ENGINEERING MECHANICS 2016

22nd INTERNATIONAL CONFERENCE

MAY 9 – 12, 2016, SVRATKA, CZECH REPUBLIC

BOOK OF FULL TEXTS

Editors: Igor Zolotarev
Vojtěch Radolf

Institute of Thermomechanics,
Academy of Sciences of the Czech Republic, v. v. i.

Institute of Theoretical and Applied Mechanics,
Academy of Sciences of the Czech Republic, v. v. i.

Institute of Solid Mechanics, Mechatronics and Biomechanics,
Faculty of Mechanical Engineering, Brno University of Technology

ŽĎAS, a.s., Žďár nad Sázavou

IFToMM Member Committee of the Czech Republic

Czech Society for Mechanics

First edition, 2016

Cover figure: Wavefronts in thick rod undergoing longitudinal impact
(J. Červ, F. Valeš - IT ASCR, V. Adámek – FAV, UWB)

ISBN 978-80-87012-59-8

ISSN 1805-8248

The Conference is hosted by the hotel ŽĎAS at Svratka

All the papers were reviewed by members of the international scientific committee.

SCIENTIFIC COMMITTEE

Chairman:

Igor Zolotarev, PhD.	**Institute of Thermomechanics AS CR, Prague, CZ**

Members:

Prof. dr. Pavol Bauer	**Delft University of Technology, NL**
Prof. Ján Benčat, PhD.	**University of Žilina, SK**
Dr. Ouadie Bennouna	**ESIGELEC, FR**
Prof. Tomáš Březina, PhD.	**Brno University of Technology, CZ**
Prof. Jiří Burša, PhD.	**Brno University of Technology, CZ**
Prof. Radim Čajka, PhD.	**VSB - Technical University of Ostrava, CZ**
Assoc. Prof. Vladimír Čech, PhD.	**OPROX, a.s., Brno, CZ**
Prof. Miloš Drdácký, DSc.	**ITAM AS CR, Prague, CZ**
Prof. Paola Forte	**University of Pisa, IT**
Assoc. Prof. Karel Frydrýšek, PhD.	**VSB - Technical University of Ostrava, CZ**
Assoc. Prof. Vladimír Fuis, PhD.	**Institute of Thermomechanics AS CR, Prague, CZ**
Prof. Ardeshir Guran, PhD.	**Institute of Structronics, Ottawa, Canada**
Prof. Ivo Herle	**TU Dresden, DE**
Jaromír Horáček, DSc.	**Institute of Thermomechanics AS CR, Prague, CZ**
Assoc.Prof. Lidia Ilieva-Mitutsova, PhD.	**Bulgarian Academy of Sciences, Sofia, BG**
Prof. Přemysl Janíček, DSc.	**Brno University of Technology, CZ**
Prof. Zbyněk Jaňour, DSc.	**Institute of Thermomechanics AS CR, Prague, CZ**
Prof. Miroslav Jícha, PhD.	**Brno University of Technology, CZ**
Prof. Milan Jirásek, DrSc.	**Czech Technical University in Prague, CZ**
Prof. Zdeněk Kala, PhD.	**Brno University of Technology, CZ**
Prof. Zbyněk Keršner, PhD.	**Brno University of Technology, CZ**
Prof. Alena Kohoutková, PhD.	**Czech Technical University in Prague, CZ**
Prof. Anne-Maria Laukkanen, PhD.	**University of Tampere, FI**
Prof. Dušan Maga, PhD.	**Czech Technical University in Prague, CZ**
Prof. Eduard Malenovský, DSc.	**Brno University of Technology, CZ**
Prof. František Maršík, DSc.	**Institute of Thermomechanics AS CR, Prague, CZ**
Prof. Arkadiusz Mężyk	**Silesian University of Technology, Gliwice, PL**
Prof. Dr. Damijan Miljavec	**University of Ljubljana, Ljubljana, SI**
Jiří Minster, DSc.	**ITAM AS CR, Prague, CZ**
Jiří Náprstek, DSc.	**ITAM AS CR, Prague, CZ**
Prof. Bořek Patzák, PhD.	**Czech Technical University in Prague, CZ**
Assoc. Prof. Michail Pavlenko	**Moscow State Mining University, RU**
Prof. Dr. Paolo Pennacchi	**Politecnico di Milano, Milan, IT**

Prof. Kazimierz Peszynski, PhD.	**Univ. of Technol. and Life Science, Bydgoszcz, PL**
Prof. Jindřich Petruška, PhD.	**Brno University of Technology, CZ**
Jiří Plešek, PhD.	**Institute of Thermomechanics AS CR, Prague, CZ**
Assoc. Prof. Stanislav Pospíšil, PhD.	**ITAM AS CR, Prague, CZ**
Prof. Jaromír Příhoda, PhD.	**Institute of Thermomechanics AS CR, Prague, CZ**
Ladislav Půst, DSc.	**Institute of Thermomechanics AS CR, Prague, CZ**
Vojtěch Radolf, PhD.	**Institute of Thermomechanics AS CR, Prague, CZ**
Prof. Ján Sládek, DSc.	**ICA, SAS, Bratislava, SK**
Prof. Vladimír Sládek, DSc.	**ICA, SAS, Bratislava, SK**
Prof. Pavel Šafařík, PhD.	**Institute of Thermomechanics AS CR, Prague, CZ**
Prof. Michal Šejnoha, DSc.	**Czech Technical University in Prague, CZ**
Prof. Alexander Tesár, DSc.	**ICA, SAS, Bratislava, SK**
Prof. Václav Tesař, PhD.	**Institute of Thermomechanics AS CR, Prague, CZ**
Prof. Tomasz Topoliński	**Univ. of Technol. and Life Science, Bydgoszcz, PL**
Prof. Michael Valášek, DrSc	**Czech Technical University in Prague, CZ**
Prof. Pavel Vlasák, DSc.	**Institute of Hydrodynamics AS CR, Prague, CZ**
Prof. Yuri Sergeevich Vorobiev	**NAS of Ukraine, Kharkov, UA**
Radek Votrubec, PhD.	**Technical University of Liberec, CZ**
Prof. Jaroslav Zapoměl, DSc.	**Institute of Thermomechanics AS CR, Prague, CZ**
Prof. Vladimír Zeman, DSc.	**University of West Bohemis in Pilsen, CZ**
Prof. Anatoly P. Zinkovskii, DSc.	**NAS of Ukraine, Kiev, UA**
Prof. Rudolf Žitný, PhD.	**Czech Technical University in Prague, CZ**
Prof. Milan Žmindák, PhD.	**University of Žilina, SK**

HONORARY COMMITTEE:

Miroslav Šabart, MSc.	**Managing Director of the ŽĎAS, Inc.**
František Mládek	**Mayor of Svratka**

List of sections:

BIO	**Biomechanics**	**KIN**	**Kinematics**
DYN	**Dynamics**	**MIN**	**Mini-symposium WAVES**
FLU	**Fluid Mechanics**	**MTC**	**Mechatronics**
FRA	**Fracture Mechanics**	**REL**	**Reliability**
HIS	**Historical structures**	**SOL**	**Mechanics of Solids**
KEY	**Keynote Lectures**	**TER**	**Thermodynamics**

Table of Contents

KEYNOTE LECTURE

PAPERS

KEYNOTE LECTURE

22nd International Conference
ENGINEERING MECHANICS 2016
Svratka, Czech Republic, 9 – 12 May 2016

MULTI-LEVEL CABLE MECHANISMS WITH ADDED ACTIVE STRUCTURES

Z. Šika[*], P. Svatoš[*], P. Beneš[*], J. Dupal[**], M. Hajžman[**]

Abstract: *The multi-level mechanisms including superimposed active structures can significantly improve the positioning accuracy and operational speed of the end-effectors with respect to pure cable-driven parallel mechanisms. The objective of the paper is description of the current state of the ongoing research project concerning complex research of active structures superimposed to cable-driven mechanisms. Different possible architectures of active structures have been investigated by simulation as well as by preliminary experiments on primary demonstrator. The complex simulation model has been prepared using identified dynamical models.*

Keywords: Multi-level mechanism, superimposed active structure, parallel mechanism, cable-driven mechanism, hierarchical motion control.

1. Introduction

Parallel kinematic mechanisms (PKM) proved their supremacy over serial structures in many mechanical parameters including dynamics and stiffness. On the other hand the ratio between the effective workspace and installation space is usually worse. The cable-driven variants of the PKM have the further advantages, namely the light-weight, large range of motion, possibility of anti-backlash property (Valášek & Karásek, 2009) and easy reconfiguration. Their application area ranges from the cargo handling (Patel & George, 2012) and astronomic applications (Zi, et al., 2011), (Meunier, et al., 2009) to humanoid-arm manipulators (Chen, et al., 2013) and snakelike manipulators (Taherifar, et al., 2013). The typical disadvantages of the cable-driven PKM are the relatively narrow frequency bandwidth of their feedback motion control and the problems with the accurate positioning of the end-effector. In (Merlet, 2015) it is stated that the over-constrained 6 DOF cable-driven parallel manipulator is always in configuration where at most 6 cables are under tension. The reason is that the cable coiling mechanism is SISO system and therefore it is not possible to control both cable length and tension simultaneously and hence the redundant cables become slack. The second reason should be that discrete time controllers are not capable to ensure the precise cable length with all cables under tension at all time (Merlet, 2014). However the results of our experiments show, that this opinion is problematic. The promising research direction for solution of weaknesses of cable-driven mechanisms comes from the concept of multi-level mechanisms with the hierarchical structure composed from the parallel cable-driven mechanism for large and slow motions and the active structure for the small and high frequency motions (Duan, et al., 2011).

Consequently the ongoing research project „Multi-Level Light Mechanisms with Active Structures“ has the following objectives: 1) To investigate possible architectures of the active structures superimposed to the end-effectors of cable-driven parallel mechanisms. 2) To investigate influence of vibrational phenomenas of the cable manipulated end-effector to the control strategies and their stability. 3) To investigate different possible strategies of the control of active structures in order to improve end-effector positioning accuracy. Some topics of the first year of project solution are described within the presented paper.

[*] prof. Ing. Zbyněk Šika, Ph.D., Ing. Petr Svatoš, Ing. Petr Beneš, Ph.D. : Czech Technical University in Prague, Faculty of Mechanical Engineering, Technická 4, CZ-16607 Praha 6, Zbynek.Sika@fs.cvut.cz, Petr.Benes@fs.cvut.cz.

[**] prof. Dr. Ing. Jan Dupal, Ing. Michal Hajžman, Ph.D.: University of West Bohemia in Pilsen, Faculty of Applied Sciences, Univerzitní 8, CZ-30614 Plzeň, dupal@kme.zcu.cz, Mhajzman@kme.zcu.cz.

2. Variants of active structures superimposed to end-effectors of cable-driven mechanisms

The important part of the research is the investigation of possible types of multi-level mechanisms. The recently developed cable-driven parallel mechanisms with high tilting capability are the main light structures taken into consideration. The cable-driven parallel manipulators can be classified with respect to different characteristics, namely the number of DOF (spatial, spherical, planar), the mounting of cables (cables) with respect to gravity (suspended, general) and some others (Beneš, et al., 2015). As the range of the active structure motion is small, the kinematic analysis in terms of the reachable workspace, the dexterity and possible collisions within the workspace is focused especially on the cable-driven part of mechanism. The main limitation that must be respected is that cables are either under tension or slack. We cannot exert the pushing force by cables. The total stiffness of the system is influenced by the type of applied control. The mixed position-tension control enables the tension in redundant number of cables in spite of statements in (Merlet, 2014) and (Merlet, 2015). The most general variant of the cable-driven and consequently the multi-level mechanisms is the system with 6 DOF positioned platform (Svatoš, et al., 2015). The typical example with 6 DOFs and 8 driven cables is in Fig. 1. This structure was the target of optimization. Besides the 6 DOF cable-driven structures, also the newly rebuilt 3 DOF cable-driven tilting mechanisms (Fig. 2.) developed within the project „Tilting Mechanisms Based on Cable Parallel Kinematical Structure with Antibacklash Control" (Procházka, et al., 2016), (Skopec, et al., 2015) are considered as the base for the multi-level mechanisms. The current project follows the results of the previous project in order to widening the servo control bandwidth and consequently to improve feedback position control of cable-driven mechanisms by the superimposed active structures.

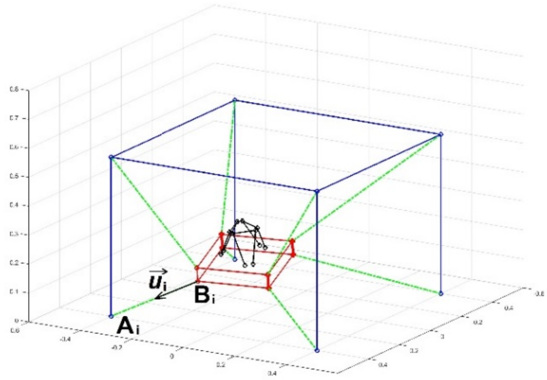

Fig. 1: Over-constrained multi-level mechanism with 6 DOF.

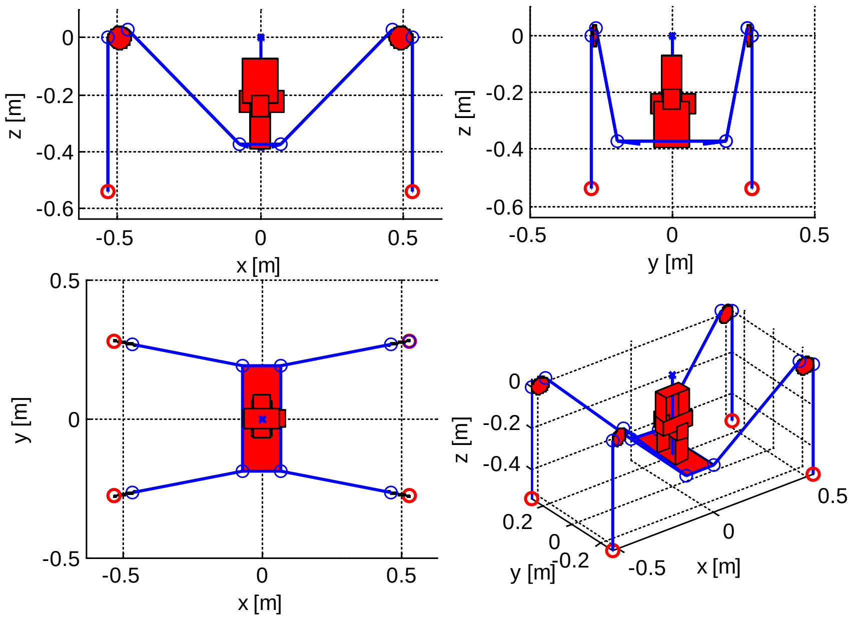

Fig. 2: Cable-driven tilting mechanism QuadroSphere with 3 DOF and angular position measurements.

The dynamical properties of the different concepts of attached active structures have been investigated not only by simulation and mathematical modelling, but also using the primary experiments

(Svatoš, et al., 2015). The demonstrator with the cable driven tilting platform has been reassembled and the piezoactuators available from the earlier times have been used for the setup of active platform (Fig. 3). The cubic architecture of 6 piezoactuators has been used. The parameters of the piezoactuators (stiffness, lengthening range, frequency range, etc.) used for these preliminary experiments are certainly given and their optimality in tested mechanism isn't guaranteed. The final specification (type and parameters) of appropriate actuators will be the result of ongoing optimization with complex model during the second project year.

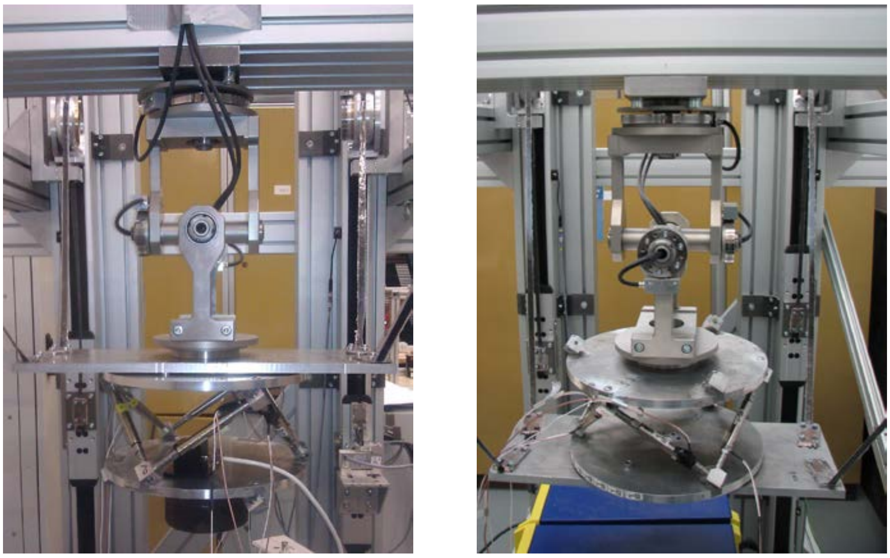

a) external placement of active structure *b) internal placement of active structure*

Fig. 3: Two tested variants of active structure placement in stand with cable mechanism.

The external variant in Fig. 3 a) according to concept in Fig. 2 a) has the active structure outside the main kinematic loops created by cables and positioned tilting platform. The cubic architecture piezohexapod has been assembled below the cable-positioned platform. The principle of acting in this configuration is in fact the 6 DOF active vibration absorber. The response level and the eigenfrequencies of the system can be influenced by the mass added to the lower desk of active absorber (the results are for 4 kg). The system was excited by the chirp signal 10÷140 V with the frequency up to 100 Hz and time length 60 s that was applied to particular piezoactuators P1-P6. The position of tilting platform was measured by three incremental revolute sensors (Fig. 4). The results for excitation by piezoactuator P4 are in Fig. 5 a).

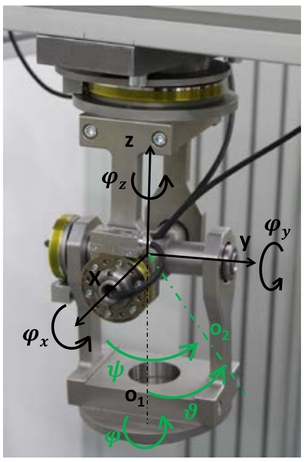

Fig. 4: Revolute incremental sensors and corresponding coordinates

The internal variant in Fig. 3 b) according to concept in Fig. 2 b) has the active structure inside the main kinematic loops created by cables and positioned tilting platform. The same type of excitations by particular piezoactuators P1-P6 have been applied. The results for excitation by piezoactuator P4 are in

Fig. 5 b). The experiments prove that the internal active structure inside the mechanism kinematical loops has significantly higher influence in the low frequency range (Svatoš, et al., 2015), nevertheless both variants are further investigated. The early experimental identification of the system variants is useful despite the fact, that the currently used piezoactuators are available from the earlier times and haven't been optimized for the given platform. Besides this the measured network of transfer functions for both variants has been the input for the state space model identification (Fig. 7) and is currently used for the control law synthesis.

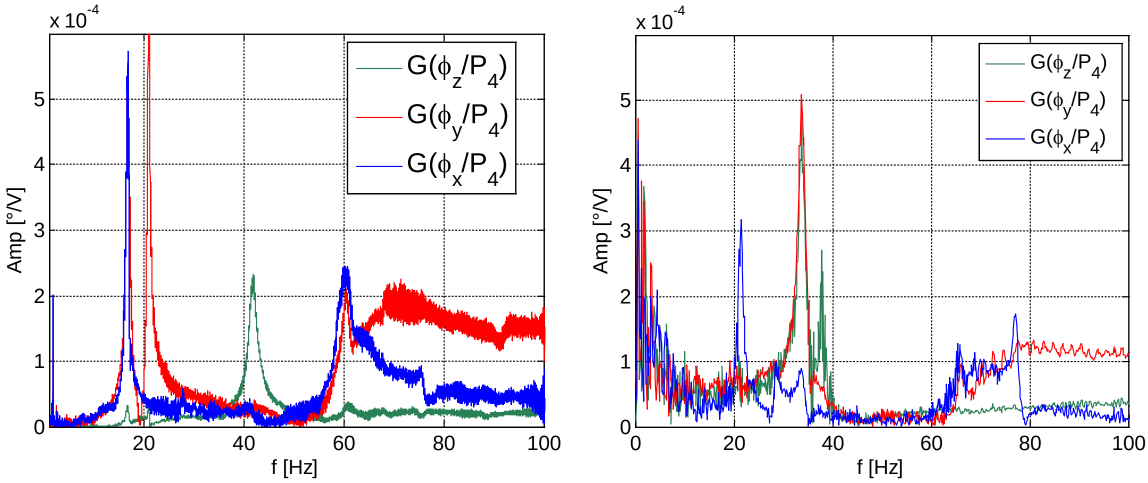

a) external placement of active structure *b) internal placement of active structure*

*Fig. 5: Measured transfer functions from piezoactuator **P4** to platform position sensors.*

3. Investigation of nonlinear dynamic behaviour of cables for manipulation of end-effector and superimposed active structure

During the first year of the project solution, different approaches to cable modelling were studied and compared. The main viewpoint of the models is their robustness and capability to be suitable for further usage, particularly for the mechanism control.

The first approach used is based on a continuous model of a cable described by following governing equation

$$\rho \frac{d^2 \boldsymbol{r}(s,t)}{dt^2} = \frac{\partial}{\partial s}[EA\varepsilon(s,t)\boldsymbol{b}(s,t)] + \boldsymbol{a}(s,t) \tag{1}$$

This equation is spatially discretized by difference method in absolute coordinate system. Used symbols have following significance ρ is linear density, E is Young's modulus, A is cross-sectional area of the cable, $\boldsymbol{b}(s,t)$ is unit tangent vector to the cable curve at point given by length coordinate s, $\boldsymbol{a}(s,t)$ is external force acting per unit length, $\varepsilon(s,t)$ is axial strain in cable, $\boldsymbol{r}(s,t)$ is position vector of an arbitrary point P at cable given by s. The range of the model (in sense of number of degrees of freedom) depends on the number of considered discretization points. This approach showed very numerically unstable behaviour and has been neglected for further considerations.

The second approach is based on variations of total energy of the system and uses Galerkin's a collocation methods with 6-th degree polynomial approximation for cable displacement. In both cases their application leads to the system of strongly nonlinear algebraic equations whose solution has to be submitted to various rearrangements to achieve numerical convergence of applied methods. Numerical implementation of the mathematical model and developed methodology was performed in computational system MATLAB. Following basic case studies have been solved and debugged.

1) Static equilibrium determination of individual cables. In spite of existence of chainsaw analytical solution taking into account a dynamic solution in future two approximate numerical methods were developed. Their outputs are in very good agreement with analytical solution.

2) Static equilibrium determination of end effector – EF (considered as a mass point) and adjoining cables by means of presented methods in 2D space. Here, the 6-th degree polynomial approximation for cable displacement was used.

3) Dynamic behaviour investigation of EF and adjoining cables by means of presented methods in 2D space. The 6-th degree polynomial approximation for cable dynamic displacement was used again. It is supposed that motion of pulleys with deployed cables is prescribed. The application of approximating function leads to the system of nonlinear ordinary differential equations whose solution corresponds to time functions for dynamic displacement approximations individual of cables end EF motion (Dupal & Byrtus, 2015).

The first analysis of the dynamic interactions between the cable-driven mechanism and the selected variant of the active structures has been done using this second type of cable model, the experimental identification of the second (internal) variant of the active structure placement, and the setup of first complex dynamical model (Fig. 3 a), Fig. 5 a)) (Svatoš, et al., 2015).

The third approach of modelling is based on so called Absolute Nodal Coordinate Formulation (ANSF) which allows to consider detailed interaction of a cable and a pulley (Fig. 6) including its nonlinear dynamic behaviour (Hajžman, et al., 2015). Global position $\boldsymbol{r} = [r_x, r_y]^T$r $= [\mathrm{r_x}, \mathrm{r_y}]^{\mathrm{T}}$ of and arbitrary beam point determined by parameter p can be written as

$$\boldsymbol{r}(p) = \boldsymbol{S}(p)\boldsymbol{e}, \quad \boldsymbol{e} = [e_1, e_2, \dots e_8]^T, \tag{2}$$

where $\boldsymbol{S}$ is a global shape function matrix, $\boldsymbol{e}$ is a vector of element nodal coordinates and $p \in (\,0, l\,)$ is a parameter of a curve. The complete model of a cable-pulley system based on the ANCF planar beam element is of the form

$$\boldsymbol{M}\ddot{\boldsymbol{q}} + \boldsymbol{B}(\dot{\boldsymbol{q}}, \boldsymbol{q})\dot{\boldsymbol{q}} + \boldsymbol{K}(\boldsymbol{q})\boldsymbol{q} = \boldsymbol{Q}_k, \tag{3}$$

where $\boldsymbol{q}$ is the vector of all elastic coordinates of the cable. This model can be combined with the models of other flexible or rigid bodies and with model of kinematic joints using a standard ways.

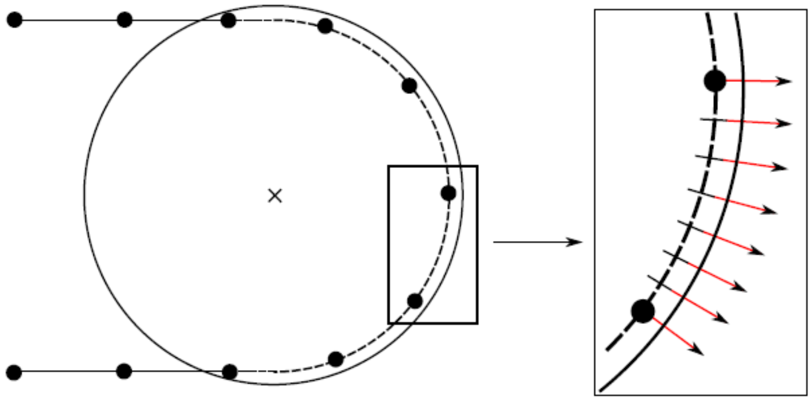

Fig. 6: Interaction of a cable and a pulley

The ANCF approach can employ cable-pulley interaction in the sense of circumferential contact forces between cable and pulley. The contact can be described i.e. by Hertz contact model. The behaviour of the cable-pulley system was modeled also using standard multibody simulation tool Alaska, where different models of velocity dependent stiffness and damping of the cable were investigated. Simultaneously, the stiffness and damping coefficients were analyzed based on records of experimental measurement and simulation results (Polach & Hajžman, 2015).

4. Development of complex dynamical models of multi-level mechanism

The models of multi-level mechanisms corresponding to the experimental demonstrator in external as well as internal variants (Fig. 3 a), Fig. 3 b)) have been used as the first modelling targets. Active structure with six piezoactuators is integrated between or on the top of the end-effector platform suspended and moved by four cables. The piezoactuators are mounted in the cubic configuration. The physical modelling have been combined with the experimental identification. Especially the experimentally identified transfer functions from the piezoactuators **P1-P6** to the platform position sensors (Fig. 4) are of special interest because of their importance for the platform controllability by piezoactuators or other added micro-actuators. The core project idea is the collaborative control of platform motion. The experimental identification has been successful as demonstrated by the example in

Fig. 7. The presented result corresponds to the external variant (Fig. 3 a)) and the response of incremental sensor ϕ_x (Fig. 4) for the chirp input excitation from the piezoactuator **P3**.The developed models are devoted to the optimization and control synthesis usage. The concept of a complex simulation dynamical model has been fixed during the first year of the project solution. The model integrates cable-driven mechanism and active structures, taken into account the advanced models of cables. The research consists in finding proper and suitable approach integrating the above mentioned parts from the model complexity point of view. The complexity of the model determines its usability especially from the computational time point of view and its potential employment in real-time simulations.

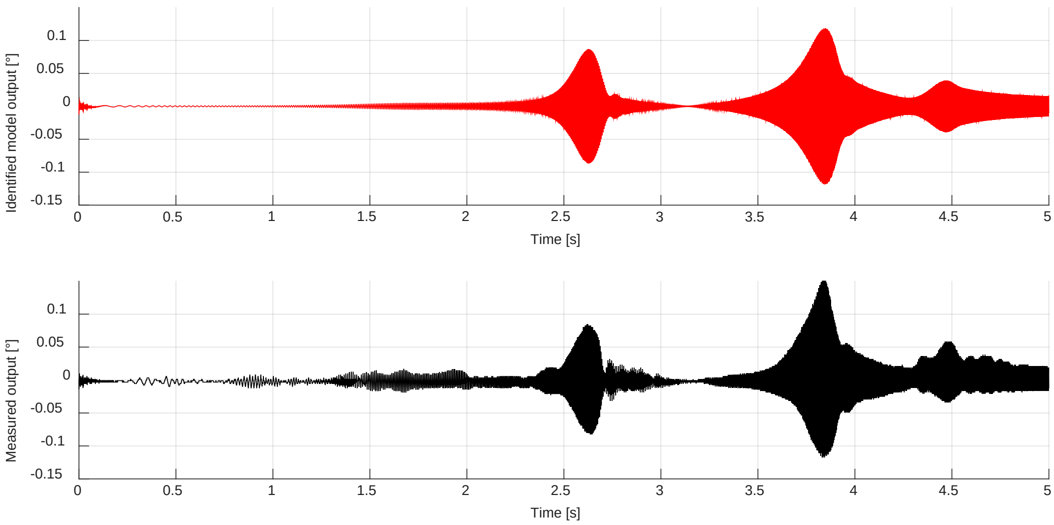

*Fig. 7: Comparison of experimental and model response of multi-level platform (piezo **P3** to ϕ_x sensor)*

5. Conclusions

The target of this paper was to present some results of the first year of solution of Czech Science Foundation research project „Multi-Level Light Mechanisms with Active Structures". Firstly the variants of active structures superimposed to end-effectors of different cable-driven mechanisms have been analyzed by simulation. The planar, spherical as well as fully spatial variants have been taken into account. The most general variant of spatial cable-driven mechanisms has been optimized for 6 DOF and 8 driven cables. The demonstrator of 3 DOF cable-driven tilting mechanism has been newly rebuilt and considered as the base for the tilting variant of multi-level mechanisms. The piezoactuators available from the earlier times have been used for the setup of preliminary active platform. The cubic architecture with 6 piezoactuators has been reassembled and included to the system. The internal as well as external (from the point of view of kinematical loops) placement of the piezo-platform has been tested. The experiments prove that the internal active structure inside the mechanism kinematical loops has significantly higher influence in the low frequency range, nevertheless both variants are further investigated. The measured network of transfer functions from piezoactuators to revolute incremental sensors has been used for the successful state space model identification. The second important topic has been the investigation of several variants of modelling of nonlinear dynamic behaviour of cables. Three main variants of modelling have been tested. The first approach is based on a continuous model of a cable spatially discretized by difference method in absolute coordinate system. This approach showed very numerically unstable behaviour and has been neglected for further considerations. The second approach is based on variations of total energy of the system and uses Galerkin's a collocation methods with 6-th degree polynomial approximation for cable displacement. The third approach of modelling is based on so called Absolute Nodal Coordinate Formulation which allows to consider detailed interaction of a cable and a pulley including its nonlinear dynamic behaviour. The problem of third formulation is very high computational complexity. The most promising seems to be the second variant of formulation. The further steps of the project will be finalization of complex simulation models and consequently the investigation of different possible strategies of the control of active structures superimposed to the end-effector of cable-driven mechanism in order to improve end-effector positioning accuracy and operational speed.

Acknowledgement

The authors appreciate the kind support by the grant GA15-20134S “**Multi-Level Light Mechanisms with Active Structures**” of the Czech Science Foundation.

References

Beneš, P. et al., 2015. Kinematic analysis of possible concepts of multi-level mechanisms combining active structures and cable-driven mechanisms. *Proc. of 31-th conference with international participation Computational Mechanics 2015, November 9 - 11, Špičák.*

Duan, X. et al., 2011. *Real-time motion planning for the macro-micro parallel manipulator system.* Shanghai: s.n.

Dupal, J. & Byrtus, M., 2015. Methodology of behaviour simulation of cable-driven manipulators with varying cable lengths. *Proc. of 31-th conference with international participation Computational Mechanics 2015, November 9 - 11, Špičák .*

Hajžman, M., Bulín, R. & Polach, P., 2015. Nonlinear analysis of the cable-pulley interaction. *Proc. of ECCOMAS Thematic Conference on Multibody Dynamics 2015, June 29 - July 2, Barcelona,* pp. 554-564.

Chen, Q., Chen, W., Yang, G. & Liu, R., 2013. An Integrated Two-Level Self-Calibration Method for a Cable-Driven Humanoid Arm. *IEEE Transactions on Automation Science and Engineering*, Volume 10 No.2, pp. 380-391.

Merlet, J., 2014. Checking the cable configuration of cable-driven parallel robots on a trajectory. *IEEE Internatiopnal Conference on Robotics & Automation (ICRA),* pp. 1586-1591.

Merlet, J., 2015. On the Redundancy of Cable-Driven Parallel Robots. *New Trends in Mechanism and Machine Science*, Volume 24, pp. 31-39.

Meunier, G., Boulet, B. & Nahon, M., 2009. Control of an Overactuated Cable-Driven Parallel Mechanism for a Radio Telescope Application. *IEEE Transactions on Control Systems Technology*, Volume 17 No. 5, pp. 1043-1054.

Patel, Y. & George, P., 2012. Parallel Manipulators Applications—A Survey. *Modern Mechanical Engineering*, Volume 2, pp. 57-64.

Polach, P. & Hajžman, M., 2015. Influence of the fibre spirng-damping model in simple laboratory mechanical system on the coincidence with the experimental measurement results. *Proc. of ECCOMAS Thematic Conference on Multibody Dynamics 2015, June 29 - July 2, Barcelona,* pp. 356-365.

Procházka, F., Valášek, M. & Šika, Z., 2016. Robust sliding mode control of redundantly actuated parallel mechanisms with respect to geometric imperfections. *Multibody System Dynamics*, March, 36(3), pp. 221-236.

Skopec, T., Šika, Z. & Valášek, M., 2015. Calibration using adaptive model complexity for parallel and fiber-driven mechanisms. *Robotica*, Published online: 10 July 2015, http://dx.doi.org/10.1017/S0263574715000429, pp. 1-20.

Svatoš, P. et al., 2015. Cable Driven Mechanisms with Added Piezo Active Platform. *Bulletin of Applied Mechanics*, 11(38), pp. 19-24.

Taherifar, A., Salarieh, H. & Alasty, A., 2013. Kinematic control of a new hyper-redundant manipulator with lockable joints. *Scienta Iranica B*, Volume 20(6), pp. 1742-1752.

Valášek, M. & Karásek, M., 2009. Kinematical Analysis of HexaSphere. *Conference Proceedings of Engineering Mechanics*, p. 1371–1378.

Zi, B., Zhu, Z. & Du, J., 2011. Analysis and control of the cable-supporting system including actuator dynamics. *Control EngineeringPractice*, Volume 19, pp. 491-501.

PAPERS

22nd International Conference
ENGINEERING MECHANICS 2016
Svratka, Czech Republic, 9 – 12 May 2016

TRANSIENT RESPONSE OF LAYERED ORTHOTROPIC STRIP TO TRANSVERSE LOAD

V. Adámek*, F. Valeš, J. Červ*****

Abstract: *This work concerns the transient response of an infinite two-layered strip subjected to a transverse load of impact character. The material of each layer is assumed to be specially orthotropic, i.e. the material and geometric axes coincide. Moreover, the material is modelled as linear viscoelastic using the model of standard linear viscoelastic solid such that the damping behaviour of the strip for long wavelengths and long times can be addressed. The non-stationary wave phenomena in the strip are studied using analytical approach. The system of equations of motion for the case of 2D plane-stress problem is solved using the classical method of integral transform. Once the formulas for the Laplace transforms of fundamental mechanical quantities are derived, the numerical inverse Laplace transform is used to obtain the response in time domain for a strip with free-fixed boundaries. The results for a strip composed of two orthotropic layers of specific material properties are presented in this work. Finally, this solution is confronted with the results of numerical simulations reached by a professional FE code.*

Keywords: Wave propagation, Layered strip, Orthotropic material, Viscoelastic material, Analytical solution.

1. Introduction

Propagation of stationary and transient stress waves through layered structures is the subject of intensive interest for many years. This interest is related to the application of layered materials as vibration isolators and impact absorbers. Most of existing works concerning the optimal design of layered structures is based on numerical approaches but several papers making the use of analytical methods exist, e.g. Luo et al. (2009) or Velo & Gazonas (2003). Analytical and semi-analytical approaches enable deeper insight into the problem and more efficient design process in such cases.

This work deals with the transient wave problem of an infinite viscoelastic strip composed of two orthotropic layers. The analytical solution of the problem with free-fixed boundaries is derived by means of classical method of integral transforms. Fourier and Laplace transforms are applied in spatial and time domains, respectively. This paper follows our previous works Adámek & Valeš (2015) and Adámek et al. (2015) in which the solutions for a single-layer strip problem and for a two-layered strip with free-free boundaries are presented.

2. Problem formulation

The scheme of the problem solved is depicted in Fig. 1. We will assume an infinite strip composed of two layers of the same thickness *d* and of special orthotropic properties such that the material and geometric axes coincide. Each layer will be identified by the index *n*, the index $n = 1$ corresponds to the lower layer, while $n = 2$ denotes the upper layer. Further, the material of both layers will be assumed to be linear viscoelastic and the model of standard orthotropic viscoelastic solid will be used for its representation (see Sobotka, 1984).

* Ing. Vítězslav Adámek, Ph.D.: NTIS – New Technologies for the Information Society, University of West Bohemia; Univerzitní 8; 306 14, Pilsen; CZ, vadamek@kme.zcu.cz

** Ing. František Valeš, CSc.: Institute of Thermomechanics AS CR, v.v.i.; Veleslavínova 11; 301 14, Pilsen; CZ, vales@it.cas.cz

*** Assoc. Prof. Jan Červ, CSc.: Institute of Thermomechanics AS CR, v.v.i.; Dolejškova 1402/5; 182 00, Prague 8; CZ, cerv@it.cas.cz

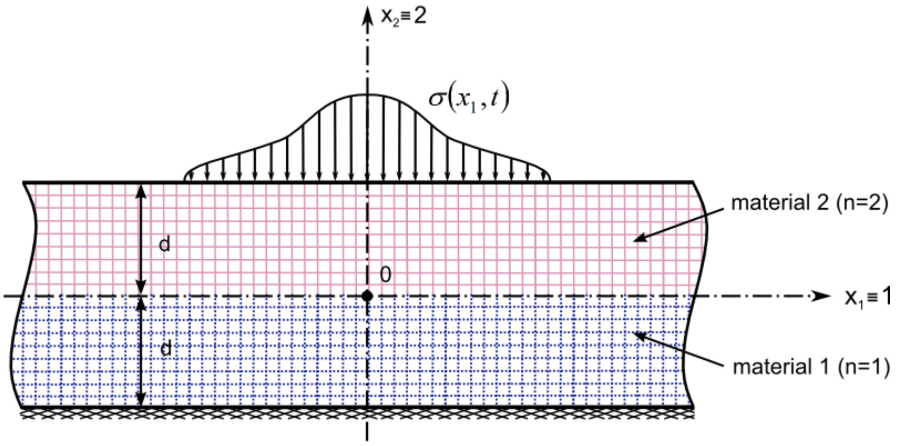

Fig. 1: The scheme of the problem solved.

The boundary and initial conditions of the problem can be specified as follows: (i) the upper edge of the strip is loaded in vertical direction by pressure/tension described by a function even in horizontal coordinate; (ii) the lower edge of the strip is fixed, i.e. zero vertical and horizontal displacements are prescribed; (iii) zero initial conditions for displacement components and their time derivatives will be assumed. Given the above, the problem will be solved as a plane stress problem in the coordinate system x_1-x_2 which is advantageously chosen in such a way that both axes represent the axes of problem symmetry. It means that the axis x_1 coincides with the layer interface (see Fig. 1).

3. Governing equations and analytical solution

In fact, the motion of waves in each layer is described by the same equations used in the paper Adámek et al. (2015). Then $u_{1,n}$ (x_1, x_2, t) and $u_{2,n}$ (x_1, x_2, t) for n = 1, 2 are the functions of displacement components which we are looking for. Applying the Laplace transform in time domain, taking into account the zero initial conditions and introducing the complex functions $\bar{u}_{1,n} = \bar{u}_{1,n}(x_1, x_2, p)$ and $\bar{u}_{2,n} = \bar{u}_{2,n}(x_1, x_2, p)$ as the Laplace transforms of $u_{1,n}$ and $u_{2,n}$ ($p \in$ C), the transformed equations of motion can be written as

$$p^2\bar{u}_{1,n} = C_{11,n}^2\left(\frac{\partial^2\bar{u}_{1,n}}{\partial x_1^2} + \nu_{21,n}\frac{\partial^2\bar{u}_{2,n}}{\partial x_1\partial x_2}\right) + C_{12,n}^2\left(\frac{\partial^2\bar{u}_{1,n}}{\partial x_2^2} + \frac{\partial^2\bar{u}_{2,n}}{\partial x_1\partial x_2}\right), \tag{1}$$

$$p^2\bar{u}_{2,n} = C_{22,n}^2\left(\frac{\partial^2\bar{u}_{2,n}}{\partial x_2^2} + \nu_{12,n}\frac{\partial^2\bar{u}_{1,n}}{\partial x_1\partial x_2}\right) + C_{12,n}^2\left(\frac{\partial^2\bar{u}_{2,n}}{\partial x_1^2} + \frac{\partial^2\bar{u}_{1,n}}{\partial x_1\partial x_2}\right), \tag{2}$$

where the constants $\nu_{12,n}$ and $\nu_{21,n}$ denote the Poisson ratios of orthotropic material corresponding to the nth layer. For simplicity, the appropriate Poisson ratios of viscous and elastic elements in the material model are assumed to be equal. The complex functions $C_{11,n}(p)$, $C_{12,n}(p)$ and $C_{22,n}(p)$ present in (1)-(2) reflect the elastic and viscous properties of the material of each layer and are expressed by standard material parameters analogously as in Adámek et al. (2015).

Due to the symmetry of the problem with respect to the axis x_2, it is clear that the solution of the coupled system (1)-(2) can be found in the form of the following Fourier integrals:

$$\bar{u}_{1,n} = \frac{1}{\pi}\int_0^\infty A(\omega, x_2, p)\sin(\omega x_1)\,d\omega \quad \text{and} \quad \bar{u}_{2,n} = \frac{1}{\pi}\int_0^\infty B(\omega, x_2, p)\cos(\omega x_1)\,d\omega. \tag{3}$$

Introducing the expected solutions (3) into the system (1)-(2) and after some algebra, one obtains a system of two PDEs for the unknown Fourier spectra $A(\omega, x_2, p)$ and $B(\omega, x_2, p)$. The solution of such a system can be expressed in a general form

$$A(\omega, x_2, p) = P_n\,\mathrm{sh}(\Lambda_{1,n}x_2) + Q_n\,\mathrm{ch}(\Lambda_{1,n}x_2) + R_n\,\mathrm{sh}(\Lambda_{2,n}x_2) + S_n\,\mathrm{ch}(\Lambda_{2,n}x_2), \tag{4}$$

$$B(\omega, x_2, p) = L_{1,n}\big(P_n\,\mathrm{ch}(\Lambda_{1,n}x_2) + Q_n\,\mathrm{sh}(\Lambda_{1,n}x_2)\big) + L_{2,n}\big(R_n\,\mathrm{ch}(\Lambda_{2,n}x_2) + S_n\,\mathrm{sh}(\Lambda_{2,n}x_2)\big), \tag{5}$$

in which sh and ch stand for the hyperbolic functions sinh and cosh, respectively. The symbols $\Lambda_{1,n}$ and $\Lambda_{2,n}$ represent the roots of the characteristic biquadratic equation associated with the mentioned system of PDEs and they are dependent on the frequency ω and on p. The other quantities $L_{1,n}$ and $L_{2,n}$ depend on $\Lambda_{1,n}$ and $\Lambda_{2,n}$ and their definition can be deduced from the relations presented in Adámek et al. (2015).

At this moment, the Fourier spectra (4)-(5) are expressed in terms of eight unknown functions $P_n(\omega, p)$, $Q_n(\omega, p)$, $R_n(\omega, p)$ and $S_n(\omega, p)$ for $n = 1, 2$. These functions can be determined by using the boundary conditions of the problem. Based on the problem formulation made above, the boundary conditions can be formulated as follows:

$$\begin{gathered}\sigma_{22,2}(x_1,d,t)=\sigma(x_1,t), \quad \sigma_{12,2}(x_1,d,t)=0, \quad \sigma_{22,1}(x_1,0,t)=\sigma_{22,2}(x_1,0,t),\\ \sigma_{12,1}(x_1,0,t)=\sigma_{12,2}(x_1,0,t), \quad u_{1,1}(x_1,0,t)=u_{1,2}(x_1,0,t), \quad u_{2,1}(x_1,0,t)=u_{2,2}(x_1,0,t),\\ u_{1,1}(x_1,-d,t)=0, \quad u_{2,1}(x_1,-d,t)=0.\end{gathered} \tag{6}$$

Using the conditions (6) and the constitutive relations for appropriate stress components, a system of eight equations is obtained for P_n, Q_n, R_n and S_n. The analytical or numerical solution of this system can be found. Due to some overflow problems during the numerical computations performed in double precision in Matlab environment, the exact solution in a closed form was derived using the symbolic system Maple in this work. Substituting this solution into (4)-(5) and subsequently into relations (3), the resulting formulas for the Laplace transforms of displacement components are obtained. On the basis of these results, the Laplace transforms of other mechanical quantities, such as velocity or stress components, can be derived.

In the last step of the solving procedure, the inverse Laplace transform back to time domain needs to be performed. Based on the complexity of the resulting formulas and on the experiences gained by authors in their previous works (e.g. Adámek & Valeš, 2012), numerical approach to the inversion was chosen. In particular, an algorithm based on the combination of FFT and Wynn's epsilon accelerator was used. For details about this method see e.g. Cohen (2007).

4. Results and discussion

The evaluation of derived solution was made for a strip the material properties of which were estimated based on the parameters for composite lamina found in Soden et al. (1998). Concretely, following material parameters have been used: the material density ρ = 2250 kg m^{-3}; the Young moduli, shear modulus and the Poisson ratio of the alone-standing elastic element in the material model, see Sobotka (1984), $E_{0,1} = 35\cdot10^9$ Pa, $E_{0,2} = 11.584\cdot10^9$ Pa, $G_{0,12} = 4\cdot10^9$ Pa, $\nu_{0,12} = 0.278$; the Young modulus and the shear modulus of the second elastic element in the material model $E_1 = 18.48\cdot10^9$ Pa, $G_{12} = 1.83\cdot10^9$ Pa and the coefficients of normal and shear viscosities $\lambda_1 = \eta_{12} = 5\cdot10^4$ Pa s^{-1}. These parameters have been used in such a way to model a material with fibers oriented horizontally in the bottom layer of the strip ($n = 1$) and vertically in the upper layer ($n = 2$). The height of each layer was chosen as d = 20 mm. Finally, the function representing the external load applied to the upper strip edge (see Fig. 1) was assumed to be non-zero only for $x_1 \in \langle -h, h\rangle$ and had the form $\sigma(x_1,t) = -\sigma_a \cos(\pi/2\cdot x_1/h)\,\mathrm{H}(t)$, where σ_a = 1 MPa, h = 2 mm and H(t) denotes the Heaviside function.

Fig. 2 shows a sample of results reached by the evaluation of the formulas derived (thick lines). The time histories of horizontal and vertical velocity components at two selected points (x_1 = 6, 10 mm) lying at the interface of the layers ($x_2 = 0$) are presented for $t \in \langle 0, 50\rangle$ μs. To validate the procedure of analytical solution derivation and its evaluation, these results were compared to those obtained by FE simulation (thin dashed lines in Fig. 2). The simulation was performed in the professional FE code MSC.Marc/Mentat using linear isoparametric 4-node elements of basic size 0.4 × 0.4 mm. The Newmark algorithm with time step $2\cdot10^{-8}$ s was used for the integration in time domain. It is obvious from this comparison that a good agreement between both types of results was achieved and that the finite element model needs to be improved to reduce the oscillations of the time courses of velocity components for short times. This can be expected since relatively coarse mesh has been used to capture the waves of high frequencies. Additionally, it is clear from Fig. 2 that the major part of transient phenomena subsides in short times which is related to the material and geometric properties of the strip.

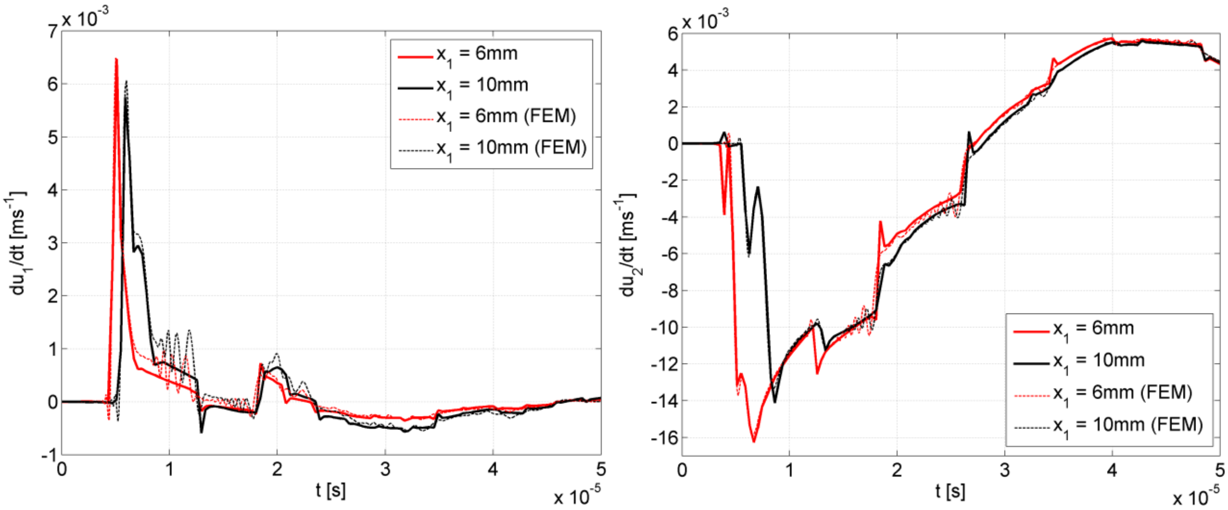

Fig. 2: Comparison of analytical (thick lines) and numerical (thin dashed lines) results for $x_2 = 0$ mm and for different values of x_1: (a) the horizontal velocity du_1/dt, (b) the vertical velocity du_2/dt.

5. Conclusions

This work presents the analytical solution for transient wave problem of an infinite viscoelastic strip composed of two specially orthotropic layers. Results for specific transversal load and free-fixed boundaries are obtained. Given the relatively general description of the strip material properties, this solution can be used for studying wave phenomena in strongly heterogeneous two-dimensional strips made of elastic, viscoelastic, isotropic or orthotropic layers. The advantage of this solution consists in the fact that it can be used not only for studying plane wave propagation through a layered structure as in most of existing works but also waves generated by a local load of impact character can be investigated. This can be utilised by the process of finding the optimal design of layered materials used for impact absorbers.

Acknowledgement

This publication was supported by the project LO1506 of the Czech Ministry of Education, Youth and Sports and by the project GA CR P101/12/2315.

References

Adámek V. & Valeš F. (2012) Analytical solution of transient in-plane vibration of a thin viscoelastic disc and its multi-precision evaluation. Mathematics and Computers in Simulation, 85, pp.34–44.

Adámek, V. & Valeš, F. (2015) Analytical solution for transient waves in layered orthotropic viscoelastic strip, in: Proc. Computational Mechanics 2015, University of West Bohemia, Pilsen, pp.1-2.

Adámek, V., Valeš, F. & Červ, J. (2015) Problem of non-stationary waves in viscoelastic orthotropic strip solved using analytical method, in: Proc. 5th ECCOMAS Thematic Conference on Computational Methods in Structural Dynamics and Earthquake Engineering (M. Papadrakakis & V. Papadopoulos eds), National Technical University of Athens, Athens, pp.1995-2003.

Cohen, A.M. (2007) Numerical Methods for Laplace Transform Inversion. Springer, New York.

Luo, X., Aref, A.J. & Dargush, G.F. (2009) Analysis and optimal design of layered structures subjected to impulsive loading. Computers and Structures, 87, pp.543-551.

Sobotka, Z. (1984) Rheology of Materials and Engineering Structures. Elsevier, Amsterdam.

Soden, P.D., Hintonb, M.J. & Kaddoura, A.S. (1998) Lamina properties, lay-up configurations and loading conditions for a range of fibre-reinforced composite laminates. Composites Science and Technology, 58, pp.1011–1022.

Velo, A.P. & Gazonas, G.A. (2003) Optimal design of a two-layered elastic strip subjected to transient loading. International Journal of Solids and Structures, 40, pp.6417-6428.

22nd International Conference
ENGINEERING MECHANICS 2016
Svratka, Czech Republic, 9 – 12 May 2016

COMPARISON OF THE MECHANICAL PROPERTIES OF THE STEEL GUIDES CARDIOLOG

M. Andryszczyk[*], A. Andrzejewska[**], T. Topoliński[***]

Abstract: *This article demonstrates results of the tests of mechanical properties of steel guidewires used in cardiac surgical procedures. The established research methodology embracing specimen geometry and simulated operating environment allowed determining the maximum strength of a guidewire during surgeries. The results of the tests were subjected to statistical analysis, on the basis of which the differences in mechanical strength of material were determined. Results indicate differences in the strength of cardiac guidewires which are in the same group characteristics and end uses. This study considered on three types of steel guidewire strength: Amplatz Ultra Stiff; Lunderquist Extra Stiff; Back – Up Meier Steerable. The AMPLATZ guidewire showed the lowest tensile strength, stiffness and the highest torsion with Young's modulus. The BACK – UP MEIER guidewire has very similar properties to the LUNDERQUIST guidewire.*

Keywords: Guides, Cardiolog, Mechanical properties, Medical applications

1. Introduction

Technological development and the changing lifestyle in highly developed countries result in the occurrence and higher incidence of the so-called civilisation diseases. One of such diseases is sclerosis, which can result in ischaemic heart disease, cardiac infarction and at worst in death. Progressing atherosclerotic plaque is a long-term process that begins as early as in childhood. That is why, introducing preventive actions from as early as possible is very important.

When it comes to the already advanced arteriosclerotic vascular disease, the constantly developing vascular surgery is applied. The most commonly used is angioplasty, which is a procedure that makes a blood vessel passable, using a balloon or a stent. In the first case, after inserting a balloon, it is inflated in order to widen the blood vessel diameter, and then it is removed. The second method, which uses a stent, involves decompressing a balloon with a small metal spring (stent) attached to it, which, after being extended, permanently expands blood vessel diameter.

Requirements concerning medical equipment specified in international standards provide strict conditions that the equipment must meet in order to be applied in treatment. When it comes to guidewires, the most significant factors are the precision in reaching to the location of stenosis (which depends on its rigidity), torque, bend strength, and proper durability (so that the guidewire does not break during a surgery). Furthermore, it is also extremely important to select proper material of the guidewires to meet the expectations of medical professionals (Murray, 2006, Sarkissian, 2012).

There are many kinds of angiographic guidewires, which differ in terms of material, type of guidewire tip and coating. These aspects affect not only the appearance of guidewires, but, above all, their mechanical properties. During a surgery, it is very important to match the equipment to a given clinical case (Murray, 2006, Sarkissian, 2012).

[*] M.Sc. Eng. Marek Andryszczyk: Faculty of Mechanical Engineering, UTP University of Sciences and Technology in Bydgoszcz, Al. Prof. S. Kaliskiego 7; 85- 796, Bydgoszcz; PL, Marek.Andryszczyk@utp.edu.pl

[**] M.Sc. (Eng.) Angela Andrzejewska: Faculty of Mechanical Engineering, UTP University of Sciences and Technology in Bydgoszcz, Al. Prof. S. Kaliskiego 7; 85- 796, Bydgoszcz; PL, Marek.Andryszczyk@utp.edu.pl

[***] Prof. Tomasz Topoliński: Faculty of Mechanical Engineering, UTP University of Sciences and Technology in Bydgoszcz, Al. Prof. S. Kaliskiego 7; 85- 796, Bydgoszcz; PL, Tomasz.Topolinski@utp.edu.pl

The analysed aspects make it necessary to define common possibilities and expectations for the materials used in medical guidewires. In order to implement new and to improve the existing treatment methods, the equipment we use must be improved.

Guidewires used in coronary angioplasty should be flexible due to difficult access to the location of stenosis and small artery sizes. When it comes to introducing stents/stent grafts to larger blood vessels, guidewires with more rigid body will be used. This is because peripheral arteries have larger lumen and require larger catheters which will carry heavier elements, such as stent grafts (Murray, 2006, Sigwart 2015).

Also, when there are large calcified atherosclerotic deposits, it is necessary to use rigid guidwires, as excessively flexible ones would not be able get through the narrowings, which would make it impossible to introduce a stent or decompress a balloon.

We should also remember that a guidewire should not damage vascular walls and atherosclerotic plaque. It may lead to the risk of tearing off a part of the plaque or forming clots which may cause sudden closure of vascular lumen in other location. Therefore, guidewire tip has been designed to be more flexible than guidewire shaft. Another characteristic element is the shape of tip, which can be curved (J-shaped) to facilitate passing through vascular branching points. However, it can also be straightened by applying force in order not to damage the vessel.

The knowledge of properties and mechanical strength of guidewires may considerably facilitate the work of doctors. The results obtained will help a doctor to select an optimum guidewire suitable for a given clinical case.

It happens quite often that stenosis is so advanced that a flexible guidewire is not sufficient to pass through the narrowed vessel diameters. Knowing the mechanical properties of guidewires may prevent a wrong choice of equipment and lower the cost and duration of a surgery.

2. Purpose

This paper is aimed at comparing physical and mechanical properties of angiographic guidewires used in artery angioplasty procedures.

3. Materials and Methods

3.1. Material characterisation

This paper describes a study on steel guidewire strength. Three types of guidewires were used: Amplatz Ultra Stiff; Lunderquist Extra Stiff; Back – Up Meier Steerable.

The table below describes feathers of the guidewires used in the study.

Tab 1. Guidewire parameter

Name:	Coating	Length [mm] / diameter [mm]	Type and length of tip
Amplatz	PTFE	2600 / 0.89	J-type tip, 70mm, radius 3 mm
Lunderquist	TFE	2600 / 0.89	Straight tip, 40mm
Back – Up Meier	PTFE	3000 / 0.89	C-type tip, 110mm

Tests were carried out on specimens which were fragments of core wires of the above listed guidewires. Distal parts (tips) were not used in the study because of too little number of specimens. Appropriate lengths of specimens were established based on standards that govern the tests. Lengths of specimens were: 220 mm for tensile test, 67 mm for torsion test.

3.2. Figures and tables

Material characterisation results were processed with the STATISTICA 12.5 software. Consistency of distribution of the tested parameters with normal distribution was determined with the Shapiro-Wilk test. For further analysis, parametric and non-parametric tests were employed. Statistical significance of differences among the obtained results was determined with one-way analysis of variance (ANOVA) and by way of the Tukey multiple comparison test. Correlation analysis was performed with the Pearson test. Level of significance $p<0.05$ was assumed as statistically significant.

4. Results and Discussion

Studies aimed at acquiring detailed knowledge on the properties of angioplasty guidewires are carried out worldwide. Most of them are concerned with the same properties as these analysed in this paper.

Guidewires of the same group and intended purpose should be characterised by very similar or even identical strength parameters. Differences may depend on a manufacturing method, coating or addition of trace amounts of other elements to the alloys in order to improve their qualitative parameters (Sarkissian, 2012).

This paper is focused on steel guidewires only, which belong to rigid guidewires. The obtained results show differences between guidewires which should have very similar strength characteristics. The analysis of the data demonstrates that the three guidewires concerned considerably differ from one another, which translates into their practical application during surgeries (Maguire, 2005).

The above test results have been obtained during strength tests and demonstrate differences among the selected guidewires. Tests were carried out in identical conditions. It should be noted that the coating of the AMPLATZ guidewire were removed due to its spring-like structure.

The statistical tensile test showed that elongation of all the guidwires reached similar levels. However, significant differences were observed when it comes to breaking force, Young's modulus and rigidity.

Breaking force indicates which guidewire has the highest tensile strength, which may be a key feature if a guidewire becomes wedged in a vessel. The LUNDERQUIST guidewire showed the highest tensile strength and the AMPLATZ guidewire – the lowest.

The highest Young's modulus, was demonstrated by the AMPLATZ guidewire, and the lowest by the BACK – UP MEIER guidewire. The situation is opposite when it comes to rigidity. AMPLATZ is characterised by the lowest rigidity.

During the torsion test carried out until the point of breaking of guidewire, the highest angle of torsion (almost two times higher) was also observed in the AMPLATZ guidewire, with means its torque is two times lower than in the LUNDERQUIST and BACK – UP MEIER guidewires.

Availability of different types of material for manufacturing guidewires may be both very practical (possibility to match a guidewire to a given clinical case) and problematic (too many possibilities make the selection process more difficult and longer). Therefore, the optimum solution would be to make a guidewire, using material which is universal and which would be suitable for both large stenoses and those difficult to reach. This will lead to reduced costs and complications of the procedure due to the use of only one guidewires during surgery, instead of several as at present.

Tab 2. Aggregated results medium parameters obtained from research

Nazwa	AMPLATZ	LUNDERQUIST	BACK - UP MEIER
ΔL [mm]	3.4	3.5	3.3
Fm [N]	850.4	1268.2	1130.5
Young's modulus [MPa]	2341.5	2085.1	1858.7
Stiffness [N/mm]	427.2	675.1	653.1
Torsion [°]	4871.3	2993.3	2804.4
Torque [Nm]	0.1	0.2	0.2

5. Conclusions

The highest rigidity of the tested guidewires is demonstrated by the LUNDERQUIST guidewire, and therefore it will be the optimum choice for restoring patency of vessels with a high number of stenoses.

Thanks to the best elasticity and the lowest torque, the AMPLATZ guidewire can be used for smaller stenoses which are hard to reach. The lower torque means better controllability of the guidewire.

The BACK – UP MEIER guidewire has very similar properties to the LUNDERQUIST guidewire, which leads to the conclusion that they can be used interchangeably. These guidewires have different coating, which may be a key-factor when it comes to choosing the right one.

References

Murray. C.J.. S.C. Kulkarni. and M. Ezzati: Understanding the coronary heart disease versus total cardiovascular mortality paradox: a method to enhance the comparability of cardiovascular death statistics in the united states. Circulation. 113/2006. P. 2071-2081.

Sigwart u. Treatment of coronary artery disease from the inside: light at the end of the tunnel? Glob cardiol sci pract. 2015. 2015(4).s.53

M. Wirwicki. T. Topoliński. "Shear Strength Testing of Bonded Joints of Dental Materials". Solid State Phenomena. Vol. 224. pp. 198-203. 2015Kuramitsu S.. Shirai S.. Ando K.. Mechanism of in-stent restenosis after second-generation drug-eluting stents (des): is it different from bare-metal stents and first-generation des? J thorac dis 2015. dec. 7 (12). s. E599 – e602

Sarkissian C.. Korman E.. Hendlin K.. Monga M.. Systematic evaluation of hybrid guidewires: shaft stiffness. lubricity. and tip configuratiion. Urology 2012. mar 79(3). s. 513-7

Maguire P.D.. McLaughlin J.A.. Okpalugo t.i.t. I wsp.. mechanical stability. corrosion performance and bioresponse of amorphous diamond-like carbon for medical stents and guidewires. Diamond and related materials 2005. nr 14(8). s. 1277 – 1288

22nd International Conference
ENGINEERING MECHANICS 2016
Svratka, Czech Republic, 9 – 12 May 2016

EFFECT OF WATER ABSORPTION ON THE MECHANICAL PROPERTIES OF BIODEGRADABLE MATERIALS FOR MEDICAL APPLICATIONS

A.Andrzejewska*, M. Andryszczyk, T. Topoliński*****

Abstract: *This article presents results of conducted studies of mechanical properties offered by biodegradable polymers in the production of biodegradable implants. The adopted research methodology comprising specimen geometry and simulating the implant functioning environment allowed the determination of the impact of water absorption during hydrolytic degradation on changes of mechanical properties of polylactide injection moulded pieces. The obtained test results were then analysed statistically, and on this basis a value correlation was defined for the obtained results in change of specimen mass in relation to change in mechanical strength of the given material.*

Keywords: Hydrolytic degradation, Biodegradable implants, Mechanical properties, Water absorption, Medical applications

1. Introduction

Poly(lactide acid), also called polylactide, is a biopolymer, the basic synthesis method of which is polymerisation with Ring-Opening-Polimerization, ROP. As an effect of ROP polymerisation a biopolymer is obtained having a molecular weight (M) within the range of 103≤M≤106 and with specified terminal groups and macro particle structure. Depending on the type of used lactide acid enantiomer, which is the input product in the polylactide polymerisation process, polylactide with defined terminal groups is obtained. Both lactide and lactic acid are characterised by the occurrence of two chilarity centres (asymmetric carbon atom), and consequently the type of lactide acid enantiomer used in the synthesis affects the form of obtained lactide. There is L(-)-lactide, D(+)-lactide or DL- lactide, which following polymerisation allows obtaining poly(L-lactide), poly(D-lactide) or poly(D,L-lactide). Polymerisation executed by the ROP method was described in an article of Żenkiewicz M., Richert J. (2009), and Foltynowicz Z., Jakubiak P. (2002).

Polylactide is a semi-crystalline aliphatic thermoplastic polymer, which is used in medical applications for the production of biodegradable implants. Those implants are made of pure polymer, conformation of pure polymer or copolymers. Polylactide has become widely used as material for the production of stents and vascular grafts, surgical suturing materials, facial fracture fixation plates or plates for osteosynthesis. Taking into account the capability of hydrolytic degradation, polylactide decays in the patient's organism to dioxide and water within a period of circa 12 – 18 months or in an appropriately shorter time, depending on the copolymer type it is comprised by (Das D., et all (2012))

The hydrolytic degradation of polymer occurs in a process involving a chemical factor - water. The human organism is to a large extent built of water, and so placing an implant made of hygroscopic polylactide in the organism of a patient leads to the absorption of water by material. By permeating into the material, the absorbed water changes the water concentration gradient between its surface and the internal part. The impact of water and polymer particles contributes to material erosion in the surface or

* M.Sc. (Eng.) Angela Andrzejewska: Faculty of Mechanical Engineering, UTP University of Sciences and Technology in Bydgoszcz, Al. Prof. S. Kaliskiego 7; 85- 796, Bydgoszcz; PL, Angela.Andrzejewska@utp.edu.pl

** M.Sc. (Eng.) Marek Andryszczyk: Faculty of Mechanical Engineering, UTP University of Sciences and Technology in Bydgoszcz, Al. Prof. S. Kaliskiego 7; 85- 796, Bydgoszcz; PL, Marek.Andryszczyk@utp.edu.pl

*** Prof. Tomasz Topoliński: Faculty of Mechanical Engineering, UTP University of Sciences and Technology in Bydgoszcz, Al. Prof. S. Kaliskiego 7; 85- 796, Bydgoszcz; PL, Tomasz.Topolinski@utp.edu.pl

throughout the material, as a result of which the mechanical strength of biodegradable material changes (Vieira A.C at all (2010)). There are different ways to analyze the mechanical properties of biomaterials. One of them is testing through gradually increasing load method (Wirwicki M. at all (2014)).

The aim of this study was to investigate the impact of absorbed degrading medium on changes of mechanical strength of polylactide, subjected to tests of monotonic stretching in the function of time of controlled hydrolytic degradation.

2. Materials and Methods

2.1. Material

In the study use was made of sample of biopolymer characterised by average viscosity - poly(lactide acid), PLA (Ingeo™ Biopolymer 3100HP), manufactured by NatureWorks LLC.

2.2. Material processing

The adopted specimen geometry is appropriate for standard polymer moulded parts had a cross-section of the working specimen amounting on average to 43mm (PN-EN ISO527-2). Polymer moulded parts were prepared in the process of injection moulding. The initially prepared granulate was dried for 3 hours in a vacuum drier at a temperature of 100°C, and then injected at injection parameters allowing obtaining amorphous material.

2.3. Characterization

2.3.1. Hydrolytic degradation

Controlled hydrolytic degradation was carried out in accordance with the adopted technology, which comprises the type of degrading medium and its temperature, as well as time intervals between successive degradation periods.

The samples were weighed (analytical scales RADWAG, d=0.1mg) to determine the initial weight of samples prior to their degradation, and then placed in heated up degrading media. In the tests use was made of three degrading media, and namely distilled water, phosphate buffered saline solution (PBS) and 0.9% sodium chloride solution, which were heated up to a temperature conforming to the temperature of the warm-blooded human organism (T=37 ± 1°C).

The samples were removed from the degrading medium after 1, 2, 6, 12, 26 weeks, dried with paper towels and then weighed and characterised using the following methods.

2.3.2. Mass change

To determine changes in specimen weight as a result of absorption of the degrading medium, the samples were weighed before and after degrading. The specimen mass change percentage was determined from the following dependence: *% change of sample mass = [(final mass – initial mass)/initial mass]* 100*

3.3.3. Mechanical strength

Degradable and non-degradable specimen were subjected to the single-axial tensile test on the Instron 8874 tensile tester. The adopted test conditions were in conformity to the standard PN-EN ISO527-2: distance between grips being 115mm, stretching speed of 1mm/min. The deformation of the tested material was determined with the use of a static clip-on extensometer.

2.4. Statistical analysis

Results of the characteristic description of the material were developed with the use of the STATISTICA 12.5 software. The conformity of decomposition of the tested parameters in relation to normal decomposition was determined by the Shapiro-Wilk test. In the further part of the analysis use was made of parametric and nonparametric tests. The statistical significance of differences in the obtained results was set out using the ANOVA one-way test and by multiple comparisons made using the Tukey algorithm. A review of the correlations was made using the Pearson test. The level of $p<0.05$ was adopted as one of statistical significance.

3. Results and Discussion

It is assumed that an important factor that characterises biodegradable polymers is an assessment of a change in specimen mass over the degradation time. The determination of the actual specimen mass loss is possible by subjecting it to the process of vacuum drying, however, specimen subjected to this process cannot be used in mechanical durability tests. For this reason in this project the adopted method for assessing changes in specimen mass is the determination of water absorption percentage in relation of specimen not subjected to degradation. The specimen mass loss during degradation was calculated for H_2O: T1 = 0.0085%, T6 = 0.0093%, T12 = 0.0103%, T26 = 0.0150%, for PBS: T1 = 0.0088%, T6 = 0.0095%, T12 = 0.0102%, T26 = 0.0106% and for NaCl: T1 = 0.0085%, T6 = 0.0093%, T12 = 0.0099%, T26 = 0.0133%. Results of a specimen mass loss percentage during degradation were presented on fig. 1. tensile strength at break (σ_B).

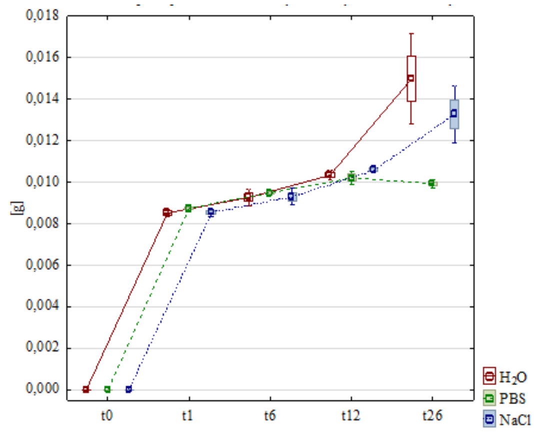

Fig. 1. Percentage mass loss

The initial tensile strength (σ_M), was 57,56 MPa. The average value of mechanical strength in time-points of degradation was measure for H_2O: T1 = 49.78 MPa, T6 = 49.78 MPa, T12 = 55.30 MPa, T26 = 32.95 MPa; for PBS: T1 = 50.12 MPa, T6 = 50.14 MPa, T12 = 55.48 MPa, T26 = 39.45 MPa and for NaCl: T1 = 50.37 MPa, T6 = 50.33 MPa, T12 = 55.46 MPa, T26 = 37.45 MPa. Results of a specimen mechanical strength were presented on fig. 2

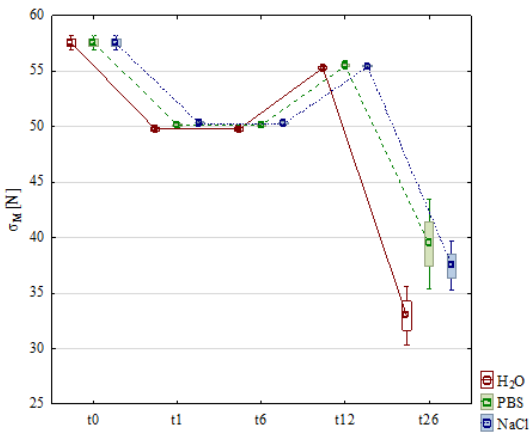

Fig. 2. Tensile strength (σ_M)

The initial tensile strength at break (σ_B), was 56.05 MPa. The average value of mechanical strength in time-points of degradation was measure for H_2O: T1 = 38.24 MPa, T6 = 39.48 MPa, T12 = 48.60 MPa, T26 = 30.53 MPa; for PBS: T1 = 39.03 MPa, T6 = 39.89 MPa, T12 = 47.91 MPa, T26 = 39.45 MPa and for NaCl: T1 = 39.84 MPa, T6 = 40.24 MPa, T12 = 47.32 MPa, T26 = 36.91 MPa. Results of a specimen mechanical strength were presented on fig. 3

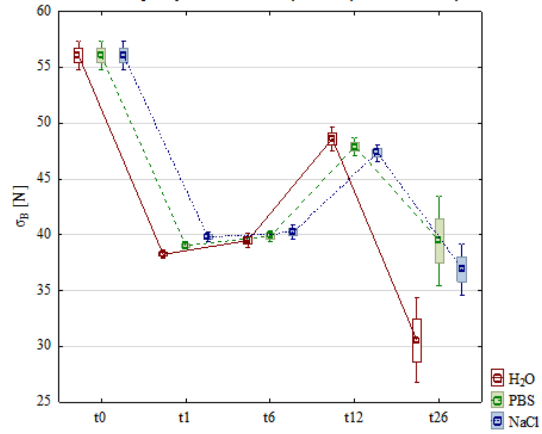

Fig. 3. Tensile strength at break (σ_B).

The implemented correlation analysis pointed to a robust linear dependence between the increase in the mass of tested specimens and their lower strength defined as parameter σ_M and σ_B. The analysed dependencies occurred in a similar way for the H_2O, PBS and NaCl medium (Tab.1). In addition a significant statistical dependency may be indicated between changes between changes in parameters given the degrading medium in which the tested specimens were immersed.

Tab. 1. Correlation table

Parameter		Degradation medium		
		H2O	PBS	NaCl
σ_M	R^2	-0.7461	-0.4936	-0.6905
	p-value	p=0.000	p=0.001	p=0.000
σ_B	R^2	-0.7646	-0.7402	-0.8131
	p-value	p=0.000	p=0.000	p=0.000

4. Conclusions

The changes in tensile strength and tensile strength at break are the effect of absorption degradation medium. The results show that with the time of degradation increase a degradation medium absorption and at the same time are reduced mechanical properties of investigated material. It has been shown that in the early stages of hydrolytic degradation (up to 12 weeks), degradation medium in which were polymer specimens immersed, has influence on polymer plasticization. But a follow up of degradation, shown that specimens, after 26 weeks time of immersion, were brittle. On this basis can conclude that the amount of absorbed fluid by amorphous material and aging time, is changing the arrangement of the polymer linkages within the specimen volume.

References

Das D., Zhang Z., Winkler T., Mour M., Günter Ch.I., Morlock M.M., Hans- Machens H.G., Schilling A.F. (2012) Bioresorption and Degradation of Biomaterials, Advances in Biochemical Engineering/Biotechnology, 126: pp. 317-333

Foltynowicz Z., Jakubiak P. (2002) Poli(kwas mlekowy) – biodegradowalny polimer otrzymywany z surowców roślinnych. Polimery 2002, 47, 11-12, pp. 769-774

Vieira A.C., Vieira J.C., Guedes R.M., Marques A.T. (2010) Degradation and Viscoelastic properties of PLA-PCL, PGA-PCL, PDO and PGA fibres. Materials science forum, 636-37, pp. 825-832

Żenkiewicz M., Richert J. (2009) Synteza, właściwości i zastosowanie polilaktydu. Przetwórstow Tworzyw, 5, pp.192-199

Wirwicki M. Topolinski T. (2014) Analysis of P-M damage accumulation in zirconium dioxide; testing through gradually increasing load method, Key Engineering Materials, Vol. 598, pp 255-260

22nd International Conference
ENGINEERING MECHANICS 2016
Svratka, Czech Republic, 9 – 12 May 2016

INFLUENCE OF UNBALANCED BENDING MOMENTS ON PUNCHING RESISTANCE OF FLAT SLABS

T. Augustín*, Ľ. Fillo, A. Bartók*****

Abstract: *Unbalanced bending moments influence punching resistance of flat slabs depending on position of columns in structure. Paper presents methods of calculation of this phenomenon by different approaches with different levels of accuracy. The contribution begins with an analysis of forces distribution depending on position of columns and continues with an analysis of stresses round the column and also brings explanation and simplification of Eurocode approaches.*

Keywords: Flat slab, Punching, Shear resistance, Unbalanced bending moment, Eurocodes.

1. Introduction

There are two possible ways of structural failure due to punching. The first one is strut diagonal failure (crushing of concrete) at control perimeter u_0 of the column (Fig. 1a). The second one is the failure in shear crack surrounded by control perimeters u_i, which are analysed in distances 2*d* from face of column (Fig. 1b).

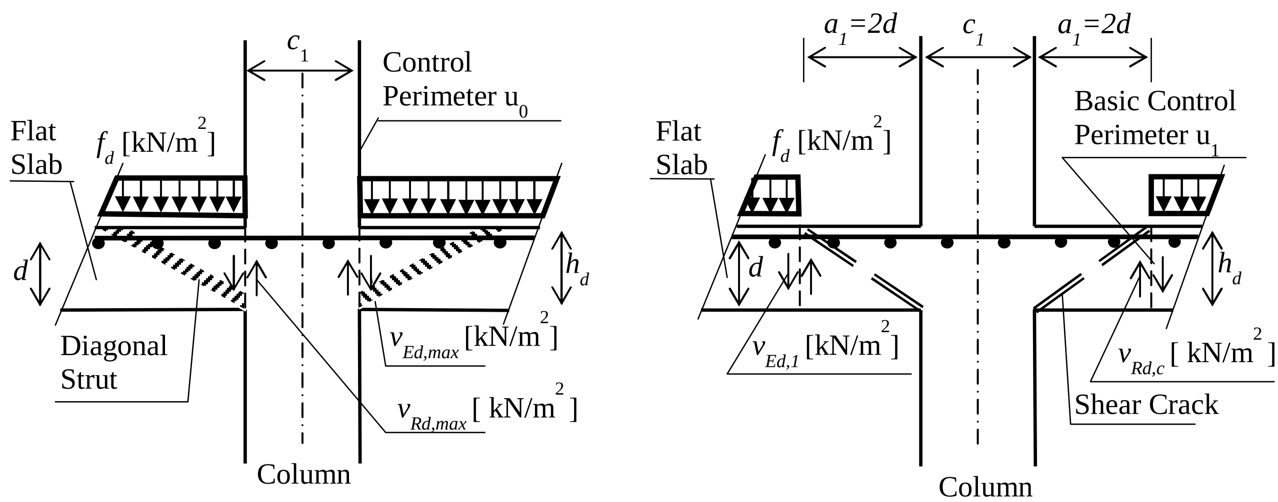

Fig. 1: a) Strut diagonal failure model (left), b) model of failure in shear crack (right)

Crushing of the struts at column perimeter is controlled by reduced compressive strength of concrete (EN 1992-1-1:2004/AC (2010)) (1).

$$v_{Ed,max} = \frac{\beta V_{Ed,max}}{u_0 d} \le v_{Rd,max} = 0.4\, \nu\, f_{cd} \tag{1}$$

* Ing. Tomáš Augustín: Faculty of Civil Engineering, SUT in Bratislava, Radlinského 11; 810 05, Bratislava; SK, tomas.augustin@stuba.sk

** Prof. Ing. Ľudovít Fillo, PhD.: Faculty of Civil Engineering, SUT in Bratislava, Radlinského 11; 810 05, Bratislava; SK, ludovit.fillo@stuba.sk

*** Ing. Andrej Bartók, PhD.: Faculty of Civil Engineering, SUT in Bratislava, Radlinského 11; 810 05, Bratislava; SK, andrej.bartok@stuba.sk

The failure in shear crack is limited by shear resistance of concrete without shear reinforcement (2). The maximum shear resistance with shear reinforcement in basic control perimeter is limited by $k_{max}\, v_{Rd,c}$ where k_{max} (1.4 - 1.9) depends on form of shear reinforcement (EN 1992-1-1:2004/AC (2010)) (3).

$$v_{Ed,1} = \frac{\beta V_{Ed,1}}{u_1 d} \;\leq\; v_{Rd,c} = \frac{0.18}{\gamma_C} k_h \left(100 \rho_l f_{ck}\right)^{1/3} \tag{2}$$

$$v_{Ed,1} \;\leq\; v_{Rd,cs} = 0.75 v_{Rd,c} + \left(\frac{1.5d}{s_r}\right) \frac{A_{sw} f_{ywd,ef}}{u_1 d} \;\leq\; k_{max} v_{Rd,c} \tag{3}$$

2. Unbalanced Bending Moment

Punching failure also depends on a position of a column in a plan of a building – corner, edge and internal position of the column. This position is very important because of unbalanced bending moment coefficient β calculation. There are several levels of calculation accuracy by Eurocodes. For the structure up to 25% adjacent span difference is allowed to use recommended values of coefficient β (corner column – β = 1.5, edge column – β = 1.4, internal column – β = 1.15). It is also possible to use simplified equations for the calculation of coefficient β for the complete perimeter of internal column (4) and reduced perimeters for corner (5) and edge column (6).

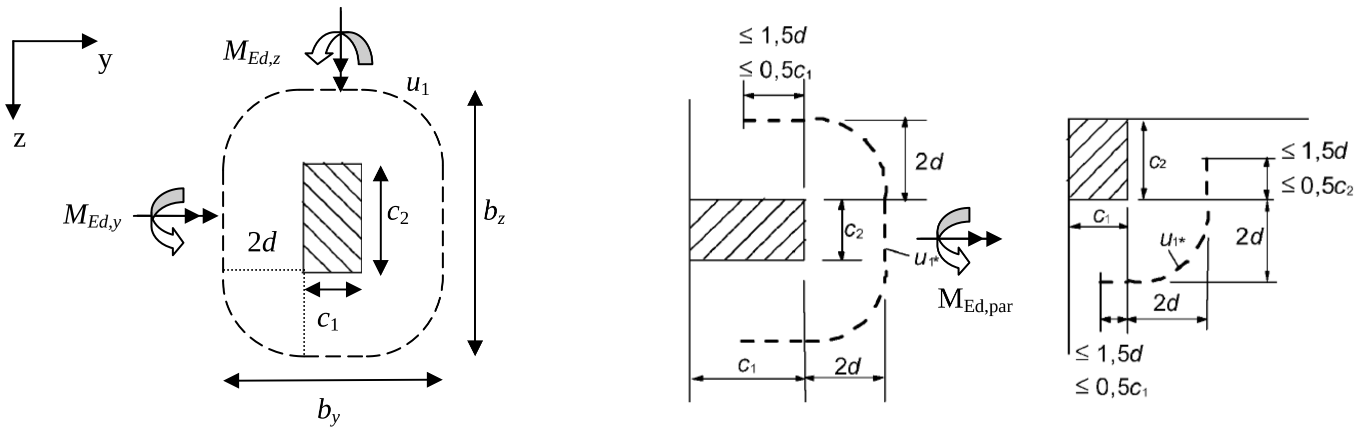

Fig. 2: Perimeter for internal column position (left), reduced perimeters for edge (middle) and corner (right) column position

$$\beta = 1 + 1.8 \sqrt{\left(\frac{M_{Ed,z}}{b_z V_{Ed,1}}\right)^2 + \left(\frac{M_{Ed,y}}{b_y V_{Ed,1}}\right)^2} \tag{4}$$

$$\beta = \frac{u_1}{u_1^*} \tag{5}$$

$$\beta = \frac{u_1}{u_1^*} + k \frac{M_{Ed,par}}{V_{Ed,1}} \cdot \frac{u_1}{W_1} \tag{6}$$

All cases of column positions can be calculated by general equation.

$$\beta = 1 + k \frac{M_{Ed}}{V_{Ed}} \cdot \frac{u_1}{W_1} \tag{7}$$

Where: u_1 is the length of the basic control perimeter; u_1^* is the length of the reduced basic control perimeter; M_{Ed} – unbalanced bending moment; k is a coefficient dependent on the ratio of the column dimensions c_1 and c_2, this value represents proportion of the unbalanced bending moment transferred by shear into column (EN 1992-1-1:2004/AC (2010)).

Tab. 1: Coefficient k - ratio of the column dimensions c_1 and c_2

c_1/c_2	≤ 0.5	1.0	2.0	≥ 3.0
k	0.45	0.60	0.70	0.80

W_1 corresponds to a distribution of shear stresses as illustrated in Fig. 3 and it is a function of the basic control perimeter u_1. The parameter W_1 is determined by the formula (8) and also by simplified equations (Fingerloos et al., 2012).

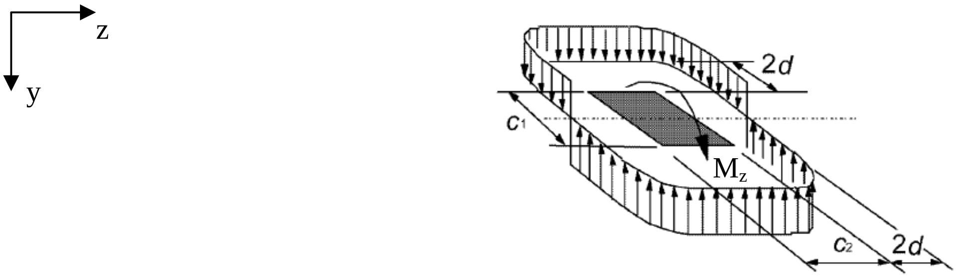

Fig. 3: Shear stresses distribution due to an unbalanced moment at a slab-column connection

$$W_1 = \int_0^{u_i} |\, e \,|\, dl \tag{8}$$

Where: dl – the length increment of the perimeter; e - the distance of dl from the axis about which the moment M_{Ed} acts.

3. Analysis of coefficient β

The analysis was done for following data: four floor apartment building, with height of one floor 3200 mm (the second floor was chosen for analysis), h_d = 200 mm (260 mm for slab overhang 300 mm), column span in "x axis" 7000 mm, column spans in "y axis" 7000 x 5000 x 7000 mm, slab overhang 1750 mm (300 mm alternative), column dimensions 400 x 400 mm, characteristic permanent load g_k = 2 kN/m^2 (without self-weight) and variable load q_k = 2.5 kN/m^2.

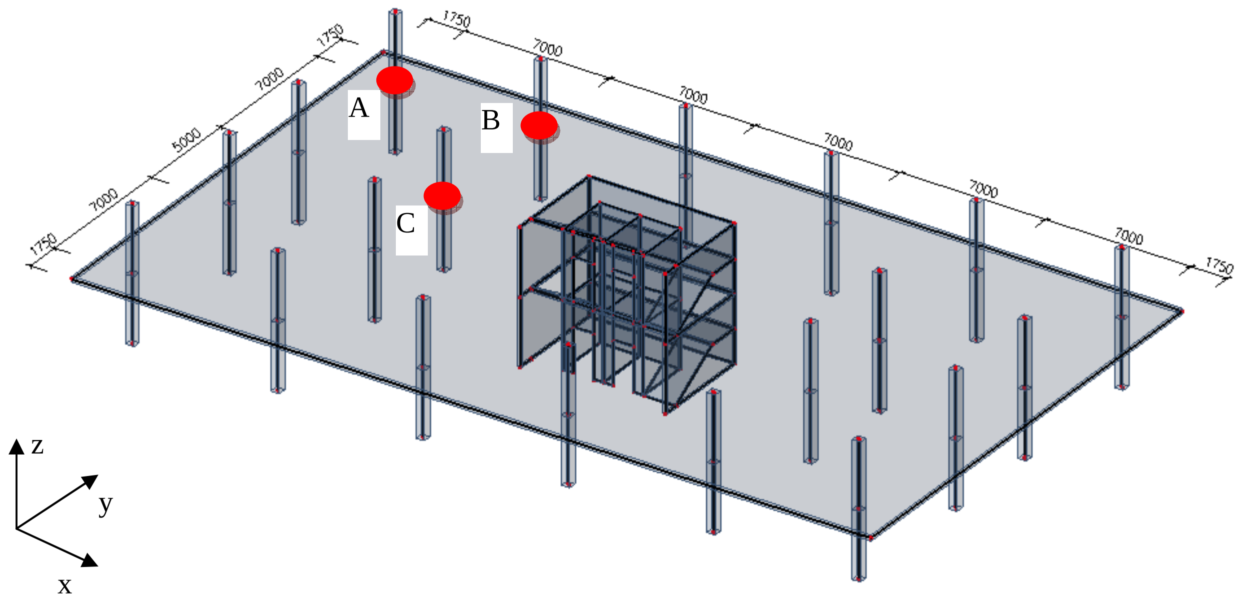

Fig. 4: Analysed plan of flat slab

Tab. 2: Comparison of the coefficient β for columns

	Columns				
	Corner – A (overhang 1750 mm)	Corner - A (overhang 300 mm)	Edge – B (overhang 1750 mm)	Edge - B (overhang 300 mm)	Internal - C
V_{Ed} [kN]	362	232	505	435	590
M_{yEd} [kNm]	113	130	136	208	90
M_{zEd} [kNm]	106	130	9	11	16
W_{1y} [m^2]	1.182	1.039	1.182	1.495	1.182
W_{1z} [m^2]	1.182	1.039	1.182	0.993	1.182
β Simplified calculation	1.81 (4)	1.96 (5)	1.51 (4)	1.52(6)	1.29 (4)
β General calculation (7)	1.77	1.52	1.48	1.56	1.28
β Recommended	1.5		1.4		1.15

4. Conclusions

In the paper is presented a contribution to the problem of flat slab punching. Two possible ways of structural failure due to punching are introduced on Fig.1. Punching failure also depends on a position of the column in a plan of a building – corner, edge and internal. This position is very important because of a coefficient β calculation (4)-(7), which depends on unbalanced bending moments. Paper presents methods of calculation of this phenomenon by different approaches with different levels of accuracy. Tab. 2 brings results of the coefficient β comparison for the different calculation methods and two possible overhangs of the edge slab cantilever (Fig.4). It’s obvious that simplified calculation brings values on the safe side, but the Eurocode recommended values of the coefficient β are on the unsafe side.

Acknowledgement

Authors gratefully acknowledge Scientific Grant Agency of the Ministry of Education of Slovak Republic and the Slovak Academy of Sciences VEGA č. 1/0696/14.

References

EN 1992-1-1:2004/AC (2010), Eurocode 2: Design of concrete structures – Part 1-1: General rules and rules for buildings.

Fillo Ľ., Halvonik J. (2013): The Maximum Punching Shear Resistance of Flat Slabs. In: Concrete and Concrete Structures, Conference Vrátna SK 376-381.

Fingerloos F., Hegger J., Zilch K. (2012) - Eurocode 2 für Deutschland, Beuth Verlag GmbH Berlin · Wien · Zurich, Wilhelm Ernst & Sohn, 388 p.

Hanzel J., Majtánová L., Halvoník J. (2014): Punching Resistance of Flat Slabs without Shear Reinforcement. In 21. Concrete Days, Proceedings of Conference. Praha: ČCS, 2014. 6p.

22nd International Conference
ENGINEERING MECHANICS 2016
Svratka, Czech Republic, 9 – 12 May 2016

BEHAVIOUR OF BOX-GIRDER UNDER SYMMETRICAL ACTION

I. Baláž[*], Y. Koleková[**], M. Kováč[***], T. Živner[****]

Abstract: *Theoretical investigation of 8 m long steel experimental model of one cell trapezoidal box-girder under four symmetrically arranged transverse forces. Buckling of wide flange in compression when girder was in normal position, buckling of narrow flange in compression when girder was in reverse position, and buckling of box-girder web in combined shear and bending. Global and local buckling. Shear lag. Comparison of experimental and theoretical values and evaluation of results.*

Keywords: Steel, box-girder, buckling of stiffened flange, buckling of web in shear, shear lag

1. Introduction

The following phenomena were investigated:

1. distribution of direct, shear and comparison stresses in box-girder;
2. resistance of compressed stiffened flange when box-girder was in normal position (the wide flange was in compression, the narrow one in tension);
3. resistance of compressed stiffened flanges when box-girder was in reverse position (the narrow flange was in compression, the wide one in tension);
4. influence of shear lag in both flanges;
5. resistance of the box-girder web under combination of shear and bending;
6. measurements of imperfections of the wide flange in compression and imperfections of the web in combined shear and bending by photogrammetric way;
7. influence of imperfections on buckling resistance of box-girder wide flange and web.

The total length of experimental box-girder is 8,4 m. Its span is 8 m and weight 2000 kg. There are 11 longitudinal L-stiffeners in wide flange and 4 flat longitudinal stiffeners in narrow flange (Fig. 2). Spacing of 9 transverse stiffening frames is 1 m (Fig. 4). The frames are strengthened by diaphragm in the cross-sections where loading is introduced (Fig. 3) and at the supports (Fig. 5). The width of the opening in diaphragm is 470 mm (Figs. 3 and 5). The strength properties of the used steel are: yield strength f_y = 262 MPa and ultimate tensile strength f_u = 390 MPa.

The box-girder was loaded by 2 pairs of antisymmetrically arranged transverse forces *F* (case a) in Fig. 4) and by 4 symmetrically arranged transverse forces *F* (case b) in Fig. 4). In this paper only two cases b) are described. The box-girder was first loaded by 4 symmetrical forces *F* in normal position when the wide flange was in compression (Figs. 1, 2, 3, 4). This is denoted as case b1). After that the experimental model was loaded by 4 symmetrical forces *F* in reverse position when the narrow flange was in compression (Fig. 5). This is called case b2). In the case b2) it was necessary before loading to weld another strengthening in the form of stiffened plate to the box-girder from its outer side in the sections where loading was introduced. It is possible to see it in Fig. 5. The purpose was to keep distance of pair of hydraulic jacks in transverse direction 1606 mm as it was in normal position (case b1).

[*] Prof. Ing. Ivan Baláž, PhD.: Department of Metal and Timber Structures; Faculty of Civil Engineering,, Slovak University of Technology, Radlinského 11; 810 05 Bratislava, Slovak Republic; ivan.balaz@stuba.sk

[**] Assoc. Prof. Ing. Yvona Koleková, PhD.: Department of Structural Mechanics; Faculty of Civil Engineering,, Slovak University of Technology, Radlinského 11; 810 05 Bratislava, Slovak Republic; yvona.kolekova@stuba.sk

[***] Ing. Michal Kováč, PhD.: Department of Metal and Timber Structures; Faculty of Civil Engineering,, Slovak University of Technology, Radlinského 11; 810 05 Bratislava, Slovak Republic; michal.kovac@stuba.sk

[****] Ing. Tomáš Živner, PhD.: Department of Metal and Timber Structures; Faculty of Civil Engineering,, Slovak University of Technology, Radlinského 11; 810 05 Bratislava, Slovak Republic; tomas.zivner@stuba.sk

The maximum capacity each of 4 hydraulic jacks was 500 kN. The strains and stresses were evaluated in 204 points with the help of the logger TSA-63. The deformations were measured with the exactness 0,1 mm in the sections 0, L/8, L/2, 3L/8 and L.

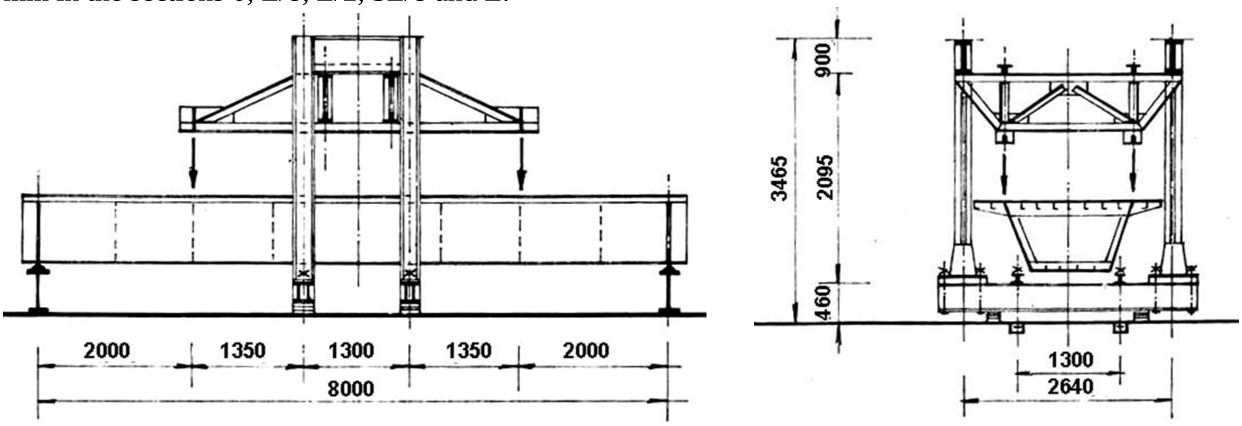

Fig. 1: Arrangement of loading frame. Four hydraulic jacks with capacity 500 kN each

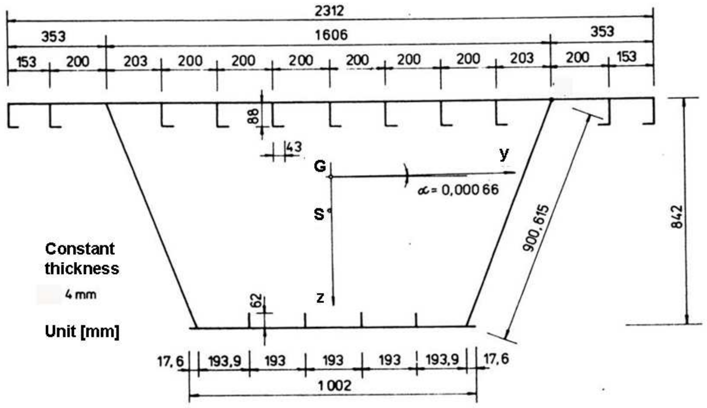

Fig. 2: Box-girder cross-section

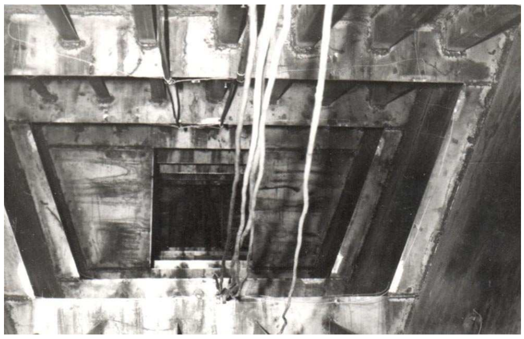

Fig. 3: Transverse stiffening frames

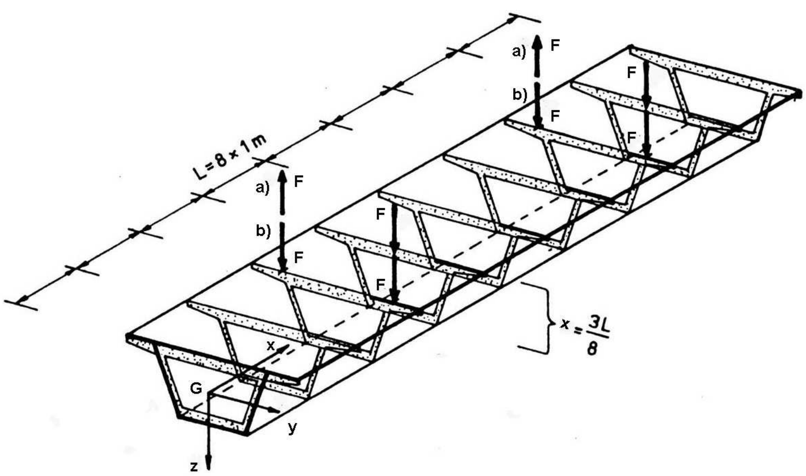

Fig. 4: Normal position of experimental box-girder

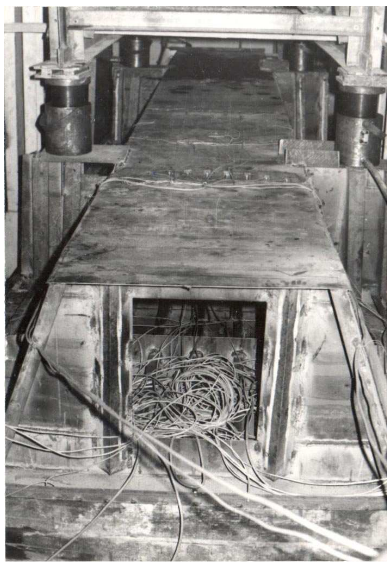

Fig. 5: Reverse position

The 5 tests were preformed in the following order in which the box-girder was under: 1) verification symmetrical loading, 2) the first antisymmetrical loading, 3) the second antisymmetrical loading, 4) symmetrical loading of girder in normal position, 5) symmetrical loading of girder in reverse position.

2. Experimental box-girder in normal position under symmetrical action

At one end of the box-girder in the field between sections 7 m and L = 8 m the both box-girder webs were strengthened in the middle by longitudinal stiffener to increase their shear resistance. At other end of the box-girder in the field between sections 0 m and 1.0 m the both box-girder webs were unstiffened. The shear resistance of this webs limited the resistance of the box-girder under symmetrical action.

2.1 Theoretical calculation of the box-girder in normal position according to EN 1993-1-5

Material, geometrical and cross-sectional properties and resistances:

$$E = 210GPa\,,\ \nu = 0.3\,,\ f_y = 262MPa\,,\ a = 1m\,,\ h = 842mm\,,\ d = 900.6mm\,,\ t = 4mm\,,\ z_G = 277.7mm \quad (1)$$

The elastic bending moment of the cross-section resistance $M_{el.R}$ and related force $F_{el,R}$ are

$$W_{el} = 5475.22cm^3\,,\ M_{el,R} = W_{el} f_y = 1434.51kNm\,,\ F_{el,R} = M_{el,R} / 2m / 2 = 358.63kN \quad (2)$$

The plastic bending moment of the cross-section resistance $M_{pl.R}$ and related force $F_{pl.R}$ are

$$W_{pl} = 7142.29cm^3\,,\ M_{pl,R} = W_{pl} f_y = 1871.28kNm\,,\ F_{pl,R} = M_{pl,R} / 2m / 2 = 467.82kN \quad (3)$$

The bending moment resistance $M_{f,R}$ of cross-section consisting of flanges only and related force $F_{f.R}$ are

$$W_f = 4018.46cm^3\,,\ M_{f,R} = W_f f_y = 1052.84kNm\,,\ F_{f,R} = M_{f,R} / 2m / 2 = 263.21kN \quad (4)$$

The box-girder cross-section is Class 4. The upper flange is under compression stress

$$\sigma_{com} = f_y z_G / h = 86.41MPa \quad (5)$$

For such small compression stress the plate and longitudinal stiffeners may be taken as fully effective concerning local buckling even if the plate and height and flange of the longitudinal L-stiffener of the girder wide flange are Class 4. Consequently all reduction factors of local buckling of all compressed parts of upper flange are ρ = 1. The shear lag reduction factors calculated by adopting elastoplastic model are in wide flange also negligible because they do not differ much from 1.0:

$$b_0 = 803mm\,,\ \alpha_0 = 1.253\,,\ \beta^{\kappa} = 0.908^{0.126} = 0.988\,,\ \text{for part of wide flange between girder webs} \quad (6)$$

$$b_0 = 353mm\,,\ \alpha_0 = 1.32\,,\ \beta^{\kappa} = 0.979^{0.058} = 0.999\,,\ \text{for cantilever parts of wide flange of box-girder} \quad (7)$$

Consequently the bending moment resistance $M_{eff,R}$ of effective^{p} cross-section taking into account only local buckling of inclined webs in bending (ψ = -2.032, k_σ =54.98, ρ = 0.844, b_{e1} = 100.3 mm, b_{e2} = 150.4 mm) and related force $F_{eff.R}$ are

$$W_{eff} = 5479.35cm^3\,,\ M_{eff,R} = W_{eff} f_y = 1435.59kNm\,,\ F_{eff,R} = M_{eff,R} / 2m / 2 = 358.90kN \quad (8)$$

Also this influence is negligible because of very short part of inclined web in compression and small contribution of the inclined web to the bending moment resistance of girder cross-section.
The shear resistance of the box-girder web and related force $F_{V,R}$ are

$$\varepsilon = 0.947\,,\ k_\tau = 8.584\,,\ \bar{\lambda}_w = 2.17\,,\ \chi_w = 0.378\,,\ V_{bw,R} = \chi_w d t f_y / \sqrt{3} = 205.96kN \quad (10)$$

$$b_f = 17.6mm + 15\varepsilon t = 74.42mm\,,\ c = a\left(0.25 + 1.6 b_f t^2 / t / d^2\right) = 250.59mm \quad (11)$$

$$V_{bf,R} = b_f t^2 f_y / c = 1.245kN\,,\ V_{b,R} = V_{bw,R} + V_{bf,R} = 207.205kN\,,\ F_{V,R} = V_{b,R} h / d = 193.722kN \quad (12)$$

The force F with minimum value from above calculated values is resistance of the box-girder

$$F_R = \min(F_{eff,R} \approx F_{el,R}, F_{V,R}) = \min(358.90kN \approx 358.63kN, 193.72kN) = 193.72kN \quad (13)$$

Verification conditions according to EN 1993-1-5 evaluated for the force F_R = 193.72 kN are

$$M_{E,\max} = 2F_R\, 2m = 774.89kNm\,,\ M_{E,\max,red} = \min(0.4a, 0.5d) M_{E,\max} = 309{,}96kNm \quad (14)$$

$$\bar{\eta}_3 = F_R / (V_{b,R} h / d) \le 1\,,\ \bar{\eta}_1 = M_{E,\max,red} / M_{pl,R} = 0.166\,,\ M_{E,\max,red} / M_{f,R} = 0.294 \le 1.0 \quad (15)$$

$$\bar{\eta}_1 + \left(1 - M_{f,R} / M_{pl,R}\right)\left(2\bar{\eta}_3 - 1\right)^2 = 0.603 \le 1.0\,,\ M_{E,\max} / M_{eff,R} = 0.54 \le 1.0 \quad (16)$$

2.2 Experimental data from the test of the box-girder in normal position

The strains and displacements were measured in desired places for the following 4 transverse forces F (Fig. 4): F = 0 kN – 200 kN – 0 kN – 250 kN – 300 kN – 325 kN. The clearly visible buckling shape of unstiffened girder web under shear was achieved at F = 250 kN. The value of the transverse force at collapse was F_{coll} = 340 kN. The transverse stiffening frame creates very weak non-rigid end post. At the value F_{coll} the welds in the anchorage of the web tension field were broken at the upper flange.

3. Experimental box-girder in reverse position under symmetrical action

This test was not originally planned. Nevertheless, after the first symmetrical test the box-girder was put in reverse position and the second symmetrical test was performed on the same partly damaged girder.

3.1 Theoretical calculation of the box-girder in reverse position according to EN 1993-1-5

The narrow flange in reverse position is under compression stress f_y = 262 MPa. The local buckling reduction factor of longitudinal stiffener ρ_{st} = 0.914 (ψ = 0.926, k_σ = 0.456) and reduction factor of flange plate is ρ_p = 0.841 (ψ = 1, k_σ = 4). The reduction factor for global buckling of the whole stiffened narrow flange ρ_c = 0.632 (for column-like buckling: $\sigma_{cr,c}$ = 529.33MPa, α = 0.49, e = 54 mm, α_e = 0.796, χ_c = 0.632; for plate-like buckling: $k_{\sigma.p}$ = 144.755, $\sigma_{cr,p}$ = 170.435MPa; ξ = 0). The shear lag reduction factor $\beta^\kappa = 0.917^{0.065}$ = 0.998. The reduction factor of the girder inclined web due to local buckling in bending ρ = 0.409 (ψ = -0.492, k_σ = 13.274,). The section modulus of effective box-girder section was calculated for reduced height and thickness of longitudinal stiffeners, reduced thickness of the narrow flange plate and reduced width of girder inclined webs as follows

$$h_{st.eff} = h_{st}\,\rho_{st} = 62\text{ mm } 0.914 = 56.66\text{ mm},\quad t_{st,eff} = t\,\rho_c\,\beta^\kappa = 4\text{ mm } 0.632\ 0.998 = 2.521\text{ mm} \tag{17}$$

$$t_{p.eff} = t\,\rho_p\,\rho_c\,\beta^\kappa = 4\text{ mm } 0.841\ 0.632\ 0.998 = 2.122\text{ mm},\ b_{e1} = 98.77\text{ mm},\ b_{e2} = 148.16\text{ mm} \tag{18}$$

$$W_{eff} = 2900.86cm^3,\quad M_{eff,R} = W_{eff}\,f_y = 760.025kNm,\quad F_{eff,R} = M_{eff,R}/2m/2 = 190kN \tag{19}$$

Verification conditions according to EN 1993-1-5 evaluated for the force F_R = 190 kN are

$$M_{E,\max} = 2F_R\,2m = 760kNm,\quad M_{E,\max,red} = \min(0.4a,0.5d)M_{E,\max} = 304kNm \tag{20}$$

$$\bar{\eta}_3 = F_R/(V_{b,R}h/d) = 0.981 \le 1,\ \bar{\eta}_1 = M_{E,\max,red}/M_{pl,R} = 0.162,\ M_{E,\max,red}/M_{f,R} = 0.289 \le 1.0 \tag{21}$$

$$\bar{\eta}_1 + \left(1 - M_{f,R}/M_{pl,R}\right)(2\bar{\eta}_3 - 1)^2 = 0.567 \le 1.0,\qquad M_{E,\max}/M_{eff,R} = 1.0 \le 1.0 \tag{22}$$

3.2 Experimental data from the test of the box-girder in reverse position

The strains and displacements were measured in desired places for the following 4 values of transverse forces F (Fig. 4): F = 0 kN – 100 kN – 0 kN – 200 kN. The value of the transverse force at collapse was F_{coll} = 275 kN. The reason was buckling and big plastic deformation of all longitudinal stiffeners in compressed flange because intermittent fillet welds were used there (in normal position the narrow flange was in tension). Consequently plate of narrow flange buckled and big plastic deformation occurred in it.

4. Conclusions

The resistance of the box-girder under symmetrical action was limited: a) by the shear buckling resistance of girder inclined unstiffened webs when box-girder was in normal position, b) by the resistance of the stiffened narrow flange when box-girder was in reverse position. The theoretical values in the cases: a) F_R = 193,72 kN , and b) F_R = 190 kN were confirmed by experimental data. Experimentally achieved collapse values of transverse forces were: a) F_{coll} = 340 kN, and b) F_{coll} = 275 kN.

Detailed comparisons of experimental and theoretical values, shapes of initial imperfections in plate of compression wide flange and in plate of inclined web in shear and relevant shapes of plates buckling modes measured by photogrammetric way, distributions of the stresses, displacements in chosen points of box-girders and photographs from experimental tests will be published in the full paper.

Acknowledgement

Project No. 1/0819/15 was supported by the Slovak Grant Agency VEGA.

References

Baláž, I. (1980) Chapter: Stresses and Deformations in Girder with Trapezoidal Cross-Section and its Experimental Measurements in: Research Report III-8-2/16: Limit States of Orthotropic Stiffened Structural Systems. Faculty of Civil Engineering, STU in Bratislava, pp.V.1-V.58, VI.1-VI-66.

EN 1993-1-5 (2006) Eurocode 3 Design of Steel Structures – Part 1-3 Plated Structural Elements. CEN Brussels.

22nd International Conference
ENGINEERING MECHANICS 2016
Svratka, Czech Republic, 9 – 12 May 2016

BEHAVIOUR OF BOX-GIRDER UNDER ANTISYMMETRICAL ACTION

I. Baláž[*], Y. Koleková[**], M. Kováč[***], T. Živner[****]

Abstract: *Steel experimental trapezoidal box-girder loaded by two pairs of antisymmetrical transverse forces. Torsional and distortional cross-section properties of exact and simplified models of cross-section. Internal forces of torsion and distortion calculated by analogy with bending. Solutions of difficult torsion and distortion problems using analogies with solutions of simple bending problems describe behaviour of box-girder in well understandable form. Comparison of experimental stresses with theoretical ones.*

Keywords: Steel, box-girder, torsion, distortion, analogies

1. Introduction

The set up of loading frame is given in (Baláž, 2016). The trapezoidal cross-section and 9 transverse stiffening frames of 8.4 m long experimental box-girder are in Fig.1 and Fig. 2.

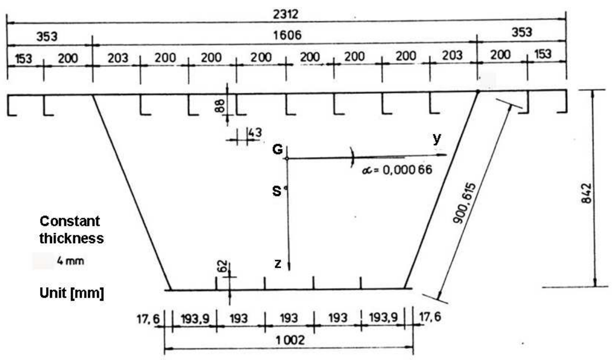

Fig. 1: Box-girder cross-section

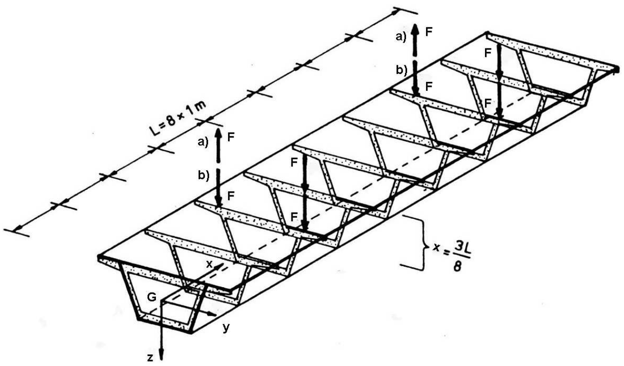

Fig. 2: Normal position of experimental box-girder

Dimensions of parts of transverse stiffening frame: a) transverse stiffener of upper wide flange: 167 mm x 4 mm, b) transverse stiffener of girder webs: 80 mm x 4 mm, c) transverse stiffener of bottom narrow flange: 120 mm x 4 mm. The transverse stiffening frames at the girder ends and in the cross-sections of the load application were strengthened by diaphragm with opening height h = 551 mm (between edges of upper and bottom transverse stiffeners) and opening width b = 440 mm.

The box-girder was loaded by 2 pairs of antisymmetrically arranged transverse forces F (case a) in Fig. 2) and by 4 symmetrically arranged transverse forces F (case b) in Fig. 2). In this paper only the case a) is described. Antisymmetrical loading required another strengthening in the form of plate stiffened by vertical stiffeners added to the box-girder from its outer side (see section A-A in Fig. 10). It enables to introduce the left forces in Fig. 2 a) to act from bottom side and to keep distance of pair of hydraulic jacks in transverse direction 1606 mm as it was in the case of symmetrical loading (Fig. 10). The maximum capacity of each of 4 hydraulic jacks was 500 kN.

[*] Prof. Ing. Ivan Baláž, PhD.: Department of Metal and Timber Structures; Faculty of Civil Engineering,, Slovak University of Technology, Radlinského 11; 810 05 Bratislava, Slovak Republic; ivan.balaz@stuba.sk

[**] Assoc. Prof. Ing. Yvona Koleková, PhD.: Department of Structural Mechanics; Faculty of Civil Engineering,, Slovak University of Technology, Radlinského 11; 810 05 Bratislava, Slovak Republic; yvona.kolekova@stuba.sk

[***] Ing. Michal Kováč, PhD.: Department of Metal and Timber Structures; Faculty of Civil Engineering,, Slovak University of Technology, Radlinského 11; 810 05 Bratislava, Slovak Republic; michal.kovac@stuba.sk

[****] Ing. Tomáš Živner, PhD.: Department of Metal and Timber Structures; Faculty of Civil Engineering,, Slovak University of Technology, Radlinského 11; 810 05 Bratislava, Slovak Republic; tomas.zivner@stuba.sk

The strains and stresses were evaluated in 204 points with the help of the logger TSA-63. The deformations were measured with the exactness 0,1 mm in the sections 0, L/8, L/2, 3L/8 and L.

The 5 tests were preformed in the following order in which the box-girder was under: 1) verification symmetrical loading, 2) the first antisymmetrical loading, 3) the second antisymmetrical loading, 4) symmetrical loading of girder in normal position, 5) symmetrical loading of girder in reverse position.

2. Experimental tests

During verification symmetrical loading local crushing of the bottom part of inclined girder web occurred at movable support (Fig. 4). Therefore the edge of diaphragm at support was strengthened by vertical L-profiles (see Fig. 5 in Baláž (2016)).

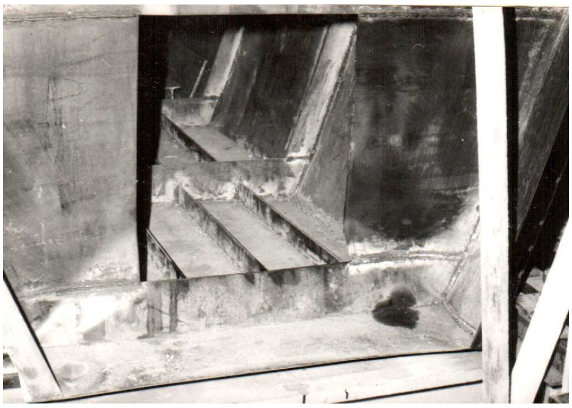

Fig. 3: Diaphragm at the box-girder end

Fig. 4: Local crushing of the web at support

The following phenomena were investigated during antisymmetrical loading:

1. distribution of direct stresses in longitudinal direction in the box-girder cross-section;
2. distribution of direct stresses in the transverse stiffening frames;
3. rotation of box-girder under antisymmetrical loading.

The strains and displacements were measured in desired places for the following transverse forces *F* values (Fig. 2 a) during (i) the first antisymmetrical loading: *F* = 0 kN – 100 kN – 0 kN – 100 kN – 150 kN – 200 kN and (ii) the second antisymmetrical loading: *F* = 0 kN – 100 kN – 0 kN – 150 kN – 200 kN – 0 – 250 kN – 300 kN. The further increasing of transverse forces *F* was limited by tension resistance of anchorage bolts. The weakest place was located in the right bottom edge of the transverse stiffening frame where the local plastification occurred.

3. Theoretical results

The distributions of the torsion bimoment and distortion bimoment are on Fig. 5 and Fig. 6.

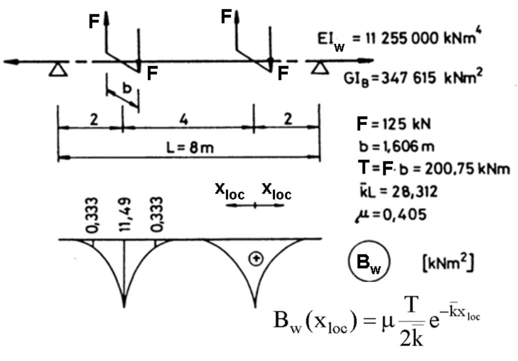

Fig. 5: Torsion bimoment taking into account influence of shear

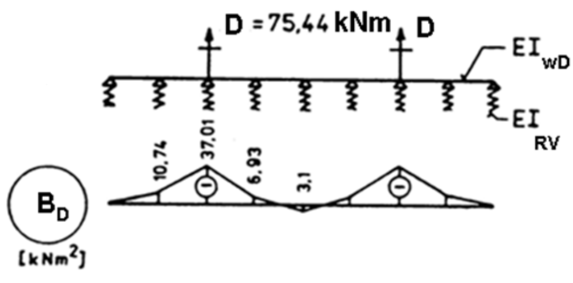

Fig. 6: Distortion bimoment

Details of calculation of cross-sectional properties of distortion and torsion are given in (Baláž, Agócs, 1994). Details of calculation of internal forces, direct and shear stresses are given in (Baláž, 2004).

Theoretical results given here are valid for F = 125 kN. They may be used for any value of F by multiplying F / 125 kN.

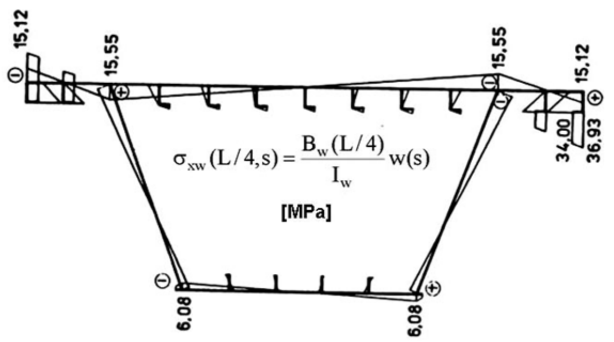

Fig. 7: Torsion direct stresses due to F = 125kN

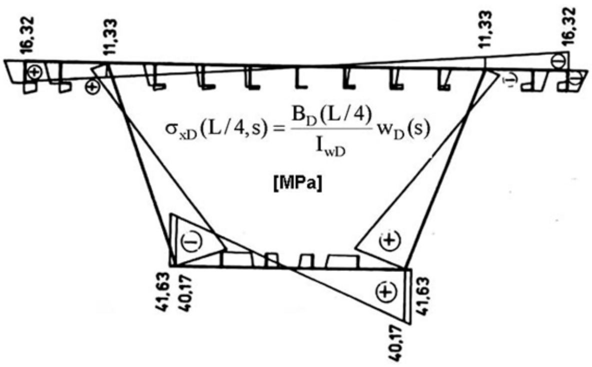

Fig. 8: Distortion stresses due to F = 125kN

4. Comparison of experimental and theoretical values and conclusions

The experimental and theoretical results show that transverse stiffening was relatively weak and therefore direct stresses due to cross-section distortion (Fig. 8) are greater than those due to torsion (Fig. 7). On the cross-section axis of symmetry the direct stresses due to antisymmetrical loading (Fig. 2 a) are zero (Fig. 7, Fig. 8) . This was not true for the experimentally measured values of direct stresses (Fig. 9).

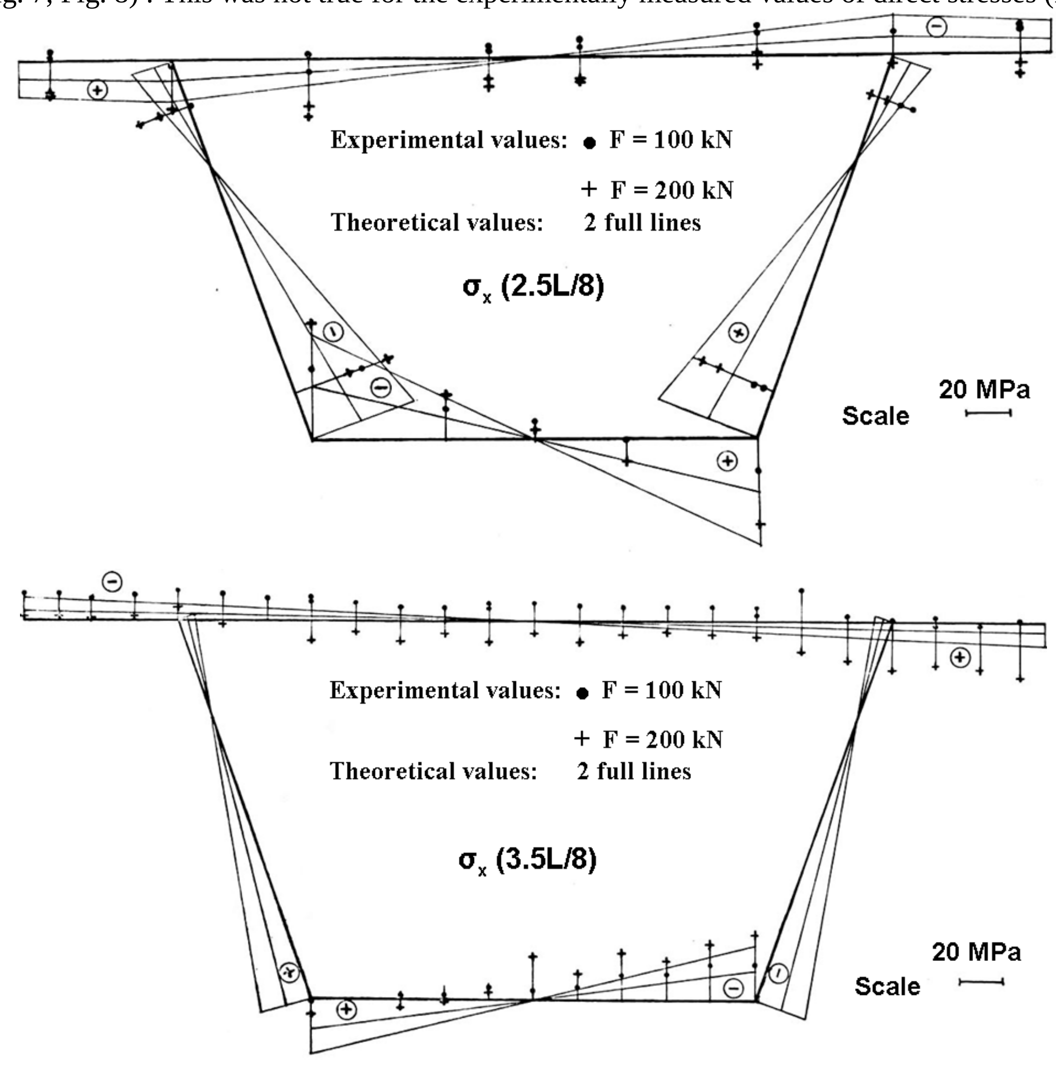

Fig. 9: Graphical comparison of experimental and theoretical values of direct stress σ_x in longitudinal direction due to distortion and torsion in two sections x = 2.5L/8, 3.5L/8

The reasons are: a) the experimental beam was at the ends elastically supported in torsion, b) it was necessary to weld additive transverse stiffener outside of cross-section in sections 2L/8 and 6L/8 only on the left side to enable to load the trapezoidal cross-section of the box-girder by the left hydraulic jacks from bottom side (Fig. 10). These two reasons are responsible for not perfectly antisymmetrical distribution of experimental direct stresses (Fig. 9).

Distortional bimoment B_D changes the sign along the box-girder length (Fig. 6). The same phenomenon may be seen in distribution of experimental direct stresses. Compare direct stresses in sections 2.5L/8 with those in section 3.5L/8 (Fig. 9).

Theoretical direct stresses in transverse stiffening frames are greater than experimental ones (Fig. 10). The comparison of theoretical and experimental values shows, that behaviour of experimental box-girder loaded by antisymmetrical loading may be described by the values obtained by hand calculation based on analogies with beam in bending (Fig. 5 and 6).

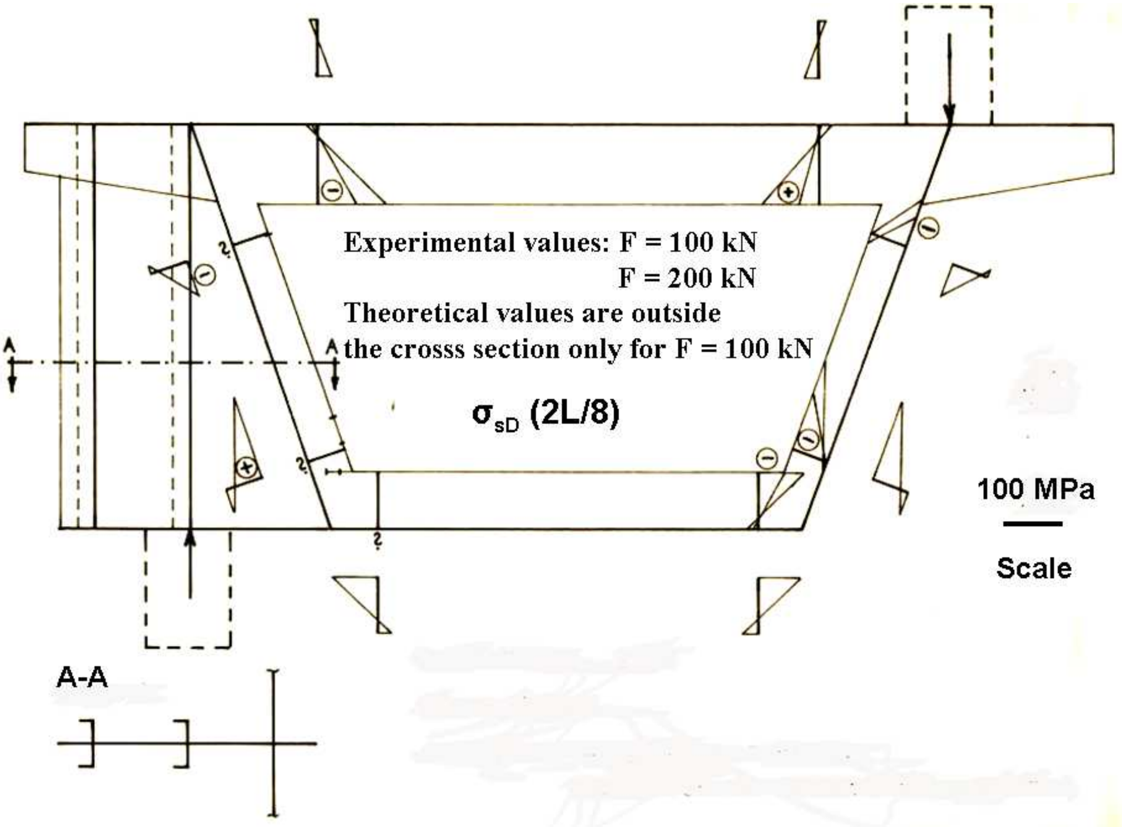

Fig. 10: Graphical comparison of experimental and theoretical values of direct stress σ_{sD} in transverse direction due to distortion in transverse stiffening frame in the section x = 2L/8

Acknowledgement

Project No. 1/0819/15 was supported by the Slovak Grant Agency VEGA.

References

Baláž, I. (1980) Chapter: Stresses and Deformations in Girder with Trapezoidal Cross-section and its experimental measurements in: Research Report III-8-2/16: Limit States of Orthotropic Stiffened Structural Systems. Faculty of Civil Engineering, STU in Bratislava, pp.V.1-V.58, VI.1-VI-66, (In Slovak).

Baláž I. (2004) Thin-walled steel structures. Influence of torsion in thin-walled bridge systems. Textbook, STU in Bratislava, 1st edition 1984, 5th edition 2004, (In Slovak).

Baláž I, Agócs Z. (1994) Metal structures I, Handbook for design of elements of steel structures, I. part, Textbook, Alfa Bratislava, 1st edition 1985, 5th edition 1994, (In Slovak).

Baláž, I., Koleková, Y., Kováč, M., Živner, T. (2016) Behaviour of Box-Girder Under Symmetrical Action. 22nd International Conference, Engineering Mechanics 2016, Svratka, Czech Republic, 9-12 May 2016.

EN 1993-1-5 (2006) Eurocode 3 Design of Steel Structures – Part 1-3 Plated Structural Elements. CEN Brussels.

22nd International Conference
ENGINEERING MECHANICS 2016
Svratka, Czech Republic, 9 – 12 May 2016

THERMO-MECHANICAL FATIGUE OF SI-MO 4.06 TURBINE HOUSING OF TURBOCHARGER - DAMAGE OPERATOR BASED LIFETIME PREDICTIONS

M. Bartošák[*], M. Španiel[**], M. Nesládek[***]

Abstract: *The paper presents application of damage operator based lifetime calculation for cast iron turbine housing of the turbocharger. Combination of thermo-mechanical fatigue and creep is considered, oxidation effect is taken into account indirectly. Results from transient thermal and elastoplastic finite element analysis are used for fatigue and creep damage calculation. Viscoplastic approximation based on nonlinear, strain controlled Maxwell model is used. Critical zones on the turbine housing of the turbocharger have been observed. Different damage parameters including dissipated energy for continuous damage calculation will be discussed.*

Keywords: Thermo-mechanical fatigue, Kinematic hardening, Creep, Hysteresis operator, Turbine housing of the turbocharger.

1. Introduction

Turbine housing of the turbocharger provides kinetic energy, needed for charging, using remaining enthalpy of the exhaust gas. Inhomogeneous distribution of temperature and boundary conditions of the component constrains thermal expansion, resulting in inelastic strains and stresses. Operating status is nearly cyclically stable. Also, at high temperature, creep and relaxation effects cannot be neglected.

Turbine housing of the turbocharger operating under thermo-mechanical cycle is considered for damage calculation. Temperature loading results from transient thermal finite element analysis (FEA), stress-strain response is obtained from elastoplastic FEA with non-linear temperature dependent kinematic hardening. Viscoplastic approximation is done as part of the post-processing step. Fatigue and creep damage are calculated separately. Oxidation is taken into account indirectly, as material tests were performed under ambient conditions. So called damage operator for variable temperature, developed especially by Nagode et al. (2010), enabling continuous calculation for non-isothermal thermo-mechanical loading, is used for fatigue damage calculation. Equivalent cycle temperature and separate rainflow counting aren't needed.

2. Material data assessment

Elastoplastic material response has been numerically modeled in ABAQUS. Constitutive model used represents mathematically Bauschinger's effect and other effects observed for materials subjected to cyclic loading, using associated flow rule and von Mises yield criterion. Widely accepted and commonly implemented in commercial software - Chaboche nonlinear temperature dependent kinematic hardening is selected from available models of incremental plasticity, capable to describe cyclic loading scenario, both isotropic and kinematic hardening, ratcheting and other phenomena. Three term backstress Chaboche model is proposed. Rather than on current temperature, model parameters have been calibrated to follow monotonic downward trend depending on temperature, mathematically described as Boltzmann function. Only cyclically stable hysteresis loops are point of the interest for thermo-mechanical fatigue. Elastoplastic

[*] Ing. Michal Bartošák: Faculty of Mechanical Engineering, CTU in Prague; Technická 4; 166 07, Prague; CZ, michal.bartosak@fs.cvut.cz

[**] Assoc. Prof. Miroslav Španiel, CSc.: Faculty of Mechanical Engineering, CTU in Prague; Technická 4; 166 07, Prague; CZ, miroslav.spaniel@fs.cvut.cz

[***] Ing. Martin Nesládek: Faculty of Mechanical Engineering, CTU in Prague; Technická 4; 166 07, Prague; CZ, martin.nesladek@fs.cvut.cz

material model has been calibrated from isothermal strain controlled low-cycle fatigue tests, attained at high strain rates for a few distinct temperatures, fully covering temperature range of the investigated component.

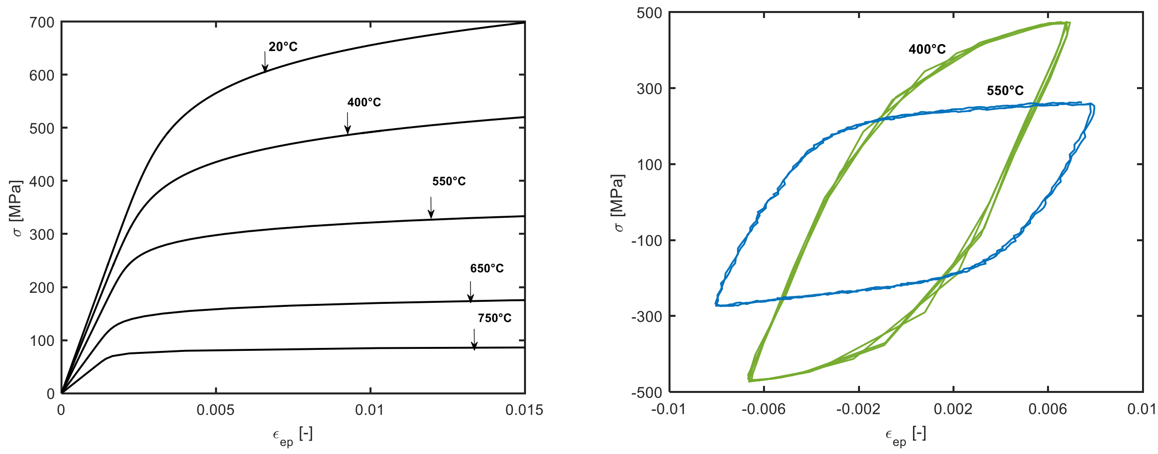

Fig. 1: Cyclically stable cyclic stress-strain curves and test hysteresis loops at mid-life.

Cyclic creep or relaxation curves are needed for time-dependent plasticity modelling. Visco-parameters have been assessed from LCF tests performed at two different strain rates at three selected temperatures. Viscoplastic approximation is proposed as a part of postprocessing step. Law of perfect viscoplasticity with the elastic domain, used for approximation, is defined as follows:

$$\dot{\varepsilon}_{vp} = \langle\frac{\sigma-k(T)}{K(T)}\rangle^{N(T)} \tag{1}$$

Where $k(T), K(t)$ and $N(T)$ are material and temperature dependent parameters.

3. Damage calculation

3.1. Fatigue damage

It has been shown, that commonly used and standardized rainflow method corresponds directly to elastoplastic material behavior and memory rules. Continuous damage calculation could be modelled using hysteresis operators.

First, nodal temperatures and equivalent stresses are transferred from elastoplastic FEA. Uniaxial total strain is assessed, expressed in the form of so-called Prandtl type operator. Subtracting viscoplastic strain from total strain using nonlinear strain controlled Maxwell model results in elastoplastic strain that contributes to fatigue damage. True stress can be expressed in the form of Prandtl type operator. For selected damage parameter, using linear damage accumulation, fatigue damage can be expressed as a total variation, representing cyclic fatigue damage evolution:

$$D_f(t_i) = \sum_{j=1}^{i} |\mathcal{D}(t_j) - \mathcal{D}(t_{j-1})| \tag{2}$$

$$\mathcal{D}(t_i) = \sum_{j=1}^{n_p} \gamma_j(T_i)P_{\gamma j}(t_i) \tag{3}$$

The damage parameter dependent play operator with general initial value is given as follows:

$$P_{\gamma j}(t_i) = max\left\{P(t_i) - p_j, min\left\{P(t_i) + p_j, \frac{\gamma_j(T_{i-1})}{\gamma_j(T_i)}P_{\gamma j}(t_{i-1})\right\}\right\} \tag{4}$$

Where the Prandtl densities $\gamma_j(T_i)$ and fictive yield damage parameters p_j in the range $j = 1, \dots, n_p$ could be derived explicitly from available temperature dependent damage parameter – life curves (fatigue curves). Damage parameter follows kinematic hardening and Masing memory rules.

3.2. Creep and total damage calculation

For a creep damage calculation widely accepted Robinson's rule (time fraction rule) is used:

$$D_c(t) = \int_0^t \frac{dt}{t_R(\sigma(t), T(t))} \tag{5}$$

Where t_R is rupture time for current stress and temperature. Total damage including creep, fatigue and oxidation is obtained as follows:

$$D(t) = D_c(t) + D_f(t) \tag{6}$$

4. Turbocharger housing lifetime predictions

Heat transfer coefficients have been determined experimentally from known temperature history from test stand. Transient thermal and elastoplastic FEA has been performed for whole model (coarse mesh) and for submodels in ABAQUS, too. Thermal shock with maximum temperature up to 600°C is considered.

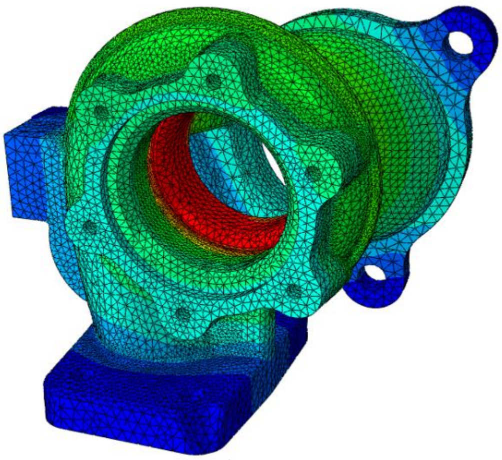

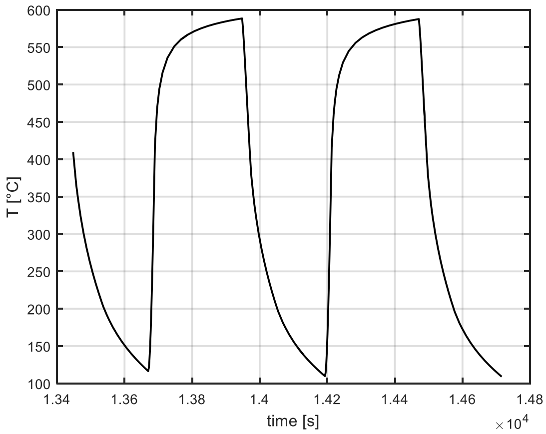

Fig. 2: Simulated thermal shock.

User C/C++ post-processing program with fast computation speed has been developed for viscoplastic approximation and damage calculation, implemented in ABAQUS. Critical zones for the turbine housing of the turbocharger subjected to thermo-mechanical fatigue and creep have been identified.

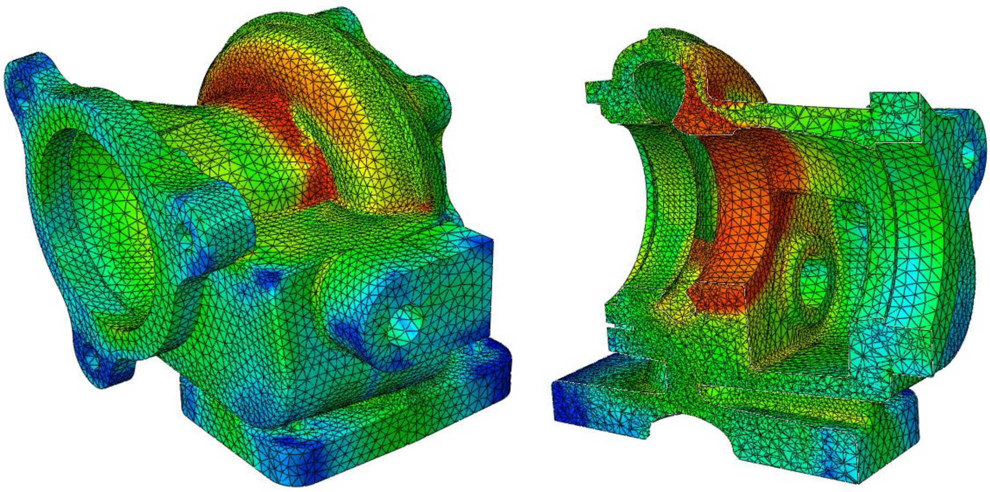

Fig. 3: Observed critical zones.

5. Conclusions

Proposed elastoplastic material model in FEA is capable of describing time independent behavior of the component. Viscoplastic approximation enables fast computation of viscous strain, using nonlinear Maxwell model. Critical zones for the turbine housing of the turbocharger have been identified according to simulated loading. Damage operator enables continuous damage calculation, which is especially suited for thermo-mechanical fatigue.

Future research will be directed especially to viscoplasticity modelling and multiaxial temperature dependent fatigue criterion. Also, other types of thermal loadings should be simulated on turbine housing of the turbocharger. Finally the results should be verified experimentally by partial destruction or total destruction of the component on the test stand.

Acknowledgement

The authors would like to acknowledge support from Technology Agency of the Czech Republic, grant No. TE01020020, and support from the Grant Agency of the Czech Technical University in Prague, grant No. SGS15/187/OHK2/3T/12.

References

ABAQUS/CAE 6.14. User's Manual, Online Documentation Help, Dassault Systemes.

Armstrong, P.J. & Frederick, C.O. (1996) A mathematical representation of the multiaxial Bauschinger effect,Central Electricity Generating Board & Berkeley Nuclear Laboratories, Research & Development Department, Berkeley.

Betten, J. (2002) Creep mechanics. Springer, Berlin.

Brokate, M., Dreßler K. & Krejči P. (1996) Rainflow counting and energy dissipation for hysteresis models in elastoplasticity. European Journal of Mechanics A/Solids, 15, 4, pp. 705–737.

Brokate, M. & Sprekels J. (1996) Hysteresis and Phase Transitions. Applied Mathematical Sciences, 121, Springer Verlag New York Inc., New York.

Chaboche, J.L. (1989) Constitutive equations for cyclic plasticity and cyclic viscoplasticity. International Journal of Plasticity, 5, 3, pp. 247-302.

Chaboche, J.L. (1993) Cyclic Viscoplastic Constitutive Equations, Part I: A Thermodynamically Consistent Formulation. Journal of Applied Mechanics, 60, 4, pp. 813.

Chaboche, J.L. & Jung, O. (1997) Application of a kinematic hardening viscoplasticity model with thresholds to the residual stress relaxation. International Journal of Plasticity, 13, 10, pp. 785-807.

Chouman, M., Gaubert, A., Chaboche, J.L., Kanouté, P., Cailletaud, G. & Quilici, S. (2014) Elastic-viscoplastic notch correction methods. International Journal of Solids and Structures, 51, 18, pp. 3025-3041.

Gosar, A. & Nagode, M. (2015) Dissipated energy-based fatigue lifetime calculation under multiaxial plastic thermo-mechanical loading. International Journal of Damage Mechanics, 24, 1, pp. 41-58.

Hosseini, E., et al. (2015) Temperature Dependent Representation for Chaboche Kinematic Hardening Model. Materials at High Temperatures, 32, 4, pp. 404-12.

Lemaitre, J. & Chaboche, J.L. (2000) Mechanics of Solid Materials. Cambridge University Press, Cambridge.

Nagode, M. (2014) Continuous damage parameter calculation under thermo-mechanical random loading. MethodsX, 1, pp. 81-89.

Nagode, M. & Fajdiga, M. (2007) Coupled elastoplasticity and viscoplasticity under thermomechanical loading. Fatigue & Fracture of Engineering Materials & Structures, 30, 6, pp. 510-519.

Nagode, M., Hack M. & Fajdiga, M. (2009) Low cycle thermo-mechanical fatigue: Damage operator approach. Fatigue & Fracture of Engineering Materials & Structures, 33, 3, pp. 149–160.

Nagode, M., Längler, F. & Hack M. (2011) Damage operator based lifetime calculation under thermo-mechanical fatigue application on Ni-resist D-5S turbine housing of turbocharger. Engineering Failure Analysis, 18, 6, pp. 1565–1575.

Norton, F.H. (1929) The creep of steel at high temperature. McGraw Hill, New York.

Penny, R.K. & Marriott, D.L. (1971) Design for creep. MacGraw Hill, London.

Visintin, A. (1994) Differential models of hysteresis. Springer-Verlag, Berlin.

22nd International Conference
ENGINEERING MECHANICS 2016
Svratka, Czech Republic, 9 – 12 May 2016

HEALTH MONITORING OF BUILDING STRUCTURES: PRELIMINARY CONSIDERATIONS ON A CASE STUDY

J. Bayer[*], S. Urushadze[**], P. Zíma[***]

Abstract: *Ageing, erosion, local damage or increase of the operating loads can decrease the reliability and load bearing capacity of building structures. Vibration monitoring may provide a promising solution of this problem, however robust health monitoring techniques are needed before wider practical applications. The presented analytical and experimental case study on a simple supported steel beam is an introductory practical investigation into this topic. It shows the sensitivity of chosen parameters to artificially induced damage and outlines possible directions or further research in conclusions. Special attention is paid to simultaneous monitoring of deformations and strains which can provide us with a useful information about the stress redistribution in monitored or tested structures.*

Keywords: Damage Detection, Dynamic Loading Tests, Modal Parameters, Relative Strain Vibration, Comparison of Analysis and Experiments

1. Introduction

Vibration monitoring of bridges, historical towers, high-rise buildings, dams or off-shore platforms are quite frequently cited in professional literature (e.g. Alampalli 2008, Foti 2012; Fujino 2010). These are usually case to case different research investigations which is far from standard use for health monitoring purposes. But the technological progress together with advances in theory promises new practical applications.

A very good overview about damage detection using vibration monitoring gives Doebling et al., 1989. A few authors point out (e.g. Padney 1991, Montazer 2014, Yu 2014) that measuring of strains (or strain modes) may provide a more sensitive parameters for damage detection than measuring just the displacements. This was also the incentive to focus beside the frequencies also on strains.

In the beginning there was a question if it is possible to indicate gradually increasing damage before the ultimate limit state (ULS) of bearing capacity is reached? As the answer to this question is not an easy one in general case a special case of a simple supported beam loaded to 60% of the ULS was chosen. Then a damage was induced at another place than where the maximum stresses from the dead load occurred. The damage was gradually increased in three stages until the ULS was reached at the damaged location.

The influence of the progressing damage on natural frequencies, transfer functions and strains was studied using numerical analysis and experiment.

2. Analysis

The investigated structure is shown on the Figure 1. It was made out of hollow steel profile 40/10mm, thickness 2mm. In the frequency band up to 100 Hz there are 8 natural frequencies, which means 5

[*] Ing. Jan Bayer, CSc.: ITAM AS CR, v.v.i., Prosecká 809/76, 190 00 Praha 9 bayer@itam.cas.cz
[**] Ing. Shota Urushadze.: ITAM AS CR, v.v.i., Prosecká 809/76, 190 00 Praha 9 urushadze@itam.cas.cz
[***] Ing. Pavel Zíma.: ITAM AS CR, v.v.i., Prosecká 809/76, 190 00 Praha 9 zima@itam.cas.cz

bending frequencies (three symmetrical and two anti-metrical). Under the dead load 60% of the first ultimate limit state was reached in the middle section. Than a damage was assumed 910 mm from the end of the beam in the form of a cut into the upper flange of the length 17, 28 and 34 mm subsequently. The calculation was made by the program ANSYS.

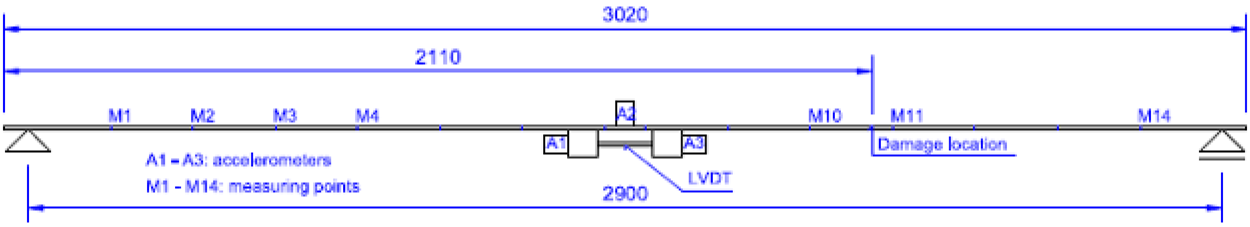

Fig. 1: The geometry of the structure

The changes of natural frequencies are presented in the Table 1. The relation of strains and displacement in the middle of the span (further designated as relative strains) and there changes are shown in the Table 2. The question is if the resolution of the measuring devices will be sufficient to reflect the damage also experimentally.

Tab. 1: Changes of natural frequencies due to the damage

bending modes	no damage	Damage DMG1 (cut 17 mm)		Damage DMG2 (cut 28 mm)		Damage DMG3 (cut 34 mm)	
	f 0,i [Hz]	f 1,i [Hz]	Δ1,i [%]	f 2,i [Hz]	Δ2,i [%]	f 3,i [Hz]	Δ3,i [%]
1	2,487	2,482	-0,17	2,471	**-0,61**	2,458	**-1,16**
2	14,38	14,34	-0,26	14,24	**-0,94**	14,1	**-1,78**
3	26,71	26,69	-0,07	26,64	-0,26	26,58	-0,49
4	54,02	53,99	-0,04	53,94	-0,15	53,9	-0,28
5	79,74	79,57	-0,21	79,14	**-0,75**	78,62	**-1,41**

Tab. 2: Changes of relative strains due to the damage

bending modes	no damage	DMG0	DMG1 (cut 17 mm)		DMG2 (cut 28 mm)		DMG3 (cut 34 mm)	
	f 0,i [Hz]	δ [m/strain]	δ [m/strain]	Δ1,i [%]	δ [m/strain]	Δ2,i [%]	δ [m/strain]	Δ3,i [%]
1	2,487	20,13	20,20	0,35 /**0,34**	20,37	1,22/**1,16**	20,59	2,31/**2,17**
2	14,38	2,921	0,830	-	1,152	-	1,227	-
3	26,71	0,928	0,927	-0,05/**-0,83**	0,927	-0,06/**-3,13**	0,927	-0,07/**-6,08**
4	54,02	1,726	0,251	-	0,228	-	0,216	-
5	79,74	0,166	0,167	0,26/**4,18**	0,168	1,00/**13,86**	0,170	1,92/**23,63**

The transfer function for the relative strains (see Fig.2) have a convenient property: it does not have extremes at the natural frequencies – it is monotonous which means that you can use for the comparison of changes the integral values around the natural frequencies. These values are written in bold in the Table 2 and it is obvious that these relative changes are much more sensitive to the damage than the discrete values on peaks which is promising from the monitoring point of view.

3. Experiments

Analytical results were verified also experimentally using two types of excitation: ambient vibrations simulated by stream of air pressure and deterministic excitation by hammer equipped with a load cell.

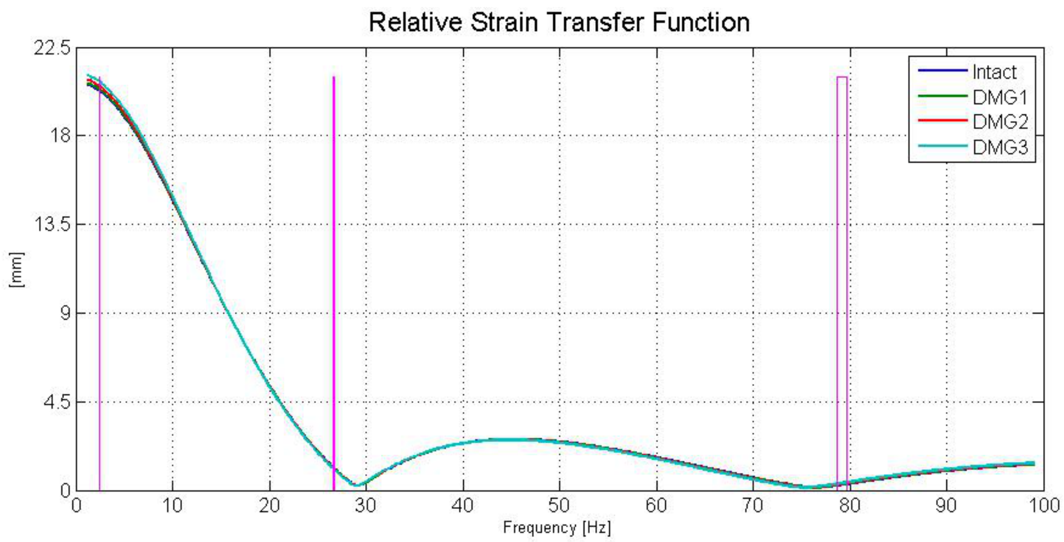

Fig. 2: The relative strain transfer function (displacement/strain)

Tab. 3: Changes of natural frequencies from the experiments

Bending modes	No damage	DMG1 (cut 17 mm)		DMG2 (cut 28 mm)		DMG3 (cut 34 mm)	
	f 0,i [Hz]	f 1,i [Hz]	Δ1,i [%]	f 2,i [Hz]	Δ2,i [%]	f 3,i [Hz]	Δ3,i [%]
1	1,962	1,955	-0,36	1,952	-0,51	1,945	-0,87
2	13,277	13,277	0,00	13,17	-0,80	13,1	**-1,63**
3	25,99	26,05	0,20	26,03	0,13	25,94	-0,19
5	78,65	78,57	-0,10	78,20	-0,57	77,52	**-1,43**

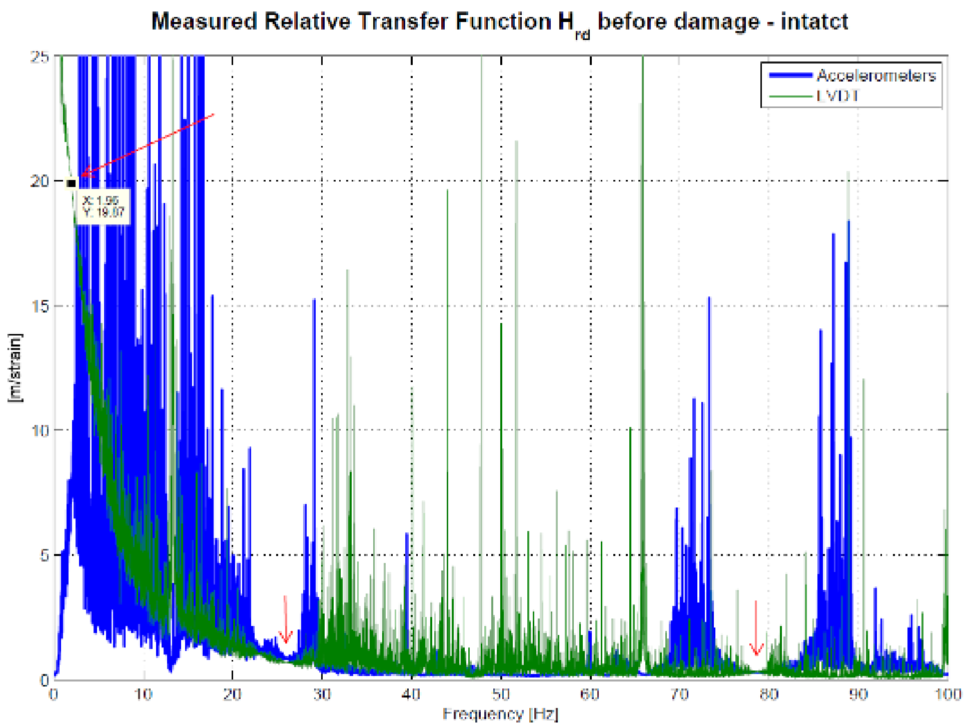

Fig. 3: Measured relative transfer function between the displacements and strains

There were no essential differences between the two sets of experimental results, therefore just the evaluation from “ambient” vibrations is presented here. The changes of natural frequencies from experiments are presented in the Table 3. The whole spectrum of frequencies was lower than the calculation but because the relative changes were of interest the model was considered to be sufficient and was not updated to the experimental results. Both experimental methods proved to be sensitive enough to reflect the stages of the progressing damage. So the measurement of natural frequencies could indicate the “dangerous” condition before the ultimate limit state would be reached.

The strains were measured as displacements on the basis of 20 cm with an LVDT-0,5mm sensor. There was also made an attempt to measure the displacements with two accelerometers. The arrangement can be seen in the Fig.1. The measured transfer function between displacements and strains corresponding to the one in Fig.2 is plotted in the Fig. 3. The measurement of displacements on low levels is covered by noise. Nevertheless, in the vicinity of frequency peaks, (marked with red arrows in the Fig. 3) the level of noise much lower. But in spite of it and of the promising theoretical premises the measurements of changes of relative strains hasn´t been quite successful until now because of very low levels of measured displacements.

4. Conclusions

The experiments confirmed that natural frequencies were sensitive enough to warn in time before the ultimate limit state would be reached in the chosen case.

The relation of displacements and strains represents a quantity that is sensitive to damage and thus promising from the health monitoring point of view, however it is quite difficult to measure.

It is desirable that the vibration measurements provide a save prevention against damage in any location which is going to be the direction of future investigations. A damage localization using dynamic test is also the next planned research program. The measurement uncertainties coming from various sources like environmental effects, limits of equipment applied etc. is another field that imposes limits on health monitoring of building structures and has therefore be focused on before practical applications.

Acknowledgement

There is very appreciated the sponsorship by the grant GAČR 15-01035S and institutional support RVO 68378297. Many thanks also to my colleges in ITAM, who helped me to carry out the experiments.

References

Alampalli S., Ettouney M. (2008) Role of structural health monitoring in bridge security, Bridge Structures, Vol. 4, No. 3–4, September–December 2008, p.143–154.

Doebling S.W., Farrar Ch.R., Prime M.B. (1998) A Summary review of vibration-based damage identification methods, The Shock and Vibration Digest 03/199.

Foti D., Diaferio M., Giannoccaro I.N., Mogelli M, (2012) Ambient vibration testing, dynamic identification and model updating of a historic tower (2012), NDT&E International 47, p. 88-95.

Fujino Y., Siringoringo D. M., Nagayama T., Su D., (2010) Control, simulation and monitoring of bridge vibration – Japan´s recent development and practice, IABSE-JSCE Joint conf. on Advances in Bridge Engineering-II, August 8-10, Bangladesh, ISBN: 978-984-33-1893-0, p.61-74.

Montazer M., Seyedpoor,S.M. (2014) A New Flexibility Based Damage Index for Damage Detection of Truss Structure, Shock and Vibration, Vol. 2014, March.

Pandey, A.K., Biswas, M., Samman, M.M. (1991) Damage detection from changes in curvature mode shapes, Journal of Sound and Vibration, 2/1991.

Yu Ch-P. , Chia-Chi Cheng Ch., Ke Y., Chih-Hung Chiang Ch., Pan Ch., (2014) Damage Assessment of Bridges with Continuous Spans by Curvature Data Derived from Displacement Responses under Moving Truck Loading, 11th European Conference on Non-Destructive Testing (ECNDT 2014), October 6-10, 2014, Prague, Czech Republic.

22nd International Conference
ENGINEERING MECHANICS 2016
Svratka, Czech Republic, 9 – 12 May 2016

THE IMPACT OF SHAPE ADJUSTMENTS OF A VALVE CHAMBER ON LOSSES IN THE CONTROL VALVE OF THE STEAM TURBINE

L. Bednář[1], L. Tajč[2], M. Miczán[3], M. Hoznedl[4], P. Kočárník[5], S. Jirků[6]

Abstract: *Computational study of pressure and energy losses in the control valve of the steam turbine is carried out. The impact of misalignment of a valve cone toward the valve chamber while changing the width of a parting rib in the chamber is assessed. The impact of the dimensions of the valve chamber on losses is examined. An optimal solution to misalignment of a valve cone, dimensions of the valve chamber and the width of a parting rib is established.*

Keywords: Steam turbine, control valve.

1. Introduction

There are certain practices, recommendations and rules for designing dimensions and shapes of the valve chamber of control valves. DOOSAN ŠKODA POWER applies rich historical experience in constructing control valves. The findings from experiments on models of valves are implemented too. Experience from the valve operations in power stations is considered as well. It is always necessary to harmonize the requirement of minimum losses in the particular operation of the turbine with the reliable and safe operation during the start-up and the reduced performance of the turbine. Current computational possibilities enable examination of some recommendations as well as certain practices in terms of their impact on energy losses. They enable assessment whether there are also certain reserves of shape adjustments of the chamber which would lead to minimization of losses. Based on analysing published data the Czech Technical University in Prague conducted a computational study focused on assessing different connections to the different shape adjustments of the chamber valve and formation of pressure losses in the valve chamber and the output diffuser [Kočárník, 2011]. Computations are confined to operating at full valve opening.

2. Impact of the energy loss in the valve on reducing the turbine output

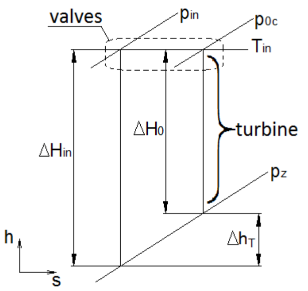

Fig. 1: Process of throttling steam when TV and CV valves are fully opened and expansion on the turbine

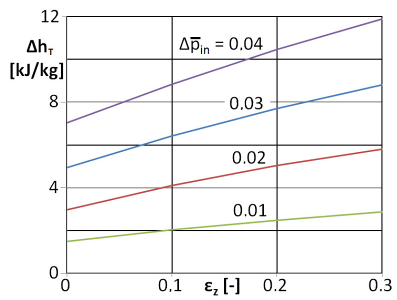

Fig. 2: Reduction of enthalpy drop in valves depending on the pressure loss $\Delta p/p_{in} = 0{,}03 \; (p_{in} = 13 \; MPa, \; t_{in} = 545 \; ℃)$

[1] Ing. Lukáš Bednář: Doosan Škoda Power s. r. o., Tylova 1/57, 301 28 Plzeň; CZ, lukas.bednar@doosan.com
[2] Ing. Ladislav Tajč, CSc.: University of West Bohemia, Univerzitní ul. 8, 306 14 Plzeň; CZ, ladislav.tajc@doosan.com
[3] Ing. Martin Miczán: Doosan Škoda Power s. r. o., Tylova 1/57, 301 28 Plzeň; CZ, martin.miczan@doosan.com
[4] Ing. Michal Hoznedl, Ph.D.: Doosan Škoda Power s. r. o., Tylova 1/57, 301 28 Plzeň; CZ, ladislav.tajc@doosan.com
[5] Ing. Petr Kočárník, PhD.: ČVUT Praha, Technická 2, A3-516a, 166 27 Praha 6 - Dejvice; CZ, kocarnik@fel.cvut.cz
[6] Doc. Ing. Slavomír Jirků, CSc.: ČVUT Praha, Technická 2, A3-516a, 166 27 Praha 6 - Dejvice; CZ, jirku@fel.cvut.cz

The requirement to reduce losses in the valve is related to its impact on the loss of the turbine output. The process of throttling the steam in the tripping valve (TV) and the control valve (CV) is presented in fig. 1.

The energy loss of the turbine depending on the pressure loss in the valve can be expressed as:

$$\Delta h_T = \frac{k\, RT_{in}}{k-1}\left[\left(\frac{p_z}{p_{oc}}\right)^{\frac{k-1}{k}} - \left(\frac{p_z}{p_{in}}\right)^{\frac{k-1}{k}}\right] \tag{1}$$

p_z is the pressure behind the high pressure (HP) part of the turbine, k is isentropic exponent.

If we apply designation $\varepsilon_z = p_z/p_{in}$ and $\Delta\overline{p}_{in} = \left(p_{in} - p_{oc}\right)/p_{in}$, thus we get for the energy loss:

$$\Delta h_T = \frac{k\, RT_{in}}{k-1}\,(\varepsilon_z)^{\frac{k-1}{k}}\left(\frac{1}{(1-\Delta\overline{p}_{in})^{\frac{k-1}{k}}} - 1\right) \tag{2}$$

The unexploited turbine output is specified using the formula $N = \dot{m}\Delta h_T \eta$, where $\dot{m}$ is the mass flow through HP part of the turbine and η is its efficiency.

The energy loss in the valve for the different pressure conditions ε_z on HP part of the turbine and for the proportional pressure loss in the valve $\Delta\overline{p}_{in}$ is shown in fig. 2. Formation of the unexploited turbine output is related to it in fig. 3. The proportional pressure loss in the valve is very important. According to results of measurement on the type version of a balance control valve [Mackovič & Němec, 2012] and on stop valve [Tajč & al., 2005] this loss is cca 3 % of the inlet total pressure. In the control valve itself the loss generates at the level of 2 %. The resulting pressure loss can be effected by the choice of valve dimensions. The performed computational study could clarify whether there is another possibility how to reduce this loss.

3. Computations of losses in the valve at a rated operation of the turbine

Scheme of the layout of the valve chamber is shown in fig. 4. A valve parting rib having the width A shall stabilize the flow in the valve chamber and support the formation of two symmetrical flows entering the diffuser under the cone. Its importance was experimentally confirmed in various works [Kamyrin & Revzin, 1954; Robozev, 1963]. Formation of two vortices under the cone is connected to the flow bend by 90°. The screen, which prevents strange particles from penetrating from the boiler to the turbine, contributes to reducing formation of vortices.

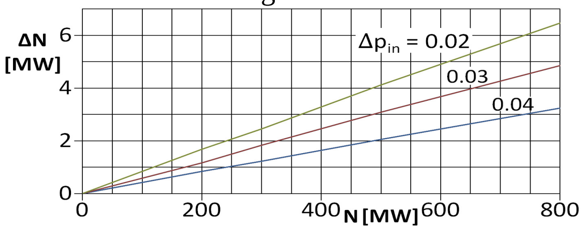

Fig. 3: Impact of the pressure loss in the valve on the loss of turbine performance

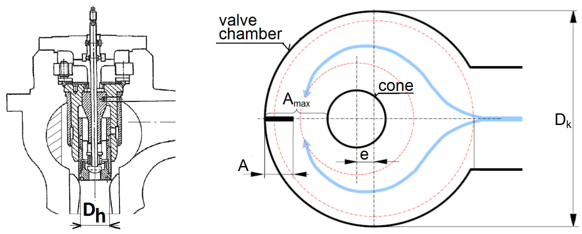

Fig. 4: Scheme of the valve chamber

Velocity conditions in the valve chamber are affected by misalignment of the valve towards the valve chamber. When there is an inappropriate ratio between the valve chamber diameter and the diffuser throat diameter, complicated circulating flows are related to the increase in pressure loss which may arise [Kamyrin, 1969]. Therefore, the basic version of computation studies focused on assessing the impact of a rib and misalignment of the valve on the size of the loss coefficient. An optimal size of the valve chamber was researched too.

The loss coefficient may be evaluated as the proportion of the pressure loss to the dynamic pressure in the inlet pipes:

$$\zeta_A = \frac{p_1 - p_2}{\frac{1}{2}\rho c_{1ax}^2} - \frac{c_{2ax}^2 - c_{1ax}^2}{c_{1ax}^2} \tag{3}$$

It may also be elaborated as the difference between input and output energy related to the kinetic energy in the input section:

$$\zeta_B = \frac{E_z}{E_{k1}} = \frac{E_{k1} + E_{p1} - (E_{k2} + E_{p2})}{E_{k1}} \tag{4}$$

The kinetic as well as potential energy E_k and E_p is included. The advantage of numerical computations is also the possibility to map the dimensionless components of velocity as well as components of energy in the entire channel. Computation study is based on the assumption of input velocity $c_{in} = 50\ m/s$ with the volume flow $1.272\ m^3/s$.

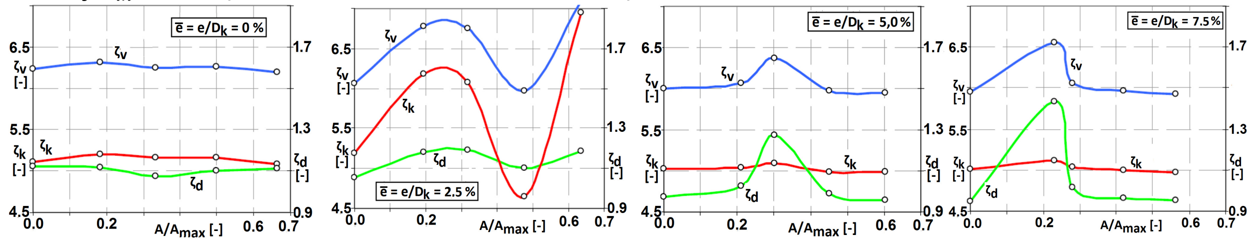

Fig. 5: The energy loss in the valve

Fig. 5 shows the course of the energy loss coefficient of the valve ζ_v, the valve chamber ζ_k and the diffuser ζ_d. In the diffuser, its path from the throat at the entry to the follow-up pipes is considered. It is shown that in a certain configuration of valve misalignment and the size of the rib, the loss coefficient of the valve increases. In small misalignment ($\bar{e}$ = 2.5 %) the loss in the valve chamber increases. In misalignment $\bar{e}$ = 5 and 7.5 % the loss in the diffuser increases. It is essential that the minimum value of the loss coefficient of the valve virtually does not differ from the layout with zero misalignment and without a rib. In a fully open valve the loss in the valve chamber is always bigger than the loss in the diffuser section.

Fig. 6 shows the values of loss coefficients as the function of eccentricity e for the variant with a zero width of the rib. There is also presented the minimum value ζ_{vmin} for optimal dimensions of a rib. ζ_{vmax} appears to be for the least appropriate dimensions of a rib. It is evident that omission of a rib has no significant effect on the final value of the loss coefficient. The losses are reduced by the increase of the eccentricity. The eccentricity of 7.5 % is optimal. The flow in the diffuser mainly contributes to the drop of the loss coefficient. Misalignment of the valve toward the valve chamber has no significant impact on the irregularity in velocity distribution in the valve. Their course for a throat and exit from the diffuser is shown in fig. 7. Irregularities of velocity equalise between the throats to the end of the diffusor.

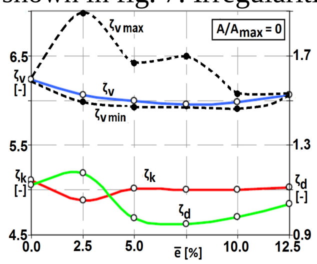

Fig. 6: Courses of loss coefficients

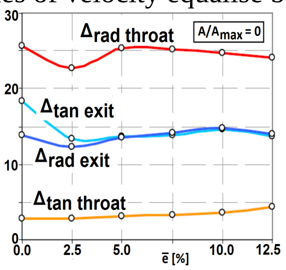

Fig. 7: Irregularities of flow distributions

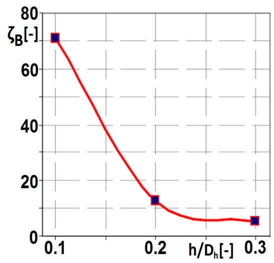

Fig. 8: Loss coefficient of the valve

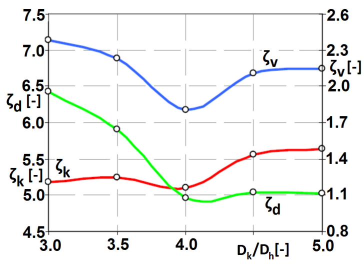

Fig. 9: Impact of the chamber diameter on the losses

A computation study was also undertaken. It focused on determining the loss coefficients in the valve with the misalignment of 10 % with applying a rib and without a rib [Kočárník, 2010]. The dimensions of the valve chamber and a rib correspond to the valve which is ready for experimental verification. The results of computations for misalignment of 0 and 10 % are processed in table 1.

Table 1: Results of computations for misalignment of 0 and 10 % with a rib and without it

variant	rib	ζ_A [-]	ζ_B [-]	η [%]	$\bar{c}_{tan}$ [%]	$\bar{c}_{rad}$ [%]	$\bar{E}_{ktan}$ [%]	$\bar{E}_{krad}$ [%]	Δc_{ax} [%] Tangential course	Δc_{ax} [%] Radial course
1	no	6.77	6.18	30.70	1.10	4.30	0.30	0.40	25.10	38.50
$\bar{e}$ = 0 %	yes	6.86	6.21	31.00	0.50	4.60	0.40	0.50	27.30	39.20
2	no	6.54	5.91	32.30	15.80	4.30	0.30	0.50	28.00	42.30
$\bar{e}$ = 10 %	yes	6.56	5.08	33.30	0.00	4.30	0.20	0.60	30.10	41.80

The lowest values of loss coefficients are shown by variant 2. $\bar{c}^*_{tan}$ and $\bar{c}^*_{rad}$ are dimensionless mean tangential and radial components of velocity standardized to the mean value of an axial component of velocity $\bar{c}^{*}_{ax}$.Mean values of the dimensionless kinetic energy in tangential course and radical course $\bar{E}^{*}_{ktan}$ a $\bar{E}^{*}_{krad}$ are standardized by the mean value of the kinetic energy in axial course $\bar{E}^{*}_{kax}$

For the other variant with a rib, for three values of a relative lift of the cone is created the characteristics of the valve $\zeta = \zeta(h/D_h)$. Computed parameters are shown in table 2, course of the loss coefficient is shown in fig. 8.

Table 1 also shows the mean square error of the distribution of an axial component of velocity $\Delta\bar{c}^{*}_{ax}$ for a specified course. Average values of velocity components and the kinetic energy are relating to the output cross-section of the diffuser. Although the kinetic energy in the output is based on the axial course of the flow, the value of the loss coefficient ζ_B with the precise calculation is by cca 1.5 % lower than the value ζ_A. The differences between the variant 1 and 2 are according to the values ζ_B insignificant. When assessing the adjustments of the chamber according to parameter ζ_A the difference comes up to 1 %. It is also confirmed by the difference of efficiency, which is up to 3 %. Efficiency is defined as the ration between output and input energy.

Table 2: Computed parameters of the other variant with a rib

h/D_h	ζ_A	ζ_B	η	$\bar{c}^{*}_{tan}$	$\bar{c}^{*}_{rad}$	$\bar{E}^{*}_{ktan}$	$\bar{E}^{*}_{krad}$	Δc^{*}_{ax} [%]	
[-]	[-]	[-]	[%]	[%]	[%]	[%]	[%]	Tangential course	Radial course
0.1	74.1	70.8	6.3	0.5	4.7	0.4	0.3	30.5	77.6
0.2	13.2	12.8	16.5	0.5	2.8	0.0	0.2	11.8	28.3
0.3	6.56	5.08	33.3	0.0	4.3	0.2	0.6	30.1	41.8

With the lift declining and reducing the flow area in the valve, the value of the loss coefficient increases. For this computation, the assessment of the loss itself in the valve chamber and the diffuser was not performed. It is highly probable that the increase of the losses is related to the velocity conditions in the diffuser. The accuracy of the choice of the diameter D_k of the valve chamber was checked. In practice, the ratio D_k/D_h an interval from 3.3 up to 4.3 is recommended. Therefore, for verification five models with the ratio $D/D_k = 3; 3.5; 4; 4.5;$ 5 were built. Courses of the loss coefficient are shown in fig. 9. From the computations it is clear that the minimum value of the loss coefficient roughly corresponds to the value of the ratio $D_k/D_h = 4$, for lower values the losses in the output diffuser increase significantly, in higher values the loss in the valve chamber increases.

4. Conclusions

The energy loss in the valve reduces the turbine performance. It is desired that in the design operating conditions of the turbine the pressure or energy loss in the valve would be minimized. Installation of a rib in the valve chamber may reduce, but may also significantly increase the value of the loss coefficient of the valve. After omitting a rib its value is comparable with its minimum value ζ_{vmin}. Misalignment of the valve toward the valve chamber helps to reduce losses. The eccentricity of 7.5 % is the most appropriate. The diameter of the valve chamber has impact on the losses. $D_k/D_h = 4$ is optimal. Under non-designing operating conditions the reduction of the pressure in the valve is desirable. The increased value of the loss coefficient is probably related to the increase of the losses in the diffuser, where the effect of the abrupt change of the cross-section is applied.

References

Камырин В. И. (1969) О характере движения пара в клапанной каробке. Энергомашиностроение, № 11, с. 38 - 49.

Камырин В. И. & Ревзин Б. С. (1954) Снижение потерь давления в регулирующих клапанах турбин высокого давления, Энергомашиностроение, № 1.

Робожев А. В. (1963) К вопросу о снижении потерь давления в регулирующих клапанах паровых турбин, Тр. МЭИ, Вып. 47, с. 117 – 127.

Kočárník P. (2011) Výpočty tvaru ventilové komory při použití dvou tečných vstupů, vliv vyosení výstupu a přepážky, výpočty reálné geometrie ventilu. Zpráva č. 43/100018/13114.

Mackovič M. & Němec M. (2012) Proměření vlastností záchytného ventilu. Výzkumná zpráva VZLU, R-5365.

Tajč L., Bednář L., Poskočilová M. &, Krejčík J. (2005) Regulační ventily parních turbín. Výzkumná zpráva ŠKODA POWER, VZTP 0974.

Kočárník P. (2010) Výpočtová studie tlakových ztrát ve ventilové komoře, optimalizace ventilové komory. Zpráva č. 43/100004/13114.

22nd International Conference
ENGINEERING MECHANICS 2016
Svratka, Czech Republic, 9 – 12 May 2016

EXPERIMENTAL ANALYSIS OF SLENDER HPC COLUMNS AT THE STABILITY FAILURE

V. Benko[*], T. Gúcky[**], P. Kendický[***], M. Čuhák[****]

Abstract: *The European standard for design of compressed concrete members allows the use of non-linear calculations. The required reliability within design of slender members subjected to axial force and bending moment is not yet satisfyingly verified and confirmed for cases when the buckling failure precedes the breach in the critical cross-section. In order to verify and compare the reliability of the standard design methods, a comparison with experiment results is necessary. In cooperation with STRABAG Bratislava LTD, the Faculty of Civil Engineering at the Slovak University of Technology in Bratislava, carried out an applied research covering an experimental verification of slender high-performance concrete columns. In the following paper, the authors present the preparation and progress of the third series of experimental verifications for six slender high-performance concrete columns of the concrete strength class C80/95. The reinforcement and shape of the columns together with the initial eccentricity of axial force were designed so that the columns fail due to stability loss before reaching the resistance in the critical cross-section.*

Keywords: Slender columns, concrete, stability failure, experiment, reliability

1. Introduction

Within the design of concrete members which are subjected to axial force and bending moment, it is often important to take the second order effects into account. Current European standard (EN 1992-1-1, 2004) offers three methods of second order analysis. Namely, a general method, based on non-linear analysis, and two simplified methods: Method based on nominal stiffness and Method based on nominal curvature.

The increase of total bending moment within the critical cross-section is markedly influenced by slenderness of the column (Koenig et al., 1997; Koteš & Vičan 2013; Pfeiffer & Quast, 2003). The increase of total eccentricity due to increase of axial force may be so significant, that the buckling failure of compressed concrete members occurs inside the domain of the cross-section's design interaction diagram M-N, considerably earlier before the design resistance in the critical cross-section is reached (Benko et al., 2015; Fillo et al., 2013). In such cases, the partial factors of materials cannot apply and do not contribute to the overall reliability. Therefore, defining a partial reliability factor for buckling failure of compressed concrete members is appropriate.

2. Geometry, reinforcement, fabrication and materials of the tested columns

The tested columns were of a rectangular cross-section with dimensions of 240 x 150 mm. Total length of the columns, including spread steel plates and steel heads, was 3890 mm. Both ends of the columns were inserted into a press with a hinged connection. Steel heads, 25 mm thick, ensured the initial eccentricity e_1 = 40 mm (Fig. 1).

[*] Prof. Dipl.-Ing. Dr. Vladimír Benko, PhD.: Faculty of Civil Engineering, Slovak University of Technology, Radlinského 11; 810 05, Bratislava; SK, vladimir.benko@stuba.sk

[**] Ing. Tomáš Gúcky: Faculty of Civil Engineering, Slovak University of Technology, Radlinského 11; 810 05, Bratislava; SK, tomas.gucky@stuba.sk

[***] Ing. Peter Kendický: Faculty of Civil Engineering, Slovak University of Technology, Radlinského 11; 810 05, Bratislava; SK, peter.kendicky@stuba.sk

[****] Ing. Marek Čuhák, PhD.: Self-employed, Hviezdoslavova 63; 956 31, Krušovce; SK, marek.cuhak@gmail.com

Fig. 1: Steel head for ensuring of initial eccentricity

The columns were reinforced with four bars with diameter of 14 mm. In the critical places, the longitudinal reinforcement was supplemented with additional bars of 14 mm in diameter and 600 mm in length, which were at each end welded to spread steel plates with thickness of 20 mm. The amount of stirrups with diameter of 6 mm was doubled for the places with additional longitudinal reinforcement in order to increase the resistance of ending parts in the columns, as a local failure in these locations can precede the buckling failure (Fig. 2). The concrete cover of stirrups was 20 mm.

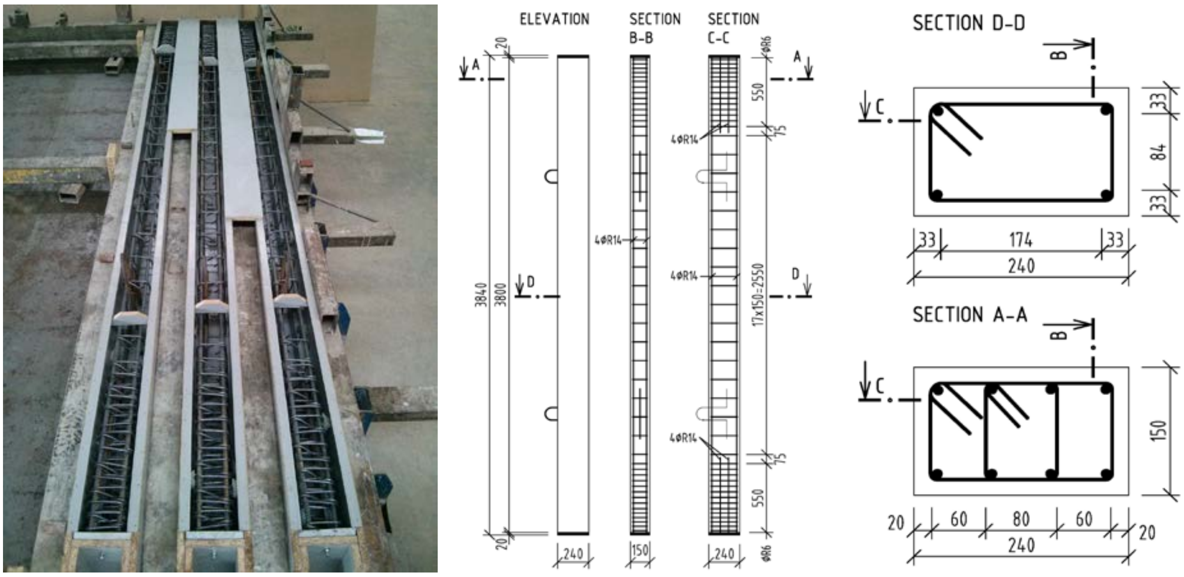

Fig. 2: The shape and reinforcement of columns for S3 series (λ=89)

Thirty testing samples were made during the production of columns - cylinders, cubes and prisms were to be checked for the standard concrete characteristics both after 28 days and at the actual time of testing of columns. After completing the tests of columns, core samples for testing concrete material characteristics were taken (Fig. 3). The evaluation of the material tests proved the concrete strength class C80/95.

Fig. 3: The core samples for testing of concrete material characteristics

3. Experimental verification

The slender concrete columns were tested in the laboratory of Faculty of Civil Engineering SUT in Bratislava (Fig. 4). The diagrams of tested columns within S3 series and calculated columns by non-linear methods are shown in Fig. 5. Diagram on the left shows the relation between axial force and bending moment while taking the second order effects into account. Curves "S3-1" – "S3-6" show M-N relation of tested columns, curves "Stab2D-NL" and "NL Method" show M-N relation of calculated columns, while first column (red curve) was calculated in non-linear software Stab2D-NL and second column (green curve) was calculated in one's of the authors own software based on non-linear calculations. The diagram on the right side shows ε - N relation on both sides of cross-section.

Fig. 4: Column testing (on the left), column after failure (on the right)

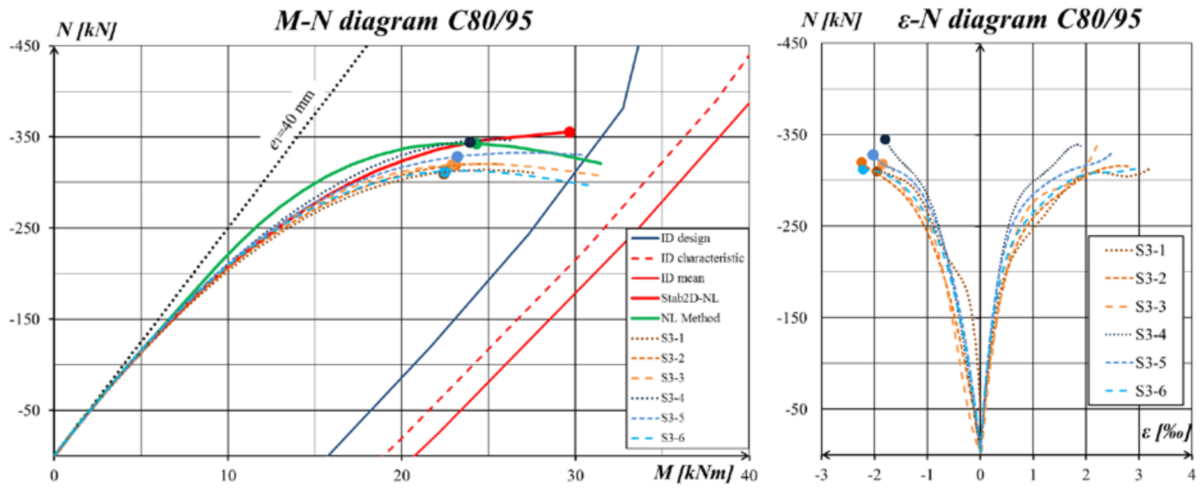

Fig. 5: Bending moment – axial force diagram (on the left), b) strain – axial force diagram (on the right)

4. Summary

The experimental analysis confirmed the predictions of the authors. The buckling failure of slender concrete columns occurred in the domain of the design interaction diagram of the column cross-section much earlier than the designed resistance of critical cross-section was reached. The compressive strain at the collapse of the columns was around 2 ‰ (Fig. 5). In such cases the definition of partial reliability factor for stability failure would be appropriate, as the partial factors of materials could not be put into effect. The importance of right definition of partial reliability factor for stability failure of compressed members is increased by the fact that the buckling failure occurs without warning. It is a brittle failure which requires higher overall reliability than the signalized failures.

Acknowledgement

This work was supported by the Scientific Grant Agency of the Ministry of Education of Slovakia and the Slovak Academy of Sciences VEGA under the contract No. 1/0696/14. We also thank the company STRABAG Bratislava LTD for the cooperation and for their aid at the production of the columns and the testing samples.

References

Benko, V., Kendický P., Križma M., Kišac M. & Beleš I. (2015) Overall Reliability of the Concrete Columns in Case of Stability Loss. In Advanced Materials Research Vol. 1106 pp 229-232, ISSN 1022-6680

EN 1992-1-1: Eurocode 2: Design of concrete structures - Part 1-1: General rules and rules for buildings (2004)

Fillo, L., Čuhák, M. & Porubský, T. (2013) Reliability of Asymmetrically Reinforced Columns. In: Concrete and Concrete Structures, Conference Vrátna SK pp 387-392

Koenig, G., Tue, N. & Ahner, C. (1997) Non-linear analysis. Lausanne, Switzerland: fib - International Federation for Structural Concrete

Koteš, P. & Vičan, J.(2013) Reliability levels and partial safety factors according to eurocodes for evaluation of existing bridges. IABSE, ISBN 978-3-85748-123-9

Pfeiffer, U., Quast, U. (2003) “Nichtlineares Berechnen stabförmiger Bauteile” Beton- und Stahlbetonbau, vol. 98, pp. 529–538

22nd International Conference
ENGINEERING MECHANICS 2016
Svratka, Czech Republic, 9 – 12 May 2016

INJECTION OF LIQUID LPG THERMODYNAMICS

S. Beroun*, P. Brabec**, A. Dittrich***

Abstract: *This paper explains the events that accompany the injection of liquid LPG into the intake air in the intake manifold of an engine. A simple calculation shows that the injection of liquid LPG is associated with extremely low temperatures injected LPG and icing on the outflow nozzle. The results of experimental research on vehicle spark-ignition engine with the formation of the mixture by injecting liquid LPG into the engine intake manifold demonstrate that the anti-icing on the discharge nozzle requires optimization for reliable construction embodiment of the end of the injector. In conclusion, the article summarizes the findings from previous research injection of liquid LPG into the engine intake manifold.*

Keywords: Injection, liquid LPG, SI engine, thermodynamics, optimization.

1. Introduction

Fuel systems of automotive gasoline LPG engines usually works with the formation of a mixture of vaporized LPG blowing into the intake tract of the engine, and in this embodiment, the spark-ignition engine operating on LPG lower output by about (5-8)% versus engine operation on petrol. The cause of decrease of the engine power is to reduce the amount of intake fresh air due to the volume of gaseous fuel in the intake mixture. Prospective solution mixture formation by injecting liquid LPG into the intake air, which reduces the temperature of the intake mixture increases the volumetric efficiency of the motor and ensures during operation with LPG the same or even better performance than when running on petrol. Effect very rapid evaporation of the injected liquid LPG however arises in the intake tract of the engine icing (wet steam LPG has a discharge nozzle injector temperature below freezing, about -30 to -40 °C) which was breaking off and clogging intake air into the engine cylinders which causes occasional misfire. Trouble-free operation of the gasoline engine with injection liquid LPG must therefore be designed in such a solution provided the injection of liquid LPG to the engine intake manifold (generally the engine) to prevent icing of the outlet nozzles or injectors in the intake manifold.

2. Injection of liquid LPG into the engine intake manifold

A configuration diagram of the injection of liquid LPG shows a sketch of FIG. 1. Injector liquid LPG is formed by a solenoid valve (EV), from which the LPG in batches (synchronized with inlet of each cylinder of the engine) is introduced into the end portion of the injector (EPI) in the intake manifold to the individual cylinders (concept MPI). After the effluent from the LPG EV occurs due to a significant drop in pressure of LPG in the EPI to the very rapid evaporation of a portion of LPG: the heat required for evaporation is removed from the thermal energy supplied to the LPG EPI and a small proportion of the evaporation of LPG the heat transmission from the environment into the EPI. Into the intake air is injected wet steam LPG, which is due to intensive evaporation of LPG in the EPI very low temperature. Simplified computational modeling processes EPI were screened connection geometry flow channel state variables LPG EPI and during the injection of liquid LPG to the engine intake manifold. Solution procedure changes the status of LPG in the EPI briefly described in the following paragraphs.

* prof. Ing. Stanislav Beroun, CSc.: Institute for Nanomaterials, Advanced Technology and Innovation, Technical University at Liberec, Studentská 1402/2; 140 00, Liberec; CZ, stanislav.beroun@tul.cz

** Ing. Pavel Brabec, Ph.D.: Institute for Nanomaterials, Advanced Technology and Innovation, Technical University at Liberec; Studentská 1402/2; 140 00, Liberec; CZ, pavel.brabec@tul.cz

*** Ing. Aleš Dittrich: Institute for Nanomaterials, Advanced Technology and Innovation, Technical University at Liberec; Studentská 1402/2; 140 00, Liberec; CZ, ales.dittrich@tul.cz

Delivery of liquid LPG is injected during dose supplied by a solenoid valve EV of elementary amounts $\Delta m_{LPG/liq}$ in EPI. The whole volume of the channels V_{BON} before the discharge orifice portion of LPG in the channels EPI evaporated portion remains in the liquid state and in the state arises EPI wet steam LPG. The density of wet steam can be expressed as the sum of the density of saturated vapor (gas) LPG and density of droplets dispersed in the volume V_{BON} channels EPI:

$$\rho_{LPG/V_{BON}} = \rho_{LPG/gas/V_{BON}} + \rho_{LPG/liq/V_{BON}} \quad (1)$$

The share of vaporized LPG in the channels of EPI determines the heat balance in the state of LPG EPI. The density of the gaseous phase in the volume of LPG V_{BON} depends on pressure and temperature LPG EPI (volume V_{BON}):

$$\rho_{LPG/gas/V_{BON}} = \frac{p_{LPG/V_{BON}}}{r_{LPG} \cdot T_{LPG/V_{BON}}} \;. \;(2)$$

The density of the liquid phase in EPI represent LPG droplets dispersed throughout the volume V_{BON}. To express the proportion of vaporized LPG was introduced in EPI equation for the density of wet steam, LPG:

$$x = k_{evapor} \cdot \left(1 - \frac{\rho_{LPG/V_{BON}}}{\rho_{LPG/liquid}}\right) \;(3),$$

$$\rho_{LPG/liquid} \cong 550 kg/m^3 \;(4).$$

The size of the correction factor evaporation k_{evapor} is determined by calibrating the model calculation using measured during wet steam pressure of LPG in the EPI. (Cengel et al., 2008, Šesták et al., 2004)

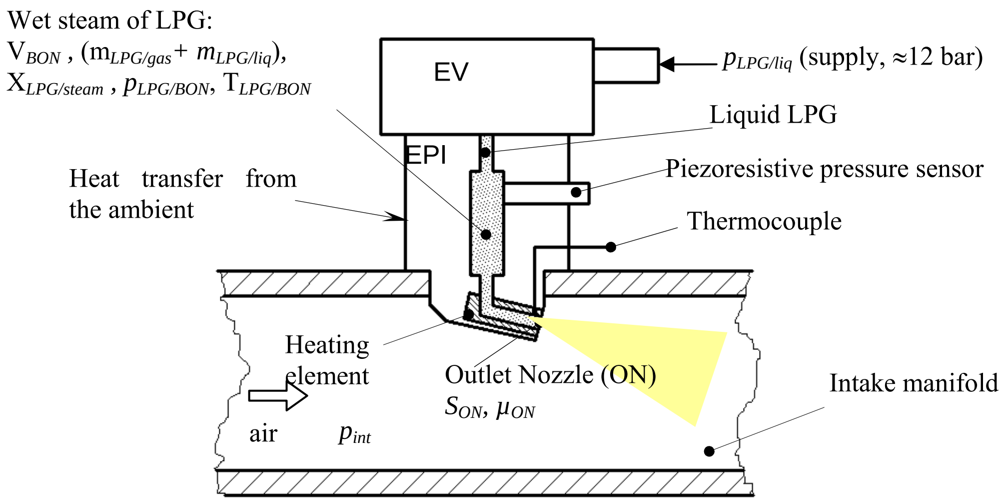

Fig. 1: The scheme of the injector for the liquid LPG injection. Heating element (HI) in the bottom of the EPI provides only heating the outlet nozzle (measures against freezing of the nozzle), heat transmission from HI to EPI EPI structure is minimized.

Heat balance for wet steam LPG EPI includes items (Beroun et al., 2013):

-Heat in the LPG (LPG_{liq} + LPG_{gas}) at the beginning of each calculation step $\Delta\tau$ (0.2 ms) in EPI.

-Heat the feed liquid LPG to the amount of EPI $\Delta m_{LPG/liq}$ at the beginning of each calculation step.

- The heat that the comparison stage permeate from around the body EPI to LPG.

-The heat required for evaporation of the LPG in the comparison step for estimating the density of wet steam. Correction coefficient estimate of wet steam saturation was measured by means of pressure in the EPI conducted a computational model calibration.

-From the heat balance for LPG in the EPI down temperature wet steam, LPG EPI and then conversion between temperature and saturation vapor pressure of LPG LPG pressure is determined in the EPI. The relationship between temperature and saturation vapor pressure of LPG for the intended ratio of propane and butane in LPG in size 50/50 shown in the graph in Figure 2.

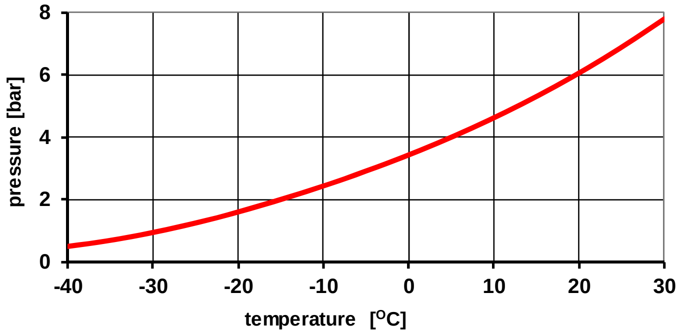

Obr.2: The vapor pressures of the ratio of propane and butane in the LPG size 50/50 depending on the temperature. The illustrated dependence (in reverse relation) clearly documents the problem which is associated with the injection of liquid LPG into the suction line: after the discharge of the liquid LPG from EV to EPI pressure decreases from $p_{LPG/liq} \cong 12$ *bar to* $p_{LPG/V_{BON}} \cong 1 bar$ *and begins intensive evaporation temperature drops LPG until* $t_{LPG/V_{BON}} \approx -30^0 C$.

- The effluent of wet vapor of LPG into the intake air is designed as a flow of gas (with respect to the critical stages of expansion during discharge). Properties of gas is only saturated steam, which at the outlet entrains droplets LPG (wet steam outlet). In calculating the amount of elemental vaunted liquid phase (droplets) involves using a proportion of vaporized LPG (x values for wet steam saturation) in the EPI.

-The calculation procedure is repeated until the entire batch feeding LPG EPI and terminates discharge the entire dose of wet steam outlet nozzle into the intake air.

Comparison of the results of model calculations of pressure in EPI discharge of wet vapor of LPG into the intake air with the results of the measured waveforms of pressure of LPG in EPI showed that the algorithm calculation model gives a very good agreement with the measurement when using the correction (calibration) coefficients for the density of wet steam in size $k_{evapor} = 0.8$. Model calculations are primarily educational in nature, but the findings were used for design solutions EPI version with heating outlet nozzle.

3. Experiment

Measurement was carried out on the Skoda engine, whose parameters are shown in Table 1. The engine was controlled by an electronic control unit with version control software SIMOS 11. Measurement were made for two configuration of EPI (with and without heating) – both configurations had the same parametres of internal dimension. Selected results of experimental verification measurements are illustrated and described in FIG. 3.

Tab. 1: The engine parameters specified for laboratory measurements.

Type	SI, 12 valves, DOHC
Bore X Stroke	76.5 x 86.9 mm
Number of cylinders	3
Swept volume of engine	1198 cm3
Maximum power	51 kW
Maximum torque	112 Nm
Compression ratio	10.5 ± 0.3 :1
Cooling	water

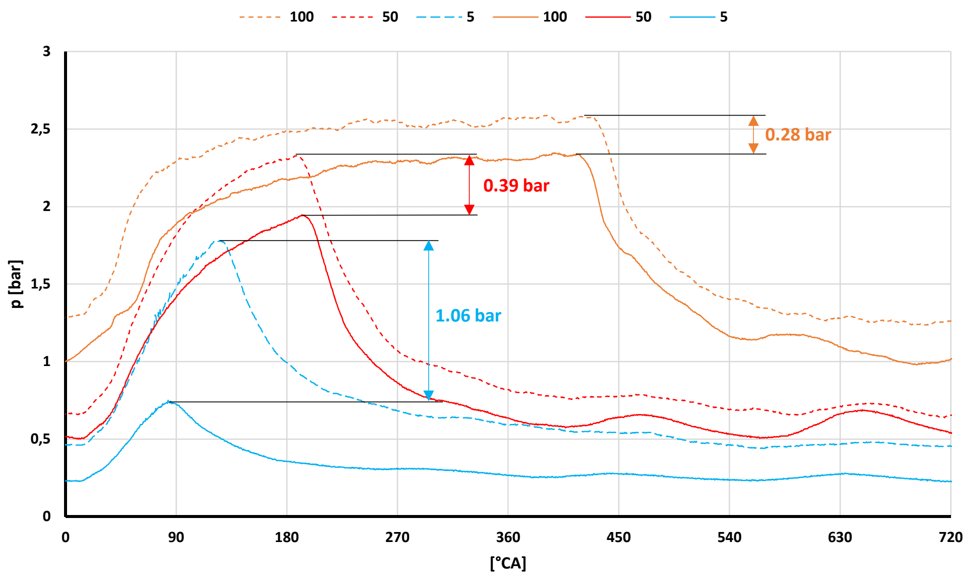

Obr.3: The picture shows the course of pressure in the end part of the injector at a speed of 3700 1 / min for three different loading modes (100 - fully open throttle, 50 - medium load, 5 - low load) depending on the rotation of the crankshaft. The dashed line shows the progress of the pressure in the end part heated, the solid line shows the progress of the pressure in the end portion without heating. At the end portion is heated with heat balance a shift to higher temperatures (see. Fig. 2) due to the heat input into the end portion of the injector.

4. Conclusions

Research injection of liquid LPG into the intake manifold of the engine revealed that the decisive factor for the smooth operation of the engine on LPG is suitable structural solution for the end of the injector, placed in the engine intake manifold. Dimensions and insertion end portion of the injector into the intake manifold must minimize the reduction of the flow cross section in the suction pipe.

To avoid the formation of ice on the front surface of the discharge nozzle is an effective measure heating of the discharge nozzle with minimizing the effect of heating wet steam LPG before the outlet nozzle.

The effluent from the wet steam outlet nozzle must be directed to the central parts of the flow cross section in the intake manifold (on impact of wet steam LPG to the inner wall of the suction pipe there is also the risk of frost). In terms of the total discharge time of wet steam LPG from EPI is suitable EV with a larger flow cross section and to shorten the opening time EV significantly this will increase the pressure of wet steam LPG EPI and increase in speed of discharge of the ON and range compact beam to the suction channels in cylinder head (this will reduce the flow of wet steam contact with the inner wall of the plastic suction pipe and the formation of frost on the wall).

Acknowledgement

This research has been realized using the support of Technological Agency, Czech Republic, Programme of Centers Competence, Project TE01020020 Josef Božek Centre for Automotive Industry. This support is gratefully acknowledged.

References

Beroun, S., Brabec, P., Dittrich, A., Dráb, O., Nguyen, T., T.: Computational Modeling of the liquid LPG Injection into the suction Manifold of an SI Vehicle Engine. Applied Mechanics and Materials Vol. 390 (2013) pp 355-359. ICMAE 2013, Moscow.

Cengel, Y. A., Boles, M. A.: Thermodynamics. 6th edition. McGrow - Hill Comp., New York, 2008. ISBN 978-0-07-352921-9.

Šesták, J., Bukovský, J., Houška, M.: Tepelné pochody, Transportní a termodynamická data. Skripta ČVUT v Praze, 2004. ISBN 80-01-02934-4.

22nd International Conference
ENGINEERING MECHANICS 2016
Svratka, Czech Republic, 9 – 12 May 2016

PARAMETRIC ANALYSIS OF PIEZOELECTRIC TRANSDUCER USED FOR SIGNAL PROCESSING

M. BLASIAK*

Abstract: *A two dimensional model of interdigital transducer (IDT) used for processing particular physical quantities into electric signal was presented in this paper. The results of numerical calculations of the above mentioned model were presented as well as a parametric analysis was conducted in order to obtain information concerning stress distribution in the transducer.*

Keywords: Piezoelectric Crystals, Interdigital Transducer, Surface Acoustic Waves, Stress

1. Introduction

Piezoelectric transducers are basic elements of components which use surface acoustics waves in order to process particular physical quantities into electric signal. The physical quantities that are measured might include: displacements, velocities, accelerations and acoustic pressure. The principle of operation of piezoelectric transducers involves using direct and converse piezoelectric effect: as a result of mechanical stresses, piezoelectric materials produce electrical current (Blasiak & Kotowski, 2009). Such attributes are characteristic of some monocrystals: barium titanate, quartz, Seignette's salt. Currently natural crystals are substituted with polycrystals, i.e. artificially polarized ceramic products (e.g. piezoceramic PZT6). Transducers made of piezoelectric crystals are used for building various devices in different branches of industry. They are widely used for measuring the vibrations in non-contacting face seals (Blasiak, 2015a, 2015b), the vibrations in the cutting process (Miko & Nowakowski, 2012a, 2012b), vibrations and control in mechanical devices (Takosoglu et al., 2012) and building gyroscopes (Koruba et al., 2010). Piezoelectric materials are widely applied as well in aviation industry, e.g. to building flying objects (Krzysztofik & Koruba, 2012). The aim of this paper is to show the stress distribution in the interdigital transducer, used for signal processing.

2. Methods

The subject of the research was interdigital transducer (IDT), built of two electrodes in the form of combs combined with each other with the use of metal rails and placed on a piezoelectric surface. A two-dimensional model of the transducer consists of an interdigital transducer that is fixed on a piezoelectric layer, and a metal plate (Fig. 1).

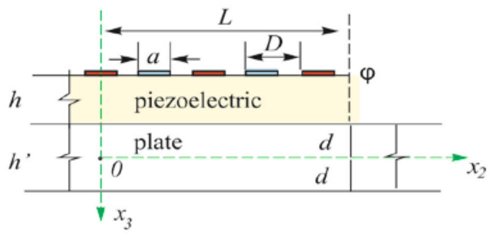

Fig. 1: A two-dimensional model of the interdigital transducer, where: $a-$ *width of the electrode,* $D-$ *gap between the electrodes,* $L-$ *length of the transducer,* $2d-$ *thickness of the plate,* $h-$ *thickness of the piezoelectric layer,* φ $-$ *potential.*

* Małgorzata Błasiak, PhD.: Department of Mechanics, Kielce University of Technology; Aleja Tysiąclecia Państwa Polskiego 7; 25-314 Kielce; PL, mdrab@tu.kielce.pl

Voltage put against electrodes of the transducer creates electric field and thus, generates mechanical waves that result from piezoelectric effect. Under the influence of electromechanical coupling, a cooperation between the transducer and the plate might be expected. The surface of the transducer was modelled in the form of a metal plate. Moreover, a strong electro-mechanical coupling as well as a finite number of electrodes in the transducer were assumed. It was assumed that the potential distribution on the surface of the transducer is continuous and it was described with a cosine potential distribution along x_2 axis (Blasiak & Kotowski, 2009, Jin et al., 2003).

For consideration piezoelectric crystal dynamic equation of motion and electric displacement satisfying Maxwell equation have the form:

$$\sum_{j=1}^{3} \sigma_{ij,j} = \rho \ddot{u}_i, \quad \sum_{i=1}^{3} D_{i,i} = 0 \tag{1}$$

where $i = 1, 2, 3$; σ_{ij} – stress tensor, u_i – displacement, ρ – mass density, D_i – electric displacement. Hooke's law and the electric displacement written in the form of constitutive equations:

$$\sigma_{ij} = c_{ijkl} u_{k,l} - e_{kij} E_k \tag{2}$$

$$D_i = e_{ikl} u_{k,l} - \varepsilon_{ij} E_j \tag{3}$$

where c_{ijkl}, c'_{ijkl} – tensor of the elastic modul, e_{ikl}, e'_{ikl} - piezoelectric constants, ε_{ij}, ε'_{ij} - dielectric constants for the piezoelectric crystal and the plate, respectively (Moulin et al., 2000).

Because it considered the wave propagating in the direction (x_2, x_3), of developing the equations (1) and (2,3), an electro-mechanical coupled equation of motion for the piezoelectric layer was obtained which was expressed with a mechanical displacement and electrical potential.

$$\left.\begin{aligned} c_{11} u_{2,22} + c_{44} u_{2,33} + (c_{13} + c_{44}) u_{3,23} + (e_{31} + e_{15}) \varphi_{,23} = \rho \ddot{u}_2 \\ (c_{13} + c_{44}) u_{2,32} + c_{44} u_{3,22} + c_{33} u_{3,33} + e_{15} \varphi_{,22} + e_{33} \varphi_{,33} = \rho \ddot{u}_3 \\ (e_{15} + e_{31}) u_{2,23} + e_{15} u_{3,22} + e_{33} u_{3,33} - \varepsilon_{11} \varphi_{,22} - \varepsilon_{33} \varphi_{,33} = 0 \end{aligned}\right\} \tag{4}$$

Equations of motions for the plate, without taking the piezoelectric and dielectric effects into consideration, take the following form:

$$\left.\begin{aligned} c'_{11} u_{2,22} + c'_{44} u_{2,33} + (c'_{13} + c'_{44}) u_{3,23} = \rho' \ddot{u}'_2 \\ (c'_{13} + c'_{44}) u_{2,32} + c'_{44} u_{3,22} + c'_{33} u_{3,33} = \rho' \ddot{u}'_3 \end{aligned}\right\} \tag{5}$$

In the boundary conditions it was assumed that the upper surface of the piezoelectric layer and the lower surface of the plate are free from stresses: $\sigma_{33} = \sigma_{23} = 0$, $\sigma'_{33} = \sigma'_{23} = 0$. The electric condition is regulated with an input electric signal that is described with an equation (Jin et al., 2003)

$$\varphi(k)\big|_{x_3=-h-d} = \frac{1}{\sqrt{2\pi}} \int_{-\infty}^{\infty} f(x_2) e^{ikx_2} dx_2 \tag{6}$$

On the border of two media, principles of continuity were presented in the following form $(\varphi = 0)$:

$$\left.\begin{aligned} u_2 = u'_2, \quad u_3 = u'_3 \\ \sigma_{33} = \sigma'_{33}, \quad \sigma_{23} = \sigma'_{23} \end{aligned}\right\} \tag{7}$$

In the model transducer it was assumed that the surface in the form of a metal plate has finite length. In case of introducing a finite number of points of computational grid, in order to avoid volatility of numerical calculations - absorbing layers on the plate edges connected with the direction x_2 were introduced. The physical sense of the layers that were applied is to simulate the exponentially disappearing vibration amplitude of the propagating waves. The equations of motion in the absorbing layer take the following form:

$$\begin{aligned}\rho\ddot{u}_2 &= c_{11}u_{2,22} + c_{44}u_{2,33} + (c_{13} + c_{44})u_{3,23} + \tau\dot{u}_2 \\ \rho\ddot{u}_3 &= (c_{13} + c_{44})u_{2,32} + c_{44}u_{3,22} + c_{33}u_{3,33} + \tau\dot{u}_3\end{aligned} \tag{8}$$

where τ – coefficient absorbing vibrations.

The mathematical model of the interdigital transducer was solved numerically with the use of the finite difference method and the elementary control volume method. It was assumed for this calculation that the piezoelectric layer has a hexagonal crystal structure of *6mm*, and an aluminium plate is the surface. Material constants PZT6 and aluminium were assumed in accordance with the paper (Blasiak & Kotowski, 2009). Dimensions of the transducer: $L = 0.02\,m$, $h = 0.001\,m$, $D = 0.002\,m$, dimensions of the aluminium plate: $L' = 0.02\,m$, $h' = 0.002\,m$.

3. Results

As a result of the numerical calculations, the distribution of displacement elements in the transducer (which were not presented here) as well as of stress elements σ_{23} (Fig.2) i σ_{33} (Fig.3) along the thickness direction x_3 were obtained. The frequency of the applied signal was $600\,kHz$, potential $\varphi = 5\,V$, thickness of the transducer $z = 0.001\,m$ (output parameters).

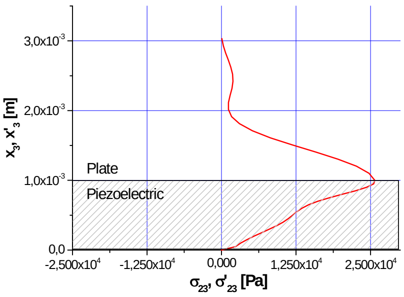

Fig. 2: Distribution of the stress element σ_{23} in the transducer.

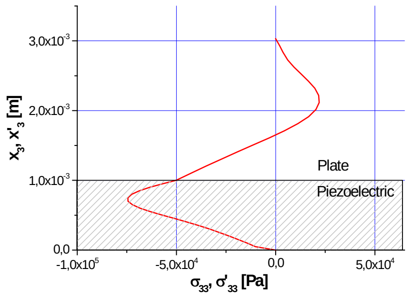

Fig. 3: Distribution of the stress element σ_{33} in the transducer.

The next was to conduct a parametric analysis of the transducer. The aim of the research was to verify, which quantities have the biggest impact on the distribution of stress elements in the interdigital transducer. All calculations were made for the same moment, namely $t = 1\times10^{-5}$. Potential, frequency and layer thickness were subsequently changed. Some results are presented below in the form of graphs. Fig. 4 presents the distribution of stress elements for various values of the potential φ (the remaining output parameters remain unchanged).

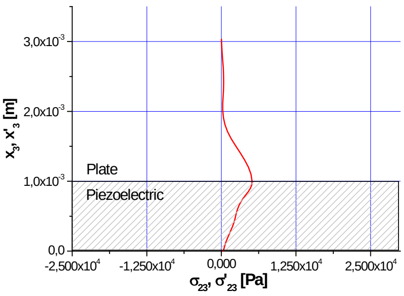

Fig. 4: Distribution of the stress element σ_{23} in the transducer for $\varphi = 1V$.

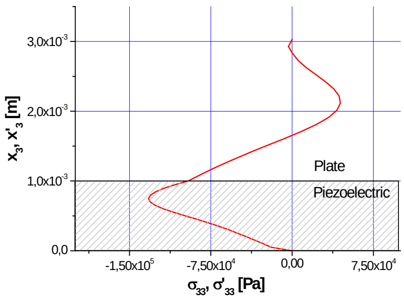

Fig. 5: Distribution of the stress element σ_{33} in the transducer $\varphi = 10V$.

Fig. 6 and 7 present the distribution of stress elements for various thicknesses of the piezoelectric layer (the remaining output parameters remain unchanged).

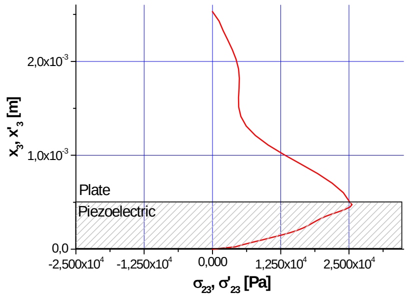

Fig. 6: Distribution of the stress element σ_{23} *in the transducer for* $z = 0.00005\ m$.

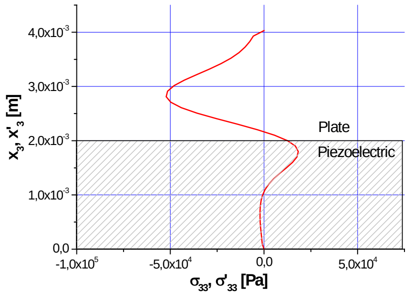

Fig. 7: Distribution of the stress element σ_{33} *in the transducer* $z = 0.0002\ m$.

Graphs (2-7) present the distribution of acoustic field in the coupled structure. Nil value on both ends connected with the thickness x_3 means that they are free from stresses. Moreover, the stress of the field is continuous along the piezoelectric layer and the aluminium plate which proves the fact that they cooperate with each other.

4. Conclusions

On the basis of the results of the parametric analysis of the transducer it was stated that with the potential increase, the stress value increases in a linear manner. It confirms the occurrence of the converse piezoelectric effect in the layer. The change in the thickness of the piezoelectric layer influences the stress distribution in the whole transducer the most. The impact of the stress distribution in piezoelectric crystals is crucial, because a lot of operating properties of piezoelectric devices depend on the stress state. Acquaintance of such stress states enables i.a. to determine the degree of the defects in the structure, limit the number of defects and modify the manner of production of the desired devices.

References

Blasiak, M. & Kotowski, R. (2009) Propagation of acoustic waves in piezoelectric crystals, Przeglad Elektrotechniczny ISSN 0033-2097, Vol. 85, NR 12/2009, pp.40-43.

Blasiak, S. (2015a) An analytical approach to heat transfer and thermal distorions in non-contacting face seals. International Journal of Heat and Mass Transfer**,** Vol. 81, pp. 90-102.

Blasiak, S. (2015b) The two dimensional thermohydrodynamic analysis of a lubrication in non-contacting face seals. Journal of Thermal Science and Technology, Vol. 10, pp. 1-8.

Jin, J., Quek, S. T. & Wang, Q. (2003) Analytical solution of excitation of Lamb waves in plate by inter-digital transducers. Proc. R. Soc. Lond. A 459, pp.1117-1134.

Koruba, Z., Dziopa, Z. & Krzysztofik, I. (2010) Dynamics and control of a gyroscope-stabilized platform in a self-propelled anti-aircraft system. Journal of Theoretical and Applied Mechanics, Vol. 48, No. 1, ISSN 1429-2955 pp.5-26.

Krzysztofik, I. & Koruba, Z. (2012) Model of Dynamics and Control of Tracking-Searching Head, Placed on a Moving Object. Journal of Automation and Information Sciences, Vol. 44, Issue 5, ISSN 1064-2315, pp.38-47.

Miko, E. & Nowakowski, Ł. (2012a) Analysis and Verification of Surface Roughness Constitution Model After Machining Process, XIIITH International scientific and engineering conference hermetic sealing, Vibration reliability and ecological safety of pump and compressor machinery-HERVICON-2011.Vol. 39, pp.395-404.

Miko, E. & Nowakowski, Ł. (2012b) Vibrations in the Machining System of the Vertical Machining Cente XIIITH International scientific and engineering conference hermetic sealing, Vibration reliability and ecological safety of pump and compressor machinery-HERVICON-2011 Vol. 39, pp. 405-413.

Moulin, E., Assaad, J., Delebarre, C., Grondel, S. & Balageas, D. (2000) Modeling of integrated Lamb waves generation system using a coupled finite element-normal modes expansion method. Ultrasonics 38, pp. 522-526.

Takosoglu, J. E., Laski, P. A. & Blasiak, S. (2012) A fuzzy logic controller for the positioning control of an electro-pneumatic servo-drive, Proceedings of The Institution of Mechanical Engineers Part I-Journal of Systems and Control Engineering, Vol. 226 Issue: I10, pp. 1335-1343.

22nd International Conference
ENGINEERING MECHANICS 2016
Svratka, Czech Republic, 9 – 12 May 2016

HEAT CONDUCTION PROBLEM IN NON-CONTACTING FACE SEALS

S. Blasiak[*]

Abstract: *A mathematical model describing the phenomenon of heat transfer in the system "sealing rings – fluid film" for non-contacting face seal was presented in this paper. The presented model was solved with the use of analytical methods for two cases of installation of the stationary ring. The first one, when the stator is completely isolated from the surrounding operating medium and the second, when heat transfer takes place via convection between the outer cylindrical ring surface and the operating factor on the processing part. The distributions of temperature fields in sealing rings were determined with the use of the method of separation of variables, which were recorded with the use of trigonometric series in the form of surface functions for the ring cross-section.*

Keywords: Mechanical seal, Non-contacting face seal, Heat transfer, Trigonometric polynomials.

1. Introduction

Mechanical seals, in particular non-contacting face seals, belong to machine elements that are characterized by a large complexity of physical phenomena. A flow of operating medium through the radial gap, heat transfer between the cooperating elements as well as fluid solid interaction occur there. What is more, in many papers one may find mathematical models describing the dynamics of the sealing rings, whose form of record is similar to the one included in the papers (Koruba et al., 2010a, 2010b; Krzysztofik & Koruba, 2012; Krzysztofik, 2012). Taking vibrations of sealing rings into consideration, attempts of controlling them (Takosoglu et al., 2009, 2012) using control schemes that are based i.a. on (Laski et al., 2015) were made. Materials used for producing operating rings as well as connecting elements made of plastics or produced with the use of the additive technology (Adamczak et al., 2014, 2015; Bochnia & Kozior, 2014; Bochnia, 2012), play a crucial role in the production of non-contacting face seals. Due to the nature of operation of non-contacting face seals, roughness of rollers of cooperating rings constitutes a crucial problem that needs to be taken into consideration. The materials for production of rings must be chosen in such a way so that one ring is produced from a material of large hardness, e.g. carborundum, tungsten carbide or stainless steel. Counter-ring, however, should be made of a soft material, e.g. impregnated graphite. Another aspects regarding the production and installation of the elements of non-contacting face seals are dimensional accuracy as well as consideration of proper shape and location tolerances (Miko & Nowakowski, 2012a, 2012b). Another phenomena which might influence the proper operation of the described type of sealing are phenomena related to heat transfer and associated thermal deformations that were presented in a detailed way in the paper (Blasiak, S. et al., 2012; Blasiak, S., 2015a). Research posts, where sensors for measuring temperature and vibrations were applied (Blasiak, M. & Kotowski, 2009), are widely described in the literature. The specificity of operation of non-contacting face seals, i.e. high angular velocity of the rotating elements, small gap of ($\sim 1 \mu\text{m}$) (Takosoglu et al., 2014), roughness of the cooperating surfaces or thermos-elastic deformations of the operating rings as well as many more other factors influence the operation of non-contacting face seals. Preparing and developing the mathematical models describing the above mentioned phenomena allow to obtain more and more detailed results of the analyses. Moreover, the choice of proper materials for sealing rings adjusted to the working conditions as well as determining the temperature value at the design stage or during bench studies allow to avoid excessive wear of the surface of sealing rings and prolong the lifetime of the cooperating elements. The subject of this paper was to identify the phenomena related to heat transfer in particular elements of non-contacting face seals.

[*] Eng. Slawomir Blasiak, PhD.: Faculty of Mechatronics and Mechanical Engineering, Department of Mechanical Technology and Metrology, Kielce University of Technology, Aleja Tysiaclecia Panstwa Polskiego 7; 25-314, Kielce; PL, sblasiak@tu.kielce.pl

2. Non-contacting face seal model

The overall scheme of non-contacting face seal for two cases of installation of the stationary ring was presented in Fig. 1. Non-contacting face seal consists of two cooperating rings – stator (1), which is firmly fixed in the casing, and rotor (2), which rotates together with the shaft (6) of the rotating machine and is pressed with the spring (3) against the stator.

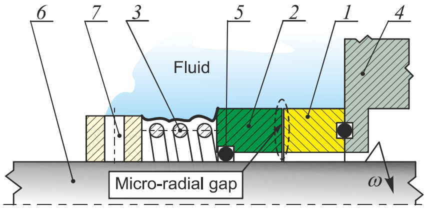

Fig. 1. Scheme of non-contacting face seal. a) stator convection, b) stator insulation; 1 – stator, 2 – rotor, 3 – spring, 4 – casing, 5 – O-ring, 6 – shaft, 7 – retainer.

The mathematical model describing the phenomenon of heat transfer was presented in papers (Blasiak, S., 2015b). As one of the boundary conditions was assumed the fact that the surfaces of operating rings (Fig.2) with no direct contact with the surrounding liquid are completely isolated. It was recorded in a general form $\frac{\partial \theta}{\partial n} = 0$, where n – means a direction normal to the surface. On the face ring surfaces (stator and rotor) limiting the radial gap, and with direct contact with the medium layer, the condition regarding the case of heat transfer via conduction is fulfilled.

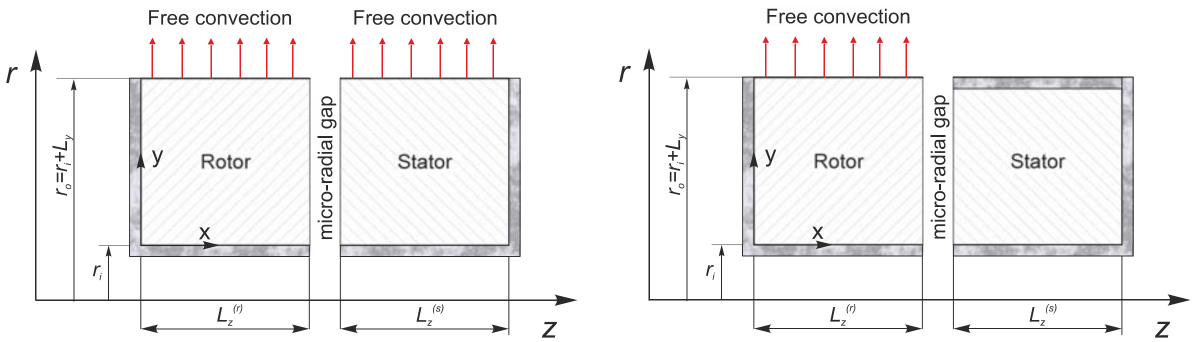

Fig. 2. Heat transfer boundary conditions, a) stator convection, b) stator insulation.

The values of heat flow on the surfaces of the element and medium under consideration are respectively:

on the stator surface: $q^s{}_v(x) = \lambda^s \frac{\partial \theta^s}{\partial x} = \lambda^f \frac{\partial \theta^f}{\partial x} = 0$ and $\theta^s = \theta^f$ on the rotor surface

$\lambda^f \frac{\partial \theta^f}{\partial x} = \lambda^r \frac{\partial \theta^r}{\partial x} = q^r{}_v(r)$ and $\theta^f = \theta^r$. It means that the maximal temperature it to be found on the border between the fluid film and stator, where there is the biggest friction of the fluid against the stationary ring surface. Thus, almost the whole heat flow is transferred by the second ring, namely the rotor. On the rotating surface of the stator and rotor (Fig.2) that contacts the surrounding medium, heat is transferred via free convection. It was generally recorded in the form: $-\lambda^i \left.\frac{\partial \theta^i}{\partial y}\right|_{y=L_y} = \alpha^i \left.\theta^i\right|_{y=L_y}$, where

$i = r, s$ rotor and stator respectively.

2.1. Analytical solution

The model of heat transfer in non-contacting face seal was solved analytically. In the first phase, the temperature distributions in sealing rings were determined by stipulating a general form of functions satisfying Laplace's equation (1), both for stationary ring (stator) as well as rotor, with accepted boundary conditions. Used in this case, the transition from the cylindrical coordinate system to the Cartesian coordinate system, considerably simplifies the analytical calculations. Appearing for the cylindrical coordinate system, Bessel functions increase the calculation time in mathematical programs.

$$\frac{\partial^2\theta}{\partial x^2}+\frac{\partial^2\theta}{\partial y^2}=0 \tag{1}$$

The presented analytical calculations were conducted similarly as in the paper (Blasiak, S., 2015b). The final formulas describing the temperature distributions in sealing rings are presented below:

in the rotor:

$$T^r=T_0+\sum_{n=1}^{\infty}\frac{-\int_0^{L_y}\bar{q}\cos(s_n y)dy}{s_n\sinh(s_n L_x)\int_0^{L_y}\cos^2(s_n y)dy}\cosh\left(s_n\left(L_x-x\right)\right)\cos(s_n y) \tag{2}$$

and the in insulated stator:

$$T^s=T_0+\sum_{n=1}^{\infty}\frac{2\cdot\int_0^{L_y}\theta^f\cos\left(\frac{n\pi}{L_y}y\right)dy}{\cosh\left(\frac{n\pi}{L_y}(L_x)\right)L_y}\cosh\left(\frac{n\pi}{L_y}(L_x-x)\right)\cos\left(\frac{n\pi}{L_y}y\right)+\frac{\int_0^{L_y}\left(\theta^f\right)\mathrm{d}y}{L_y}, \tag{3}$$

as well as in the non-insulated stator:

$$T^s=T_0+\sum_{n=1}^{\infty}\frac{\int_0^{L_y}\theta^f\cos(s_n y)dy}{\cosh(s_n L_x)\int_0^{L_y}\cos^2(s_n y)dy}\cosh(s_n x)\cos(s_n y) \tag{4}$$

The above dependencies served to determine the temperature distributions in the system “fluid film - sealing rings”.

3. Numerical results

The calculations were conducted for operating and geometric parameters from the paper (Blasiak, S., 2015b). It was assumed that water T_o of $20\,^{\circ}C$ was the operating medium. In the geometry of mechanical seal it was assumed that the outer radius was 45 mm, and the inner 40 mm for both cooperating rings. It was assumed as well that the rotor rotates with the angular velocity of 500 rad/s. Thermal conductivity for the rotor of $\lambda^r = 130\ (\mathrm{W/m\cdot K})$, and for the stator of $\lambda^s = 15\ (\mathrm{W/m\cdot K})$ was taken into consideration. The height of the radius gap on the assumed level 1 μm .was taken into account.

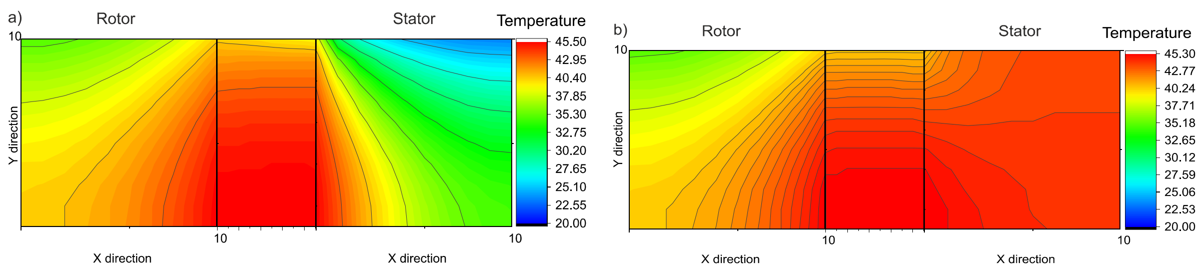

Fig. 3. Temperature distribution, a) stator convection, b) stator insulation.

On the basis of the obtained results, it might be concluded that the temperature distribution in the gap is at the same level. The temperature differences are visible only in case of stator what results from the method of its installation in the casing. For the insulated stator (Fig. 3b), the temperature is practically in the entire cross section at the level of 43 °C. For the stator (Fig. 3a), which is not insulated, the temperature on the outer radius is similar to the temperature of the working medium on the processing part. On the basis of (Fig. 3a), uneven temperature distributions in cooperating rings might be observed. It results from various physical properties of the materials that the rings are produced from. Diversification of temperature distributions in sealing rings changes the geometry of the radial gap, which results from thermos-elastic deformations.

4. Conclusions

The main task of non-contacting face seals is to keep tightness regardless of external factors. There is a tight relation between the geometry of the radial gap and the leakage. Deformations due to uneven temperature distribution in the sealing rings are main connecting factors. Developing more detailed mathematical models and determining temperature values already at the design stage provide the researchers and constructors with crucial knowledge that is essential while designing such devices. This knowledge, in turn, translates into huge reliability and longevity of the constructions.

References

Adamczak, S., Bochnia, J., & Kaczmarska, B. (2014) Estimating the uncertainty of tensile strength measurement for a photocured material produced by additive manufacturing, Metrology and Measurement Systems, 21, 3, pp. 553–560. doi:10.2478/mms-2014-0047

Adamczak, S., Bochnia, J., & Kaczmarska, B. (2015) An analysis of tensile test results to assess the innovation risk for an additive manufacturing technology, Metrology and Measurement Systems, 22, 1, pp. 127–138. doi:10.1515/mms-2015-0015

Blasiak, M., & Kotowski, R. (2009) Propagation of acoustic waves in piezoelectric crystals, Przeglad Elektrotechniczny, 85, 12, pp. 40–43.

Blasiak, S. (2015a) An analytical approach to heat transfer and thermal distortions in non-contacting face seals, International Journal of Heat and Mass Transfer, 81, pp. 90–102. doi:10.1016/j.ijheatmasstransfer.2014.10.011

Blasiak, S. (2015b) The two dimensional thermohydrodynamic analysis of a lubrication in non-contacting face seals, Journal of Thermal Science and Technology, 10, 1, pp. JTST0016–JTST0016. doi:10.1299/jtst.2015jtst0016

Blasiak, S., Kundera, C., & Bochnia, J. (2012) A Numerical Analysis of the Temperature Distributions in Face Sealing Rings, Procedia Engineering, 39, pp. 366–378. doi:10.1016/j.proeng.2012.07.040

Bochnia, J. (2012) Ideal Material Models for Engineering Calculations, Procedia Engineering, 39, 0, pp. 98–110. doi:http://dx.doi.org/10.1016/j.proeng.2012.07.013

Bochnia, J., & Kozior, T. (2014) Methods of Prototyping Process Using Modern Additive Technologies, Solid State Phenomena, 223, pp. 199–208. doi:10.4028/www.scientific.net/SSP.223.199

Koruba, Z., Dziopa, Z., & Krzysztofik, I. (2010a) Dynamics and control of a gyroscope-stabilized platform in a self-propelled anti-aircraft system, Journal of Theoretical and Applied Mechanics, 48, 1, pp. 5–26.

Koruba, Z., Dziopa, Z., & Krzysztofik, I. (2010b) Dynamics of a controlled anti-aircraft missile launcher mounted on a moveable base, Journal of Theoretical and Applied Mechanics, Vol. 48 nr, pp. 279–295.

Krzysztofik, I. (2012) The Dynamics of the Controlled Observation and Tracking Head Located on a Moving Vehicle, Solid State Phenomena, 180, pp. 313–332. doi:10.4028/www.scientific.net/SSP.180.313

Krzysztofik, I., & Koruba, Z. (2012) Model of Dynamics and Control of Tracking-Searching Head, Placed on a Moving Object, Journal of Automation and Information Sciences, 44, 5, pp. 38–47.

Laski, P. A., Takosoglu, J. E., & Blasiak, S. (2015) Design of a 3-DOF tripod electro-pneumatic parallel manipulator, Robotics and Autonomous Systems, 72, pp. 59–70. doi:10.1016/j.robot.2015.04.009

Miko, E., & Nowakowski, L. (2012a) Analysis and Verification of Surface Roughness Constitution Model After Machining Process, Procedia Engineering, 39, pp. 395–404. doi:10.1016/j.proeng.2012.07.043

Miko, E., & Nowakowski, L. (2012b) Vibrations in the Machining System of the Vertical Machining Center, Procedia Engineering, 39, pp. 405–413. doi:10.1016/j.proeng.2012.07.044

Takosoglu, J. E., Dindorf, R. F., & Laski, P. A. (2009) Rapid prototyping of fuzzy controller pneumatic servo-system, International Journal of Advanced Manufacturing Technology, 40, 3-4, pp. 349–361. doi:10.1007/s00170-007-1349-5

Takosoglu, J. E., Laski, P. A., & Blasiak, S. (2012) A fuzzy logic controller for the positioning control of an electro-pneumatic servo-drive, Proceedings of the Institution of Mechanical Engineers. Part I: Journal of Systems and Control Engineering, 226, 10, pp. 1335–1343. doi:10.1177/0959651812456498

Takosoglu, J. E., Laski, P. A., & Blasiak, S. (2014) Innovative Modular Pneumatic Valve Terminal With Self-Diagnosis, Control and Network Communications, In V. Fuis (Ed.), Engineering Mechanics 2014 (pp. 644–647). Dolejskova 5, Prague 8, 182 00, Czech Republic: Acad Sci Czech Republic, Inst Thermomechanics.

22nd International Conference
ENGINEERING MECHANICS 2016
Svratka, Czech Republic, 9 – 12 May 2016

ANISOTROPHY OF MECHANICAL PROPERTIES OF A MATERIAL WHICH IS SHAPED INCREMENTALLY USING POLYJET TECHNOLOGY

J. Bochnia*, S. Blasiak**

Abstract: *This paper discusses the results of static tensile test of rectangular cross-section specimens made of a photo-curable material – FullCure 720. The specimens were prepared applying an incremental shaping method with the use of PolyJet technology. An analysis of the results was conducted and uncertainty in the measurements of tensile strength was estimated. Direction of specimens on a working platform of the machine was taken into account. The occurrence of anisotrophy of mechanical properties of the materials depending on the direction of the elements on the working table of a 3D printer was confirmed.*

Keywords: Additive technologies, tensile strength, anisotrophy of mechanical properties of materials.

1. Introduction

More than thirty years ago, appearance of the first 3D printing technology gave rise to new technologies, initially known as Rapid Prototyping, which found their application in the production of solid models of prototypes. Currently, more and more often we use the term 'incremental technologies' (additive manufacturing technology), since creation of models using incremental technologies involves adding material in layers where each subsequent layer is an exact reflection of any section of a model in a given plane. The current state and the prospects for development of incremental technologies was discussed, inter alia, in the study by Campbell (Campbell et al., 2012), presenting the possibilities of industrial applications, material development and design intentions. A body (solid), having substantially different properties from those of a semi-finished product is produced during a technological process of building a model on the working platform of a 3D printer. During the manufacturing (printing) process of a model, mechanical properties of a material are shaped as well (Adamczak et al., 2014, 2015; Bochnia & Kozior, 2014).

With the development of materials used in incremental technologies, there are more and more studies on their properties. It is worth quoting the study (Puebla et al., 2012), which presents the results of studies on the effects of environmental conditions (ageing) and orientation (i.e. arrangement on the working platform of the printer) on mechanical properties of the specimens made with the use of stereolithography. The studies have shown anisotrophy of materials manufactured using stereolithography as well as a reduction in mechanical properties under the influence of environmental conditions. The study (Bassoli et al., 2012) discussed the effect of the direction of deposition of layers (virtual arrangement of an element on the working platform) and laser sintering of polyamide powders on mechanical properties of produced materials of specimens for the tests. Significant differences were found, indicating anisotrophy of materials obtained using this technology. Many researchers used 3D materials for modeling various elements, e.g. sealing rings, membranes, viscoelastic elements, cable guides, muscle models and other structural components (Laski et al., 2015; Miko & Nowakowski, 2012; Takosoglu et al., 2012, 2014). The authors of this work, taking into consideration the issues outlined above as well as the possibility of using both incremental materials and technologies to build the models of mechanical seals (Blasiak et al., 2014; Blasiak, 2015a, 2015b), tried to estimate tensile strength on the

* Eng. Jerzy Bochnia, PhD.: Kielce University of Technology, Al. 1000-lecia P. P. 7, 25-314 Kielce, Poland, Department of Machine Technology and Metrology (jbochnia@tu.kielce.pl)

** Eng. Slawomir Blasiak, PhD.: Kielce University of Technology, Al. 1000-lecia P. P. 7, 25-314 Kielce, Poland, Department of Machine Technology and Metrology (sblasiak@tu.kielce.pl)

basis of static stretching of specimens shaped incrementally using photo-curable rosin FullCure720, taking into account the directions of printing. Further considerations involved the preparation of specimens, static tensile test and an analysis of the results.

2. Methods

Test specimens were made of photo-curable rosin FullCure 720 using PolyJet technology (http://objet.com/3d-printing-materials), with the use of the printer Connex350 by Objet. Specimens with the size according to the (ASTM, 2013) standard with the following dimensions: width of the narrow section of the specimen 13±0.02 mm, length of the narrow section 57±0,02 mm, thickness of the specimen 4±0.4 mm, width of the handle 19±0.025 mm, total length of the specimen 165 mm were used to conduct the static tensile test.

Solid model of the specimen was drawn in CAD 3D and saved in a digital file with the extension *.stl*, using triangulation parameters in export options: resolution – adjusted, deviation – tolerance of 0.016 mm, angle – toleration of 5^0. Then, using the program Objet Studio, models of specimens were placed on the working platform of a machine Connex350 in three different positions in accordance with longitudinal movement of printhead:

- direction X – specimen placed sidewise on the working platform,
- direction Y – flat side of the specimen placed on the working platform,
- direction Z – specimen placed vertically on the working platform.

Specimens were prepared in the mode Glossy in order to obtain a smooth surface.

Models arranged virtually on the working platform with the use of the program Objet Studio are shown in Fig 1.

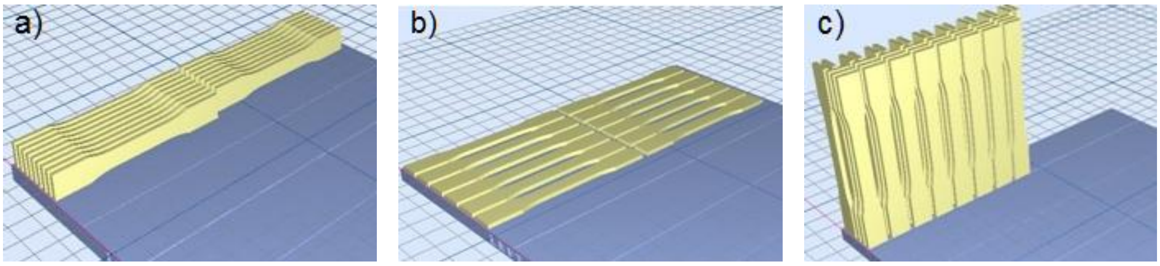

Fig. 1: Arrangement of specimens on the working platform; a) sidewise – direction X, b) flat side – direction Y, c) vertical – direction Z.

After printing, the specimens were carried away from the machine's working platform and then the supporting material was removed. They were then prepared for carrying out the static tensile test. The test was conducted with the use of a testing machine Inspect mini and an extensometer for strain measurement. In the program Labmaster, which is supplied with the machine Inspect mini, the test speed was set at 5 mm/min.

3. Results

Specimen all-in-one charts illustrating loading forces applying to specimens in displacement function obtained directly from the testing machine's computer are shown in Fig. 2, 3 i 4.

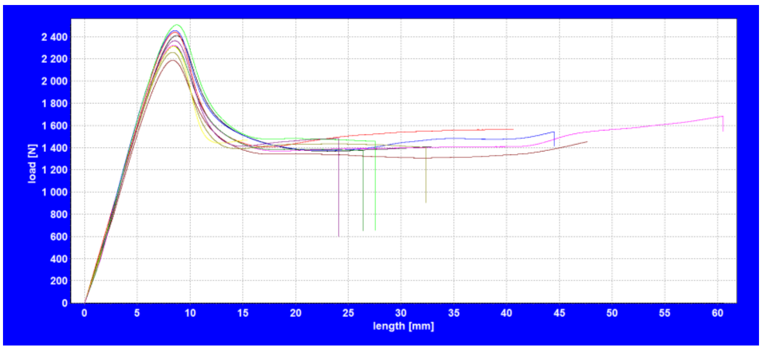

Fig. 2: Graph illustrating specimens placed sidewise in direction X on the working platforms undergoing tensile tests.

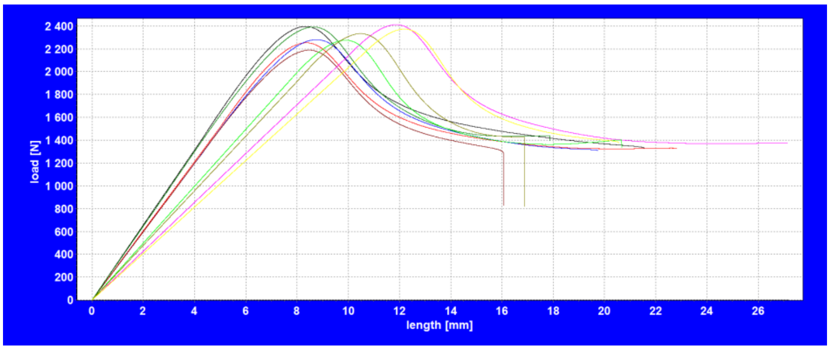

Fig. 3: Graph illustrating specimens placed with the flat side in direction Y on the working platforms undergoing tensile tests.

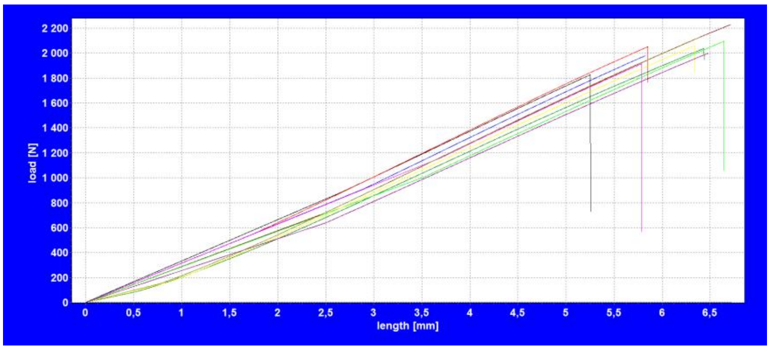

Fig. 4: Graph illustrating specimens placed vertically in direction Z on the working platforms undergoing tensile tests.

The program Labmaster, after entering data, such as width and thickness of the specimen, while recording the maximum tensile force, calculates tensile strength Rm. Standard results uncertainty regarding tensile strength *Rm* for specimens made in individual positions was calculated using the formula (1) (Adamczak et al., 2011).

$$u_{R_m} = \sqrt{\left(\frac{1}{\overline{a}_0 \overline{b}_0}\right)^2 u_{F_m}^2 + \left(\frac{-\overline{F}_m}{\overline{a}_0^2 \overline{b}_0}\right)^2 u_{aA}^2 + \left(\frac{-\overline{F}_m}{\overline{a}_0 \overline{b}_0^2}\right)^2 u_{bA}^2} \qquad (1)$$

where: – $\overline{F}_m$ – the average value of the maximum tensile force calculated for individual directions of printing (Table 1),

u_{F_m} – uncertainty of an average value of the maximum tensile force,

$\overline{a}_0$ – average thickness of specimens,

u_{aA} – uncertainty of an average thickness of specimens,

$\overline{b}_0$ – average width of specimens,

u_{bA} – uncertainty of an average width of specimens.

Values of tensile strength obtained in individual tests and uncertainties of measurements are listed in Table 1.

Tab. 1: Results of tensile strength tests.

Orientation of specimens (Fig. 1)	**Average value of tensile strength $\overline{R}_m$ [MPa]**	**Values of uncertainties of measurements u_{R_m} [MPa]**
X direction	45.17	0.591
Y direction	44.28	0.450
Z direction	37.79	0.657

The studies have shown that tensile strength *Rm* of specimens made in vertical position is 19.5% lower than the strength of specimens made in direction X and 17.2% lower than the strength of specimens made in direction Y. The lack of a typical plastic deformation comes as a surprise, as shown in Fig. 4. Uncertainty of measurements u_A for specimens placed on the working platform vertically is 11.1% higher than for specimens printed in direction X and 46% higher than for specimens printed in direction Y. These results show marked anisotrophy of material properties in relation to the directions of printing.

4. Conclusions

The studies have proven, as shown in the all-in-one graphs (Fig. 2, 3) illustrating tensile tests of specimens made in horizontal position, a good reproductivity of results in terms of tensile strength and, when exceeded, in the field of plastic deformations, specimens broke up in the case of longer elongations. Specimens made in vertical positions have shown poorer properties, as shown in an all-in-one graph (Fig. 4). Material of specimens built incrementally in direction Z (vertical) have not shown plastic properties, its tensile strength was lower than the strength of specimens built in horizontal direction. Uncertainty of tensile strength measurements was also lower than uncertainty of specimens built horizontally, which indicates greater dispersion of results. The studies have shown that material built using incremental technology has marked anisotropic properties determined by the directions of consecutive layers.

Acknowledgement

The paper was prepared with the use of both facilities and equipment purchased for European Union funds within the scope of the Development of Eastern Poland Operational Program for 2007 – 2013, Project LABIN Apparatus Support for Innovative Scientific Laboratories of the Kielce University of Technology, Priority axis I – Modern Economy, Measure 1.3 – Support for Innovations and research project No. POIG 02.02.00-26-023/08-00.

References

Adamczak, S., Bochnia, J., & Kaczmarska, B. (2014) Estimating the uncertainty of tensile strength measurement for a photocured material produced by additive manufacturing, Metrology and Measurement Systems, 21, 3, pp. 553–560.

Adamczak, S., Bochnia, J., & Kaczmarska, B. (2015) An analysis of tensile test results to assess the innovation risk for an additive manufacturing technology, Metrology and Measurement Systems, 22, 1, pp. 127–138.

Adamczak, S., Janecki, D., & Stepien, K. (2011) Cylindricity measurement by the V-block method - Theoretical and practical problems, Measurement, 44, 1, pp. 164–173. doi:10.1016/j.measurement.2010.09.039

ASTM (2013) ASTM: D638, Standard test method for tensile properties of plastics, ASTM Standards, pp. 1–16.

Bassoli, E., Gatto, A., & Iuliano, L. (2012) Joining mechanisms and mechanical properties of PA composites obtained by selective laser sintering, Rapid Prototyping Journal, 18, 2, pp. 100–108. doi:10.1108/13552541211212087

Blasiak, S. (2015a) An analytical approach to heat transfer and thermal distortions in non-contacting face seals, International Journal of Heat and Mass Transfer, 81, pp. 90–102. doi:10.1016/j.ijheatmasstransfer.2014.10.011

Blasiak, S. (2015b) The two dimensional thermohydrodynamic analysis of a lubrication in non-contacting face seals, Journal of Thermal Science and Technology, 10, 1, pp. JTST0016–JTST0016. doi:10.1299/jtst.2015jtst0016

Blasiak, S., Takosoglu, J. E., & Laski, P. A. (2014) Heat transfer and thermal deformations in non-contacting face seals, Journal of Thermal Science and Technology, 9, 2, pp. JTST0011–JTST0011. doi:10.1299/jtst.2014jtst0011

Bochnia, J., & Kozior, T. (2014) Methods of Prototyping Process Using Modern Additive Technologies, Solid State Phenomena, 223, pp. 199–208. doi:10.4028/www.scientific.net/SSP.223.199

Campbell, I., Bourell, D., & Gibson, I. (2012) Additive manufacturing: rapid prototyping comes of age, Rapid Prototyping Journal, 18, 4, pp. 255–258. doi:10.1108/13552541211231563

Laski, P. A., Takosoglu, J. E., & Blasiak, S. (2015) Design of a 3-DOF tripod electro-pneumatic parallel manipulator, Robotics and Autonomous Systems, 72, pp. 59–70. doi:10.1016/j.robot.2015.04.009

Miko, E., & Nowakowski, L. (2012) Analysis and Verification of Surface Roughness Constitution Model After Machining Process, In A. Martsynkovskyy, V and Zahorulko (Ed.), XIIIth International Scientific and Engineering Conference Hermetic Sealing, Vibration Reliability and Ecological Safety of Pump and Compressor Machinery-Hervicon-2011 (Vol. 39, pp. 395–404). doi:10.1016/j.proeng.2012.07.043

Puebla, K., Arcaute, K., Quintana, R., & Wicker, R. B. (2012) Effects of environmental conditions, aging, and build orientations on the mechanical properties of ASTM type I specimens manufactured via stereolithography, Rapid Prototyping Journal, 18, 5, pp. 374–388. doi:10.1108/13552541211250373

Takosoglu, J. E., Laski, P. A., & Blasiak, S. (2012) A fuzzy logic controller for the positioning control of an electro-pneumatic servo-drive, Proceedings of the Institution of Mechanical Engineers. Part I: Journal of Systems and Control Engineering, 226, 10, pp. 1335–1343. doi:10.1177/0959651812456498

Takosoglu, J. E., Laski, P. A., & Blasiak, S. (2014) Innovative Modular Pneumatic Valve Terminal With Self-Diagnosis, Control and Network Communications, In V. Fuis (Ed.), Engineering Mechanics 2014 (pp. 644–647). Dolejskova 5, Prague 8, 182 00, Czech Republic: Acad Sci Czech Republic, Inst Thermomechanics.

22nd International Conference
ENGINEERING MECHANICS 2016
Svratka, Czech Republic, 9 – 12 May 2016

NUMERICAL METHODS IN PROCESSES OF DESIGN AND OPERATION IN PNEUMATIC CONVEYING SYSTEMS

G. Borsuk*, S. Pochwała*, J. Wydrych*

Abstract: *During design and operation of large dust boilers systems one of the main problems is to provide the required distribution of the air-dust mixture to individual burners. Further, the higher concentration of particles in certain areas of the flow can cause uncontrolled erosion wear of these fragments. For boilers with burners in the corners, just behind the outlet of the mill four-path separator is built-in, whose task is even distribution of air-dust mixture. For numerical analysis Psi-CELL method was used to determine velocity distributions and for calculating particle trajectories Lagrangian method. Numerical calculations of the air-pulverized coal mixture flow through a pipeline with built-in elbow and a four- path separator were prepared. The result of the study showed when a small modification of the test system - by installing the threshold scattering - can reduce dust segregation intensity in the section downstream the elbow. It is also shown that the method adopted to calculate the system allows optimization of the flow for other very complex geometries.*

Keywords: Pneumatic conveying, two-phase flow, CFD, particle concentration distribution.

1. Introduction

During the design and operation of large power boilers systems there are many problems that impede the optimal operation of these systems. One of the main problems is to provide the required separation of a gas-particle mixture to each burner (Wydrych J., 2010, Xiliang C. et al, 2012). This problem is important not only because of the limitation of losses incomplete combustion, but also because of the life of parts of the combustion installation and nitrogen oxide emissions. In the case of boilers with corner burners, downstream to the outlet form the mill there is a four-path separator, where it should be uniform gas-particle mixture distribution.

2. Methods

The presence of particles in the gas volume has an effect on gas velocity and this effect depends on the particle concentration (Taylor T., 1998). For modeling the movement of diluted gas-particle mixture method in which the individual particles are considered as material moving points in space with the interaction with the gas and the walls is used (Liang C. et al, 2014). The Lagrangian method provides good quality of results for the volume fraction of particles less than 12% (Lain et al. 2012). Because of the potential movement analysis of the polidisperse gas-particle mixture PSICell method were used (Crowe C. et al. 1977). Neglecting the phase changes and assuming that both phases are microscipically incompressible, and the flow is isothermic and stationary, the gas motion can be described in the uniform, generalized conservative form, isolating convection, diffusion and source components. In a consequence we obtain

$$\frac{\partial(\rho\phi)}{\partial t} + \frac{\partial(\rho U_i \phi)}{\partial x_i} = \frac{\partial}{\partial x_i}\left(\Gamma_\phi \frac{\partial \phi}{\partial x_i}\right) + S_\phi + S_{\phi p} \tag{1}$$

where ϕ is a generalized dependent variable, Γ_ϕ is the coefficient of diffusion transport, and the source term S_ϕ contains all the remaining components of the differential equations (except for convection and

* Grzegorz Borsuk, PhD., Sławomir Pochwała, PhD., Jacek Wydrych PhD.:Opole University of Technology, Department of Thermal Engineering and Industrial Facilities, ul. Mikołajczyka 5, 45-271 Opole, g.borsuk@po.opole.pl

diffusion ones). The coefficients Γ_ϕ i S_ϕ are dependent on the variable ϕ. In the PSICell method it is assumed that particles of the disintegrated phase are the sources of mass, momentum and energy occurring as additional components $S_{\phi p}$ in equations of the continuous (gaseous) phase.

The system of equations is accompanied by suitable boundary and initial conditions. This system of partial differential equations is non-linear. Particular equations are coupled, so they have to be solved with special numerical techniques. The particle trajectory should be known during calculation of the mentioned source components. The particle trajectory is calculated according to its equation of motion (Lain et al. 2012). If the phase density difference is large, the equation of particle motion can be written as

$$m_p \frac{du_p}{dt} = \frac{3}{4} C_D \frac{\rho m_P}{\rho_p dp} u \left| u - u_p \right| (u - u_p) + g \tag{2}$$

where m_P is mass of the particle, and C_D is the aerodynamic drag coefficient. Special attention should be paid to the case when the particle collides with the wall. In such a case, components of the particle velocity vector after the collision are calculated from equations included normal and tangential coefficients of restitution. These coefficients are heavily depend on the particle impact angle, material properties of the particles and the walls as well as wall surface smoothness and particle shape.

3. Results

Analyzed flow system shown in Fig. 1. a) is an outlet straight section of the pipeline from the mill with the elbow.

a)

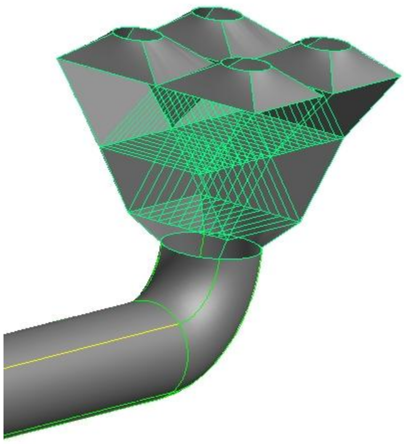

b)

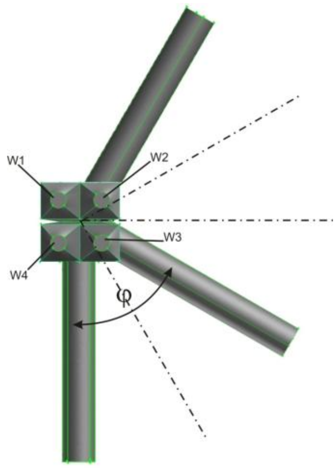

Fig.1. a) General view of four-part seperator with the elbow,
b) The tested system „ four-path separator" for different inlet locations.

Directly downstream the elbow there is a four-path separator. There were velocity and concentration measurements in the cross-sections upstream and downstream the elbow, as well as the fractional particle analysis. Measurements and numerical research were realized with an average load for the mill RP1043x ie. 40 t/h and the air flow of 70000 Nm^3/h. Based on the mathematical algorithm a series of numerical calculations were implemented, using FLUENT (Ansys Package). As a result of calculation obtained concentration of solid phase, as shown in Fig. 2.

To improve the flow conditions in the separator a special diffusion element was built. The purpose of the construction was to change the direction of gas flow and the particle concentration downstream the elbow. During the numerical calculations it was found that installing this element have an effect on the particle concentration change in the cross-section in the pipe downstream the elbow. It was determined that the diffusion element should be located in the area where is a high concentration of particles, i.e. in the final section of the elbow. As a result of particle collision with diffusion element formed mass distribution homogenize in the pipe downstream this element. On the basis of completed series of calculations it was found that the optimum ratio of diffusion element height h to the radius of bend R is 0.29. Moreover element placed in the elbow under an angle β=13,5° relatively best equalize the distribution of particle concentration upstream the separator.

a) b)

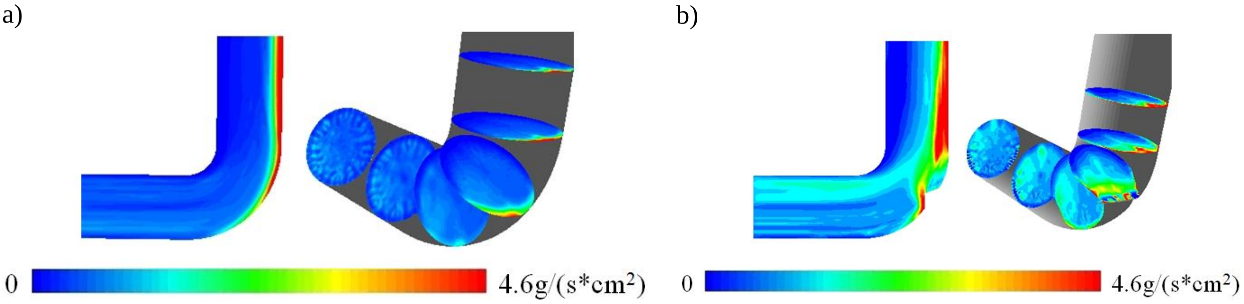

Fig. 2. Paricle concentration distribution in axis plane and selected cross-sections for the geometry a) without, b) with diffusion element

Further part of this paper was to evaluate the effect of the supplying pipe configuration to the four-path separator on the particle distribution uniformity downstream the separator. It was made an attempt to assess the effect of the configuration for six different settings of the entry section to the separator, at different velocities as well as particle diameters. In the calculation domain considered the complex internal structure of the separator, which is schematically shown in Fig. 1a. Setting the inlet compared to the position of the four-path separator is shown in Fig. 1b. The results was prepared for different inlet angles φ. The inlet plane illustrated as being vertical was marked as set of 0°, and further setting the set inlet of 30°, 60°, 90°, 120° and 150°. Fig. 1b shows a flow system in a top view with symbols of outlet cross-sections. The calculation results for trajectories of the particles delivered to the system from the point inlets of the system 90° and 150° are presented in Fig. 3.

a) b)

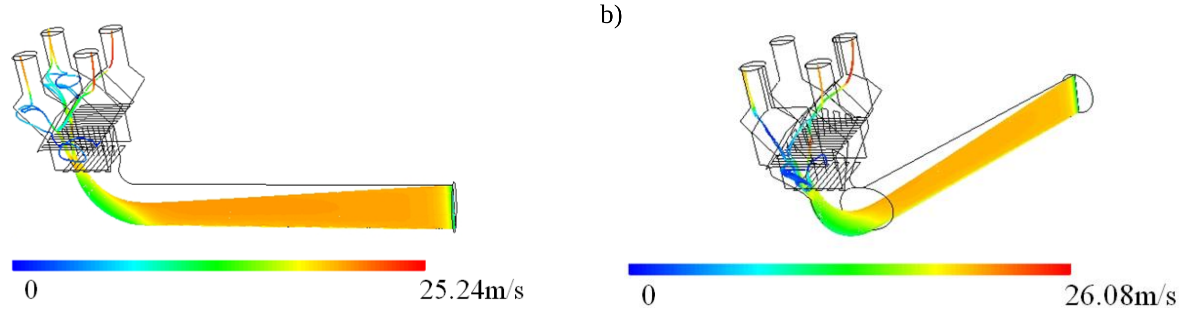

Fig. 3. Trajectories of the particles 100μm for the inlet velocities 25m/s for the system. a) *φ*=90°, b) *φ=150° (color indicates particle velocity)*

The tests concerned dispersed coal particles of 5, 10, 25, 50 and 100 μm. The calculations were performed for the stationary flow with the interfacial coupling. At the inlet to the calculation area, three stationary velocity distributions of the gaseous phase were assumed (25, 30 and 35 m/s).

Assuming that uniform separation (25% of particles for each outlet) provides the best service conditions of the boiler installation, at the next stage deviations of the calculated separations from the expected were estimated according to the following relation:

$$ED = \frac{D - 25}{25} \cdot 100 \qquad (2)$$

where *D* is the calculated separation, and *ED* deviation of separation from the expected value.

Analysis of calculated distribution deviations demonstrate that the increasing of inlet velocity of gas-particle mixture increases the uniformity of the particle distribution to the respective outlets, especially for systems with the angle of the inlet in relation to the separator within the range of 50-100°. For lower velocity to improve the uniformity of the distribution is at an angle φ approx. 90°.

The presented results allowed to formulate the sets of moduli of the averaged deviations from all the outlets for whole the polidysperse mixture. From these sets was built chart presented in Fig. 4, where changes of these moduli related to changes of velocity and angle of inlet location φ was compared.

Application of the smallest inlet velocity to the system causes occurrence of the largest non-uniformities in dust distribution to the outlets. At this velocity, the angle φ=60° is the optimum inlet angle in relation to the separator. Increase of the inlet velocity to 30 m/s causes a change of the optimum inlet angle to 80°. At the highest tested inlet velocity 35 m/s, the optimum inlet angle reduces to 70°. Such results testify strong influence of the inlet system on effectiveness of particle separation by the four-path separator. Moreover, we can find that particular inlet locations are optimum for the given service loadings, and a change of these conditions can cause a worse separation of particles to particular outlets.

a) b)

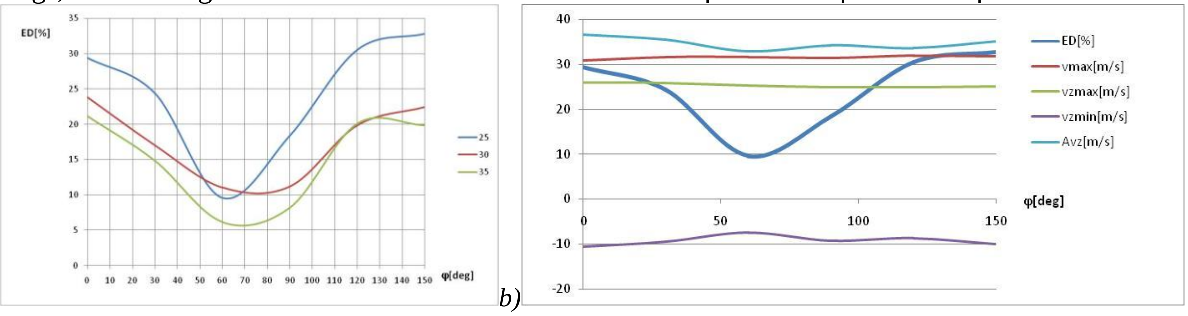

Fig. 4. a) Modulus of the averaged deviation for all the outlets
b) Changes of deviations, extreme velocities and velocity amplitudes versus the inlet location angle φ

The further part of analysis includes an attempt of a relation between deviations of particle separation from the expected values and gas velocities for different inlet-separators systems determination. Fig. 4a shows changes of separation deviations, maximum gas velocities, maximum, minimum and component vertical gas velocities caused by changes of locations of the inlet angle φ.

The data presented in Fig. 4b allowed to determine correlations between them, and calculated correlation coefficients allow to state that there are not important relations between the maximum moduli v_{max} and vertical component v_{zmax} gas velocities and separation deviations. On the other side, high convergence between the minimum values v_{zmin} and amplitudes A_{vz} of vertical velocity components with separation deviations from the expected values can be seen.

4. Conclusions

Completed numerical calculations lead to the conclusion that placing the diffusion element significantly affects the concentration of dust in the cross-section of the pipe downstream the elbow and very important for diffusion element localization. Measurements of concentration before and after installing the diffusion element made explained the desirability of the building. It is advisable to conduct further numerical calculations carried out mainly for optimization of diffusion element shape.

Regarding the elbow and four-path separator analysis leads to the conclusion that due to the method used, it is possible to define the geometry of the four-path separator, which ensure optimum distribution of particles into selected outlet sections. It has been found that the use of minimum inlet velocity for the system affects the occurrence of nonuniformity in the largest section of particle outlets. Changing the inlet velocity influences the optimum angle of the inlet. These results indicate a major impact on the efficiency of the inlet particle separation by the four-path separator.

References

Crowe Clayton T., Stock David E. & Sharma M.P., (1977) The particle-sources-in cell /PSI-CELL/ model for gas-droplet flows. Journal of Fluid Engineering No. 99, pp. 325-332.

Lain S. & Sommerfeld M. (2012) Numerical calculation of pneumatic conveying in horizontal channels and pipes: Detailed analysis of conveying behavior. International Journal of Multiphase Flow, No. 39, pp. 105–120.

Liang C., et al, (2014) Comparison of pressure drops through different bends in dense-phase pneumatic conveying system at high pressure. Experimental Thermal and Fluid Science, No. 57, pp. 11-19.

Schuh M.J., Schuler C.A. & Humphrey J.A.C., (1989) Numerical calculation of particle laden gas flows past tubes. AIChE Journal, No. 35, 3, pp. 466-480.

Sommerfeld M. & Huber N., (1999) Experimental analysis and modelling of particle–wall collisions. International Journal of Multiphase Flow, No. 25, 6,7, pp. 1457–1489.

Taylor T., (1998) Specific energy consumption and particle attrition in pneumatic conveying. Power Technology, No. 95, pp. 1-6.

Wydrych J., (2010) Comparative analysis of the methods of simulation of flow in boiler dust systems. Chemical and Process Engineering, No. 31, 4, pp. 603-623.

Xiliang C., et al, (2012) Investigations of pulverized coal pneumatic conveying using CO2 and air. Powder Technology, No. 219, pp. 135–142..

22nd International Conference
ENGINEERING MECHANICS 2016
Svratka, Czech Republic, 9 – 12 May 2016

ON PARALLELIZATION OF ASSEMBLY OPERATIONS IN FINITE ELEMENT SOFTWARE

M. Bošanský[*], B. Patzák[**]

Abstract: *Current development in computer hardware brings in new opportunities in numerical modelling. Computers with a single processing unit, where only one instruction can be processed at any moment in time, allow us to run simulation codes only sequentially. The performance of single processing units is reaching the physical limits, given by transmission delays and heat build-up on the silicon chips. The future of scientific computing seems to be in parallel computing, that allows to overcome the limitations of traditional sequentional processing units. Parallel computing is based on simultaneous use of multiple processing units. The fundamental paradigm in parallel computing is based on work decomposition into pieces of work that can be processed simultaneously. This contribution focuses on parallelization of sparse matrix and global vector assembly operations, which are typical to any finite element code. The aim of presented work is to propose an alternative approach to assembly operation based on decomposition of the work into independent element groups, members of which can be processed concurrently without blocking operation. The individual groups contain elements contributing to distinct entries in sparse matrix or global vector. Such decomposition is done using colouring algorithm. As the elements in group contribute to distinct locations, there is no need to prevent the race condition, that can occur when the same location is updated simultaneously. It is only necessary to enforce synchronization before processing each element group. Efficiency of implemented approach is compared to approach based on decomposition of assembly loop using OpenMP directives and explicit locking of updated locations in sparse matrix or global vector, which was published by the authors in (Bosansky & Patzak, 2016a) and (Bosansky & Patzak, 2016b).*

Keywords: Finite element method, shared memory, colouring algorithm.

1. Introduction

Parallelization can significantly reduce computational time by more efficient use of available hardware resources (Patzak, 2010). The existing parallel computers can be divided by type of memory architecture. The main types include shared, distributed, and hybrid memory systems (Hughes C. & Hughes T., 2003). shared memory systems are characterized by a common, global memory space, which is accessible to all individual processing units. Efficient and scalable parallel algorithms are more difficult to design than serial ones, because parallelism introduces new sources of complexity. The design of any parallel algorithm requires to split the work into the set of smaller tasks, which are solved concurrently by the simultaneous use of multiple computing resources (Barney, 2010). Additional care must be taken to establish communication and synchronization between the tasks. The scalability of a parallel algorithm, represents the ability to reduce required solution time with increasing number of processing units. However, the ideal linear trend is difficult to obtain due to additional overhead of parallel algorithm (synchronization, locking) and due to the fact that some parts may have to be processed serially.

In this paper we use Open Multi-Processing (OpenMP) programming model to implement different variants of parallel assembly operations. OpenMP is a shared memory programming model that supports multi-platform shared memory multiprocessing programming in C, C++ (Stroustrup, 1997), and Fortran, on most processor architectures and operating systems (Barney, 2014). It consists of a set of compiler directives, library routines, and environment variables that influence run-time behaviour. OpenMP parallel constructs allow us to overcome relatively straightforward parallelization of serial code, by

[*] Ing. Michal Bošanský, Department of Mechanics, Faculty of Civil Engineering, CTU in Prague, Thákurova 7/2077; 166 29, Prague; CZ, michal.bosansky@fsv.cvut.cz

[**] Prof. Bořek Patzák, Department of Mechanics, Faculty of Civil Engineering, CTU in Prague, Thákurova 7/2077; 166 29, Prague; CZ, borek.patzak@fsv.cvut.cz

providing constructs enabling to parallelize the for-loops (Chapman et al., 2008). This is achieved by marking such a loop by special compiler directives as a parallel loop. The rest is done almost automatically by a compiler, which splits the loop into parts that are subsequently assigned to individual threads of execution. The user can adjust certain parameters that affect the work assignment (static or dynamic), and the scope (local or shared) of variables inside the loop.

Finite Element Method (FEM) is the most popular method to solve various problems in engineering. It actually identifies a broad spectrum of methods for finding an approximate solution to boundary value problems for partial differential equations. The differential equations are converted to the algebraic system of equations by using variational methods and by decomposing the problem domain into sub-domains called elements. In structural mechanics, the resulting algebraic equations correspond to the discrete equilibrium equations at nodes of the computational mesh. In matrix notation we can write

$$\mathbf{K}\,\mathbf{r} = \mathbf{f} \tag{1}$$

where **K** and **f** are global stiffness matrix and load vector, and **r** is vector of unknown displacements.

The vector as well as the stiffness matrix are assembled from individual elements contributions

$$F_i = \sum F_i^e\ ;\ f_i = \sum f_i^e\ ;\ K = \sum K^e\ ; \tag{2}$$

The assembly process is relying on global numbering of discrete equilibrium equations yielding so called code-numbers assigned to nodes (identifying equilibrium equations assembled in given node) and to elements (identifying equilibrium equation into which the element end-forces contribute). The typical serial algorithm for vector assembly is following

Algorithm 1: Prototype code - Assembly of element part of load vector

```
for elem=1, nelem
    F^e = computeElementVecto(elem)
    Loc^e = giveElementCodeNubmer(elem)
    for i = 1, Size(Loc^e)
        F(Loc^e(i))+ = F^e(i)
```

This assembly operation evaluates individual element contributions. This operation in case of nonlinear problem can be repeated several times and can be costly.

The parallelization strategy of the assembly operation is typically based on domain decomposition paradigm, where the elements are divided into disjoint subsets (called sub domains), that are processed by individual threads. The individual element contributions are computed in parallel and then assembled into the corresponding global form a equilibrium equations. However, as elements processed by individual threads may contribute to the same global equilibrium equation, it is necessary to ensure that multiple threads do not update the same value in global force vector or stiffness matrix at the same time, as this will lead to unpredictable and incorrect results.

2. The flow of control of the Assembly Loop and Parallelization of the Assembly Loop

The traditional approach, as discussed in previous paragraph, requires explicit locking of updated memory cells to prevent simultaneous update. Such locking and its associated overhead have negative impact on overall parallel efficiency.

The idea followed in this work is based on alternative decomposition of elements into disjoint groups, where contributions of individual elements in a group do not update the global entry updated by another element within the same group. The elements in the same group should not share any common node to satisfy this requirement. Such decomposition can be obtained by a so-called colouring algorithm, described in (West, 2001), for example.

The direct consequence of this decomposition is the possibility to process all elements within a group in parallel without the need of any locking or synchronization. The serial assembly procedure has to be decomposed into outer loop over element groups and inner loop over elements of individual group, that can be processed concurrently. The optimum performance can be expected when the number of groups will be minimal and when the inner loop will be optimally decomposed into available processing nodes, either using static or dynamic load balancing.

3. Results

The approach with colouring algorithm was evaluated using a benchmark problem of a 3D finite element model of nuclear containment. The mesh consists of 899780 nodes and 114878457 tetrahedral elements with linear interpolation. The total number of equations was 3013128 and number of colours was 15. The structure has been loaded with self-weight, resulting in nonzero contribution of every element to external load vector. The individual approaches have been tested on Linux workstation (running Ubuntu 14.04 OS) with the two CPU Intel(R) Xeon(R) CPU E5-2630 v3 @ 2.40GHz and 126GB RAM. The two CPU units consists of eight physical and sixteen logical cores, allowing up to thirty-two threads to run simultaneously. All the tests fit into a system memory.

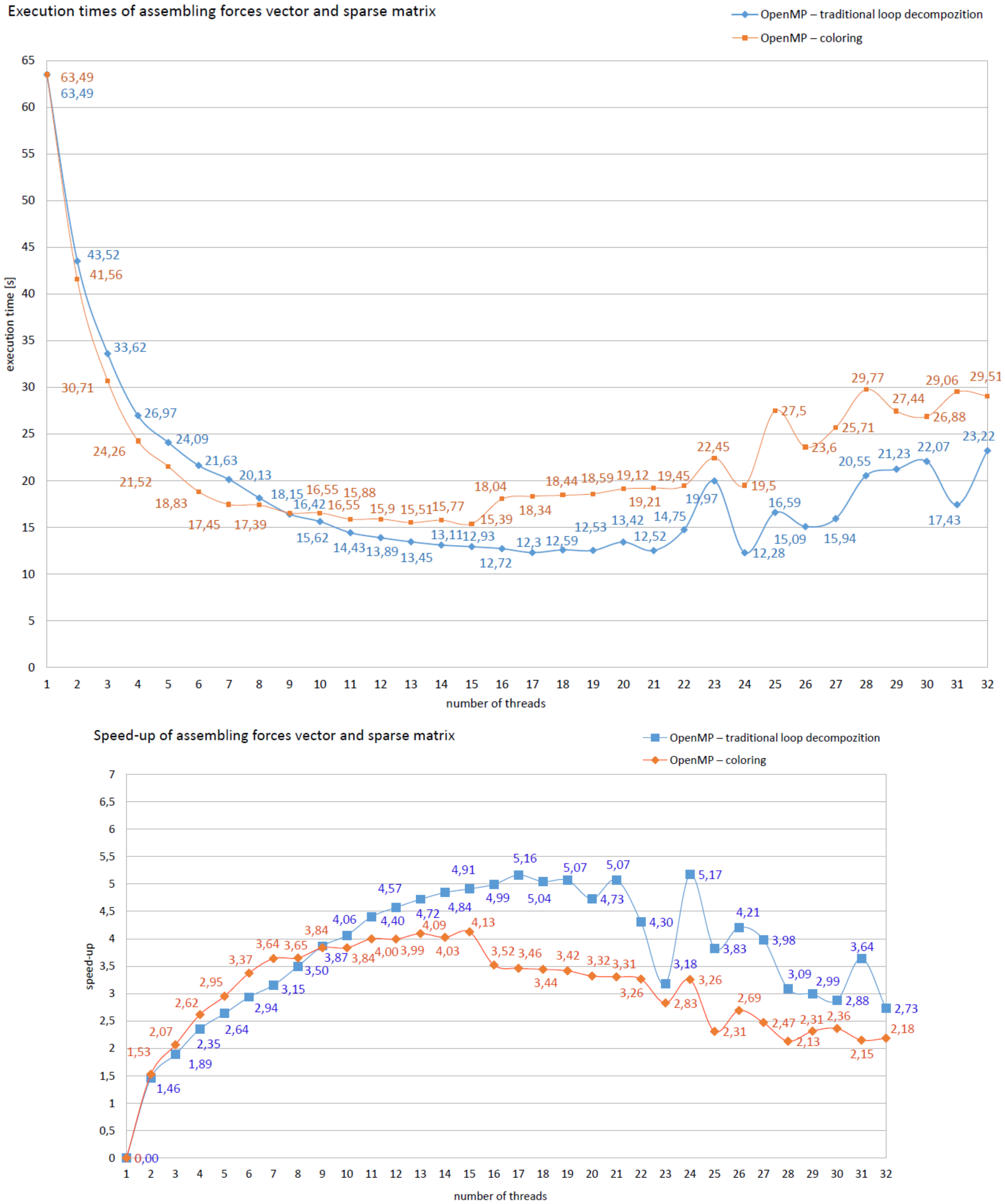

Fig. 1: Execution times and speed-ups.

Executions times and speed-ups of assembly operations based on previously mentioned strategies using OpenMP parallel constructs (synchronization using Critical sections or Simple locks) using different numbers of threads were taken from (Bosansky & Patzak, 2016a) and (Bosansky & Patzak, 2016b). Executions times and speed-ups for assembly operations obtained using decomposition based on colouring algorithm are presented in Fig. 1. The reported execution times have been obtained as an average from five consecutive runs. It can be observed that time needed for calculation is reduced as number from threads gets bigger. Nevertheless, the impact of overhead is dominant with number of threads bigger than twenty and the overall speed-up is clearly not ideal, see Fig. 1. This is partially due to the additional overhead associated with parallel implementation (thread creation and management, synchronization) that is not present in the serial version. Compared to traditional loop based decomposition, the colouring decomposition performs better, reducing the parallel overhead. However, the overall trend is similar. Additional performance decrease (see Fig. 1) can be attributed to the hyper-threading technology specific to Intel processors, leading to sharing of CPU resources (execution engine, caches, and bus interface) between the hyper-threaded cores, but this is the factor common for both approaches.

The results indicate that the colouring strategy performs better for lower number of threads involved. In our opinion this is the consequence of avoiding the need for explicit synchronization. However, for higher number of threads, the OpenMP with synchronization performs better. It seems that part of the problem would be in less optimal use of shared L3 cache on the processor. The nodes are numbered in a way that allows to minimize sparse profile and reduce data transfer to/from cache memory. However, the parallelization approach using the colouring scheme accesses the individual elements in non-sequential order, which results in less optimal use of cached data with higher ratio of cache misses. However, the reasons for this behaviour are not yet fully understood and further evaluation is required.

4. Conclusions

In this work we compare two approaches for parallelization of assembly operation. The first is based on traditional loop-based decomposition using OpenMP constructs, while the other uses alternative decomposition into element groups based on connectivity considerations, allowing to process elements in individual group in parallel without any extend synchronization or locking. The latter approach performs slightly better, but further optimization can improve it performance.

Acknowledgement

This work was supported by the Grant Agency of the Czech Technical University in Prague, grant No. SGS15/031/OHK1/1T/11 “Advanced algorithms for numerical modelling in mechanics of structures and materials”.

References

Barney B. (2010) Task scheduling for parallel systems. https://computing.llnl.gov/tutorials/parallel comp/.

Barney B., Lawrence Livermore National Laboratory (2014) OpenMP - An Application Program Interface. https://computing.llnl.gov/tutorials/openMP/.

Bosansky M., Patzak B. (2016a) Different Approaches to Parallelization of Vector Assembly. In Applied Mechanics and Materials, Trans Tech Publications, Vol. 821, pp. 341-348.

Bosansky M., Patzak B. (2016b) Different Approaches to Parallelization of Sparse Matrix Operation. Applied Mechanics and Materials, Trans Tech Publications, Vol. 825, pp. 91-98.

Hughes C., Hughes T. (2003) Parallel and Distributed Programming Using C++. ISBN 0-13-101376-9, Pearson Education.

Chapman B., G. Jost, R.V.D. Pas (2008) Using OpenMP - portable shared memory parallel programming. Morgan Kaufmann Publishers, Inc.

Patzak B. (2010) Parallel computations in structural mechanics. ISBN 978-80-01-04565-7, Czech Technical University in Prague.

Stroustrup B. (1997) The C++ programming language. Murray Hill, AT Labs Murray Hill, New Jersey.

West, D. B. (2001) Introduction to graph theory. Vol. 2, Upper Saddle River: Prentice hall.

22nd International Conference
ENGINEERING MECHANICS 2016
Svratka, Czech Republic, 9 – 12 May 2016

A NUMERICAL STUDY OF TEMPERATURE AND STRESS DISTRIBUTIONS IN THE BRAKING DISK

P. Brabec[*], K. Fraňa[**], R. Voženílek[***], T. Zvolský[****]

Abstract: *Peak temperatures in the brake system have been identified numerically using calculation procedures. These calculation approaches were validated on the simple rotating disk involving the heat transfer by a convection, conduction and radiation. Furthermore the stress calculation was carried out in order to identify the stress peaks. Calculations have been performed on the real train path including braking, accelerating and waiting at the train stations. Generally, the temperature peaks have been identified immediately after several braking periods within a short time interval. These temperature maxima, however, drop quickly due to the heat conduction and simultaneously the higher stresses in the disk material have been observed.*

Keywords: Temperature distributions, brake disc, simulations, braking systems, brake cycles.

1. Introduction

The objective of the paper is to investigate a temperature distribution on the rotating disk and indirectly on the surface of brake elements. Results of the temperature distribution in time and space were used to identify temperature peaks at surfaces of the rotating disk. Furthermore, the stress analysis was performed. Peak temperatures determined for the particular train path including braking, waiting at stations and acceleration can predict service conditions of the braking system and help to find appropriate materials for the brake elements in regarding to the temperature performance.

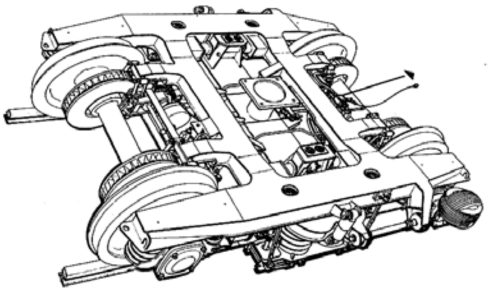

Fig. 1: The example of disc brakes for rail vehicles - GP 200 S chassis for wagon Amee and Bmee without axle generator [Reference 5]

Calculation procedures including settings of the boundary conditions were verified by the experimentally provided data. Temperature distributions obtained numerically were used for the structural analysis. The cast iron material commonly denoted as EN-GJL-250 (CSN 42 2425) was proposed by designer as the main material of brake discs with material properties as follows: the tensile modulus $E = 110000\,\mathrm{MPa}$; the Poisson number $\mu = 0.26$; the density $\rho = 7200\,\mathrm{kg \cdot m^{-3}}$; the specific heat capacity $c_p = 460\,\mathrm{J \cdot kg^{-1} \cdot K^{-1}}$; the thermal expansion coefficient $\alpha_1 = 11.7 \cdot 10^{-6}\,\mathrm{K^{-1}}$ and the thermal conductivity $\lambda_t = 48.5\,\mathrm{W \cdot m^{-1} \cdot K^{-1}}$.

[*] Ing. Pavel Brabec, Ph.D.: Technical University of Liberec, Studentská 2; 461 17, Liberec 1; CZ, pavel.brabec@tul.cz
[**] Doc. Ing. Karel Fraňa, Ph.D.: Technical University of Liberec, Studentská 2; 461 17, Liberec 1; CZ, karel.frana@tul.cz
[***] Ing. Robert Voženílek, Ph.D.: Technical University of Liberec, Studentská 2; 461 17, Liberec 1; CZ, robert.vozenilek@tul.cz
[****] Ing. Zomáš Zvolský: Technical University of Liberec, Studentská 2; 461 17, Liberec 1; CZ, tomas.zvolsky@tul.cz

2. Methods

To identify temperature peaks at the surface brake elements, the numerical analysis of the heat flux balance was performed. The heat was generated because of a friction during the braking phases and the cooling of the brake disk was controlled by the convection and the heat transfer to surroundings. This heat transfer to surroundings was carried out by a force or natural convection, heat conduction and radiations. The intensity of the heat transfer for different heat transfers is given by parameters such as a speed of the rotating disk, the coefficient of the heat conductivity, size of surfaces, temperature differences etc. Details about fundamental aspects of the heat transfer can be found e.g. in the reference 1. The commonly used non-dimensional parameter for convection is the Nusselt number which takes a form as

$$N_U = \alpha \cdot \frac{l_{ch}}{\lambda} \tag{1}$$

where α is the heat transfer coefficient for a convection, l_{ch} is characteristic length and λ is the heat transfer coefficient for a conduction. From experiments of the simple rotating disk, the Nusselt number varies between values from tens to thousands depending on the Reynolds number (references 2 and references 3). The Reynolds number is defined as

$$R_e = \omega \cdot \frac{R^2}{\upsilon}. \tag{2}$$

where ω is the angular velocity, R radius and υ is a kinematic viscosity. The Nusselt number for different Reynolds numbers is shown in Figure 2.

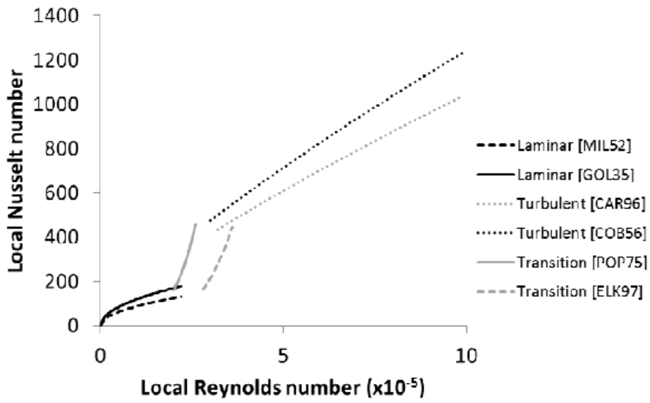

Fig. 2: Local Nusselt numbers over a rotating disc in quiescent air for isothermal surface

In our study, The Reynolds number is lower than $3 \cdot 10^5$ so that the laminar flow conditions were considered. the Nusselt number took values from 10 to 200. Taking into account the heat transfer by a radiation, the estimated heat flux of the rotating disk can be calculated. The combination of the theoretical calculation and experimental results provided the heat flux value which can be used further as the boundary conditions for simulations. However, the averaged surface temperature field, the constant surrounding conditions and many other simplifications can consequently reduce the accuracy of the heat flux prescription. In our study the heat transfer balance was simulated for the service condition including braking, acceleration and waiting with short time steps.

Because of the short time step, the influence of the radiation in respect to the small surface and the lower temperature can be neglected. Therefore, only natural and force convection can be considered for calculations. In this particular case, only the heat convection was taken into account and the heat coefficient for convection was directly prescribed at boundary conditions. The solver calculates automatically the amount of the heat transfer due to convection based on the actual local temperate difference between disk surfaces and surroundings. Results were validated by experiments which described declines of the heat at the disk surface during rotations or breaks. The figure 3 shows the drop of the surface temperature calculated numerically and validated by experiments. For the particular heat transfer coefficient prescribed in the simulation, the satisfied match could be found between experimentally and numerically provided surface temperature of the brake disk.

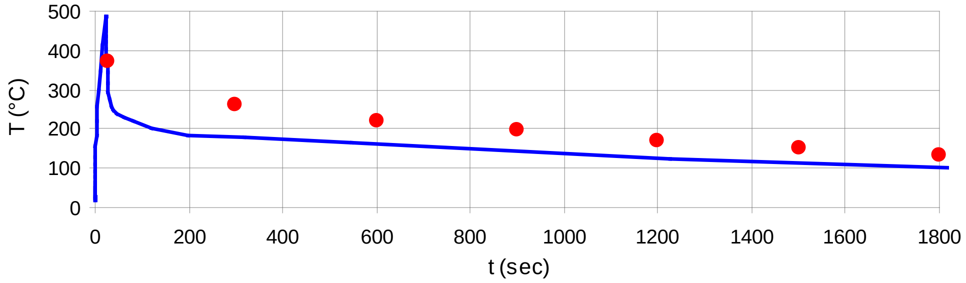

Fig. 3: The temperature drop in time during braking. The blue colour indicates the heat convection and red points express measured values.

Measured surface temperatures on the disk at the beginning and at the end phase helped to precise the value of the heat convection coefficient (see Fig. 3). Besides the convection, the heat accumulation was considered for calculations as well. However, the heat accumulation effect was significant only in particular service regimes mostly at the beginning. The amount of the heat accumulated into materials was estimated from the proportion of temperature changes provided by experiments.

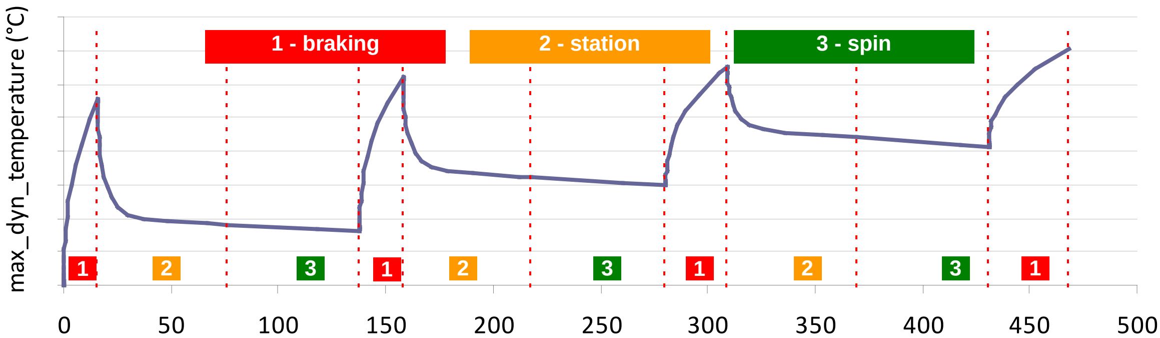

Fig. 4: The development of the maximum temperature on the model versus time (simulation of experiment)

3. Simulation of driving cycle - calculation of surface temperature on the brake disc

For setting of boundary conditions, data about service train path e.g. speed limits in time etc., were used.. Furthermore, the simulation study considered different slopes of the train track expressed in ‰ which took the positive or negative value based on the climbing or descending of the train. Moreover the braking by the engine was taken into account in the study which finally led to a reduction of the loading of the braking system. Results such as peak surface temperatures etc. were plotted in time of the train movement. Other effects such as the heat conduction in the brake elements were not considered in calculations because of the complexity. Nevertheless, experiments demonstrated obviously that the amount of the heat transported towards brake elements accounted approximately 3% of the total generated heat due to braking. Therefore, this part of conduction was neglected for further calculations.

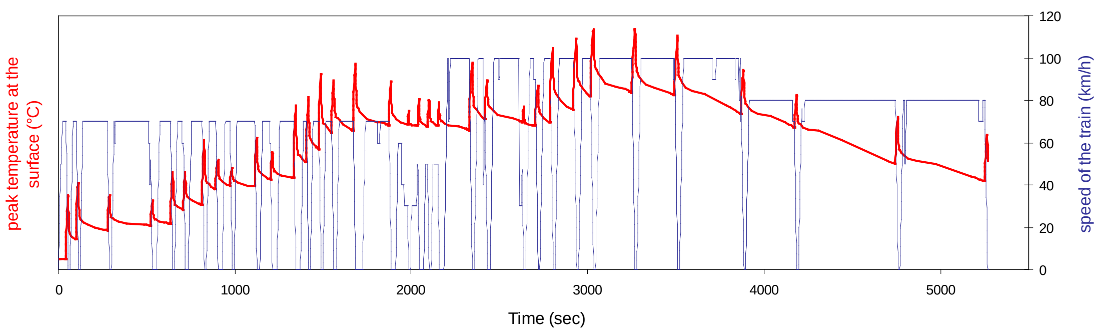

Fig. 5: Graph of maximum instantaneous surface temperature at the contact surface of the brake disc with the brake pads on the time (simulations of the driving cycle)

4. Stress analysis on the brake disc

Following calculations deal with the stress identification on brake discs for stop mode of train during one braking period, from the speed of 100 km/h to stall. The simulated model consisted of three components - brake disc, hub and ground cloth. Because of the complexity, all three parts of the model were considered as a one solid body without any gaps between them. Simultaneously, the pre-stressed bolt connections were neglected. The great influence on the stress results had a fixed storage of the brake disc to the hub through screw connections. The stiffness of the hub did not allow deformations because of temperatures and the thermal expansion coefficient of the material of the disc. For materials of the brake disc the ultimate tensile strength (R_{mt} = 250 MPa) was lower than the limit of the compressive strength (R_{md} = 950 MPa). The classical hypothesis HMH (Huber-Mises-Hencky) was applied for tough materials and it was inappropriate for our calculations. For our particular problems the basic hypothesis of strength for brittle materials, like e.g. Mohr hypothesis (basic linear variation also known as Mohr-Coulomb) was suitable and therefore it was preferred.

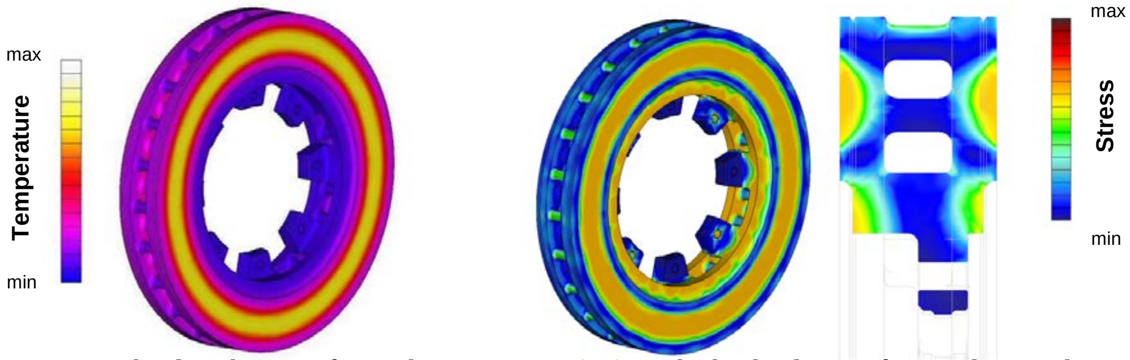

Fig. 6: The distribution of actual temperature (°C) on the brake disc surface and equivalent stress (von Mises) (MPa) on the brake disc at the end of the braking phase

5. Conclusions

The paper presented possibilities to numerically predict temperature and stress distributions in time of the train path. Thermodynamics knowledge and experiments were used to determine values of the natural or force convection coefficients. The obtained results e.g. peak surface temperatures determined service conditions under which the brake element materials must survive. The train path contained several braking, acceleration and waiting periods. For particular train path, temperature peaks were identified in time. The temperature maxima appeared immediately after the braking. In several seconds after the braking, this peak surface temperature rapidly dropped due to intensive heat conduction in the brake disc. However, even the short exposition by the higher temperature can be crucial for several materials used commonly for braking elements. Furthermore, stress analyses were performed and the peak stress was located. This numerical study demonstrated a feasibility to predict several operating conditions and limits which can be take into account for a design of the brake system.

Acknowledgement
This publication was written at the Technical University of Liberec, Faculty of Mechanical Engineering with the support of the Institutional Endowment for the Long Term Conceptual Development of Research Institutes, as provided by the Ministry of Education, Youth and Sports of the Czech Republic in the year 2016.

References

Incropera, F.P. et al. (2007) Introduction to Heat Transfer, John Wiley&Sons.

Harmand, S., Pelle, J., Poncet, S. & Shevchuk, I.V. (2007) Review of fluid flow and convective heat transfer within rotating disk cavities with impinging jet.

Shevchuk, I.V. (2009) Convective Heat and Mass Transfer in Rotating Disk Systems. Springer Verlag, Berlin, Heidelberg, pp.1-239.

Brabec, P., Fraňa, K. & Voženílek, R. (2015) Calculation of the braking discs, technical reports, Technical university of Liberec.

http://www.parostroj.net/katalog/ov/clanky/vozy_A_Bmee/vozy_A_Bmee.php3

22nd International Conference
ENGINEERING MECHANICS 2016
Svratka, Czech Republic, 9 – 12 May 2016

MODELING A PNEUMATIC CYLINDER WITH FRICTION

G. F. Bracha*

Abstract: *This article shows method of obtaining a mathematical model of a pneumatic actuator including changes in pressure, temperature, simplified flow of heat to the environment and friction. Position and velocity graph of real pneumatic drive and its mathematical model implemented in Matlab with LuGre and Stribeck friction was presented.*

Keywords: pneumatics, mathematical model, friction.

1. Introduction

One of the basic elements used in the industry is a pneumatic drive, in most cases is used for tasks that require dynamic pivot of action as well as a huge amount of work cycles. Pneumatic actuators are also used for positioning elements which do not require high precision or because of the operating environment is not possible to use a different drive. There are also application of pneumatic drives for manipulators with several degrees of freedom(Laski et al., 2014). In these cases, the pneumatic control requires the use of more stringent controls than other types of actuators.

2. Mathematical model of the pneumatic cylinder

The mathematical model of the pneumatic cylinder is based on the energy balance resulting from the assumptions: pneumatic actuator converts the energy of compressed air entering to the cylinder Q_i to work L, at the moment the compressed air in the chamber has a stored energy U and a stream of energy transmitted through the housing to the environment as a heat Q_T.

$$Q_i = Q_o + dL + dU + Q_T \tag{1}$$

Eq. 1: Energy equation; Q_i – flowing energy, Q_o – outflow energy, dL – the work done by the actuator, U – changes in internal energy, Q_T – energy fed back into the environment.

The energy entering and leaving in the form of compressed air can be written as the product of the air mass and its enthalpy: $Q = h \cdot dm$, assuming that the air supplied to the actuator has a constant pressure, enthalpy of the air express as a specific heat at a constant pressure with a known temperature $h = c_p \cdot T$. We assume that the air entering temperature is constant and equal to an ambient temperature and the outflow temperature is variable and corresponds to the actual temperature of air in the cylinder. The work done by the drive will be described as the product of pressure and volume change of the chamber: $L = p \cdot dV$ and internal energy as the product of specific energy and the current air mass: $dU = du \cdot m + dm \cdot u$, where $u = c_v \cdot T$ (c_v - specific heat at constant volume). The energy dissipated by the cylinder actuator housing will be described in a simplified form as a product of the coefficient of heat transmission α, heat casting surface $S = \pi D x$ (D – diameter of the piston, x – the current position of the piston) and the temperature difference between the actuator and the environment:

$$Q_T = \alpha\pi(Dx + 0,25D^2)\Delta \mathrm{T dt}. \tag{2}$$

Using these dependencies we will write:

* M.sc. Gabriel Franciszek Bracha.: Department of Applied Computer Science and Armament Engineering, Kielce University of Technology, Al. Tysiąclecia P.P. 7; 25-314, Kielce; PL, gbracha@tu.kielce.pl

$$c_p T_i dm_i - c_p T_o dm_o - pdV - c_v dTm - dmc_v T - \alpha\pi(Dx + 0,25D^2)\Delta \mathrm{T}_o \mathrm{dt} = 0 \qquad (3)$$

For further considerations, we assume that the working medium is ideal gas which satisfies the Clapeyron equation in form: $mRT = pV$, heat capacity ratio $k = c_p / \mathrm{c}_v$ and the gas constant $R = c_p - c_v$.
Changes in internal energy, which depends on weight changes we describe in the form of: $dm = \frac{1}{RT}\left(dpV + dVp\right)$, and then, after simple transformations balance equation takes the form:

$$kRT_i dm_i - kRTdm_o - kpdV - \frac{pVdT}{T} - dpV - (k-1)\alpha\pi(Dx + 0,25D^2)\Delta \mathrm{T}\mathrm{dt} - = 0 \qquad (4)$$

And after pulling out pressure we obtain the differential equation describing the pressure changes:

$$\dot{p} = \frac{1}{V}\left(kRT_i\dot{m}_i - kRT\dot{m}_o - kp\dot{V} - \frac{pV}{T}\dot{T} - (k-1)\alpha\pi\left(Dx + 0,25D^2\right)\Delta \mathrm{T} \right) \qquad (5)$$

The equation of the temperature in the chamber of the actuator is obtained from the differential equation of the ideal gas: $R \cdot dm \cdot dT = dV \cdot dp$, which after calculation and re-substitution Clapeyron equation instead of the air mass and $V = Ax$ where A is a surface of piston:

$$\frac{dT}{dt} = T\left(\frac{1}{p}\frac{dp}{dt} + \frac{1}{x}\frac{dx}{dt} - \frac{\dot{m}RT}{pV} \right) \qquad (6)$$

On the piston acts pressure difference between the chambers of the actuator, and the friction force F_T , from Newton's law we determine the equation:

$$\frac{d^2x}{dt^2} = \frac{1}{m}\left[A\left(p_1 - p_2\right) - F_T \right]. \qquad (7)$$

These equations describe the pressure and temperature in a single chamber into a full description of the operation of the actuator also requires a model of the second chamber. The realization of such a system in Matlab is shown in Figure 1. More complex model which takes into account the flow of heat between the chambers of the actuator, can be obtained from work relating to heat flow through the seal. (Blasiak et al., 2014)

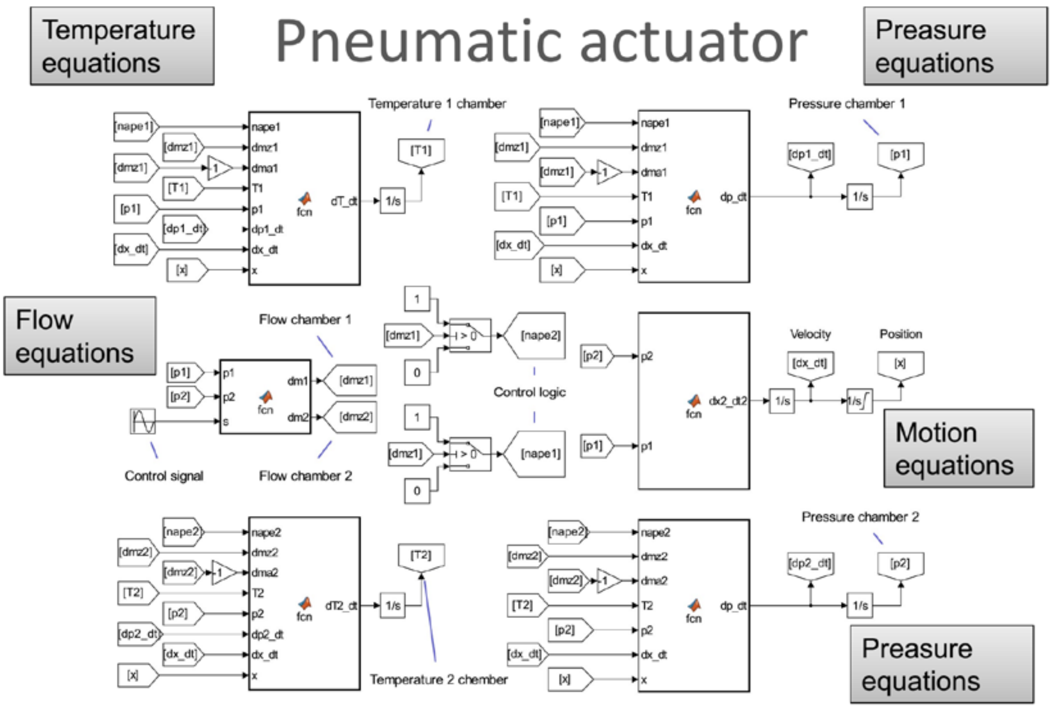

Fig. 1: Pneumatic actuator model implemented in Matlab - Simulink.

3. Model of friction in pneumatic drives

The forces of friction in pneumatic drives are especially important at low speeds as well as during starting when the transition from static friction to kinetic occurs. Mathematical models describing the physical phenomena occurring in the sealing elements have been described, for example. in the works: (Blasiak, 2015),(Blasiak & Zahorulko, 2016). There are several basic models of friction, which allows the actuator to create a model suitable for simulation, selection of controls and control systems. One such model is the model of friction Lund – Grenoble (Olsson, 1996). This model besides typical representation of drive operation with friction, also allows simulations of well-known and very negative phenomenon of stick-slip, which makes precise positioning of pneumatic drives for low speeds practically impossible. Mathematical notation of friction equations is as follows:

$$\frac{dz}{dt} = v - \sigma_0 \cdot \frac{|v|}{g(v)} \cdot z \qquad g(v) = F_c + (F_s - F) \cdot e^{-(v/v_s)^2} \qquad F_f = \sigma_0 z + \sigma_1 \dot{z} + F_v v \qquad (8)$$

where z – average deviation bristles, v – velocity of the piston, σ_0 – stiffness of bristles, σ_1 – damping,

F_v – viscous friction, F_c – Coulomb force, F_s – stiction force.

The realization of friction LuGre is shown in Fig. 2.

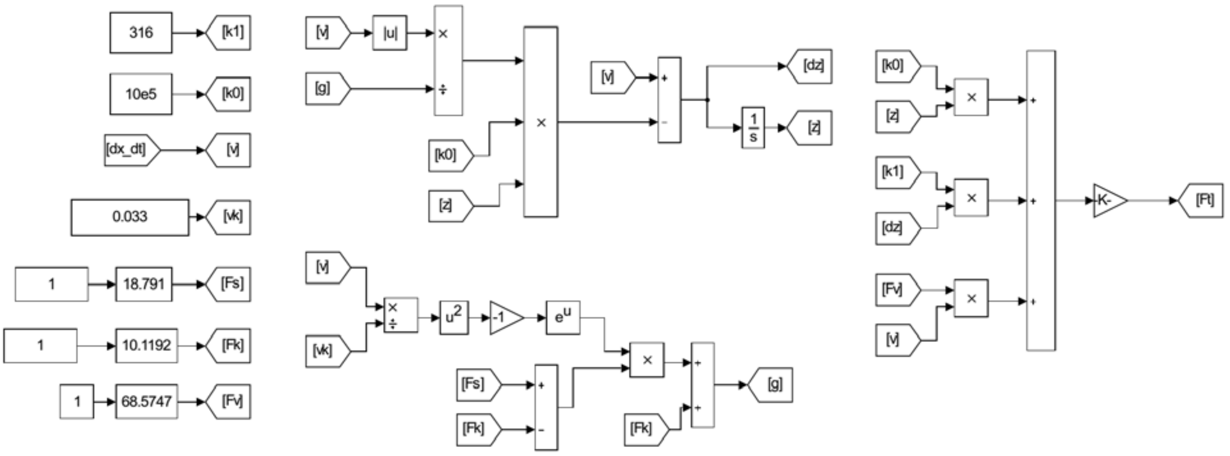

Fig. 2: Implementation of LuGre friction model in Matlab – Simulink .

Figure 3 shows the speed and movements of a real cylinder, on this graph is possible to observe the phenomenon of stick-slip. The figure also shows simulation results of pneumatic piston model with LuGree friction.

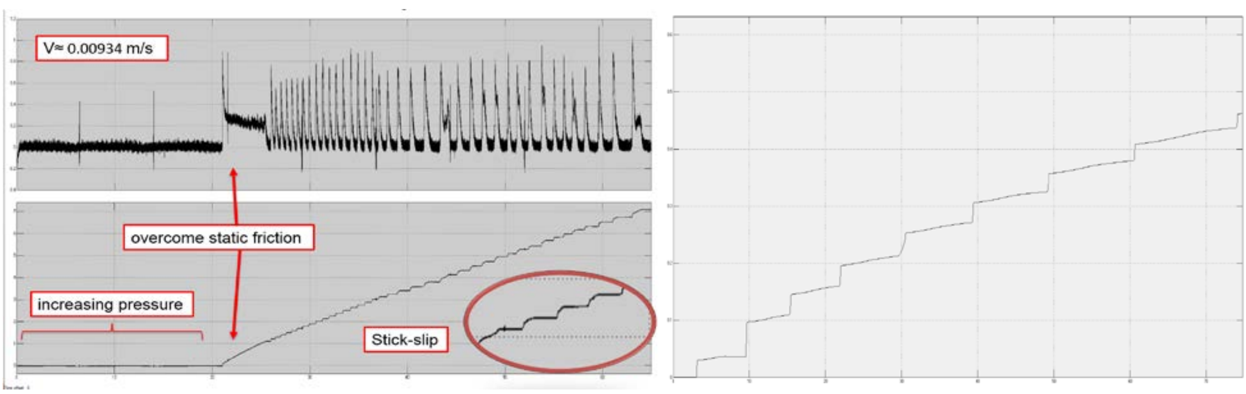

Fig. 3: Graph of speed and the actual position of the pneumatic cylinder and the simulation model of the actuator with LuGre friction (right side).

Another much simpler approach to modeling the pneumatic actuator with friction is the combination of Coulombs friction with Stribeck curve. Studies have shown that this model pretty well simulates the behavior of a pneumatic drive and with comparison to the model of LuGre is much easier to implement in control systems.

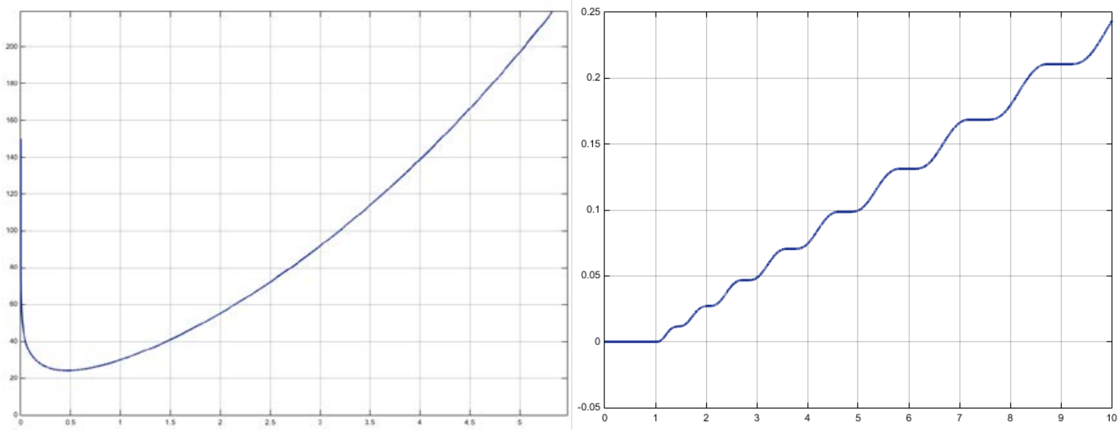

Fig. 4: The dependence of friction force on the relative speed for the combined Stribeck and Coulomb friction. On the right side of the graph movement for a very small constant flow.

4. Conclusions

The selection of controllers and control systems for compressed air devices requiring precision work often requires the development of accurate mathematical model and carry out large amounts of simulations. An important element in creating a model is to include relevant operating parameters, for fast and less precise movements can be taken a simplified model without the influence of temperature or friction, while for relatively slow processes essential element may be predictive controller for which is required knowledge of the friction influence to control the pneumatic drive (Schindele & Aschemann, 2009). Another approach to control pneumatic actuators is the use of special fuzzy logic controllers that allow you to skip the creation of a mathematical model but require more expertise knowledge (Takosoglu et al., 2012).

References

Blasiak, S. (2015) The two dimensional thermohydrodynamic analysis of a lubrication in non-contacting face seals, Journal of Thermal Science and Technology, 10, 1, pp. JTST0016–JTST0016. doi:10.1299/jtst.2015jtst0016

Blasiak, S., Takosoglu, J. E., & Laski, P. A. (2014) Heat transfer and thermal deformations in non-contacting face seals, Journal of Thermal Science and Technology, 9, 2, pp. JTST0011–JTST0011. doi:10.1299/jtst.2014jtst0011

Blasiak, S., & Zahorulko, A. V (2016) A parametric and dynamic analysis of non-contacting gas face seals with modified surfaces, Tribology International, 94, pp. 126–137. doi:10.1016/j.triboint.2015.08.014

Laski, P. A., Takosoglu, J. E., & Blasiak, S. (2014) Design of a 3-DOF tripod electro-pneumatic parallel manipulator, Robotics and Autonomous Systems. Elsevier.

Olsson, H. (1996) Control Systems with Friction, Department of Automatic Control, Lund Institute of Technology, 1045, October, pp. 172. doi:10.1103/PhysRevE.51.6235

Schindele, D., & Aschemann, H. (2009) Adaptive friction compensation based on the LuGre model for a pneumatic rodless cylinder, In *IECON Proceedings (Industrial Electronics Conference)* (pp. 1432–1437). doi:10.1109/IECON.2009.5414726

Takosoglu, J. E., Laski, P. A., & Blasiak, S. (2012) A fuzzy logic controller for the positioning control of an electro-pneumatic servo-drive, PROCEEDINGS OF THE INSTITUTION OF MECHANICAL ENGINEERS PART I-JOURNAL OF SYSTEMS AND CONTROL ENGINEERING, 226, I10, pp. 1335–1343. doi:10.1177/0959651812456498

22nd International Conference
ENGINEERING MECHANICS 2016
Svratka, Czech Republic, 9 – 12 May 2016

NUMERICAL ANALYSIS OF THE MODAL PROPERTIES OF A SHROUDED TURBINE BLADING

J. Brůha*, V. Zeman**

Abstract: *Presented work is concerned with the numerical analysis of natural frequencies and corresponding mode shapes of twisted blades with contacts between blade shrouds. The blades are modelled by means of the Finite Element Method (FEM) using Rayleigh beam elements with varying cross-sectional parameters along the elements and six degrees of freedom (DOFs) in each of nodes, while the rhomboid-shaped shrouds are considered to be rigid. The blades are clamped into a rotating rigid disk. Since the finite element models based on the Rayleigh beam theory tend to slightly overrate natural frequencies and underrate deflections in comparison with finite element models including shear deformation effects, parameter tuning of the blades is performed. The modelling of interactions at the contact surfaces of neighbouring blade shrouds is carried out using a multipoint frictionless contact approach with constant normal contact stiffness. In order to compare the natural frequencies, three different geometries of the blade shroud as well as three different values of the pre-twist angle induced by preloads at the contact interfaces are tested.*

Keywords: Turbine blade, Finite element method, Parameter tuning, Contact, Modal analysis.

1. Introduction

Turbine blades are the most important parts of gas and steam turbines. Due to the crucial role they play during the operation, blades and bladed disks require special attention and very careful design. One of the key factors that affect service life of turbine blades is associated with vibration prevention techniques. Blade vibration as a side effect of the operation of steam and gas turbines is very dangerous because of the high cycle fatigue. The failure of a single blade can be responsible for large economic losses or, in the worst-case scenario, even a human loss. Since prediction of all excitation sources is very difficult, the blades should be designed in such a way that they can absorb vibration caused by unexpected or unusual excitation. One of the most effective types of damping devices is a blade shroud. When surfaces in contact of the neighbouring blade shrouds move relative to each other, the rubbing dissipates energy (Pešek et al., 2015; Petrov, 2008; Zeman et al., 2010). Moreover, the blade shrouds stiffen the blading and, in consequence, they affect natural frequencies of a bladed disk.

Today, a large-scale FE model of a bladed disk contains $10^4 - 10^6$ DOFs (Petrov, 2008). However, utilization of these models can be, especially in cases of large contact problems, inefficient because of the time-consuming computation. Therefore, the blade modelling by means of various types of beam FEs can be perceived as a suitable alternative.

In this paper, a method for the numerical analysis of modal properties of shrouded turbine blades has been developed. The method is based on a blade modelling by means of Rayleigh beam FEs with varying cross-sectional parameters along the FEs (Brůha & Rychecký, 2016). In order to attenuate the handicap of overrated natural frequencies due to omitted shear deformation effects in Rayleigh beam theory, parameter tuning is performed. The interactions between neighbouring blade shrouds are modelled using a multipoint frictionless contact model (Hajžman & Rychecký, 2012). As a test example, the effects of three different geometries of the blade shroud and three different values of the pre-twist angle (induced by preloads at the shroud contact interfaces) on the natural frequencies are analysed.

* Ing. Jan Brůha: Department of Mechanics, Faculty of Applied Sciences, University of West Bohemia, Univerzitní 22, 306 14, Plzeň, CZ, bruhaj@ntis.zcu.cz

** prof. Ing. Vladimír Zeman, DrSc.: Department of Mechanics, Faculty of Applied Sciences, University of West Bohemia, Univerzitní 22, 306 14, Plzeň, CZ, zemanv@kme.zcu.cz

2. Computational modelling of interacting blades

In the framework of the computational modelling using FEM, we consider a model of M twisted blades with variable cross-section along the blades and rigid rhomboid-shaped tip shrouds (see Fig. 1). The blades are clamped into a rigid disk rotating with constant angular velocity ω_0 around the Y axis. As noted previously, the blades are divided into $N-1$ Rayleigh beam finite elements (blade finite elements) with varying cross-sectional parameters along each FE and six DOFs in each of the nodes on rotating x_j axis, $j = 1, 2, \dots, M$. Due to zero displacements in the first node of each blade, described model has $n = 6M(N-1)$ DOFs.

The equations of motion of the individual blades can be expressed in generalized coordinates

$$\boldsymbol{q}_j = [\ldots\ u_i, v_i, w_i, \varphi_i, \vartheta_i, \psi_i, \ldots]^T, \quad i = 1, 2, \dots, N, \quad j = 1, 2, \dots, M \tag{1}$$

in following form

$$\boldsymbol{M}_j \ddot{\boldsymbol{q}}_j + (\boldsymbol{B}_j + \omega_0 \boldsymbol{G}_j)\dot{\boldsymbol{q}}_j + [\boldsymbol{K}_{s,j} + \omega_0{}^2(\boldsymbol{K}_{stiff,j} - \boldsymbol{K}_{\omega,j})]\boldsymbol{q}_j = \boldsymbol{0}, \tag{2}$$

where symmetric matrices $\boldsymbol{M}_j$, $\boldsymbol{B}_j$, $\boldsymbol{K}_{s,j}$, $\omega_0{}^2\boldsymbol{K}_{stiff,j}$, $-\omega_0{}^2\boldsymbol{K}_{\omega,j}$ are mass, material damping, static stiffness, centrifugal stiffening under rotation and softening because of modelling in the rotating coordinate system, respectively. The skew symmetric matrix $\omega_0\boldsymbol{G}_j$ represents gyroscopic effects. Since the Rayleigh beam theory does not take account of shear deformation effects, turbine blade models based on this approach tend to slightly overestimate natural frequencies and underestimate deflections. In order to attenuate this handicap, the Young's modulus E as well as the torsion resistance J_t were being tuned (Brůha & Rychecký, 2016).

In order to include the mutual interactions between the neighbouring blade shrouds, a multipoint frictionless contact model is taken into account. In such a case, the rectangular contact areas are decomposed into a set of elementary contact areas (marked with the subscript e) and the contact forces are distributed among them. The coupling stiffness matrix $\boldsymbol{K}_C$ of all M interacting blades can be derived from the strain energy (Zeman et al., 2010)

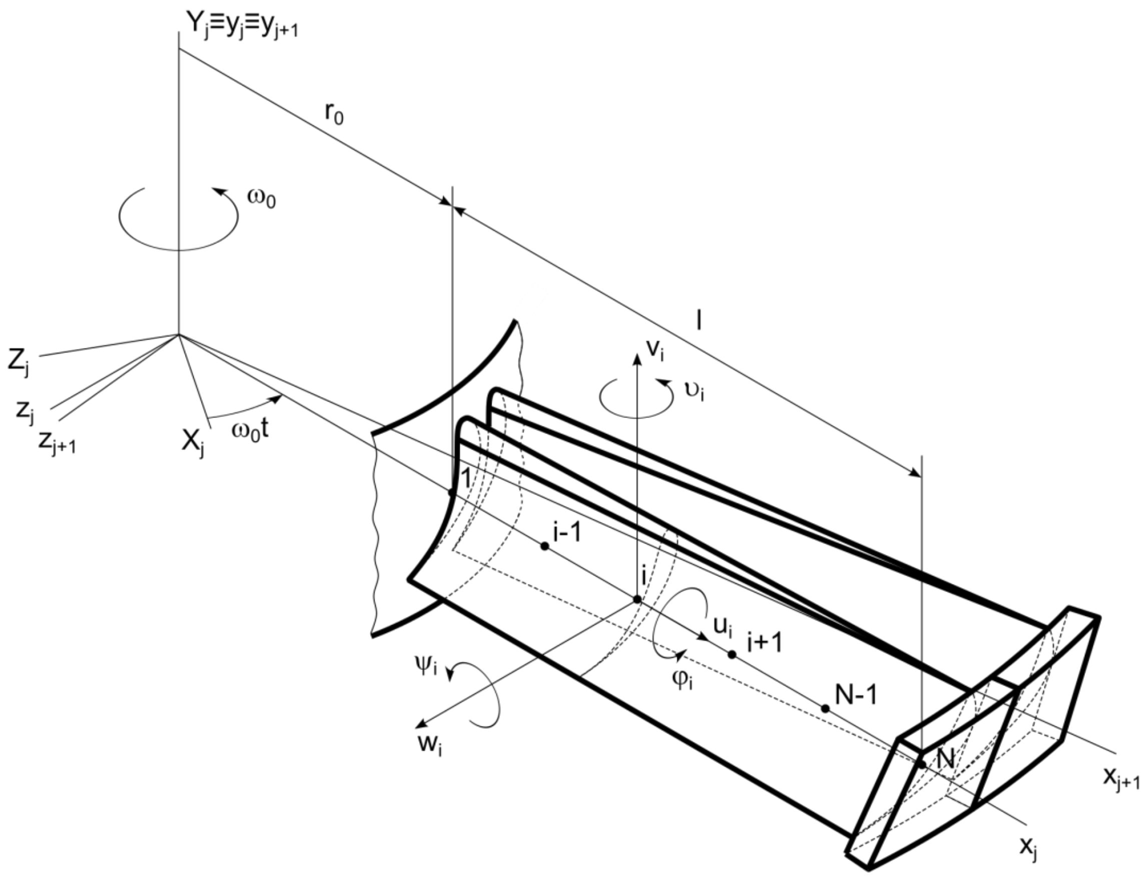

Fig. 1: A sector of a bladed disk.

$$E_S = \frac{1}{2}\sum_{j=1}^{M}\sum_e k_{j,e} d_{j,e}^2 \ , \tag{3}$$

where $k_{j,e}$ represents normal contact stiffness in eth elementary contact area of interaction between the jth and the $(j+1)$th blade and $d_{j,e}$ is relative displacement of the elementary contact areas in normal direction. Subscript $j = M$ corresponds to interaction between the Mth and the $1st$ blade. Then, the coupling stiffness matrix is given by the equivalence

$$\frac{\partial E_S}{\partial \boldsymbol{q}} = \boldsymbol{K}_C \boldsymbol{q} \ , \quad \boldsymbol{q} = [\boldsymbol{q}_1^T, \boldsymbol{q}_2^T, \dots, \boldsymbol{q}_M^T]^T \ . \tag{4}$$

Finally, the equation of motion of the whole structure (of M interacting blades) can be written in the form

$$\boldsymbol{M}\ddot{\boldsymbol{q}} + (\boldsymbol{B} + \omega_0 \boldsymbol{G})\dot{\boldsymbol{q}} + \left[\boldsymbol{K}_s + \omega_0{}^2\left(\boldsymbol{K}_{stiff} - \boldsymbol{K}_\omega\right) + \boldsymbol{K}_C\right]\boldsymbol{q} = \boldsymbol{0} \ . \tag{5}$$

In accordance with equation of motion (2), below presented matrices have a block-diagonal structures

$$\begin{gathered} \boldsymbol{M} = diag(\boldsymbol{M}_1, \dots, \boldsymbol{M}_M) \ , \quad \boldsymbol{B} = diag(\boldsymbol{B}_1, \dots, \boldsymbol{B}_M) \ , \\ \boldsymbol{G} = diag(\boldsymbol{G}_1, \dots, \boldsymbol{G}_M) \ , \quad \boldsymbol{K}_s = diag\left(\boldsymbol{K}_{s,1}, \dots, \boldsymbol{K}_{s,M}\right) \ , \\ \boldsymbol{K}_{stiff} = diag\left(\boldsymbol{K}_{stiff,1}, \dots, \boldsymbol{K}_{stiff,M}\right) \ , \quad \boldsymbol{K}_\omega = diag\left(\boldsymbol{K}_{\omega,1}, \dots, \boldsymbol{K}_{\omega,M}\right) \ . \end{gathered} \tag{6}$$

3. Numerical results

The presented method was tested on a bladed disk consisting of 100 steel turbine blades MTD30 stage HP15 (Kubín & Hlous, 2013). For this purpose, an in-house code in MATLAB computing environment was developed. Either of the blades was divided into six Rayleigh beam finite elements and each of the shroud contact surfaces was decomposed into a set of 100 elementary contact areas. In order to compare calculated natural frequencies, three different values of the pre-twist angle (see Table 1) and three different geometries of the blade shroud were considered. As shown in Table 1, the pre-twist of the blades induced by preloads at the shroud contact interfaces has a positive effect on blading stiffening.

Tab. 1: Natural frequencies of the blading.

Family number	Pre-twist angle (°)	Natural frequency (Hz)	
		$\omega_0 = 0$ (rev/min)	$\omega_0 = 5\,500$ (rev/min)
1	0.1	1 129.3 — 2 661.0	1 152.0 — 2 671.3
	0.466	1 129.4 — 2 661.2	1 152.1 — 2 671.4
	1	1 129.4 — 2 661.2	1 152.1 — 2 671.4
2	0.1	2 680.4 — 3 895.5	2 690.6 — 3 895.8
	0.466	2 681.2 — 3 898.3	2 691.4 — 3 898.6
	1	2 681.4 — 3 899.0	2 691.6 — 3 899.3
3	0.1	5 849.0 — 6 380.8	5 868.0 — 6 402.9
	0.466	5 904.9 — 6 386.8	5 924.5 — 6 409.0
	1	5 918.7 — 6 388.1	5 938.5 — 6 410.3

The natural frequencies (and corresponding mode shapes) of the turbine blading are grouped into several distinct families. Each family is characterized by a certain number of nodal circles (NCs) and the mode shapes in the family have from 0 to $\frac{M}{2} = 50$ nodal diameters (NDs). Chosen mode shapes of the considered turbine blading are shown in Fig. 2. In Fig. 2(c), the nodal diameters pass between each two neighbouring blades.

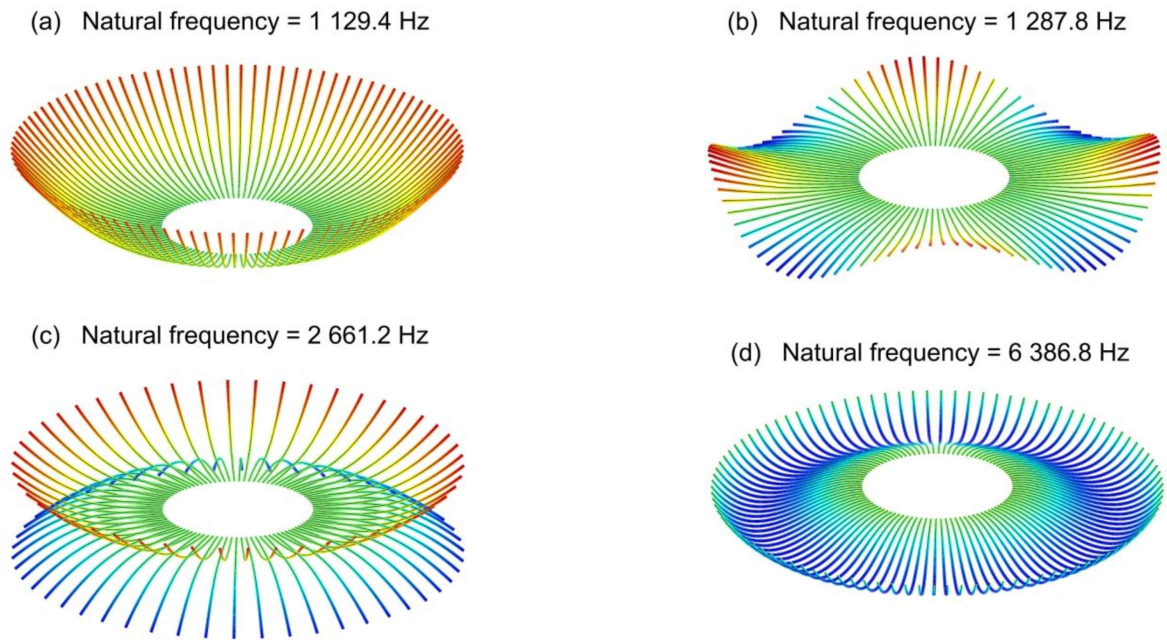

Fig. 2: Chosen mode shapes characterized by: (a) 0 NDs / 0 NCs, (b) 4 NDs / 0 NCs, (c) 50 NDs / 0 NCs, (d) 0 NDs / 1 NC.

4. Conclusions

Presented method deals with the numerical analysis of modal properties of interacting turbine blades. The twisted blades with variable cross-sectional parameters were modelled by means of the FEM using Rayleigh beam elements, while rhomboid-shaped tip shrouds were considered to be rigid. In order to attenuate the handicap of overrated natural frequencies due to omitted shear deformation effects in Rayleigh beam theory, parameter tuning was performed. The interactions between neighbouring blade shrouds were modelled using a multipoint frictionless contact model. The developed in-house code in MATLAB computing environment is capable to analyse the effects of the shroud geometry and the pre-twist angle (induced by preloads at the shroud contact interfaces) on natural frequencies as well as visualize corresponding mode shapes. Described methodology can be perceived as an alternative to complex commercial codes especially due to less time-consuming computation. It is the first step in the analysis of the tip shroud design effect on the dynamic behaviour of a turbine blading with contact interfaces.

Acknowledgement

This work was supported by the project LO1506 of the Ministry of Education, Youth and Sports of the Czech Republic and by the project TE01020068 “Centre of research and experimental development of reliable energy production” of the Technology Agency of the Czech Republic.

References

Brůha, J. & Rychecký, D. (2016) Modelling of rotating twisted blades as 1D continuum, in: Applied Mechanics and Materials 821, pp. 183-190.

Hajžman, M. & Rychecký, D. (2012) Multipoint contact approach to the analysis of interacting flexible bodies vibration, in: Advances in Mechanisms Design 8, pp. 181-186.

Kubín, Z. & Hlous, J. (2013) Measurement of rhombic bladed disk. Research report, Doosan Škoda Power, Pilsen.

Pešek, L., Hajžman, M., Půst, L., Zeman, V., Byrtus, M. & Brůha, J. (2015) Experimental and numerical investigation of friction element dissipative effects in blade shrouding, in: Nonlinear Dynamics 79, pp. 1711-1726.

Petrov, E.P. (2008) Explicit finite element models of friction dampers in forced response analysis of bladed disks, in: Journal of Engineering for Gas Turbines and Power 130.

Zeman, V., Byrtus, M. & Hajžman, M. (2010) Harmonic forced vibration of two rotating blades with friction damping, in: Engineering Mechanics 17, pp. 187-200.

22nd International Conference
ENGINEERING MECHANICS 2016
Svratka, Czech Republic, 9 – 12 May 2016

ON ADVANCED SHIP EVACUATION ANALYSIS

V. Bucci[1], A. Marinò[2], F. Mauro[3], R. Nabergoj[4], C. Nasso[5]

Abstract: *New cruise passenger ships are trending towards "gigantism", consequently together with size also the number of passengers and crew increases. For this reason, international regulations known as "Safe Return to Port" are more and more aimed at upgrading intrinsic ship safety in event of fire or flooding. When the accident exceeds a fixed threshold, a ship safe evacuation must be guaranteed. To this end evacuation analysis becomes a primary task in passenger ship design, since the early stages. According to IMO Regulations, evacuation analysis can be tackled in two different ways: a simplified method or an advanced one. The latter involves the use of specific certified computational tools. In this work an advanced evacuation analysis for a cruise passenger ship with about 3600 persons on board is presented.*

Keywords: Safe Return to Port, Ship Evacuation Analysis, Ship Safety.

1. Introduction

In the last years, the construction of new cruise passenger ships reported even larger ships carrying thousands of persons (both passengers and crew). For such ships the survivability in event of fire or flooding has become of paramount importance. The SOLAS Regulations II-2/21-23 known as *Safe Return to Port* state that the ship should be able to return to port if the specified casualty threshold, defined by the regulation in event of fire or flooding, is not exceeded. Otherwise, it is necessary to evacuate and abandon the ship within 3 hours. If instead the accident is below the casualty threshold persons involved should be only moved towards Safe Areas. Anyway, an evacuation analysis must be performed in order to check the effective time necessary to abandon the ship, putting in evidence possible congestion points along the escape routes.

This paper presents the results of a study carried out with a simulation tool (AENEAS) within a wider research program oriented to check the capability of different certified software to simulate consistently the evacuation of new cruise passengers ships.

2. Regulations

Until now, the evacuation analysis is mandatory, in the simplified form, only for ro-ro passenger ships, while the new requirements (IMO circular MSC.1/Circ.1238 "Guidelines for evacuation analysis for new and existing passenger ship") extend it to all types of passenger ships and offer the possibility to use two different methods for the evacuation analysis: the "simplified method" and the "advanced method". Within the simplified method, the total evacuation time is calculated and compared with an allowable time which depends on both the vessel type and the number of Main Vertical Zones (MVZ). The advanced method uses computational tools to calculate the total evacuation time taking into account many

[1] Aggr. Prof. Vittorio Bucci: Dept. of Engineering and Architecture, University of Trieste, via Valerio 10; 34127, Trieste; I, vbucci@units.it

[2] Assoc. Prof. Alberto Marinò: Dept. of Engineering and Architecture, University of Trieste, via Valerio 10; 34127, Trieste; I, marino@units.it

[3] Ir. Francesco Mauro: Dept. of Engineering and Architecture, University of Trieste, via Valerio 10; 34127, Trieste; I, fmauro@units.it

[4] Assoc. Prof. Radoslav Nabergoj: Dept. of Engineering and Architecture, University of Trieste, via Valerio 10; 34127, Trieste; I, nabergoj@units.it

[5] Dr. Carlo Nasso: Dept. of Engineering and Architecture, University of Trieste, via Valerio 10; 34127, Trieste; I, nassocarlo88@gmail.com

parameters like the behaviour of each passenger while is escaping and the interactions between human factor (gender, age, reduced mobility) and ship layout by means of a virtual reality software.

SOLAS II-2/13.2 requires that at least two separated means of escape from all spaces on board must be ensured. Each MVZ owns a primary means of escape while the secondary one are placed in the adjacent MVZs. All the means of escape along an escape route like doorways, stairways and corridors, are sized in accordance with Chapter 13 of the International Code for Fire Safety Systems (FFS Code). In that Regulation two main cases are considered:

Case 1 (by night) – all passengers in cabins with maximum berthing capacity fully occupied; crew members 2/3 in cabins and 1/3 in service spaces.
Case 2 (by day) – all passengers in public spaces occupied to 3/4 of maximum capacity; crew members 1/3 in public spaces, 1/3 in service spaces and 1/3 in cabins.

The evacuation analysis must be performed for the following scenarios:

Scenario 1 – persons as per Case 1; entire ship; evacuation along the main means of escape.
Scenario 2 – persons as per Case 2; entire ship; evacuation along the main means of escape.
Scenario 3 – persons as per Case 1; MVZ with longest evacuation time; evacuation along:
Alternative 1 – secondary means of escape.
Alternative 2 – main means of escape (plus 50% of persons from adjacent MVZ)
Scenario 4 – persons as per Case 2, evacuation as per Scenario 3.

The final objective of the evacuation analysis is the evaluation of the *total evacuation time* and compare it with an *allowable time n* equal to 80 minutes reduced to 60 minutes for ro-ro passenger ships and passenger ships with no more than 3 MVZs.

In the simplified method, the check to be done is the following:

$$\textit{total evacuation time} = 1.25\,(A+T) + 2/3\,(E+L) \leq n \tag{1}$$

where A is the *awareness time* equal to 10 minutes for the night scenarios and 5 minutes for the day scenarios; T is the *travel time* given by the sum of tabular values related to flow time, deck travel time, stairway travel time and assembly travel time properly defined in Circ.1238; E is the *embarkation time* and L is *launching time*, which sum is equal to 30 minutes.

In the advanced method, the travel time, including also the awarnes time, is calculated by virtual reality software that considers the probabilistic nature of the process. Then:

$$\textit{total evacuation time} = 1.25\,T + 1/3\,(E+L) \leq \mathrm{n} \tag{2}$$

Embarkation, lanching and allowable times are the same as the simplified method. For each scenario, 50 simulations must be run, considering 10 randomly generated populations. Another important result from the simulations is the identification of possible congestion points along the escape routes. The *congestion* is defined as an area where population density exceeds 4 person/m^2 for a significant time. If there are more than 10% of simulations with significant congestions, some means of escape must be modified.

3. Tools

The virtual reality simulators are based on different pedestrian algorithms using statistical models, queuing theory, route-choise models, kinetic theory of gases, etc. The main certified software are:

- EVI: developed by University of Glasgow and Strathclyde.
- AENEAS: developed in cooperation between DNV-GL and TraffGo.
- EXODUS: developed by University of Greenwich.
- ODIGO: developed by Principia.
- VELOS: developed by University of Athens.

3.1 AENEAS

AENAES is a multi-agent software in which persons are represented as individuals (called *agents*) with independent attitudes, abilities and goals. The software requires a square-cell discretisation of the decks. The cell side is 0.4 m long and each agent can occupy only one cell at each time step.

The following types of cell can be used:

- Free cells: for the areas where the agents are allowed to move (white cells).
- Wall cells: for the areas where the agents are not allowed to move (black cells).
- Goal cells: for the areas the agent must reach (yellow cells).
- Door cells: for doors on the deck (red cells).
- Steep cells: for stair between decks (cyan cells).

During each time step of the simulations, agents move from cell to cell in order to reach the goal cells, using neighbor free cells only.

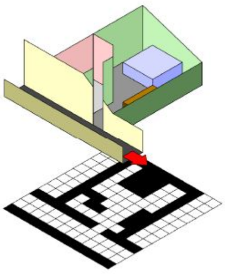

Fig. 1: Detail of a cabin in AENEAS.

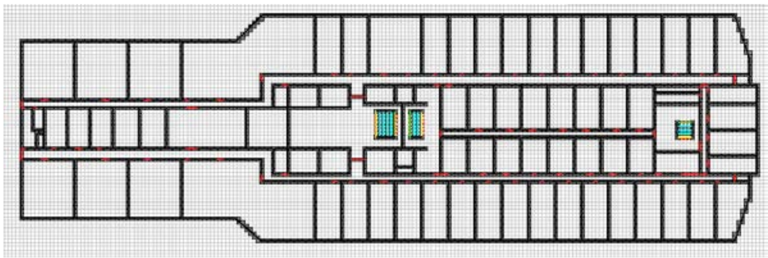

Fig. 2: Deck discretization in AENEAS

The software is composed by 3 modules: *AENEASed* (to model the ship, place agents and define goal cells), *AENEASsim* (to run the simulation), *AENEASview* (to view the results).

4. Case Study

An existing cruise passenger ship has been considered to carry out an advanced evacuation analysis. The main dimensions of the ship are indicated in Figure 3 together with a view of the analyzed MVZs.

Length, overall	285.00	m
Breadth, moulded	32.20	m
Gross Tonnage	86300	GT
Speed, max	24.00	kn
Speed, cruise	22.00	kn
Deck	11	
Passengers	2667	
Crew	933	

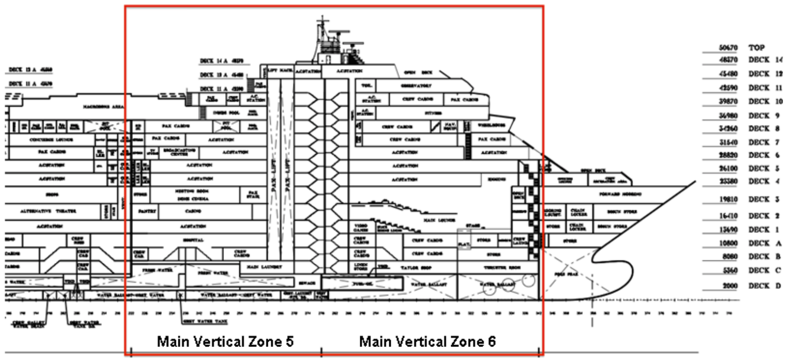

Fig. 3: The MVZs considered in the evacuation analysis.

Tab. 1: Population distribution for each scenario.

	Night scenarios 1-3		Day scenarios 2-4	
Deck	**Passengers**	**Crews**	**Passengers**	**Crews**
C	/	8	/	12
B	/	175	/	88
A	/	89	/	51
1	142	4	202	15
2	0	11	402	22
3	0	17	324	23
4	121	4	0	2
5	150	4	0	2
6	173	4	0	6
7	124	4	0	2
8	108	4	0	2
9	0	14	268	28
10	92	20	0	10
11	20	7	198	12
TOT	***930***	***365***	***1324***	***275***

Tab. 2: Travel times calculated by AENEAS.

Scenario	**1**	**2**	**3**	**4**
$\mathbf{t_I}$ [s]	980	667	1483	2344
T [s]	2344			

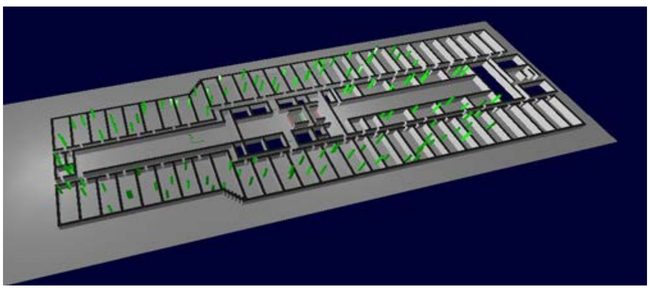

Fig. 4: Screenshot of a simulation time step.

Passenger cabins are located on decks 4 through 8, passenger public areas are on decks 2, 3 and 9, while accommodation and recreation areas for the crew are located on deck D, C, B and A. All the muster stations (assembly stations) are on deck 3.

The evacuation has been simulated for the most populated Main Vertical Zones (MVZ 5 and MVZ 6). The population distributions for night and day scenarios are detailed in Table 1. For each scenario the imposed 50 random-generated simulations have been run and the relevant travel times t_I has been determined (Table 2). Finally, the travel time T is obtained as the maximum of the times t_I. Scenario 4 presents the highest travel time (2344 s). Analyzing more deeply this simulation, a congestion point on the deck 2 at the entrance of secondary stairway has been noted.

Applying equation (2) the total evacuation time has been determined, and results 4130 s. The requirement of MSC.1/Circ.1238, which states for a cruise passenger ship an allowable time of 4800 s, is fully satisfied. Despite the performance standard is met, the results obtained could suggest a possible modification of the ship layout in order to further reduce the evacuation time.

5. Conclusions

New IMO Regulations (MSC.1/Circ.1238) for cruise passenger ship impose to perform an evacuation analysis in order to guarantee a safe abandonment of the ship when significant fire or flooding casualty occurs. It is foreseen also the use of specific software to tackle in an advanced manner the dynamics of the escaping crowd. Currently, only five certified software are available on the market. Up to now the simulation software have been mainly used for ro-ro passenger ship, dealing with at most 1000-1500 persons. In this study, the capabilities of a specific software (AENEAS) to manage a very high number of individuals (about 3600) have been successfully tested.

Acknowledgement

This research has been carried out with the financial support of the “Università degli Studi di Trieste – Finanziamento di Ateneo per progetti di ricerca scientifica – FRA 2014”.

References

Brown R., Galea E.R., Deere S., Filippidis L. (2012) “IMO Inf paper summary – Response time data for large passenger ferries and cruise ship”, Safeguard Passenger Evacuation Seminar, London, United Kingdom.

Chu C., Lu h., Pan C., (2013) “Emergency evacuation route for the passenger ship”, Journal of Marine Science and Technology, Vol. 21, No. 5, pp. 515-521.

Dongkon L., Hongtae K., Jin-Hyoung P., Beom-Jin P. (2003) “The current status and future issues in human evacuation from ships”, Safety Science, Vol. 41, pp. 861-876.

Galea E.R., Brown R.C., Filippidis L., Deere S. (2010) “Collection of evacuation data for large passenger vessels at sea”, PED 2010, Maryland, USA.

Ginnis A.I., Kostas K.V., Politis C.G., Kaklis P.D. (2010) "VELOS: A VR platform for ship-evacuation analysis", Computer-Aided Design, Vol. 42 pp. 1045-1058.

Lopez Piñeiro A., Pérez Arribas F., Donoso R., Torres R., (2005) "Simulation of passengers movement on ship emergencies. Tools for IMO regulations fulfilment", Journal of Maritime Research, Vol. II, No. 1, pp. 105-125

Vassalos D., Christiansen G., Kim H.S., Bole M., Majumder J. (2002) "Evacuability of passenger ship at sea", SASMEX.

Vassalos D., Guarin L., Vassalos G.C., Bole M., Kim H.S., Majumder J. (2003) "Advanced evacuation analysis – Testing the ground on ship", Second International Conference in pedestrian and evacuation dynamics, London, United Kingdom.

Wang W.L., Liu S.B., Lo S.M., Gao L.J. (2014) "Passenger ship evacuation simulation and validation by experimental data sets", Procedia Engineering, Vol. 71 pp. 427-432.

Bucci V., Marinò A., Trincas G., Zanutto G. (2015) "Innovative tools for advanced evacuation analysis of passenger ships", 18th International Conference on Ships and Shipping Research, Lecco, Italy.

22nd International Conference
ENGINEERING MECHANICS 2016
Svratka, Czech Republic, 9 – 12 May 2016

NUMERICAL MODELLING OF FIRE AND SMOKE DEVELOPMENT IN RAILWAY TUNNEL

K. Cábová*, M. Bernas, F. Wald*****

Abstract: *Simulation of fire spread and development of toxic gases during a fire accident in a rail tunnel allows prepare and validate models of safe evacuation of people. Highly complex problem of fire dynamics in a tunnel can be solved by the aid of CFD method. It can simulate the temperature resolution and toxic gases development in a tunnel, which can be together with visibility considered as the most important parameters affecting the safety of persons involved in tunnels accidents. In order to check the degree of qualitative agreement of model prediction, verification and validation process is applied. Prediction method of fire and smoke development by the aid of numerical model in FDS is applied to a real construction of tunnel Špičák.*

Keywords: Railway tunnel, Fire and smoke development, Fire safety, CFD method, FDS code.

1. Introduction

According to international statistics, fire accidents in tunnels are less frequent than on the open space. However, consequences of a fire in a tunnel may be more serious comparing to fire on the open road (Carvel & Marlair, 2005). During the fire in a tunnel higher amount of heat released thanks to ventilation and geometry of a structure is generated. Extreme radiation inducing high temperatures may destroy structure of a tunnel. It leads to several days of infrastructure lay-by and financially demanding repairs. Considering railway tunnels potential for a large number of casualties and lost of transported material in the event of a fire is even higher comparing to road tunnels.

In the design phase fire safety is evaluated from the length of a tunnel of 350 m, which is considered as the length with higher risk for human safety. Temperature resolution and development of toxic gases in a tunnel are together with visibility considered as the most important parameters affecting the safety of people involved in tunnel accidents. In order to provide models of safe evacuation of people, numerical simulation of highly complex problem of fire dynamics in tunnels by the aid of CFD method provides safe and economically optimized solution.

2. Numerical modelling

Nowadays, mathematical modelling of fire dynamics plays a key role in fire engineering. Together with the development of computer technology, a number of sophisticated software tools, which implement the so-called Computational Fluid Dynamics method (CFD) dramatically increases. Computational Fluid Dynamics modelling is a numerical approach to representing fluids that divides a fluid domain into number of smaller subdomains, resulting in the generation of a mesh of cells (control volumes). Three-dimensional, time-dependant partial differential equations of conservation of mass, momentum and energy transfer and conservation of species are written for each control volume based on fundamental equations of fluid dynamics, thermodynamics, chemical reactions and mechanics. Appropriate initial boundary conditions are then applied to find numerical solutions to these equations. Currently available

* Ing. Kamila Cábová, PhD.: Department of Steel and Timber Structures, Faculty of Civil Engineering, Czech Technical University in Prague, Thákurova 7; 166 29, Prague; CZ, kamila.cabova@fsv.cvut.cz

** Ing. Martin Bernas: Faculty of Civil Engineering, Czech Technical University in Prague, Thákurova 7; 166 29, Prague; CZ, martin.bernas@fsv.cvut.cz

*** prof. Ing. František Wald, CSc.: Department of Steel and Timber Structures, Faculty of Civil Engineering, Czech Technical University in Prague, Thákurova 7; 166 29, Prague; CZ, wald@fsv.cvut.cz

CFD models include sub-models for solution of burning and heat transfer, so they provide a framework for including all phenomena which are present during fire in a tunnel into a calculation.

One of the freely available numerical code, Fire Dynamics Simulator (FDS), developed by National Institute of Standards and Technology (NIST), is frequently used for simulation of fires. It is a numerical solver to simulate a flow and movement of fluids, also caused by burning. FDS solves numerically a form of the Navier-Stokes equation appropriate for low-speed, thermally-driven flow with an emphasis of the transport of heat and smoke from fires (McGrattan, et al., 2010). The code consists of several independent models, for example model of burning. To interpret data obtained from FDS postprocessor Smokeview is used. The computer program Fire Dynamics Simulator (McGrattan et al., 2007) is used in this study.

2.1. Verification and validation

Despite the rapid software development there are many contradictory opinions about the reliability of computer predictions. Therefore, verification and validation is always recommended to evaluate reliability and accuracy of numerical predictions.

In order to verify the accuracy of the model of fire and smoke development in a railway tunnel in FDS v6, a model of a single-track railway tunnel of simple geometry (length of 50 m and a rectangular cross section with dimensions of 5.0 x 5.0 m) was subjected to calculation in software Smartfire v4.3 (Ewer et al., 2013). Results of statistical relationships introduced in (Cabová & Wald, 2016) demonstrate that the verification of the numerical model undertaken in both software has reached a good agreement (Paerson´s correlation coefficient is equal to 0.97). Details of the verification study including sensitivity analysis of influence of mesh density on attained results may be found in (Cabová & Wald, 2016) and (Horová et al., 2015).

For the process of validation which enables to evaluate a level of agreement between a computer prediction and a physical model, meaning experimentally reached results, data measured during the fire test in road tunnel Valík (Pokorný & Hora, 2007) were used. Numerical model was validated with experimental results by the aid of gas temperature which is calculated in three height levels (4.0 m, 6.5 m and 7.9 m) and several vertical sections from the source of fire (0 m, 5 m, 10 m and 15 m). Results of the small-scale model and the model of real dimensions, presented in (Cabová & Wald, 2016) were in agreement with measured values during the fire test. For more information about validation see (Cabová & Wald, 2016).

2.2. Practical application to Špičák tunnel

After the evaluation of acceptable level of accuracy of mathematical model, the prediction of fire and smoke development by the aid of FDS code is applied to a real tunnel construction. The tunnel Špičák which represents one of the longest old tunnel in the Czech Republic is chosen. The tunnel is 1747 m long. Along the tunnel length cross-section of the tube changes. In total there are twenty different cross-section areas. Material of the tunnel linings is also variable. High difference of both portals is negligible.

2.2.1. Model description

In numerical model the cross-section of 6.97 m width and 5.33 m high, which covers the longest part of the tunnel and which has the minimum high, is used. Arc shape of the tube is replaced by staircase shape of the cross-section in the model, as illustrated on Fig. 1a. The tunnel lining is formed by 0.4 m thick layer of concrete with density of 2200 kg/m^3, conductivity of 1.3 W/mK and specific heat of 1.02 kJ/kgK. Tunnel portals opened throughout the cross-sectional area provide natural gas flow (in FDS code plane surface type VENT is OPEN).

Fire scenario of burning inside a passenger train wagon is simulated by uniform heat release rate of 20 MW (input data corresponds to results of fire test of passenger train wagon described in (White, 2010)). The heat flux is released through four window openings, each of area of 1,44 m^2, situated 2 m above the ground level. The fire (areas releasing the heat flux) is located in the third wagon from the total of five wagons. The train stopped after 935 m after entering its portal (stands between 810 m and 935 m of the tunnel length). In FDS burning is simulated by mixed-fraction ratio of polyurethane (defined by fractions of carbon, hydrogen, oxygen, nitrogen and soot yield particles). Development of rate of heat release is based on t-quadratic curve for ultra-fast fire (Bernas, 2016).

Computational domain of dimensions 1747 m x 6.97 m x 5.33 m consists of five meshes. Size of mesh is determined according to rules given in (McGrattan et al., 2007). Cell size in axis (x, y, z) equals to (0.345 m, 0.348 m and 0.355 m). In the region of fire source the grid is refined to half size, in axis (x, y, z) cell size equals to (0.182 m, 0.174 m, 0.178 m). The total number of cells is 1 530 600.

In the tunnel there is negligible natural gas flow as the high difference of both portals is very small. Initial gas flow velocity is therefore set to 0 m/s. Gas temperature before fire ignition is considered as 10°C. In FDS turbulence model is applied by Smagorinski formulas of large eddy simulation (LES) with coefficient Cs equals to 0.2. Heat transfer by radiation is applied by 100 discrete angles.

In the model there are sensor to measure high of smoke layer, temperature of hot gas layer and temperature of gas layer below the smoke level. These sensors are situated in 50 m span sections in the axis of the tunnel tube and in the position of 0.6 m from the side lining, which should control the area of safety evacuation path.

2.2.2. Results

After fire ignition layer of hot smoke gases accumulated below the tube arch. The tunnel linings cooled hot gases down and smoke sank to lower level of the tunnel. Visualisation of fire and smoke development originated form the fire of passenger train wagon in 600 s is given in Fig. 1a. Fig. 1b shows decrease of smoke layer high along the tunnel length in 5 min. In the diagram three curves are introduced – curve of smoke layer high calculated by numerical model in the axis of evacuation path (0.6 m from the tunnel linings), curve of smoke layer high calculated in the axis of the tunnel cross-section and a curve indicating the level of maximal smoke layer decrease according to ČSN 73 7508. In the figure it is visible that the calculated high of smoke layer in the axis of evacuation path is lower than the level of 2.2 m. This level is considered as the maximal limit for safe evacuation.

Gas temperature calculated in the axis of fire source in the same time is illustrated in Fig. 2a. The maximal value calculated in 600 s is 800°C which is denoted to temperature of flames. From the view of safe evacuation temperature of 80°C is usually controlled in the high of 2 m above the evacuation path. Temperature of tunnel linings calculated in 600 s of fire reaches about 150°C directly above the fire source.

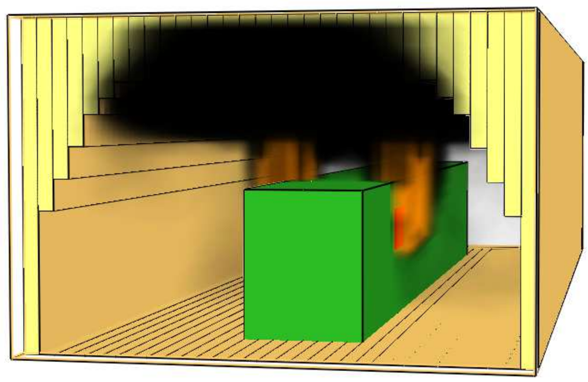

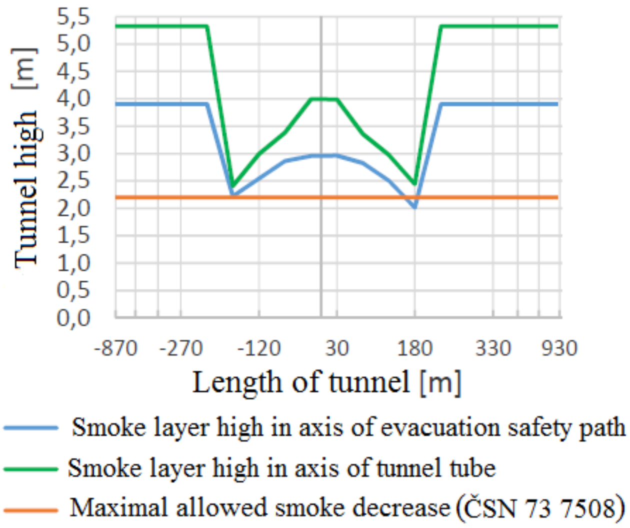

a) *b)*

Fig. 1: Model of passenger train fire in railway tunnel – a) smoke development in 600 s; b) smoke layer high along the tunnel length in 5 min.

3. Conclusions

Findings from the numerical simulations of fire and smoke development in railway tunnels enables to improve models of human evacuation during fires in tunnels. Similarly to shown study of model of passenger wagon fire in Špičák tunnel, gas temperature resolution, development of smoke layer together with visibility, toxicity of smoke and other parameters which are beyond the capabilities of CFD codes may be evaluated. Except optimization of fire safety equipment and evacuation scenarios, by the aid of numerical models it is possible to improve emergency procedures of IRS, provide accurate gas temperature resolution for the design phase, evaluate material behavior of tunnel linings and rail bed at elevated temperatures and during rapid cooling caused by firefighters.

Correctly applied CFD models may reproduce the qualitative behaviour of fire in each tunnel. The degree, to which qualitative agreement is achieved, is necessary to find out by the aid of verification and validation process. Accurate prediction of fire and smoke spread in tunnels on the bases of physical properties is a promising approach how to stress the human safety and fire design economy.

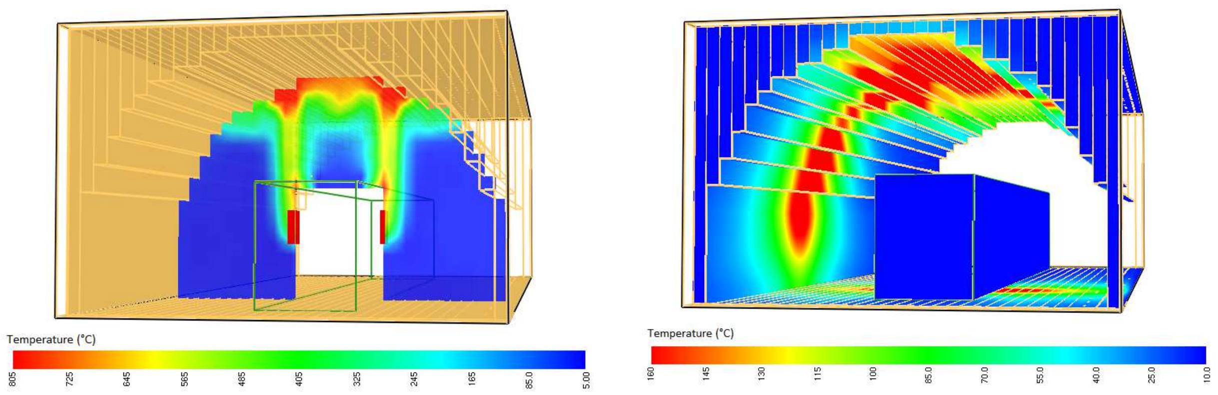

a) *b)*

Fig. 2: Model of passenger train fire in railway tunnel – a) gas temperature in 600 s; b) temperature of tunnel linings in 600 s.

Acknowledgement

Work on the research presented in this paper is supported by project no. VI20162019036, *Výzkum a vývoj ověřených modelů požáru a evakuace osob a jejich praktická aplikace při posuzování požární bezpečnosti staveb*, in the frame of Research project of security of Ministry of interior of the Czech Republic and project no. TE01020168 – Centre for Effective and Sustainable Transport Infrastructure, in the frame of Competence Centres program of Technology Agency of the Czech Republic (TA CR).

References

Bernas, M. (2016) Modelling of fire in railway tunnels. Master thesis, Czech Technical University in Prague.

Cábová, K. & Wald, F. (2016) Verification and validation of numerical model of fire and smoke development in railway tunnel. Acta Polytechnica, Czech Technical University in Prague.

Carvel, R. & Marlair, G. (2005) A history of fire incidents in tunnels. Handbook of Tunnel Fire Safety, ICE Publishing, 3-20 p.

Ewer, J., et al. (2013) Smart Fire – User guide and technical manual. Smartfire tutorials, Greenwich, United Kingdom.

Horová, K., et al.: Verification of numerical model of fire and smoke development in railway tunnel. Proceedings of the Internalitonal Conference in Dubrovnik, 15-16 October 2015, Applications of Structural Fire Engineering, DOI: http://dx.doi.org/10.14311/asfe.2015.058

McGrattan, K. et al. (2007) Fire Dynamics Simulator (Version 5), Technical Reference Guide. NIST Special Publication 1018-5, p. 86, U.S. Government Printing Office, Washington.

Pokorný, J. & Hora, J. (2007) Požární zkoušky v tunelu Valík, Praktická aplikace některých poznatků. Sborník přednášek konference Červený kohout.

White, N. (2010) Fire development in passenger trains. Master thesis, Victoria University, Australia.

22nd International Conference
ENGINEERING MECHANICS 2016
Svratka, Czech Republic, 9 – 12 May 2016

A DYNAMIC ANALYSIS OF AN INDUSTRIAL CNC PLOTTER

D. Cekus*, D. Skrobek**, T. Zając***

Abstract: *In the paper the drive parameters for a planned machining process have been determined. For this purpose, a dynamic analysis of a CNC plotter has been carried out in the Motion module of the SolidWorks program. The results have been used in the design stage of an industrial plotter for a Polish company producing CNC machines.*

Keywords: dynamics, CNC plotter, SolidWorks.

1. Introduction

This work illustrates how the parameters of drives, for the planned machining process, can be determined using the SolidWorks software (Weber & Verma, 2014). The research was conducted for an industrial CNC plotter (Fig. 1b) which is produced by the Kimla company. This machine tool is designed for processing materials such as non-ferrous metals, plastics, composite materials and wood.

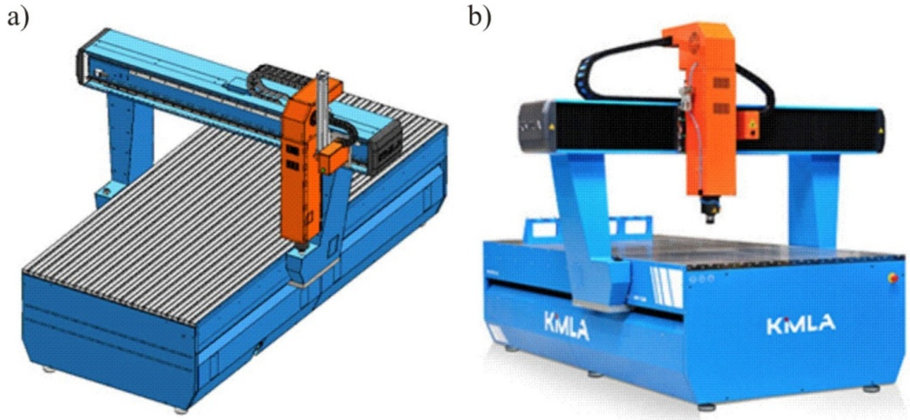

Fig. 1: An industrial CNC plotter: a) geometrical model, b) real object (www.kimla.pl).

2. Simulation of duty cycle

For the dynamical research (Cekus, 2013; Posiadała et al., 2013; Waryś et al., 2014) a parametric geometrical model (Fig. 1a) (Cekus et al., 2014) was worked out in the SolidWorks program. The study was conducted in the Motion module. It was assumed that some parts of the machine could be treated as rigid assemblies during the analysis. This procedure is not required, but can significantly reduce computation time. During the computation, those parts, located inside the rigid assembly, were constructed as being stationary relative to each other. This is to avoid errors caused by the insufficient restraint of some components.

The conducted research concerned the machining processing of an aluminium plate. The task was divided into three stages (Nagata & Watanabe,2014; Zhao et al., 2014; Siciliano et al., 2009) (Fig. 2):

* Assoc Prof. Dawid Cekus Phd. Eng., Institute of Mechanics and Machine Design Foundations, Czestochowa University of Tehnology, Street Dąbrowskiego 73; 42-201, Częstochowa; PL, cekus@imipkm.pcz.pl

** M.Sc. eng. Dorian Skrobek., Institute of Mechanics and Machine Design Foundations, Czestochowa University of Tehnology, Street Dąbrowskiego 73; 42-201, Częstochowa; PL, skrobek@imipkm.pcz.pl

*** M.Sc. eng.Tomasz Zając, Kimla, Street Bałtycka 30, 42-202 Częstochowa, PL, tomasz.zajac@gmail.com

- start-up - the tool length and the start position is set,
- working of the detail,
- tool retracting - the gateway machine moves away from the working area in order to facilitate the removal of the made details.

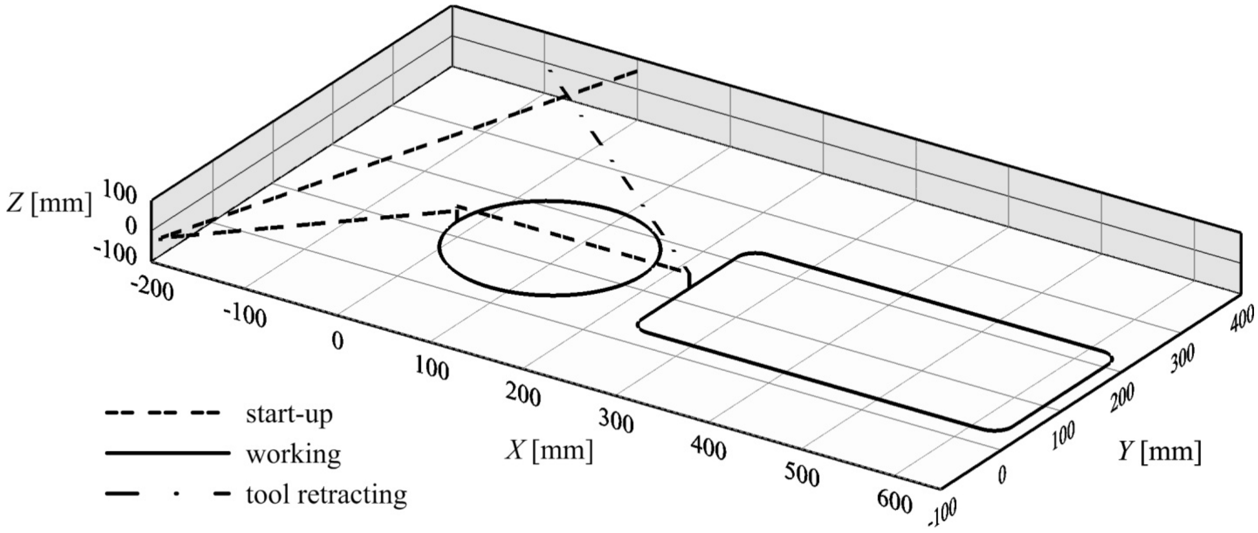

Fig. 2: Tool path.

For each machine axis (X, Y, Z) a separate drive was defined and, on the basis of the planned duty cycle (Fig. 2), the dependence of the position versus time was assigned (Fig. 3). These functions were imported into the SolidWorks using a function generator.

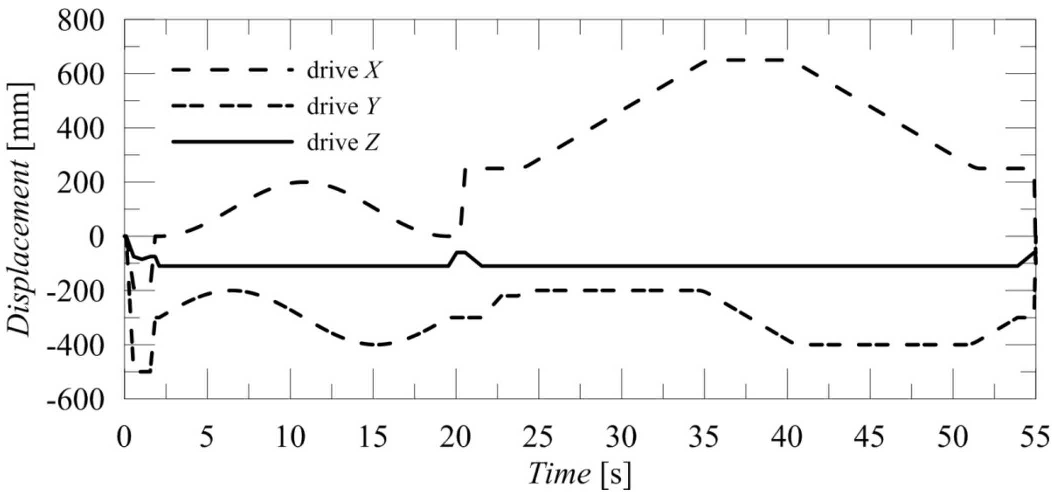

Fig. 3: The dependence of the position versus time for the drives.

3. The results of dynamic analysis

The loads of the plotter drives during the planned working cycle were determined using the above assumptions. The obtained results are presented in Figures 4-6.

The force values (Fig. 4-6) required to move the drive contain many overstated values, which are visible as so called "pins". Therefore, statistical computations were performed to determine the arithmetic mean value (1), standard deviation (2) and typical area of variability (3) (Table 1).

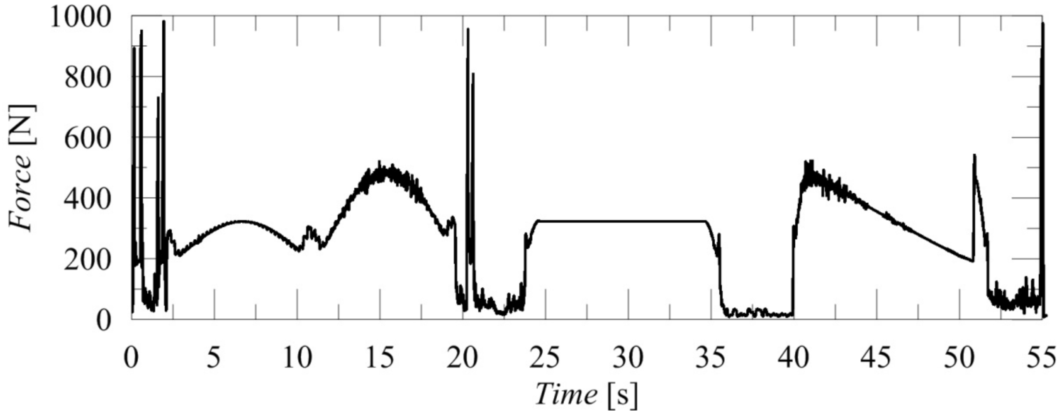

Fig. 4: The load of drive X during the duty cycle.

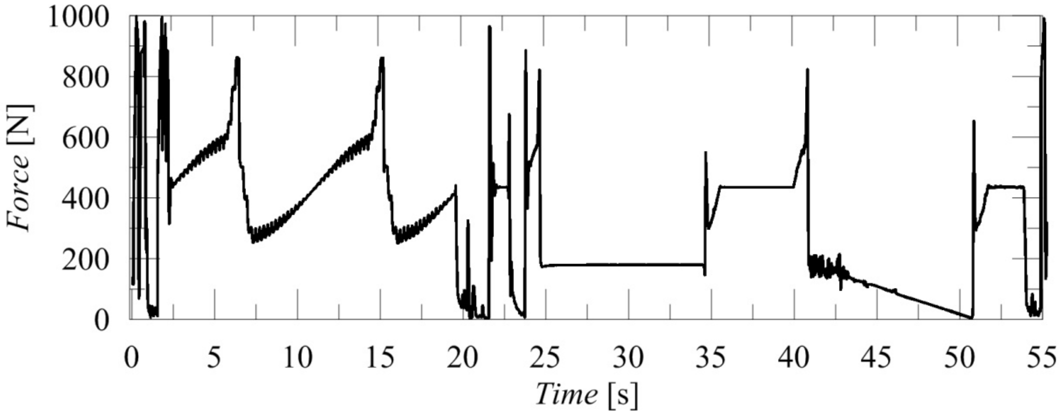

Fig. 5: The load of drive Y during the duty cycle.

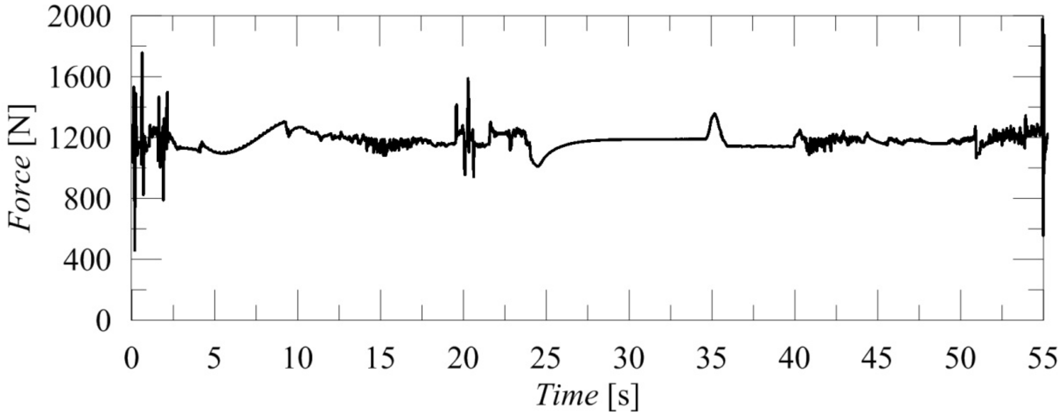

Fig. 6: The load of drive Z during the duty cycle.

$$\bar{x} = \frac{\sum_{i=1}^{n} x_i}{n}, \; s = \sqrt{\frac{\sum_{i=1}^{n} (x_i - \bar{x})^2}{n}}, \; \bar{x} - s < x_{typ} < \bar{x} + s \tag{1-3}$$

Tab. 1: The results of statistical analysis

	X axis	***Y axis***	***Z axis***
The arithmetic mean value of the force	*287 N*	*395 N*	*1179 N*
Standard deviation	*465 N*	*1123 N*	*145 N*
Typical area of variability	*-178 ÷ 752 N*	*-728 ÷ 1517 N*	*1034 ÷ 1324 N*

Using the obtained values (Table 1), the drive and transmission parameters can be determined. For drive X and Y the torques are:

$$M_x = P\frac{d_w}{2} = 16.75 \text{ Nm}, \; M_y = P\frac{d_w}{2} = 33.82 \text{ Nm}, \qquad (4, 5)$$

where: d_w - the pitch diameter (44.56 mm), P - circumferential force (the maximum value of variability interval for the respective axis)

The torque for drive Z for the reversing mode is:

$$M_z = \frac{F_b L \eta}{2000\pi} = 2.34 \text{ Nm}, \qquad (6)$$

wherein: F_b - the axial load [N] (the maximum value of variability interval for the Z axis), L - pitch of thread (10 mm), η - efficiency of machine (0.9).

4. Conclusions

It is possible to use the SolidWorks program to determine the load drives at the design stage of machine sets. This helps to reduce significantly the cost of making a prototype. The determined values of the driving forces are of minimum values to provide motion. Drives with higher parameters must be selected in order to ensure adequate dynamics and the reliability of the machine.

The dynamic computation method presented in this paper has been implemented by Kimla, a Polish company producing CNC machines.

References

Cekus D., (2013) Modelowanie, identyfikacja i badania dynamiki układów mechanicznych, seria Monografie nr 275, Wydawnictwo Politechniki Częstochowskiej, Częstochowa.

Cekus D., Posiadala B. & Warys P., (2014) Integration of modelling in SolidWorks and Matlab/Simulink environments, Archive of Mechanical Engineering, Volume 61, Issue 1, pp. 57–74.

Nagata F. & Watanabe K., (2013) Controller design for industrial robots and machine tools, Woodhead Publishing.

Posiadała B., Waryś P., Cekus D. & Tomala M., (2013) The dynamics of the forest crane during the working cycle, International Journal of Structural Stability and Dynamics, Vol. 13, No. 7, October, (DOI: 10.1142/S0219455413400130).

Siciliano B., Sciavicco L. Villani L. & Oriolo G., (2009) Robotic – Modelling, Planning and Control, Springer, London.

Waryś P., Cekus D. & Skrobek D., (2014) Modelling and Simulation Research of 4DOF manipulator, Machine Dynamics Research, Vol.38, No1, pp.5-11.

Weber M. & Verma G., (2014) SolidWorks 2015 Black Book, CREATESPACE.

Zhao J., Feng Z., ChuF.& Ma N., (2014) Advanced Theory of Constraint and Motion Analysis for Robot Mechanisms, Elsevier.

22nd International Conference
ENGINEERING MECHANICS 2016
Svratka, Czech Republic, 9 – 12 May 2016

THE INFLUENCE OF MESH MORPHOLOGY ON THE SCF IN 2D FEM ANALYSIS OF FLAT BARS WITH OPPOSITE V-NOTCH UNDER TENSION

A. Cichański*

Abstract: *The paper covers an issue of accuracy of numerical determination of stress concentration factor values for flat specimens with opposite V-notch. Own calculations were performed with finite element method with application of both meshes types, free mesh and mapped mesh. Dependency of K_t on finite element characteristic size was determined with application of the taken into consideration meshes. Based upon the obtained results, the mesh morphology influence on the accuracy of K_t calculations for the discussed notches was specified. The presented considerations allow for determination of optimum mesh morphology and size for obtaining the precise K_t value at minimum DOF number.*

Keywords: ***Notch, Stress concentration factor, Finite element method, Mesh morphology.***

1. Introduction

Analytical solution to the issue of stress concentration in the flat specimens with opposite V-notch under tension was described in the paper (Nisitani & Noda, 1986). With approximating formulae (Noda et al., 1995) one can estimate K_t values for any notch with the accuracy of up to 1%. Higher accuracy of K_t determination can be achieved by the approach presented in the paper (Noda & Takase, 2002) which proposes a division of notches into six groups, distinguished by depth and radius with separate dependencies in each group. Approximate values of K_t can be estimated with simplified method described in the specific handbooks (Pilkey & Pilkey, 2008). Numerical verification of handbook values of K_t values performed by FEM in the paper (Shin et al., 1994) for flat specimens notch under tension revealed discrepancy of K_t values of up to 8%.

The paper (Karolczuk, 2013) shows that oversized mesh size in the notch may cause up to 8% error in the calculated fatigue life, and undersized mesh may even double the duration of analyses made by Finite Element Method FEM. The problem of the influence of finite element order on calculation accuracy was addressed in the paper (Cichański, 2011). Based upon the conducted analyses it was determined that second order elements are characterized by good accuracy relation to the problem size. The issue of mesh morphology impact on the accuracy of FEM analyses was discussed in the paper (Cichański, 2015). It was stated that the mapped mesh with sub-area in the shape of a circle ring segment guarantees calculation accuracy control in the whole range of dimension variability of the finite element size. The issue of specimen geometry shaping with respect to the mesh was discussed in the paper (Soltysiak & Boronski, 2015). In geometrical model of notch specimen, apart from sub-areas specified for modelling of various material properties in weld zones, sub-areas for control of mesh structure with respect to accuracy were introduced. In the paper (Blacha, 2013) in the notch area, subsequent sub-areas were distinguished, allowing for the control of finite elements size increase along with distancing from the notch root.

The paper discusses the issue of the mesh morphology influence in the notch area on K_t value determined by FEM for flat specimens under tension. During the analyses, comparison of the accuracy of free meshes with triangular and quadrate elements with quadrilateral mapped meshes was performed. The calculations estimated the mesh quality parameters and degree of freedom DOF number change along with the change of finite element characteristic size.

* Ing. Artur Cichański, Ph.D.: University of Science and Technology, Mechanical Engineering Faculty, Kaliskiego 7; 85-789, Bydgoszcz; PL, e-mail: artur.cichanski@utp.edu.pl

2. The object and test conditions

The tests were conducted in plane stress condition for flat specimens of W width with opposite V-notch (Fig. 1). The analyses were performed for the specimen of W=100mm width and L=200mm length, corresponding to L=2W. The notch of ρ=1.5mm radius was adopted for considerations, corresponding to 2ρ/W = 0.03. For the adopted notch, it was analytically determined (Nisitani, 1986) that the extreme K_t=5.58 value was present for the depth of t=15mm, corresponding to 2t/W=0.3.

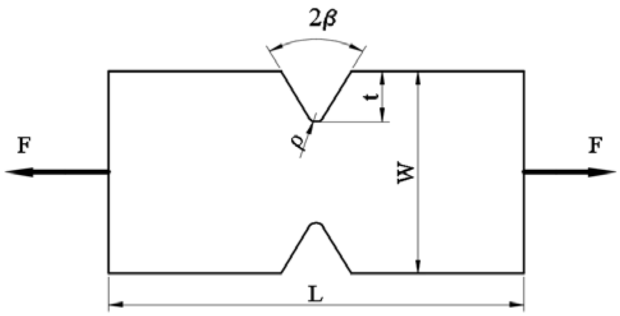

Fig. 1: Specimen adopted for tests.

Linear numerical analyses were conducted with finite element method in ANSYS software environment. Due to the symmetry of geometrical shape and boundary conditions a quarter of the specimen was adopted for the analysis. The analyses were performed with second order finite elements PLANE183 (Cichański, 2011). For free mesh and mapped mesh each, two different morphology variants were adopted (Fig. 2).

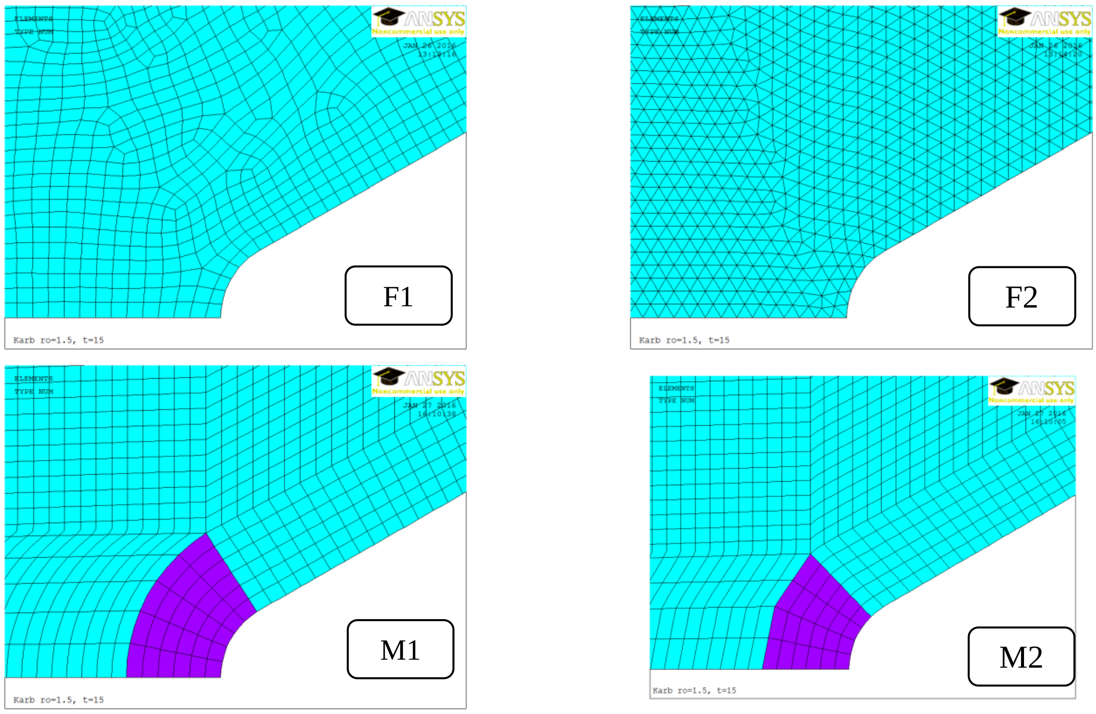

Fig. 2. Mesh morphology in the notch area: F1) free mesh with quadrate elements; F2) free mesh with triangle elements; M1) mapped mesh with circular sub-area; M2) mapped mesh with polygonal sub-area.

For free meshes the whole specimen surface was modelled with a single area. The tests were performed with quadrate elements (Fig. 2, F1) and triangular elements (Fig. 2, F1). In this case the shape of each element was determined by meshing algorithm. For the purpose of the notch root element shape control mapped meshes with application of two different sub-areas specified in the notch area were used. In the first variant, the sub-area is of a circular ring segment shape (Fig. 2, M1). The second variant assumed determination of the sub-area in the notch area in such manner that its two delimiting lines are the chords of the concentric circle with the notch arch (Fig. 2, M2).

3. Test results

For the discussed methods of mesh modelling (Fig. 2) a number of calculations with application of meshes with various characteristic element sizes was performed. For each mesh the relative error δK_t was calculated based upon analytical value of K_t for the tested notch (Nisitani & Noda, 1986). Along the decrease of the mesh characteristic size, the analysis accuracy increased which was reflected in decrease of δK_t relative error (Fig. 3a). The increase of calculation accuracy was connected with the increase of finite elements number, necessary for specimen area meshing which was reflected in the increase of degree of freedom DOF number (Fig. 3b).

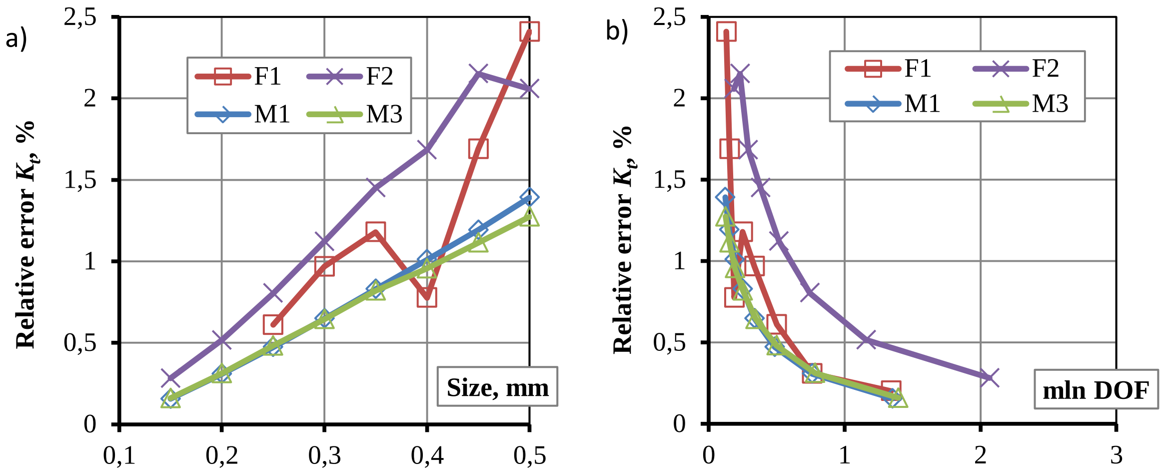

Fig. 3: Dependency of δK_t relative error on: a) element size; b) DOF number

During analyses was collected the mesh quality factors for the notch root element. The course of aspect ratio being a measure of its distortion is presented on Fig. 4a. The improvement of shape along with the decrease of the element size was observed for both mapped meshes. For free meshes, low correlation between the size and the element quality factors was observed. The course of the error of stress discontinuity described by absolute value of the maximum variation of any nodal stress component SDSG is presented on Fig. 4b. Stress discontinuities in triangular elements are much greater than those which were set for both meshing methods with use of quadrate elements. F1 mesh for element size 0.4mm exhibit deviation of δK_t error course (Fig. 3a) as a result of the finite element distortion which is described by the aspect ratio increase (Fig. 4a). For this particular case the notch root element belongs to the free mesh distortion which involves sharing one node by five elements.

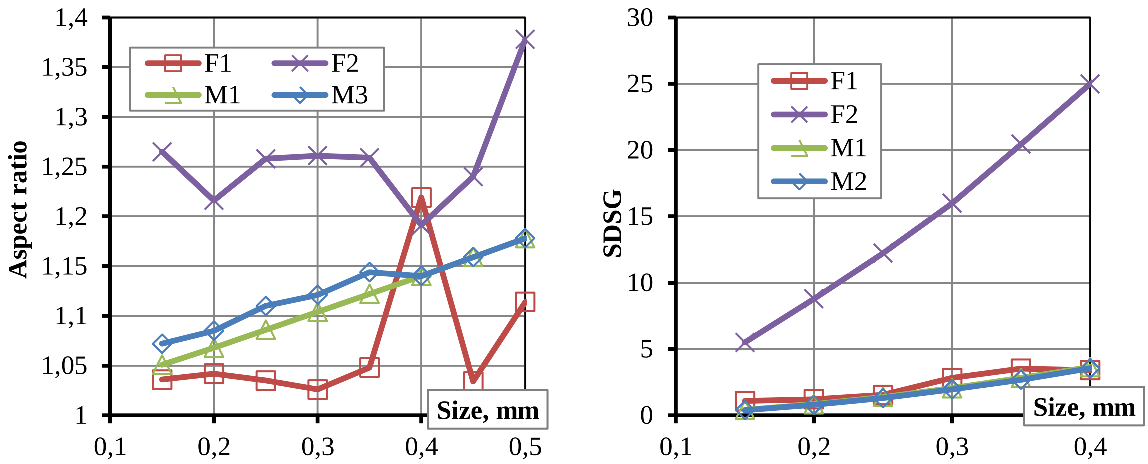

Fig. 4: Mesh quality factors at notch root: a) aspect ratio; b) stress discontinuity error.

The analysis of graphs on Fig. 3b shows that, depending on the mesh preparation method, the assumed calculation accuracy can be obtained for various model sizes. Additional estimation was conducted to establish the problem size for which the assumed error level could be obtained with each model. The estimated problem sizes are presented in Tab. 1 with DOF number and in DOF relative values determined for individual meshes corresponding to DOF for M1 mesh.

Tab. 1: Estimated problem size for obtaining of the assumed δK_t relative error

δK_t, %	F1	F2	M1	M2	F1	F2	M1	M2
	mln DOF				DOF / (DOF for M1)			
2	0.144	0.251	0.076	0.055	1.90	3.31	1.00	0.73
1	0.324	0.604	0.195	0.179	1.66	3.11	1.00	0.92
0.2	1.354	2.385	1.182	1.197	1.14	2.02	1.00	1.01

The quality of free mesh is lower than the quality of mapped meshes for which we can observe the linear influence of the element size on aspect ratio. Triangular elements, compared to quadrate elements, require three times as much as DOF quantity in order to reach the error over 1% and double the number of DOF for more precise analyses in which models are of the size above 1 mln of DOF. The shape of the notch sub-area borders has an influence on the calculation accuracy for mapped models of the dimension below 0.1 mln of DOF.

4. Conclusions

The accuracy of FEM analyses for flat specimens with opposite V-notch under tension is not only influenced by the size of the finite element, but also by mesh morphology. Quadrate elements allow for more precise estimation of high gradient stresses which are present at the notch root. Introduction of mapping to the mesh significantly improves the calculation accuracy.

For the mapped meshes, preparation of the notch root surrounding sub-area, in the manner that the generated mesh consists of non-deflected elements, gains crucial importance. The geometrical form of this sub-area border has an impact on the accuracy of analyses for relatively large characteristic sizes of finite elements.

In order to guarantee the clarity of our discussion, the paper assumes a homogeneous value of the finite elements characteristic size in the whole specimen area, also in its gripping part. It allows for separation of effect of the mesh morphology influence on calculation accuracy for each mesh variant. In practice, it is often used the approach which assumes variation of the elements size and the mesh morphology, between the notch area and the rest of the specimen, by refining the mesh at locations of stress gradients. Also, in such cases, the tendencies of relations of estimation accuracy of K_t to DOF number remain unchanged in the terms of quality. It should be expected that quantity measures shall be subject to change.

References

Blacha, L., Karolczuk, A., Banski, R. & Stasiuk, P. (2013) Application of the weakest link analysis to the area of fatigue design of steel welded joints, Engineering Failure Analysis, 35, pp 665-677.

Cichanski, A. (2011) Influence of finite element order on SCF precision for U-shaped notches in flat bars under tension, Proceedings of XVII 17th International Conference Engineering Mechanics 2011, Svratka - Czech Republic, 2011, pp.79-82.

Cichanski, A. (2015) The influence of mesh morphology on the accuracy of FEM analysis of bar with a ringed notch under tension, Solid State Phenomena, 224, 2015, pp. 204-209.

Karolczuk, A. & Palin-Luc, T. (2013) Modelling of stress gradient effect on fatigue life using Weibull based distribution function, Journal of Theoretical and Applied Mechanics, 51, 2, pp. 297-311.

Nisitani, H & Noda, N.A. (1986) Stress concentration of a strip with double edge notches under tension or in-plane bending, Engineering Fracture Mechanics, 23, pp.1051-1065.

Noda, N.A., Sera, M. & Takase, Y. (1995) Stress concentration factors for round and flat specimens with notches. International Journal of Fatigue, 17, 3, pp.163-178.

Noda, N.A., & Takase, Y. (2002) Stress concentration factors formulas useful for all notches shapes in a flat test specimen under tension and bending, Journal of Testing and Evaluation, 30, 5, pp.369-381.

Pilkey, W.D. & Pilkey D.F. (2008) Peterson's stress concentration factors. John Wiley & Sons, Inc.

Shin, C.S, Man, K.C. & Wang C.M. (1994) A practical method to estimate the stress concentration of notches, International Journal of Fatigue, 16, 4, pp.242-256.

Soltysiak, R. & Boronski, D. (2015) Strain analysis at notch root in laser welded samples using material properties of individual weld zones, International Journal of Fatigue,74, 71-80.

22nd International Conference
ENGINEERING MECHANICS 2016
Svratka, Czech Republic, 9 – 12 May 2016

MORPHOLOGICAL DILATION AS THE METHOD OF MINERAL FRACTION LOSS COMPENSATION IN RECONSTRUCTION OF TRABECULAR BONE STRUCTURE

A. Cichański*, K. Nowicki

Abstract: *The paper presents the issue of compensation of mineral fraction loss during bone reconstruction performed with application of own algorithms. The algorithm of the image morphological dilation was adopted for such compensation. The algorithm efficiency was proved during numerical analyses of bone structures reconstructed with First-Second and First-Last methods for the selected eight sizes of voxels. Application of the image morphological dilation allowed for improvement of the accuracy of structure reconstruction with First-Last method.*

Keywords: ***bone structure reconstruction, finite element method, morphological dilation***

1. Introduction

The content of mineral fraction is decisive for the stiffness of the tested trabecular structure (Topoliński et al. #1, 2012). At the structure modelling stage the voxel size is a significant parameter with respect to stiffness. Decrease of stiffness of the structure modelled with hexahedral elements which accompanies the voxel size increase can be reduced by compensation of the modelled sample volume or by application of tetrahedral elements (Urlich et al., 1998). Other method for stiffness decrease minimization is to apply hexahedral elements for elongated voxels (Topoliński et al. #2, 2012). Application of elements with quadratic interpolation between nodes does not improve accuracy of modelling of the structure resilience properties (Depalle et al., 2013).

Mathematical morphology is vastly applied in processing of medical images. It is mostly used for denoising of images generated with basic methods of medical imagining (Mittal et al., 2013). Morphological filters are also applied in analysis of biological structures, including trabecular bone structures. Skeletal images of trabecular bone structure generated with morphological filters are the basis for determination of structural parameters (Sakoda et al., 2004).

The paper presents the issue of compensation for mineral fraction loss in samples modelled with own structure reconstruction algorithms. The image morphological dilation algorithm was adopted for correction of the structure. Verification of the proposed method for samples of variable structure in the vast range of voxel size variability was performed. During numerical analyses the impact of the proposed compensation method on accuracy of modelling of stiffness of the reconstructed trabecular bone structure was specified.

2. Test object

Modelling was applied to samples of trabecular structure in cylindrical form, of 10mm diameter and 7.5mm height, cut from human femoral neck. Samples preparation method was described in the work by (Topoliński et al. #1, 2012). Trabecular structure samples obtained were subject to µCT80 (Stanco A.G., Switzeland) microtomograph tests. As a result of tests conducted with 36µm resolution, a set of 210 images of layers of structures perpendicular to sample axis were obtained. The images were processed to binary form by thresholding, with threshold value as 18% of maximum brightness of the received image.

* Dr.Eng. Artur Cichański: University of Science and Technology, Mechanical Engineering Faculty, Kaliskiego 7; 85-789, Bydgoszcz; PL, e-mail: artur.cichanski@utp.edu.pl

Three structural models were prepared for each sample: base model SC, model First-Second FS model and First-Last FL model (Topoliński et al. #2, 2012). The models differed in the number of μCT required for their preparation. SC model was based on all images generated with images μCT. FS and FL models were based on the selected μCT images, and the subsequent layers of the reconstructed structure were composed of axially elongated voxels (Fig. 1). During construction of FS models, two subsequent scans, set 36μm apart, were compared. During construction of FL models, two subsequent scans, set total multiple of the base 36μm dimension apart, were compared. For FS and FL models, voxel *d* size varied from 72 to 324μm, with 36μm increment.

a)

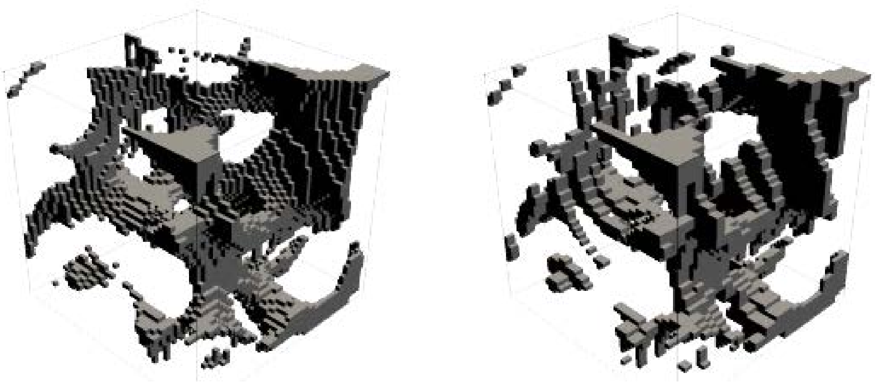

Fig. 1: An example of reconstructed structure: a) SC method; b) FS method, d=108μm.

Application of FS and FL models results in reduction of a number of scans necessary for structure reconstruction, thus it allows for reduction of radiation dose a diagnosed person is exposed to. Mineral fraction loss and the loss of connections between trabeculae in the reconstructed structure and the resulting sample stiffness decrease are undesirable effects of these models . For *BV/TV*=0.353 sample, average volume decrease of models reconstructed with FS method referenced to volumes for SC method is below 1% (Fig 2a), and average Young apparent modulus decrease, referenced to Young apparent modulus for SC method reaches 17% (Fig 2b). For the same sample reconstructed with FL method volume decrease is 43% (Fig 2a), and strength decrease reaches 72% (Fig 2b).

The work uses morphological dilation algorithm for compensation of mineral fraction loss (Gonzalez & Woods, 1992). The applied method realized dilation algorithm with three dimensional structural element 3x3x3 applied for each image in image stack representing individual cross-sections of trabecular bone structure and images in the adjacent stack, above and below the processed image. Dilation algorithm was activated if the original number of pixels representing mineral fraction on the reconstructed image was less than on the unprocessed image. The mask corresponding to actual location of the structural element was placed on the unprocessed image. If the pixels of such mask covered the mineral fraction representing pixels on the unprocessed image, then additional mineral fraction representing pixel was additionally created. As a result of algorithm operation, gradual expansion of edges of the unprocessed image objects and diminishing of openings took place. Such prepared morphological dilation was conducted until the least possible difference in the number of pixels between unprocessed and reconstructed image was reached, upon maintaining lower number of reconstructed image pixels then the number of unprocessed image pixels.

3. Test conditions

For each of three models sample stiffness was specified with finite elements method FEM in ANSYS software environment. The mesh was created with direct voxel to element geometry conversion (Boutroy et al., 2008). Analysis was performed on 8 node SOLID186 elements in the form of cube of side length 36μm. In case of elongated voxels, characteristic for FS and FL methods, several elements were created for the voxel and distributed along its length. Elements not connected with the whole sample structure were eliminated from such prepared mesh. Isotropic material properties E = 10GPa and ν=0.3 were adopted for the analyses. Threshold conditions mapped cylindrical sample compression in axial direction ε=0.8% (Topoliński et al. #2, 2012). Apparent Young modulus for the sample was determined on the basis of the analysis results.

Tab. 1: Selected structural indicators for the modelled samples.

value	*BV/TV*	*Tb.Th* [mm]	*Tb.Sp* [mm]	*Tb.N* [1/mm]
min	0.068	0.76	0.089	0.331
max	0.377	1.956	0.23	1.223
mean	0.224	1.446	0.147	0.612
standard deviation	0.111	0.407	0.044	0.31

Numerical analyses used 9 samples selected from population of 42 samples. As the first the sample of *BV/TV* value closest to *BV/TV* average value for the whole population was selected. Then, 4 samples of *BV/TV* values close to average *BV/TV* plus 0.5, 1, 1.5 and 2 multiple of standard deviation SD for the whole population were selected. The same procedure was applied for subsequent 4 samples for which *BV/TV* value was lower than the average by similar SD multiples. Basic structure indicators specifying the selected samples are presented in Table 1. Significant variability of the indicators and their standard deviations indicates significant variation of the analysed structures. For each selected sample the following calculations were performed: for 1 SC model and 8 FS models without compensation and for 8 FS models with compensation and 8 FL models without compensation and 8 FL models with compensation.

4. Test results

No change was observed for FS method as its characteristic volume decrease was so insignificant that it did not triggered the dilation algorithm. As a result of dilation algorithm application, structure reconstruction error for FL method was reduced. For sample with *BV/TV* =0.353 volume decrease is 20% (FL,CP designation on Fig 2a), Young modulus decrease reaches 48% (FL,CP designation on Fig 2b).

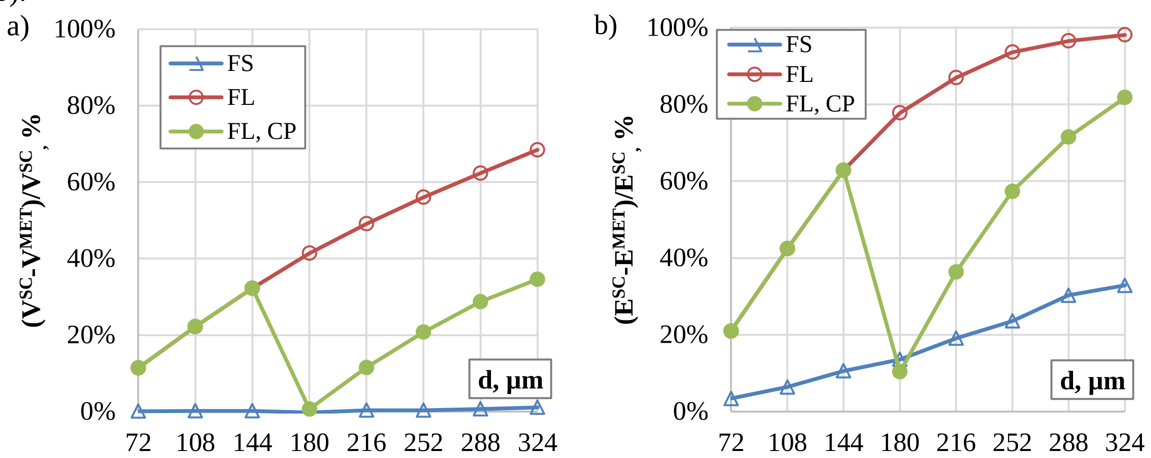

Fig. 2. Structure reconstruction errors for sample BV/TV=0.353, a) volume V; b) apparent modulus E.

Analyses results for 9 samples modelled with FS method and FL method are presented in table 1 for the models without NC compensation and with CP volume compensation. Relative errors of δV^{MOD} volume were calculated from dependency (1) on the basis of FEM analysis results for all eight voxel sizes *d* changing in the range from 72 to 324µm, with 36µm increment. For the set voxel size *d* V_d^{SC} volume was determined on the basis of SC model and V_d^{MOD} volume was determined on FS or FL model. Maintaining similar convention of designations, averaged values of relative errors of Young apparent modulus δE were determined.

$$\delta V^{MOD} = \frac{1}{8}\sum_{d=72}^{324}\frac{V_d^{SC}-V_d^{MOD}}{V_d^{SC}} * 100\% \qquad (1)$$

For FS method, values of δV^{FS} volume error and values of δE^{FS} apparent Young modulus error remain unchanged for models with and without compensation. For FL method, application of the image morphological dilation resulted in reduction of δV^{FL} volume error and δE^{FL} apparent Young modulus error. For both methods, absolute values of δE apparent Young modulus error are higher than the values of δV volume errors. Along with *BV/TV* increase the values of both errors are decreased.

Tab. 1: Reconstruction errors, averaged for all voxel sizes

BV/TV	δV^{FS}		δV^{FL}		δE^{FS}		δE^{FL}	
	NC	CP	NC	CP	NC	CP	NC	CP
0.377	0%	0%	33%	18%	10%	10%	56%	32%
0.353	0%	0%	43%	20%	17%	17%	72%	48%
0.32	0%	0%	46%	18%	18%	18%	72%	45%
0.259	1%	1%	58%	30%	32%	32%	82%	62%
0.217	4%	4%	65%	38%	45%	45%	89%	83%
0.171	9%	9%	69%	52%	52%	52%	90%	85%
0.145	10%	10%	69%	51%	59%	59%	92%	88%
0.107	17%	17%	71%	48%	60%	60%	92%	83%
0.068	31%	31%	74%	53%	70%	70%	95%	90%
mean	**8%**	**8%**	**59%**	**36%**	**40%**	**40%**	**82%**	**68%**

5. Conclusions

FS method maps the modelled structure accordingly. For the samples characterised with high mineral fraction *BV/TV*>0.3 share the method allows for structure reconstruction without volume decrease for voxels of up to 0.3mm length. For this method, the image morphological dilation algorithm was not triggered. The observed decrease of the sample stiffness is influenced by the loss of connections between trabeculae resulting from omission of some µCT images which is characteristic for FS method.

FL method is sensitive to voxel size increase resulting from the increase of distance between µCT images, selected for the structure reconstruction. Even the samples of the highest mineral fraction share modelled with the method show high volume losses. Values of the structure reconstruction errors are comparable to the values obtained for the samples characterised with the lowest mineral fraction share but modelled with FS method.

Application of the image morphological dilation allowed for improvement of the structure reconstruction accuracy with FL method. Average difference between FL and FS models stiffness decreased for all samples. Higher increase of the structure reconstruction efficiency for samples characterized with higher mineral fraction share was observed. For both tested methods, the structure reconstruction accuracy increases with the mineral fraction quantity increase.

References

Boutroy, S., Van Rietbergen, B., Sornay-Rendu, E., Munoz, F., Bouxsein, M. L., Delmas, P. D., 2008, Finite element analysis based on in vivo HR-pQCT images of the distal radius is associated with wrist fracture in postmenopausal women, J Bone Miner Res, 23, 3, pp. 392-399.

Depalle B., Chapurlat R., Walter-Le-Berre H., Bou-Said B., Follet, H. (2013). "Finite element dependence of stress evaluation for human trabecular bone." J Mech Behav Biomed Mater, 18, pp.200-212.

Gonzalez R., Woods R., (1992), Digital Image Processing, Addison-Wesley Publishing Company.

Mittal U., Anand S.,(2013), Effect of morphological filters on medical image segmentation using improved watershed segmentation, Int J of Computer Science & Engineering Technology, 4, 6, pp.631-638

Sakoda S., Kawamata R., Kaneda T., Kashima I., (2004), Application of the digital radiographic bone trabecular structure analysis to the mandible using morphological filter, Oral Science Int, May 2004, pp.45-53

Topoliński T., Cichański A., Mazurkiewicz A., Nowicki K., (2012), Microarchitecture Parameters Describe Bone Structure and Its Strength Better Than BMD, The Scientific World Journal, 2012, Article ID 502781, doi:10.1100/2012/502781, pp.1-7.

Topoliński T., Cichański A., Mazurkiewicz A., Nowicki K., (2012), The Relationship between Trabecular Bone Structure Modeling Methods and the Elastic Modulus as Calculated by FEM, The Scientific World Journal, 2012, Article ID 827196, doi:10.1100/2012/827196, pp.1-9.

Ulrich D., van Rietbergen B., Weinans H., Ruegsegger P., (1998), Finite element analysis of trabecular bone structure: a comparison of image-based meshing techniques, Journal of Biomechanics, 31, 12, pp.1187-1192.

22nd International Conference
ENGINEERING MECHANICS 2016
Svratka, Czech Republic, 9 – 12 May 2016

MECHANICAL CONCEPT OF WHIRL FLUTTER AEROELASTIC DEMONSTRATOR

J. Čečrdle*, J. Maleček**, O. Vích***

Abstract: *This paper deals with the design of the whirl flutter aeroelastic demonstrator. It gives a theoretical background of the whirl flutter phenomenon. The main part is focused on the new aeroelastic demonstrator "W-WING", designed at the VZLU. The demonstrator represents wing and engine nacelle of a twin turboprop commuter aircraft. It enables changes of the main structural parameters influencing whirl flutter stability characteristics. Moreover, it includes thrusting propeller. The demonstrator is intended for experimental investigations at the VZLU 3m-diameter low-speed wind tunnel. The results will be used for validation of analytical methods and software tools as well as in the frame of research projects.*

Keywords: Aeroelasticity, Whirl Flutter, Aeroelastic experiment, W-WING demonstrator.

1. Introduction

Whirl flutter is a specific kind of aeroelastic flutter instability, which may appear on turboprop aircraft owing to the effect of rotating parts (propeller or gas turbine engine rotor). Rotating mass generates additional forces and moments and increases the number of degrees-of-freedom. Rotating propeller also causes aerodynamic interference effect with a nacelle and a wing. Whirl flutter instability is driven by motion-induced unsteady aerodynamic propeller forces and moments acting in the propeller plane. It may cause unstable vibration, which can lead to a failure of an engine installation or a whole wing.

The complicated physical principle of the whirl flutter requires the experimental validation of the analytically gained results, especially due to the unreliable analytical solution of the propeller aerodynamic forces. Further, a structural damping is a key parameter, to which whirl flutter is extremely sensitive and which needs to be validated. Therefore, the aeroelastic models are used. This paper takes up the previous work on the subject by authors (Čečrdle & Maleček, 2010) and summarizes the new achievements in the aeroelastic demonstrator development process.

2. Theoretical Background

The principle of whirl flutter phenomenon is described on the simple mechanical system with two degrees-of-freedom, where an engine flexible mounting is represented by two rotational springs (stiffness K_Ψ, K_Θ), while a propeller is considered rigid (see figure 1). This system has two independent mode shapes (yaw and pitch) with angular frequencies ω_Ψ and ω_Θ. Considering a propeller rotation with the angular velocity Ω, the gyroscopic effect causes both independent mode shapes merge into the whirl motion. A propeller axis shows an elliptical movement with a trajectory dependent on both angular frequencies ω_Ψ and ω_Θ. The orientation of the gyroscopic movement is backward relative to the propeller rotation for the mode with the lower frequency (backward whirl mode) and forward relative to the propeller rotation for the mode with the higher frequency (forward whirl mode).

The gyroscopic motion results in changes of the propeller blades' angles of attack. It causes generating of unsteady aerodynamic forces, which may under specific conditions induce whirl flutter

* Ing. Jiří Čečrdle, Ph.D.: Strength of Structures Dept., Aeronautical Research and Test Institute (VZLU), Beranovych 130; 199 05, Prague - Letnany; CZ, cecrdle@vzlu.cz

** Ing. Jaromír Maleček, CSc.: Strength of Structures Dept., Aeronautical Research and Test Institute (VZLU), Beranovych 130; 199 05, Prague - Letnany; CZ, malecek@vzlu.cz

*** Ing. Ondřej Vích: Strength of Structures Dept., Aeronautical Research and Test Institute (VZLU), Beranovych 130; 199 05, Prague - Letnany; CZ, ondrej.vich@vzlu.cz

instability. The critical flutter state is defined as the neutral stability with no damping of the system and the corresponding air velocity (**$V_\infty = V_{FL}$**) is called critical flutter speed. If the air velocity is lower than flutter speed (**$V_\infty < V_{FL}$**), the system is stable and the gyroscopic motion is damped. If the airspeed exceeds the flutter speed (**$V_\infty > V_{FL}$**), the system becomes unstable and gyroscopic motion divergent.

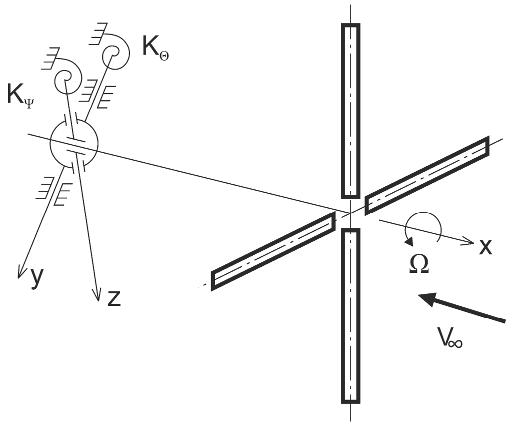

Fig. 1: Gyroscopic system with propeller

The analytical solution is focused on a determination of the aerodynamic forces caused by the gyroscopic motion on each of propeller blades. Presented equations of motion were derived for the gyroscopic system shown in figure 1 using Lagrange's approach. The kinematical scheme is shown in figure 2. Three angles (**φ, Θ, Ψ**) are independent generalised coordinates, the propeller angular velocity is constant (**$\varphi = \Omega\, t$**). The rotating part is assumed cyclically symmetric with respect to both mass and aerodynamics. Non-uniform mass moments of inertia of an engine with respect to pitch and yaw axes (**$J_Z \neq J_Y$**) are considered. Considering small angles, the equations of motion become:

$$
\begin{aligned}
J_Y\ddot{\Theta} + \frac{K_\Theta \gamma_\Theta}{\omega}\dot{\Theta} + J_X \Omega \dot{\Psi} + K_\Theta \Theta &= M_{Y,P} - a.P_Z \\
J_Z\ddot{\Psi} + \frac{K_\Psi \gamma_\Psi}{\omega}\dot{\Psi} - J_X \Omega \dot{\Theta} + K_\Psi \Psi &= M_{Z,P} + a.P_Y
\end{aligned}
\tag{1}
$$

Propeller aerodynamic forces are determined using aerodynamic derivatives (Ribner, 1945; Houbolt & Reed, 1962). Seeking for the critical (flutter) state assuming the harmonic motion has a character of an eigenvalue problem. The whirl flutter matrix equation then has a following form:

$$
\left(-\omega^2\left[M\right] + j\omega\left(\left[D\right] + \left[G\right] + q_\infty F_P \frac{D_P^2}{V_\infty}\left[D^A\right]\right) + \left(\left[K\right] + q_\infty F_P D_P \left[K^A\right]\right)\right)\begin{bmatrix}\overline{\Theta} \\ \overline{\Psi}\end{bmatrix} = \{0\} \tag{2}
$$

The critical state emerges when the angular velocity **ω** is real. The critical state can be reached by increasing either **V_∞** or **Ω**. The increase of the propeller advance ratio **(V_∞ / (ΩR))** has destabilizing effect. Structural damping is a significant stabilization factor. On the contrary, the influence of the propeller thrust is negligible. The most critical state is **$\omega_\Theta = \omega_\Psi$**, when the trajectory of the gyroscopic motion is circular. Considering the rigid propeller blades, the whirl flutter inherently appears at the backward gyroscopic mode.

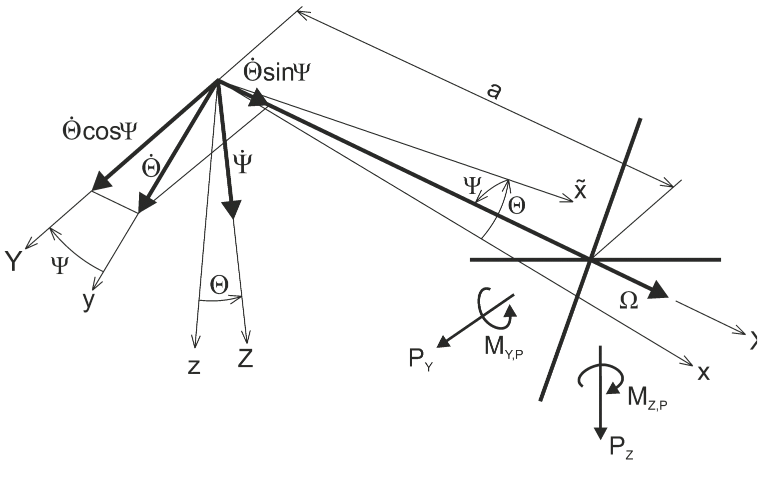

Fig. 2: Kinematical scheme of gyroscopic system

The described model with a rigid propeller is applicable to conventional propellers, for which the propeller blade frequencies are much higher compared to the nacelle pitch and yaw frequencies. In case of the large multi-bladed propellers of heavy turboprop aircraft, the consideration of a rigid propeller appears too conservative and the blade flexibility must also be modelled.

3. Experimental Research on Whirl Flutter

The first experimental investigations of whirl flutter characteristics were accomplished by Houbolt & Reed (1962) on the simple model of a propeller in the windmilling mode. Further investigations were conducted by Bland & Bennet (1963), who measured the propeller forces and stability of the propeller-nacelle component model. The comparison of the experimental results with theory demonstrated that the theoretical aerodynamic derivatives underestimate the whirl flutter speed. Another broad experimental campaign was conducted following the accidents of two L-188C Electra II airliners in the frame of the accident cause investigation (Abbott, Kelly & Hampton, 1963).

4. W-WING Whirl Flutter Aeroelastic Demonstrator

"W-WING" (Whirl-Wing) is the new whirl flutter demonstrator designed and developed by the Aeronautical Research and Test Institute (VZLU), Prague, Czech Republic. The demonstrator was adapted from the former aeroelastic model of the L-610 commuter aircraft, which was used for assessment of the flutter and the aeroelastic dynamic response issues during the development of the aircraft. The starboard wing including the nacelle was later utilised as the research demonstrator.

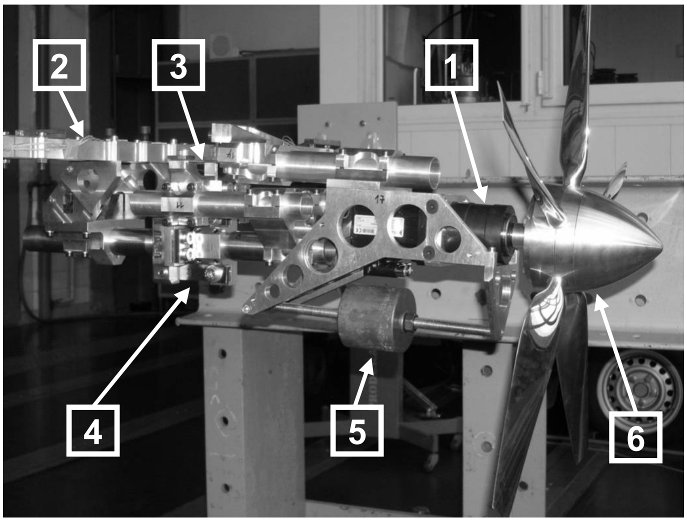

Fig. 3: W-WING demonstrator uncoated nacelle with motor and propeller (1 - motor; 2 - wing spar; 3 - pitch attachment; 4 - yaw attachment; 5 - massbalancing weight; 6 - propeller)

The wing with span of 2.56 m is fixed at the root to the pylon and attached in a wind tunnel. The wing structure is modular. The wing stiffness is modelled by the duralumin spar with the variable H-cross-section; the aileron stiffness is modelled by the spar with a variable rectangular cross-section. The inertial characteristics are modelled by lead weights. The aerodynamic shape is covered by the modular balsa and plastic foil segments.

The nacelle structure is replaceable. The W-WING demonstrator represents the new nacelle structure (it does not represent any specific type of aircraft). The demonstrator is capable of simulating changes of all the important parameters influencing the whirl flutter. The nacelle model has two degrees of freedom - engine pitch and yaw. The stiffness parameters in both pitch and yaw are modelled by means of cross spring pivots with changeable spring leaves (stiffness constants are independently adjustable by replacing these spring leaves). Both pivots can be independently moved in the direction of the propeller axis within the range of 0.15 m to adjust the pivot points of both vibration modes. The centre of the gravity of the nacelle can be adjusted by means of the movable balance weight with a nominal mass of 4.22 kg. The plastic nacelle cowling is manufactured using the 3D print technology. The gyroscopic effect of the rotating mass is simulated by the mass of the propeller blades. Two sets of blades made of duralumin and steel are available. The propeller diameter is 0.7 m. It represents a geometrically scaled-down real 5-blade Avia V-518 propeller. The propeller blades' angle of attack is adjustable at the standstill by means of the special tool.

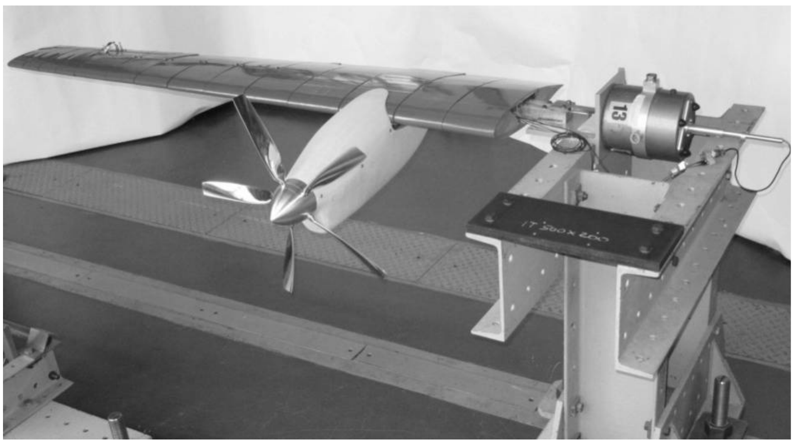

Fig. 4: W-WING demonstrator

Contrary to the most of former experimental applications, the W-WING demonstrator’s propeller is powered by an electric motor. Its nominal power is 597 W and nominal revolutions are 3000 rpm. Although the propeller thrust influence on the whirl flutter stability is low, the powered propeller solution was chosen to obtain wider options in the combination of the wind-flow velocity and the propeller revolutions. The demonstrator may be excited either by the wind flow turbulence or aerodynamically by means of the aileron deflection using various excitation signals (harmonic, swept sine, impulse). The system is controlled by the special in-house SW tool prepared in the LabVIEW v2012 environment. It provides acquisition of measured quantities from the strain gauges, accelerometers and the propulsion system, and also the safeguard preventing the destruction of the demonstrator by turning off the motor and the aerodynamic excitation, provided the response is exceeding the preselected limits.

5. Conclusion and Outlook

The paper deals with the mechanical concept of the new aeroelastic demonstrator for whirl flutter simulation (W-WING). The demonstrator represents wing and engine with the thrusting propeller of a turboprop commuter aircraft. The demonstrator's concept allows adjusting of all main parameters influencing whirl flutter. The W-WING demonstrator underwent the functionality tests and tests of the structural parameters. A broad testing campaign in the VZLU 3m-diameter wind tunnel is planned. The test schedule includes the measurement up to wind flow velocity of 45 $m \cdot s^{-1}$. In the first phase of testing, the influence of pitch and yaw stiffness and mass balance weight station will be primarily evaluated. The second phase will be focused mainly on the influence of the different sets of propeller blades (gyroscopic effect) and their angle of attack. The experimental results will be subsequently utilized for verification of the analytical methods and tools used for the certification of turboprop aircraft.

In parallel with the demonstrator hardware, the analytical model for FE flutter calculations was prepared. The model was used for preliminary analytical studies. First, the parametric calculations using optimization-based approach (Čečrdle, 2012) to find the stability margins and to predict the flutter behaviour of the system during the wind tunnel tests were performed. The stations of both hinges and balance weight were kept at the centre of their ranges, while both vertical and lateral stiffness as well as the propeller revolutions became parameters. The example of results is shown in the figure 5. It shows the stability margin (expressed in terms of required stiffness for the neutral stability) for a fixed propeller revolutions and variable wind flow velocity. Next, the influence of both engine attachment hinge points as well as balance weight stations was evaluated.

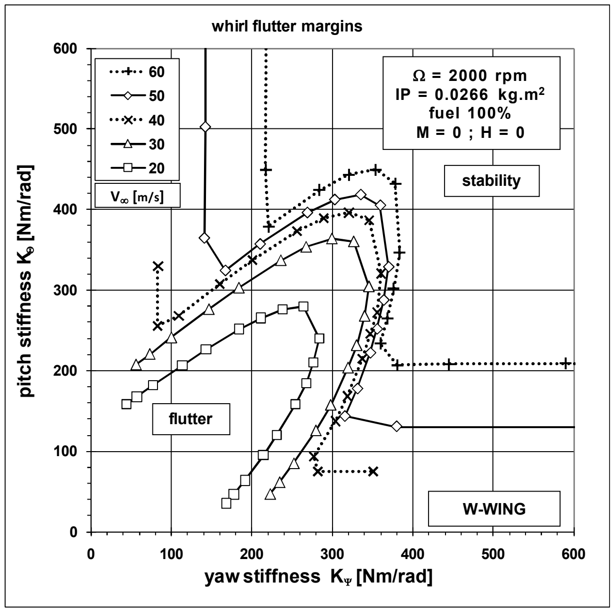

Fig. 5: W-WING analytical results example - required stiffness for neutral stability

References

Abbott, F.T., Kelly, H.N. & Hampton, K.D. (1963) Investigation of Propeller-Power-Plant Autoprecession Boundaries for a Dynamic-Aeroelastic Model of a Four-Engine Turboprop Transport Airplane, NASA TN D-1806.

Bland, S.R. & Bennett, R.M. (1963) Wind-Tunnel Measurement of Propeller Whirl-Flutter Speeds and Static Stability Derivatives and Comparison with Theory, NASA TN D-1807.

Čečrdle, J. (2012) Analysis of Twin Turboprop Aircraft Whirl-Flutter Stability Boundaries. Journal of Aircraft, Vol.49, No.6, Nov – Dec 2012, pp.1718 – 1725.

Čečrdle, J. (2015) Whirl Flutter of Turboprop Aircraft Structures, Elsevier Science Ltd., ISBN 978-1-782421-85-6.

Čečrdle, J. & Maleček, J. (2010) Conceptual Design of Aeroelastic Demonstrator for Whirl Flutter Simulation, World Academy of Science, Engineering and Technology (WASET), Issue 68, pp.132-136.

Houbolt, J.C. & Reed, W.H. (1962) Propeller Nacelle Whirl Flutter, Journal of Aerospace Sciences, Vol.29, March 1962, pp.333-346.

Ribner, H.S. (1945) Propellers in Yaw, NACA Rep.820.

Náprstek, J. & Pospíšil S. (2012) Response Types and General Stability Conditions of Linear Aero-elastic System with Two Degrees-of-freedom, Journal of Wind Engineering and Industrial Aerodynamics, Vol.111, Nr.1, 2012, pp.1-13

22nd International Conference
ENGINEERING MECHANICS 2016
Svratka, Czech Republic, 9 – 12 May 2016

NUMERICAL SOLUTION OF A SECULAR EQUATION FOR RAYLEIGH WAVES IN A THIN SEMI-INFINITE MEDIUM MADE OF A COMPOSITE MATERIAL

J. Červ[*], V. Adámek[**], F. Valeš[*], S. Parma[*]

Abstract: *The traditional way of deriving the secular equation for Rayleigh waves propagating along the stress-free edge of a thin semi-infinite composite is presented. It means that it is necessary to find a general steady-state solution that vanishes at infinity. The secular equation is then obtained by vanishing of the surface traction at the stress-free edge. For the solution of such secular equation it is necessary to precompute some roots of characteristic quartic equation. The method shown in this paper, based on displacement formulation, leads to the so-called implicit secular equation. The numerical approach to the solution is shown.*

Keywords: Rayleigh Waves, Composite Material, Secular Equation.

1. Introduction

A thin semi-infinite composite structure is considered. The kind of the composite material in mind is one in which a matrix material is reinforced by strong stiff fibres which are systematically arranged in the matrix. The fibres are considered to be long compared to their diameters and the fibre spacing, and to be densely distributed, so the fibres form a substantial proportion of the composite. A composite of this kind for sufficiently long wavelength can be regarded as a homogeneous orthotropic material. It is also assumed that composite thickness is small compared to the shortest wavelength taken into account. Under these conditions one can consider the composite structure as an orthotropic solid in the state of plane stress. The traditional way of deriving the secular equation for Rayleigh-edge waves propagating in the direction of the x_1- axis in a thin semi-infinite composite $x_2 \geq 0$ is to find a general steady-state solution for the displacement components that vanishes at $x_2 = +\infty$. The secular equation is then obtained by vanishing of the surface traction at $x_2 = 0$. For the solution of such secular equation it is necessary to precompute some roots of characteristic quartic equation. The method shown in this paper (based on displacement formulation) leads to the so-called implicit secular equation. The details can be seen in the paper Cerv & Plesek (2013).

2. Preliminaries

We suppose that material and body axes of the 2D orthotropic linear elastic medium in the state of plane stress are denoted by X_1, X_2 and x_1, x_2 respectively. The third axis x_3 is identical with the material axis X_3 and constitutes axis of possible rotation (through an angle ϑ) of the principal material axes X_1, X_2 from thre body axes x_1, x_2, see Fig. 1. Due to the plane stress it holds $\sigma_{33} = \sigma_{23} = \sigma_{13} = 0$. For considered material, the relationship between the stress σ_{ij} and strain ε_{ij} components is given by the formula (1), where $C_{ij} = C_{ij}(\vartheta)$ denote the elastic stiffnesses.

[*] Assoc. Prof. Jan Červ, PhD: Institute of Thermomechanics AS CR, v.v.i.; Dolejškova 5; 182 00, Prague; CZ, cerv@it.cas.cz
[**] Vítězslav Adámek, PhD.: NTIS – New Technologies for the Information Society, University of West Bohemia; Univerzitní 8; 306 14, Pilsen; CZ, vadamek@kme.zcu.cz
[*] František Valeš, PhD.: Institute of Thermomechanics AS CR, v.v.i.; Veleslavínova 11; 301 14, Pilsen; CZ, vales@it.cas.cz
[*] Slavomír Parma, MSc.: Institute of Thermomechanics AS CR, v.v.i.; Dolejškova 5; 182 00, Prague; CZ, parma@it.cas.cz

$$\begin{Bmatrix} \sigma_{11} \\ \sigma_{22} \\ \sigma_{12} \end{Bmatrix} = \begin{bmatrix} C_{11} & C_{12} & C_{16} \\ C_{12} & C_{22} & C_{26} \\ C_{16} & C_{26} & C_{66} \end{bmatrix} \cdot \begin{Bmatrix} \varepsilon_{11} \\ \varepsilon_{22} \\ 2\varepsilon_{12} \end{Bmatrix} \tag{1}$$

The strain components ε_{ij} are related to the displacement components u_1, u_2 through

$$2\varepsilon_{ij} = \left(u_{i,j} + u_{j,i}\right). \tag{2}$$

The equations of motion, written in the absence of body forces, are

$$\sigma_{ij,j} = \rho \cdot \ddot{u}_i \,, \tag{3}$$

where ρ is the mass density and the comma denotes differentiation with respect to x_j.

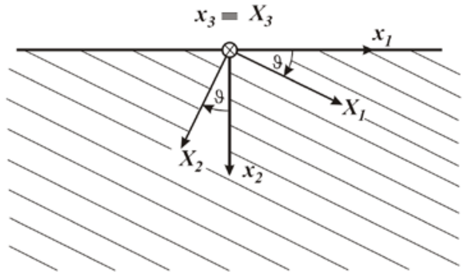

Fig. 1: A thin semi-infinite orthotropic medium.

3. Solution

Equations of motions in terms of displacements are considered, see Cerv & Plesek (2013). The solution to these equations is supposed in the form

$$\begin{aligned} u_1(x_1, x_2, t) &= U_{01} e^{q x_2} e^{\mathrm{i}k(x_1 - ct)} \,, \\ u_2(x_1, x_2, t) &= U_{02} e^{q x_2} e^{\mathrm{i}k(x_1 - ct)} \,, \end{aligned} \tag{4}$$

where k is the wavenumber, c the unknown velocity and q a complex parameter dependent on C_{ij}, c and ρ. It is stipulated that $\mathrm{Re}(q) < 0$. This solution represents a harmonic wave propagating in the positive direction of the x_1-axis. Boundary conditions can be stated as

$$\lim_{x_2 \to +\infty} u_1(x_1, x_2, t) = \lim_{x_2 \to +\infty} u_2(x_1, x_2, t) = 0 \,, \tag{5}$$

$$\sigma_{12} = \sigma_{22} = 0 \quad \text{at} \quad x_2 = 0 \,. \tag{6}$$

Substituting (4) into equations of motions one obtains a homogeneous system for displacement amplitudes, U_{01}, U_{02} as

$$\begin{aligned} &[k^2 C_{11} - 2\mathrm{i}kqC_{16} - q^2 C_{66} - \rho k^2 c^2] U_{01} + [k^2 C_{16} - \mathrm{i}kq(C_{12} + C_{66}) - q^2 C_{26}] U_{02} = 0 \,, \\ &[k^2 C_{16} - \mathrm{i}kq(C_{12} + C_{66}) - q^2 C_{26}] U_{01} + [k^2 C_{66} - 2\mathrm{i}kqC_{26} - q^2 C_{22} - \rho k^2 c^2] U_{02} = 0. \end{aligned} \tag{7}$$

This system will have a nontrivial solution if and only if its determinant vanishes. This leads to a quartic characteristic equation in $p := \mathrm{i}q$, which may be written as

$$Ap^4 + Bkp^3 + Ck^2p^2 + Dk^3p + Ek^4 = 0 \,. \tag{8}$$

Due to the boundary condition (5) we are only interested in the roots satisfying $\mathrm{Im}(p) < 0$. The real coefficients A, B, C, D, E are functions of velocity c and material constants, see Cerv & Plesek (2013).

Using Ferrari's method it is possible to prove that it is sufficient to solve the quartic equation (8) for $k = 1$ only. All the roots must then be scaled by the true value of the wavenumber of interest, k. A quartic equation has four roots. In this case, the equation coefficients are real, hence the complex roots always come in conjugate pairs. It can be seen that the fulfilment of the boundary conditions at infinity $x_2 \to +\infty$ can only be guaranteed by the roots with $\mathrm{Im}(p) < 0$. Let us consider that $p_2,\ p_4,\ p_2 \neq p_4$ are such roots of (8) taken for $k = 1$. It turns out, without going into the details, that in the interval of velocities, where $\mathrm{Im}(p_2)$ and $\mathrm{Im}(p_4)$ are negative, the general solution to the equations of motion takes the form

$$
\begin{aligned}
u_1(x_1, x_2, t) &= [U_{01}^{(1)} e^{-\mathrm{i}kp_2x_2} + U_{01}^{(2)} e^{-\mathrm{i}kp_4x_2}]\, e^{\mathrm{i}k(x_1 - ct)}\ , \\
u_2(x_1, x_2, t) &= [U_{02}^{(1)} e^{-\mathrm{i}kp_2x_2} + U_{02}^{(2)} e^{-\mathrm{i}kp_4x_2}]\, e^{\mathrm{i}k(x_1 - ct)}\ .
\end{aligned}
\tag{9}
$$

Now it is possible to express the stress components σ_{12} and σ_{22}. It holds that

$$
\begin{aligned}
\sigma_{22} &= C_{12}\varepsilon_{11} + C_{22}\varepsilon_{22} + C_{26}2\varepsilon_{12}\ , \\
\sigma_{12} &= C_{16}\varepsilon_{11} + C_{26}\varepsilon_{22} + C_{66}2\varepsilon_{12}\ .
\end{aligned}
\tag{10}
$$

The stress free boundary conditions at $x_2 = 0$, equation (6), yield another homogeneous system for displacement amplitudes $U_{01},\ U_{02}$ as

$$
\begin{aligned}
&[C_{12} + C_{22}p_2D1 - C_{26}(p_2 + D1)]U_{01} + [C_{12} + C_{22}p_4D2 - C_{26}(p_4 + D2)]U_{02} = 0\ , \\
&[C_{16} + C_{26}p_2D1 - C_{66}(p_2 + D1)]U_{01} + [C_{16} + C_{26}p_4D2 - C_{66}(p_4 + D2)]U_{02} = 0\ .
\end{aligned}
\tag{11}
$$

This system will have a nontrivial solution if its determinant vanishes. This leads to a secular equation. The implicit secular equation may be written symbolically as (details may be seen in Cerv & Plesek (2013))

$$
F(C_{ij}, \vartheta, \rho, c, p_j(C_{ij}, \vartheta, \rho, c)) = 0\ . \tag{12}
$$

4. Results

The determination of Rayleigh wave velocity by means of implicit secular equation (12) may be illustrated by the following example. Let us consider the thin composite SE84LV (Cerv et al., 2010). Let us also assume that the orientation of the principal material axes is given by $\vartheta = 45^{\circ}$.

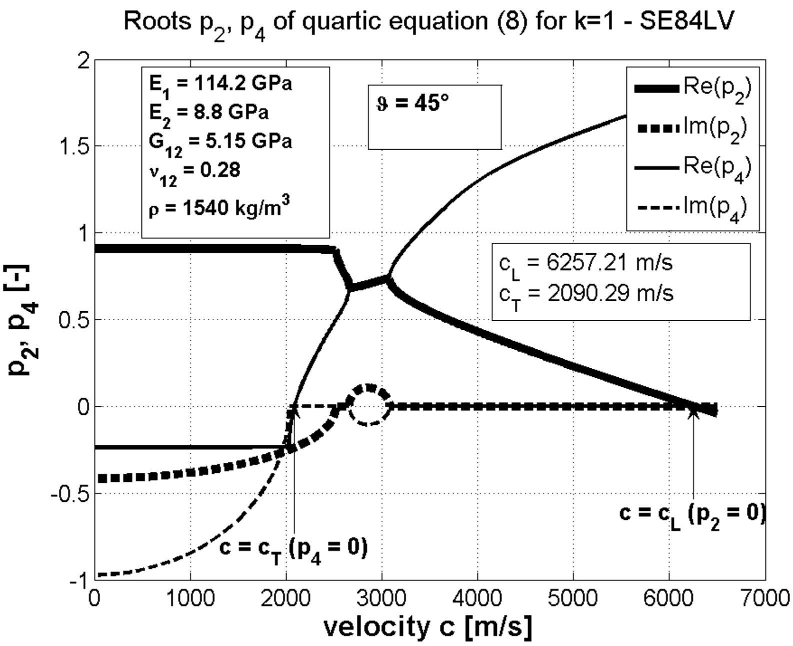

Fig. 2: Roots p_2, p_4 of eq. (8) for $k = 1$ versus c.

Before evaluating the left-hand side of the equation (12) as a function of velocity c one has to compute the four roots p_j of the quartic equation (8) taken for $k = 1$. It can be seen that the fulfilment of boundary conditions at infinity $x_2 \to +\infty$ is guaranteed only by the roots p_2, p_4 with negative imaginary parts, see Fig. 2. A graph of the function F is shown in Fig. 3. In an interval of speeds, where simultaneously $\mathrm{Im}(p_j) < 0$, the equation (12) has just one root $c_R = 1967.224$ m/s.

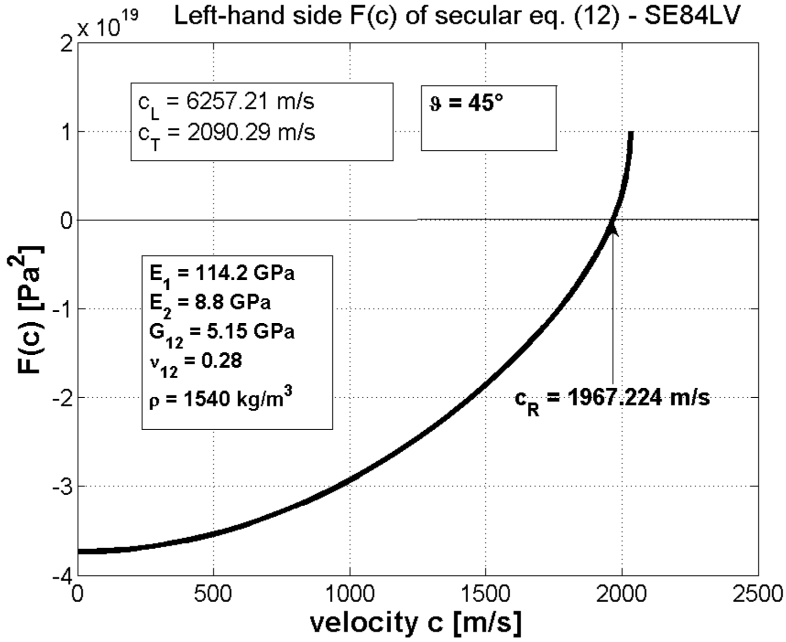

Fig. 3: Left-hand side of eq. (12) versus velocity c.

5. Conclusions

It has been confirmed, in accord with Ting's (2004), that the Rayleigh wave propagation exhibits no geometric dispersion. This means that the Rayleigh wave velocity is independent of frequency. In the case of orthotropic materials (thin composites) it has been found that Rayleigh wave velocity depends significantly, as with bulk waves, on the directions of the principal material axes. All numerical computations were performed in Matlab R2010b.

Acknowledgement

The work was supported by the projects GAP101/12/2315 (GA CR) and TH01010772 (TA CR) with institutional support RVO: 61388998.

References

Cerv, J. & Plesek, J. (2013) Implicit and explicit secular equations for Rayleigh waves in two-dimensional anisotropic media. Wave Motion, 50, pp. 1105-1117.

Cerv, J., Kroupa, T. & Trnka J. (2010) Influence of principal material directions of thin orthotropic structures on Rayleigh-edge wave velocity. Composite Structures, 92, pp. 568-577.

Ting T.C.T. (2004) Explicit secular equations for surface waves in an anisotropic elastic half-space from Rayleigh to today, in: R.W. Goldstein, G.A. Maugin (Eds.), Surface Waves in Anisotropic and Laminated Bodies and Defects Detection, Kluwer Academic Publishers, Dordrecht, pp. 95–116.

22nd International Conference
ENGINEERING MECHANICS 2016
Svratka, Czech Republic, 9 – 12 May 2016

DEVELOPMENT OF COMPUTATIONAL MODEL OF PISTON DYNAMICS BEHAVIOUR

J. Dlugoš*, P. Novotný, O. Maršálek***, P. Raffai****, J. Knotek*******

Abstract: *Sooner or later, the development process of each technical product, inevitably, reaches a phase when several other design proposals are being compared. But based on what is the best design chosen? Engineers all around the world have a challenging task to find the best compromise among numerous aspects—e.g. manufacturing, cost, functionality, reliability etc.—especially in contemporary phenomenon of endless minimization of all kinds of losses. To estimate the operational lifetime characteristics, i.e. wear, friction, noise and vibration and others, test benches are widely used. Most of the time, they offer accurate results, but the insight in to the physics is lost. On the other hand, simulation tools can clarify the details during the product's operational cycle but the disadvantage lays within the adequacy of the algorithms used. Therefore, computational models are often verified by the test results. Only then their full potential can be exploited, providing fast and reliable results with translucent insights into the true physics behind it. The following paper presents the development of one such computational model focused on the investigation of piston dynamics behavior.*

Keywords: Piston, Tribology, Mechanical loss, Multibody dynamics, Elastohydrodynamic lubrication

1. Introduction

The piston of internal-combustion engine (ICE) is primarily designed to transfer released fuel energy into the mechanical work as a rotational motion of the crankshaft. This way piston, together with piston rings, has an additional task to seal the combustion chamber (in order to prevent the exhaust gas leakage into the crankcase) and to dissipate the released heat energy into the liner. In addition, the piston crown shape is designed to enhance the air/fuel mixture creation.

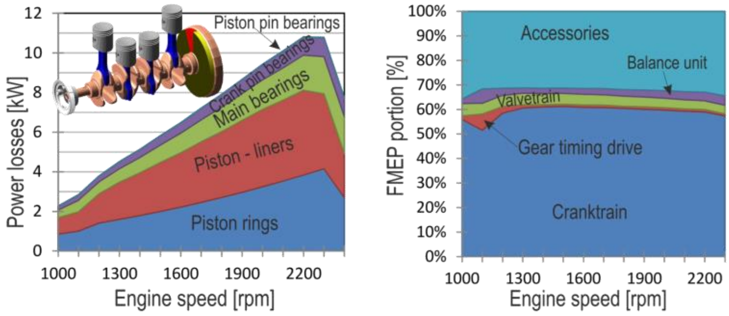

Fig. 1: Mechanical loss contribution in a 4.2L diesel engine (Novotný et al., 2010)

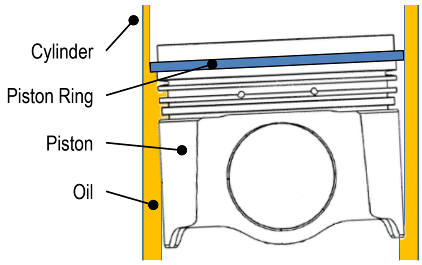

Fig. 2: Piston/Liner Interaction

* Ing. Jozef Dlugoš: Institute of Automotive Engineering, Brno University of Technology, Technická 2896/2; 616 69, Brno; CZ, dlugos@iae.fme.vutbr.cz

** doc. Pavel Novotný, PhD.: Institute of Automotive Engineering, Brno University of Technology, Technická 2896/2; 616 69, Brno; CZ, novotny.pa@fme.vutbr.cz

*** Ing. Ondřej Maršálek, PhD.: Institute of Automotive Engineering, Brno University of Technology, Technická 2896/2; 616 69, Brno; CZ, marsalek@fme.vutbr.cz

**** Ing. Peter Raffai: Institute of Automotive Engineering, Brno University of Technology, Technická 2896/2; 616 69, Brno; CZ, raffai@fme.vutbr.cz

***** Ing. Jiří Knotek: Institute of Automotive Engineering, Brno University of Technology, Technická 2896/2; 616 69, Brno; CZ, knotek@fme.vutbr.cz

The piston has to fulfill requirements such as structural strength, adaptability to operating conditions, low friction, low wear, seizure resistance and simultaneous running smoothness, low weight with sufficient shape stability, low oil consumption, and low pollutant emissions values (Mahle GmbH, 2012). The piston group is the main contributor to the overall ICE mechanical loss as depicted in Fig. 1.

2. Theoretical background

The piston has to withstand very high thermal and mechanical loads during its demanding utilization. It is guided by piston skirt/liner interaction via lubrication oil – journal bearing (Fig. 2).

2.1. Hydrodynamic and asperity contact model

Oil response is mathematically represented by the Reynolds equation (RE) in the following form:

$$\frac{\partial}{\partial x}\left(\frac{\rho h^3}{12\eta}\frac{\partial p_H}{\partial x}\right)+\frac{\partial}{\partial y}\left(\frac{\rho h^3}{12\eta}\frac{\partial p_H}{\partial y}\right)-\frac{\partial\left(u\rho h\right)}{\partial x}-\frac{\partial\left(\rho h\right)}{\partial t}=0 \qquad (1)$$

where x is direction of liner rotational axis, y is circumferential direction, h is oil film thickness, p_H is elastohydrodynamic (EHD) pressure, u is relative sliding velocity, η is oil dynamic viscosity and ρ is oil density. Oil film thickness consists of the following contributors:

$$h = h_{rigid} + h_{thermal}^{piston} + h_{elastic}^{piston} + h_{thermal}^{liner} + h_{elastic}^{liner} \qquad (2)$$

where h_{rigid} is the clearance between the piston (undeformed with specific ovality and contour shape) and the liner (deformed due to the assembling – head bolts, gasket, etc.), $h_{thermal}^{piston}$ and $h_{thermal}^{liner}$ are the thermal expansion of the piston and the liner, respectively; $h_{elastic}^{piston}$ and $h_{elastic}^{liner}$ are the elastic deformation of the piston and the liner, respectively.

The asperity contact pressure may be calculated by the Greenwood and Tripp (1970) as:

$$p_c = \frac{8\pi}{5}\left(\eta\beta\sigma\right)KF_{5/2}\left(\frac{h}{\sigma}\right) \qquad (3)$$

where p_c is the pressure caused by the contact of surface solids, β is the radius of curvature at asperity peak, σ is the standard deviation of the sum of the summit heights, and $F_{5/2}$ is the statistical function for Gaussian distribution of the summit heights.

Oil film thickness h is affecting the hydrodynamic and asperity contact pressure and vice versa (oil density and viscosity may be pressure dependent as well). Therefore, Gauss-Seidel solver enhanced by the Successive Over Relaxation (SOR) method with overrelaxation parameter is used.

2.2. Elastic deformation

To be able to calculate the overall oil film thickness h, elastic deformations have to be known. To do so, Multibody Dynamics (MBD) software, namely MSC Adams (Chapter 3.1.), can be augmented by the flexibility of simulated bodies. In this case, the elastic deformation is assessed as the combination of multiple mode shapes – modal superposition. It has to be kept in mind that this approach assumes only small linear deformations relative to a local reference. The number and type of chosen modal shapes determines the accuracy of calculated deformed shape. To be able to detect correct deformations, the Craig-Bampton method is applied (MSC Software, 2015).

2.3. Thermal load

To predict the piston behavior accurately, the temperature distribution has to be estimated since it affects not only mechanical properties but also thermally deformed shapes – $h_{thermal}^{piston}$ and $h_{thermal}^{liner}$ in eq. (2). For this purpose Computational Fluid Dynamics (CFD) simulation can be used. Unfortunately, this method is very sensible to the input variables which are not always known. Therefore, a much more industrially used approach is preferred for the piston temperature. It is the calibration of thermal Finite Element Analysis (FEA) to the measured peak temperatures at the piston's specific locations. This may be done by use of templugs inserted into the measurement locations of the piston. The temperature is estimated by the decrease in the templug hardness (Mahle GmbH, 2012). The liner does not perform large body motion as the piston does, therefore the temperature distribution may be measured by the thermocouples placed in the specific distances across its thickness.

3. Simulation strategy

Commercial MBD software (MSC Adams) is used for the solution of the piston/liner model. It solves the force balance and the equation of motion of the whole system with respect to the nonlinear system response, i.e. force/motion two-way dependence arisen from the RE eq. (1). The EHD pressure is calculated simultaneously in the user-written subroutine in Fortran programming language. The solver/subroutine exchange is clear from Fig. 3.

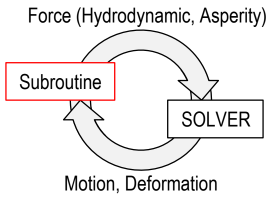

Fig. 3: MBD/subroutine exchange

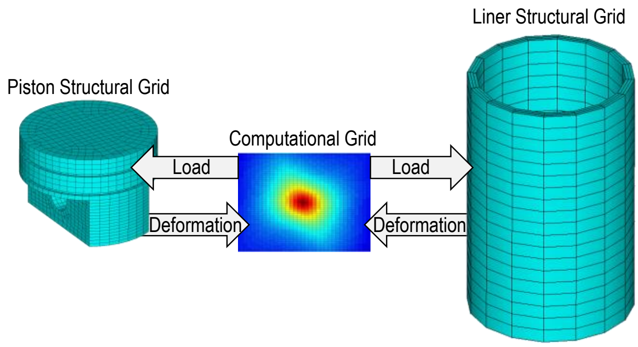

Fig. 4: Mapping process with different structural and computational grids

3.1. Mapping

For the HD and asperity contact solution (Chapter 2.1.) the computational grid is fixed to the piston. Since this grid simulates the piston/liner interaction, the calculated load distribution has to be mapped onto the liner surface. Furthermore, the liner deformation response has to mapped back onto the computational grid (Fig. 4). There are two kinds of mapping: the load and the deformation mapping, each having different requirements.

The load mapping has to preserve force and momentum static equilibrium between the *source* and the *target* – the *source* and the *target* load has to lead to the same body dynamic response. The *source* pressure distribution is transferred by the bilinear shape functions into the analytical form. Then it is analytically integrated per each of *target* cells – *target* force distribution. This approach satisfies the previously mentioned requirements.

For the purpose of good numerical stability, the deformation mapping has to lead to the smooth deformation shape. The 2D cubic Hermit spline is created from the *source* deformation and the *target* deformations are estimated as a functional values of this cubic spline.

Further investigations lead to the fact that computational grid has to be much finer than the structural one. Very fine structural grid is causing long computational times, because it is a major contributor of Degree of Freedom (DOF) in the simulation. In order to avoid that, different structural and computational grids are used on the piston – load and deformation mapping is required.

4. Example of results

The simulation of 4-stroke Spark Ignited (SI) single cylinder engine with bore of 86 mm and stroke of 86 mm is used. The nominal radial clearance is set to 50 μm, skirt profile and piston dimensions are taken from McNally (2000). Only piston-side EHD simulation is performed, with fully-flooded conditions, constant oil density and viscosity. Piston secondary motion is one of the most significant piston behaviors which is often experimentally measured. It affects engine optimization parameters like noise, friction loss, wear, etc.

Graph in Fig. 5 shows the piston secondary motion in a firing engine at 1000 rpm. The major portion of the side force is caused by the gas pressure acting on the piston crown. At the Top Dead Centre (TDC) the piston changes position from one side to the other very rapidly – piston slap. The biggest impact of the piston's elastic deformation is during the expansion stroke, where the higher loads are present. Overall piston motion history is smooth and damped – effect of the fully-flooded oil conditions.

Some authors introduce piston flexibility only as the stiffness matrix of the piston skirt nodes. However, looking at the piston deformation in Fig. 6, the piston pin bosses are deformed as well and significantly affect the piston skirt shape.

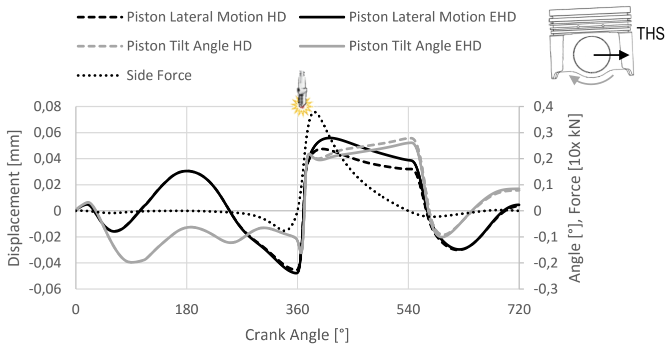

Fig. 5: Piston secondary motion by HD and EHD solution

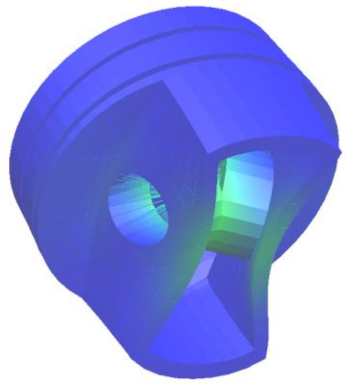

Fig. 6: Piston deformation due to the flexibility of pin bosses

5. Conclusion

The presented computational model is combining advantages of two approaches. Firstly, it uses commercial MBD software which is very stable and meant to simulate varied set of dynamic analyses. Secondly, developed computational model augments commercial MBD to be able to catch the most of the major physical processes acting on the piston during the operational cycle.

However, there are some difficulties. Current HD solver in user-written subroutine (SOR) does not seem to be the most efficient when finer computational grids are applied – multigrid might be needed. Too many time consuming mapping processes are calculated during each of the MBD solver iterations – optimization is inevitable.

The usage of the flexible liner incorporated into the cylinder block would allow to investigate the engine block noise and vibration caused by the piston motion – piston shape optimization in terms of NVH.

Acknowledgement

The research leading to these results has received funding from the Ministry of Education, Youth and Sports under the National Sustainability Programme I (Project LO1202).

References

Greenwood, J. A., & Tripp, J. H. (1970) The contact of two nominally flat rough surfaces. Proceedings of the Institution of Mechanical Engineers, pp. 625-633.

Mahle GmbH (2012) Pistons and engine testing: With 269 illustrations and 20 tables (1. ed.). Wiesbaden: Vieweg+Teubner.

McNally, C. P. (2000) Development of a Numerical Model of Piston Secondary Motion for Internal Combustion Engines (Master's Thesis). Massachusetts Institute of Technology.

MSC Software (2015) MSC. *ADAMS/Solver C++ Users Manual 2015r1.*

Novotný, P., Píštěk, V., & Svída, D. (2010) Solution of powertrain friction losses by virtual engine. Mecca: Journal of Middle European Construction and Design of Cars, pp. 12-61.

22nd International Conference
ENGINEERING MECHANICS 2016
Svratka, Czech Republic, 9 – 12 May 2016

MICROSTRUCTURE-INFORMED ENRICHMENT FUNCTIONS IN EXTENDED FINITE ELEMENT METHOD

M. Doškář[*], J. Novák[**], J. Zeman[***]

Abstract: *The present contribution reports on preliminary results of enhancing the approximation space of the Finite Element Method by means of pre-generated displacement fluctuation fields. The formulation builds on the Wang tile based compression of investigated microstructures and expands the application potential of the tiling compression into numerical methods. Enrichment functions are precomputed as responses of the compressed system to a set of load cases and synthesized analogously to the synthesis of the microstructure. The performance is illustrated with a two-dimensional linear diffusion problem.*

Keywords: Wang tiles, heterogeneous materials, fluctuation field synthesis, microstructure-informed enrichment functions, eXtended Finite Element Method.

1. Introduction

The issue of incorporating knowledge of a material microstructure into coarser scale analyses remains a vivid topic in Computational Mechanics. In the case of separation of scales, i.e., when the characteristic microstructural length is by orders of magnitude smaller than the size of a macro-scale task, the material can be treated as homogeneous from the macro-scale viewpoint. The microstructural characteristics are then propagated into upper scales by means of homogenization when either parameters of a given constitutive model are identified from numerical tests performed on a Representative Volume Element or the macroscopic constitutive model is obtained in an incremental form arising from the solution of a boundary value problem for each integration point of the macroscopic discretization, see (Geers et al., 2010) and reference therein.

In this work, we aim at tasks in which the separation of scales is not valid. In such a case, the standard Finite Element Method requires detailed resolution of the underlying microstructural geometry. As a result, the complexity of the macro-scale model significantly increases. The second disadvantage of such an approach stems from its dependence on a specific microstructure realization, which is stochastic in the majority of real-world materials. Therefore, Monte Carlo-like simulations are necessary to assess the model response under different realizations of the microstructure in an attempt to account for unfavorable compositions.

We have recently demonstrated, e.g., in (Novák et al., 2012; Doškář et al., 2014), that the representation based on Wang tiles is particularly appealing when multiple stochastic realizations of a microstructure should be efficiently generated, featuring spatial statistics similar to that of the reference sample. In the present contribution, we exploit the compressed form of a microstructure in the framework of eXtended Finite Element Method (XFEM), which allows to circumvent the requirement of the detailed resolution by enhancing the approximation space with specifically designed enrichment functions. In particular, we construct the enrichment functions as responses of the compressed system to prescribed loadings while preserving continuity of the functions across the corresponding edges of individual tiles. The global enrichment functions for a macro-scale analysis are then assembled in the same way the microstructure

[*] Ing. Martin Doškář: Department of Mechanics, Faculty of Civil Engineering, Czech Technical University in Prague; Thakurova 2077/7; 160 00, Praha; CZ, martin.doskar@fsv.cvut.cz

[**] Ing. Jan Novák, Ph.D.: Experimental Centre, Faculty of Civil Engineering, Czech Technical University in Prague; Thakurova 2077/7; 160 00, Praha; CZ, novakj@cml.fsv.cvut.cz

[***] doc. Ing. Jan Zeman, Ph.D.: Department of Mechanics, Faculty of Civil Engineering, Czech Technical University in Prague; Thakurova 2077/7; 160 00, Praha; CZ, zemanj@cml.fsv.cvut.cz

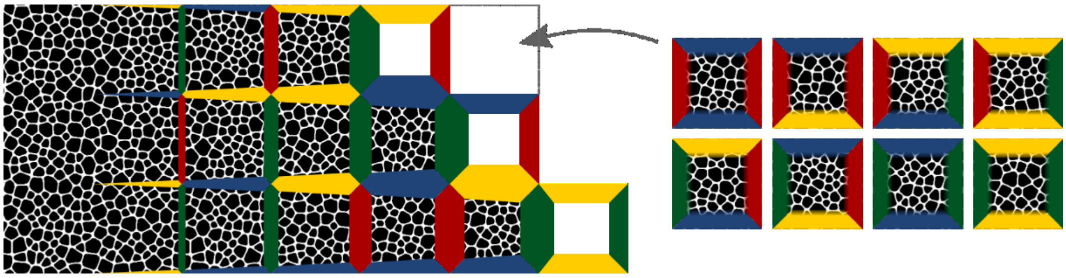

Fig. 1: Illustration of a reconstructed microstructure with the highlighted Wang tile codes defining the compatibility constraint during an assembly (left) and a set of Wang tiles (right).

realization is generated. We illustrate the proposed methodology with a preliminary results for the two-dimensional diffusion problem.

2. Wang tiles

Originally developed as a decidability procedure in Mathematical Logic (Wang, 1961), Wang tiles are currently a well-established tool for efficient synthesis of naturally looking textures in Computer Graphics (Cohen et al., 2003). The direct correspondence between goals of texture synthesis and representation of heterogeneous materials motivated our current effort and allowed us to introduce the concept of Wang tiles as a promising generalization of the Statistically Equivalent Periodic Unit Cell (SEPUC) approach to modelling of heterogeneous materials (Novák et al., 2012). We replace the single cell with a set of piecewise compatible domains—Wang Tiles—and employ the formalism of the original tiling concept in order to formulate the compatibility constraint during the assembly of tiles into a realization of the compressed microstructure, see Fig. 1. Microstructural information can be compressed into the tile set by making use of the methods developed for SEPUC generation, modified in order to account for the generalized periodic boundary conditions arising in the tiling concept (Novák et al., 2012). In order to alleviate computation cost of the optimization approach, we have proposed an alternative method, see (Doškář et al., 2014), that was inspired by the approach of Computer Graphics (Cohen et al., 2013), and employs a provided sample of the microstructure. The major merit of Wang tiles is their ability to reconstruct instantly stochastic realizations of arbitrary size with suppressed artificial periodicity inherent to PUC. Therefore, the concept is appealing for a wide range of tasks in which multiple statistically coherent realizations of the investigated microstructure are needed, for instance in numerical homogenization (Doškář & Novák, 2016). With the present contribution, we expand its application potential into enrichment based numerical methods.

3. Methodology

The standard formulation of Finite Element Method (FEM) builds on the weak form of the governing equations which in general reads as

$$Find\ u \in V: a(u,v) = b(v),\ \forall v \in V_0. \tag{1}$$

The quality of the solution directly follows from the finite-dimensional approximation space $V^h \subset V$, which in the case of FEM is constructed from element-wise polynomials. As mentioned above, this construction requires a mesh refinement in order to properly account for microstructural details. The eXtended Finite Element Method (XFEM), also called the Generalized Finite Element Method[1], supplements the approximation space with a priori knowledge of a (local) character of the solution. As a result, significantly smaller number of degrees of freedom (DOFs) is necessary.

In mechanics of solids and modelling of materials in particular, XFEM is usually used to capture crack propagation, shear bands, or complex microstructural geometries, see (Belytschko et al., 2009; Fries & Belytschko, 2010) for a comprehensive review. Usually, analytical enrichment functions derived for a single microstructural feature are used to enhance the approximation space, e.g., (Strouboulis et al., 2001). However, numerical "handbook" functions have been already introduced by Strouboulis et al. (2003) for the case of multiple closely packed inclusions. A similar approach has been recently proposed by Plews and Duarte (2014). The both approaches rely on computing Boundary Value Problems on subdomains of

[1] Description of etymology of the names can be found in (Belytschko et al., 2009).

the original task and extracting the dominant response of the microstructure. In this perspective, our approach can be understood as their off-line counterpart. The original idea of employing the Wang tiles for a synthesis of enrichment functions dates back to (Novák et al., 2013), where the constraint of stress compatibility among congruent tile edges was incorporated into the objective function of the optimization algorithm used to design tile morphology. However, this condition led to a nearly periodic arrangement of particles. In this work, we generate enrichment functions separately after a microstructure is compressed in the tile set. Each tile is discretized with an FE mesh that is compatible across the congruent edges. Inspired by the first-order numerical homogenization, we consider the decomposition of the displacement field into the fluctuation part and the part corresponding to a prescribed macroscopic gradient tensor. We assemble a stiffness matrix for each tile, condensate out inner fluctuation DOFs, and localize the remaining unknowns according to the edge codes into the stiffness matrix for the whole tile set. The resulting system is then solved for a prescribed unit macroscopic gradient and the edge fluctuation unknowns are obtained. The fluctuation fields inside each tile are then reconstructed from the edge DOFs. This treatment ensures continuity of the enrichment fields across the corresponding tile edges.

With the displacement fluctuation fields pre-computed for each tile, we can define n_j enrichment functions for every microstructure reconstructed with the Wang tile set as an assembly of the fluctuation fields derived from n_j loading cases. The approximate solution of Eq. (1) then takes the form

$$u^h(x) = \sum_{i=1}^{n_i} N_i(x)u_i + \sum_{i=1}^{n_i}\sum_{j=1}^{n_j} N_i(x)\left(\psi_j(x) - \psi_j(x_i)\right)u_i^j, \tag{2}$$

where $N_i(x)$ and u_i are the standard polynomial shape functions and DOFs while $\psi_j(x)$ denotes an enrichment function (in our case global) with the corresponding DOF u_i^j. The enrichment function is (i) shifted by $\psi_j(x_i)$ and (ii) multiplied by the shape functions $N_i(x)$ in order to (i) restore the Kronecker delta property $u^h(x_i) = u_i$ and (ii) preserve the banded structure of the resulting algebraic system.

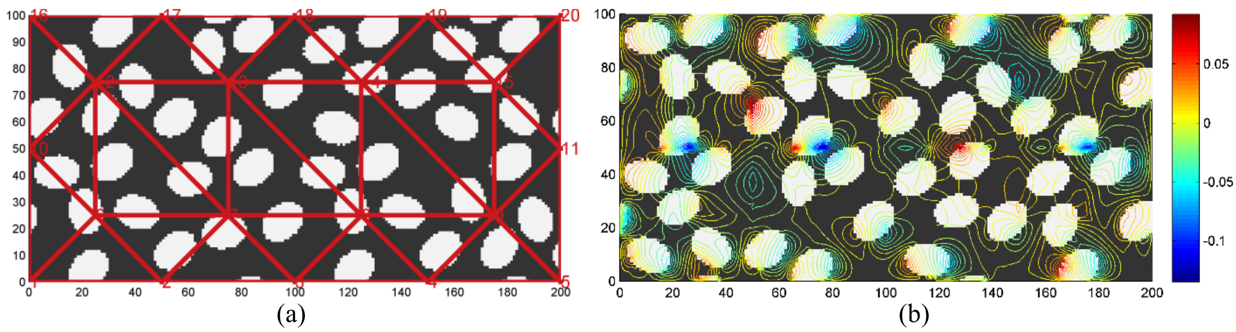

Fig. 2: The discretization and the microstructure of the considered task (a) and (b) contours of the discrepancy between the XFEM solution (24 DOFs) and the fully resolved FEM (nearly 20k DOFs).

4. Numerical example

As an illustrative example, we considered the Laplace equation for a simple rectangular domain with a microstructure generated from a tiling composed of 4×2 tiles. The loading of the domain was induced through Dirichlet boundary conditions prescribed with a macroscopic gradient in x direction (horizontal) of magnitude 0.02. At the tile level, the microstructure was discretized using a regular grid of quadrilateral linear elements corresponding to pixel representation of the tiles, the resolution of a tile was 50×50 px. Two global enrichment functions related to a unit gradient in each direction were provided to XFEM. At the macro-scale level, linear triangular elements were used. The discretization of the macro-scale task is depicted in red in Fig. 2a along with the considered microstructure, dimensions of the domain are given in px. The integration of the weak form (1) was performed employing the tile discretization and the 9 point Gauss quadrature rule. The obtained XFEM solution (24 DOFs) was compared to the reference solution of the fully resolved microstructure (nearly 20k DOFs). The absolute discrepancy between the two solutions is plotted in Fig. 2b. Note that the errors concentrate mainly along the tile edges and near the boundary of the domain which is due to the pre-computed nature of the enrichment functions. The boundary related errors can be compensated for by a finer discretization near the domain boundary whilst the discrepancies related to the tile edges would be reduced by taking more enrichment functions into account.

5. Conclusions

With a simple example, we have demonstrated that the proposed methodology can provide comparable results to the fully resolved FEM with a significantly smaller number of DOFs. The geometry of the macro-scale task is not restricted to rectangular shapes and can be arbitrary due to the multiplication of the enrichments functions by the standard shape functions in Eq. (2). On the other hand, our approach shares the main sore common to XFEM, namely the integration of the discretized weak form, which can in turn dissipate the computation savings arising from less DOFs. Moreover, the integration has to be carried out carefully in the regions where the macro-scale elements intersect the tile-level elements. Strouboulis et al. (2003) also showed that the XFEM solution is particularly sensitive to the accuracy of the provided enrichment, which is only approximate in our approach. Thus, our particular attention will be devoted to the question of an appropriate formulation of the enrichment functions and efficient integration. The method holds promise also for a non-linear regime. The assembled enrichment functions will address only the linear mode and will allow for identification of regions with onset of the non-linearity. Additional enrichment functions reflecting the non-linear mode will be supplemented on-the-fly only locally for the identified regions, similarly to the proposed strategy by Plews and Duarte (2014).

Acknowledgement

The authors gratefully acknowledge the financial support from the Grant Agency of the Czech Technical University in Prague, project No. SGS16/037/OHK1/1T/11 “Algorithms for numerical analysis and modeling comprising uncertainties and spatial nonuniformities”, and the Czech Science Foundation through projects No. 15-07299S and 16-11473Y.

References

Belytschko, T., Gracie, R. & Ventura, G. (2009) A review of the extended/generalized finite element methods for material modeling. Modelling and Simulation in Materials Science and Engineering, 17, 4, 043001.

Cohen, M.F., Shade, J., Hiller, S. & Deussen, O. (2003) Wang Tiles for image and texture generation. ACM Transactions on Graphics, 22, 3, pp. 287-294.

Doškář, M., Novák, J. & Zeman, J. (2014) Aperiodic compression and reconstruction of real-world material systems based on Wang tiles. Physical Review E, 90, 6, 062118.

Doškář, M. & Novák, J. (2016) A jigsaw puzzle framework for homogenization of high porosity foams. Computers & Structures, 166, pp. 33-41.

Fries, T-P. & Belytschko, T. (2010) The extended/generalized finite element method: An overview of the method and its applications. International Journal for Numerical Methods in Engineering, 84, 3, pp. 253-304.

Geers, M.G.D., Kouznetsova, V.G. & Brekelmans. W.A.M. (2010) Multi-scale computational homogenization: Trends and challenges. Journal of Computational and Applied Mathematics, 234, 7, pp. 2175-2182.

Novák, J., Kučerová, A. & Zeman, J. (2012) Compressing random microstructures via stochastic Wang tilings. Physical Review E, 86, 4, 040104.

Novák, J., Kučerová, A. & Zeman, J. (2013) Microstructural enrichment functions based on stochastic Wang tilings. Modelling and Simulation in Materials Science and Engineering, 21, 2, 025014.

Plews, J.A. & Duarte, C.A. (2014) Bridging multiple structural scales with a generalized finite element method. International Journal for Numerical Methods in Engineering, 102, 3-4, pp. 180-201.

Strouboulis, T., Copps, L. & Babuška, I. (2001) The generalized finite element method. Computer methods in applied mechanics and engineering, 190, 32-33, pp. 4081-4193.

Strouboulis, T., Zhang, L. & Babuška, I. (2003) Generalized finite element method using mesh-based handbooks: application to problems in domains with many voids, 192, 28-30, pp. 3109-3161.

Wang, H. (1961) Proving Theorems by Pattern Recognition – II. Bell System Technical Journal, 40, 1, pp. 1-41.

22nd International Conference
ENGINEERING MECHANICS 2016
Svratka, Czech Republic, 9 – 12 May 2016

DESIGN AND PRODUCTION OF THE MOTION THREADED MECHANISM

L. Drahorádová [*], V. Andrlík [**]

Abstract: *This short article includes introduction to different designs of screws for linear motion, their advantages, disadvantages and problems. Ball screws and cheaper lead screws are the most common in the industry. An innovative screw mechanism is described in the next part of the article – motion threaded mechanism which solves problems with balls inside the nut of a ball screw, for example circulation of balls (it is complicated for the nut with a multiple thread) and greater threaded pitch. The next two parts feature the production of a motion threaded mechanism and future measuring of qualities and then a comparison between a motion threaded mechanism and a ball screw.*

Keywords: motion threaded mechanism, ball screw, nut.

1. Introduction

The basic function of lead screws and ball screws is the transformation of rotating motion to linear motion. Their basic parameters are stroke, speed, acceleration, indispensable force, accuracy of positioning and efficiency. The shaft of the lead screw is in direct touch with the nut. Thanks to this friction, lead screws have a lesser efficiency. The friction also produces heat energy and causes thermal expansion of material. It is the reason why friction has to be decreased, for example by application of new materials or higher accuracy of production.

The solution of the friction is to use a lead screw with roller elements – usually ball screws. Balls are inside the nut and transmit the load by rolling. Passive resistance is reduced to rolling resistance only. The advantages of ball screws are high efficiency, long lifetime, possibility of creating preload (for higher stiffness and accuracy), prevention of jerky movements and possibility of transformation of linear motion to rotating motion. On the other hand, the nut of a ball screw is more complicated and expensive because it is necessary to ensure a circulation of balls. The transmission of balls inside the nut can be a reason for formation of vibrations and noise. Important parameters for ball screws are the following: nominal diameter, screw pitch, speed, load capacity, static and dynamic stiffness, efficiency, lifetime, passive resistance, thread profile groove, ball diameter, load force and preload.

For lower friction, there are special types of screws such as a planetary roller screw which uses threaded rollers instead of balls. Qualities are better than those of a ball screw but the price is higher. Another variant is a lead screw with a hydrostatic nut. A liquid is pressed between threaded shaft and nut by hydraulic pump.

A motion threaded mechanism is one of the unconventional designs of the screw for linear motion. Its design and production are described in the following chapters. The screw was invented by doc. Ing. Vladimír Andrlík, CSc. and won a competition Best Cooperation of the Year 2014 and a competition Innovative Idea in the year 2014.

[*] Ing. Lucie Drahorádová: Faculty of Mechanical Engineering, Czech Technical University in Prague, Horská 3; 128 00, Prague; CZ, Lucie.Drahoradova@fs.cvut.cz

[**] Doc. Ing. Vladimír Andrlík, CSc.: Faculty of Mechanical Engineering, Czech Technical University in Prague, Horská 3; 128 00, Prague; CZ, Vladimir.Andrlik@fs.cvut.cz

2. Design of the Motion Threaded Mechanism

The shaft of the motion threaded mechanism has the same circular thread profile groove as a ball screw shaft. The nut consists of four rings with sheaves and two end flanges (Fig. 1). Constituent rings and end flanges are fitted with seals and all parts are clipped by bolted rods. Modular conformation of the nut has advantage in universal production for different loads.

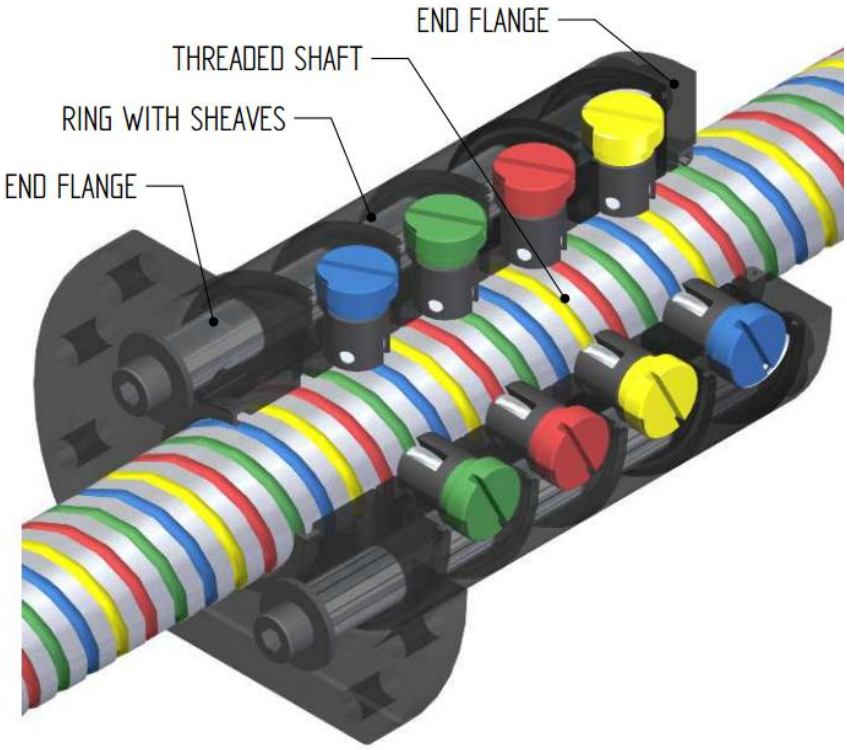

Fig. 1: Section of the motion threaded mechanism.

Radially supported sheaves replace balls which circulate inside the nut. It is a completely new solution of the disposition. A sheave assembly contains four parts, sheave with the pintle is put inside the cylindrical bushing (Fig. 2). The bushing is pressed on the shaft of the screw by the threaded bushing. Sheave assemblies are four in one ring and each of them copies one groove of the four-threaded screw. The nut is also equipped with lubricator and seals. The advantage of this solution is silence and smoothness during the motion.

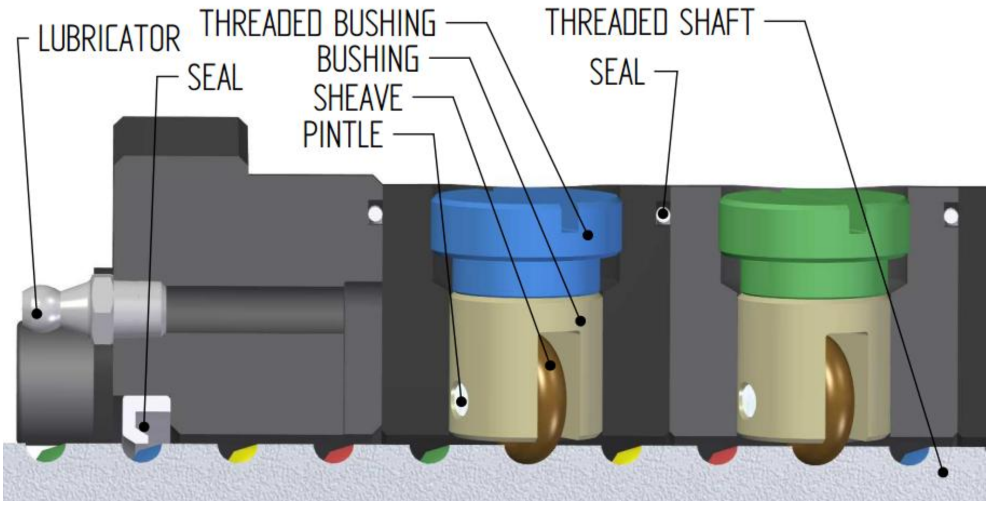

Fig. 2: Detail of shaves inside rings.

3. Production of Motion Threaded Mechanism and Nut

The nut of motion threaded mechanism (Fig. 3) and the threaded shaft were made according to technical drawings. The production was simple in comparison with ball nut and usual production technologies are sufficient.

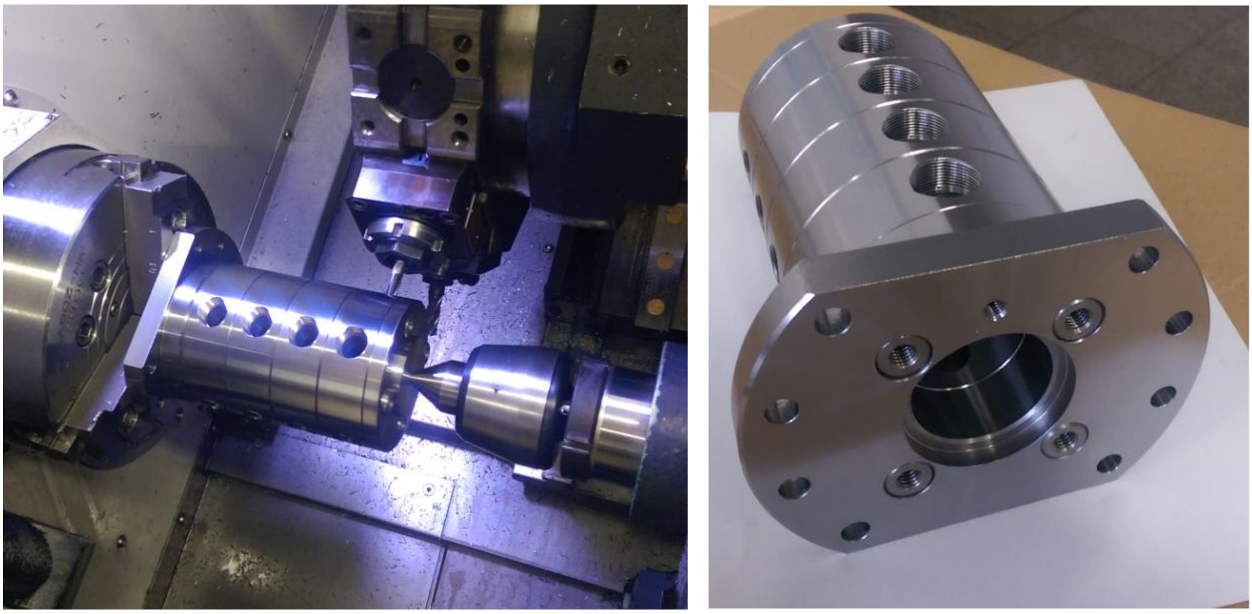

Fig. 3: On the left: the nut cutting by a CNC machining centre, on the right: finished nut without standardized part.

4. Future Experimental Research of Difference between Motion Threaded Mechanism and Ball Screw

Because the motion threaded mechanism is a completely unique mechanism for transforming rotary movement to linear movement, it is necessary to perform experimental research to identify the behaviour during the process, such as a vibration, noise, smoothness during running, stiffness etc. At present a real test bed is being prepared (Fig. 4), together with a threaded shaft, a sheave nut with three rings (Fig. 4) and a ball nut. The results of the nut of the motion threaded mechanism and the ball nut will be evaluated and compared with each other.

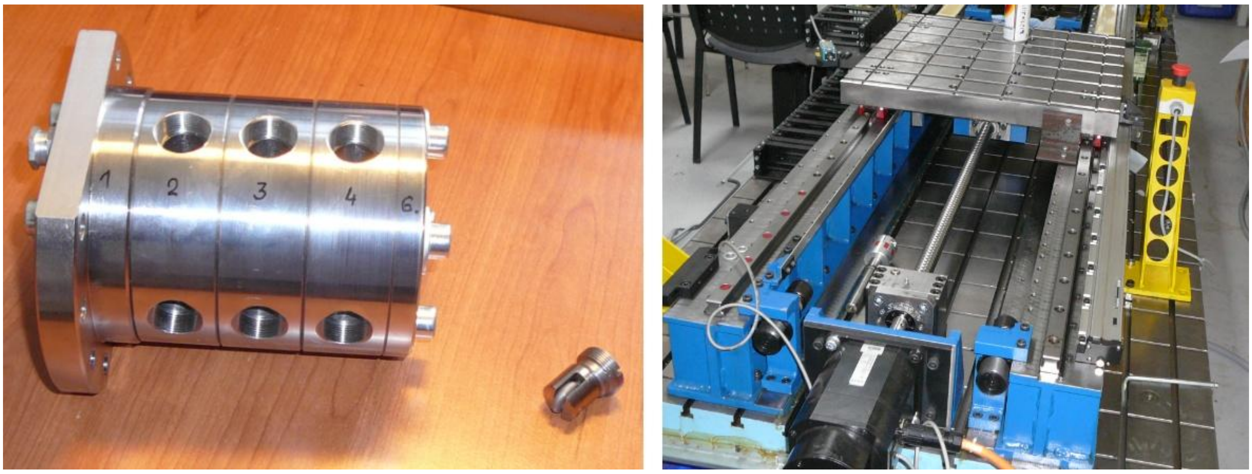

Fig. 4: On the left: the nut with three rings and sheave assembly, on the right: the test bed for measuring of qualities.

5. Preparation for the Measurement of the Stiffness

As the first measurement, the stiffness of the all mechanism will be tested on the test bed. The table of this test bed is stopped against the fixed body and the motor is operating (the table is creating pressure on the fixed body). Sensors are used for sensing of the angle and path difference in three positions (Fig. 1). Sensor number 1 is hidden inside the motor and measures running speed (spin). Sensor 2 is located on the nut, coaxially to the threaded shaft and checks the angle difference. The last sensor number 3 controls linear position of the body deformation. The measurement should be supported by the calculation.

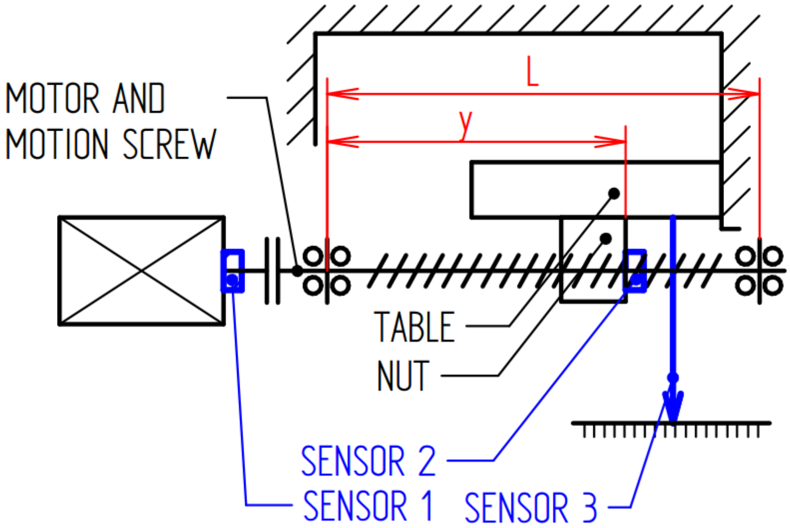

Fig. 5: Schematic picture of the test bed and measurement of the stiffness.

6. Conclusions

For the linear motion, an innovative motion threaded mechanism was designed which uses tightly supported sheaves in the threaded groove instead of balls. This solved problems with balls inside the nut of a ball screw, for example circulation and greater threaded pitch. Because of the completely unique mechanism, it is necessary to perform experimental research on qualities of this motion threaded mechanism such as vibration, noise, smoothness during running, stiffness etc. Now, measuring of these parameters is being prepared and then the motion threaded mechanism will be compared with a usual ball screw.

Acknowledgement

The research is supported by the grant SGS13/189/OHK2/3T/12.

The nut was made by Ing. Petr Konečný, PhD, Final Hlinsko, s.r.o. and ZPS Modřany, a.s.

The threaded shaft was made by the company Kuličkové šrouby Kuřim, a.s.

References

Souček, P. (2004) Servomechanisms in Production Machines of the Monograph. Czech Technical University in Prague, ISBN 80-01-02902-6 (in Czech)

Souček, P. (2015) Didactic text: Submitted Transfers in Drive of NC Machines. Department of Production Machines and Equipment, Faculty of Mechanical Engineering, Czech Technical University in Prague, pp. 1-70 (in Czech)

Czech Technical University in Prague, Faculty of Mechanical Engineering, Department of Production Machines and Equipment. Motion Threaded Mechanism. Inventor: Andrlík, V. National utility model application. CZ, registration number: 24842, 21.1.2013

Czech Technical University in Prague, Faculty of Mechanical Engineering, Department of Production Machines and Equipment. Multiple Motion Threaded Mechanism. Inventors: Andrlík, V., Kolář, M. National utility model application. CZ, application number: 2014-30202, 3.11.2014

22nd International Conference
ENGINEERING MECHANICS 2016
Svratka, Czech Republic, 9 – 12 May 2016

ON THE ISOGEOMETRIC FORMULATION OF PLANAR CURVED BEAMS

E. Dvořáková*, B. Patzák**

Abstract: *An isogeometric formulation of planar Timoshenko beams with variable curvature is presented. The Non-Uniform Rational B-Splines (NURBS) are used for both the geometry and unknown approximations. The NURBS capability of exact geometry representation, which is independent of a mesh density, is very advantageous in the analysis of curved beams as there is no loss of accuracy caused by the geometry approximation. The high accuracy results can be obtained while keeping the computational cost low. A beam element for arbitrarily curved planar beams is implemented and its performance is verified by means of few simple tests. The problem of shear locking is observed and is overcome by using reduced integration.*

Keywords: Curved Beams, Finite element analysis, Isogeometric analysis, NURBS, Shear locking.

1. Introduction

The finite element method is undoubtedly the most powerful tool in nowadays structural analysis. Its popularity has grown over past few decades and at the moment we can hardly imagine another approach which would substitute the need of finite element analysis completely. A large effort has been made to improve convergence and accuracy of the results, however most of the researchers concentrate only on the analysis itself. If we want to make the design and the analysis really efficient it is necessary to look at the design from the very beginning.

The geometry used for the analysis is usually represented by CAD files. The biggest drawback of such a representation is the need for its discretization prior the analysis. In this phase the geometry approximation and meshing take a turn. This process usually cannot be made fully automatic and it requires about 80% of overall analysis time. Moreover, the loss of the exact geometry can rapidly reduce the accuracy. The gap between CAD model and the finite element analysis can be eliminated by the concept proposed by Hughes et al. (2005) which is referred to as isogeometric analysis.

In isogeometric analysis the same representation of geometry is shared between CAD and FEM models. The exact geometry representation appears to be a big advantage especially for curved geometries such as curved beams and shells. The main emphasis of this paper is on two-dimensional curved beams. In general, curved beams can be modeled using sufficient number of straight beam elements but this approach can lead to the smaller accuracy and the higher computational cost. Among curved beam elements most of the literature is dedicated to the shapes with constant curvature. In this paper the isogeometric formulation of the planar beam element applicable to beams with variable curvature based on work of Bouclier et al. (2012) is presented.

2. NURBS-based curved beam element

The NURBS are generated using B-splines which can be defined recursively using the Cox-de Boor formulas (Cox, 1971, de Boor, 1972). The starting point are the piecewise constant functions

$$N_{i,0}(\xi) = \begin{cases} 1 & \text{if } \xi_i \leq \xi < \xi_{i+1} \\ 0 & \text{otherwise} \end{cases}, \tag{1}$$

* Ing. Edita Dvořáková: Department of Mechanics, Faculty of Civil Engineering, CTU in Prague; Thákurova 7, 166 27, Prague; CZ, edita.dvorakova@fsv.cvut.cz

** Prof. Dr. Ing. Bořek Patzák: Department of Mechanics, Faculty of Civil Engineering, CTU in Prague; Thákurova 7, 166 27, Prague; CZ, borek.patzak@fsv.cvut.cz

where ξ_i is the coordinate of the i^{th}-knot and parameter $\xi \in (0,1)$ runs through the entire patch (subdomain of knot spans which are seen as "elements" in isogeometric analysis). See Fig. 1 or Piegl and Tiller (1997) for better understanding of NURBS geometry. A pth-degree B-spline function is defined recursively

$$N_{i,p}(\xi) = \frac{\xi - \xi_i}{\xi_{i+p} - \xi_i} N_{i,p-1}(\xi) + \frac{\xi_{i+p+1} - \xi}{\xi_{i+p+1} - \xi_{i+1}} N_{i+1,p-1}(\xi) . \tag{2}$$

Finally, to generate the NURBS from its non-rational counterparts we use

$$R_i^p(\xi) = \frac{N_{i,p}(\xi) w_i}{\sum_{\hat{i}=1}^{n} N_{\hat{i},p}(\xi) w_{\hat{i}}} , \tag{3}$$

where w_i are the weights associated with the corresponding basis function. The NURBS curve is given by

$$\boldsymbol{C}(\xi) = \sum_{i=1}^{n} R_i^p(\xi) \boldsymbol{P}_i, \tag{4}$$

where $\boldsymbol{P}_i$ are the Cartesian coordinates of the i^{th}-control point, all control points define a control net of the NURBS curve. The advantage of NURBS over classical polynomial function is the inter-element continuity. While traditional polynomial shape functions provide C^0-continutity between the elements, the NURBS provide up to C^{p-1}-continuity. The lower continuity can be achieved by increasing a knot multiplicity. For the purposes of this paper we restrict ourselves to 2nd order NURBS.

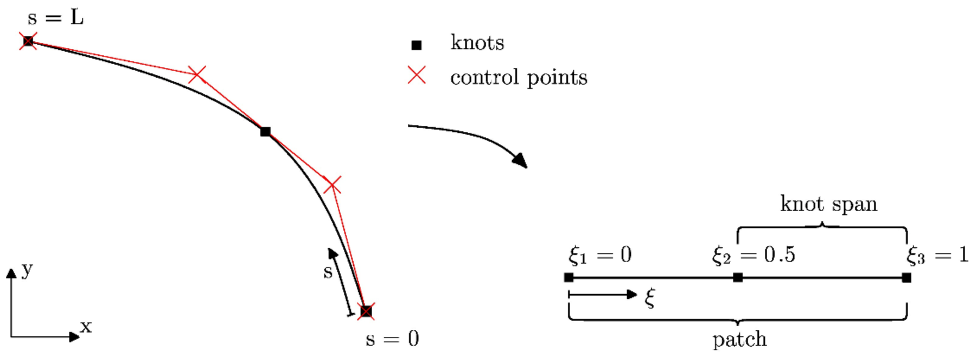

Fig. 1: Description of NURBS finite element geometry.

A curved Timoshenko beam placed in x-y plane is considered. The degrees of freedom are tangential displacement $u_t(s)$, normal displacement $u_n(s)$ and rotation $\theta(s)$. Curvilinear coordinate s runs along the midline of the beam. Membrane, transverse shear and bending strains are given by

$$\varepsilon_m = u_t' - \frac{u_n}{R}, \qquad \gamma_s = \frac{u_t}{R} + u_n' - \theta, \qquad \chi_b = \theta', \tag{5}$$

where the prime indicates a derivation with respect to the curvilinear coordinate s. Formulas for strain components (5) are used to derive strain-displacement matrix $\boldsymbol{B}$, which is defined as

$$\boldsymbol{\varepsilon} = \boldsymbol{Br}, \tag{6}$$

where $\boldsymbol{\varepsilon} = \{\varepsilon_m, \gamma_s, \chi_b\}^T$ and $\boldsymbol{r} = \{u_t, u_n, \theta\}^T$. Stiffness matrix is evaluated using

$$\boldsymbol{K} = \int_0^L \boldsymbol{B}^T \boldsymbol{DB} \, ds, \tag{7}$$

where **D** is a material matrix resulting from

$$N = EA\varepsilon_m, \qquad Q = GA\gamma_s, \qquad M = EI\chi_b, \tag{8}$$

where N, Q and M are axial force, transverse shear force and bending moment, respectively. Young's modulus E, shear modulus G, area A and moment of inertia I are the material and cross-section characteristics. To evaluate the stiffness matrix $\boldsymbol{K}$ the Gauss quadrature is used, three point rule is sufficient for the integration.

3. Numerical results

A NURBS beam element has been implemented and its performance has been verified by means of three simple tests (see Fig. 2). Firstly, the analysis of a cantilever beam has been performed and results have been compared with the exact solution. In case of moment loading, the linear distribution of rotation is expected. It has been proven (see Fig. 3) that the right results can be obtained only in case of parametrization which leads to constant Jacobian. For constant Jacobian the non-uniformly distributed control points are needed. When the control points are distributed uniformly, the Jacobian is not constant and the patch test is not satisfied.

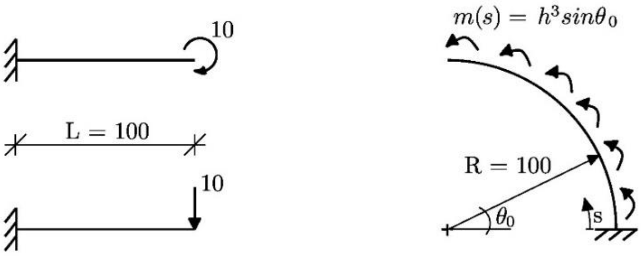

Fig. 2: Cantilever beam subjected to force load and moment load and curved beam with sinusoidal moment loading. ($E = 10^5, I = 0.0833, h = 1.0, b = 1.0, \nu = 0.0$)

In case of a cantilever beam subjected to force load the shear locking phenomena is observed and the expected linear curvature is not obtained (Fig. 4). Selective reduced integration has been used to remove shear locking and thus only two Gauss points have been used for integration of shear components, instead of three Gauss points used for membrane and bending components. This treatment is sufficient to overcome shear locking. Note that Bouclier et al. (2012) have proposed even more efficient quadrature schemes, which use the fact that due to the higher inter-element continuity (in comparison with classical polynomial functions) less Gauss points can be used over entire patch.

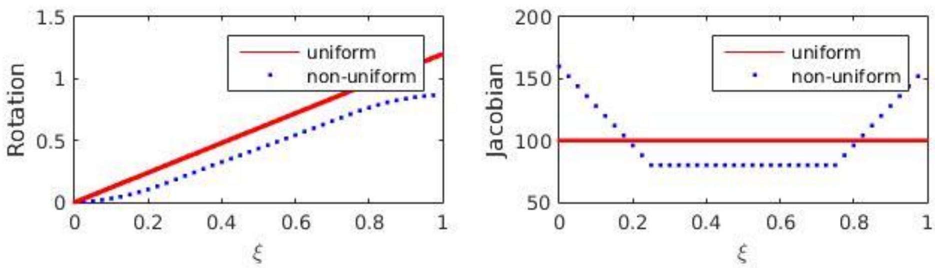

Fig. 3: Cantilever beam (moment load): Rotation and Jacobian corresponding to the linear parametrization (non-uniformly distributed control points) and the non-linear parametrization (uniformly distributed control points).

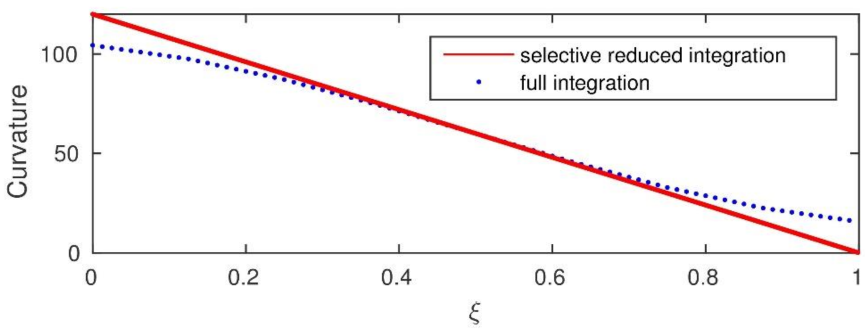

Fig. 4: Cantilever beam (force load): Selective reduced integration involving two Gauss points sufficiently removes shear locking and linear curvature is obtained.

Finally, a curved beam subjected to the sinusoidal loading has been analyzed. In Fig. 5a) the convergence of NURBS elements is compared to the classical polynomial straight beam elements implemented in the OOFEM finite element code (Patzák, 2014). With the NURBS element we can obtain almost the exact solution for small number of nodes while the high number of elements would be needed when traditional straight elements are used. In Fig. 5b) the relative error of NURBS elements is shown.

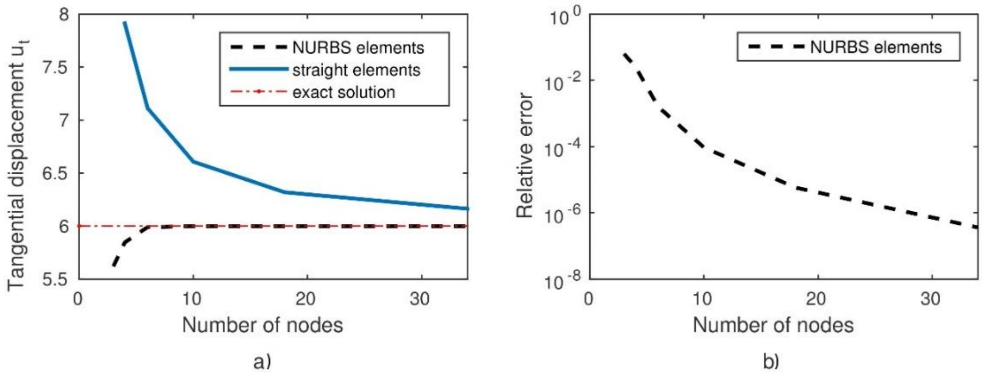

Fig. 5: Curved cantilever beam (sinusoidal moment loading): a) Comparison of tangential displacement of the tip obtained using traditional straight beam elements and NURBS elements. b) Dependence of the relative error of the NURBS elements solution on the number of nodes.

4. Conclusions

The formulation of NURBS beams has been presented. The element is formulated using NURBS approximation and therefore the exact geometry description is used for the analysis. The implementation enabled us to test the element and to compare its performance with traditional straight beam elements which use polynomial shape functions.

The necessity of linear parametrization to satisfy case of constant curvature is observed. Furthermore, while running the numerical tests, it has been proven that the element suffers from shear locking. The problem is solved by selective reduced integration. This treatment sufficiently removes shear locking and obtained results matches the expected ones.

Finally the curved structure has been analyzed. Superior convergence properties over the use of straight beam element is shown. Only small number of nodes is necessary to express exact solution and thus the computational cost is kept low.

Acknowledgement

The financial support of this research by the Grant Agency of the Czech Technical University in Prague (SGS project No. SGS16/038/OHK1/1T/11) and by the Technology Agency of the Czech Republic (TAČR project No. TA02011196) is gratefully acknowledged.

References

Adam, C., Bouabdallah, S., Zarroug, M., Maitournam, H. (2014) Improved numerical integration for locking treatment in isogeometric structural elements, Part I: Beams. Comput. Methods Appl. Mech. Engrg., 279, pp. 1-28.

Bouclier R. & Elguedj, T. (2012) Locking free isogeometric formulations of curved thick beams. Comput. Methods Appl. Mech. Engrg., 245-246, pp. 144-162.

Cottrell, J.A, Reali, A., Bazilevs, Y., Hughes, T.J.R. (2006) Isogeometric analysis of structural vibrations. Comput. Methods Appl. Mech. Engrg. 195, pp. 5257-5296.

Cottrell, J.A, Hughes, T.J.R., Bazilevs, Y. (2009) Isogeometric analysis: Toward integration of CAD and FEA, Wiley.

Cox, M.G. (1971) The numerical evaluation of B-splines. Technical report, National Physics Laboratory DNAC 4.

De Boor, C. (1972) On calculation with B-splines. Journal of Approximation Theory, 6, pp. 50-62.

Echter, R. & Bischoff, M. (2010) Numerical efficiency, locking and unlocking of NURBS finite elements. Comput. Methods Appl. Mech. Engrg. 199, pp. 374-382.

Hughes, T.J.R., Cottrell, J.A., Bazilevs, Y. (2005) Isogeometric analysis: CAD, finite elements, NURBS, exact geometry and mesh refinement. Comput. Methods Appl. Mech. Engrg. 194, pp. 4135-4195.

Hughes, T.J.R., Reali, A., Sangalli, G. (2010) Efficient quadrature for NURBS-based isogeometric analysis. Comput. Methods Appl. Mech. Engrg. 199, pp. 301-313.

Patzák, B. (2014) OOFEM project home page, http://www.oofem.org, 2014.

Piegl, L., Tiller, W. (1997) The NURBS Book. Springer-Verlag Berlin Heidelberg, New York.

22nd International Conference
ENGINEERING MECHANICS 2016
Svratka, Czech Republic, 9 – 12 May 2016

INFLUENCE OF POLYMERIC INTERLAYERS ON THE STRESS DISTRIBUTION IN LAMINATED GLASS PANES

M. Eliášová[*], M. Vokáč[**], K. Machalická[***]

Abstract: *Glass is nowadays one of the most progressive materials in civil engineering. It is used not only as a filling material but also as a material for load-bearing structures. Unlike widely-used materials (steel, aluminium, etc.), glass behaves elastically until it breaks by a brittle fracture without any warning. The insufficient tensile strength of float glass is solved by using a tempering process that enables the production of heat-strengthened or heat-toughened glass. However, increased tensile strength is not the only requirement for safe design. Laminated glass panels should be used in the reliable and effective design of glass elements as parts of a load-bearing system. The composite action of laminated glass under loading is influenced mainly by the shear modulus of the interlayers, which is dependent on time and on temperature. This paper presents experimental research performed at the Klokner Institute of CTU in Prague on the material properties of visco-elastic interlayers under various temperatures and under various load rates.*

Keywords: Glass, Interlayers, Shear modulus, Lamination, Visco-elastic material, Polymer.

1. Introduction

Modern trends in materials and in production technologies have been emerging in civil engineering. Glass is a material that has been used for a long time in windows as a filling material. It has much to offer for this purpose, due to its very high compressive strength and its transparency. There is now a growing trend to extend the use of glass sheets to load-carrying elements. These sheets are used for floors, staircases, beams, columns and shear panels that are not loaded only by self-weight but that are also able to transfer wind or snow loads and service loads. Laminated glass needs to be used, in order to achieve sufficient ultimate resistance of structural glass elements and also residual resistance.

At the present time, there is a lack of information, design rules and procedures for considering the potential mechanical participation of various interlayers for glass elements under loading. The safety considerations and the really conservative approaches that are widely adopted in practical applications are based on the assumption that the laminated glass is considered without any composite action. This leads to conservative tensile stress values, and therefore to the use of expensive, thick glass panes. To improve the design process, it is necessary to determine the real shear modulus of the interlayers that are used, because the material properties are generally unknown. The main issue in the experimental research presented in this paper has been to define the influence of temperature and load duration on the shear modulus of the transparent interlayers that are widely used for laminated glass panes.

2. Laminated glass

Laminated glass consists of at least two glass panes, which are connected by transparent interlayers. Various kinds of polymers and other plastics are used as materials for the interlayers. Widely-used interlayers are poly-vinyl-butyral (PVB), ionoplast (SentryGlass), ethylene vinyl-acetate (EVA), polyethylene (PE) and thermoplastic polyurethane (TPU). Full surface connection offers many ways to

[*] Assoc. Prof. Martina Eliášová, CSc.: Faculty of Civil Engineering, Czech Technical University in Prague; Thákurova 7/2077; 166 29, Prague; CZ, eliasova@fsv.cvut.cz

[**] Ing. Miroslav Vokáč, PhD.: Klokner Institute, Czech Technical University in Prague; Šolínova 7; 166 08, Prague; CZ, miroslav.vokac@cvut.cz

[***] Ing. Klára Machalická, PhD.: Klokner Institute, Czech Technical University in Prague; Šolínova 7; 166 08, Prague; CZ, klara.machalicka@cvut.cz

modify the mechanical properties of laminated glass, depending on the component layers that are selected, their thickness and the sequence of the layers. The main consideration for load-bearing glass elements is their post-breakage behaviour. After failure of one or all of the glass layers, the pieces of glass remain on the interlayer. Following significant improvements in load-bearing behaviour, post fracture integrity and robustness, laminated glass also acts under loading as a composite element. The full load-bearing capacity and the residual load-bearing capacity of laminated glass are influenced by the strength of the individual layers, and above all by the composite action effect of the interlayers. The behaviour of the interlayer is strongly influenced by temperature and by load duration, Fig. 1. This means that under high temperatures laminated glass has no composite action, because the polymer materials are not able to transfer the shear forces, and the shear modulus will be close to zero. However, temperatures below 20°C lead to hardening of the material and to higher shear modulus values. The second crucial factor influencing the shear modulus is load duration. Typically, there is creeping of the polymer interlayers under long-term loading, and the shear modulus value decreases (Wurm 2007).

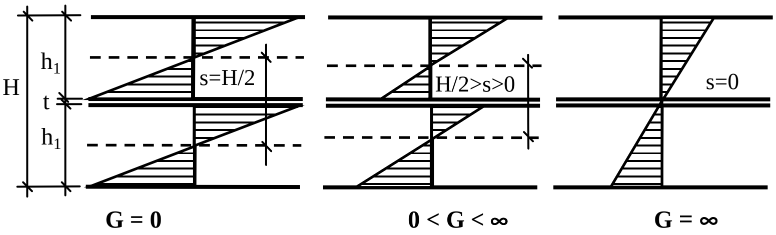

Fig. 1: Normal stress distribution of laminated glass, depending on the shear modulus G of the interlayer.

This kind of behavior influences the stress distribution in real structures, e.g. glass floors or roofs which are exposed to temperatures between 0° and 80°C. According to the temperature and the load duration, the connection between the glass panes is semi-rigid. The relation between the maximal normal stress σ and the shear modulus G of the interlayer is shown in Fig. 2. The study was performed for a squared pane simply supported along four sides made from double-layered laminated glass. Curve σ_h shows the normal stress on the tensile side of the upper pane, while curve σ_d demonstrates the normal stress on the tensile side of the bottom pane. It is obvious that full composite action between glass panes occurs if the shear modulus G is close to 10 MPa. In this case, the normal stress σ_h on the tensile side of the upper pane is equal to zero, see the picture on the right in Fig. 1.

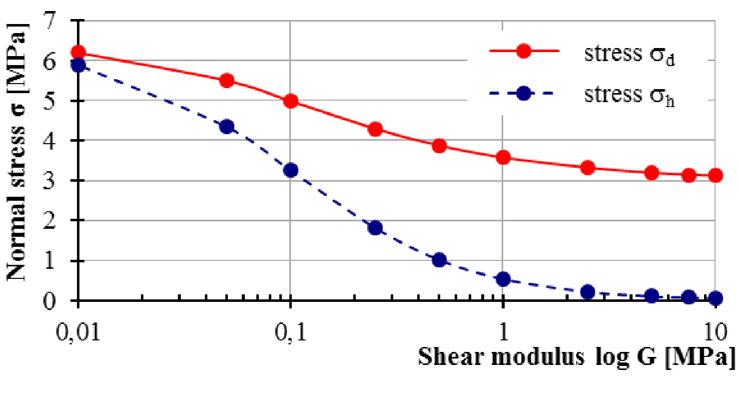

Fig. 2: The relation between normal stress and shear modulus in the middle of glass pane.

The influence of the shear modulus on the stress redistribution also depends on the boundary conditions. In case of glass panes simply supported along two sides, the differences between the full composite action and the composite action without a connection (e.g. due to high temperature) are more significant than when the panes are simply supported along four sides.

3. Experimental programme

As a pilot phase of the research project, small-scale tests aimed at determining the shear modulus of transparent foils were carried out at the Klokner Institute, CTU in Prague, in 2015. Laminated glass test specimens were tested under various boundary conditions – at temperature levels of 0°C, 20°C, 40°C and 60°C and at a load rate of 2 mm / min, 0.5 mm / min and 0.125 mm / min. Two types of EVA interlayers (EVALAM-80-120, EVASAFE), two types of PVB foils (TROSIFOL-BG-R-20, TROSIFOL-ES) and TPU (KRYSTALFLEX PE399) were chosen for the experimental programme. A total of 315 test specimens were tested.

3.1. Test set-up

Test specimens with geometrical dimensions of 50 x 150 mm, were produced from double layered laminated float glass 10 + 10 mm with thickness of the interlayer 0.76 mm, Fig. 3a). The tested area of 50 x 50 mm in the middle of the specimen was subjected to shear. A special steel frame, Fig. 3b), was used for introducing the appropriate load.

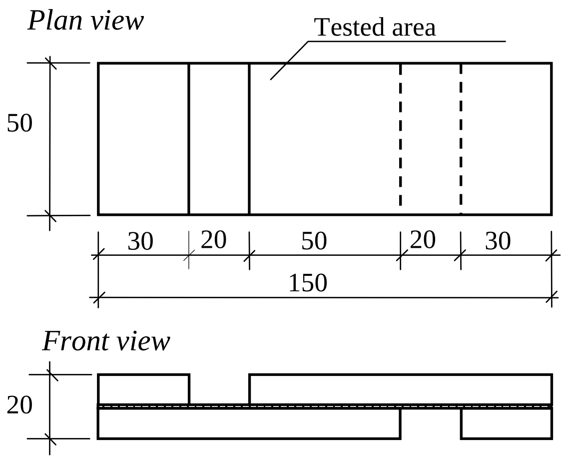

Fig. 3: a) Geometrical dimensions of the test specimens, b) Steel frame for introducing the load.

All experiments were carried out in the laboratory of the Klokner Institute, using the TIRA testing machine, which was supplemented by a climatic chamber for experiments at above and below room temperature 20°C. Additionally, the displacements of each test specimen were measured by two potentiometers. A total of 10 test specimens are planned for each type of interlayer, temperature and load rate.

3.2. Evaluation of the experiments

The first part of the experimental results was evaluated. The number of test samples was sufficient for obtaining the shear modulus of the interlayers under various conditions and for determining the statistical values (average, dispersion, standard deviation). Tab. 1 presents an overview of the specified initial shear modulus *G* for all tested interlayers, temperatures and a one-load rate of 2 mm/min.

Tab. 1: Overview of shear modulus G for a load rate of 2 mm/min.

Type of interlayer	**Shear modulus G [MPa]**			
	Load rate 2 mm/min			
	0°C	**20°C**	**40°C**	**60°C**
EVA - Evalam	7.31	1.67	0.68	0.32
EVA - Evasafe	-	5.30	2.74	1.48
PVB - Trosifol	-	1.66	0.44	0.26
PVB - Trosifol ES	-	155.34	-	-
TPU - Krystalflex	-	2.56	1.68	0.64

A preliminary summary of the results shows that the strongest interlayer is PVB-Trosifol-ES, which is almost without deformation at a temperature of 20°C. It should be mentioned that the same chemical composition does not mean the same shear modulus (e.g. a comparison between EVA-Evalam and EVA-Evasafe). For high temperatures (60^{o}C), all tested interlayers are much less strong. PVB-Trosifol resisted only a very small force (100-200 N), and there was sliding of the interlayer instead of the usual failure mode. All of the tested interlayers are more resistant with lower temperature and with a higher load rate, see Fig. 4. The load rate has a significant impact on the shear modulus, depending on the type of interlayer. In the case of PVB-Trosifol, we can observe almost the same shear modulus for a load rate of 2 mm/min and for a load rate of 0.5mm/min, but for a load rate of 0.125 mm/min there is a substantial reduction in the shear modulus. By contrast, EVA-Evalam has the same stiffness for practically all tested load rates. For practical reasons, the load rates were chosen with respect to the testing time, and do not correspond to the long-term behavior under self-weight.

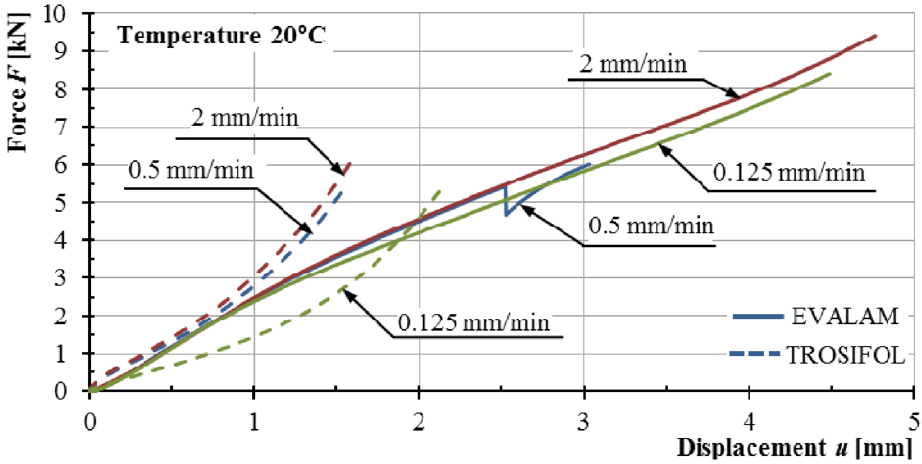

Fig. 4: Force displacement relation of two interlayers for a different load rate.

4. Conclusions

For load-bearing laminated glass panes with a load perpendicular to the surface, the material properties of visco-elastic transparent foils are very important. The composition of the laminated structural elements as a whole needs to be chosen with respect to the static function, the design load and the environmental conditions, e.g. temperature, which affect the shear modulus G of the interlayers and consequently the stress distribution as well as the deflection. This has motivated intensive research in Europe (Galuppi & Royer-Carfagni, 2013).

The shear modulus has different values not only for different interlayer materials but also under different environmental conditions (temperature) and load duration. Under high temperatures, laminated glass generally works without any composite action, because polymer materials are not able to transfer the shear forces, and in this case the shear modulus is close to zero. Temperatures below 20°C lead to stiffening of the material and to higher shear modulus values. Under long-term application of the load there is a creeping effect in the polymer interlayers, which has to be taken into account (e.g. self-weight).

Approaches that are suggested for the design of laminated glass elements, in particular, the method described in Draft prEN 16612 (2013), are based on an evaluation of the effective thickness. These approaches are too simplified and need to be improved. The test results presented here form a small part of a future study under various conditions and for a wider range of interlayer materials in order to obtain all the necessary data (shear modulus values) for the improved design of laminated glass elements.

Acknowledgement

This paper has been written with support from GAČR No. 16-17461S.

References

Wurm, J. (2007) Glass structures – Design and construction of self-supporting skins, Birkhäuser Verlag AG, Germany.

Galuppi, L. & Royer-Carfagni, G. (2013) The design of laminated glass under time-dependent loading. International Journal of Mechanical Sciences, 68, pp. 67–75.

Draft prEN 16612 (2013) Glass in building - Determination of the load resistance of glass panes by calculation and testing, CEN, Brussels.

22nd International Conference
ENGINEERING MECHANICS 2016
Svratka, Czech Republic, 9 – 12 May 2016

STABILITY ANALYSIS OF THE LATERAL OSCILLATIONS OF A FLEXIBLY SUPPORTED VISCOELASTIC JEFFCOTT ROTOR

P. Ferfecki[*], J. Zapoměl[**], J. Kozánek[***], V. Dekýš[****]

Abstract: *Material damping has a significant influence on vibrations of flexible rotors and can induce their self excited oscillations. The squeeze film dampers inserted in the rotor supports are frequently used to suppress occurrence of these undesirable operating conditions. Modelling the shaft by means of a Kelvin-Voigt material can arrive at the overestimation of the effect of internal damping on the rotor movement. This was a motivation to develop a procedure based on utilization of the Zener material (standard solid theoretical material) to represent the shaft of a Jeffcott rotor supported by squeeze film dampers. The development and testing of this procedure, the experimental determination of the appropriate material constants, and learning more on the influence of material damping on the stability and vibration attenuation of flexible rotors are the principal contributions of the presented article.*

Keywords: Jeffcott rotor, Zener material, squeeze film dampers, vibration amplitude and stability.

1. Introduction

Material damping has a significant effect on vibrations of flexible rotors. When the speed of their rotation exceeds a limit value, it becomes a source of self excited oscillations. The often used technological solution making it possible to suppress these undesirable operating conditions consists in adding the squeeze film dampers to the rotor supports.

A great attention must be paid to representing the shaft material in mathematical models of rotor systems. The experience shows that the most frequently used Kelvin-Voigt theoretical material characterized for a linear dependence of the specific damping capacity on the vibration frequency can overestimate the influence of internal damping on the rotor motion. The nonlinear dependence of the damping capacity is provided by the Zener material which is considered to be a standard solid material model.

In this paper there is presented a procedure developed for investigation of the stability and the vibration attenuation of a Jeffcott rotor excited by the disc unbalance. The shaft material is represented by a Zener one. The rotor is supported at both its ends by classical squeeze film dampers. The steady state response is determined by application of a trigonometric collocation method. The stability vibration is evaluated by means of the Floquet theorem. The pressure distribution in the gap of the squeeze film dampers is determined by solving the Reynolds equation. The development and testing of the new computational procedure, the experimental determination of the material constants, and learning more on the influence of internal damping on the vibration of flexible rotors are the principle contributions of this article.

[*] Ing. Petr Ferfecki, PhD.: IT4Innovations National Supercomputing Center, VŠB - Technical University of Ostrava, 17. listopadu 15, 708 33 Ostrava-Poruba; CZ,
Department of Applied Mechanics, VSB-Technical University of Ostrava, 17. listopadu 15, 708 33 Ostrava-Poruba; CZ
petr.ferfecki@vsb.cz

[**] prof. Ing. Jaroslav Zapoměl, DrSc.: Institute of Thermomechanics, Dolejškova 5; 182 00 Prague; CZ,
Department of Applied Mechanics, VSB-Technical University of Ostrava, 17. listopadu 15, 708 33 Ostrava-Poruba; CZ
jaroslav.zapomel@vsb.cz

[***] Ing. Jan Kozánek, CSc.: Institute of Thermomechanics, Dolejškova 5; 182 00, Prague; CZ
kozanek@it.cas.cz

[****] doc. Ing. Vladimír Dekýš, CSc.: Department of Applied Mechanics, Zilina University, Univerzitná 8215/1, 010 26 Žilina; SK
vladimir.dekys@fstroj.uniza.sk

2. The investigated rotor system

The investigated rotor system consists of a shaft and of one disc (Fig 1). At both its ends it is supported by squeeze film dampers lubricated with classical oil. The rotor turns at constant angular speed, is loaded by its weight and excited by the disc unbalance. Both squirrel springs are prestressed to be eliminated their deflection caused by the rotor weight. The disc can be considered as thin and absolutely rigid and the whole system as symmetric relative to the disc middle plane.

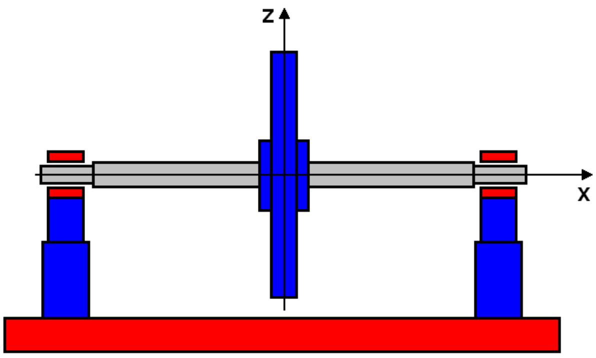

Fig. 1: The investigated rotor system

The shaft of the rotor is made of steel. The carried out measurements provided the value of the modulus of elasticity (isothermal) 200 GPa and dependence of the specific damping capacity on the vibration frequency. Based on analysis discussed in Zapoměl et al., 2015 behaviour of the investigated material is close to the viscoelastic Zener one (the standard solid material model). The corresponding specific damping capacity ψ is expressed by the relation (Zapoměl, 1998)

$$\psi = 2\pi\omega T_R \frac{\frac{E_S}{E_T} - 1}{1 + T_R^2 \omega^2 \frac{E_S}{E_T}}, \qquad (1)$$

where T_R is the time relaxation constant, E_T, E_S are the isothermal and adiabatic Young's moduli, and ω is the angular frequency of the vibrations. The comparison of the measured data with those obtained by their approximation is depicted in Fig. 2. The values of the moduli ratio and the time relaxation constant were determined by application of the nonlinear least square method ($E_S/E_T = 1.008$, $T_R =$ 185 ms).

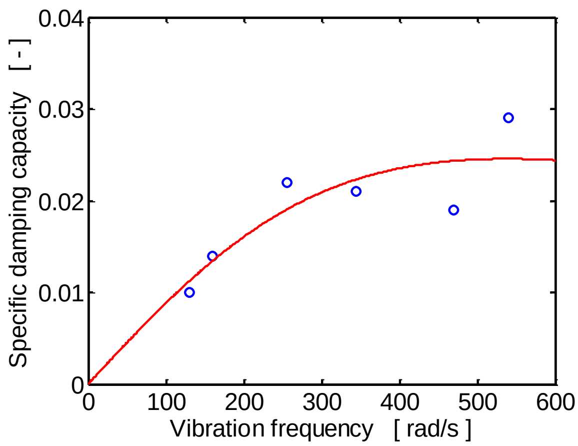

Fig. 2: The dependence of the specific damping capacity on the vibration frequency

3. The motion equations

In the computational model the rotor is considered to be a Jeffcott one. The shaft is massless represented by a viscoelastic Zener material and the squeeze film dampers are implemented by springs with no itertia effects and by force couplings (Zapoměl, 2007, Szeri, 1980).

Because of the system symmetry, the rotor vibration is governed by four nonlinear motion equations that have the form with respect to the fixed (inertial) frame of reference

$$m\ddot{y}_R + b_P \dot{y}_R = -F_{my} + m e_T \omega^2 \cos\omega t\,, \tag{2}$$

$$m\ddot{z}_R + b_P \dot{z}_R = -F_{mz} + m e_T \omega^2 \sin\omega t - mg\,, \tag{3}$$

$$0 = F_{my} - 2k_D y_D + 2F_{hy} + 2F_{psy}\,, \tag{4}$$

$$0 = F_{mz} - 2k_D z_D + 2F_{hz} + 2F_{psz}\,. \tag{5}$$

m is the disc mass, b_P is the coefficient of external disc damping (damping caused by the environment), F_{my}, F_{mz} are the y and z components of the viscoelastic force by which the flexibly deformed shaft acts on the disc, e_T is the eccentricity of the disc centre of mass, k_D is the stiffness of one squirrel spring, F_{hy}, F_{hz} are the y and z components of the hydraulic force acting on the rotor journal (Zapoměl, 2007, Szeri, 1980), F_{psy}, F_{psz} are the y and z components of the prestress force, g is the gravity acceleration, y_R, z_R are the y and z displacements of the disc centre, y_D, z_D are the y and z displacements of the journal centre, t is the time, and $(\dot{\ })$,$(\ddot{\ })$ denote the first and second derivative with respect to time.

The components $F_{m\eta}$, $F_{m\zeta}$ of the viscoelastic force by which the shaft acts on the disc can be expressed in the coordinate system rotating together with the rotor

$$F_{m\eta} = k_T(\eta_R - \eta_D) + \int_0^t b_M \mu (\dot{\eta}_R - \dot{\eta}_D)\, e^{-\mu(t-\vartheta)} d\vartheta\,, \tag{6}$$

$$F_{m\zeta} = k_T(\zeta_R - \zeta_D) + \int_0^t b_M \mu (\dot{\zeta}_R - \dot{\zeta}_D)\, e^{-\mu(t-\vartheta)} d\vartheta\,. \tag{7}$$

k_T, k_S are the shaft isothermal and adiabatic stiffnesses, η_R, ζ_R, η_D, ζ_D are the η and ζ displacements of the disc and of the journal centre, respectively, μ is the inverse value of the time relaxation constant, ϑ is the time parameter, and b_M is the coefficient of the shaft material damping (Zapoměl, 1998)

$$b_M = T_R(k_S - k_T)\,. \tag{8}$$

After performing a series of manipulations one obtains a matrix equation referred to the fixed frame of reference that governs the Jeffcott rotor vibrations

$$\begin{bmatrix} \mathbf{M} & \mathbf{O} \\ \mathbf{O} & \mathbf{O} \end{bmatrix} \begin{bmatrix} \ddot{\mathbf{x}} \\ \ddot{\mathbf{g}} \end{bmatrix} + \begin{bmatrix} \mathbf{B}_\mathrm{P} + \mathbf{B}_\mathrm{M} & -\frac{1}{\mu}\mathbf{B}_\mathrm{M} \\ -\mu\mathbf{I} & \mathbf{I} \end{bmatrix} \begin{bmatrix} \dot{\mathbf{x}} \\ \dot{\mathbf{g}} \end{bmatrix} + \begin{bmatrix} \mathbf{K} - \omega\mathbf{K}_\mathrm{C} & \frac{\omega}{\mu}\mathbf{K}_\mathrm{C} \\ \mu\mathbf{\Omega} & \mu\mathbf{I} - \mathbf{\Omega} \end{bmatrix} \begin{bmatrix} \mathbf{x} \\ \mathbf{g} \end{bmatrix} = \begin{bmatrix} \mathbf{f} \\ \mathbf{o} \end{bmatrix}. \tag{9}$$

$\mathbf{M}$, $\mathbf{K}$, $\mathbf{B}_\mathrm{P}$, $\mathbf{B}_\mathrm{M}$ are the mass, stiffness, external and material damping matrices, $\mathbf{K}_\mathrm{C}$ is the circulation matrix, $\mathbf{I}$ is the unity matrix, $\mathbf{\Omega}$ is the matrix of the rotor angular velocity, $\mathbf{O}$ is the zero matrix, $\mathbf{x}$ is the vector of physical displacements, $\mathbf{f}$ is the vector of applied forces, $\mathbf{g}$ is the vector of auxiliary (internal) coordinates, and $\mathbf{o}$ is the zero vector.

As the forces induced by the disc unbalance are of a harmonic time history, the trigonometric collocation method was used to determine the steady state component of the rotor vibration. Its stability was evaluated by application of the Floquet theorem.

4. Results of the simulations

The technological and operating parameters of the investigated rotor system are: the disc mass 130 kg, the shaft stiffness (isothermal) 7 MN/m, the stiffness of one squirrel spring 3 MN/m, the coefficient of external damping of the disc 4 kg/s, the disc unbalance 7.8 kg.mm, the mean diameter and the length of the damper 120 mm, 40 mm, the width of the damper clearance 200 μm, the dynamic viscosity of the lubricant 0.08 Pa.s, the oil input pressure 300 kPa, the specified angular speed range 0 ÷ 600 rad/s.

The (isothermal) stiffness of the shaft 7 MN/m, the measured values of the time relaxation constant 185 ms and the adiabatic/isothermal stiffness ratio 1.008 give the magnitude of the material damping coefficient of 101.8 kg/s.

The frequency responses of the disc and of the rotor journal referred to the vibration in the horizontal direction are drawn in Fig. 3. The maximum displacements correspond to the rotor critical speed the value of which is approximately 220 rad/s. Amplitude of the disc vibrations approaches with rising angular speed of the rotor rotation to the disc centre of mass eccentricity.

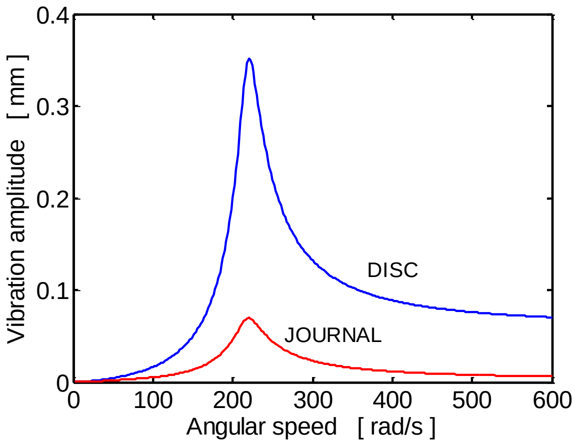

Fig. 3: The rotor frequency response

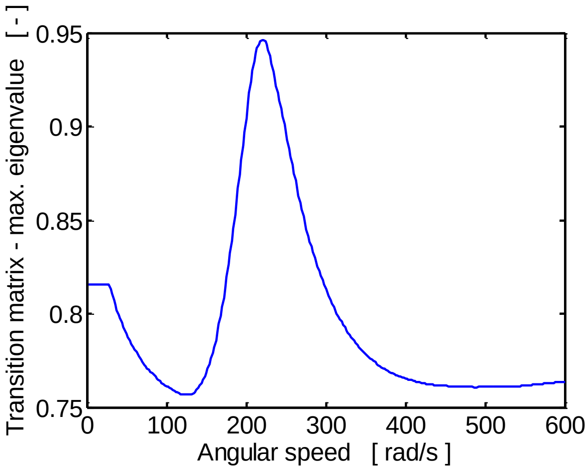

Fig. 4: The vibration stability evaluation

The dependence of the maximum eigenvalue of the transition matrix set up over the span of time of one period on the rotor angular speed is depicted in Fig. 4. The results show that all magnitudes of the maximum eigenvalues are less than 1 which implies the rotor vibration is stable in the specified range of the angular speed.

5. Conclusions

The lateral vibration of rotors is significantly influenced by the shaft elastic properties and material damping. It implies a great attention must be paid to the choice of the theoretical material to implement the shaft in the computational model. The approach for investigation of the oscillation amplitude and evaluation of the vibration stability of a Jeffcott rotor supported by squeeze film dampers is presented in this paper. The rotor shaft is made of a Zener material which is characterized for a nonlinear dependence of the specific damping capacity on the vibration frequency. A trigonometric collocation method was applied to determine the steady state response of the rotor. The stability of the forced vibration was evaluated by means of the Floquet theorem. The development of a new computational procedure, the experimental determination of the appropriate material constants, and learning more on the effect of the internal damping and the squeeze film dampers on the vibration attenuation of flexible rotors are the principle contributions of this article.

Acknowledgement

This work was supported by the Czech Science Foundation (GA 15-06621S), The Ministry of Education, Youth and Sports from the National Programme of Sustainability (NPU II) project „IT4Innovations excellence in science - LQ1602“, the Slovak Research and Development Agency (contract No. APVV-0736-12), and the Slovak Grant Agency (proj. VEGA 1/0983/15).

References

Szeri, A. Z. (1980) Tribology: Friction, Lubrication, and Wear. Hemisphere, Publishing Corporation, Washington, New York, London

Zapoměl, J. (1998) Přístupy k zahrnutí materiálového tlumení do počítačových modelů mechanických soustav, the habilitation thesis, VŠB - Technical University of Ostrava, Faculty of Mechanical Engineering, Ostrava

Zapoměl, J. (2007) Počítačové modelování příčného kmitání rotorů uložených v hydrodynamických ložiskách a squeeze filmových tlumičích, VŠB - Technical University of Ostrava, Ostrava

Zapoměl, J., Ferfecki, P., Dekýš, V. & Žmindák, M. (2015) Modelling and investigations of influence of material damping on vibrations of flexible rotors, Proceedings of the conference Computational Mechanics 2015, Špičák, CD 1-2

22nd International Conference
ENGINEERING MECHANICS 2016
Svratka, Czech Republic, 9 – 12 May 2016

CONCRETE PLASTICITY MODEL AND ITS APPLICATION TO PLANE STRESS STATE

J. Fiedler*, T. Koudelka**

Abstract: *Two Drucker-Prager criteria are employed to define a nonlinear material model for concrete that is capable to solve tri-axial analysis of plasticity. The model consists of one Drucker-Prager criterion set to approximate tensile stress area and the other to describe compression area. The first derivative singularities are treated by using an imaginary tangent as a local yield function and the model is modified for specific application for the plane stress state. The model is implemented into the SIFEL solver using the finite element method.*

Keywords: Double Drucker-Prager, Concrete plasticity model, Plane stress state, SIFEL solver, Finite element method.

1. Introduction

Since behaviour of concrete in tension and compression is diverse, single yield criterion for this material is not sufficient enough to describe both stress areas. In this case, two Drucker-Prager yield criteria can be employed to form a concrete plasticity model capable to capture more general stress-strain states. Combining these two criteria nevertheless leads to the first derivative singularities which need to be treated separately. Compared to other concrete models, e.g. Drucker-Prager + Tresca (Feenstra & de Borst, 1996), this plasticity model incorporates less singularities. Moreover, whole plasticity calculation of the model can be performed at the level of stress invariants and the treatment of the singularities can be thus considerably simplified. The model is also modified for the plane stress state where the correction of the out-of-plane elastic strain is needed. The model has been implemented into the SIFEL software package (Krejčí, Koudelka & Kruis, 2011) using the finite element method.

In the first part of the paper, the principle of general plasticity and the single Drucker-Prager criterion is described. The second part is dedicated to the treatment of the singularities and especially to the out-of-plane strain correction regarding the plane stress state. In the end, an example of calculation using the model is presented where the correction for the plane stress state should be demonstrated.

2. Plasticity in finite element method

The state, in which material exhibits plastic flow, is generally expressed by the following yield criterion

$$f(\boldsymbol{\sigma},\boldsymbol{q}) = 0 \tag{1}$$

where $\boldsymbol{\sigma}$ is the stress vector, $\boldsymbol{q}$ is the vector of internal variables and f is the yield function. If values of the yield function are negative $f < 0$, material is located in the elastic stress area. Stress states where the yield function provides positive values, are not admissible.

Assuming elastoplastic behaviour and small strains, relation between stress and strain can be determined by

$$\boldsymbol{\sigma} = \boldsymbol{D}_e(\boldsymbol{\varepsilon} - \boldsymbol{\varepsilon}_p) \tag{2}$$

* Ing. Josef Fiedler: Faculty of Civil Engineering, Czech Technical University in Prague, Thákurova 7/2077; 166 29, Prague; CZ, josef.fiedler@fsv.cvut.cz

** Ing. Tomáš Koudelka, Ph.D.: Faculty of Civil Engineering, Czech Technical University in Prague, Thákurova 7/2077; 166 29, Prague; CZ, koudelka@cml.fsv.cvut.cz

where $\boldsymbol{\varepsilon}$ is total strain vector, $\boldsymbol{\varepsilon}_p$ is plastic strain vector and $\boldsymbol{D}_e$ denotes elastic stiffness matrix. In the case of the concrete plasticity model, the associated flow rule is selected as an expression of plasticity

$$\dot{\boldsymbol{\varepsilon}}_p = \dot{\gamma} \frac{\partial f}{\partial \boldsymbol{\sigma}} \tag{3}$$

where $\dot{\boldsymbol{\varepsilon}}_p$ represents the rate of plastic strains, $\dot{\gamma}$ is the rate of plastic multiplier that indicates the magnitude of plastic strains, and the gradient of the yield function dictates the direction of plastic flow.

A nonlinear analysis is usually carried out by an iterative calculation with increments of load. As the first step, the evaluation of the trial stress state $\boldsymbol{\sigma}_{tr}$ is performed using the following expression

$$\boldsymbol{\sigma}_{tr} = \boldsymbol{D}_e \left(\boldsymbol{\varepsilon}^{(n)} - \boldsymbol{\varepsilon}_p^{(n-1)} \right) \tag{4}$$

where the superscript n indicates the iteration step of the global iterative procedure. The trial stress state that is calculated from total strains of the current step and plastic strains of the previous step, is determined whether it belongs to the admissible stress area. If it does, no further computation of plasticity is performed. Otherwise, the trial stress state is necessary to return to the admissible stress area by, for example, the cutting plane method (de Souza Neto, Perić & Owen, 2008).

Assuming incremental calculation, eq. (3) can be rewritten as

$$\Delta \boldsymbol{\varepsilon}_p^{(n)} = \Delta \gamma^{(n)} \frac{\partial f^{(n-1)}}{\partial \boldsymbol{\sigma}} \tag{5}$$

The cutting plane method is specifically used for determination of the increment of the plastic multiplier $\Delta\gamma$. With the help of the newly calculated increment of the plastic strain vector using eq. (5), the corrected stress state is then possible to evaluate

$$\boldsymbol{\sigma}^{(n)} = \boldsymbol{\sigma}^{tr} - \boldsymbol{D}_e \Delta \gamma^{(n)} \frac{\partial f^{(n-1)}}{\partial \boldsymbol{\sigma}} \tag{6}$$

3. Double Drucker-Prager concrete plasticity model

The single Drucker-Prager plasticity is described by the following yield function

$$f(\boldsymbol{\sigma}) = \alpha_\phi I_1(\boldsymbol{\sigma}) + \sqrt{J_2(\boldsymbol{\sigma})} - \tau_0 \tag{7}$$

where τ_0 is the parameter representing shear strength and the parameter α_ϕ is connected with friction angle. I_1 is the first invariant of the stress tensor and J_2 is the second invariant of the deviatoric stress tensor. Exploiting of these two yield functions with different setup of the parameters leads to a suitable plasticity model that describes concrete in both compression and tension (Jirásek & Bažant, 2002). By employing concrete strength in single compression f_c and in biaxial compression f_b, parameters for yield function that approximates compressive behavior, can be calculated

$$\alpha_{\phi,c} = \frac{\sqrt{3}}{3} \frac{f_b - f_c}{2 f_b - f_c}, \quad \tau_{0,c} = f_c \frac{\sqrt{3} - 3\alpha_{\phi,c}}{3}. \tag{8}$$

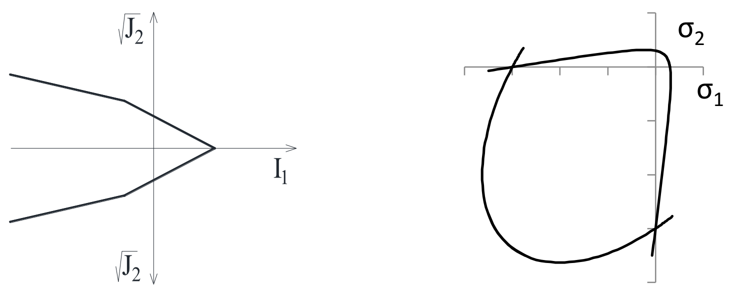

a) *b)*

Fig. 1: Double Drucker-Prager criterion: a) coordinate system of stress invariants, b) plane stress state

The tensile stress area can be then described by adding concrete strength in tension f_t

$$\alpha_{\phi,t} = \frac{\sqrt{3}}{3}\frac{f_c - f_t}{f_c + f_t}, \quad \tau_{0,t} = f_c \frac{\sqrt{3} - 3\alpha_{\phi,t}}{3}. \tag{9}$$

The resulting yield surface, created by two separate Ducker-Prager yield criteria, is represented by an angular cone whose characteristic sections are displayed in fig. 1.

4. Singularities treatment

As depicted in fig. 1a, the first derivative singularities are located at the vertex of the cone and at the intersection of the criteria. By these singularities, so called stress return areas are established where the value and the derivative of the relevant yield functions are evaluated. The whole problem is solved at the level of the stress invariants and the derivative of the yield functions are substituted by

$$\frac{\partial f}{\partial \boldsymbol{\sigma}} = \frac{df}{dJ_2} \cdot \frac{\partial J_2}{\partial \boldsymbol{\sigma}} + \frac{df}{dI_1} \cdot \frac{\partial I_1}{\partial \boldsymbol{\sigma}}. \tag{10}$$

Return to the point of the first derivative singularity is solved by using an imaginary tangent which is defined as a normal to the connecting line between the singularity and the trial stress state point. The tangent serves as a local yield function and its value together with its derivative is used further in calculation, specifically in the cutting plane method.

5. Correction for plane stress state

The plane stress state is constrained by the following expressions

$$\sigma_z = \tau_{xz} = \tau_{yz} = 0 \qquad \gamma_{xz} = \gamma_{yz} = 0. \tag{11}$$

Elastic stiffness matrix for the plane stress state is derived from general Hooke's law in a way that it is assumed that, apart from other conditions, the component σ_z is in elastic form equal to zero. However, if a tri-axial plasticity model is used, a stress return algorithm usually generates in the case of the plane stress state non-zero out-of-plane stress component σ_z which may negatively influence whole plasticity calculation. Stress correcting procedure that deals with this problem, has been firstly suggested by (Aravas, 1987) and the following algorithm, used in SIFEL, has been designed by (Dodds, 1987).

The non-zero stress components together with corresponding strains are assembled as follows

$$\boldsymbol{\sigma} = \{\sigma_{11} \quad \sigma_{22} \quad \sigma_{12}\}^T, \quad \boldsymbol{\varepsilon} = \{\varepsilon_{11} \quad \varepsilon_{22} \quad 2\varepsilon_{12}\}. \tag{12}$$

In the first step of the procedure, a trial out-of-plane strain component is calculated

$$\varepsilon_{33}^{e\,trial} = -\frac{\nu}{1-\nu}\left(\varepsilon_{11}^e + \varepsilon_{22}^e\right). \tag{13}$$

As the next step, a stress return algorithm is called while using an extended stiffness matrix (as for axisymmetric problem) for calculating trial stresses

$$\left[\begin{array}{c} \boldsymbol{\sigma}^{trial} \\ \hline \sigma_{33}^{trial} \end{array}\right] = \boldsymbol{D}_{ext}\left[\begin{array}{c} \boldsymbol{\varepsilon}^{e} \\ \hline \varepsilon_{33}^{e\,trial} \end{array}\right]. \tag{14}$$

After the stress return algorithm is finished, the stress state $[\boldsymbol{\sigma}^T \quad \sigma_{33}]^T$ that satisfies a plasticity criterion, is obtained. The stress correcting algorithm is terminated if the out-of-plane stress component σ_{33} is lesser than tolerable inaccuracy. Otherwise, the following correction of the out-of-plane strain is applied

$$\varepsilon_{33}^e = \varepsilon_{33}^{e\,trial} - \frac{\sigma_{33}}{D_{44}} \tag{15}$$

where D_{44} is the element of the extended stiffness matrix at the 4,4 position. The newly acquired out-of-plane strain then enters to the stress return algorithm and again the value of the out-of-plane stress component is tested. This procedure continues until the required value of the out-of-plane stress is reached. The general iterative form of eq. (15) can be then written as

$$\varepsilon_{33}^{i+1} = \varepsilon_{33}^{i} - \frac{\sigma_{33}^{i}}{D_{44}}. \tag{16}$$

6. Calculation example

The plasticity model is tested on the example of a concrete beam with following parameters: 0.6 m height, 3.6 m length, 0.3 m depth, concrete C30/37 f_c = 30 MPa, f_t =3 MPa, f_b = 1.2 f_c. The beam is fixed alongside the left edge and loaded by vertical force at the upper right corner. The results are shown for the 33,5 kN value of the loading force. In accordance to the development of the plastic multiplier (fig. 2), the distribution of the out-of-plane stress component can be observed from fig. 3. In the areas where behaviour of concrete is elastic, the out-of-plane stress is automatically equal to zero. However, in the case of the plastic yielding area, minor values that corresponds with tolerable inaccuracy (1 kPa), can be recognized at the upper left edge. These small values in the plastic yielding area prove the presence of the stress correcting algorithm inside the plasticity model.

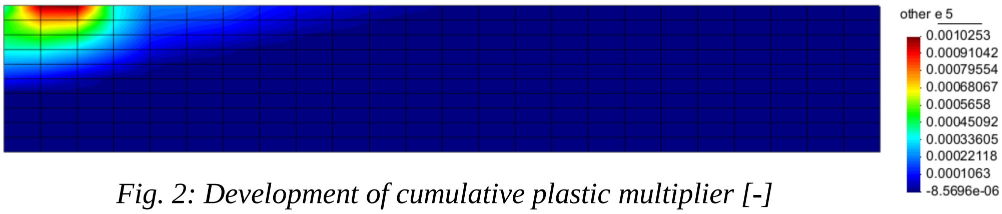

Fig. 2: Development of cumulative plastic multiplier [-]

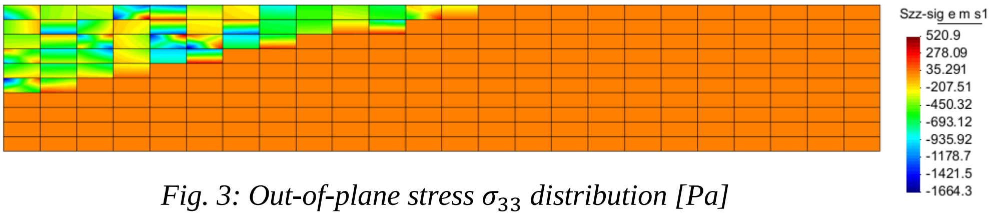

Fig. 3: Out-of-plane stress σ_{33} distribution [Pa]

7. Conclusions

The concrete plasticity model using two Drucker-Prager criteria has been presented in the paper while emphasizing the solution of the first derivative singularities and the importance of the stress correcting algorithm in case of the plane stress state. The validity of the algorithm has been demonstrated in the plastic yielding area of the concrete beam.

Acknowledgement

This paper was supported by project SGS15/031/OHK1/1T/11 – Advanced numerical modeling in mechanics of structures and materials.

References

Aravas N. (1987) On the Numerical Integration of a Class of Pressure-Dependent Plasticity Models. Int. J. Num. Meth. Engng, 24, pp. 1395–1416.

Dodds R.H. Jr. (1987) Numerical Techniques for Plasticity Computations in Finite Element Analysis. Comput. Structs, 26, pp. 767–779.

Feenstra P. H. & Borst, R. de (1996) A Composite Plasticity Model for Concrete, International Journal of Solids and Structures, 33, pp. 707-730.

Jirásek M. & Bažant Z. P. (2002) Inelastic Analysis of Structures. 1st ed. Wiley, Chichester.

Krejčí T., Koudelka T. & Kruis J. (2011) Modeling of building constructions in SIFEL environment, Czech Technical University in Prague, 1. ed., Prague.

Souza Neto E.A. de, Perić D. & Owen D.R.J. (2008) Computational Methods for Plasticity – Theory and Applications. 1st ed. Wiley, Chichester.

22nd International Conference
ENGINEERING MECHANICS 2016
Svratka, Czech Republic, 9 – 12 May 2016

APPROXIMATION OF THE MOVEMENT OF THE SPHERICAL PENDULUM

C. Fischer*, J. Náprstek**

Abstract: *The horizontally driven two-degrees of freedom spherical pendulum is an auto-parametric system which exhibits a wide variety of response types. Depending on the amplitude and frequency of the excitation the response can vary from stationary to chaotic regime. It has been already shown that the response can be described using time variable parameters of an inscribed ellipse. Such a description has a potential to close the gap between description of stationary, quasi-periodic and chaotic types of response. This study presents methodology and results of an analysis of the experimentally measured data providing the time dependent parameters of a twisting ellipse. The obtained results are discussed and some open problems are indicated.*

Keywords: Spherical pendulum, quasi-periodic response, data analysis.

1. Introduction

The spherical pendulum, which is kinematically driven in its suspension point, is a very popular auto-parametric system. In fact it is the simplest system, which exhibits complex response types, ranging from stationary periodic response to chaotic regime for certain driving conditions. Thus, many authors dealt various aspects of behaviour of the spherical pendulum until now, however, most of them are referencing papers by J. Miles (1962, 1984), where the weakly non-linear resonant response of a damped spherical pendulum is discussed. Among other papers dealing with aspects close to currently discussed topic can be mentioned, e.g., Petrov (2005) and Leung (2006), who analysed various types of kinematic or force excitation in suspension, where the harmonic excitation in the suspension point in both vertical and horizontal directions are considered. The experimental verification of the theoretical model was carried out by Tritton (1986).

Contribution of the authors to theoretical description of behaviour of the spherical pendulum comprises several publications; see, e.g., Náprstek & Fischer (2009, 2013). In first paper the non-linear mathematical model was introduced and its stability was analysed using the harmonic balance approach. In the latter paper, the concept of "virtual ellipse" was introduced and used for analysis of the quasi-periodic part of the response. The research was later supplemented by an experimental work by Pospíšil et. al (2014). The experimental setup was aimed to study the influence of uneven damping in both directions (lateral and transversal) with respect to direction of excitation. The current work returns to the concept of "virtual ellipse" and uses the experimental data to illustrate validity of the mathematical model.

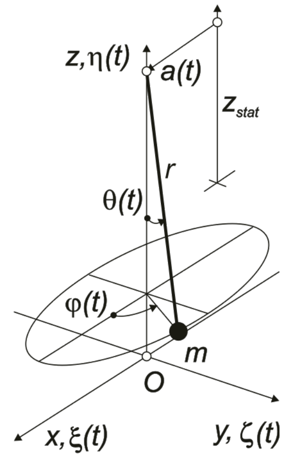

Fig. 1: Sketch of the system.

2. Theoretical model

The mathematical model of the spherical pendulum follows from the mechanical energy balance. Using the Hamilton principle and quadratic form of the Rayleigh function, a system of two Lagrange equations in Cartesian coordinates can be set up, for details see Náprstek & Fischer

*RNDr. Cyril Fischer, PhD., Institute of Theoretical and Applied Mechanics AS CR, v.v.i., Prosecká 76, 190 00 Praha 9, fischerc@itam.cas.cz

**Ing. Jiří Náprstek, DrSc., Institute of Theoretical and Applied Mechanics AS CR, v.v.i., Prosecká 76, 190 00 Praha 9, naprstek@itam.cas.cz

(2009) and Fig. 1. Neglecting terms of order $O(\varepsilon^6)$; $\varepsilon^2 = (\xi^2 + \zeta^2)/r^2$, the approximate system reads:

$$
\begin{aligned}
\ddot{\xi} + \frac{1}{2r^2}\xi\frac{\mathrm{d}^2}{\mathrm{d}t^2}(\xi^2+\zeta^2) + 2\beta_\xi\dot{\xi} + \omega_0^2\xi\left(1+\frac{1}{2r^2}(\xi^2+\zeta^2)\right) = -\ddot{a} \\
\ddot{\zeta} + \frac{1}{2r^2}\zeta\frac{\mathrm{d}^2}{\mathrm{d}t^2}(\xi^2+\zeta^2) + 2\beta_\zeta\dot{\zeta} + \omega_0^2\zeta\left(1+\frac{1}{2r^2}(\xi^2+\zeta^2)\right) = 0
\end{aligned}
\tag{1}
$$

Here ξ stands for horizontal component of the response in direction of the excitation $a = a(t)$, while ζ describes the transverse motion. Symbols m, r represent mass and suspension length of the pendulum and β_ξ, β_ζ are the coefficients of linear viscous damping in the individual directions. The natural frequency of the corresponding linear pendulum is $\omega_0^2 = g/r$. The above equations are mutually independent if only the linear terms are considered; their interaction is given by the non-linear terms only.

With respect to assumption of the harmonic excitation and continuous character of the mathematical model and taking into account previously obtained analytical, numerical, and experimental results the system response can be approximated by following expressions:

$$\xi(t) = a_c(t)\cos\omega t + a_s(t)\sin\omega t\,, \quad \zeta(t) = b_c(t)\cos\omega t + b_s(t)\sin\omega t \tag{2}$$

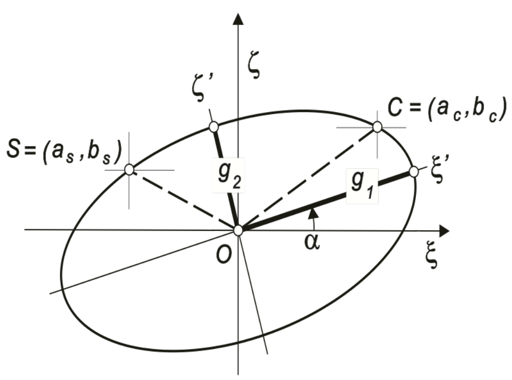

Fig. 2: Description of an ellipse in the xy plane

The partial amplitudes $a_c(t), a_s(t), b_c(t), b_s(t)$ in Eqs (2) are supposed to be the functions of a "slow" time and ω is the driving frequency of harmonic excitation. Enumeration of these amplitude functions is possible if the harmonic balance procedure is applied on the original system (1). As a result, a system of four first order ordinary differential equations can be obtained. Properties of the partial amplitudes reflect properties of different response types of the pendulum. The assumed solution (2) represents a parametric form of an ellipse in central position. It can be outlined in components ξ, ζ see Fig. 2, where $\alpha = \alpha(t)$ is orientation of principal axes; $g_1 = g_1(t)$ is the length of major axis and $g_2 = g_2(t)$- length of minor axis.

The three parameters α, g_1, g_2 determining properties of the inscribed ellipse are again functions of "slow" time. Variability of these functions is the same as variability of partial amplitudes (2). Their relation to the partial amplitudes is given as (see Náprstek & Fischer (2009) for details):

$$g_1 = \pm\frac{\sqrt{2S_A^4}}{\sqrt{R_A^2 + \sqrt{R_A^4 - 4S_A^4}}}\,, \quad g_2 = \pm\frac{\sqrt{2S_A^4}}{\sqrt{R_A^2 - \sqrt{R_A^4 - 4S_A^4}}}\,, \tag{3}$$

where R_A^2, S_A^2 are given as

$$R_A^2 = a_c^2 + a_s^2 + b_c^2 + b_s^2\,, \qquad S_A^2 = a_s b_c - a_c b_s\,. \tag{4}$$

The orientation of principal axes is given as:

$$\alpha(t) = \frac{1}{2}\arctan\frac{2(a_c b_c + a_s b_s)}{a_c^2 + a_s^2 - b_c^2 - b_s^2} \tag{5}$$

The curvature of the ξ, ζ trajectory considered as a planar curve is given as (Ruttler 2000):

$$k^2(t) = \frac{\left(\dot{\xi}\ddot{\zeta} + \ddot{\xi}\dot{\zeta}\right)^2}{\left(\dot{\xi}^2 + \dot{\zeta}^2\right)^3} \tag{6}$$

The approximation algorithm will be based on curvature of the experimental trajectory.

3. Approximation of experimental data

The ellipse in central position, which is supposed to approximate the experimental data (ξ_e, ζ_e), is fully described by three time dependent parameters α, g_1, g_2. The general expression reads:

$$\xi_e = g_1 \cos\alpha \cos\omega t - g_2 \sin\alpha \sin\omega t \,, \quad \zeta_e = g_1 \sin\alpha \cos\omega t + g_2 \cos\alpha \sin\omega t \tag{7}$$

The experimental (measured) data describe the trajectory of the pendulums bob in time; the driving frequency is ω known. In following it is assumed, that the measured data are filtered in such a way that they do not contain any spurious oscillations and thus that they represent a sufficiently smooth functions. This assumption eliminates cases when the trajectory degenerates into a line segment.

The basic idea of the algorithm is simple. In the first step, the maxima of the curvature of the experimental data have to be found. The radius vectors then allow determining orientation α of the ellipse and lengths of both major axis g_1 and minor axis g_2 at the corresponding time instants:

$$g_1 = \|(\xi_e, \zeta_e)\| \,, \quad g_2 = \sqrt{\frac{g_1}{k}} \,, \quad \alpha = \tan^{-1}\frac{\zeta_e}{\xi_e} \tag{8}$$

The relations (8) are valid for static ellipse; however, they provide sufficiently accurate initial values for subsequent optimization. This behaviour is illustrated in Figs. 3. Plot (A) shows the expected interpolation of the artificial data, which originate from discretization of a rotating ellipse (7), whereas the plot (B) uses real measured data. In both plots the dark solid lines represent the data to be approximated and dark dashed lines correspond to the ellipses inscribed in points of maximal curvature (shown as black dots). In case (A) the normal direction (dotted line) in the point of maximal curvature directs correctly to the origin. Thus, the approximation by an ellipse in central position is correct. For real measured data (B) is the incidence of the trajectory and approximating ellipse not as good. The normal direction in the point of maximal curvature (thin dotted lines) deviates from the radius vectors (thin dashed lines) significantly and the data trajectory is not symmetrical with respect to the normal. On the other hand, it seems that the ellipse in central position still provides acceptable approximation. Indeed, when the osculating circle (dotted circle) is shifted towards radius vector (dashed circle) in plot (B), it provides better approximation of the experimental trajectory than the osculating circle in the sense of least squares.

It seems that a similar approach can be used for points of minimal curvature; these points should directly provide length of the minor axis g_2. Unfortunately, because the trajectories are partly almost straight the search for a minimum leads to an ill-conditioned problem. On the other hand, the point of minimal curvature could be determined approximately dividing the angle between radius vectors of two adjacent points of maximal curvature or dividing the length of the arch. Because the curvature in such parts of the trajectory is low, the introduced error would be small and an additional point can improve the overall accuracy.

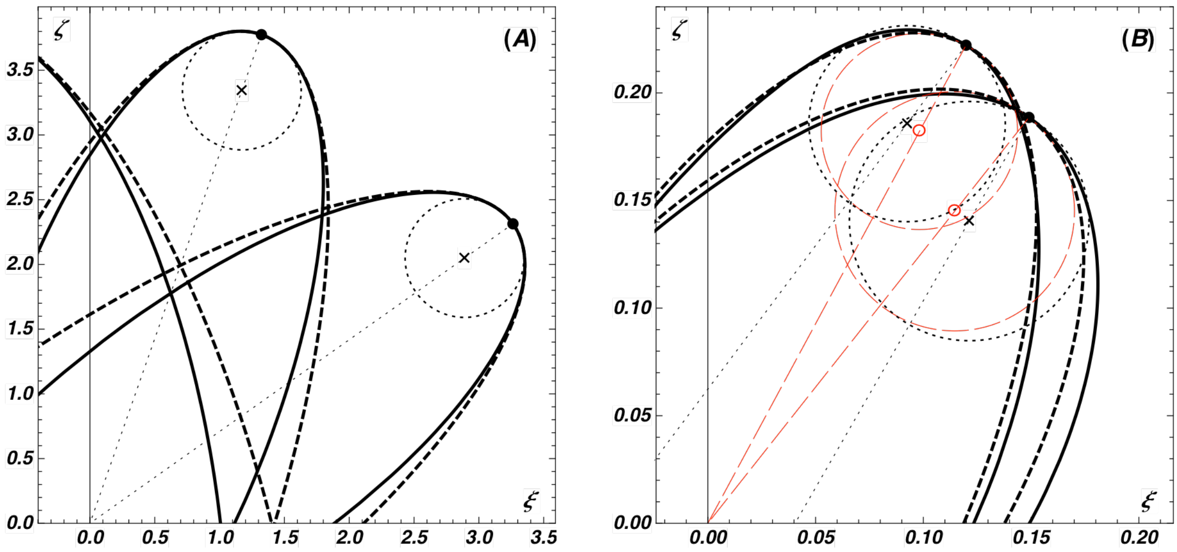

Fig. 3: Approximation of the rotating ellipse. (A) idealized case, (B) measured data. Thick solid curve - approximated data, thick dashed curve – inscribed ellipse, dotted circle - osculating circle

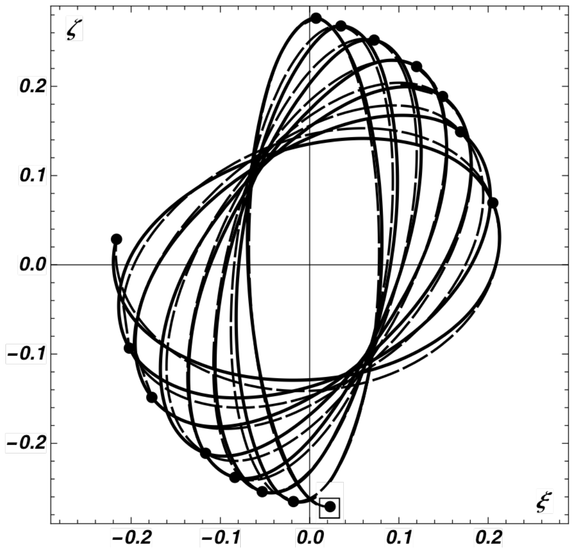

Fig. 4: Approximation of experimental data (solid) by the rotating ellipse (7), (dashed).

Figure 4 presents an example result of real approximation. The original data trajectory is shown as a solid curve, approximating ellipse (7) is dashed. The points of maximal curvature are indicated using black dots, starting point is denoted by a small square. It should be noted that the approximation in Figure 4 uses only curvatures computed in vertices of the ellipses. The numerically obtained values of α, g_1, g_2 were linearly interpolated as well as the computed "frequencies" $\omega = \pi/\Delta t$, which varied slightly around the driving frequency of the pendulum (Δt is the time difference between two instants of maximal curvature). The time coordinate had to be adjusted by introduction of a time (phase) shift in intervals between two instants of maximal curvature. No additional numerical optimization has been performed for results shown in Figure 4. For real usage, it would be worth to smoothen the obtained functions and improve the agreement using the least squares optimization method.

4. Conclusions

One of promising approaches for description of movement of the spherical pendulum is based on rotating ellipses. Presented contribution sketches out a procedure, which matches the experimental data to the theoretical model. The data are supposed to be sufficiently smooth or approximated by a smooth curve (e.g. spline). The approach based on observation of the curvature of the measured trajectory and usage of the extremal values to enumerate desired parameters proves to be usable. Using of non-extremal curvature values is feasible, but it brings some additional difficulties. Although it was not shown in this contribution, the similar approach is usable – after some modification – even for cases where the trajectory forms more complex geometrical curves (e.g., lemniscate). However, the degenerated cases (zero or infinite curvature) have to be dealt separately.

The presented approach is based purely on geometric curvature of the observed trajectory. It could be improved utilizing other geometrical relations. Compared to more traditional least squares interpolation approach the presented procedure can very quickly provide the approximate results. If necessary, these data could serve as a good initial approximation for subsequent optimization.

Acknowledgement

The kind support of the Czech Scientific Foundation No. GA CR 15-01035S and RVO 68378297 institutional support are gratefully acknowledged.

References

Miles, J.W. (1984) Resonant motion of spherical pendulum, Physica D, 11, 309–323

Miles J.W. (1962),Stability of forced oscillations of a spherical pendulum. Quarterly Journal of Applied Mathematics, 20 21–32.

Náprstek J. & Fischer C. (2009) Auto-parametric semi-trivial and post-critical response of a spherical pendulum damper, Computers and Structures, 87, 19–20, pp. 1204–1215, 2009

Náprstek J. & Fischer C. (2013) Types and stability of quasi-periodic response of a spherical pendulum, Computers and Structures, 124, 8, 74 – 87.

Petrov A.G. (2005) On the equations of motion of a spherical pendulum with a fluctuating support, Doklady - Physics, 50, 11, pp. 588–592.

Pospíšil S., Fischer C. & Náprstek J. (2014) Experimental analysis of the influence of damping on the resonance behavior of a spherical pendulum, Nonlinear Dynamics, 78, 1, pp. 371–390.

Rutter J.W. (2000) Geometry of Curves, CRC Press, 2000.

Tritton D.J. (1986) Ordered and chaotic motion of a forced spherical pendulum, European Journal of Physics. 7, 162–169.

22nd International Conference
ENGINEERING MECHANICS 2016
Svratka, Czech Republic, 9 – 12 May 2016

THE STEEL CORE COVERED BY REINFORCED CONCRETE IN THE COMPOSITE STEEL-CONCRETE COLUMNS

J. Frólo[*], Š. Gramblička[**]

Abstract: *Design of the composite steel concrete columns with the massive solid steel profiles, called steel cores, is not covered in Eurocode 4 by using of simplified design method. Reasons are related to the problems about the residual stresses arising during the fabrication process of the solid steel profile and strain limitation in concrete section of the column. The available results of German research gives recommendations to design the composite steel concrete columns with the section of the concrete filled tubes with the central steel core according to Eurocode 4. Studies of the composite steel-concrete columns with the section of the steel core covered by reinforced concrete have not been covered in this research. This paper deals with the experimental and numerical analysis of this type unverified columns. 6 columns were tested with column lengths of 3.85 m and 3.0 m. Description and results of the experimental analysis are given. Numerical analysis consists of calibrated 3D models in the FEM program ATENA 3D with the conformity to the results of the experimental study. Presently these calibrated models are used as a background for the analysis of the columns with the variable geometrical and material modifications.*

Keywords: Composite steel-concrete column, steel core, experimental study, resistance, imperfection

1. Introduction

The solid steel profile, called steel core too, can increase the plastic axial stiffness significantly of the section of the composite steel-concrete column. Column with the steel core reaches higher resistance by higher slenderness. High resistance and high slenderness are the most required structural and architectural attributes for the columns of high-rise buildings. In general, there are two basic section-types of the composite steel-concrete columns with steel core:

- concrete filled steel tube with central steel core (Fig.1a),
- steel core covered by the reinforced concrete (Fig.1b).

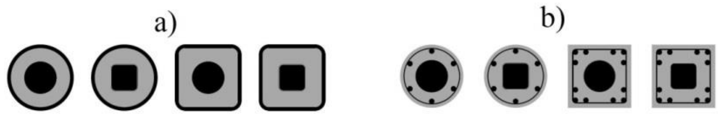

Fig. 1: Section-types of composite steel-concrete columns with steel core.

Design of the composite steel-concrete columns with steel core is not covered in actual standard Eurocode 4 by using of simplified method because of two reasons. Residual stresses in the section of the steel core, which arise during its fabrication process (Roik, 1980) and strain limitation in concrete. German research has given recommendations for design of the steel-concrete columns with the section of concrete filled steel tubes with central steel core (Fig.1a) according to Eurocode 4. These recommendations are based on close experimental and numerical analysis, where the main studied parts are reduction factor of the plastic bending resistance α_M, initial bow imperfection and buckling curve (Lippes, 2008). This paper deals with experimental and numerical analysis on the composite steel-concrete columns with the section of the steel core covered by reinforced concrete (Fig.1b). Our research should lead to recommendation for safe and economical design of the columns with section according to Fig.1b by using the simplified design method of the Eurocode 4.

[*] Ing. Juraj Frólo: Department of Concrete Structures and Bridges, Faculty of Civil Engineering, Slovak University of Technology in Bratislava, Radlinského 11; 810 05, Bratislava; SK, juraj.frolo@stuba.sk

[**] Doc. Ing. Štefan Gramblička, PhD.: Department of Concrete Structures and Bridges, Faculty of Civil Engineering, Slovak University of Technology in Bratislava, Radlinského 11; 810 05, Bratislava; SK, stefan.gramblicka@stuba.sk

2. Experimental analysis

2.1. Description of experimental tests

Experimental analysis included fabrication and tests of 6 specimens of columns divided into 2 length series. S1-serie consisted of 3 columns by length of 3.85 m with the relative slenderness $\overline{\lambda}$ =1.37. S2-serie consisted of 3 columns by length of 3.0 m with the relative slenderness $\overline{\lambda}$ =1.06. The assumed resistances and cross-section of columns are shown in Fig.2. Columns were concreted in vertical position.

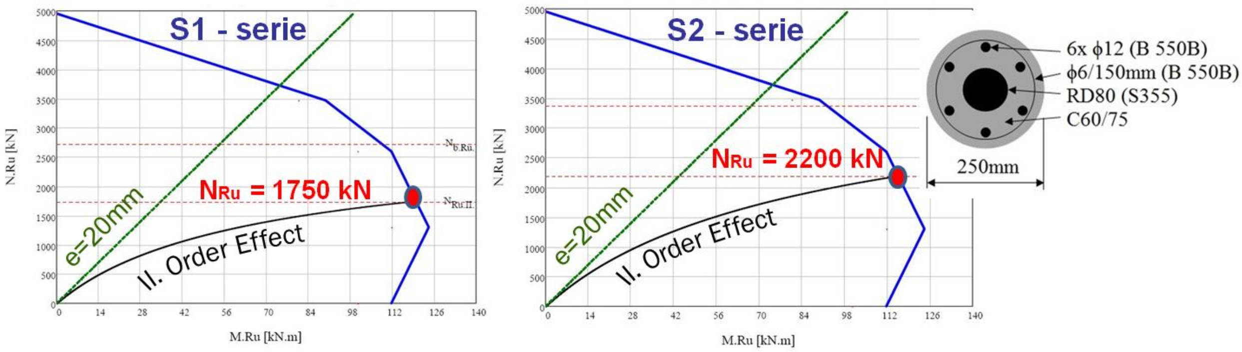

Fig. 2: The assumed ultimate resistances and cross-section of columns series S1 and S2.

First of all geometrical imperfection were measured and material tests were performed before load tests of columns. Measured geometrical imperfections were from 0.15 mm to 2.51 mm. The concrete cylinder strength was 63.9 MPa, the yield strength of reinforcement was 548.7 MPa and the yield strength of steel cores was 327.3 MPa. Measuring system of columns consisted of strain gauges on the steel core, strain gauges on concrete, mechanical strain measuring on concrete, measuring of deflections and measuring of depression of testing system between top and bottom of column. Force was received from the hydraulic cylinder machine. The columns were hinge-supported in the hydraulic cylinder machine with axial eccentricity of 20 mm. The columns were subjected to short-term load tests. Each test was performed by increasing and decreasing load steps with taking into account stabilizing deformation between individual load steps. This loading process should take into account slight influence of long-term loads, negative influence of irreversible effects like irreversible deflection and it should lead to earlier failure of column.

2.2. Results of experimental study

All columns failed approximately in middle of the length (Fig. 3) during the holding constant load by uncontrollable increasing of deflection, known as second order effect. Measurement results suggest that all failures were caused by run out of the concrete capacity. Before each failure the strain was about 3.5‰ in compression zone of concrete cross-section. Strains of column cross-section in the middle of the length are shown in Fig. 4b. Ultimate resistance of each column is shown in Tab. 1.

Fig. 3: a) The column before test; b) the column after failure; c), d) the detail of column failure

Tab. 1: Measured geometrical imperfections, experimental resistances and deflections of columns.

	Length L [m]	Relative slender-ness $\bar{\lambda}$ [-]	Measured geometrical imperfection w_0 [mm]	Eccentricity of axial force e_0 [mm]	Assumed axial resistance N_{Ra} [kN]	Ultimate axial resistance N_{Ru} [kN]	Ultimate deflection w_u [mm]	Accuracy N_{Ra} / N_{Ru}
S1.1	3.85	1.37	1.09	20	**1 734**	**1 829**	**34.7**	**95%**
S1.2			0.15		**1 756**	**1 811**	**41.1**	**97%**
S1.3			2.51		**1 703**	**1 777**	**40.4**	**96%**
S2.2	3.0	1.06	1.04		**2 207**	**2 294**	**23.5**	**96%**
S2.3			0.99		**2 209**	**2 292**	**24.8**	**96%**

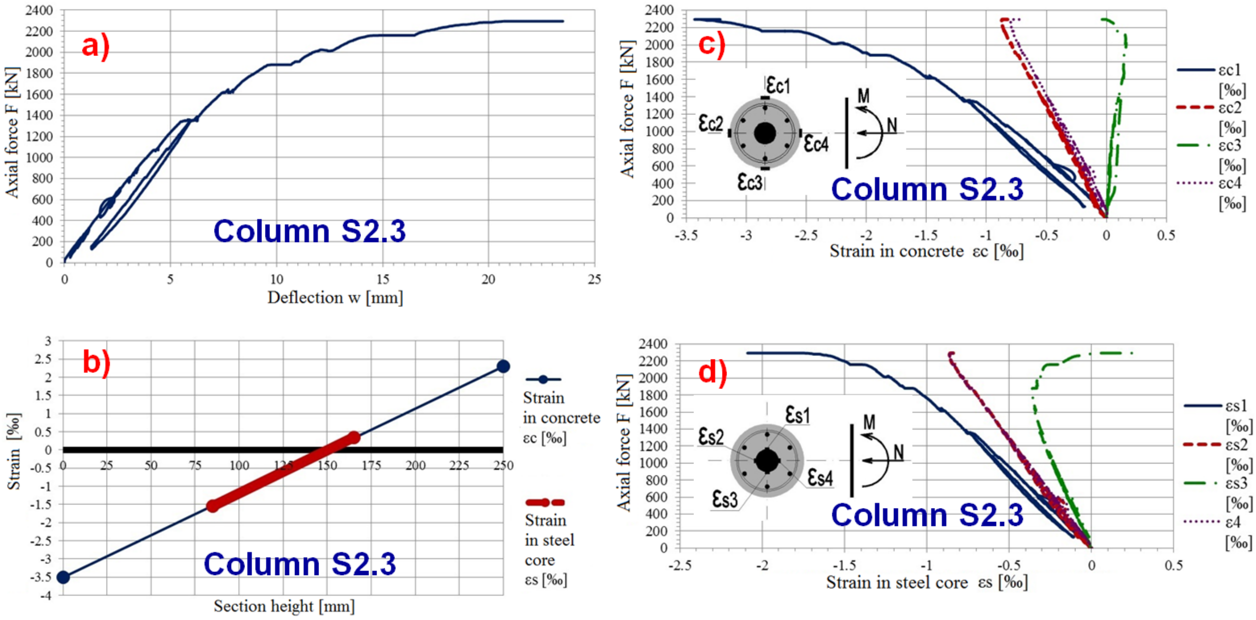

Fig. 4: Recordings during the test of column S2.3: a) deflection; b) strain in the section before failure; c) strain on the concrete surface; d) strain on the steel core surface.

3. Numerical analysis

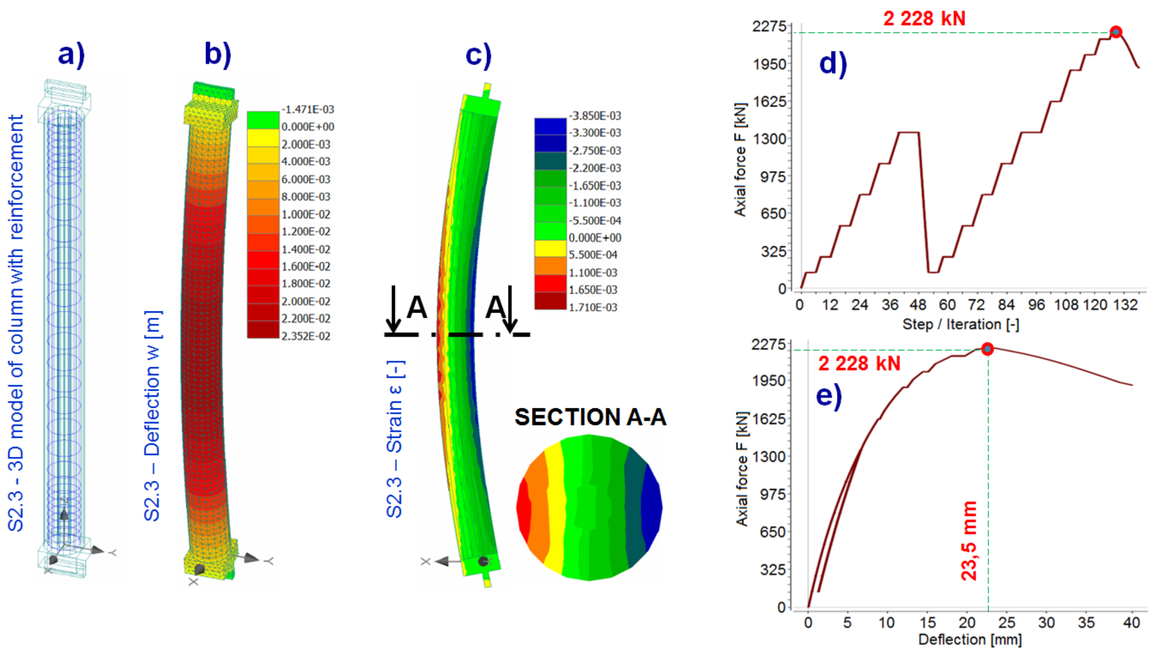

Fig. 5: Column S2.3 in ANTENA 3D: a) 3D model with reinforcement; b) deformed 3D model; c) strain in the column before failure; d) load steps, e) deflection during the load steps.

Numerical analysis was performed by nonlinear FEM calculation with 3D models by software ATENA 3D. Each column was modeled with same geometrical dimensions, material properties and boundary conditions as columns in experimental part. Geometrical imperfection was taken into account by additional eccentricity w_0 to basic eccentricity e_0. Load steps were defined the same as load steps in experimental tests. Model calibrations were based on optimizing the mash of 3D elements in order to reach the closest results to experimental results. Results comparison between experimental and numerical analysis is shown in Tab. 2. Calibrated models are presently used as a background for further analysis of the columns with various geometrical and material modifications. Columns with variable relative slenderness have been calculated yet. These columns are of the same material and section properties and boundary conditions as columns S1.1-S2.3.

Tab. 2: Results comparison between experimental and numerical analysis.

	L [m]	w_0 [mm]	e_0 [mm]	Experiment. ultimate axial resistance $N_{Ru,EPX}$ [kN]	Numerical ultimate axial resistance $N_{Ru,NUM}$ [kN]	Accuracy $N_{Ru,NUM}$ / $N_{Ru,EXP}$	Experiment. ultimate deflection $w_{u,EXP}$ [mm]	Numerical ultimate deflection $w_{u,NUM}$ [mm]	Accuracy $w_{u,NUM}$ / $w_{u,EXP}$
S1.1		1.09		**1 829**	**1 754**	**96%**	**34.7**	**31.1**	**90%**
S1.2	3.85	0.15		**1 811**	**1 797**	**99%**	**41.1**	**30.4**	**74%**
S1.3		2.51	20	**1 777**	**1 686**	**95%**	**40.4**	**33.8**	**84%**
S2.2	3.0	1.04		**2 294**	**2 226**	**97%**	**23.5**	**23.3**	**99%**
S2.3		0.99		**2 292**	**2 228**	**97%**	**24.8**	**23.5**	**95%**

Tab. 3: Results of numerical analyzed columns with variable relative slenderness.

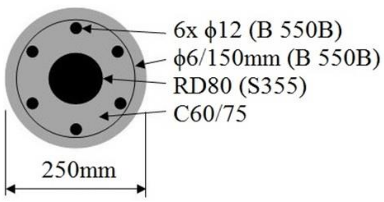

Relative slenderness $\bar{\lambda}$ [-]	Buckling length L_{cr} [m]	Basic eccentricity of axial force e_0[mm]	Ultimate axial resistance N_{Ru} [kN]	Ultimate deflection w_u [mm]
0.2	0.66		**4 217**	**1.72**
0.5	1.65		**3 323**	**6.70**
1.0	3.29	20	**2 277**	**17.60**
1.5	4.93		**1 361**	**33.61**
2.0	6.58		**880**	**37.48**

4. Conclusion

Experimental tests have been performed and numerical 3D models have been calibrated in research of the composite steel-concrete columns with the steel core covered by reinforced concrete. Presently columns with variable material and geometrical modification are investigated. The columns with steel cores of dimension size over 100 mm will be investigated with the influence of residual stresses in the section of massive steel profile. From new available evaluated research we conclude the necessary adjustment for tested and analyzed type of composite steel-concrete columns for design them according to Eurocode 4 by using the simplified design method.

Acknowledgement
This contribution was prepared with the financial support of Slovak Grant Agency VEGA 1/0696/14.

References

EN 1994-1-1 Design of composite steel and concrete structures, Part 1-1 General rules and rules for buildings, (2004)

Lippes, M.(November 2008), Zur Bemessung von Hohlprofil – Verbundstutzen aus hochfesten Stahlen und Betonen. Institut für Konstruktiven Ingenieurbau Bergische Universität Wuppertal

Roik, K. & Schaumann, P. (1980), Tragverhalten von Vollprofilstutzen – Fliesgrenzenverteilung an Vollprofilquerschnitten, Institut für Konstruktiven Ingenieurbau, Ruhr-Universität Bochum

22nd International Conference
ENGINEERING MECHANICS 2016
Svratka, Czech Republic, 9 – 12 May 2016

THEORY, EXPERIMENT AND NUMERICAL APPROACH FOR THE BEAM RESTED ON NONLINEAR ELASTIC FOUNDATION

K. Frydrýšek[*], Š. Michenková[**]

Abstract: *This work presents theory, approximations of experiments and numerical approaches suitable for the solution of straight plane beams rested on an elastic (Winkler's) foundation. The nonlinear dependence of the reaction force can be described via bilateral tangent-linear or secant-linear or nonlinear (linear + arcus tangent) approximations. These applications lead to linear or nonlinear differential equations of 4th-order (Central Difference Method, Newton-Raphson Method).*

Keywords: Elastic foundation, Beam, Central Difference, Nonlinearity, Experiment.

1. Introduction

Beams on elastic foundations are frequently used in the practice. In mechanics, the beam is described by differential equation $\frac{d^4v}{dx^4} - \frac{q_R}{EJ_{ZT}} = 0$, where $v = v(x)$ [m] is deflection of the beam, E [Pa] is the modulus of elasticity of the beam, J_{ZT} [m^4] is the major principal second moment of the beam cross-section and $q_R = q_R(x, v, ...)$ [Nm^{-1}] is the nonlinear reaction force in the foundation (Frydrýšek et al. 2013; Frydrýšek et al. 2014). Our work focuses on the solution of straight 2D beams on an elastic foundation with nonlinear behaviour (evaluation of experiments, curve fitting). For typical cases, the linear Bernouli's beam theory is coherent with nonlinear response of reaction force in foundation.

2. Evaluation of Experiment

The methodology for measuring of elastic foundation applied in this paper is based on the pressing of a beam into the foundation; see Fig. 1, Table 1 and reference (Klučka et al., 2014)) (i.e. dependence $q_R = q_R(v)$ which is based on the foundation load-settlement behaviour is evaluated and approximated).

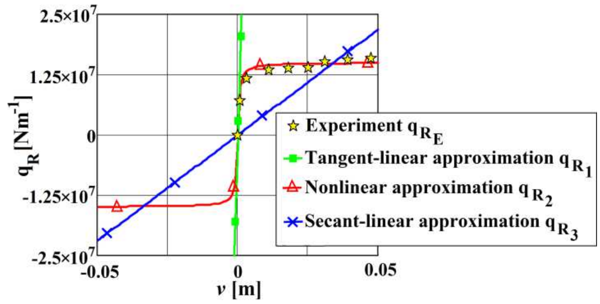

Fig. 1: Dependence of reaction force on deflection (i.e. foundation load-settlement behavior for a sand) - experiment and its suitable linear and nonlinear approximations.

The measured nonlinear behaviour of reaction force on displacement in the foundation (i.e. dependence $q_R = q_{R_E}$) can be approximated by bilateral tangent-linear q_{R_1} or bilateral nonlinear q_{R_2} or bilateral secant-linear q_{R_3} functions; see Table 1 and Fig. 1. From Fig. 1, in comparing with

[*] Assoc. Prof. M.Sc. Karel Frydrýšek, Ph.D.: Department of Applied Mechanics, Faculty of Mechanical Engineering, VSB-Technical University of Ostrava; 17. listopadu 15/2172; 708 33, Ostrava; Czech Republic, karel.frydrysek@vsb.cz

[**] M.Sc. Šárka Michenková: Department of Applied Mechanics, Faculty of Mechanical Engineering, VSB-Technical University of Ostrava; 17. listopadu 15/2172; 708 33, Ostrava; Czech Republic, sarka.michenkova@vsb.cz

experiment, the best curve fitting is performed via nonlinear behaviour of foundation prescribed by function $\mathrm{q_{R_2}} = k_1 v + k_a \mathrm{arctg}(c_a v)$.

Tab. 1: Approximations for reaction forces in the foundation.

Description	Constants:
Tangent-linear approx.: $\mathrm{q_{R_1}} = k_1 v$, linear diff. equation $\frac{d^4v}{dx^4} - \frac{k_1 v}{EJ_{ZT}} = 0$. Good fitting for small values of v.	k_1=1.7422×10^{10} Nm^{-2}, k_a=0 Nm^{-2}, c_a=0 m^{-1}.
Nonlinear approx.: $\mathrm{q_{R_2}} = k_1 v + k_a \mathrm{arctg}(c_a v)$, nonlinear diff. equation $\frac{d^4v}{dx^4} - \frac{k_1 v + k_a \mathrm{arctg}(c_a v)}{EJ_{ZT}} = 0$. Good fitting for all values of v (i.e. the closest to the experiment).	k_1=5.21×10^5 Nm^{-2}, k_a=9.52×10^6 Nm^{-2}, c_a=1.83×10^3 m^{-1}.
Secant-linear approx.: $\mathrm{q_{R_3}} = k_1 v$, linear diff. equation $\frac{d^4v}{dx^4} - \frac{k_1 v}{EJ_{ZT}} = 0$. Good fitting for bigger values of v.	k_1=4.3866×10^8 Nm^{-2}, k_a=0 Nm^{-2}, c_a=0 m^{-1}.

3. Central Differences

The FEM is frequently used for solutions of nonlinear problems. However, in this article, the central differences (CD) are applied for their easy derivation of problem. The CD proceed by replacing the derivatives $v_{\mathrm{i}}^{(1)}$, $v_{\mathrm{i}}^{(2)}$, $v_{\mathrm{i}}^{(3)}$ and $v_{\mathrm{i}}^{(4)}$ in the differential equations at the point "i" with step $\Delta = \frac{\mathrm{L}}{\mathrm{n}}$ [m], where L [m] is length and n [1] is number of divisions. Hence, $v_{\mathrm{i}}^{(1)} = \frac{dv}{dx} \approx \frac{v_{\mathrm{i+1}} - v_{\mathrm{i-1}}}{2\Delta}$, $v_{\mathrm{i}}^{(2)} = \frac{d^2v}{dx^2} \approx \frac{v_{\mathrm{i+1}} - 2v_{\mathrm{i}} + v_{\mathrm{i-1}}}{\Delta^2}$, $v_{\mathrm{i}}^{(3)} = \frac{d^3v}{dx^3} \approx \frac{v_{\mathrm{i+2}} - 2v_{\mathrm{i+1}} + 2v_{\mathrm{i-1}} - v_{\mathrm{i-2}}}{2\Delta^3}$, $v_{\mathrm{i}}^{(4)} = \frac{d^4v}{dx^4} \approx \frac{v_{\mathrm{i+2}} - 4v_{\mathrm{i+1}} + 6v_{\mathrm{i}} - 4v_{\mathrm{i-1}} + v_{\mathrm{i-2}}}{\Delta^4}$, see Jones, 1997 and Frydrýšek et al., 2014.

4. Solved Example and its Boundary Conditions

The beam of length 2L with cross-section b×h=0.2×0.4 m^2 is resting on an elastic foundation and loaded by force F = 7×10^6 N; see Fig. 2. Beam properties are E = 2×10^{11} Pa, $J_{ZT} = \frac{\mathrm{bh}^3}{12} = \frac{0.2 \times 0.4^3}{12}$ m^4. Foundation properties are described as an evaluation of experiment in Tab. 1. The beam is symmetrical (i.e. it is sufficient to solve ½ of the beam $x \epsilon \langle 0; \mathrm{L} \rangle$). Hence, the beam is described by the equation

$$\frac{d^4v}{dx^4} - \frac{k_1 v + k_a arctg(c_a v)}{EJ_{ZT}} = 0. \qquad (1)$$

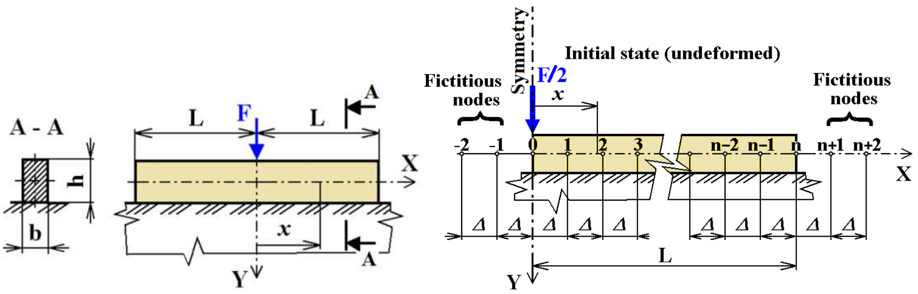

Fig. 2: Beam of length 2L resting on an elastic foundation and loaded by force F and divisions of the beam (CDM – one half of the beam).

From the boundary conditions prescribed in points x = 0 m and x = L follow equations

$$\left.\begin{aligned} &\frac{dv(x=0)}{dx} = 0, \\ &T(x=0) = -\frac{\mathrm{F}}{2} => -EJ_{ZT}\frac{d^3v(x=0)}{dx^3} = -\frac{\mathrm{F}}{2} => \frac{d^3v(x=0)}{dx^3} = \frac{\mathrm{F}}{2EJ_{ZT}}, \\ &M_o(x=\mathrm{L}) = 0 => -EJ_{ZT}\frac{d^2v(x=\mathrm{L})}{dx^2} = 0 => \frac{d^2v(x=\mathrm{L})}{dx^2} = 0, \\ &T(x=\mathrm{L}) = 0 => -EJ_{ZT}\frac{d^3v(x=\mathrm{L})}{dx^3} = 0 => \frac{d^3v(x=\mathrm{L})}{dx^3} = 0, \end{aligned}\right\} \qquad (2)$$

where $T(x)$ [N] is shearing force and $M_o(x)$ [Nm] is bending moment.

5. Solved Example and Central Difference Method (CDM)

The beam and its surroundings can be divided into n+5 nodes "i"; see Fig. 2. Denote for simplicity $b = \frac{F\Delta^3}{EJ_{ZT}}$, $a_1 = \frac{k_1\Delta^4}{EJ_{ZT}}$, $a_2 = \frac{k_a\Delta^4}{EJ_{ZT}}$ and $c = 6 + a_1$. Boundary conditions (2) can be approximated by CD, for node "0" (i.e. $\mathrm{i} = 0, x = 0$) and for node "n" (i.e. $\mathrm{i} = \mathrm{n}, x = \mathrm{L}$) as

$$\left.\begin{aligned} \frac{v_{\mathrm{i}+1}-v_{\mathrm{i}-1}}{2\Delta} = 0 &=> v_1 - v_{-1} = 0, \\ \frac{v_{\mathrm{i}+2}-2v_{\mathrm{i}+1}+2v_{\mathrm{i}-1}-v_{\mathrm{i}-2}}{2\Delta^3} = \frac{\mathrm{F}}{2EJ_{ZT}} &=> v_2 - 2v_1 + 2v_{-1} - v_{-2} = b,, \\ \frac{v_{\mathrm{i}+1}-2v_{\mathrm{i}}+v_{\mathrm{i}-1}}{\Delta^2} = 0 &=> v_{\mathrm{n}+1} - 2v_{\mathrm{n}} + v_{\mathrm{n}-1} = 0, \\ \frac{v_{\mathrm{i}+2}-2v_{\mathrm{i}+1}+2v_{\mathrm{i}-1}-v_{\mathrm{i}-2}}{2\Delta^3} = 0 &=> v_{\mathrm{n}+2} - 2v_{\mathrm{n}+1} + 2v_{\mathrm{n}-1} - v_{\mathrm{n}-2} = 0. \end{aligned}\right\} \tag{3}$$

Similarly, differential equation (1) can be approximated via CD for q_{R_1}, q_{R_2} and q_{R_3} as

$$v_{\mathrm{i}-2} - 4v_{\mathrm{i}-1} + (6 + a_1)v_{\mathrm{i}} - 4v_{\mathrm{i}+1} + v_{\mathrm{i}+2} + a_2\mathrm{arctg}(c_a v_{\mathrm{i}}) = 0, \quad \mathrm{i} = 0,2, \ldots, \mathrm{n}, \tag{4}$$

Now, the variables v_{-2}, v_{-1}, $v_{\mathrm{n}+1}$ and $v_{\mathrm{n}+2}$ (i.e. results in fictitious nodes -2, -1, n+1 and n+2, see Fig. 2) can be expressed from boundary conditions (3). Hence the set of nonlinear equations can be written in the matrix form as

$$f_i = [\mathrm{M}]\{v\} + a_2\mathrm{arctg}(c_a\{v\}) - \{\mathrm{b}\} = 0, \tag{5}$$

where

$$[\mathrm{M}] = \begin{bmatrix} c & -8 & 2 & 0 & 0 & 0 & 0 & \ldots & 0 \\ -4 & 7+a_1 & -4 & 1 & 0 & 0 & 0 & \ldots & 0 \\ 1 & -4 & c & -4 & 1 & 0 & 0 & \ldots & 0 \\ 0 & 1 & -4 & c & -4 & 1 & 0 & \ldots & 0 \\ \vdots & \vdots & \vdots & \vdots & \ddots & \vdots & \vdots & \ldots & \vdots \\ 0 & \ldots & 0 & 1 & -4 & c & -4 & 1 & 0 \\ 0 & \ldots & 0 & 0 & 1 & -4 & c & -4 & 1 \\ 0 & \ldots & 0 & 0 & 0 & 1 & -4 & 5+a_1 & -2 \\ 0 & \ldots & 0 & 0 & 0 & 0 & 2 & -4 & 2+a_1 \end{bmatrix}, \{b\} = \begin{Bmatrix} b \\ 0 \\ \vdots \\ 0 \end{Bmatrix}, \{v\} = \begin{Bmatrix} v_0 \\ v_1 \\ \vdots \\ v_n \end{Bmatrix} \tag{6}$$

6. Iterative Approach and Solutions

The system of coupled nonlinear equations can be solved iteratively via Newton–Raphson Method as

$$\left\{{}^{\langle \mathrm{j}+1\rangle}v\right\} = \left\{{}^{\langle \mathrm{j}\rangle}v\right\} - \left[{}^{\langle \mathrm{j}\rangle}\mathrm{J}\right]^{-1}\left\{[\mathrm{M}]\left\{{}^{\langle \mathrm{j}\rangle}v\right\} + a_2\mathrm{arctg}\left(c_a\left\{{}^{\langle \mathrm{j}\rangle}v\right\}\right) - \{\mathrm{b}\}\right\}, \tag{7}$$

where vectors $\left\{{}^{\langle \mathrm{j}+1\rangle}v\right\}$ and $\left\{{}^{\langle \mathrm{j}\rangle}v\right\}$ are new and old iterations and matrix $\left[{}^{\langle \mathrm{j}\rangle}\mathrm{J}\right] = \left(\frac{\partial f_{\mathrm{i}}}{\partial\, {}^{\langle \mathrm{j}\rangle}v_{\mathrm{k}}}\right)_{\mathrm{i,k}=0,1,2,\ldots,\mathrm{n}}$ is the Jacobian matrix. Some results are presented in Fig. 3.

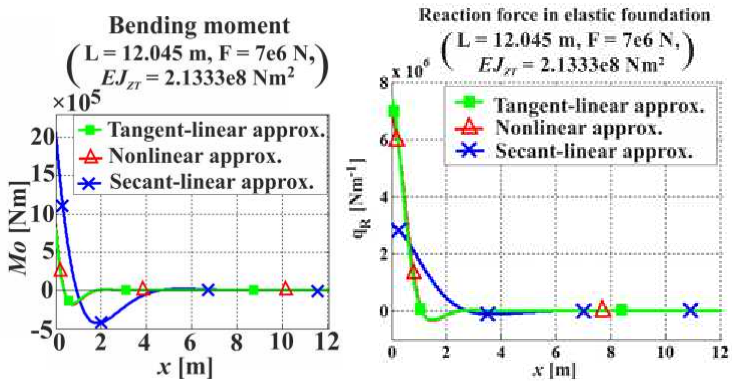

Fig. 3. Dependence for bending moment and distributed reaction forces on coordinate x of the beam for different types of foundation approximations.

The differences between the linear and nonlinear approximations are evident.

7. Conclusions

The use of an elastic foundation including nonlinearities is a suitable way of performing numerical/experimental modelling of engineering problems in the branch of mechanics and biomechanics; see some applications in references (Frydrýšek et al., 2013). Our team is in the process of application of elastic foundation as a suitable simplification of the complicated interaction between implants and bones in traumatology and orthopaedics, see Fig. 4.

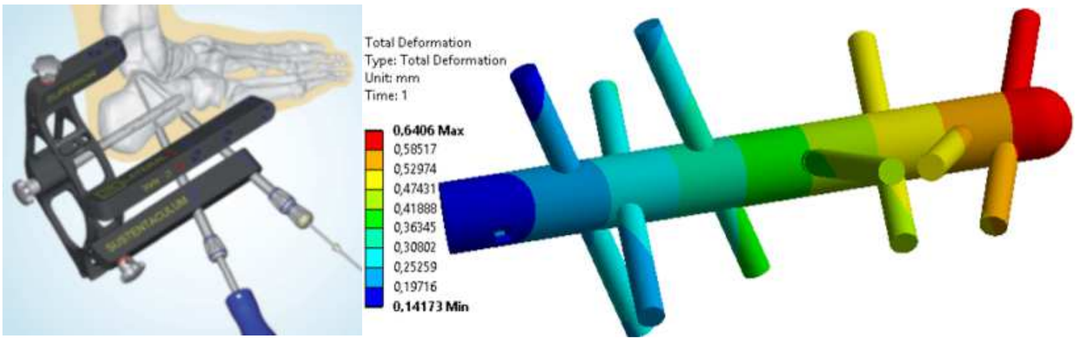

Fig. 4. The intramedullary nail C-NAIL for minimal-invasive fixation of intraarticular calcaneal fractures (application of FEM and evaluation as structures on elastic foundation).

The derivation, rapid solutions and application of our own simple numerical model based on the Central Difference Method (CDM) open up a new avenue for further applications using a stochastic approach (i.e. millions of solutions with random inputs). The Simulation-Based Reliability Assessment Method (i.e. the direct Monte Carlo approach) can be applied. For more information see (Frydrýšek et al., 2013; Marek et al., 1995).

This work is a continuation of our previous work. The measured material properties of the elastic foundation were evaluated and approximated in three ways (via bilateral tangent-linear, bilateral nonlinear and secant-linear functions). Beams on elastic linear/nonlinear foundations were solved via CDM and Newton's (Newton-Raphson) Method.

Theory, experiment, CDM and numerical approach are exposed for the beams rested on linear/nonlinear foundations. The best approximation is the bilateral nonlinear function $\mathrm{q}_{\mathrm{R}_2} = k_1 v + $ $+ k_a \mathrm{arctg}(c_a v)$.

Acknowledgement

The authors gratefully acknowledge the funding from the Czech projects TA03010804 "Osteosynthesis of Leg and Arm Fractures" and SP2016/145.

References

Frydrýšek, K., Michenková, Š. & Nikodým, M. (2014) Straight Beams Rested on Nonlinear Elastic Foundations – Part 1 (Theory, Experiments, Numerical Approach). In: Applied Mechanics and Materials. Volume 684, Trans Tech Publications, Switzerland, pp. 11-20.

Frydrýšek. K., Tvrdá, K., Jančo, R., et al. (2013) Handbook of Structures on Elastic Foundation. VŠB - Technical University of Ostrava, Ostrava, pp. 1-1691.

Jones, G. (1997) Analysis of Beams on Elastic Foundations Using Finite Difference Theory. Thomas Telford Publishing, London, pp.164.

Klučka, R., Frydrýšek, K. & Mahdal, M. (2014) Measuring the Deflection of a Circular Plate on an Elastic Foundation and Comparison with Analytical and FE Approaches. In: Applied Mechanics and Materials, Trans Tech Publications, Switzerland, Vol. 684, pp 407-412.

Marek, P., Guštar, M. & Anagnos, T. (1995) Simulation-Based Reliability Assessment for Structural Engineers, CRC Press, Boca Raton, USA, pp.365.

22nd International Conference
ENGINEERING MECHANICS 2016
Svratka, Czech Republic, 9 – 12 May 2016

USE AND EFICIENCY OF MULTIPLE MASS DAMPERS IN CONSTRUCTION FOUNDATIONS

I. Gołębiowska*, M. Dutkiewicz**

Abstract: *In the first part of the paper an overview of methods for vibration reduction of construction is presented from the point of solutions of dampers, as well as excitation of dynamic harmonic and seismic forces. In the second part of the paper the vibration of circle foundation under the harmonic excitation is analyzed. The spring-mass system is attached to the foundation. The horizontal and rotational vibrations of rigid foundation is analyzed. Foundation rests on the elastic half space. Based on the theory of body resting on the half space under dynamic excitation, the problem is described by means of differential and then matrix equation. The effects of reduction of foundation vibration are studied in detail. Several plots of the amplitude deflections of the foundation are also given and discussed.*

Keywords: Multiple mass dampers, tuned vibrations, dynamic absorbers.

1. Introduction

Technological progress and needs of civil engineering development in the area of dynamic excitations: seismic, para-seismic loads cause searching methods and means of protection building objects against vibration. Considerable attention has been paid to researches of effectiveness of multiple mass dampers. Snowdon J.C. (1974) summarize methods in order to reduce level of vibrations such as removal of vibration source, balancing, aligning of device resting on the foundation, modification of technological process, sliding of devices producing vibrations in a distance from object sensitive to vibrations, increasing base stiffness, active, semi-active, passive, hybrid vibration isolation, application of passive, active, semi-active, hybrid dynamic dampers, use of passive, active, semi-active, hybrid bracing. Cox S.J.(1998), Soong T.T., Spencer B.F. (2002) and Soong T.T., Constantinou M.C. (1993) in their researches showed wide application of dynamical protection of structure in civil engineering. What is important in practice vertical or sloping trenches filled with isolation materials are applied to protect structures against seismic or para-seismic excitation. Reducing of propagation of surface waves is possible by covering the base surface with dynamical vibrations dampers, as well Nashif A., Johes D., Henderson J. (1985) presented the direction of development of reduction vibrations. A well accepted strategy in utilizing dynamic control systems is based on the increase of structural damping. As a first idea damping devices can be installed. Then, they have the task to damp the relative motion between two structures, two parts of the same structure, or the structure and the 'rigid' vicinity. The damping effects may be obtained by friction, plastic deformation or viscose behavior inside the device. The protection of the environment from vibrations is a priority requirement to be achieved. Methods of vibration reduction using absorbers are an effective way to reduce vibrations, which was presented among others at work Warburton G.B. (1982). The problem of vibration of structural systems and their reduction was analyzed in terms of the seismic excitation. In the papers of Dutkiewicz M. (2005) and Dutkiewicz M. (2006) is shown the effectiveness of the reduction of such vibrations model stamp and beams under seismic excitation.

2. Horizontal and rotational vibrations of foundation with multiple tuned mass damper

* Prof. Dr Eng. Irena Gołębiowska: Department of Building Construction, University of Technology and Life Sciences in Bydgoszcz, ul. Prof. S. Kaliskiego 7, 85-796 Bydgoszcz, Poland; tel.: +48 052 340 85 79, fax: +48 052 340 82 25; e-mail: igolebio@utp.edu.pl
** Dr Eng. Maciej Dutkiewicz: Department of Building Construction, University of Technology and Life Sciences in Bydgoszcz, ul. Prof. S. Kaliskiego 7, 85-796 Bydgoszcz, Poland; tel.: +48 510 035 090, fax: +48 052 340 82 25; e-mail: macdut@utp.edu.pl

Application of dynamic dampers in order to reduce vibration foundations for the machine or reduce the harmful effects of vibration transmitted on structures and buildings was the subject of research of Szwec H.S., Sedin W.Ł., Kiriczek A. (1987) and Gołębiowska I, Dutkiewicz M. (1999). Dynamic damper can be used both at the design stage as well as on the existing foundations. Efficiency one mass dynamic dampers for vibration foundations, resting directly on the ground floor, loaded with harmonic forcing limited unstable frequency was investigated by Korieniew B. G., Reznikow L. M. (1988). Foundations rest on the ground, have an increased damping properties. This is most evident with the vibration of vertical and horizontal vibrations, regardless of the adopted model, describing the deformable surface. In such situations, the effectiveness one mass vibration dampers may be insufficient, particularly in the case where the forcing frequency is unstable. The frequency narrow-band dampers can be removed using eg. multiple mass damper (MMD). The issue of the use of MMD to reduce vibration massive foundation is still insufficiently explored. In this section the use of MMD for horizontal and rotational vibrations is analysed

This analytical analysis can be useful as computational schemes of foundations of many real objects, eg. foundations for antennas and chimneys, have a circular base, besides the circular base of the foundation may be accepted also as a result of approximation of the foundations of other complex geometric form.

2.1. Assumptions

Horizontal and rotational vibrations of foundation equipped with two mass damper were analysed. Foundation with the circle basement rests on the spring half space. Two cases of excitation are analyzed: horizontal harmonic force and rotational momentum. The effectiveness of tuned mass damper fixed to foundation is studied.

The differential equation of motion can be written in the form:

$$M\ddot{X} + C\dot{X} + KX = P(t) \tag{1}$$

where M, C, K represent the mass, damping and stiffness matrices, respectively. P(t) is force excitation, in the first part of analyses is a horizontal harmonic force, in the second part of analysis is the harmonic momentum.

The following non-dimensional parameters are defined as:

$$\xi_k = \frac{k}{2m_0\omega_0}, \quad \xi_c = \frac{c}{2m_0\omega_0} \quad \mu_1 = \frac{m_1}{m_0}, \quad \mu_2 = \frac{m_2}{m_1}, \quad M_0 = \frac{m_0}{\rho_0 R^3}, \quad g = \frac{\nu}{\omega_0}, \quad k_c = R\nu\sqrt{\frac{\rho}{G}}$$

m_0 – mass of the foundation, m_1 is the first mass damper, m_2 is the second mass damper, k,c are parameters of the damping system, ρ is the density of the half space, R is the radius of the circle foundation, υ is force frequency, G is the shear frequency of the half space,

μ_1 ratio of masses of the TMDs on the first level to the main mass,

μ_2 ratio of masses of the TMDs on the second level to the main mass. In above expressions ω_0 is the natural frequency

The equations of dynamic equilibrium of the horizontal vibration stamp have a similar form to that of the vertical vibration, except that the coefficients γ and δ depending on dimensionless force frequency and shear modulus.

2.2. Horizontal vibrations

Selection of the optimum parameters of dynamic vibration dampers in case of horizontal vibrations of foundation was carried out in such a way as to obtain reducing vibration amplitudes in the greatest band without exceeding the allowable predetermined value of amplitude. As a result, the optimum parameters for the horizontal vibrations were found for m_0 = 25; A_{1max} = 4.9715, for one mass damper μ_1=0,075, $\xi_{k,1}$= 0,472, $\xi_{c,1}$= 0,472 and for two mass damper is μ_1=0,075, μ_2=0,0375 $\xi_{k,1}$= 0,486, $\xi_{c,1}$= 0,105,

$\xi_{k,2} = 0{,}493$, $\xi_{c,2} = 0{,}146$. The effectiveness of the one- and two mass damper in case of horizontal vibrations of the foundation is illustrated in figure 1. The use of the one mass damper provides the reducing of the maximum amplitude by 12% in relation to amplitude of vibration of foundation without the damper and by 25% in case with two mass damper. The wide band frequency in which the vibration amplitude reaches the similar values is achieved.

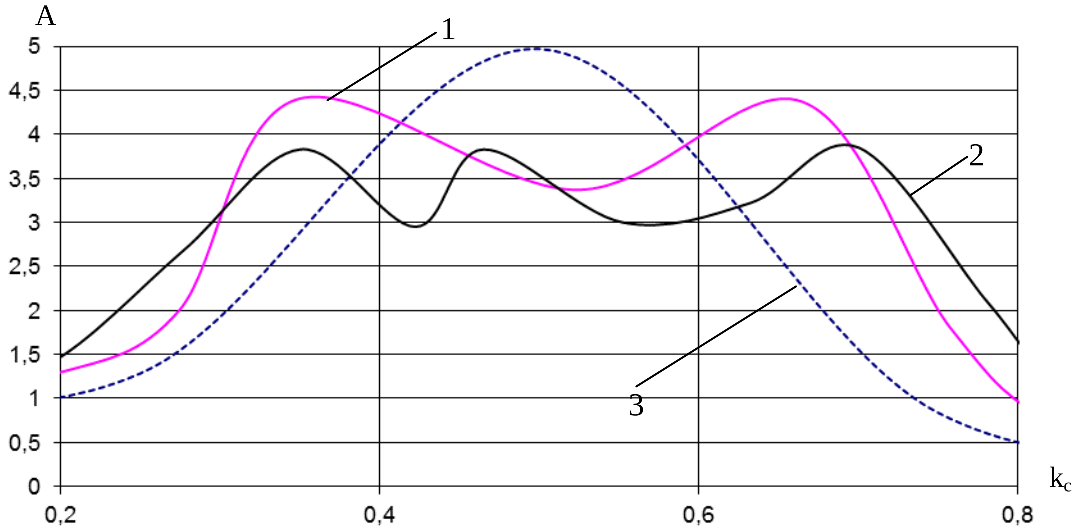

Fig.1. Amplitude – frequency characteristic of horizontal vibrations for foundation with one- and two mass damper in case of optimal parameters:1- for one mass damper, 2- for two mass damper, 3- without mass damper.

2.3. Rotational vibrations

Analyzing the vibration of rotating foundation with circular base one can use the equilibrium equations describing the vertical vibrations, in which the displacement are replaced to rotating angles, and masses can be replaced to respective moments of inertia of damper and foundation. Selection of the optimum parameters of dynamic dampers for rotation vibration was carried out as in previous analyzed cases, ie. for reducing of vibration amplitudes of foundation in the greatest frequency band, without exceeding the allowable predetermined value of amplitude. The optimum parameters were found for the case of rotational vibration of the foundation equipped with:

$M_0 = 30$; $A_{1max} = 6.3121$ for one mass damper $\mu_1=0{,}095$, $\xi_{k,1} = 0{,}439$, $\xi_{c,1} = 0{,}138$ and for two mass damper is $\mu_1=0{,}095$, $\mu_2=0{,}0475$ $\xi_{k,1} = 0{,}484$, $\xi_{c,1} = 0{,}136$, $\xi_{k,2} = 0{,}491$, $\xi_{c,2} = 0{,}127$. Effectivennes of two mass damper fixed to the foundation is illustrated in the figure 2.

3. Conclusions

In this paper the posibility of reducing the foundation using the multiple mass vibration damper is investigated. The study can be concluded as follows: effectiveness of multiple mass dampers arises with increase of number of masses from one to two masses, use of damper mass causes of amplitude vibration peaks.

The performed analysis can be useful in real solutions as computational schemes of foundations of many real objects, eg. foundations for antennas and chimneys, have a circular base, besides the circular base of the foundation may be accepted also as a result of approximation of the foundations of other complex geometric form.

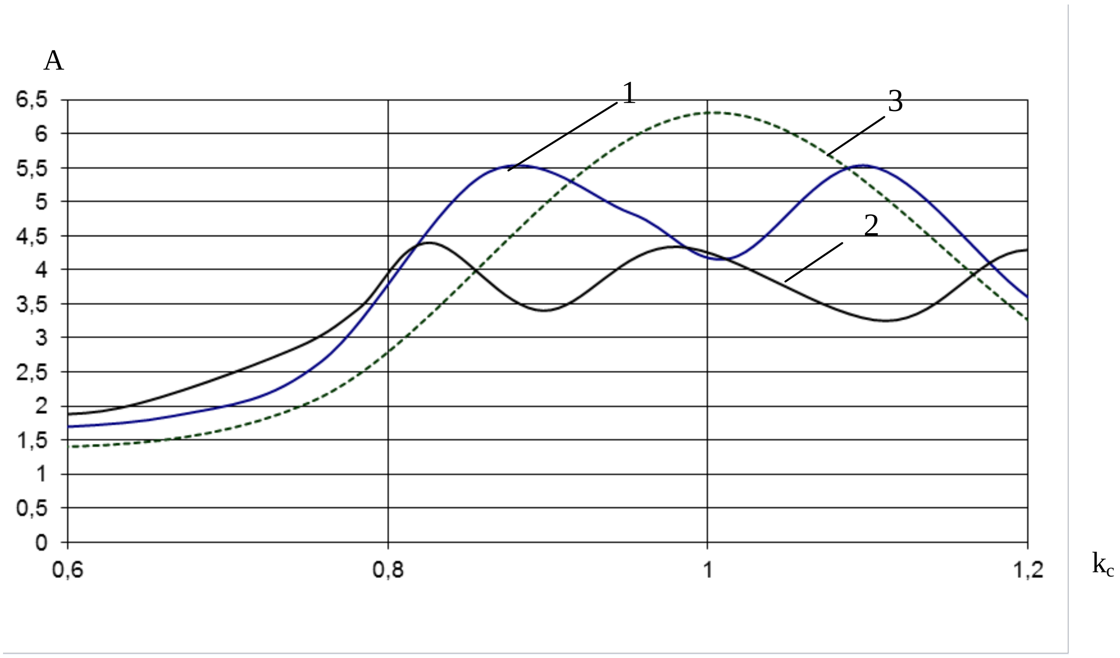

Fig.2. Amplitude – frequency characteristic of rotational vibrations for foundation with one- and two mass damper in case of optimal parameters:1- for one mass damper, 2- for two mass damper, 3- without mass damper.

References

Cox S.J.(1998): Designing for optimal energy absorption, Part 1, Lumped parameter systems. J. Vibr. Acoust,Stress and Rel. Des. Trans. ASME., V.120, №2, , 339-345.

Dutkiewicz M. (2005): Vibration control of random excited footing resting on the elastic half-space. Prace Naukowe Politechniki Radomskiej. Transport nr 3(23), s. 143-148.

Dutkiewicz M. (2006): Vibration of Euler-Bernoulli beam under random load carrying spring-mass system. 10th International Conference „Computer Systems Aided Science, Industry and Transport, pp. 199-204.

Gołębiowska I, Dutkiewicz M. (1999): Vibration of a footing on the elastic half-space with damping system. Lightweight, Structures in Civil Engineering, Local Seminar of IASS Polish Chapter, Warsaw, 3 December, 1999 (s.30-33).

Korieniew B. G., Reznikow L. M. (1988): Dinamiczeskije gasitieli koliebanij: Teorija techniczeskie priłożenija.-M.: Nauka,.-304 s.

Nashif A., Johes D., Henderson J. (1985): Vibration damping.- New York:John Wiley &Sons,. 470 p.

Snowdon J.C. (1974): Dynamic vibration absorber that have increased effectiveness. Journal of Engineering for Industry. Trans. ASME, V. 96. №3, 940-945.

Soong T.T., Constantinou M.C. (1993): Passive and active vibration control in civil engineering, Springer, Vien.

Soong T.T., Spencer B.F. (2002): Supplemental energy dissipation: state-of-the-art and state-of-the-practice. Engineering Structures, 243-259.

Szwec H.S., Sedin W.Ł., Kiriczek A. (1987): Konstruktiwnyje spasoby snirzienija wibracji fundamientow maszin dynamiczeskimi nagruzkami, Moskwa Stroizdat.

Warburton G.B. (1982): Optimum absorber parameters for various combinations and excitation parameters. Earthquake Engineering and Structural Dynamics, vol. 10, pp. 381-401.

22nd International Conference
ENGINEERING MECHANICS 2016
Svratka, Czech Republic, 9 – 12 May 2016

REDUCTION OF CABLE VIBRATIONS CAUSED BY WIND

I. Golebiowska*, K. Peszynski**

Abstract: *The cables are important components of civil engineering structures. Due to their low internal damping, mass and rigidity, they are very sensitive to the dynamic action of the wind. Frequent and excessive cable vibrations are the cause of fatigue failure in the fixing location. Restricting the damage possibility caused by the wind is very important not only because of the safety of the construction, but also for economic reasons. The paper presents an analysis of experimental and theoretical research on ways to reduce the cables vibrations level and reviewing selected their application. Attention was drawn to merge the various methods in order to obtain the most effective way of damping.*

Keywords: Cable vibrations, damping methods, aerodynamic and mechanical methods

1. Introduction

With the development of innovative materials, technology, and advanced methods of calculations, people erect increasingly higher and longer constructions. Such structures as cable-stayed bridges, suspension bridges, masts, stacks, overhead power lines etc. are usually characterized by low rigidity and relatively low damping, and therefore are strongly affected by natural environment, such as wind. Cables are commonly used as structural components in such constructions. They have very low internal damping and are not capable of total dissipation of excitation energy, hence they can reach high amplitudes of vibrations. Damping coefficients of cables in serviced bridges range between 0.001 to 0.005 [Fujino Y., Kimura K, Tanaka H., 2012]. An increased span length of modern bridges requires longer cables, which leads to hazards related to their safety. High amplitudes of vibrations may induce excessive stress and fatigue damage in cables and in their connections to structural elements. Therefore, reduction of cable destruction possibilities caused by vibrations is very important not only in terms of economy but for structural safety as well.

Cables of bridges exhibit a variety of different aerodynamic and aeroelastic phenomena. In order to assume an effective and efficient method of lowering the level of cable vibrations, we need to have deep understanding of physical phenomena that take place under the influence of wind, such as: vortex excitation, vortex excitation at high velocity, rain-wind induced excitation, galloping, galloping of dry inclined cables, wake galloping for groups of cables, buffeting, etc.

This work is devoted to overview and analysis of the methods of damping the vibrations of bridge cables, as well as their application.

2. Vibration damping methods

General vibration damping methods are divided into passive, semi-active and active. Passive vibration control equipment are devices with fixed parameters (rigidity and damping). They do not require external power supply to work and are relatively cheap in comparison with active and semi-active control methods. These devices are relatively easy to design, manufacture, and service.

In comparison with the passive method, the active method of structure vibration damping is characterized by two basic features. The first one is the necessity to supply the required external energy to

*Assoc. Prof. Irena Golebiowska, PhD.: UTP University of Science and Technology, Faculty of Civil and Environmental Engineering and Architecture, Al. prof. S. Kaliskiego 7, 85-796 Bydgoszcz; PL, irena_golebiowska@wp.pl

**Assoc. Prof. Kazimierz Peszynski, PhD.: UTP University of Science and Technology, Faculty of Mechanical Engineering, Al. prof. S. Kaliskiego 7, 85-796 Bydgoszcz; PL, kazimierz.peszynski@utp.edu.pl

the control system. The second one is the need to implement feedback, as the process is based on real-time measurement data. Active control system is substantially a closed control system and it includes four basic components: structure treated as an object of control, measuring devices (vibration sensors), controller, and actuators. These devices are connected in a feedback loop. Measuring system is especially sensitive; it is composed of sensors carefully positioned on the structure, which primarily measure the structure responses to dynamic excitations. More complex active control systems may also measure external interference (such as wind velocity) and then the control system is a branched system with measurement of interfering value. After proper processing, measurement signals are input signals to the controller, which develops controlling signals for the actuators on the basis of a strictly specified algorithm. Practically, all the power supply is used for the actuators, which are responsible for counteracting the enormous forces of dynamic interference, hence their power of sometimes several dozen kilowatts.

A compromise between the passive control system and the active control system is semi-active control system. It combines advantages of passive and active systems, but it also has some of their drawbacks. In this system, external energy is used to set the parameters of the passive controller (damping and/or rigidity). Characteristics of such device must be modified during its operation. Energy requirements of the semi-active control system are low – several dozen watts. This type of control is substantially a passive control with an internal built-in controlling system.

Currently, passive dampers are divided into three categories: hysteresis dampers, viscous dampers, and mass dampers. The first category of dampers uses materials and systems with hysteresis damping features. The second category uses fluids whose resistive force affecting a body is directly proportional to its velocity. The most common are fluids with high viscosity, such as engine oil. Mass dampers use the inertia of additional mass added to the structure. Frequency of a damper's own vibrations is usually set to the value of basic frequency of the structure's own vibrations in order to transfer the energy of vibrations from the structure to the damper.

There are several possible methods of damping cable vibrations. They include: surface modification (aerodynamic methods), increasing rigidity of a cable system (structural methods), and increasing the damping level (mechanical methods).

2.1. Aerodynamic methods

The reference literature suggests numerous different cable surface modifications [Zdravkovich M.M., 1981]. One of the most common modifications are helical strakes and ribs (spiral turbulators). Helical strakes with a rectangular section and sharp edges break the vortex structures, help to avoid rain-wind excitations through preventing the forming of water rivulets, and induce three-dimensional flow interferences, which, as a consequence, helps in reducing the level of vibrations caused by vortexes.

The paper [Lee S.J., Kim H.-B., 1997] presents results of a test on a cylinder with three rods wound on it. It was established that surface ridges (wound structures) lengthen the area of vortex formation and their frequency and wake width are reduced. The publication [Novak M., 2001] proposes the installation of separate little rectangular plates (wing-like turbulator) on the cylinder surface, making a helical line. This solution is based on the same concept as that described above, but the plates arranged helically do not block water rivulets. Another solution is to add extended rectangular plates to the cylinder surface by welding. This circumferential solution provides multi-directional efficiency of this surface modification, which is backed up by 70% reduction of vortex excitation in resonance [Alexandre M., 1970].

In order to reduce aerodynamic interactions between two parallel hanger cables on the Akashi-Kaikyo suspension bridge (Japan), wires were wounded around the hanger cables. Spiral turbulators proved to be effective in reducing the level of vortex-induced vibrations and wake-induced instabilities [Fujino Y., Kimura K, Tanaka H., 2012]. Another effective method of aerodynamic damping are channels made on the cable surface along the axis so that water can flow through this channels without the possibility of transverse movement. Such type of modification has been implemented on the Higashi-Kobe bridge (Japan).

This solution is very efficiently when it comes to reducing inclined cable vibrations at rain-wind excitation [Saito T., Matsumoto M., Kitazawa M., 1994]. The paper [Bearman P.W. and Harvey J.K. 1993] describes the results of tests on a cylinder with evenly arranged indentations within its entire circumference, with the proportion between the indentation depth and the cable diameter corresponding to the one in a typical golf ball. The cylinder with these indentations demonstrated a lower critical Reynolds number than a smooth cylinder, because the irregular surface made the boundary layer increase in thickness and led to earlier detachment of the flow [Holmes, J.D., 2001].

Another type of surface modification is making a regularly arranged pattern on the cable surface in the form of discreet indentations, which prevent water rivulets from forming [Miyata T., Katsuchi H., Tamura Y., 1999]. Such an indentation conduces to stabilization of flow separation from the cable surface. Cables of such type has been used on the Tatara bridge (Japan).

Cable surface can also be modified by applying proper perforated shrouds or longitudinal bars parallel to the cylinder axis or rods attached to a ring mounted on the cylinder. Paper [Wong H.Y. and Kokkalis A., (1982)] presents results of experimental tests carried out in an aerodynamic tunnel on selected types of cylinder surface modifications. The tests demonstrate that all the modifications were effective in reducing the level of vibrations induced by vortexes; the highest reduction of aerodynamic resistance coefficient was observed in the case of the perforated shroud, although it was not the most effective method of vortex damping.

2.2. Mechanical methods

There are many various solutions for reducing vibrations of cables in cable-stay bridges and hanger cables in suspension bridges. The simplest solution, often used, are additional lines that tie the cables; they can be installed vertically, horizontally or diagonally, as needed, which increases the rigidity of the cables within their plane (structural method). This damping method has been used in many bridges around the world, e.g. in the Normandie bridge (France), Second Severn (Great Britain), and Yobuko (Japan).

Many cables of cable-stay bridges are equipped with passive internal dampers at the point where the cables are connected with the deck (inside the stay pipe of the anchorage area). This method shows highly-effective passive internal dampers (VSL), which can be also used as external dampers.

Friction damper dissipates the energy through friction between two specially designed elements (a pair of sliding discs and composite pads). The contact force is regulated through deformation of the spring blades. A change in the contact force leads to a change in the damping characteristics. 120 VSL friction dampers have been used for the cables of the Udevala bridge (Sweden). Optimum damping of the friction damper is independent from the type of vibrations, i.e. the friction damper will be effective for any type of vibrations.

VSL GENSUI damper dissipates energy through deformation of elastic elements made of high-durability rubber with high fatigue strength. Several damping elements are placed between two discs, one of which is rigidly attached to the stay cable and the other to the guide pipe. In this case, the characteristics of the damper is determined by the number and type of damping elements used.

If cable damping is still insufficient, using the above damping method, external dampers are used that are placed within a short distance from the cable anchoring point. External oil dampers have been applied to cables in, for example, the Normandie bridge (France) and the Aratsu bridge (Japan).

Drawing 10 shows an oil damper applied to cables of the Aratsu bridge. Advantages of oil damper: wide range of damping capabilities, low costs, simple technology. Oil damper may provide axial damping force along the direction of its cylinder. In order to control the cable vibrations in both planes (in the cable plane and beyond it), installation of two oil dampers transversely to the cable axis at a specific angle of inclination is required. Passive viscous dampers (oil, hydraulic) can be effective, providing optimum damping level only for a chosen type of vibrations, while for the other types the added damping will be lower than optimum. It is commonly known that vibrations induced by the rain-wind excitation are dominated by the first several types of vibrations, mainly by the second type. That is why, these dampers designed to damp the first type of vibrations will be less effective in minimizing vibrations induced by the rain-wind excitation. Damper effectiveness is higher when it is mounted at the anti-node (maximum amplitude) point of the cables; however, due to practical and aesthetic reasons, external dampers are mounted near the anchoring point of the cable, i.e. within a distance of 2-6% of the cable length [Gimsing N., Georgakis Ch., 2012].

Today, semi-active dampers of MR type (magnetorheological) are also widely used to damp cable vibrations. MR dampers are filled with MR fluid controlled by a magnetic field with the use of an electromagnet, which allows a continuous control of damping characteristics through the change of energy. Its rheological characteristics will change in the presence of a magnetic field: without a magnetic field, MR fluid acts as a Newtonian fluid; if a magnetic field is applied, MR fluid acts as a Bingham fluid. MR fluid consists of three basic components: base fluid (carrier fluid), metal particles, stabilizing additives.

The base fluid serves as a carrier in which magnetic particles are suspended. Hydrocarbon oils, mineral oils, and silicone oils are commonly used as carrier fluids for manufacturing MR fluids. If there is no magnetic field, an MR fluid has similar characteristics to those of the carrier fluid, but upon applying a magnetic field, the rheological characteristics may change rapidly. Thus in a matter of milliseconds, a fluid may change its properties into properties similar to a solid body [Kciuk M, Turczyn R. 2006].

There are three types of MR dampers: mono-tube, twin-tube, and double-ended MR dampers [Ashfak A et al., 2009]. Mono-tube MR damper is the most commonly used MR damper to control cable vibrations. It consists of only one MR fluid reservoir and an accumulator to compensate changes in volume caused by piston rod movement. MR damper may ensure optimum or sub-optimum damping for any type of vibrations and any type of cable through the change of input voltage.

In 2002, 312 semi-active MR dampers were used to control rain-wind-induced vibrations in the Doingting Lake cable-stay bridge (China). That was the first time in the world that MR dampers had been applied to bridge cables. Thanks to their mechanical simplicity, low energy requirements, and ability to produce high damping forces, MR dampers are one of the most promising devices used in mechanical control of cable vibrations. The only problem is related to the requirement of an external energy source.

3. Conclusions

High amplitudes of cable vibrations may lead to their destruction, and thus a shorter service life. Therefore, reducing the level of cable vibrations is so important with regard to the safety of an entire structure. Common methods of minimizing cable dynamic response are: additional tying cables, appropriate external surface finish, and the use of mechanical passive and semi-active dampers. A combination of particular methods seems to be a more effective solution. As opposed to passive dampers, semi-active dampers applied to cables offer permanent optimum level of effectiveness, even when various different types of vibrations are to be damped. What is more, there is a low energy requirement to power a semi-active damper and the energy can be supplied for example from solar cells.

References

Alexandre M., (1970) Experimental study of the action of vortex shedding on cylinders with longitudinally welded fins. Euromech Colloq. 17, Cambridge (U.K.), 1970.

Ashfak A et al., (2009) Design, Fabrication and Evaluation of MR Damper, University of Kerala, India. World Academy of Science, Engineering and Technology 53, pp 358-363.

Bearman P.W. and Harvey J.K. (1993) Control of Circular Cylinder Flow by the Use of Dimples. AIAA Journal, Vol. 31, No. 10, 1993, pp. 1753-1756.

Fujino Y., Kimura K, Tanaka H., (2012) Wind Resistant Design of Bridges in Japan, Springer.

Gimsing N., Georgakis Ch., (2012) Cable Supported Bridges: Concept & Design, Wiley, 3rd Edition.

Holmes, J.D., (2001) Wind Loadings of Structures, Spon Press, New York.

Kciuk M, Turczyn R. (2006) Properties and application of magnetorheological fluids. Journal of Achievements in Materials and Manufacturing Engineering, Volume 18.

Lee S.J., Kim H.-B., (1997) The Effect of Surface Protrusions on the Near Wake of a Circular Cylinder. Journal of Wind Engineering and Industrial Aerodynamics 69-71, pp. 351-361.

Miyata T., Katsuchi H., Tamura Y., (1999) Comprehensive Discussions on Structural Control for Wind- Induced Responses of Bridges and Buildings, Wind Engineering into the 21st Century. Balkema, Rotterdam, 1999, pp. 487-494.

Novak M., (1966) The Wind Induced Lateral Vibration of Circular Guyed Masts, Tower-Shaped Steel and Reinforced Concrete Structures, Symp. Int. Ass. Shell Struct., Bratislava, 1966.

Wong H.Y. and Kokkalis A., (1982) A Comparative Study of Three Aerodynamic Devices for Suppressing Vortex-Induced Oscillation. J. Wind Eng. Indust. Aerodyn., 10:32-29.

Zdravkovich M.M., (1981) Review and Classification of Various Aerodynamic and Hydrodynamic Means for Suppressing Vortex Shedding. Journal of Wind Engineering and Industrial Aerodynamics 7/1981, pp. 145-189.

22nd International Conference
ENGINEERING MECHANICS 2016
Svratka, Czech Republic, 9 – 12 May 2016

THE USE OF SPECIAL ALGORITHM TO CONTROL THE FLIGHT OF ANTI-AIRCRAFT MISSILE

M. Grzyb[*], K. Stefański[**]

Abstract: *The paper analyzes a possibility of using the special algorithm to control the flight of a homing air target missile. The method is based on the signum function and utilizes the phase trajectories of errors resulting from the adopted homing method (proportional navigation). The results obtained via Matlab package are presented in graphical form.*

Keywords: dynamics, phase trajectories, homing, missile, control.

1. Introduction

A constant rise in the number of combat operations involving air defence systems requires that the missile flight control methods be refined. Guidance to a moving target dictates that the missile should reach the target as fast as possible and meet the system performance requirements at the same time. The selection of the guidance method is an important factor as it has a profound effect on the likelihood of intercepting the target. Deviation of a missile motion from the ideal constraints is an error, which is used to formulate the guidance control rule. The special control algorithm proposed here is based on phase trajectories of control errors. The method utilizes the signum function for switching the control forces at appropriate points of the phase plane (Hsu & Meyer, 1968; Osiecki & Stefański, 2008). The flight of the anti-aircraft missile will be controlled with the use of aerodynamic forces. The homing of the flying object on the aerial target was executed with the proportional navigation method. The device providing the identification and tracing the target, and also precise and reliable lead the missile to it along the proper trajectory, could be the optical scanning-tracing head (Dziopa et al., 2015; Gapiński et al., 2014; Krzysztofik & Koruba, 2012), but in the paper this concept was not considered.

2. Missile flight dynamic and kinematic equations

Figure 1 summarizes the coordinate systems in which the missile flight equations were introduced. Figure 2 shows the forces that act on the moving missile. The following symbols are used (Koruba & Nocoń, 2015): α, β – attack angle and sideslip angle [rad]; ψ, ϑ, φ – pitch angle, yaw angle and roll angle of the missile [rad]; γ, χ – flight-path angle in vertical plane and horizontal plane – pitch angle and yaw angle of missile velocity vector [rad], $S\xi\eta\zeta$ – coordinate system for the missile; $Sxyz$ – velocity coordinate system; $Sx_g y_g z_g$ – coordinate system with the missile as an origin, parallel with the starting system $\vec{V}_m$ – missile velocity vector; $\vec{P}$ - thrust; $\vec{A}$ – resultant of aerodynamic forces; $\vec{G}$ – gravitational force; $\vec{Q}$ – control force; $\vec{M}$ – sum of moments of forces acting on the missile; ε, σ – pitch and yaw angles of the line-of-sight (LOS) [rad].

[*] Research Assistant Marta Grzyb, M.Sc. Eng.: Faculty of Mechatronics and Machinery Design, Kielce University of Technology, al. 1000-lecia P.P. 7; 25-345, Kielce; PL, mgrzyb@tu.kielce.pl

[**] Assistant Prof. Konrad Stefański, Ph.D. Eng.: Faculty of Mechatronics and Machinery Design, Kielce University of Technology, al. 1000-lecia P.P. 7; 25-345, Kielce; PL, kstefanski@tu.kielce.pl

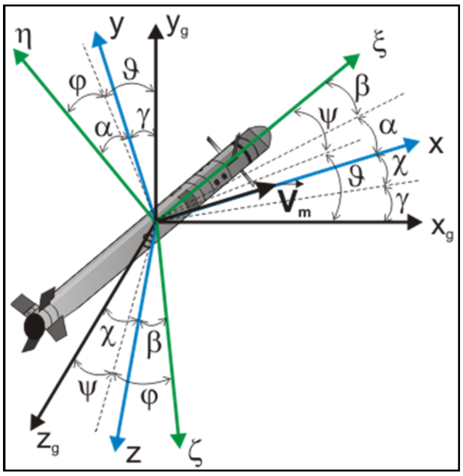

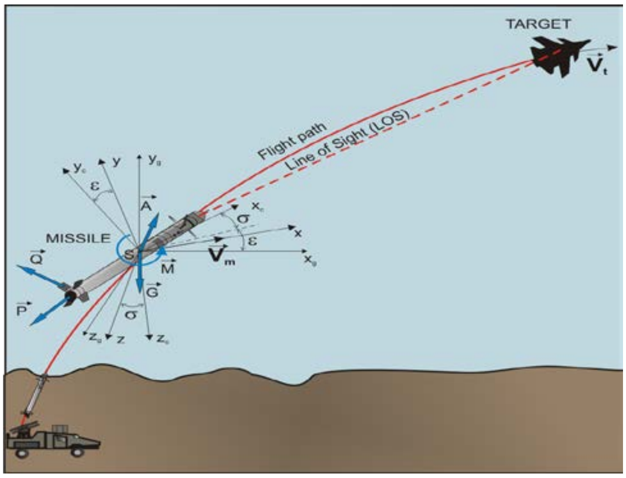

Fig. 1:Coordinate system with angles of rotation

Fig. 2: Forces acting on a missile

For the purposes of these calculations, the rocket is assumed to be a rigid body which does not rotate around its longitudinal axis and the motion of the missile and the target is restricted to a common vertical plane. The flat motion (vertical plane) is considered in order to simplify the analysis of the process of homing the missile on the aerial target. In practice, if the target does not make rapid manoeuvres, the homing process departs only slightly from the vertical plane (also due to autopilot stabilization system), thereby the motion in the horizontal plane can be neglected. Thus, $\psi = 0$, $\varphi = 0$, $\beta = 0$; $\chi = 0$, $\sigma = 0$. With these assumptions applied, the missile dynamic equations are as follows (Koruba & Osiecki, 1999):

$$\dot{V}_m = \frac{P}{m}\cos\alpha - g\sin\gamma - \lambda_x V_m^2, \quad \dot{\gamma} = \frac{1}{V_m}\left(\frac{P\sin\alpha + Q_y}{m} - g\cos\gamma\right) + \lambda_y V_m \alpha \tag{1a}$$

$$\ddot{\vartheta} = -D_1\frac{V_m^2}{l}\alpha - D_2 V_m\dot{\alpha} - D_3 V_m\dot{\vartheta} + \frac{Q_y e}{J_k}, \lambda_x = \frac{c_x S_x \rho}{2m}, \lambda_y = \frac{c_y S_y \rho}{2m}, D_{1,2,3} = \frac{C_i l}{J_k} \tag{1b}$$

where: l – length of the missile body [m]; ρ – air density [kg/m^3]; S_x – cross-sectional area of the missile; S_y – lifting area [m^2]; m – mass of the missile [kg]; J_k – moments of inertia of the missile in relation to its transverse axis [kgm^2]; γ – actual angle of missile flight-path [rad]; Q_y – missile flight control force [N]; e – distance between control force and aerodynamic pressure centre [m]; g – acceleration of gravity [m/s^2]; $\lambda_x, \lambda_y, D_{1,2,3}$ – relative aerodynamic coefficients of aerodynamic forces and moments [1/m] (Koruba & Osiecki, 1999); c_x, c_y – coefficients of aerodynamic forces; C_i – coefficients of moments of aerodynamic forces; V_m – flight velocity of the missile [m/s].

Kinematic relationships between the missile and target have the form (Koruba et al., 2010):

$$\dot{r} = V_t\cos(\varepsilon - \gamma_t) - V_m\cos(\varepsilon - \gamma_d), \qquad -r\dot{\varepsilon} = V_t\sin(\varepsilon - \gamma_t) - V_m\sin(\varepsilon - \gamma_d) \tag{2}$$

where: V_t – target velocity [m/s]; γ_t – angle of the target flight-path [rad]; γ_d – desired angle of the missile flight-path [rad]; r – distance between the missile and the target [m].

To satisfy the missile total kinematic overload requirement, the following equations are used

$$n_x = -\left(\frac{\dot{V}_m}{g} + \sin\gamma\right), \quad n_y = -(\dot{V}_m\dot{\gamma} + \cos\gamma), \quad n = \sqrt{n_x^2 + n_y^2} \tag{3}$$

3. The algorithm of homing and determination of the control force

To realize the homing guidance on the target, the following proportional navigation algorithm was used (Yanushevsky, 2011; Koruba & Osiecki, 1999):

$$\dot{\gamma}_d = a\dot{\varepsilon} \tag{4}$$

where: a – constant dimensionless coefficient of proportional navigation

To determine the control force for the rocket flight, the method based on phase trajectories of control errors was applied. This method consists in bringing the error to zero through switching the control force at appropriate points on the phase plane, as reported in detail by (Hsu & Meyer, 1968; Osiecki & Stefański, 2008). The control force was calculated from

$$Q_y = -u\left(p_1 \operatorname{sgn} e_1 + p_2 \operatorname{sgn} e_2 + p_3 \operatorname{sgn} e_3\right) \tag{5}$$

where: u, $p_{1,2,3}$ – control coefficients: $e_1 = \gamma - \gamma_d$, $e_2 = \dot{\gamma} - \dot{\gamma}_d$, $e_3 = \int_{t_0}^{t_k} (\gamma - \gamma_d) dt$

4. Digital simulation results

Numerical simulations were conducted for a hypothetical missile attacking an aerial target from the front quarter. The following numerical values were used: starting missile position: x_{m0} = 0 [m], y_{m0} = 0 [m]; starting target position: x_{t0} = 5500 [m], y_{t0} = 3500 [m]; angle of a missile launch: γ_0 = 0.7667 [rad]; starting angle of pitch of a target velocity vector: γ_{t0} = 0.01 [rad]; starting missile velocity: V_{m0} = 20 [m/s]; target velocity: V_c = const = 300 [m/s]; l = 1.6 [m]; m = 10.8 [kg]; J_k = 2.304 [kgm^2]; λ_x = 0.000171 [1/m]; λ_y = 0.0051 [1/m]; D_1 = 0.081 [1/m], D_2 = 0.0821 [1/m], D_3 = 0.00041 [1/m]; a = 4; t – time. The flight path of the target was described as follows: $\gamma_t(t) = \pi - 0.003t$.

Graphical representation of the results is shown in Figs 3-8.

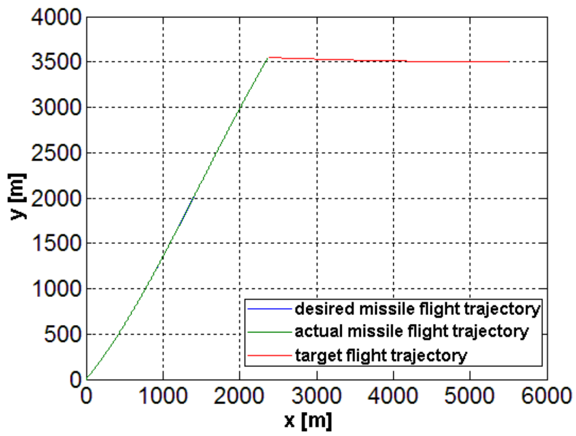

Fig. 3: The missile and target flight paths

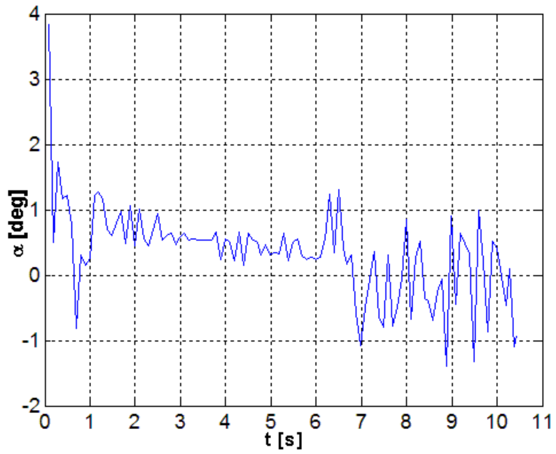

Fig. 4: The angle of attack realized during the missile flight

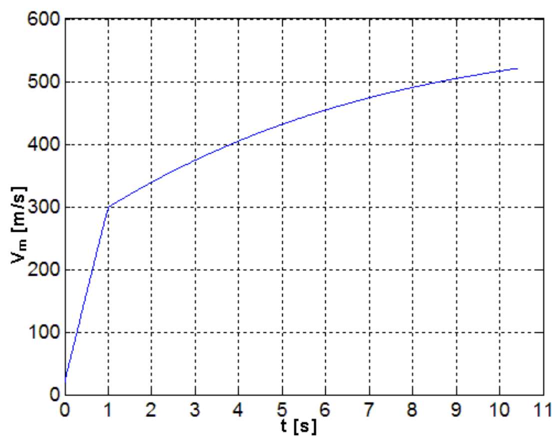

Fig. 5: Flight velocity of the missile

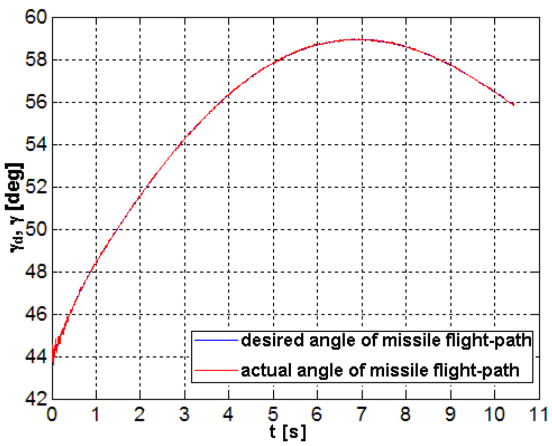

Fig. 6: Desired and actual angles of missile flight path

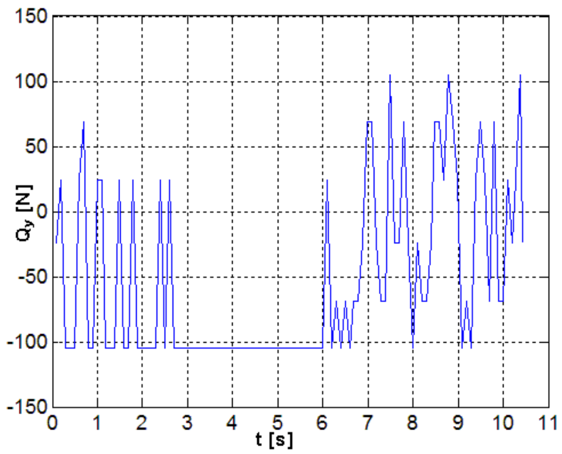

Fig. 7: Values of control forces required for homing the missile on the target

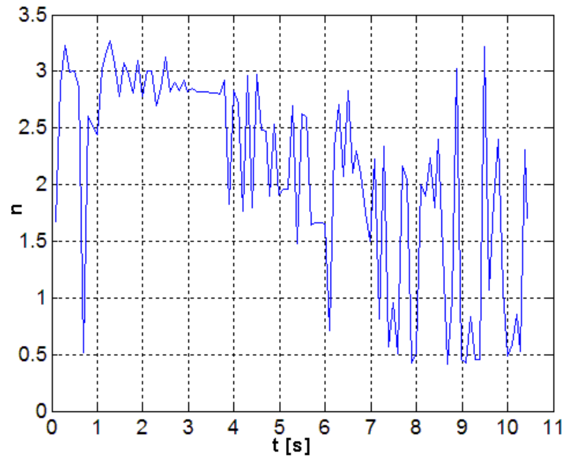

Fig. 8: Kinematic overloads acting on the missile during the flight

The results of the simulations are as follows: starting distance between the missile and the target: r_0 = 6519.2 [m]; starting values of pith angle of line-of-sight: $\varepsilon_0 = 0.5667$ [rad] (32.47 [deg]); final target position: x_{tk} = 2367 [m], y_{tk} = 3549 [m]; accuracy of missile hit: r_k = 5.04 [m]; time from a missile drop to hit a target: t_k = 10.44 [s].

5. Conclusions

The results of the simulations point to the following conclusions: the method proposed for the control of the air defence missile flight (with optimally selected controller gain rates (Gapiński et al., 2014)) allowed hitting the moving target; the hitting accuracy of 5.04 [m] is sufficient because most of the anti-aircraft missile are fitted with proximity fuses; minor oscillations of the rocket's actual flight path and angle result from the use of signum function - reduction of these oscillations should be considered; the control force reached low values, possible to attain in real conditions; overload acting on the flying rocket also reached acceptable values; the application of the proposed method, based on the phase trajectories of control errors, to the guidance of a missile on a target is possible and viable.

In the future, an attempt will have to be made to use the proposed method of missile control in a spatial approach.

References

Dziopa, Z., Buda, P., Nyckowski, M. & Pawlikowski, R. (2015) Dynamics of an Unguided Missiles Launcher. Journal of Theoretical and Applied Mechanics, 53, 1, pp.69-80.

Gapiński, D., Koruba, Z. & Krzysztofik, I. (2014) The Model of Dynamics and Control of Modified Optical Scanning Seeker in Anti-Aircraft Rocket Missile. Mechanical Systems and Signal Processing, 45, 4, pp.433-447.

Hsu, J.C. & Meyer A.U. (1968) Modern Control Principles and Application. McGraw-Hill, New York.

Koruba, Z., Dziopa, Z. & Krzysztofik I. (2010) Dynamics and Control of a Gyroscope-Stabilized Platform in a Self-Propelled Anti-Aircraft System. Journal of Theoretical and Applied Mechanics, 48, 1, pp.5-26.

Koruba, Z. & Nocoń, Ł. (2015) Automatic Control of an Anti-Tank Guided Missile Based on Polinomial Functions. Journal of Theoretical and Applied Mechanics, 53, 1, pp.139-150.

Koruba, Z. & Osiecki, J.W. (1999) Constructions, Dynamics and Navigation of the Short Range Rocket Missile (in polish). 1st part, Academy Course Book, 348, Kielce University of Technology.

Krzysztofik, I., Koruba, Z. (2012) Model of Dynamics and Control of Tracking-Searching Head, Placed on a Moving Object. Journal of Automation and Information Sciences, 44, 5, pp.38-47.

Osiecki, J.W. & Stefański, K. (2008) On a Method of Target Detection and Tracking Used in Air Defence. Journal of Theoretical and Applied Mechanics, 46, 4, pp.909-916.

Yanushevsky, R. (2011) Guidance of Unmanned Aerial Vehicles. Taylor & Francis Group, New York.

22nd International Conference
ENGINEERING MECHANICS 2016
Svratka, Czech Republic, 9 – 12 May 2016

MODELLING OF THERMO-MECHANICAL FATIGUE ON ENGINE GENERATOR TURBINE

J. Had*, T. Jamróz**

Abstract: *Presented paper is dealt with thermo-mechanical fatigue analysis of the generator turbine. Only elastic stress and temperature field are taken from FEM analysis. Elasto-plastic stress and strain are calculated with temperature dependent hysteresis model of stabilized stress-strain relation. Generalized Prandtl-Ishlinskii model is used for this purpose. For every point in loading history is found closed hysteresis loop. Damage for damage parameter corresponding to current hysteresis loop is evaluated by using Prandtl-Ishlinskii model. This procedure was implemented and applied to the generator turbine.*

Keywords: thermo-mechanical fatigue, hysteresis modeling, Prandtl-Ishlinskii model, damage prediction, turbine engine

1. Introduction

Rotating parts are crucial parts in the every aspect of turbine engine. During the service of an engine, a multitude of material damage such as foreign object damage, erosion, high cycle fatigue, low cycle fatigue, fretting, hot corrosion/oxidation, creep, and thermo-mechanical fatigue (TMF) is induced in these parts. The mechanical loading and effects based on the temperature gradient were stated as the most important factors in operational life. A common engineering practice in the fatigue analysis is based on the isothermal fatigue. This approximation is very raw estimation of complex loading state of working engine.

A promising concept for analysis of TMF is proposed by Nagode, et al. (2010). Actual damage is calculated in every step of loading history. Evolution of damage can be calculated cheap and very quickly using widely available isothermal fatigue curves. Proposed concept overcame hysteresis loop closure problems; loop's end can't intersect starting point in the case of changing temperature during the cycle. The closure problem is solved by identification of origin of hysteresis loop to current analyzing point. Temperature dependent damage is based on interpolation of experimental fatigue data for the current temperature. Actual damage is evaluated with damage operator. Prandtl-Ishlinskii model of hysteresis is applied on interpolated iso-thermal fatigue curves fur current temperature.

Objective of this paper is a demonstration of this approach in the case of real engine part. Theoretical background is introduced at first. An application of damage operator approach to the calculation of TMF on generator turbine loaded by simplified rotation speed spectrum follows.

2. Hysteresis modeling

Modelled stress and strain in actual time step are controlled with stabilized cyclic stress-strain curves corresponding to actual temperature. According Nagode, et al. (2010) stress input is suggested to be used from elastic FEM analysis. Elastoplastic behavior is modeled with generalized Prandtl-Ishlinskii model of hysteresis. Similar to the stress and strain, same hysteresis modeling approach is used in the case of damage.

2.1. Prandtl-Ishlinskii model of stress-strain relation

Brief theoretical background of hysteresis modeling is introduced in this paragraph. An example of stress modeling from stress input is described. Prandtl-Ishlinskii model is based on two fundamental models: Prandtl's and Prager's model.

* Ing. Jiří Had, PhD.: VZLÚ a.s, Beranových 130 Praha 9, Prague; CZ, +420 225 115 593, had@vzlu.cz
** Ing. Tomáš Jamróz: VZLÚ a.s, Beranových 130 Praha 9, Prague; CZ, +420 225 115 593, jamroz@vzlu.cz

Prandtl model of elasto-plasticity, also named stop, is based on simple rheological spring-slider model. There are two parts; linear elastic element is coupled in series with rigid perfectly plastic element, see Fig. 1. Further, Prager's model of perfect plasticity, called play, is dual model of the stop, see Fig. 2. There is linear elastic element coupled in parallel with perfectly plastic part. Despite Prandtl's model, Prager's model can account for rigid plasticity with the strain hardening. Mathematical expressions of abovementioned models can be found in Bertotti, et al. (2006).

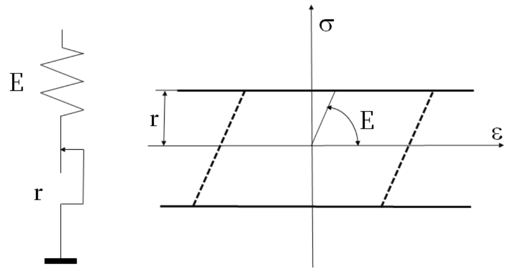

Fig. 1: Prandtl's model (stop) of elasto-plasticity

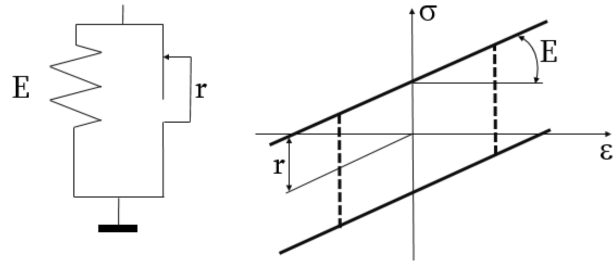

Fig. 2: Prager's model (play) of perfect plasticity

Model of elastoplasticity with strain hardening can be assembled with "stops" connected in series. Because of duality, same results can be done with construction of "plays" connected in parallel. This type of model is called Prandtl-Ishlinskii model, see Fig. 3.

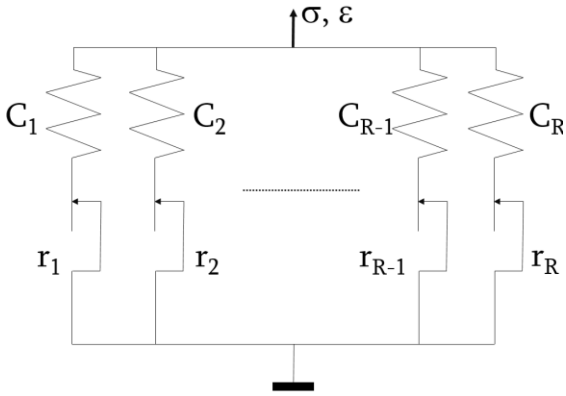

Fig. 3: Prandtl-Ishlinskii model

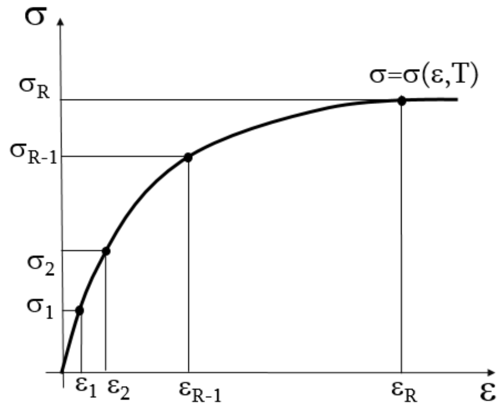

Fig. 4: Approximation of cyclic stress-strain curve

Let's assume stress controlled model loaded with stress stepwise history $\sigma = \sigma(t_i)$. Elasto-plastic stress is calculated with Neuber's approximation. Strain $\epsilon(t_i)$ in time step t_i in the Fig. 3 can be expressed as sum of elemental strain contributions from each individual spring-slider sub-models according to (1).

$$\epsilon(t_i) = \sum_{r=1}^{R} C_r(T_i) * \left(\sigma(t_i) - \sigma_r^{pl}(t_i)\right) \tag{1}$$

Instead of original procedure published in Nagode, et al. (2010), identification of parameters C_i and r_i of sub-model is used according to Grzesikiewicz, et al. (2012) and this leads to equations (2) and (3). Number of sub-models is chosen based on sufficiently approximated stabilized cyclic stress-strain curve as schematically depicted in Fig. 4.

$$\mathrm{C_r(T_i)} = \frac{\epsilon_\mathrm{r} - \epsilon_\mathrm{r-1}}{\sigma_\mathrm{r} - \sigma_\mathrm{r-1}} - \sum_{\mathrm{j=r+1}}^{\mathrm{R}} \mathrm{C_j(T_i)}$$

$$\mathrm{r = R-1, R-2, \dots 2} \tag{2}$$

Play operator in r-th sub-model of eq. (1) is expressed in equation (3).

$$\sigma_r^{pl}(t_i) = max\left\{\begin{matrix} \sigma(t_i) - r_r \\ min\left\{\begin{matrix} \sigma(t_i) + r_r \\ \sigma_r^{pl}(t_{i-1}) \end{matrix}\right\} \end{matrix}\right\} \tag{3}$$

Aforementioned relations are expressed for temperature T_i in analyzed time step t_i. As usual, experimental stress-strain curves are available for only a few temperatures. Therefore, to obtain stress and strain at any temperature, one can interpolate from experimental available curves.

2.2. Damage evaluation

Similar as strain modeling, current damage can be calculated from Prandtl-Ishlinskii model applied to description of fatigue curves. This approach was published in Nagode, et al. (2010). Current damage is calculated according to equations (4).

$$\mathrm{D_f}(t_i) = \sum_{j=1}^{i} \left| D(t_j) - D(t_{j-1}) \right| \tag{4}$$

Damage $D(t_j)$ is calculated as a sum of contributions of spring-slider models, see (5).

$$D(t_j) = \sum_{p=1}^{P} F_p(T_i) * \left(P_{SWT}(t_i) - p_p(t_i)\right) \tag{5}$$

Similar to Prandtl-Ishlinskii model of strain, fatigue curves (for available temperature) are approximated with number of spring-slider sub-models. For this purpose fatigue curve is expressed depending on damage level $d_f = (1/N_f)$ instead of number of cycles (reversals). In the case of low cycle fatigue, the damage parameter SWT (or generally other one) is expressed instead of $P_{SWT}=P_{SWT}(2N_f)$ as $P_{SWT}=P_{SWT}(2/d_f)$. Damage level d_f is non-decreasing value varies in range of $0 \leq d_f \leq 1$. Due to always bounded damage level, numerical difficulties are avoided in the case of $N_f \rightarrow \infty$.

Play operator $p_p(t_i)$ in (5) is expressed in (6). It depends on damage parameter $P_{SWT}(t_i)$ in current time.

$$p_p(t_i) = max \left\{ \begin{matrix} P_{SWT}(t_i) - r_r \\ min \left\{ \begin{matrix} P_{SWT}(t_i) + r_r \\ p_p(t_{i-1}) \end{matrix} \right\} \end{matrix} \right\} \tag{6}$$

Current damage parameter is calculated from closed hysteresis loop. This closed loop is created from current analyzing stress-strain point and corresponding origin in the loading history. Procedure for searching and storing these origins are published in Nagode (2014).

3. Fatigue analysis of generator turbine

Damage operator approach was applied to fatigue assessment of generator turbine. It is known from previous work, crucial point is a connection of bladed disk with other parts. Therefore, modeling approach was focused on this detail. A third section of generator turbine assembly was modeled. Cutting planes with appropriate boundary conditions were placed far from screw connection, see Fig. 5. The model and all subsequent FEM analyses were performed in commercial software ABAQUS.

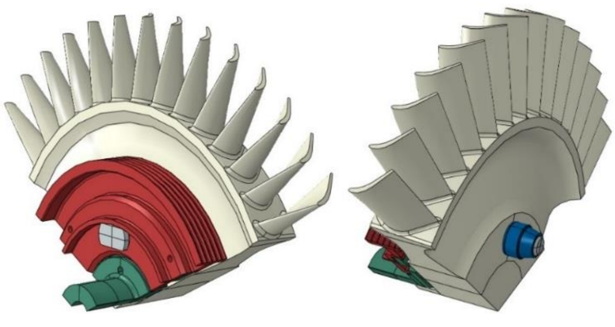

Fig. 5 Analyzed assembly of the generator turbine

Firstly, heat transport analysis was performed to solve convection and conduction of heat from gas to structural parts. Gas temperature was calculated according to the rotational speed spectrum using in-house software for calculation of thermodynamic variables in the engine. The spectrum can be seen in Fig. 6. The spectrum represents start of the engine, followed by single pre-heating cycle and subsequent 5 working cycles. A special attention was paid to the contact connection, where heat transfer condition is included in the contact definition.

Temperature field is assumed from previous heat analysis as a boundary condition in subsequent structural analysis. Furthermore, the structural model (finer mesh) is loaded by rotational speed spectrum and by aerodynamic force depending on current RPM. In general, linear analysis (elastic material) is recommended for subsequent fatigue analysis; strain is reconstructed from elasto-plastic stress calculated from Neuber‘s approximation. In the case of present contact, large plastic area with higher strain can be expected (and confirmed by analysis) and therefore Neuber's approximation isn't suitable approach. Therefore, nonlinear analysis with plasticity and included contact definition was performed.

According to Nagode, et al. (2010) FEM results (stress-strain state, temperature) in every loading increment are stored from FEM analysis as an input to damage calculation briefly described ahead. Because of considered plasticity in the structural analysis both stress and strain distribution can be used. Set of nodes inside of hole and in adjacent surface were analyzed. Fatigue analysis was implemented in MATLAB. All imported FEM entities was analyzed, a crucial one is the node with maximal damage at the end of the analyzed loading sequence. Limit number of repetitions of working cycles N can be calculated from (7). Term d_{N_i} stands for damage up to the beginning of last fifth cycle; N_i stands for number of already analyzed working cycles (N_i=4) and d_{last} is increased damage during the last fifth cycle.

$$D_{total} = 1 = d_{N_i} + (N - N_i) * d_{last} \tag{7}$$

Stress and temperature results in crucial point as well as predicted damage progression are shown in Fig. 6.

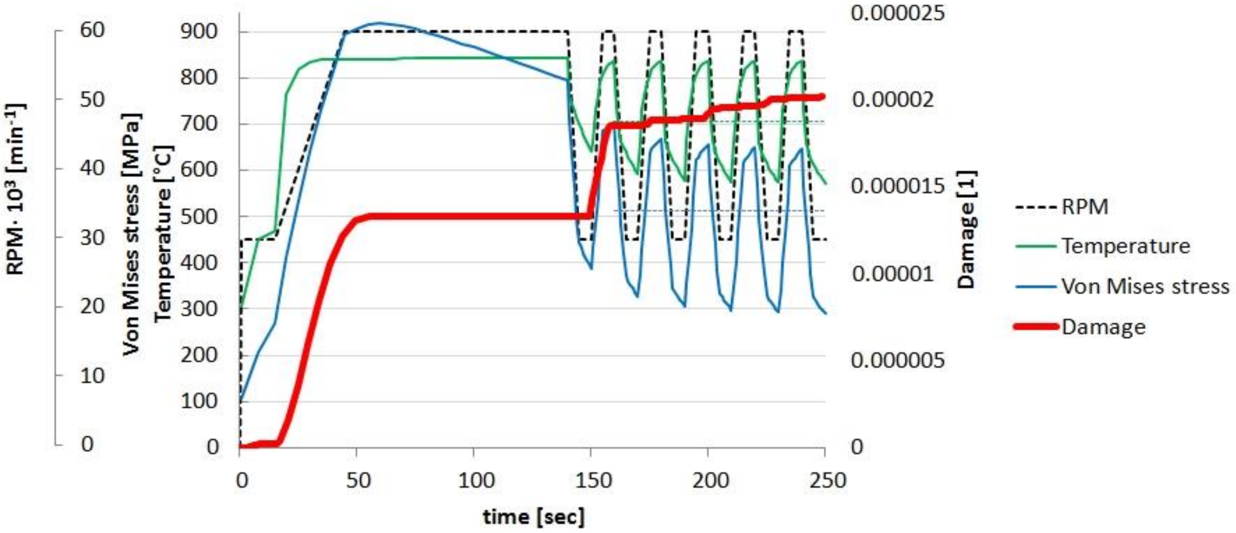

Fig. 6 Predicted damage progression and FEM results

4. Conclusions

Presented paper demonstrates continuous damage calculation during the non-isothermal loading of engine generator turbine. Duration of loading cycles is suggested long enough to enforce temperature is changing significantly. More straightforward identification procedure of parameters of spring-slider sub-model was used compare to the original paper. Verification of implemented damage calculation approach should be the inevitable next step in the future work.

Acknowledgement

This work was supported by the ESPOSA project in Work package WP5.1 and by VZLU, a.s. in project HC TMF, project number IP4406.

References

Bertotti, G. & Mayergoyz, I. D. (2006) The Science of Hysteresis: Physical modeling, micromagnetics, and magnetization dynamics. Vol. 2. Gulf Professional Publishing.

Grzesikiewicz, W. & Zbiciak, A. (2012) Study of generalized Prandtl rheological model for constitutive description of elastoplastic properties of materials. Journal of Achievements in Materials and Manufacturing Engineering, 55.2, pp. 501-510.

Nagode, M., Hack, M. & Fajdiga, M. (2010) Low cycle thermos-mechanical fatigue: damage operator approach. Fatigue & Fracture of Engineering Materials & Structures, 33.3, pp. 149-160.

Nagode, M. (2014) Continuous damage parameter calculation under thermo-mechanical random loading. MethodsX, 1, pp. 81-89.

22nd International Conference
ENGINEERING MECHANICS 2016
Svratka, Czech Republic, 9 – 12 May 2016

NUMERICAL SIMULATION OF THE EFFECT OF STIFFNESS OF LAMINA PROPRIA ON THE SELF-SUSTAINED OSCILLATION OF THE VOCAL FOLDS

P. Hájek*, P. Švancara*, J. Horáček, J. G. Švec*****

A two-dimensional (2D) finite element (FE) model of the fluid-structure-acoustic interaction during self-sustained oscillation of the human vocal folds (VF) is presented in this paper. The aim is to analyze the effect of stiffness of lamina propria on VF vibrations. Such stiffness change can be caused by some VF pathologies. The developed FE model consists of the FE models of the VF, trachea and a simplified human vocal tract. The vocal tract model shaped for simulation of phonation of Czech vowel [a:] was created by converting data from the magnetic resonance images (MRI). The developed FE model includes VF contact, large deformations of the VF tissue, fluid-structure interaction (FSI), moving boundary of the fluid mesh (Arbitrary Lagrangian-Eulerian (ALE) approach), airflow separation during the glottis closure and solution of unsteady viscous compressible airflow described by the Navier-Stokes equations. The numerical simulations showed that higher values of lamina propria Young's modulus (stiffer lamina propria) result in a decrease of the maximum glottis opening. Stiffer lamina propria also requires the use of higher subglottal pressure to initiate self-sustained vibration of the VF.

Keywords: Simulation of phonation, Fluid-structure-acoustic interaction, Finite element method, Biomechanics of voice

1. Introduction

Production of human voice is a complex fluid-structure-acoustic interaction problem, where the air flow induced self-oscillations of the vocal folds generate acoustic waves propagating through the vocal tract. Besides experimental studies, numerical modelling can be used to investigate this complex phenomenon. Traditional approach is to use low degree of freedom mass models of the vocal fold vibration (Ishizaka & Flanagan, 1972; Story & Titze, 1995; Horáček et al., 2005). Presently higher-level FE models are used. They allow to deal with complex geometry of the vocal folds and vocal tract and allow to solve fluid-structure-acoustic interaction. Xue et al. (2014) used immersed boundary method for solving fluid-structure interaction and studied phonation on three-dimensional human larynx model. Hybrid numerical approach to analyze human voice production was used by Šidlof et al. (2015), where first the fluid flow problem is solved using finite-volume method with prescribed motion of the VF and then Lighthill's acoustic analogy or acoustic perturbation equations are used to solve propagation of acoustic waves in the vocal tract.

In previous works of the authors (Švancara et al., 2011; Švancara et al., 2014) the FE model of flow-induced oscillations of the VF in interaction with acoustic spaces of the vocal tract was developed. In this study a new 2D FE model of phonation was constructed using four-layered VF structure and in literature widely used M5 geometry of the vocal folds (Scherer et al. 2001). Effect of stiffness and damping of

* Ing. Petr Hájek: Institute of Solid Mechanics, Mechatronics and Biomechanics; Brno University of Technology; Technická 2896/2; 616 69, Brno; CZ, y126528@stud.fme.vutbr.cz

* Ing. Pavel Švancara, Ph.D.: Institute of Solid Mechanics, Mechatronics and Biomechanics; Brno University of Technology; Technická 2896/2; 616 69, Brno; CZ, svancara@fme.vutbr.cz

** Ing. Jaromír Horáček, DrSc.: Institute of Thermomechanics; Academy of Sciences of the Czech Republic; Dolejškova 1402/5; 182 00, Prague; CZ, e-mail: jaromirh@it.cas.cz

*** RNDr. Jan G. Švec, Ph.D.: Department of Biophysics; Palacky University Olomouc; 17. listopadu 12; 771 46, Olomouc; CZ, e-mail: svecjang@gmail.com.cz

lamina propria on VF vibrations was also studied in previous paper of the authors (Hájek et al. 2016), where the model was excited by constant velocity prescribed at the entrance to the subglottal space. In this study model is excited by the constant lung pressure which corresponds better to real human voice production (Titze, 2006).

2. Methods

The FE model was created using the program system ANSYS 16.2. Fig. 1a) shows the 2D FE model of the four-layered tissue of the vocal folds. The overall dimensions of the one VF are width 9.5 mm and height 11 mm, thicknesses of individual layers are also depicted in Fig. 1. The FE model of the trachea and the simplified acoustic spaces of the human vocal tract shaped for simulation of phonation of the Czech vowel [a:] is shown in Fig. 1 b) together with used boundary conditions and measuring points. Layers of the VF was considered to be homogenous and isotropic with the Young's modulus of 25 kPa for epithelium, 1÷5 kPa for the lamina propria (see Tab. 1), 8 kPa for the ligament and 65 kPa for the muscle. The material density of 1040 kg.m^{-3} was used for all four layers. Poisson's ratio of 0.49 was used for all layers except the muscle with 0.40. Other details of the model can be found in Hájek et al. (2016). The change of lamina propria stiffness was simulated by change of Young's modulus (E_{SLP}) of this layer (see Tab. 1). In order to initiate self-sustained vibrations of the VF for the stiffer lamina propria it was necessary to increase the lung pressure at the entrance to the model of trachea. Three values of the lung pressure (p_{Lu}) were considered: 190 Pa, 275 Pa and 400 Pa.

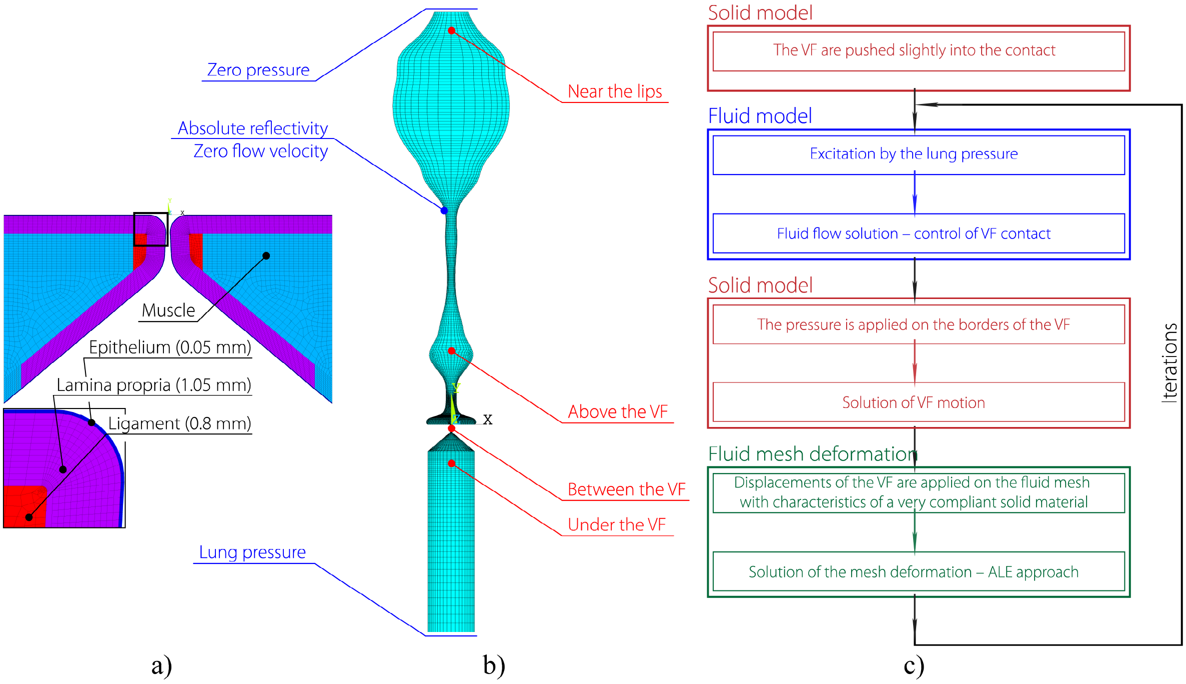

Fig. 1: a) FE model of the four-layered tissue of the VF, b) FE model of the acoustic spaces of the trachea and the vocal tract for the Czech vowel [a:], c) computational algorithm.

In the beginning of the numerical simulation, the VF are pushed slightly into the contact to the phonatory position. Then the fluid-structure interaction is solved using explicit coupling scheme with separated solvers for the structure and fluid domains. Computational algorithm is shown in Fig. 1 c). More details can be found in Švancara et al. (2014). Each computation (up to 0.1 s) took approximately 11 hours on PC with Intel i7–960 3.20 GHz (4 cores / 8 threads) and 12 GB of RAM.

3. Results and discussion

Fig. 2 shows an example of the vocal folds self-oscillations computed for $E_{SLP} = 2$ kPa and $E_{SLP} = 3$ kPa, the thickness of the lamina propria $t_{SLP} = 1.05$ mm and the lung pressure $p_{Lu} = 275$ Pa. Output pressure characteristics and sensitivity of the results on E_{SLP} can be found in Hájek et al. (2016). The oscillations of the VF are stabilized after the first few periods of the transient regime. We can also observe that the stiffer lamina propria (E_{SLP} = 3 kPa) decreased the maximum of the VF displacement in *x* direction and the fundamental frequency – see Tab. 1. For the fluid velocity we can see in Fig. 2 two peaks, the smaller peak is in the initial (opening) phase and the higher peak appears during closing phase of the oscillation period. The maximum magnitude of the fluid velocity remained approximately constant for both E_{SLP} values when the lung pressure was unchanged.

For each variant of the model (changing E_{SLP}) the following parameters widely used in laryngology (Titze, 2006) were then evaluated (see Tab. 1): the maximum glottis width, the open quotient OQ (i.e., duration of open phase divided by cycle duration), the closed quotient CQ (i.e., duration of closed phase divided by cycle duration), the closing quotient ClQ (i.e., duration of closing phase divided by cycle duration), the speed quotient SQ (i.e., duration of opening phase divided by duration of closing phase), the speed index SI (i.e., difference between the durations of the opening and closing phases divided by sum of these) and the fundamental oscillation frequency *f*.

Tab. 1: Characteristics of VF oscillation depending on Young's modulus of the lamina propria E_{SLP} and lung pressure p_{Lu}.

E_{SLP} [kPa]	p_{Lu} [Pa]	Max. glottal width [mm]	OQ [–]	CQ [–]	ClQ [–]	SQ [–]	SI [–]	*f* [Hz]
1	**190**	0.53	0.31	0.69	0.07	3.14	0.52	105
1.5		0.42	0.25	0.75	0.04	4.50	0.64	75
2	**275**	0.55	0.47	0.53	0.07	5.33	0.68	123
2.5		0.48	0.47	0.53	0.09	4.29	0.62	127
3		0.42	0.55	0.45	0.07	6.83	0.74	116
3.5		0.38	0.57	0.43	0.07	6.86	0.75	103
4	**400**	0.59	0.52	0.48	0.10	4.33	0.62	164
4.5		0.58	0.55	0.45	0.14	2.88	0.48	179
5		0.56	0.54	0.46	0.11	4.17	0.61	175

Results show that the stiffer lamina propria (higher E_{SLP}) causes a decrease of the maximum of glottal width and in some cases decrease of the fundamental frequency. Same conclusions were observed for the model excited by constant flow velocity (Hájek et al., 2016). Actual model excited by the lung pressure shows the values of the quotients more corresponding to clinical results (Lohscheller, 2013). For example the open quotient is for higher values of E_{SLP} slightly above 0.5. From the results we can also see that the fundamental frequency is increasing with the lung pressure which is also in agreement with clinical data (Titze, 2006). As a next step it is planned to use vocal tract shaped for other Czech vowels, which will allow to analyze the influence of vocal tract geometry on computed results.

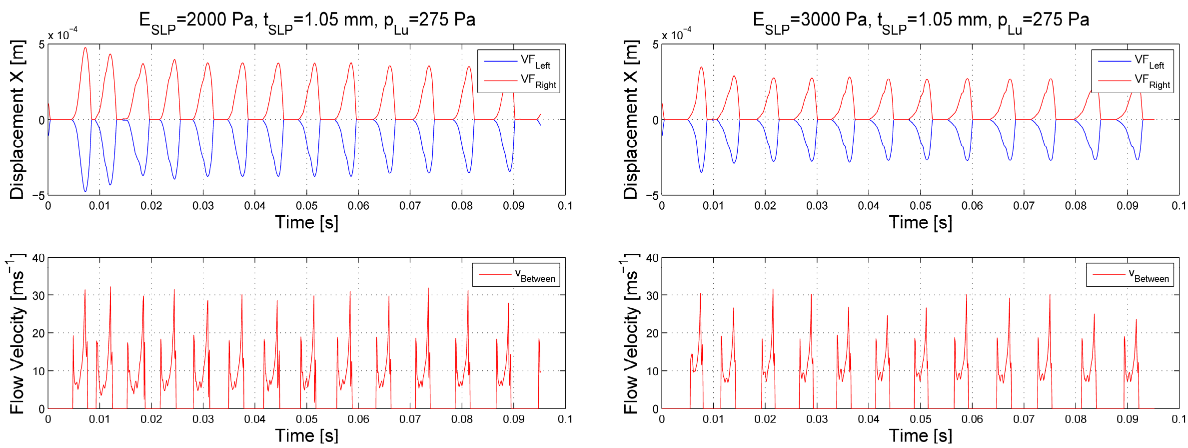

Fig. 2: Computed displacement in x direction of selected nodes on the face of the left and right VF located in the middle of the VF height and flow velocity in selected node between the VF for E_{SLP} = 2 kPa (left graphs) and E_{SLP} = 3 kPa (right graphs).

4. Conclusions

The 2D FE model of the vocal fold self-oscillations in interaction with the vocal tract acoustics was created and the effect of stiffness of lamina propria on the VF vibrations was analyzed. The results of the numerical simulations showed that the excitation of the model by the constant lung pressure produces the VF self-oscillations. Numerically simulated results showed characteristics similar as in human phonation.

The computed results showed that by increasing stiffness of the lamina propria the maximal glottis opening decreases. The lower vibration frequency observed in some cases was probably caused by the fact, that for the lower Young's modulus (E_{SLP}) the lamina propria was vibrating while the muscle remained almost still, whereas for the higher values of E_{SLP} the VF were vibrating as a whole body. The developed model excited by the lung pressure showed that the quotients characterising the phonation regime correspond better to the clinical data comparing to the previous model excited by the constant flow velocity. The numerical simulations also showed that with increasing lung pressure the fundamental frequency increases which is in accordance with clinical results. The developed FE model can be used for simulations how the various pathological changes in VF tissue can change the resulting VF vibrations and the produced sound.

Acknowledgement

This research is supported by Grant Agency of the Czech Republic by the project No 16-01246S „Computational and experimental modelling of self-induced vibrations of vocal folds and influence of their impairments on human voice."

References

Hájek P., Švancara, P., Horáček, J., Švec, J.G. (2016) Finite Element Modelling of the Effect of Stiffness and Damping of Vocal Fold Layers on their Vibrations and Produced Sound. in: Applied Mechanics and Materials, 821, pp. 657–664.

Horáček, J., Šidlof, P., Švec, J.G. (2005) Numerical simulation of self-oscillations of human vocal folds with Hertz model of impact forces. Journal of Fluids and Structures, 20, pp. 853–869.

Ishizaka, K., Flanagan, J.L. (1972) Synthesis of voiced sounds from two-mass model of the vocal cords. Bell Syst. Tech. J., 51, pp. 1233–1268.

Lohscheller J., Švec J., Döllinger, M. (2013) Vocal fold vibration amplitude, open quotient, speed quotient and their variability along glottal length: kymographic data from normal subjects. Logoped. Phoniatr. Vocol., 38/4, pp. 182–92.

Scherer, R. C., Shinwari, D., De Witt, K. J., Zhang, C., Kucinschi, B. R., & Afjeh, A. A. (2001). Intraglottal pressure profiles for a symmetric and oblique glottis with a divergence angle of 10 degrees. Journal of the Acoustical Society of America, 109, 4, pp. 1616–1630.

Story, B.H., Titze, I.R. (1995) Voice simulation with a body-cover model of the vocal folds, Journal of the Acoustical Society of America, 97, pp. 1249–1260.

Šidlof, P., Zörner, S., Hüppe, A. (2015) A hybrid approach to the computational aeroacoustics of human voice production. Biomechanics and Modeling in Mechanobiology, 14/3, pp. 473–488.

Švancara, P., Horáček, J., Hrůza, V. (2011) FE modelling of the fluid-structure-acoustic interaction for the vocal folds self-oscillation. in: Vibration Problems ICOVP 2011 (Náprstek, J., Horáček, J., Okrouhlík, M., Marvalová, B., Verhulst, F., Sawicki, J.), Springer, Berlin, pp. 801–807.

Švancara, P., Horáček, J., Martínek, T., Švec J.G. (2014) Numerical simulation of videokymographic images from the results of the finite element model. in: Engineering Mechanics, Svratka, pp. 640–643.

Titze, I.R.(2006) The Myoelastic Aerodynamic Theory of Phonation, National Centre for Voice and Speech, Denver and Iowa City.

Xue, Q., Zheng, X., Mittal, R., Bielamowicz, S. (2014) Subject-specific computational modeling of human phonation. Journal of the Acoustical Society of America, 135/3, pp. 1445–56, 2014.

22nd International Conference
ENGINEERING MECHANICS 2016
Svratka, Czech Republic, 9 – 12 May 2016

DETERMINATION OF STEEL CORROSION RATE

K. Hájková[*], L. Jendele[**], V. Šmilauer[***]

Abstract: *Carbonation and chloride ingress are considered as the most serious damaging mechanisms for steel corrosion in reinforced concrete. The service life is divided into two main phases. The initial phase and propagation phase. The initial phase was explored recently and results show high influence of cracks on accelerating of carbonation and chloride ingress in concrete structures. Our model focuses on the propagation period and predicts x_{corr} presents a loss of mass for radial corrosion depth, including cracking and spalling of concrete cover. The presented model was implemented in ATENA software. A prestressed box-girder bridge is analyzed in greater detail, showing corrosion of reinforcement and its impact on bridge's bearing capacity.*

Keywords: Concrete, Corrosion, Propagation phase, Carbonation, Chlorides

1. Introduction

Reinforcement corrosion due to carbonation and chloride ingress are the most damaging mechanisms in reinforced concrete structures (P. Basheer at al., 1996).

The service life t_l of reinforced concrete structures is generally divided into two time phases, Figure 1. The initiation period t_i and the propagation period t_p. Calculation of the initiation period was solved in the previous project and preliminary results show high influence of cracks to transport properties and acceleration of damaging mechanisms. For traditional CBM, cracks 0.3 mm decrease induction time approximately 6x for carbonation and approximately 9x for chloride ingress in salt water. Preventing macrocracks and designing proper concrete is essential for durable concrete (V. Červenka et al., 2012)

Our model is focused on the propagation period t_p where corrosion of reinforcing steel take place. During this time is reinforcement weakened and grow corrosion products on the surface of reinforcement. In the model, two types of corrosion are considered. A uniform corrosion (corrosive attack proceeding evenly over the entire surface area) typical for carbonation and pitting corrosion (caused by depassivation of a small area, leads to the creation of small holes in the material) typical for chlorides (F. Duprat, 2007).

2. Model for carbonation and chloride penetration

Model for steel cross section loss during the propagation period. Model is based on Faraday's law (Rodriguez, 1996).

2.1 The corrosion rate for the carbonation

The corrosion rate for the carbonation depends on the corrosion current density i_{corr} [$\mu A / cm^2$], which ranges between 0.1-10 and depends on the quality and the relative humidity of the concrete (Page CL,

[*] Ing. Karolina Hájková: Czech Technical University in Prague, Faculty of Civil Engineering, Thákurova 7; 166 29, Prague 6; CZ, karolina.hajkova@fsv.cvut.cz

[**] Doc. Ing. Vít Šmilauer, PhD.: Czech Technical University in Prague, Faculty of Civil Engineering, Thákurova 7; 166 29, Prague 6; CZ, vit.smilauer@fsv.cvut.cz

[***] Doc. Ing. Libor Jendele CSc, Ph.D.: Červenka Consulting s.r.o., Na Hřebenkách 55, 150 00, Prague, CZ, libor.jendele@cervenka.cz

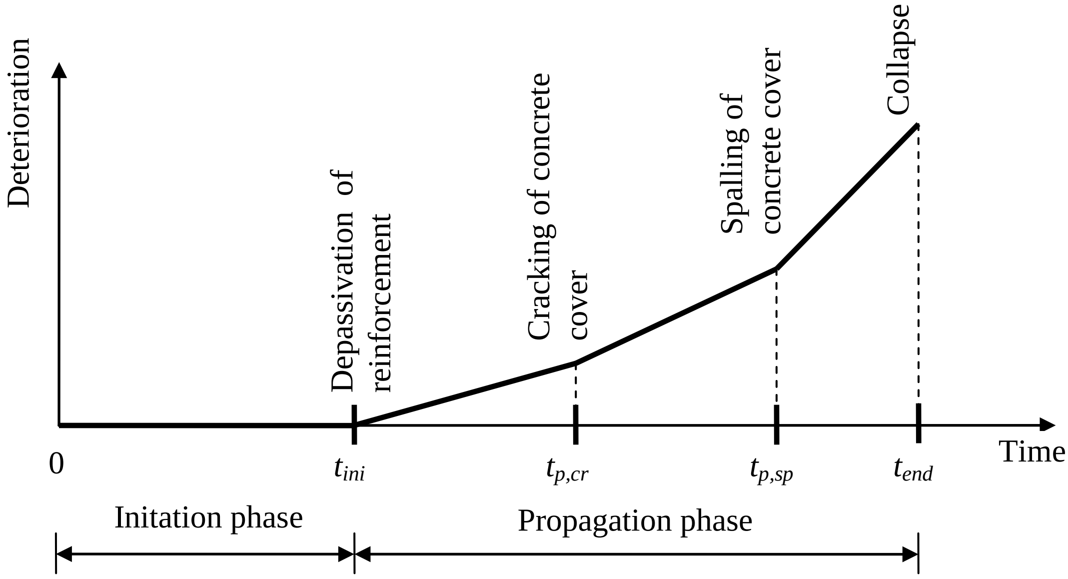

Fig. 1: Initiation and propagation phase

1992). This model is suitable for prediction of steel cross section loss during the whole propagation period t_p. Principal task is to determine the proper current density, i_{corr} in each stage of the propagation period. The corrosion rate is determined as follows:

$$\dot{x}_{corr}(t) = 0.0116 i_{corr}(t) \tag{1}$$

where $\dot{x}_{corr}$ is the average corrosion rate in the radial direction [mm/yr], i_{corr} is corrosion current density [µA/cm^2] and t is calculated time after the end of induction period [years].

2.2 The corrosion rate for chlorides

The corrosion rate for chlorides is more complicated because it is affected by concentration of chlorides in the concrete and their transport. For this calculation is used model Liu and Weyer (Y. Liu et al., 1998):

$$i_{corr} = 0.926 * \exp\left[7.98 + 0.7771 \ln(1.69 C_t) - \frac{3006}{T} - 0.000116 R_C + 2.24 t^{-0.215}\right] \tag{2}$$

Where i_{corr} is corrosion current density [µA/cm^2], C_t Total chloride content [kg/m^3 of concrete], C_t must exceed the threshold (about 0.36 kg/m^3 of concrete). This is computed from ATENA model for chloride ingress, T is temperature at the depth of reinforcement [K] and R_c is ohmic resistance of the cover concrete [Ω] (Y. Liu, 1996) and t is time after initiation [years]:

$$R_C = \exp[8.03 - 0.549 \ln(1 + 1.69 C_t)] \tag{3}$$

The average corrosion rate in radial direction is determined according to Eq. (1).

After spalling of concrete cover, corrosion of reinforcement take place in direct contact with the environment. To determine the rate of corrosion of reinforcement after spalling is used direct determination of the value of the rate of corrosion of reinforcement (Spec-net).

Table 1: Corrosion rates of steel under atmospheric exposition

Corrosivity zones (ISO 9223)	***Typical environment***	***Corrosion rate for first year (µm/yr)***

Category	*Description*		*Mild stell*	*Zinc*
C1	*Very low*	*Dry indoors*	*≤1,3*	*≤0,1*
C2	*Low*	*Arid/Urban inland*	*>1,3 a ≤25*	*>0,1 a ≤0,7*
C3	*Medium*	*Coastal and industrial*	*>25 a ≤50*	*>0,7 a ≤2,1*
C4	*High*	*Calm sea-shore*	*>50 a ≤80*	*>2,1 a ≤4,2*
C5	*Very High*	*Surf sea-shore*	*>80 a ≤200*	*>4,2 a ≤8,4*
CX	*Extreme*	*Ocean/Off-shore*	*>200 a ≤700*	*>8,4 a ≤25*

2.2. Cracking of concrete cover

The cracking of concrete cover in propagation period $t_{p,\ cr}$ corresponds to the depth of corrosion $x_{corr,cr}$ (DuraCrete, 2000). The critical penetration depth of corroded steel $x_{corr,cr}$ is formulated as:

$$x_{corr,cr} = a_1 + a_2 \frac{C}{d_{ini}} + a_3 f_{t,ch} \tag{5}$$

where parameter a_1 is equal 7.44e-5 [m], parameter a_2 is equal 7.30e-6 [m], a_3 is [-1.74e-5 m/MPa], C is cover thickness of concrete [m], d_{ini} initial bar diameter [m], $f_{t,ch}$ is characteristic splitting tensile strength of concrete [MPa].

2.3. Spalling of concrete cover

The time of spalling of concrete cover $t_{p,sp}$, which again corresponds to the depth of penetration $x_{corr,sp}$. The critical penetration depth of corroded steel $x_{corr,sp}$ is calculated from (DuraCrete, 2000):

$$x_{corr,sp} = \frac{w^d - w_0}{b} + x_{corr,cr} \tag{6}$$

where parameter b depends on the position of the bar (for top reinforcement 8.6 µm/µm and bottom 10.4 µm/ µm), w_d is critical crack width for spalling (characteristic value 1 mm), w_0 is width of initial crack (known from previous ATENA computation) and $x_{corr,cr}$ depth of corroded steel at the time of cracking [m].

3. Implementation of presented model in ATENA software

The model is used on a structure of a pre-stressed reinforced concrete bridge of Mr. Pavel Wonka over the river Elbe in Pardubice, Czech Republic. The bridge is modeled by 4500+ shell elements. The pre-stressed reinforcement is realized by special "external cable" elements. For more details see (J. Červenka et al., 2016).

The concrete of the girder box was classified as C35/45. Estimated composition yields CEM 42.5, C_p= 350 kg/m^3 and water, W= 175 kg/m^3. Concrete box girder was loaded on its surface by carbonation and chlorides load and used the following parameters for carbonation: CO_2 = 0.00036, RH = 0.60. K_{CO2} has no influence since there are no SCM, for chlorides: mean value D_{ref} = 7.72e-13·86400 = 6.67e-08 m^2/day (assumed 90% confidence which is 1.19e-7), t_{Dref} = 3650 days, m_{coeff} = 0.37, t_{mcoeff} = 10950 days, C_s = 0.103, Cl_{crit} = 0.0185. Progressive period for both loads: a_1 = 7.44e-5 m, a_2 = 7.30e-6 m, a_3 = -1.74e-5 m/MPa, $f_{t,ch}$ = 3.5 MPa, d_{ini} = 0.001 m, pitting corrosion R_{corr} = 1, corrosion rate after spalling 30 µm/year.

The Figure 2 shows calculated reduction coefficient for reinforcement cross sectional area with concrete cover 20 mm. For the first 50 years the reinforcement does not corrode, but at the age of 100 years about 50% of the reinforcement has corroded and at 150 years there is only about 30% of the original reinforcement.

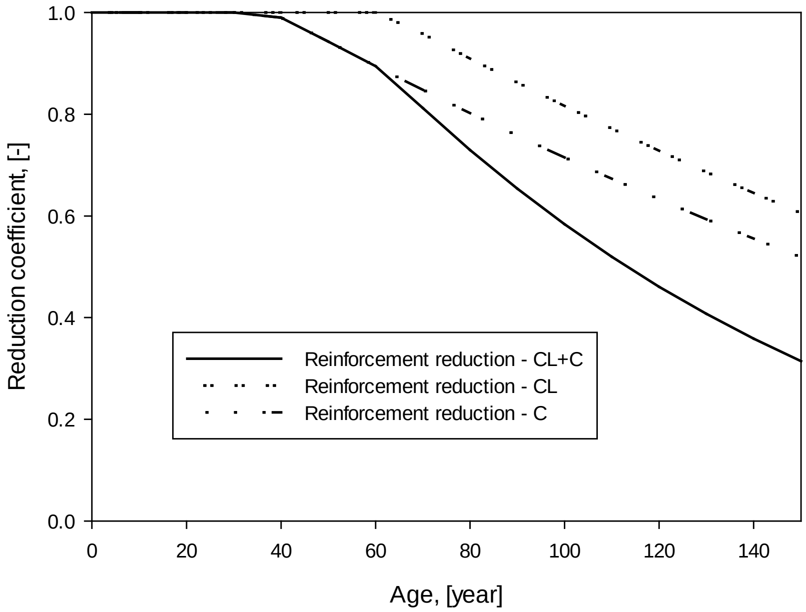

Fig. 2: The worst reinforcement reduction coefficient for bars with concrete cover 20 mm with the influence of cracks.

4. Conclusions

The presented model was implemented in ATENA software and allows us to model reinforcement mass loss during the propagation phase due to two main corrosion mechanisms, carbonation and chloride ingress. The results shows that durability analysis could be a part of design of structures. It allows simulate negative effects of external environmental conditions on the structure and to modify its design accordingly, increase depth of reinforcement cover, modify properties of concrete mixture, improve surface isolations, etc.

Acknowledgement

We gratefully acknowledge the financial support from the Technology Agency of the Czech Republic TAČR under the project TA04031458 and SGS12/116/OHK1/2T/11 granted by CTU in Prague.

References

Basheer, P., Chidiact, S., Long, A. (1996) Predictive models for deterioration of concrete structures. Construction and Building Materials, 10, 1, pp.27-37.

Červenka, V., Červenka, J., Bittnar, Z. (2009-2012) Projekt CerHyd MPO TIP FR-TI1/612. Výpočetní program pro simulaci procesů v průběhu tvrdnutí betonu s využitím mikroúrovňových modelů hydratace.

Duprat, F. (2007) Reliability of RC Beams Under Chloride-ingress. Construction and Building Materials, 21, 1605.

DuraCrete (2000) Final Technical Report, Gouda.

Rodriguez, J., Ortega, L. M., Casal, J. & Diez, J. M. (1996) Corrosion of Reinforcement and Service Life of Concrete Structures. In Proc. of Int. Conf. on Durability of Building Materials and Components, 7, 1:117-126.

Page CL (1992) Nature and properties of concrete in relation to environment corrosion, Corrosion of Steel in Concrete, Aachen.

Liu, Y., Weyers, R.E. (1998) Modeling the Dynamic Corrosion Process in Chloride Contaminated Concrete Structures. Cement and Concrete Research, 28(3), 365-367.

Liu, Y. (1996) Modelling the Time-to-corrosion Cracking of the Cover Concrete in Chloride Contaminated Reinforced Concrete Structures. Ph.D. dissertation, Virginia Polytechnic Institute.

Spec-net (2015) Corrosivity zones for steel construction [online] available from: http://www.spec-net.com.au/press/1014/gaa_081014/Corrosivity-Zones-for-Steel-Construction-Galvanizers-Association.

Červenka, J. & Sajdlová, T. (2016) Most Pavla Wonky v Pardubicích, Nelineární model nosné konstrukce - reprodukce zatěžovací zkoušky a výpočet únosnosti. Červenka Consulting, Prague, Czech Republic.

22nd International Conference
ENGINEERING MECHANICS 2016
Svratka, Czech Republic, 9 – 12 May 2016

ANALYSIS OF TRADITIONAL CARPENTRY BUTT JOINT FINITE-ELEMENT MESH

M. Hataj*, P. Kuklík**

Abstract: *The aim of this article is to compare a quality of butt joint 3D finite-element meshes. FEM solution accuracy and calculation convergence speed are the main factors for a mesh quality evaluation. Numerical model of the subjected butt joint includes material nonlinearities. Material model of wood presume elasto-plastic behaviour and has orthotropic – transversal isotropic property. Contact elements are modeled among the individual structural components of the joint. The finite-element meshes introduced herein differ one from other by element type and their quantity applied, type of mapping and local density of mesh. Number of nodes and elements, calculation convergence speed, FEM solution exactness, symmetry and mapping of elements are observed.*

Keywords: Finite element method, Mesh, Butt joint, Carpentry, Timber structures.

1. Introduction

Wood is one of the first structural material applied in the civil engineering practice. It disposes of beneficial structural properties which make it, together with its renewability, convenient for primary load-bearing element application. Timber elements often constitute bearing part of roof structures. A connection is usually the weakest point of a timber frame structure. Traditional carpentry joints are still frequently performed despite the great technological progress in timber joining. However, these types of connections are not supported by the applicable standards much and therefore their design normally considers only simple and empirical relationships based on a carpenter's experience. The aim of the carpentry joints research is to derive analytical relationships supported by modern numerical calculations and experiments and so enable their effective application in a structural practice. For instance, a lapped scarf joint with inclined faces and wooden dowels starts was applied within a historical structure reconstruction process, Arciszewska-Kedzior et al. (2015).

This article is focused on a perpendicular butt joint examination. The connection is composed of two structural elements – one is longitudinal and one is transversal, see Fig. 1. A traditional butt joint is usually fixed by a carpentry iron dog. The transversal timber element is exposed to compression parallel to the grains. Longitudinal element is subjected to compression perpendicular to the grains.

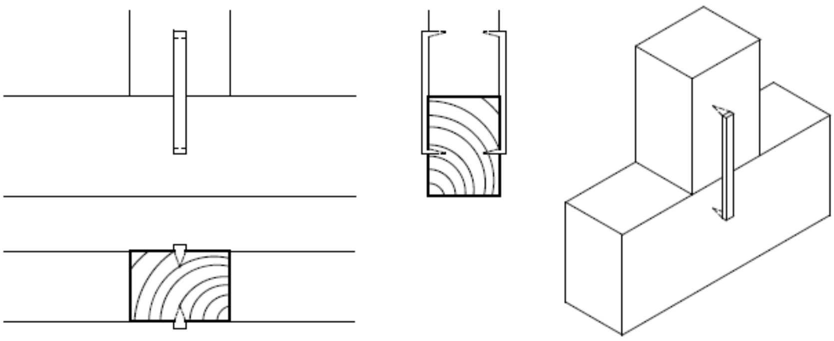

Fig. 1: Traditional carpentry butt joint.

* Ing. Martin Hataj: Department of Steel and Timber Structures, Czech Technical University in Prague, Thákurova 7; 166 29, Prague; CZ, martin.hataj@fsv.cvut.cz

** Assoc. Prof. Ing. Petr Kuklík, Ph.D.: University Centre for Energy Efficient Buildings CTU, Czech Technical University in Prague, Třinecká 1024; 273 43, Buštěhrad; CZ, kuklik@uceeb.cz

Compression strength perpendicular to the grain flow is noticeably lower comparing to compression strength parallel to the grain flow. Characteristic values of compression strength for a commonly applied timber strength class in the Czech Republic - C24 - are listed in standard ČSN EN 338 (2003):

$$f_{\mathrm{c,0,k}} = 21\,\mathrm{MPa} \tag{1}$$

$$f_{\mathrm{c,90,k}} = 2,5\,\mathrm{MPa} \tag{2}$$

where $f_{\mathrm{c,0,k}}$ is characteristic value of compression strength parallel to the grains and $f_{\mathrm{c,90,k}}$ is characteristic value of compression strength perpendicular to the grains. Regarding the fact, that $f_{\mathrm{c,0,k}}$ is approx. ten times higher that $f_{\mathrm{c,0,d}}$, the strength perpendicular to grains is often exceeded in linear elements and undesired local deformations occur.

2. Methods

This research is focused on 21 numerical models of a traditional carpentry butt joint. All calculations are conducted on a mutual desktop computer. Hardware parameters are consisted from CPU Intel Xeon E5-1650, 6 cores 3,2 GHz, RAM 16 GB. Numerical models are created in software ANSYS 16.0, Academic. All the inputs, except for an appertaining finite-element mesh, are identical in all the numerical models examined within the research.

Tab. 1: Finite-element mesh types.

Mesh type	Model No.	El. size [mm]	Element type	Elem. number	Node number	Time [h:m:s]
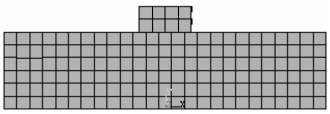	1_1_1	20	SOLID45 hex	873	1115	0:00:15
	1_1_2	10	SOLID45 hex	5940	6741	0:01:46
	1_1_3	5	SOLID45 hex	43728	46631	0:22:01
	1_1_4	20	SOLID95 hex	873	3897	0:00:48
	1_1_5	10	SOLID95 hex	5940	25063	0:08:11
	1_1_6	5	SOLID95 hex	43728	179531	5:58:24
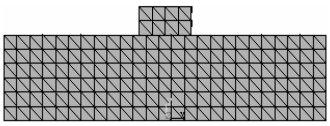	1_2_1	20	SOLID95 pent	1921	4737	0:00:49
	1_2_2	10	SOLID95 pent	12596	30887	0:09:03
	1_2_3	5	SOLID95 pent	90320	222795	5:03:21
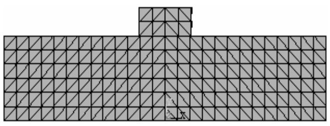	1_3_1	20	SOLID95 pent	1994	4911	0:00:48
	1_3_2	10	SOLID95 pent	12596	30887	0:08:13
	1_3_3	5	SOLID95 pent	90320	222795	5:18:57
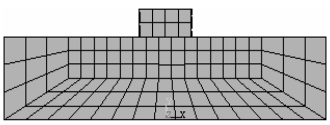	1_4_1	20	SOLID95 hex	767	2903	0:00:29
	1_4_2	10	SOLID95 hex	4382	16413	0:04:25
	1_4_3	5	SOLID95 hex	30536	117255	2:14:44
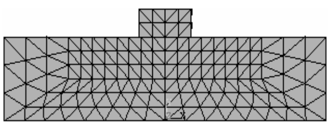	1_5_1	20	SOLID95 pent	1456	3693	0:00:37
	1_5_2	10	SOLID95 pent	8176	20207	0:04:57
	1_5_3	5	SOLID95 pent	58720	145439	1:53:31
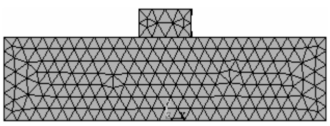	1_6_1	20	SOLID92 tetr	5371	8434	0:00:21 [1]
	1_6_2	10	SOLID92 tetr	40960	59123	0:06:20 [2]
	1_6_3	5	SOLID92 tetr	326167	451800	18:39:58

Numerical models of the traditional carpentry butt joint include orthotropic elasto-plactic wood definition. This material model expects a bilinear stress-strain relation, published by Moses & Prion (2002). Different types of finite-element meshes applied in the particular simulations can be found in Tab.1. Individual meshes differ one from other by types of element and their quantity, by type of mapping and local density of the mesh. Computing time for individual models is listed in the right column of Tab.1. Models 1_6_1 and 1_6_2 are not convergent and so time for 30 % [1] a 42 % [2] of the final computing time is listed in the table. Elements SOLID45 and SOLID95 are used for mapped finite-element mesh whereas element SOLID95 forms free mesh. Applied elements are demonstrated in Fig. 2.

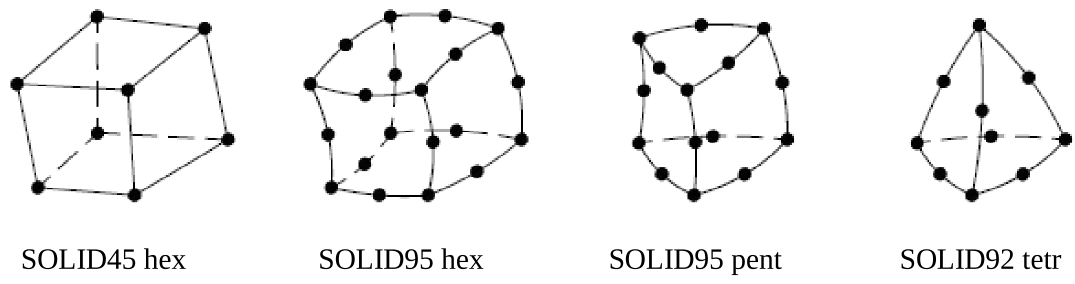

Fig. 2: Used element types.

A solution quality and calculation convergence speed with finite-element meshes listed above are compared with each other. Load-displacement behaviour of joint is depicted in Fig. 3 respectively. Loading is applied on the horizontal surface of the transversal timber element. Elasto-plastic behaviour of numerical model sets 1 – 6 is marked with a grey line. The most exact numerical solution that is reached by the procedure is marked with the black dashed line.

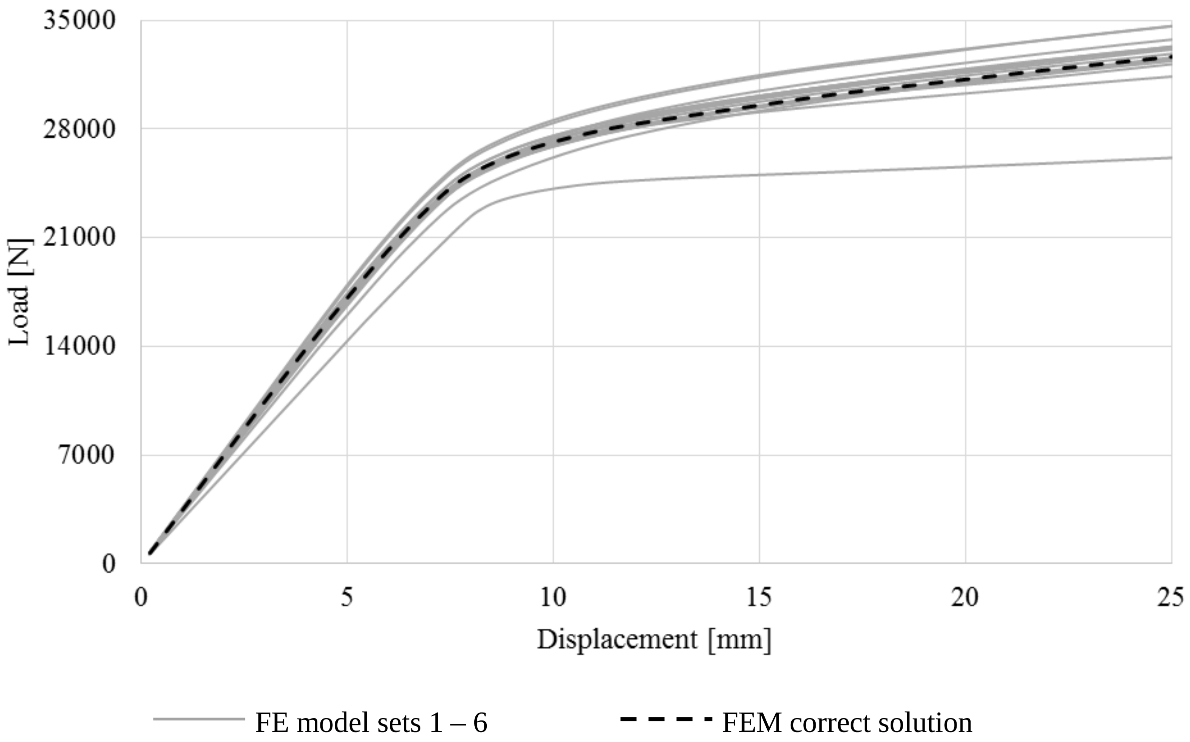

Fig. 3: Load-displacement diagram of FE model sets 1-6 and correct solution.

In Tab. 2, percentage equality of the individual finite-element types' solution with the most exact numerical result is presented. The value of compression stress linked to the vertical displacement equal to 25 mm is the dominant result assessed within the numerical simulation analyses. Finite-element models 1_6_1 and 1_6_2 are not evaluated due to non-convergence of numerical calculation.

Tab. 2: Finite-element mesh quality.

Mesh number	1_1_1	1_1_4	1_2_1	1_3_1	1_4_1	1_5_1	1_6_1
Quality [%]	75	106	102	103	106	101	-
Mesh number	1_1_2	1_1_5	1_2_2	1_3_2	1_4_2	1_5_2	1_6_2
Quality [%]	93	101	101	101	101	100	-
Mesh number	1_1_3	1_1_6	1_2_3	1_3_3	1_4_3	1_5_3	1_6_3
Quality [%]	98	100	100	100	100	100	100

3. Conclusions

In contrast with application of SOLID95 hex elements, an application of SOLID45 hex elements leads to an accurate result with increasing number of elements. Symmetric element configuration does not significantly affect a solution quality and calculation convergence speed in comparison with asymmetrical configuration of the same elements (SOLID95 pent). Application of SOLID92 elements resulted into a poor calculation convergence. Calculation converges in the case the number of elements is high however computation is rather time-consuming. Application of SOLID95 pent elements proves to be more advantageous than SOLID45 hex elements. Numerical model with SOLID95 pent elements delivers a better result accuracy comparing to the model with twice smaller elements SOLID45 hex. Furthermore, calculation is approximately twice faster in favour of finite-element mesh with SOLID95 pent. SOLID95 pent element application is also useful in comparison with elements SOLID 95 hex. SOLID 95 pent elements collect results in two other nodes. Both these simulations are almost the same time-consuming, although SOLID95 pent elements are twice longer than SOLID95 hex elements in compared finite-element meshes and calculation results are more precise. Parts of volume that are discrete distributed by the described elements are mutually compared and depicted in Fig. 4. Numerical models with a mesh locally densified in the interface (connecting area), where the timber elements are connected and where prismatic elements SOLID95 pent are applied, appear to be the most favourable in the aspects of results quality and calculation speed.

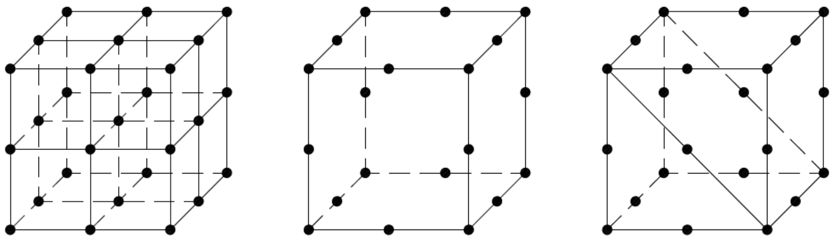

8 x SOLID45 hex 1 x SOLID95 hex 2 x SOLID95 pent

Fig. 4: Applied element types for comparison.

Acknowledgement

This work has been supported by project of University Centre for Energy Efficient Buildigs and by Czech Technical University in Prague project no. SGS14/178/OHK1/3T/11.

References

Arciszewska-Kedzior, A., Kunecký, J., Hasníková, H. & Sebera, V. (2015) Lapped scarf joint with inclined faces and wooden dowels: experimental and numerical analysis. Engineering Structures, 94:2015, pp.1-8.

ČSN EN 338: Konstrukční dřevo – Třídy pevnosti. (2003) Český normalizační institut, Prague.

Moses, D. M. & Prion, G. L. (2002) Anisotropic Plasticity and Failure Prediction in Wood Composites. Research Report, University Of British Columbia, Vancouver.

22nd International Conference
ENGINEERING MECHANICS 2016
Svratka, Czech Republic, 9 – 12 May 2016

ACCELERATED CHLORIDE MIGRATION TESTS IN CONCRETE

P. Hlaváček*, J. Němeček**

Abstract: *Accelerated chloride migration tests are performed on cylindrical samples made of Portland cement concrete. Low voltage electric field is applied as a driving force for both chloride accelerated penetration and extraction. It is verified that the chloride concentration profile measured in samples after 48 hours of electromigration approximately corresponds to the chloride profile after six months of natural diffusion. Potential and effectiveness of the chloride extraction process for the rehabilitation of concrete in terms of lowering the chloride concentration using the DC current is discussed. Experiments show up to 50% decrease in chloride concentration in concrete after 48 hours of extraction driven by electric field with the reverse polarity. Simulation of the process is provided using analytical and numerical solutions of partial differential equations with a simplification in form of the constant diffusion coefficient.*

Keywords: Concrete, Chlorides, Diffusion, Electromigration, Chloride Extraction

1. Introduction

The resistance to penetration of chlorides is one of critical properties of steel-reinforced concrete. The chloride-induced corrosion of steel rebar largely affects the durability of the concrete in saline environments, such as offshore structures, tidal zone structures or in highway engineering (due to the winter deicing maintenance). There are two primary mechanisms by which the ion can migrate inside the pore solution in the concrete. The first one is diffusion where the ions are transported via the concentration gradient; the second one is a convection of ions due to internal (inter-ionic) or externally applied electric potential. As soon as the concentration of chlorides on the rebar surface reaches a critical level, the corrosion of the steel reinforcement starts. The corrosion is accompanied by an expansion of the rust products causing high pressures and, concrete cracking, internal damage and finally spalling of a cover layer. The critical chloride concentration, modeling of the steel corrosion and various concrete impregnation approaches are in researchers' spotlight for more than 30 years (e.g. Blankenhorn, 1978; Tuutti, 1982; Cabrera, 1996; Šmilauer et al., 2013; Němeček & Xi, 2015).

An effectiveness and numerical modeling of chloride extraction from concrete using an external electric field is studied in this paper. Chloride penetration of concrete using both natural diffusion and electromigration and a subsequent chloride extraction in an electromigration chamber is examined.

2. Materials and Methods

2.1 Experimental part

Concrete specimens made of ordinary Portland cement, sand and natural crushed aggregate were used in all experiments used within this study. Table 1 shows its mixture composition. The compressive strength at 28 days was found as 49.7±4.2 MPa and the open (water accessible) porosity ~ 7%.

The concrete was mixed for 2 minutes in a 50l laboratory mixer, subsequently cast into cylindrical and cubic molds and vibrated for approximately 30 seconds. The forms were covered with a foil to prevent water evaporation. The samples were unmolded and submerged into water bath after 48 hours. Cubes

* Ing. Petr Hlaváček, PhD.: Faculty of Civil Engineering, Czech Technical University in Prague, Thákurova 7; 166 29, Prague 6; CZ, petr.hlavacek@fsv.cvut.cz

** Doc. Ing. Jiří Němeček, Ph.D..: Faculty of Civil Engineering, Czech Technical University in Prague, Thákurova 7; 166 29, Prague 6; CZ, jiri.nemecek@fsv.cvut.cz

150x150x150 mm^3 were used for compressive strength determination; 50 mm thick slices from cylinders with 100 mm in diameter were used for the chloride migration tests.

Tab. 1: Concrete mixture composition, mass per 1m^3.

CEM I-42,5R	Sand 0-4	Aggregates 4-8	Aggregates 8-16	Water	w/c
432 kg	865 kg	288 kg	576 kg	184 kg	0.43

Two kinds of tests on matured samples (at least 28 days old) were performed. First, a natural chloride diffusion test in which the samples were sealed from all sides but the upper surface was submerged in 3% NaCl solution in constant laboratory temperature for 173 days. Second, the accelerated chloride penetration/extraction tests were performed in an electromigration chamber. The chamber consisted of two containers with electrolyte solutions. In case of chloride penetration tests, a 3% NaCl solution was used in the upstream compartment and 0.3 M NaOH solution in the downstream compartment. In case of chloride extraction, both compartments were filed with 0.3 M NaOH and the polarity was switched. A DC power source with a constant electric potential difference 20V was connected to stainless steel mesh electrodes submerged in the electrolytes. The analyzed sample was placed between the two electrodes, and the whole chamber was sealed (Figure 1). The accelerated chloride penetration/extraction run for 48 hours.

After the tests, the total (acid soluble) chloride concentration was analyzed in 5 mm depth-steps. The concrete specimens were drilled in 5 mm steps, the powder collected and mixed with 20% HNO_3. The concentration of chlorides was determined using a chloride ion selective electrode.

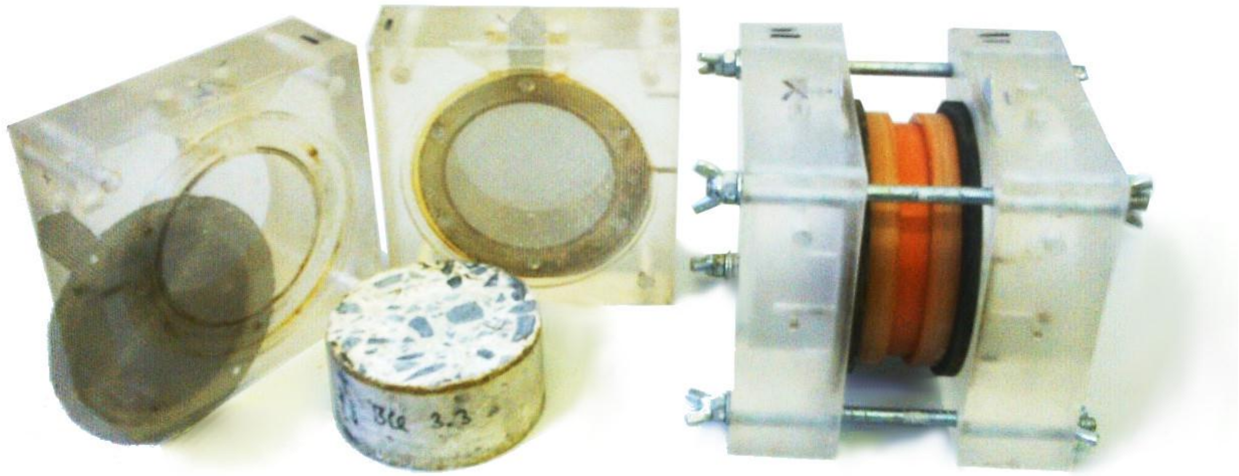

Fig. 1: An electromigration chamber used for accelerated chloride penetration/extraction tests.

2.2. Numerical Part

The concentration profiles were used for the assessment of a diffusion coefficient by employing a non-steady state diffusion equation (the Fick's second law, Eq. 1). The Fick's second law can be used for a pure 1-D diffusion problem in the reference sample and can be written as:

$$\frac{\partial C}{\partial t} = D \frac{\partial^2 C}{\partial x^2} . \tag{1}$$

For a given boundary conditions of the reference sample, there exists an analytical solution in form of an error function:

$$C(x,t) = C_0 \left(1 - erf\left(\frac{x}{2\sqrt{Dt}} \right) \right), \tag{2}$$

where x is a distance from the surface exposed to NaCl, t time, $C(x,t)$ is the ion concentration and D is diffusion coefficient.

For modeling of an electromigration experiment, a combination of ion diffusion and ion migration under non-steady state conditions a Nernst-Planck equation can be used (Tang & Nilsson, 1995):

$$\frac{\partial C}{\partial t} = D\left(\frac{\partial^2 C}{\partial x^2} + \frac{zF}{RT}\frac{\partial C}{\partial x}\frac{\partial \Phi}{\partial x}\right), \qquad (3)$$

where z is the ion valence, R is universal gas constant, F is Faraday's constant and, Φ stands for an electric potential, which is assumed to be constant in time in our case. In this stage of investigation, the diffusion coefficient is, in a simplified way, considered to be constant. The Nernst-Planck equation was solved numerically using the finite difference method (Němeček and Xi, 2015).

3. Results and discussion

The results of natural diffusion test are depicted in Figure 2 which shows a concentration profile of the reference sample after 173 days of a natural diffusion. The chloride diffusion coefficient $D= 4.98\cdot10^{-12}\,m^2s^{-1}$ was evaluated from the Eq. 2 as a best fit minimizing the least square error. The red line in Figure 2 exhibits the analytical solution using this diffusion coefficient. The solution agrees well with the experimental results. Chloride concentration profiles of penetrated/extracted samples using the electromigration method are depicted in Figure 3.

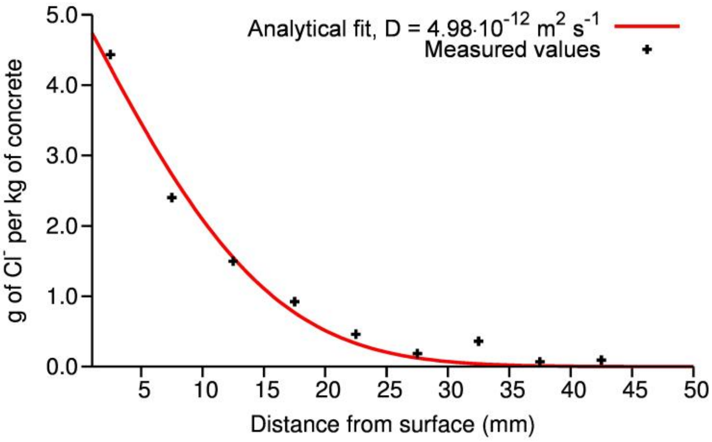

Fig. 2: Chloride concentration profile, natural 1D diffusion of 3% NaCl, 173 days.

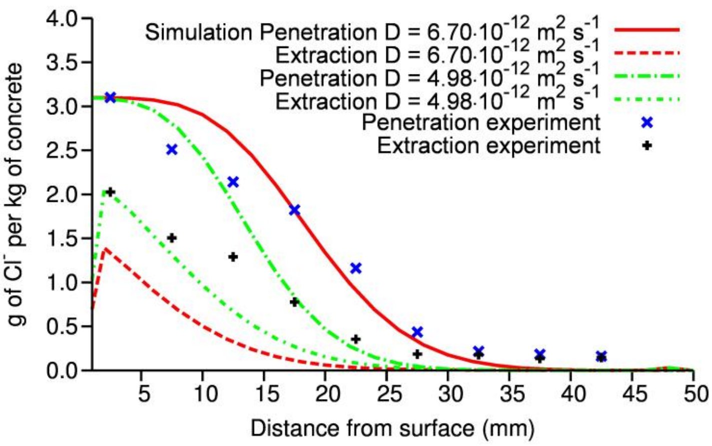

Fig. 3: Chloride concentration profile, chloride penetration/extraction by electromigration at 20 Volts for 48 hours; experiments present an average from three measurements.

The same diffusion coefficient was used for the numerical modeling of the accelerated penetration experiment (Eq. 3). The diffusion coefficient identified from 1-D natural diffusion ($4.98 \cdot 10^{-12}$ m^2s^{-1}) seems to be underestimated for the electromigration (the green dash-and-dotted line in Fig. 3). Using the least-square-minimization procedure, the diffusion coefficient for chloride electro-penetration was identified as $6.70 \cdot 10^{-12}$ m^2s^{-1} (the red line in Fig. 3). On the other hand, with this diffusion coefficient the subsequent chloride electro-extraction is significantly overestimated. The difference between the predicted concentrations after extraction (the red dashed line in Fig. 3) and the measured ones can be related to chloride binding in the concrete sample (Yuan et al., 2009; Němeček, 2015). If the original diffusion coefficient ($4.98 \cdot 10^{-12}$ m^2s^{-1}) is used for modeling the extraction process, a better agreement to experimental values is found (the green dash-and-dotted line in Fig. 3) also suggesting the reduction in the diffusion coefficient is caused by the binding. Incorporation of the binding phenomena is provided by more sophisticated model (Xi and Bažant, 1999) but is beyond the scope of this paper. Further investigation on the mechanism of chloride extraction and the chloride binding is required.

4. Conclusions

Chloride electromigration experiments showed a speedup in chloride penetration into concrete up to 90 times compared to the natural diffusion test performed at laboratory temperature. Approximately 50% reduction in the chloride concentration was measured after 48 hours of applying a low voltage (20 V) electric field. Therefore, it was found the extraction of chlorides from concrete driven by an electric field is feasible and exhibits a high level of efficiency (i.e. large Cl concentration decrease). The constant diffusion coefficient for the natural diffusion was identified from the experimental data using Fick's second law. The same diffusion coefficient, however, cannot be used in the case of electromigration suggesting different underlying mechanism takes place in the concrete. The diffusion coefficient for chloride penetration in electromigration experiments was identified from experiments numerically using the Nernst-Planck equation solved by finite difference method and it appears to be slighty higher compared to natural diffusion. Also, the numerical predictions of chloride extraction were found to be approximately two times overestimated. It is assumed that the effect of chloride binding (not modeled here) is responsible for such discrepancy.

Acknowledgement

Financial support of the Czech Science Foundation (project 16-11879S) and the Grant Agency of the Czech Technical University in Prague (OHK1-074/16) is gratefully acknowledged.

References

Blankenhorn, P.R., Evans, V.A., Kline, D.E. & Cady, P.D. (1978) Chloride penetration of concrete impregnated with various linseed oil/mineral spirits combinations, Cement and Concrete Research, 8(5), pp. 565-570.

Cabrera, J.G. (1996) Deterioration of concrete due to reinforcement steel corrosion, Cement and Concrete Composites, 18(1), pp. 47-59.

Němeček, J, Xi, Y. (2015) Simulation of Chloride Extraction Tests on Concrete Specimens, in: Proceedings of the Fifteenth International Conference on Civil, Structural and Environmental Engineering Computing, (J. Kruis, Y. Tsompanakis & B.H.V. Topping eds), Civil-Comp Press, Stirlingshire, Scotland

Šmilauer, V., Jendele, L. & Červenka, J. (2013) Prediction of Carbonation and Chloride Ingress in Cracked Concrete Structures, in: Proceedings of the Fourteenth International Conference on Civil, Structural and Environmental Engineering Computing, (B.H.V. Topping & P. Iványi eds), Civil-Comp Press, Stirlingshire, Scotland

Tang, L. & Nilsson L.-O. (1995) A Discussion of the Paper "CALCULATION OF CHLORIDE DIFFUSIVITY IN CONCRETE FROM MIGRATION EXPERIMENTS, IN NON-STEADY-STATE CONDITIONS" by C. Andrade, D. Cervigijn, A. Recuero and 0. Rio, Cement and Concrete Research 25(5), pp. 1133-1137.

Tuutti, K. (1982) Corrosion of steel in concrete. Dissertation, Swedish Cement and Concrete Research Institute, Stockholm.

Yuan, Q., Shi, C., De Schutter, G., Den, D. & Audenaert, K. (2009) Chloride binding of cement-based materials subjected to external chloride environment, A review, Construction and Building Materials 23, pp.1-13.

Xi, Y., Bažant, Z. (1999) Modeling Chloride Penetration in Saturated Concrete, Journal of Materials in Civil. Engineering, 11(1), pp. 58–65.

22nd International Conference
ENGINEERING MECHANICS 2016
Svratka, Czech Republic, 9 – 12 May 2016

ANALYSIS OF INNOVATIVE METHODS FOR CAR TIRE COMMINUTION

H. Holka[*], T. Jarzyna[**]

Abstract: *This paper deals with an analysis of two innovative methods for tire recycling: high pressure method – Waterjet and mechanical method Rotarex Fast&Easy. Both methods have been developed on the basis of earlier patents. In the Waterjet method the particles of rubber separate from the tread by means of high pressure water jets flowing out from a water spray head. The mechanical method is based on milling of blocked tires.*

Keywords: tire recycling, tire comminution, Waterjet method, Rotarex Fast&Easy method

1. Introduction

Although used car tires have always been an ecological issue, currently we are able to cope successfully with it. Legal norms introduced by the European Union have encouraged the member states to start dealing with the problem of used car tire management. According to the available norms, as many as 75% of manufactured tires are supposed to be recycled in some way or another which is the responsibility of the manufacturers. The cheapest way to manage used car tires is the so called energy recovery, that is burning. Contrary to common beliefs it is environment friendly and generates relatively little contamination. It allows to obtain large amounts of heat as its energy value 32 GJ/Mg and is similar to energy value of coal. Burning is carried out in high temperature furnaces, power plants, and paper mills, guaranteeing small pollution. The number of tires which undergo burning accounts approximately for 60-75% of tires intended for recycling. The remaining tires have to be reused in a different way. This is the so called material recycling which involves obtaining rubber granulate from tires.
There are two industrial methods for obtaining granulate from tires: cryogenic and mechanical methods.

Briefly speaking, a cryogenic method involves freezing tires down to temperature equal to -85°C, and then breaking the frozen tire into tiny parts. This technology is being introduced into new companies. Mechanical methods (cost of a company is very expensive) involve comminution of tires as required into granulate with particles of 150 μm do 0,8 mm and more. In order to achieve the final effect it is necessary to perform a few operations of comminution.

The above mentioned operations are accompanied by separation of rubber from wires and textile parts of the tire. The most commonly used method is the mechanical one. The disadvantage of all the mechanical methods is that the granulate contains parts of wire that has not been caught by magnets.

2. New innovative methods for tire comminution

In search of more effective methods for tire utilization, new solutions are being constantly created. The number of patents connected with this area is quite impressive. Unfortunately, most of them will never be analyzed or implemented.

This paper presents two new methods for tire utilization which have been developed at the University of Science and Technology Bydgoszcz and Hydrapress Sp. z o.o. company also from Bydgoszcz. The first water based method is called “Waterjet” solution and it was developed at the University as part of the

[*] Prof. Henryk Holka, PhD.: University of Bydgoszcz, Unii Lubelskiej 4C Street; 85 059, Bydgoszcz; PL, hhenryk@vp.pl

[**] Tomasz Jarzyna, PhD.: Institute of Mechanics and Machine Design, University of Science and Technology; Al. prof. S. Kaliskiego 7; 85 796, Bydgoszcz; PL, tomasz.jarzyna@utp.edu.pl

Ministry Development Project. The authors of this paper were involved in this Project. The second method “Rotarex Fast&Easy Method” was developed on the basis of a patent of Hydrapress Sp. z o.o. company, and the authors of this paper belonged to the project team.

2.1. Waterjet method

The authors of this paper started research on tire decomposition by using the high pressure method with application of a patent in 2004 entitled “Tire Utilization Method” and a subsequent patent in 2010. On this basis another patent application has been submitted (Holka&Jarzyna, 2010), whose operation principle is presented in figure 1.

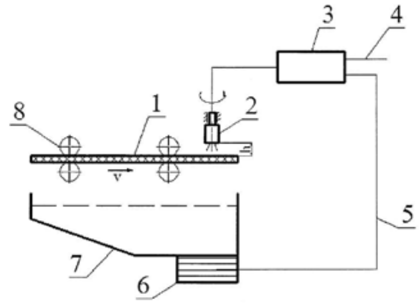

Fig. 1: Scheme of tire utilization by Waterjet method: 1-tire, 2-rotary head, 3-pump, 4-water supply system, 5- technological system for secondary circulation, 6-set of filters , 7-tank, 8- driving rollers

In this method water which after compression is directed to at least one rotary head equipped with at least two nozzles is fed to the respective device, generating high pressure, from where it continuously or cyclically hits the tire surface separating rubber and textile parts from the metal mesh. After removal of rubber and metal parts from a tire, the wastes with water flow down to the tank. Thanks to the secondary circulation the water is resupplied to the pump. Before recycling tires were cut and flattened. During the process a tire moves with v velocity under a water spray head. Velocity of the move and the distance between the head and the tire need to be adjusted to the pump parameters, the type of tire, and the assumed efficiency of the process.

Experimental tests were supposed to find out whether the proposed method can be an alternative for currently used methods (especially mechanical comminution) and how steel wires are separated from the remaining materials of the tire. A special test stand was built to be used for all experimental tests, fig. 2.

Fig. 2: Overall view if the test stand *Fig. 3: A view of a tire after Waterjet method application*

The results of experimental tests after application of single water jets as well as a three nozzle head have confirmed that complete separation of steel wires from the remaining materials is possible, fig. 3.

Another important issue is the size of particles after the process. Relevant measurements were performed with the use of a microscope equipped with an ocular with a scale, calibrated by means of a 1 mm long model and a scale of 0,01 mm. The measurement was made using x80 zoom. Specimens were random taken from comminuted rubber and maximum sizes of particles were determined for each view. A division row was developed on the basis of this population which was featured by variability range (difference in measurement results) $R=a_{max}-a_{min}=688,2+9,3=688,2$ µm and arithmetic mean of measurement results $\bar{a}=146$ µm. Moreover, the average square deviation was determined for s=139,8 µm as well as a mean error of the mean value $\bar{s}=8,82\,\mu m$.Value ranges for n=251 of measurements, for probability value level p=0,95 were $131,91 < E(a) < 160,95\,\mu m$. In figure 4 there is a histogram of the division row of rubber particles (Holka&Jarzyna, 2011).

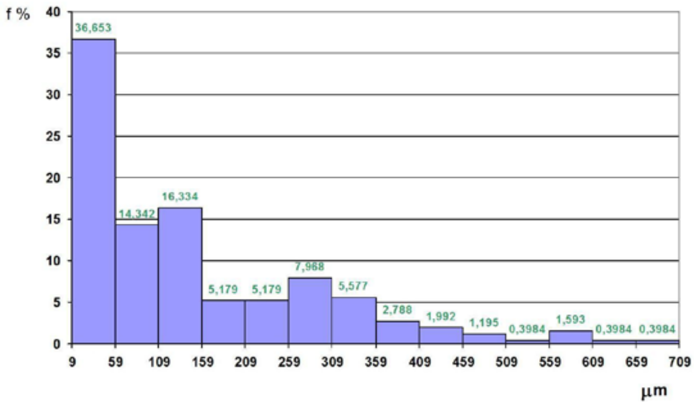

Fig. 4: Histogram of the division row of rubber particle dimensions (non-modal row)

Fig. 5: Overall view of a three nozzle spray head

The water spray head is an important element of the test stand, fig. 5. The head consists of three nozzles mounted at certain angles. A proper choice of nozzles facilitates penetration of the jet into the rubber turning the head simultaneously. Thus, the nozzles shift by translational and rotary motion leaving the wires clean.

Conclusions for Waterjet method

a) The tests have revealed that the method can be used in industrial conditions as an alternative for mechanical comminution methods.

b) Application of high pressure water jets (min. 200 MPa), enables total separation of steel wires from the remaining materials. The obtained rubber is characterized by high degree of disintegration and does not contain wires.

c) Utilization of a bigger number of spray nozzles allows simultaneous treatment of a tire throughout its width.

d) Due to small dimensions of the device and its mobility it can be used it in tire collection points.

2.2. Rotarex Fast&Easy method

This technology uses a tool for milling in the form of a special quick rotating head patented by a company from Jarocin: RBB-STAL SA, (P.392203, 2010 (fig. 6).

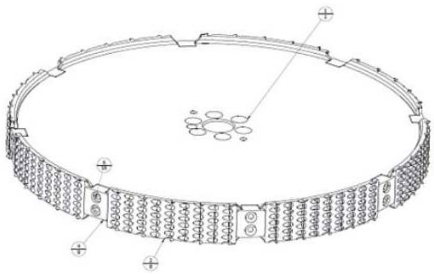

Fig. 6: Milling head (Holka&Wełnowski, 2012)

a) b)

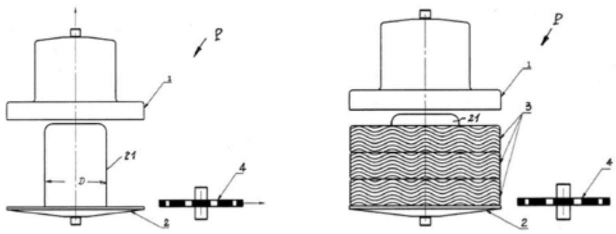

Fig. 7: Device for tire recycling: a) device without tires, b) device with tires; 1-upper plate of the press , 2-lower table of the press, 3-tires, 4 – machining disk , 21 – guiding roll, P - press (Wełnowski, 2012)

Being in possession of a good milling tool, engineers from Hydrapress Sp. z o.o. company applied for a patent entitled (Wełnowski, 2012). The scheme of the device operation is presented in fig. 7. Comminution of tires by the presented method involves compression of tires stapled between the upper and the lower plate of the press (fig. 7b) in a special device (fig. 7a). The tires compressed to a given degree are set into rotary motion by means of the upper and lower plate sets. They are exposed to a rotating machining disk until complete disintegration of the compressed tires. The disk of the tool is fixed proportionally and is slidingly in relation to the upper and lower rotary axes of the plates. A guiding roll with a conical end protrudes from the lower plate (Wełnowski, 2012).

Patent description contains the idea of the machine operation. The real machine is somewhat different than the description, fig. 8.

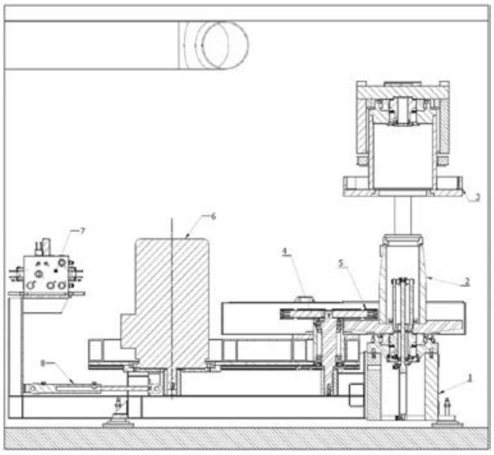

Fig. 8: Machine for mechanical tire recycling ; 1-body, 2-table with an arbor , 3-press bed, 4-spindle , 5-millig disk , 6-motor , 7- hydraulic block, 8-press actuator (Holka&Wełnowski, 2012)

In the considered method the height of compressed tires is equal to the height of the mill and machining can be performed concurrently and backwardly. Tests are being performed in order to determine optimal parameters of the machining. One of the most important issue will be to determine the obtained granulate size in the function of the tire and mill rotation and in the function of the feed.

The considered machine is a mechatronic one which combines numerous innovative technological solutions in the field of mechanics, hydraulics, pneumatics, electronic control, ergonomics and OHS. Its spindle and drive plates are powered electrically and hydraulically with smooth control of pressure force, compressing module and feed of the whole spindle. It is characterized by the following technical parameters: arrangement of operation: vertical, operation modes: manual, automatic, CNC control: controller FACET (Holka&Wełnowski, 2012).

3. Conclusions

1. It should be noted that the companies which deal with traditional recycling are stationary ones due to big size of their equipment. Thus they have one big disadvantage. If their efficiency is high the surrounding area soon becomes devoid of tires and in order to maintain continuity of production the tires have to be supplied from more and more distant places which has a negative impact on the company profits. Waterjet machines and Rotarex Fast&Easy are relatively small which makes them easy to transport. A complete device Rotarex Fast&Easy with the whole tooling can be placed in a portable container.

2. Waterjet method produces rubber particles which are free from contamination with metal. Besides, like in the Fast&Easy method it is a mobile system, that is, due to its small size it can be transported to a given location or increase the company efficiency through installation of a new station.

References

Holka H., Jarzyna T. (2010) Method of retrieval of gum from used car tires and installation for its application - patent registered in UPRP, on 17.08.2010, under number P.392151.

Holka H., Jarzyna T. (2011) Zastosowanie trójdyszowych głowic natryskowych w metodzie water-jet do recyklingu opon samochodowych. Inżynieria i Aparatura Chemiczna, 3, pp. 29-30.

Holka H., Wełnowski J. (2012) ROTAREX FAST&EASY - nowa metoda recyklingu materiałowego opon. Inżynieria i Aparatura Chemiczna, 3, pp. 53-55.

Wełnowski J. (2012) Sposób i urządzenie do rozdrabniania zużytych opon - patent registered in UPRP, on 08.06.2012, under number 399461.

22nd International Conference
ENGINEERING MECHANICS 2016
Svratka, Czech Republic, 9 – 12 May 2016

RECTILINEARITY OF LARGE SIZED SHAFTS

H. Holka*, T. Jarzyna**

Abstract: *The article deals with the problems connected with straightening of large sized shafts. They are used, among others, in papermaking industry and their length ranges up to several meters. Due to the complex manufacturing technology only few factories can meet its requirements. The criterion of geometric axis rectilinearity poses significant difficulties, hence the process involves the necessity of using straightening by means of heat. The study includes a description of an automated test stand, using a modern measurement system, as well as a difficult process of strengthening.*

Keywords: large shafts, centering shaft, centering plugs, straightening pipes

1. Introduction

Large sized shafts are used in different industries e.g. cement industry, paper making industry or wood industry. They are constructed from pipes with plugs on their ends, fig. 1 . The length of such an element can range up to several meters.

Fig. 1: A pipe with plugs

Shafts perform their function in technological processes by rotating e.g. they squeeze out excessive amount of water from the paper pulp by exerting pressure and stress, and therefore they need to be rectilinear. The rotation speeds are not high. In order to provide stable and long operation of the shaft, the pipe that makes up the shaft, should be straight and have possibly small shape deformities. Moreover, the plugs of the pipe should be mounted coaxially in relation to it. Operation of an element, manufactured in such a way, is characterized by a small radial beating. In practice, the most important operations involved in shaft manufacturing are:

-measurement and potential correction of rectilinearity of the pipe geometric axis,

-mounting and positioning of plugs in the pipe.

Displacement sensors located along the axis are used to verify performance correctness of the above mentioned operations. The traditional method uses mechanical clock sensors whose indications are manually recorded in the function of rotation. Simultaneous recording of the values measured from a few sensors is time consuming. Therefore, in order to facilitate the process, a fully automated test stand for straightening pipes and alignment of pipe plugs has been constructed. As compared to the traditional method, the time of manufacturing has been shortened, the process accuracy has been improved and the probability of error occurrence on the side of the operator has been reduced.

The purpose of this work is to present technological operations which are involved in large sized shafts manufacturing, with special emphasis on the process of straightening.

* Prof. Henryk Holka, PhD.: University of Bydgoszcz, Unii Lubelskiej 4C Street; 85 059, Bydgoszcz; PL, hhenryk@vp.pl

** Tomasz Jarzyna, PhD.: Institute of Mechanics and Machine Design, University of Science and Technology; Al. prof. S. Kaliskiego 7; 85 796, Bydgoszcz; PL, tomasz.jarzyna@utp.edu.pl

2. Characteristics of the stand

The test stand for pipe straightening and alignment of plugs is presented in figures 2, 3.

Fig. 2: A test stand for straightening pipes and centering plugs

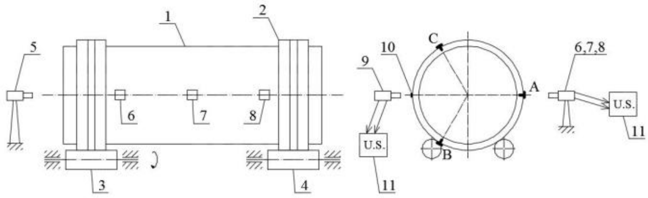

Fig. 3: Scheme of a test stand for straightening pipes and centering plugs

First, pipe 1 is mounted in centering rings 2 by means of twelve bolts located in two rows, six in each row, fig. 4.

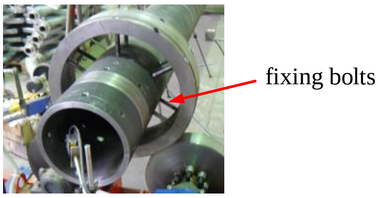

Fig. 4: Pipe mounted in centering rings

The main positioning of a pipe in the rings is performed by A, B, C rings placed, at every 120°. The remaining bolts are supposed to improve stability of the mounting. Then the pipe is put on positioners 3 and 4 (element 3 is a drive element, whereas 4 - guides the pipe) and checks centricity of its mounting in the rings. Laser sensors 6, 7, 8 which record displacement of the shaft in three planes (during centering plugs 6 and 8, while straightening 7) play a very important role in centering a pipe in the rings and mounting the plugs. Sensors 6 and 8 are placed on the ends of the pipe, whereas sensor 7 in half of its length. Correctness of the sensors position in relation to the pipe axis is checked by means of a laser beam generated by laser 5, projected the pipe external plane. Measurements of displacements are performed in the function of the shaft rotary motion. A rotary - impulse converter was used for synchronization of readings of parameters from sensors with the current diameter of the shaft. Its initial location is marked by magnetic marker 10, whose position is recorded by photo - optic sensor 9. Signals from all the listed sensors will be transmitted to control device 11. It consists of control and steering systems based on a freely programmable controller as well as an operating system, fig. 5. The elements work in Ethernet system. The terminal is equipped with control functions, and it enables recording and imaging of measurement results in the form of diagrams and tables with the shaft displacement (Kasprzyk, 2002).

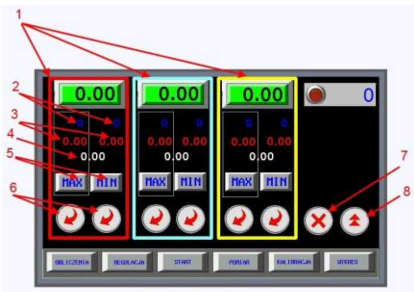

Fig. 5: A control terminal: 1 - measurement columns,2,3 - values of angular positions and maximum and minimum displacements, 5 - search for maximum and minimum values of measurements, 6 - automatic rotation of shaft into its maximum and minimum position, 7 - deletion of search, 8 - rotation by 90° in relation to actual position

3. Straightening a pipe in centering rings

Before straightening the pipe is mounted in centering rings (fig.4) and put on positioners. The pipe straightening can be started after it is properly centered in both rings. This is done on the basis of measurements performed by means of three laser displacement sensors. The measurement procedure is carried out in three steps:

- calibration of the measurement system,
- measurement of strains and assigning to them angular values of the rotating pipe,
- searching for characteristic points, maximum and minimum values assigned to the angular position.

Measurement results in the form of three diagrams (fig. 6) allow, in the first place, to center the pipe in rings and then its straightening.

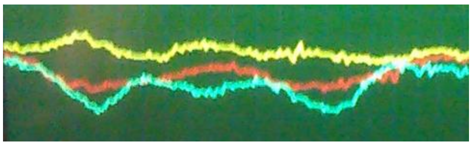

Fig. 6: Diagrams obtained from three measurement sensors

Centering the pipe in plugs is considered to be correct if diagrams of sensors 6 and 8 approach horizontal lines within the assumed tolerance. Interpretation of the diagrams in terms of pipe straightening, which is performed on the basis of the recordings from sensor 7, is similar.

The most difficult stage of pipe centering and straightening is the process of straightening. It is done with the use of a burner, fig. 7.

Fig. 7: Heating a pipe with a burner to straighten it

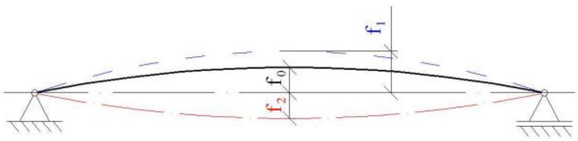

Fig. 8: Deformation of the pipe depends on its heating

In the first place the pipe flexure value is determined on the basis of the diagram from figure 6. Then the pipe is turned so that flexure f_o will be on its top (fig. 8). The pipe is heated in the area of its maximum flexure. During heating the flexure arrow grows to reach position f_1, and position f_2 after gradual cooling. This process will be finished if f_2 is equal to 0. So far searching for $f_2=0$ has been done by operators with the use of their intuition. The pipe was repeatedly heated and cooled. Thus, it is planned to carry out experiments in such a way that relations between f_o and f_1, will be $f_2=0$. For this purpose a laboratory test stand has been built (fig. 9), where a certain section of a pipe will be heated and cooled. During this time measurements of strains will be performed by means of an extensometer placed in the middle of the pipe and traditional clock sensors mounted on its ends (Jajubiec&Lesiński&Czajkowski, 1980; Czuchryj&Papkała&Wniowski A, 2005; Karlikowski, 2005).

Fig. 9: A test stand for measurements of the pipe flexure

Fig. 10: Examination of a pipe whose one side was fixed

The authors plan to find the discussed dependencies in a theoretical way. However, it is an extremely difficult task. In order to confirm the phenomenon, initial experiments were carried out with the use of a simple model. It was a pipe whose one side fixed and it was heated downward the fixing zone (fig. 10). Measurement of the flexure was performed on the pipe free end. The pipe was being heated to reach the temperature to make its free end fall by 1,66 mm and rise, in relation to the initial position after cooling, by 0,06 mm above the initial.

During industrial straightening it is necessary to remember that under the influence of the deadweight it undergoes a static strain (fig. 11), which has to be included in calculations.

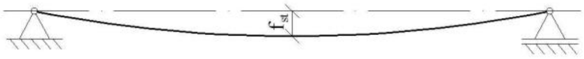

Fig. 11: Static flexure of a pipe under its own weight

It is the highest in the middle of its length. Equation of the flexure arrow is as follows:

$$f_{st} = \frac{1}{EI}\left[\frac{5ql^4}{384}\right] \tag{1}$$

where: E – module of longitudinal elasticity [MPa], I – moment of inertia [mm^4], q – constant loading [N/mm], l – length of the beam [mm] (Holka & Jarzyna, 2014).

4. Centering plugs in the pipe

The successive step in the shaft manufacturing is its mounting and centering plugs in the pipe. It is carried out in the following way:
- plugs are inserted into both ends of the pipe, fig. 12,

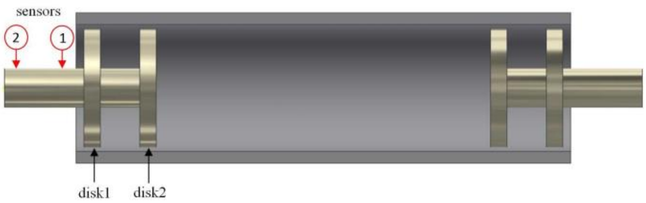

Fig. 12: Plugs mounted in the pipe

openings for mounting fixing bolts

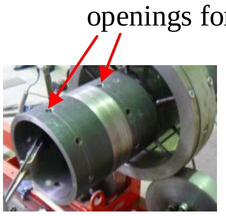

Fig. 13: Openings for fixing bolts

- four bolts, uniformly arranged on the circumference, situated in two rows per each plug, whose task is to perform initial positioning of the plugs, are screwed into the mounting holes, fig. 13,
- centering a plug in the plane of sensor 1 is performed by turning and stopping the shaft with the use of bolts fixing the disk 1 (fig. 12),
- beating of the shaft against the plane of sensor 2, which is corrected by bolts fixing disk 2 (the system behaves like a lever), is performed in a similar way
- correction in both planes is carried out until obtainment of satisfactory results,
- fillet weld is used to connect disk 1 with the pipe,
- another verification of beating is performed by means of sensors 1 and 2 or it is corrected by welds in the remaining openings presented in figure 13,
- after the fixing bolts are unbolted the holes are welded and correctness of the plug centering is checked,
- the procedure is repeated for the second plug.

5. Conclusions

1. The discussed, fully automated test stand enables significantly faster performance of pipe straightening and plug centering processes for large sized shafts. The number of processes has been increased and the number of errors has been decreased.

2. Precise assessment of strains that can occur after heating the pipe is very difficult. The carried out experimental tests and attempts to describe the analytical process will allow to improve the whole processes of heating and straightening.

References

Kasprzyk J. (2002) Programowanie sterowników przemysłowych. WNT, Warszawa.

Holka H., Jarzyna T. (2014.) Statyka i wytrzymałość materiałów. WUUTP, Bydgoszcz

Jajubiec M., Lesiński K., Czajkowski H. (1980) Technologia konstrukcji spawanych. WNT, Warszawa.

Czuchryj J., Papkała H., Wniowski A. (2005) Niezgodność w złączach spajanych. Istytut Spawalnictwa, Gliwice

Karlikowski J. (2005) Thermal stresses from one – side heating of asymmetric composite span. Archivest of Civil Engineering 4.

22nd International Conference
ENGINEERING MECHANICS 2016
Svratka, Czech Republic, 9 – 12 May 2016

MODELING OF REINFORCEMENT CORROSION IN CONCRETE

I. Hollý*, J. Bilčík**

Abstract: *Chloride-induced steel corrosion is one of the major deterioration problems for steel reinforced concrete structures. The accumulated corrosion products on the bar surface cause longitudinal cracking of the concrete cover. Loss of concrete cover leads to reduction in bond strength at the interfacial zone between the two materials. In addition, the deterioration of the ribs of the deformed bars causes a significant reduction of the interlocking forces between the ribs of the bars and the surrounding concrete keys. This deteriorates the primary mechanism of the bond strength between deformed bars and concrete, and hence, the bond strength decreases significantly. In this paper the effect of reinforcement corrosion on the bond strength between reinforcement and concrete was investigated for different corrosion levels. The effect of corrosion was simulated by the nonlinear numerical analysis with the FEM program using the 3D models.*

Keywords: Concrete, reinforcement, corrosion, bond, numerical analysis.

1. Introduction

It is known that, in good quality concrete the embedded reinforcing steel is protected against corrosion due to the formation of a sub-microscopically thin film. The corrosion of reinforcements in the construction of a transport infrastructure (especially bridges), parking areas, etc., is primarily initiated by chlorides from de-icing salts. In prestressed concrete structures the reinforcing steel elements are subjected to high mechanical stresses, therefore corrosion of the tendons can lead to consequences far more serious than in the case of conventionally reinforced concrete structures. This may result in failure of the steel and consequently of structure, or part of it, with a great potential for life losses, life disruption, and a huge economic impact. When corrosion is initiated, active corrosion results in a volumetric expansion of the corrosion products around the reinforcing bars against the surrounding concrete. Higher corrosion rates can lead to the cracking and spalling of the concrete cover. Continued corrosion of reinforcement causes a reduction of total loss of bond between concrete and reinforcement.

2. Experimental measurements

Numerical modeling is based on data obtained from previous experimental investigation of the effect of reinforcement corrosion on bond behavior. A total number of 48 reinforced concrete specimens were made. The dimensions of specimens were 200 x 200mm, height 130mm, Fig 1. The specimens were divided into 6 groups (types A to F), depending on the diameter of the reinforcement (Ø8 - types A, C, E, and Ø10 - types B, D, F), the thickness of concrete cover (30 and 40 mm respectively), and with or without stirrups, Tab.1. In the next part of paper, results for specimens with Ø10 diameter of reinforcement are discussed.

To accelerate the reinforcement‘s corrosion, the impressed current technique was used. The actual degree of corrosion, (corrosion level C_L) was measured as the loss in weight of the reinforcement steel bar to that of the bond length before corrosion, and thereby representing an average corrosion level along the bond length. The bond strength has been calculated using the initial (un-corroded) cross-sectional dimension of the bars.

* Ing. Ivan Hollý, PhD. : Department of Concrete Structures and Bridges, Faculty of Civil Engineering SUT in Bratislava; Radlinskeho 11; 810 05, Bratislava; SK, ivan.holly@stuba.sk

** Prof. Ing. Juraj Bilčík, PhD. : Department of Concrete Structures and Bridges, Faculty of Civil Engineering SUT in Bratislava; Radlinskeho 11; 810 05, Bratislava; SK, juraj.bilcik@stuba.sk

Tab. 1: Geometrical parameters of specimens.

Type	main rebar d_{sl} [mm]	stirrups d_{ss} [mm]	main rebar cover c [mm]	c/d_{sl} [-]
A1-A8	***8***	***6***	***40***	***5.0***
B1-B8	***10***	***6***	***40***	***4.0***
C1-C8	***8***	***6***	***30***	***3.75***
D1-D8	***10***	***6***	***30***	***3.0***
E1-E8	***8***	***-***	***30***	***3.75***
F1-F8	***10***	***-***	***30***	***3.0***

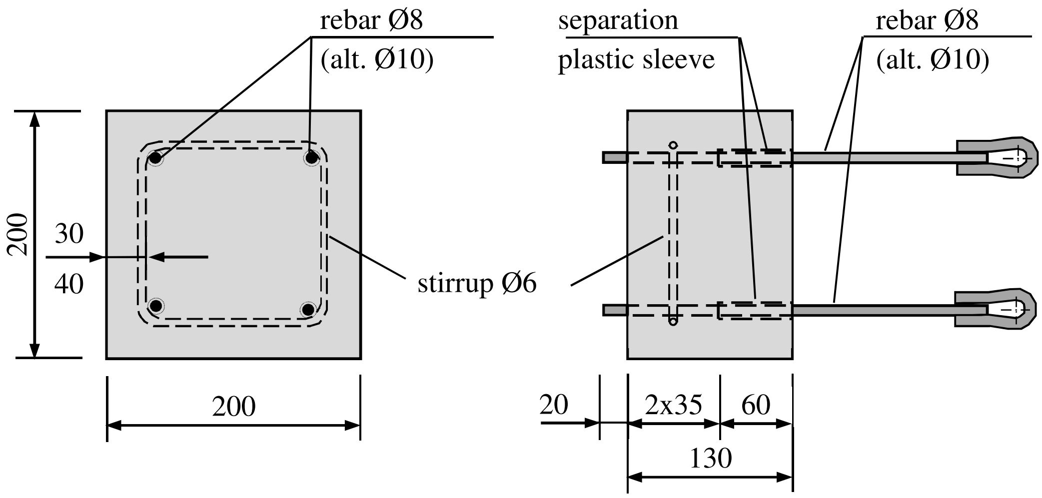

Fig. 1: Geometry of experimental specimens with stirrups

3. Numerical analysis

The Atena 3D software was used for numerical modeling. A total of 3 models, depending on geometrical parameters of specimens were developed. Due to symmetrical shape and for decrease of numerical solution, only 1/4 of specimens were modeled (Fig. 2). The reinforcement ribs were also modeled due to effect of mechanical interlock of the reinforcement ribs into concrete. The reinforcement cross-section was modeled as hexagon with the same cross-section area as original the circle, because the 3D version of Atena does not allow to model circular cross-sections.

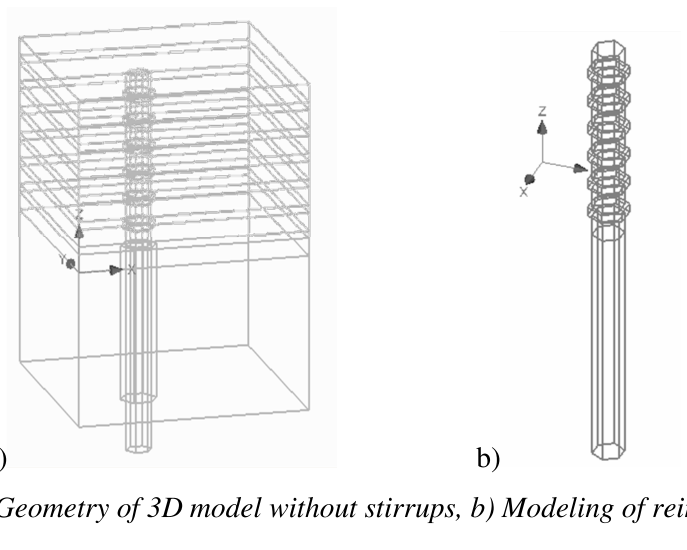

a) b)

Fig. 2: a) Geometry of 3D model without stirrups, b) Modeling of reinforcements ribs.

The reinforcement cross-section area is decreasing due to corrosion, while the volume of the corrosion products increases. Due to this phenomenon, it was necessary to recalculate the reinforcement diameter *d*(t) at time *t* and also the percentage loss of reinforcement area, (Fig. 3). The value of percentage loss of reinforcement area was calculated depending on the generated corrosion products (Fe_2O_3, Fe_3O_4...) during the accelerated corrosion.

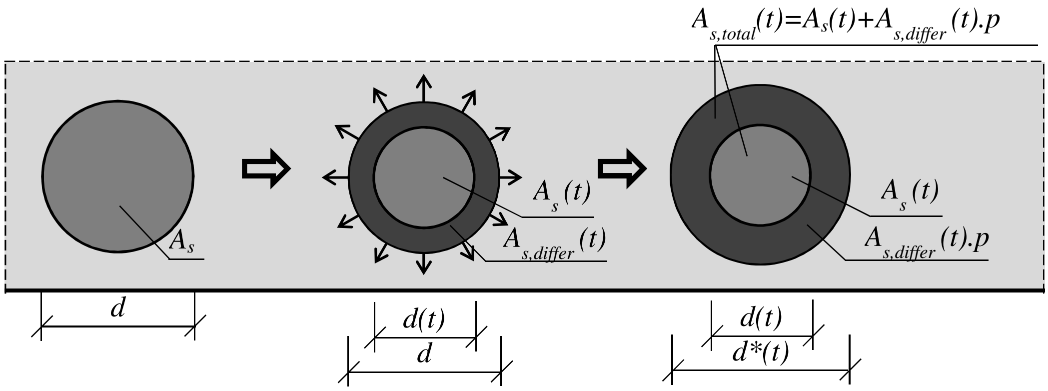

Fig. 3: Change of reinforcement cross-section area due to corrosion – theoretical approach.

The contact between concrete and reinforcement was modeled with material characteristic "3D interface", which is based on Mohr-Coulomb criterion with tension cut off. The constitutive relation for a general three-dimensional case is given in terms of tractions on interface planes and relative sliding and opening displacements and it is given by Eq. (1).

$$\begin{Bmatrix} \tau_1 \\ \tau_2 \\ \sigma \end{Bmatrix} = \begin{bmatrix} K_{tt} & 0 & 0 \\ 0 & K_{tt} & 0 \\ 0 & 0 & K_{nn} \end{bmatrix} \begin{Bmatrix} \Delta v_1 \\ \Delta v_2 \\ \Delta u \end{Bmatrix} \qquad (1)$$

Where τ is the shear stress in the x and y directions, σ is the normal stress, Δv is the relative displacement on surface, Δu is the relative opening of contact, K_{tt} is the initial elastic shear stiffness and K_{nn} is the initial elastic normal stiffness.

The reinforcement volume increase due to the corrosion from experimental research was put into the model as load using the shrinkage function, with the opposite sign so as to cause increase of reinforcement volume. This load was evenly distributed within the cross-section and incrementally increases with the load steps. Subsequently, the reinforcement was loaded with a tension force with a value of 1 kN per one step. The monitor was added on free end of reinforcement for the measurement of the displacements.

4. Comparison of results

Comparison of results obtained from experimental and numerical analysis for specimens with rebars Ø 10mm, are presented on Fig.4. The general trend of bond strength curves for all specimens is similar: the bond strength decreases with increases corrosion level. Also, results from numerical solution confirmed the results from experiments. A good match of both methods is shown. The regression functions for results from numerical analysis are line, but for results from experiment are curve. Comparison of results obtained from experimental and numerical analysis for specimen type B and D, are presented on Fig.4. The curve shows that the bond strength obtained from experiment was higher than the numerical analysis (Atena 3D software). But, for specimens without stirrup (series F), the results from experiment were lower than the numerical analysis. However, the relative differences between the both methods are small and within the range of acceptable variation (approximately 2 MPa). Comparison results for specimens with stirrups (series B and D) and without stirrups (series F) also showed that the transverse reinforcement (stirrups) provides positive effect on bond strength. For example, for corrosion revel of reinforcement CL= 6%, the decrease on bond strength for specimens with stirrups are approximately 20%, but for specimens without stirrups are more than 35%.

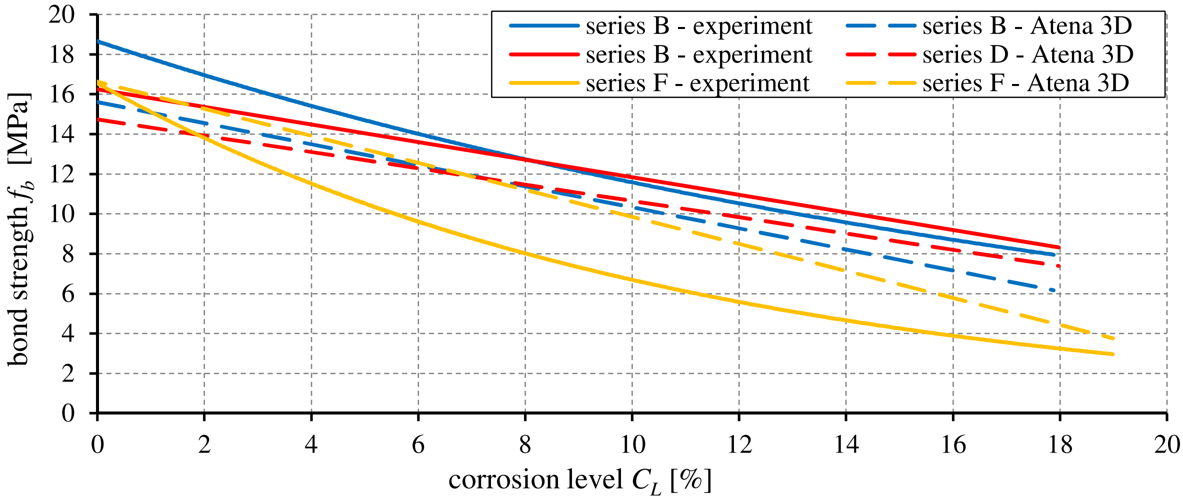

Fig. 4: Comparison of experimental and numerical results (rebars Ø 10mm)

5. Conclusions

The paper analyses the effect of steel corrosion on bond behavior between a reinforcement and concrete. The experimental and numerical results confirmed that:

1. The corrosion of the reinforcing steel adversely affects the bond strength. The loss of bond strength is potentially more severe than the loss of the bar's cross section. The results demonstrated that due to the reinforcement corrosion, the bond strength can be reduced by 50% while the loss of the reinforcement area is only 12%.

2.Compared to specimens without stirrups, specimens with stirrups show higher residual bond strength and less influence of corrosion on bond resistance. The numerical and experimental results lead to the conclusion that for specimens with stirrups, the bond strength of specimens with stirrups is much less sensitive to the corrosion of main reinforcement.

3.For the given degrees of corrosion rate, the risk for cracking, spalling and decrease in bond strength mainly depends on the geometry of the cross section (concrete cover) and the transverse rebars (links).

4.By comparing numerical and experimental results, regarding the bond strength dependency on the corrosion level, good results are obtained. The results obtained from experiment were higher than numerical analysis results circa 12.40 % for the specimen series B, 8.97 % for the specimen series D respectively. For specimen series F, the results obtained from numerical analysis were higher than experiment results circa 29.43 %.

Acknowledgement

The financial support of the Scientific Grant Agency of the Ministry of Education, Science, Research and Sport of the Slovak Republic by Grant No. 1/0583/15 is greatly acknowledged.

References

Bilčík, J. (2007) Repair of panel buildings, Bratislava: SUT, 2007. 200 p., ISBN 978-80-227-2763-1 (in Slovak).

fib Bulletin 10. Bond of reinforcement in concrete. August 2000, 427 pp.

Hollý, I. (2014) Effect of steel corrosion on bond between reinforcement and concrete: Dissertation thesis. Slovak University of Technology Bratislava. 2014, 151 p. (in Slovak)

Červenka, V. – Jendele, L. – Červenka, J. (2012): ATENA Program Documentation Part 1: Theory. Praha: Cervenka Consulting Ltd., 2012. 281 pp.

Weizhong, G. – Raupach, M. – Wei-Liang, J. (2010): Korrosionsprodukte und deren Volumenfaktor bei der Korrosion von Stahl in Beton. In: Beton- und Stahlbetonbau. ISSN 1434-1006, 2010, vol. 105, 9, p. 572–578.

Koteš, P. – Brodňan, M. (2012): Numerical modeling of the reinforcement corrosion. 18th International Conference Engineering Mechanics Svratka, Czech Republic, May 14 – 17, 2012, pp. 673–679.

Koteš, P. (2013): Influence of Corrosion on Crack Width and Pattern in an RC Beam. In: Concrete and Concrete Structures 2013. Procedia Engineering, Vol. 65. Terchová. 2013. ISSN 1877-7058, pp. 311 – 320.

22nd International Conference
ENGINEERING MECHANICS 2016
Svratka, Czech Republic, 9 – 12 May 2016

ROOT-FINDING METHODS FOR SOLVING DISPERSION EQUATIONS

P. Hora*

Abstract: *Contribution deals with the methods of rootfinding in a plate and cylindrical waveguide. The methods are based on: classic root-finding, interval arithmetics, Chebyshev interpolation, marching squares and marching triangles. All methods have been implemented both in Matlab (ChebFun toolbox) and Julia (ApproxFun module).*

Keywords: Dispersion curves, Rootfinding, Interval arithmetic, Chebyshev interpolation.

1. Interval arithmetic

Wave propagation in thick plates is well solvable problem. One of part of task solution is to find the waveform dispersion curves. This problem has been chosen for the first trial using interval arithmetic (Moore, Kearfott & Cloud, 2009), because of its relative simplicity. In calculating the dispersion curves is needed to quantify the only trigonometric functions, hyperbolic functions, and square roots. All of these functions are already included in INTLAB (Rump, 1999) and therefore need not to be newly programmed.

The thick plate is defined as that it has a nonzero thickness $2d$ and endless remaining dimensions. To calculate the stress wave propagation in plates it is used the integration along the dispersion curves for thick plates. These dispersion relations are (for the stress-free boundary conditions of the plate surfaces and for symmetric modes) defined as

$$(\xi^2-2)^2\tanh(\gamma d\sqrt{1-\xi^2})-4\cdot\sqrt{1-\xi^2}\sqrt{1-\kappa\xi^2}\tanh(\gamma d\sqrt{1-\kappa\xi^2})=0,$$

where γ is wavenumber ($\gamma=2\pi/\lambda$), ξ is the ratio of the phase velocity and the shear wave velocity and κ mean the ratio of the squares of the phase velocities for the plate's material.

To avoid computation in the complex domain it was necessary to break up calculation into the parts according to parameter ξ value (see Tab. 1) as the algorithm was implemented in INTLAB. For each interval are the equations shown in tab 1. To quantify the equations and finding the waveform dispersion curves is used interval arithmetic.

Tab. 1: Dispersion equation: $(\xi^2-2)^2\cdot\alpha-4\cdot\beta\cdot x_1x_2=0$.

	$0<\xi<1$	$1<\xi<1/\sqrt{\kappa}$	$1/\sqrt{\kappa}<\xi$
x_1	$\sqrt{1-\xi^2}$	$\sqrt{\xi^2-1}$	$\sqrt{\xi^2-1}$
x_2	$\sqrt{1-\kappa\xi^2}$	$\sqrt{1-\kappa\xi^2}$	$\sqrt{\kappa\xi^2-1}$
α	$sinh(\gamma dx_1)\,cosh(\gamma dx_2)$	$sin(\gamma dx_1)\,cosh(\gamma dx_2)$	$sin(\gamma dx_1)\,cos(\gamma dx_2)$
β	$cosh(\gamma dx_1)\,sinh(\gamma dx_2)$	$cos(\gamma dx_1)\,sinh(\gamma dx_2)$	$-cos(\gamma dx_1)\,sin(\gamma dx_2)$

Interval arithemic is an extension of arithmetic over real numbers, where for each real function $f(x_1,\ldots,x_n)$, the interval function $F(X_1,\ldots,X_n)$ is called an interval extension of the function f if for each

* Assoc. Prof. Petr Hora, PhD.: Institute of Thermomechanics, Dolejškova 1402/5; 182 00, Prague; CZ, hora@cdm.cas.cz

intervals $I_1,\ldots,I_n$ function $F(I_1,\ldots,I_n)$ returns interval I such that $\forall y_1 \in I_1 \ldots \forall y_n \in I_n(f(y_1,\ldots,y_n) \in I)$. For other applications it is particularly important the interval Newton method, according to which each continuously differentiable function f each interval I must be $\forall a, x \in I, \exists \varepsilon \in I(f(x) = f(a)+(x-a)f'(\varepsilon)$. Specifically then, the function f continuously differentiable on the interval I has all the roots in I in interval $N_a = a-(F(a)/F'(I))$ where a is an arbitrary element of I and F, F' is an interval extension function of f, f'.

For quantification of interval arithmetic was used MATLAB's toolbox INTLAB, which are defined not only the basic functions for interval arithmetic, but their automatic differentiation too (Bücker, Corliss, Hovland, Naumann, & Norris, 2005).

When trying to use the Newton method in INTLAB was needed to solve the problem by dividing intervals. INTLAB always returns the result $\langle -\infty, \infty\rangle$ for each I/J where $0 \in J$. However, for this case, it was necessary defined alternative way of dividing, when the interval is divided into two portions, and finding roots thus diverges into two tasks. The actual calculation is solved in recursive steps. In a single step in the equation $N_a = a-(F(a)/F'(I))$ is substituted middle I per a, yielding a new interval $J = I \cap N_a$. This one is used in the next recursive step. The calculation continues until the result interval width falls under a predetermined accuracy.

2. Chebyshev interpolation

To calculate the stress wave propagation for a longitudinal impact of semi-infinite thick cylindrical bars it is used the integration along the dispersion curves. These dispersion relations $f(\xi, \gamma a)$ is defined as

$$(2-\xi^2)^2 J_0(\gamma a\, A)\, J_1(\gamma a\, B) + 4AB\, J_1(\gamma a\, A)\, J_0(\gamma a\, B) - \frac{2\xi^2}{\gamma a} A\, J_1(\gamma a\, A)\, J_1(\gamma a\, B) = 0,$$

where a is radius of the semi-infinite bar, γ is wavenumber, ξ is the ratio of the phase velocity and the shear wave velocity, κ means the ratio of the squares of the phase velocities for the bar's material, $A = \sqrt{\kappa\xi^2 - 1}$, $B = \sqrt{\xi^2 - 1}$ and J is the Bessel function of the first kind.

Summary of the Chebyshev expansion algorithm (Boyd, 1995):

1. Choose the following:
   1. γa
   2. Search interval, $\xi \in [a, b]$.

      The search interval must be chosen by physical and mathematical analysis of the individual problem. The choice of the search interval $[a, b]$ depends on the user's knowledge of the physics of his/her problem, and no general rules are possible.
   3. The number of grid points, N.

      N may be chosen by setting $N = 1+2^m$ and the increasing N until the Chebyshev series displays satisfactory convergence. To determine when N is sufficiently high, we can examine the Chebyshev coefficients a_j, which decrease exponentially fast with j.
2. Compute a Chebyshev series, including terms up to and including T_N, on the interval $\xi \in [a, b]$.

   1. Create the interpolation points (Lobatto grid):

      $$\xi_k \equiv \frac{b-a}{2}\cos\left(\pi\frac{k}{N}\right) + \frac{b+a}{2}, \qquad k = 0,1,2,\ldots,N.$$
   2. Compute the elements of the $(N+1)\times(N+1)$ interpolation matrix.

      Define $p_j = 2$ if $j = 0$ or $j = N$ and $p_j = 1$, $j \in [1, N-1]$. Then the elements of the interpolation matrix are

$$I_{jk} = \frac{2}{p_j p_k N}\cos\left(j\pi\frac{k}{N}\right).$$

3. Compute the grid-point values of $f(\xi)$, the function to be approximated:

$$f_k \equiv f(\xi_k), k = 0,1,\dots,N.$$

4. Compute the coefficients through a vector-matrix multiply:

$$a_j = \sum_{k=0}^{N} I_{jk} f_k\,, \qquad j = 0,1,2,\dots,N.$$

The approximation is

$$f_k \approx \sum_{j=0}^{N} a_j T_j\left(\frac{2\xi-(b+a)}{b-a}\right) = \sum_{j=0}^{N} a_j \cos\left\{j\cos^{-1}\left(\frac{2\xi-(b+a)}{b-a}\right)\right\}.$$

3. Compute the roots of f_N as eigenvalues of the Chebyshev–Frobenius matrix

   Frobenius showed that the roots of a polynomial in monomial form are also the eigenvalues of the matrix which is now called the *Frobenius companion matrix*. Day and Romero (2005) developed a general formalism for deriving the *Frobenius matrix* for any set of orthogonal polynomials.

4. Refine the roots by Newton iteration with $f(\xi)$ itself.

   Once a good approximation to a root is known, it is common to *polish* the root to close to machine precision by one or two Newton iterations.

Computations were performed with the normalized Bessel functions that eliminate the large fluctuations in magnitude. For numerical experiments were used MATLAB's toolbox CHEBFUN (Driscoll, Hale & Trefethen, 2014) and Julia's package ApproxFun (ApproxFun).

3. Conclusions

Fig. 1 shows the dispersion curves as calculated using a classic root-finding algorithm and the Chebyshev method. It can be seen, that both approaches provide equivalent results.

Both the interval arithmetic and the Chebyshev interpolation provide a robust method for finding the roots of the dispersion equation.

For relatively low speed, these methods are not suitable to complete the calculation, it is however possible to use the first approach with low accuracy, or when using the Gaussian integration method along the dispersion curves.

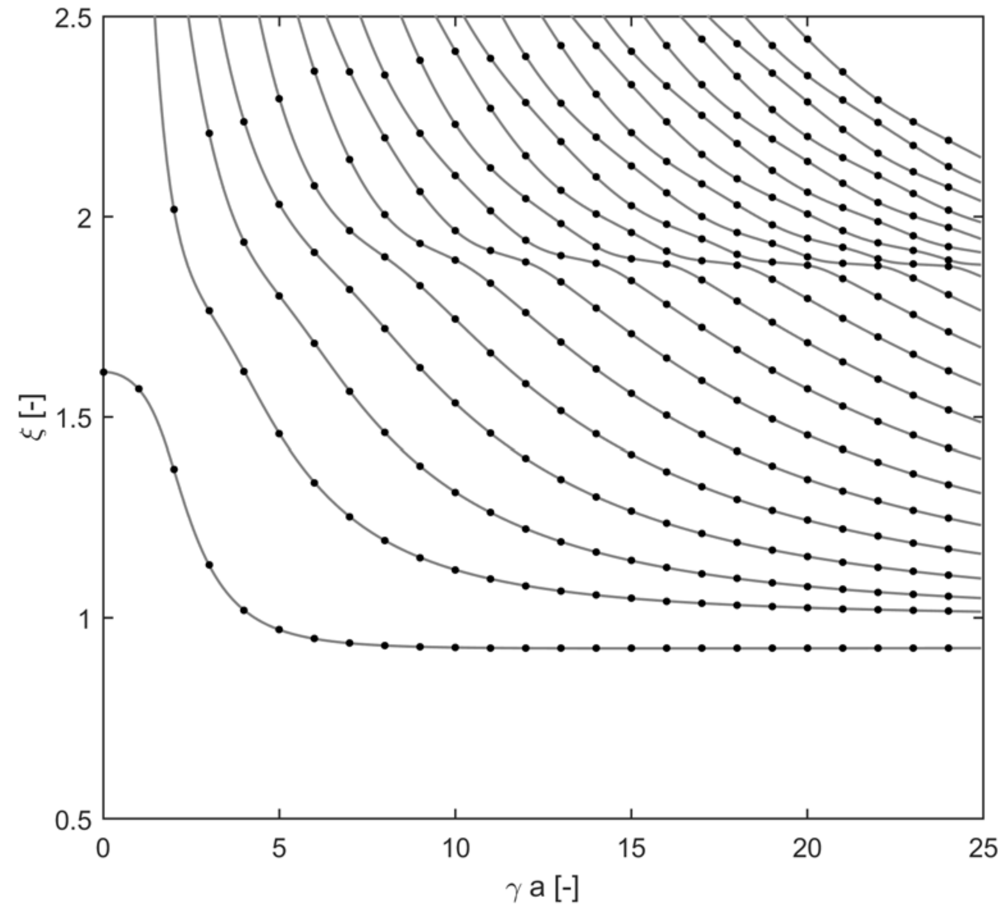

Fig. 1: Dispersion curves computed using a conventional mode tracing algorithm (gray lines) and the Chebyshev method (black dots).

Acknowledgement

The work was supported by the institutional support RVO: 61388998.

References

Boyd, J.P. (1995) A Chebyshev Polynomial Interval-Searching Method ("Lanczos Economization") for Solving a Nonlinear Equation with Application to the Nonlinear Eigenvalue Problem. Journal of Computational Physics. 118. pp. 1–8.

Bücker, H.M., Corliss, G., Hovland, Naumann, U., Norris, B., eds. (2005) Automatic Differentiation: Applications, Theory, and Implementations. Lect. Notes Comput. Sci. Eng. 50. Springer, New York.

Day, D.M. & Romero, L. (2005) Roots of polynomials expressed in terms of orthogonal polynomials. SIAM J. Numer. Anal. 43. pp. 1969–1987.

Driscoll, T.A., Hale, N. & Trefethen, L.N. editors, (2014) Chebfun Guide. Pafnuty Publications, Oxford.

Graff, K.F. (1975) Wave Motion in Elastic Solids. Dover Publications.

Moore, R.E., Kearfott, R.B. & Cloud, M.J. (2009) Introduction to Interval Analysis. SIAM.

Rump, S.M. (1999) INTLAB - INTerval LABoratory. Kluwer Academic Publishers. pp. 77–104.

URL: github.com/ApproxFun/ApproxFun.jl.git

22nd International Conference
ENGINEERING MECHANICS 2016
Svratka, Czech Republic, 9 – 12 May 2016

PHONATION CHARACTERISTICS OF SELF-OSCILLATING VOCAL FOLDS REPLICA WITH AND WITHOUT THE MODEL OF THE HUMAN VOCAL TRACT

J. Horáček[*], V. Bula[**], J. Košina[***], V. Radolf[****]

Abstract: *The experimental study presents in vitro measurements of phonation characteristics performed on the developed 1:1 scaled replica of human vocal folds. The aerodynamic, vibration and acoustic characteristics measured with and without the model of the human vocal tract for vowel [u:] are compared.*

Keywords: Fluid-Structure-Acoustic Interaction, Biomechanics of Voice, Modelling of Phonation.

1. Introduction

Voice production is a complex physical process, which involves airflow coming from the lungs, self-oscillating vocal folds and acoustics of the resonance cavities of the human vocal tract. The vocal folds, excited by the airflow, generate a primary sound which propagates in the airways of the vocal tract modifying its spectrum and producing the final acoustic signal radiated from the mouth (Titze, 1994). Understanding basic principles of voice production is important for detection of laryngeal pathologies and treatment of laryngeal disorders. The physical models of voice production are important tools for experimental verification of developed theoretical models of phonation and in the development of the vocal folds prosthesis (Verkerke & Thomson, 2014).

2. Methods

The design of the geometry (size and shape) of the vocal folds replica was based on computer tomography (CT) measurement of the subject during phonation. The replica is made of ca 1 mm thin silicon cover filled by water (Horáček et al. 2015). The fundamental frequency of the self-oscillations can be controlled by changing the hydrostatic pressure inside the vocal folds and by their slight static pretension in the anterior - posterior direction. A simplified plexiglas model of the human vocal tract was developed from the 3D finite element (FE) model designed from the CT images of the subject taken during phonation (Vampola et al. 2015). To ensure the correspondence with reality the straight model of the vocal tract of the circular shape has the same areas in the 47 cross-sections along the vocal tract as the 3D FE model. The model begins with a simple model of the laryngeal cavity near the ventricular folds and ends at the lips by modelling the oral cavity.

The vocal folds were excited by the manually controlled airflow rate with synchronous measurement of the subglottic and oral air pressures (the fluctuating compound and the mean values) and the radiated sound. A general scheme of the measurement set up is shown in Fig. 1. The airflow is coming from the compressor through the float and orifice flowmeters to the model of subglottal spaces created by a simplified model of the human lungs and trachea (diameter 18 mm), then enters the glottal region with the vocal folds and finally the vocal tract model for the vowel [u:]. The airflow rate was increased step by step from the phonation onset up to the airflow rate and the subglottic pressure, which are in the range of physiologically relevant values for a normal human voice production.

[*] Ing. Jaromír Horáček, DrSc.: Institute of Thermomechanics, Dolejškova 1402/5, 182 00 Prague; CZ, jaromirh@it.cas.cz
[**] Ing. Vítězslav Bula: Institute of Thermomechanics, Dolejškova 1402/5, 182 00 Prague; CZ, bula@it.cas.cz
[***] Ing. Jan Košina: Institute of Thermomechanics, Dolejškova 1402/5, 182 00 Prague; CZ, Kosina@it.cas.cz
[***] Ing. Vojtěch Radolf, PhD.: Institute of Thermomechanics, Dolejškova 1402/5, 182 00 Prague; CZ, radolf@it.cas.cz

The personal computer (PC I) was joint to the measurement system B&K Pulse with the Controller Module MPE 7537A, where all time signals measured by the pressure transducer, the two digital manometers, the contact sensor and two microphones were synchronously recorded using 16.384 kHz sampling frequency. The fundamental frequencies F_0 of the vocal folds vibration were analyzed using the FFT spectra of the time signals in the frequency range 0 - 6.4 kHz.

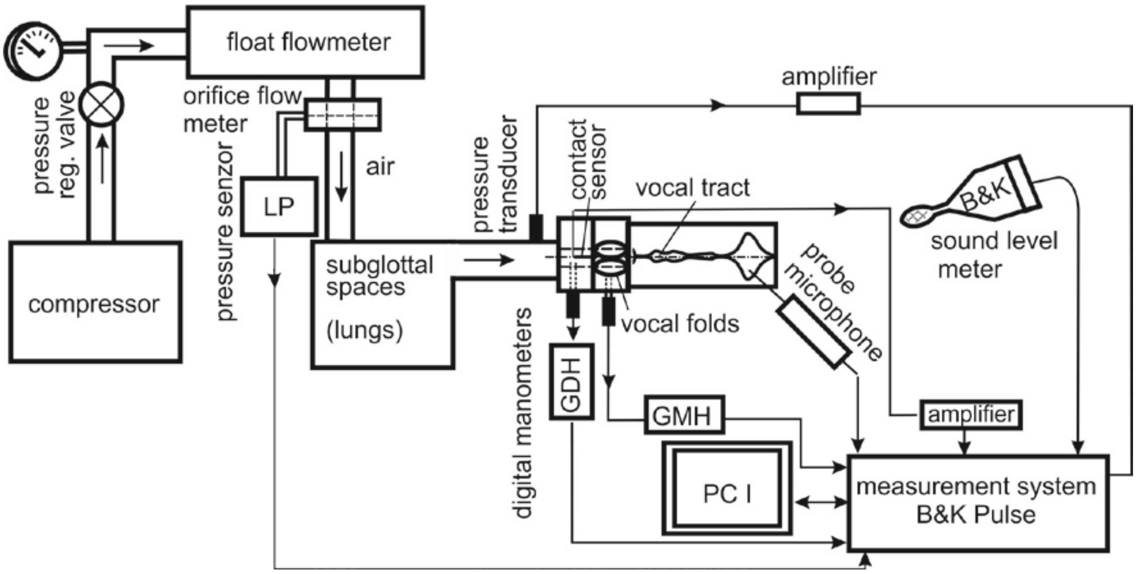

Fig. 1: Scheme of the measurement set up.

The miniature pressure sensor (Precision Measurement Company, model 060, range 0-350 kPa, diameter 1.5 mm, thickness 0.3 mm) used for measurement of the contact stress was mounted on a thin metal lamella and installed freely in the center of the glottis between the vibrating vocal folds. When the glottis is opened, the sensor measures the intraglottal pressure. The signal was amplified by an especially developed measurement amplifier. The acoustic signal was recorded by the sound level meter B&K 2239 installed at the distance of 30 cm from the vocal folds model or from the end of the oral cavity.

3. Results

Before starting the measurements, the vocal folds setting was tuned in order to obtain the regular phonation in the airflow range Q=0.2-0.4 *l*/s both for the vocal folds with and without the vocal tract. The original length (20 mm) of the vocal folds was prolonged by 8.25% (1.65 mm) and the hydrostatic pressure of water inside the vocal folds was adjusted to 1.75 kPa.

Several examples of the measured time signals are shown in Fig. 2 and the spectra of the generated sound measured by the external microphone placed outside the vocal tract are presented in Fig. 3. The peak sound level of the generated acoustic pressure signal (P_{out}) at the distance 30 cm from the lips is higher than the peak sound level measured without the vocal tract (see Fig. 2), however, the most of the energy of the microphone signal for the vowel [u:] is concentrated in the region of the first and second formant frequencies, i.e. the acoustic resonances of the vocal tract: $F_1 \simeq 350$ Hz and $F_2 \simeq 550$ Hz, while the primary signal generated by the vocal folds contains many higher harmonics up to 6 kHz, see Fig. 3. The maximum of the impact (contact) stress *IS* is evaluated from the intraglottal pressure $P_{intraglot}$ measured by the miniature pressure sensor in the glottis taking into account a time delay between the *IS* and the synchronously measured subglottal pressure P_{sub} , see Fig. 2. The relatively high fluctuation amplitudes (peak-to-peak values) of the P_{sub} were reduced by the acoustic-structure interaction of the vocal tract joint to the self-oscillating vocal folds.

Figure 4 shows the effects of acoustic-structural interaction on the vibration, acoustic and airflow characteristics measured with and without vocal tract in the whole region of the flow rates Q=0.2-0.4 *l/s*. The fundamental vibration frequency F_0 for the joint system (vocal tract and vocal folds) increased by cca 5-10 Hz and similarly as expected increased the P_{sub} by ca 0.3 – 0.75 kPa and the flow resistance P_{sub}/Q, see Fig. 4. On the other hand the following positive changes can be concluded. The vocal tract decreased the *IS* by ca 0.3-0.6 kPa and peak-to-peak amplitudes of the subglottal pressure from cca 50% for the lower flow rates Q and up to 100% for the higher values of Q. The difference in the sound pressure level SPL of the acoustic signal are smaller.

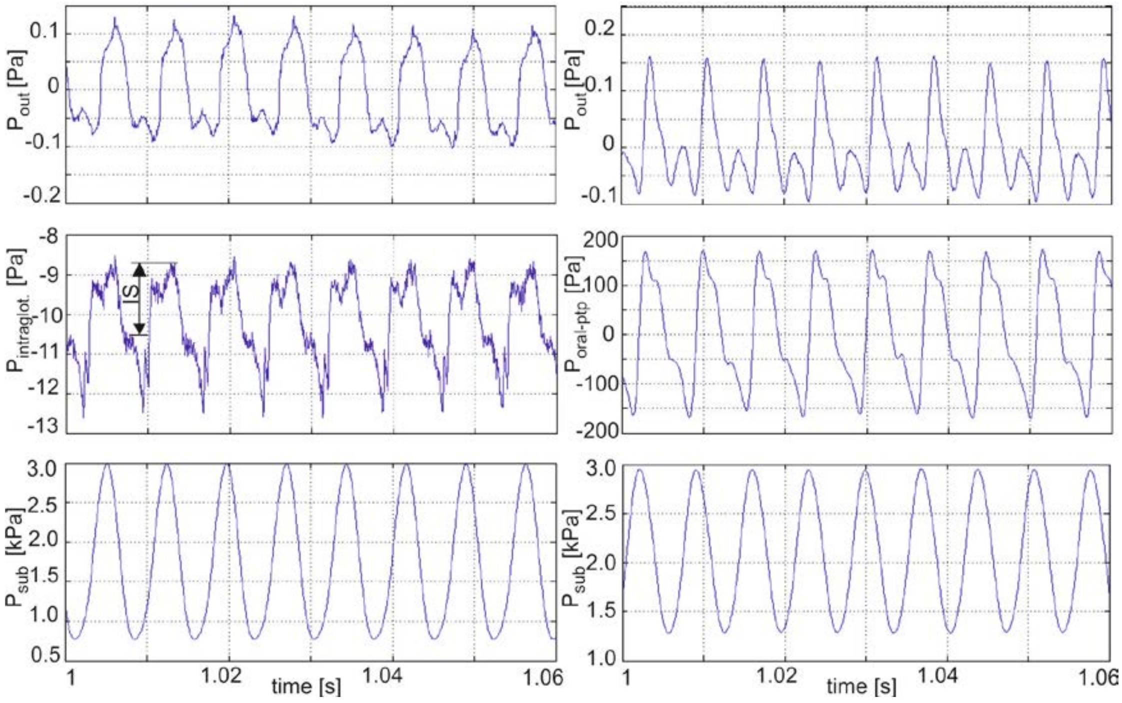

Fig. 2: Measured time signals for the airflow rate Q=0.25 l/s: a) without the vocal tract (left column), and b) with the vocal tract model for the vowel [u:] (right column). P_{out} - the generated acoustic signal measured by external microphone, $P_{intraglot}$ - the intraglottal pressure measured by the miniature pressure transducer in the glottis, $P_{oral-ptp}$ - fluctuations of the oral pressure and P_{sub} - the subglottal pressure.

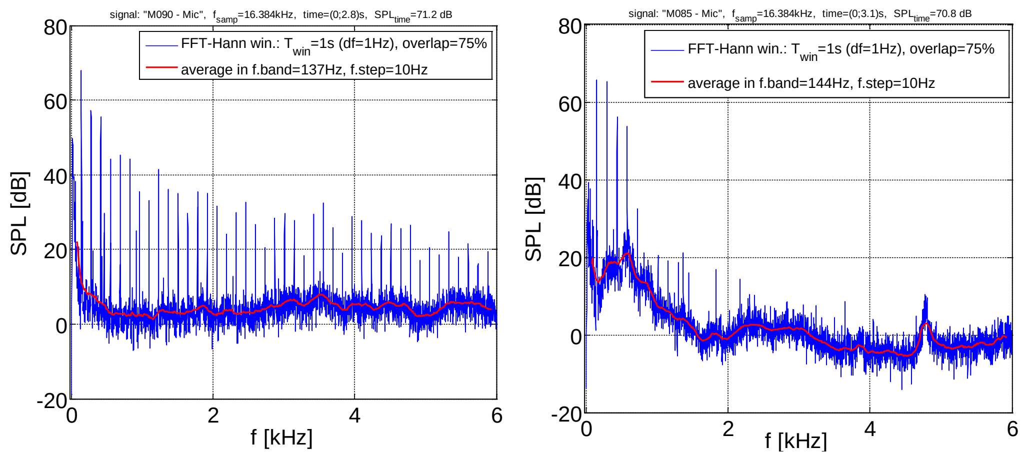

Fig. 3: Spectra of the generated sound measured by the external microphone for the airflow rate Q=0.25 l/s: a) without the vocal tract (left), and b) with the vocal tract model for the vowel [u:] (right).

4. Conclusions

The study was focused on modelling the effects of interaction of the supraglottal acoustic cavities with the self-oscillating vocal folds. The vocal fold model created by the silicon cover filled by water phonated in the intervals of the airflow rates *Q*=0.2-0.4 *l/s* and subglottic pressure $P_{sub} \cong 1.5 - 2.75\,\mathrm{kPa}$ that are realistic values in humans. The fundamental frequency F_0 which corresponded to a tenor voice increased when the vocal tract was joint system with the vocal folds. The highest impact (contact) stress during the vocal folds collisions was found ca $IS \cong 3.5\,\mathrm{kPa}$, which is also in the range of values measured in humans (Jiang & Titze, 1994). Important finding is that the vocal tract decreased the *IS* and peak-to-peak amplitudes of the subglottal pressure. A high contact stress is one of the most detrimental factor causing nodules and other pathologies in the vocal fold tissue. The influence of the vocal tract on the sound pressure level of the acoustic signal was found small. The measured aerodynamic, vibration and acoustic characteristics are in good agreement with the values found in humans.

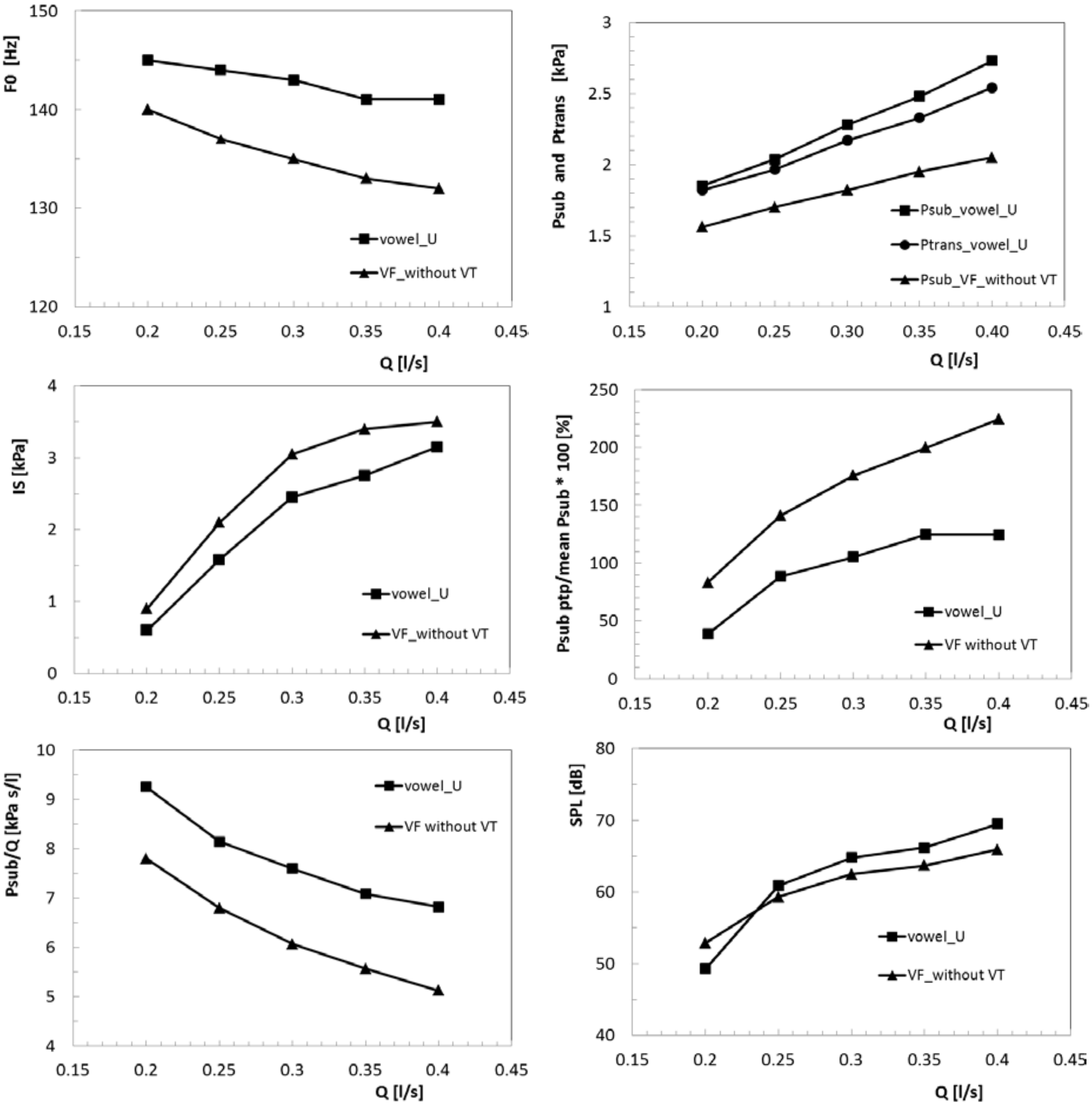

Fig. 4: Comparison of the vibration, acoustic and airflow characteristics of phonation measured on the vocal folds replica without and with the vocal tract model for the vowel [u:].

Acknowledgement

The work has been supported by the grant project GACR No 16-01246S.

References

Horáček, J., Bula, V., Radolf, V., Vampola, T. & Dušková, M. (2016) Development of self-oscillating human vocal folds prosthesis, in Proc. 12th Int. Conf. on Vibration Problems, ICOVP 2015, Procedia Engineering 2016, 8. pp. (in print).

Jiang, J. & Titze, I. (1994) Measurement of vocal fold intraglottal stress and impact stress. Journal of Voice, 8, pp. 132-144.

Titze, I.R. (1994) Principles of voice production. Prentice Hall.

Vampola, T., Horáček, J., Laukkanen, A.M. & Švec, J.G. (2015) Human vocal tract resonances and the corresponding mode shapes investigated by three-dimensional finite-element modelling based on CT measurement. Logopedics Phoniatrics Vocology, 129, pp. 310-315.

Verkerke, G.J. & Thomson, S.L. (2014) Sound-producing voice prostheses: 150 years of research. Annu. Rev. Biomed. Eng. 16, pp. 215–45.

22nd International Conference
ENGINEERING MECHANICS 2016
Svratka, Czech Republic, 9 – 12 May 2016

IMPACT OF HYDROPHOBIC MODIFICATIONS ON MICROSTUCTURE AND MICROMECHANICS OF CEMENTITIOUS MATERIAL

V. Hrbek[*], V. Petráňová[**], J. Němeček[***]

Abstract: *This paper compares recent methods of internal hydrophobization of cementitious composite by silicon-based solutions and a crystalline admixture used as the alternation of external coatings. The study focuses on the overall hydrophobic performance of the admixtures as well as on their impact on the microstructure and micromechanical properties. Results contained in this paper show both positive influence of the admixtures and limitations with respect to their micromechanical performance measured by nanoindentation.*

Keywords: Cementitious composite, Hydrophobization, Crystalline admixture, Nanoindentation

1. Introduction

The majority of corrosion degradation process is related to water propagation through pores in structural material. Thus, with the development of new materials, modern concept in the field of civil engineering is to increase the structure durability by limiting the penetration of the water. Formerly, the materials have been modified by external hydrophobic coatings. Based on the latest researches, other problems can result from the approach, such as degradation of the coating layer itself and the sustainability of the material properties. In order to lower the degradation of the hydrophobic agent, internal hydrophobization is taken into consideration as a possible solution. As such, crystalline admixtures were recently used in cementitious composite. In some cases, this method was considered ineffective thanks to the lack of the knowledge about the admixture behavior on the micro-scale and its microstructural interaction within the material. This paper deals with both water-repellent performances of the selected hydrophobic admixtures as well as with their micromechanical influence assessed with nanoindentation.

2. Theoretical background

2.1. Hydrophobization

The hydrophobic coatings used for external treatment of cementitious materials are typically silicon based water solutions, in which silanes and siloxanes oligomers are represented. Their reaction is closely discussed e.g. in Hrbek et al. (2016). The simplification of their evolution can be described as poly-condensation process leading to the development of a thin layer of silica polymeric chain connected to the surface over the hydrogen-oxygen bonds. The degree of polymer chain depends on the presence of the "free" water during the condensation process and on the type of silicon based solution. This also results in decrease of water necessary for

[*] Ing. Vladimír Hrbek: Czech Technical University in Prague, Faculty of Civil Engineering, Department of Mechanics, Thákurova 7/2077,166 29 Praha 6, vladimir.hrbek@fsv.cvut.cz

[**] Mgr. Veronika Petráňová: Czech Technical University in Prague, Faculty of Civil Engineering, Department of Mechanics, Thákurova 7/2077,166 29 Praha 6, veronika.petranova@fsv.cvut.cz

[***] doc. Ing. Jiří Němeček, PhD.: Czech Technical University in Prague, Faculty of Civil Engineering, Department of Mechanics, Thákurova 7/2077,166 29 Praha 6, jiri.nemecek@fsv.cvut.cz

hydration of cement. In case of external hydrophobization, the formed coating is subjected to the degradation, mostly caused by the de-bonding of the hydrogen-oxygen link.

The crystalline admixtures are usually described as active chemicals coupled with very fine sand and cement as an admixture used as a sealant in waterproof concrete structures. The hydrolytic active particles, in reaction with water or the calcium-silica-hydrate (C-S-H) gel, increase the C-S-H density or produce the crystalline deposits that block the penetrating water into the material. This provides the material with calcium silicate crystals that integrally bond with the cement paste and enclose the pores and the cracks. This reaction can thus be, based on the space and water available, repeated over the service life of the structure. By now, this method of waterproofing provides the largest resistance to penetrating water under pressure.

2.2. Micromechanical properties and nanoindentation

The nanoindentation, as a method of micromechanical testing, is today a widely used technique of direct estimation for elastic and plastic properties of the material on the microscale. Its principle is based on the measurement of penetration of a rigid tip into the material surface. Standardly, load-penetration depth diagrams of small material volumes allow determination of mechanical properties of small material volumes, such as hardness H or reduced modulus E_r as

$$H = \frac{P}{A_c} \qquad\qquad E_r = \frac{1}{2\beta}\frac{\sqrt{\pi}}{\sqrt{A_c}}\frac{dP}{dh} \tag{1}$$

where P is the maximum load, A_c is the projected contact area of the tip, dP/dh is the unloading stiffness, β is the geometrical constant. The reduced (combined) modulus can be used for calculation of Young's modulus with the knowledge of the material Poisson's ratio (Oliver and Pharr, 1992). Even though the method was found for homogeneous-like materials (metals, ceramics, etc.), it can be successfully used for microscopically heterogeneous material, such as cementitious composites by using a method of statistical grid indentation coupled with deconvolution of the material phase distributions (Constantinides et al., 2006, Němeček et al., 2013, Leal Da Silva et al., 2014).

3. Methodology of testing

3.1. Sample description

The investigated samples were made of a cementitious composite mixture consisting of CEM I-42,5R and micro-silica as binders, fine aggregate perlite (with diameter lower than 200 μm) and 3M glass micro-bubbles as filler. The water cement ratio of the mixture was 0.35 and the Sika-Crete plasticizer (with ratio 0.12 to binders) was used to obtain an optimum workability.

The enhancement of the hydrophobic properties by use of sodium-methyl-siliconate (SMS) in SMS to binder weight ratio 0.10% to 0.15% was proved by previous research (Hrbek et. al., 2016). In this paper, substitution of 0.00%, 0.10%, and 0.20% of SMS solution were compared to specimens with the crystalline admixture used as a binder replacement of 0%, 1% and 2%, as recommended by the producer (Xypex). Samples were matured in water over the period of 28 days. Further sample labeling used in this work is HYFx.xx for samples with silicone based solution and XYPx.xx for Xypex crystalline admixture replacement, where x.xx indicates the SMS or Xypex to binder ratio, respectively.

3.2. Macro-scale hydrophobicity

The macroscopic properties of water repellence were tested on samples 40x40x160 mm. 28 days after the production short term water absorption was tested after specimens drying in 30°C for 3 days. Then, samples were placed on wetted linen by one surface and the increments of samples' weight were measured over the next 4 hours. In order to obtain the terminal dry weight, samples were placed in 45°C for the next 14 days. Then, samples were saturated with water for 24 hours in a vacuum chamber under the pressure of 150 mbar, their weight gain was measured and the full saturation ratio with respect to their dry weight calculated.

3.3. Mechanical properties based on nanoindentation

The effect of hydrophobic alternation of the sample micromechanical properties was quantified by the change in distribution of reduced elastic moduli measured over large representative areas of the sample that were previously polished by a metallographic procedure to minimize their roughness. The indentation was performed with diamond Berkovich tip in several 20 by 20 indent grids with mutual indents' separation of 25 μm in ambient conditions (~21 ^{o}C, ~20-40% r.h.). The linear loading lasting for 5 seconds with 0.4 mN/s loading rate was prescribed and maximum load of 2 mN was reached for all indents leading to the maximum penetration depth of 335±124 nm. The following constant holding of the force over 20 seconds allowed material for creep so the following unloading part, from which elastic material parameters are evaluated, can be supposed unaffected by a time-dependent process. The unloading again lasted for 5 seconds.

4. Results

4.1. Macroscopic water absorption

Based on the data from Fig. 1a), the internal hydrophobization by silicon based solution exhibits lower short term absorption compare to crystalline admixture. Such effect can be explained by a lower level of saturation of near surface pores in the crystalline-modified sample during the measurement. In other words, the efficiency of the crystalline admixture is, unlike the silicon-based modification, water-supply and time dependent. In case of full saturation, as depicted in Fig. 1b), the SMS solution proved insufficient ability to repel water under pressure and the results may indicate de-bonding of the polymeric agent from the surface. As for the crystalline particles, the water-supply ensures sealing of the pores resulting in a rapid decrease of saturation ratio.

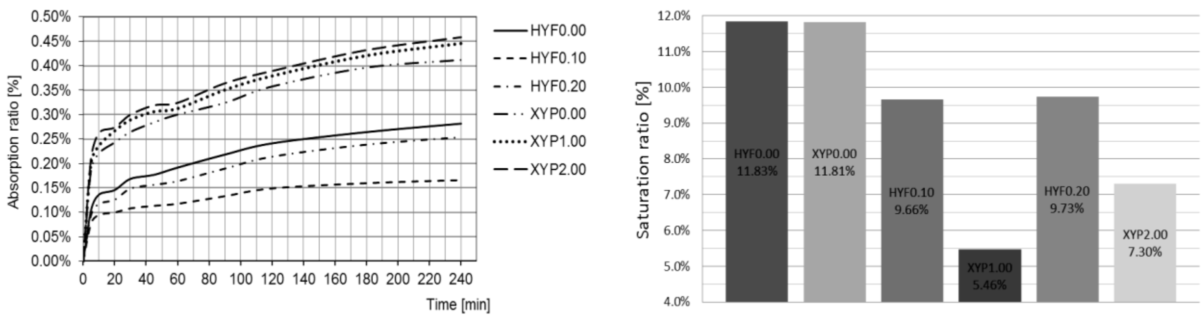

Fig. 1: Comparison of a) average short term absorption ratio and b) full saturation ratio

4.2. Micromechanical performance

Results presented in Fig. 2 show the probability density of reduced moduli merged from all measured positions, i.e. containing mechanical response from different microstructural phases. Based on the local and overall shifts in the histograms the effect of hydrophobic modification can be established. Clearly, the silicon based admixture interacts with other reactive components and shifts the phase stiffness towards lower or higher values (Fig. 2a). In the case of low concentration (HYF0.10) the reduced moduli of the main hydrated phases are lower compared to untreated samples. The possible reason for that is an altered reaction kinetics and the formation of more low-density C-S-H phase. In contrast, reduced moduli for the sample with higher SMS ratio (HYF0.20) and thus lower w/c ratio are shifted towards higher values. This can be explained by the reaction rate of the cement minerals, where fastly reactive tricalcium silicate reacts with the water prior to other minerals which may lack water later. Their hydration products, ettringite and portlandite, exhibit higher stiffness corresponding to presented data. Further evolution of lower stiffness C-S-H phases then can be lowered due to the lack of water supply. The active particles in crystalline admixtures that are several tens of micrometers large are mostly dissolved in the mixture by the alkaline environment with partial integration to the matrix. In Fig. 2b, the presence of non-dissolved particles is indicated by a low stiffness (local peak bellow 10 GPa for the sample XYP 2.00). On the other hand, the low stiffness portion of the material in this case has a potential of a further reaction (not studied here). The lower concentration of the particles (XYP1.00) alters the reduced modulus in the least amount as compared to reference samples.

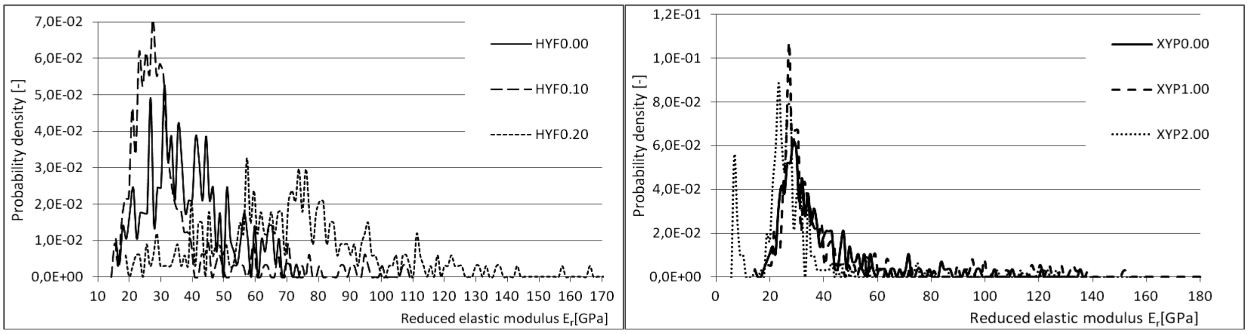

Fig. 2: Probability density of E_r – a) SMS solution, b) Xypex crystalline admixture

5. Conclusions

It has been shown that the crystalline admixtures can be used as internal hydrophobic agents similarly to silicon based solutions. They are highly efficient for surface hydrophobization in lower concentrations (Hrbek, 2016) and can be dispersed in the mixture also internally as shown in this paper. It was proved by micromechanical tests that the SMS admixture interacts with hydrating phases of cement and causes a shift in their stiffness. The conclusion provided here is based on a short term testing. A long term performance should be studied in the future. The crystalline admixture shows higher hydrophobic potential in under-pressure water intake. However, competing mechanisms of the admixture dissolution and pore sealing takes place in the microstructure which is again manifested by the shift in their micromechanical performance. Based on the short term studies an optimum replacement ratio of the crystalline admixture seems to be around 1% with respect to the binder.

Acknowledgement

Financial support of the Czech Science Foundation (project 16-11879S) and Grant Agency of the Czech Technical University in Prague (SGS16/135/OHK1/2T/11) is gratefully acknowledged.

References

Hrbek V., Petráňová V. & Němeček, J. (2016) Enhancing engineered cementitious composite by external and internal hydrophobization Key Engineering Materials vol. 677, pp 57-63.

Němeček J., Králík V. & Vondřejc, J. (2013) Micromechanical analysis of heterogeneous structural materials, Cement & Concrete composites, vol. 36, pp. 85 – 92.

Leal Da Silva W., Němeček J. & Štemberk P (2014) Methodology for nanoindentation-assisted prediction of macroscale elastic properties of high performance cementitious composites. Cement and Concrete Composites, vol. 45, pp. 57-68.

Oliver W. & Pharr G., (1992) An improved technique for determining hardness and elastic modulus using load and displacement sensing indentation experiments, Journal of Material Research 7, pp. 1564 – 1583.

Constantinides G., Chandran K. R., Ulm F.-J., Vliet K. V. (2006) Grid indentation analysis of composite microstructure and mechanics: Principles and validation, Material Science and Engineering A, pp. 189-202.

22nd International Conference
ENGINEERING MECHANICS 2016
Svratka, Czech Republic, 9 – 12 May 2016

THE USAGE OF SMOOTH OPEN-SHAPED PROFILED SHEET IN A COMPOSITE STEEL-CONCRETE SLAB

A. Hrušovská*, Š. Gramblička**

Abstract: *The steel-concrete composite slabs are often used as an alternative to monolithic concrete slabs due to the time and money savings. The trapezoidal sheets are used not only as a permanent shuttering, but can also constitute a tension reinforcement for positive bending. Design of composite slabs is regulated in Eurocode 4. The calculation of longitudinal shear resistance is very complex and can be determined only by testing on large scale samples to establish coefficients describing specific type of profiled sheeting. The usage of a smooth open-shaped profiled steel sheet is not involved in the Eurocode 4 although those sheet kinds are widely sold steel sheets worldwide. The research of smooth sheets, their interaction with concrete and a combination with end anchorages are therefore necessary. In this article we will describe the design of composite slabs with smooth open-shaped trapezoidal sheets and end anchorages, and the experimental verification on three large scale samples.*

Keywords: Composite, Slab, Sheet, Smooth, Anchorage

1. Introduction

The composite slab consists of a monolithic concrete slab and a cold-formed steel sheet. The main advantage of composite slab is in the absence of the additional shuttering. Frequent requirement of designers is to use steel sheet as a tension reinforcement for a positive bending in the critical cross-section.

The resistance of composite slab in the longitudinal shear is influenced by plenty of factors such as: the sheet thickness, shape and spacing of the embossments, the load distribution, length of the shear span, thickness of the concrete layer, the steel sheet tension, friction in the supports, the torsional displacement and many others. The connection between concrete and steel is provided by three factors: the physical-chemical adhesion (is influenced by surface properties during the casting and can be removed with higher levels of cyclic loading), the friction (is activated after the establishment of the first slip and do not depend on the size of the contact surface) and the mechanical wedge (is dependent on shape characteristics of contact surfaces and the extra connectors). Last two factors activate after appearance of first micro-cracks. When the slip between steel and concrete is completely prevented, we can speak about complete interaction, however most shear connectors have to undergo some deformation before they can supply any force. In this case the interaction is incomplete (partial), which is the most common class of the composite slab stiffness.

A composite action may be ensured by variable types of connectors (studs, perforated strips, block connectors, angle irons, different type of anchors etc.) or by shaping of the sheet ribs and flanges. According to the connection strength we know full or partial shear connection. The full shear connection is formed when the shear connection is so strong that the ultimate load is determinate by the bending moment resistance. This means, that the application of additional connectors cannot increase total resistance of composite slab. In the case of partial shear connection the failure of composite slab occurs after reaching longitudinal shear resistance value and the ultimate load depends on the number and type of shear connectors that can be also flexible or rigid.

* Ing. Andrea Hrušovská: Department of Concrete Structures and Bridges, Faculty of Civil Engineering, Slovak University of Technology, Radlinského 11; 810 05, Bratislava; SK, andrea.halabrinova@stuba.sk

** Doc. Ing. Štefan Gramblička, PhD.: Department of Concrete Structures and Bridges, Faculty of Civil Engineering, Slovak University of Technology, Radlinského 11; 810 05, Bratislava; SK, stefan.gramblicka@stuba.sk

According to deformation capacity flexible and rigid connection can be divided into: ductile and brittle (non-ductile) connection. The composite slabs with open-shaped sheets tent to act brittle while those with re-entrant shaped sheets ductile. Ductile behavior can be achieved by embossments, indentations or by adding connectors.

Design of composite slabs is regulated in the Eurocode 4 (EN 1994-1-1, 2004) The bond between concrete slab and the profiled sheet must be made in one of four ways or their combination: by adjustments on flanges or ribs of the sheets (embossments or indentations), by the re-entrant shape on the ribs creating a bond by friction, by anchorages (welds or other connectors) situated at the end of the slab only in combination with sheets described above or by end deformation of the re-entrant shaped ribs. The smooth open-shaped sheets composite slabs are not involved in the Eurocode 4.

2. The composite slab consisting of smooth open-shaped sheet and end anchorages

The design of slab with end anchorages is described in Eurocode 4 in chapter 9.7.4. The issue of longitudinal shear is defined as follows. If the test don´t prove enlargement of the longitudinal shear resistance by other shear equipment, end anchorages have to be designed to the full ultimate state tensile force. This applies only on slabs connected by adjustments on flanges or ribs of the sheets or by the re-entrant shape on the ribs. The longitudinal shear resistance can be calculated also by a partial shear connection method, when the shear resistance of sheet is enlarged by the shear resistance of additive connectors.

In case of sheets with smooth and open-shaped ribs the adhesion as a part of composite action must be neglected, so the whole longitudinal shear force must be supplied by shear connectors.

2.1. The design of composite slab consisting of smooth open-shaped sheet and end anchorages

Fig. 1: Installation of HILTI end anchorages.

For the design example the smooth open-shaped sheet RUUKKI T55-107L-976 with length 2,1m, the end anchorages HILTI X HVB 95 (Fig.1) and the class of concrete C30/35 have been chosen. The thickness of concrete layer is 110mm due to the design recommendations in Eurocode 4. The limiting values of deflection and bending moment of the profiled sheet in construction phase were verified as described in standard. It is necessary to set number of anchorages and their location in sheet ribs before analysis for the ultimate state in service limit phase is taken. If we would like to design slab for full shear connectivity, the number of connectors have to be calculated on full ultimate state tensile force:

$$N_p = A_{eff} \times f_{yd} \cong 270kN \tag{1}$$

The resistance of one anchor is influenced by the direction of anchor against the rib and the initial resistance given by the manufacturer, so the number of anchors will be:

$$\mathrm{n}_t = N_p / P_{Rd} = 270kN/28kN \cong 10 \tag{2}$$

Since the design is made on the slab width of 1 m, this means placement of 10 pieces of anchors into four ribs on each side of the slab. The condition of the minimum distance from the anchor edge to medium rib equal to 40 mm is limiting for our example (Fig.2). It means that only four anchorages on each side can be fitted to the slab with use of the selected sheet. Knowing this it was necessary to recalculate resistance to longitudinal shear and other ultimate resistances of section with partial shear connection method. The full shear connection in this type of slab is practically impossible, but as a partial connection is this solution sufficient and us designed slab can supply design load of 13,6kN/m^2 at 100% utilization in the longitudinal shear.

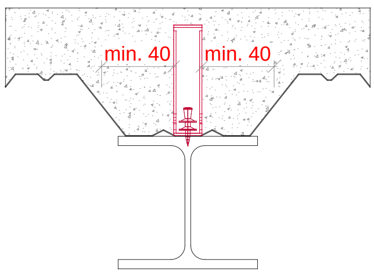

Fig. 2: Installation instruction given by manufacturer.

2.2. The experimental analysis of composite slab consisting of smooth open-shaped sheet and end anchorages

In the experimental program were verified three composite slabs as those described in Section 2.1.. The smooth open-shaped sheet RUUKKI T55-107L-976 with total length 2,2m (2,1 theoretical span), four end anchorages HILTI X HVB 95 on each side of slab and the class of concrete C30/35 were used.

Fig. 3: Composite slabs before casting.

The test was carried out as a four-point bending test (Fig.4). Following values were measured in each slab: deflection on the bottom edge of the slab in two ribs, deflection on the upper edge in the center of the slab and slip of the sheet and the concrete on both sides of the slab. The measured values were evaluated graphically.

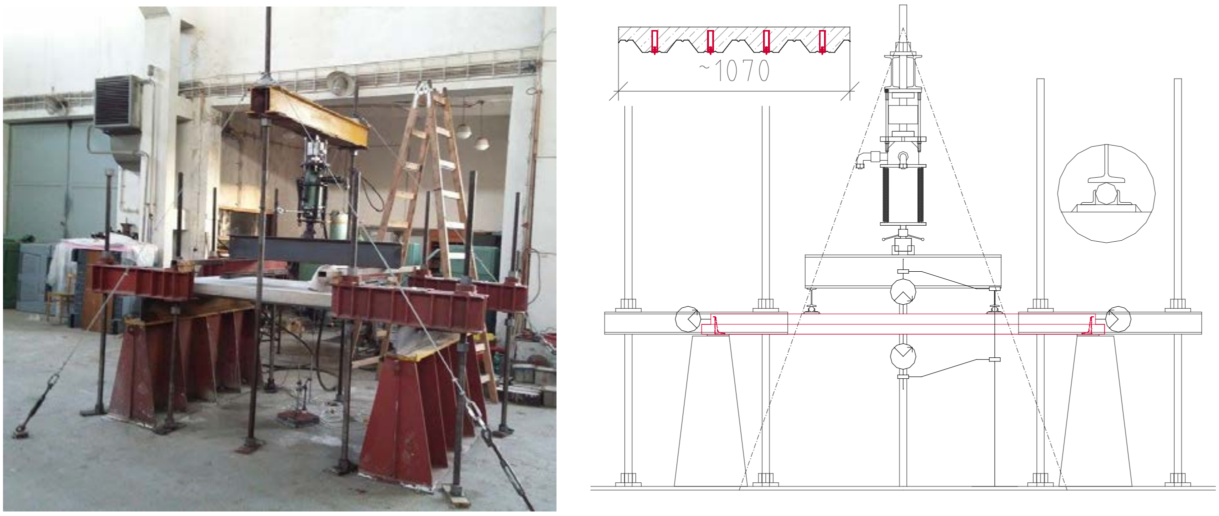

Fig. 4: The experimental set-up.

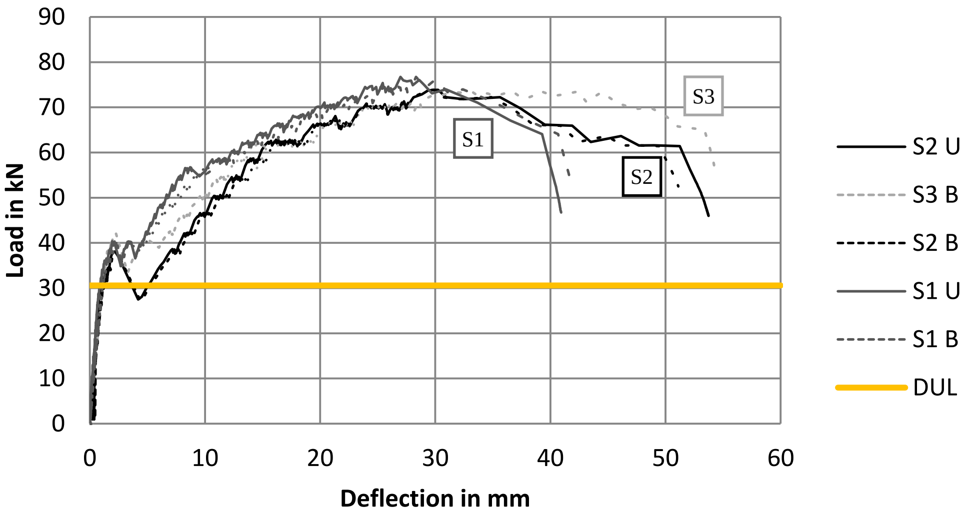

Fig. 5: The measured deflection.

Fig. 5. describes deflection, where S1, S2, S3 labels three slab samples and ending B or U are used for the bottom or upper edge measuring. Line named by shortcut DUL represents design ultimate load calculated in section 2.1.. The deflection capacity of tested slabs is markedly greater than calculated one, which means safety design. The deformation capacity can be classified as a ductile, what is caused by ductile connectors and behavior of these slabs resembles re-entrant slabs.

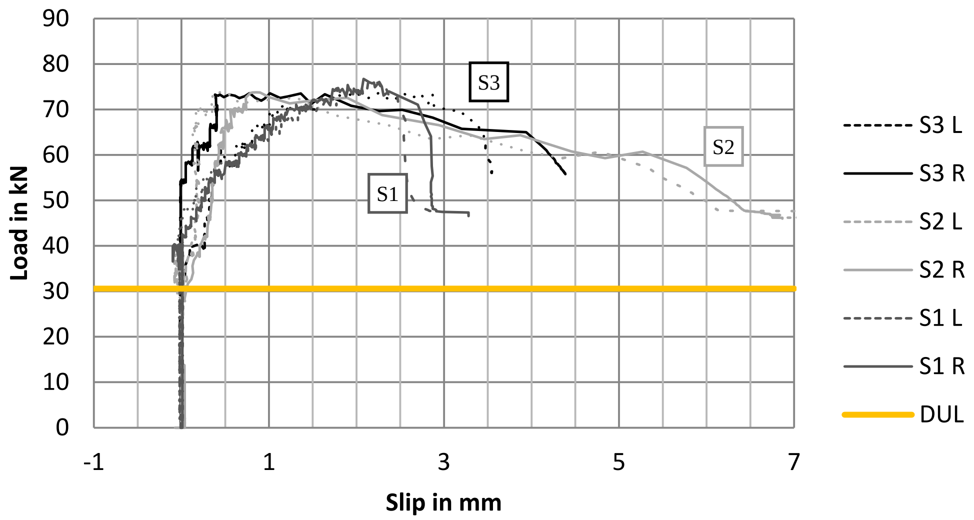

Fig. 6: The measured slip.

Fig. 6. represents slip of concrete layer against steel sheet, where ending L or R are used for left or right slab side measuring. Actually a zero slip was measured until reaching at least 38kN loading level in every case. The adhesion between the steel and the concrete is surprisingly high enough to supply designed load. Of course, composite slab cannot be designed without any anchorages, but added connectors may supply load after adhesion disappearance, which can be caused by higher levels of cyclic load or bad surface conditions during the casting. The course of slip curve is similar to those delineating slabs with profiled sheets with minor embossments although the used sheet has smooth opened ribs (Stark, 1990).

3. Conclusions

In this paper we demonstrated simple direction on how to design the composite slab with smooth open-shaped profiled sheet and end anchorages. The yet done experimental analysis showed satisfying result verification with sufficient reserve on the safe side. The partial shear connection method is an important option for the economic use of composite slabs in building industry, especially when it is practically impossible to place required numbers of connector to ensure full shear connection. We assume that the use of these slabs will have a wider application in the future and therefore future research is needed.

In the near future another three samples will be tested, two with the same proportions and connectivity parameters, but with another way of loading and one with the same dimensions, but without the end anchorages. The first two will be loaded till the first slip will appear and then the loading will start from the zero loading level again. The slab without end anchorages will allow us to do a comparison of adhesion behavior. A numerical analysis is also planned in the future.

Acknowledgement

This contribution was prepared with the financial support of Slovak Grant Agency VEGA 1/0696/14.

References

EN 1994-1-1 Design of composite steel and concrete structures, Part 1-1 General rules and rules for buildings, (2004)

Stark, J.W.B. (1990) General Methods of Design of Composite Construction: IABSE Short Course, Volume 61, pp.7-38.

22nd International Conference
ENGINEERING MECHANICS 2016
Svratka, Czech Republic, 9 – 12 May 2016

WIND FLOW AROUND AN ATYPICAL BUILDING AND BUILDING CONFIGURATIONS

O. Hubová*, L. Konečná**

Abstract: *This paper deals with a solution of air flowing around an atypical building. A result is an important parameter - the pressure coefficient on the structure. It is necessary for design of buildings and structures (or part of structures) in terms of wind load calculations. Wind tunnel measurements of wind flow and wind pressures distributions around an atypical building (a cross-section was shaped as quarter circle and building configurations with weak interaction) were performed in BLWT STU in Bratislava for 24 wind directions and different wind speeds. The results were compared with EN 1991-1-4 and they pointed to the conservative approach of standards as well as local peak pressures on the façade.*

Keywords: Wind tunnel measurements, Intensity of turbulence, Steady Wind Flow, Wind pressure Coefficient, Local angle of wind attack.

1. Introduction

Wind environment studies around idealized building and building configurations were carried out with the major focus on flow caused by strong wind with different directions. In this research, a series of parametric wind tunnel studies was carried out to investigate the effects of building width, height and the building configurations on the wind pressure distribution Beranek (1984), Statopoulos (1992), Richards (2007). In the article, we will discuss this issue for atypical high building and Twin City A1 project in Bratislava. We will indicate the high wind speed areas for strong wind conditions and try to find optimal solutions in terms of the planned new buildings groups.

2. Gust wind velocity

The effect of wind on a structure is composed of the mean wind speed increased by the turbulent component, which is reflected in the peak coefficients *g(t)*. The maximum impact velocity can be expressed as follows:

$$\hat{v} = v_m(z) + g(t)\cdot\sigma_v(z) = v_m(z)\cdot\left[1 + g(t)\cdot I_v(z)\right], \tag{1}$$

where $v_m(z)$ is mean wind velocity at a height z, $g(t)$ is peak factor, t is time, $\sigma_v(z)$ is standard deviation of the turbulence, $I_v(z)$ is turbulence intensity at height z.

The wind load - peak velocity pressure is:

$$\frac{1}{2}\cdot\rho\cdot\hat{v}^2 = q_m(z)\cdot\left[1 + g(t)\cdot I_v(z)\right]^2 = q_m(z)\cdot\left[1 + 2\cdot g(t)\cdot I_v(z) + g^2(t)\cdot I_v^2(z)\right]. \tag{2}$$

Eq. 2 is often simplified neglecting quadratic member. The peak factor due to meteorological measurements is taken to be $g(t) = g = 3 \div 3.5$. The wind pressure in EN 1991-1-4 (2005) is expressed by Eq. 3, where peak factor $g\ (t) = 3.5$.

$$w = \left(c_{pe} - c_{pi}\right)\cdot\left[1 + 7\cdot I_v(z)\right]\cdot 1/2\cdot\rho\cdot v_m^2(z), \tag{3}$$

* Assoc. Prof. Ing. Olga Hubová, PhD.: Slovak University of Technology Bratislava, Faculty of Civil Engineering, Departement of Structural mechanics, Radlinského 11, 810 05, Bratislava; SK, olga.hubova@stuba.sk

** Ing. Lenka Konečná, PhD.: Slovak University of Technology Bratislava, Faculty of Civil Engineering, Departement of Structural mechanics, Radlinského 11, 810 05, Bratislava; SK, lenka.konecna@stuba.sk

where $\rho = 1.25\ kg/m^3$ is air density, c_{pe} is external and c_{pi} is internal pressure coefficient. It is possible for typical shapes of constructions to find the values c_{pe} and c_{pi} in Section 7 - EN 1991-1-4 (2005).

2.1. Wind flow around atypical structures

The wind pressure distribution on these structures can be obtained by experimental measurements in the wind tunnel or by CFD simulation for a suitable model of turbulence. Lately, it is possible to see high-rise structures in the shape of quarter circle (see Fig.1a, b).

Experimental measurements were performed in BLWT of Slovak Technical University in Bratislava. Wind tunnel was designed with open circuit scheme with total length of 26.3 m, two operation spaces with the dimensions of the cross-section 2.6×1.6 m and with adjustable ceiling.

We tested the model of building in two spaces - in steady and turbulent wind flow (see Fig. 1c, d) by changing of wind direction and wind velocity. The measurements were conducted using pressure scanner DSA 3217 (Scanivalve). Measured profile - quarter circle with a radius of 0.16 m and length of 1.1 m was placed centrally in front of the measuring space and 0.8 m above the floor. There was measured the steady flow. Initial position of segment (rotation angle 0°), dimensions and 16 measured pressure taps are shown in Fig. 1e. Wind velocity has been set by using software LabVIEW. The model was rotated every 15º, thereby was simulated the changing of wind direction acting on the object. The evaluation of the measured data enables to determine the most unfavorable position with maximum values of suction and wind pressure for different wind speeds (Fig. 2a). A model with height h = 0.273 m and radius r = 0.11 m (scale 1:380) was placed in the middle of rotating table in turbulent wind flow. The mean wind velocity and intensity of turbulence profiles were simulated with plastic foil FASTRADE 20 and wall 150 mm. Boundary layer simulations proved to be in good agreement with logarithmic law, Hubová & Lobotka (2014). ABL simulation with value roughness length z_0 = 0.7 – 0.77 m is between terrain category III – IV according EN 1991-1-4 (2005), closer to the terrain category IV. The measurements were made at the heights z_A = 0.258 m, z_B = 0.136 m and z_C = 0.015 m above the floor. Resultant value was determined as average of 1 000 samples (in each tap). The measurements were carried out for reference wind velocities at the top of building $v_{ref,1}$ = 8.83 m/s and $v_{ref,2}$ = 12.72 m/s (see Fig.2 b).

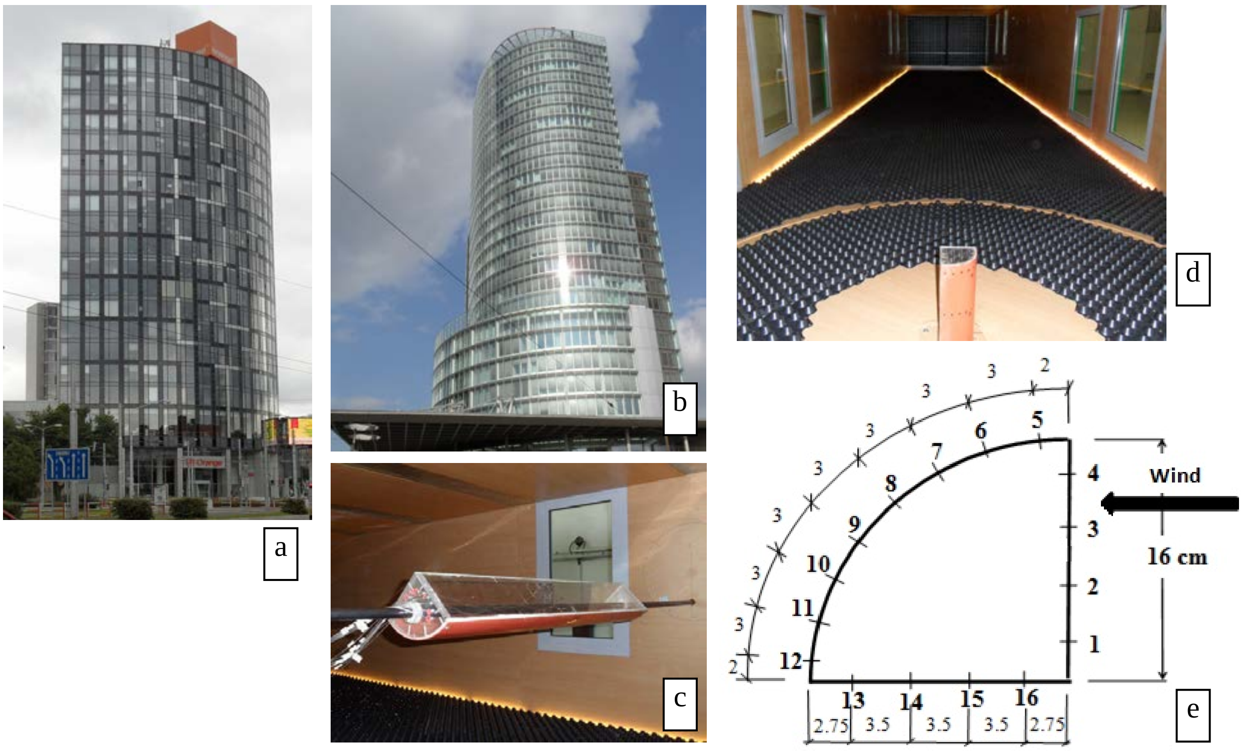

Fig. 1: High-rise building shaped as quarter circle (a, b); model of quarter circle in steady wind flow (c) and turbulent wind flow (d); cross-section of the model with dimensions in [cm] and pressure taps.

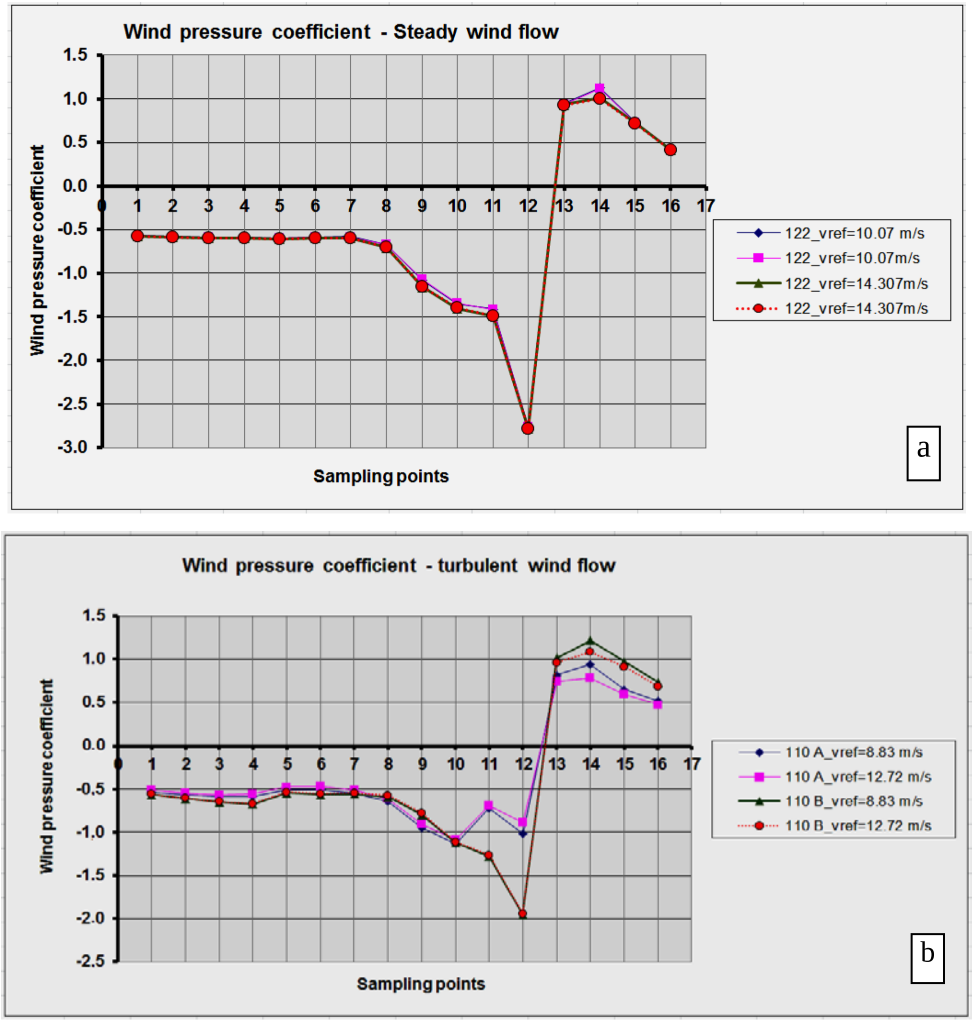

Fig. 2: External wind pressure coefficient in steady (a) and turbulent wind flow (b).

2.2. Wind flow around building configuration

The strong interaction occurs principally for all configurations if the distances between the buildings are less than 5 times the high. We monitored the distribution of wind pressure on future high-rise building TWIN A1 in the center of Bratislava. The orientation of the building in relation to the prevailing wind directions plays an important role in wind load. 90 m high buildings with surrounding lower parts (scale 1:300) were tested in BLWT in turbulent wind flow and the model was rotated every 15º (see Fig. 3).

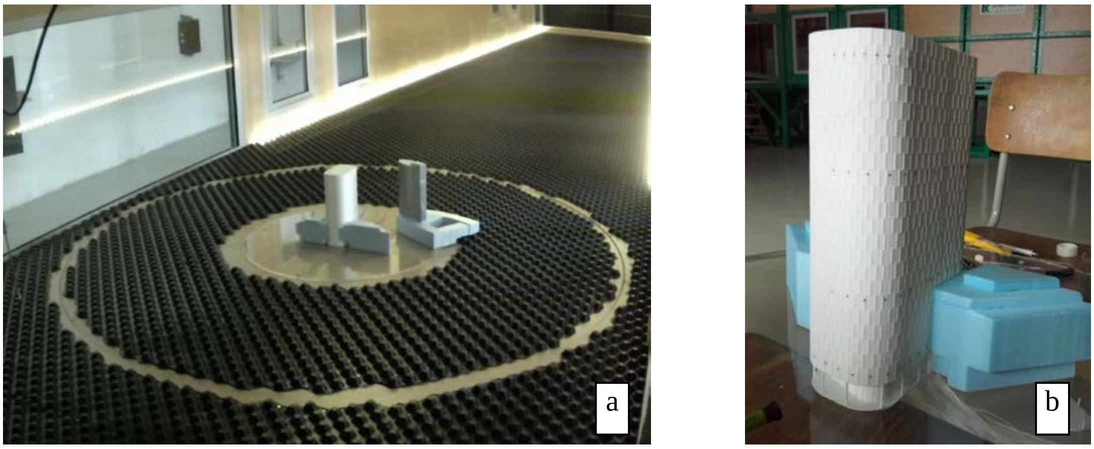

Fig. 3: Building configurations - TWIN A1 and VUB Bank buildings (in the scale 1:300) (a); detail of the TWIN A1building (b).

Comparison of the wind pressure on the facade of the white building obtained by calculation according to EN 1991-1-4 and the values obtained by experimental measurements (EXP) is shown in the graph in the Fig. 4. We used internal pressure coefficients c_{pi} = 0.2 and c_{pi} = -0.3 according to EN 1991-1-4. The resulting wind pressures on the preparing new building obtained experimentally were significantly lower than conservative values in accordance with EN standards. Local sucking on the rounded corners of the facade, was significantly higher than Normative coefficient c_{pe} = - 1.2 for the region around the corner of the building and reached values c_{pe} = - 1.47.

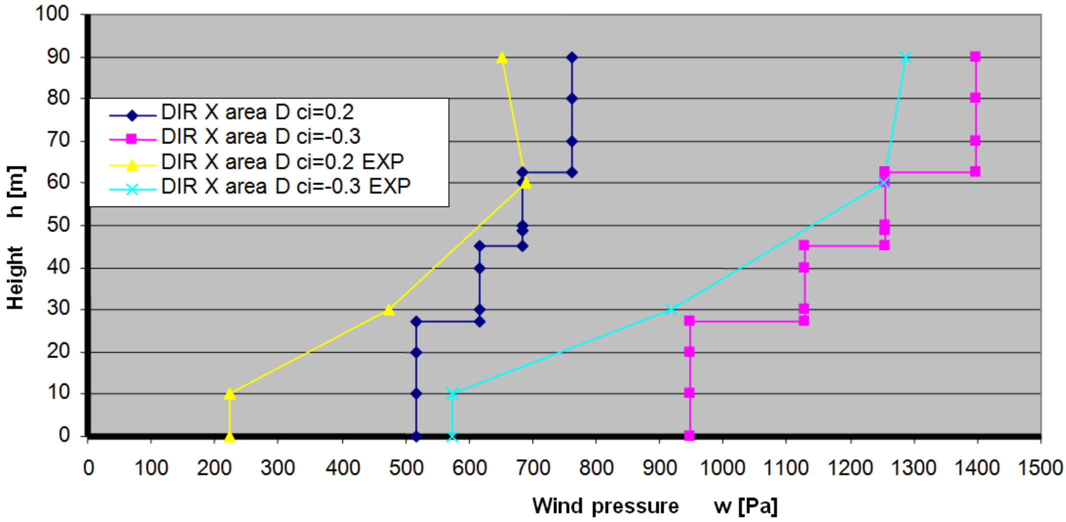

Fig. 4: Comparison of the wind pressure in X direction (prevailing wind direction).

3. Conclusions

The external wind pressure distribution and external wind pressure coefficients obtained from repeated experimental measurements made on models in steady and turbulent wind flow indicates the local extremes of suction in certain directions. Extreme values of the external wind pressure coefficients reached values of suction around -2 ÷ -2.78. It is evident from the graphs (Figs. 2 and 4), that in upper part of the structures, the pressures are affected by specific wind flow around the free end of the structure. In the case of atypical shapes of high buildings and structures in groups the wind tunnel investigation is recommended.

Acknowledgement

This paper was supported by the grants no. 01/0544/15 and no. 01/0265/16 provided by the Grant Agency of Ministry of Education, Science, Research and Sport of the Slovak Republic.

References

EN 1991-1-4: Eurocode 1: Action on structures – Part 1-4: General actions - Wind actions, (2005).

Beranek, W.J. (1984) Wind Environment around Building Configurations. HERON 29 No.1/1984, pp. 1-70. Delft, Netherlands.

Koloušek, V., Pirner, M., Fischer, O. &, Náprstek, J. (1983) Wind effects on Civil Engineering Structures. Academia Praha, Elsevier, coed, London.

Pirner, M. & Fischer, O. (2003) Zatížení staveb vetrem, ČKAIT Praha.

Hubová, O. (2007) The effect of the wind on the structure. Slovak Journal of Civil Engineering, Vol. XV, No. 3. ISSN 1210-3896.

Hubová, O. & Lobotka, P. (2014) The Natural Wind Simulations in the BLWT STU Wind Tunnel, in: Porceedings of ATF 3nd Conference on Building Physics and Applied Technology in Architecture and Building Structures. E-Book of reviewed papers, May 6-7, 2014, Austria, Vienna, pp. 78-84. ISBN 978-3-200-03644-4.

Stathopoulos, T., Wu,H. & Bédant, C. (1992) Wind environment around buildings: a knowledge –based approach. Journal of Wind Engineering and Industrial Aerodynamics, 41-44, pp.2377-2388.

Richards, P.J., Hoxey R.P, Connel B.D. & Lander D.P. (2007) Wind-tunnel modeling of the Silsoe Cube. Journal of Wind Engineering and Industrial Aerodynamics, 95, pp.1384- 1399.

22nd International Conference
ENGINEERING MECHANICS 2016
Svratka, Czech Republic, 9 – 12 May 2016

EVALUATION OF MULTIDIMENSIONAL EFFECT OF NATURAL DRAFT WET-COOLING TOWER FLOW

T. Hyhlík*

Abstract: *The computational study of the flow fields inside the natural draft wet-cooling tower has been done. Obtained results allow evaluating the influence of particular parts on the flow field inside cooling tower. The effect of rain zone, fill zone and flue gas injection are studied. It is shown that the flow field above the fill zone is mainly influenced by minor losses in cooling tower fill and by the controlling of the flow direction in this zone. This effect is leading to practically uniform velocity field just above the fill zone even though the flow field in the rain zone is multidimensional. The impact of flue gas injection is studied by using momentum and kinetic energy flux coefficients. The system of Euler equations for quasi-one-dimensional flow is generalized using momentum and kinetic energy flux coefficients. It is shown that the flow field inside cooling tower excluding rain zone can be considered as quasi-one-dimensional in the case where the flue gas injection is not taken into account. The effect of flue gas injection slightly deviates the character of the flow, which is still very close to quasi-one-dimensional flow in the whole domain excluding rain zone.*

Keywords: natural draft wet-cooling tower, momentum flux coefficient, kinetic energy flux coefficient

1. Introduction

Natural draft cooling tower of rotational hyperboloid shape with

$$A(z) = \frac{\pi}{4}(0.006977z^2 - 1.2764z + 131.61)^2 \quad (1)$$

is selected. The tower is 150m high with fill zone placed at the height of 11.5m. Fill height is assumed to be 2 m. Water inlet mass flow rate is 17200 kg/s. Inlet water temperature is 34.9°C. Air inlet temperature is 22°C, and specific humidity is 7.622 g/kg. The atmospheric pressure is 98100 Pa. Fill Merkel number is assumed to be 0.815 and Lewis factor is 0.9. Loss coefficient per meter of the fill zone is 12 m^{-1}. The flue gas mass flow rate is 350 kg/s and the temperature is 59°C. The heat and mass transfer is solved together with quasi-one-dimensional flow model in the first step by using model (Hyhlík, 2015-1). Dry air mass flow rate of 16393 kg/s is obtained in the case without flue gas injection, and 15576 kg/s is obtained with flue gas injection. Water temperature decreases to 26.4°C without flue gas and to 26.5°C with flue gas injection. Mentioned results are used as an input to the multidimensional flow field study.

2. Generalized quasi one-dimensional flow model

The system of governing equations can be written in the case of quasi-one-dimensional flow as

$$\frac{\partial(\boldsymbol{W}A)}{\partial t} + \frac{\partial(\boldsymbol{F}A)}{\partial z} = \boldsymbol{Q}, \quad (2)$$

where $A(z)$ is cross-sectional area of the cooling tower, z is spatial coordinate, and t is temporal coordinate. Vector of conservative variables $\boldsymbol{W}$ and vector of fluxes $\boldsymbol{F}$ are

$$\boldsymbol{W} = \begin{bmatrix} \rho \\ \rho v \\ \rho e \end{bmatrix}, \quad \boldsymbol{F} = \begin{bmatrix} \rho v \\ \rho v^2 \beta + p \\ \left\{\rho\left(u + \gamma \frac{v^2}{2}\right) + p\right\} v \end{bmatrix}, \quad (3)$$

* Ing. Tomáš Hyhlík, Ph.D., Department of Fluid Dynamics and Thermodynamics, Faculty of Mechanical Engineering, Czech Technical University in Prague, Technická 4; 166 07, Prague 6; CZ, tomas.hyhlik@fs.cvut.cz

where ρ is density, v is velocity, p is pressure, u is internal energy, and e is sum of internal energy and kinetic energy. The first equation is continuity equation, the second is momentum equation, and the third is equation of energy. The system of governing equations is generalized by using momentum coefficient β and by using kinetic energy coefficient γ taking into account the non uniformity of velocity field

$$\beta = \frac{A\int_A v^2 dA}{\left(\int_A vdA\right)^2}, \quad \gamma = \frac{A^2\int_A v^3}{\left(\int_A vdA\right)^3}. \tag{4}$$

Coefficient β is analogous to Boussinesq momentum correction coefficient which is a ratio of momentum flux based averaged velocity and mass flux based averaged velocity. Similarly, the kinetic energy coefficient is a ratio of kinetic energy flux based averaged velocity and mass flux based averaged velocity. These coefficients can modify momentum flux and kinetic energy flux with respect to non-uniformity of the velocity profile in the quasi-one-dimensional computation (Hyhlík, 2015-2) and, on the other hand, they allow to quantify nonuniformity of velocity profile.

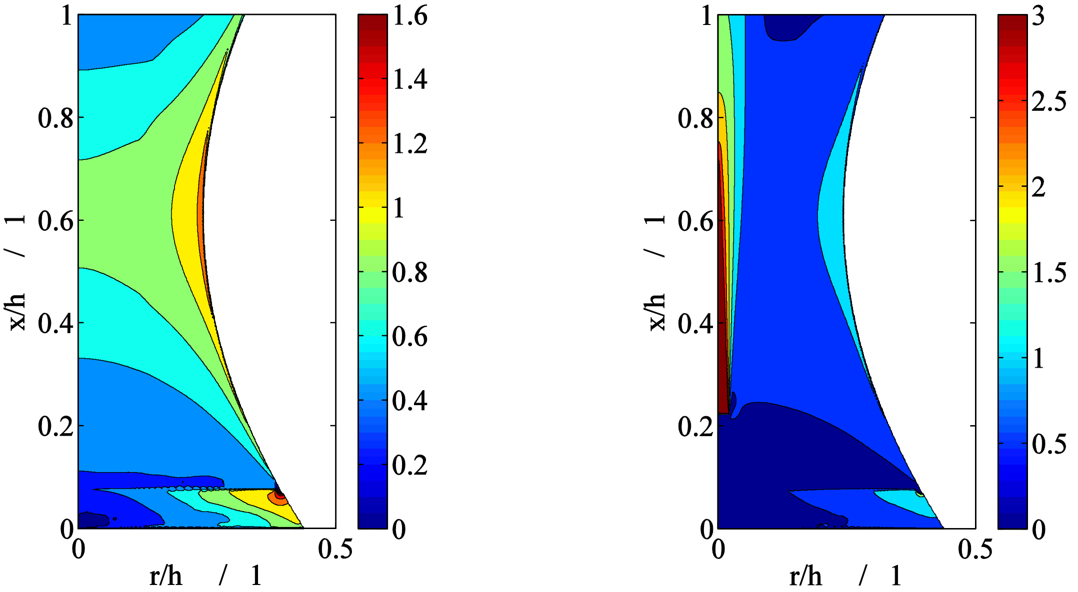

Fig. 1: Contours of velocity (non-simplified model); without flue gas injection (left) and with flue gas injection(right) .

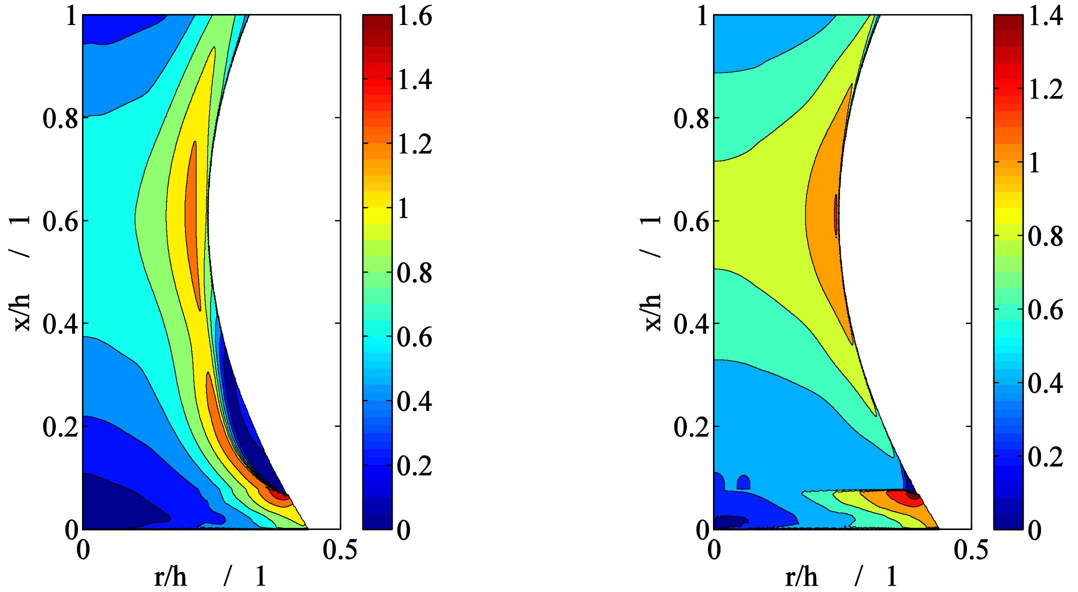

Fig. 2: Contours of velocity (simplified model); there are no minor losses in the fill (left);there are minor losses only in radial direction in the fill (right)

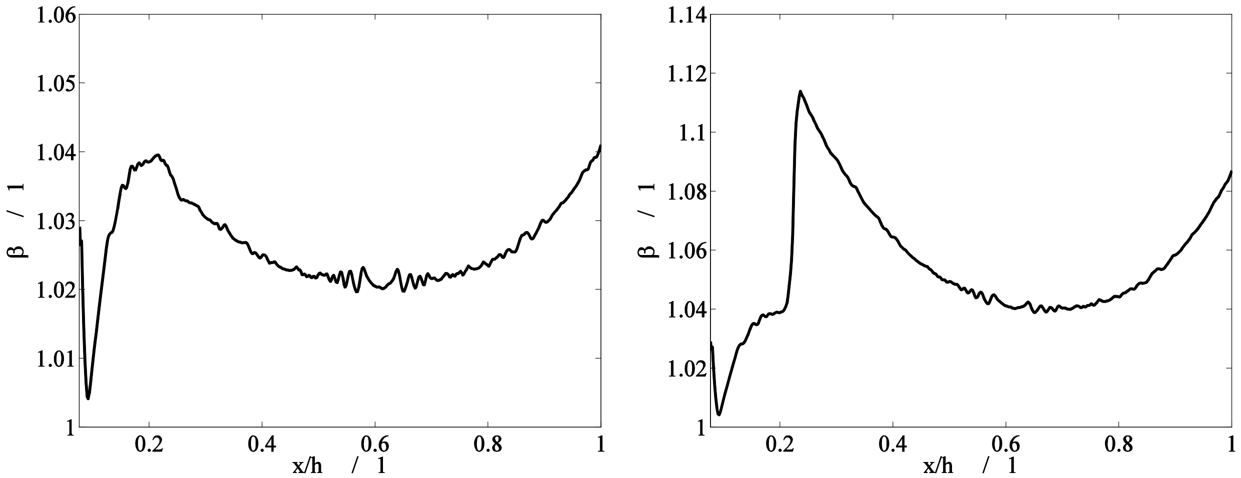

Fig. 3: Momentum coefficient (non-simplified model); without flue gas injection (left) and with flue gas injection(right).

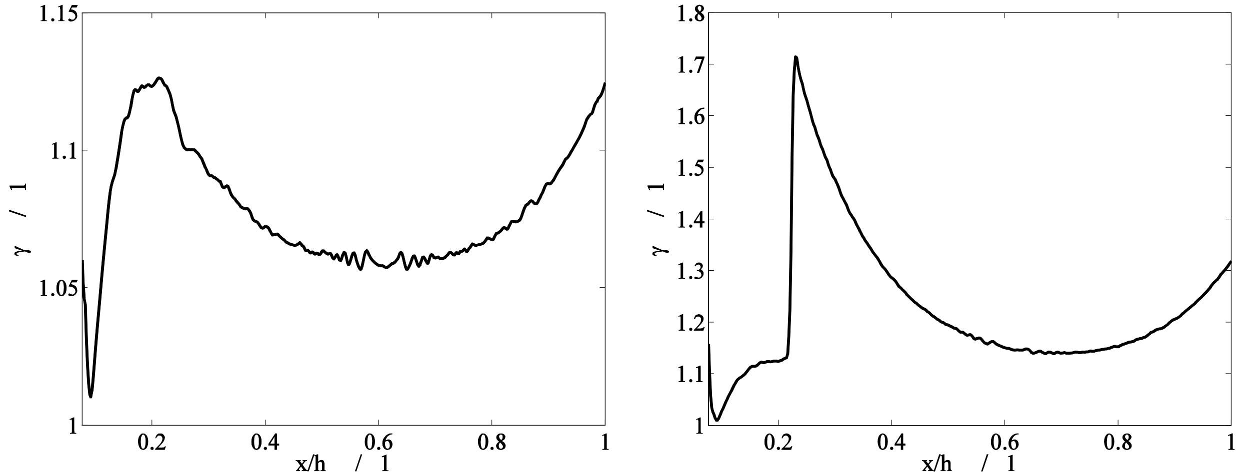

Fig. 4: Kinetic energy coefficient (non-simplified model); without flue gas injection (left) and with flue gas injection(right).

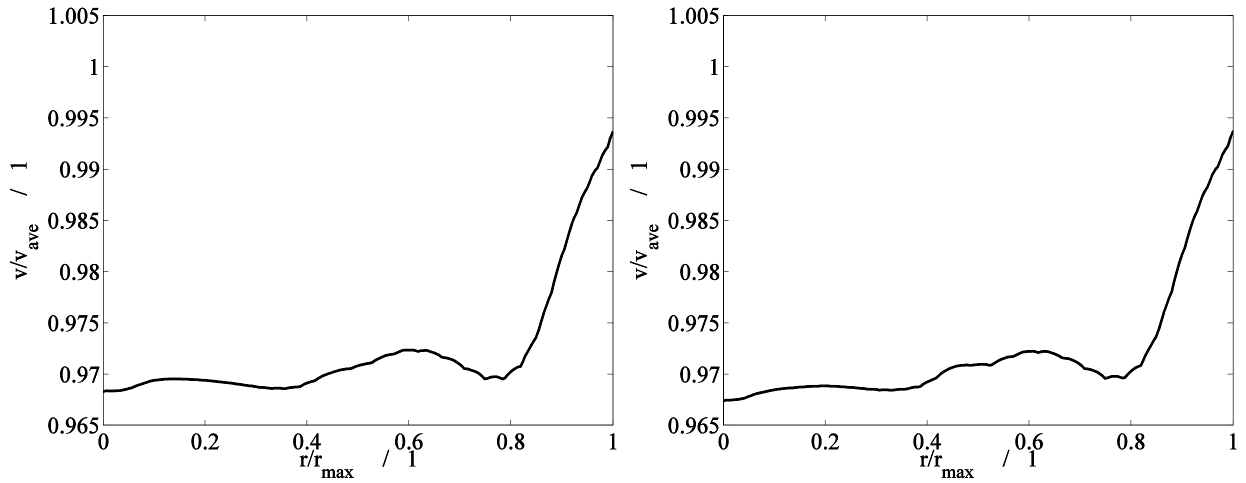

Fig. 5: Velocity distribution above the fill zone (non-simplified model); without flue gas injection (left) and with flue gas injection(right).

3. Results

The numerical solution of axisymmetric flow inside the cooling tower has been done by using ANSYS Fluent code, where air and water mass flow rates are prescribed as was mentioned in the introduction. Rain zone in the cooling tower is modeled by using discrete phase model which allowed modeling an interaction of flowing moist air and water droplets. Fill zone is prescribed by using both radial and axial direction minor loss coefficients, where radial loss coefficient is set to have very high value to prevent flow in the radial direction in this zone. There is the cooling tower cross section in figures 1 and 2, where the axis is on the left, the inlet is on the right down and outflow is on the top side. The velocity is normalized by area weighted velocity in the narrowest cross section of the cooling tower. Figure 1 shows the velocity field in the case of the flow without and with flue gas injection. The highest velocities are in the bottom part of the cooling tower close to the inlet. It is visible that the velocity field is strongly affected by flue gas injection, but the flue gas injection affects only limited region close to the cooling tower axis. The figure 2 documents importance of minor loses in the model. The left part of this figure shown the case, where minor loses in the fill zone are ignored, loses in rain zone are modeled correctly with discrete phase model. It is visible that this approach leads to the unrealistic flow field with a large separation zone. The right-hand side of figure 2 documents the case where the minor loses in the radial direction in the fill zone are included, and this approach leads to realistic flow field which in very close to the flow field in figure 1 despite the fact that the minor loses in the axial direction are ignored. From the engineering point of view is very important to evaluate the nonuniformity of the flow field because the design codes are mainly one-dimensional. Momentum and kinetic energy coefficients defined in section 2 are evaluated in figures 3 and 4 as a function of the nondimensional axial coordinate. Because the flow field in the rain zone is multidimensional, this zone is not included in figures 3 and 4. It is possible to see that the case of the flow without flue gas injection is almost one dimensional because the coefficients β and γ are very close to one. The values of momentum and kinetic energy coefficients are higher in the case of flue gas injection, but the flow field is not so far from the one-dimensional case. There is an increase in momentum and kinetic energy coefficient in the bottom part of the cooling tower above fill zone. The coefficients are decreasing in the middle of the cooling tower, and then there is an increase in the outflow part. The highest values of mentioned coefficients are connected with the place where the flue gas is injected. It is visible that the distribution of velocity above the fill is not affected by the flue gas injection as depicted in figure 5. Although the flow in the rain zone is multidimensional, the velocity above the fill is almost uniform. This effect is connected with loses in the rain zone and in the fill zone.

4. Conclusions

A computational study of the flow through the natural draft wet-cooling tower has been performed. It has been shown that the most important minor loss is the radial loss coefficient in the fill which significantly affects flow field as is documented in figures 1 and 2. The utilization of this coefficient allows flowing only in the axial direction in the fill. The character of the flow field deviates from the idealized quasi-one-dimensional flow especially in the case of flue gas injection, but the deviation is not strong. The flow field in the case without flue gas injection is almost quasi-one-dimensional. The obtained results allow being included in the model of quasi-one-dimensional flow in the section 2 which can improve the flow field prediction. Another possibility is to include presented momentum coefficient into so-called draft equation (Kröger, 2004) which is frequently used by cooling tower industry.

Acknowledgement

This work has been supported by *Technology Agency of the Czech Republic* under the project *Advanced Technologies for Heat and Electricity Production – TE01020036*.

References

Hyhlík, T. (2015) Quasi One-Dimensional Model of Natural Draft Wet-Cooling Tower Flow, Heat and Mass Transfer, EJP Web of Conferences, Volume 92, 02027, http://dx.doi.org/10.1051/epjconf/20159202027

Hyhlík, T. (2015) Mathematical Model of Two Phase Flow in Natural Draft Wet-Cooling Tower Including Flue Gas Injection, in: Experimental Fluid Mechanics 2015, Prague

Kröger, D. G. (2004) Air-cooled heat exchangers and cooling towers: thermal-flow performance evaluation and design, PennWell Corporation, Tulsa

22nd International Conference
ENGINEERING MECHANICS 2016
Svratka, Czech Republic, 9 – 12 May 2016

FINITE ELEMENT ANALYSIS OF CRANIAL IMPLANT

J. Chamrad[*], P. Marcián[**], L. Borák[***], J. Wolff[****]

Abstract: *Medical 3D-printing is a modern technology that offers the possibility to manufacture patient-specific implants offering shorter operating times and better clinical results at a lower cost. The patient-specific implants are nowadays on the rise in cranioplasty which uses e.g. polymetylmetacrylate (PMMA) implants to correct the damaged skull. The manufacturing accuracy of such constructs remain problematic and deserve a detailed investigation. The aim of this study was to assess the inaccuracy of the bone-implant interface when PMMA skull implant is employed. The assessment was performed using the computational simulation.*

1. Introduction

The most common surgery technique used for brain tumor removal is craniotomy. During this procedure, a portion of the skull is removed to allow access to the brain. Craniotomy is usually followed by cranioplasty which is a surgical procedure to correct the damaged skull. Such procedures are also performed to correct skull deformities. To date biocompatible materials such as PMMA, and titanium alloys are commonly used to manufacture implants that are subsequently used to treat such defects. Modern implants used for the treatment of the aforementioned skull defects are designed on computers and are manufactured using different rapid prototyping technologies (Narra et. al., 2014). The manufacturing accuracy of such constructs remains problematic. One approach to assess implant inaccuracy is by using computational simulations. Such techniques provide a good insight into potential problems. The purpose of this study was to assess the inaccuracy of the bone-implant contact (BIC) when PMMA implant is employed.

2. Methods

2.1 Patient-specific approach

Computer tomography (CT) is a standard diagnostic imaging tool that is commonly used prior to most skull surgeries. The acquired CT data sets can be converted into STL files and are then exported to CAD software packages to design patient specific skull implants (Huotilainen et. al, 2014). There are three basic ways how to plan the skull reconstruction and to design a skull implant:

- CT dataset of the patient’s skull taken before the injury can be used to design the implant.
- The unaffected side of the skull can be mirrored it into the damaged part of the skull. However the skull is never 100 % symmetrical.
- Cranial defects can be reconstructed using spline algorithms.

[*] Bc. Jakub Chamrad.: Institute of Solid Mechanics, Mechatronics and Biomechanics, Faculty of Mechanical Engineering, Brno University of Technology, Technická 2896/2, 616 69 Brno, Czech Republic; CZ, kuba.chamrad@seznam.cz

[**] Ing. Petr Marcián, PhD.: Institute of Solid Mechanics, Mechatronics and Biomechanics, Faculty of Mechanical Engineering, Brno University of Technology, Technická 2896/2, 616 69 Brno, Czech Republic; CZ, marcian@fme.vutbr.cz

[***] Ing. Libor Borák, PhD.: Institute of Solid Mechanics, Mechatronics and Biomechanics, Faculty of Mechanical Engineering, Brno University of Technology, Technická 2896/2, 616 69 Brno, Czech Republic; CZ, liborborak@seznam.cz

[****] Jan Wolff, DDS, PhD.: Department of Oral and Maxillofacial Surgery, VU University Medical Center Amsterdam, Amsterdam; NL, Jan.Wolff@vumc.nl

Despite the fact that patient-specific implants have advantages, design and manufacturing inaccuracies cannot be completely avoided. Moreover, the overall cost of patient-specific implants is still a limiting factor.

2.2 Computational modeling

CT images of 1 injured human skull (male, 45 yo) were used in this study. STL model of the skull was created using STL Model Creator (Marcián et. al., 2011) and SolidWorks software (Fig. 1a). The implant was designed following standard procedures described above. In order to test the influence of implant geometry inaccuracy, two versions of the implant model were created (Fig. 1b): 1. An ideal implant geometry that fitted exactly into the skull defect (labeled as "Ideal"); 2. An implant with randomly distributed inaccuracies in the BIC (labeled as "Real"). The real implant and corresponding defect were modeled using cut and Boolean operations. Both implants were assumed to be from PMMA as requested by the doctors. In the simulations, PMMA was modeled using a linear, homogeneous and isotropic material model (Young's modulus (E) = 3000 MPa, Poisson's ratio (μ) = 0.38; Preusser et. al., 2011, Gómez et. al., 2003). The implants were fixed to the skull using three micro-plates made of Ti6Al4V (KLS Martin). Micro-screws were modeled as threadless cylinders with an equivalent mean diameter. This simplification is acceptable as it does not significantly affect the results in the BIC. For the titanium alloy as well as for the bone itself, the same material model as for PMMA was used (titanium alloy: E = 110 000 MPa, μ = 0.3 (Niinomi (1998)); bone: E = 15 000 MPa, μ = 0.3 (Freedman et. al., 2013, Motherway et. al., 2009)). The computational model was finalized in ANSYS 16.2. All parts were discretized using quadratic element types SOLID186 and SOLID187. All contacting parts were connected using contact elements TARGE170 and CONTA174 (frictional contact). Number of elements and nodes were approximately 180 000 and 320 000, respectively. Friction coefficients for each contact pair (with an exception of micro-screws) were assumed to be as follows: 1. PMMA-Ti6Al4V = 0.3; 2. PMMA-Bone = 0; 3. Ti6Al4V-Bone = 0.3. The assumed coefficients were analyzed in preliminary test calculations and were conservatively set to maximize the final strains in the BIC and stresses in the fixators as presented in this paper. The screws were fixed to the implant and to the bone and no mutual movement was allowed. The models were loaded with a static force applied to the center of the implant. Specifically, the force was distributed to the nodes of the FE mesh in the small circular region (~1 cm^2) of the implant center. This loading case mimicked a relaxed person resting on a pillow as requested by the doctors. The force of 50 N corresponds to an approximate weight of the head (~5 kg (Ridwan-Pramana et. al., 2016)). In addition, the bone and implant were loaded with an intracranial pressure of 4 kPa (Czosnyka et. al., 2004). The models were fixed at the bottom side of the skull in the region where the spine is assumed.

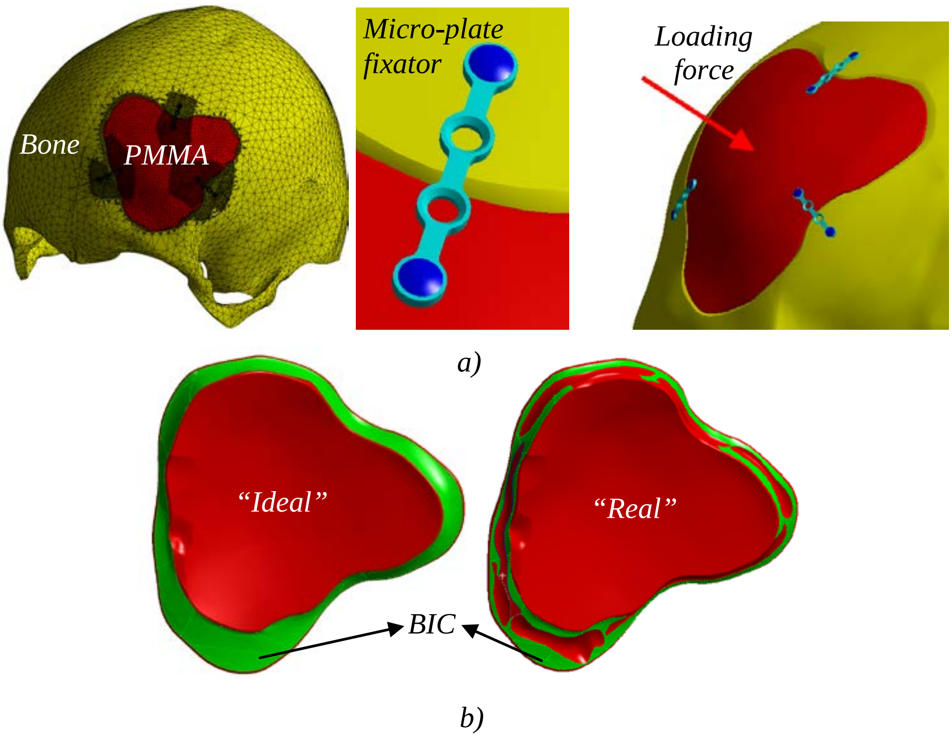

Fig. 1: a) Geometry model of whole system b) two variants of PMMA implants.

3. Results

The BIC areas of the "Ideal" and "Real" models were 870 mm^2 and 490 mm^2. This difference significantly affected the implant displacements, contact pressures, von Mises stresses and von Mises strains. Maximum implant displacements in the loading direction were observed at the point of the force application (Figure 2). These displacements were 0.033 mm and 0.042 mm for the "Ideal" and "Real" cases, respectively.

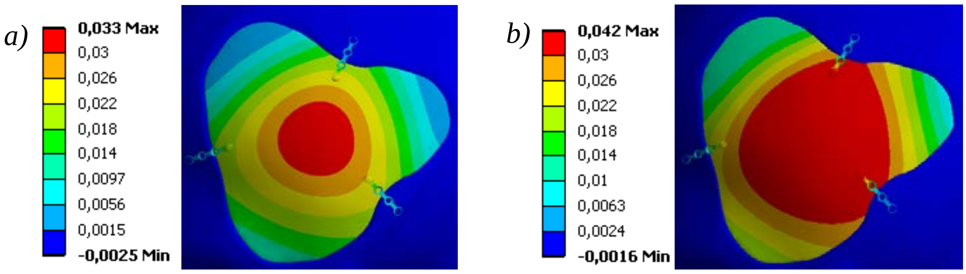

Fig. 2: Displacement [mm] a) "Ideal" b) "Real".

Contact pressures in the BIC are shown in Figure 3. Maximum contact pressure for the "Ideal" and "Real" case is 0.067 MPa and 0.100 MPa, respectively.

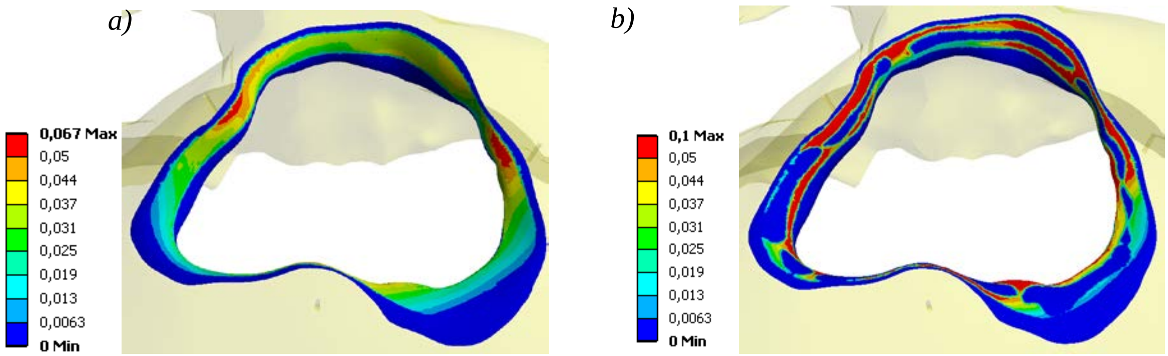

Fig. 3: Contact pressure [MPa] a) "Ideal" b) "Real".

The bone in the BIC vicinity was evaluated for von Mises strains. Higher values of these strains were observed again in the "Real" case, especially under the fixators as shown in Figure 4.

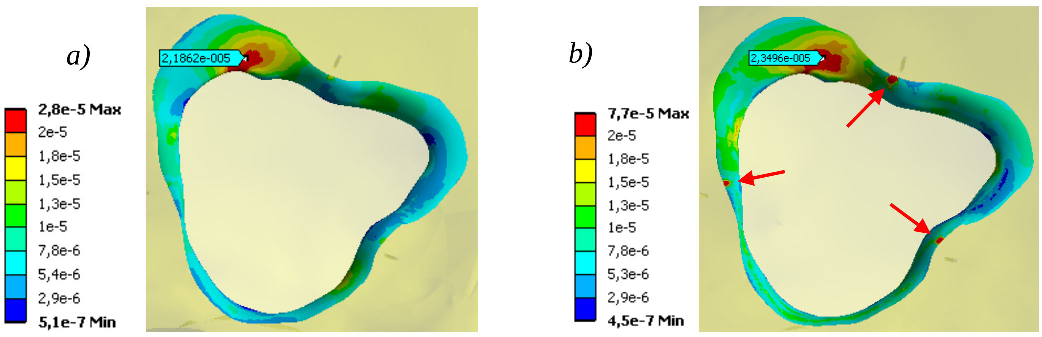

Fig. 4: von Mises strains [-] a) "Ideal" b) "Real".

The fixators were evaluated for von Mises stresses (Figure 5). The maximum stresses were observed to be 30 MPa and 78 MPa in the "Ideal" and "Real" cases, respectively.

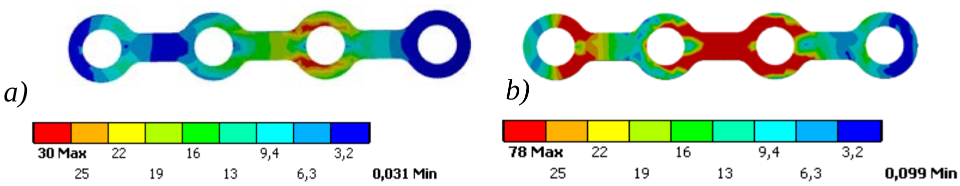

Fig. 5: von Mises stress [MPa] a) "Ideal" b) "Real".

4. Discussion

The results of the study confirm that implant manufacturing inaccuracies significantly affect the biomechanical conditions in the BIC. In case of the “Real” model, all observed results showed to be more severe than in the “Ideal” case. Maximum normal displacement in the tested “Real” case was higher by 27% and the contact pressure was higher by 49%. In the “Ideal” case, the contact pressure exceeded 0.05 MPa only at two locations in the fixator vicinity; however, in the “Real” case, the pressure exceeded this value almost everywhere in the BIC. Similarly, maximum von Mises strain in the “Real” case was higher by 275% and, as a contrary to the “Ideal” case, extreme concentrations can be observed in a close vicinity of the fixators. The “Real” case implant is also much more stressed than the “Ideal” one; maximum von Mises stress is higher by 260%. The main reason for the significant differences in all monitored results is the fact that the “Real” case lacks the uniform bone support in the BIC and is, therefore, susceptible to stress/strain concentrators which might be a source of implant failure. In this study, only one randomly generated “Real” case was tested; however, it is evident that a considerable amount of attention should be payed to the implant accuracy as well as to accuracy of the craniotomy itself.

5. Conclusion

We are witnessing a boom in medical 3D-printing. This technology offers the possibility to manufacture patient-specific implants which offer shorter operating times and better clinical results at a lower cost. However, patient-specific implants are still somewhat idealized objects and their manufacturing accuracy should be considered carefully.

Acknowledgement

The research was supported by the Czech Science Foundation by grant No. 16-08944S.

References

Czosnyka, M. & Pickard, J. D. (2004) Monitoring and interpretation of intracranial pressure. Journal of Neurology, Neurosurgery, and Psychiatry, 75, 6, pp. 813–821.

Freedman, M., Ring, M. & Stassen, L. F. A. (2013) Effect of alveolar bone support on zygomatic implants: a finite element analysis study. International Journal of Oral and Maxillofacial Surgery, 42, pp. 671-676.

Gómez, F. J. & Elices, M. (2003) Fracture of components with V-shaped notches. Engineering Fracture Mechanics, 70, pp. 1913-1927.

Huotilainen, E., Jaanimets, R., Valášek, J., Marcián, P., Salmi, M., Tuomi, J., Mäkitie, A. & Wolff, J. (2014) Inaccuracies in Additive Manufactured Medical Skull Models Caused by the DICOM to STL Conversion Process. Journal of Cranio-Maxillofacial Surgery, 42, 5, pp. e259 (e265 s.).

Marcián, P., Konečný, O., Borák, L., Valášek, J., Řehák, K., Krpalek, D. & Florian, Z. (2011) On the Level of Computational Models in Biomechanics Depending on Gained Data from Ct/Mri and Micro- Ct, in: MENDEL 2011 - 17th International Conference on Soft Computing. 1. Brno: Brno University of Technology, pp. 255-267.

Motherway, J. A., Verschueren, P., Van der Perre, G., Vander Sloten J. & Gilchrist, M. D. (2009) The mechanical properties of cranial bone: The effect of loading rate and cranial sampling position. Journal of Biomechanics, 42, pp. 2129-2135.

Narra, N., Valášek, J., Hannula, M., Marcián, P., Sándor, G., Hyttinen, J. & Wolff, J. (2014) Finite element analysis of customized reconstruction plates for mandibular continuity defect therapy. Journal of Biomechanics, 47, 1, pp. 264-268.

Niinomi, M. (1998) Mechanical properties of biomedical titanium alloys. Mater Science Engineering, 243, pp. 231-236.

Preusser, T., Rumpf, M., Sauter, S. & Schwen, L. O. (2011) 3D Composite Finite Elements for Elliptic Boundary Value Problems with Discontinuous Coefficients. SIAM Journal on Scientific Computing, 33, pp. 2115-2143.

Ridwan-Pramana, A., Marcián, P., Borák, L., Narra, N., Forouzanfar, T. & Wolff, J. (2016) Structural and mechanical implications of PMMA implant shape and interface geometry in cranioplasty – a finite element study. Journal of Cranio-Maxillofacial Surgery, 44, 1, pp. 34-44.

22nd International Conference
ENGINEERING MECHANICS 2016
Svratka, Czech Republic, 9 – 12 May 2016

COMPUTATION OF AERODYNAMIC DAMPING IN AEROELASTIC SYSTEMS BASED ON ANALYTICAL AND NUMERICAL APPROACH

Š. Chládek, J. Horáček, I. Zolotarev[1]

Abstract: *The paper describes computation of aerodynamic damping and natural frequencies of aeroelastic systems. The damping is a critical parameter for the stability analysis of aeroelastic systems. Structural damping of the system is important for very low fluid flow velocities, however by increasing the flow velocity, the aerodynamic damping dominates in the instability search. The damping can be evaluated in time or in frequency domain. The presented computation of aerodynamic damping consists of two analytical and one numerical approach. The analytical approaches are represented by the well-known pk method and the unsteady panel method. The pk method is based on Theodorsen unsteady aerodynamics and on the computation of complex eigenvalues of the system as functions of the flow velocity. The unsteady panel method enables the computation of the interaction between aeroelastic system and fluid flow. The aerodynamic damping is evaluated in time domain from the system response to given initial conditions. The numerical approach is based on the finite volume method (FVM) modelling the complete fluid-structure interaction (FSI) coupled problem. The aerodynamic damping is also computed from the system response to a given initial condition. The results of the mentioned methods are compared for the profile NACA 0012 with two degrees of freedom (2-DOF) for plunge and pitch motion around an elastic axis.*

Keywords: aeroelastic instability, aerodynamic damping and eigenfrequency analysis, fluid structure interaction

1. Introduction

Aeroelastic systems are represented by wide range of systems where vibrating structure interacts with fluid. The fluid flow affects the structure and the structure affects the flow field. It yields the coupled problem where governing equations of both structure and fluid have to be solved together. One of the basic important problems is the computation of stability boundaries of the coupled system. These boundaries are usually calculated for critical fluid flow velocities. If a certain value is achieved, the system becomes unstable. Two basic types of instability are usually defined – divergence and flutter. Divergence is defined as instability with negative damping and zero frequency of the motion of the structure. Flutter is defined as instability with negative damping and positive frequency of the motion. Calculation of the damping as a function of the fluid flow velocity represents a classical procedure for the stability investigation. For zero and very low velocities the damping of the structure is usually positive and consists mainly of the structural damping. With increasing the flow velocity the aerodynamic damping becomes more significant. At certain velocity the aerodynamic damping starts to decrease. When the total damping crosses the zero value, the instability occurs (Dowell et al., 1995).

2. Methods

Three different computational methods are introduced. They differ in the form of FSI calculation. The pk method only solves an eigenvalue problem of the FSI system, see e.g. Dowell et al. (1995). The unsteady panel method (Basu & Hancock, 1978) and the FVM (Rodden at al., 1979) enable the FSI solution in time domain. These methods are based on the evaluation of aerodynamic damping and natural frequencies. In all cases considered here, we suppose that the fluid flow is inviscid and incompressible in a 2D computational domain.

[1] Ing. Štěpán Chládek, Ing. Jaromír Horáček, DrSc., Ing. Igor Zolotarev, CSc., Institute of Thermomechanics AS CR, v. v. i., Dolejškova 1402/5, 182 00 Praha 8, Czech Republic, chladek@it.cas.cz, jaromirh@it.cas.cz, igor@it.cas.cz

2.1. Pk method

The pk method represents a technique for computation of aeroelastic stability solution where p indicates the eigenvalue and k the reduced frequency. This method is based on the computation of complex eigenvalues of the equation of motion

$$M\ddot{x}(t) + B\dot{x}(t) + Kx(t) = Q(k)x(t), \quad (1)$$

in which for the considered 2-DOF system M, B, K and Q stand for/are mass, damping, stiffness and aerodynamic forces matrices of dimension 2x2 respectively. The matrix of aerodynamic forces is derived for inviscid and incompressible fluid using the Theodorsen unsteady aerodynamics and it is a function of reduced frequency $k = \frac{\omega b}{U_\infty}$ where ω is the natural frequency, b is the reference dimension and U_∞ is the fluid flow velocity. Aerodynamic matrix $Q(k)$ for aeroelastic system with 2 degrees of freedom (DOF) can be found in classic aeroelastic literature, see e.g. Dowell et al., (1995). The eigenvalues are computed in the form of complex conjugate numbers

$$p_{j_{1,2}} = -b_{rj}\Omega_{0j} \pm i\Omega_{0j}\sqrt{1 - b_{rj}^2}\,. \quad (2)$$

The solution using the pk method is iterative and the convergence criterion is the difference of frequency ω and imaginary part of eigenvalue $\left|\Omega_0\sqrt{1 - b_r^2} - \omega\right| < \varepsilon$. Once the convergent solution is computed, the damping ratio is evaluated as

$$b_{rj} = -\frac{Re(p_j)}{|p_j|}, \quad (3)$$

and the eigenfrequency is evaluated as the positive imaginary part of (2). Results of the pk method are valid in accordance with its derivation only for zero fluid flow velocity, or for the velocity, where the flutter occurs. Nevertheless, the benefits of pk method are reflected in its implementation into commercial software NASTRAN for aeroelastic calculations (Rodden at al., 1979).

2.2. Unsteady panel method

Unsteady panel method was derived for 2D inviscid and incompressible fluid flow as a tool for fluid structure interaction calculation. The calculation of the flow field is based on the solution of the Laplace equation for the total velocity potential $\Delta\phi = 0$. The solution for the total velocity potential is considered as a sum of free stream, source and sink, and vortex components. The geometry of the structure has to be defined and the computational domain is considered to be infinite. Once the complete flow field is computed, the aerodynamic forces acting on the structure can be evaluated. The motion of the structure is described by the equation of motion

$$M\ddot{x}(t) + B\dot{x}(t) + Kx(t) = V(t), \quad (4)$$

where $V(t)$ is the vector of aerodynamic forces. The structure motion and the fluid flow have to be solved for every time step. The response of the structure can be computed for arbitrary initial displacement of the structure at defined flow field velocity. The damping ratio and natural frequencies can be evaluated based on the structure response in time domain, see e.g. Chládek et al., (2016).

2.3. Finite volume method

The inviscid incompressible 2D fluid flow field is described by the Euler equation in the conservative form

$$\mathrm{D}.W_t + F_x + G_y = 0, \quad (5)$$

where $W = \{p, u, v\}^T$ is the vector of conservative variables, $F = \{u, u^2 + p, uv\}^T, G = \{v, uv, v^2 + p\}^T$ represent inviscid physical fluxes and $\mathrm{D} = diag(0,1,1)$ represents diagonal matrix. The solution in the time domain was calculated by the finite volume method in discrete points of the computational domain where the proper initial and boundary conditions were defined. Computational domain is shown with the boundary conditions in the left-hand side of Fig. 1. On Γ_i, which represents inlet of the channel, there was the Dirichlet boundary condition prescribed in the form $[u, v] = (U_\infty, 0)$. On Γ_o, which represents outlet of the channel, a value of pressure p was prescribed. Γ_w denotes boundary condition of type wall and it was prescribed on the structure and on the walls of the channel. It defined the slip boundary condition in the case of the inviscid fluid. For given initial conditions of the structure position was the coupled FSI problem solved. In every time step the complete flow field was calculated, the aerodynamic forces were evaluated and the equation of motion (4) was solved. Based on the structure response in time domain, the damping ratios and the natural frequencies were evaluated similarly as for the unsteady panel method.

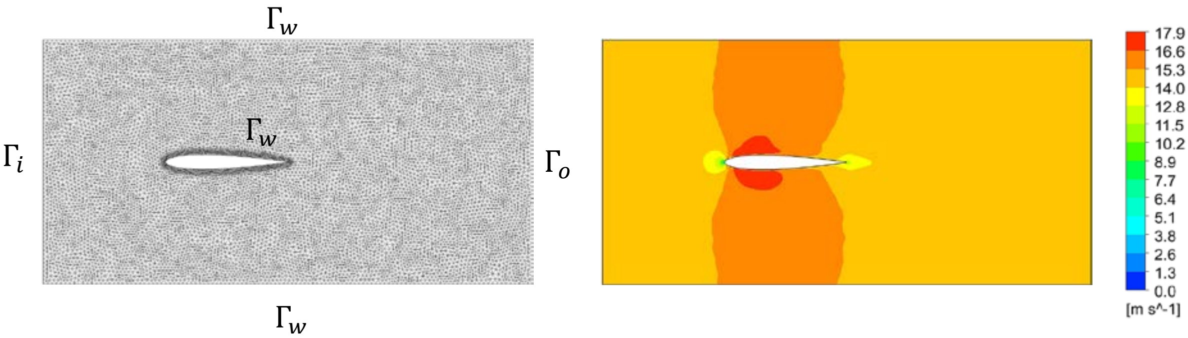

Fig. 1: Computational domain for FVM (left) and example of velocity flow field at U_∞=15 m.s^{-1}(right).

3. Results and discussion

Algorithms for the pk method and the unsteady panel method were programmed in Matlab. The FVM solution was implemented in the commercial software Ansys/Fluent and the Runge-Kutta method was used for numerical solution of the equation of motion (4) as in the case of the panel method. Structural properties of the profile NACA 0012 were taken from Sváček et al. (2012).Only the static moment was multiplied by -1 to be positive. The profile response was computed for the far flow field velocities $U_\infty = \{10, 15, 20, 26, 30\}\, m.s^{-1}$. The initial position of the profile was set to $h(0) = 2.10^{-3} m$ for the vertical translation and $\alpha(0) = 2.86^\circ$ for the rotation. The example of the FVM solution is shown in the right-hand side of Fig. 1 in the form of velocity flow field. The resulting natural frequencies are shown as a function of the flow velocity in Fig. 2 and the evaluated damping ratios are presented in Fig. 3.

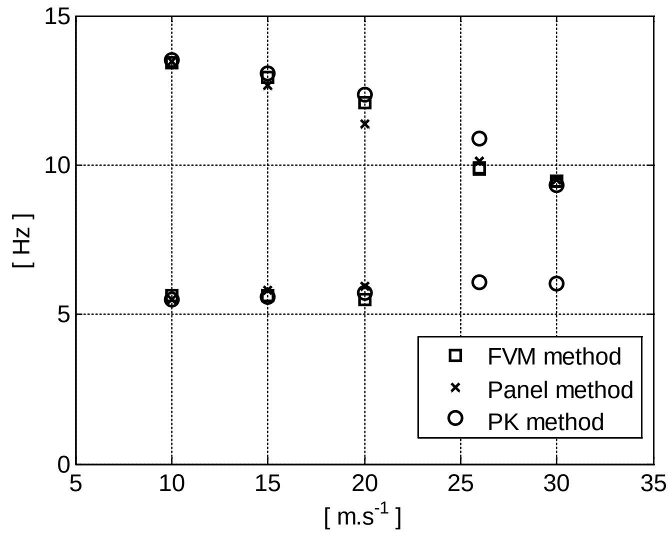

Fig. 2: Comparison of computed natural frequencies as a function of flow velocity.

Considering the data in Fig. 2 it can be concluded that for the flow velocities lower than $U_\infty = 26\, m.s^{-1}$ here is a good agreement of all three methods, however, for the higher velocities two natural frequencies were computed only by the pk method, while by the panel and FVM methods we computed only the higher natural frequency. Nevertheless, these frequencies are close to the results obtained by the pk method. The results for the damping ratio are not clear. There are some flow field velocities where the results are in good agreement but it is difficult to make some general conclusions. The results of the stability analysis are summarized in Tab. 1. The lowest stability limit was computed by the panel method when the flutter occurs at far field velocity $U_\infty = 26\, m.s^{-1}$. Using FVM method the flutter velocity was computed at $U_\infty = 28\, m.s^{-1}$. Finally, the pk method estimated the flutter instability at $U_\infty = 30\, m.s^{-1}$.

Tab. 1: Aeroelastic stability analysis based on three different computational methods.

Velocity U [m.s^{-1}]	***Stable or type on instability***		
	PK method	*Panel method*	*FVM method*
5	*stable*	*stable*	*stable*
10	*stable*	*stable*	*stable*
15	*stable*	*stable*	*stable*
20	*stable*	*stable*	*stable*
26	*stable*	*FLUTTER*	*stable*
28	*stable*	*FLUTTER*	*FLUTTER*
30	*FLUTTER*	*FLUTTER*	*FLUTTER*

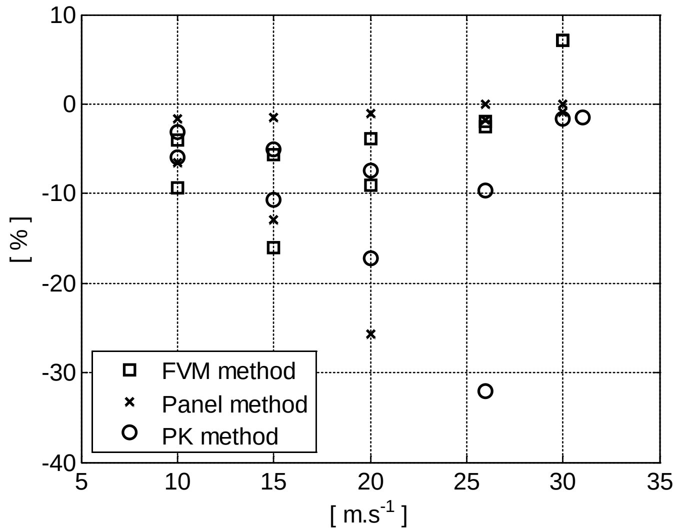

Fig. 3: Comparison of evaluated damping ratios as functions of the airflow velocity.

4. Conclusions

Three different methods for the airfoil stability calculation were compared. The results show a good agreement in case of natural frequency evaluation. Comparison of the damping ratios appeared more complicated and only for some values of the fluid flow velocity a good agreement was obtained. A more detailed study is needed for clarification of such discrepancies.

Acknowledgement

The research was supported by the project of the Grant Agency of the Czech Republic GA13-10527S „Subsonic flutter analysis of elastically supported airfoils using interferometry and CFD“.

References

Basu, B.C., Hancock, G.J. (1978) The unsteady motion of a two-dimensional aerofoil in incompressible inviscid flow. Journal of Fluid Mechanics, vol. 87, part 1, pp.159-178.

Dowell, E.H., Crawley, E.F., Curtiss, H.C., Peters, D.A., Scanlan, R.H., Sisto, F. (1995) A Modern Course in Aeroelasticity. Kluwer Academic Publishers, Dodrecht.

Chládek, Š., Horáček, J., Zolotarev, I. (2016) Evaluation of aerodynamic damping and natural frequencies from numerical simulations and experiments. Dymamesi 2016, Institute of Thermomechanics AS CR, v.v.i., Prague.

Rodden, W.P., Harder, R.L, Bellinger, E.D. (1979) Aeroelastic Addition to NASTRAN. NASA Contractor Report 3094.

Sváček, P., Horáček, J., Honzátko, R., Kozel, K. (2012) Simulation of Free Airfoil Vibrations in Incompressible Viscous Flow – Comparison of FEM and FVM. Acta Polytechnica, Vol. 52, No.6/2012, pp.105-115.

22nd International Conference
ENGINEERING MECHANICS 2016
Svratka, Czech Republic, 9 – 12 May 2016

STUDY OF LOCALIZED VIBRATIONS OF MISTUNED BLADES OF CENTRIFUGAL COMPRESSOR

T. Jamróz*

Abstract: *Presented paper deals with sensitivity analysis of a mistuning centrifugal compressor. Vibrations of blades of mistuning bladed disk generate local zoning of vibration modes as well as amplitude magnification, which primarily reduces the high cycle fatigue life of engine. The sensitivity analysis uses a criteria for determination of the level of these local mode effects depending on mistuning deviations. The analysis shows that some vibration modes of centrifugal compressor structure which are characterized by significant percentage of blades on the total bladed disk strain energy, have a significantly higher sensitivity to blade mistuning. These vibration modes are characterized with low structural coupling blades such as higher bending modes or modes with high numbers of nodal diameter lines.*

Keywords: Centrifugal compressor, mistuning, blade vibration, mode localization.

1. Introduction

Good knowledge of dynamic behaviour of bladed disk is essential during the design as well as test-phase of future aeroengine rotors. Especially in the case of integrated bladed disks (blisks) become more important aiming at more environmentally-friendly, more efficient, and more powerful aeroengines. The deletion of the heavy bladed disk connection results in reduced masses, higher maximum rotational velocities, and improved pressure ratios (increased efficiency factors). In this connection also, a number of disadvantages occur above that are mentioned in Beirow, et al. (2005) such as very low structural damping and higher sensitivity with regard to mistuning. This behaviour reduces the margin for dynamic load and consequently causes a problem that is connected to High Cycle Fatigue (HCF) as noted by Seinturier (2007) or earlier Steffens (2001).

Mistuning, which primarily results from manufacturing tolerances, but also from wear or even strain gauge instrumentation, can cause mode localizations accompanied by a severe increase of blade displacements compared to the tuned response. Almost 50 years ago a conservative limit (1) for an estimation of the maximum displacement increase of bladed disks only depending on the number of blades N by Whitehead (1966) was introduced. This formulation was more or less validated later by Petrov & Ewins (2003).

$$\gamma = \frac{\max u_{mistuned}}{\max u_{tune}} = \frac{1}{2}\left(1 + \sqrt{N}\right) \tag{1}$$

Nevertheless, mistuning can be described by other parameters such as Mode Localization and Mode Fill factor. These characteristics were described by Klauke, et al. (2009). Thus especially the mode localization has to be kept in mind during the rig test vibration monitoring because only a few blades will be instrumented with strain gauges. Therefore suitable choice of blades is essential to avoid critical misinterpretations during assessment of results from measurement. To achieve a better understanding of these contexts, free and forced vibration behaviours of updated full FE models of the centrifugal compressor from aeroengine M601 was analysed using different evaluation factors.

* Ing. Tomáš Jamróz: Aerospace Research and Test Establishment, Beranových 130 Prague 9, CZ, jamroz@vzlu.cz

2. Numerical Analysis of the Tuned Blisk

In order to get an idea about basic vibration characteristics a FE model segment is derived from the ideal design of centrifugal compressor with main blade and splitter blade (Fig. 1a). This FE model segment is rotated to make full model of the centrifugal compressor. Based on this model an eigenvalue analysis with the effect of rotational speed included is carried out, firstly to derive the nodal diameter plot (Fig. 1b) and with that to get an overview about relevant blade mode families and disk dominated modes as well.

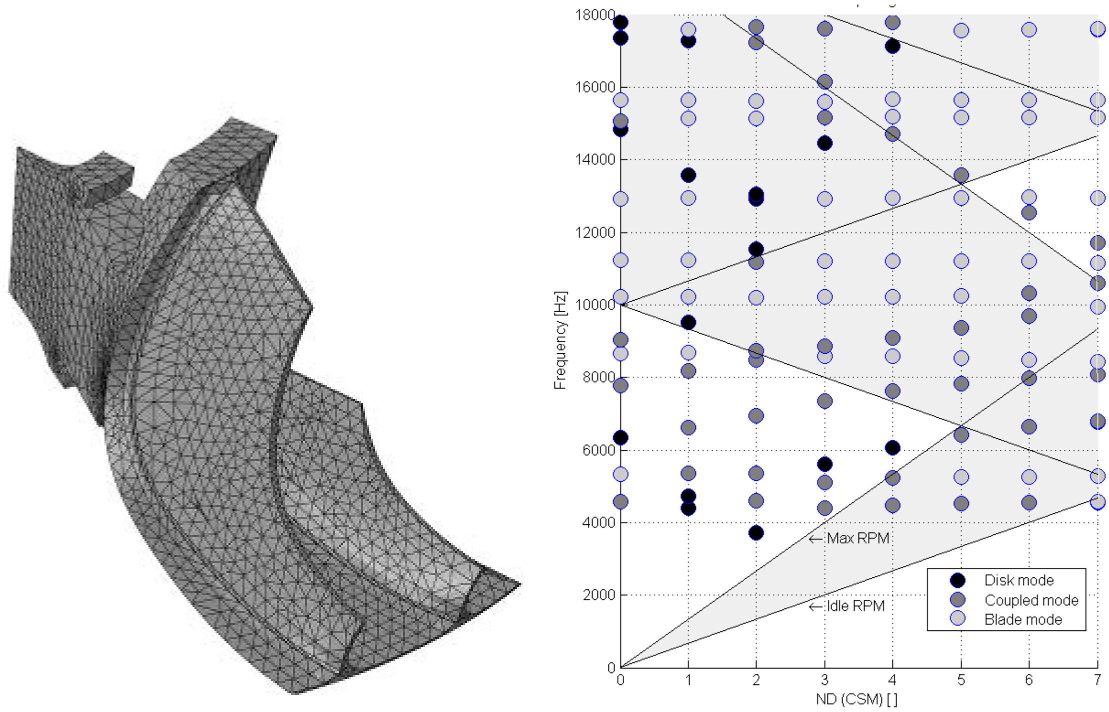

Fig. 1: a) FE model segment of centrifugal compressor and b) Nodal map diagram for tune blisk.

In the nodal diameter map (Fig. 1b), all eigenfrequencies of the tuned system are showed against nodal diameter also known as their CSM (Cyclic Symmetry Mode). Additionally, the modes can be distinguished using the blade percentage of the total blisk strain energy as a reliable indicator (Table 1). Hence, several blade-modes mode families can be easily identified. These mode families occur as nearly horizontal lines. In contrast to this, disk-modes and coupled modes show more rising frequencies with an increasing number of nodal diameters caused by increasing disk stiffness, as mentioned above can be found in Strehlau & Kühhorn (2010).

Tab. 1 Distinguish of blisk modes.

	Disk mode	Coupled mode	Blade mode
Blade percentage of total blisk strain energy	*<50%*	*50%÷75%*	*>75%*

3. Numerical Analysis of Mistuned Blisk

3.1. Modeling of Blade Mistuning

Modeling of mistuning of full model was realized by changing the material properties. This realization due to the decrease and increase in the individual blade's Young modulus E_i, the blade eigenfrequencies were modified without changing the blade geometry. The change in blade eigenfrequencies is proportional to the change in the square root of the blade's Young moduli.

Modeling of blade mistuning was performed by different artificial sinusoidal blade mistuning deviations in contrast to the measured mistuning distributions, which differ from blade mode to blade mode and can be characterized by a Weibull-distribution.

The number of full sine waves around the blisk circumference was chosen to be 1 and 4 with standard deviations of 0.33%, 0.98%, 2.62%. Generally, the mistuning of a bladed disk assembly results in several fundamental effects such as splitting of double mode and mode localization, according Srinivasan (1997).

3.2. Evaluation of Mistuning Blisk

The variation of the vibration mistuning modes of the blisk was based on a discrete Fourier transform (DFT) such as those done before by Castanier & Pierre (2002). The mistuned mode is represented as a superposition of tuned modes, where the coefficients of the single tuned modes in the modal summation characterize the level of mode distortion.

One of the fundamental parameters that is evaluated is called Mode Fill Factor (*MFF*) which has been published by Klauke, et al. (2009). This parameter is used for comparison of the magnitudes of mode filling of different blade modes with each other. This factor specifies the number of harmonics that are included in each the vibration mode. In other words, how strong is the deviation of modification of mistuning mode with regard to tune vibration mode and how many *EOs* are able to excite this *(M) CSM*.

$$MFF_i = \frac{100}{CSM_{max}}(\xi_i - 1)\ [\%], \qquad where \quad \xi_i = \left(\frac{\sum_{i=0}^{CSM_{max}} DFT_i}{DFT_{max}}\right) \tag{2}$$

Another important parameter is the Localization Factor (LF). The amplification factor alone gives no information about the number of high displacement blades during forced response analysis of a mistuned blisk. Hence, it is possible that a lot of blades reach high magnification factors or only one single blade reaches a higher displacement level. This knowledge is helpful in terms of an optimum blade selection for strain gauge instrumentation of rotor stages and vibration results analysis.

$$LF_i = \frac{100}{\sqrt{N} - x}(\varsigma_i - x)\ [\%], \qquad where \quad \varsigma_i = \frac{U_{i,max}}{RMS_i} \tag{3}$$

Where $x=1$ if $CSM=0$ or $CSM=CSM_{max}$ and $x=\sqrt{2}$ if $1 \leq CSM \leq CSM_{max}$ (odd N) or $1 \leq CSM < CSM_{max}$ (even N)

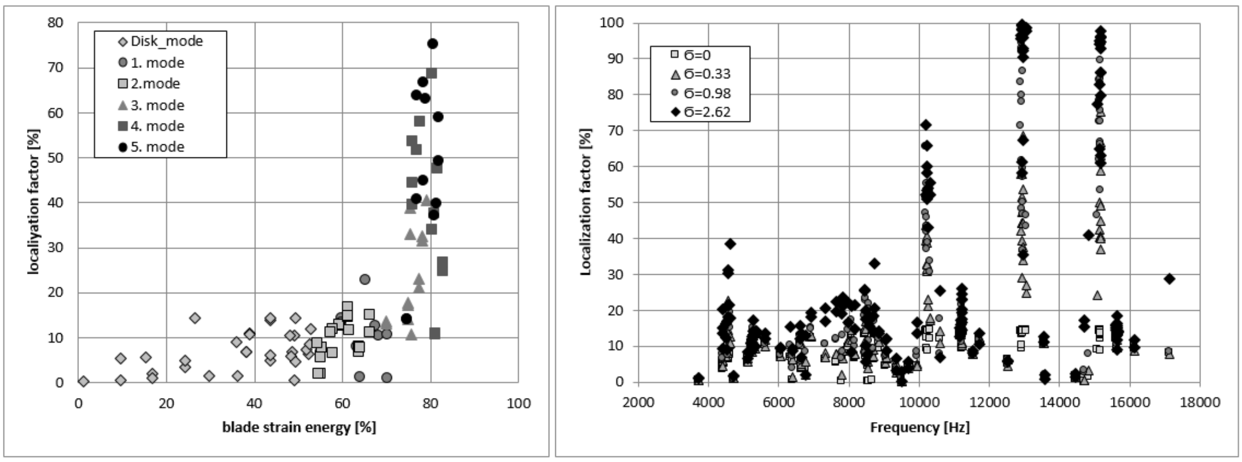

Fig. 2: Localization factor versus percentage of blades of total blisk strain energy, σ=0.33% and Localization factor of natural vibrations depending on the blade mistuning deviation.

4. Conclusions

The results of sensitivity analysis of mistuning centrifugal compressor have shown similar conclusions as those for axisal compressor according Klauke, et al. (2009). The vibration modes of blade integrated disks are very sensitive to individual blade mistuning. The reason for this behaviour is very low structural damping. The mistuning effect leads to the formation of local zoning of the vibration modes (mode localization). The determined localization factors show that in general higher bending modes have a more pronounced local zoning of the vibration modes than lower bending modes as well as modes with lower numbers of nodal diameter lines. These higher bending modes have a low structural coupling between blades and disk, which can be characterized by significant percentage of blades on the total blisk strain energy.

Other general effect of mistuning bladed disk and local zoning is the double modes splitting. These modes are split into two adjacent eigenvalues, by the symmetry loss. By increasing the mistuning of the system, the distance between the adjacent eigenfrequencies increases.

Force response analysis shows that high amplitude increases of forced vibrations appear at moderate mistuning levels for low damped systems, while the localization of blade modes constantly increases with higher blade mistuning.

An understanding of these correlations will lead in future to better preparation and analysis results from strain gauge measurement during operational condition of aeroengine that will be performed for centrifugal compressor and gas turbine.

Acknowledgement

This work was supported by VZLU, a.s. in project SPB, project number IP4405.

References

Seinturier, E. (2007) Forced Responce Computation for Bladed Disks Industrial Practices and Advanced Methods, in: Proc. 12th IFToMM World Congress, Besançon, France

Steffens, K. (2001) Advanced Compressor Technology—Key Sucess Factor for Competitiveness in Modern Aero Engines, in: Proc. 15th International Symposium on Air Breathing Engines, ISABE, Bagalore, India.

Beirow, B., Kühhorn, A., Golze, M., Klauke, T. & Parchem, R. (2005) Experimental and Numerical Investigations of High Pressure Compressor Blades Vibration Behavior Considering Mistuning, in: Proc. 10th International NAFEMS World Congress, Malta, ISBN 1174376034.

Whitehead, D. S. (1966) Effect of Mistuning on the Vibration of Turbomachine Blades Induced by Wakes. Journal Mechanical Engineering Science, 8, pp. 15-21.

Petrov, E. P. & Ewins, D. J. (2003) Analysis of the Worst Mistuning Patterns in Bladed Disk Assemblies. J Turbomach, 125, pp. 623-631.

Klauke, T., Kühhorn, A., Beirow, B. & Golze., M. (2009) Numerical Investigations of Localized Vibrations of Mistuned Blade Integrated Disks (Blisks). Journal of Turbomachinery 131, 031002.

Strehlau, U. & Kühhorn, A. (2010) Experimental and Numerical Investigations of HPC Blisks With a Focus on Travelling Waves. ASME Turbo Expo2010: Power for Land Sea and Air, Glasgow, UK, June 14–18, ASME Paper No. GT2010-22463.

Srinivasan, A., V. (1997) Flutter and Resonant Vibration Characteristics of Engine Blades. R Journal of Engineering for Gas Turbines and Power, 119, pp. 741–774.

Castanier, M. P. & Pierre, C. (2002) Using Intentional Mistuning in the Design of Turbomachinery Rotors. AIAA J., 40 (10), pp. 2077–2086.

22nd International Conference
ENGINEERING MECHANICS 2016
Svratka, Czech Republic, 9 – 12 May 2016

EPISTEMIC UNCERTAINTY IDENTIFICATION VIA DIFFERENT BAYESIAN INFERENCE METHODS

E. Janouchová*, A. Kučerová, J. Sýkora*****

Abstract: *Currently the Bayesian inference becomes increasingly popular and more widespread approach to parameter identification, which allows to estimate values of input parameters together with appropriate uncertainties by combining a priori information and experimental measurements. In this case, observations are assumed to be performed for the specific yet unknown values of input parameters and epistemic uncertainty arising from experimental errors and lack of knowledge is reduced with an increasing number of experimental observations. Bayes' rule provides an elegant solution to this inverse problem by making it well-posed. However the resulting a posteriori probability distribution usually has a complicated formulation, which cannot be treated analytically. To overcome this obstacle, several methods were developed. The most commonly referred techniques in literature are based on the Markov chain Monte Carlo method, less mentioned approaches utilize the Kalman filter or optimal transport maps. The aim of this contribution is to review and compare these methods of the Bayesian inference.*

Keywords: Epistemic uncertainty, Bayesian inference, Markov chain Monte Carlo, Kalman filter, Optimal transport map.

1. Introduction

In order to predict the behaviour of the structural system under the loading in a computational way, the corresponding numerical model has to be properly calibrated. In other words, parameters of the mathematical model of the system have to be estimated as accurately as possible to obtain realistic predictions, e.g. for usage in an appropriate reliability analysis or structural design optimisation. To infer the model parameters from indirect experimental measurements one can proceed in two principally different ways. The traditional approach is deterministic, while advances in surrogate modelling and increasing computational capacity of modern computers permitted many researches to focus on parameter identification in probabilistic setting.

The most common method of parameter estimation is based on fitting the response of the numerical model to the experimental data. This deterministic approach leads to optimising parameters so as to minimise the difference between the data and the model response. The optimisation problem is, however, often ill-posed and thus requires the employment of robust optimisation algorithms. The result of such an optimisation process is only the single-point estimate of parameter values, as you can see in Fig. 1b, thus any information beyond the mean values of parameters is omitted. Consequently, this deterministic inversion method does not provide any quantification of the uncertainty in parameter estimates which in fact exists and is caused by e.g. an insufficient number of observations and measurement errors.

In this context, uncertainties can be divided into two main categories according to whether a source of nondeterminism is irreducible or reducible (Oberkampf et al., 2002). This contribution focuses on identification of epistemic (reducible, subjective, cognitive) uncertainty arising from our lack of knowledge which is supposed to be reduced by any new measurement according to the coherence of

* Ing. Eliška Janouchová: Faculty of Civil Engineering, Czech Technical University in Prague; Thákurova 7/2077; 166 29, Prague; CZ, eliska.janouchova@fsv.cvut.cz

** Ing. Anna Kučerová, PhD: Faculty of Civil Engineering, Czech Technical University in Prague; Thákurova 7/2077; 166 29, Prague; CZ, anicka@cml.fsv.cvut.cz

*** Ing. Jan Sýkora, PhD: Faculty of Civil Engineering, Czech Technical University in Prague; Thákurova 7/2077; 166 29, Prague; CZ, jan.sykora.1@fsv.cvut.cz

learning (Mantovan & Todini, 2006; Beven et al., 2007). While the inherent stochasticity is expressed by aleatory uncertainty which cannot be reduced.

In the last decades probabilistic methods for stochastic modelling of uncertainties have become applicable thanks to a growing computational capacity of modern computers. The probabilistic approach restates the inverse problem as well-posed in an expanded stochastic space by modelling the parameters as well as the observations as random variables with their probability distributions (Kaipio & Somersalo, 2005). Several methods for the uncertainty quantification in probabilistic settings have been proposed in the literature. The last decade witnessed an intense development in the field of Bayesian updating of epistemic uncertainty (Fig. 1c) in description of deterministic material or structural parameters, see e.g. Marzouk et al. (2007). Here, a likelihood function is established to quantify our confidence in observed data, with the goal to update our prior knowledge on model parameters (Gelman et al., 2004). The increasing popularity of Bayesian methods is motivated by developments in the field of spectral stochastic finite element method, which allows to alleviate the computational burden by surrogate models such as polynomial chaos expansions (Marzouk & Najm, 2009). The most commonly referred techniques of Bayesian inference in literature are based on the Markov chain Monte Carlo method (Marzouk et al., 2007), less mentioned approaches utilize the Kalman filter (Rosić et al., 2013) or optimal transport maps (El Moselhy & Marzouk, 2012). The aim of this contribution is to review and compare these methods of the Bayesian inference.

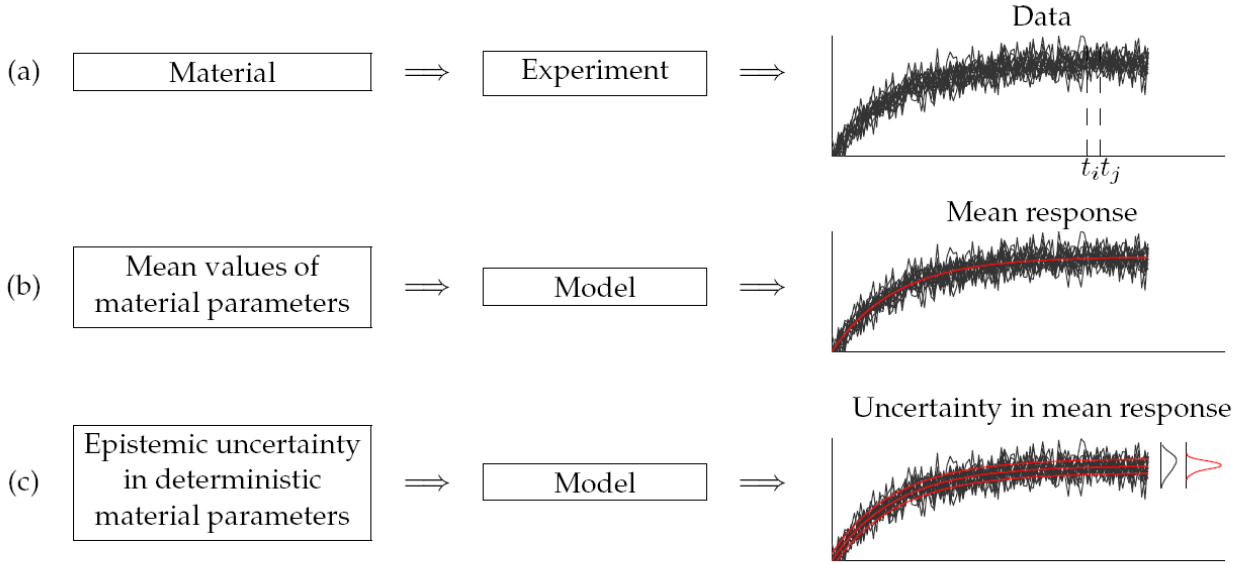

Fig. 1: Scheme of an experiment and different approaches to parameter identification.

2. Bayesian inference

Consider a stochastic problem

$$\boldsymbol{z}(\boldsymbol{x},\boldsymbol{\omega}) = \boldsymbol{y}(\boldsymbol{x}) + \varepsilon(\boldsymbol{\omega}) \tag{1}$$

with uncertain model parameters $\boldsymbol{x}$ and random observable data $\boldsymbol{z}$, which can be predicted by a model response $\boldsymbol{y}(\boldsymbol{x})$ besides a measurement error ε. In Bayesian statistics, probability represents a degree of belief about the parameter values (Tarantola, 2005). Combining the initial knowledge in the form of the prior distribution p($\boldsymbol{x}$) and the experimental data as the likelihood function p($\boldsymbol{z} \mid \boldsymbol{x}$) according to Bayes' rule

$$p(\boldsymbol{x}|\boldsymbol{z}) = \frac{p(\boldsymbol{z}|\boldsymbol{x})p(\boldsymbol{x})}{p(\boldsymbol{z})} = \frac{p(\boldsymbol{z}|\boldsymbol{x})p(\boldsymbol{x})}{\int p(\boldsymbol{z}|\boldsymbol{x})p(\boldsymbol{x})d\boldsymbol{x}}, \tag{2}$$

we obtain the posterior distribution of the parameters. The mean values of the updated distribution are equal to the best guess of the parameters' values with the uncertainty represented by the corresponding variance. However the posterior statistical moments cannot be generally computed analytically, because the identified distribution including the whole structural model is too complicated. To overcome this obstacle, several methods were developed.

2.1. Markov chain Monte Carlo

Markov chain Monte Carlo (MCMC) is a sampling method based on a creation of an ergodic Markov chain of required stationary distribution equal to the posterior (Gilks, 2005; Geyer, 2011). There are different algorithms for constructing this chain (Spall, 2003), e.g. Gibbs sampler or Metropolis-Hastings algorithm, which avoids calculating of the normalisation constant in Eq. (2) by evaluating only ratios of target probabilities. Suitable setting of the proposal distribution for a random walk is important and can be evaluated on the basis of acceptance rate (Rosenthal, 2011) or autocorrelation which is required to be minimal. The convergence speed of the procedure depends also on the appropriate choice of the starting point (Geyer, 2011). The essential advantage of this method is its versatility for usage with nonlinear models, when for an infinite number of samples it gives the exact solution. The disadvantage of this method is its high computational effort resulting from necessity of a high number of model simulations. In order to accelerate this sampling procedure in identification process, the evaluations of a numerical model can be replaced by evaluations of a computationally efficient model surrogate.

2.2. Kalman filter

The second way of obtaining updated posterior distribution comprises Bayesian linear methods, see e.g. Rosić et al. (2016), based on Kalman filtering (Kálmán, 1960). The basic idea of these methods is to update the prior random variable X_f by a linear map to a linear Bayesian posterior estimate

$$X_a = X_f + K\left(\boldsymbol{z}(\boldsymbol{x},\boldsymbol{\omega}) - Y_f\left(X_f\right)\right), \tag{3}$$

where Y_f is the prior model response and the Kalman gain

$$K = \mathbf{C}_{X_f Y_f}\left(\mathbf{C}_{Y_f} + \mathbf{C}_\varepsilon\right)^{-1} \tag{4}$$

is computed from the corresponding covariance matrices and measurement covariance $\mathbf{C}_\varepsilon$.

The posterior X_a can be estimated by so called the ensemble Kalman filter algorithm based on updating of prior Monte Carlo samples, which also serve for computation of the covariance matrices. The method requires a smaller number of samples than previous MCMC method, but the identification of the uncertainty is not generally so accurate as with MCMC. Another approach is to approximate the random variables by polynomial chaos expansions, which enables to evaluate the Kalman gain and posterior X_a in an algebraic way (Rosić et al., 2012). Its main advantage is elimination of computationally demanding model simulations. However, the result is exact only in a special case of a linear model and normally distributed random variables, in another cases these methods are only approximate.

2.3. Optimal maps

This technique is based on formulation of a transport function or a map which transforms the prior random variable X_f into the posterior random variable X_a (El Moselhy & Marzouk, 2012) and arises from the context of optimal transport theory. The authors describe the map by multivariate orthogonal polynomials and the solution is obtained by the optimisation of the corresponding polynomial coefficients. The cost function is defined with a help of the Kullback-Leibler divergence expressing the discrepancy between the prior density $p(\boldsymbol{x})$ and approximate map-dependent prior density. The prior has to be expressible by standard random variables whose probability distribution is orthogonal to the chosen polynomial basis (Xiu & Karniadakis, 2002). The posterior is then identified in the form of polynomial chaos expansion which is efficient in terms of analytical evaluation of posterior statistical moments. Thanks to deterministic expression of the map, one can easily sample from the posterior by transforming the prior samples.

3. Conclusions

The contribution is focused on presenting different numerical methods of Bayesian inference, which provides estimation of unknown model parameters along with a probability description of epistemic uncertainty corresponding to noisy experimental observations.

The most universal and well-known method is MCMC, which however, suffers from high computational demands. The sampling procedure can be accelerated by using a surrogate model instead of the full numerical model, but it brings a possible source of approximation error. The ensemble Kalman filter needs less model simulations than MCMC, but the identified uncertainty does not reach so great precision because of the problem linearisation. The polynomial chaos based variant of linear Bayesian update avoids time-consuming sampling, but its accuracy also depends on the nonlinearity of the investigated problem. The last considered method of probabilistic parameter estimation is based on optimising deterministic mapping between prior and posterior. The approach is suitable for nonlinear and high-dimensional problems, the essential part of the procedure is a creation of the map composition and optimisation of its parameters. Formulation in terms of orthogonal polynomials allows to compute posterior statistical moments and to generate posterior samples very efficiently.

Acknowledgement

The financial support of the Ministry of Education, Youth and Sports of the Czech Republic (Project No. 8F15004), the Czech Science Foundation (Project No. 16-11473Y) and the Grant Agency of the Czech Technical University in Prague (Project No. SGS16/037/OHK1/1T/11) is gratefully acknowledged.

References

Beven, K., Smith, P. & Freer, J. (2007) Comment on "Hydrological forecasting uncertainty assessment: Incoherence of the GLUE methodology" by Pietro Mantovan and Ezio Todini. Journal of Hydrology, 338, pp. 315-318.

El Moselhy, T. A. & Marzouk, Y. M. (2012) Bayesian inference with optimal maps. Journal of Computational Physics, 231, 23, pp. 7815-7850.

Gelman, A., Carlin, J. B., Stern, H. S. & Rubin, D. B. (2004) Bayesian data analysis. Chapman & Hall/CRC.

Geyer, C. J. (2011) Handbook of Markov Chain Monte Carlo. Chapman & Hall/CRC.

Gilks, W. R., Deland, S. M., Rutherford, B. M., Diegert, K. V. & Alvin, K. F. (2005) Markov Chain Monte Carlo. Encyclopedia of Biostatistics, Chichester, UK: John Wiley, 75(3), pp. 333-357.

Kaipio, J. & Somersalo, E. (2005) Statistical and Computational Inverse Problems. New York: Springer-Verlag, Applied mathematical sciences, 339 p.

Kálmán, R. E. (1960) A new approach to linear filtering and prediction problems. Transactions of the ASME-J. of Basic Engineering (Series D), 82, pp. 35-45.

Mantovan, P. & Todini, E. (2006) Hydrological forecasting uncertainty assessment: Incoherence of the GLUE methodology. Journal of Hydrology, 330, pp. 368-381.

Marzouk, Y. M. & Najm, H. N. (2009) Dimensionality reduction and polynomial chaos acceleration of Bayesian inference in inverse problems. Journal of Computational Physics, 228, pp. 1862-1902.

Marzouk, Y. M., Najm, H. N. & Rahn, L. A. (2007) Stochastic spectral methods for efficient Bayesian solution of inverse problems. Journal of Computational Physics, 224, 2, pp. 560-586.

Oberkampf, W. L., DeLand, S. M., Rutherford, B. M., Diegert, K. V. & Alvin, K. F. (2002) Error and uncertainty in modeling and simulation. Reliability Engineering and System Safety, 75, pp. 333-357.

Rosenthal, J. S. (2011) Optimal Proposal Distributions and Adaptive MCMC, in: Handbook of Markov Chain Monte Carlo. Chapman & Hall/CRC, pp. 93-140.

Rosić, B., Kučerová A., Sýkora J., Pajonk O., Litvinenko, A & Matthies, H. G. (2013) Parameter Identification in a Probabilistic Setting. Engineering Structures, 50, pp. 179-196.

Rosić, B. V., Litvinenko, A., Pajonk, O. & Matthies, H. G. (2012) Sampling-free linear Bayesian update of polynomial chaos representations. Journal of Computational Physics, 231, pp. 5761–5787.

Rosić, B., Sýkora J., Pajonk O., Kučerová A. & Matthies, H. G. (2016) Comparison of Numerical Approaches to Bayesian Updating in Computational Methods for Solids and Fluids, 41, pp.427-461.

Spall, J. C. (2003) Estimation via Markov Chain Monte Carlo. IEEE Control Systems Magazine, 23, 2, pp. 34-45.

Tarantola, A. (2005) Inverse problem theory and methods for model parameter estimation. Philadelphia, PA: Society for Industrial and Applied Mathematics, 348 p.

Xiu, D. & Karniadakis, G. E. (2002) The Wiener-Askey Polynomial Chaos for Stochastic Differential Equations. SIAM Journal on Scientific Computing, 24, 2, pp. 619-644.

22nd International Conference
ENGINEERING MECHANICS 2016
Svratka, Czech Republic, 9 – 12 May 2016

DYNAMICS MODEL OF THE THREE-WHEELED MOBILE PLATFORM

A. Jaskot[*], B. Posiadała [**], S. Śpiewak[***]

Abstract: *The dynamics model of the 3-wheeled mobile platform has been presented. The proposed model is useful to examine different configurations of the drive wheels and to analyze the relations between causes and effects of the motion parameters. The solution presented in the work allows to study the behavior of the platform also while slippage and in the circumstances to refrain the platform from falling into the skid. The problem of the forced motion and free motion of the platform with the possibility of modification the drive modulus positions has been considered. The formulated initial problem has been solved numerically and sample results are presented.*

Keywords: mobile platform, dynamics, motion parameters.

1. Introduction

Considerations about various issues, both theoretical and experimental, in mechanical systems such as mobile platforms and mobile robots are widely described in literature. The kinematic and the dynamic analysis including the trajectory tracking and path generation for nonholonomic systems are a continually common matter. In previous studies the kinematics of wheeled mobile robots have been the main subject in planning the control of nonholonomic systems. The analysis of motion planning with consideration of the dynamics equations of the three wheeled mobile robot is proposed among others in (Zohar et. al., 2011). Proposition of the trajectory planning problem for multi-objective is widely described in (Khoukhi, 2015). The formulation of tracking control of a group of mobile robots with guaranty of no collisions between robots is proposed and described in (Do, 2009). The analysis of the internal dynamics, specifically the system stability is presented in (Eghtesad & Necsulescu, 2006). Approach of the kinematic and dynamic solutions for the possible positions of the wheeled platforms are proposed in (Campion et. al., 1996). Simple or inverse task of the dynamics can be solved by establishing the differential equations of motion. Some approaches are described by using the Langrange method (Staicu, 2009). Knowing the differential equations of motion the motion parameters can be determined. The effect of this is generating and implementing the trajectory of the platforms motion.

In this paper the description of the dynamics for three-wheeled mobile platform is described. The main purpose is to know the platforms work conditionings. The proposed model is necessary for an analysis of the planar motion, including a progressive and rotational motion of the platform. Description of the dynamics of the platform in the classical approach ultimately is a base to provide the fundamental parameters, which are velocity and acceleration, taking into account the cause of the motion and allow to know the position of the platform at a particular point in time.

2. Model of 3-wheeled mobile platform

The modular construction of the design solution of the mobile platform has been adopted. The prototype model enable to creating any different configurations of selected positioning of the platform wheels by the using the drive member with electric drive. The realization of the preset trajectories of vehicular

[*] Anna Jaskot, MSc: Institute of Mechanics and Machine Design Foundations, Czestochowa University of Technology, Dabrowskiego Street 73; 42-201, Czestochowa; PL, jaskot@imipkm.pcz.pl

[**] Doctor of Technical Sciences, Professor Bogdan Posiadala, : Institute of Mechanics and Machine Design Foundations, Czestochowa University of Technology; Dabrowskiego Street 73; 42-201, Czestochowa; PL, bogdan.p@imipkm.pcz.pl

[***] Szczepan Spiewak, PhD.: Institute of Mechanics and Machine Design Foundations, Czestochowa University of Technology, Dabrowskiego Street 73; 42-201, Czestochowa; PL, spiewak@imipkm.pcz.pl

transporter is possible. The assumption that chassis of the platform is constructed from a rigid frame and the provision of possibility to separate the selected wheel drives have been made.

Description of dynamics of 3-wheeled mobile platform has been made on the basis of the model according to the geometrical scheme presented in Figure 1.

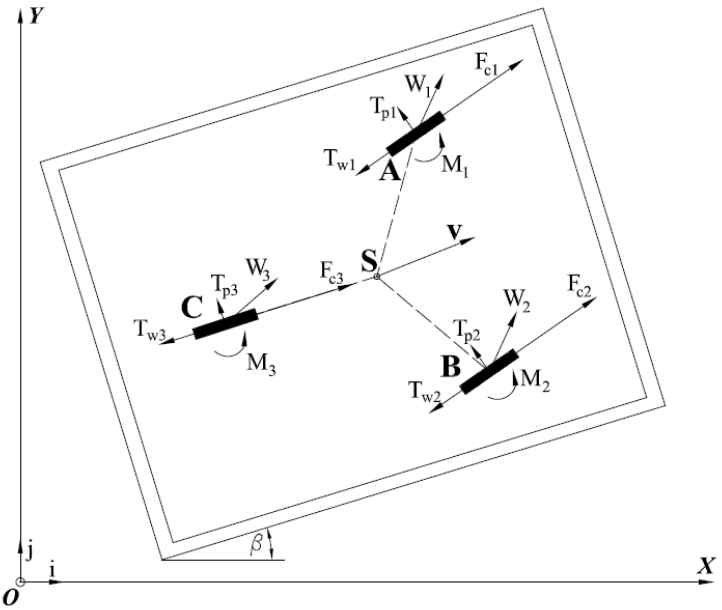

Fig. 1: The geometric scheme with distribution of forces in the platform wheels

In order to draw up a description of the mobile platforms dynamics, the motion parameters are determined with respect to the global reference frame *OXY*.

To establish the important quantities of the dynamics is an obligation. First, the form of functions, equations of motion for global coordinate system to designate the path of motion the mobile robot, and for the local coordinate systems. The analysis of platforms motion during rotational movement as well as during linear movement occurs in a planar surface. Instantaneous motion is composed of the progressive motion with the velocity of the center of the mass and the rotational motion with the velocity around the center of mass of the mobile platform.

In Fig. 2 the forces occurring in the wheels of platform during the movement are presented. The force N_i, as a reaction on the weight of the platform wheels are considered. In the figure the driving torque M_i which later is the base to determine the active force $\mathbf{F}_{ci}$ is also shown.

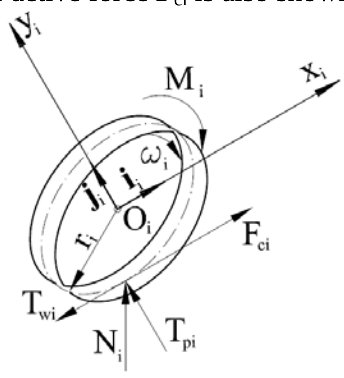

Fig. 2. Distribution of forces acting on each wheel of the platform

In Fig. 2 the following forces are presented: $\mathbf{M}_i$ – the drive torque, $\mathbf{F}_{ci}$ – the active driving force, $\mathbf{T}_{wi}$ – the friction force in the longitudinal direction, $\mathbf{T}_{pi}$ – the friction force in the transverse direction, $\mathbf{N}_i$ – the reaction force of the *i*-th wheel, ω_i – the angular velocity of the *i*-th wheel.

3. Dynamics description of 3-wheeled mobile platform

In determining the forces occurring during the motion there is a need to take into account the drive torque and the friction, which is consequent from the contact of the wheel with the raceway. It is necessary to determine the values of wheel loads on the roadway. The values of the resultant forces $\mathbf{W}_i$ have been calculated as follows:

$$\mathbf{W}_1 = \mathbf{F}_{c1} + \mathbf{T}_{w1} + \mathbf{T}_{p1}, \tag{1}$$

$$\mathbf{W}_2 = \mathbf{F}_{c2} + \mathbf{T}_{w2} + \mathbf{T}_{p2}, \tag{2}$$

$$\mathbf{W}_3 = \mathbf{F}_{c3} + \mathbf{T}_{w3} + \mathbf{T}_{p3} \tag{3}$$

The active forces acting on each wheel were calculated by the formula:

$$\mathbf{F}_{ci} = \frac{M_i}{r} \cdot \mathbf{i}_i \tag{4}$$

where: M_i – the drive torque of the i-th wheel, r – the radius of the driver wheel.

The passive forces should be determined, in addition to the active forces which cause motion of the system. The resistance forces such as friction forces $\mathbf{T}_{wi}$ in the longitudinal direction, and the friction forces $\mathbf{T}_{pi}$ in the transverse direction are considered according to the motion parameters. Because the active force $\mathbf{F}_{ci}$ is different from zero, the friction force values are also different from zero during the platform motion. The values of those forces are described below:

$$\mathbf{T}_{wi} = -\mu_w \cdot N_i \cdot sign(v_{wi}) \cdot \mathbf{i}_i \tag{5}$$

$$\mathbf{T}_{pi} = -\mu_p \cdot N_i \cdot sign(v_{pi}) \cdot \mathbf{j}_i \tag{6}$$

where: μ_w, μ_p are the coefficients of friction for the longitudinal and transverse directions and the v_{wi} and v_{pi} are the velocity components for the longitudinal and transverse directions.

Considering the formulated formulas (1-6) representing the active and passive forces the translational motion equation can be formulated in the form:

$$m\mathbf{a} = \sum_{i=1}^{3} \mathbf{W}_i \tag{7}$$

where: m – the mass of the whole object, $\mathbf{a}$ – the acceleration of the platform center of mass, $\mathbf{W}_i$ – the i-th resultant force.

By using those equations the determining of the motion parameters of the mass center under the influence of known external forces is possible. The progressive motion of the center of mass is described by Eq. (7).

The equation of the rotational motion around the center of mass for the platform can be written in the form:

$$\frac{d\mathbf{K}}{dt} = \sum_{i=1}^{3} \mathbf{s}_i \times \mathbf{W}_i + \sum_{i=1}^{3} \mathbf{M}_i \tag{8}$$

where: $\mathbf{K}$ – the angular momentum vector of the whole platform, $\mathbf{s}_i$ (i=1,2,3) – the location vectors of points: A, B, C in the global coordinate system.

By using the derived equations of motion, written in the form of differential equations, the rate of change certain physical quantities (ex. velocity, positioning) can be defined. For the local coordinate system the parameters of motion for the center of mass platform are: $\dot{x}_i$ - longitudinal velocity, $\dot{y}_i$ - transverse velocity, $\dot{\beta}_i$ - angular velocity.

The dynamic equations of motion in the global coordinate system can be written in case of the planar motion in the form:

$$\ddot{X} = \sum_{i=1}^{3} \frac{W_{ix}}{m} \tag{9}$$

$$\ddot{Y} = \sum_{i=1}^{3} \frac{W_{iy}}{m} \tag{10}$$

$$\ddot{\beta} = \frac{\sum_{i=1}^{3} (s_{ix} \cdot W_{iy} - s_{iy} \cdot W_{ix})}{I_z} \tag{11}$$

To formulate the initial problem by adding the initial conditions according to the starting values of the motion parameters the set of equations (9-11) can be used.

4. Sample simulation results

The dynamics of the mobile platform generally can be develop in two ways. First, to solve the forces acting on the system based on a motion description. Second, the so-called inverse dynamics, where the forces are well known but the motion parameters need to be determined. This work contains the inverse dynamics description. The sample simulation results has been obtain with the following assumptions. The assumed values are: drive torque M_1=0,1 kNm, coefficients of friction in the longitudinal direction μ_w=0,1 and in the transverse direction μ_p=0,1, mass of the platform m=150 kg, and the acceleration of gravity g=9,81 m/s^2.

Analysis of the dynamics of mobile platform was made by using the described formulas. The results in form of graphs of motion parameters and the sample trajectory are presented in Fig. 3.

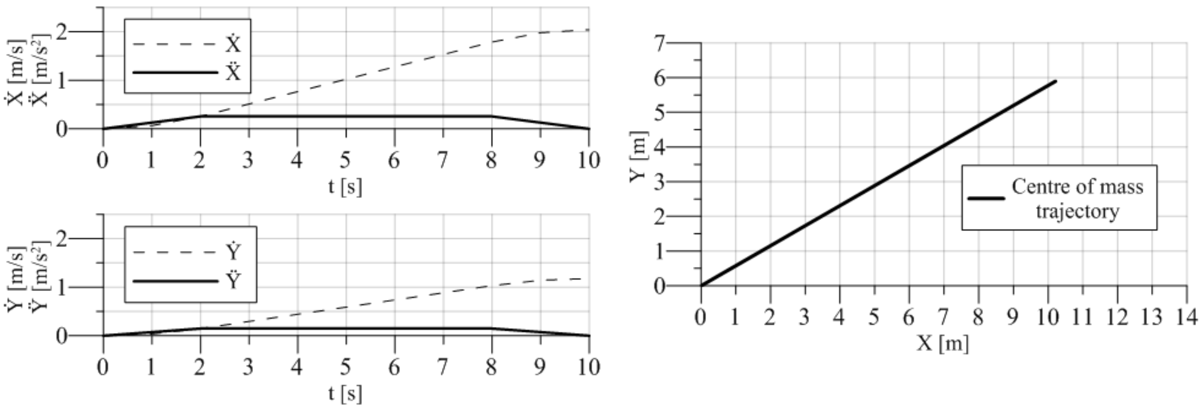

Fig. 3. Obtained motion parameters $\dot{X}$ [m/s], $\dot{Y}$[m/s], $\ddot{X}$ [m/s^2], $\ddot{Y}$ [m/s^2], and trajectory of the center of the mass for β=Pi/6.

5. Conclusions

The dynamics model of the 3-wheeled mobile platform has been presented. The model enables to know the determinants of platforms work, which in consequence allow to determine the parameters affecting to the movement of both the platform and its components. The proposed model is useful to examine different configurations of the drive wheels and to analyze the relations between causes and effects of the motion parameters. The problem of the forced motion and free motion of the platform with the possibility of modification the drive modulus positions has been considered. The formulated initial problem has been solved numerically and sample results are presented.

The solution presented in the work allows to study the behavior of the platform also while slippage and in the circumstances to refrain the platform from falling into the skid. The model can also be developed by introducing to the mathematical description other elements of the real object.

References

Campion G., Bastin G. & D’Andréa-Novel B. (1996) Structural Properties and Classification of Kinematic and Dynamic Models of Wheeled Mobile Robots. IEEE Transactions on robotics and automation, 12, 1.

Do K.D. (2009) Output-feedback formation tracking control of unicycle-type mobile robots with limited sensing ranges. Robotics and Autonomous Systems, 57, pp. 34-47.

Eghtesad M. & Necsulescu D. S. (2006) Study of the internal dynamics of an autonomous mobile robot. Robotics and Autonomous Systems, 54, pp. 342-349.

Khoukhi A. (2015) Data-driven multi-stage multi-objective motion planning of mobile robots, application to near minimum power fuzzy parking. Computers and Electrical Engineering, 43, pp. 218-237.

Staicu S. (2009) Dynamics equations of a mobile robot provided with caster wheel. Nonlinear Dyn, 58, pp. 237-248.

Zhang Y., Liu G. & Luo B. (2014) Finite-time cascaded tracking control approach for mobile robots. Information Sciences, 284, pp. 31-43.

Zohar I., Ailon A. & Rabinovici R (2011) Mobile robot characterized by dynamic and kinematic equations and actuator dynamics: Trajectory tracking and related application. Robotics and Autonomous Systems, 59, pp. 343-353.

22nd International Conference
ENGINEERING MECHANICS 2016
Svratka, Czech Republic, 9 – 12 May 2016

FLOW PARAMETERS SIMULATION TECHNIQUE IN ANNULAR TURBINE CASCADE INLET

T. Jelínek*, M. Němec*, V. Uruba**

Abstract: *This article summarizes the concept of equipment which produces the required flow parameters at the inlet of annular turbine cascade. The investigation of inlet flow parameters - i) the boundary layer on hub and tip inlet channel end-walls and ii) the inlet flow turbulence – are part of a project intent on a flow in multistage steam turbine arrangement. This variable inlet can produce the laminar or turbulent boundary layer, respectively the laminar or fully turbulent velocity profile in the inlet channel. The change of inlet turbulence level is controlled by the grid. The detailed measurement of inlet flow: the turbulence and the total pressure distribution across the height of inlet channel were performed by HWA (hot wire anemometry) probe and by total pressure probe, respectively. The measurement results characterize the inlet flow for several inlet channel arrangements and are used for the experimental investigation of the flow field inside the stage and as the inlet parameters for CFD simulations.*

Keywords: Turbulence, Boundary layer, Annular inlet flow, Grid, Axial turbine stage.

1. Introduction

The flow in axial turbine stage is a very complex phenomenon. The outlet flow field behind the turbine stage is also depending on the parameters of inlet flow. The character of inlet flow can influence the transition in boundary layer and the production of secondary structures. These are strongly depending on the inlet turbulence and the character of boundary layer. Both play significant role in secondary structures production (Seeverding, 1985, Lampart, 2009).

Many authors attend to the influence of turbine blade inlet flow characteristics by simulation of increasing the inlet flow turbulence level on outlet flow characteristics. Lot of work was done on linear blade cascades and the authors show the influence of inlet turbulence intensity on the transition in boundary layer, the formation of wake vortexes consequently (e.g. Michálek, 2015). Gregory-Smith brings the investigation of the high inlet turbulence influence to the secondary structures production in linear blade cascade. The secondary structures may change the outlet flow angles from turbine vanes. Even small vane outlet angle deviation may evoke the change in rotor work efficiency.

The understanding of the inlet flow characteristics and its accurate setting is important when the CFD (Computational fluid dynamics) simulations are performed. The accurate setting of inlet flow parameters has a strong impact on the boundary layer transition, secondary structures production and may affect the outlet flow parameters.

To study this phenomenon on the annular turbine stage the appropriate device was necessary to propose and design. The device must make change the inlet turbulence level and the thickness of boundary layer on both, the hub and tip channel wall, resp. the velocity profile in the inlet channel.

2. Concept of the inlet channel

* Ing. Tomáš Jelínek, Ing. Martin Němec, PhD.: Výzkumný a zkušební letecký ústav, a.s., Beranových 130; 199 05, Prague - Letňany; CZ, jelinek@vzlu.cz

** Prof. Ing. Václav Uruba, CSc.: Institute of Thermomechanics AS CR, v.v.i, Dolejškova 1402/5 182 00 Prgue; CZ, uruba@it.cas.cz

The device (scheme in Fig. 1) consists of four concentric circular parts of inner and outer body, forms together the turbine stage inlet channel of height *h*. Forming the different inlet channel length *l* it makes the different boundary layer thickness δ, resp. forming different inlet velocity gradient *u(y)*. Inlet turbulence level is produced by the grid which is located in proper distance l_g in front of vane leading edge. The distance l_g can be variably set to change the level of inlet turbulence. The additional parts of the turbine stage disable mounting the traversing device just in front of the vane leading edge as it should require to now the parameters of the flow just in front of the vane. The measurement plane 0 had to be placed 46 mm in front of the vane leading edge. As the parameters can be well prediction analytically it is believed that they will be just verified in the plane 0 position. The measurement plane 1 was placed 5mm behind the vane trailing edge.

The total pressure probe of 0.6 mm in diameter was used for the total pressure measurement in plane 0 and the 4-hole probe to evaluate the total and static pressure and flow angle behind the vane was used in plane 0.

In both planes the HW probes were used to evaluate the turbulence. In front of the vane the 21 points were taken across the channel height, behind the vane 21 points across the vane channel in *h/2*. The DANTEC 55P02 and 55R02 probes with straight prongs and with the sensor at an angle of 45° to probe axis was used for the turbulence measurement in both planes.

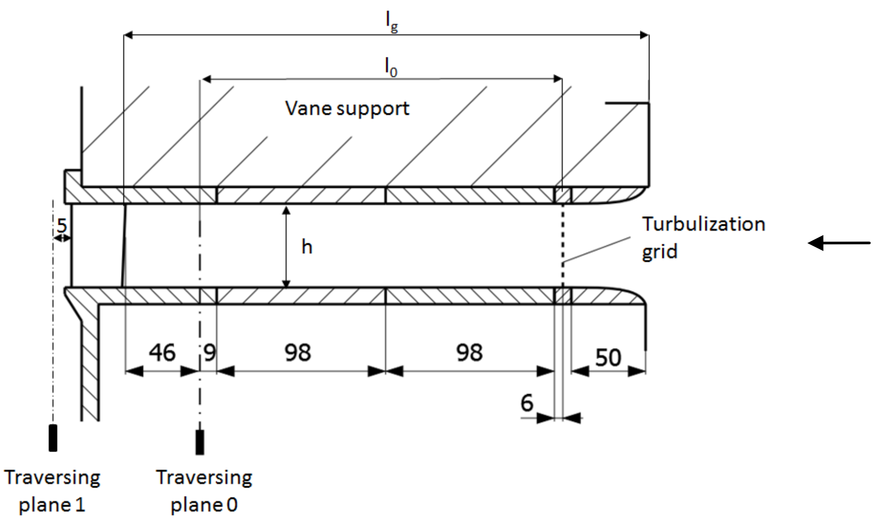

Fig. 1: Scheme of the inlet channel allows changing the inlet flow parameters.

2.1. Velocity profile

The assessment of the inlet channel length was based on the requirements to have the maximum boundary layer thickness in the position of vane leading edge δ = ¼*h*. As the flow in the channel is not considered as the channel flow defined (by Pope, 2000): *h* = 2δ ; l/δ >> 1, the assessment of the maximum channel length was based on the equation for turbulent boundary layer thickness on a flat-plate (Schlichting, 2004):

$$\delta = 0{,}382\frac{x}{\mathrm{Re}_x^{1/5}} \ . \qquad (1)$$

To ensure that the transition to turbulent boundary layer starts at a very beginning the turbulization strip was used at the channel inlet. The strip is realized by send roughness of 40 and the width is 5mm.

For the case of the shorter channel which could produce very low thickness laminar boundary layer the Blasius law was used to predict the boundary layer thickness:

$$\delta = 4{,}91\frac{x}{\sqrt{\mathrm{Re}_x}} \ . \qquad (2)$$

2.2. Turbulence production

The most useful method how to generate nearly isotropic turbulence is by means of grid. The grid are mostly used to reduce the turbulence and for elimination of pressure non-uniformities. The grids of relatively large dimensions placed normal to a uniform upstream flow can be used to increase the isotropic turbulence of inlet probe. Roach (1987) in his paper summarizes the proposal of the grid based on many experiments and mention the equation for the turbulence:

$$Tu = C.\left(\frac{x}{d}\right)^{-5/7}, \qquad (3)$$

where C is a constant which is considered for the case of uniform grid with circular wire 0.8; x is the displacement from the grid and d is the wire diameter. The exponent represents the turbulence decay. This relation is displayed in Fig.2.

The preliminary requirements on investigation of inlet flow parameters on the flow in axial turbine stage defined, that the required inlet turbulence should be in range of 8-2%. Based on this requirement the grid was defined: wire diameter d = 2mm, mesh length m = 7mm, that means the porosity of the grid $\beta = (1\text{-}2/m)^2 = 0.51$.

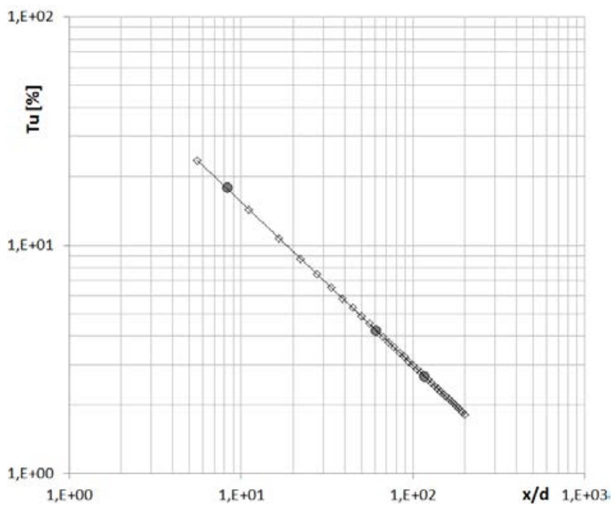

Fig. 2: The relation of turbulence on x/d: ◊ theory after Roach, • Measured values in centerline.

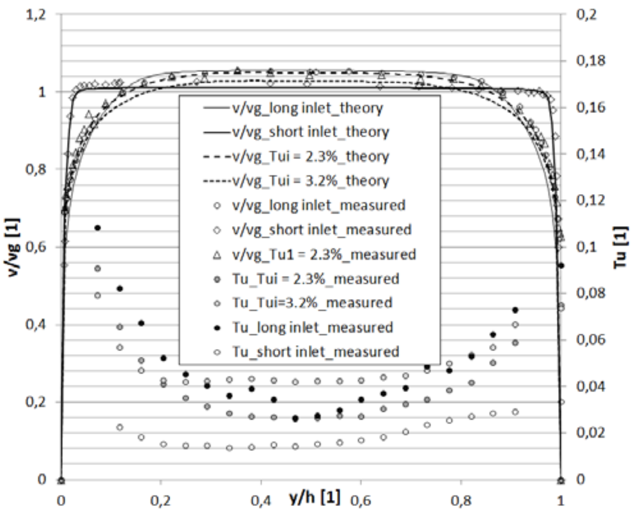

Fig. 3: Velocity and turbulence profile in plane 0 for different inlet channel configurations.

3. Velocity profile and turbulence measurement

The turbulence was measured and evaluated based on the methodology of Institute of Thermomechanics AS CR. The mean turbulence value on the channel center are displayed in Tab. 1 and also in Fig. 2 where there are compared with the theory after Roach. It is clearly visible that the measured turbulence meets the theory and thus the turbulence in the plane at the vane leading edge can be determined.

In Fig. 3 the measured velocity and turbulence profiles are shown for different inlet configurations. It is seen that the measured velocity distribution is in good accordance with the theory for both cases the laminar and turbulent boundary layer. For the cases when the grid is placed in the channel, the velocity distribution is in accordance as well. Slightly higher velocity can be observed in the lower part of the channel (y/H < 0.5) for some cases. This can be taken into consideration when the kinetic energy loss of vane is evaluated.

The effect of the inlet turbulence on the outlet stator flow field is seen in Fig. 4. The change of inlet turbulence has very minor impact on the generation of secondary flow inside the vane channel in hub and tip corners. The small changes in the secondary structures have a small effect on the outlet angle from vane as well. It is important for the rotor work efficiency, however the effect of the vane outlet parameters changes on the stage overall performance was negligible and the measured performance changes were lower than the measurement uncertainty.

Tab. 1: The measured values of three different grid positions.

Configuration No.		006	004	005
Length (from grid to plane 0) l_0	[mm]	15	113	211
Length (from grid to vane LE) l_g	[mm]	61	159	257
Turbulence measured (plane 0) Tu_0	[%]	(17,9)	4,23	2,66
Turbulence theory (plane 0) Tu_{0t}	[%]	17,59	4,24	2,67
Turbulence (vane LE) Tu_i	[%]	6,54	3,24	2,29

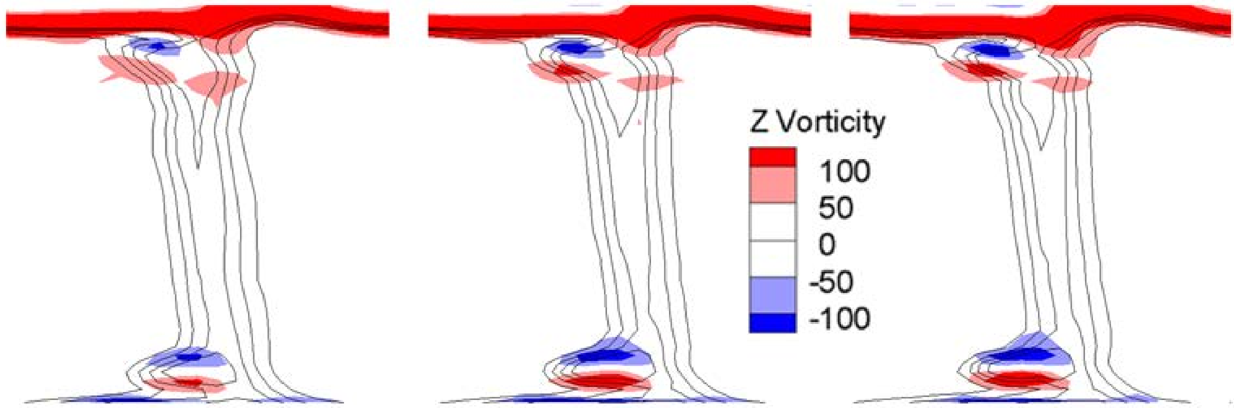

Fig. 4: The vorticity in the plane behind the vane trailing edge. Tu_i = 6.54% (left), Tu_i = 3.24% (in the middle) Tu_i = 2.29% (right)

4. Conclusions

The variable inlet channel to generate the different velocity profile and different level of turbulence in the inlet of turbine stage was design and the characteristics of inlet flow were verified by measurement using pressure probes and HW probes. The assessment of the grid produced the nearly isotropic turbulence was verified even for the application in annular channel flow.

The insight into the inlet flow parameters and the knowledge of exact values of inlet flow parameters are necessary as inputs for CFD calculations when the flow simulation can be done to analyze the flow filed in the turbine stage.

Acknowledgement

The work was performed with kindly financial support of TACR on the project TA04020129 “Investigation of flows in a multi-stage axial turbine stages arrangement”.

References

Gregory-Smith, D.G.: Secondary Flow Measurement in a Turbine Cascade with Figh Inlet Turbulence, ASME, 1990, 90-GT-20

Lampart P., “Investigation of Endwall Flows and Losses in Axial Turbines, Part I. Formation of Endwall Flows and Losses,” Journal of Theoretical and Applied Mechanics, Vol. 47, No. 2, 2009, pp. 321-342.,

Michálek J., Straka P.: Experimental investigation and steady/unsteady RANS modelling of the wake decay behind a low pressure turbine cascade, Proceedings of the 12th ISAIF 2015, Genova, Italy

Pope, S.B.: Turbulent Flows, Cambridge University Press, The Edinburgh Buiding, Cambridge, CB2 2RU, UK, 2000

Roach P.E., The Generation of Nearly Isotropic Turbulence by Means of Grids, Heat and Fluid Flow, June 87, 8 (2), pp. 82-92, June 1987

Schlichting H., K. Gersten, Boundary layer Tudory (8th edd.), Springer-Verlag 2004, ISBN 81-8128-121-7

Sieverding C.H.: Recent progress in the understanding of basic aspects of secondary flow in turbine blades passage, ASME, J. Eng. For Gas Turbine and Power, 1985, Vol. 107, pp 248-257

22nd International Conference
ENGINEERING MECHANICS 2016
Svratka, Czech Republic, 9 – 12 May 2016

SIMULATION OF ADHESION CONDITIONS ON ROAD VEHICLES

P. Jilek[*], O. Voltr[**], J. Pokorný [***]

Abstract: *The article deals with the possibilities of controlled affecting of adhesion in the contact between vehicle wheel and road. In the first part some of currently used ways of affecting of adhesion are stated. These are briefly compared subsequently. Further new proposal of system for affecting of adhesion is introduced followed by its comparison with SkidCar system. The proposed system and SkidCar system are simulated in simplified form and resultant behavior of the car is evaluated in enclosed graphs. The article is processed in primary version of particular system for verifying of vehicle stability. This article aims to highlight the fact that it is possible to change the adhesive conditions of road vehicles using an additional system without preventing the movements of a body.*

Keywords: vehicle, adhesion, shear, driver, wheel.

1. Introduction

The size of a total adhesive force between a tire and a road is the product of radial wheel reactions and an adhesion coefficient. Thus, there will be two possible ways to change the adhesive force. The first category changing the adhesion coefficient includes the Slide Surfaces, Skid Tires and Easydrift Ring. The second category, which reduces radial wheel reactions, contains the SkidCar System and our system SlideWheel.

While reducing the adhesive conditions, a vehicle reaches the limit of a skid already at a lower speed than it would do under realistic conditions. Achieving a safer border car test is thus ensured. Simultaneously, it is possible to simulate the behavior of a vehicle on ice, although in fact it moves on a surface of a higher adhesion coefficient.

The article describes the difference in the behavior of the car with systems SkidCar and SlideWheel. SlideWheel is a system designed by the authors. Both systems operate on the principle of reducing the adhesive forces transmitted by the wheels of a vehicle.

2. SkidCar system

From the perspective of the authors, it is an electrohydraulic wheeled steel frame which allows a moving vehicle to achieve various types of skids. The frame is mounted under the floor of a car and, using an electronic controller, it allows for a partial lightening of the front axle or rear axle or both axles simultaneously in any range. Lightening or lifting a car is done by changing a position of hydraulic piston and cylinder in placing of the revolving wheels to the frame using an increase in hydraulic oil pressure. This intervention will evoke the possibility of a car skid situation with a front or rear-wheel drive, taking into account the different degrees of adhesion between the wheel and the road.

Strengths:

- the system can be used on any car,
- a possibility of continuously adjustable traction for any axle of a car,
- a possibility of changing the adhesion conditions while driving,

[*] Ing. Petr Jilek.: Jan Perner transport faculty, University of Pardubice; Studentská 95; 532 10 Pardubice; CZ, petr.jilek@upce.cz

[**] Ing. Ondřej Voltr.: Jan Perner transport faculty, University of Pardubice; Studentská 95; 532 10 Pardubice; CZ, ondrej.voltr@upce.cz

[***] Ing. Jan Pokorný, Ph.D.: Jan Perner transport faculty, University of Pardubice; Studentská 95; 532 10 Pardubice; CZ, jan.pokorny@upce.cz

- a possibility of saving an adhesive setting for repeatable tests,
- keeps the car electronic systems active,
- a road bears no optical or other information on the change of adhesion conditions,
- can be used in vehicles with front, rear or with both driving axles,
- almost impossible to overturn a car,
- possible to use any tires,
- ensures a repeatability of adhesive conditions in different tests.

Weaknesses:

- a vehicle has auxiliary wheels on the sides – a larger width of the tested car is a negative feature while doing driving maneuvers,
- a car body attached to the SkidCar frame – not possible to tilt the sprung masses against the unsprung masses; the body does not tilt or incline while doing driving maneuvers,
- an operation of electrohydraulic unit and electromagnets is heard in the vehicle; a driver is notified of the change of adhesion conditions,
- increasing a car mass and reducing the elevation coordinates of a car center of gravity,
- a need for a relatively flat surface of sufficient size under the considered testing,
- changing a rolling resistance and tire directional properties of a wheel due to the reduced radial reaction transmitted around.

3. SlideWheel - Custom system design to reduce vehicle adhesion conditions

We approach to the change of adhesion conditions by changing the radial car wheel load. The first option is to pass the required proportion of the car mass to the supporting units directly from the body, which are the sprung masses (*Fig. 1*). To some extent, it is a similar system as the SkidCar, only the supporting units are placed under the vehicle. Thus, a plan profile of the test car has not increased, and at the same time, the added mass of the vehicle has decreased. The system does not contain any supporting frame, connecting each of the supporting units. Therefore it would be possible to use this system for driving corridors. The supporting units do not allow a roll of the body when the centrifugal and inertial forces resulting from a passage of a vehicle through a corner are applied, the system does not simulate the real conditions of vehicle behavior. This system is only a thorough approach to reality. This disadvantage is eliminated in the second proposed solution.

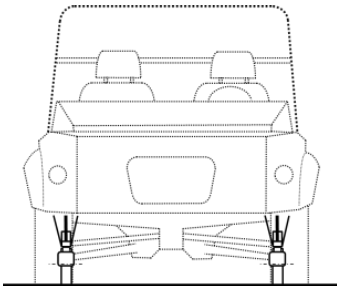

Fig. 1: Lifting the sprung masses

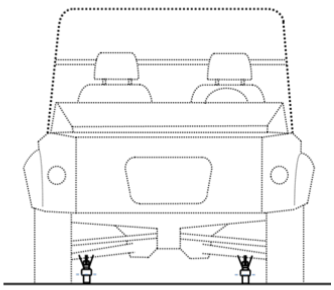

Fig. 2: Lifting the unsprung masses

The second option is to reduce the radial car wheel reaction by lifting the unsprung masses with the help of the supporting wheel units (*Fig. 2*). This system is called SlideWheel. The connection points are the lower arms of axle of the car. This ensures that the body is allowed to tilt when cornering and it can simultaneously pitch while changing a brake or thrust force.

Strengths:

- a possibility of continuously adjustable traction for any axle and any wheel,
- a body pitch corresponds to real conditions,
- the car outer outline dimensions do not change; all components are placed inside a car or under the axle arms,
- a low mass of the entire system,
- a change of adhesion conditions occurs by a primary lifting of the unsprung masses allowing for pitch and roll of the vehicle body,
- the system can be used on any car if slightly modified,
- a possibility of changing the adhesion conditions while driving,

- keeps the car electronic systems active,
- a possibility of saving an adhesive setting for repeatable tests,
- can be used in vehicles with front, rear or with both driving axles,
- possible to use any tires,
- ensures a repeatability of adhesive conditions in different tests,
- a hydraulic circuit operation is silent; a driver does not hear the change of adhesive conditions,
- a vehicle movement on a classic road, without any obvious visual differences of places with different adhesion surfaces.

Weaknesses:
- the system is for lower driving speeds,
- increasing a car mass but lower than with SkidCar,
- reducing the elevation coordinates of a car center of gravity,
- a need for a relatively flat surface of sufficient size under the considered testing,
- changing a wheel rolling resistance due to the reduced radial reaction,
- a need to calibrate the system for a given vehicle.

The system of car wheel lifting is operated electro-hydraulically using a control panel of the vehicle interior. The system can operate under the influence of random adhesion conditions or as required by an operator who is a fellow-passenger in the car.

The SlideWheel system advantages as compared to the SkidCar system are evident in allowing the body movement as seen from the below mentioned diagrams (*Fig. 3*, *Fig. 4*). The computational model of the car with the SlideWheel system (according to *Fig. 2*) has been done in SW Adams/View (Multibody dynamics simulation software) so far only in a simplified form. Also further described simulations were performed in this software.

4. Simulating the body movement

A time-varying longitudinal thrust force has been used for the movement of the model vehicle. A gradually increasing longitudinal force applied to the rear wheels in a time interval from t = 1.2 to 6.8 s has been used for a forward movement. All-wheel brake force is used at the time of from 10 to 14 s. A longitudinal force simulates the acceleration and deceleration of the vehicle.

The size of a body inclination α is determined by the equation (*1*), where H_{1i} (H_{2i}) – a distance of a measurement point on the front (rear) part bow (stern) of the body from the road at time t_i; A_x – a distance between measurement points in the longitudinal plane of the vehicle; H_{10} (H_{20}) is a distance of a measuring point corresponding to a steady vehicle velocity.

$$\alpha_i = \tan^{-1}\left(\frac{(H_{1i} - H_{1o}) - (H_{2i} - H_{2o})}{A_x}\right) \tag{1}$$

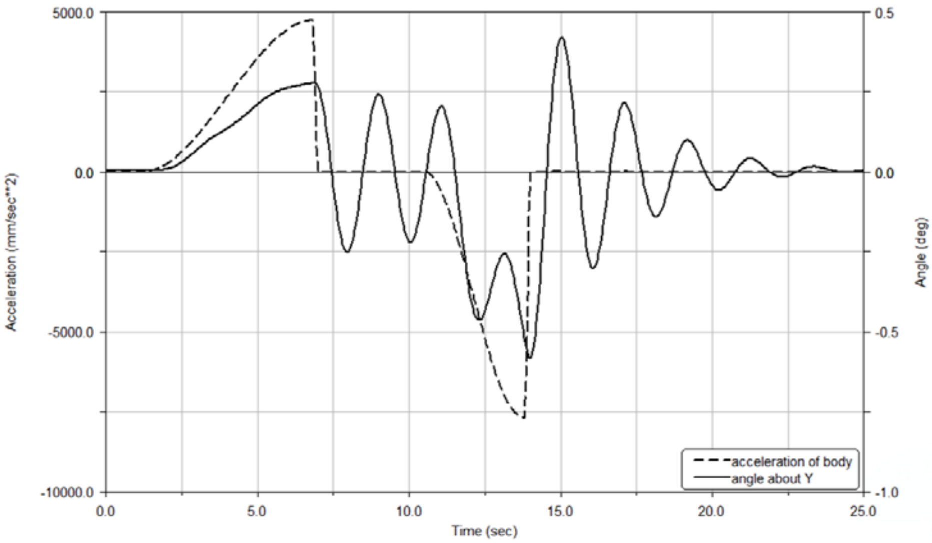

Fig. 3: Acceleration of the vehicle and body pitch according to the lateral axis

The process of the body inclination according to a lateral axis y is shown in *Fig. 3*. The maximum absolute value of the car body inclination is $\alpha = 0.58°$ which corresponds to the difference of a vertical lifting between the bow and stern of the absolute value of 38 mm on the length of the body.

When implementing the body roll examination, the model car has been set to motion at a constant velocity by the forward force applied on the front wheels. At the time $t = 15$ s, there has been a shift in a rack of the steering transmission to a left lock and further so as to make the car perform a track in the form of a figure eight and finally perform a simple lane change.

The process of the body roll according to a longitudinal axis x is shown in *Fig. 4*. The maximum absolute value of the car body inclination is $\beta = 1.53°$ which corresponds to the difference of a vertical lifting between the left and right side of the body with the absolute value of 69 mm on the width of the body.

$$\beta_i = \tan^{-1}\left(\frac{(H_{3i} - H_{3o}) - (H_{4i} - H_{4o})}{B_x}\right) \tag{2}$$

The size of a body roll angle β is determined by the equation (*2*), where H_{3i} (H_{4i}) – a distance of a measurement point on the left (right) side of the body from the road at time t_i; B_x – a distance between measurement points in the lateral plane of the vehicle; H_{30} (H_{40}) is a distance of a measuring point corresponding to a steady vehicle velocity (Zikmund T., 2006).

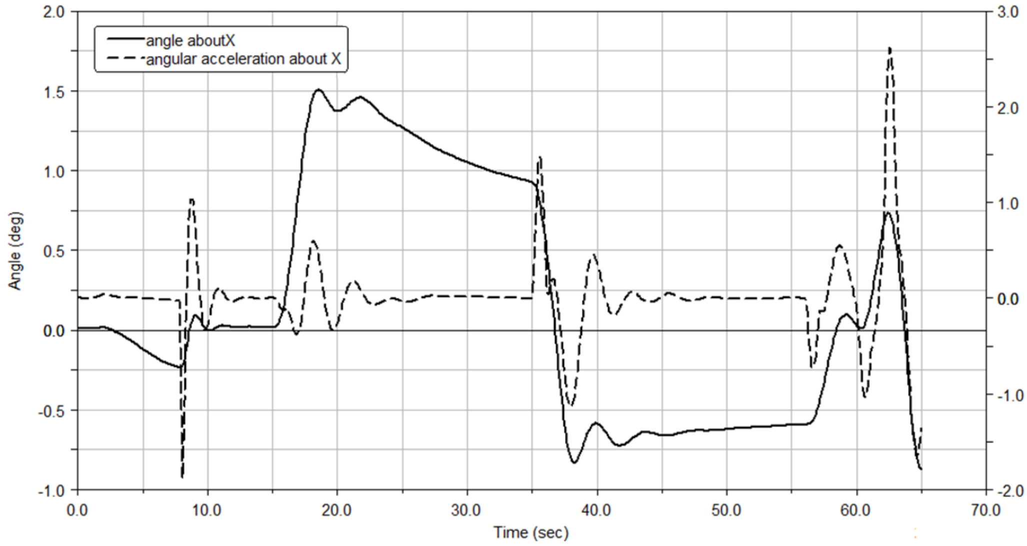

Fig. 4: Angle and acceleration of the body roll

5. Conclusion

The vehicle body movement simulation diagrams imply that every driving condition involving a change in acceleration causes a movement of the body. If it is necessary to change the adhesive conditions for the vehicle movement, it is possible to use slip surfaces or slip tires, or it is possible to influence a radial wheel reaction. To achieve the credibility of vehicle behavior change, we recommend providing the radial wheel reaction by lifting the unsprung masses. When lifting the sprung masses, the body does not change its position to a road plane and such a vehicle is applicable to a limited extent for training the drivers. Value of the body inclination for the SkidCar system is equal to zero due to its construction. From this perspective, the benefit of the SlideWheel system is evident.

A more detailed treatment of the vehicle behavior with lifting unsprung masses is subject to further work at the Department of Transport Means and Diagnostics of the University of Pardubice which aims to bring the structural solution of SlideWheel into a real form and undergo a driving test.

References

Zikmund, T. (2006) Dynamics of undercarriage parts of road, 105, pp. 71-81. University of Pardubice, Pardubice.

Multibody dynamics simulation software ADAMS/View 2012. MSC Software Corporation.

22nd International Conference
ENGINEERING MECHANICS 2016
Svratka, Czech Republic, 9 – 12 May 2016

COMPUTATIONAL MODEL FOR HEAT TRANSFER IN A TYRE CURING PRESS

J. Jirásko*, R. Kottner**

Abstract: *This paper provides an introduction to the issue of heat transfer in curing presses. It deals with a validation model for the heat transfer coefficients and transfer of boundary conditions to the newly designed variants. The article also deals with the description of materials used, links between individual components and setting of the boundary conditions for this type of task. A brief assessment of the benefits of the newly proposed variants is made in the conclusion.*

Keywords: Heat transfer, Curing press, Finite element method, Mechanical engineering.

1. Introduction

The aim of this calculation is to determine the surface temperature of two new variants of a curing press (type VL75) when the temperature of the inner surface of the pressure chamber is 145 °C. We can solve heat transmission as a stationary task (steady state) thanks to these arguments: the main interest is to find out the highest possible surface temperature that could arise; there is no significant cooling between the production cycles of the curing press (Hynek, 2011, 2013). The calculation is done using finite element method (FEM) in Abaqus 6.11. The computational model is validated by comparison of the calculated temperature field with the temperature field of a real curing press (VL95). A thermal field was obtained using a thermal imager. The validation model is modified to have the same material properties and structure as the real VL95 curing press.

2. Computational model

The curing press has one plane of symmetry so the model is only one half of the press. Individual parts of the press are meshed according to the following geometry: 3D elements with 8 nodes, shell elements with four nodes and beam elements with two nodes. The entire press is divided into several sub-units which are tied together. Figure 1 shows the entire assembly. Shell and beam elements are rendered with their thickness (section). Each unit is meshed as a single piece, which means that all real connections within a single unit are linked. Some sub-units are meshed so that it is possible to define various material properties of different machine parts elements. This allows modelling more machine parts at once without having to define additional links. The difference between the variants is shown in Figure 2. Variant 1 unlike Variant 2 has: top cover connected to the upper pressure chamber; bottom cover extended to the shoulder of the lower chamber; and there is a gap between the protective belt and the top cover. The protective belt is connected with the top part of the chamber in all models. The upper cover is connected with the chamber only for model validation. Connections are meshed using beam elements with 2 nodes. Connections distribution can be seen in the results in Figure 4. Regions where the connections occur have a higher temperature (the angle between connections is 30 °).

Material properties are listed in Table 1 (Bejan, 2003, Bonollo, 1996, Lattimer 2012). All models use insulation material S4000® for insulation boards. The S 4000® is a laminate based on glass-fibres bound with a high-temperature polymer. Foam glass insulation is used to validate the model instead of two-component hard polyisocyanurate (PIR) foam.

* Ing. Jakub Jirásko: Department of Machine Design, Faculty of Mechanical Engineering, University of West Bohemia; Univerzitni 22; 306 14, Pilsen; CZ, jirasko3@kks.zcu.cz

** Ing. Radek Kottner, Ph.D.: European Centre of Excelence, NTIS - New Technologies for Information Society, Faculty of Applied Sciences, University of West Bohemia; Univerzitni 8; 306 14, Pilsen; CZ, kottner@kme.zcu.cz

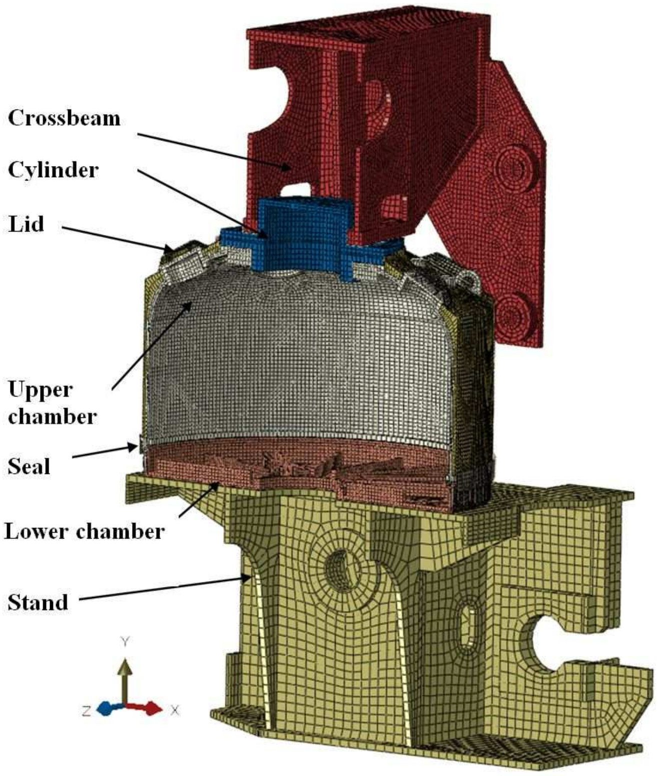

Fig. 1: Whole computational model of the curing press.

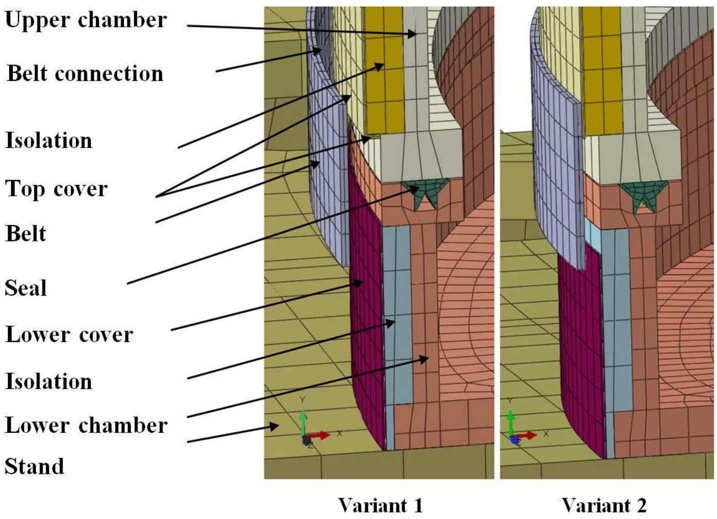

Fig. 2: Detail of the dividing plane with the seal.

Tab. 1: Material properties.

Material	Density [kg·m^{-3}]	Specific heat [J/kg·K]	Thermal conductivity [W/m·K]	Materials
Rubber	1000	450	0.14	
Steel	7800	470	53.40	
Foam glass	140	840	0.04	
PIR foam	42	1400	0.04	
S4000®	2000	900	0.12	
Bronze	8940	384	386.00	

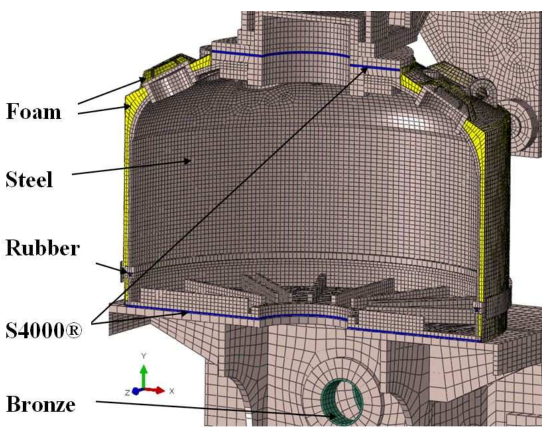

2.1 Boundary conditions

Heat transmission is solved as stationary. A constant temperature of 145 °C is set on the inner surface of the pressure chamber. The heat transfer coefficient $\alpha = 4\ \mathrm{Wm^{-2}K^{-1}}$ is set for all external surfaces of the press. The condition of air is set as still with temperature of 36°C. The protective belt is an exception and the ambient air temperature is set to 50 °C.

2.2 Validation of the model

The temperature field on the surface of the press is validated by comparing the model results with the image made by the thermal imager. The image from the imager is available for press VL95. Due to the different design of VL75 variant 1 and VL95 the following changes had to be made:

- PIR foam is replaced with foam glass.
- Pressure chamber assembly holes - insulating covers are not used.
- Connections of top cover with the upper chamber is added.

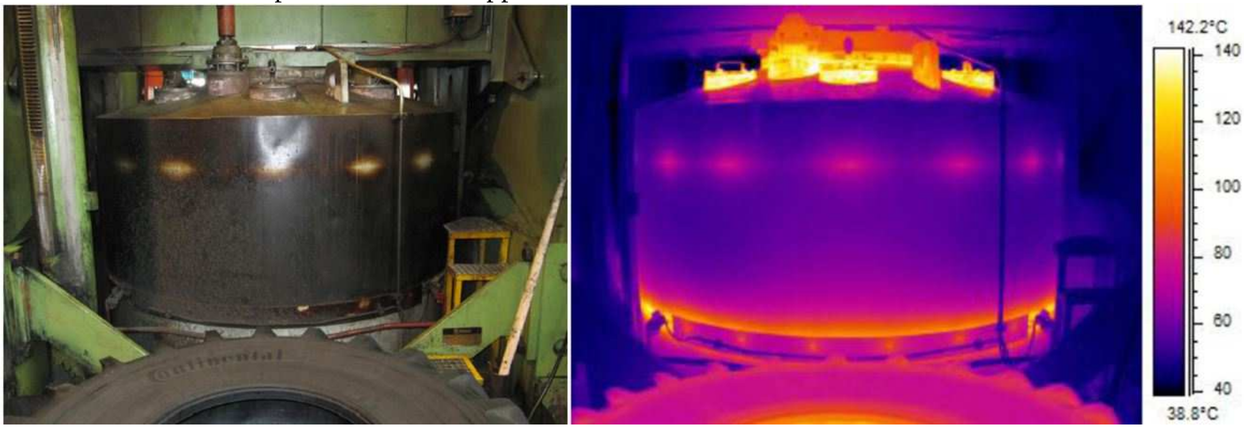

Fig. 3: The photo of the curing press and the thermal image.

The real view of the VL95 press and corresponding image from the thermal imager is shown in Figure 3. The temperature field from the validation model is shown in Figure 4. It is clear that comparison of Figure 3 and Figure 4 provides some consensuses. The differences are evident in the connection points of the upper cover and the protective belt. This difference is probably caused by the idealization of these connections into rods with a circular cross section and also there is a perfect distribution of insulation foam around the connections in the model.

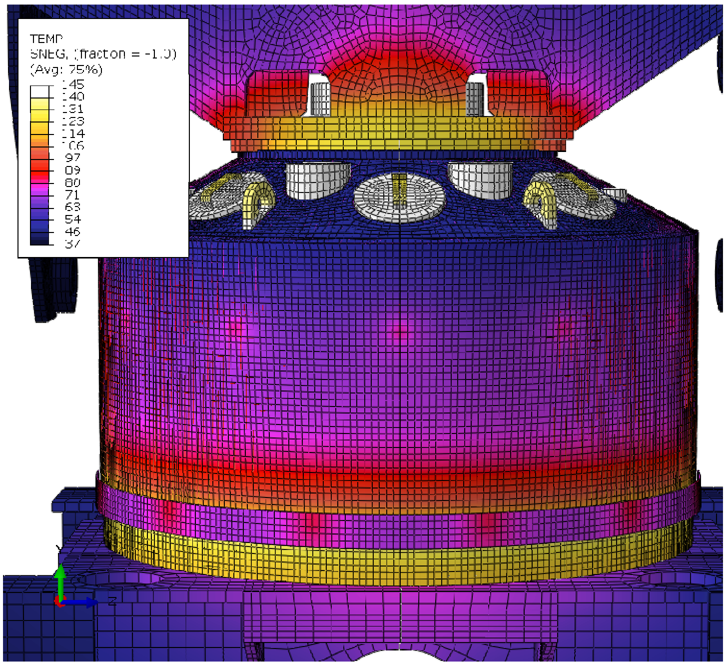

Fig. 4 Temperature field of the validation model.

3. Results

An overall view of the first variant's temperature field is shown in Figure 5 on the left. Heat bridges greatly increase the surface temperature of the press and associated heat loss. The temperature field of the second variant is on the right of Figure 5. It is obvious that in comparison with the first variant the temperature of the top cover is reduced. The temperature value above the upper edge of the protective belt is 76°C (Variant 1 has 110°C). The temperature on the bottom cover is also reduced but not so much. The reason for this is that the foam insulation is thinner than in the upper cover.

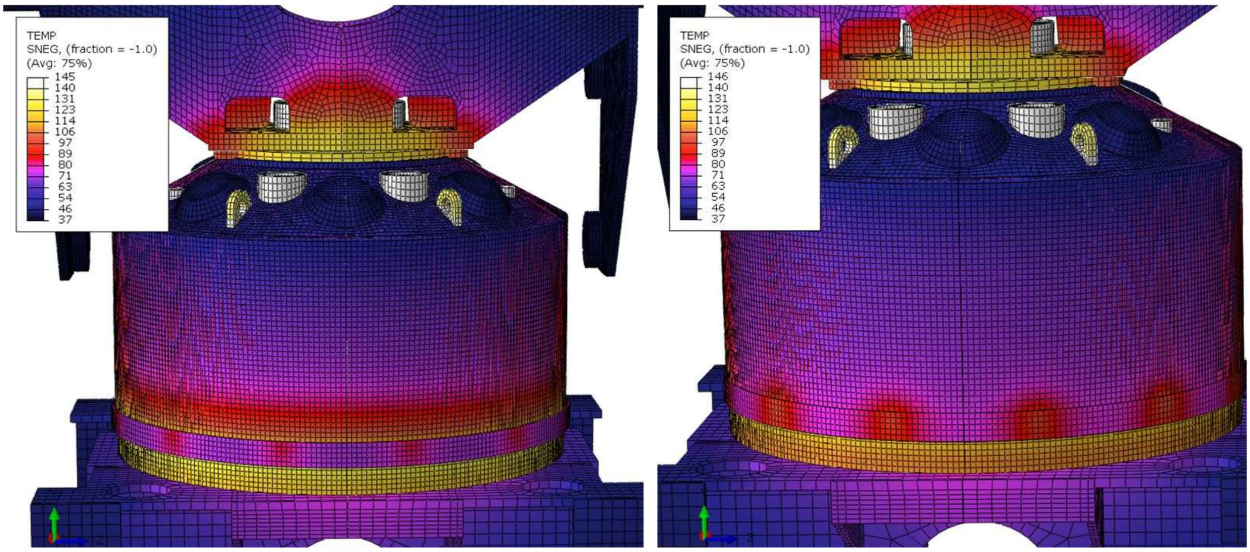

Fig. 5 Temperature fields of Variant 1 and Variant 2.

4. Conclusions

This paper describes a possible method for solving calculations for heat transmission in curing presses. The validation method and calculation setting of the model is discussed in the article. Calculations with the newly designed variants were performed based on the validated computational model.

A comparison of the validation model and Variant 1 shows a reduction in the surface temperature of the top cover connection points. Furthermore, it is obvious that if lid covers are used, the temperature in the area of the lid covers is only 53°C, so the heat loss is reduced in comparison with the VL95 press. Variant 2 compared to Variant 1 proves the reduction in temperature at the surface of the area around a plane dividing the upper and lower cover. The reduction of temperature in the area of the lower cover is not as good as on the top cover. Due to the higher temperature in the lower cover, it is appropriate to increase the thickness of the insulation in this area. The critical point in terms of heat loss and temperatures remains the connection of the pressure chamber with the crossbeam.

Acknowledgement

R. Kottner was supported by the project LO1506 of the Czech Ministry of Education,Youth and Sports. J. Jirasko was supported by the project SGS-2016-012 of the University of West Bohemia.

References

Bejan, A., Kraus, A.D. (2003) Heat transfer handbook. John Wiley & Sons, Inc., Hoboken, New Jersey.

Bonollo, F., Gramegna, N. (1996) A contribution to the correct use of heat transfer coefficients and cooling media properties in simulation of foundry process. Universita di Padova.

Hynek, M., & Votapek, P. (2013). Numerical analysis of thermal fields in the insulated cover of tire curing presses. 18th International Conference Engineering mechanics 2012.

Hynek, M., Votapek, P. (2011). Thermal analysis of tyre curing process. In IM 2011. Praha: AVČR. pp. 223-226.

Lattimer, B.Y., Goodrich, T.W., Chodak, J., Cain, Ch. (2012) Properties of composite materials for modeling high temperature response. In 17th International Conference on Composites.

22nd International Conference
ENGINEERING MECHANICS 2016
Svratka, Czech Republic, 9 – 12 May 2016

CALIBRATION PROGRAM FOR FINE GRAINED SOILS

T. Kadlíček*, T. Janda, M.Šejnoha*****

Abstract: *This paper is concern with an ongoing effort to introduce hypoplastic models into the engineering community. Attention is limited to the hypoplastic model for fine grain soils. Carefully selected samples of soils collected from various regions of the Czech Republic are examined to test the quality of the recently developed calibration software. The behavior of these soils is then compared by solving a simple example of a uniformly loaded strip footing. The results provided by the Mohr-Coulomb model are also exploited to identify some drawbacks of both models.*

Keywords: Hypoplastic model, Mohr-Coulomb model, calibration, fine grain soils

1. Introduction

During the last few decades, some advanced soil models such the Hypoplastic model for clays (HC) have underwent a significant development, see e.g. Mašín (2013). Despite an indisputable precision in the prediction of soil response, these models are still too far from being ordinary used in practice. Such a state is probably caused by theoretical and technical demands associated with tuning the material parameters of the model. We expect that robust calibration software combined with classification of soils represents the way of overcoming such obstacles. Some preliminary results of our current research effort are provided in this contribution.

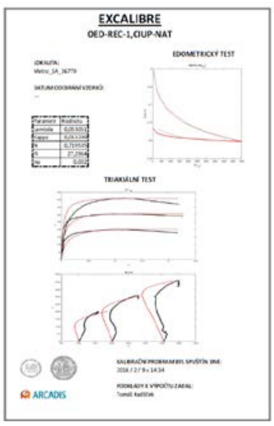

Fig. 1: Calibration report

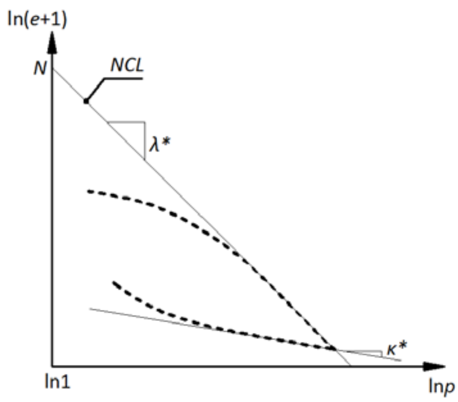

Fig. 2: Parameters of hypoplastic clay model

2. Calibration software

The calibration program is being developed to remove difficulties associated with time consuming calibration of the hypoplastic models and consequently broaden application of these advanced models in the engineering practice. The current version of the program is available free of charge at TAČR (2016) where particular details of model calibration, not listed here due to lack of space, are presented. For

* Ing. T. Kadlíček.: Czech technical University in Prague, Thakurova 7/2077, 166 29 Prague 6, tomas.kadlicek@fsv.cvut.cz
** Ing. T. Janda, Ph.D.: Czech technical University in Prague, Thakurova 7/2077, 166 29 Prague 6, tomas.janda@fsv.cvut.cz
*** Prof. Ing. M.Šejnoha, Ph.D., DSc.: Czech technical University in Prague, Thakurova 7/2077, 166 29 Prague 6, sejnom@fsv.cvut.cz

illustration we show in Fig. 1 a typical output of the program offering the calibrated data of the model together with the comparison of laboratory measurements and numerical simulations of given tests such as the oedometric test shown in Fig. 2. This figure also identifies some of the material data of the basic version of the model. Further details discussing also its extended version accounting for a high stiffness at initial stages of loading are described in Mašín (2005).

3. Soil samples

Six samples of fine grain soils were collected from various regions of the Czech Republic, see Fig. 3, and tested in the Arcadis CZ, a.s. laboratory. Soil classification according to the USCS accompanied by a brief description to identify some of the differences is presented in Tab. 1.

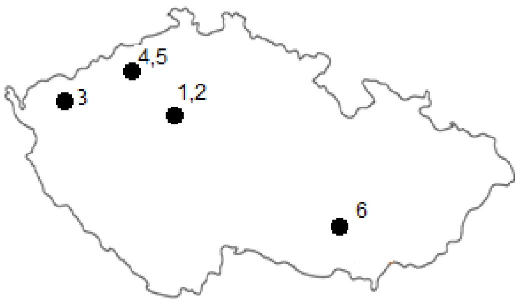

Fig.3: Locations of the tested samples

1,2 - Prague subway V.A,
3 - Odval Hajek – Karlovy Vary region,
4,5 - Bilina – dump slope
6 - Brno region

Tab. 1: Soil samples description

	USCS	DESCRIPTION
1	CL	Low plasticity clay with traces of sand, 65% passing 0.063mm sieve
2	CL	Low plasticity clay with traces of sand, 51% passing 0.063mm sieve
3	CL	Low plasticity clay, at least 55% passing 0.063mm sieve
4	CL	Low plasticity clay, with fraction of coal, 65% passing 0.063mm sieve
5	CH	High plasticity clay, 92% passing 0.063mm sieve
6	CH	High plasticity clay 90% passing 0.063mm sieve

The calibration software requires the knowledge of standard laboratory tests such as oedometric and triaxial tests. The basic parameters of the model seen in the 2nd to 6th column in Tab. 2 are found either directly from the experimental curves or by numerical simulations of these tests. Point out that the first three parameters have a direct link to the oedometric test in Fig. 2. The forth parameter stands for the angle of internal friction at critical volume and the 5th parameter controls the ratio of the shear and volumetric stiffness.

Tab. 2: Soil samples description

Sample number	$\lambda^*[-]$	$\kappa^*[-]$	$N[-]$	$\varphi_{cv}[°]$	$r[-]$	$E_0[\mathrm{MPa}]$	$k_d[\frac{\mathrm{MPa}}{\mathrm{m}}]$
1	0.047	0.010	0.662	27,3	0,235	14,73	0,099
2	0.042	0.007	0.611	32.4	0,304	14,40	0,120
3	0.039	0.006	0.677	32.6	0,385	4,41	0,172
4	0.023	0.006	0.497	25,9	0,627	5,18	0,307
5	0.051	0.011	0.891	24,2	0,731	2,84	0,138
6	0.103	0.018	1.327	25,6	0,521	10,08	0,053

In Tab. 3 we also present the parameters of the Mohr-Coulomb (MC) model for the first two soil samples as these were used in a comparative study in the next section. For details regarding the derivation of the shear strength parameters we refer the interested reader to Kadlíček et al. (2015).

Tab. 3: Soil samples description

Sample number	$E_0[\mathrm{MPa}]$	$k_d\left[\frac{\mathrm{MPa}}{\mathrm{m}}\right]$	$\upsilon[-]$	$c_{ef}[\mathrm{kPa}]$	$\varphi_{ef}[°]$
1	14,729	0,099	0,400	25	23,5
2	14,397	0,120	0,400	20	30

The last two parameters in Tab. 2, also listed in Tab. 3, deserve some special attention. These parameters are implemented in GEO5 FEM software, Fine-Ltd. (2016), to allow for the evolution of stiffness with depth. This becomes particularly important with application of classical constitutive models such as Mohr-Coulomb to properly reduce the dependency of the displacement profile on the size and boundary conditions of the computational model in finite element (FEM) simulations, see Šejnoha et al. (2015). The parameter E0 is the elastic modulus representing the soil stiffness at the terrain surface and the parameter kd shows how this modulus increases with depth h according to equation (1)

$$E(h) = E_0 + k_d h \qquad (1)$$

For this simple linear relationship the parameters E0 and h are typically derived from an oedometric test for the expected range of stresses. Therefore, they can be assumed as material properties independent of the computational model being solved. Nevertheless, the location of the bottom boundary must still be selected with caution.

4. Numerical example

A simple example of a uniformly loaded strip footing is presented to examine the behavior of relatively similar soils. The finite element mesh is plotted in Fig. 4. The computational model is 40 m long and 10 m deep. Only half of the model is analyzed due to symmetry. The strip footing is represented by a beam element with a finite stiffness. All calculations were performed adopting the GEO5 FEM software in the 2D environment assuming the state of plane strain. The results in terms of the maximum vertical displacements caused by a uniform loading of 100 kPa and measured at the center and edge of the footing are stored in Tab. 4. Note that these values are derived for the hypoplastic model assuming the basic formulation that requires only the first 5 parameters in Tab. 2. Qualitatively, these results agree well with a variable composition identified with individual soil samples.

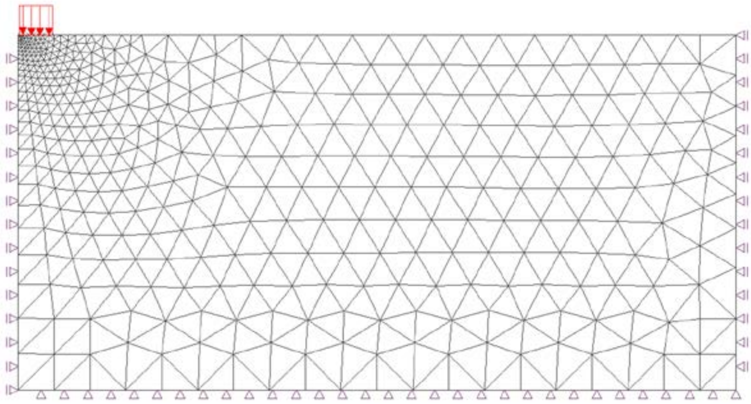

Fig.4: Finite element mesh and loading

Tab. 4: Maximum vertical displacements at edge and center of footing

Sample number	Edge [mm]	Center [mm]
1	40	53
2	44	57
3	33	43
4	28	38
5	66	87
6	83	110

To compare the settlement prediction provided by HC and MC models we run the same analysis with the MC model adopting the variable soil stiffness and the strength parameters in Tab. 3. The resulting displacements are available in Tab. 5 suggesting some possible drawbacks of the HC model when used in its basic version only.

Tab. 5: Comparison of prediction provided by extended version of HC model and MC model

Sample number	HypoClay - SS / Total loading				MC / Total loading			
	100 kPa		200 kPa		100 kPa		200 kPa	
	Edge [mm]	Center [mm]	Edge [mm]	Center [mm]	Edge [mm]	Center [mm]	Edge [mm]	Center [mm]
1	18	28	36	51	16	22	43	53
2	18	28	37	53	17	22	38	48

Clearly, this yields the soil response much too compliant as evident when comparing the MC predictions in Tab. 5 with those listed in Tab. 4. To remedy this, an extended version has been developed that takes into account a relatively large shear stiffness of soil at initial stages of loading – the so called small strain stiffness, see e.g. Niemunis & Herle (1997).

The extended version of the HC models depends on additional 5 parameters. Their determination requires application of non-standard laboratory tests. This, however, goes beyond the present scope and we refer the interested reader to (Mašín (2015); Janda & Šejnoha (2013)). Here we just point out that using this extended version considerably improves the model performance as seen by comparing the settlements in Tab. 5.

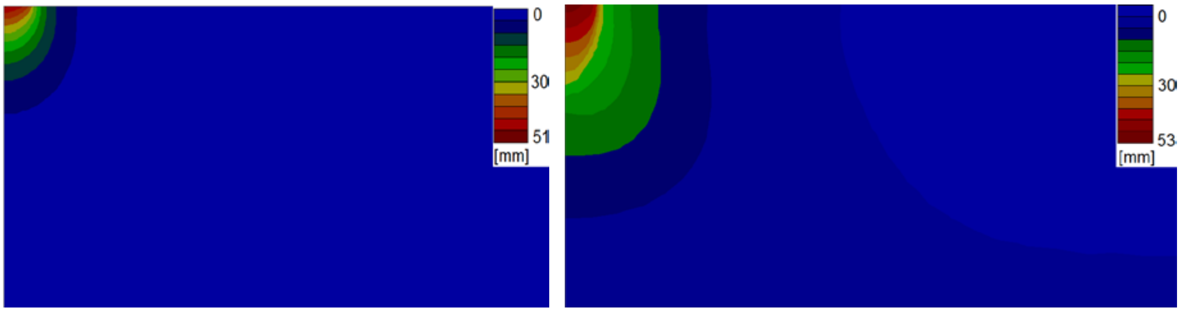

a) *b)*

Fig.5: Displacement profile provided by a) extended HC model, b) MC model

At this point, we would like to warn the reader not fall into a false impression that using the classical MC model is sufficient and that there is no need for using more complex advanced models. To that end, we plot the overall displacement soil profile associated with the uniform loading of 200 kPa for both models. It is clearly seen that the MC model even if enhanced with a variable stiffness option, recall Eq. (1), predicts much deeper progress of vertical displacements. In general, this is largely influenced by the location of the bottom boundary of the model.

5. Conclusions

This contribution addresses some of our recent achievements towards development of the calibration software to provide data for some of the advanced constitutive models including the Cam clay and Hypoplastic models for fine and coarse grained soils. This should help to increase the interest in these models among practical engineers which in turn should lead to improved and more reliable design of geotechnical structures. Further support is expected by providing a classification methodology much similar to standard classification of soils.

Acknowledgement

The financial support provided by the projects TA04031603 and SGS15/031/OHK1/1T/11 is gratefully acknowledged.

References

Janda T., Šejnoha M. (2013) Stanovení parametrů pokročilých materiálových modelů pro jemnozrnné zeminy pomocí MKP softwaru. Geotechnika 2, pp.3-13, in Czech.

Niemunis, A and L Herle. 1997. Hypoplastic model for cohesionless soils with elastic strain range: Mechanics of Cohesive-Frictional Materials, pp. 279-299.

TAČR (2016) https://mech.fsv.cvut.cz/TA04031603/#!index.md.

Mašín D. (2005) A hypoplastic constitutitve models for clays. International Journal for Numerical and Analytical Methods in Geomechanics, 29, pp 311-336.

Mašín D. (2013) Clay hypoplasticity with explicitly defined asymptotic states. Acta Geotechnica 8 (5), pp.481-496.

Mašín D. (2015). Hypoplasticity for Practical Applications, course handouts [online]. https://web.natur.cuni.cz/uhigug/masin/hypocourse, 2015.

Fine-Ltd. (2016) http://www.fine.cz/.

Šejnoha M., Janda T., Pruška J. & Brouček M. (2015) Metoda konečných prvků v geomechanice: Teoretické základy a Inženýrské aplikace, ČVUT v Praze, in Czech.

Kadlíček T., Janda T., Šejnoha M., Kuňák J., & Urbánková M. (2015) Application of hypoplastic model of fine-grained soils in numerical modelling of NATM tunnelling. Tunel, 24 (2), 69–82.

22nd International Conference
ENGINEERING MECHANICS 2016
Svratka, Czech Republic, 9 – 12 May 2016

STATIC STIFFNESS CALCULATION OF A LATHE HEADSTOCK

T. Keckstein*, Š. Pušman**, M. Hynek***

Abstract: *Checking and calculation of the headstock static stiffness for every machine tool is important because it directly influences the machine accuracy, which is one of the most important factors. This paper describes the calculation and results of the static stiffness of a bearing housing in different areas of the headstock of a universal centre lathe. To determine the stiffness, we performed a calculation using the finite element method (FEM). The computational model was loaded by maximum forces that were calculated via analytic calculations. Displacement of several important areas of the headstock was found by using this FEM calculation. Stiffness was calculated from displacements and loading forces by using well known formula.*

Keywords: Stiffness, Machine tool, Finite element method, Universal centre lathe, Headstock.

1. Introduction

Modern machining processes require machine tools to work accurately and dynamically. This leads to the necessity for a method which can analyse the stiffness of machine tools. (Lianqing and Liping, 2009) The aim of this calculation is to examine the static stiffness of the spindle bearing housing in the headstock (Fig. 1) of a universal centre lathe via calculation by finite element method (FEM). The headstock stiffness is one of several values of stiffness that are necessary for calculation of the overall static stiffness of a spindle bearing. This stiffness has a crucial influence on the machining accuracy of the lathe. Decisive criteria of machine tools quality are the productivity and working accuracy. (Šooš, 2008) In addition to these structural parameters the accuracy of the machining process is also influenced by the diameter and the geometry of the workpiece. (Chen, Wei and Tsai, 1999)

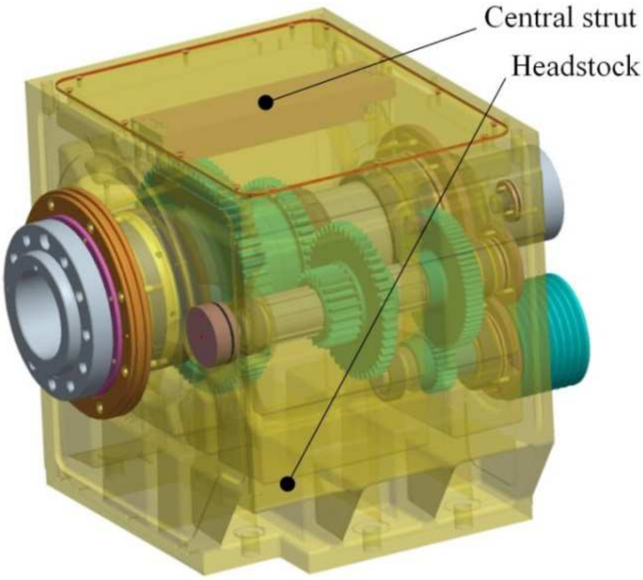

Fig. 1: Headstock of the universal centre lathe.

* Ing. Tomáš Keckstein: Department of Machine Design, Faculty of Mechanical Engineering, University of West Bohemia, Univerzitni 8; 306 14, Pilsen; CZ, tomkec@kks.zcu.cz

** Ing. Šimon Pušman: Department of Machine Design, Faculty of Mechanical Engineering, University of West Bohemia, Univerzitni 8; 306 14, Pilsen; CZ, pusmans@kks.zcu.cz

*** Doc. Ing. Martin Hynek Ph.D.: Department of Machine Design, Faculty of Mechanical Engineering, University of West Bohemia, Univerzitni 8; 306 14, Pilsen; CZ, hynek@kks.zcu.cz

Only the headstock and pliable central strut was modelled volumetrically, other parts were simplified for this calculation (Fig. 1). Stiffness was examined in three mutually orthogonal directions by loading of places where spindle bearings are in the real machine. The calculations were made in the FEM system MSC Marc 2011. Only small deformations were considered in this calculation.

2. Calculation settings

Pliable parts of the model – the headstock and the central strut were meshed using linear volume elements with 8 (hex8) or 6 (penta6) nodes. The bed of the lathe was discretized as a non-deformable surface. The spindle bearings were considered as absolutely rigid – contact surfaces between every bearing and the headstock were linked with an imaginary point on the axis of the bearing by using absolutely rigid links (Rigid Link in MSC Marc). Contact surfaces of the bolt heads with the headstock were also replaced with absolutely rigid links. Bolts were replaced by links with a possibility of preload (Overclosure link in MSC Marc). One end of the preloaded link was placed on the rigid links that connect the contact surface of the bolt head, and the second end of the preloaded link was connected to one internal node of the non-deformable surface, where there is actually a thread in the bed of the lathe (threaded holes have not been simulated). Overclosure ties were loaded with the recommended preloading force specified by the bolt manufacturer.

The validity of Hook's law (i.e. linear stress distribution on deformation) was considered for all the materials used. Their parameters are listed in Tab. 1. The headstock is made of cast iron (EN-GJL-300) and the central strut is made of steel (S235JRG2).

Tab. 1: Mechanical properties of used materials.

Material	**Density [kg·m^{-3}]**	**Young's modulus [GPa]**	**Poisson's ratio [-]**	**Compressive strength [MPa]**	**Tensile strength [MPa]**	**Yield strength [MPa]**
EN-GJL-300	7350	130	0.26	860	300	-
S235JRG2	7800	210	0.3	340		235

The contact with friction was defined between parts of the model (between the headstock and the central strut and between the headstock and the bed of the lathe). This contact does not allow transfer of tensile normal forces, but it transfers all other forces (contact touching in MSC Marc). The coefficient of friction between all contact surfaces was specified as 0.15. The size of the transmitted tangential forces was derived from this coefficient.

The computational model was used to investigate the stiffness, and for this task it was necessary to set the geometric and static boundary conditions.

Forbidding all displacements and rotations has been prescribed for the solid surface that represents the bed. All displacements and rotations were also forbidden for the selected nodes of the headstock and the central strut, but only in the first calculation step in which the model has not been loaded with any static boundary conditions. In the second and next calculation steps these geometric boundary conditions have been released.

For this calculation, a static load of the model was considered and the model was loaded with forces transmitted through the bearings and bolted connections. Forces transmitted through the bearings were always prescribed in one central node for each bearing. (See Fig. 2) The position of this central node was tied to nodes corresponding with their position to the position of the contact points between the headstock with the bearings. Similarly, the preloading force of the bolt connections was always applied to the node located on the axis of the screw, while the relative position of the central node was linked with nodes that correspond with their position to the points of contact between the headstock and the bolt head. Other possibilities of numerical modelling of preloaded bolted joints are described in Lašová & Kosnar (2006).

Loading was done in three basic steps:

- Geometric boundary conditions were activated - positions of all elements of the model were defined.
- Bolt connections were preloaded.
- Loading forces to the bearings points were applied.

During investigation of the stiffness, the last basic step of the calculation (loading forces to the bearing points) was conducted with five different settings. For each of these five different calculations always only one bearing was loaded with a simple force in one coordinate direction (see Tab. 2). For all five calculations always the maximum value of the loading force in particular bearings was chosen. The value of the loading forces was calculated via analytical calculations from the load spectrum of the lathe.

Tab. 2: Individual loading forces.

Calculation - *n*	**1**	**2**	**3**	**4**	**5**
Bearing designation	**NN 3936**	**NN 3936**	**NN 3932**	**NN 3932**	**180 TAC**
Type of bearing	**radial**	**radial**	**radial**	**radial**	**axial**
Force in the X direction [N]-$F_{X,n}$	-30 000	0	30 000	0	0
Force in the Y direction [N]-$F_{Y,n}$	0	30 000	0	-30 000	0
Force in the Z direction [N]-$F_{Z,n}$	0	0	0	0	30 000

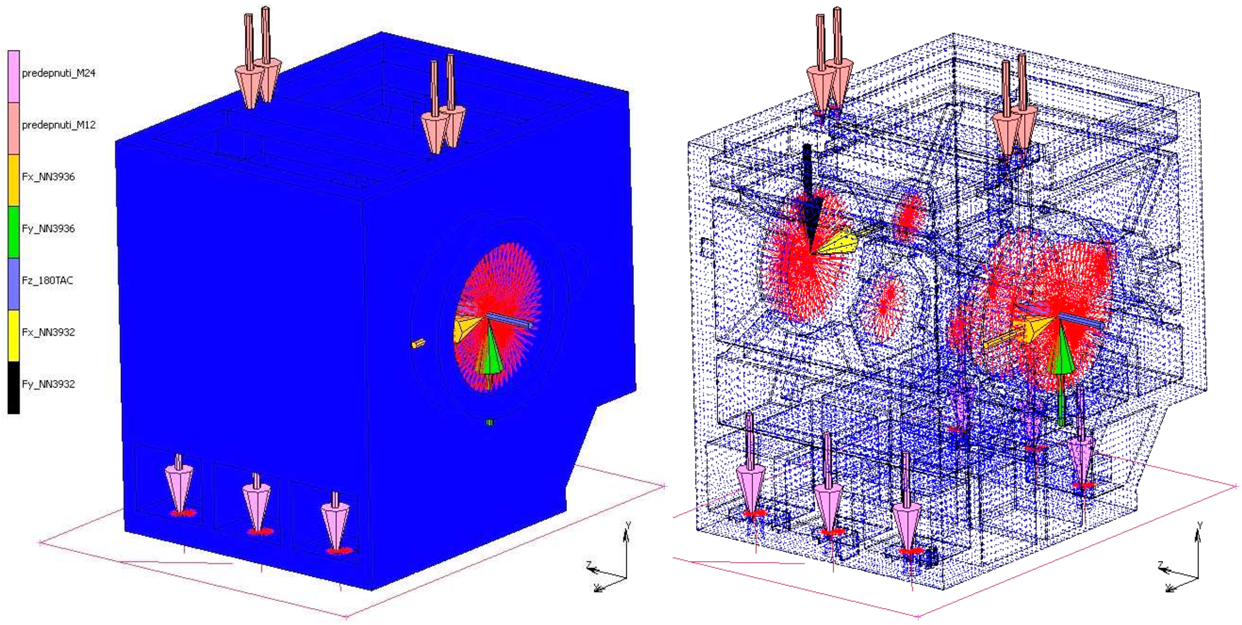

Fig. 2: Static boundary conditions.

3. Stiffness evaluation

The stiffness was examined in the directions of the coordinate axes on the basis of the specified static boundary conditions and the discovered displacements of the nodes where the loading forces was placed (node in the middle of bearings), according to the equation:

$$k_{i,n} = \frac{F_{i,n}}{u_{i,n}} \tag{1}$$

while $F_{i,n}$ is loading force from Tab. 2, where the index i is coordinate X, Y or Z and the index n is the number of calculation (1-5) from the same table.

The discovered values of the displacement of the centre points of bearings $u_{i,n}$ are given in Tab. 3 and values of stiffness calculated according to equation (1) are stated in Tab. 4. In Fig. 3 you can see an example of the calculated displacement of all nodes in the direction of the loading force (loading force $u_{x,1}$).

Tab. 3: Displacement of centre points of bearings.

Calculation - *n*	**1**	**2**	**3**	**4**	**5**
Bearing designation	**NN 3936**	**NN 3936**	**NN 3932**	**NN 3932**	**180 TAC**
Type of bearing	**radial**	**radial**	**radial**	**radial**	**axial**
Displacem. in the X direction [mm]-$u_{X,n}$	-0.016	0	0.018	0	0
Displacem. in the Y direction [mm]-$u_{Y,n}$	0	0.011	0	-0.005	0
Displacem. in the Z direction [mm]-$u_{Z,n}$	0	0	0	0	0.021

Tab. 4: Calculated stiffness of the headstock in coordinate directions.

Calculation - *n*	**1**	**2**	**3**	**4**	**5**
Bearing designation	**NN 3936**	**NN 3936**	**NN 3932**	**NN 3932**	**180 TAC**
Type of bearing	**radial**	**radial**	**radial**	**radial**	**axial**
Stiffness in the X direction [kN/mm]-$k_{X,n}$	1875	0	1667	0	0
Stiffness in the Y direction [kN/mm]-$k_{Y,n}$	0	2727	0	6000	0
Stiffness in the Z direction [kN/mm]-$k_{Z,n}$	0	0	0	0	1429

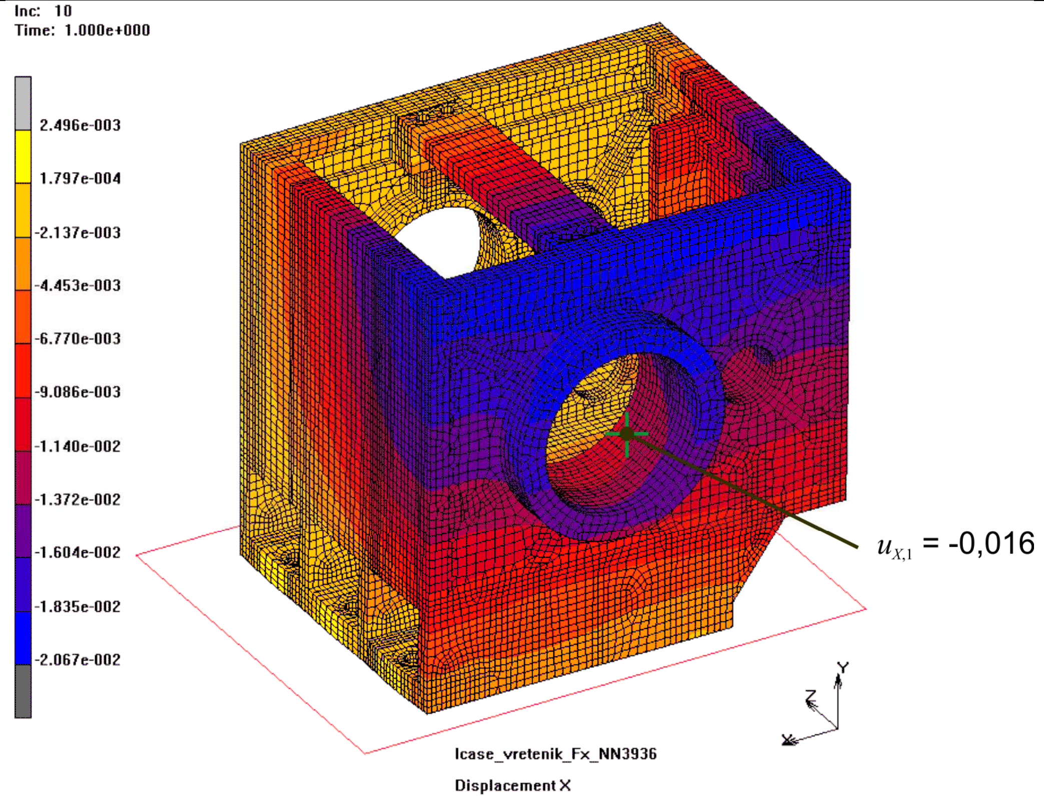

Fig. 3: Displacement in the direction of loading force [mm], calculation n=1.

4. Conclusions

The goal of this calculation was to discover the static stiffness of bearing housing areas in the headstock of a universal centre lathe via calculation by FEM. The stiffness was examined in three orthogonal directions by loading the spindle bearings. From the values gained from this calculation, it is possible to calculate the overall stiffness of the spindle bearing, which is very important for the accuracy of the designed machine. The calculated values show that the lowest stiffness of the headstock was observed in the spindle axis direction.

Acknowledgement

This paper was supported by the project SGS-2016-012 of the University of West Bohemia.

References

Chen, T. Y., Wei, W. J., & Tsai, J. C. (1999). Optimum design of headstocks of precision lathes. International Journal of Machine Tools and Manufacture, 39(12), 1961-1977.

Lašová, V., & Kosnar, M. (2006). Numerical modelling of preloaded bolted joints of machine tool. CADAM 2006. Rijeka: Zigo, 2006. s. 57-58. ISBN: 953-7142-19-1.

Lianqing, Y., & Liping, W. (2009). Stiffness analysis of machine tools using finite element method. In Intelligent Information Technology Application, 2009. IITA 2009. Third International Symposium on (Vol. 3, pp. 553-556). IEEE.

Šooš, Ľ. (2008). Quality of design engineering: case of machine tools headstock. Quality Festival, 2008, 2nd International quality conference.

22nd International Conference
ENGINEERING MECHANICS 2016
Svratka, Czech Republic, 9 – 12 May 2016

NUMERICAL MODELING OF MAGNETOSTRICTIVE MATERIALS

I. Kholmetska*, J. Chleboun, P. Krejčí*****

An operator-differential model for magnetostrictive energy harvesting proposed in the literature is used to calculate the amount of harvested energy under some uncertainty in the Preisach density function. The uncertainty is modeled through a fuzzy set approach. In galfenol, an alloy of gallium and iron, however, the hysteresis phenomenon is present only weakly. This allows to propose a simpler, but computationally faster model without hysteresis. The new, simpler model has been identified from the measured magnetic and magnetostrictive cycles. The amount of harvested energy is of the same order in both models. Again, an uncertainty in the identified model can be considered and its impact on the amount of the harvested energy calculated.

Keywords: Magnetostrictive materials, hysteresis, energy harvesting, uncertainty quantification, identification of parameters.

1. Introduction

The modern approach to the mathematical modeling of the materials with memory is based on the use of hysteresis operators. Hysteresis is a time-based dependence of a system's output on present and past inputs. Materials with memory are the subject of research and modeling in various fields, including nonlinear elasticity, moisture transport, magnetism, piezoelectricity, etc. Magnetostrictive materials are used in vibration sensors and energy harvesting devices, for instance. Energy harvesting is a technique for recovering small amounts of any kind of ambient (and otherwise wasted) energy (such as light, vibrations, heat, etc.). In our work, special attention is paid to uncertainty quantification and propagation in the models.

2. Energy harvesting device and its mathematical model

A magnetostrictive galfenol core of a coil with N loops is exposed to a known periodic uniform stress $\sigma(t)$ and produces variations in a background (bias) magnetic field h_0. As a consequence, an electric current is induced in the loops of wire and flows through a resistor (Davino et al., 2014). The phenomenon is described by the Faraday law

$$\frac{d}{dt}\left(\mu_0 f\,(t)u(t) + \mathcal{P}[u,\lambda_{-1}](t)\right) + \alpha\big(h(t) - h_0(t)\big) = 0, \qquad (1)$$

where the unknown function $u(t) = h(t)/f(t)$ is to be found for the time interval $t\epsilon[0,T]$ and an initial value $u(0) = u_0\epsilon\mathbb{R}$; h is an unknown total magnetic field in the core; μ_0 is the vacuum permeability; $f(t) = f(\sigma(t)) > 0$ is a known function that takes part in the magnetostrictive response to pre-stress; $\mathcal{P}[\cdot,\cdot]$ is the Preisach hysteresis operator; λ_{-1} is an initial memory state; α is a known model parameter dependent on the coil properties.

The model is free of spatial wave propagation, which may play a role for high frequency loading in the range of several tens or hundreds of kilohertz. Energy harvesting is a low frequency application. In addition, realistic spatially distributed data are not easy to get.

* Ielizaveta Kholmetska: Faculty of Civil Engineering, Czech Technical University in Prague, Thákurova 7; 166 29, Prague; CZ, ielizaveta.kholmetska@fsv.cvut.cz

** Jan Chleboun: Faculty of Civil Engineering, Czech Technical University in Prague; Thákurova 7; 166 29, Prague; CZ, jan.chleboun@cvut.cz

*** Pavel Krejčí: Institute of Mathematics, Academy of Sciences of the Czech Republic; Žitná 25; 115 67, Prague; CZ, krejci@math.cas.cz

The Preisach model is a multiyield model. It is particularly suitable for modeling energy harvesting due to easy parameter identification and an explicit formula for the instantaneous energy dissipation rate.

The Preisach operator $\mathcal{P}$ allows for taking hysteresis phenomena into account

$$\mathcal{P}[u,\lambda_{-1}](t) = \int_0^\infty \int_0^{\mathfrak{p}_r[u,\lambda_{-1}](t)} \psi(r,v)\mathrm{d}v\mathrm{d}r \tag{2}$$

and is determined by the Preisach density function ψ as well as the play operator $\mathfrak{p}_r\colon (u,\lambda_{-1}) \longmapsto \xi_r$, where ξ_r solves a differential variational inequality defined by u_0, u, and λ_{-1}. In (2), t is fixed and $\mathfrak{p}_r[u,\lambda_{-1}](t)$ is a function of r.

It is proved in (Davino et al., 2014) that a unique solution $u\epsilon W^{1,2}(0,T), u(0) = u_0$, exists and depends continuously on initial data. If $h_0(t)$ and $f(t)$ are T_p-periodic functions, then u is T_p-periodic, too. The proof is based on an approach that can serve as a numerical method for solving the problem (1).

A Preisach density function based on galfenol measurements is identified in Davino et al. (2014), see Fig. 5 (left).

Let us recall (1) and $u(t) = h(t)/f(t)$. The energy E harvested during a time period T_p is equal to

$$E(h_0,\alpha,\gamma) = \gamma \int_{\hat{T}}^{\hat{T}+T_p} (h_0 - h(t))^2\,\mathrm{d}t, \tag{4}$$

where γ is a known model parameter, see (Davino D. et al. (2014)).

Numerical tests indicate that the calculated harvested energy converges with the rate Cs, where s is the time-step size used in solving (1) and $C > 0$ is a constant of order 0 if the bias field h_0 is constant, but of order 2 if h_0 is nonconstant, i.e., periodic.

3. Fuzzy input data

The function ψ_{M} is approximated by a continuous piecewise bilinear function $\psi_{\mathrm{A}}{}^{\mathrm{bilin}}$ defined on a rectangular mesh. Due to the symmetry of ψ_{M}, only one half of the graph of $\psi_{\mathrm{A}}{}^{\mathrm{bilin}}$ is depicted in Fig. 1. The value of $\psi_{\mathrm{A}}{}^{\mathrm{bilin}}$ is uncertain at some mesh nodes and fixed at the others.

The uncertainty is modeled by 16 fuzzy numbers with a triangular membership function defined on $[0.9\psi_{\mathrm{M}}(r_i,v_i), 1.1\psi_{\mathrm{M}}(r_i,v_i)]$, where (r_i,v_i) are the coordinates of the nodes that bear the uncertainty. A fuzzy saturation condition is considered

$$\int_0^{r_\infty} \int_0^{v_\infty} \psi_{\mathrm{A}}{}^{\mathrm{bilin}}(r,v)\mathrm{d}r\mathrm{d}v = c_{\mathrm{fuzzy}}, \tag{5}$$

where r_∞ and v_∞ are sufficiently large and c_{fuzzy} is a fuzzy triangular number. The approximate membership function of the fuzzy harvested energy can be constructed on the basis of the worst and best case scenario problems solved on α-cuts (α-level optimization), see Chapter 5.2.2 (Möller & Beer, 2010).

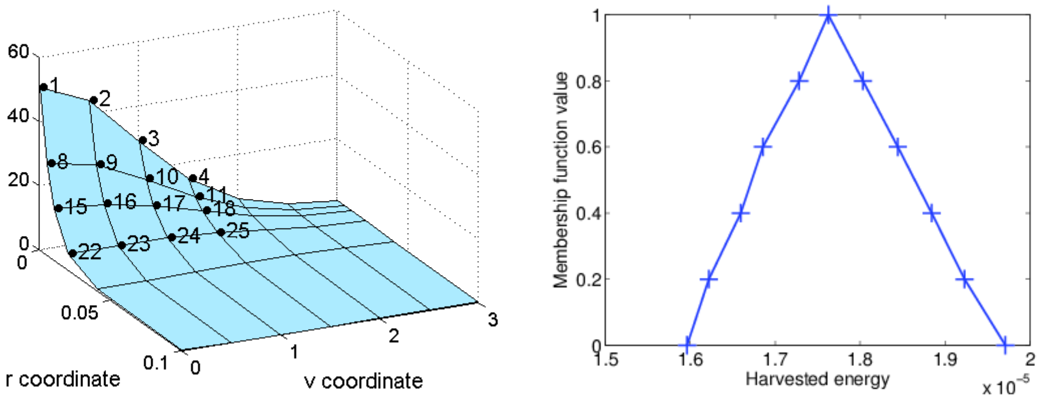

Fig. 1: Left: The graph of $\psi_A{}^{bilin}$ with 16 uncertain nodal values. Right: The calculated membership function of the harvested energy.

4. Identification of a magnetostrictive material model without hysteresis

In galfenol, an alloy of gallium and iron, the effect of the hysteresis is rather small, and this leads us to considering a simplified model where hysteresis is neglected. In this model and for a fixed stress σ, the magnetization m_σ and the strain ε_σ are assumed to depend on a function g and a value $f(\sigma)$ and to take the form

$$m_\sigma(h) = g\left(\frac{h}{f(\sigma)}\right), \qquad \varepsilon_\sigma(h) = -f^{'}(\sigma)G\left(\frac{h}{f(\sigma)}\right) \tag{6}$$

where $h \epsilon \mathbb{R}$ and $G(u) = \int_0^u vg'(v)\mathrm{d}v$, the prime stands for the derivative with respect to the indicated variable. In (6), ε_σ is the inelastic part of the total strain, that is, $\varepsilon_\sigma = \varepsilon_{\text{total}} - \frac{\sigma}{E}$, where E is the Young modulus.

Our goal is to identify g and $f(\sigma)$ from a set of measurements generously provided by Prof. Daniele Davino from Università degli Studi del Sannio di Benevento, see a selection of measured data in Fig. 2. or Davino et al. (2013). For this purpose, the weighted least squares optimization method was used, see Fig. 3 and Fig. 4. It has turned out that g and $f(\sigma)$, see Fig. 5 (right), cannot be uniquely identified unless a restrictive condition such as $G = \int_0^\infty vg'(v)\mathrm{d}v = 1$ is imposed. By (6), the shape of g corresponds to a magnetization curve, cf. Fig. 2 (left).

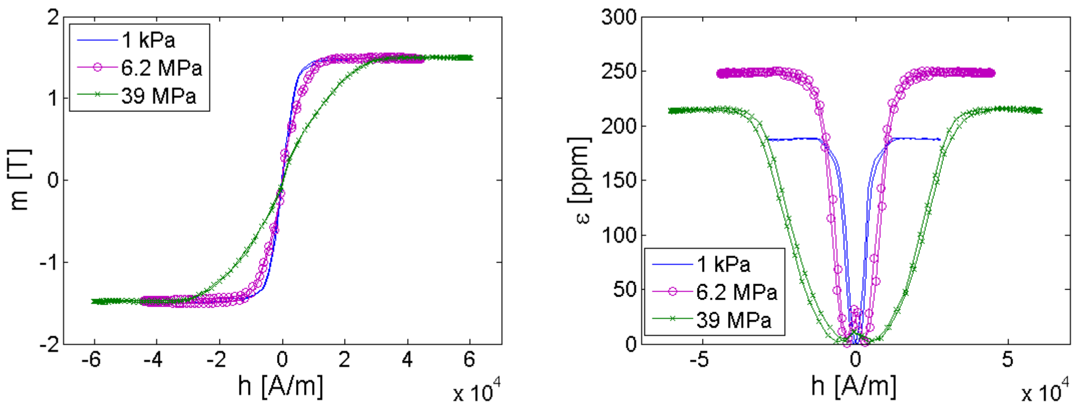

Fig. 2: Magnetic (left) and magnetostrictive (right) cycles at different constant stresses

In the hysteresis-free model, the equation (1) transforms into the following form:

$$\frac{d}{dt}\left(\mu_0 f(t)u(t) + g(u)(t)\right) + \alpha\left(h(t) - h_0(t)\right) = 0. \tag{7}$$

The energy E harvested during a time period is then determined by (4), where $h(t) = u(t) \cdot f(t)$, $u(t)$ solves (7). The difference between the energy values in the model with hysteresis ($E = 1.31061 \cdot 10^{-5}$ for a particular setting) and the model without hysteresis ($E = 2.31054 \cdot 10^{-5}$) is acceptable.

The function g can be considered uncertain and results similar to those depicted in Fig. 1 (right) can be obtained.

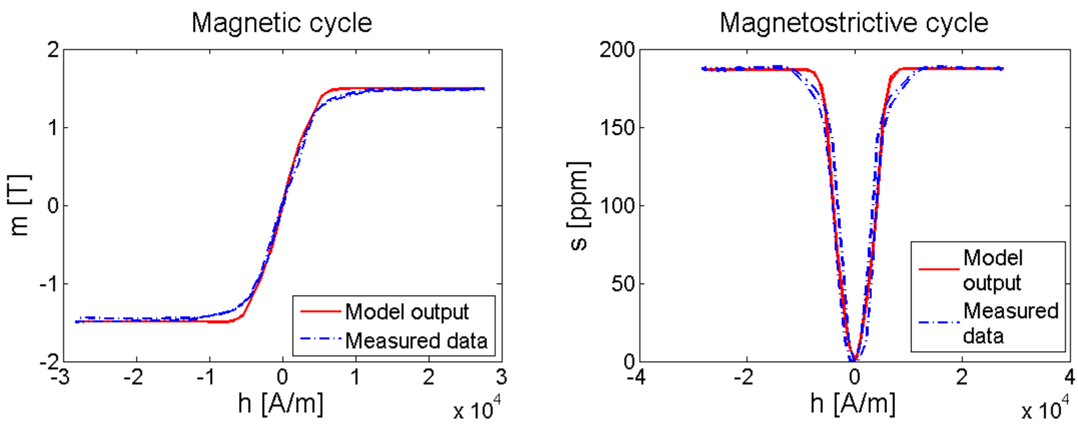

Fig. 3: Difference between the experimental data and the model output for σ_1 = 1 [kPa].

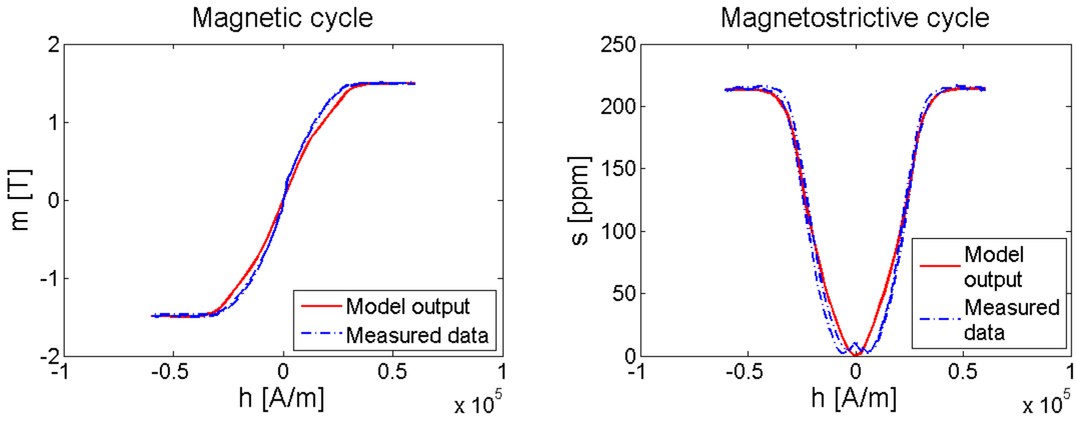

Fig. 4: Difference between the experimental data and the model output for σ_3 = 39 [MPa].

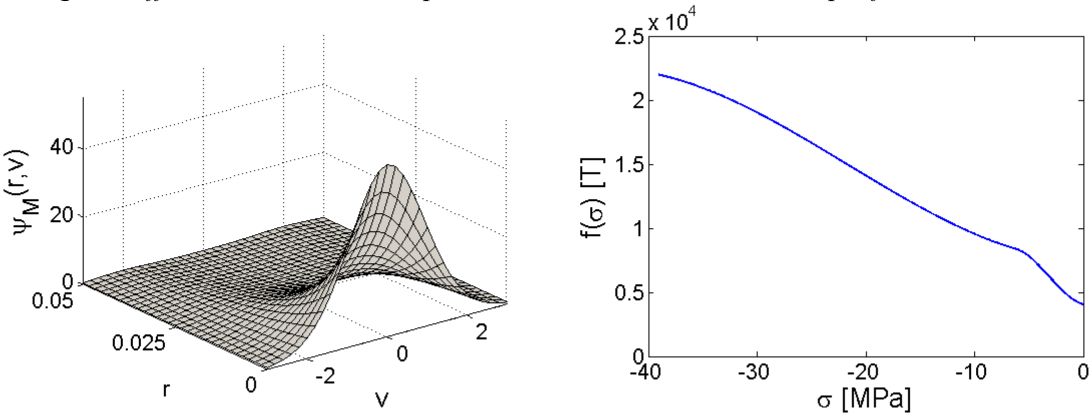

Fig. 5: Left: Identified function ψ_M. Right: Identified function f(σ) for a galfenol rod.

5. Conclusions

In the hysteresis model, the bottleneck is in solving the differential equation containing the Preisach operator. Although the best/worst case scenarios are searched for in parallel to speed up the membership function construction, the calculations take hours in the Matlab environment. The model without hysteresis is much faster and its accuracy is on par with the model with hysteresis. As a consequence, the simplified model can be used to accelerate calculations if only a small hysteresis effect is present.

A question has arisen about the degree of the correctness of the Preisach density function published in the literature. A new, nonparametric identification would be useful for further uncertainty quantification.

It can also be observed that the accuracy of the hysteresis-free model is limited especially if the stress is large, see Fig. 4 for instance. A more advanced model with a feedback is the subject of the current research.

Acknowledgement

The first author was supported by the Grant Agency of the Czech Technical University in Prague, grant No. SGS15/181/OHK1/3T/11, the other authors' work was funded by the Czech Science Foundation through grant No. 15-12227S.

References

Davino D. et al. (2014) Analysis of an operator-differential model for magnetostrictive energy harvesting. Submitted to Communications in Nonlinear Science and Numerical Simulation.

Davino D., Krejčí P., and Visone C. (2013) Fully coupled modeling of magneto-mechanical hysteresis through `thermodynamic' compatibility, Smart Materials and Structures 22, 095009 (14 pp).

Möller B., Beer M. (2010) Fuzzy Randomness - Uncertainty in Civil Engineering and Computational Mechanics. Springer-Verlag, Berlin.

22nd International Conference
ENGINEERING MECHANICS 2016
Svratka, Czech Republic, 9 – 12 May 2016

ASSESSMENT OF BALL VALVE CLOSING IN WATER HAMMER EVENT VIA VIDEO PROCESSING METHOD

C. KISTAK[*], H. EREN[**]

Abstract: *Water hammer event suddenly emerges as a result of instantly stopping or beginning the water flow through installation components and pipelines and is seen frequently in water installations. The waves emerging as a result of water hammer may lead to fractions and deformations by spreading throughout the installation. Valves and pumps are the main components of the most basic water installment schema, and are seen as the components that most frequently lead to water hammer in starting and stopping the water flow. In this study, for 3 flow velocities in a simple installment setting containing the main installment components, the event of closure of a ball valve with pneumatic actuator was examined experimentally via video processing method, and the effects of flow velocity on water hammer were investigated by visualizing the flow.*

Keywords: Water hammer, Hydraulic shock, Video processing, Ball valve, Valve closing

1. Introduction

The most used component of the installments is the valves. There are many types of valves depending on the operation systems. Furthermore, depending on the dimensions of installments, there are also different sizes of valves.

The ball valves are the vales changing the flow rate of the liquid according to the movement of the ball in those valves. Some of the main characteristics of those valves are that they can be closed and opened with a single maneuver, and that they do not create significant changes in pressure. With these valves, water hammer effect may occur when the flow is suddenly stopped. As a result of this, due to the pressure fluctuations, severe damages may occur in installment components.

The water hammer occurs as a result of the pressure changes in flow velocity of the liquid. This change occurs at the same rate and velocity with the change pressure. Suddenly stopping the liquid having high flow rate leads to dangerous pressure changes, and this may exceed beyond the operational limits of the installment components (Gürsel & Çağlar, 2014). It is necessary to sufficiently analyze this important event. Otherwise, various levels of problems may emerge (Martin, 2000). The water hammer event has typically 2 types; thermal water hammer in hot water-vapor systems and hydraulic water hammer in cold water flow systems (Wylies, 1993). When the liquid moving with its own energy crashes the closed valve, then its pressure spreads throughout the installment in wave form in order to damp the energy. The continuity of this case leads to weakening in many regions of the installment (Gürsel & Çağlar, 2014). In case of thermal water hammer, the size of surface of contact of vapor with water, the temperature differences between water and vapor, and the liquid flow velocity are the main parameters determining the blast effect (Wylies, 1993). The first study on water hammer has been carried out by Menabra (1885). In studies performed, the assessments of various flow parameters were executed. Michaud (1878), in order to ensure the controllability of water hammer event, has carried out studies on the use of air channels and safety valves. In early 19th century, Weston (1885), Carpenter (1893) and Frizell (1898) have made effort to develop the intra-pipe flow velocity changes and pressure relation. The fundamental theories of transition flow have been established by Jukowski (1898). And then, these equations have become the basis of water hammer event. Jukowsi (1898) has examined the equations, which he has obtained under different physical conditions and from various parameters, through advanced

[*] Res. Asist. Celal Kıstak, MSc.: Mechanical Engineering, Fırat University, 23100; Elazığ; TR, ckistak@firat.edu.tr
[**] Prof. Haydar Eren PhD.: Mechanical Engineering, Fırat University, 23100; Elazığ; TR, haydar@firat.edu.tr

mathematical relations (Gibson, 1908). Kavurmacıoğlu & Karadoğan (2003) have carried out studies on designing the water hammer in pumping systems due to valve actions and electricity cuts. Padmanabhan, Kochupillai & Ganesan (2004) have developed a model for liquid structure transfer in installments by developing a finite elements formulation based on flow velocity for solving the instability problem when the valve is closed. Bakeer, Barber, Sever & Boyd (2004) have experimentally examined the general characteristics of the flow through a 6-inch smooth pipe. Ramos & Almeida (2002) have examined the effect of water hammer in order to better determine the dynamic behaviors of turbo-machines.

In this study, the emergence of water hammer in case of closing the valve at different flow rates was examined in relation with the time. At the same time, the methods were discussed for preventing the effects of water hammer or minimizing the results.

2. Methods

In test setting, the components involved in a classic water installment such as pump, various valves, connection components, pipes, and tanks were utilized. In order to monitor the pressure change via camera, various colors of food coloring were utilized, and the blue color that provided the best image was preferred, and then the experiments were executed. In order to keep the closure of valve under same conditions at each of the experiments in experiment system, the ball valve was opened closed by a pneumatic actuator.

The experiment setting consists of a pump, a pipeline ensuring the integrity of installation, the valves, storage tank (250lt water in it), the pneumatic actuator, compressor, 2 cameras, and a rotameter for measuring the flow rate. The image of experiment setting is presented in Figure 1.

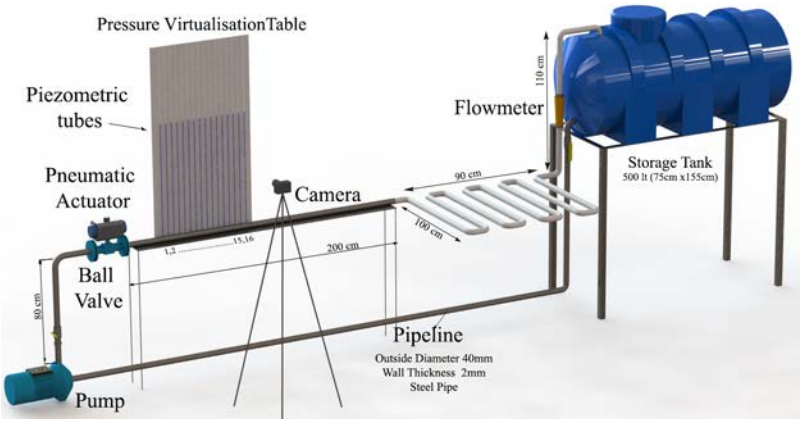

Fig. 1: Solid Model of Experiment Setting.

In order to monitor the water hammer effect throughout the experiment, various interventions were made to flow through the installment.

In this study, the closure of flanged-type ball valve through the air removal from actuator and the springs in actuator by changing the direction of solenoid valve, which directs the air to pneumatic actuator fed by compressor, emergency stop button was observed while the system was operating in actual order. During this process, the flow rates measured by the rotameter were recorded and the experiment was carried out under different flow-rate conditions.

By setting the flow rate, at which the results were obtained, the persistent flow conditions were established.

• While the video camera was recording, the valve was closed (closing time 0.66 seconds) by the closing button connected to pneumatic actuator.

• The images were translated into numeric values via an algorithm prepared in Matlab software. Video frame rate is 50 fps, in algorithm data taking ratio is 25fps/1data (two data in every second).

• The processed values were transformed into time-related graphics, and then the experiments were completed for that parameter.

3. Results and Discussions

In this study, the pressure changes due to water hammer that occurred because of the closure of a ball valve via a pneumatic actuator were examined. The data obtained from experiment setting are presented in relation to flow velocity values in Figures 2, 3 and 4.

Tab. 1: Flow rate and velocity values.

Flow Rates	**Flow Velocity Values**
0.3 m^3/h	***0.066 m/s***
0.5 m^3/h	***0.111 m/s***
0.7 m^3/h	***0.155 m/s***

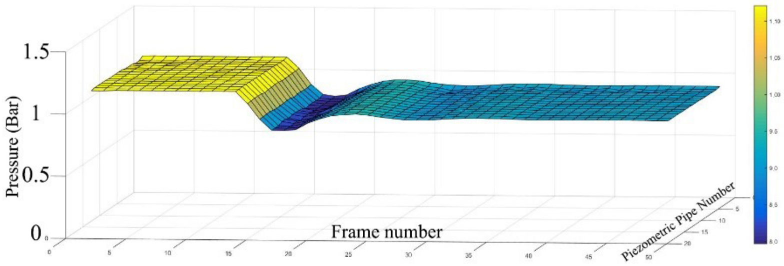

Fig. 2: Time-related pressure change for 0.066 m/s flow velocity.

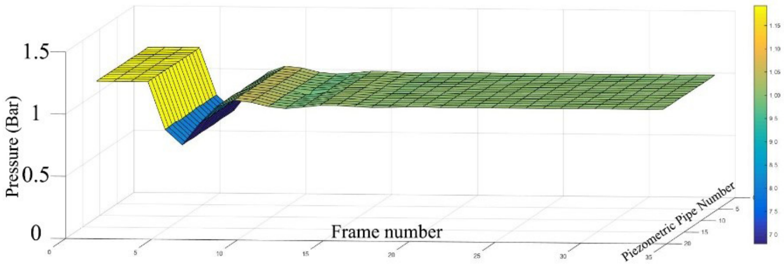

Fig. 3: Time-related pressure change for 0.155 m/s flow velocity.

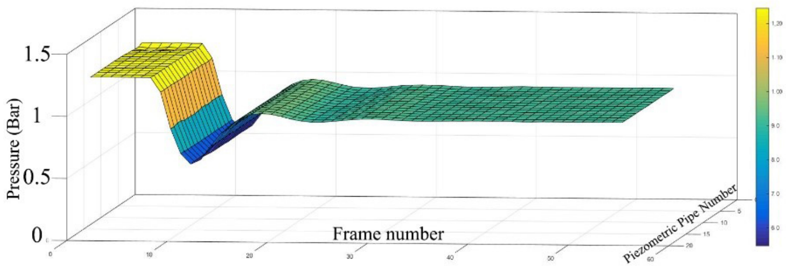

Fig. 4: Time-related pressure change for 0.111 m/s flow velocity.

Considering the results obtained as a result of experiments, it can be seen that the pressure changes occurring as a result of water hammer due to increase in flow velocity because of liquid flow rate has increased linearly. In 3D time-related graphics, the flow velocity-related changes in pressure fluctuations are clearly seen.

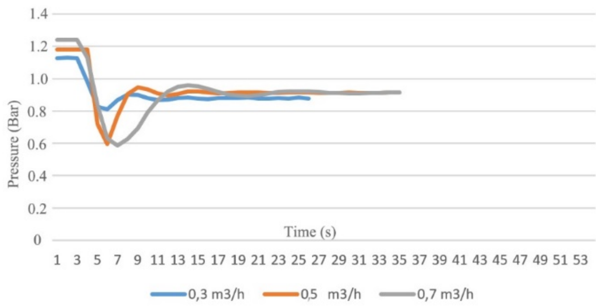

Fig. 5: Comparison of time-related pressure changes.

In Figure 5, the results obtained at 3 different flow velocities are presented in a single graphic. In this graphic, it is obviously seen that the duration of damping the pressure waves occurring due to water hammer increased in proportion to increase in flow velocity. The flow velocity's effect on occurrence of water hammer was analyzed, and the measures that can be made for decreasing the influence of water hammer are as follows:

• The water flow velocity in pipe should be decreased; the diameter of pipe should be increased for this purpose.

• Wave speed (a) should be decreased; for this purpose, PVC or polyethylene pipe should be used when possible.

• Water pressure regulator should be added into installations carrying high-pressure and the valves should be fixed via clamp (Kavurmacıoğlu & Karadoğan 2003).

The flowmeter used in this study has the accuracy tolerance of ±1%. Moreover, the data obtained from image processing method were analyzed, and it was found that the error rate in translating the images into numeric values was ±5%. Since it is not further improve the measurement differences originating from these situations in laboratory environment, they were ignored.

References

Gürsel, T.K., & Çağlar A. (2014) "Küresel Valflerde Su Darbesi Etkisinin İncelenmesi." SDÜ Mühendislik Bilimleri ve Tasarım Dergisi 2.2 : 91-101.

Martin C.S., (2000) "Waterhammer potential in pumps and systems", School of Civil and Environmental Engineering, Georgia Institute of Technology, Atlanta GA, U.S.A.

Wylie E. B., (1993) "Fluid Transients In Systems", Prentice Hall, Englewood Cliffs, NJ 07632.

Menabrea, L.F., (1885) Note sur les effects de choc de l'eau dans les conduites, C. R. Hebd.Seances Acad. Sci. 47, July–Dec., . 221–224.

Michaud, J., (1878) Coups de be´lier dans les conduites. E ´ tude des moyens employe´s pour en atteneur les effects, Bull. Soc. Vaudoise Ing. Arch. 4~3, . 56–64, 65–77.000

Weston, E.B., (1885) Description of Some Experiments Made on the Providence, RI Water Works to Ascertain the Force of Water Ram in Pipes, Trans. Am. Soc. Civ. Eng. 14, p. 238.

Carpenter, R.C., (1893) Experiments on Waterhammer, Trans.ASME, 15.

Frizell, J.P., (1898) Pressures Resulting from Changes of Velocity of Water in Pipes, Trans. Am. Soc. Civ. Eng. 39,1–18.

Joukowski, N.E., (1898) Memoirs of the Imperial Academy Society of St. Petersburg, 9~5 ~Russian translated by O Simin 1904,Proc. Amer. Water Works Assoc. 24, . 341–424.

Gibson, A.H., (1908) Water Hammer in Hydraulic Pipelines. Archibald Constable and Co. Ltd., London.

Kavurmacıoğlu, L., & Karadoğan, H., (2003) "Su Darbesi Projelendirme Hataları, VI. Ulusal Tesisat Mühendisliği Kongresi ve Sergisi Bildiriler Kitabı, MMO Yayın No: E/2003/328-1, 37-45.

Padmanabhan, C., Kochupillai, J., & Ganesan, N., (2004) "A new finite element formulation based on the velocity of flow for water hammer problems", Indian Institute of Technology Madras, Chennai 600 036, India.

Bakeer, R. M., Barber, M. E., Sever, V. F., & Boyd, G. R., (2004) "Effect of close-fit sliplining on the hydraulic capacity of a pressurized pipeline", Department of Civil and Environmental Engineering, Tulane University, New Orleans, LA 70118, U.S.A

Almeida, A. B., & Ramos, H., (2002) "Parametric analysis of water-hammer effects in small hydro schemes", Department of Civil Engineering, Instituto Superior Téchnico, 1049-001 Lisboa, Portugal.

22nd International Conference
ENGINEERING MECHANICS 2016
Svratka, Czech Republic, 9 – 12 May 2016

ANALYSIS OF CAUSES OF FALSE-NEGATIVE EVALUATION OF EUSAMA METHODOLOGY FOR SUSPENSION ASESSMENT

M. Klapka*, I. Mazůrek, O. Macháček*****

Abstract: *The article deals with recent failures of the EUSAMA methodology which is used for non-destructive testing of the car chassis without disassembling. On simulated data, there is performed an analysis of false-negative evaluation of car condition which occurs often on cars in actually good technical shape. High tire stiffness in combination with small axle load are identified as main causes of the methodology failures. Such combination of technical features is common for car chassis designed according contemporary trends in automotive industry. Adjustment of the too high excitation stroke is suggested as possible future recourse. Therefore the testing conditions should comply with contemporary quality of the road surfaces.*

Keywords: Technical diagnostics of vehicles, car suspension, EUSAMA methodology.

1 Introduction

The shock absorber is an important design element of the car chassis. It has appeared on cars in various design forms since their "birth." Nowadays, the shock absorber has at least the same importance to ensure good vehicle adhesion and crew comfort as quality of the tires or brake system have. According Calvo (2008) or Coylu (2013), worn shock absorber significantly prolongs the braking distance, causes much faster wear of other chassis parts etc. Therefore, recent pressure to perform regular technical diagnostics of car suspension condition is fully understandable.

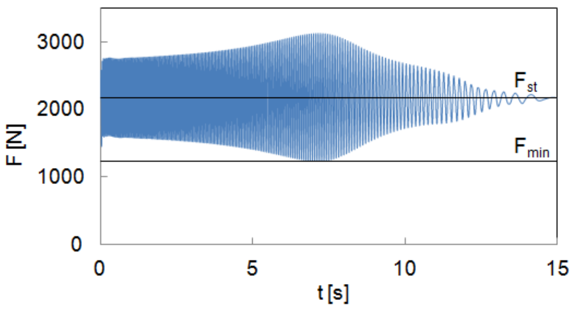

Fig. 1 Pressure force - time response during EUSAMA test procedure

These testing devices evaluate the adhesion of the wheel to the oscillating platform according to the EUSAMA methodology. This methodology was introduced by "European Shock Absorber Manufacturers Association" in the '70s last century. The wheel of the car is placed on the vertically oscillating platform. Stroke of the platform oscillations is 6 mm and it simulates road roughness. Wheel pressure force to the platform is acquired during test. Frequency of platform oscillation decreases gradually from 25 Hz to stop after the driving motor is switched off. Main goal of the test is to acquire the wheel pressure force time response during whole testing interval – i.e. frequency range. EUSAMA value is determined as division

* Ing. MilanKlapka, Ph.D.:Institute of Machine and Industrial Design, Brno University of Technology;Technická 2; 616 69,Brno; CZ, klapka.m@fme.vutbr.cz

** Assoc. Prof. Ivan Mazůrek, CSc.: Institute of Machine and Industrial Design, Brno University of Technology;Technická 2; 616 69,Brno; CZ, mazurek@fme.vutbr.cz

*** Ing. Ondřej Macháček.:Institute of Machine and Industrial Design, Brno University of Technology;Technická 2; 616 69,Brno; CZ, y126193@stud.fme.vutbr.cz

of the minimum pressure force F_{min} which acts between the wheel and the oscillating platform and the static force F_{st} which acts on the platform at rest (figure 1). The minimum permissible value of 20 % relative downforce is recommended by EUSAMA (1976) prescription.

2 Formulation of problem

The EUSAMA methodology is able to directly measure mechanical grip of the examined wheel which is huge advantage. The criterion of the wheel relative pressure to the road is easy to understand and quantifiable. However, a new phenomenon arose in the last decade when the test results were negative for a brand new cars. The faulty assessment of the rear axle suspension of the FIAT 500 car model is a typical representative of this new category of phenomenon as mentioned by Tassiaux (2009) and Winter (2010). The assessed vehicle could be declared as unfit for purpose provided that too low EUSAMA value is obtained through the test.

3 Objectives

Main goal was to elaborate the analysis of most serious causes of frequent negative EUSAMA evaluation occurrences of vehicles otherwise in good technical condition. Knowledge obtained by analysis is invaluable to further solution of the problem.

4 Methods

Selected method of solution was based on analysis of simulated dataset which imitates signals obtained by real tests at testing facilities. An explicit linear mathematical model was used to enable calculation of large number of possible input variants. There was generated curve which describes response of dynamic force acting on the oscillating platform $F_{dyn}(\omega)$ in dependency on the angular frequency (ω). Similar response curve was generated for phase shift $\Phi(\omega)$ of this force delay to excitation stroke in dependency on angular frequency. Both curves were generated from the transfer function of excitation stroke and tire deformation for each of the simulated chassis variant.

4.1 The simulation model

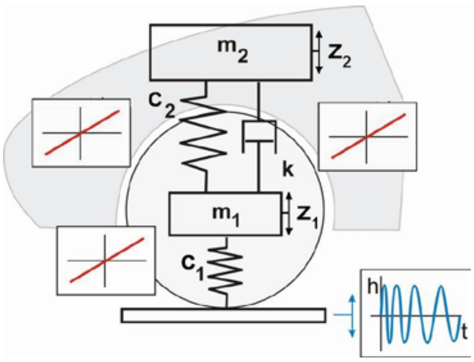

Fig. 2 ¼ model of the wheel suspension on EUSAMA testing rig

Analysis of inaccurate diagnostics results was made with ¼ simulation 2 DOF (degree of freedom) model of the wheel suspension similar to Malmedahl (2005), Simms (2002) and Sun (2002) ones, which describes motion of the masses excited by tester (figure 2). The oscillating masses m_1 and m_2 are separated by springs c_1, c_2 and by the damper k. Motion of masses can be described by transfer function between the excitation platform stroke $h(\omega)$ and the force of adhesion $F_{dyn}(\omega)$:

$$W_F(\omega) = \frac{F_{dyn}(\omega)}{h(\omega)} = c_1 \cdot \left| \frac{c_1}{c_1 + c_2 + i\omega \cdot k - \omega^2 \cdot m_1 - \dfrac{(c_2 + i\omega \cdot k)^2}{c_2 + i\omega \cdot k - \omega^2 \cdot m_2}} - 1 \right| \tag{1}$$

EUSAMA relative downforce is defined as the ratio of the minimum force acting on the platform during its oscillating motion and the static force acting on standstill platform:

$$EUSAMA = \frac{F_{\min}}{F_{st}} = \frac{F_{st} - F_{dyn\max}}{F_{st}} = \frac{g \cdot (m_1 + m_2) - F_{dyn\max}}{g \cdot (m_1 + m_2)} \tag{2}$$

The damping ratio is usually used to evaluate damping efficiency of linear dampers in dynamics branch. It is possible to determine damping ratio of the unsprung mass of the wheel suspension (fig. 2) which is given by equation:

$$\xi_1 = \frac{k}{2 \cdot \sqrt{m_1 \cdot (c_1 + c_2)}} \tag{3}$$

According to the literature by Reimpell (1996), Tsymberov (1996) and Dixon (2007), minimum damping ratio of sprung mass should be $\xi_1 = 0.1$.

5 Results and discussion

The test procedure was simulated for large dataset of the wheel suspensions with respect to current designs of suspension and chassis of cars. Overview of the range of simulated input variables is as follows: unsprung mass: m_1 = 20 to 60 kg; ratio of masses m_2 and m_1: $p_m = m_2/m_1 = 3$ to 13; static deformation of tire: $sbt = g.(m_1+m_2)/c_1$ = 7.5 to 22.95 mm; natural freq. of mass m_2: $f_2 = \sqrt{(c2/m2)}/2\pi$ = 0.95 to 2.2 Hz; damping constant: k = 100 to 2000 Ns/m.

Calculation of the transfer function $W_F(\omega)$ in simulation model enables to obtain simulated values of EUSAMA relative downforce very efficiently. Relative downforce was calculated for 11164 chassis variations using ¼ suspension model and equation (2). In figure 3, there are plotted obtained EUSAMA values proportionally to input damping ratio (each dot represents one chassis design). Unfortunately, used linear model is unable to simulate the tire's ability to flex only in pressure region. Therefore, simulated adhesion values could have negative value (in fact, they cannot fall below 0 in reality).

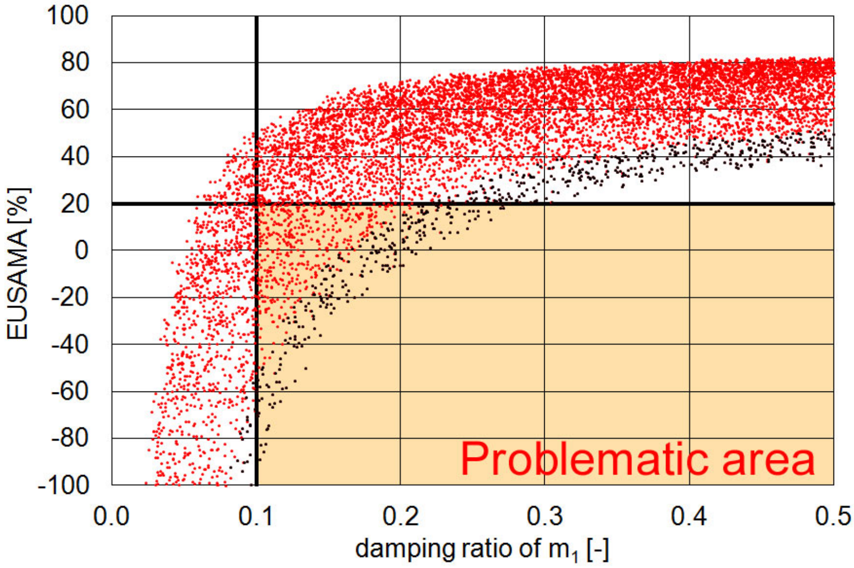

Fig. 3 Simulated EUSAMA test procedure (excitation stroke 6 mm)

Two problematic areas of the resulting values are depicted in figure 3. First group of problematic results contains EUSAMA value ≥ 20%, although ξ_1 <0.1. Second group of suspicious results contains EUSAMA values <20% despite $\xi_1 \geq 0.1$. The first group can be put aside as it is on side of high adhesion safety. On the contrary second group of results requires urgent solution. Among all simulated variants, there were 9346 of simulated test procedures with input value of the damping ratio of the unsprung mass above 0.1. However, 794 of such simulations ends with EUSAMA value below 20%, which is roughly a tenth of them. Thus, it can be concluded that inaccurate diagnostic result of the methodology is an objective phenomenon which occurs thanks to interference of several partial effects. These are the most important of them:

•High tire stiffness (low profile number, runflat design)

•Low load on axle (especially non driven rear axles)

It could be assumed that vast majority of cars which does not pass the test criteria was equipped with tires with higher stiffness. This assumption is based on many available recordings of routine test performed by PTI (periodical technical inspection) facilities. This rising trend is mainly based on the recent demands to reduce rolling resistance and thus acoustic noise generated by tires. Black points in figure 3 represents results of simulation with smallest ratio of axle load and stiffness of tire $(m_1+m_2)/c_1$. Obviously, the assessment of the relative downforce is affected severely by value of this ratio at most.

6 Conclusions

Essentially, the EUSAMA methodology simulates driving on a road with certain surface roughness. However, it was created in the '70s last century when general condition of the roads was completely different compared to the present. With some exaggeration one can say that quality of driving on modern roads approaches conditions on the racetrack. Frequently, the designers of the passenger car chassis are therefore using similar designs of suspensions as competition cars have. There are clearly visible trends such as to equip low profile tires, increasing of the tire stiffness, reduction of suspension stroke and increasing overall efficiency of suspension.

The situation requires urgent solution regarding the perspective of users and producers of the EUSAMA principle testing devices. We suggest that the possible solution is to adjust the testing hardware. Thus the test conditions should better reflect the current general quality of road surfaces (it means reduction of the excitation stroke). Such solution should lead to a significant reduction of errors in assessment of the technical condition of the car suspension occurring especially within contemporary cars. Therefore, it seems that further study of effect of excitation stroke value to the relative downforce assessment is essential in future. Provided such analysis is available there would be possible to determine the new value of the excitation stroke for testing.

Acknowledgement

The research leading to these results has received funding from the MEYS under the National Sustainability Programme I (Project LO1202) and with support of the the BUT grant nr. FSI-S-14-2329.

References

Calvo, J. A., Díaz, V. & San Román, J. L. (2008) Influence of shock absorber wearing on vehicle brake performance. International Journal of Automotive Technology, 9,4, p. 235-240. DOI: 10.4028/3-908451-21-3.235.

Dixon, J. C. (2007) The shock Absorber Handbook, SAE Inc, Warrendale, PA.

EUSAMA - Recommendations for a performance test specification of an "on car" vehicle suspension testing system, (1976) TS-02-76.

Koylu, H. & Cinar, A. (2013) Dynamical investigation of effects of variable damper settings induced brake pressure oscillations on axle and wheel oscillations during ABS-braking based on experimental study. Meccanica. 48,5, p. 1093-1115. DOI: 10.1007/s11012-012-9654-y.

Malmedahl, G., et al. (2005) Analysis of automotive damper data and design of a portable measurement system, in SAE 2005 World Congress & Exhibition, no. 2005-01-1043. SAE International, 2005.

Reimpell, J., & Stoll, H. (1996) The Automotive Chassis: Engineering Principles, SAE Inc. Warrendale, PA, USA.

Simms, A., & Crolla, D. (2002) The Influence of Damper Properties on Vehicle Dynamic Behavior, SAE Paper, 2002-01-0319.

Sun, T., Zhang, Y. & Barak, P. (2002) Quarter Vehicle Ride Model, SAE Paper, 2002-01-1581.

Tassiaux, I., Question de Madame la Députée Isabelle Tasiaux-De Neys à Monsieur Etienne Schouppe, Secrétaire d'Etat à la Mobilité, (2009) concernant les problèmes de passage au contrôle technique de la Fiat 500., Available at http://tasiaux.exxoss.com/wp-content/uploads/2010/02/contr%C3%B4le-technique-Fiat.pdf.

Tsymberov, A. (1996) Improved Non-Intrusive Automotive Suspension Testing Apparatus with Means to Determine the Condition of the Dampers. SAE Technical Paper., č. 26.

Winter, S. (2010) Analysis of the influence of the Eusama-Value on the vehicle dynamic performance. In: FKA [online].

22nd International Conference
ENGINEERING MECHANICS 2016
Svratka, Czech Republic, 9 – 12 May 2016

STATISTICAL ANALYSIS OF PARAMETERS OF RAIL VEHICLES

L. Knopik*, K. Migawa, P. Kolber*****

Abstract: *In this paper we propose a mixture of two different normal distributions to model heterogeneous of rail vehicles parameters. Maximum likelihood estimations of the parameters of mixture are obtained by using expectation algorithm. Illustrative examples based on real data (speed, number of axles, length of train, number of railway carriage and mass of train) are given.*

Keywords: Statistical analysis, mixture of distributions, rail vehicles, speed of train, mass of train, maximum likelihood method, expectation algorithm

1. Introduction

Monitoring the values of parameters of rail vehicles is a very important factor of safety in rail transportation. Values of these parameters are collected by DSAT system. This system screens the values of parameters of rail vehicles with various types of construction of bearing axles and train brake. It is applicable to various diameters of the wheels. System DSAT is installed on a straight rail line. System DSAT finds the following symptoms:

improvement of temperature of a bearing axle,
no working brakes – function,
exceeded pressure on axle or exceeded linear pressure.
deformation of surface wheels – function.

The system DSAT registers the following values of parameters:

speed [km/h],
number of axles,
length of train [m],
number of railway carriage,
mass of train [t].

The values of these parameters are the heterogeneous sets. It is a result of the fact that the rail vehicles moving on the analyzed path execute different tasks, such as transportation of people and cargo. In this paper, we use the mixture model for investigating a complex distribution of parameters of the rail vehicles. The mixture model has a wide variety of applications in technical and life science. Because of their usefulness as extremely flexible method of modeling, finite mixture models have continued to receive increasing attention over the recent years, from both practical and theoretical points of view, and especially for lifetime distributions. The problem application of the mixture of distributions to lifetime analysis is considered by Knopik (2010). Fitting the mixture distributions can be handled by variety of techniques, this includes graphical methods, the methods of moments, maximum likelihood and Bayesian approaches (Titterington et al., 1985; McLachan & Basford, 1988; Lindsay, 1995; McLachlan & Peel, 2000; Furhwirth-Schnatter, 2006). Now extensive advances have been introduced in the fitting of the mixture models especialy via maximum likelihood method. Among all, the maximum likelihood method becomes the first preference due to the existence of an associated statistical theory. The maximum

* Assoc. Prof. Leszek Knopik, PhD.: Faculty of Management, UTP University of Science and Technology, Fordońska Street 430, 85-790 Bydgoszcz, Poland, knopikl@utp.edu.pl

** Assoc. Prof. Klaudiusz Migawa, PhD.: Faculty of Mechanical Engineering, UTP University of Science and Technology, Prof. S. Kaliskiego Street 7, 85-789 Bydgoszcz, Poland, klaudiusz.migawa@utp.edu.pl

*** RNDr. Piotr Kolber, DSc.: Faculty of Mechanical Engineering, UTP University of Science and Technology, Prof. S. Kaliskiego Street 7, 85-789 Bydgoszcz, Poland, piotr.kolber@utp.edu.pl

likelihood method is making by expectation maximization algorithm (EM algorithm). The key property of the EM algorithm has been established in by Dempster et al. (1977) and McLachan & Krishan (1997). The EM algorithm is a popular tool for solving maximum likelihood problems in the context of a mixture model. We will focus on maximum likelihood techniques in this paper since the estimates tend to converge to true parameters values under general conditions. Maximum likelihood estimation procedures seek to find the parameters values that maximize the likelihood function evaluated at the observations. The purpose of this paper is to show that the mixture of the different normal distributions is the appropriate model distribution for the heterogeneous data of value of rail vehicle parameters.

2. Model of distribution of parameters

The fact that the analyzed sets are heterogeneous caused that in order to analyze the probability distribution of parameters of the rail vehicles is not applicable to the various distributions such Weibull and gamma. In this paper, we analyze two-component mixture distribution of distributions as the distribution of examined parameters. Let X_1 and X_2 be the independent random variables with the density functions $f_1(x)$ and $f_2(x)$, the cumulative distribution functions $F_1(x)$ and $F_2(x)$, the reliability functions $R_1(x)$ and $R_2(x)$, the failure rate function (hazard function) $\lambda_1(t)$ and $\lambda_2(t)$. Reliability function of the mixture X_1 and X_2 is described by the following formula:

$$R(x) = p\, R_1(x) + (1-p)\, R_2(x) \tag{1}$$

where p is the mixing parameter and $0 \leq p \leq 1$.

The failure rate function of the mixture can be written as the mixture (Knopik, 2010):

$$\lambda(t) = \omega(t)\, \lambda_1(t) + (1 - \omega(t))\, \lambda_2(t) \tag{2}$$

where $\lambda(t) = f(t) / R(t)$, $\omega(t) = pR_1(t) / R(t)$. Understanding the shape of the failure rate function is important in reliability theory and practice.

The basic problem is to infer about unknown parameters, on the basis of a random sample of size n on the observable random variable X. The first opinion of the data from the DSAT system shows that the mixture of two normal distributions is a proper model for analyzed parameters. The density function of the mixture of two normal distributions can be written in the following form:

$$f\left(x; m_1, m_2, \sigma_1^2, \sigma_2^2, p\right) = \frac{p}{\sqrt{2\pi\sigma_1^2}} \exp[-\frac{(x-m_1)^2}{2\sigma_1^2}] + \frac{1-p}{\sqrt{2\pi\sigma_2^2}} \exp[-\frac{(x-m_2)^2}{2\sigma_2^2}] \tag{3}$$

We will estimate five parameters $m_1, m_2, \sigma_1, \sigma_2$, p of the density (3). To estimate parameters $\Theta = (m_1, m_2, \sigma_1^2, \sigma_2^2, p)$ we will use the likelihood method (see Hasti et al. 2001). The likelihood function for the mixture (3) is:

$$L\left(x_1, x_2, ..., x_n; m_1, m_2, \sigma_1^2, \sigma_2^2, p\right) = \prod_{i=1}^{n} f(x_i : m_1, m_2, \sigma_1^2, \sigma_2^2, p) \tag{4}$$

We compute the first partial derivative of the logarithm of likelihood function:

$$\frac{\partial \ln L}{\partial m_1} = \sum_{i=1}^{n} \left(\frac{1}{A} \frac{p}{\sqrt{2\pi\sigma_1^2}} \exp[-\frac{(x_i-m_1)^2}{2\sigma_1^2}] \times \frac{(x_i-m_1)}{\sigma_1^2} \right) = 0 \tag{5}$$

$$\frac{\partial \ln L}{\partial m_2} = \sum_{i=1}^{n} \left(\frac{1}{A} \frac{1-p}{\sqrt{2\pi\sigma_2^2}} \exp[-\frac{(x_i-m_2)^2}{2\sigma_2^2}] \times \frac{(x_i-m_2)}{\sigma_2^2} \right) = 0 \tag{6}$$

$$\frac{\partial \ln L}{\partial \sigma_1^2} = \sum_{i=1}^{n} \left(\frac{1}{A} [-\frac{p}{2\sqrt{2\pi}} (\sigma_1^2)^{-\frac{3}{2}} \exp[-\frac{(x_i-m_1)^2}{2\sigma_1^2}] + \frac{p}{\sqrt{2\pi\sigma_1^2}} \exp[-\frac{(x_i-m_1)^2}{2\sigma_1^2}] \frac{(x_i-m_1)^2}{2(\sigma_1^2)^2}] \right) = 0 \tag{7}$$

$$\frac{\partial \ln L}{\partial \sigma_2^2} = \sum_{i=1}^{n} \left(\frac{1}{A} [-\frac{p}{2\sqrt{2\pi}} (\sigma_2^2)^{-\frac{3}{2}} \exp[-\frac{(x_i - m_2)^2}{2\sigma_2^2}] + \frac{1-p}{\sqrt{2\pi\sigma_2^2}} \exp[-\frac{(x_i - m_2)^2}{2\sigma_2^2}] \frac{(x_i - m_2)^2}{2(\sigma_2^2)^2}] \right) = 0 \quad (8)$$

$$\frac{\partial \ln L}{\partial p} = \sum_{i=1}^{n} \left(\frac{1}{A} (\frac{1}{\sqrt{2\pi\sigma_1^2}} \exp[-\frac{(x_i - m_1)^2}{2\sigma_1^2}] - \frac{1}{\sqrt{2\pi\sigma_2^2}} \exp[-\frac{(x_i - m_2)^2}{2\sigma_2^2}]) \right) = 0 \quad (9)$$

where $A = f(x_i; m_1, m_2, \sigma_1^2, \sigma_2^2, p)$.

To find the maximum log – likelihood function, we set the first partial derivative equal to zero. In finite mixture model, the EM algorithm has been used as an effective method to find maximum likelihood parameters estimation.

3. Real data set

In this chapter, we will estimate the parameters m_1, m_2, σ_1^2, σ_2^2, p of the mixture of two normal distributions for the random variable X_1 – speed of train, X_2 – number of axles, X_3 – length of train, and X_4 – mass of train. By λ we describe the value of the goodness of fit statistics Kolmogorov-Smirnov. We used procedure (EM algorithm) given for special case of normal mixtures by Hastie et al. (2001). The estimated parameters, K-S test statistics and p-values for four random variables are given in Table 1. All the considered the parameters of rail vehicles shown good conformity with the empirical distributions and the mixture distributions.

Tab.1: Values of parameters of mixtures

Random variable	Parameters of mixture					goodness of fit statistic λ-KS	p-value
	m_1	m_2	σ_1	σ_2	P		
X_1 – speed	51.27	78.11	7.82	2.69	0.531	0.3780	0.99
X_2 – axles	37.60	151.49	12.57	43.10	0.531	0.6102	0.85
X_3 – length	191.92	599.77	72.52	109.84	0.547	0.9153	0.56
X_4 – mass	381.66	2051.8	39.21	788.59	0.738	0.8543	0.53

The graphs of the empirical distribution functions (Fe) and the mixture distribution function (Ft) are shown in Figure 1.

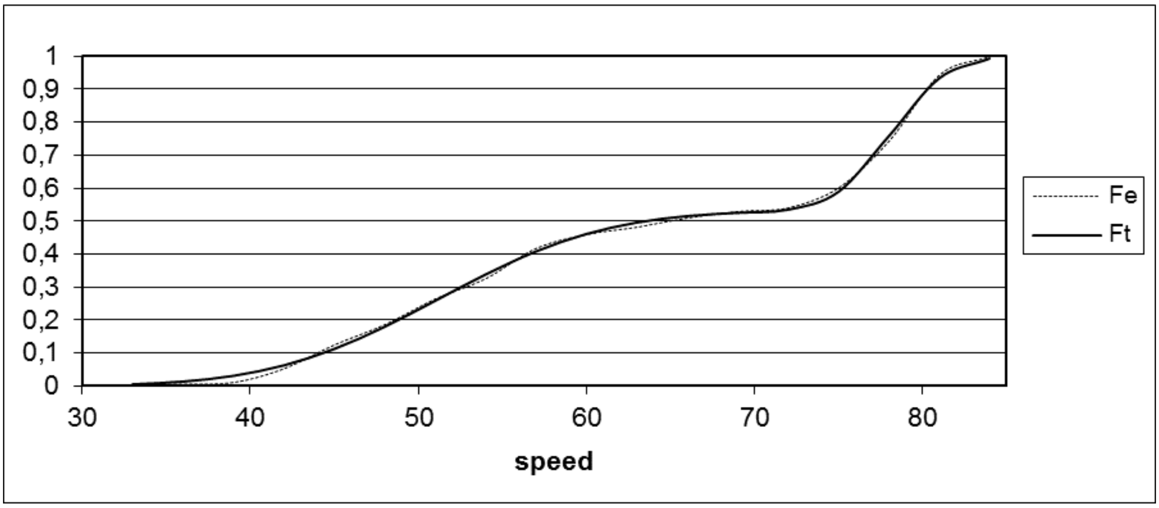

Fig. 1: Empirical distribution function and distribution function of mixture model for number of the speed

A graphical comparison of empirical distribution function and distribution function of the mixture model for number of axles is given in Figure 2.

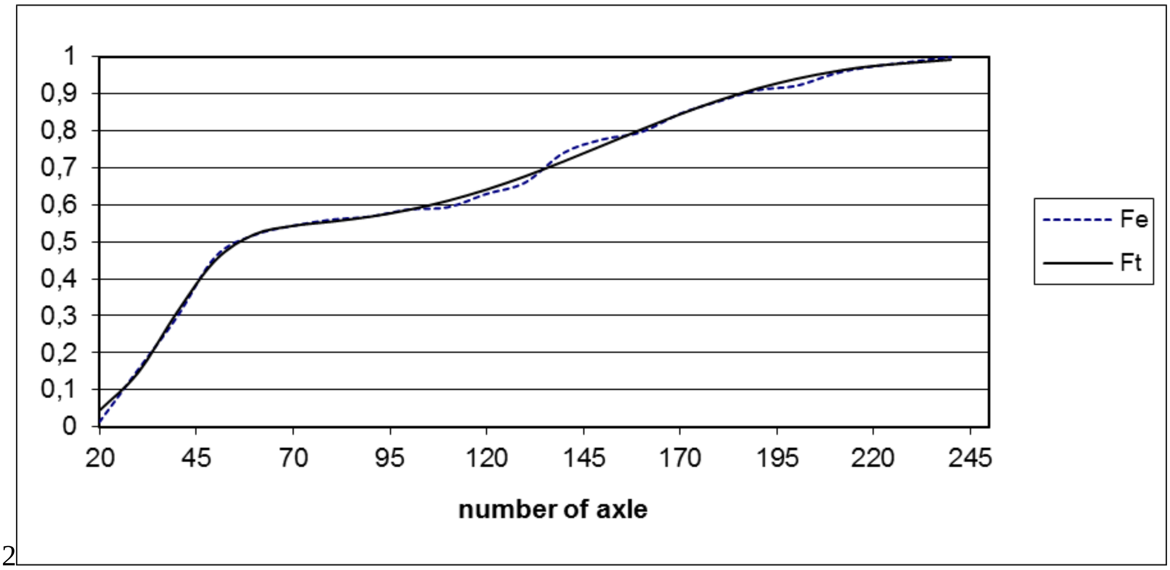

Fig.2: Empirical distribution function and distribution function of mixture model for number of axles

4. Conclusions

We use the mixture of two-normal distributions for investigating complex probability distributions of parameters of the rail vehicles. It is shown that the mixture of the different normal distributions is useful for exploring the complex distributions. The probability distributions of all measured system parameters (speed, number of axles, length of rail vehicle, mass) are compatible with the calculated mixture of two normal distributions. Knowledge of the probability distributions of the load parameters of the railway line is useful for the design of the modernization of these lines. Lastly we fit the two-component mixture normal distribution to data set using EM algorithm to maximize the likelihood function.

References

Dempster, A.P., Larid, N.M. & Rubin, D.B. (1977) Maximum likelihood from incomplete data via the EM algorithm. Journal Statistical Society, Series B, 39, pp. 1-38.

Hastie, T., Tibshirani, R. & Friedman, J. (2001) The Elements of Statistical Learning: DataMining, Inference and Prediction. Springer Verlag.

Fruhwirth-Schnatter, S. (2006) Finite Mixture and Markov, Switching Models. Springer Verlag, New York.

Knopik, L. (2010) Mixture of distributions as a lifetime distribution of a technical object. Scientific Problems of Machines Operation and Maintenance, Vol. 162, No. 2, pp. 53-61.

Lindsay, B.G. (1995) Mixture Model: Theory, Geometry and Applications. Harward Institute of Mathematical Statistics.

MacLachan, G. J. & Basford, K. E. (1988) Mixture Model: Inference and Applications to Clustering. Marcel Dekker, New York.

MacLachlan, G. & Peel, D. (2000) Finite Mixture Models. John Wiley & Sons, New York.

MacLachan, G.J. & Krishan, T. (1997) The EM algorithm and extensions. John Wiley & Sons, New York.

Titterington, D.M., Smith, A.F.M. & Makov, U.E. (1985) Statistical Analysis of Finite Mixture Distribution. John Wiley & Sons, New York.

22nd International Conference
ENGINEERING MECHANICS 2016
Svratka, Czech Republic, 9 – 12 May 2016

DESIGN OF SINGLE LAP JOINTS WITH MILD STEEL ADHERENDS

İ. Kocabaş[*], A. Özdemir[**], P. Svanda[***]

Abstract: *Adhesively bonded single lap joints are a candidate structure fastening technique to riveted, welded and bolted joints, attaining a better load transfer and more uniform stress distributions. It is quite important to establish a relationship between static strength of a single lap joint and design parameters such as geometrical parameters, material response, type of loading and etc. This paper presents a conceptual design methodology for single lap joints with mild steel adherend S255 considering geometrical and material parameters. In order to perform this task, ductile (Veropal Super HE-20) and brittle (Carboresin) two component structural epoxy adhesives are implemented to examine influence of material behavior. Single lap joints are manufactured at various overlap lengths and undergone simple uni-axial tensile tests to identify static tensile strengths. Then a numerical model is created in a commercial finite element package program (ABAQUS™) to make a comparison between experimental and numerical failure loads, which implements well-known maximum value criteria for both adhesive and adherend failure. The results express that the material response and overlap length plays a substantial role in the design stage of bonded structures up to a certain point. Consequently, strength of a single lap joint is no longer dependent on increase of overlap length at which the failure mechanism is dictated by adherend yielding.*

Keywords: Single lap joint, Epoxy adhesive, Static strength, Mild steel, Finite element method

1. Introduction

Adhesively bonded joints are practical, economical and easy to manufacture and thus have been commonly implemented in a variety of engineering applications including railway, automotive, aircraft and other mechanical industries. The strength estimations and failure analysis of adhesively bonded structural joints in numerous applications are critical point of interest. For the prediction of failure loads of single lap joints, geometrical design parameters such as overlap length, adhesive and adherend thickness, type of loading and environmental conditions are critical issues as much as the material behavior of both adhesive and adherend.

For the case of low strength steel, adherend yielding occurs during the joint loading and the interpretation of the joint failure mechanisms is radically different from that seen with high strength (elastic) steel adherends (da Silva et al., 2013). Adherend yielding often occurs in engineering structures where metals such as aluminum and mild steel (automotive) are used (Harris JA and Adams RD., 1984). There are many researchers in the literature that include adherend yielding using finite element (FE) analysis with a continuum mechanics approach (Dorn L and Liu W., 1993), or alternative tools such as cohesive zone modelling (Zhao X, et al., 2011). It was first recognized by Hart-Smith (Zhao X, et al., 2011), Adams et al. (Clarke JD and Mcgregor IJ., 1993), (Grant et al., 1981) and da Silva et al. (Hunston DL. et al. 1984 and Duan K. et al., 2004) that adhesive yielding could be rather simple and solely controlled by adherend yielding.

This paper aims to contribute design of the single lap joints considering the effect of overlap length and material response (ductile or brittle adhesive). A simple failure theory based on maximum equivalent stress and strain values is presented to evaluate failure loads of the single lap joints under uni-axial tensile

[*] İbrahim Kocabaş, M.Sc.: Jan Perner Transport Faculty, Pardubice University, Studentska 95, 53009 Pardubice; CZ, ibrahimkocabas@anadolu.edu.tr

[**] Alp Özdemir, M.Sc.: Jan Perner Transport Faculty, Pardubice University, Studentska 95, 53009 Pardubice; CZ, alpozdemir@anadolu.edu.tr

[***] Assoc. Prof. Pavel Svanda, PhD.: Jan Perner Transport Faculty, Pardubice University, Studentska 95, 53009 Pardubice; CZ, Pavel.Svanda@upce.cz

loading. It is quite advantageous that the presented approach only requires such mechanical properties to estimate failure strength, which can be obtained from a basic stress-strain diagram of corresponding bulk samples of adhesive and adherend.

2. Material and Methods

2.1. Materials

Two different types of structural epoxy adhesive, Veropal Super HE-20 (ductile) and Carboresin (brittle), were used to manufacture single lap joints. Adherend material was selected to be S255 mild steel with a low yielding strength of 255 N/mm^2 to asses influence of adherend yielding on static strength of single lap joints.

Since the main objective is to evaluate failure mechanism of both adhesive and adherend, the bilinear elastic-plastic material properties are needed. For this case, bi-linear material properties (Tab. 1.) of both adherend and adhesive materials were specified as a result of true stress-strain diagrams of bulk samples. The Poisson's ratio values of adherend, Veropal Super HE-20 and Carboresin are 0.3, 0.34 and 0.28, respectively.

Tab. 1: Mechanical properties of adhesive and adherend materials.

	Modulus of elasticity, E (MPa)	Yield Strength, S_y (MPa)	Tensile strength, S_u (MPa)	Elongation at break, ε_f (%)
Mild Steel S255	200000	255	380	20
Veropal Super HE-20	1150	31.2	34.7	12.5
Carboresin	7460	20.9	23.6	1.5

2.2. Joint Geometry

The same geometry as that prescribed in ASTM D1002 were used for manufacture of the joints (Fig. 1.). Single lap joints were manufactured and modelled for four different overlap lengths of 20, 30, 40 and 50 mm, respectively. Two alignment tabs 25mm in length were placed equally at the both ends of each adherend material in order to avoid eccentricity, which creates a high amount of peeling stresses at the joint extremities. The joints were manufactured with an adhesive bond-line thickness of 0.2 mm.

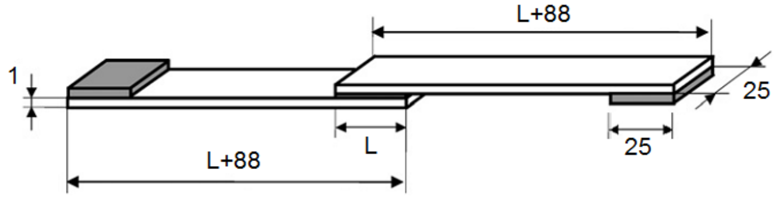

Fig. 1: Single lap joint geometry (Dimensions in mm).

2.3. Numerical Model

The finite element analysis was performed to estimate failure loads and details were covered in this section. The strength of the joint is highly affected by the plasticization of mild steel adherend material since they have quite ductile and relatively low yield stress. Beyond a critical point of adherend material stiffness, the joint strength remains almost the same. For this reason, bi-linear elastic-plastic material model, which is nearly exhibited by low strength mild steels, was implemented in the numerical analysis. In the same way, structural epoxy adhesives are mainly characterized by bi-linear material model. After reaching a critical stress value, the joint can sustain no extra load, global stiffness dramatically decreases then failure is assumed to be completed as a result of limit state consideration. For the numerical analysis, the single lap joint geometry (Fig. 2.) was created in 2-D since the static strength of bonded joints are almost directly proportional to width of the joint. In order to stimulate real case, displacement constraints are applied over the grip lengths and loaded in the uni-axial direction. A refined mesh zones were created at the joint extremities (Fig.2) where shear and peeling stresses attain the highest peak values.

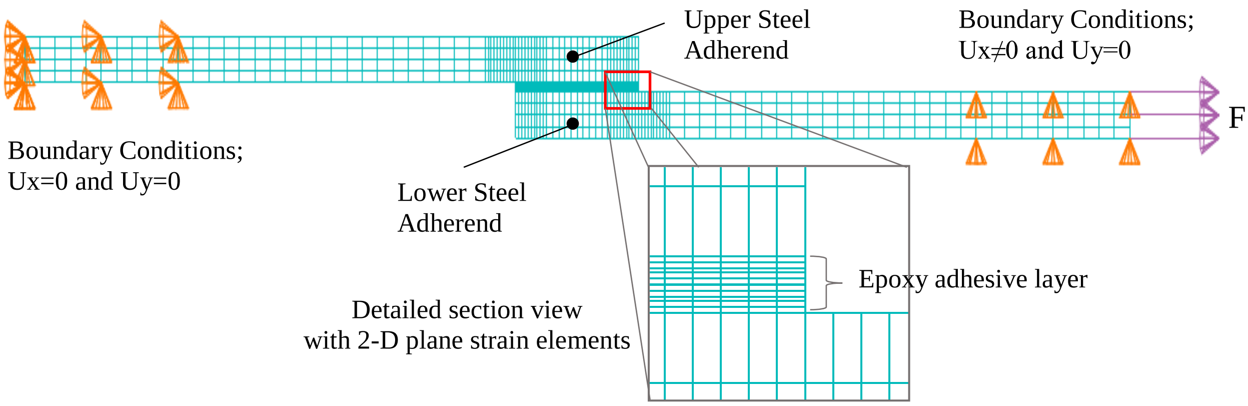

Fig. 2: Two dimensional numerical model of the single lap joint with mesh structure.

An eight node quadrilateral plane strain element was selected with the element dimensions of 0.01x0.1 mm^2 and 0.2x0.25 mm^2 for refined and coarse meshed zones, respectively. For the modelling of metal adherends, classical Von-Mises yield criterion is used with isotropic hardening which is offered by ABAQUS™. Adhesive failure is estimated based on peak values of longitudinal plastic strain together maximum stresses at the local elements for both ductile and brittle yielding mechanisms.

3. Results and Discussion

Experimental tensile test results for both adhesive type are given in Fig.3. It was clearly observed that the failure load remains nearly constant beyond a critical overlap (40mm) for ductile adhesive. Contrary, the joint strength with brittle adhesive is still sensitive to overlap length, for the case of loading under the yielding limit of adherend material. Hence, it may be effective for high strength brittle adhesives.

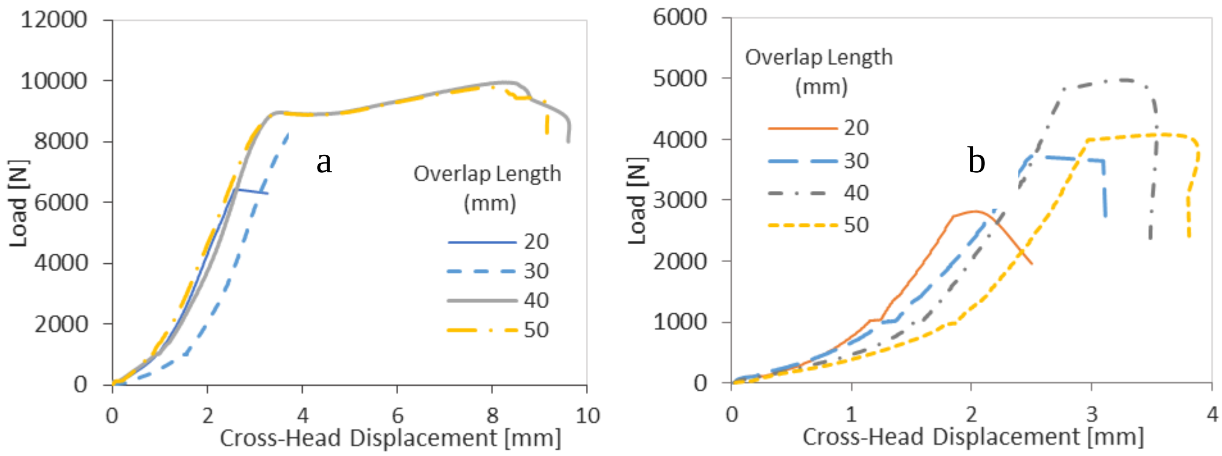

Fig. 3: Experimental load-displacement curves for a) Ductile Veropal HE-20 b) Brittle Carboresin adhesive at various overlap lengths.

In order to replicate the case, a numerical failure approach based on the maximum value of plastic principal strain in longitudinal direction (ε_{11}) was considered as a failure parameter at the critical zones positioned at the interfaces of steel and adhesive gometry. Failure parameter corresponding to 0.12 and 0.015 plastic strain for ductile and brittle adhesive, respectively was utilized. The model is also checked to ensure yielding stress is reached for each load step. Then, the trends of numerical failure load with respect to overlap length is presented (Fig. 4) with the deviations from experimental work.

Deviations of numerical results is found out to be lower than roughly 10% assumed to be in acceptable limits. From both experimental numerical results, strength of the joints with ductile adhesive exihibit an increasing trend upto a critical overlap length of 40mm where adherend yielding appeared then becomes nearly the similar. However, brittle ones have almost linear response with overlap length since the yielding point of

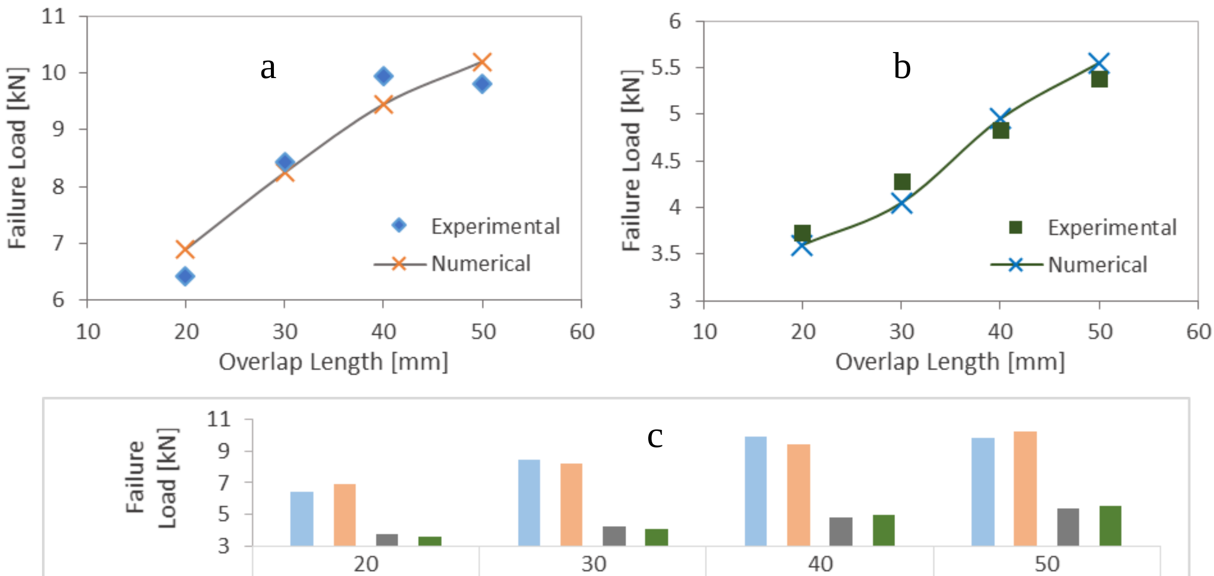

	20	30	40	50
Ex. Ductile	6.437	8.426	9.948	9.816
Num. Ductile	6.9	8.25	9.45	10.2
Ex. Brittle	3.732	4.28	4.83	5.38
Num. Brittle	3.6	4.05	4.95	5.55

Fig. 4: Trends of the experimental and numerical failure loads for (a) Veropal HE-20 ductile, (b) Carboresin brittle adhesive, (c) the discrete failure load values for each configuration.

adherend is not reached. Failure mode of the joints is mainly dictated by interfacial failure mode due to lack of adhesion at the interfaces.

4. Conclusions

It is concluded that the determining of critical overlap length depends on adherend yielding point. Simply, the strength of the brittle joint has emerged a quasi-linear trend with increasing overlap length if the adherend remains in the elastic region. Failure estimation for brittle material behavior is very conservative since the maximum principal strain parameter is very small comparing to ductile material model.

References

Karachalios E.F., Adams R.D., da Silva Lucas F.M.,(2013) Single lap joints loaded in tension with high strength steel adherends. International Journal of Adhesion & Adhesives Vol. 43 pp. 81–95.

Harris JA, Adams RD.,(1984) Strength prediction of bonded single lap joints by the non-linear finite element methods. Int J Adhes Adhes;4:65–78.

Dorn L, Liu W., (1993) The stress state and failure properties of adhesive-bonded plastic/metal joints. Int J Adhes Adhes;13:21–31.

Zhao X, Adams RD, (2011) da Silva LFM. Single lap joints with rounded adherend corners: Stress and strain analysis. J Adhe Sci Technol;25:819–36.

Zhao X, Adams RD, da Silva LFM., (2011) Single lap joints with rounded adherend corners: experimental results and strength prediction. J Adhe Sci Technol;25:837–56.

Clarke JD, Mcgregor IJ., (1993) Ultimate tensile criterion over a zone: a new failure criterion for adhesive joints. J Adhe;42:227–45.

Kinloch AJ, Shaw SJ., (1981) A fracture mechanics approach to the failure of structural joints. In: Kinloch AJ, editor. Developments in adhesives: 2. London: Applied Science Publishers; p. 82–124.

Hunston DL, Kinloch AJ, Shaw SJ, Wang SS., (1984) Characterization of the fracture behavior of adhesive joints. In: Mittal KL, editor. Adhesive joints, formation, characteristics and testing. New York: Plenum Press; p. 789–807.

Duan K, Hu X, Mai Y-W., (2004) Substrate constraint and adhesive thickness effects on fracture toughness of adhesive joints. J Adhe Sci Technol; 18:39–54.

22nd International Conference
ENGINEERING MECHANICS 2016
Svratka, Czech Republic, 9 – 12 May 2016

COMPUTATIONAL HOMOGENIZATION OF FRESH CONCRETE FLOW AROUND REINFORCING BARS

F. Kolařík[*], B. Patzák[**], J. Zeman[***]

Abstract: *Motivated by casting of fresh concrete in reinforced concrete structures, we introduce a numerical model of a steady-state non-Newtonian fluid flow through a porous domain. Our approach combines homogenization techniques to represent the reinforced domain by the Darcy law with an interfacial coupling of the Stokes and Darcy flows through the Beavers-Joseph-Saffman conditions. The ensuing two-scale problem is solved by the Finite Element Method with consistent linearization and the results obtained from the homogenization approach are verified against fully resolved direct numerical simulations.*

Keywords: fresh concrete flow, porous media flow, homogenization, Stokes-Darcy coupling.

1. Introduction

This work is motivated by the computational modeling of self-compacting concrete (SCC). In contrast to the conventional concretes where the aim during its design lies in achievement of desirable compressive strength, SCCs must meet additional rheological requirements, such as higher liquidity, in order to fill in all the possible gaps in the whole form-work while keeping the risk of phase segregation at low level, see (Roussel et al. 2007). For this reason, the focus of the numerical modeling of SCC is not only on the structural, but also on the casting performance, and thus it relies on techniques of computational fluid mechanics.

The constitutive models suitable for structural-scale applications consider concrete as a homogeneous non-Newtonian fluid and the concrete flow can be then efficiently simulated using the Finite Element Method. The efficiency relies on how much details are involved in the computational model. Therefore, sub-scale phenomena can only be accounted for approximately. For example, the effect of traditional reinforcement can be accounted for by heuristic modification of constitutive parameters. This is critical especially in case of modeling of casting processes in highly-reinforced structures, which represent the major field of application for SCC.

In this paper, we propose an efficient approach which incorporates the effects of traditional reinforcement on fresh concrete flow. The tools of computational homogenization will be utilized to avoid the need to resolve flows around each reinforcing bar, which would lead to excessive simulation costs comparable to those of the particle-based models. To this purpose, the structure is decomposed into three parts: reinforcement-free zone occupied by a homogeneous non-Newtonian fluid, reinforced zone where a two-scale homogenization scheme is employed, and homogenization-induced interface separating the reinforced and reinforcement-free zones. At his stage, we restrict ourselves only to steady state flows.

In the reinforced domain, we assume that the reinforcing bars are rigid, acting as obstacles to the flow, and that their size is small compared to a characteristic size of the structure or of the concrete form-work. It now follows from the results of mathematical homogenization theory, that the flow in this region can be accurately approximated by a homogeneous Darcy law, see (Jäger et al. 2001). The relation between the macro-scale pressure gradient and the seepage velocity is defined implicitly, via a micro-

[*] Ing. Filip Kolařík: Faculty of Civil Engineering, Czech Technical University in Prague, Thákurova 7; 166 29, Prague; CZ, kolarfil@cml.fsv.cvut.cz.

[**] Prof. Dr. Ing. Bořek Patzák: Faculty of Civil Engineering, Czech Technical University in Prague, Thákurova 7; 166 29, Prague; CZ, borek.patzak@fsv.cvut.cz.

[***] Doc. Ing. Jan Zeman, PhD.: Faculty of Civil Engineering, Czech Technical University in Prague, Thákurova 7; 166 29, Prague; CZ, zemanj@cml.fsv.cvut.cz.

scale boundary value problem that represents a Stokes flow in the representative volume element (RVE) of the reinforcing pattern, driven by the gradient of the macro-scale pressure. For the numerical treatment of the ensuing two-scale model, we will rely on the variationally-consistent approach developed recently in Sandström & Larsson (2013), which combines the variational multi-scale method with first-order computational homogenization, see also (Hughes et al. 1998).

As a result of the homogenization procedure, an artificial interface appears that separates the Stokes domain from the Darcy domain. In order to couple the flows in both domains, we will employ the Beavers-Joseph-Saffman interface conditions. The ensuing interface constants, relating the traction vector and the relative tangential slip in velocity, can be estimated from an auxiliary boundary value problem at the cell level.

2. Formulation of the Problem

As a point of departure, we consider a Stokes flow over a perforated domain as shown in Fig. 1. We denote, in agreement with Fig. 1, Ω_F as the reinforcement-free part of the domain and Ω_P as a part of the domain with the obstacles (further called perforated sub-domain). Boundary of the obstacles is denoted as $\partial\Omega_P$, while the outer boundary $\partial\Omega_F$ is split into two disjoint parts $\partial\Omega_F^P$ and $\partial\Omega_F^u$ corresponding to the type of applied boundary condition; Γ stands for the interface between the perforated, Ω_F, and the un-perforated, Ω_P, domains. By $\mathbf{n}$, we denote both the outer unit normal vector to $\partial\Omega_F$ and Γ , in the latter case pointed from Ω_P to Ω_F.

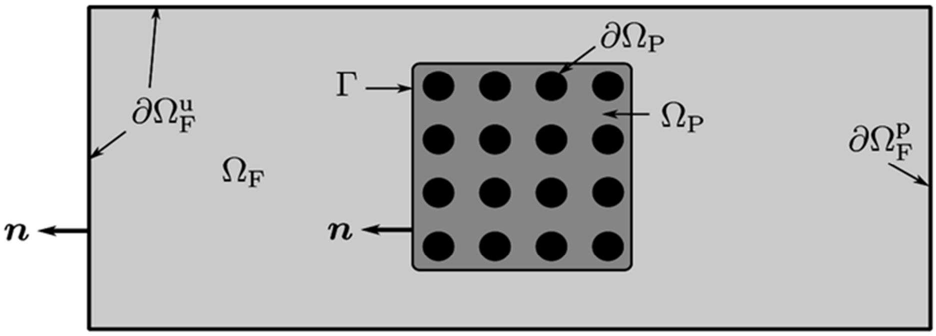

Fig. 1 Stokes flow over the bars modeled as a perforated domain.

The governing equations of the steady-state flow of an incompressible fluid in the union of domains Ω_P and Ω_F take the form

$$\begin{gathered}
-\boldsymbol{\nabla}\cdot\boldsymbol{\tau}\big(\boldsymbol{D}(\boldsymbol{u})\big)+\boldsymbol{\nabla}p=\rho\boldsymbol{b}\quad \text{in } \Omega_F\cup\Omega_P \\
\boldsymbol{\nabla}\cdot\boldsymbol{u}=0\quad \text{in } \Omega_F\cup\Omega_P \\
\boldsymbol{u}=\boldsymbol{0}\quad \text{on } \partial\Omega_P \\
(\boldsymbol{\tau}-p\boldsymbol{I})\cdot\boldsymbol{n}=-\hat{p}\boldsymbol{n}\quad \text{on } \partial\Omega_F^P \\
\boldsymbol{u}=\hat{u}_n\boldsymbol{n}\quad \text{on } \partial\Omega_F^u
\end{gathered} \tag{1}$$

Our notation is standard; $\boldsymbol{\tau}$ stands for the deviatoric part of a stress tensor, the strain rate tensor $\mathbf{D}$ is obtained as the symmetrized gradient of the unknown velocity field $\mathbf{u}$, p denotes pressure, $\rho\mathbf{b}$ are body forces, $\mathbf{I}$ is a unit second order tensor and $\hat{u}_n$ and $\hat{p}$ refer to the boundary data.

In order to properly average the flow in the perforated domain Ω_P, we follow the idea of the variational multi-scale method and its application to porous media. The next step then consists in formulation of (1) in a weak sense and in introduction of a decomposition of the unknown pressure field p and its corresponding test funcion δq into the macro-scale and subscale parts as

$$p = p^M + p^S, \quad \delta q = \delta q^M + \delta q^S. \tag{2}$$

By substitution of (2) into the weak formulation of (1), we can split the equations according to the macro-scale and sub-scale part of the test function δq into the the macro-scale and sub-scale problem respectively. Following the procedure introduced in Sandstrom & Larsson (2013), which we skip here for the sake of brevity, the equations on macro-scale can be transformed using the averaging rule and employing the first order homogenization, see (Jäger et al. 2001), into the form of a conservation equation

$$\int_{\Omega_D} \delta q \, (\nabla \cdot \bar{\boldsymbol{u}}) \mathrm{dx} = 0, \tag{3}$$

where Ω_D refers to the homogenized macro-scale domain covered by RVE's. As $\bar{\boldsymbol{u}}$, we denote so called seepage velocity, obtained from the sub-scale problem by a simple averaging rule; the bar refers to the homogenized domain. The relation (3) can be recognized as a Darcy law which governs the flow in a porous media. The flow inside the homogenized domain Ω_D is coupled with the flow in the un-perforated domain Ω_F through the interface Γ with the help of so called Beavers-Joseph-Saffman conditions. These conditions prescribe continuity of the velocities and stresses in the normal direction and relates stress and velocity in the tangential direction (with respect to the interface) through the parameter β, which can be interpreted as a friction parameter. The conditions have the following form

$$\begin{aligned} u_n - \bar{u}_n &= 0 \\ p - \bar{p} &= \boldsymbol{n} \cdot \boldsymbol{\tau} \cdot \boldsymbol{n} \\ \beta(u_t - \bar{u}_t) &= \boldsymbol{n} \cdot \boldsymbol{\tau} \cdot \boldsymbol{t}, \end{aligned} \tag{4}$$

and have to be satisfied on the interface Γ. The parameter β in the last equation of (4) can be determined, in case of a linear Newtonian fluid, from the geometry of the domain. However, up to our best knowledge, there is no way how to determine this parameter in case of non-Newtonian fluid, which is used in our work as a constitutive relation for the concrete. Therefore, the parameter β has to be set up in advance by the rule of a thumb. The sub-scale problem itself represents the Stokes flow solved over the RVE. It comes from the sub-scale part of the weak formulation of (1) with the help of localization of the test functions, see Sandström & Larsson (2013) for the details. It consists in finding $(\boldsymbol{u}^{\boldsymbol{S}}, p^S)$ such that

$$\begin{aligned} \int_{\Omega_S} \nabla \delta \boldsymbol{w}^{\boldsymbol{S}} \colon \boldsymbol{\tau}\left(\boldsymbol{D}(\boldsymbol{u}^{\boldsymbol{S}})\right) \mathrm{dx} - \int_{\Omega_S} (\nabla \cdot \delta \boldsymbol{w}^{\boldsymbol{S}}) p^S \mathrm{dx} &= \int_{\Omega_S} \delta \boldsymbol{w} \cdot (\rho \boldsymbol{b} - \bar{\boldsymbol{g}}) \mathrm{dx} \\ \int_{\Omega_S} \delta q (\nabla \cdot \boldsymbol{u}^{\boldsymbol{S}}) \mathrm{dx} &= 0. \end{aligned} \tag{5}$$

In above, we denote Ω_S the domain of the RVE and also the super script S refers to the sub-scale problem. The macro-scale problem (3) is coupled with the sub-scale problem (4) in the following way. The sub-scale velocity field u^S is averaged over the domain Ω_S, resulting in $\bar{\boldsymbol{u}}$, which acts on the macro-scale, while the flow on the sub-scale is drive by the macroscopic pressure gradient, in (5) denoted as $\bar{\boldsymbol{g}}$**.**

3. Numerical Examples

In this section, a benchmark test is presented to illustrate the capability and performance of the proposed method. The example illustrates the complex flow of the concrete over the reinforced area. The solution based on the homogenization technique is verified against a fully resolved solution computed by Direct Numerical Simulation (DNS). The reinforced area is located in the middle of the problem domain, so the fluid is not forced to go through the reinforcing bars and the whole situation is closer to real casting problems. The schematic setup of the situation is outlined in Fig. 2, bottom right corner. Uniform velocity is prescribed on the left side, no friction on the top and the bottom and zero "do nothing" boundary condition on the right. The radius of the obstacle in the RVE is chosen as r = 0.25. The fresh concrete is modeled as a Bingham fluid. For numerical purposes, we used modified Bingham model, which has the following form

$$\boldsymbol{\tau} = \left[\mu_0 + \frac{\tau_0}{\sqrt{J_2^D}}\left(1 - \exp(-m\sqrt{J_2^D}\right)\right] \boldsymbol{D} \tag{6}$$

It has two physical parameters, plastic viscosity μ_0 and yield stress τ_0. Additional parameter m governs how close the exponential curve of the modified Bingham model is to the original bilinear one. In the numerical example, the parameters were chosen as $\mu_0 = 20Pa.s$, $\tau_0 = 20Pa$, $m = 15$. The results obtained from the homogenized procedure are in excellent agreement with the DNS, the maximal error is less than 13%. In presented examples, computational time in both approaches is comparable but we assume that in more complex situations, the advantage of the multi-scale approach would be obvious.

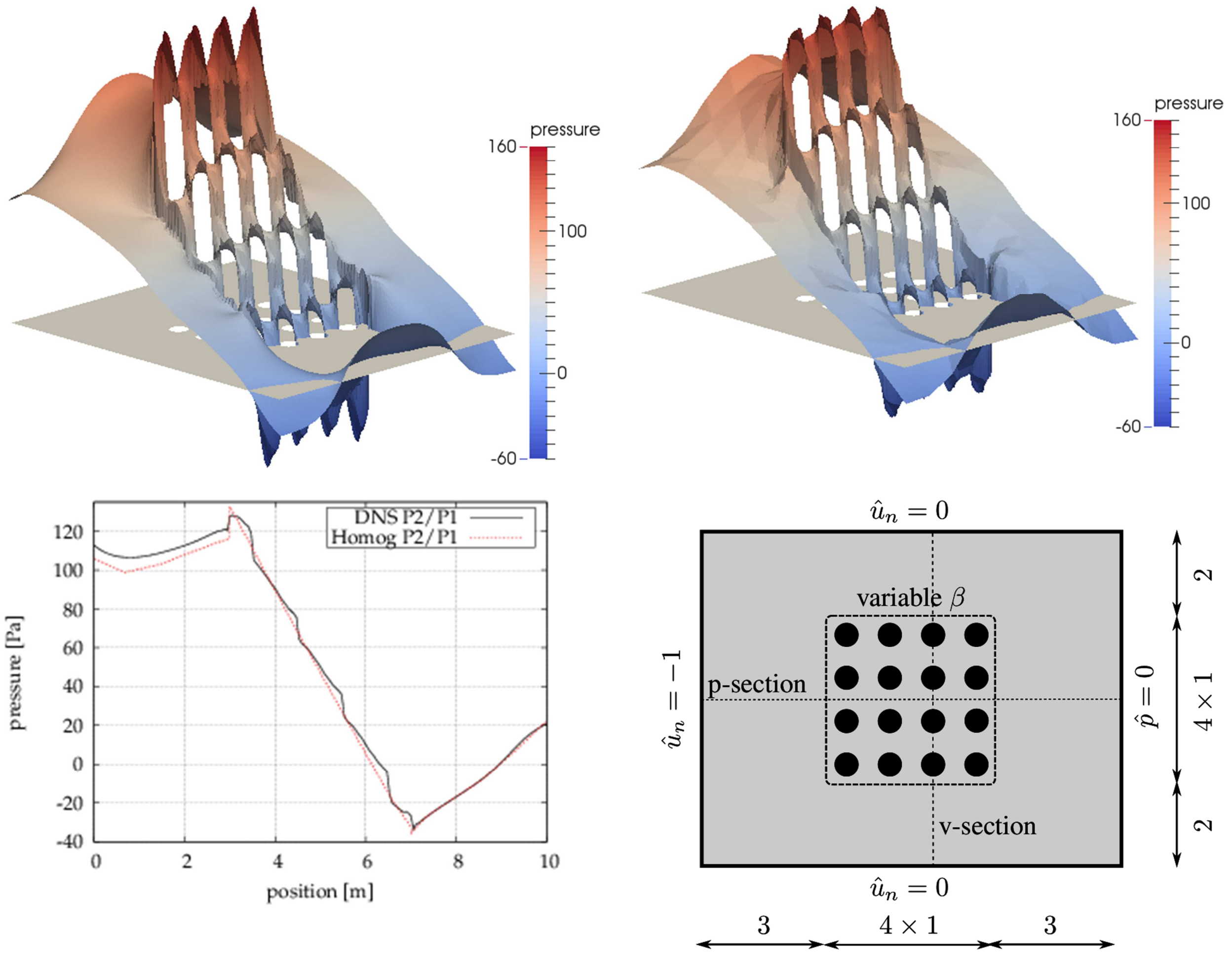

Fig. 2 Top left – fully resolved (DNS) pressure distribution. Top right – pressure distribution obtained with the homogenization approach, reconstructed from the micro-scale. Bottom left Comparison of the pressures along the horizontal section according to the scheme in the bottom left picture.

4. Conclusions

In this paper, the homogenization approach to flow of a Bingham fluid through a porous media is presented. The paper presents unified formulation of coupled Stokes and Darcy flows obtained by consistent homogenization of Stokes flow in porous sub-domain.

Acknowledgement

The research was carried out within the project SGS - Advanced algorithms for numerical analysis and modeling of structures and materials, Project No. SGS16/038/OHK1/1T/11 and the authors gratefully acknowledge the financial contribution of the MŠMT ČR.

References

Roussel N., Geiker M.R., Dufour F., Thrane L.N. & Szabó P. (2007) Computational modeling of concrete flow: general overview, Cement and Concrete Research 37, 9 pp. 1298–1307.

Sandström C., Larsson F. (2013) Variationally consistent homogenization of Stokes flow in porous media, Journal for Multiscale Computational Engineering, 11, pp. 117-183.

Hughes T.J.R., Feijóo G.R, Mazzei L. & Quincy J.B (1998) The variational multiscale method - a paradigm for computational mechanics, Computer Methods in Applied Mechanics and Engineering, 166, pp. 3-24.

Jäger, W., Mikelic, A. & Neuss, N.(2001) Asymptotic Analysis of the Laminar Viscous Flow Over a Porous Bed, SIAM Journal on Scientific Computing, 6, 22, pp. 2006-2028.

22nd International Conference
ENGINEERING MECHANICS 2016
Svratka, Czech Republic, 9 – 12 May 2016

THE CONTROL SYSTEM OF THE STEPPER MOTOR MOTION WITH POSITIONING ACCURACY VERIFICATION

Kolber P.* Perczyński D.* Landowski B.* Wawrzyniak S.*

Abstract: *The paper demonstrates the laboratory stand for the stepper motor control. It was developed on the basis of the two-phase stepper hybrid motor with two shaft ends operated as bipolar. For the stand the following Wobit components were used: the stepper motor controller, the programmable trajectory generator for the stepper motor controllers, the rotary encoder, the programmable pulse and speed counter, a power supply designed for the stepper motor controllers, a power supply for the encoder, the pulse counter, and the trajectory generator. The stand was used for the positioning accuracy measurements and on their basis the errors were determined for several motion parameters such as: minimum speed, maximum speed, and acceleration. The tests were made for three values of the basic step division:1/2, 1/8, and 1/16 as well as for different values of the load moment. The stand also allows the implementation of various stepper motor motion trajectories by developing control programs.*

Keywords: Step motor, basic step, accuracy, bipolar control.

1. Introduction

The stepper motor is a motor that transforms electrical control pulse series into angular displacement series of a rotor or linear displacement of an "unrolled" rotor. The stepper motor is an electro mechanical energy converter, which is characterised by discrete mechanical displacement [Glinka T., Kulesza B., 2004], [Przepiórkowski J., 2012]. The motor converts the control signal (pulse) directly on the fixed position of the shaft without using feedback as, for example, in servomechanisms. The angular displacement of the rotor is proportional to the number of pulses and the rotational speed is proportional to the control impulse frequency of motor winding. The direction of the rotation depends on the control impulse sequences.

2. Description of the laboratory stand

For the research at the measurement stand, ECM 268-E2.8B-1 two-phase stepper motor with two shaft ends was used with rating: current rating 2.8 A (unipolar connection of the windings), current rating 4.0 A (parallel bipolar connection of the windings), rated voltage 2.8 V, basic step 1.8°, holding torque 1.2 Nm.

The motor can work as unipolar or bipolar, because there are eight wires ending the windings [Wróbel T., 1993]. The motor works with parallel bipolar connection of the windings in the laboratory stand.

The other basic functional components are subassemblies of Wobit company.

The motor is connected to SMC 104 controller with power stage designed for two-phase stepper motor with bipolar winding (8 or 4 wire) or unipolar 6-wire set as bipolar. This enables the motor control with division of the step in the range from 1/2 to 1/64 forcing the constant current value in the winging

* Assist. Prof. Piotr Kolber, PhD, UTP University of Science and Technology, Faculty of Mechanical Engineering, Al. prof. S. Kaliskiego 7, 85-796 Bydgoszcz; PL, piotrl.kolber@utp.edu.pl

* Assist. Prof. Daniel Perczyński, PhD, UTP University of Science and Technology, Faculty of Mechanical Engineering, Al. prof. S. Kaliskiego 7, 85-796 Bydgoszcz; PL, daniel.perczynski@utp.edu.pl

* Assist. Prof. Bogdan Landowski, PhD, UTP University of Science and Technology, Faculty of Mechanical Engineering, Al. prof. S. Kaliskiego 7, 85-796 Bydgoszcz; PL, bogdan.landowski@utp.edu.pl

* Assist. Prof. Sylwester Wawrzyniak, PhD, UTP University of Science and Technology, Faculty of Mechanical Engineering, Al. prof. S. Kaliskiego 7, 85-796 Bydgoszcz; PL, sylwester.wawrzyniak@utp.edu.pl

independently of the power supply voltage value. The controller has an option of choosing the current value in the range from 1.2 to 3.8A through configuration micro-switches located on the front panel. It is also possible to turn on the reduction, which limits the power consumption by half if CLK clock signals have a frequency lower than 1.5Hz. The motor starts working by giving the signal (+5 ÷ 24V) to the EN input (ENABLE). The direction of the rotation is controlled by DIR input [www.wobit.com.pl].

The controller is powered by ZN200-L unregulated power supply, which is designed for stepper controllers with rating: current 4A, voltage 36V, power 100W. The power supply enables reception of the motor return energy through the output capacitors of capacitance 4700μF.

At the laboratory stand, SMC104 controller is clocked by MG-ZT1 programming device, which is a programming trajectory generator for the controllers of the stepper motors. From the programming device to the controller two signals are primarily sent: clocking (CLK) that determines intervals between motor steps and direction signal (DIR) that determines the direction of the motion. The programming device in combination with the controller enables generation of stepper motor motion trajectory with parameters such as: position, speed, acceleration. It is possible to set the device and program the motor motion trajectory due to menu placed on the external panel. Therefore, it is not necessary to connect the module to the computer [www.wobit.com.pl].

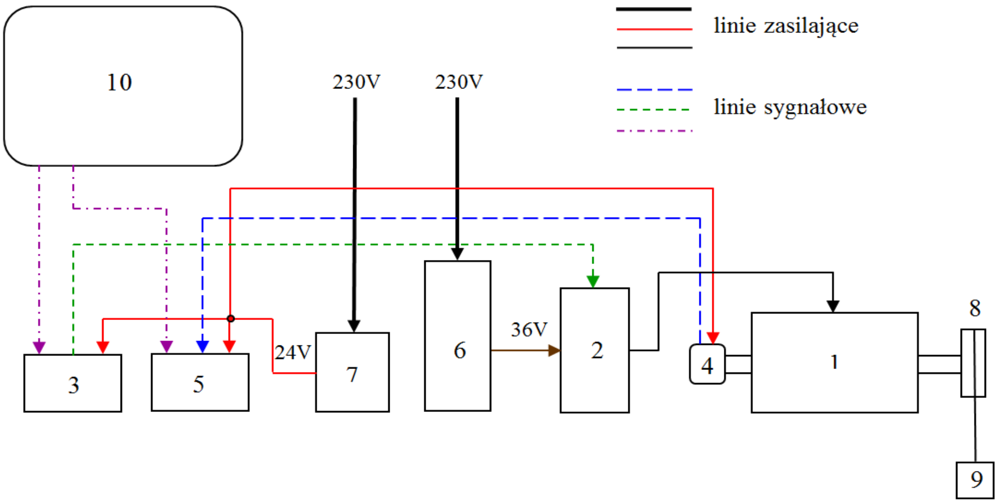

Fig. 1: Block diagram of the laboratory stand for controlling the stepper motor: 1-stepper motor, 2-SMC104 controller, 3-MG-ZT1 programming device, 4-enkoder, 5-MD 150E pulse counter, 6-ZN200-L power supply, 7-DR-4524 power supply, 8-rope reeler, 9-changeable load, 10-PC computer.

The stepper motor has two shaft ends. Rope reeler is attached to the one of them, which enables suspension of the load with different values on it. MHK-40 rotary-pulse encoder with a hole for axle with resolution of 3600 divisions per rotation.

The encoder is connected to MD 150E programmable pulse and speed counter. On the external panel there is the menu and the display which presents the number of counted pulses, cycles and pulse frequency (speed).

MG-ZT1 *programming device,* MD 150E counter and the encoder are powered by DR-4524 power supply with a voltage of 24V. The *programming device* and the counter can be connected to the PC computer through USB interfaces whereby it is easier to control the stepper motor and visualisation of measurement results.

3. Positioning accuracy measurements

Positioning accuracy measurements were carried out for specific motion parameters, such as: minimum speed $v_{\min} = 1\,\text{impuls/s}$, maximum speed $v_{\max} = 1600\,\text{impuls/s}$, maximum acceleration $a_{\max} = 800\,\text{impuls/s}^2$.

The values of the measurement are determined for the programming device in pulses, which sends the clocking signal CLK to the controller of the stepper motor. The measurements were carried out for the following settings of the basic step division (1.8°): 1/2, 1/8, 1/16. The settings were conducted in the front panel of the controller by using micro-switches. The accuracy positioning tests were carried out for various values of rope reeler loads, i.e.: without load m_1 = 0 kg, load of m_2 = 0.5 kg, load of m_3 = 1 kg, load of m_3 = 1.32 kg (load torque M_0 = 0.42 Nm).

The radius of the rope reeler disc (fig. 1, item 8) r = 32.5 10^{-3} m. Load torque M_0 was determined from the formula

$$M_{\text{o}} = m_i g r \quad i = 1, 2, 3, 4 \tag{1}$$

During the research, there were carried out repeatedly measurements of positioning for selected setting of the basic step division of the stepper motor as well as for given load value during a rotation of the motor shaft. The number of pulses corresponding to one rotation for set basic step division was entered from the programming device. Whereas the actual position of the stepper motor shaft after one rotation was determined by the encoder and the pulse counter. For the used encoder there were 10 pulses for 1° of rotation sent from the encoder to the counter.

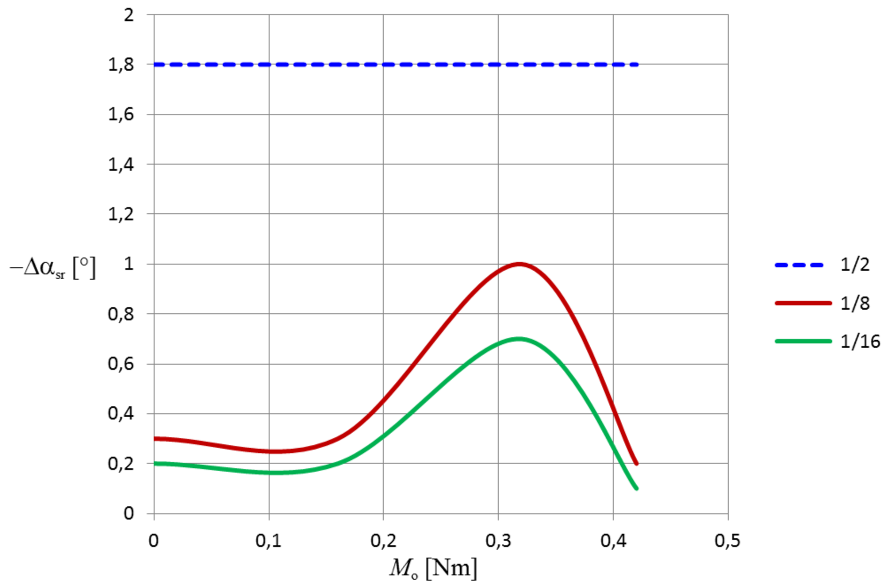

Fig. 2: Diagram of positioning errors for the function of load torque for different basic step divisions.

Based on the measurement, the following could be determined:

– the average absolute angular error of positioning for full 360$^{\text{o}}$ rotation

$$\Delta\alpha_{\text{sr}} = \sum_{i=1}^{n} \frac{\Delta\alpha_i}{n} \tag{2}$$

where: $\Delta\alpha_i$ – absolute error of positioning to the ith implementation of the measurement, n – the number of measurements.

–the average relative percentage error of positioning for full 360° rotation

$$\delta\alpha_{\text{sr}} = \frac{\Delta\alpha_{\text{sr}}}{360} \cdot 100 \tag{3}$$

A diagram of average angular error of positioning for the function of load torque for different basic step divisions is presented in Fig.2, whereas a diagram of the same error in the function of basic step division multiplicity in Fig.3.

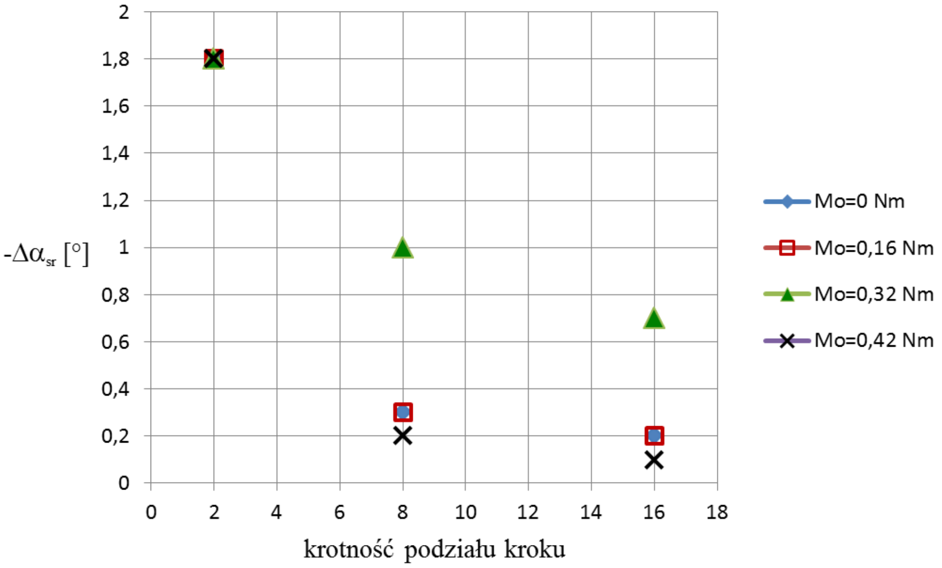

Fig. 3: Diagram of positioning errors in the function of basic step division multiplicity for different values of load torque.

4. Summary

Based on the measurements, it can be stated that the increase of basic step division affects the decrease of positioning error value, which is between -1.8° (-0.5%) and -0.1° (-0. 03%) depending on the loads.

The positioning error has the same value -1.8° (-0.5%) for applied basic step division ½ independently from the load torque. For the divisions 1/8 and 1/16 under the load torque $M_o = 0,32 \mathrm{N \cdot m}$ ($m = 1 \mathrm{kg}$), there are increased positioning error values, respectively -1.0° (-0.28%) and -0.7° (-0.19%) as compared to the other loads as well as no load.

There is repeatability of measurements for the same settings of the basic step divisions and load values for right rotations (lifting a load) as well as for left rotations (lowering a load). The breaking, which means losing a step, happens only in case of the basic step division 1/2 (400 pulses from the programming device) and the load torque $M_o = 0,42 \mathrm{N \cdot m}$ ($m = 1,32 \mathrm{kg}$) for left rotations (in the direction of load).

References

Glinka T., Kulesza B. (2004) Laboratorium elektromechanicznych elementów wykonawczych (Eng. Laboratory of electro-mechanical actuators), Wydawnictwo Politechniki Śląskiej, Gliwice 2004

Przepiórkowski J.: Silniki elektryczne w praktyce elektronika (Eng. Electric motors in practice electronic), Wydawnictwo btc Warszawa 2012

Wróbel T.: Silniki skokowe (Eng. Stepper motors), WNT Warszawa 1993

22nd International Conference
ENGINEERING MECHANICS 2016
Svratka, Czech Republic, 9 – 12 May 2016

DISPERSION PROPERTIES OF FINITE ELEMENT METHOD: REVIEW

R. Kolman[*], M. Okrouhlík[**], J. Plešek[***], D. Gabriel[****]

Abstract: *Review of the dispersion properties of plane square bilinear finite element used in plane elastic wave propagation problems is presented. It is assumed the grid (spatial) dispersion analysis and, further, the temporal-spatial dispersion analysis for explicit direct time integration based on the central difference method. In this contribution, the dispersion surfaces, polar diagrams and error dispersion graphs for bilinear finite element are depicted for different Courant numbers in explicit time integration. Finally, recommendation for setting the mesh size and the time step size for the explicit time integration of discretized equations of motion by the bilinear finite element method is provided.*

Keywords: Finite element method, dispersion properties, wave speed, explicit time integration.

1. Introduction

For accuracy analysis of the finite element method (FEM) (Hughes, 2000; Belytschko, 1983) in solving of wave propagation problems in solids is necessary to know dispersion properties of temporal-spatial semi-discretization. Generally, finite element (FE) solution is polluted by dispersion errors as an effect of spatial FE discretization [Belytschko, 1978; Mullen, 1982; Abboud, 1992] and by period elongation errors and numerical damping of direct time integration (Hughes, 2000; Belytschko, 1983). The dispersion errors are caused by differences of numerical wave speeds from the wave speeds in the 'ideal' continuum. Moreover, the FEM dispersion error is dependent on the frequency of propagating wave and on its orientation in a FE grid. For more information about dispersion properties of FEM see [Okrouhlík, 1993; Brepta, 1996; Červ, 1996; Plešek, 2010; Gabriel, 2010; Kolman, 2013; Kolman, 2015].

The temporal-spatial dispersion analysis of FEM in implicit and explicit direct time integration has been studied in [Schreyer, 1983; Marfurt, 1984]. The central difference method with the diagonal (lumped) mass matrix [Dokainish, 1989] is widely utilized in explicit time integration, while the Newmark method with the consistent mass matrix [Newmark, 1959] is employed in implicit computations. In principle, implicit computation needs a much larger computational effort per time step due to the solving a linear equation system. On the other hand, explicit methods with a diagonal mass matrix require a vector solver only, but mostly they are merely conditionally stable. Thus, the time step size must satisfy the stability limit, [Park, 1977]. In wave propagation and impact problems, the explicit time integration is preferred, therefore we focus only on the central difference method [Dokainish, 1989].

2. Wave propagation in an elastic unbounded domain

It is known that two types of elastic waves propagate through an elastic unbounded domain (Achenbach, 1973). The first wave is the longitudinal one propagating with the wave speed given by $c_1 = \sqrt{(\Lambda + 2G)/\rho}$ and the second one is the transverse wave with the wave speed $c_2 = \sqrt{G/\rho}$, where Λ and G are the Lamé's constants and ρ is the mass density.

[*] Ing. Radek Kolman, PhD.: Institute of Thermomechanics, Czezh Academy of Science, Dolejškova 1402/5; 182 00, Prague; CZ, kolman@it.cas.cz

[**] Prof. Ing. Miloslav Okrouhlík, CSc.: Institute of Thermomechanics, Czech Academy of Science, Dolejškova 1402/5; 182 00, Prague; CZ, ok@it.cas.cz

[***] Ing. Jiří Plešek, CSc.: Institute of Thermomechanics, Czech Academy of Science, Dolejškova 1402/5; 182 00, Prague; CZ, plesek@it.cas.cz

****Ing. Dušan Gabriel, PhD.: Institute of Thermomechanics, Czech Academy of Science, Dolejškova 1402/5; 182 00, Prague; CZ, gabriel@it.cas.cz

In dispersion analysis, we assume a plane wave solution for components of a displacement field in the form $u_i = U_i \exp[\mathrm{i}\, k\,(\mathbf{x}\,\mathbf{p} \pm c\,t)]$, $i = 1,2$, where $\mathrm{i} = \sqrt{-1}$, $\mathbf{k} = (k_x, k_y)$ is the wave vector, $k = \sqrt{k_x^2 + k_y^2}$ is the wavenumber, $\mathbf{x}$ is the position vector, $\mathbf{p}$ is the unit vector describing direction of wave propagation, c is the phase speed, t is the time and U_i is the *i*-th component of displacement vector. Relationship for the angular velocity of wave ω is given by $\omega = k\,c$ and the wavelength λ is computed as $\lambda = 2\pi / k$. The positions of nodes with the indexes m, n in the bilinear FE mesh are prescribed as $x_m = mH$, $y_n = nH$, where H marks the edge length of a bilinear finite element. The components of the unit vector $\mathbf{p}$ are defined by the angle θ: $p_x = \cos\theta$, $p_y = \cos(\pi/2 - \theta)$ (Fig. 1).

A dimensionless time step size is defined by the Courant number as $Co = \Delta t c_1 / H$, where Δt is the time step size.

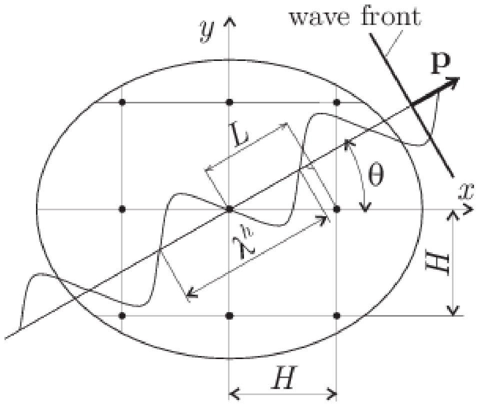

Fig. 1: A plane infinite bilinear regular finite element mesh and plane wave inclined by angle θ.

3. Dispersion properties of the bilinear finite element method

Results of spatial and temporal-spatial dispersion analysis of the bilinear finite element and for the explicit time integration based on the central difference method with the lumped mass matrix are presented on Figs. 2, 3 and 4. The results are depicted for several Courant numbers, where the value $Co = 1.0$ corresponds to the critical time step size for the bilinear finite element with the lumped mass matrix [Park, 1977].

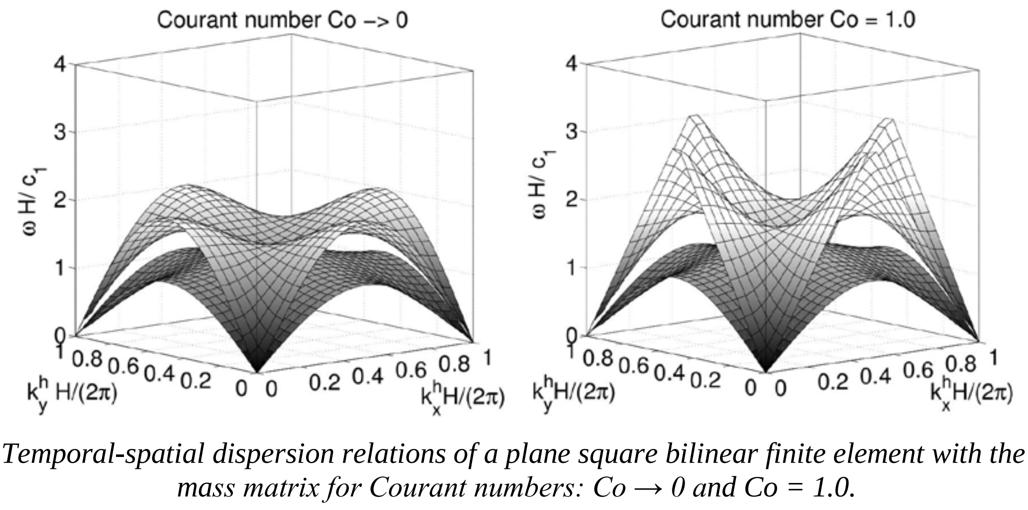

Fig. 2: Temporal-spatial dispersion relations of a plane square bilinear finite element with the lumped mass matrix for Courant numbers: Co → 0 and Co = 1.0.

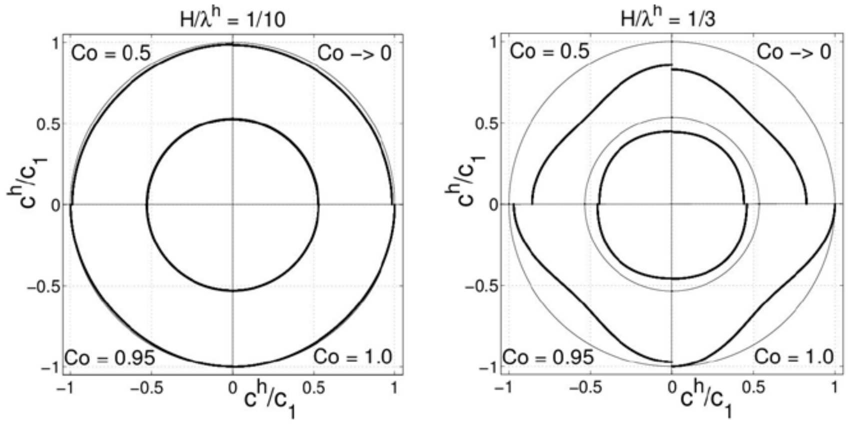

Fig. 3: Polar temporal-spatial dispersion diagrams of a plane square bilinear finite element with the lumped mass matrix for Courant numbers Co={→0, 0.5, 0.95, 1.0} for H/λ^h = 1/10 and H/λ^h =1/3.

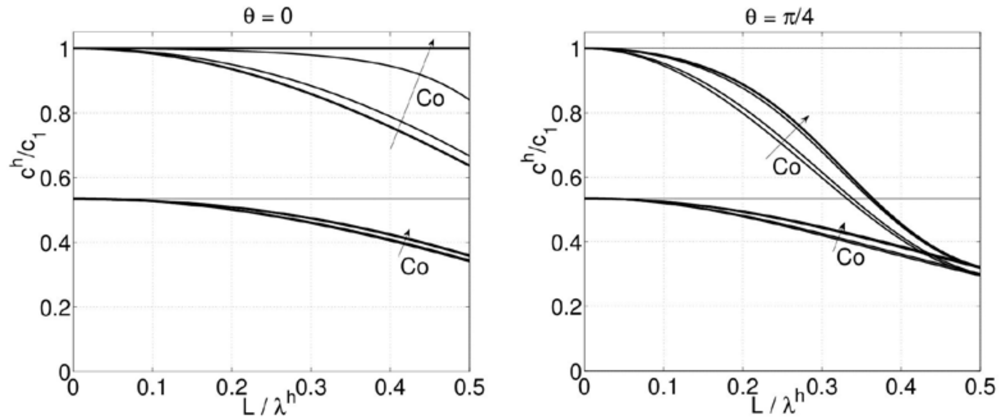

Fig. 4: Dispersion errors in phase velocity of a plane square bilinear finite element with the lumped mass matrix for Courant numbers Co = {→ 0, 0.5, 0.95, 1.0} for propagation directions given by angles θ = 0 and θ = π/4.

Based on the temporal-spatial dispersion analysis of the bilinear finite element, we can see an effect of improving dispersion errors for longitudinal waves for the critical time step (the Courant number close to $Co = 1.0$) and for wave direction given by $\theta = 0$. On the other hands, this effect is not seen for the transverse waves. Therefore, the best choice for the time step size with respect to accuracy of the linear FEM and explicit time integration is the time step size given by the stability limit [Park 1977].

4. Conclusions

Based on the dispersion analysis of the bilinear finite element method, the edge length of the finite element H is recommended to choice so that it is satisfied the conditions $H_{\max} \le \lambda/10$. The wavelength can be estimated as $\lambda = c_2 / f_{\max}$, where $f_{\max}$ is the maximal loading frequency in Hz.

Further, it was shown that dispersion errors in explicit FE modelling can be improved only for longitudinal waves, where we should integrate with the critical time step size by the central difference method. In principle, the dispersion errors for transverse waves are independent of a choice of the stable time step size. Other way how to eliminate dispersion errors also for transverse waves is to use the partitioned wave explicit scheme presented in [Kolman, Cho, Park, 2015].

This contribution is dedicated to the seventy-fifth birthday of Professor Miloslav Okrouhlík.

Acknowledgement

The work has been supported by the Czech Science Foundation (GACR) (Grant No. GAP101/12/2315 and 16-03823S) and by the Technology Agency of the Czech Republic (TACR), (Grant Number TH01010772). All grant projects supported by GACR and TACR were realized within institutional support RVO:61388998.

References

Abboud, N.N. & Pinsky P.M. (1992) Finite element dispersion analysis for the three-dimensional second-order scalar wave equation. International Journal for Numerical Methods in Engineering, 35, 6, pp. 1183-1218.

Achenbach, J.D. (1973) Wave propagation in Elastic Solids. North-Holland Publishing Comp., American Elsevier Publishing Comp., Inc., New York.

Belytschko, T, & Mullen, R. (1978) On dispersive properties of finite element solutions. In: Modern Problems in Elastic Wave Propagation (J. Miklowitz, J. Achenbach eds), John Wiley & Sons Inc., pp. 67-82.

Belytschko, T. & Hughes, T.J.R. (1983) Computational Methods for Transient Analysis. North-Holland: Amsterdam.

Brepta, R., Valeš, F., Červ, J. & Tikal B (1996) Rayleigh wave dispersion due to spatial (FEM) discretization of a thin elastic solid having non-curved boundary. Computers & Structures, 58, 6, 1233-1244.

Červ, J. & Brepta, R. & Valeš, F. (1996) Acoustic surface waves in media discretized by FEM. Acustica, 82, 1, pp. 235. Computational Technology Reviews, Vol. 1, pp. 251-279.

Dokainish, M.A. & Subbaraj, K.(1989) A survey of direct time-integration methods in computational structural dynamics - I. Explicit methods. Computers & Structures, 32, 6, pp. 1371-1386.

Gabriel, D., Plešek, J. Kolman, R. & Valeš, F. (2010) Dispersion of elastic waves in the contact-impact problem of a long cylinder. Journal of Computational and Applied Mathematics, 234, 6, pp. 1930-1936.

Hughes, T.J.R. (2000) The Finite Element Method: Linear and Dynamic Finite Element Analysis. Dover Publications: New York.

Kolman, R., Cho, S.S. & Park, K.C. (2015) Efficient implementation of an explicit partitioned shear and longitudinal wave propagation algorithm, International Journal for Numerical Methods in Engineering, accepted.

Kolman, R., Plešek, J., Červ, J., Okrouhlík, M. & Pařík, P. (2015) Temporal-spatial dispersion and stability analysis of finite element method in explicit elastodynamics, International Journal for Numerical Methods in Engineering, accepted, DOI: 10.1002/nme.5010.

Kolman, R., Plešek, J., Okrouhlík, M. & Gabriel, D. (2013) Grid dispersion analysis of plane square biquadratic serendipity finite elements in transient elastodynamics. International Journal for Numerical Methods in Engineering, 96, 1, 1-28.

Marfurt, K.J. (1984) Accuracy of finite-difference and finite-element modeling of the scalar and elastic wave equations. Geophysics, 49, 5, pp. 533-549.

Mullen, R. & Belytschko T. (1982) Dispersion analysis of finite element semidiscretizations of the two-dimensional wave equation. International Journal for Numerical Methods in Engineering 18, 1, pp. 11-29.

Newmark, N. (1959) A method of computation for structural dynamics. Journal of the Engineering Mechanics Division 85, 3, pp. 67-94.

Okrouhlík, M. & Höschl, C. (1993) A contribution to the study of dispersive properties of one-dimensional Lagrangian and Hermitian elements. Computers & Structures 49, 5, pp. 779-795.

Park, K.C. (1977) Practical aspect of numerical time integration. Computers & Structures, 7, 3, pp. 343-353.

Plešek, J., Kolman, R. & Gabriel, D. (2010) Dispersion Error of Finite Element Discretizations in Elastodynamics.

Schreyer, H.L. (1983) Dispersion of semidiscretized and fully discretized systems. In Computational Methods for Transient Analysis, (T. Belytschko, T.J.R. Hughes eds). North-Holland: Amsterdam; pp. 267-299.

22nd International Conference
ENGINEERING MECHANICS 2016
Svratka, Czech Republic, 9 – 12 May 2016

EXPERIMENT E7/0,3 – DISPLACEMENT PROCESSES IN NON-COHESIVE SAND MASS DURING ACTIVE TRANSLATIVE MOTION OF RETAINING WALL

P. Koudelka*

Abstract: *The first part of information on the new experiment denominated as E7/0,3 with* active *pressure of non-cohesive quartz sand on time behaviour of the mass was presented at the last Conference (P. Koudelka, 2015). The second part is object of this Paper. The experiment was performed at the Institute of Theoretical and Applied Mechanics in 2014. The moved rigid front wall of the experimental equipment was translatively moved towards active direction (out of the mass) at a position of supposed acting of active pressure value, then the wall motion was stopped and time pressure stability was monitored. After more than three months the wall was moved at the last position of 100 mm from original position before the experiment. The experiment ran four and a half months. The paper presents firstly results on the deforming mass through the course of the wall movement at a supposed position for active pressure mobilization of 1.357 mm and after the further movement. The experiment was repeated to be the results proved (Experiment E8/0,3). New results are analysed.*

Keywords: Retaining wall, active lateral earth pressure, non-cohesive material, sandy mass behaviour, wall movement modus, displacements.

1. Introduction

Long-term experiment E7/0,3 with *active* lateral pressure of sandy mass is a part of a long-term research of lateral earth pressure of non-cohesive granular masses at the Institute of Theoretical and Applied Mechanics running from 1998. A complete set of experiments with *passive* pressure ran in period 2010 - 2014 (P. Koudelka, 2013) when all three basic modes of wall movement (rotations about the top and toe, translative motion) were tested two times (experiment sets E5 and E6), altogether six long-term experiments using the same sand to be proved mass behaviour during each wall movement modus. The presented experiment E7/0,3 ran in the second half of 2014 year. A repeated same experiment E8/0,3 ran after in the first half of 2015 and its results are analysed.

Each of experiments brought huge volume of different data. Data of bi-component pressure sensors (normal pressure and friction), movement sensors and temperature sensor were registered digitally using record frequency of 1-100 Hz (max. frequency is of 1000 Hz), cameras of visual monitoring of small globule displacements in the mass on left side and surface of the mass registered pictures with record frequency 1 picture per minute. The digital registering is complemented and secured by “handmade” data registering of sensors and namely uplift/settlement of red sandy strips in the mass on right side and their disruptions which show slip surfaces in the mass much more preciously than globule displacement vectors on the opposite side. The Paper presents some results of an analysis of the strip registering (“handmade” data and photos).

2. Experimental equipment and techonology

Experimental equipment and technology were mentioned at the last Conference in the paper P. Koudelka (2015). A brief survey follows. It was availed the same developed advanced equipment with transparent side walls (glass) such as for the previous experiments with passive pressure (P. Koudelka, 2013) however, with shorter sandy sample space. Sizes of sandy sample were as follows: wide of 0.98 m, height

* Petr Koudelka, DSc.,PhD.,AEng.,CEng.: Institute of Theoretical and Applied Mechanics, Czech Academy of Sciences, Prosecká 76; 190 00, Prague; CZ, koudelka@itam.cas.cz

of 1.20 m, length of 1.375 m (previous experiments – length of 3.0 m). Numbers of bi-component pressure sensors in a front moved wall (5) and a stable back wall (6) were the same but more sensitive sensors for lower pressures were used. It is used the same sharp quartz material of size of 0.3 mm repeatedly and as well as for the experiment E7/0,3. Compaction of the mass was homogeneous and not too high similarly to previous masses using also a special exact compacting instrument ($n=47.0$ %, $I_D = 0.55$, unit weight $\gamma = 1494\ kg/m^3$).

2.1. Experiment Flow

The **e**xperiment was in progress in three motional phases applying front wall translative motion and three reconsolidation phases (without a motion). The first motional phase tested an influence of *active* micro movement of the front wall from an original position of $u = 0$ *mm* to position of $u = -0.28$ *mm*, i.e. behaviour in a range of pressure at rest. The second motional phase followed after 5 days at wall position of $u = -1.36$ *mm*, i.e. supposed full mobilization position of *active pressure* according to EN 1997-1 (Annex C). Then time behaviour of the mass consolidated along of 97 days was monitored. The last motional phase at position of $u = 100.42$ *mm* made it possible to monitor behaviour of the mass in a range of full shear strength mobilization and further during destruction of the mass. Consolidation pressures of the failed mass were monitored 23 days after. A movement velocity of the front wall during all motional phases was of *0.0049 mm/min.*, the same as during other experiments.

Fig. 1: View at the right side of the sample after active translative motions of the front wall (left):
a) Movement of 1.36 mm to left. Deformations are not yet visible.
b) Movement of 9.13 mm to left. Deformations and the first main slip surface are visible.
c) Movement of 74.04 mm to left. Displacements are very obvious in a frontal active mass part and create very complicated system of slip surfaces.

3. Results of slow processes in the mass

The wall motion velocity was very slow to be near to behaviour velocity of natural soil masses which, unfortunately, can vary in wide limits. The applied wall velocity about of 0.0049 mm/min. is about fifty times faster than a continental drift between Europe and America or grows of human nails only. The velocity corresponds approximately to behaviour of long term retaining structures under pressure of less cohesive soils.

3.1. The mass deformation

The mass shows two parts which are visibly distinct almost from the motion beginning. A frontal wedge shaped part touching the wall subsides according to the wall motion. A pure deformation process does not continue during a longer motion owing to a process of slip surface creating. It can be seen comparing Fig. 2a and Fig 2b, resp. less obviously in Fig. 1a (very slight subside) and Fig. 1b. Absolute wall motion values in figures are denominated like *u* and a note minus signifies active direction, i.e. out of the mass.

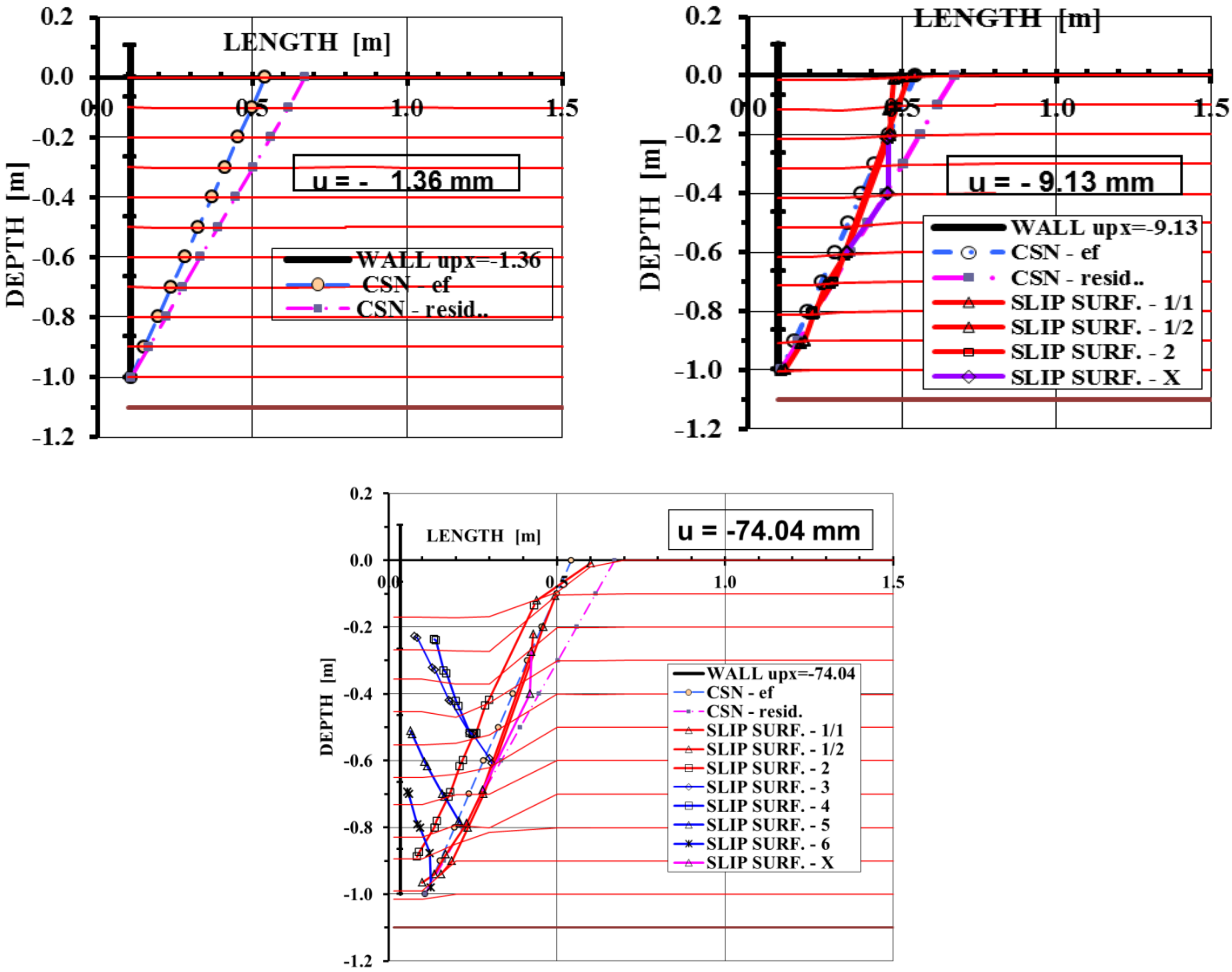

Fig. 2: Graphs of real drop of the red strips in the sample and real slip surfaces according to mass states in Figs. 1:
a) State after motion of 1.36 mm to left. Deformations are not yet visible.
b) State after motion of 9.13 mm to left. Deformations and the first main slip surface are visible.
c) State after motion of 74.04 mm to left - state of the frontal mass part destruction. Displacements are very obvious in a frontal active mass part and create very complicated system of slip surfaces.

Vertical thick full lines in figures demarcate positions of the wall and horizontal line marks give positions of the pressure sensors. Inclined lines in Fig. 2a are shear surfaces supposed according to the classic earth pressure theory (also by ČSN 73 0037) considering angle of effective shear strength (dashed blue line) and angle of residual shear strength (dash-dotted violet line).

The code EN 1997-1 presents in Annex C, Table C.1 values of ratios v_a/h for non-cohesive soils where v_a is the wall motion to mobilise active earth pressure and h is the height of the wall. The values depend on kind of wall movement and compaction of the soil. Translative motion values in cases of loose and dense soils are of *0,2,* resp. *0.05-0.1*. The mentioned compaction of the mass of $I_D = 0.55$ accords to approximately medium compacted soils and the motion value of $u=-1.36$ *mm* accords about to suppositions of the code for active pressure mobilisation. The mass deformation near after this value begins to be influenced due to displacements along slip surfaces creating themselves.

3.2. Slip surfaces

The first slip surface zone appeared before reaching of the wall motion value of $u=-9.13$ *mm*. The zone involves the slip surfaces 1 and 2. Unfortunately, an equipment structure post covers an area around length of *0.4 m* and a substantial part of histories of the slip surfaces was not visible (see Fig. 1b). Owing to this fact the missing part was interpolated. However, a more probable history of this part of slip surface 1 may be a history according to the slip surface X.

A further history of transfiguring of the mass begins by widening of the first slip surfaces zone (slip surface 1 and 2) and by slipping of the frontal mass part along the zone. Next slip surfaces create themselves outside the zone step by step (e.g. slip surface 2). The second opposite system of slip surfaces begins to create about of wall motion of *25 mm*. This system is very complex and it causes subsidence process of a middle part of the mass frontal part (Figs. 1c and 2c). This is after the point of the destruction process beginning.

4. Conclusion

Known wider physical experiments with lateral earth pressure appear sporadic. There can be mentioned an excellent research of lateral passive pressure in Cambridge presented by Roscoe (1970), unfortunately without detailed results for wall rotation about the top and not concerning with active pressure. Also, there can be mentioned experiments of Gudehus (1980) monitoring total forces acting on the whole wall.

Owing to this research situation the long term wide research at the institute can be useful and applicable for a putting more exactly of lateral earth pressure theory and practice.

5. Acknowledgement

The author thanks to Jan Bryscejn, EEng. for driving the equipment and data registering a transforming.
Of course, exact collaboration of institute technicians was requisite and meritorious.

References

EN 1997-1: Eurocode 7: Geotechnical design – Part 1: General rules. CEN, Bruxeles 2004, 168 ps.

Gudehus G.(1980): *Materialverhalten von Sand: Anwendung neuerer Erkentnise im Grundbau.* Bauingenieur,55/9,351-359.

Koudelka, P. (2015) Experiment E7/0,3 – Displacement Processes in Non-cohesive Sand Mass during Active Wall Translative Motion, in: Proc. 21st IC on Engineering Mechanics 2015 (J. Náprstek & C. Fischer eds), Institute of Theoretical and Applied Mechanics, v.v.i., Praha, Czech Republic. ISBN 978-80-86246-42-0, ISSN 1805-8248, pp. 146-147.

Koudelka, P.(2013) Double Case of Passive Pressure Acting on Wall Rotated about the Top. Proc.7th IC on Case Histories in Geotechnical Engineering (#3.15b), Wheeling (Chicago, Ill.), Apr.29-May 4, 2013. S. Prakash, Missouri University of Science and Technology, Rolla, MO, USA. ISBN 1-887009-18-3 (Abs.v.), ISBN 1-887009-17-5, ps.10.

Roscoe, K.H. (1970): The Influence of Strains in Soil Mechanics. *Géotechnique 20*, No. 2, pp. 129-170.

22nd International Conference
ENGINEERING MECHANICS 2016
Svratka, Czech Republic, 9 – 12 May 2016

PROBABILISTIC NONLINEAR ANALYSIS OF THE HERMETIC CIRCULAR COVER OF MAIN COOLANT PUMP FAILURE DUE TO EXTREME PRESSURE AND TEMPERATURE

J. Králik*

Abstract: *This paper describes the probabilistic nonlinear analysis of the hermetic circular cover of main coolant pump failure due to extreme pressure and temperature. The scenario of the hard accident in nuclear power plant (NPP) and the methodology of the calculation of the fragility curve of the failure overpressure using the probabilistic safety assessment PSA 2 level is presented. The model and resistance uncertainties were taken into account in the response surface method (RSM).*

Keywords: Nuclear power plant, Reactor cover, Nonlinearity, Fragility curve, PSA, RSM, ANSYS.

1. Introduction

After the accident of nuclear power plant (NPP) in Fukushimi the IAEA in Vienna adopted a large-scale project "Stress Tests of NPP", which defines new requirements for the verification of the safety and reliability of NPP under extreme effects of the internal and external environments and the technology accidents (ENSREG, 2012). The experience from these activities will be used to develop a methodology in the frame of the project ALLEGRO, which is focused to the experimental research reactor of 4th generation with a fast neutron core. The new IAEA safety documents (IAEA, 2010) initiate the requirements to verify the hermetic structures of NPP loaded by two combinations of the extreme actions.

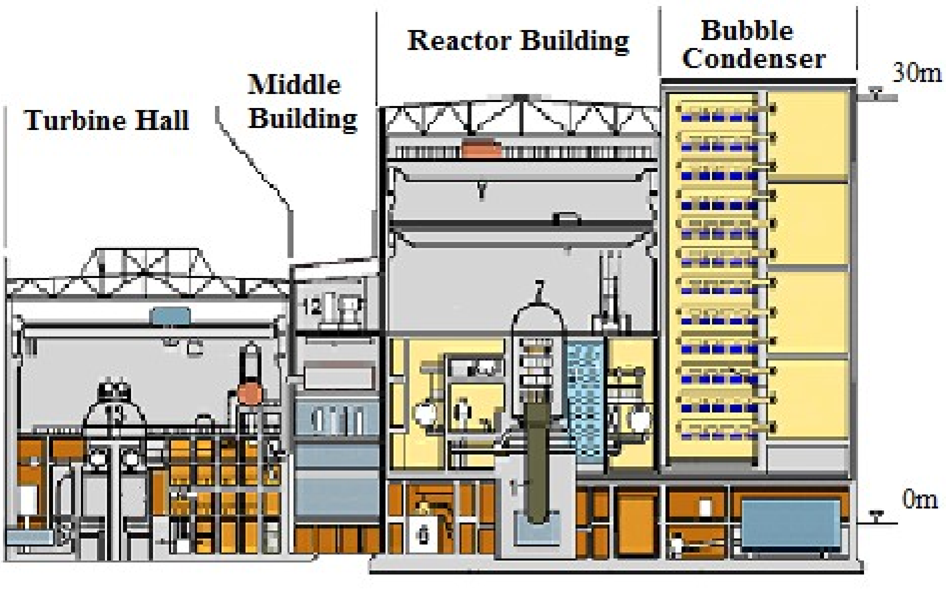

Fig 1: Section plane of the NPP with reactor VVER440/213

In the case of the loss-of-coolant accident (LOCA) the steam pressure expand from the reactor hall to the bubble condenser (IAEA, 2010). The reactor and the bubble condenser reinforced structures with steel liner are the critical structures of the NPP hermetic zone (Králik, 2009, 2015). The critical technology steel segments are at level +18.9 (Fig.1). The safety and reliability of these segments were tested

* Prof.Ing.Juraj Králik,CSc.: Faculty of Civil Engineering, Slovak University of Technology Bratislava Radlinského 11; 810 05 Bratislava; SK, juraj.kralik@stuba.sk

considering the scenario of the hard accidents. The previous analysis was achieved for the overpressure value of 100kPa due to design basic accident (DBA), which corresponds of the loss of coolant accident due to guillotine cutting of the coolant pipe (Králik, 2009). When the barbotage tower operates in the partial or zero performance the overpressure is equal to the 150 - 300 kPa.

Type	Duration	Overpressure in HZ [kPa]	Internal temperature [^{o}C]
I.	1hour - 1day	150	127
II.	2hours - 7days	250	150
III.	1year	-	80 - 120

Tab. 1: The assumed scenarios of the accidents in the hermetic zone

The SE-ENEL proposes the maximum temperature in the reactor shaft is equal about to 1 800^{o}C and in the containment around the reactor shaft is equal about to 350^{o}C (Králik, 2015). The possibility of the temperature increasing to the containment failure state is considered in the scenario too. In the case of the hard accident the overpressure can be increased linearly and the internal and external temperature are constant. Three types of the scenarios were considered (Tab.1). The critical was the accident during 7 days with the overpressure 250kPa, internal temperature 150^{o}C and external temperature -28^{o}C.

2. Calculation model of MCP Steel covering

The steel coverings are located at the boundary of the confinement at floor level +18.90 m. In the assembled state, the steel covering fulfils both the sealing and shielding functions. The technology segments of the NPP hermetic zone are made from the steel. The FEM model of MCP steel covering structure is shown in Fig.2. The technical parameters of the covering basic parts are specified in Tab. 2. The shielding cover is fitted in the frame cast in concrete and sealed to the frame with double rubber packing of 15 mm in width. The shielding cover is provided with 30 mechanical closures.

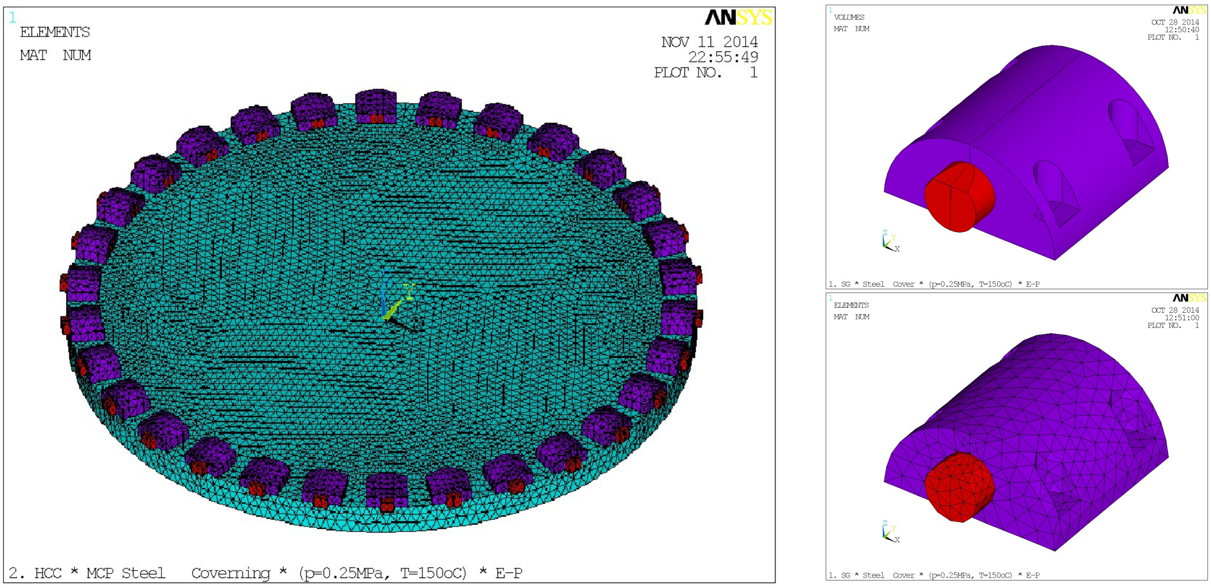

Fig.2: FEM model of the MCP Steel covering and the mechanical closure segments

Two calculation FEM models of the MCP steel covering structure with the mechanical closure were considered with two variants of the material properties of mechanical closure segments. The original closure segment is made from two materials - material 42 2430 for mechanical closures, material 11 700 for sliders. The FEM model has 107 212 solid and surface elements with 22 593 nodes.

Part	Basic dimension [mm]	Weight [kg]	Material
Welded frame	∅4000x500	1317	11373
Shielding cover	∅3710x160	13400	11378
Double protect. cover	2x∅4000x30	2x632=1264	11373
Mechanical closures	30x235x180x150	420	422430/11700

Tab.2: Basic part of MCP Steel Covering

3. Probability and sensitivity nonlinear analysis

Huber-Mises-Hencky model (HMH) of the elastic - plastic steel material properties for MCP steel covering was used. The "Central Composite Design Sampling" (CCD) method of the “Response Surface Method” (RSM) is based on 45 nonlinear simulations depending on the 6 variable input data. The nonlinear solution for the one simulation consists about the 50 to 150 iteration depending on the scope of the plastic deformations in the calculated structures. The uncertainties are coming from the standard requirements and the other publications (Handbook 5, 2005, JCSS, 2011, Krejsa,M. Králik,J. 2015, Sýkora M. Holický, M. 2013). The mean values and standard deviations were defined in accordance of the experimental test and design values of the material properties and the action effects (see Tab.3). Based on the results from the simulated nonlinear analysis of the technology segments and the variability of the input parameters 10^6 Monte Carlo simulations were performed in the software ANSYS.

Quantity	Charact. value	Variable	Histog. type	Mean μ	Deviat. σ[%]	Minim. value	Maxim. value
			Material				
Strength	F_k	f_{var}	N	1.1	6.6	0.774	1.346
			Action effects				
Dead load	G_k	g_{var}	N	1	5	0.808	1.195
Live load	Q_k	q_{var}	GU	0.643	22.6	0.232	1.358
Pressure LOCA	p_k	p_{var}	N	1	8	0.698	1.333
Temperature	T_k	t_{var}	GU	0.667	14.2	0.402	1.147
			Model uncertainties				
Action	E_k	e_{var}	N	1	5	0.813	1.190
Resistance	R_k	r_{var}	N	1	5	0.812	1.201

Tab. 3: Variability of input parameters

The sensitivity analyses give us the informations about the influences of the variable properties of the input data to the output data (Fig.3). These analyses are based on the correlations matrixes.

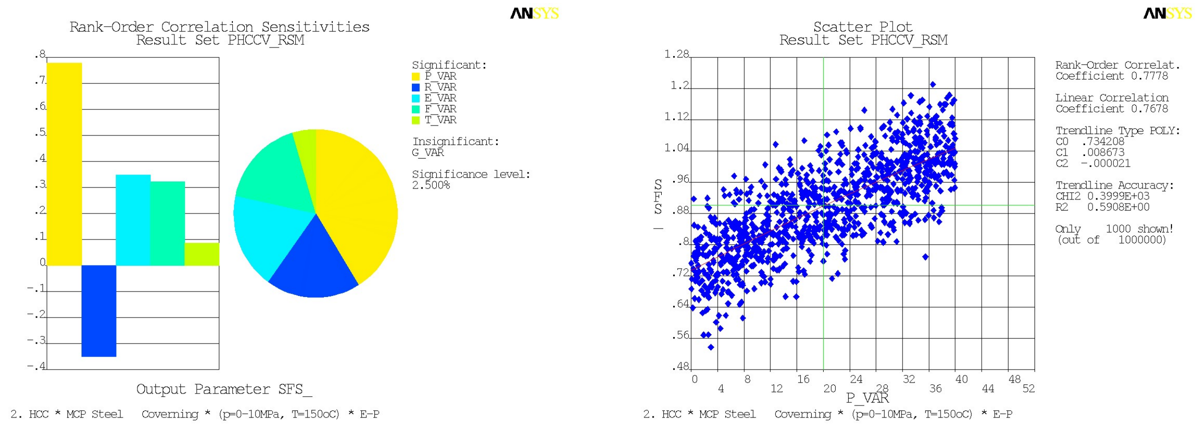

Fig.3: Sensitivity and trend analysis of the safety function of MCP steel covering for uniform distribution of overpressure

4. Fragility curves of failure pressure

The PSA approach to the evaluation of probabilistic pressure capacity involves limit state analyses (Králik,J. 2009). The limit states should represent possible failure modes of the confinement functions. The failure of the steel structure is limited with the max. strain values or with the stability of the nonlinear solution (Abraham, 1998). The standard STN EN 1993 1-2 (Handbook 5, 2005) define following characteristic values of the strain for the structural steel – the yield strain $\varepsilon_{ay,\theta} = 0.02$, the ultimate strain $\varepsilon_{au,\theta} = 0.15$, the max. limite strain $\varepsilon_{ae,\theta} = 0.20$. The fragility curve of the failure pressure (Fig.4) was determined using 45 probabilistic simulations using the RSM approximation method with the experimental design CCD for 10^6 Monte Carlo simulations for each model and 5 level of the overpressure. The various probabilistic calculations for 5 constant level of overpressure next for the variable overpressure for gauss and uniform distribution were taken out. The failure criterion of the steel structures using HMH plastic criterion with the multilinear kinematic hardening stress-strain relations for the various level of the temperatures and the degradation of the strength were considered.

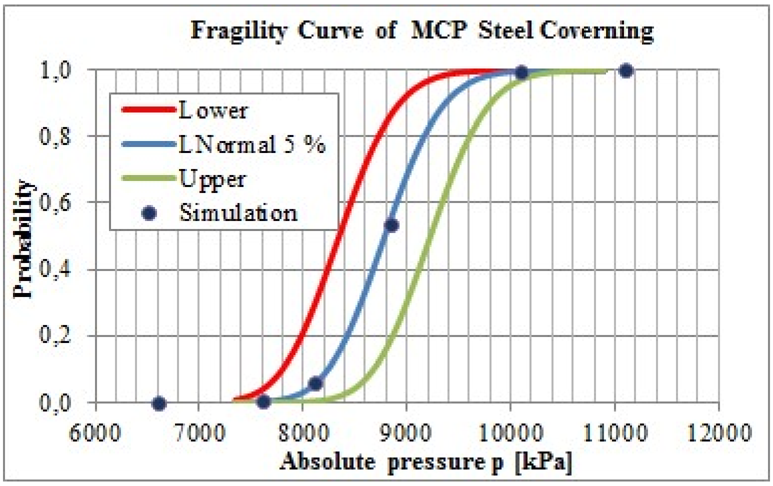

Fig.4: Fragility curves of MCP steel covering determined for normal distribution with 5% envelope

5. Conclusions

This report is based on the methodology of the probabilistic analysis of structures of the hermetic zone of NPP with reactor VVER44/213 detailed described in the work (Králik, J. 2009, 2015). The uncertainties of the loads level, the material model of the steel structures as well as the inaccuracy of the calculation model and the numerical methods were taken into account in the approximation RSM method for CCD experimental design and 10^6 Monte Carlo simulations (Králik, J. 2009).

One from the critical technology segments of the containment is MCP steel covering with the failure pressure $p_{u.0,05}$= 8023.7kPa. The mean value of pressure capacity of MCP steel covering is $p_{u.0,50}$= 8795.5kPa, the upper bound of 95% is $p_{u.0,95}$= 9971.7kPa. These fragility curves (Fig.4) are the input data for the following risk analysis of the NPP safety.

Acknowledgements

The project was performed with the financial support of the Grant Agency of the Slovak Republic (VEGA 1/0265/16).

References

Abraham, (1998) ASME Boiler and Pressure Vessel Code, Section III, Div. 1, Appendix F, "*Rules for Evaluation of Service Loadings with Level D Service Limits*," American Society of Mechanical Engineers.

ENSREG, (2012) *Post-Fukushima accident. Action Plan. Follow-up of the peer review of the stress tests performed on European nuclear power plants*.

HANBOOK 5. (2005) *Implementation of Eurocodes Reliability Backgrounds. Design of Buildings for the Fire Situation. Development of Skills Facilitating Implementatio of Eurocodes*. Leonardo Da Vinci Pilot Project CZ/02/B/F/PP-134007. Prague, CR.

IAEA (2010) *Safety Series No. SSG-4, Development and Application of Level 2 Probabilistic Safety Assessment for Nuclear Power Plants*, Vienna.

JCSS 2011. *JCSS Probabilistic Model Code.* Zurich: Joint Committee on Structural Safety. <www.jcss.byg.dtu.dk>.

Králik,J. (2009) *Safety and Reliability of Nuclear Power Buildings in Slovakia. Earthquake-Impact-Explosion.* Ed. STU Bratislava, 307pp. ISBN 978-80-227-3112-6.

Králik,J. et al. (2015) Structural Reliability for Containment of VVER 440/213 Type, In *Safety and Reliability: Methodology and Applications - Nowakowski et al.* (Eds) © Taylor & Francis Group, London, p.2279-2286.

Krejsa, M. Králik,J. (2015) Probabilistic Computational Methods in Structural Failure Analysis, Journal of Multiscale Modelling, Vol. 6, No. 2 (5 pages), Imperial College Press, DOI: 10.1142/S1756973715500067.

Sýkora,M. Holický,M. (2013) Assessment of Uncertainties in Mechanical Models, *Applied Mechanics and Materials*, Vol. 378 pp 13-18, © Trans Tech Publications, Switzerland, doi:10.4028/www.scientific.net/AMM.378.13.

22nd International Conference
ENGINEERING MECHANICS 2016
Svratka, Czech Republic, 9 – 12 May 2016

NONLINEAR ANALYSIS OF STEEL CONCRETE COLUMNS FIRE RESISTANCE

J. Králik[*], M. Klabník[**], A. Grmanová[***]

Abstract: *The aim of this work is the design of the steel and concrete composite column subjected to fire considering material and geometrical nonlinearity. The paper presents the detailed analysis of the structural fire resistance in accordance with the Eurocode requirements. On the base of the nonlinear analysis using ANSYS software, the fire resistance of two types of columns – a reinforced concrete column and a steel and concrete composite column - has been investigated. The load of column section is considered alternatively. The Drucker-Prager yield function for the concrete, and Von Mises function for steel, have been taken. The theory of large deformations is regarded in geometrical nonlinearity. The FEM model is made from the solid (SOLID65), shell (SHELL181) and link (LINK180) elements. The comparison studies present the differences of the steel and concrete composite columns in comparison with the reinforced concrete columns, or steel.*

Keywords: fire resistance, material and geometrical nonlinearity

1. Introduction

Experiences from fire cases and their consequences are the main reasons for the developing of the fire safety standards. A list of codes, standards, and other legal documents being used to achieve this aim are based on the simple numerical methods. This paper particularly shows the possibility of solution the fire resistance problem. The fire resistance of the structure could be verified by simplified or exact computational model. From the structural behaviour point of view we consider a plastic model. The definition of the material properties, as well as the load condition, can be defined by deterministic or probabilistic access. Fire resistance of the structure is evaluated by discrete histogram obtained from the probabilistic analysis. The fire resistance of composite steel-concrete structures is calculated according to EN1994-1-2. Three methods are available in order to evaluate the fire resistance: the tabulated data method, the simple calculation models and the advanced calculation models. The tabulated data method is based on observations resulted from experimental study. It is the easiest to apply, but it is limited by the geometrical conditions imposed to the composite cross-section. The simple calculation models compute the ultimate load of the element by means of formulas or design charts, established on the basis of experimental data. The advanced calculation models suppose an advanced numerical analysis of the elements, parts of the structure, or of the entire structure under fire, using specialized software for the mechanical analysis of structures under elevated temperatures.

The nominal standard temperature-time ISO 854 fire curve does not take into account any physical parameter, and can be far away from reality. From the beginning, the nominal curve supposes that the entire compartment is in the flashover phase and the temperature is increased continuously, without taking into account the cooling phase.

The fire is considered an accidental situation which requires, with some exceptions, only verifications against the ultimate limit state. The combinations of actions for accidental design situations are given in the European Standard for basis of structural design EN1990, by the following formulas:

[*] Prof. Ing: Juraj Králik, PhD.: Departement of Structural Mechanics, Slovak University of Technology, Radlinského 11; 81101, Bratislava; SK, juraj.kralik@stuba.sk

[**] Ing. Maroš Klabník, Departement of Structural Mechanics, Slovak University of Technology, Radlinského 11; 81101, Bratislava; SK, xklabnik@stuba.sk

[***] Mgr. Alžbeta Grmanová, Departement of Structural Mechanics, Slovak University of Technology, Radlinského 11; 81101, Bratislava; SK, alzbeta.grmanova@stuba.sk

$$G_k + P_k + \Psi_{1,1} Q_{k,1} + \sum_{i>1} \Psi_{2,i} Q_{k,i} \qquad \text{or} \qquad G_k + P_k + \sum_{i\geq 1} \Psi_{2,i} Q_{k,i} \tag{1}$$

2. Composite steel-concrete structure analysed

The paper presents the calculation of the fire resistance for the composite columns of high rise building. This column is critical structure element with required fire resistance R90 in accordance with Eurocode 4. The composite steel-concrete column consists the steel profile I600 from S235, concrete rectangular section 550/800mm from C30/37 and the reinforcement 8∅28mm from B500B (Fig.1) .

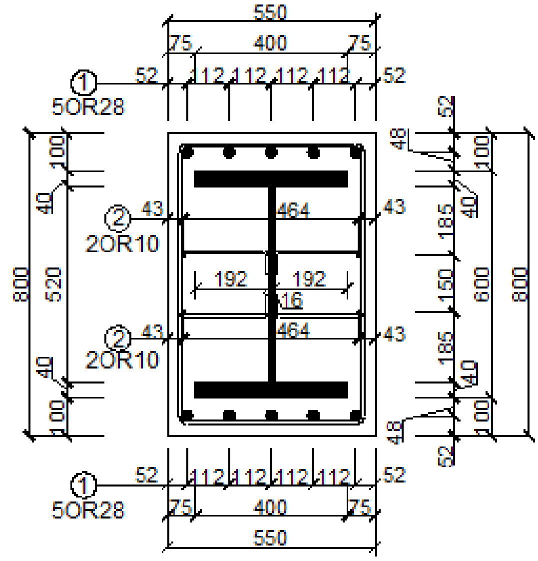

Figure 1: Section of the composite steel-concrete column

3. Geometric and material nonlinearity

The resistance of the composite steel-concrete column was calculated considering the material and geometric nonlinearity depended on temperature. The geometric nonlinearity is based on the theory of the large strain, which is often used for elastic-plastic elements. The motion vector $\{u\}$ is formulated by the position vectors for undeformed $\{X\}$ and deformed $\{x\}$ state

$$\{u\} = \{x\} - \{X\} \tag{2}$$

The deformation gradient $[F]$ is defined as

$$[F] = \left[\frac{\partial\{x\}}{\partial\{X\}} \right] \tag{3}$$

which can be written in terms of the displacement here $[R_{1/2}]$ is the rotation matrix computed from the polar decomposition of the deformation gradient evaluated at the midpoint configuration:

$$[F_{1/2}] = [R_{1/2}][U_{1/2}] \quad \text{and} \quad [F_{1/2}] = [I] + \frac{\partial\{u_{1/2}\}}{\partial\{X\}} \tag{4}$$

where $\{u_{1/2}\} = (1/2)(\{u_n\} + \{u_{n-1}\})$ is the midpoint displacement.The computed strain increment $[\Delta\varepsilon_n]$ (or equivalently $\{\Delta\varepsilon_n\}$) can then be added to the previous strain $\{\varepsilon_{n-1}\}$ to obtain the current total Hencky strain. The strain increment is also computed from the midpoint configuration.

$$\{\Delta\varepsilon_n\} = [B_{1/2}]\{\Delta u_n\} \tag{5}$$

where $\{\Delta u_n\}$ is the displacement increment over the time step and $[B_{1/2}]$ is the strain-displacement relationship evaluated at the midpoint geometry

$$\{X_{1/2}\} = \frac{1}{2}\left(\{X_n\} + \{X_{n-1}\}\right) \tag{6}$$

This method is an excellent approximation to the logarithmic strain if the strain steps are less than ~10%. This method can be used by the standard 2-D and 3-D solid and shell elements. For the case of nonlinear materials the stress increment can be computed via the elastic stress-strain relations

$$\{d\sigma\} = [D_{el}]\{d\varepsilon^{el}\} \tag{7}$$

where $[D_{el}]$ is the stress-strain matrix and the elastic strain is defined in the form of:

$$\{\varepsilon^{el}\} = \{\varepsilon\} - \{\varepsilon^{th}\} - \{\varepsilon^{pl}\} \tag{8}$$

where ε^{el} is an elastic strain vector, ε - total strain vector, ε^{th} - thermal strain vector, ε^{pl} - plastic strain vector. The incremental theory of plasticity provides a mathematical relationship that characterizes the elastic-plastic response of materials. There are three ingredients in the rate-independent plasticity theory: the yield criterion, flow rule and the hardening rule. The increment of the plastic strain results from the flow rule by Drucker (condition of positive plastic work)

$$\{d\varepsilon^{pl}\} = d\lambda\left\{\frac{\partial Q}{\partial\sigma}\right\} \tag{9}$$

where $d\lambda$ is plastic multiplier (which determines the amount of plastic straining) and Q is plastic potential (which determines the direction of plastic straining). The plastic multiplier $d\lambda$ express from consistency condition of yield function $dF(\sigma,\kappa,\alpha) = 0$

$$d\lambda = \frac{\left\{\frac{\partial F}{\partial\sigma}\right\}^T [D_{el}]\{d\varepsilon\}}{-\frac{\partial F}{\partial\kappa}\{\sigma\}^T\left\{\frac{\partial Q}{\partial\sigma}\right\} - C\left\{\frac{\partial F}{\partial\alpha}\right\}^T\left\{\frac{\partial Q}{\partial\sigma}\right\} + \left\{\frac{\partial F}{\partial\sigma}\right\}^T [D_{el}]\left\{\frac{\partial Q}{\partial\sigma}\right\}} \tag{10}$$

The yield function F defines the state, when the plastic strain ε^{pl} is started. Generally the yield criterion can be defined as follows

$$F(\sigma,\kappa,\alpha) = 0 \tag{11}$$

where κ is the hardening parameter (plastic work) and α is the back stress (location of the centre of the yield surface). The yield function was taken by Von Mises for the steel material and by Drucker-Prager for the concrete material in following form- Von Mises yield function

$$F(\sigma,\kappa,\alpha) = \sqrt{3J_2} - \sigma_y(\kappa) \tag{12}$$

where J_2 is the second invariant of the stress tensor, $\sigma_y(\kappa)$ is the yield parameter.

- Drucker-Prager yield function for the concrete

$$F(\sigma,\kappa,\alpha) = \beta I_1 + \sqrt{J_2} - \sigma_y(\kappa) \tag{13}$$

where I_1 is the first invariant of the stress deviator, J_2 is the second invariant of the stress deviator, the parameter β and the yield parameter $\sigma_y(\kappa)$ is defined as follows

$$\sigma_y(\kappa) = \frac{6c.\cos\varphi}{\sqrt{3(3-\sin\varphi)}}, \quad \beta = \frac{f_T}{f_c} = \frac{1-\sin\varphi}{1+\sin\varphi}, \quad \varphi = \arcsin\left(\frac{1-\beta}{1+\beta}\right), \quad c = \frac{\sqrt{2}}{2} f_c \tag{14}$$

where C is the cohesion coefficient and φ is the angle of interior material friction.

4. FEM model of the composite steel-concrete column

The FEM model consist of 3.800 solid elements (SOLID65), 784 shell elements (SHELL181) and 1396 link elements (LINK180) in program ANSYS. The material model of the steel elements was defined for the Von Mises yield function and multilinear isotropic hardening stress-strain diagram. In the case of concrete the Drucker-Prager yield function was taken.

5. Recapitulation of the nonlinear analysis

The fire resistance of two types of column - composite steel-concrete (SC) and reinforced concrete (RC) in four models was considered – M1 (SC column loaded by full section), M2 (SC column loaded by steel profile), M3 (RC column only), M4 (S column from I600 only).

Temperature °C	$N_{,fi,Rd,z}$ kN	$N_{\cdot fi.Ed}$ kN	Capacity ratio %
20	19224.3108	9027.82477	46.96046
200	17776.4928	9027.82477	50.785185
400	13890.2026	9027.82477	64.9941908
500	10187.6206	9027.82477	88.6156357
700	3547.04101	9027.82477	254.517068
900	1021.70869	9027.82477	883.600662

Table 1: Design values of the normal forces of SC column

6. Conclusions

This paper deals with the analysis of the fire resistance of two types of column - composite steel-concrete (SC) and reinforced concrete (RC) for four models – M1 (SC column loaded by full section), M2 (SC column loaded by steel profile), M3 (RC column only), M4 (S column from I600 only). The load was considered for 20%, 40%, 60% and 80% level of design normal force N_{Rd} and temperature of 200, 400, 500, 700 and 900^{o}C. The limit state was achieved for following situations : model M1 - 40% N_{Rd} and 820°C, M2 - 60% N_{Rd} and 900°C, M3 - 40% N_{Rd} and 700°C, M4 - 40% N_{Rd} and 900°C. The composite steel-concrete column (model M2) loaded by steel profile has the highest level of fire resistance.

Acknowledgement

The project was realized with the financial support of the Grant Agency of the Slovak Republic (VEGA). The project registration number is VEGA 1/1039/12

References

CARVALHOA, L.T. et al. Numerical modelling of steel columns in fire, *Applications of Structural Fire Engineering*, February 2009, Prague, Czech Republic.

CADORIN, J.F et al. : A tool to design steel elements submitted to compartment fires-Ozone V2. Part2: Methodology and application, *Fire safety journal*, Elsevier, 38, 439-451, 2003.

LAUSOVÁ, L. KREJSA, M. Experimentální testování ocelové konstrukce za požáru. *Sborník vědeckých prací VŠB-TUO, řada stavební,* VŠB TU Ostrava, 2012, s. 261-268.

KODUR,V. : Guidelines for Fire Resistant Design of Concrete-Filled Steel HSS Columns - State-of-the-Art and Research Needs, *Steel Structures* 7 (2007) 173-182.

PARK,S.H. et al.: Fire resistance of Bar-Reinforced Concrete-Filled Steel Tube Columns, In Proc. *Application of Structural Fire Engineering*, 19-20 February 2009, Prague, CR.

STN EN 1991 – 1 – 2 : *Eurokod 1, Zaťaženia konštrukcii, Časť 1-2: Všeobecne zaťaženia – Zaťaženie konštrukcii namáhaných požiarom*. SUTN Bratislava 2006.

22nd International Conference
ENGINEERING MECHANICS 2016
Svratka, Czech Republic, 9 – 12 May 2016

PROBABILISTIC CALCULATION USING PARALLEL COMPUTING

M. Krejsa[*], J. Brozovsky[**], P. Janas[***], R. Cajka[****], V. Krejsa[*****]

Abstract: *The paper is focused on methods for the calculations of failure probabilities in structural failure and reliability analysis with special attention to newly developed probabilistic method: Direct Optimized Probabilistic Calculation (DOProC), which is highly efficient in terms of calculation time and the accuracy of the solution. The novelty of the proposed method lies in an optimized numerical integration that does not require any simulation technique. The algorithm of the DOProC based probabilistic calculation is easy to adjust for parallel computing on multiprocessor computers or supercomputers.*

Keywords: Parallel computation, Probabilistic Methods, Monte Carlo, Direct Optimized Probabilistic Calculation, DOProC.

1. Introduction to parallel computing

In recent years computers have become faster and faster due to series of improvements of their individual components. Operating speeds are approaching their physical limits. In spite of all the advantages, current computers still cannot solve many problems in reasonable time. One way to achieve further increase in performance is through the use of a collection of processors that cooperate in the solution process (Kindervater et al., 1989).

New computational techniques are still evolving. Along with powerful computing technology, it enables to solve complex engineering problems (e.g. Brozovsky & Pankaj, 2007; Cajka et al., 2014; Kormanikova & Kotrasova, 2014). Parallelization has found wide application for FEM based calculations and analysis (Kruis et al., 2002; Cho & Hall, 2012; Cermak et al., 2014) and last but not least in probabilistic calculations (Reh et al., 2006) and reliability assessments (Kralik, 2010).

2. Probabilistic methods

Probabilistic methods are used in engineering where a computational model contains random variables (Janas & Krejsa, 2012; Cajka & Krejsa, 2014; Janas et al., 2015). Some works deal with parallel process systems in which the input and output data are fuzzy (e.g. Lozano, 2013). For solution of the theoretical time-invariant structural reliability problem have been developed series of probabilistic methods (summary e.g. Krejsa & Kralik, 2015). The largest and most popular group of probabilistic approaches consists of techniques based on Monte Carlo simulation.

Crude Monte Carlo simulations are employed in several scientific domains due to their capacity to produce realistic results from repeated sampling of events generated by pseudo-random algorithms (Oran et al., 1998). Correct results require a large number of statistically independent events, which has a strong impact on the computing time of the simulation. Nevertheless, Monte Carlo simulations are easily

[*] Assoc. Prof. Ing. Martin Krejsa, Ph.D.: Department of Structural Mechanics, Faculty of Civil Engineering, VSB-Technical University of Ostrava, Ludvika Podeste 1875/17; 708 33, Ostrava - Poruba; CZ, martin.krejsa@vsb.cz

[**] Assoc. Prof. Ing. Jiri Brozovsky, Ph.D.: Department of Structural Mechanics, Faculty of Civil Engineering, VSB-Technical University of Ostrava, Ludvika Podeste 1875/17; 708 33, Ostrava - Poruba; CZ, jiri.brozovsky@vsb.cz

[***] Assoc. Prof. Ing. Petr Janas, CSc.: Department of Structural Mechanics, Faculty of Civil Engineering, VSB-Technical University of Ostrava, Ludvika Podeste 1875/17; 708 33, Ostrava - Poruba; CZ, petr.janas@vsb.cz

[****] Prof. Ing. Radim Cajka, CSc.: Department of Structures, Faculty of Civil Engineering, VSB-Technical University of Ostrava, Ludvika Podeste 1875/17; 708 33, Ostrava - Poruba; CZ, radim.cajka@vsb.cz

[*****] Ing. Vlastimil Krejsa: Department of Structural Mechanics, Faculty of Civil Engineering, VSB-Technical University of Ostrava, Ludvika Podeste 1875/17; 708 33, Ostrava - Poruba; CZ, vlast.krejsa@seznam.cz

parallelized (e.g. Camarasu-Pop et al., 2013), using various platforms, e.g. in MatLab (Vasek & Krejsa, 2014) or on supercomputer (Konecny et al., 2009). More advanced ways to increase parallel computing efficiency of this simulation technique are under development also (Qiu & Wang, 2011; Nishihara et al., 2014; Vrugt, 2016). As a very powerful tool for parallel programming seems to be currently MatLab included Parallel Computing Toolbox (Sharma & Martin, 2009).

3. Direct Optimized Probabilistic Calculation

The probabilistic method Direct Optimized Probabilistic Calculation – DOProC, is under development now. DOProC solves the probabilistic tasks in a purely numerical way that is based on basis of probability theory and does not require any simulation technique. This is highly effective way of probabilistic calculation in terms of computation time and accuracy of the solution for many probabilistic tasks. The novelty of the proposed method lies in an optimized numerical integration. Summary was published e.g. in (Janas et al., 2010). Application of the DOProC method in solving reliability problems described publications (Krejsa et al., 2013, 2014, 2016).

3.1. Optimization of basic calculation algorithm

Probabilistic calculations of especially complex tasks can be technically and temporally difficult. The computational complexity of the DOProC method is in particular due to:

- The number of random input variables $j = 1, ..., n$.

- The number of classes (intervals) in histogram for each random input variables N_j.

- Difficulty of the solved task (computational model).

- Algorithm of the probabilistic calculation and the way how the calculation model is defined in the relevant software, e.g. in text mode or in machine code as a dynamic library.

Logically, there should get on optimization techniques that can be applied for two random and independent variables, and also for three or more independent random quantities.

In the probabilistic calculation with two statistically independent input variables come into consideration using of following optimizing steps:

- Interval optimization.

- Zone optimization.

- Simple trend optimization.

Three independent input variables come into consideration in addition to the above:

- Complex trend optimization,

- Grouping of input and output variables,

- Parallelization of probabilistic calculation.

The proposed optimization techniques have been published in details e.g. in (Janas et al., 2010) except the parallelization, which is aimed at further description.

3.2. Parallelization of probabilistic calculation

Probabilistic calculations by DOProC method can be very time consuming, but some parts of computing can proceed simultaneously. The calculation algorithm of DOProC method is advantageous for use on machines with two or more processing units, or their cores. All of computational operations of the DOProC basic algorithm can be divided to as many parts as there are available execution units. After partial calculations partial results can be summarized e.g. into the resulting histogram of safety margin when probabilistic assessment is performed.

Division of probabilistic calculation into sub-sections is appropriate to combine with grouping of input random variables, but this may not be required. Let the resulting random variable B is any function f of independent random variables A_j where j ranges from 1 to n. Then

$$B = f(A_1, A_2, A_3, ..., A_j, ..., A_n). \quad (1)$$

Relationship (1) is possible to adjust otherwise. Histogram of random variable B can be e.g. divided into parts:

$$B = B_1 + B_2 + B_3 + ... + B_p + ... + B_s, \tag{2}$$

where $B_p = f(A_{1,p}, A_2, ..., A_j, ..., A_n)$.

Parts of the histogram of random variable B_p are calculated from all histograms of random variables A_j for $j = 2$ to n, and from the part p of the histogram of random variable A_1, which is marked as $A_{1,p}$. If the number of these parts is equal to s, then:

$$A_1 = A_{1,1} + A_{1,2} + ... + A_{1,p} + ... + A_{1,s}. \tag{3}$$

Parts of the histogram of random variable B in the equation (2) are not summed up by relation (1) but such that is selected width of the class $\Delta b_{1,p}$ for all parts the same, i.e. whether for the histogram of random variable B, and totaled probabilities in each class of all parts of histograms B_p of random variable B for $p = (1, ..., p, ..., s)$.

This procedure ensures that the result of parallel computing is theoretically identical with the results of non-parallel calculation. In case of computing with different widths of classes $\Delta b_{1,p}$ of all parts of histograms B_p under calculation the resulting histogram of random variable B according (2), the parallel computing of the histogram of the random variable B may vary somewhat from the non-parallel computing. The difference of results is not usually significant and even this method of calculation can be considered as correct.

4. Conclusions

This paper discussed possibilities of probabilistic calculation using parallel computing with special focus on new method under development – the Direct Optimized Probabilistic Calculation ("DOProC"). The highlight of the DOProC lies in an efficient and accurate optimized numerical integration and the possibility of straightforward implementation on parallel systems. Thanks to these properties DOProC method can be useful for solution of many probabilistic tasks and failure analysis.

Acknowledgement

This outcome has been achieved with the financial support of the project GACR No. 16-08937S „State of stress and strain of fiber reinforced composites in interaction with the soil environment". In this undertaking, theoretical results gained by conceptual development of research, development and innovations for 2016 at the VSB-Technical University of Ostrava (granted by the Ministry of Education, Youths and Sports of the Czech Republic) were partially exploited. Their financial assistance is gratefully acknowledged.

References

Brozovsky, J. & Pankaj, P. (2007) Towards modelling of a trabecular bone. Computers & Structures, 85, 9, pp. 512-517. DOI: 10.1016/j.compstruc.2006.08.037.

Cajka, R. & Krejsa, M. (2014) Measured data processing in civil structure using the DOProC method. Advanced Materials Research, 859, pp. 114-121. DOI: 10.4028/www.scientific.net/AMR.859.114.

Cajka, R., Burkovic, K. & Buchta V. (2014) Foundation Slab in Interaction with Subsoil. Advanced Materials Research, 838-841, pp. 375-380. DOI: 10.4028/www.scientific.net/AMR.838-841.375.

Camarasu-Pop, S., Glatard, T., da Silva, R.F., Gueth, P., Sarrut, D. & Benoit-Cattin, H. (2013) Monte Carlo simulation on heterogeneous distributed systems: A computing framework with parallel merging and checkpointing strategies. Future Generation Computer Systems, 29, 3, pp. 728-738. DOI: 10.1016/j.future.2012.09.003.

Cermak, M., Kozubek, T., Sysala, S. & Valdman, J. (2014) A TFETI domain decomposition solver for elastoplastic problems. Applied Mathematics and Computation, 231, pp. 634–653. DOI: 10.1016/j.amc.2013.12.186.

Cho, I.H. & Hall, J.F. (2012) Parallelized Implicit Nonlinear FEA Program for Real Scale RC Structures under Cyclic Loading. J. Comput. Civ. Eng., 26, 3, pp. 356-365, DOI: 10.1061/(ASCE)CP.1943-5487.0000138.

Janas, P., Krejsa, M. & Krejsa, V. (2010) Using the Direct Determined Fully Probabilistic Method for determination of failure, in: Proc. European Safety and Reliability Conference ESREL 2009, Reliability, Risk and Safety:

Theory and Applications. Taylor & Francis Group, London, pp. 1467-1474, ISBN: 978-0-415-55509-8, DOI: 10.1201/9780203859759.ch203.

Janas, P. & Krejsa, M. (2012) Statistical Dependence of Input Variables in DOProc Method. Transactions of the VSB - Technical University of Ostrava, Civil Engineering Series, 12, 2, pp. 48-58. DOI: 10.2478/v10160-012-0017-3.

Janas, P., Krejsa, M., Krejsa, V. & Bris, R. (2015) Structural reliability assessment using Direct Optimized Probabilistic Calculation with respect to the statistical dependence of input variables, in: Proc. Conference ESREL 2015: Safety and Reliability of Complex Engineered Systems (L.Podofillini, B.Sudret, B.Stojadinovic, E.Zio & W.Kröger eds), Zurich, Switzerland, CRC Press, pp. 4125–4132, ISBN: 978-1-138-02879-1, eBook ISBN: 978-1-315-64841-5, DOI: 10.1201/b19094-540.

Kindervater, G.A.P., Lenstra, J.K. & Rinnooy Kan, A.H.G (1989) Perspectives on Parallel Computing. Operations Research, 37, 6, pp. 985-990, DOI: 10.1287/opre.37.6.985.

Konecny, P., Brozovsky, J. & Krivy, V. (2009) Simulation Based Reliability Assessment Method using Parallel Computing, in: Proc. First International Conference on Parallel, Distributed and Grid Computing for Engineering (B.H.V.Topping & P.Iványi eds), Civil-Comp Press, Stirlingshire, UK, pp. 542-549, DOI: 10.4203/ccp.90.38.

Kormanikova, E. & Kotrasova, K. (2014) Finite Element Analysis of Damage Modeling of Fiber Reinforced Laminate Plate. Applied Mechanics and Materials, 617, pp. 247-250, DOI: 10.4028/www.scientific.net/AMM.617.247.

Kralik, J. (2010) A RSM method for probabilistic nonlinear analysis of reinforced concrete bubbler tower structure integrity, in: Proc. European Safety and Reliability Conference ESREL 2009, Reliability, Risk and Safety: Theory and Applications. Taylor & Francis Group, London, pp. 1369-1372, ISBN: 978-0-415-55509-8, DOI: 10.1201/9780203859759.ch188.

Krejsa, M., Janas, P., Yilmaz, I., Marschalko, M. & Bouchal, T. (2013) The Use of the Direct Optimized Probabilistic Calculation Method in Design of Bolt Reinforcement for Underground and Mining Workings. Scientific World Journal, 2013, DOI: 10.1155/2013/267593.

Krejsa, M., Janas, P. & Cajka, R. (2013) Using DOProC Method in Structural Reliability Assessment. Applied Mechanics and Materials, 300-301, pp. 860-869. DOI: 10.4028/www.scientific.net/AMM.300-301.860.

Krejsa, M. (2013) Probabilistic failure analysis of steel structures exposed to fatigue. Key Engineering Materials, 577-578, pp. 101-104, DOI: 10.4028/www.scientific.net/KEM.577-578.101.

Krejsa, M. (2014) Probabilistic reliability assessment of steel structures exposed to fatigue, in: Proc. Safety, Reliability and Risk Analysis: Beyond the Horizon, CRC Press-Taylor & Francis Group, pp. 2671-2679, ISBN: 978-1-315-81559-6; 978-1-138-00123-7, DOI: 10.1201/b15938-404.

Krejsa, M., Janas, P. & Krejsa, V. (2016) Application of the DOProC Method in Solving Reliability Problems. Applied Mechanics and Materials. 821, pp. 717-724. DOI: 10.4028/www.scientific.net/AMM.821.717.

Krejsa, M. & Kralik, J. (2015) Probabilistic Computational Methods in Structural Failure Analysis. Journal of Multiscale Modelling, 6, 2. DOI: 10.1142/S1756973715500067.

Kruis, J., Matous, K. & Dostal, Z. (2002) Solving laminated plates by domain decomposition. Advances in Engineering Software, 33, 7-10, pp. 445–452. DOI: 10.1016/S0965-9978(02)00075-3.

Nishihara, R., Murray, I. & Adams, R.P. (2014) Parallel MCMC with Generalized Elliptical Slice Sampling. Journal of Machine Learning Research, 15, 1, pp. 2087-2112.

Lozano, S. (2014) Computing fuzzy process efficiency in parallel systems. Fuzzy Optimization and Decision Making, 13, 1, pp. 73-89. DOI: 10.1007/s10700-013-9170-0.

Oran, E.S., Oh, C.K. & Cybyk, B.Z. (1998) Direct Simulation Monte Carlo: Recent Advances and Applications. Annual Review of Fluid Mechanics, 30, pp. 403-441. DOI: 10.1146/annurev.fluid.30.1.403.

Qiu, Z. & Wang, J. (2011) New direct probabilistic approach for static responses of structures with uncertainties. International Journal of Computer Mathematics, 88, 4, pp. 714–730. DOI: 10.1080/00207161003774230.

Reh, S., Beley, J.D., Mukherjee, S. & Khor, E.H. (2006) Probabilistic finite element analysis using ANSYS. Structural Safety, 28, 1-2, pp. 17-43, DOI: 10.1016/j.strusafe.2005.03.010.

Sharma, G. & Martin, J. (2009) MATLAB: A Language for Parallel Computing. International Journal of Parallel Programming, 37, 1, pp. 3-36. DOI: 10.1007/s10766-008-0082-5.

Vasek, J. & Krejsa, M. (2014) Probabilistic Reliability Assessment of Truss Construction in Matlab Software Platform. Transactions of the VSB – Technical University of Ostrava, Civil Engineering Series, 14, 1, pp. 100–109, DOI: 10.2478/tvsb-2014-0013.

Vrugt, J.A. (2016) Markov chain Monte Carlo simulation using the DREAM software package: Theory, concepts, and MATLAB implementation. Environmental Modelling & Software, 75, pp. 273-316. DOI: 10.1016/j.envsoft.2015.08.013.

22nd International Conference
ENGINEERING MECHANICS 2016
Svratka, Czech Republic, 9 – 12 May 2016

NUMERICAL MODELING OF STEEL WELDED SUPPORTING ELEMENTS

M. Krejsa[*], J. Brozovsky[**], D. Mikolasek[***], P. Parenica[****], R. Halama[*****]

Abstract: *The paper is focused on the numerical modeling of steel welded supporting elements and their verification using experiment. Currently, for the stress-strain analysis of the elements in supporting structures it is possible to use many commercial software systems, based on the finite element method - FEM. It is important to check and compare the results of FEM analysis with the results of physical verification test, in which the real behavior of the bearing element can be observed. The results of the comparison can be used for calibration of the computational model. The article deals with the physical test of steel supporting elements, whose main purpose is obtaining the material, geometry and strength characteristics of the fillet and butt welds. The main aim was at defining the tested samples numerical models for using FEM analysis and for the commercial software ANSYS. The tension test was performed during the experiment, wherein the totals load value and the corresponding deformation of the specimens under the load was monitored. Obtained data were used for the calibration of numerical models of test samples and they are necessary for further strain analysis of steel supporting elements.*

Keywords: Numerical modeling, Experiment, Steel structure, FEM, Fillet weld, Butt weld.

1. Introduction

Numerical modeling is increasingly promoting into design practice. Using powerful computers and efficient software systems can provide valuable results, which serve to increase the reliability of the proposed support systems and elements (Kotes & Vican, 2013). Complex mathematical procedures take into account physical and geometric nonlinearities of the structure (Janas et al., 2016). An important tool for mathematical modeling is particularly the Finite Element Method - FEM, whose principle is to discretize continuum to a certain (finite) number of elements and the determination of calculated parameters in individual nodes.

Numerical modeling finds its application in all sorts of areas of engineering. There are publications that analyze problems of mathematical modeling of structures based on thin-walled cold-rolled cross-section (Flodr et al., 2014) or round timber bolted joints with steel plates (Lokaj & Klajmonova, 2014). The results of numerical modeling have usually limited use without the experimental verification or without the load tests (Cajka & Krejsa, 2014). Test results may lead to calibration and validation of mathematical model, which should ensure compliance of the numerical model and the actual behavior of the investigated structure. Valuable results of mathematical modeling are also conditional on defining the material models, which are often associated with laboratory-obtained material properties (Major & Major, 2010). Some particular and selected problems of numerical modeling are aimed at ultimate limit state and probability-based studies (Kala, 2015; Kotrasova et al., 2015; Protivinsky & Krejsa, 2015; M Kralik & Kralik, 2013).

[*] Assoc. Prof. Ing. Martin Krejsa, Ph.D.: Department of Structural Mechanics, Faculty of Civil Engineering, VSB-Technical University of Ostrava, Ludvika Podeste 1875/17; 708 33, Ostrava - Poruba; CZ, martin.krejsa@vsb.cz

[**] Assoc. Prof. Ing. Jiri Brozovsky, Ph.D.: Department of Structural Mechanics, Faculty of Civil Engineering, VSB-Technical University of Ostrava, Ludvika Podeste 1875/17; 708 33, Ostrava - Poruba; CZ, jiri.brozovsky@vsb.cz

[***] Ing. David Mikolasek, Ph.D.: Department of Structural Mechanics, Faculty of Civil Engineering, VSB-Technical University of Ostrava, Ludvika Podeste 1875/17; 708 33, Ostrava - Poruba; CZ, david.mikolasek@vsb.cz

[****] Ing. Premysl Parenica: Department of Structures, Faculty of Civil Engineering, VSB-Technical University of Ostrava, Ludvika Podeste 1875/17; 708 33, Ostrava - Poruba; CZ, premysl.parenica@vsb.cz

[*****] Assoc. Prof. Ing. Radim Halama, Ph.D.: Department of Applied Mechanics, Faculty of Mechanical Engineering, VSB-Technical University of Ostrava, 17. listopadu 15/2172; 708 33, Ostrava - Poruba; CZ, radim.halama@vsb.cz

The stress analysis of welds has got also the considerable attention in the past. In (Hobbacher, 1993) it was defined stress intensity factor of welded joint for typical structural details, among others for cruciform joint fillet weld. In (Lazzarin & Tovo, 1998) the authors discuss the derivation of the so called notch stress intensity factors for welded joints, using which can be accurately described stress distributions in the toe neighborhood of weld toes.

With the development of commercial computing systems there have been emerging works which aim at describing the state of stress in the welds through FEM analysis. In (Meneghetti & Guzzella, 2014) is described the approach for a determination of the notch stress intensity factor in welded joints using three-dimensional finite element models (SOLID 45) in software system ANSYS. In (Cerit et al., 2010) authors focused on modeling of fillet welded cylindrical joints under tension and torsion loading with regard to the fatigue resistance (Krejsa, 2013, 2014). The work (Anca et al., 2011) deals with the mechanical analysis with the simulation of fusion welding by the Finite Element Method, where the implemented models include a moving heat source, temperature dependence of thermophysical properties, elastoplasticity and non-steady state heat transfer. Using software systems MSC Marc and ANSYS is possible to simulate and model the welding process and the rise of residual stresses (Barsoum & Lundback, 2009).

Application of the finite element method to predict thermal, material and mechanical effects of welding are comprehensively described in (Lindgren, 2006). Real behavior of welds in terms of stress analysis can be examined through physical tests. Publication (Kanvindea et al., 2009) contains the results from twenty-four cruciform weld experiments and complementary finite element simulations to study the effect of the weld root notch on strength and ductility of fillet welds. In (Lee et al., 2015) the real stress state in steel butt welds subjected to cyclic mechanical loading is evaluated. From the above summary of publications aimed at mathematical modeling of structures, focusing on the problems of welded oriented problems is obvious that this is a very current topic.

The further interpretation is dedicated to problems of mathematical modeling of welded bearing elements in steel structures. Some works focused on numerical modelling of a steel fillet welded joints based on experimental verification have been published (Krejsa et al., 2015). This article focuses on numerical modelling of different types of steel welded bearing elements - fillet welded lap joint and double V butt welded joints.

2. Numerical modelling of special designed specimens

Three types of specimens were designed to investigate the state of stress in fillet of butt welds. Specimens were designed to reflect the fact that the stiffness of connected elements has to be higher than the stiffness of the welded joints (see Fig. 1 to Fig. 3). It can therefore be assumed that the stress-strain diagram will reflect the behavior of strains and stresses in welds. It has to be noted also that for comparison of the behavior of the weld sample in Fig. 3 was made special specimen with the same geometrical parameters, which is not welded, but is formed by only the base material.

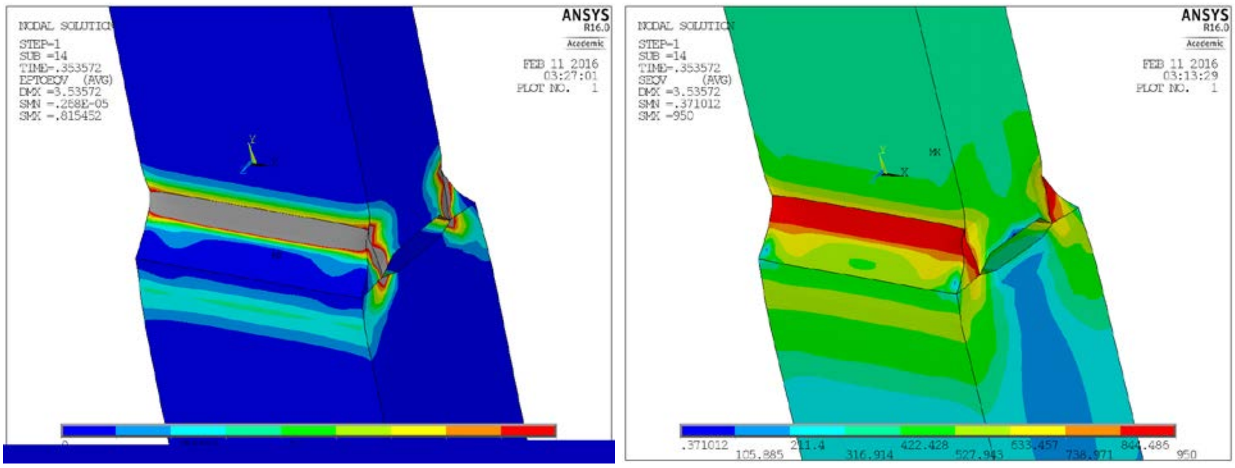

Fig. 1: Resulting total strain (left) and von Mises stress (right) in numerical model of fillet welded lap joint with densest FEM mesh and for the maximal achieved strength in tested sample

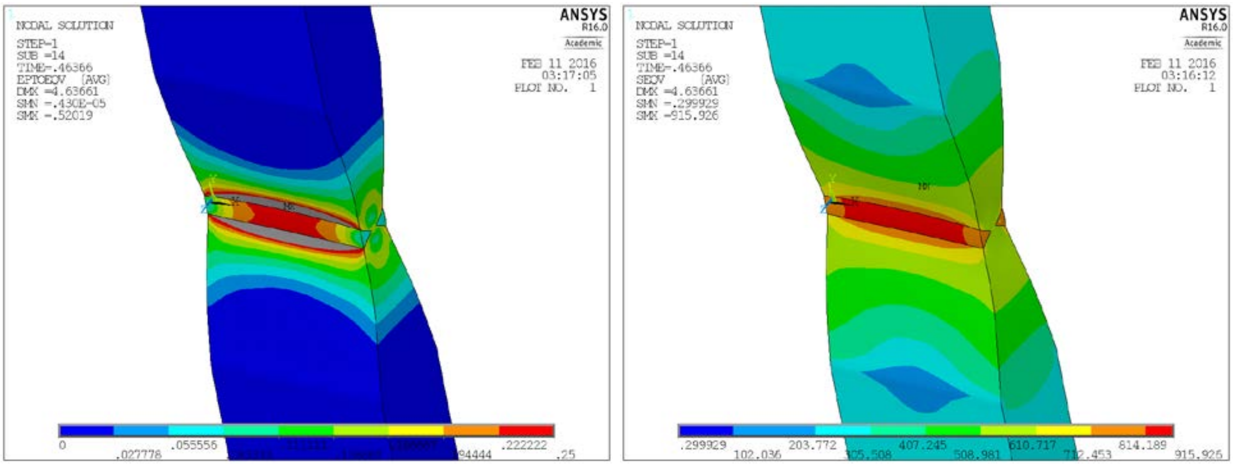

Fig. 2: Resulting total strain (left) and von Mises stress (right) in numerical model of double V butt welded joint with densest FEM mesh and for the maximal achieved strength in tested sample

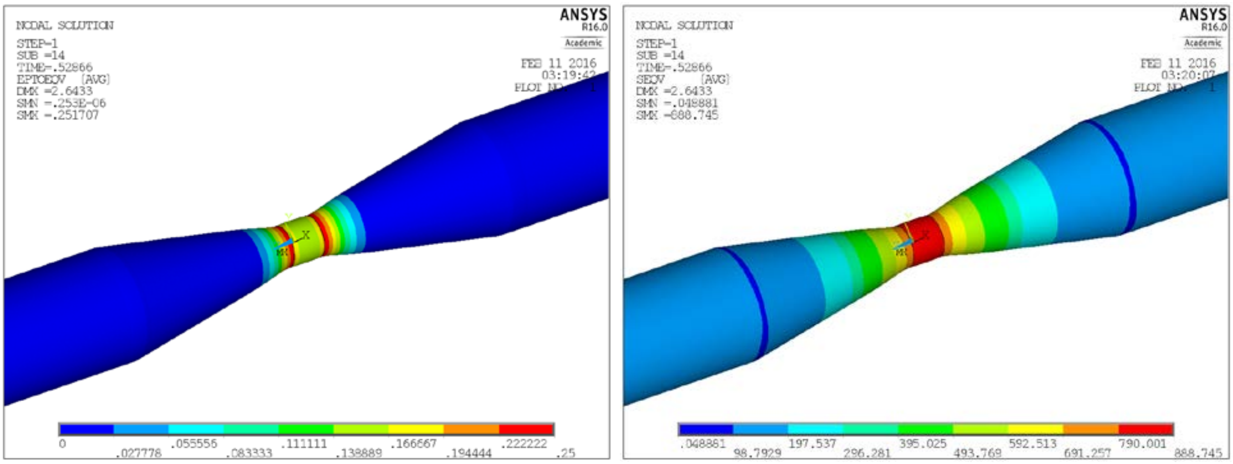

Fig. 3: Resulting total strain (left) and von Mises stress (right) in rotationally symmetric double U butt welded joint with densest FEM mesh and for the maximal achieved strength

The 20-node isoparametric SOLID186 finite elements and the ANSYS software were used. For each of the model were performed three variants of FEM mesh density (size of elements was 3 mm, 2 mm and 1 mm). For each model and FEM mesh density were performed compare/sensitivity stress-strain analysis based on bilinear and multilinear stress-strain diagrams of basic steel material and weld material. These diagrams were verified using measurement data from experiments. Resulting total strain and von Misses stress for numerical models with the densest FEM mesh and for maximal achieved strength in tested samples is possible to see for all three types of tested and modeled specimens in Figs. 1 to 3.

3. Conclusions

The article described experimental tests and numerical analysis in the program system ANSYS focused on steel fillet and butt welded supporting elements. On the basis of these experiments there were obtained parameters of a real stress-strain relations that will be used as input data for further works in the area of modeling of specific types of welded components, which can be used in steel structures of buildings.

Acknowledgement

This paper has been completed thanks to the financial support provided to VSB - Technical University of Ostrava by the Czech Ministry of Education, Youth and Sports from the budget for conceptual development of science, research and innovations for the year 2016.

References

Anca, A., Cardona, A., Risso, J. & Fachinotti, V.D. (2011) Finite element modeling of welding processes. Applied Mathematical Modelling, 35, 2, pp. 688-707, DOI: 10.1016/j.apm.2010.07.026.

Barsoum, Z. & Lundback, A. (2009) Simplified FE welding simulation of fillet welds 3D effects on the formation residual stresses. Engineering Failure Analysis, 16, 7, pp. 2281-2289, DOI: 10.1016/j.engfailanal.2009.03.018.

Cajka, R. & Krejsa, M. (2014) Validating a computational model of a rooflight steel structure by means of a load test. Applied Mechanics and Materials, 501-504, pp. 592-598, DOI: 10.4028/www.scientific.net/AMM.501-504.592.

Cerit, M., Kokumer, O. & Genel, K. (2010) Stress concentration effects of undercut defect and reinforcement metal in butt welded joint. Engineering Failure Analysis, 17, 2, pp. 571-578, DOI: 10.1016/j.engfailanal.2009.10.010.

Flodr, J., Krejsa, M., Mikolasek, D., Sucharda, O., Zidek, L. (2014) Mathematical Modelling of Thin-Walled Cold-Rolled Cross-Section. Applied Mechanics and Materials, 617, pp. 171-174, DOI: 10.4028/www.scientific.net/AMM.617.171.

Hobbacher, A. (1993) Stress intensity factors of welded joints. Engineering Fracture Mechanics, 46, 2, pp. 173-182, DOI: 10.1016/0013-7944(93)90278-Z.

Janas, P., Koubova, L. & Krejsa, M. (2016) Load Carrying Capacity of Steel Arch Reinforcement Taking Into Account the Geometrical and Physical Nonlinearity. Applied Mechanics and Materials, 821, pp. 709-716, DOI: 10.4028/www.scientific.net/AMM.821.709.

Kala, Z. (2015) Reliability and Sensitivity Analysis of Welded Shell Tanks for Crude Oil Storage, in: AIP Proc. Int. Conf. on Numerical Analysis and Applied Mathematics (ICNAAM), 1648, DOI: 10.1063/1.4913078.

Kanvindea, A.M., Gomeza, I.R., Robertsa, M., Fella, B.V. & Grondinb, G.Y. (2009) Strength and ductility of fillet welds with transverse root notch. Journal of Constructional Steel Research, 65, 4, pp. 948-958. DOI: 10.1016/j.jcsr.2008.05.001.

Kotes, P. & Vican, J. (2013) Recommended Reliability Levels for the Evaluation of Existing Bridges According to Eurocodes. Structural Engineering International, 23, 4, pp. 411-417, DOI: 10.2749/101686613X13627351081678.

Kotrasova, K., Grajciar, I., Kormanikova, E. (2015) A Case Study on the Seismic Behavior of Tanks Considering Soil-Structure-Fluid Interaction. Journal of Vibration Engineering & Technologies, 3, 3, pp. 315-330.

Kralik, J. & Kralik, Jr. (2013) Probability Assessment of Analysis of High-Rise Buildings Seismic Resistance. Advanced Materials Research, 712-715, pp. 929-936, DOI: 10.4028/www.scientific.net/AMR.712-715.929.

Krejsa, M. (2013) Probabilistic failure analysis of steel structures exposed to fatigue. Key Engineering Materials, 577-578, pp. 101-104, DOI: 10.4028/www.scientific.net/KEM.577-578.101.

Krejsa, M. (2014) Probabilistic reliability assessment of steel structures exposed to fatigue, in: Proc. Safety, Reliability and Risk Analysis: Beyond the Horizon, CRC Press-Taylor & Francis Group, pp. 2671-2679, ISBN: 978-1-315-81559-6; 978-1-138-00123-7, DOI: 10.1201/b15938-404.

Krejsa, M., Brozovsky, J., Mikolasek, D., Parenica, P., Zidek, L. & Kozak, J. (2015) An Experimental Testing of Fillet Welded Specimens. Applied Mechanics and Materials, 752-753, pp. 412-417, DOI: 10.4028/www.scientific.net/AMM.752-753.412.

Krejsa, M., Brozovsky, J., Mikolasek, D., Parenica, P. & Halama, R. (2015) Experimental Verification of a Steel Fillet Welded Joint Model, in: Proc. of the Fifteenth Int. Conf. on Civil, Structural and Environmental Engineering Computing (J. Kruis, Y. Tsompanakis & B.H.V. Topping eds.), Civil-Comp Press, DOI: 10.4203/ccp.108.34.

Lazzarin, P. & Tovo, R. (1998) A notch intensity factor approach to the stress analysis of welds. Fatigue & Fracture of Engineering Materials & Structures, 21, 9, pp. 1089-1103, DOI: 10.1046/j.1460-2695.1998.00097.x.

Lee, C.H., Chang, K.H. & Do, V.N.V. (2015) Finite element modeling of residual stress relaxation in steel butt welds under cyclic loading. Engineering Structures, 103, pp. 63-71, DOI: 10.1016/j.engstruct.2015.09.001.

Lindgren, L.E. (2006) Numerical modelling of welding. Computer Methods in Applied Mechanics and Engineering, 195, 48-49, pp. 6710-6736, DOI: 10.1016/j.cma.2005.08.018.

Lokaj, A. & Klajmonova, K. (2014) Carrying capacity of round timber bolted joints with steel plates under cyclic loading. Advanced Materials Research, 838-841, pp. 634-638, DOI: 10.4028/www.scientific.net/AMR.838-841.634.

Major, M. & Major, I. (2010) Acceleration wave in a thin segmental hyperelastic rod. Archives of Civil and Mechanical Engineering, 10, 1, pp. 59-67.

Meneghetti, G., Guzzella, C. (2014) The peak stress method to estimate the mode I notch stress intensity factor in welded joints using three-dimensional finite element models. Engineering Fracture Mechanics, 115, pp. 154-171, DOI: 10.1016/j.engfracmech.2013.11.002.

Protivinsky, J. & Krejsa, M. (2015) Reliability Assessment of the Dissipative Link in Steel Boiler Structure with Regard to Seismic Load, in: Proc. 4th Int. Conf. on Materials Engineering for Advanced Technologies (ICMEAT), London, pp. 202-206, ISBN: 978-1-60595-242-0.

22nd International Conference
ENGINEERING MECHANICS 2016
Svratka, Czech Republic, 9 – 12 May 2016

FUZZY CONTROL OF THE OBSERVATION AND TRACKING HEAD PLACED ON A MOVEABLE BASE

I. Krzysztofik*

Abstract: *The Observation and Tracking Head is a significant element of equipment of self-propelled anti-aircraft missile systems. It is used for detecting, identifying and tracking air and ground targets in different lighting conditions. The paper contains the analysis of fuzzy control of the head. The impact of kinematic excitations caused by the movement of the base on which the head is mounted on the operation of head has been taken into account. Selected results of numerical research are presented in a graphical form.*

Keywords: Observation and Tracking Head, Control, Fuzzy logic.

1. Introduction

The Observation and Tracking Head (OTH) is a significant element of equipment of remotely controlled modules of weaponry, mounted on combat vehicles. The head is used for detecting, identifying and tracking air and ground targets during the day and at night, also in the conditions of dense smoke and fog (Krzysztofik & Koruba, 2012; Krzysztofik, 2012).

OTH is a modern optoelectronic system which integrates many sensors (M. Blasiak & Kotowski, 2009). First of all, it is equipped with a thermographic camera, daylight camera and an eye-safe laser range finder. Moreover, it can be equipped with a weak light camera which increases the possibility of head operation to dawn and dusk. Manufacturers frequently equip their observation systems with an indicator or a laser illuminator as well as an internal GPS/IMU navigation system. Thanks to that it is possible to determine the geographical location of a target. The mentioned sensors are placed on a controlled and gyroscope-stabilized platform which ensures stability of image regardless of manoeuvres made by the vehicle (Koruba et al., 2010a).

The head performs movements in two planes: a vertical one, in an angular scope usually up to 90 degrees, and a horizontal one, in the full angular scope. During the search of the air space, the head performs the programmed movement. After detecting a target, it automatically passes into the tracking mode. Simultaneously, strong disruptions coming from the deck of the self-propelled missile system on which the head is located affect the head (Koruba et al., 2010b). Hence, a careful selection of parameters of the automatic control system is important so that, independently of the said disruptions, the process of searching and tracking a detected target went stably.

2. Formulation of problem

It is necessary to determine a suitable physical model and then to formulate a mathematical model for conducting simulation research on the dynamics of the Observation and Tracking Head, as shown in papers (Baranowski, 2013; S. Blasiak et al., 2013; S. Blasiak et al., 2014; S. Blasiak, 2015a, 2015b).

In this paper, the spatial model of the Observation and Tracking Head placed on the deck of a movable object shown in Fig. 1 was adopted for the research. The head consists of an outer frame of mass m_{ex} and moments of inertia $J_{x_{h1}}, J_{y_{h1}}, J_{z_{h1}}$ as well as an inner frame, including an observation and tracking device of mass m_{in} and moments of inertia $J_{x_h}, J_{y_h}, J_{z_h}$. We determine head movement with the

* Eng. Izabela Krzysztofik, PhD.: Department of Applied Computer Science and Armament Engineering, Faculty of Mechatronics and Mechanical Engineering, Kielce University of Technology, Aleja Tysiaclecia Panstwa Polskiego 7; 25-314, Kielce; PL, pssik@tu.kielce.pl

use of two functions: $\psi_h(t)$ – the angle of rotation of the head around axis y_h and $\vartheta_h(t)$ – the angle of rotation of the head around axis z_h.

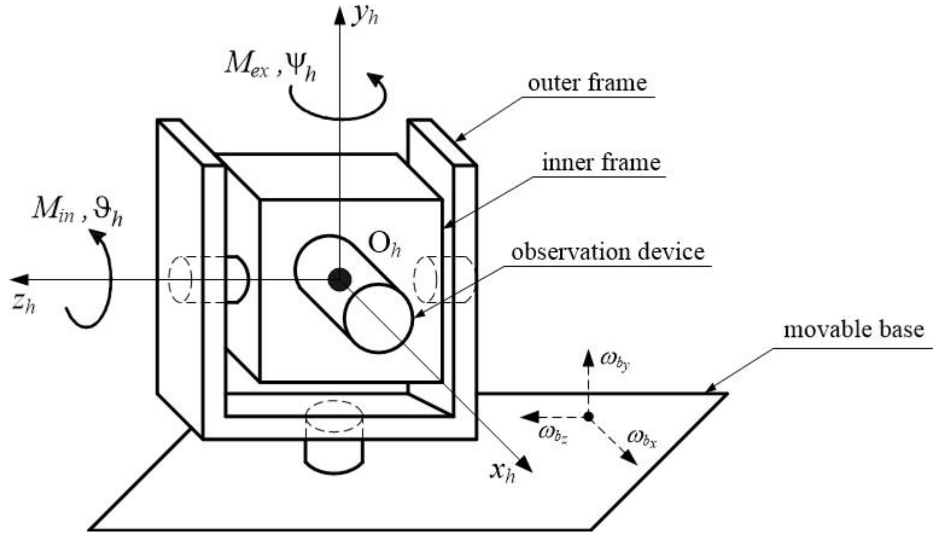

Fig. 1: The view of the Observation and Tracking Head.

The head is affected by base vibrations $\omega_{b_x}, \omega_{b_y}, \omega_{b_z}$ which were adopted in the harmonic form:

$$\omega_{b_x} = \omega_{xo} \cdot \sin(\nu_b t + \phi_x) \tag{1}$$

$$\omega_{b_z} = \omega_{zo} \cdot \sin(\nu_b t + \phi_z) \tag{2}$$

where: $\omega_{b_y} = 0$, $\omega_{xo} = 1.5\ \text{rad}$, $\omega_{zo} = 1.5\ \text{rad}$, $\nu_b = 10\ \text{rad/s}$, $\phi_x = 0.314\ \text{rad}$, $\phi_z = -0.314\ \text{rad}$.

The equations of dynamics of the head were introduced with the use of Lagrange II-nd kind of equations with the assumption that the centre of mass of the head overlaps with the centre of movement. The following system of equations was obtained:

$$\begin{aligned}
&\left[J_{y_{h1}} + J_{y_h} + \left(J_{x_h} - J_{y_h}\right)\sin^2\vartheta_h\right]\left(\ddot{\psi}_h + \dot{\omega}_{b_y}\right) + \frac{1}{2}\left(J_{x_h} - J_{y_h}\right)\left(\dot{\omega}_{x_{h1}} + \omega_{y_{h1}}\dot{\vartheta}_h\right)\sin 2\vartheta_h \\
&- \left[J_{y_h} + \left(J_{x_h} - J_{y_h}\right)\sin^2\vartheta_h\right]\omega_{x_{h1}}\dot{\vartheta}_h + J_{x_h}\omega_{x_h}\omega_{z_h}\cos\vartheta_h - J_{y_h}\omega_{y_h}\omega_{z_h}\sin\vartheta_h \\
&+ \left(J_{x_{h1}} - J_{z_{h1}}\right)\omega_{x_{h1}}\omega_{z_{h1}} - J_{z_h}\omega_{z_h}\omega_{x_{h1}} + \eta_{ex}\psi_h = M_{ex}
\end{aligned} \tag{3}$$

$$J_{z_h}\left(\ddot{\vartheta}_h + \dot{\omega}_{z_{h1}}\right) - \left(J_{x_h} - J_{y_h}\right)\omega_{x_h}\omega_{y_h} + \eta_{in}\vartheta_h = M_{in} \tag{4}$$

where:

$\omega_{x_{h1}} = \omega_{b_x}\cos\psi_h - \omega_{b_z}\sin\psi_h$, $\omega_{y_{h1}} = \omega_{b_y} + \dot{\psi}_h$, $\omega_{z_{h1}} = \omega_{b_x}\sin\psi_h + \omega_{b_z}\cos\psi_h$;

$\omega_{x_h} = \omega_{x_{h1}}\cos\vartheta_h + \omega_{y_{h1}}\sin\vartheta_h$, $\omega_{y_h} = -\omega_{x_{h1}}\sin\vartheta_h + \omega_{y_{h1}}\cos\vartheta_h$, $\omega_{z_h} = \omega_{z_{h1}} + \dot{\vartheta}_h$;

η_{ex}, η_{in} – friction coefficient in suspension bearings of the outer and inner frame, respectively;

M_{ex}, M_{in} – moment of forces interacting on outer and inner frame, respectively.

3. Fuzzy control

In order to achieve precision when searching and tracking a detected target it is necessary to isolate the observation and tracking device completely from angular movements of the base. It can be done by properly formulated controls M_{ex} and M_{in}, applied to two mutually perpendicular axes of the head (Gapiński & Stefański, 2013; Krzysztofik & Koruba, 2012, 2014; Osiecki & Stefański, 2008). In the

Matlab/Simulink software fuzzy controllers Mamdani's PD type were designed (Driankov et al., 1996; Sivanandam et al., 2007). Input signals to head deflection controller are error $e_1 = \psi_{hr} - \psi_h$ and error change Δe_1, whereas the output signal is the control M_{ex}. Analogously, input signals to head inclination controller are error $e_2 = \vartheta_{hr} - \vartheta_h$ and error change Δe_2, whereas the control M_{in} is the output signal. Angles $\psi_{hr}, \vartheta_{hr}$ mark a set angle of head deflection and inclination, respectively. The inference was conducted based on 25 fuzzy rules. Trapezium and triangular functions were adopted as membership functions (Takosoglu et al., 2009; Takosoglu et al., 2012).

In order to assess the proposed fuzzy control of the Observation and Tracking Head mounted on a movable base, numerical simulations were conducted with the Matlab/Simulink software, with the use of *ode3* procedure, with a fixed constant of integration amounting to $dt = 0.0001$, for the following parameters: $I_{x_{h1}} = 0.22\ \text{kgm}^2$, $I_{y_{h1}} = 0.114\ \text{kgm}^2$, $I_{z_{h1}} = 0.117\ \text{kgm}^2$, $I_{x_h} = 0.061\ \text{kgm}^2$, $I_{y_h} = 0.035\ \text{kgm}^2$, $I_{z_h} = 0.029\ \text{kgm}^2$, $\eta_{ex} = 0.05\ \text{Nms}$, $\eta_{in} = 0.05\ \text{Nms}$.

Figs. 2-3 show the set and real head trajectory as well as control errors for the programmed movement on the surface of a circular cone.

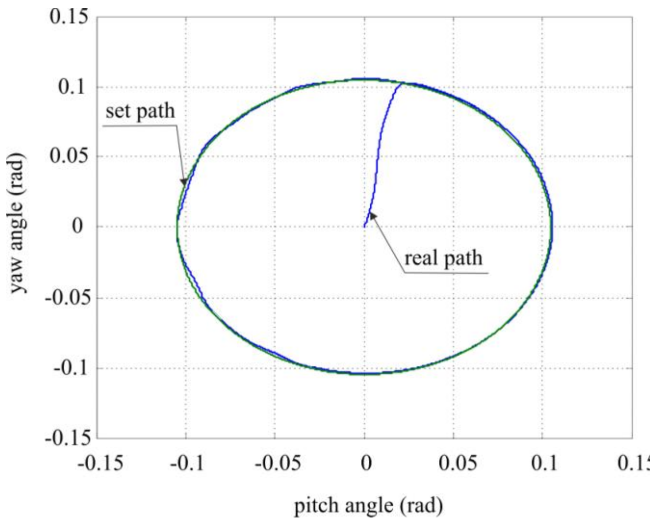

Fig. 2: The set and real head trajectory.

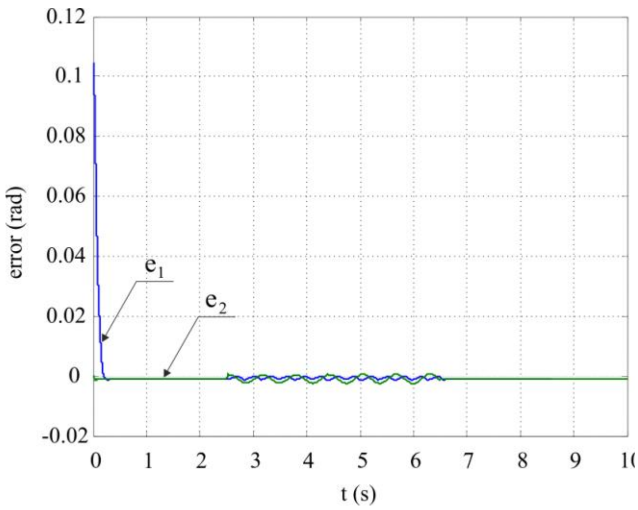

Fig. 3: Control errors.

Figs. 4-5 show the set and real head trajectory as well as control errors for the programmed movement on the unwinding spiral.

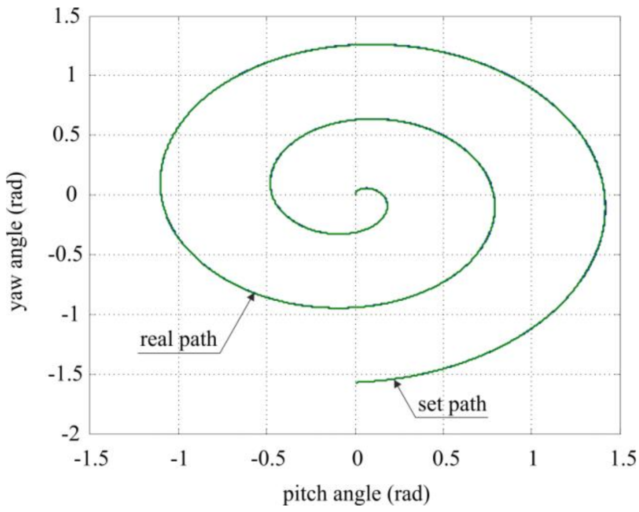

Fig. 4: The set and real head trajectory.

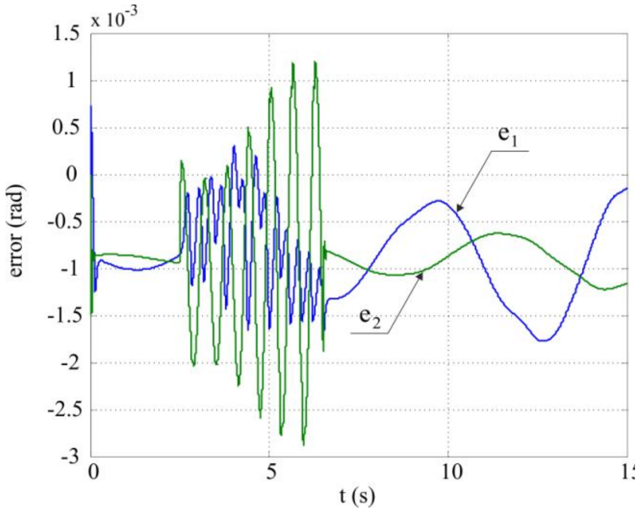

Fig. 5: Control errors.

4. Conclusions

The task of Observation and Tracking Head consists in effective identification and subsequent tracking of targets which are to be destroyed. Therefore, the reliability and precision of operation of the head are important.

The presented research results confirm the correct operation of the designed fuzzy controllers for controlling OTH in deflection and inclination movement. The programmed movement is fulfilled with high precision. Base vibrations affecting the head are simply imperceptible. Slight deviations from the set location occur. It is particularly visible in Fig. 2.

In the next stage of research, tests of effectiveness of operation of the proposed control system at the moment of the head passing from searching to tracking a detected target should be conducted.

References

Baranowski, L. (2013) Equations of motion of a spin-stabilized projectile for flight stability testing. Journal of Theoretical and Applied Mechanics, 51, 1, pp. 235–246.

Blasiak, M. & Kotowski, R. (2009) Propagation of acoustic waves in piezoelectric crystals. PRZEGLAD ELEKTROTECHNICZNY, 85, 12, pp. 40–43.

Blasiak, S. (2015a) An analytical approach to heat transfer and thermal distortions in non-contacting face seals. International Journal of Heat and Mass Transfer, 81, pp. 90–102. http://doi.org/10.1016/j.ijheatmasstransfer.2014.10.011

Blasiak, S. (2015b) The two dimensional thermohydrodynamic analysis of a lubrication in non-contacting face seals. Journal of Thermal Science and Technology, 10, 1, pp. JTST0016-JTST0016. http://doi.org/10.1299/jtst.2015jtst0016

Blasiak, S., Laski, P. A. & Takosoglu, J. E. (2013) Parametric analysis of heat transfer in non-contacting face seals. International Journal of Heat and Mass Transfer, 57, pp. 22–31. http://doi.org/10.1016/j.ijheatmasstransfer.2012.09.058.

Blasiak, S., Takosoglu, J. E. & Laski, P. A. (2014) Heat transfer and thermal deformations in non-contacting face seals. Journal of Thermal Science and Technology, 9, 2, pp. JTST0011-JTST0011. http://doi.org/10.1299/jtst.2014jtst0011

Driankov, D., Hellendoorn, H. & Reinfrank, M. (1996) An Introduction to Fuzzy Control. Springer-Verlag Berlin Heidelberg.

Gapiński, D. & Stefański, K. (2013) A Control of Modified Optical Scanning And Tracking Head To Detection And Tracking Air Targets. Solid State Phenomena, 210, pp. 145–155. http://doi.org/10.4028/www.scientific.net/SSP.210.145

Koruba, Z., Dziopa, Z. & Krzysztofik, I. (2010a) Dynamics and control of a gyroscope-stabilized platform in a self-propelled anti-aircraft system. Journal of Theoretical and Applied Mechanics, 48, 1, pp. 5–26.

Koruba, Z., Dziopa, Z. & Krzysztofik, I. (2010b) Dynamics of a controlled anti-aircraft missile launcher mounted on a moveable base. Journal of Theoretical and Applied Mechanics, 48, 2, pp. 279–295.

Krzysztofik, I. (2012) The Dynamics of the Controlled Observation and Tracking Head Located on a Moving Vehicle. Solid State Phenomena, 180, pp. 313–322. http://doi.org/10.4028/www.scientific.net/SSP.180.313

Krzysztofik, I. & Koruba, Z. (2012) Model of Dynamics and Control of Tracking-Searching Head, Placed on a Moving Object. Journal of Automation and Information Sciences, 44, 5, pp. 38–47.

Krzysztofik, I. & Koruba, Z. (2014) Mathematical Model of Movement of the Observation and Tracking Head of an Unmanned Aerial Vehicle Performing Ground Target Search and Tracking. Journal of Applied Mathematics, 2014, Article ID 934250, 11 pages. http://dx.doi.org/10.1155/2014/934250

Osiecki, J. W. & Stefański K. (2008) On a method of target detection and tracking used in air defence. Journal of Theoretical and Applied Mechanics, 46, 4, pp. 909–916.

Sivanandam, S. N., Sumathi, S. & Deepa, S. N. (2007) Introduction to Fuzzy Logic using MATLAB. Springer-Verlag Berlin Heidelberg.

Takosoglu, J. E., Dindorf, R. F. & Laski, P. A. (2009) Rapid prototyping of fuzzy controller pneumatic servo-system. International Journal of Advanced Manufacturing Technology, 40, 3-4, pp. 349–361. http://doi.org/10.1007/s00170-007-1349-5

Takosoglu, J. E., Laski, P. A. & Blasiak, S. (2012) A fuzzy logic controller for the positioning control of an electro-pneumatic servo-drive. Proceedings of the Institution of Mechanical Engineers, Part I: Journal of Systems and Control Engineering, 226, 10, pp. 1335–1343. http://doi.org/10.1177/0959651812456498

22nd International Conference
ENGINEERING MECHANICS 2016
Svratka, Czech Republic, 9 – 12 May 2016

HYDRAULIC RESISTANCE OF MAGNETORHEOLOGICAL DAMPER VISCOUS BYPASS GAP

M. Kubík*, O. Macháček, Z. Strecker, J. Roupec, I. Mazůrek

Abstract: *The paper presents hydraulic resistance of viscous bypass gap in magnetorheological damper using FEM system Ansys. The appropriate design of bypass gap is essential for efficient function of MR damper in automotive. In the paper, a numerical hydraulic model of bypass gap filled with MR fluid is compared with experiments on the designed test rig. Maximal difference between numerical model and experiments for various geometries and MR fluids is 24%.*

Keywords: Magnetorheological fluid, MR fluid, magnetorheological damper, MR damper, bypass gap.

1. Introduction

Magnetorheological (MR) fluid is composed of micro-scale ferromagnetic particles, carrier fluid and additives. Upon the application of an external magnetic field, the MR fluid is able to change their behaviour from a fluid state to a semi-solid or plastic state, and vice-versa, in a couple of milliseconds (Wang et al., 2011). This effect is caused by arrangement the particles in the direction of the magnetic field fig.1. This phenomenon is known as the MR effect. MR fluids are attractive because they provide a simple and rapid response interface between electronic control systems and mechanical systems. This behaviour of MR fluid uses magnetorheological (MR) damper.

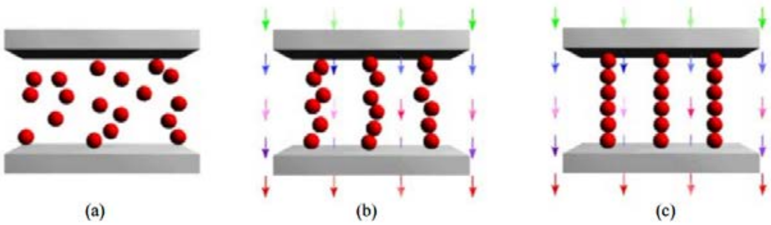

Fig. 1: MR effect (Yang et al., 2002), a) without magnetic field, b) and c) in magnetic field.

MR damper is device which can resize the dissipated energy depending on the current in the coil. MR damper is using in automotive industry (Nguyen et al., 2009), in railway industry (Guo et al., 2014), for damping in stay cable bridges (Choi at al., 2007) or for the control of seismic vibrations in buildings (Yang et al., 2002). The common design of MR damper is composed of electromagnetic coil, magnetic circuit and MR fluid fig. 2. One of the important curves describing the behaviour of MR damper is damping force dependency on piston velocity and electric current (F-v-I). MR damper exhibits rapid growth of force in dependence on piston velocity for small velocities followed by small increase of force in dependence on piston velocity for higher velocities. This non-linearity in F-v dependency causes an undesirable hardness to the vehicle, which might degrade ride comfort (Sohn et al., 2015). Foister et al. (2009) proposed parallel connection of magnetic and bypass gap in MR damper which is not exposed to magnetic field fig. 2(b). This gap is usually designed as nozzle in the piston of MR damper. MR fluid flows through the viscous bypass gap in case the active zone exhibits high hydraulic resistance. The proposed change caused inclination of slope of F-v dependency in low piston velocity fig. 2(b). Sohn et. al (2015) describes essential analytical hydraulic model of bypass gap operating in MR fluid. However, this model does not include turbulent flow or entrance losses.

* All autors: Institute of Machine and Industrial Design, Brno University of Technology, Technická 2896/2;616 69, Brno; CZ, y115760@stud.fme.vutbr.cz

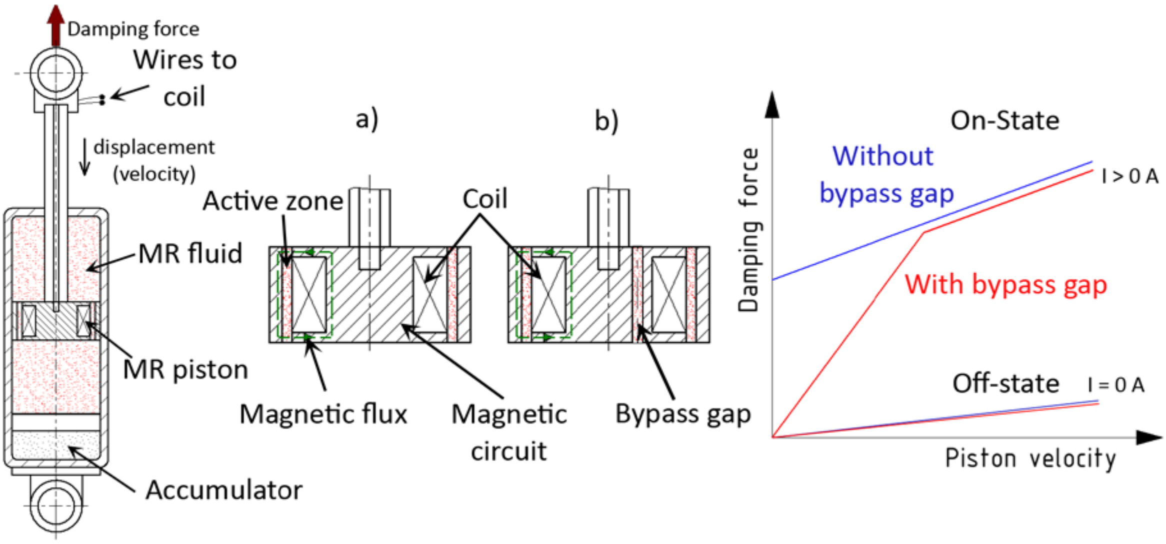

Fig. 2: MR damper; a) piston without bypass gap; b) piston with bypass gap.

The main goal of this paper is to propose the numerical hydraulic model of viscous bypass gap operating in MR fluid and to compare the results from simulation with experiments.

2. Methods

2.1. Experimental unit and methodology of testing

The experimental unit was design for efficient testing of hydraulic resistance of bypass gap filled by MR fluid. This equipment simulates behaviour of bypass gap in MR damper when current is applied. The experimental unit (fig. 3 left) is composed of commercially available hydraulic cylinder (1), hydraulic fittings (8, 9, 10, 11, 12) and block (3). In the block, there are located replaceable nozzle (bypass gap) (2), expansion tank (7) with hydraulic valve (6) and temperature sensor (4).

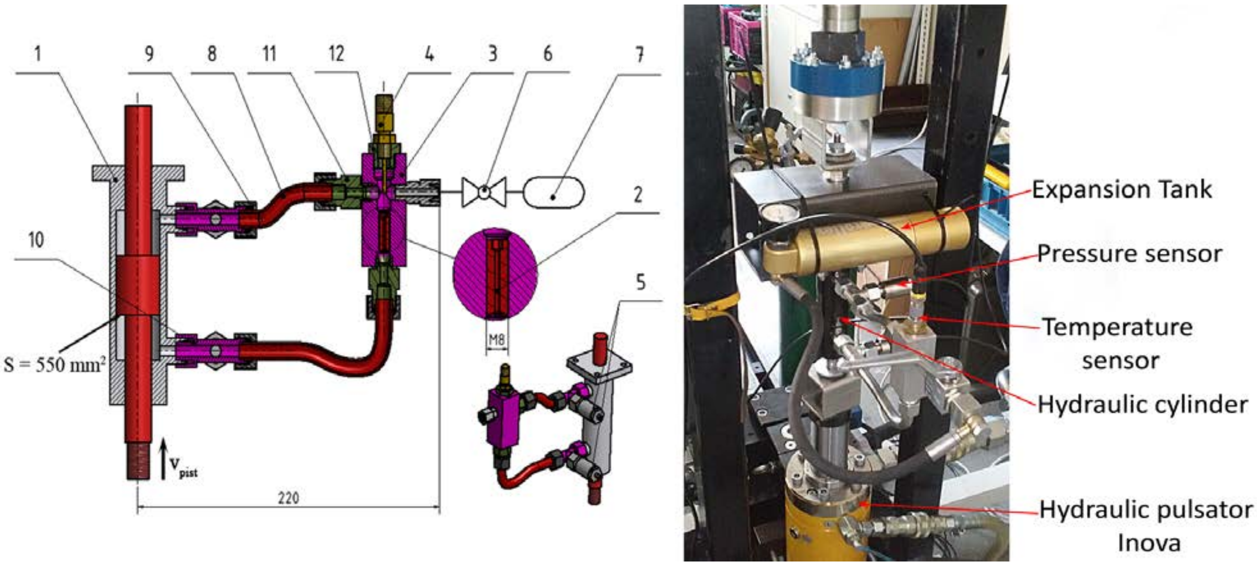

Fig. 3: Experimental unit.

The experimental unit was mounted to the stand with hydraulic pulsator Inova. Hydraulic pulsator Inova moves with the piston (1), which creates a flow of MR fluid through the test nozzle (bypass gap). Stroke, temperature, pressure above and under piston was measured fig. 3(5). The logarithmic sweep with constant amplitude of stroke 10 mm was used. Using the expansion tank, the tested system was pressurized to 10 bars. Expansion tank was separated from tested system by hydraulic valve before the experiment. Therefore, an expansion tank stiffness did not affect the experiment. The data was measured with sampling frequency 2000 Hz.

2.2. Numerical model

Hydraulic model of test nozzle was created by FEM software Ansys CFX. The parabolic velocity profile with mean velocity v_s and intensity of turbulence 5% was set on inlet. The average static pressure 0 bar was set on the outlet. The boundary conditions were smooth wall and no slip wall. The k-ε turbulent model was used. MR fluid was described by dynamic viscosity for each average temperature obtained from experiment. Residual target (RMS) was set 0.0001. The geometry of nozzle fig. 4 was discretized by 45 726 tetrahedral elements.

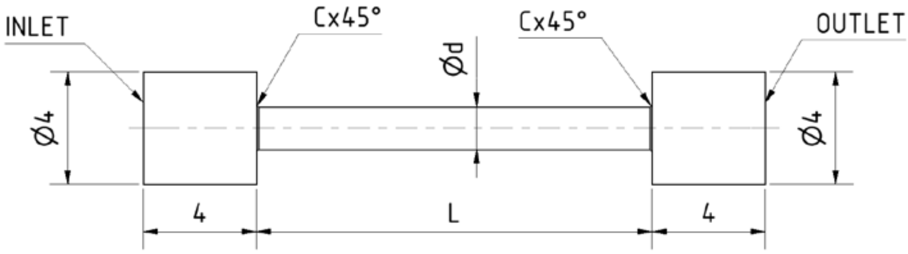

Fig. 4: Geometry.

2.3. MR fluids and geometry of nozzles

Commercially available MR fluids Lord MRF 122-EG (solids content by weight 72%) and Lord MRF 140-CG (85%) were tested. The diameter and length of nozzles are in tab. 1.

Tab. 1: Geometry of nozzles.

�d [mm]	L [mm]	C [mm]	�d [mm]	L [mm]	C [mm]
1.65	4.2	0.07	1.63	14.8	0.07
1.6	7.2	0.09	1.5	14.8	0.08
1.66	13.8	0.08	1.95	14.8	0.08

3. Results

3.1. Lord MRF 122-EG

The different diameters of nozzles with constant length 14 mm filled with MR 122-EG were tested. The results show the biggest difference between the pressure drop calculated from simulation and pressure drop measured from experiment for 2 mm nozzle. This difference at velocity 0.2 m/s is 19.5%. The next experiment was for different lengths of nozzles at the same diameter 1.6 mm. The difference between experiment and model was 14% for length 4 mm.

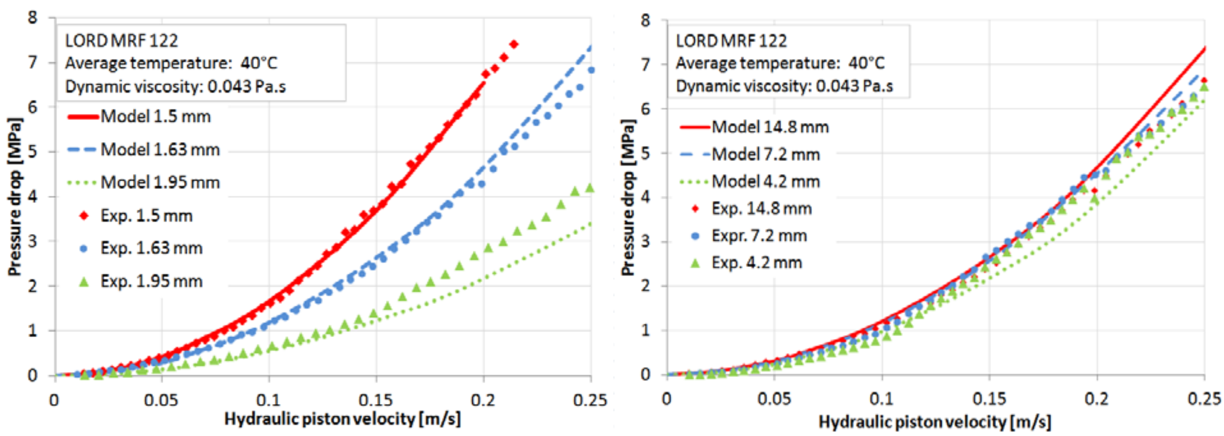

Fig. 5: Influence of diameter (left) and length (right) of nozzle.

3.2. Lord MRF 140-CG

The different diameter of nozzles with constant length 14 mm filled with MR 140-CG was tested. The results show the biggest difference between model and experiment for velocity higher than 0.15 m/s. The next experiment was for different length of nozzles with the same diameter of 1.6 mm. The difference between experiment and model was 24% for the length 7.2 mm.

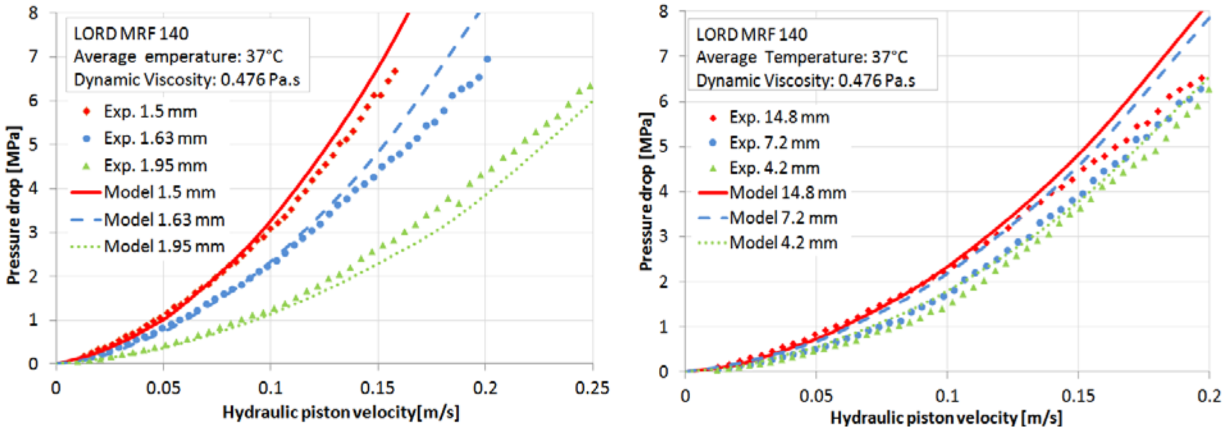

Fig. 6: Influence of diameter (left) and length (right).

4. Conclusions

In this paper, the result from hydraulic numerical model of viscous bypass gap in MR damper was published. For Lord MRF 122-EG and Lord MRF 140-CG, the numerical model with different geometry of bypass gap was compared with experiment. A difference between numerical model and experiments was observed especially for velocity higher than 0.15 m/s. The maximal error of numerical model is 24%. This error was observed for MRF 140-CG, diameter of nozzle 1.6 mm and length 7.2 mm. Presented numerical model is sufficiently accurate for majority of MR damper designs.

Acknowledgement

The research leading to these results has received funding from the MEYS under the National Sustainability Programme I (Project LO1202), FSI-S-14-2329, FEKT/FSI-J-15-2777, FV 15-13, FV 16-17, FEKT/FSI-J-16-3 and GAČR 13-31834P.

References

Choi, K.-M., Jung, H.-J., Cho, S.-W., Lee, I.-W. (2007) Application of smart passive damping system using MR damper to highway bridge structure. Journal of Mechanical Science and Technology 21, pp. 870-874

Foister, R.T., Nehl, Kruckemeyer, W.C. Raynauld, O. (2009) Magnetorheological (MR) piston assembly with primary and secondary channels to improve mr damper force

Guo, C., Gong, X., Zong, L., Peng, C., Xuan, S. (2014). Twin-tube- and bypass-containing magneto-rheological damper for use in railway vehicles. Proceedings of the Institution of Mechanical Engineers, Part F: Journal of Rail and Rapid Transit 229, pp.48-57.

Nguyen, Q.-H. & Choi, S.-B. (2009) Optimal design of MR shock absorber and application to vehicle suspension. Smart Materials and Structures, 18, pp.1-11.

Sohn, J.W., Oh, J.-S., Choi, S.-B., Lee, I.-W. (2015). Design and novel type of a magnetorheological damper featuring piston bypass hole. Smart Materials and Structures 24, pp.810-823.

Wang, D.H. & Liao, W.H. (2011) Magnetorheological fluid dampers: a review of parametric modelling. Smart Materials and Structures, 20, pp. 839-873.

Yang, G., Spencer, B.F., Carlson, J.D. & Sain, M.K. (2002) Large-scale MR fluid dampers: modeling and dynamic performance considerations. Engineering Structures 24, pp. 309-323.

22nd International Conference
ENGINEERING MECHANICS 2016
Svratka, Czech Republic, 9 – 12 May 2016

AUTOMATIC DIFFERENTIAL LOCK CONTROL IN A TRUCK – STRAIGHT DRIVE

P. Kučera[*], V. Píštěk[**], P. Porteš[***]

Abstract: *The paper deals with the creation of control algorithm for locking differential of the truck. This algorithm is based on assumptions of the ZF ADM system and it is created using software Simulink-Stateflow. The article describes the function of algorithm and its application to the computational model of vehicle with 4x4 drive. In conclusion, a simulation of driving manoeuvres is done to verify the functionality of the assembled control algorithm of the differential.*

Keywords: Control Algorithm, Simulink, Stateflow, Computational Model of Vehicle, Differential

1. Introduction

Mechatronic systems aimed at controlling of the vehicle differential locking can be used for more efficient use of a vehicle torque. The available systems are very sophisticated. For example Torque Vectoring System works with a continuous change of the torque control. In case of trucks, simple systems of a torque step change are used. This principle is used by ZF Company which has developed an algorithm for the control of the dog clutch with special teeth for the differential lock. This system is known as ZF ADM system. According to the literature (Stelzeneder, F. H. & Aitzetmüller, H., 2000), the system is intended for a vehicle up to 6x6 drive. Basic philosophy of this control is monitoring of each wheel speed and a slip evaluation then the algorithm determines a lock and open of the differential.

The article deals with the creation of a partially independent control algorithm for the differential lock which is based on assumptions of the ZF ADM system. This means that there is not a sequential lock of the differential in all cases as in the case of the ZF ADM system. The algorithm is also extended for a vehicle up to 8x8 drive. The algorithm was created in the Simulink-Stateflow software. In order to verify the algorithm function, the vehicle computational model was assembled. This vehicle model was built with the use of own libraries with blocks containing computational models of basic vehicle powertrain elements. A more detailed description can be found in (Kučera, P. 2015; Kučera, P. & Píštěk, V., 2014; Kučera, P. & Píštěk, V., 2013).The article describes the application of the control algorithm on the vehicle computational model, as well as simulation of the drive in muddy conditions. The aim was to develop a control algorithm which could be easily compiled into an appropriate language and used on the National Instruments hardware and software. This will allow initial testing of the control algorithm on a real vehicle.

2. Control algorithm of the differential lock

Knowing of the ZF ADM system (Stelzeneder, F. H. & Aitzetmüller, H., 2000) is the basis required to generate the algorithm. The created control algorithm for the control needs a speed monitoring of each wheel. The slip between the left and right wheel of a single axle is calculated from this wheel speed. The slip between the drive shafts of the respective axles is calculated, too. However, a problem may occur when turning because the individual wheels rotate at different angular velocity. Then the control system

[*] Ing. Pavel Kučera, Ph.D.: Institute of Automotive Engineering, University of Technology, Technická 2896/2; 616 69, Brno; CZ, kucera@fme.vutbr.cz

[**] Prof. Ing. Václav Píštěk, DrSc.: Institute of Automotive Engineering, University of Technology, Technická 2896/2; 616 69, Brno; CZ, pistek.v@fme.vutbr.cz

[***] Doc. Ing. Petr Porteš, Ph.D.: Institute of Automotive Engineering, University of Technology, Technická 2896/2; 616 69, Brno; CZ, portes@fme.vutbr.cz

would evaluate a condition as a slip. For this reason, the steering angle sensor is used, and a slip correction is carried out. For example, the slip of the front axle is described by the equation in the created algorithm

$$s=\frac{\max(\omega_L,\omega_R)-\min(\omega_L,\omega_R)}{\max(\omega_L,\omega_R)}-s_{cor},\ \text{if}\ \max(\omega_L,\omega_R)=0,\ s=0, \tag{1}$$

where s is the slip between the right and left wheel, s_{cor} – slip correction, ω_L – angular velocity of the left wheel and ω_R – angular velocity of the right wheel. The speed difference is controlled to prevent the destruction of powertrain parts. The brake pedal is another control element. In case of braking, axle differentials must be opened because the vehicle stability must be preferred. The braking state of the engine is a similar case. The throttle is used to control a state of the engine braking. In terms of vehicle velocity, a function of an axis differential lock is limited. The last of the main sensors is the clutch sensor, which is used for the changing gear. The control algorithm is created in the Simulink software using the Stateflow library, which is intended primarily for creating logic algorithms. The algorithm is divided into two main parts and the user has four control buttons. The first button sets a manual or automatic control of the differential lock. The diagram of the automatic control is shown in Fig. 1. In case of manual control, another three buttons are used for locking.

3. Computational model of the vehicle

The available literature (Dabney, J. B. & Harman T. L., 2004; Grepl, R., 2007) was used to create computational models. The vehicle computational model with 4x4 drive was used for the differential lock simulation of the truck. The basic parameters of the vehicle are the weight 20000 kg, front axle track 1.994 m, rear axle track 1.774 m, wheelbase 3.7 m, engine power 265 kW at 1500-1900 rpm and engine torque 1775 Nm at 1000-1410 rpm. To assemble a computational model of a commercial vehicle, blocks from own library are used and its powertrain is assembled from an engine block (Paccar MX Euro 5), clutch, transmissions (ZF 16S 2530), auxiliary transmission with the option of turning on and off of the front drive, two axles with axial differentials, drum brakes, computational models of tyres (315/80 R22.5) and vehicle block. The control unit block, differential block, tyre block and road block are the most important elements in the computational model. The computational model of the differential allows a simulation where the differential is locked. It is an important aspect for testing the control algorithm. In this case, the differential can be closed or opened. The tyre block (Pacejka, H. B., 2006) has been extended by a possibility to change the value of the scale factor for the peak friction coefficient $\lambda_{\mu x}$, $\lambda_{\mu y}$ and the rolling resistance coefficient q_{sy1}. It is important for simulation of the slip.

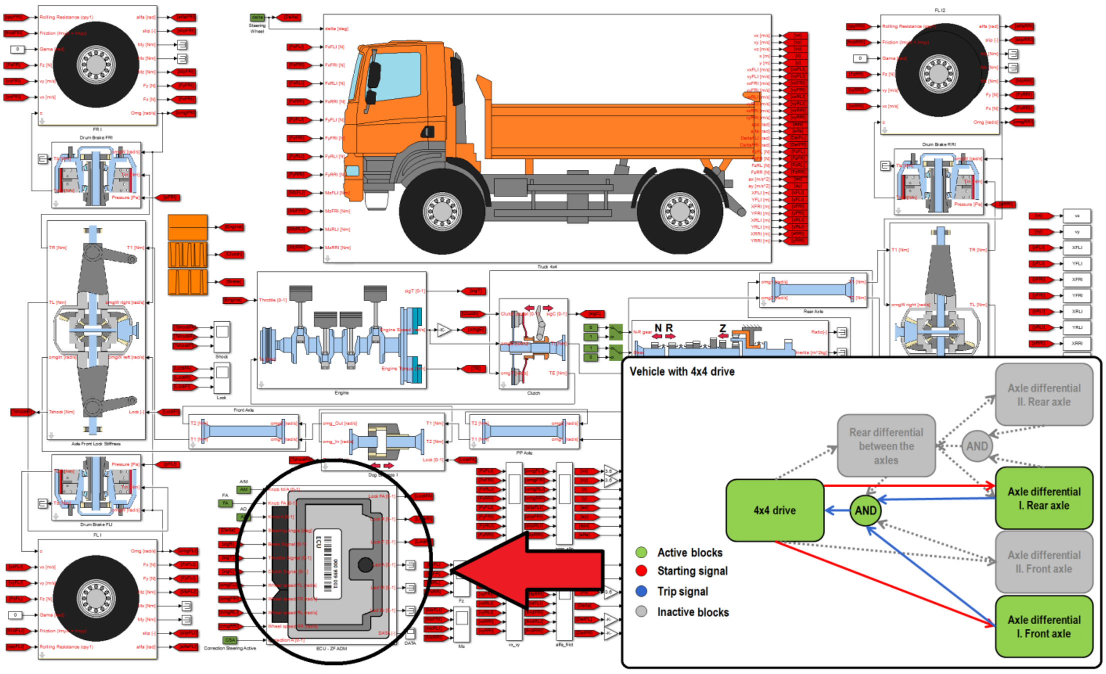

Fig. 1: The vehicle computational model with the differential lock control algorithm.

4. Simulation of the automatic control

The simulation was performed on the computational model of a vehicle with 4x4 drive. In order to conduct a test of the differential lock, it was necessary to simulate the slip of the individual wheels of the vehicle. For this purpose, the road block has been created with the matrix describing the road adhesion between the tyre and the road, and with the rolling resistance coefficient. These values are input parameters of the tyre block depending on a tyre position on the road. This principle can simulate various road surfaces and simulates a crossing between them.

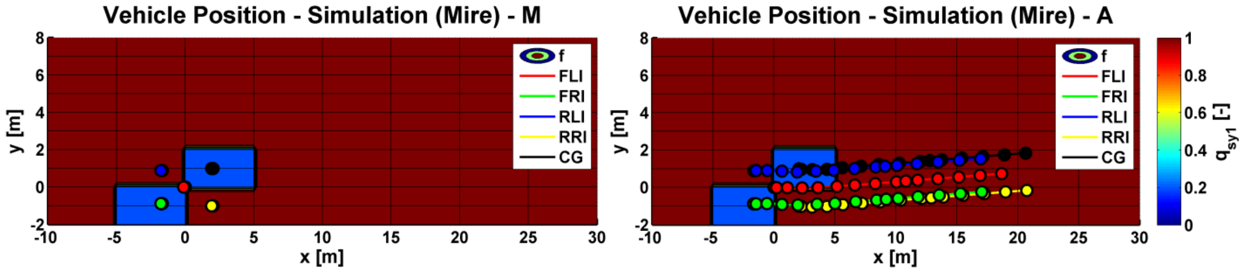

Fig. 2: Vehicle position (manual control and automatic control)

The simulation describes starting of the vehicle from zero velocity on an even road. This simulation is divided into automatic and manual control for driving without a change of the steering angle. Both combinations of simulation have three input signals which are accelerator, clutch and brake signal.

The first simulation can be described in more detail as follows: the vehicle began to move without changing of the steering angle. The manual control of the differential was set, and no differential or the front-wheel drive were activated. The dependence of the scale factor of the peak friction coefficient on a vehicle position is shown in Fig. 2. The blue region describes a value of 0.3. Other areas have the scale factor of the peak friction coefficient of 1. The rolling resistance of these blue areas reaches 0.4 which corresponds to the muddy surface of the road. The position of each wheel (FLI – left front wheel, FRI – front right wheel, RLI – left rear wheel, RRI – right rear wheel) and the centre of gravity of the vehicle in the simulation drive are displayed, too.

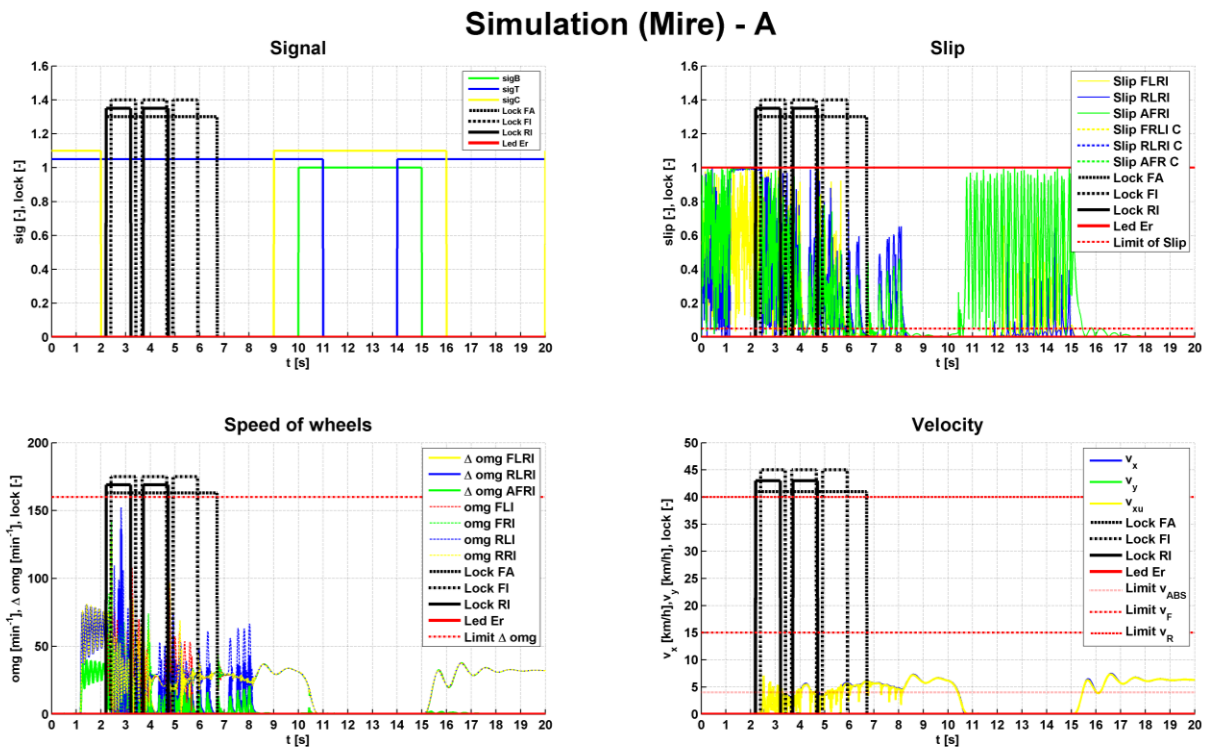

Fig. 3: Input and output signals of the control algorithm.

In the simulation process of a vehicle move, there was the rear wheel slip caused by a different condition of the rear wheels and the vehicle remained standing in one place. In that case, the driver would have to use buttons to control differential locking. The second simulation is shown in Fig. 4 where the control system is set to automatic control. The vehicle began to move and the slip of the right rear wheel occurred again. In this case, the control algorithm evaluated the slip by Eq. 1 and other control parameters. There are four graphs in Fig. 3 describing all parameters. The first graph describes a throttle, brake and clutch signal. The second graph shows the slip signals and the slip correction (not applied in this simulation). The third graph displays the differences of the wheel speed. The fourth graph represents the vehicle velocity and the velocity limit for controlling. The activated front wheel drive or differential lock can be found in each of these graphs of simulation. In case of all differential locks, the algorithm does not have the slip value used for evaluation. Therefore, a 1s test was performed. Axial differentials were opened and input parameters for locking of the differential were checked again. The test status is visible in the results of the second simulation. The algorithm was tested three times before the vehicle drove from a muddy field to the asphalt road.

5. Conclusions

The aim was to create a control algorithm for the differential lock of the truck. This algorithm was created in the software Simulink-Stateflow. The created algorithm was based on the ZF ADM system.

The created algorithm can be described as a mechatronic system which evaluates the input wheel speed signal, steering angle, throttle, clutch and the brake signal. The evaluation of algorithm determines locking or opening of the differential. In order to verify the created algorithm, the simulation was carried out and described in the relevant chapter. The computational model of the vehicle with 4x4 drive was made to test the algorithm. The results achieved in the simulation and the theoretical predictions suggest that the response behaviour of the algorithm is correct. Errors occurred in the algorithm before the initial testing on a real vehicle. This simulation could save costs if the algorithm was applied incorrectly to a real control unit.

The algorithm will be expanded and improved to be applicable to the vehicles with more axles. It will be adapted to different types of vehicles as well. It would also be appropriate to test the algorithm on a real vehicle using NI 3110 RT hardware. This hardware would serve as a control unit. But for this testing on a real vehicle, it is necessary to create an appropriate dog clutch for the differential lock. This work has already started in cooperation with one a truck manufacturer.

Acknowledgement

This work is an output of the internal BUT research project Reg. No. FSI-S-14-2334 and was also supported through NETME CENTRE PLUS (LO1202) by financial means from the Ministry of Education, Youth and Sports under the „National Sustainability Programme I".

References

Dabney, J. B. & Harman T. L. (2004) Mastering Simulink. Pearson Prentice Hall, Upper Saddle River.

Grepl, R. (2007) Modelování mechatronických systémů v Matlab SimMechanics. BEN, Praha.

Kučera, P. (2015) Mechatronic Approach to Vehicle Dynamics. Brno University of Technology, Faculty of Mechanical engineering, Brno

Kučera, P. & Píštěk, V. (2013) Transmission Computational Model in Simulink. Perner's Contacts, 8, 4, pp. 37-48.

Kučera, P. & Píštěk, V. (2014) Virtual prototype of a heavy duty off-road truck driveline in Simulink software, in: Transport means 2014 Proceedings of 18th International Conference, Technologija, Kaunas, pp. 5-8.

Pacejka, H. B. (2006) Tyre and vehicle dynamics. Butterworth-Heinemann, Oxford.

Stelzeneder, F. H. & Aitzetmüller, H. (2000) ADM Drive-Train Management, in: FISITA World Automotive Congress, Korea Society of Automotive Engineers, Seoul, pp. 1-7.

ATMOSPHERIC DISPERSION SIMULATIONS - PASSIVE GAS MIXTURE FLOW

M. Kyncl *, J. Pelant **

Abstract: *Here we work with the system of equations describing the non-stationary compressible turbulent multi-component flow in the gravitational field, and we focus on the numerical solution of these equations. The mixture of perfect inert gases is assumed. The RANS equations are discretized with the use of the finite volume method. The exact solution of the modified Riemann problem (original results) is used at the boundary faces. The roughness of the surface is simulated using the alteration of the specific dissipation at the wall. The presented computational results are computed with the own-developed code (C, FORTRAN, multiprocessor, unstructured meshes in general).*

Keywords: Gas Mixture, RANS, Riemann Problem, Software, 3D.

1. Introduction

The physical theory of the compressible fluid motion is based on the principles of conservation laws of mass, momentum, and energy. The mathematical equations describing these fundamental conservation laws form a system of partial differential equations. The aim of this work is to numerically simulate the complicated behaviour of the perfect gas mixture. In this contribution we consider the Reynolds-Averaged Navier-Stokes equations with the k-omega model of turbulence. This system is equipped with the equation of state in more general form, and with the mass conservation of the additional gas specie.

$$\frac{\partial \rho Y_1}{\partial t} + \frac{\partial \rho Y_1 v_2}{\partial x_1} + \frac{\partial \rho Y_1 v_2}{\partial x_2} + \frac{\partial \rho Y_1 v_2}{\partial x_3} = \sum_{s=1}^{3} \frac{\partial}{\partial x_s}(\sigma_C \mu_T \frac{\partial Y_1}{\partial x_s}) + S_{Y_1} \qquad (1)$$

Here t is time, x_1, x_2, x_3 are the space coordinates, v_1, v_2, v_3 are the velocity components, Y_1 is the mass fraction of the additional gas specie, $\sigma_C \mu_T$ is the diffusion coefficient, and S_{Y_1} denotes the source term. We focus on the numerical solution of these equations.

2. Methods

For the discretization of the system we proceed as described in Kyncl & Pelant (2000). We use either explicit or implicit finite volume method in order to discretize the analytical problem, represented by the system of equations in generalized (integral) form. In order to apply this method we split the area of the interest into the elements, and we construct a piecewise constant solution in time. The crucial problem of this method lies in the evaluation of the so-called fluxes (and its Jacobians) through the edges/faces of the particular elements. One of the most accurate method (and perhaps the most accurate method) is based on the solution of the so-called Riemann problem for the 2D/3D split Euler equations. The analysis of this problem can be found in many books, i.e. see M. Feistauer, J. Felcman, and I. Straškraba (2003), E. F. Toro (1997). Unfortunately, the exact solution of this problem cannot be expressed in a closed form, and has to be computed by an iterative process (to given accuracy). Therefore this method is also one of the most demanding. Nevertheless, on account of the accuracy of the Riemann solver, we decided to use the analysis of the exact solution also for the discretization of the fluxes through the boundary edges/faces. The right-hand side initial condition, forming the local Riemann problem, is not known at the boundary

* RNDr. Martin Kyncl, PhD.: Výzkumný a zkušební letecký ústav, a. s., Beranových 130, 199 05 Prague; CZ, kyncl@vzlu.cz
** RNDr. Jaroslav Pelant, CSc.: Výzkumný a zkušební letecký ústav, a. s., Beranových 130, 199 05 Prague; CZ, pelant@vzlu.cz

faces. In some cases (far field boundary) it is wise to choose the right-hand side initial condition here as the solution of the local Riemann problem with given far field values, which gives better results than the solution of the linearized Riemann problem. It can be shown, see Kyncl (2011), that the right-hand side initial condition for the local problem can be partially replaced by the suitable complementary condition. In order to prescribe some variable (for example pressure) by chosen value at the boundary, the local modified Riemann problem must have a solution, otherwise the value cannot be used at the boundary. This was the main idea behind the construction of the shown boundary conditions by preference of certain variable. On the contrary to the solution of the initial-value Riemann problem, the solution of the modified boundary problems can be written in a closed form. Therefore it is not computationally expensive to use the constructed boundary conditions in the code. Various original modifications of the Riemann problem (and exact solutions of these modifications) are used at the boundary. In general we prefer the given pressure distribution combined with the given total variables at the inlet.

The own-developed software (C,FORTRAN) is based on the finite volume method with implicit or explicit time discretization, solution is computed on unstructured 3D meshes in general, OpenMPI and MPI parallelizations are used. The large linear systems within the implicit method are solved with the implemented preconditioned GMRES matrix solver. The roughness of the surface is simulated by the adjustment of the specific dissipation at the wall, shown in Wilcox (1998).

3. Examples

In order to simulate the wall roughness we choose the simple channel flow. The air flows over the smooth and rough surface, the channel is 30 m long, regime 15 $m \cdot s^{-1}$. Comparison of the computed values of the normed velocity U^+ (red lines) at the $x_1 = 25m$ (red cut) with the law of the wall, described in Wilcox (1998), shown in Y^+, U^+ graph, figure 1.. Here Y^+ is the normed distance from the wall y.

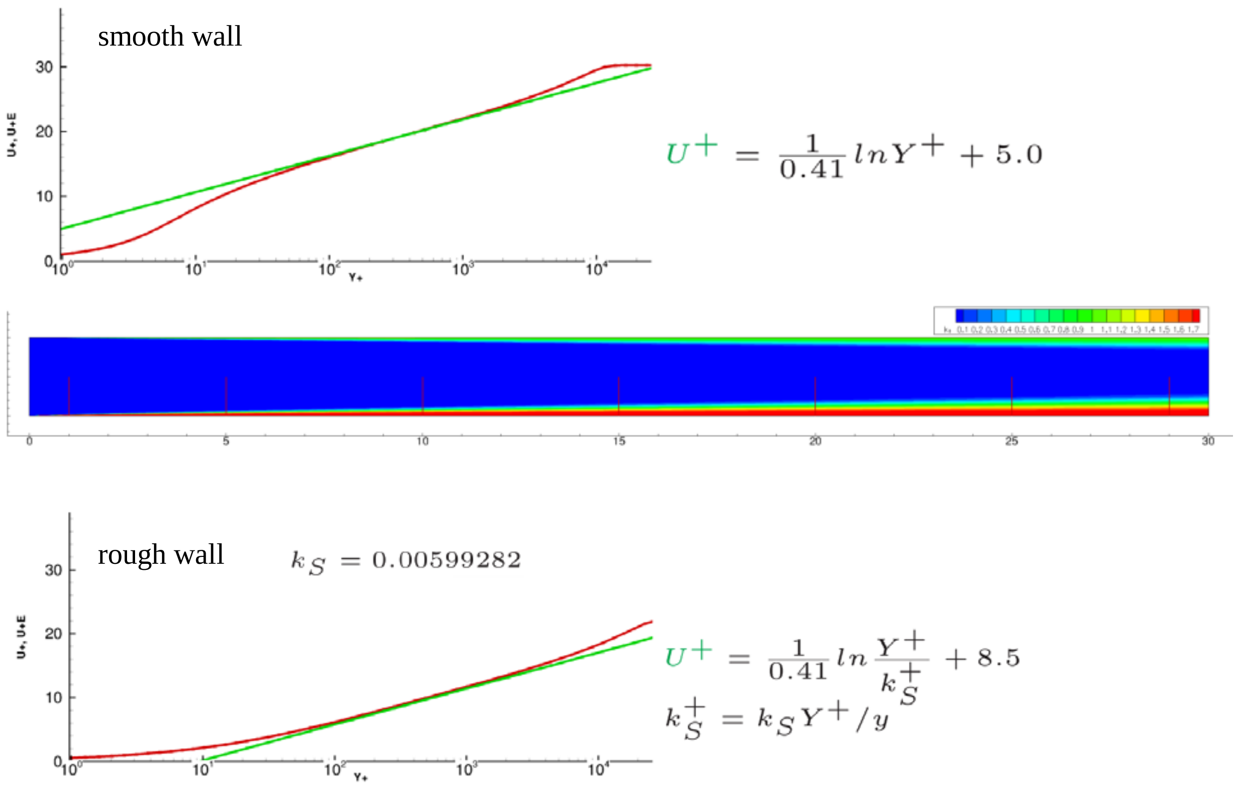

Fig. 1: The wall roughness simulation, channel flow. Isolines of the turbulent kinetic energy and the comparison of the computed data (red line) with the law of the wall (green line).

Further we show the simulation of the gas mixture. The 17 m long channel (with the bump at the bottom wall at the distance 14m) is filled with the air, regime15 $m \cdot s^{-1}$. At the inlet, the boundary condition with the preference of total quantities ($T_0 = 273.15K$, $p_0 = 101325$ Pa) and the direction of velocity (1,0,0) was used, together with the turbulent kinetic energy intensity set to 0.1, turbulent viscosity ratio set to 0.01. Outlet boundary condition by the preference of pressure was used, the pressure value was estimated using the Bernoulli equation for the compressible flow (isentropic relations) for the given regime 15 $m \cdot s^{-1}$. Figure 2. shows the computed distribution of the velocity and the turbulent kinetic energy in the channel, and also in the selected section of the further interest. The computed data from this computation were used for the initial and boundary conditions (the total values conservation at the inlet, pressure preference at the outlet) for the next simulation of the gas mixture propagation. Here the computational area was restricted to the channel section (by x coordinate) from -1 to 2.

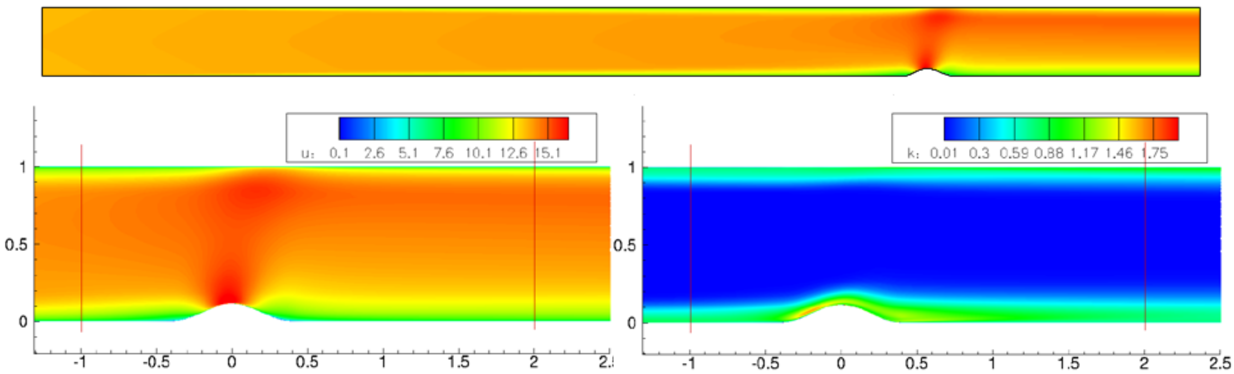

Fig. 2: Channel flow simulation, isolines of the velocity and the specific turbulent kinetic energy.

The additional gas specie enters the area through the boundary condition, fixed source, or with the use of initial condition. The picture sequences in figure 3. demonstrate the propagation of the additional gas specie into the area. Here we tested the various types of the possible pollution source. The computations for the fixed source are visually comparable to the experimentally obtained data.

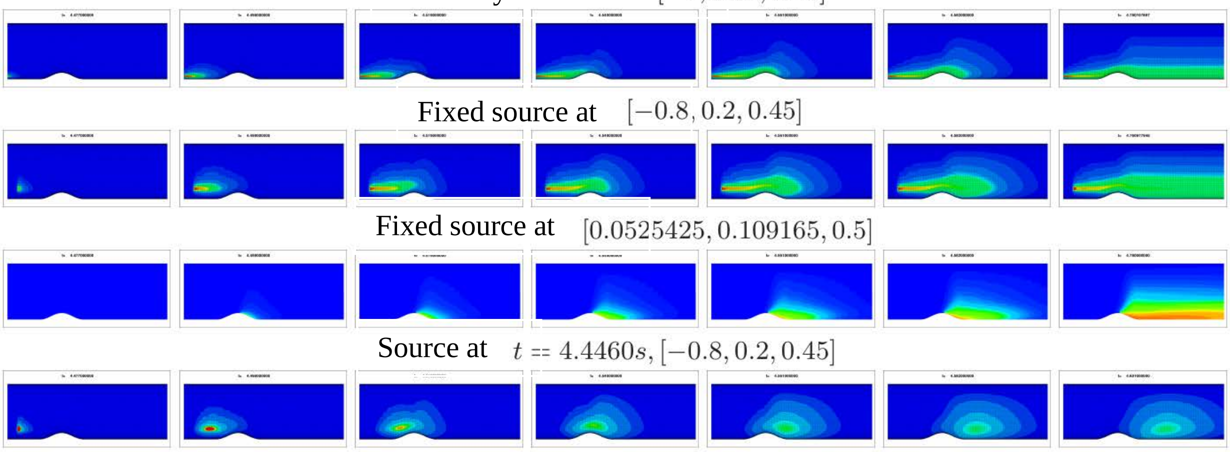

Fig.3: Propagation of the additional gas specie in time, isolines of the mass fraction Y_1.

The figure 4. shows the simplified simulation of the gas mixture flow over the simple terrain. Surface data were given by a set of point coordinates (left picture). Then the surface mesh was constructed and volumes created using own software. Computation run with the regime velocity 4 $m \cdot s^{-1}$, and fixed emission source located at the chosen point. The aim of this computation was to achieve relatively quickly some estimate of the gas dispersion in the case of some possibly dangerous pollution.

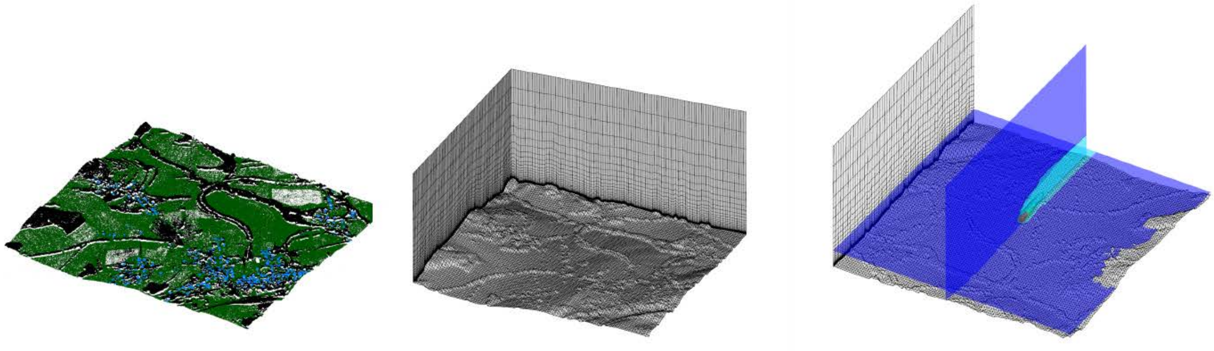

Fig.4: The gas specie dispersion over simple terrain.

4. Conclusions (style - EM 2016 Main chapter)

This paper shows the numerical simulation of the mixture of two inert perfect gases in 3D. The numerical method (finite volume method) is applied for the solution of these equations. Own software was programmed. The modification of the Riemann problem and its solution was used at the boundaries. Elementary examples show good coincidence with the experimentally obtained results. The desired intention was to use the modified software for the quick estimation of the gaseous pollution of the air, which may be critical in the case of the sudden leakage of the substances hazardous to health. The estimates computed with this software are undoubtedly more precise than a set of concentric circles, which is being used now days. Further comparisons with the experimental data (from the wind tunnel) are still in the process.

Acknowledgement

This result originated with the support of Ministry of the Interior of the Czech Republic, project SCENT. The authors acknowledge this support.

References

D. C. Wilcox (1998) Turbulence Modeling for CFD, California, USA

C. J. Kok (2000) Resolving the dependence on free-stream values for k-omega turbulence model, in: AIAA Journal, Vol. 38., No. 7.

M. Kyncl and J. Pelant (2012) Implicit method for the 3d RANS equations with the k-w (Kok) Turbulent Model, Technical report R-5453, VZLU, Beranovych 130, Prague.

M. Feistauer (1993) Mathematical Methods in Fluid Dynamics, Harlow, England

E. F. Toro (1997) Riemann Solvers and Numerical Methods for Fluid Dynamics, Berlin, Germany

M.Feistauer, J.Felcman, and I.Straškraba (2003). Mathematical and Computational Methods for Compressible Flow, Oxford, England

M. Kyncl (2011) Numerical solution of the three-dimensional compressible flow, Doctoral Thesis, Prague

J. Pelant (1996-2000) Arti reports VZLÚ, z-65, z-67 to z-73. Prague

22nd International Conference
ENGINEERING MECHANICS 2016
Svratka, Czech Republic, 9 – 12 May 2016

NUMERICAL ANALYSIS OF THE APPROACH SLAB EXPERIMENT FOR PARAMETRICAL STUDY

K. Laco*, V. Borzovič**

Abstract: *The approach slab function is to overcome the transition between the abutment and the soil embankment. The issue is in the different stiffness of those elements and its foundation, what causes the differential settlement. The main goal of this work is to optimise the numerical analysis of the prepared experiment of the approach slab according to the results of experiment itself. The task is not only in getting nonlinear material characteristic of the soil, or the concrete material of the slab, but also in the accurate representation of the behaviour when cyclic load is applied. This type of loading represents the load implicated by the vehicle passing. The correct adjusting of the numerical model could lead to further parametrical study of the whole transition zone in full scale.*

Keywords: **approach slab, transition zone, non-linear time-step analysis, bridge abutment, embankment**

1. Introduction

The approach slab is designed to compensate the different settlement of the bridge abutment and a road embankment. In Fig. 1 the typical cross section of the transition zone represented by FEM model can be seen. It is prepared for the parametric study. Main subject of the interest is the difference in stiffness of the foundation.

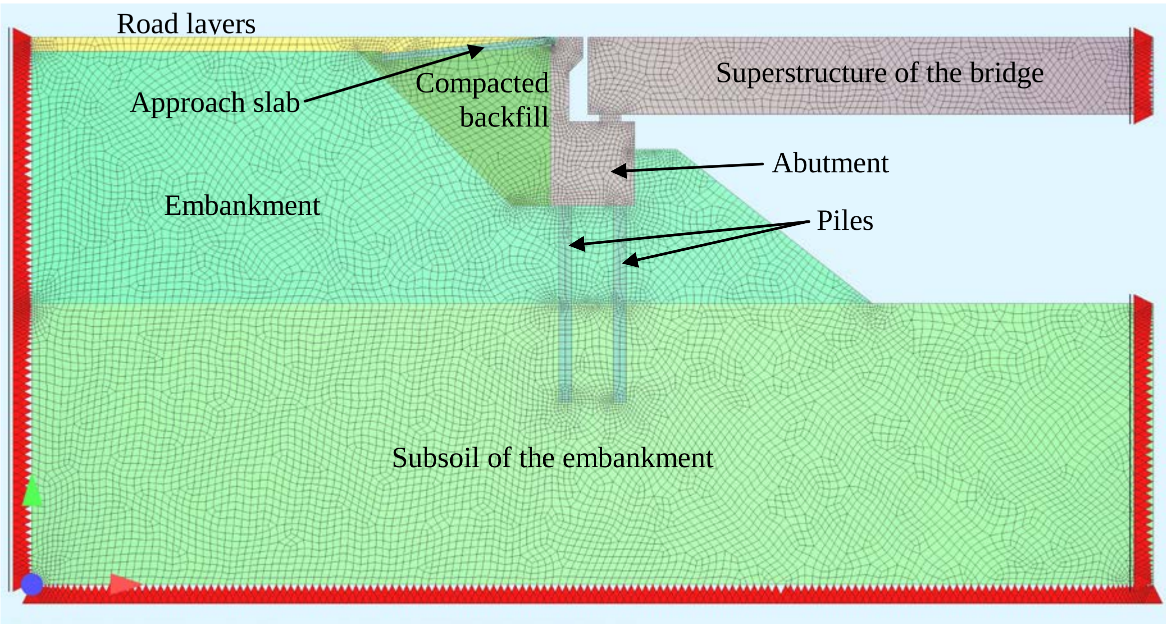

Fig. 1: FEM model of the transition zone typical cross-section.

* MSc. Kamil Laco: Slovak University of Technology, Faculty of Civil Engineering, Radlinského 11, 810 05 Bratislava, SR, kamil.laco@stuba.sk

** assoc.prof. Viktor Borzovič, PhD.: Slovak University of Technology, Faculty of Civil Engineering, Radlinského 11, 810 05 Bratislava, SR, kamil.laco@stuba.sk

Driving comfort can be interrupted by the so called “bump” on both ends of the bridge. These disorders caused by the exceeded size of the different settlements should be eliminated by the approach slabs. Among many reasons of the uneven settlement the most common ones are the consolidation of the soil embankment and its subsoil.

2. Structural Model of the Approach Slab

For the estimation of the structural member behaviour, proper structural scheme should be used. The simplest, but also the most conservative model is represented by simple supported slab, with hinges on both ends. One in the place of connection to abutment. The other, at free end in specific distance according to resultant of the bedding pressure. Conservative model is assumed in Slovak standard (OTN 73 6244, 1981).

More precise schemes include elastic support under the slab, whether along the whole length, or only partially at the free end. Stiffness of this support beneath the slab can also develop in time. Problem with right structural description comes with the type of acting load. Behaviour of the approach slab is changing in time with consolidation of the backfill, embankment or subsoil, or by any accidental situation such as soil erosion resulting in void development in mid-span of the slab. Detailed study comparing various models was already published in Laco, Borzovič and Panuška (2014)

In this paper the nonlinear analysis with the nonlinear soil and concrete parameter was performed. Despite the accuracy of this type of analysis, its usage is limited only for the scientific or experimental works. It is not only because of the longer computational time, but mainly because of required soil properties and their uncertainties.

3. Numerical Model of The Approach Slab Experiment

Fig. 2 represents the numerical model in FEM software SOFiSTiK and it shows the arrangement of the experiment being in preparation. Dimensions of the soil tank are 3.9 m in width, 4.2 m in length and 2.25 m in height. Soil will be filled up to 2 m. The walls will be constructed by DOKA framed formwork system. Specimen of the approach slab will be in geometrical scale 1:2 with reduction of width. As a load pattern, one axle of the tandem system will be used. Reinforcement arrangement will be set to maintain the same reinforcement ratio as it is in approach slabs designed for real structure.

Analytical model consists of beam (1D) elements represented by the incline struts and frames of the formwork. 2D elements are used for laminated slabs of the formwork and the approach slab itself. Soil is represented by 3D tetrahedral elements. All elements are linear. Contact between the slab and 3D soil elements is represented by node to node springs, with soil properties.

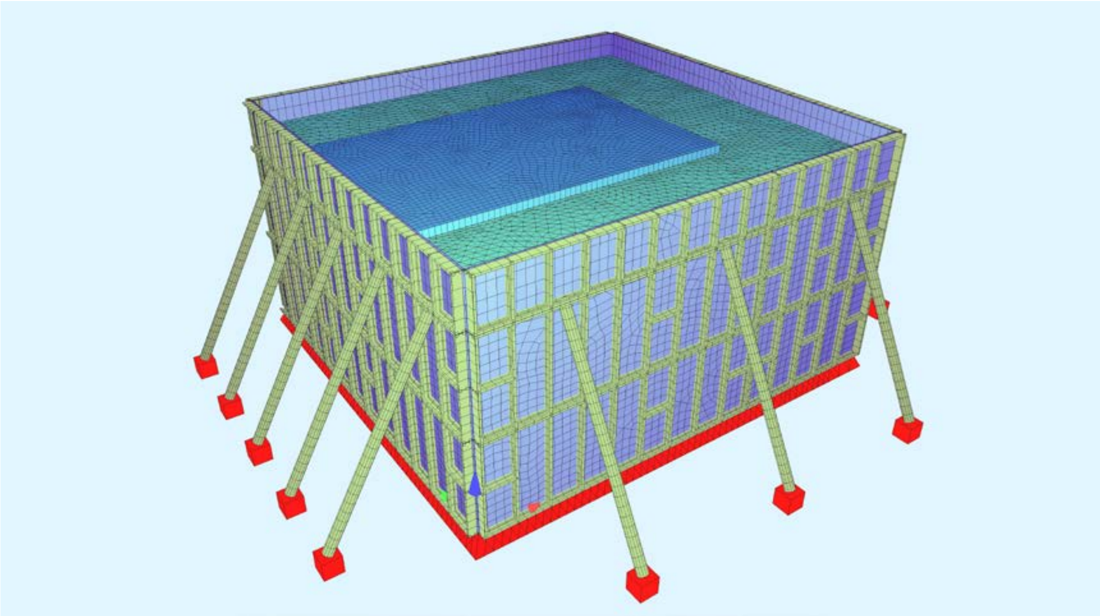

Fig. 2: Numerical model of the approach slab experiment

Material nonlinearities are fully included in all types of elements. In the concrete slab, estimated areas of the reinforcement were entered and 2D elements are later computed via layers dividing the height of the cross-section. Concrete properties and stress–strain curves were set as normative values according EC 2.

Hardening soil nonlinearity was chosen for the subsoil material, because of the type of soil elements. Due to its stress-strain curvature and possibility of changing the material properties in time, it is suitable for the nonlinear time-step analysis.

Reference load of the FEM analysis was 150 kN at each of two loaded areas, which should represent the contact pressure caused by wheels of the vehicles. Period of the sinus loading function was 0.35 s. The factor of the acting load was set as time variable of this function. The highest peak was 1.0, the lowest 0.1.For last two seconds of the loading function the factor was set to 0.

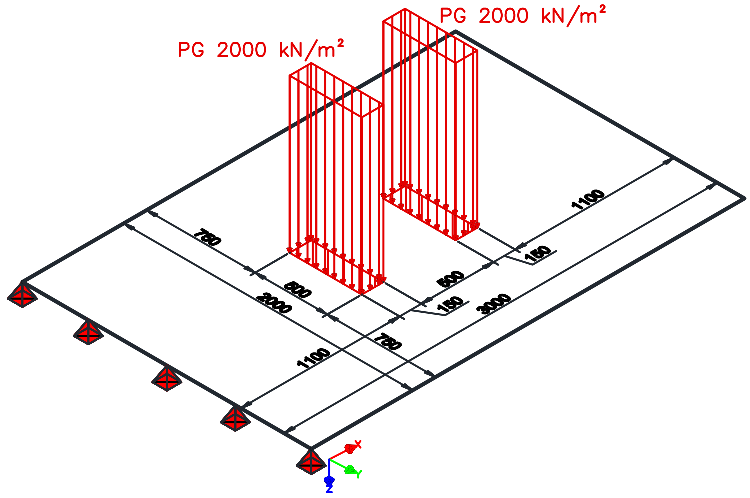

Fig. 3: Approach slab with applied load in the numerical model

The FEM analysis was focused on the behaviour of the slab and its interaction with subsoil. Soil pressure under the load areas was increasing in time, and after the end of cyclic loading, bedding stress goes to 0 MPa. Soil pressure development in time is shown in Fig. 4. With the consideration that the self-weight is acting during whole analysis, zero bedding stress suggest the creation of the void under the slab.

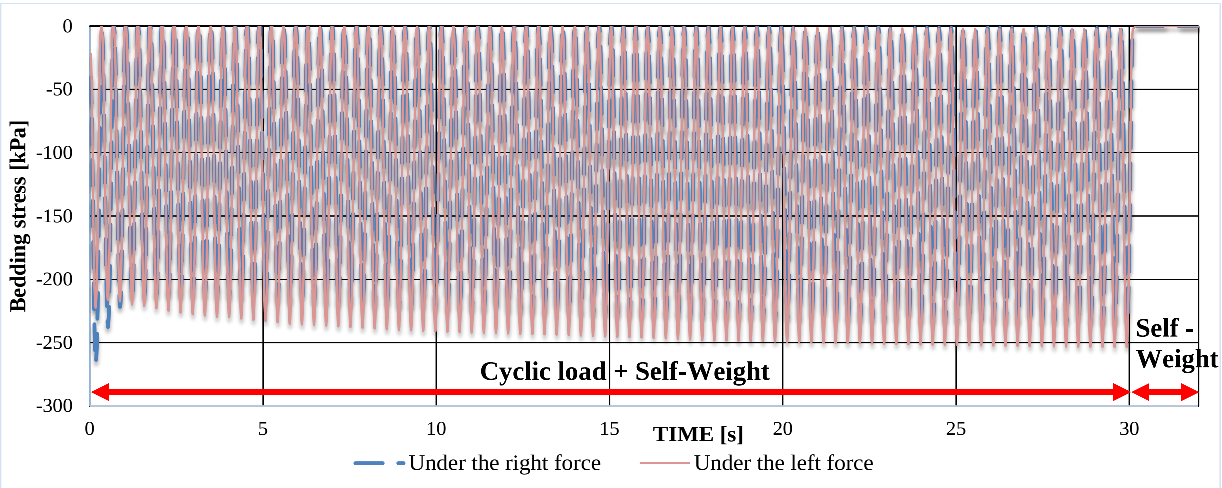

Fig. 4: Development of bedding stresses under applied loading areas in time

Another interesting behaviour was observed in support reaction of the assumed abutment. Because of the development of another theoretical soil support in front of the line support representing the abutment, reaction in all nodes of the line support are decreasing. Results prove the gap creation under the acting loads. It is necessary to mention, that the vehicle load is moving, and in real structure, the cyclic loading is not located only in the middle of the slab.

From the graph in Fig. 5 can be the changes of the structural scheme of the analysed slab assumed. On the horizontal axis, the position of the centre line along the span length of the slab is displayed. Vertical axis represents the deflections, and the time steps are described by depth axis. Deflection in the middle of the slab is decreasing in time and the free edge is rising. It can be presumed, that soil-hardening support on this edge is developing, what could explain all the observed behaviour of the slab from the performed analysis.

Further investigation in bigger time scale is advised as well as improving the meshing for better energy convergence and smaller numerical errors.

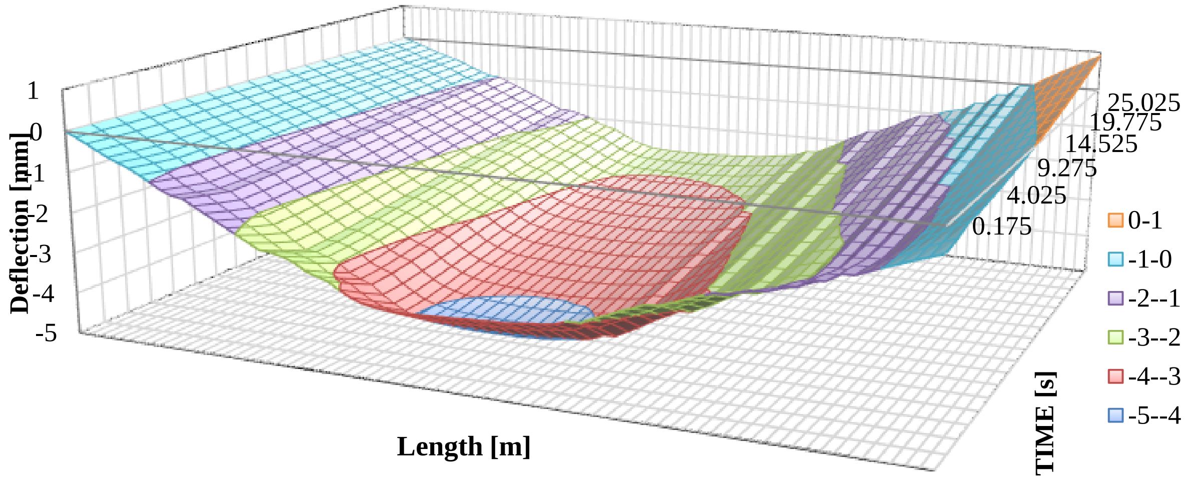

Fig. 5: Deflection development of the centre line of the analysed slab in time

4. Conclusion

In this work some problems concerning with estimation of the actual behaviour of the approach slabs were presented. Interaction of the slab structural member with the subsoil is complex problem and a discussed question among many researchers. When effect of a time and also a cyclic loading is added, even more questions are appearing.

After series of experiments, numerical model, as well as material properties will be carefully optimised according to the results. Main goal is to match the behaviour, deflection and reinforced concrete strain in highest possible accuracy. With right computational method and the material properties, 2D FEM model of the transition zone can be used for parametrical study. In this case, the possibility of using the moving cyclic load could be implemented.

Extended study could also use complete 3D FEM model, with consideration of wings of the abutment, or pile foundation and transverse strain of the elements. It is suggested to compare the results with in-situ measurements for the analysis verification.

Acknowledgement

This work was supported by the Slovak Research and Development Agency under the contract No APVV–0442-12.

Authors gratefully acknowledge technical support provided by company YIT Reding.

References

OTN 73 6244 : Transition zones of the roadway and highway bridges. Praha, 1981. (in Slovak)

K. Laco, V. Borzovič, J. Panuška, Analysis of the behaviour of the approach slab, in: Concrete days 2014 a 5. post-conference colloquium SNK fib : Collective volume, 1. edition, Bratislava : STU in Bratislava, 2014, ISBN 978-80-8076-114-1, pp. 303-308. (in Slovak)

22nd International Conference
ENGINEERING MECHANICS 2016
Svratka, Czech Republic, 9 – 12 May 2016

AN EXAMPLE OF MARKOV MODEL OF TECHNICAL OBJECTS MAINTENANCE PROCESS

B. Landowski [*], D. Perczyński[*], P. Kolber[*], Ł. Muślewski[*]

Abstract: *The paper presents the usefulness diagnosis method of the technical objects to realise the tasks received by the controlling subsystem. The investigation object being the basis to illustrate the considerations presented here in, is a municipal-transport bus maintenance system in a selected urban agglomeration. In order to solve the discussed problem it has been assumed that the mathematical model of the bus maintenance process is homogenous Markov process. As a criterion to select (purchase) a specific bus type to be maintained, the usefulness potential usage rate. The paper does not cover investigation of the economic aspects related to the purchase of a specific bus type.*

Keywords: diagnosis, homogenous Markov process, maintenance process.

1. Introduction

The investigation object is the urban transport bus maintenance system in the chosen urban agglomeration. The effects resulting from the activity of the analysed system are precisely associated with efficiency of management, which is defined as an ability to control resources, processes and information for their optimal use in the business. There are various different technical objects on the market, and therefore it is useful to develop a tool, for decision-makers, which enables the rational (based on accepted criterion) selection of buses in the analysed system.

The primary aim of studied system is an effective and safe carriage of passengers by urban transport buses in defined quantitative and territorial range (Landowski B., Woropay M., Neubauer A., 2004, Woropay M., Knopik L., Landowski B., 2001).

An Example of Markov Model of Technical Objects Maintenance Process

A subsystem which is directly responsible for performing tasks of the system is the executive subsystem which contains basic subsystems of type <C – OT> (driver – bus), wherein a man is coupled by serial structure with a technical object. Reliability of operated technical objects is maintained at an appropriate level as a result of the operating processes in the subsystem ensuring roadworthiness.

The analysed system have two bus depots in which service stations are located.

The roadworthiness and diagnosis processes are ensured in the service stations and in particular: daily services, periodic maintenance, current repairs and technical inspections of the vehicles.

The subsystem ensuring roadworthiness also contains another subsystems so called mobile decentralised departments, the set of emergency technical service units. The main task of these departments is to restore as soon as possible the roadworthiness of buses which are outside the bus depots or, in case it is impossible to fix the buses outside the depots, to tow out-of-order buses to a service station.

[*]Assist. Prof. Bogdan Landowski, PhD, UTP University of Science and Technology, Faculty of Mechanical Engineering, Al. prof. S. Kaliskiego 7, 85-796 Bydgoszcz; PL, bogdan.landowski@utp.edu.pl

[*]Assist. Prof. Daniel Perczyński, PhD, UTP University of Science and Technology, Faculty of Mechanical Engineering, Al. prof. S. Kaliskiego 7, 85-796 Bydgoszcz; PL, daniel.perczynski@utp.edu.pl

[*]Assist. Prof. Piotr Kolber, PhD, UTP University of Science and Technology, Faculty of Mechanical Engineering, Al. prof. S. Kaliskiego 7, 85-796 Bydgoszcz; PL, piotrl.kolber@utp.edu.pl

[*]Assoc. Prof. Łukasz Muślewski, PhD, UTP University of Science and Technology, Faculty of Mechanical Engineering, Al. prof. S. Kaliskiego 7, 85-796 Bydgoszcz; PL, lukasz.muslewski@utp.edu.pl

The result of assumption and limitation analysis shows that Markov process and the theory of the process analysis has been considered as the best tool, from research purpose point of view, for mathematical modelling of real maintenance process of the investigation object.

2. Selected results of the preliminary maintenance tests

The time analysis in selected operating states were carried out during the preliminary maintenance tests conducted in real urban transport bus maintenance system (Woropay M, Landowski B, Perczyński D., 2004). The tests were carried out in natural conditions of maintenance by using passive observation method.

The results presented in the following part of the paper refer to Mann (16 vehicles) and Volvo bus brand (90 vehicles) which are operated in the analysed system. Table 1 and Table 2 present the results of preliminary tests regarding selected time statistics of proper bus operation (T_1), bus repair done by emergency technical service units (T_2) and bus repair done by service stations (T_3) (Woropay M, Landowski B, Perczyński D., 2004).

Tab. 1. Values of selected statistics of examined characteristics for Volvo bus brand

Volvo			
Statistics	$\mathbf{T_1}$	$\mathbf{T_2}$	$\mathbf{T_3}$
Number of observations	823	474	407
Average value	242.5	1.13	1.67
Standard deviation	289.9	0.72	0.85
Minimum	0.34	0.03	0.47
Maximum	2237.67	4.88	7.23
Range	2237.33	4.85	6.76
Variance	84092.40	0.51	0.73
Median	143.65	143.65	1.40
Mode	24	1.00	1.07

Tab. 2. Values of selected statistics of examined characteristics for Mann bus brand

Mann			
Statistics	$\mathbf{T_1}$	$\mathbf{T_2}$	$\mathbf{T_3}$
Number of observations	174	89	87
Average value	295.06	1.11	1.71
Standard deviation	353.74	0.54	1.15
Minimum	7.22	0.05	0.23
Maximum	1824	2.75	6.17
Range	1816.78	2.70	5.94
Variance	125131.0	0.29	1.32
Median	165.81	1.15	1.30
Mode	48	1.67	0.92

3. Maintenance process model carried out in the investigation object

The investigation object identification resulted in defining three, important for research purposes, maintenance states of the buses, i.e. (Woropay M, Landowski B, Perczyński D., 2004):

S_1 - operating state, realisation of transport tasks,

S_2 - repair state done by emergency technical service units,

S_3 - repair state done by service stations,

It is assumed that the preliminary mathematical model of bus maintenance process is stochastic process $\{X(t), t \geq 0\}$. Analysed stochastic procces $\{X(t), t \geq 0\}$ has finite phase space S, S=$\{S_1 , S_2 , S_3 \}$. It is assumed that the theory of homogenous Markov processes is used for description of maintenance process of analysed technical objects. Bus state space and maintenance event analysis enables to create a digraph, presented in Fig. 1, that imitate the maintenance process carried out in the investigation object.

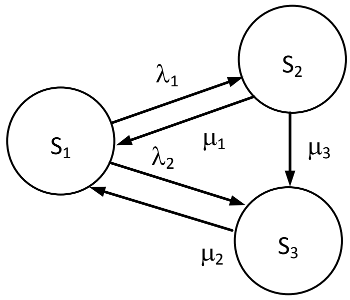

Fig. 1: Digraph of maintenance process state

Transition intensity of analysed process is included in so called transition intensity matrix Λ:

$$\Lambda = \begin{bmatrix} -(\lambda_1+\lambda_2) & \lambda_1 & \lambda_2 \\ \mu_1 & -(\mu_1+\mu_3) & \mu_3 \\ \mu_2 & 0 & -\mu_2 \end{bmatrix}$$

Through using the theory of Markov processes it possible to determine probabilities $P_i(t)$, i = 1, 2, 3, of technical objects positions in selected maintenance states S_i at the moment t for maintenance process model. For that purpose it is needed to solve A. N. Kolmogorov system of differential equations:

$$P'(t) = P(t)\Lambda,$$

where:

$P'(t)$-column vector composed of derivatives $P_i'(t)$,

$P(t)$-unconditional probability vector $P_i(t)$,

Λ-transition intensity matrix of process states.

A calculation algorithm has been developed to determine values $P_i(t) = P(X(t)=S_i)$, i=1, 2, 3, and a computer programme has been designed (Knopik L., Landowski B., Perczyński D. 2002).

One of the research aims is to determine the distribution of random variables T_i, i = 1, 2, 3, indicating duration of analysed maintenance states $S_i \in S$ of Mann and Volvo bus brands. The null hypothesis H_0, stating that empirical distribution of random variable T_i complies with exponential distribution, is verified for each of the states S_i (i=1,2,3). Compatibility test χ^2 (Pearson) is used to verify the hypothesis. There is no scientific basis to reject the verified hypothesis (level of significance α=0.05) for random variables T_i, i=1,2,3, (Mann) and T_i=2,3, (Volvo). The verified hypothesis is rejected for random variable T_1 (meaning time of proper operation state of Volvo bus brand). However, the positive result of compliance of the analysed random variable empirical distribution with Erlang distribution has been obtained. Then it is possible to present random variable T_1 as follows (Buslenko N., Kałasznikow W., Kowalenko I., 1979):

$$T_1 = T_{11} + T_{12} + ...+T_{1k},$$

where: T_{1i} - independent random variables with exponential distribution with parameter λ.

Transition from state S_{1i} ($1\leq i \leq k-1$) to state $S_{1\,i+1}$ is the only possible transition.

Minimum sum of squared deviations of Erlang distribution function F(x) from the value of empirical distribution $F_e(x)$ is assumed as the criterion of optimal selection of parameters λ and k.

The calculation algorithm has been developed to estimate values for parameters k and λ.

The process $\{X(t), t \geq 0\}$with state space S_i has been transformed into the process $\{Y(t), t \geq 0\}$ with state space ST for which time distributions of states are exponential distributions. on the cost of state space enlargement.

Various different technical objects are used in the urban transport maintenance system. When there is a need to purchase buses, the important problem for decision-makers is which brand should be chosen. In the paper, the roadworthiness potential is the criterion for buying specific technical object and can be written as:

$$W_u(t_a) = \frac{\int_0^{t_a} P_1(t)dt}{t_a},$$

where:

t_a–analysis time,

$P_1(t)$–probability of bus operating state.

The value of the indicator depends on the value of parameters which characterise the model (maintenance process of selected brand bus) and can be a diagnostic signal for decision-makers regarding usefulness of selected technical object for maintenance under operating conditions of the system.

The value of the indicator $W_u(t_a)$ for two selected brands of buses has been determined to present the key idea of the paper.

The analysis of the indicator shows that purchase Volvo buses (W_u=0,9961) is a better choice than Mann buses (W_u=0, 9912).

4. Conclusions

The aim of the study was to present the possibilities of using Markov process model operation of technical facilities for pre-diagnose their suitability for the tasks adopted by the controlling subsystem, forecasting the state of the system operation after changing the input parameters of the model. By changing the input parameters there were simulated the impact of internal and external factors on the behaviour of the system.

References

Woropay M, Landowski B, Perczyński D. (2004) Metoda doboru obiektów technicznych do użytkowania w systemie eksploatacji (Eng. The method of technical objects selection for use in system operation), Diagnostyka vol. 32/2004.

Knopik L., Landowski B., Perczyński D. (2002), Prognozowanie stanu systemu eksploatacji transformatorów rozdzielczych na podstawie badań modelowych (Eng. Forecasting of the system operation state of distribution transformers on the basis of model tests). Zagadnienia eksploatacji maszyn nr 4 (132), vol. 37, PAN, Radom.

Buslenko N., Kałasznikow W., Kowalenko I. (1979) Teoria systemów złożonych (Eng, Theory of complex systems). PWN, Warszawa.

Landowski B., Woropay M., Neubauer A. (2004) Sterowanie niezawodnością w systemach transportowych (Controlling reliability in the transport systems). Biblioteka Problemów Eksploatacji, Wydawnictwo Instytutu Eksploatacji Maszyn, Bydgoszcz – Radom.

Woropay M., Knopik L., Landowski B. (2001) Modelowanie procesów eksploatacji w systemie transportowym (Modelling of maintenance processes in a transport system). Biblioteka Problemów Eksploatacji. Wydawnictwo Instytutu Eksploatacji Maszyn, Bydgoszcz – Radom.

22nd International Conference
ENGINEERING MECHANICS 2016
Svratka, Czech Republic, 9 – 12 May 2016

THE DESIGN OF A PROPORTIONAL SLIT VALVE WITH A PIEZOELECTRIC ACTUATOR

P.A. Laski*

Abstract: *The article is devoted to a proportional valve controlling the direction of flow in liquid pneumatic systems. Based on the analysed reference books, it can be stated that there are no power saving proportional flow and pressure valves with control times shorter than 0.005s with retaining mass intensity of flow at the level of 0.06kg/s or higher. The article presents the design of a slit separating valve and model determination of characteristics of mass intensification of flow for working paths (flow surface).*

Keywords: power saving, proportional valve, piezoactuator, fast response pneumatic valve.

1. Introduction

The main purpose for which the valve had been designed is programmed and follow-up control of pneumatic drives, including muscles and actuators. Shaping curvilinear characteristics of movement of pneumatic drives is a difficult problem, but it is necessary in advanced and developed robots and manipulators with parallel structures (Andrs et al., 2012) (Huscio & Kolodziejczyk, 2013)(Trochimczuk, 2013)(Koruba et al., 2010). Sometimes in technological processes the synchronization of drives is required and it is particularly difficult for muscles and pneumatic actuators. The follow-up control of pneumatic valves requires ultra-quick valves with the controlled flow of the working agent (Krzysztofik, 2012). As a result of conducted research it was found that that there are no valves for follow-up control of pneumatic drives for diameters above 40 mm with ensuring sufficient accuracy of recreation of the set movement trajectory. It results from the lack of sufficiently quick and precise proportional flow and pressure valves. Most often slide separating valves are used for controlling pneumatic and hydraulic actuators (Krzysztofik & Koruba, 2012). Their task is to separate the stream of liquid between valve flow surface (Janecki, Dariusz & Zwierzchowski, 2015). Separation of the stream is done by suitably shaped edges of the valve slide and its body (Miko & Nowakowski, 2012)(Janecki, D et al., 2015). With the use of the CFD software, vector speed fields and pressure distributions were determined and presented in the cross-sections of valve flow surface. Based on the conducted research, flow characteristics in the function of slide valve shift were determined. On the basis of the determined characteristics, it can be stated that the construction of a proportional pneumatic separating valve with high flow values is possible.

2. Actuators used in valves

In the solutions used for controlling fluid valves described in the reference books and patent applications two types of piezoactuators are used. In the first type, the piezoactuator (Błasiak & Kotowski, 2009) (Tuma et al., 2013) has the shape of a plate of small thickness and usually it is fixed with one end with the body, while the other end moves opening and closing the flow surface of the mini-valve. In such a solution, the piezoactuator may move with high frequency with great displacement of several millimetres, but the force does not exceed several Newtons. This type of valves are mostly used as preliminary degrees of control for pressure valves and separation with much greater flows (Ohuchi et al., 2000) (Yun et al., 2010). A similar group of valves encompasses the valves in which the controlling element has the shape of a disc of small thickness in relation to the diameter. As a result of polarization of the piezoactuator the middle part is moved and flow surface are opened (Sobocinski et al., 2009). The second group of valves where at present piezoactuators are used includes structures in which a piezoeletric

* Pawel Anrzej Laski, PhD.: Department of Automation and Robotics, Faculty of Mechatronics and Machine Design, Aleja Tysiaclecia Panstwa Polskiego 7; 25-314 Kielce; PL, pawell@tu.kielce.pl

actuator has the form of a multi-layer stack. There are solutions in which a piezoactuator directly opens and closes flow surface, but the displacements of the piezoelectric drive usually do not exceed 100 μm. Such a small displacement makes the construction more difficult and requires the application of high precision when making elements. The solutions in which the valves with the multi-layer actuator are directly used include injectors and pump-injectors of diesel engines (Bart, 1977) (MacLachlan et al., 2004). Another type of valves with multi-layer piezoeletric stacks includes structures where a slight displacement of the actuator is multiplied by levers and mechanical cams. In this way, a greater displacement of the drive can be seen at the cost of the decrease of force and frequency of operation (Reuter, 2013) (Claeyssen et al., 2007). In the considered structure of the valve, the drive and at the same time control element is the multi-layer piezoactuator with a mechanical amplifier in the form of a clamp. The maximum displacement of the applied drive amounts to 500 μm, and the maximum blocking force amounts to 570 N, the frequency of operation amounts to 460 Hz. The multi-layer actuator of the valve in the form of a piezoeletric stack allows in an ultraquick way to displace slit separating plates opening proportionally the flow surface of the valve(Suranek et al., 2013).

2.1. The principle of operation of a slit separating valve type 5/3

In a valve, the flow and separation of the liquid stream is done by properly shaped groups of slits creating flow surface. In this solution there is no classic separating slide. It appears from the experimental research carried out by the author that programmed positional control for pneumatic valves with the diameter of 25 mm requires the valves that have the frequency of operation at the level of at least 70 Hz and the flow of 700 l/min with power pressure of 0.6 MPa. It can similarly be observed in the case of muscle drives the only difference being that they require precise control of pressure changes. The principle of operation of the valve is shown on Fig. 1 to Fig 3. In the said valve, a single slit has the shape of a rectangle with one side equal to a half of piezoactuator's displacement. On the other hand, the size of the other side of the rectangle of the flow window is adjusted to the designed flow value and the total number of slits. In each flow window of the valve the flows from individual slits are summed up and the nominal valve flow is obtained. The selection of the number of slits in a unit corresponds to the surface of a flow window for a single valve path. The valve has the following flow paths: *1, 2, 3, 4, 5* in marked body (10) and slit groups: *1',2', 3', 4', 5'* in the upper plate cylinder (6) as well as the corresponding groups of slits: *1'', 2'', 3'', 4'', 5''* in any plate cylinder (7). The lower plate cylinder is joined with the possibility of disconnection with one of the arms (8) of the amplifier of displacement piezoactuator (9). The second arm of the amplifier of displacement is mounted to the body (10) of the valve. In neutral position (Fig 1) the flow paths of the valve are completely closed. Outermost positions of slit plane of the valve are shown on Fig 3. The piezoactuator allows for controlling the valve in a proportional way, then the lower plate cylinder may occupy an intermediate position in relation to the upper plate cylinder, and the flow through flow paths will depend on the degree of opening of the groups of slits.

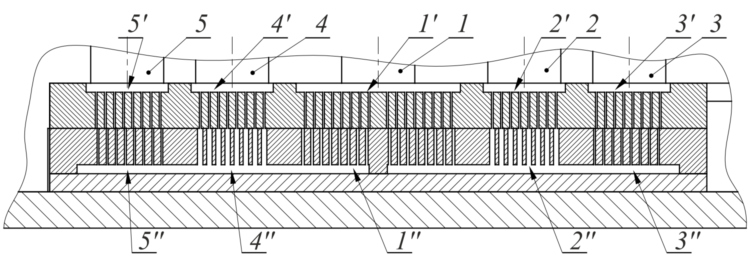

Fig. 1: A fragment of the cross-section of 5/3 valve. a) neutral position, b) a graphic symbol of the valve with a pneumatic actuator.

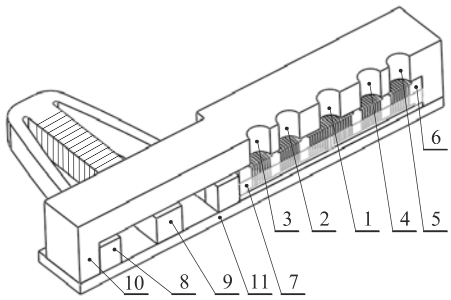

Fig. 2: An axonometric view with a partial cross-section, a) lower plate cylinder and a piozoelectric actuator.

The total surface of slits in a group creating a flow window is at least equal to the surface of the service line of valve G1/4" (~34mm2). The increase of the surface of flow does not constitute a structural problem because it is done by adding new groups of slits and maintaining the distance of piezoactuator's displacement. In the considered separating valve, a single slit has the size of 0.25x45x5 mm. Fig.2. shows the valve in an axonometric view with a partial cross-section.

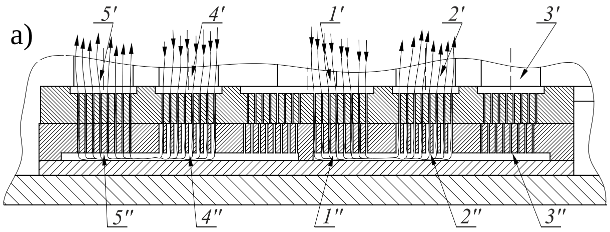

Fig. 3: 5/3 valve in outermost positions of the lower slit cylinder, a) full flow between paths 1-2 and 4-5, b) full flow through flow paths 1-4 and 2-3.

3. Flow simulation (CFD)

Fig. 5 shows the results of simulation research in the CFD software (Wawrzyniak & Peszynski, 2014)(Blasiak, Slawomir, 2015a)(Blasiak, Slawomir, 2015b)(Blasiak, S & Zahorulko, 2016). In order to conduct the analysis, a spatial computational grid with irregular structure was adopted. Groups of slits in which the minimum size of a grommet amounted to 1μm were the pivotal area of grid assumption. In order to shorten the time of performing numerical calculations, the model was divided along symmetrical axes. Half of the volume of the analysed air amounted to $1.0047 \cdot 10^{-5} m^3$ where the number of units amounted to ~3.3 million of units corresponds to 14.7 million elements. Fig. 4 shows an enlarged fragment of the grid of slit flow surface of the valve.

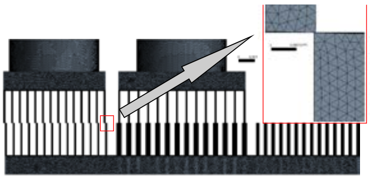

Fig. 4: The view of a computational grid for the valve filling agent.

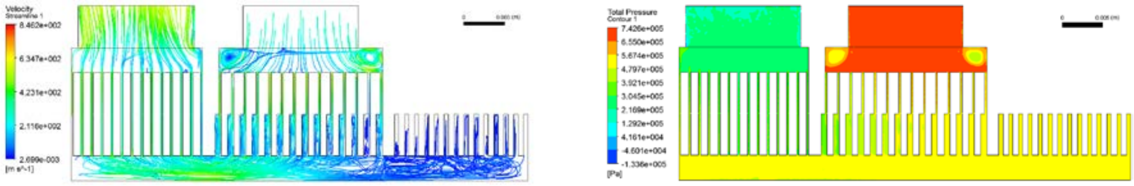

Fig. 5: The view of the cross-section of the capacity of valve slits, a) medium speed distribution (streamline), b) medium pressure distribution.

The conducted model research confirmed the conjecture that a small asymmetry of the working agent flow may occur in the valve. It appears directly from the width of flow surface in the moving cylinder of the valve. Varied width of flow surface of the moving cylinder is necessary to perform the function of a 5/3 valve and close in-flow and out-flow paths. Fig. 6 shows minimum differences of flow values for different feed paths 1-2 and 1-4 in relation to out-flow paths 2-3 and 4-5. In extreme positions of the valve, more dynamic outflow will occur on outflow paths. Maximum mass flow rate for routes 1-2 and 1-4 amounts to 0.058kg/s

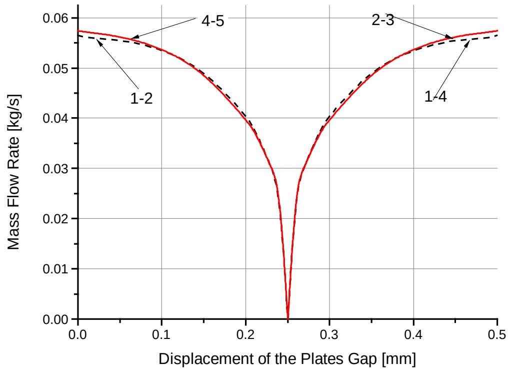

Fig. 6: Mass flow rate vs signal and measurement set-up.

4. Conclusions

The presented valve has many features that differentiate it from the produced comparable products. It appears from the analysis of the market of producers of pneumatic devices, and the patent applications that there is no solution that would allow for achieving the flow through the flow surface of the valve above 0.06 kg/s and actuation times above 75 Hz. The slit structure of separating plates of the valve allows for adding up the flow from individual surface and thereby the construction of a valve of flows unattainable till now amounting to a couple thousand litres per minute. Moreover, the innovative structure of flow surface allows to design valves with any flows adjusted to technological processes. The valve is protected with patent no. PL 213836 B1. **Acknowledgement:** The work was performed within the framework of the research project NCN and NCBiR TANGO no. TANGO1/270131/NCBR/2015.

Reference

Andrs, O., Brezina, T., & Kovar, J. (2012) Design of Fuzzy Logic Controller for DC Motor, , pp. 9–18. doi:10.1007/978-3-642-23244-2_2

Bart, H. U. (1977) Piezoelectric fuel injector valve, . Retrieved from http://www.google.com.br/patents/US4022166

Blasiak, S. (2015a) An analytical approach to heat transfer and thermal distortions in non-contacting face seals, International Journal of Heat and Mass Transfer, 81, pp. 90–102. doi:10.1016/j.ijheatmasstransfer.2014.10.011

Blasiak, S. (2015b) The two dimensional thermohydrodynamic analysis of a lubrication in non-contacting face seals, Journal of Thermal Science and Technology, 10, 1, pp. JTST0016–JTST0016. doi:10.1299/jtst.2015jtst0016

Blasiak, S., & Zahorulko, A. V (2016) A parametric and dynamic analysis of non-contacting gas face seals with modified surfaces, Tribology International, 94, pp. 126–137. doi:10.1016/j.triboint.2015.08.014

Błasiak, M., & Kotowski, R. (2009) Propagacja fal akustycznych w kryształach piezoelektrycznych, Przegląd Elektrotechniczny, R. 85, nr, pp. 40–43.

Claeyssen, F., Le Letty, R., Barillot, F., & Sosnicki, O. (2007) Amplified Piezoelectric Actuators: Static {&} Dynamic Applications, Ferroelectrics, 351, 1, pp. 3–14. doi:10.1080/00150190701351865

Huscio, T., & Kolodziejczyk, W. (2013) Haptic Devices Based on Planar Stepping Motors - Introductory Concept, In Gosiewski, Z and Kulesza, Z (Ed.), *Mechatronic Systems And Materials IV* (Vol. 198, pp. 313–317). LAUBLSRUTISTR 24, CH-8717 STAFA-ZURICH, SWITZERLAND: TRANS TECH PUBLICATIONS LTD. doi:10.4028/www.scientific.net/SSP.198.313

Janecki, D., & Zwierzchowski, J. (2015) A method for determining the median line of measured cylindrical and conical surfaces, Measurement Science & Technology, 26, 8. doi:10.1088/0957-0233/26/8/085001

Janecki, D., Zwierzchowski, J., & Cedro, L. (2015) A problem of optimal cylindricity profile matching, Bulletin of The Polish Academy of Sciences-Technical Sciences, 63, 3, pp. 771–779. doi:10.1515/bpasts-2015-0088

Koruba, Z., Dzipa, Z., & Krzysztofik, I. (2010) Dynamics and control of a gyroscope-stabilized platform in a self-propelled anti-aircraft system, Journal of Theoretical and Applied Mechanics, 48, 1, pp. 5–26.

Krzysztofik, I. (2012) The Dynamics of the Controlled Observational and Tracking Head Located on a Moving Vehicle, Solid State Phenomena, 180, pp. 313–332. doi:10.4028/www.scientific.net/SSP.180.313

Krzysztofik, I., & Koruba, Z. (2012) Model of Dynamics and Control of Tracking-Searching Head, Placed on a Moving Object, Journal of Automation and Information Sciences, 44, 5, pp. 38–47.

MacLachlan, B. J., Elvin, N., Blaurock, C., Keegan, N. J., & Anderson, E. H. (2004) Piezoelectric valve actuator for flexible diesel operation: Smart Structures and Materials 2004: Industrial and Commercial Applications of Smart Structures Technologies, , pp. 167–178. doi:10.1117/12.545625

Miko, E., & Nowakowski, L. (2012) Analysis and verification of surface roughness constitution model after machining process, In Martsynkovskyy, V and Zahorulko, A (Ed.), *XIIITH International scientific and engineering conference hermetic sealing, vibration reliability and ecological safety of pump and compressor machinery-HERVICON-2011* (Vol. 39, pp. 395–404). doi:10.1016/j.proeng.2012.07.043

Ohuchi, H., Akasaka, H., & Osada, T. (2000) Pneumatic pulse flow conrtol valve driven by successive impulsive force of a piezoelectric multilayer actuator: FLUCOME 2000, 6th Triennial International Symposium on Fluid Control Meausrement and Visualization, Universit{é} de Sherbrooke, , pp. 54–57.

Reuter, M. (2013) Valve, . Retrieved from http://www.google.com/patents/US8490575

Sobocinski, M., Juuti, J., Jantunen, H., & Golonka, L. (2009) Piezoelectric unimorph valve assembled on an LTCC substrate, Sensors and Actuators A: Physical, 149, 2, pp. 315–319. doi:10.1016/j.sna.2008.11.025

Suranek, P., Mahdal, M., & Tuma, J. (2013) Comparising of Antialiasing Filters in A/D Converters, In Petras, I and Podlubny, I and Kacur, J and Nawrocka, A and Sapinski, B (Ed.), *Proceedings of the 2013 14TH International Carpathian Control Conference (ICCC)* (pp. 373–376). 345 E 47TH ST, New York, NY 10017 USA: IEEE.

Trochimczuk, R. (2013) Conception of Arm of Medical Robot Dedicated to Application of Minimally Invasive Surgery, In Gosiewski, Z and Kulesza, Z (Ed.), *MECHATRONIC SYSTEMS AND MATERIALS IV* (Vol. 198, pp. 3–8). LAUBLSRUTISTR 24, CH-8717 STAFA-ZURICH, SWITZERLAND: TRANS TECH PUBLICATIONS LTD. doi:10.4028/www.scientific.net/SSP.198.3

Tuma, J., Simek, J., Skuta, J., & Los, J. (2013) Active vibrations control of journal bearings with the use of piezoactuators, Mechanical Systems and Signal Processing, 36, 2, pp. 618–629. doi:10.1016/j.ymssp.2012.11.010

Wawrzyniak, S., & Peszynski, K. (2014) Modeling and simulation of the recuperative heat exchanger, In Fuis, V (Ed.), *ENGINEERING MECHANICS 2014* (pp. 700–703). DOLEJSKOVA 5, PRAGUE 8, 182 00, Czech Republic: ACAD SCI Czech Republic, INST THERMOMECHANICS.

Yun, S.-N., Ham, Y.-B., Park, J.-H., Kim, H.-H., & So, H.-J. (2010) Design Strategy of Piezoelectric Valve for Color Sorter, Journal of the Korean Physical Society, 57, 41, pp. 913. doi:10.3938/jkps.57.913

22nd International Conference
ENGINEERING MECHANICS 2016
Svratka, Czech Republic, 9 – 12 May 2016

FRICTIONLESS BELLOWS UNIT CONNECTED WITH THE MAGNETORHEOLOGICAL VALVE

O. Macháček*, M. Kubík, I. Mazůrek, Z. Strecker, J. Roupec

Abstract: *Dynamic range is one of the key parameter for effective control of magneto-rheological (MR) dampers in suspensions controlled by semi-active algorithms. This article discusses dynamic range increase ensured by elimination of friction in a device which forces fluid to flow through MR valve. The friction affects a force velocity dependency. It is a part of force that cannot be controlled. Therefore friction is unwanted in MR dampers or valves. This article describes the two versions of volumetric unit with MR valve. First, the fluid was forced by hydraulic cylinder with high friction. In order to eliminate friction, a unique volumetric unit was designed and used instead of hydraulic cylinder. It uses elastic metal bellows which can be sealed by static seals, therefore there is no contact between moving parts. Measurement of force velocity dependency was carried out for original and new volumetric unit connected with the same MR valve. The results showed that the frictionless unit exhibits a significant improvement of dynamic range for the whole range of velocities compared to original piston unit. That has positive impact to efficiency of vibration elimination of MR valve using semi-active control.*

Keywords: Vibration, Dynamic range, Magneto-rheological valve, Frictionless, Bellows

1. Introduction

Vibrations – an accompanying feature of movement are usually unwanted. Therefore, there are understandable efforts to reduce them according to Housner's study (1997). One of possible way is semi-active control using magneto-rheological (MR) damper or valves. Fundamental part of these smart devices is a coil. The coil allows creating the magnetic field with different intensity that causes various yield stress of medium – MR fluid. Carlson (1996) describes the MR fluid as suspension of iron particles, oil and additives. Yang (2002) said that efficiency of MR damper for semi-active control is affect by two factors: dynamic range and time response. Until now, the fastest damper was developed by Strecker (2015). Time necessary to change the damping of this damper is approximately 2 ms. Dynamic range (1) depends on the piston velocity and it can be calculated as ratio of the damping force in active state (F_{on}) and the force in inactivated state (F_{off}). The off state force can be determined according to Yang (2002) and Bai (2014) as the sum of force caused by flowing of viscous fluid F_η and the friction F_f. It is necessary to add a yield stress force F_τ in sum for active state.

$$D(v) = \frac{F_{on}(v)}{F_{off}(v)} = \frac{F_\tau + F_\eta + F_f}{F_\eta + F_f} = 1 + \frac{F_\tau}{F_\eta + F_f} \qquad (1)$$

Couple ways of increasing the maximal dynamic range were described. Carlson (1996) increased the maximal magnetic field strength in the gap. Yang (2002) optimized geometry of gap and piston. Cvek (2015) choses fluid that exhibits the greatest differences between the yield stress in ON and OFF states. Above mentioned authors however did not investigate the influence of sealing friction. The friction in off-state can cause significant part of damper overall force, but it is negligible in on-state. Therefore, elimination of the friction force should improve the dynamic range of MR damper. The elimination of friction was discussed in papers from Davis (1994), Seong (2013) and Lee (2015).

All authors: Institute of Machine and Industrial Design, Brno University of Technology, Technická 2896/2, 616 69 Brno; CZ, * Ing. Ondřej Macháček: y126193@stud.fme.vutbr.cz

In this article, the impact of friction force on dynamic range is investigated. The frictionless unit with bellows is compared to the classical concept with hydraulic cylinder with friction force caused by usual sealing.

2. Methods

The first version, where the fluid was forced to flow through MR valve by commonly used hydraulic cylinder is shown in Figure 1 – left. There are seals between cylinder and piston or piston rod. These seals are the most significant cause of friction force. That force cannot be controlled, consequently it decreases the dynamic range of MR valve. Therefore the cylinder was replaced by newly designed bellows unit shown in Figure 1 – right. When the pulsator moves relative to the frame, the fluid is forced to flow through MR valve. Damping force of MR valve was controlled by electric current in coil.

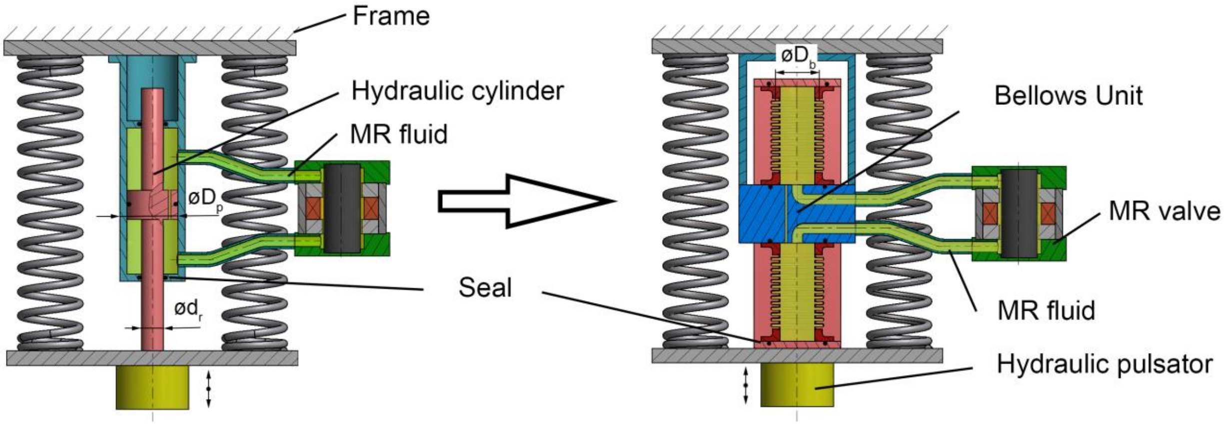

Fig. 1: Scheme of first (left) and second (right) volumetric unit

2.1. Measurement set-up

The damping and spring force F was measured by strain gauge load cell INTERFACE 1730ACK-50kN mounted between the upper plate and the frame. Velocity $\underline{v_o}$ was measured by sensor integrated in pulsator INOVA AH 40-150 M56. Force caused by springs was calculated and subtracted from total force by our software.

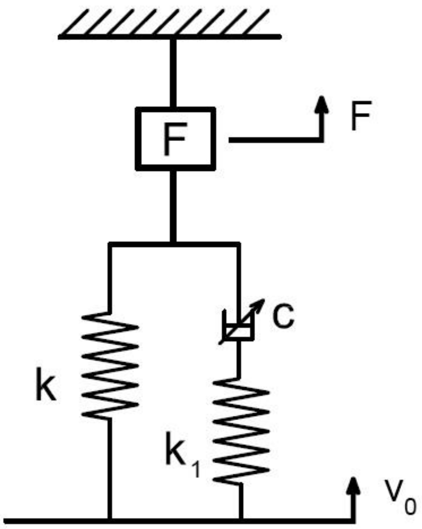

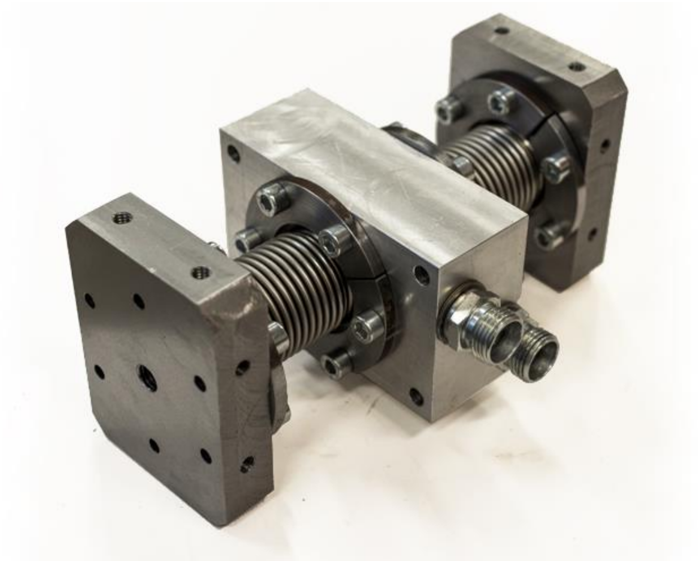

Fig. 2: Scheme of measurement (left) and manufactured bellows unit (right)

Damping of MR valve was investigated in conjunction with both volumetric units with the same settings:

Fluid	***MRF 132 DG (LORD)***
Excitation	***Linear Sweep sine***
Exc. Amplitude	***5 mm***
Exc. Frequency	***0.1 – 8 Hz***
Coil currents	***0A, 0.5A, 1A***
Bypass diameter	***1.45 mm***

3. Results

Primary stiffness k is 402 N/mm, secondary k_1 2860 N/mm and damping coefficient c cannot be determined, because force and velocity dependency of the MR valve is non-linear.

3.1. Force and velocity dependency

Force - velocity dependency of bellows unit differs especially for current 0A compared to hydraulic cylinder, because of friction decrease. This also affects the states with other currents in coil, therefore the force is lower. We can observe different slope of curves in measurement for cylinder and bellows. It is caused by different effective area. For hydraulic cylinder, the effective area is the piston area, which is given by diameter of piston $D_p = 36\ mm$ and piston rod $d_r = 18mm$ (Fig. 1). But bellows unit has no piston, therefore the middle diameter $D_b = 30.25\ mm$ of bellows waves was taken as an effective area shown in Fig. 1. Presumption that middle diameter can be considered as virtual piston was verified by test. These areas were not absolutely similar because of limited sizes of bellows and cylinders offered by manufacturers. The different effective areas for bellows and hydraulic cylinder have however minimal impact on dynamic range.

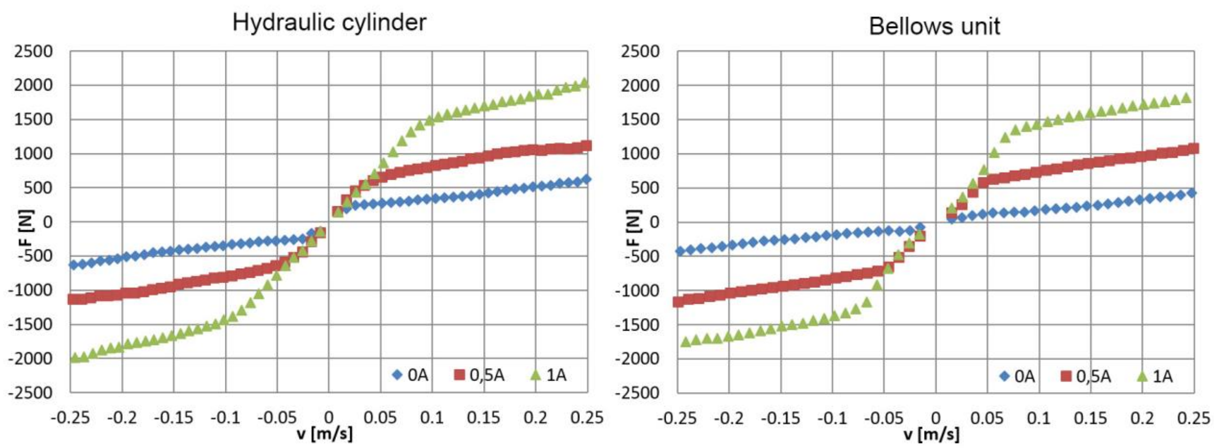

Fig. 3: Force velocity dependency of MR valve connected with the hydraulic cylinder (left) and bellows unit (right)

3.2. Dynamic range

The dynamic range $D(v)$ of MR valve can be counted using the equation (1) so the ratio between damping force with maximal current in coil ($I = 1\ A$) and no current in coil ($I = 0\ A$). The dependency of Dynamic range and velocity is shown in Fig. 4. It is obvious that the new design has a higher dynamic range for all velocity range. For the lower velocity value v < 0.08 m/s is the increase more than 100%.

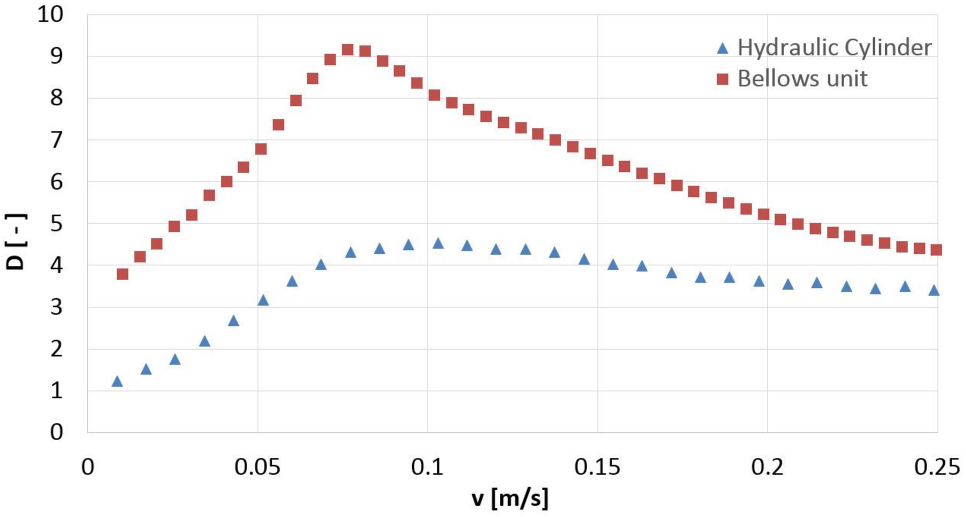

Fig. 4: Comparison of dynamic range

4. Conclusions

Two versions of volumetric unit which forced fluid flow through MR valve was designed manufactured and tested. The first version was a standard solution with hydraulic cylinder with friction caused by sealing and the second version was frictionless bellows unit. The measurement proved that the force caused by friction in damping system with MR valve has significant impact on dynamic range of such devices. The increase of dynamic range for frictionless bellows unit is more than 100% for velocity of pulsator in range 0 – 0.08 m/s. This fact should according to Yang (2002) significantly improve quality of damping using a semi-active algorithm.

Acknowledgement

The research leading to these results has received funding from the MEYS under the National Sustainability Programme I (Project LO1202), FSI-S-14-2329, FEKT/FSI-J-15-2777 and GAČR 13-31834P.

References

Bai, X. & N.M. Wereley (2014) A fail-sefe magnetorheological energy absorber fot shock and vibration. Journal of Applied Physics, 115, 17, pp.17B535.

Carlson JD & BF Spencer Jr. (1996) Magneto-rheological fluid dampers: scalability and design issues for application to dynamic hazard mitigation. Proceedings of 2nd Workshop on Structural Control: Next Generation of Intelligent Structures, Hong Kong

Cvek M., M. Mrlik et. al. (2015) A facile controllable coating of carbonyl iron particles with poly(glycidyl methacrylate): a tool for adjusting MR response and stability properties. J. Mater. Chem., 3, 18, pp. 4646-4656

Davis P., D. Cunningham & J. Harrell. Spencer Jr. BF. (1994) Advanced 1.5 Hz passive viscous isolation system. 35th Structures, Structural Dynamics, and Materials Conference, Reston

Housner, G. W., L. A. Bergman, et al. (1997) Structural Control: Past, Present, and Future. Journal of Engineering Mechanics, 123, 9, pp.897-971.

Lee D. G. & J. H. Han. (2015) Experimental study on on-orbit and launch environment vibration isolation performance of a vibration isolator using bellows and viscous fluid. Aerospace Science and Technology, 45, pp. 1-9.

Seong, M. S., S.B. Choi & C.H. Kim (2013) Damping force of frictionless MR damper associated with hysteresis modeling. 13th International Conference on Electrorheological Fluids and Magnetorheological Suspensions, Ankara

Strecker Z., J. Roupec et. al. (2015) Design of magnetorheological damper with short time response. Journal of Intelligent Material Systems and Structures, 26, 14, pp. 1951-1958.

Yang, G. B. F., J.D. Carlson & M.K. Sain (2002) Large-scale MR fluid dampers: modeling and dynamic performance considerations. Engineering Structures, 24, 3, pp. 309-323.

22nd International Conference
ENGINEERING MECHANICS 2016
Svratka, Czech Republic, 9 – 12 May 2016

WAVE PHENOMENA IN COMPOSITE RUBBER-SANDSTONE STRUCTURES USING ADINA PROGRAM

I. Major[*], M. Major[**]

Abstract: *In this paper the numerical solution of vibrations damper in form of cube made of sandstone and rubber cross located inside during technological process with the use of ADINA program is discussed. These days there exists many solutions at the market, which allow to reduce the mechanical waves caused by dynamical loads. Despite that fact there is just a few solutions involving composite materials application. By performing the numerical solution with the use of ADINA program significant mechanical wave reduction could be observed in the proposed composite. Moreover presented solution can be applied in the production process with such an ease and it could also be produced in modular form. Adopted sandstone material model to the performed analysis had very similar properties as widely available material, which is utilized in production of the YTONG airbricks. The rubber cross was described with the Mooney-Rivlin material model which is basically implemented in the ADINA program. It should be noted that presented solution can be treated as an innovative product, which not only allow to reduce vibrations from machines on the wall structures without the necessity of use additional anti-vibrations systems but also can be treated as an ecological product made of materials, which can be easily recycled.*

Keywords: Composite structures, wave phenomena, ADINA, rubber-sandstone, vibrations damping

1. Introduction

Wave phenomena due to its wide range of applications, are the subject of interest by many researchers, who in order to describe the problem of wave propagation in various different types of materials used both classical mathematical and finite element method approach. Mathematical models concerning the description of various types of wave phenomena was presented by Coulson (1982). The numerical analysis performed to validate the repaired lightweight steel roof structure, which had an excessive deformations due to the act of static and dynamical forces was presented in (Čajka, Krejsa, 2014). The problem of wave propagation in simple elastic structures was discussed in (Major, Major, 2014a), where authors presented both mathematical description of phenomena and the possibility of numerical solutions with the use of finite element method in the ADINA program. Sam authors afterwards published paper (Major, Major, 2014b), which concerned the comparative analysis of shockwave propagation in rubber material described by Zahorski (1959) and rubber described by Mooney-Rivlin (Mooney 1940; Rivlin 1948). Considerations of wave phenomena description in composite structures were presented by Kosiński (2007), Zhuang, Ravichandran G. & Grady (2003) and Verma (2013), whereas the vast literature overview covering all aspects of wave phenomena was included in (Wesołowski, 1989).

In case of civil engineering the wave propagation in material or structure is a phenomena, which should be strongly avoided therefore in that structures various additional elements reducing the dynamical and acoustic effects have to be utilized such as vibro-isolators and soundproof mats. The disadvantage of the above mentioned solutions is the lack of possibility to transfer significant static loads resulting in the necessity of application additional support components. That additional materials makes the construction more complex and the dimensions of such a structure may increase resulting in reduced usable area of the object.

[*] Associate Professor Izabela Major: Department of Technical Mechanics, Częstochowa University of Technology, Akademicka 3 street, 42-200, Częstochowa, PL, imajor@bud.pcz.czest.pl

[**] Eng. Maciej Major, PhD.: Department of Technical Mechanics, Częstochowa University of Technology, Akademicka 3 street, Częstochowa, PL, mmajor@bud.pcz.czest.pl

In this paper the numerical finite element method approach is presented in order to determine the mechanical wave propagation resulting from impulse load in a raw sandstone material and in a composite sandstone-rubber. Performed numerical analysis is an introduction to the research of this type of composite materials with the further possibility of application in construction industry as low cost material, easy in production as well as ecological product, which can be recycled. It should be noted that presented composite could be applied as the wall structure, which is exposed to the negative influence of vibrations, as a support system under machines, without the necessity of application other additional vibro-isolators.

2. Methods

In order to obtain approximate solutions of effective stress arising along the wave propagation through specified material under the influence of impulse load the ADINA program was chosen. The object of study comprised of the cube and three dimensional cross located at the center of cube gravity. The side of cube was assumed of 10 cm length, while the individual prism with a square base had dimensions 8×2×2 cm. At the bottom surface of the cube all six degrees of freedom were fixed, whereas on the top surface the impulse pressure load was assumed. In the time from 0 s to $1.111 \cdot 10^{-6}$ s the pressure increases from 0 kN/m^2 to 10 kN/m^2, releasing energy of load in the so-called first time step. Adopted model to the numerical analysis is presented in Fig. 1.

a)

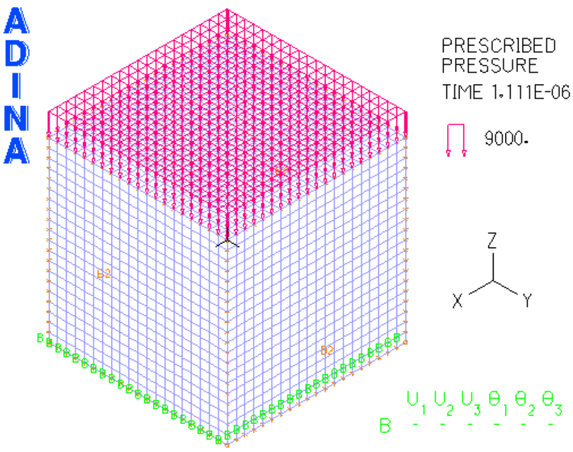

b)

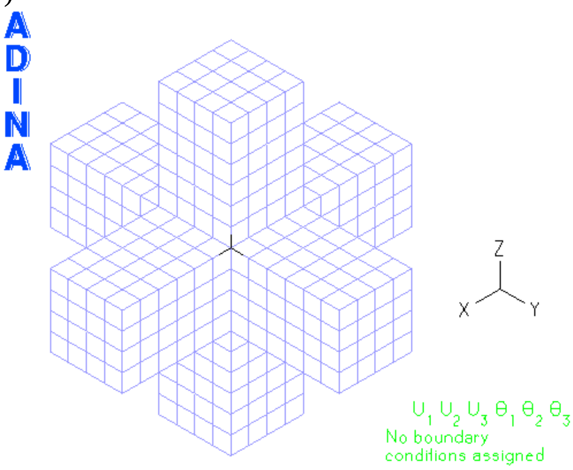

Fig. 1: Numerical model of composite rubber-sandstone cube (a), three dimensional cross made of Mooney-Rivlin material (b), respectively. Cross center of gravity lays exactly in cube center of gravity.

In order to describe cross rubber like material, existing Mooney-Rivlin ADINA program module allowing to describe rubber and foam material models was chosen. The sandstone material was assumed to be simplified to the linearly elastic material model. Properties of both materials utilized in the numerical analysis were shown in Table 1.

Tab. 1: Material properties of rubber and sandstone

Mooney-Rivlin material		**Sandstone material**	
Property	**Value**	**Property**	**Value**
C_1	*62780 [Pa]*	E	*86.00 [GPa]*
C_2	*8829 [Pa]*	ν	*0.125 [-]*
ρ	*1190 [kg/m^3]*	ρ	*2650 [kg/m^3]*

Discretization of the cube and cross area was done with the use of 8-node 3D-Solid finite elements, 0.5×0.5×0.5 cm each. In the case of model made of pure sandstone without rubber 8345 finite elements were obtained for the whole structure, whereas in the composite 7705 finite elements were described with sandstone material and 640 with rubber material, respectively. In both model cases there were 9265 nodes.

3. Numerical results

In this chapter in Fig. 2 the approximate numerical results in the graph form of effective stress plot concerning the mechanical wave propagation under the influence of impulse load for the pure sandstone model cross-section and composite sandstone-rubber cross-section with the use of ADINA program have been presented. Mentioned cross-sections comprise the transition of YZ plane on X axis at distance equal 5 cm from the beginning of the global coordinate system.

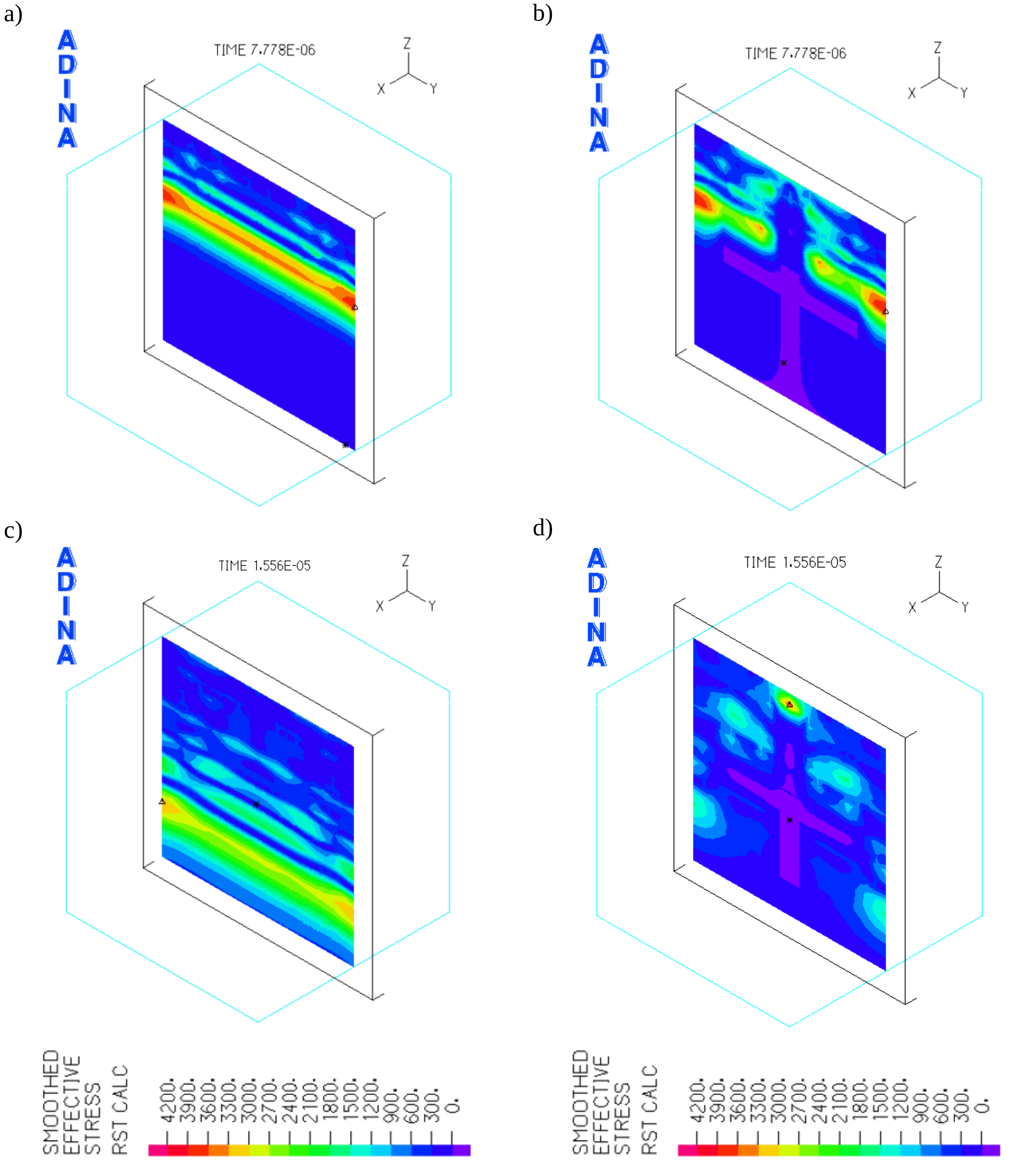

Fig. 2: Wave propagation under the impulse load for a different time steps in the sandstone material (a, c,) and in the composite rubber-sandstone (b, d), respectively. Scales presented in Pa units.

By analysis of the obtained numerical results, it can be clearly visible that at the $7.778\cdot10^{-6}$ s time step in case of the composite material (Fig. 2b) characteristic refraction of the effective stress distribution was obtained where wave pass through rubber material and wave propagate almost only in the sandstone material in comparison with the homogeneous cube made of sandstone (Fig. 2a). Moreover the value of effective stress near the outer part of cross-section area is almost the same in presented composite and pure sandstone, however in the inner area of the composite (Fig. 2b) near the rubber, cross wave propagation is damped around twice. Comparing both numerical models at the time step equal $1.556\cdot10^{-5}$ s it can be observed that in the composite, the mechanical wave propagation is significantly reduced (Fig. 2d) and values of presented effective stress are four times lowered than in the homogeneous sandstone cube (Fig. 2c).

Significant differences between homogeneous sandstone cube and the composite allow to conclude that the presented composite is a well vibrations damper, while the rubber cross structure allow to reduce vibrations for about the same value with the assumption that the value of dynamical force placed on any surface of cube is exactly the same. An additional advantage of the presented solution is fact, that in the realization process of any structure, which have to reduce vibrations, the problem of correct positioning of element can be neglected due to the utilized plane symmetry in all three mutually orthogonal planes passing through the cube center of gravity.

4. Conclusions

In this paper the finite element method approach was presented in order to obtain approximate solutions of wave propagation phenomena in two different materials – pure sandstone and composite made of sandstone and rubber.

Performed numerical analysis allowed to observe the dispersion of mechanical wave resulting from impulse load in the composite model in comparison with the homogeneous cube made of sandstone. Due to the significant reduction of dynamic effects and the ability of transferring the static load, presented solution may be treated as desirable to utilize from the civil engineering point of view in any construction which is exposed to soil vibrations, machines vibrations or it is necessary to reduce the acoustic waves and also it is required to transfer significant values of static load. Moreover applied plane symmetry of discussed composite allow to utilize it in the building structures without the risk of incorrect placement of the element. It should also be noted that connection of sandstone and rubber material allow to obtain environmental friendly elements since both materials can be easily recycled. It is also important that despite of obtained satisfactory results from the numerical analysis, it is recommended to make the experimental studies which would confirm the validity of presented solution.

References

Čajka R. & Krejsa M. (2014) Validating a computational model of a rooflight steel structure by means of a load test, Applied Mechanics and Materials, 501, pp. 592-598.

Coulson C.A. & Jeffrey A. (1982) Fale. Modele matematyczne. WNT, Warszawa.

Kosiński S. (2007), Fale sprężyste w gumopodobnych kompozytach warstwowych. Wydawnictwo Politechniki Łódzkiej, Łódź.

Major I. & Major M. (2014) Modeling of wave propagation in the ADINA software for simple elastic structures, Advanced Materials Research, 1020, pp. 171-176.

Major M. & Major I. (2014) Comparative analysis of the distribution of effective stress in Mooney and Zahorski materials using ADINA software, Advanced Materials Research, 1020, pp. 165-170.

Mooney M. (1940) A theory of large deformations, Journal of Applied Physics, 11, pp. 582-592.

Rivlin R.S. (1948) Large elastic deformations of isotropic materials, I Fundamental concepts, Philosophical Transactions of the Royal Society of London A 240, 822, pp. 459-490.

Verma K. L. (2013) Wave propagation in laminated composite plates, International Journal of Advanced Structural Engineering, 5:10, Springer Open Journal

Wesołowski Z. (1989) Akustyka ciała sprężystego. Państwowe Wydawnictwo Naukowe, Warszawa / Poznań.

Zahorski S. (1959) A form of elastic potential for rubber-like materials, Archives of Mechanics, 5, pp. 613-617.

Zhuang S., Ravichandran G. & Grady D.E. (2003) An experimental investigation of shock wave propagation in periodically layered composites, Journal of the Mechanics and Physics of Solids, 51, 2, pp. 245–265.

22nd International Conference
ENGINEERING MECHANICS 2016
Svratka, Czech Republic, 9 – 12 May 2016

EVALUATION OF SAFETY OF MODELS FOR ASSESSMENT OF THE PUNCHING SHEAR RESISTANCE OF FLAT SLABS WITHOUT SHEAR REINFORCEMENT

L. Majtánová[*], J. Hanzel[**], J. Halvonik[***]

Abstract: *Reinforced concrete flat slabs are frequently used structural members in buildings construction. The most dangerous failure of these systems, as well as the most usual damage, is punching of the slab by column. Safety verification and avoidance of failure due to punching in the vicinity of a column is currently performed using empirical model which is introduced in Eurocode 2 (EC2 model). However, extensive discussions are held about safety of the EC2 model. The paper deals with statistical evaluation of EC2 model safety and with its comparison with the other relevant models for assessment of punching resistance (Model Code 2010, ČSN 731201, etc.). Database which includes results of more than 400 experimental tests of flat slab specimens has been used for the statistical evaluation*

Keywords: Punching Shear Resistance, Flat Slab, Safety, Reinforced Concrete

1. Introduction

Reinforced concrete slabs supported on columns are common in residential and commercial buildings. The most usual damage of these systems is punching of slab by support (column or corner walls). Punching of the slabs is caused by shear forces which are concentrated on the small area at the vicinity of a column. Such failures are usually associated with very small deformations and crack widths prior to failure and, as such, can occur without noticeable warning signs. Furthermore, the mechanism of punching failure is still poorly understood. The punching provisions in codes of practice are based on different theories or on empirical formulae, thus in some cases leading to very different strength predictions.

Design model for assessment of punching resistance in EC2 is model which was originally published in Model Code 1990. The model is very empirical because main parameters having influence on punching resistance were statistically determined using results of some experiments. The most of the experiments used for calibration were performed on the slab specimens with inner column. Therefore a question was raised if calibrated model is applicable also for slab in areas with edge or corner columns or for foundation slabs and footings.

Because database of experimental results has been significantly increased within last 20 years it is interesting to check reliability of currently used models and if necessary to recalibrate them. This is example of EC2 model update, which was released in January 2016 (*Hegger*, *Siburg*, *Kueres*) from RTWH Aachen. Besides empirical models there were developed new mechanical models within last decade. Among them is model based on the Critical Shear Crack Theory (CSCT), developed by *Muttoni and Schwartz* and updated by *Muttoni and Ruiz (2008, 2012)* or model of *A. Marí, A. Cladera* from Spain. Because many flat slabs were design using ČSN 731201 standard on the territory of Czech and Slovak republic the statistical evaluation has been also carried out for this model.

[*] Ing. Lucia Majtánová.: Department of Concrete Structures and Bridges, Slovak Universtity of Technology; Radlinského 11; 810 05; SR, lucia.majtanova@stuba.sk

[**] Ing. Ján Hanzel.: Department of Concrete Structures and Bridges, Slovak Universtity of Technology; Radlinského 11; 810 05, Bratislava; SR, jan.hanzel@stuba.sk

[***] Prof. Ing. Jaroslav Halvonik, PhD.: Department of Concrete Structures and Bridges, Slovak Universtity of Technology; Radlinského 11; 810 05, Bratislava; SR, jaroslav.halvonik@stuba.sk

2. Models for assessment of the shear resistance of flat slabs without shear reinforcement

As it has already been mentioned the statistical safety evaluation was carried out for several different models. The first one is ČSN model, the second one is current EC2 model, the third one is German update of EC2 model from 2016 and the others are models based on CSCT theory.

2.1. Control perimeter

The models for assessment of punching resistance differ each other with position of basic control perimeter and with the inclination of modeling shear crack. Current Eurocode has basic control perimeter at distance $2d$ from edge of a column, the others $0.5d$ and ČSN model $0.5h$ where d is average effective depth of a slab at column area and h is a thickness of slab, see fig. 1.

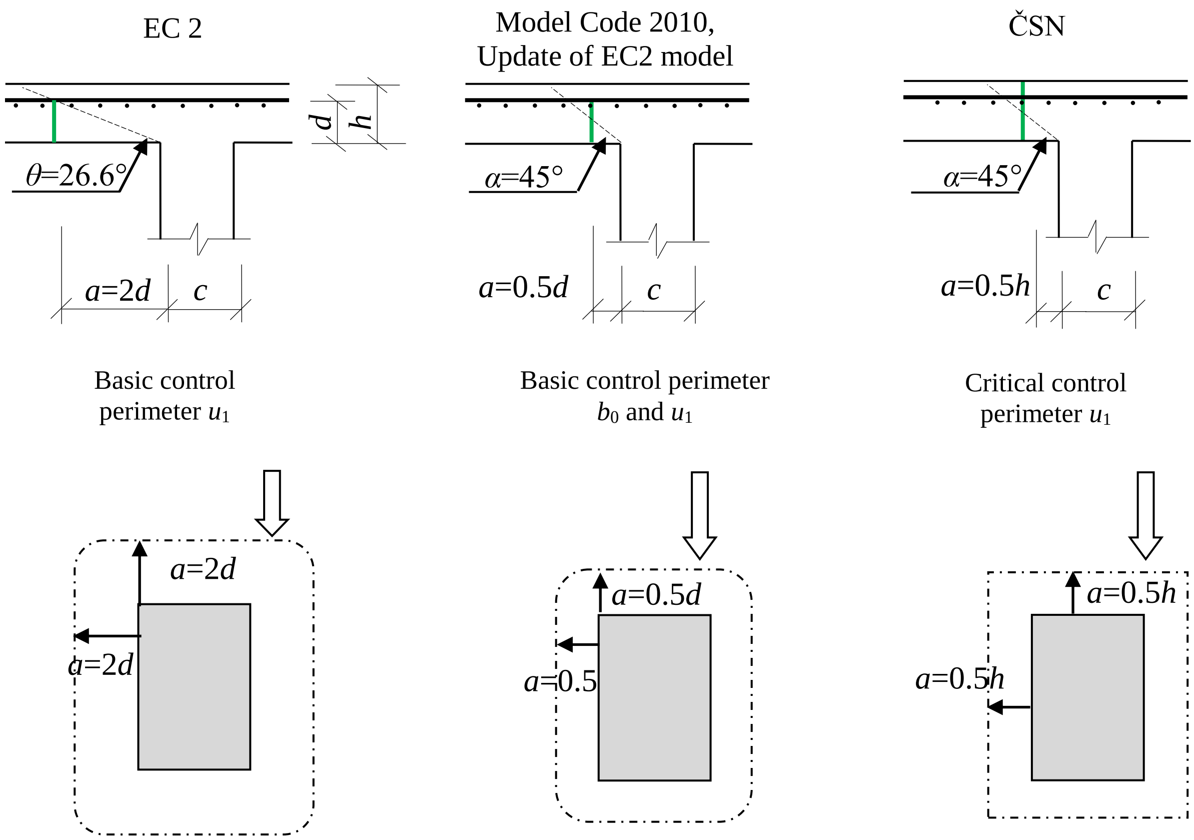

Fig. 1: Control perimeters for punching verification in codes of practice

2.2. Calculation of the shear resistance

In all major codes of practice, punching strength of flat slabs is verified by comparing the design shear strength $v_{Rd,c}$ of an element to a design shear stress v_{Ed} on a unit length of a control perimeter around a column or a loaded area. Effect of unbalanced moments is taking into account by factor β.

$$v_{Ed} = \beta * V_{Ed}/(u_1 * d) \leq v_{Rd,c} \quad (1)$$

The shear resistance $v_{Rd,c}$ generally depends on the following factors. Tensile strength of concrete, slab effective depth (size effect), maximum aggregate size $d_{g,max}$, slab rotation ψ, shear slenderness a_λ/d.

2.2.1 Empirical EC2 models and its update

Punching shear resistance without shear reinforcement can be determined using formula (2), according to current EC2 model, model “B”.

$$v_{Rd,c} = C_{Rd,c} * k * (100 * \rho_l * f_{ck})^{1/3} \text{ [MPa]} \quad (2)$$

Where design value of empirical factor $C_{Rd,c} = C_{Rk,c}/\gamma_C$ [MPa], with $C_{Rk,c} = 0.180$ MPa, ρ_l is reinforcement ratio [-] and f_{ck} is characteristic compressive strength of concrete [MPa].

German group proposed amendment of EC2 model. The model, released in January 2016 (*Hegger, Siburg, Kueres*), (model "B") is based on the similar formula with current EC2 model, see (3), where basic control perimeter u_1 has been moved closer to the column, at distance 0.5d from the edge of loaded area:

$$v_{Rd,c} = C_{Rd,c}*k_d*\ k_\lambda*(100*\rho_l*f_{ck})^{1/3}\ \text{[MPa]} \qquad (3)$$

Moreover, new factors were calibrated taking into account influence of shear slenderness and dimension of column periphery by coefficient $k_\lambda = [(a_\lambda/d)*(u_0/d)]^{-1/5}$, where a_λ is the distance between the edge of the loaded area and the line of contra flexure, u_0 is the perimeter of the loaded area. Coefficient taking into account size has been updated by formula $k_d = 1/[1+(d/200)]^{1/2}$. Empirical factor $C_{Rk,c}$ has a new value of $C_{Rk,c} = 1.80$ MPa.

2.2.2 Model of Critical Shear Crack Theory (CSCT)

CSCT is mechanical model for assessment of punching resistance. The principles of the theory came out from the assumption of critical crack development at the vicinity of a column. Punching resistance is ensured by aggregates interlocking in the critical crack and by tensile strength of the concrete. Shear resistance $v_{Rd,c}$ then depends on friction in the critical crack which is directly influenced by the crack width and by the maximum aggregate size d_g . The crack width is proportional to the slab rotation (ψ) at the vicinity of a column.

$$v_{Rd,c} = k_\psi*\ \sqrt{f_{ck}}/\gamma_C \quad \text{[MPa]} \qquad (4)$$

According to MC2010/CSCT $\qquad k_\psi= 0.67/(1+0.6*k_{dg}*\ \psi*d) \leq 0.6 \qquad (5)$

According to EC2/CSCT $\qquad k_\psi= 0.7/(1+0.45*k_{dg}*\ \psi*d) \leq 0.6 \qquad (6)$

Where coefficient k_{gd} depends on the maximum aggregate side d_g, k_{dg}=32/(16+d_g) [mm].

Rotation of the slab ψ depends on several factors, mainly on strains in bending reinforcement crossing critical shear crack and on the shear slenderness r_s/d , where r_s is distance of zero radial bending moments with respect to support axis. The rotation can be calculated simply by assuming of steel yielding (7), level of approximation LoA I, e.g. for preliminary design, or by more precise procedure (8) LoA II and (9) LoAIII, where m_{Ed} is average design moment per unit length and m_{Rd} is bending resistance. Because all tests used for statistical evaluation have had concentric load, the m_{Ed} has been calculated by $m_{Ed} = V_{R,test}/8$.

$$\psi = 1.5*(r_s/d)*(f_{yd}/E_s) \qquad (7)$$

$$\psi = 1.5*(r_s/d)*(f_{yd}/E_s)*(m_{Ed}/m_{Rd})^{1.5} \qquad (8)$$

$$\psi = 1.2*(r_s/d)*(f_{yd}/E_s)*(m_{Ed}/m_{Rd})^{1.5} \qquad (9)$$

Together four different CSCT models were analyzed. The model "D" where k_ψ was determined by (5) and (7), model "E" using (5) and (8), model "F" using (5) and (9), and finally "G" with (6) and (9).

3. Statistical evaluation of the models for punching resistance

Statistical evaluation of the models for punching resistance without shear reinforcement has been carried out for six models with partial safety factor γ_c = 1,0. Cylinder strength of concrete f_{ck} introduced by authors of the experiments has been used. Control perimeters were assumed at distance 2d from the face of column for current EC2 model, h/2 for ČSN model, and d/2 for the other models. Main statistical variable in the evaluation was ratio $P_i = (V_{R,test}/V_{Rd,c})_i$, where "i" is number of a test, $V_{R,test}$ is a resistance obtained from an experimental test and $V_{Rd,c}$ (Q_{bu}) is punching resistance obtained from theoretical model. Only variables P_i which satisfy condition $0.5 < P_i < 2.0$ have been used in statistical evaluation. Mean value P_m was calculated using formula $P_m = (\Sigma P_i)/n$ where n is a number of assumed tests. Characteristic value was determined as 5% fractile for Gaussian distribution $P_{k,0.05} = P_m(1\text{-}1{,}645.V_p)$, where V_P is coefficient of variation $V_P = \sigma_P/P_m$ and σ_P is standard deviation $\sigma_{P2} = [\Sigma(P_i-P_m)^2]/(n-1)$. The target value of $P_{k,0.05}$ is 1.0 according to EN1990. However resistance models can be assumed reliable if $P_{k,0.05} > 0,85$, e.g. due to membrane forces which are present in real structures.

Tab. 1: Statistical evaluation of model safety

Models		Number of specimens [n]	Average value [P_m]	Variation coef. [V_p]	Characteristic value [$P_{k,0.05}$]
"A"	ČSN 731201	406	1.1219	0.2344	0.689
"B"	EC2 model	408	1.1679	0.2007	0.782
"C"	EC2 update 2016	389	1.1786	0.1614	0.866
"D"	MC2010 (LoA I)	127	1.6297	0.1607	1.199
"E"	MC 2010 (LoA II)	182	1.4109	0.2177	0.906
"F"	MC 2010 (LoA III)	192	1.3058	0.2130	0.848
"G"	CSCT/EC2	194	1.1213	0.1992	0.754

4. Conclusions

Technical committee CEN TC250/SC2/WG1/TG4 holds extensive discussions how to proceed with model for punching resistance in Eurocode 2 in connection with works on the second generation of Eurocodes. Based on our assessment the models with accepted level of reliability are German EC2 update (2016) and models that are based on CSCT theory from Model Code 2010. Current EC2 model "B" and model with EC2 format based on CSCT "G" does not have required safety. Opposite model "D" based on CSCT for level of approximation LoA I is pretty uneconomical and therefore does not suits much for standards. The best solution for Eurocode 2 represents empirical model "C" with $P_{k,0.05} = 0,87$ and physical model "F" with $P_{k,0.05} = 0,85$. The advantage of "C" model is similarity with current EC2 model, which is very convenient for engineers. However the model has some limitations in application for FRC, LWAC, members reinforced by FRP and for design of strengthening for punching. Physical models based on CSCT theory can be much simpler adapted for above mentioned issues.

Acknowledgement

This work was supported by the Slovak Research and Development Agency under the contract NO APVV-0442-12. Many thanks for providing us the database of experiments to Carsten Siburg and prof. Joseph Hegger from RWTH Aachen University.

References

Muttoni A., Fernández Ruiz M. (2008) Shear strength of members without transverse reinforcement as function of critical shear crack width, ACI Structural Journal, V. 105, No 2, 2008, pp. 163-172

Muttoni, A., Fernández Ruiz, M., (2012) The levels-of-approximation approach in MC 2010: applications to punching shear provisions, Structural Concrete, Ernst & Sohn, Germany, Vol. 13, No. 1, 2012, pp. 32-41

Hegger J., Häusler F., Ricker M.(2008) Critical review of the punching shear provisions according to Eurocode 2 (in German: Zur Durchstanzbemessung von Flachdecken nach Eurocode 2), Beton- und Stahlbetonbau, Vol. 103, No. 2, 2008, pp. 93-102

Siburg C., Hausler F., Hegger,J. (2012) Flat slab punching design according to German annex of Eurocode 2, Bauinginieur, Volum 87,May 2012, pp.216-225

EN1992-1-1 Design of Concrete Structures, Part 1-1 General Rules and Rules for Buildings, May 2004

Fédération Internationale du Béton (fib), Model Code 2010 - Final draft, Vol. 1, fédération internationale du béton, Bulletin 65, Lausanne, Switzerland, 2012, Vol. 2

ČSN 731201/86 Navrhovaní betónových konstrukci

22nd International Conference
ENGINEERING MECHANICS 2016
Svratka, Czech Republic, 9 – 12 May 2016

BRIDGE STRUCTURE LOADED BY TERRORIST CHARGE

D. Makovička[*], D. Makovička, Jr.[**]

Abstract: *During explosion of terrorist charge the structure is loaded by the blast wave. The charge mass of 100 kg TNT was situated firstly above the bridge floor and secondly under the bridge on the level of terrain in the vicinity of one its piers. The reinforced concrete continuous four span bridge beam of chamber sections, supported by thin square piers was used for the determination of the dynamic response of the whole structure. The dimensions and distribution of structure parts were modelled while respecting the structure geometry and its dimensions, in order to obtain the most precise model of the bridge's mass and stiffness. The calculated bridge response in time histories of displacements and angles of rotation of bridge parts are used for structure assessment.*

Keywords: Bridge, Explosive charge, Blast load, Dynamic analysis, Response assesment.

1. Introduction

Usually terroristic charge is located in vehicle on bridge or its proximity. After initiation and during resulting explosion of charge propagates blast wave, whose characteristics depend partly on size of explosive and on the spacing of charge from bridge surface. If come to explosion on roadway in vehicle, then parameters of blast load are effected by height of explosion above roadway and it is possible then this effect simplified interpolate among effect of surface or air burst comprehends at the bridge surface level, or at close vicinity above or near this surface. Propagating blast wave load the bridge surface below angle of incidence, given by the direction ray, connecting focus of explosion and immediate stand of loaded blast wave.

2. Bridge structure

The reinforced concrete bridge structure was used for the dynamic analysis of blast loading and bridge response. The bridge includes four long spans (30 m, 2×45 m, 30 m) with intermediate piers (12.25 m, 17.25 m, 15.25 m) and was made of concrete C 30/37. The computational model and its cross sections in the middle of spans and in supports are illustrated on Fig. 1. The dimensions and distribution of structure parts were modelled while respecting the structure geometry and its dimensions, in order to obtain the most precise model of the bridge's mass and stiffness. Besides bridge dead load, the mass of asphalt part of the roadway were included in the bridge mass.

The bridge was analyzed under blast load of the explosion 100 kg TNT above the mid span above the bridge floor in height 2 m or in the case of charge location under bridge in the vicinity of one its pier in height 2 m above terrain and in the distance 2 m from pier (Fig. 2).

The blast load exerted on bridge floor surface was considered as series of blast sequences (by equations 5 to 10) acting in the selected points of central part of the floor span (Fig. 2) and graduated in some zones in terms of intensity as well as the whole history action on the basis of the real overpressure and underpressure phase of blast wave – dynamic load histories, as a function of the impact wave velocity of propagation. The explosion load is usually burdened with a number of uncertainties, related to determining the amount of explosive medium, its location in relation to the loaded structure, and the conditions of surroundings (Makovička, 2008). These load effects were derived by the authors based on

[*] Assoc. Prof. Ing. Daniel Makovička, DSc.: CTU in Prague, Klokner Institute, CZ 166 08 Prague 6, Šolínova 7, Czech Republic, daniel.makovicka@cvut.cz

[**] Ing. Daniel Makovička: Static and Dynamic Consulting, CZ284 01 Kutná Hora, Šultysova 170/8, Czech Republic, d.makovicka@makovicka.cz

the experimental results of small charge explosions. They may be used for an engineering estimation of the probable blast loads. This methodology enables us to determine with sufficient accuracy the time course of the impacting shock wave and its interaction with the structure itself.

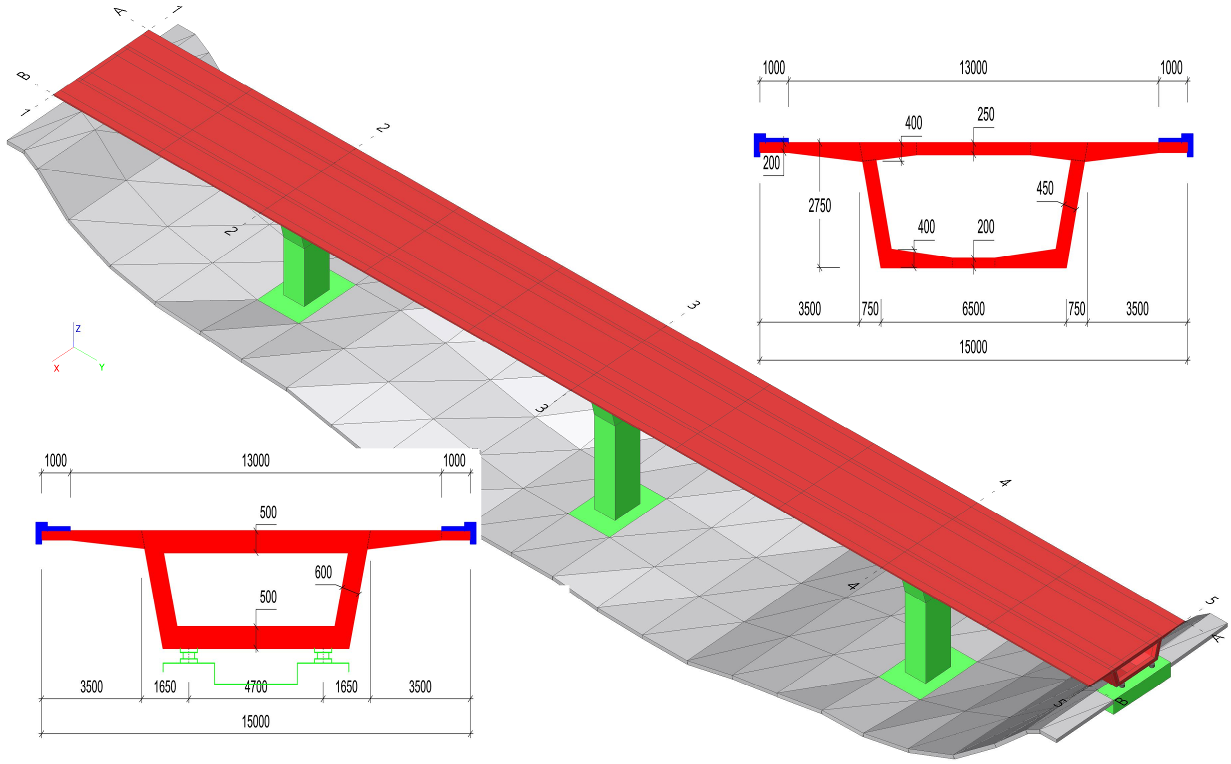

Fig. 1: Bridge structure.

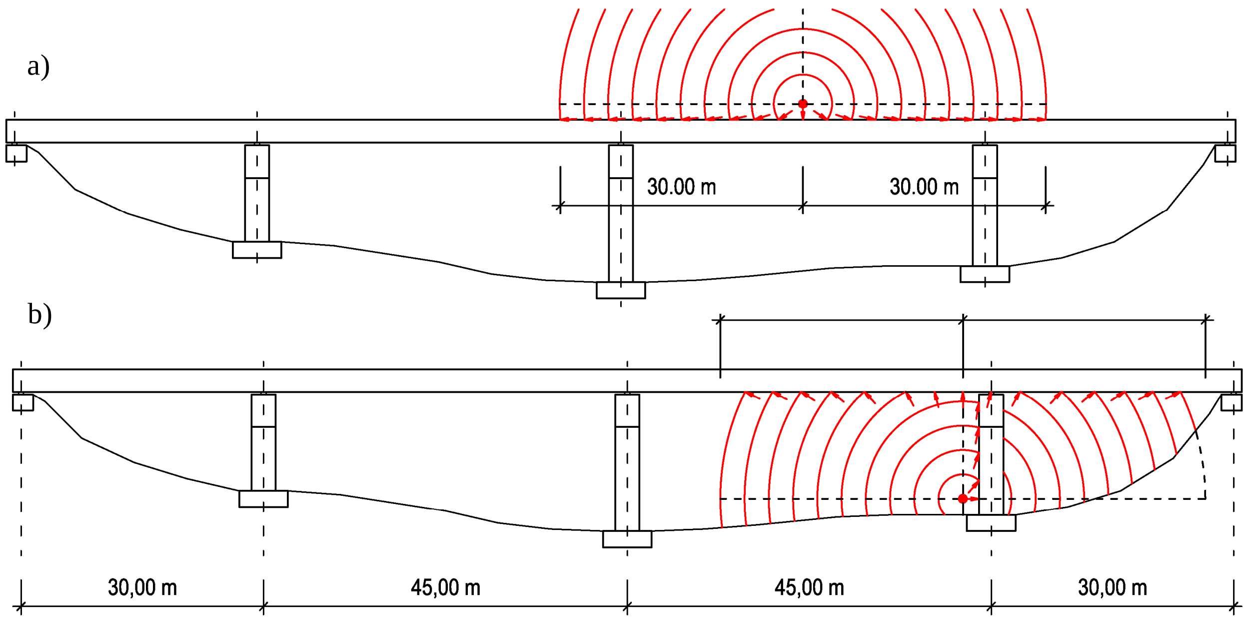

Fig. 2: Location of explosion, a) above the bridge, b) in the vicinity of pier.

3. Load history

The overpressure determined at the face of the air impact wave that spreads from the explosion site to the surroundings stems from the reduced distance (Makovička, 2014, 2015) is:

$$\overline{R} = R/\sqrt[3]{C_W} \tag{1}$$

where $\overline{R}$ is the reduced separation distance from the epicentre of the explosion [m/kg$^{1/3}$], R is the distance from the explosion epicentre [m], and C_W is the equivalent mass of the charge [kg TNT].

On the basis of comparing various resources in the literature (namely Makovička & Janovský, 2008, Ngo et al., 2007) and our own results of tests walls structures during explosions of small charges, the authors of this paper proposed the application of realistic formulas. Their resulting form corresponds to the impact wave effects from a small solid charge in an open air during this explosion. Maximum overpressure p_+ and underpressure p_- at the face of the air impact wave, velocity v of the wave face propagation and its durations τ_+ and τ_- are applicable both to ground and above-ground explosions:

$$p_+ = 1.07/\overline{R}^3 - 0.1 \text{ [MPa]} \quad \text{for } \overline{R} \le 1 \text{ m/kg}^{1/3} \quad \text{[MPa]} \qquad (2)$$

$$p_+ = 0.0932/\overline{R} + 0.383/\overline{R}^2 + 1.275/\overline{R}^3 \quad \text{for } 1 < \overline{R} \le 15 \text{ m/kg}^{1/3} \quad \text{[MPa]} \qquad (3)$$

$$p_- = 0.035/\overline{R} \quad \text{[MPa]} \qquad (4)$$

$$\tau_+ = 1.6 \cdot 10^{-3} \cdot \sqrt[6]{C_W} \cdot \sqrt{R} \quad \text{[s]} \qquad (5)$$

$$\tau_- = 1.6 \cdot 10^{-2} \cdot \sqrt[3]{C_W} \quad \text{[s]} \qquad (6)$$

$$v = 340 \cdot \sqrt{1 + 8.3 \cdot p_+} \quad \text{[m/s]} \qquad (7)$$

After a normal (perpendicular) impact of the explosion wave on a solid obstacle, a reflected wave is formed with the reflection overpressure p_{ref} that loads the building structure from the front side. The overpressure value in the reflected wave corresponds to approximately twice the value of the overpressure for low overpressure values p+ of approximately up to 5 MPa (up to eight times the value for high overpressures of the order of several MPa) in the incident wave.

$$p_{ref+} \approx 2\, p_+ \qquad (8)$$

$$p_{ref-} \approx 2\, p_- \qquad (9)$$

4. Bridge response

The decomposition of dynamic load history to the natural modes of vibration is used for the forced vibration analysis by means of Scia Engineer program. 100 lowest natural modes and frequencies of vibration in the interval 1.9 Hz to 21.6 Hz were considered in the computation. The damping of the structure of the building has been set as a damping ratio of 4 %. The calculation of forced vibration has been made with 1000 time steps of 0.0005 s. The dynamic analysis was made for linear elastic behaviour of the structure material. As an example of the bridge deformation, vertical displacements are shown in Fig. 3, and Fig. 4 presents angle of rotations.

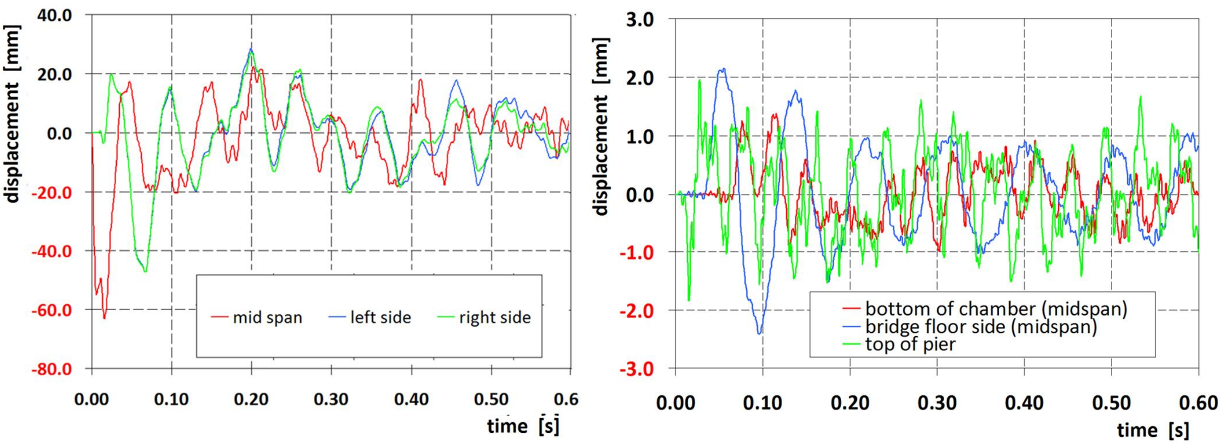

Fig. 3: Time histories of displacements U_z for above (at left) and under (at right) bridge explosion

The calculated rotations (angle ψ) of the middle surface of structural parts are used for structure assessment. The maximal angle of the rotation is 1.3 degrees round the both horizontal axes. The limit rotation for RC prestressed beam and plate structure for mean damages is 1 degree (Mc Cann, 2007; Makovička, 2008, 2015). It is clear that damages for above floor explosion are greater then the limit value. For the under bridge explosion the effects of explosion are much smaller. The bearing capacity of the whole bridge structure may in the case of above floor explosion be serious threatened.

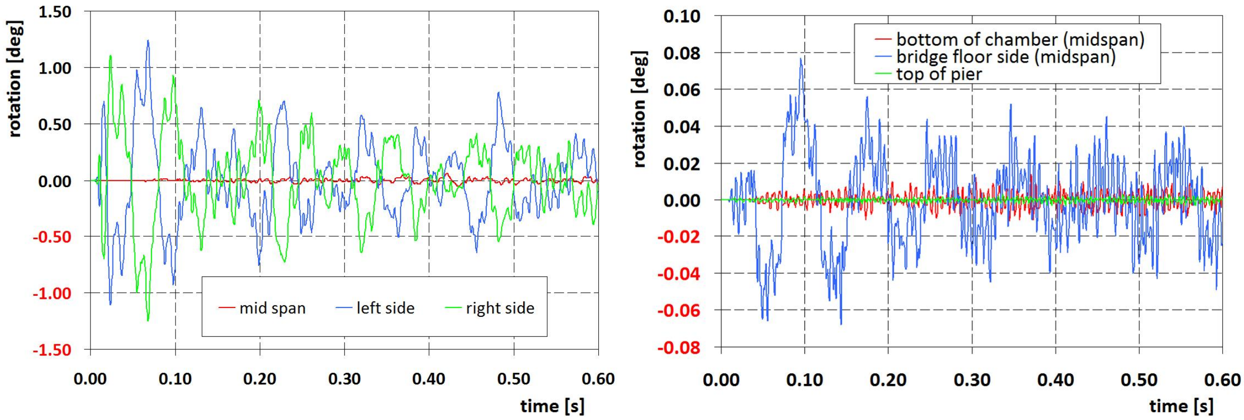

Fig. 4: Time histories of rotations F_y for above (at left) and under (at right) bridge explosion

5. CONCLUSIONS

Paper is determined to the problem of an explosion and the threat to the safety of the structure due to the explosion of an explosive charge installed in a car and initiated on the bridge or under bridge. The explosion load is usually burdened with a number of uncertainties, related to determining the amount of explosive medium, its location in relation to the loaded structure, and the conditions in the surroundings. These load effects were derived by the authors based on the experimental results of small charge explosions (Makovička. 2015). They may be used for an engineering estimation of the probable blast loads. This methodology enables us to determine with sufficient accuracy the time course of the impacting shock wave and its interaction with the structure itself.

The authors have used limit rotation values (angle of failure), as an efficient method for response assumption. Evaluating a structure on the basis of the limit rotation is a methodology under development at present, and is in accordance with recent research trends for structure loaded by blast wave of explosion. The results for the response of the bridge to this load are presented in parts, together with the principles for evaluating the structure according to the displacements and to the angle of failure corresponding to the given explosion load and its location.

Acknowledgement

There is very appreciated a kind sponsorship of the research project VG20122015089 supported by the Ministry of the Interior of the Czech Republic.

References

Makovička, D. & Makovička, D. (2015) Impact of outdoor blast wave on building structure, In: Krivanek, V.: ICMT'15, International Conference on Military Technologies 2015, May 19-21, Brno, Faculty of Military Technology, University of Defence in Brno, pp. 183-187.

Makovička, D. & Makovička, D. (2015) Structure response under blast wave load, In: Papadrakis, M. et al.: Compdyn 2015, May 25-27, Crete Island, ICMES, paper No: C1158.

Makovička, D. & Janovský, B. (2008) Handbook of Explosion Protection for Buildings (in Czech), Prague: CTU Publishing House.

Makovička, D. & Makovička, D. (2014) Blast resistant design of structure to terrorist explosion, Proceeding of EURODYN 2014, June 30 - July 2 July, Porto, pp. 3519-3524.

McCann, D. M. & Smith, S. J. (2007) Blast resistant design of reinforced concrete structures, STRUCTURE magazine, pp. 22-26.

Ngo, T., Mendis, P., Gupta, A. & Ramsey, J. (2007) Blast loading and blast effects on structures - An overwiev, EJSE Special Issue: Loading of structures, pp. 79-91.

22nd International Conference
ENGINEERING MECHANICS 2016
Svratka, Czech Republic, 9 – 12 May 2016

ESTIMATION OF ORTHOTROPIC MECHANICAL PROPERTIES OF HUMAN ALVEOLAR BONE

P. Marcián[*], P. Lošák[**], J. Kaiser[***], L. Borák[****]

Abstract: *In computational simulations of biomechanical problems, cancellous bone has often been modeled as a homogeneous, linear isotropic or orthotropic continuum. However, a need for higher modeling level is topical when it comes to simulations related to the dental implantology. The purpose of this study is to analyze cancellous bone specimens from alveolar bone, to estimate their apparent mechanical properties (assuming linear orthotropy) and to discuss their applicability in computational simulations of dental implantology problems. For this purpose, four cancellous bone segments from the first premolar region of human mandible were scanned on μCT device and subsequently analyzed using methods of biomechanical finite element simulations. In combination with the standard equations of mechanics of materials for calculating beam stiffness, nine independent elastic constants of linear orthotropic material model were determined for all analyzed segments. The results confirmed that the elastic constants are strongly dependent on the quality of the analyzed segment and its topology. It was concluded that this type of material model should be used only in cases where the stresses and strains in the bone itself are not of main concern. Otherwise, the information about the histomorphometry data should be inseparable part of each such model.*

Keywords: Bone, Mandible, FEM, micro-CT.

1. Introduction

Bone tissue is a complex living structure that undergoes a continual change of topology during the lifetime. The change of topology (known as a bone modeling or remodeling) is believed to be driven by a mechanical stimulus and a typical example of this phenomena is the gradual resorption of underloaded alveolar ridge in the mandible. The underloading is usually caused by the absence of tooth or teeth in this region and might be eliminated by a dental implant therapy. After the implant is placed into the bone, the surrounding tissue will be stimulated by the mechanical loading and the affected bone will start to remodel.

Dental implant therapy is an interdisciplinary task that includes not only medical treatment itself but also pre-medical planning and preparations, among others using methods of biomechanics. A powerful tool that can be used for development of dental implants, analysis of the treatment prospects or estimation of the dental implant performance is the computational simulation. Nowadays, the most frequent way of the computational simulation is based on the finite element method. This method itself became routine; however, the input data and some components of the computational models in biomechanics are still debatable, not fully established or even unknown. Widely discussed is the model of material of living tissues. For instance, the bone in the aforementioned example, and especially its cancellous part, has often been modeled as a homogeneous, linear and isotropic or orthotropic continuum. Such approach may be fully sufficient and justifiable in some cases; however, in case of simulations related to the dental

[*] Ing. Petr Marcián, PhD.: Institute of Solid Mechanics, Mechatronics and Biomechanics, Faculty of Mechanical Engineering, Brno University of Technology, Technická 2896/2, 616 69 Brno, Czech Republic; CZ, marcian@fme.vutbr.cz

[**] Ing. Petr Lošák, PhD.: Institute of Solid Mechanics, Mechatronics and Biomechanics, Faculty of Mechanical Engineering, Brno University of Technology, Technická 2896/2, 616 69 Brno, Czech Republic; CZ, losak@fme.vutbr.cz

[***] Prof. Jozef Kaiser, PhD.: Institute of Physical Engineering, Faculty of Mechanical Engineering, Brno University of Technology, Technická 2896/2, 616 69 Brno, Czech Republic; CZ, kaiser@fme.vutbr.cz

[****] Ing. Libor Borák, PhD.: Institute of Solid Mechanics, Mechatronics and Biomechanics, Faculty of Mechanical Engineering, Brno University of Technology, Technická 2896/2, 616 69 Brno, Czech Republic; CZ, liborborak@seznam.cz

implantology (e.g. including implant performance analyses, bone remodeling predictions etc.), the level of cancellous bone modeling is extremely important and using such simplifications might be inappropriate. Efforts to increase this level is evident and highly topical.

The aim of this study is to analyze mandibular cancellous bone specimens, estimate their apparent mechanical properties (assuming linear orthotropy) and discuss their applicability in the computational simulations of dental implantology problems.

2. Methods

Four cancellous bone segments from the first premolar regions of four human mandibles were subjected to the micro-computed tomography (μCT; GE vtomexL240 μCT device, General Electric, USA). The bone segments were selected to represent typical location for dental implant placements. The segments were of maximum possible cubic shape (5x5x5 mm) with the orientation as indicated in Figure 1.

The μCT images (voxel size of 20 μm) were first analyzed in Image J software (Schneider et al., 2012) using software extension Bone J (Dougherty et al., 2007) and basic histomorphometric parameters were obtained. Bone volume fraction (BVF), mean trabecular thickness (Tb.Th) and mean trabecular spacing (Tb.Sp) were adopted as representative characteristics of the segments. The images were further processed in STL Model Creator software (Marcián et al., 2011) to obtain 3D models of the segments (Fig. 2). The models were subsequently imported into the FEM software ANSYS 16.2. The models were meshed by quadratic tetrahedral elements SOLID187 with a general element size of 0.02 mm. At the micro level, the bone is assumed to be homogeneous, linear and isotropic with a typical values of Young's modulus (E) and Poisson's ratio (μ) of 15 GPa and 0.3, respectively (Shefelbine et al., 2005).

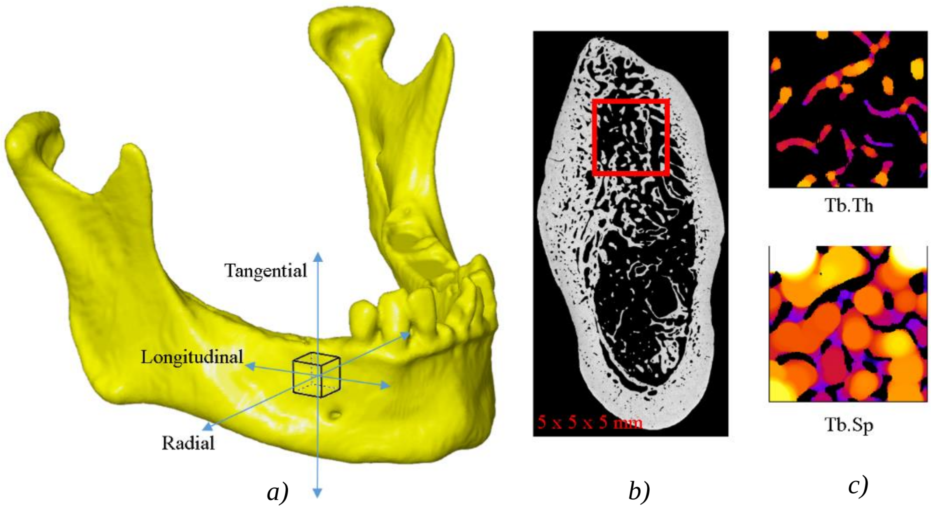

Fig. 1: Bone histomorphometry analysis: a) Segment position and orientation; b) μCT image of the mandible section with highlighted position of the segment; c) Typical image from the analysis in Image J.

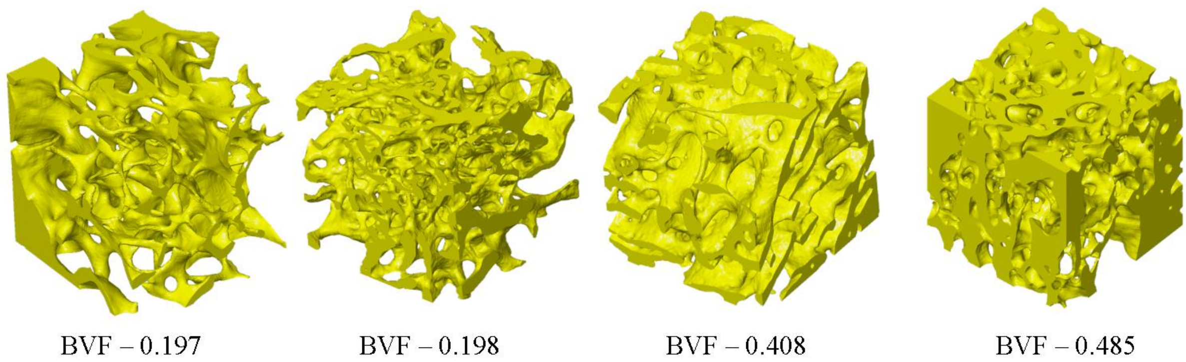

Fig. 2: Bone segment models created from the μCT images.

Nine independent elastic constants of the orthotropic material representing the apparent mechanical properties of each cancellous bone segment were estimated from six computational experiments: 1. Three tensile tests for the estimation of the Young's moduli and major Poisson's ratios (E_x, E_y, E_z, μ_{xy}, μ_{yz}, μ_{zx}); 2.

Three shear tests for the estimation of the shear moduli (G_{xy}, G_{yz}, G_{zx}). Each computational test was performed as indicated in Figure 3 and the elastic constants were calculated using Eq. (1) through (3). In those equations, F_i is a calculated reaction force [N], F_j is a loading force [N], u_i is a predefined displacement [mm], u_j is a calculated displacement [mm], l_i is the segment dimension [mm], S_i is the segment cross-section area [mm^2] and J_i is the segment second moment of area [mm^4]. Indices i and j represent directions x, y and z. As for the shear modulus and Poisson's ratio, index ij represent any combination of directions x, y and z. Therefore, G_{ij} is the shear modulus in direction j on the plane with the normal in direction i and μ_{ij} corresponds to the contraction in direction j when the extension is applied in direction i. Eq. (1) and (2) follow the classical mechanics of materials method for calculation of bar elongation and transverse contraction. Eq. (3) is derived from the formula for calculating the deflection of the Timoshenko cantilever beam. The shear coefficient κ_{ij} for the rectangular section is dependent on the Poisson's ratio and can be calculated using Timoshenko's expression (Eq. (4)).

$$E_i = \frac{F_i \cdot l_i}{S_i \cdot u_i} \qquad (1) \qquad \mu_{ij} = \frac{u_j \cdot E_i \cdot S_i}{l_i \cdot F_i} \qquad (2) \qquad G_{ij} = \frac{F_j \cdot l_i}{\kappa_{ij} \cdot S_i \cdot \left(u_j - \dfrac{F_j \cdot l_i^3}{3 \cdot E_i \cdot J_i} \right)} \qquad (3)$$

$$\kappa_{ij} = \frac{5 \cdot (1 + \mu_{ij})}{6 + 5 \cdot \mu_{ij}} \qquad (4) \qquad \frac{\mu_{ij}}{E_i} = \frac{\mu_{ji}}{E_j} \qquad (5)$$

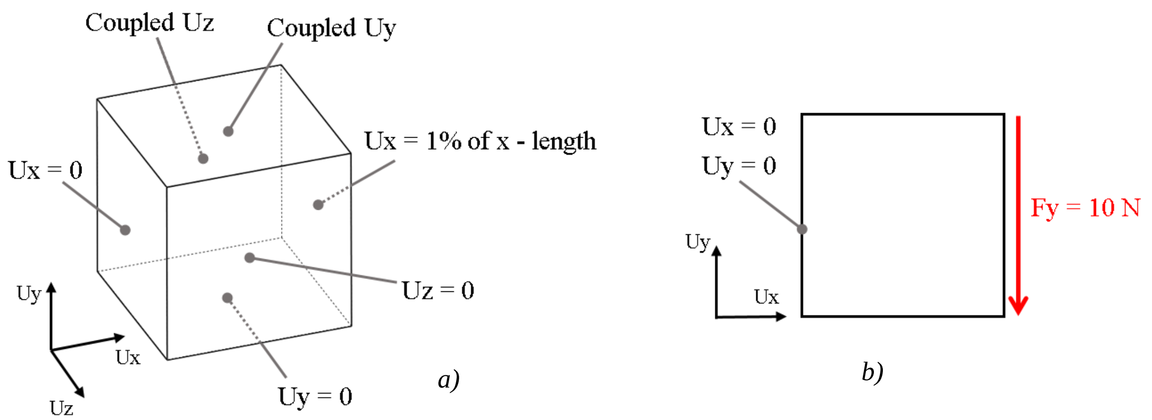

Fig. 3: Computational experiment setting: a) E_x and μ_{xy} calculation; b) G_{xy} calculation.

Prior the computational experiments on the cancellous bone segments, the methodology (especially the calculation of the shear moduli) were tested on the fully homogeneous cube with an acceptable accuracy (maximum error of 5%). To increase the credibility of the results, the minor Poisson's ratios (μ_{yx}, μ_{zy}, μ_{xz}) are also calculated and tested whether the relations in Eq. (5) is satisfied.

3. Results

Results of the histomorphometry analysis are shown in Figures 4. The Young's moduli, major Poisson's ratios and shear moduli for all bone segments are presented in Figures 5. The minor Poisson's ratios were checked using the expression in Eq. (5) and the calculated values differ from the theoretical ones by a maximum of 0.5 %.

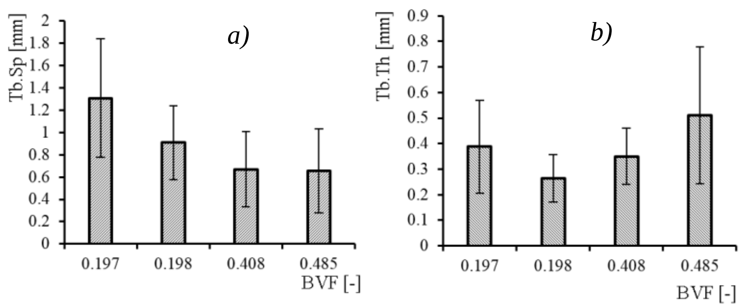

Fig. 4: Histomorphometry analysis results: a) Trabecular bone spacing; b) Trabecular bone spacing.

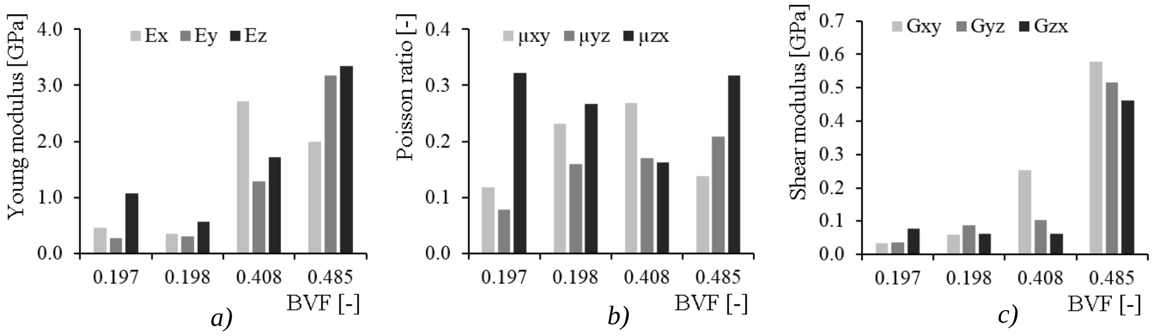

Fig. 5: Computational experiment results: a) Young's moduli E_i; b) Major Poisson's ratios μ_{ij}; c) Shear moduli G_{ij}.

4. Discussion

The calculated elastic constants are strongly dependent on the quality of the analyzed segment. The specific values are consistent with those presented in (van Eijden et al., 2006); however, authors of the referred paper studied different part of human mandible (mandibular condyle) and did not provide constants for bone in the vicinity of teeth. The results indicate that the higher the BVF, the higher the apparent Young's modulus. Alternatively, similar link might be seen between the apparent Young's modulus and Tb.Th. For the precise quantification of these relationships, much larger statistical data set would be required. This faces difficulties with suitable specimen acquisition. However, the variability of the results that depend on various histomorphometric parameters indicates that using homogeneous, linear and orthotropic material model in computational simulations related to mandibular cancellous bone might be extremely untrustworthy if the information about the histomorphometry data are not provided (and if they do not correspond with the actual bone under consideration). The segments were not analyzed for the principal material directions in this study; however, the necessity of having information about the principal material directions for the computational simulation using the orthotropy is obvious.

5. Conclusion

It is evident that using homogeneous, linear and orthotropic material model in the computational simulations related to cancellous bone is precarious and should be used only when the cancellous bone is not of the main concern. If the cancellous bone is analyzed for the effect of the interaction with dental implants, higher level of modeling is strongly advised to be adopted. Typical example of higher level in this case might be using detailed 3-dimensional model of the cancellous bone structure. Although this approach is more complex in terms of topology definition and much more computational time consuming, the results would be much more trustworthy than using simplified continuum. This approach is becoming powerful part of the patient-specific concept not only in biomechanics but in general.

Acknowledgement

The research was supported by the Czech Science Foundation by grant No. 16-08944S.

References

Dougherty, R. & Kunzelmann, K. (2007) Computing local thickness of 3D structures with ImageJ. Microscopy and Microanalysis, 13, pp. 1678-1679.

Marcián, P., Konečný, O., Borák, L., Valášek, J., Řehák, K., Krpalek, D. & Florian, Z. (2011) On the Level of Computational Models in Biomechanics Depending on Gained Data from Ct/Mri and Micro- Ct, in: MENDEL 2011 - 17th International Conference on Soft Computing. 1. Brno: Brno University of Technology, pp. 255-267.

Schneider, C.A., Rasband, W.S. & Eliceiri, K.W. (2012) "NIH Image to ImageJ: 25 years of image analysis". Nature Methods, 9, pp. 671-675.

Shefelbine, S.J., Simon, U., Claes, L., Gold, A., Gabet, Y., Bab, I., Müller, R. & Augat, P. (2005) Prediction of fracture callus mechanical properties using micro-CT images and voxel-based finite element analysis. Bone, 36, 3, pp. 480-488.

van Eijden, T. M., van der Helm, P. N. , van Ruijven, L. J. & Mulder, L. (2006) Structural and mechanical properties of mandibular condylar bone. Journal of Dentistry Research, 85, 1, pp. 33-37.

22nd International Conference
ENGINEERING MECHANICS 2016
Svratka, Czech Republic, 9 – 12 May 2016

WING TIP VORTEX RANS AND LES SIMULATION AND MEASUREMENT OF THE MEAN CHARACTERISTICS

J. Matějů*, P. Griffin**, J. O’Brien***, P. Zikmund****

Abstract: *LES, $RANS\ \ SST\ k-\omega$ and $uRANS-RST$ simulation of mean wing tip vortex characteristics at x/c = 6 position were compared to experiments. The wing tip vortex was generated by a wing at $AoA = 10\ deg$, $U_\infty = 34\ m \cdot s^{-1}$, $Re = 3.22 \times 10^5$. Star CCM+ CFD solver and a wind tunnel with a five hole probe located at University of Limerick were used. The study is an extension of Dr. O’Regan and Dr. Griffin research, O'Regan et al. (2014). Good results in the mean characteristics were achieved only by LES simulation. RANS simulation predicted faster dissipation of a tip vortex and didn’t capture a jet-like axial velocity in a vortex core position.*

Keywords: Wing tip vortex, RANS, LES, wind tunnel tests.

1. Introduction, physical description of a wing-tip vortex and literature review

A correct model of downstream tip vortex flow is important for modelling interaction of tip vortex with other object. The origin of the vortex is caused by a pressure difference between upper and down side of a wing. The pressure difference leads to a development of a crossflow velocity. Secondary effect is a development of an axial velocity. The vortex can be divided into three sub-regions, analogous to a turbulent boundary layer over solid walls fig. 1, Zheng & Ramaprian (1993). Region I is viscous core region, region II semi-logarithmic law region and region III defect law region.

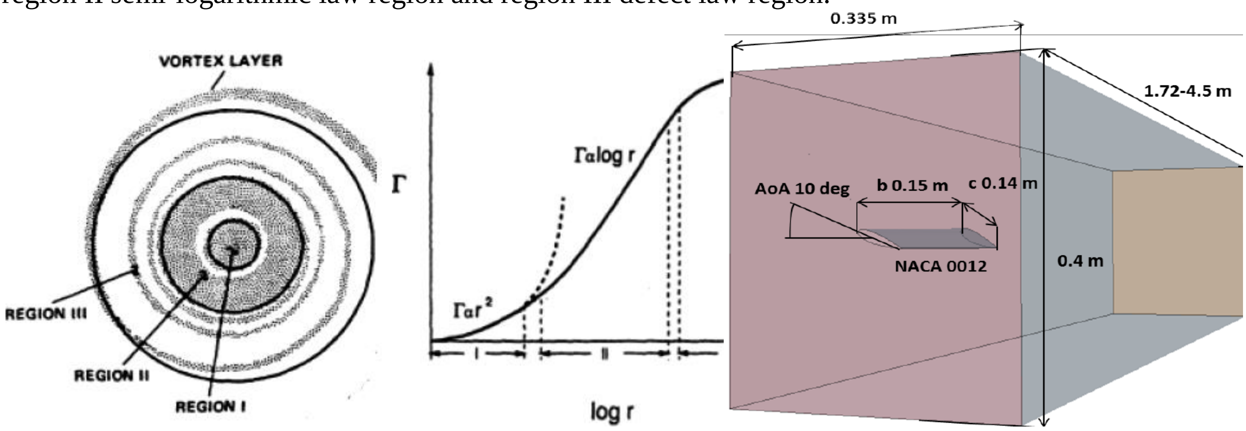

Fig. 1: Left and middle: The structure of the fully developed turbulent vortex Zheng & Ramaprian (1993), Right: Geometry of the wind tunnel and the wing

Results of comprehensive measurements and detail description of physical structure can be found in Chow et al. (1997) and Zheng & Ramaprian (1993). Experimental work was also done in Giuni, & Green (2013) and O'Regan et al. (2014). The tab. 1 shows the survey of performed CFD simulations. While some

* Ing. Jiří Matějů.: Institute of Aerospace Engineering, Brno University of Technology, Technická 2896/2; 616 69, Brno; CZ, mateju@lu.fme.vutbr.cz

** Dr. Phillip Griffin.: Department of Mechanical, Aeronautical and Biomedical Engineering, University of Limerick; National Technological Park, Limerick, IE, Philip.Griffin@ul.ie

*** B. E. Jeremiah O‘Brien.: Department of Mechanical, Aeronautical and Biomedical Engineering, University of Limerick; National Technological Park, Limerick, IE, Jerry.OBrien@ul.ie

**** Ing. Pavel Zikmund, Ph.D.: Institute of Aerospace Engineering, Brno University of Technology, Technická 2896/2; 616 69, Brno; CZ, zikmund@lfme.vutbr.cz

of RANS based models were able to capture mean characteristics, high turbulent structure of the tip vortex is possible to capture only by DES, LES or DNS models as can be found in the literature.

Tab. 1: CFD simulations of wing tip vortex. M - mean, T - turbulent characteristics

CFD Method	*Examined*	*Resource*
RANS-SA, SADM, SARC	*M*	*Nash'at et al. (2013)*
LES/ILES, RANS/URANS	*M, T*	*Jiang et al. (2007)*
RST and LES with VC	*M, T*	*O'Regan et al. (2014)*
RANS-SA, DDES	*M*	*Liang & Xue (2014)*
RANS linear EVM, nonlinear EVM, RST-TCL	*M, T*	*Craft et al. (2006)*
RANS - $k-\omega$, *DRSM, Hybrid RANS-LES*	*M, T*	*Kolomenskiy et al. (2014)*

2. Description of physical conditions, numerical simulations and experiments

International standard atmosphere conditions at 0 m ISA were used. Inlet velocity of $34\ \mathrm{m \cdot s^{-1}}$ was chosen as used at O'Regan et al. (2014) work. Free stream turbulent intensity of 0.5 % was measured in the wind tunnel. The geometry is described in the fig. 1 right. A coordinate system orientation is depicted in the fig. 2 left.

Four different meshes were used for a sensitivity study (tab. 2). Surface mesh was modified by Remesher and Wrapper and refined on the wing edges. A volume mesh was generated by Polyhedral mesher and Optimizer.

Tab. 2: Mesh description (TS – target size, PL – number of prism layers)

$Mesh$	$Coarser$	$Average$	$Finer$	$Very\ Fine$
$No.of\ elements$	$2.86 \cdot 10^6$	$4{,}8 \cdot 10^6$	$7 \cdot 10^6$	$10 \cdot 10^6$
$Volumetric\ Control\ TS\ (mm)$	2.8	2.1	1.82	1.68
$TS\ (tunnel/wing)(mm)$	35/1.4	14/2.8	11/1.82	17/1.4
$PL\ (tunnel/wing)$	5/10	0/0	0/4	5/10

Three different CFD turbulent models were tested in Star CCM+ software CD-Adapco (2014); $RANS\ SST\ k-\omega$, $uRANS-RST$ with 0.001 s time step and LES with $10^{-4}\ s$ time step. All the models were used with Vorticity Confinement, All Y+ treatment, constant density gas fluid, segregated flow model and implicit solver.

An open wind tunnel with a closed test section 1 x 0.335 x 0.4 m was used for measurements. Mean characteristics were measured by a five hole probe. Each position was measured for 10 s with a frequency of 1000 Hz on coarse grid (80x80 mm, step 6 mm) and fine grid (40x40 mm, step 2 mm) (fig. 2, middle).

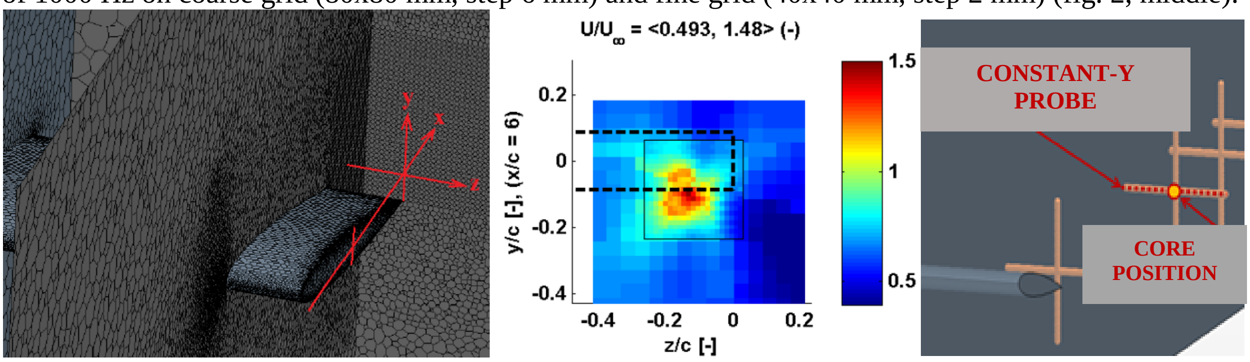

Fig. 2: Left: mesh and coordinate system, Middle: Coarseness of measurement (Normalized axial velocity), Right: Constant y probe position

3. Results

Mean velocity characteristics are evaluated at constant y probe placed at the core position (fig. 2 right). The position of the core is well captured by the all tested models. The fig. 3 left shows a V-component of the normalized velocity at the constant y probe for different turbulent models. The value of the peak V-velocity at the border of the vortex, determined from LES simulation, corresponds to measurements as well as the velocity gradient in the core. RANS based methods predict more than twice lower peak value. The V-velocity decreases faster outside of the core (in defect law region) in comparison to measurement. The fig. 3 right shows deformation of the vortex core, which is caused probably by wall interference. CFD simulations did not capture the core deformation. Reason can be coarse mesh between volumetric control and the tunnel walls.

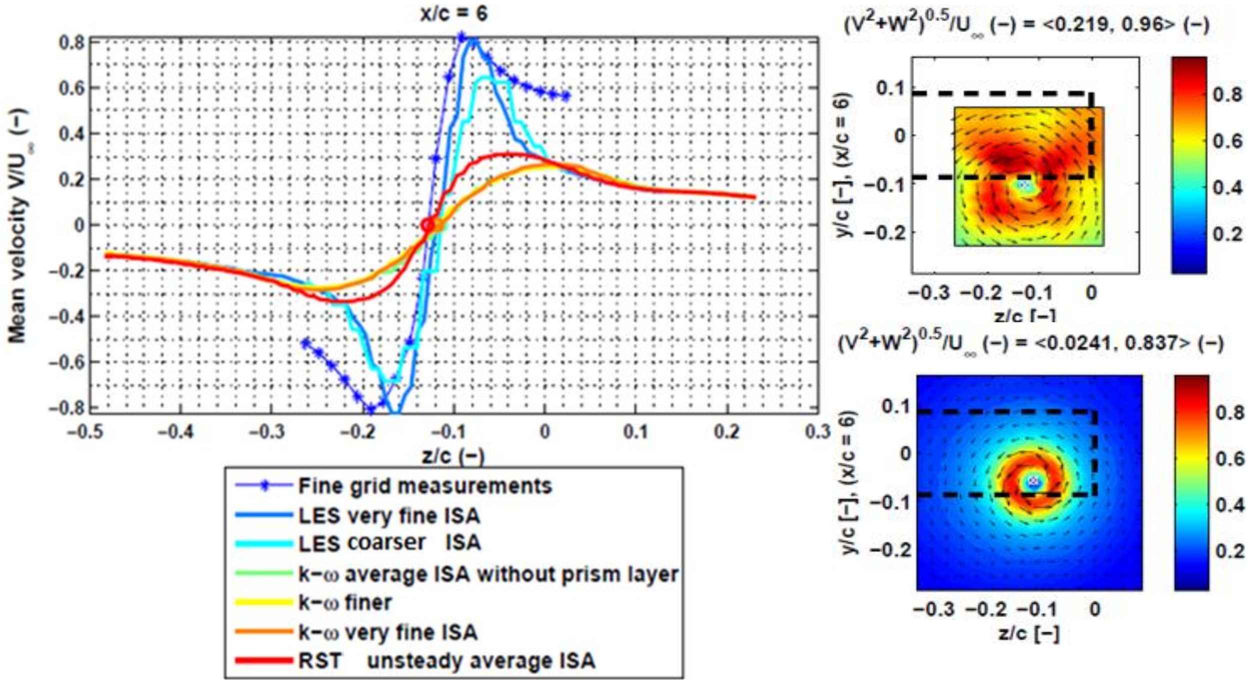

Fig. 3: Left: Different turbulent models and measurement comparison on a V-velocity. Right up: The measured mean crossflow velocity, Right down: LES simulation of the mean crossflow velocity.

The sensitivity study of a normalized mean axial velocity in different models of turbulence and comparison to the measurement can be seen in the fig. 4 left. A Jet-like axial velocity up to 1.5 U_∞ in the core is evident in the measurement. RANS based models do not capture it. The Jet-like velocity is evident also in LES, but not as high as in the measurement. CFD simulation didn't capture a gradient of the axial velocity in a defect law region outside the vortex core. Fig. 4 (right up) shows measured axial velocity, fig. 4 (right down) shows LES axial velocity. LES simulation has potential to capture the jet-like axial velocity profile. Using finer mesh and longer physical time than three seconds could improve the results.

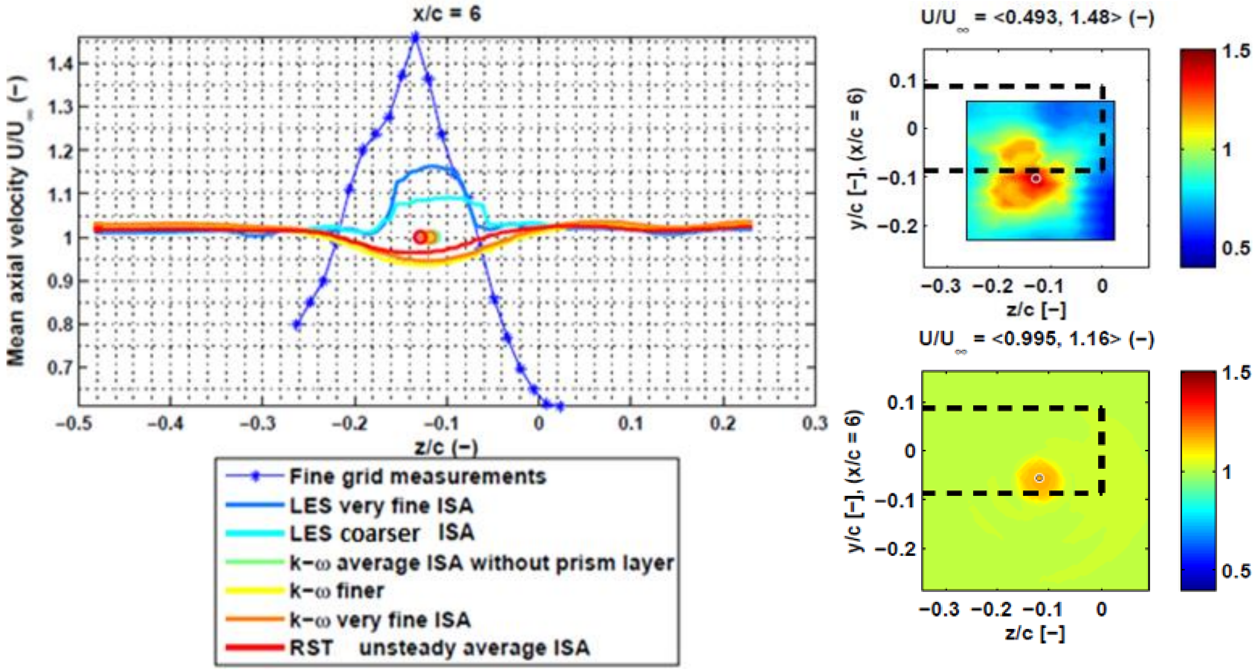

Fig. 4: Left: Different turbulent models and measurement comparison on a mean axial velocity. Right up: The measured mean axial velocity, Right down: LES simulation of the mean axial velocity.

4. Conclusion

The study shows different results of the mean characteristics obtained by using different methods. Reasonably good results of the mean characteristics were achieved by LES simulation, although the gradient of crossflow velocity with a core distance outside of the core boundary was much steeper and axial velocity didn't reach the measured peak axial velocity. RANS $k-\omega$ and RST models predicted a lower peak crossflow velocity and did not capture a jet-like axial velocity. Any CFD method didn't capture the core deformation. It can be caused by too coarse mesh between the tunnel walls and volumetric control. The core location was in the same position for the all methods and measurement. The turbulent characteristics simulation are presented in the extended version of this article.

References

CD-Adapco (2014) User Guide Star-CCM+ Version 9.02.

Chow, J., Zilliac, G. & Bradshaw, P. (1997) Turbulence Measurements in the Near Field of a Wingtip Vortex, NASA Technical Memorandum 110418.

Craft, T. J., Gerasimov A. V., Launder, B. E. & Robinson C. M. E. (2006), A computational study of the near-field generation and decay of wingtip vortices, International Journal of Heat and Fluid Flow, 27, 4, 684-695.

Giuni, M. & Green, R. B. (2013) Vortex formation on squared and rounded tip, Aerospace Science and Technology, 29, 1, 191-199.

Jiang, L., Cai, J. & Liu, C. (2007) Large-eddy simulation of wing tip vortex in the near field, Tech. rep., University of Texas.

Kolomenskiy, D., Paoli, R. & Boussuge, J. F. (2014) Hybrid RANS-LES simulation of wingtip vortex dynamics, 4th Joint US-European Fluids Engineering Division Summer Meeting and 12th International Conference on Nanochannels, Microchannels, and Minichannels, Chicago, Illinois, USA, ASME, 11.

Liang, Z. C. & Xue, L. P. (2014) Detached-eddy simulation of wing-tip vortex in the near field of NACA 0015 airfoil, Journal of Hydrodynamics, Ser. B, 26, 2, 199-206.

Nash'at, N. A. Proctor, F. H. & Perry, R. B. (2013) Numerical Simulation of the Aircraft Wake Vortex Flowfield, 5th AIAA Atmospheric and Space Environments Conference, American Institute of Aeronautics and Astronautics.

O'Regan, M. S., Griffin, P. C. & Young, T. M. (2014) Numerical and experimental investigation of the mean and turbulent characteristics of a wing-tip vortex in the near field, Proceedings of the Institution of Mechanical Engineers Part G: Journal of Aerospace Engineering, 228, 13, 2516-2529.

O'Regan, M. S., Griffin, P. C. & T. M. Young. (2014): A Vorticity Confinement Model Applied to URANS and LES Simulations of a Wing-tip vortex in the Near-field, unpublished.

Zheng, Y. & Ramaprian, B. R. (1993) An Experimental Study of Wing Tip Vortex in the Near Wake of Rectangular Wing.

Abbreviations

LES, ILES	Large Eddy Simulation, Implicit LES	EVM	Eddy-viscosity model
DES, DDES	Dettached Eddy simulation, Delayed DES	TCL	two-component limit
DNS	Direct numerical simulation	$k-\omega$	$k-\omega$ turbulent model
ISA	International standard atmosphere	SST	Menter's Shear Stress Transport
uRANS	unsteady RANS	RST	Reynolds stress transport model
SA	Spallart - Allmaras	SGS	Subgrid-scale model
SADM	SA with Dacles-Mariani correction	WALE	Wall-Adapting-Local-Eddy-Viscosity
SARC	SA with Splart-Shur correction	BUT	Brno University of Technology
VC	Vorticity confinement or Volumetric control	AoA	Angle of Attack

Nomenclature

Description	Symbol	Normalization
$Mean\ streamwise(axial)\ velocity$	U	$/U_\infty$
$Mean\ crossflow\ velocity$	$\sqrt{V^2+W^2}$	$/U_\infty$
$Position$	x, y, z	$/c$

22nd International Conference
ENGINEERING MECHANICS 2016
Svratka, Czech Republic, 9 – 12 May 2016

EXTREME VALUES CALCULATION OF MULTI-MODAL PEAK DISTRIBUTIONS

F. Mauro*, R. Nabergoj**

Abstract: *To search for the extreme value of a measured quantity from the peak analysis of a time series it is common practice in the field of offshore engineering to perform the analysis by means of a Weibull distribution. Usually the peaks distribution is quite well described by a common two or at most three parameters Weibull. However, when severe sea states are investigated or the analyzed structure presents particular geometries, the representation on the Weibull plane can be nonlinear, even adopting a three parameters distribution. In such a case the standard Weibull distributions are no more suitable to describe the peaks population, which presents a multi-modal form. To overcome this problem, the Mixed Weibull distribution was here used to describe the populations and a procedure based on genetic algorithms has been established to fit the parameters of the multi-modal function. Thereafter the extreme value predictions by the developed procedure have been compared with the one coming from standard Weibull analysis.*

Keywords: Mixed Weibull distribution, extreme values, genetic algorithm.

1. Introduction

In ship design and offshore applications, the extreme values of motions or loads acting on the ship/structure are needed, hence it is usual to perform model tests or numerical simulations. Analyzing the time traces of the quantities under investigation and considering all the peaks obtained by a zero mean extraction process, it results that the extreme values can be evaluated by fitting a Weibull distribution on the obtained population. For standard quantities the use of a simple two parameters or at most a three parameters Weibull distribution is satisfactory to describe the peaks population and then evaluate the values of the extremes. However, for particular cases, considering severe sea states or very large and complex structures, the adoption of the standard Weibull distribution can be no more satisfactory, maybe leading to an excessive over/under estimation of the extreme values needed for the design application. This problem arises when the peaks are distributed with a multi-modal trend. For this purpose, the Mixed Weibull distribution has been used to fit the peaks population of the loads on a ship structure. A procedure based on genetic algorithm has been developed to find the regression coefficients of the multi-modal distribution to perform automatically the extreme values analysis. Through this paper an overview of the newly implemented procedure is given and the results are compared with the one obtained from the standard Weibull analysis for a sample time record. Proper regression analysis has avoided a highly over dimensioned structure and, therefore, a substantial cost reduction.

2. Two-parameters Weibull distribution

The simplest case of Weibull distribution is the two parameter distribution with a probability density function (PDF) defined as follows:

$$p(x) = \frac{\beta}{\eta}\left(\frac{x}{\eta}\right)^{\beta-1} e^{-(x/\eta)^{\beta}} \qquad (1)$$

* Ir. Francesco Mauro: University of Trieste, Department of Engineering and Architecture, Via Valerio 10; 34100, Trieste; IT, fmauro@units.it

** Prof. Radoslav Nabergoj: University of Trieste, Department of Engineering and Architecture, Via Valerio 10; 34100, Trieste; IT, nabergoj@units.it

The cumulative density function (CDF) results in:

$$F(x) = \int_0^\infty p(x)dx = 1 - e^{-(x/\eta)^\beta} \tag{2}$$

where $\beta \in (0,+\infty)$ is the *shape parameter* and $\eta \in (0,+\infty)$ is the *scale parameter*.

The two parameters Weibull distribution has another property. By adopting a representation of the distribution in a particular Q-Q plot (Weibull plane) where *x* axis is represented by *ln x* and *y* axis by *ln(-ln(1-F(x)))*, the function can be linearized in the following way:

$$\begin{aligned} F(x) &= 1 - e^{-(x/\eta)^\beta} \\ \ln\left(-\left(\ln\left(1 - F(x)\right)\right)\right) &= \beta \ln x - \beta \ln \eta \end{aligned} \tag{3}$$

At the end the obtained regression equation is of the type $y=mx+q$. That means, by using this particular plot (Weibull plane), it is possible to fit the peak distribution of a sample data with a straight line.

3. Three parameters Weibull distribution

In some particular cases, the Weibull plot representation of the analyzed population does not properly follow a straight line, but the data follow a curve with a single convexity or concavity. Thus it is possible to reconstruct the 2 parameters case by adopting a simple change of variable. To do this it is necessary to introduce a third parameter γ called location parameter, and the PDF of the distribution assumes the following form:

$$p(x) = \frac{\beta}{\eta}\left(\frac{x-\gamma}{\eta}\right)^{\beta-1} e^{-\left(\frac{x-\gamma}{\eta}\right)^\beta} \tag{4}$$

Consequently the CDF of the distribution is similar to equation (2) just adding the location parameter in the exponential. It must be noted that the three parameters Weibull distribution is defined for $x > \gamma$ with no limitation in sign for the location parameter.

4. Mixed Weibull distribution

For particularly complicated systems, the sample data on the Weibull plane could be not only far away of a straight line fit, but could also present more than one convexity. In such a case the linear regression is no more sufficient to correctly describe the population even with the three parameters extension. This is the typical case of multi-modal responses, i.e. sample data could contain more than one population. To give a reliable description of the population, use can be made of the so-called Mixed Weibull distribution. This distribution is a combination of two or more standard Weibull distributions (with 2 or 3 parameters). Then the PDF and CDF assume the following forms:

$$p(x) = \sum_{i=1}^{N} p_i \frac{\beta_i}{\eta_i}\left(\frac{x-\gamma_i}{\eta_i}\right)^{\beta_i-1} e^{-\left(\frac{x-\gamma_i}{\eta_i}\right)^{\beta_i}} \tag{5}$$

$$F(x) = 1 - \sum_{i=1}^{N} p_i e^{-\left(\frac{x-\gamma_i}{\eta_i}\right)^{\beta_i}} \tag{6}$$

where N is the number of subpopulations and p_i is the percentile of the subpopulation in the total population ($\sum p_i = 1$). The other parameters are the same of the previously mentioned Weibull distributions. There are no limitations on the number of subpopulations, just the number of parameters increases. To give a rough example, to fit a 2 subpopulations Mixed Weibull using 3 parameters Weibull distributions, 7 parameters should be estimated, in case of 3 subpopulations the parameters became 12 and so on.

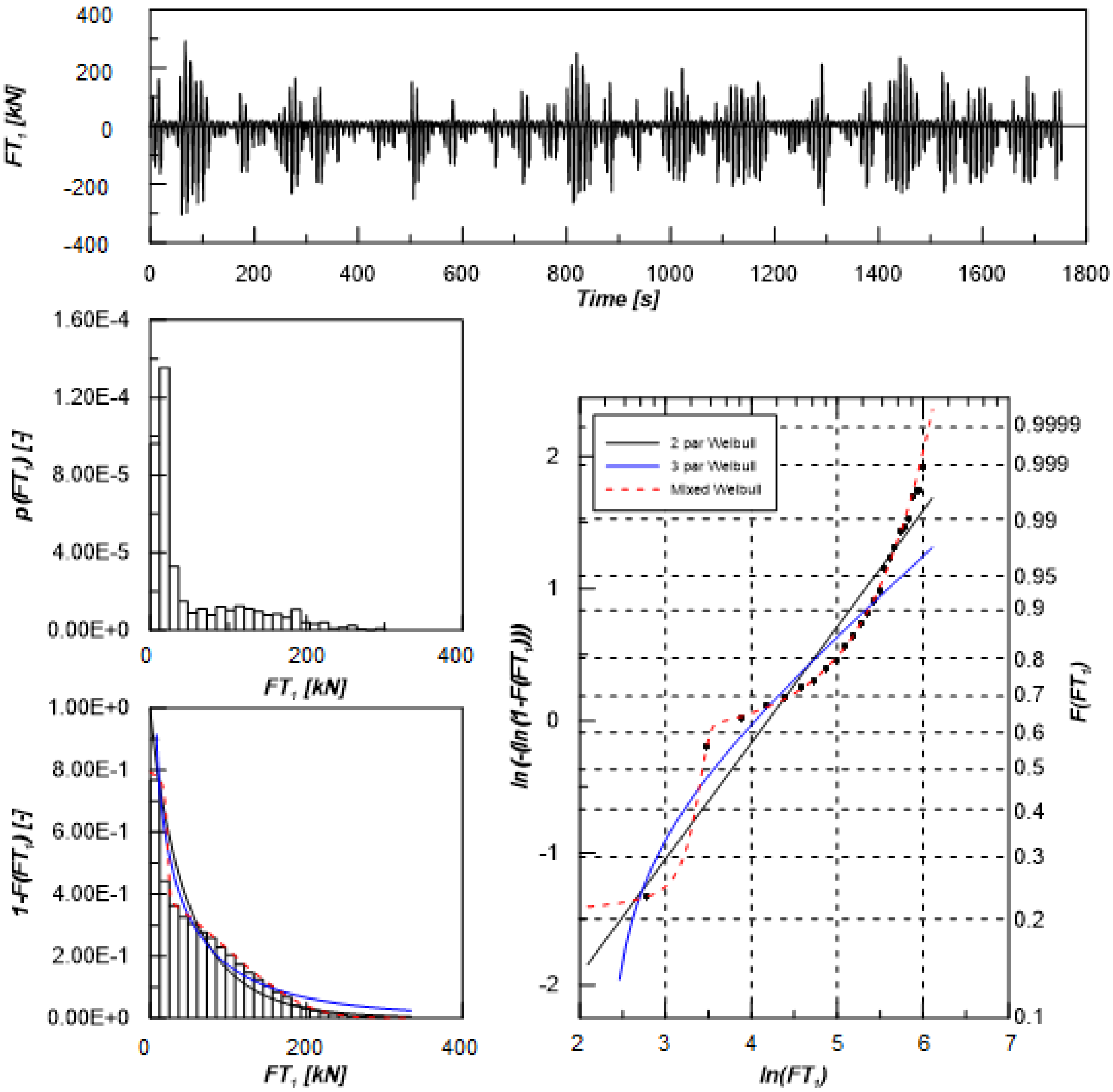

Fig. 1 Weibull data analysis

5. Parameters determination

To estimate the parameters of a Weibull distribution different methods can be adopted like least square fitting, method of moments, maximum likelihood and so on. All these methods have been implemented for the 2 parameters and thereafter extended for the 3 parameters distribution, but the scope of this work is not centered on the differences between the estimation methods. Due to the high number of unknowns, once the Mixed Weibull distribution should be analyzed, the above mentioned methods cannot be directly used, and it is a common practice to perform a 'manual fitting' of data. To build up an automatic procedure for the parameter estimation a general evolutionary algorithm has been here used, performing an extended version of the last square fitting method. The same estimation method has been used in this work also for the standard 2 and 3 parameters Weibull distribution as well.

6. Extreme values calculation

After the parameters determination process, the extreme values of the population can be predicted from the fitted distribution. Usually the values of interest are the events with the following probability *p*, i.e., 3%, 1% and 0.1%. To know these values, one should use the quantiles (inverse cumulative distribution) of the selected Weibull or Mixed Weibull distribution. For the different distributions the quantiles have the following forms, respectively:

$$Q(p,\eta,\beta)=\eta(-\ln(1-p))^{\frac{1}{\beta}} \tag{7}$$

$$Q(p,\gamma,\eta,\beta)=\gamma+\eta(-\ln(1-p))^{\frac{1}{\beta}} \tag{8}$$

$$Q(p,p_i,\gamma_i,\eta_i,\beta_i)=\sum_{i=1}^{N}p_i\left(\gamma_i+\eta_i(-\ln(1-p))^{\frac{1}{\beta_i}}\right) \tag{9}$$

which are representative of the 2, 3 parameters and Mixed Weibull distribution respectively.

7. Numerical example

To highlight the differences between the predictions of extreme values, different distributions have been used to analyze the time series of a generic structural load which was recorded during a seakeeping test of an offshore vessel in severe sea state conditions. Data shown in Figure 1 present clearly a bi-modal shape, and for this reason a 2 population Mixed Weibull distribution has been selected for fitting. The results of the time series analysis are presented in Table 1.

Tab. 1 Weibull analysis results

Regression Type	Force T1 [kN]		
	p 3%	p 1%	p 0.1%
2 parameters	281	376	580
3 parameters	296	465	921
Mixed	264	294	342

The standard 2 and 3 parameters regressions are estimating much higher extreme values than the Mixed Weibull distribution. Analyzing the Weibull plot in Figure 1 it can be noted that the standard regressions (2 and 3 parameters Weibull) are not fitting well the data points for large force values. This fact is generating a huge overestimate of the extremes.

8. Conclusions

The Mixed Weibull distribution is reproducing well the behavior of a multi modal population and therefore is suitable to perform an accurate prediction of the extreme values of load responses. The parameters determination procedure based on a genetic algorithm allows to perform quickly and automatically the parameters computation to be used for fitting the population distribution. Further study must be carried out to determine the regression technique sensitivity with the sample interval.

References

Hahn, G.J. & Samuel, S.S. (1967). Statistical Models in Engineering. John Wiley & Sons, New York.

Lawless, J.F. (1982). Statistical Models and Methods for Lifetime Data. John Wiley & Sons, New York.

Weibull, W. (1951). A Statistical Distribution Function of Wide Applicability. Journal of Applied Mechanics, 18, pp 293-297.

22nd International Conference
ENGINEERING MECHANICS 2016
Svratka, Czech Republic, 9 – 12 May 2016

DYNAMIC ANALYSIS OF CNC MILLING MACHINE FRAME

A. Max*, M. Hynek**, L. Řehounek***

Abstract: *The aim of this paper is to discuss specific dynamic properties of the main frame of a particular CNC milling machine. Key issues of the preparation of a computational model using the process of FE model including assessment of the loading forces, as well as the results of modal and harmonic response analyses are presented here. Recommendations for setting up the operating conditions are in included in the summary.*

Keywords: CNC, Milling machine frame, dynamic analysis, modal analysis, harmonic analysis.

1. Introduction

Even though there is a continuous development of new technologies for the production of components, it can be stated that 'the machine tool has been, is and no doubt will be, a key factor in industrial and equipment evolution, and as such, improving man's quality of life' (López De Lacalle & Lamikiz, 2009). Total engineering design of a CNC milling machining centre is a complex process and calculation, which should correspond to reality, and can be considered as art (Marek et al., 2014). Modern computational software and sufficient computer power mean that a computational model can be created that approaches reality. FEM models are most often used for these static and dynamic analyses, created based on pre-built CAD models.

2. Analysis of CNC milling machine frame

2.1. CAD and FEM model

From the complete CAD model of CNC milling machine (see Fig. 1), all major structural and connecting parts were used in the preparation of the computational FE model (see Fig. 1).

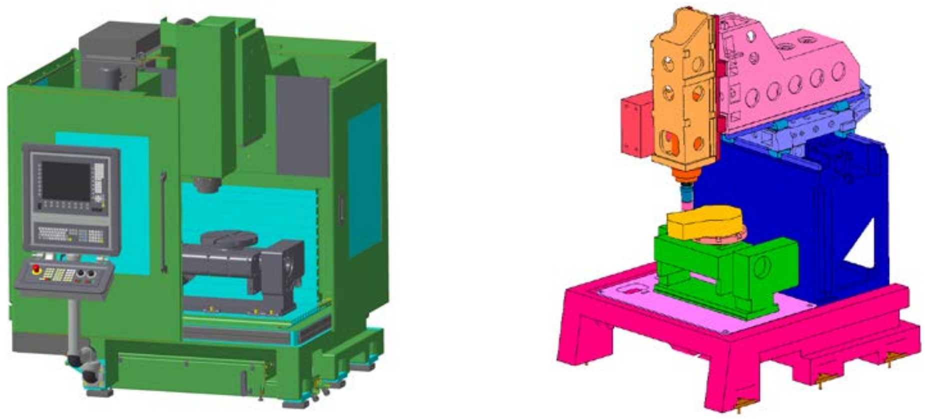

Fig. 1: Complete CAD model (left), simplified FE model for numerical calculation (right)

* Ing. Antonín Max.: Department of Machine Design, Faculty of Mechanical Engineering, University of West Bohemia, Univerzitni 22; 306 14, Pilsen; CZ, antoon@kks.zcu.cz

** Doc. Ing. Martin Hynek, Ph.D.: Department of Machine Design, Faculty of Mechanical Engineering, University of West Bohemia, Univerzitni 22; 306 14, Pilsen; CZ, kynek@kks.zcu.cz

*** Ing. Luboš Řehounek, Ph.D.: Department of Physics, Faculty of Science, University of Hradec Králové, Rokitanského 62; 500 03, Hradec Králové; CZ, lubos.rehounek@uhk.cz

Because of the complexity of the frame’s structural design, a FE model was created by combining structured and unstructured mesh (elaborately shaped castings with large changes of thickness were meshed by unstructured elements; rotationally symmetrical parts, plates and linear guides were meshed by structured elements).

Mutual connections of neighboring parts have been accomplished with merging properly selected nodes and by introducing rigid connection (e.g. in case of substitution of screw mountings, see Fig. 2) or by incorporating of linear springs between corresponding pairs of nodes (this was the case of motion screws and the connections between the carriages and the linear guide rails, see Fig. 2).

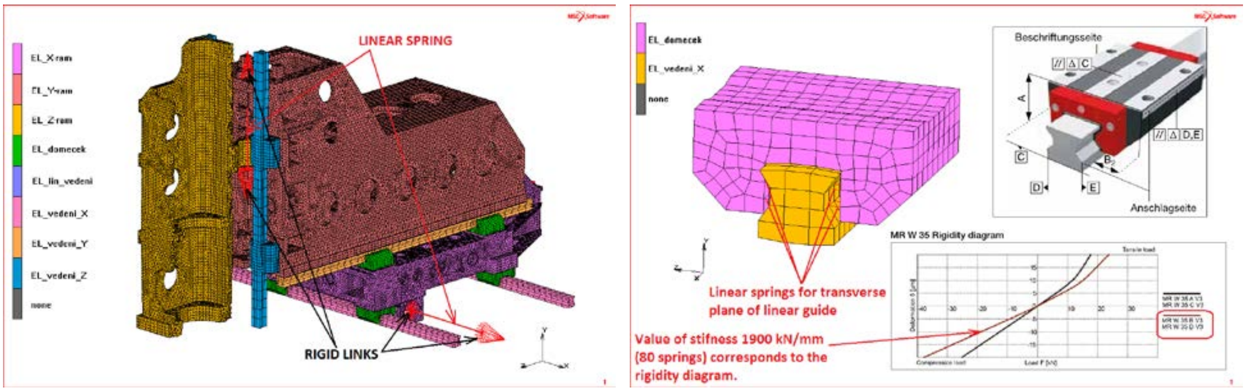

Fig. 2: Replacements of ball screws (right) and definition of linear guide (left)

An overview of the operating parameters and load parameters for tool load according to recommended cutting conditions for steel HB 90-200 are listed in Tab.1. Based on the analysis of the geometry and operating conditions of the load condition (see Tab. 1) it is apparent, that during one revolution of the tool the number of teeth in engagement varies from 2 to 3. From these parameters it case be deduced that is necessary to focus on eigenfrequencies in the range 130-200Hz.

Tab. 1: Operating parameters and load parameters for the tool

Description	***Value***	**Description**	***Value***
Tool diameter D *[mm]*	63	Cutting resistance of steel k_c *[N.mm-2]*	*1700*
Number of cutting edges *[-]*	6	Spindle power P_c *[kW]*	*8.5*
Cutting rate v_c *[m.min-1]*	330	Spindle torque M_L *[N.m]*	*48.7*
Cutting width a_e *[mm]*	50		
Cutting depth a_p *[mm]*	4	Focused circumferential force F_O *[N]*	*1546*
Spindle speeds n *[min-1]*	1667	Axial force F_A *[N]*	*928*
Feed per rev f_n *[mm]*	0.90	Radial force F_R *[N]*	*1237*

At the first step, modal analysis was conducted in order to assess dynamic properties of the frame (see Fig. 4 and 5). Subsequently, several harmonic response analyses were prepared with amplitudes of the loading forces specified according to operating conditions of individual machine tools and the resulting displacements were evaluated in three specific nodes (see Fig.3). Frequency response diagrams are shown in Fig. 6, deformed shapes of the harmonically excited frames in Fig. 7 and 8.

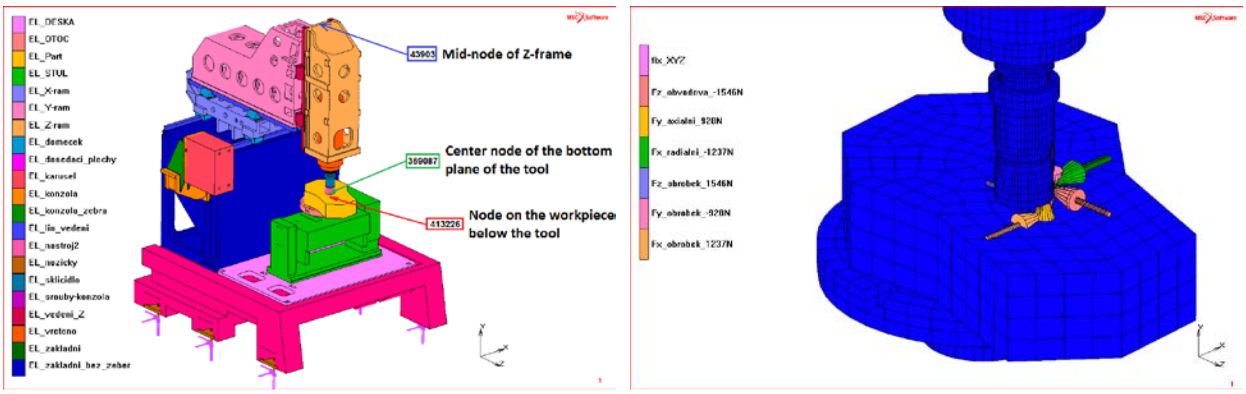

Fig. 3: Location of the nodes (left), Position of load conditions (right)

2.2. Modal analysis results

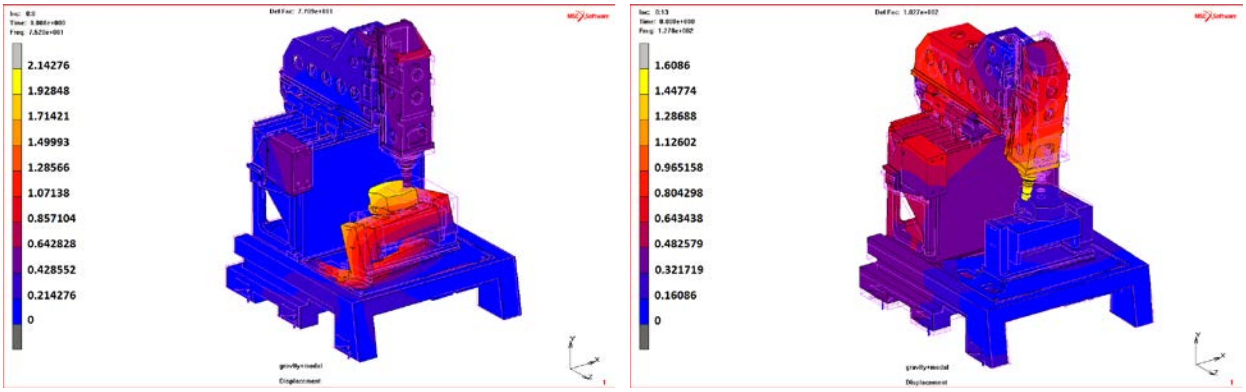

Fig. 4: Displacement of the frame for eigenfrequency: n.8, 75.2Hz (left) and n.13, 127,8Hz (right)

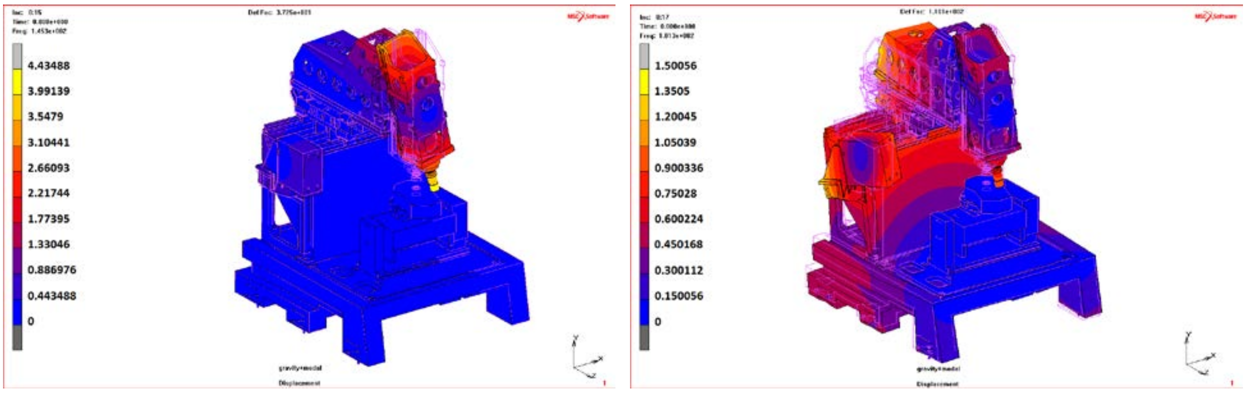

Fig. 5: Displacement of the frame for eigenfrequency: n.15 145.3Hz (left); n.17, 181,3Hz (right)

2.3. Harmonic analysis results

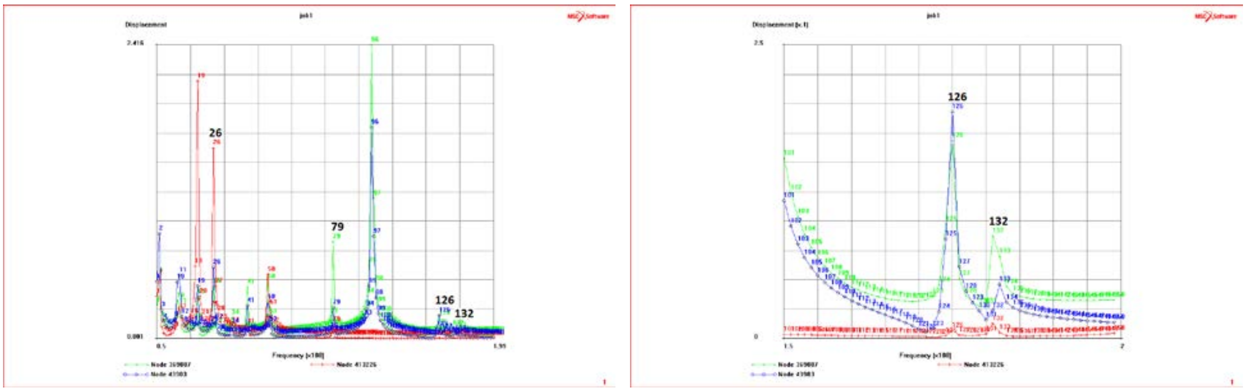

Fig. 6: Diagram of dependence of displacement for selected nodes and the excitation frequency: the entire range (left) and frequency range 150 Hz - 200 Hz (right)

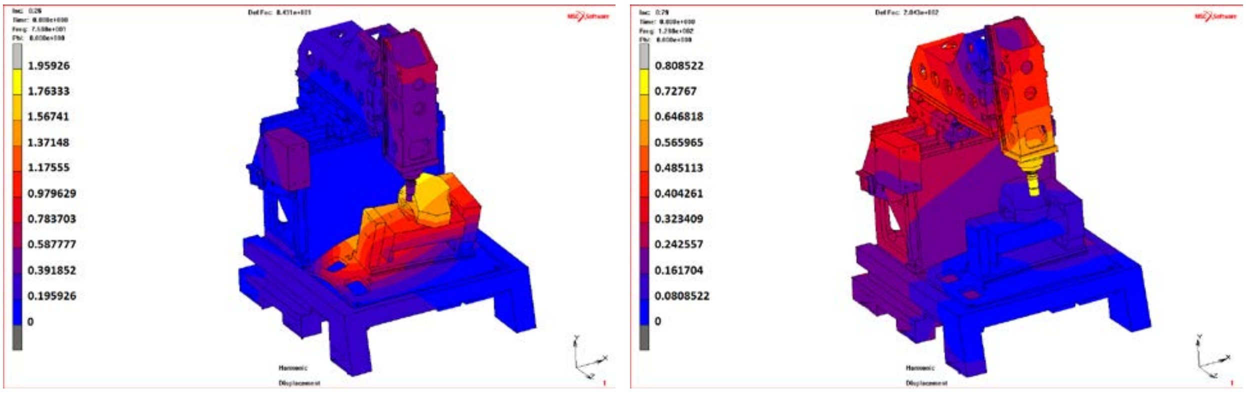

Fig. 7: Displacement caused by harmonic excitation: f=75Hz peak 26 (left); f=128Hz peak 79 (right)

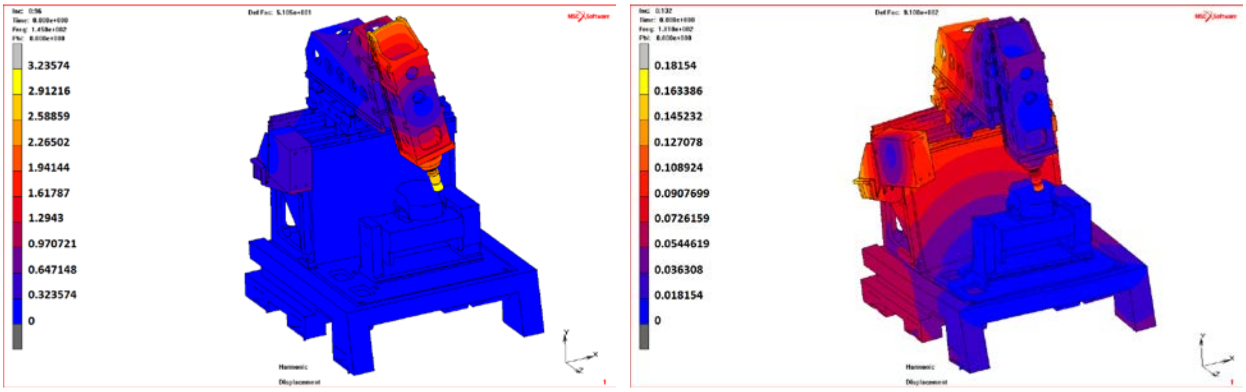

Fig. 8: Displacement caused by harmonic excitation: f=145Hz peak 96 (right); f=181Hz peak 132 (left)

2.4. Summary of results

Modal analysis showed that the eigenmodes occurring in the range of 50 - 200 Hz are reflected in the vibrations of the carousel with a workpiece (see Fig.4) and also in the mutual tilting and rotation of the individual parts of the frame (see Fig.4). Therefore, harmonic analysis was also performed. Comparison of peak frequencies from harmonic response analyses and eigenfrequencies from modal analysis, as well as the displacement amplitudes in specific nodes are shown in the Tab. 2.

Tab. 2: Summary of displacements of selected nodes

Excitation frequency [Hz]	*Displacement (harmonic analysis) [mm]*			*Closest eigenfrequency [Hz]*
	node 369087	*node 413226*	*node 43903*	
75	*0.432*	*1.571*	*0.590*	*75.2*
128	*0.798*	*0.119*	*0.257*	*127.8*
145	*2.416*	*0.011*	*1.741*	*145.3*
181	*0.088*	*0.013*	*0.024*	*184.3*

Based on the results it can be concluded that operating conditions for the tool specified in Tab.1 are not suitable for this particular frame structure of milling machine. It is advisable to choose tools with a higher number of teeth or increase the spindle speed within the recommended cutting conditions at least by 35%. This remedy should shift the main excitation frequencies above 200 Hz, i.e. to the range where eigenmodes do not include a resonance of main parts of the frame.

3. Conclusion

Even though there is a satisfactory agreement between the results of the modal analysis and the harmonic response analysis one should realize that without experimental verification the results of numerical simulations can hardly ever be taken for granted. The major source of the error in the application presented in this paper is probably the specification of the stiffness of the rail guides and the simplified representation of the ball screws and bearings. All contact conditions had to be substituted with either suitable linear springs or by simple node merging - without these simplifications both modal and harmonic response analyses could not have been conducted as they are both linear analyses.

Acknowledgement

This work was supported by the project SGS-2016-012 of the University of West Bohemia.

References

López De Lacalle, L. N. and Lamikiz, A. (2009) *Machine tools for high performance machining, Machine Tools for High Performance Machining,* Springer London.

Marek, J., Novotný, L., Březina, T., Blecha, P., Dobřický, J., Mrkvica, I., Sulitka, M., Dvořák, R., Král, M., Šooš, L., Učen, O. and Svoboda, J. (2014) *Konstrukce CNC obráběcích strojů III*, 3rd ed. MM Speciál.

22nd International Conference
ENGINEERING MECHANICS 2016
Svratka, Czech Republic, 9 – 12 May 2016

APPLICATION OF GENETIC ALGORITHM TO CONTROL THE AVAILABILITY OF TECHNICAL SYSTEMS

K. Migawa*, L. Knopik, S. Wawrzyniak*****

Abstract: *This study presents the problems connected with control of operation and technical objects maintenance systems. In particular, it discusses assessment and control of the availability of technical objects. In case of complex operation and maintenance systems, in order to control the availability it is essential to use the proper and effective methods and mathematical tools. The factors influencing the running and efficiency of the operation and maintenance process introduced in a complex system are of random nature. Most often the stochastic processes are used in mathematical modelling of the operation and in maintenance. In order to control the availability of technical systems, the following genetic algorithm was implemented on the basis of the semi-Markov model of operation and maintenance. Genetic algorithm may serve as a convenient tool to implement and facilitate the use of a complicated rational control decision making process in complex operation and maintenance systems. These include: systems operating machines, construction equipment, and means of transport. Due to its general character, the presented method may be implemented to solve a broad spectrum of optimization issues concerning the operation and maintenance systems. Among them are: controlling availability and reliability, analysis of costs and profits, and analysis of risk and safety.*

Keywords: Technical systems, Availability, Genetic algorithm.

1. Introduction

In actual complex operation and maintenance systems, the process of making control decisions should be implemented with the use of proper methods and mathematical tools. It should not be limited to the “intuitive” system based only on knowledge and experience of the decision-makers. Implementation of proper mathematical methods to control the process makes the choice of sensible decisions easier. Proper and effective implementation of the tasks ascribed to the system is thus provided.

Genetic algorithm may serve as a convenient tool. Its implementation facilitates the use of a complicated rational control decision making processes in a complex technical object operation and maintenance system (Goldberg, 2003).

2. Decisive model of availability control

The research paper presents an example of the implementation of control semi-Markov processes. They control availability in the operation and maintenance system for the means of transport. In order to implement them, a mathematical model of the operation and maintenance process was prepared on the basis of the event model of this process shown in figure 1.

* Assoc. Prof. Klaudiusz Migawa, PhD.: Faculty of Mechanical Engineering, UTP University of Science and Technology, Prof. S. Kaliskiego Street 7, 85-789 Bydgoszcz, Poland, klaudiusz.migawa@utp.edu.pl

** Assoc. Prof. Leszek Knopik, PhD.: Faculty of Management, UTP University of Science and Technology, Fordońska Street 430, 85-790 Bydgoszcz, Poland, knopikl@utp.edu.pl

*** Assist. Prof. Sylwester Wawrzyniak, PhD.: Faculty of Mechanical Engineering, UTP University of Science and Technology, Prof. S. Kaliskiego Street 7, 85-789 Bydgoszcz, Poland, sylwester.wawrzyniak@utp.edu.pl

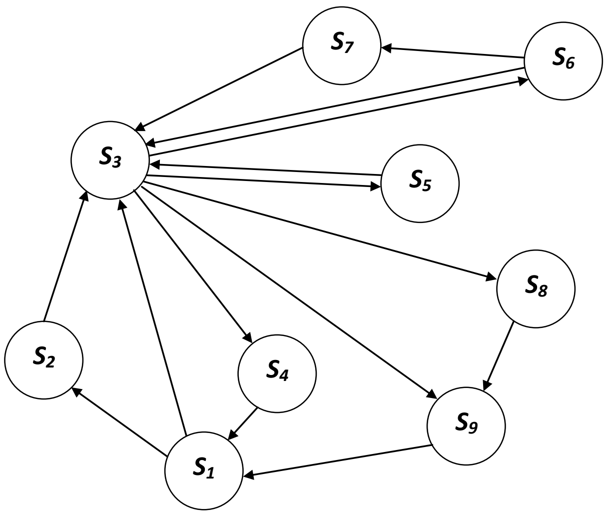

Fig. 1: Directed graph representing the transport means operation process

S_1 – refuelling, S_2 – awaiting the carrying out of the task at the bus depot parking space, S_3 – carrying out of the transport task, S_4 – awaiting the carrying out of the task between transport peak hours, S_5 – repair by technical support unit without losing a ride, S_6 – repair by the emergency service with losing a ride, S_7 – awaiting the start of task realization after technical support repair, S_8 – repair in the serviceability assurance subsystem, S_9 – maintenance check on the operation day

In order to assign the values of limit probabilities p_i^* of remaining in the states of semi-Markov model of operation and maintenance process, matrix $P = \lfloor p_{ij} \rfloor$ of the states change probabilities and matrix $\Theta = \left[\overline{\Theta}_{ij}\right]$ of conditional periods of duration of the states in process *X(t)* were created. Based on matrix *P* and matrix *Θ*, average values of non-conditional duration periods of process states $\overline{\Theta}_i, i = 1,2,...,9$ were defined.

Therefore, the limit probability p_i^* for remaining in the states of semi-Markov processes can be determined. It is based on the limit statement for the semi-Markov process (Grabski, 2014; Kulkarni 1995):

$$p_i^* = \lim_{t \to \infty} p_i(t) = \frac{\pi_i \cdot \overline{\Theta}_i}{\sum\limits_{i \in S} \pi_i \cdot \overline{\Theta}_i} \tag{1}$$

where probabilities $\pi_i, i \in S$ constitute the stationary layout of the implemented Markov's chain in the process *X(t)*.

Availability of an individual technical object is defined on the basis of the semi-Markovian model of operation and maintenance process. It is determined as the sum of limit probabilities p_i^* of remaining in the states belonging to the set of availability states $S_i \in S_G$:

$$G^{OT} = \sum_i p_i^* = \frac{p_{12} \cdot (p_{34} + p_{38} + p_{39}) \cdot \overline{\Theta}_2 + \overline{\Theta}_3 + p_{34} \cdot \overline{\Theta}_4 + p_{35} \cdot \overline{\Theta}_5 + p_{36} \cdot p_{67} \cdot \overline{\Theta}_7}{\left[(p_{34} + p_{38} + p_{39}) \cdot \left(\overline{\Theta}_1 + p_{12} \cdot \overline{\Theta}_2\right)\right] + \overline{\Theta}_3 + p_{34} \cdot \overline{\Theta}_4 + p_{35} \cdot \overline{\Theta}_5 + \left[p_{36} \cdot \left(\overline{\Theta}_6 + p_{67} \cdot \overline{\Theta}_7\right)\right] + p_{38} \cdot \overline{\Theta}_8 + (p_{38} + p_{39}) \cdot \overline{\Theta}_9} \tag{2}$$

The decisive semi-Markov process is a stochastic process $\{X(t): t \geq 0\}$. Its implementation depends on the decisions made at the beginning of the process t_0 and at the moments of changing the process t_1, t_2, …, t_n, … . In case of implementation of the decisive semi-Markov processes making the decision at the moment of t_n, *k*-controlling decision in *i*-state of the process means a choice of *i*-verse of the core of the matrix from the following set (Cao, 2003; Kashantov, 2010; Puterman, 1994):

$$\left\{Q_{ij}^{(k)}(t): t \geq 0,\ d_i^{(k)}(t_n) \in D_i,\ i, j \in S\right\} \tag{3}$$

where:

$$Q_{ij}^{(k)}(t) = p_{ij}^{(k)} \cdot F_{ij}^{(k)}(t) \tag{4}$$

The choice of the *i*-verse of the core of the process specifies the probabilistic mechanism of evolution of the process in the period of time ‹t_n, t_{n+1}). This means that for the semi-Markov process, in case of the change of the state of the process from one into *i*-one (entry to the *i*-state of the process) at the moment t_n, the decision $d_i^{(k)}(t_n) \in D_i$ is made. According to the schedule $\left(p_{ij}^{(k)} : j \in S\right)$, *j*-state of the process is generated. It is entered at the moment of t_{n+1}. At the same time, in accordance with the schedule specified by the distributor $F_{ij}^{(k)}(t)$, the length of the period of time is generated ‹t_n, t_{n+1}). It leaves the *i*-state of the process, when the next state is the *j*-state. Then, as the strategy we understand the δ sequence, where the words are the vectors. They comprise of the decision $d_i^{(k)}(t_n)$ made in the following moments of the t_n changes of the state of the process $X(t)$:

$$\delta = \left\{ \left[d_1^{(k)}(t_n), d_2^{(k)}(t_n), \ldots, d_9^{(k)}(t_n) \right] : \quad n = 0,1,2,\ldots \right\} \tag{5}$$

The choice of the proper control strategy δ is called the optimal strategy δ^*. It refers to the situation when the function being the criterion of the choice of the optimal strategy (e.g. availability of individual technical object) takes an extreme value. The choice of the optimal strategy δ^* is made on the basis of the following criterion:

$$G^{OT}\left(\delta^*\right) = \max_{\delta}\left[G^{OT}(\delta)\right] \tag{6}$$

The genetic algorithm is a convenient tool for choosing the optimal strategy δ^* of process control operation of technical objects. It is bases on developed semi-Markov model of the process. General scheme of choice of the optimal strategy using genetic algorithm is presented in Figure 2 (Vose, 1998).

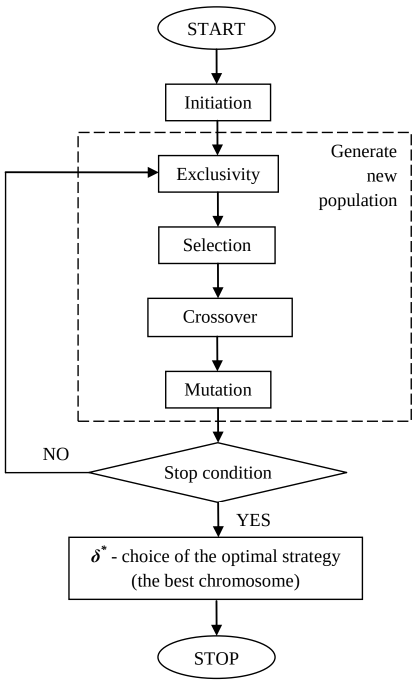

Fig. 2: General scheme of the genetic algorithm of choice of the optimal strategy δ^*

When using the genetic algorithm to determine the optimal strategy process control operation of technical objects, the following assumptions should be adopted:

–in each state one of the two ways of proceeding can be used (called the decision),

–if decisions are labelled 0 and 1, the set of stationary and deterministic strategies will be the set of function $\delta : S \to D$, where *S* is the set of states of the process, $S = \{1, 2, \ldots, m\}$ and *D* – is the set of decisions made in the state of the process, $D = \{0,1\}$;

This determines the possible control decisions in the state of the analyzed model of the process of operation of technical objects. It also estimates the value of the items of the kernel process *Q(t)* of the matrix *P* probabilities of transitions and the matrix Θ durations of the states of the process. For the analyzed model of transport means operation process, the values of genetic algorithm input parameters and possible decisions made in decision-making process states were determined (table 1).

Tab. 1: The control decisions in the states of the analyzed operation process

Process state	Decision „0" - $d_i^{(0)}$	Decision „1" - $d_i^{(1)}$
S_1	non decision-making process state	
S_2	non decision-making process state	
S_3	The route marked code L ('easy' conditions of delivery task)	The route marked code D ('difficult' conditions of delivery task)
S_4	non decision-making process state	
S_5	Treatment by a PT type B (basic range)	Treatment by a PT type E (extended range)
S_6	Treatment by a PT type B (basic range)	Treatment by a PT type E (extended range)
S_7	Non decision-making process state	
S_8	Treatment in positions PZZ type N (normal)	Treatment in positions PZZ type I (extensive)
S_9	Operate in positions OC type N (normal)	Operate in positions OC type I (extensive)

Next, calculations were made with the help of developed computer software. Genetic algorithm was implemented. As a result of the calculations performed, the optimal control strategy was determined in the tested system for the adopted criterion (6). Calculation results were presented in table 2.

Tab. 2: Availability function value, determined on the basis of genetic algorithm

Optimal strategy δ^*	$G^{OT}(\delta^*)$
[1,1,1,0,0,1,0,0,1]	0.8426

3. Conclusions

Due to its general character, the presented method can be implemented for solving a broad spectrum of optimization issues. They concern the operation and maintenance systems for the technical objects. Among them are the following: controlling availability and reliability, analysis of costs and profits, analysis of risk and safety etc.. In each case there is a necessity to form the definition of the criterion properly. It is also required to specify possible control decisions made in the states of the tested operation and maintenance process of the technical objects.

References

Cao, X.-R. (2003) Semi-Markov decision problems and performance sensitivity analysis. IEEE Transactions on Automatic Control, Vol. 48, No. 5.

Goldberg, D. E. (2003) Algorytmy genetyczne i ich zastosowanie. WNT, Warszawa.

Grabski, F. (2014) Semi-Markov processes: Applications in system reliability and maintenance. Elsevier, Amsterdam.

Kashtanov, V. A. (2010) Controlled semi-Markov processes in modeling of the reliability and redundancy maintenance of queuing systems, Applied Statistics and Operation Research, Vol. 14.

Kulkarni, V. G. (1995) Modeling and analysis of stochastic systems. Chapman & Hall, New York.

Puterman, M. L. (1994) Markov decision processes. John Wiley, New York.

Vose, M.D. (1998) The simple genetic algorithm. Foundations and theory. MIT Press, Cambridge.

22nd International Conference
ENGINEERING MECHANICS 2016
Svratka, Czech Republic, 9 – 12 May 2016

CENTRAL DIFFERENCE METHOD APPLIED FOR THE BEAM RESTED ON NONLINEAR FOUNDATION (PROGRAMMING AND EVALUATION OF RESULTS)

Š. Michenková*, K. Frydrýšek**

Abstract: *This work presents practical applications of experimental and numerical approaches in the solution of straight beams on elastic foundations. There are tangent-linear, nonlinear (i.e. linear + arcus tangent) and secant-linear approximations for dependencies of distributed reaction forces on deflection in the foundation. For solutions of nonlinear problems of mechanics, the Central Difference Method is applied in combination with the Newton Method. The results acquired by linear/nonlinear solutions are evaluated and compared.*

Keywords: Elastic foundation, Beam, Central difference, Nonlinearity, Programming.

1. Introduction

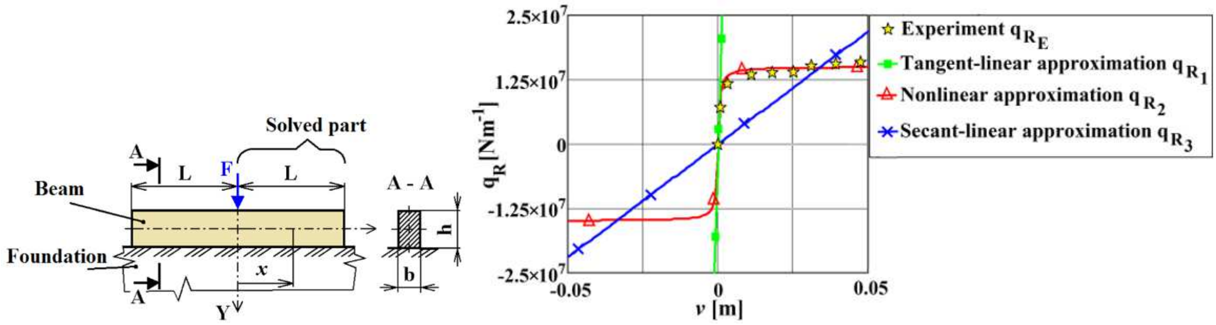

Fig. 1. Solved beam of length 2L resting on an elastic foundation and dependence of reaction force on deflection (i.e. foundation load-settlement behaviour).

Beams on elastic foundations are frequently used in engineering; see (Frydrýšek et al., 2013). This work is a continuation of our previous works. The symmetrical beam of length 2L = 2×12.045 m with cross-section b×h (b = 0.2 m, h = 0.4 m) is resting on an elastic foundation. The beam is loaded by force F = 7×10^6 N. The modulus of elasticity of the beam is $E = 2\times10^{11}$ Pa and the principal quadratic moment of the beam cross-section is $J_{ZT} = \frac{bh^3}{12}$. The nonlinear behaviour $q_R = q_R(v)$ [Nm^{-1}] of the distributed reaction force on deflection v [m] in the foundation was approximated by tangent-linear $q_{R1} = k_1 v = 1.7422 \times 10^{10} v$, non-linear $q_{R2} = k_1 v + k_a \text{arctg}(c_a v) = 5.21 \times 10^5 v + 9.52 \times 10^6 \text{arctg}(1.83 \times 10^3 v)$ and secant-linear $q_{R3} = k_1 v = 4.3866 \times 10^8 v$ functions. The nonlinear approximation q_{R2} fits the best with experiment. The solution deals with nonlinear differential equation $\frac{d^4 v}{dx^4} - \frac{k_1 v + k_a \text{arctg}(c_a v)}{E J_{ZT}} = 0$. In the cases of linear solutions (i.e. tangent-linear and secant-linear approximations), the function $k_a \text{arctg}(c_a v) = 0$. The parameters k_1, k_a and c_a were acquired from measurements q_{RE} by curve fitting; see (Frydrysek et al., 2013).

* M.Sc. Šárka Michenková: Department of Applied Mechanics, Faculty of Mechanical Engineering, VSB-Technical University of Ostrava; 17. listopadu 15/2172; 708 33, Ostrava; Czech Republic, sarka.michenkova@vsb.cz

** Assoc. Prof. M.Sc. Karel Frydrýšek, Ph.D.: Department of Applied Mechanics, Faculty of Mechanical Engineering, VSB-Technical University of Ostrava; 17. listopadu 15/2172; 708 33, Ostrava; Czech Republic, karel.frydrysek@vsb.cz

2. Central Difference Method (CDM) – Study case of Beam on Elastic Foundation

According to CDM (see Fig. 2 and (Frydrýšek et al., 2013), i.e. discretization of a nonlinear differential equation), the system of n+1 nonlinear equations for approximations q_{R1}, q_{R2} and q_{R3} can be derived.

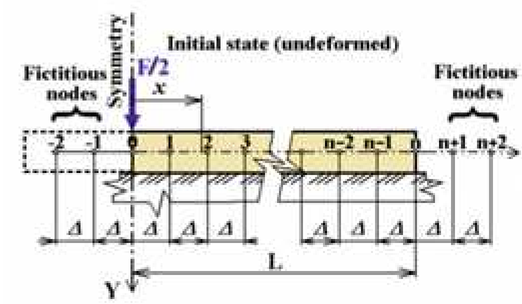

Fig. 2. CDM - Divisions of the beam (study case).

Hence, the system of nonlinear equations includes boundary conditions,

$$[\mathrm{M}]\{v\} + a_2 \mathrm{arctg}(c_a\{v\}) - \{\mathrm{b}\} = \{0\}, \tag{1}$$

where $[\mathrm{M}] = \begin{bmatrix} c & -8 & 2 & 0 & 0 & 0 & 0 & \dots & 0 \\ -4 & 7+a_1 & -4 & 1 & 0 & 0 & 0 & \dots & 0 \\ 1 & -4 & c & -4 & 1 & 0 & 0 & \dots & 0 \\ 0 & 1 & -4 & c & -4 & 1 & 0 & \dots & 0 \\ \vdots & \vdots & \vdots & \vdots & \ddots & \vdots & \vdots & \dots & \vdots \\ 0 & \dots & 0 & 1 & -4 & c & -4 & 1 & 0 \\ 0 & \dots & 0 & 0 & 1 & -4 & c & -4 & 1 \\ 0 & \dots & 0 & 0 & 0 & 1 & -4 & 5+a_1 & -2 \\ 0 & \dots & 0 & 0 & 0 & 0 & 2 & -4 & 2+a_1 \end{bmatrix}$, $\{b\} = \begin{Bmatrix} b \\ 0 \\ \vdots \\ 0 \end{Bmatrix}$, $\{v\} = \begin{Bmatrix} v_0 \\ v_1 \\ \vdots \\ v_n \end{Bmatrix}$,

$\Delta = \frac{\mathrm{L}}{\mathrm{n}}$ (see Fig. 2), $b = \frac{\mathrm{F}\Delta^3}{EJ_{ZT}}$, $a_1 = \frac{k_1\Delta^4}{EJ_{ZT}}$, $a_2 = \frac{k_a\Delta^4}{EJ_{ZT}}$, $c = 6 + a_1$.

3. Newton Method Iterative Approach

The nonlinear equations (1) can be solved iteratively via Newton Method as

$$\left\{{}^{\langle \mathrm{j}+1\rangle}v\right\} = \left\{{}^{\langle \mathrm{j}\rangle}v\right\} - \left[{}^{\langle \mathrm{j}\rangle}\mathrm{J}\right]^{-1}\left\{[\mathrm{M}]\left\{{}^{\langle \mathrm{j}\rangle}v\right\} + a_2\mathrm{arctg}\left(c_a\left\{{}^{\langle \mathrm{j}\rangle}v\right\}\right) - \{\mathrm{b}\}\right\}. \tag{2}$$

Where vectors of displacement $\left\{{}^{\langle \mathrm{j}\rangle}v\right\}$ and $\left\{{}^{\langle \mathrm{j}+1\rangle}v\right\}$ are old and new iterations and $\left[{}^{\langle \mathrm{j}\rangle}\mathrm{J}\right]$ is the Jacobian defined by

$$\left[{}^{\langle \mathrm{j}\rangle}\mathrm{J}\right] = \left(\frac{\partial\left[[\mathrm{M}]\left\{{}^{\langle \mathrm{j}\rangle}v\right\} + a_2\mathrm{arctg}\left(c_a\left\{{}^{\langle \mathrm{j}\rangle}v\right\}\right) - \{\mathrm{b}\}\right]}{\partial\, {}^{\langle \mathrm{j}\rangle}v_{\mathrm{k}}}\right)_{\mathrm{k}=0,1,2,\dots,\mathrm{n}}, \tag{3}$$

Matrix $\left[{}^{\langle \mathrm{j}\rangle}\mathrm{J}\right]$ is changing for each iteration $\langle \mathrm{j}\rangle$. However, matrix $\left[{}^{\langle \mathrm{j}\rangle}\mathrm{J}\right]$ is "similar" to matrix [M] (i.e. both are sparse and their distinctions are only in main diagonals of these matrices) which is suitable for programming. For more information, see (Frydrýšek et al., 2014; Michenková et al., 2014).

4. Evaluation of Acquired Results

Some basic results for a long beam are presented in Fig. 3 (i.e. dependencies for deflection, slope, bending moment, shear force and reaction force on length coordinate x for q_{R1}, q_{R2} and q_{R3} approximation of foundation). The slope of the beam is defined as $\frac{dv}{dx}$, the bending moment is defined as $M_o = -EJ_{ZT}\frac{d^2v}{dx^2}$, the shear force is defined as $T = -EJ_{ZT}\frac{d^3v}{dx^3}$ and the reaction force in the foundation is defined via q_{R1}, q_{R2} and q_{R3} functions. The distinctions between each type of foundation are evident. For presented inputs, the tangent-linear approximation q_{R1} and nonlinear approximation q_{R2} of foundation give nearly the same results (i.e. good agreement with experiment noted in chapter 1). However the secant-linear approximation q_{R3} gives unreal results. This is caused by "quite small" loading force F = 7×10[6] N.

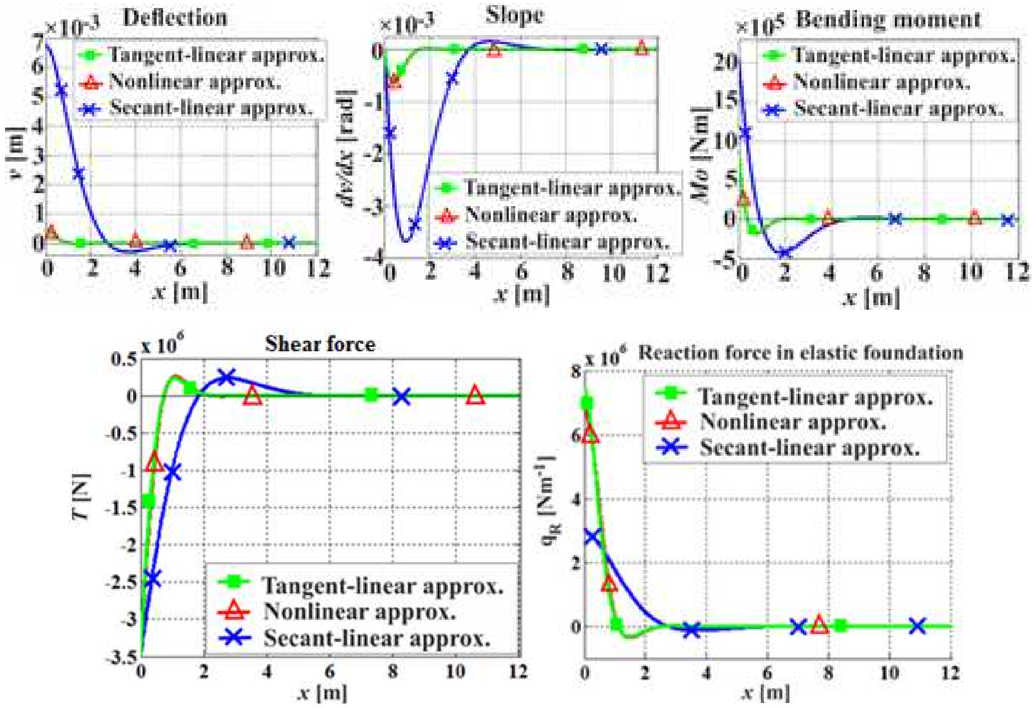

Fig. 3. Dependence of deflection, slope, bending moment, shear force and distributed reaction force on coordinate $x\epsilon\langle 0; L\rangle$ of the beam for different types of foundation approximations (results acquired by CDM with MATLAB).

However, increasing of external force F brings higher influence of nonlinearity (i.e. bigger differences between linear and nonlinear solutions). Hence, dependencies of maximum values of displacement v_{MAX} [m], bending moment Mo_{MAX} [Nm] and reaction forces q_{RMAX} [Nm^{-1}] on force F are presented in Fig. 4. These figures were printed for the same beam rested on elastic linear/nonlinear foundation.

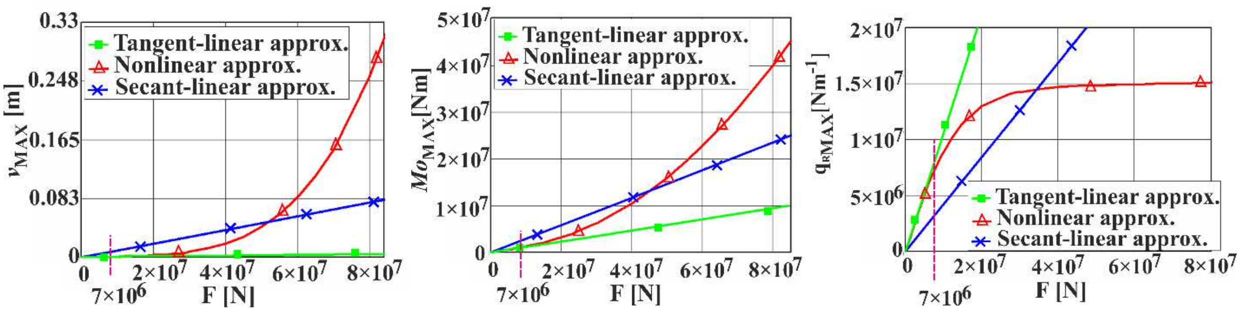

Fig. 4. Dependence of maximum deflection, maximum bending moment and maximum reaction force on external force for the beam on different types of foundation approximations (results acquired by CDM with MATLAB).

Now, the distinctions between each type of foundation approximations (i.e. influences of nonlinearities) are evident. As it was mentioned, the nonlinear approximation q_{R2} is the best approximation of the reality. Therefore, for the small deflections of foundation fit well tangent-linear approximations q_{R1} (i.e. for $F \in \langle 0; 3\times 10^7\rangle$ N). Otherwise, for larger deflections fits well secant-linear approximation q_{R3} (i.e. for $F \in \langle 4\times 10^7; 6\times 10^7\rangle$ N). However, nonlinear approximation q_{R2} fits well for all cases of deflections (i.e. for $F \in \langle 0; 8\times 10^7\rangle$ N). To put that into context, in Fig. 4, there is marked the value of loading force F = 7×10[6] N which is connected with the solution presented in Fig. 3.

5. Future Application

The use of an elastic foundation including nonlinearities is a suitable way of performing numerical/experimental modelling of engineering problems. For example modelling of external fixators designed for the treatment of complicated bone fractures, modelling of femoral screws designed for the treatment of "collum femoris" fractures (see Fig. 5 and reference Frydrýšek et al., 2013).

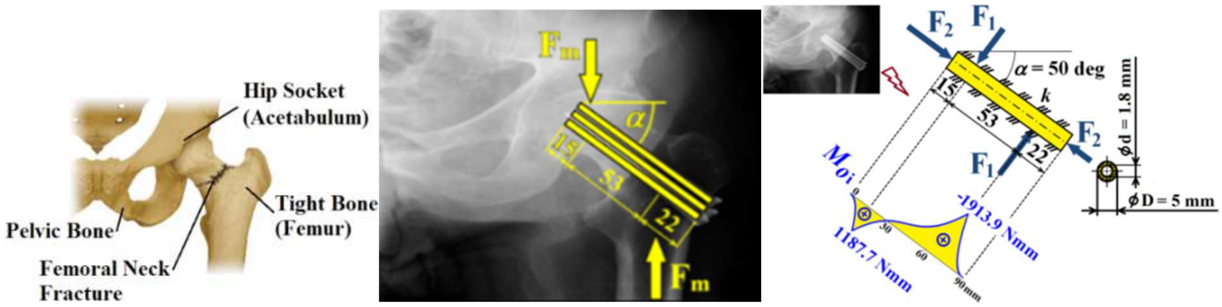

Fig. 5. Examples of beams on elastic foundations in the field of biomechanics (collum femoris fracture and its treatment and numerical solutions of femoral cannulated screw).

The derivation, rapid solutions and application of our own simple numerical model based on CDM open up new possibilities for further applications using a stochastic approach (i.e. millions of solutions with random inputs and outputs can be easily simulated). Therefore, the application of the CDM + probabilistic approach connected with the probabilistic reliability assessment of femoral screws is the main focus of the future work, see (Marek et al., 1995).

6. Conclusions

The measured material properties of the elastic foundation were evaluated and approximated in three ways (via easy bilateral tangent-linear $q_{R1} = k_1 v = 1.7422 \times 10^{10} v$, complicated but complex bilateral nonlinear $q_{R2} = k_1 v + k_a \mathrm{arctg}(c_a v) = 5.21 \times 10^5 v + 9.52 \times 10^6 \mathrm{arctg}(1.83 \times 10^3 v)$ and easy secant-linear $q_{R3} = k_1 v = 4.3866 \times 10^8 v$ functions). Beams on elastic linear and nonlinear foundations were solved via the CDM and iterative Newton Method using MATLAB software. The iterative approach is necessary for nonlinear solutions. From the results, it is evident that the nonlinear approximation for the behaviour of an elastic foundation fits very well with experiments and gives the best results. However, the application of the CDM and iterative Newton Method (i.e. solutions of nonlinear problems) is possible, though complicated (i.e. time-consuming). Tangent/secant-linear approximations of the elastic foundations behaviour give worse results, though acceptable in some cases. It could be dangerous to place blind faith in the easy linear approximation of the foundation.

In references (Frydrýšek et al., 2013; Frydrýšek et al., 2014; Michenková et al., 2014) are presented other approximations and solutions of similar beam rested on elastic foundation with different behaviour. Possible future improvements are explained too. The application of CDM is quite easy, comprehensible and suitable for beam structures. Numerical approaches used in this article could be applied in many engineering solutions.

Acknowledgement

The authors gratefully acknowledge the funding from the Czech projects TA03010804 and SP2016/145.

References

Frydrýšek, K., Michenková, Š. & Nikodým, M. (2014) Straight Beams Rested on Nonlinear Elastic Foundations – Part 1 (Theory, Experiments, Numerical Approach). In: Applied Mechanics and Materials. Volume 684, Trans Tech Publications, Switzerland. pp. 11-20.

Frydrýšek. K., Tvrdá, K., Jančo, R., et al. (2013) Handbook of Structures on Elastic Foundation. Ostrava: VŠB - Technical University of Ostrava, Ostrava, pp. 1-1691.

Marek, P., Guštar, M. & Anagnos, T. (1995) Simulation-Based Reliability Assessment for Structural Engineers, CRC Press, Boca Raton, USA, pp.365.

Michenková, Š., Frydrýšek, K. & Nikodým, M. (2014) Straight Beams Rested on Nonlinear Elastic Foundations – Part 2 (Numerical Solutions, Results and Evaluation). In: Applied Mechanics and Materials. Volume 684, Trans Tech Publications, Switzerland, pp. 21-29.

22nd International Conference
ENGINEERING MECHANICS 2016
Svratka, Czech Republic, 9 – 12 May 2016

COMPARISON OF QUASICONTINUUM APPROACHES USING VARIOUS LEVELS OF SIMPLIFICATION

K. Mikeš[*], M. Jirásek[**]

Abstract: *Atomistically based simulations of materials with disordered microstructure often lead to a high number of degrees of freedom (DOFs) and extreme computational costs. The quasicontinuum method (QC) is a multiscale simulation technique which combines fast continuum and exact atomistic approaches. The key idea of QC is to reduce the computational cost by reducing degrees of freedom of the fully atomistic approach. In the present work, the QC idea is applied to particle systems with elastic-brittle links representing a specific material microstructure. Three approaches using various levels of simplification based on the idea of QC are described and implemented. Accuracy and specific properties of QC-inspired approaches are evaluated by comparing the results with the fully resolved particle model.*

Keywords: Quasicontinuum method, finite elements, discrete particle model, elasto-brittle material.

1. Introduction

The quasicontinuum method (QC) was originally proposed in (Tadmor et al., 1996). The original application of this multi-scale technique was a simplification of large atomistic lattice models described by long-range conservative interaction potentials. In this paper the idea of QC is applied to discrete disordered particle systems with short-range elastic-brittle interactions.

2. Methods

The key idea of QC is to reduce the number of DOFs and the associated computational cost without losing the exact atomistic description in regions where it is required. Therefore, two types of regions in the investigated domain are considered. In regions of high interest, the pure particle approach is required and all particles carry their own independent DOFs. By contrast, in regions of low interest, continuum assumptions are used (Miller & Tadmor, 2002). The simplification is then implemented in two steps: interpolation of DOFs and homogenization of microstructure. In this work, three approaches that differ by the level of simplification based on the QC idea are outlined, implemented in the OOFEM platform (Patzák, 2012) and compared with the pure particle model in 2D. All presented approaches have been developed and explained in more detail in (Mikeš & Jirásek 2015).

2.1. Pure particle approach (A1)

This approach does not use any simplification. Every single particle represents a node with independent DOFs. All links are taken into account explicitly and contribute directly to the stiffness matrix. Consequently, this approach provides the "exact" result, which is used as a reference solution for evaluation of accuracy and efficiency of the following simplified approaches.

2.2. Hanging nodes approach (A2)

The first model reduction technique is based on approximation of certain DOFs. In the regions of low interest, only a small subset of particles is selected to carry independent DOFs. These so-called *repnodes*

[*] Ing. Karel Mikeš: Faculty of Civil Engineering, Czech Technical University in Prague; Thákurova 7/2077; 166 29 Praha; CZ, Karel.Mikes.1@fsv.cvut.cz

[**] Prof. Ing. Milan Jirásek, DrSc.: Faculty of Civil Engineering, Czech Technical University in Prague; Thákurova 7/2077; 166 29 Praha; CZ, Milan.Jirasek@fsv.cvut.cz

represent the vertices of a triangular mesh which is used to interpolate the DOFs of other particles called hanging nodes because their DOFs are not independent but are "hanging" on appropriate repnodes. By contrast, in the regions of high interest, all particles are selected as repnodes to provide the exact particle representation.

2.3 Global homogenization approach (A3)

In this approach, 2D or 3D finite elements are used not only to interpolate DOFs but also to replace the stiffness that corresponds to the microstructure, so that a substantial number of links can be removed from the particle model. Material properties of 2D elements are identified by homogenization of one global effective elastic stiffness tensor, which is assembled from the contribution of all links. According to (Stránský et al., 2010), such a tensor can be evaluated as

$$\boldsymbol{D}_e = \frac{1}{V}\sum_{i=1}^{N_t} L_i E_{t_i} A_i (\boldsymbol{n}_i \otimes \boldsymbol{n}_i \otimes \boldsymbol{n}_i \otimes \boldsymbol{n}_i) \tag{1}$$

where $\boldsymbol{n}$ is the unit vector specifying the direction of the given link, E_t is the Young modulus of the link, A is its cross-section area and L is its length. The sum is taken over N_t links occupying volume V.

2.4 Local isotropic (A4) and anisotropic (A5) homogenization approach

The idea of these approaches is the same as for A3 with the difference that the evaluation of the effective material stiffness tensor is done for each element separately. The stiffness tensor of each element is obtained only from the contributions of the parts of the links that are located in this element. Then the material parameters are identified from the corresponding stiffness tensor for each element. The A4 approach identifies the stiffness of all elements as isotropic whereas A5 considers all elements as arbitrarily anisotropic with the exact anisotropic stiffness matrix.

3. Results and conclusions

The presented example is an L-shaped beam with geometry and boundary condition according to Fig. 1. The material of the links is considered as elastic-brittle, with failure occuring at the critical level of tensile strain. Before the critical value is reached, the link is considered as purely elastic. The region of high interest is located around the nonconvex corner and along the expected crack trajectory; see Fig. 1 (right). The geometry of microstructure is generated randomly. Five different realizations with the same parameters have been used. Different realizations of microstructure lead to different crack trajectories and force-displacement diagrams; see Fig. 2. The results are evaluated as an average over all five random realizations of microstructure.

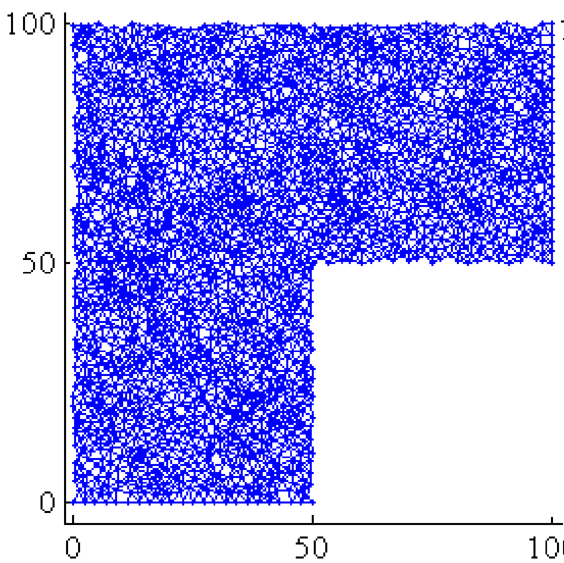

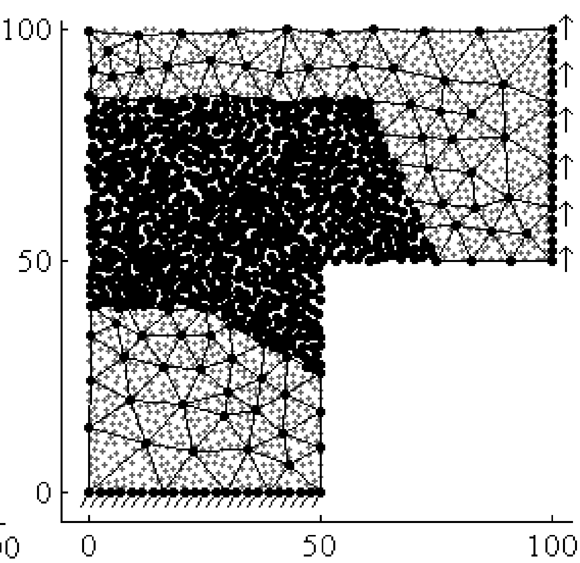

Fig. 1: Example of microstructure geometry (left). Quasicontinuum model with boundary conditions (right), regions of high interest, repnodes with interpolation elements (black), hanging nodes (grey).

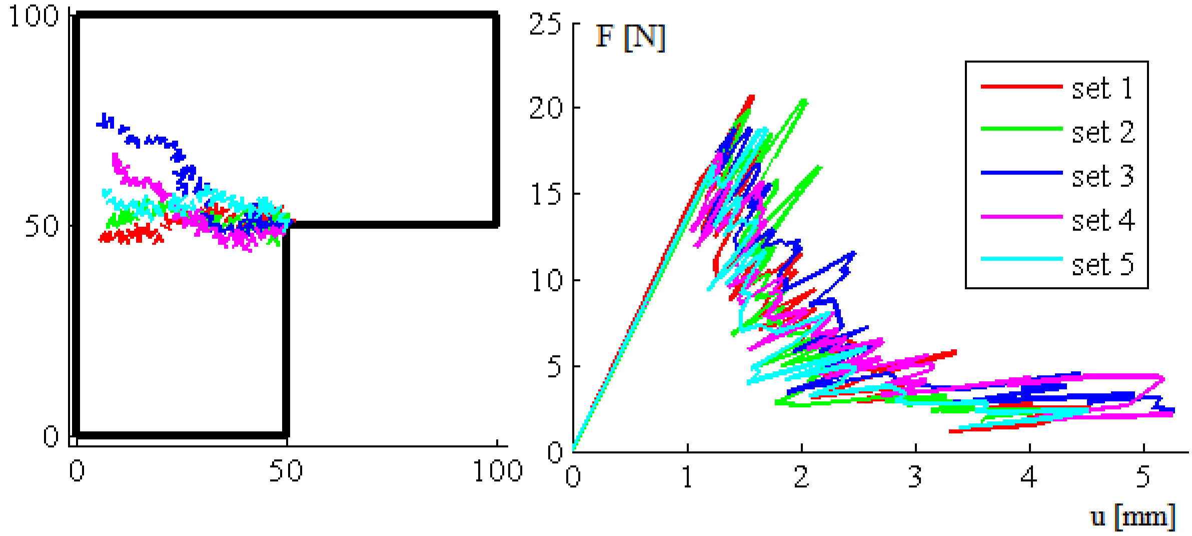

Fig. 2: Crack trajectories (left) and corresponding force-displacement diagrams (right) for five random microstructures generated with the same parameters.

The accuracy of the presented simplifying approaches A2-A5 is evaluated with respect to the exact approach A1. Relative errors in terms of displacement and force are plotted in Fig. 3. The relative error in macroscopic stiffness and the error measured in the terms of a global strain error indicator defined as

$$e^2{}_{A2} = \frac{1}{2}\sum_{i=1}^{N_t} L_i E_{t_i} A_i \left(\varepsilon_{A2_i} - \varepsilon_{A1_i}\right)^2 \tag{2}$$

are plotted in Fig. 4. Numerical values of all errors in the first step are listed in Table 1. The initial response of A3 is significantly stiffer. The error of A3 decreases as the crack propagates because the major part of deformation takes place in the region of high interest. It is surprising that A4 is less stiff (more accurate) than A5 with more sophisticated homogenization and even than A2 with the exact microstructure. It is because both the interpolation and the anisotropic homogenization make the final response stiffer. By contrast, isotropic approximation of an anisotropic stiffness tensor may

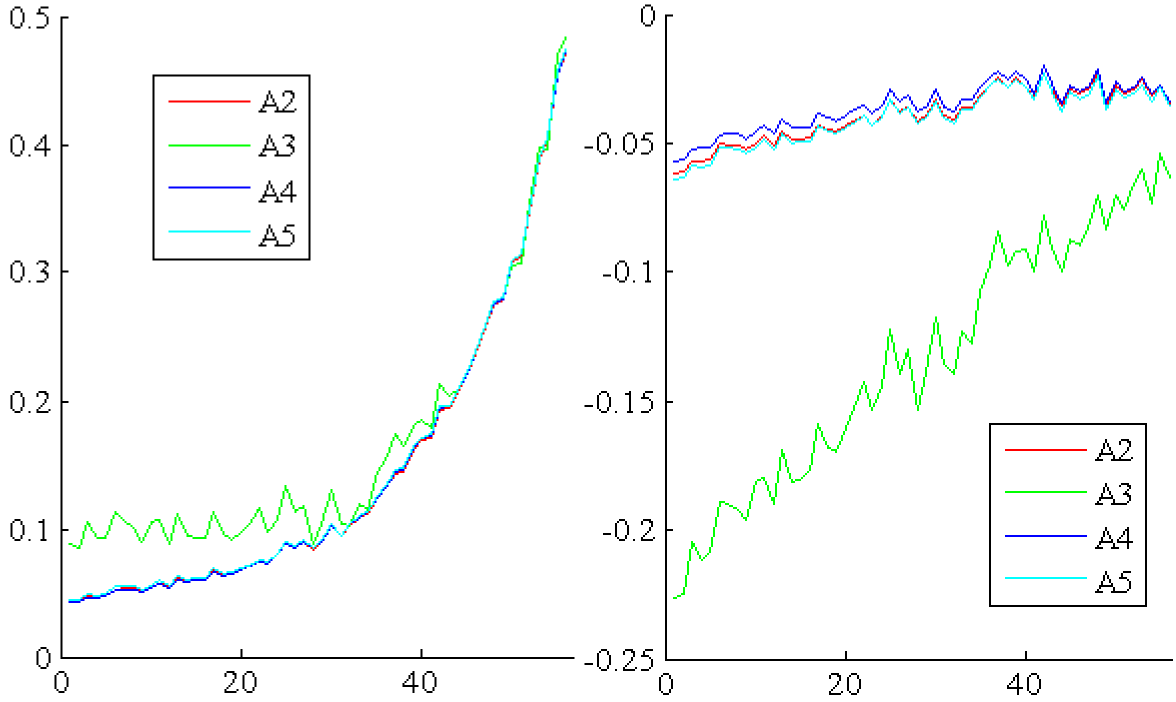

Fig. 3: Relative force error (left) and relative displacement error (right) as a function of number of cracked links.

result in a loss of stiffness in some directions. In A4 these two types of error act against each other and thus A4 appears to be the most accurate (in terms of stiffness) but its accuracy cannot be guaranteed. This can be observed if the error is measured in strain. According to the strain error indicator, the best approach is A2 with interpolation only, while A5 with the most accurate anisotropic homogenization is only slightly worse and A4 takes the 3rd place; see Table 1.

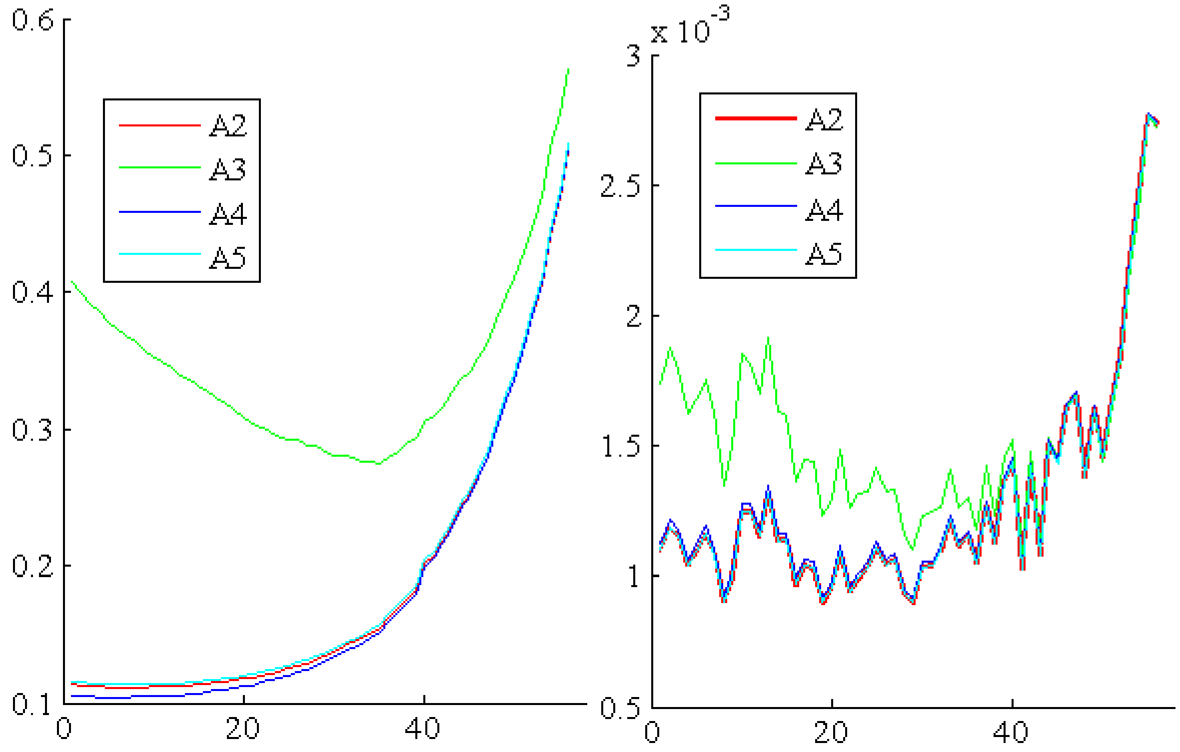

Fig. 4: Relative stiffness error (left) and global strain error indicator (right) as a function of number of cracked links.

Tab. 1: Table of accuracy of different approaches.

Method	Displacement error	Force error	Stiffness error	Global strain error indicator
A2 hanging nodes	-6.18%	4.47%	11.33%	2.258E-03
A3 global homogenization	-22.63%	8.88%	40.75%	3.622E-03
A4 local isotropic homog.	-5.73%	4.23%	10.56%	2.324E-03
A5 local anisotropic homog.	-6.38%	4.48%	11.58%	2.264E-03

Acknowledgement

Financial support of this research received from the Grant Agency of the Czech Technical University in Prague (SGS16/038/OHK1/1T/11) and from the Czech Science Foundation (GAČR project No. 14-00420S) is gratefully acknowledged.

References

Mikeš, K. & Jirásek, M. (2015) Quasicontinuum Method Extended to Disordered Materials, in: Proc. 15th Int. Conf. on Civil, Structural and Environmental Engineering Computing, Civil-Comp Press Ltd, Stirling.

Miller, R. E., & Tadmor, E. B. (2002). The quasicontinuum method: Overview, applications and current directions. Journal of Computer-Aided Materials Design, 9, 3, pp. 203-239.

Patzák, B. (2012). OOFEM—an object-oriented simulation tool for advanced modeling of materials and structures. Acta Polytechnica, 52, 6.

Stránský, J., Jirásek, M., & Šmilauer, V. (2010). Macroscopic elastic properties of particle models, in Proc. Int. Conf. on Modelling and Simulation, Prague.

Tadmor, E. B., Ortiz, M., & Phillips, R. (1996). Quasicontinuum analysis of defects in solids. Philosophical Magazine A, 73, 6, pp. 1529-1563.

22nd International Conference

ENGINEERING MECHANICS 2016

Svratka, Czech Republic, 9 – 12 May 2016

EXPERIMENTAL DETERMINATION OF HEAD LOSSES IN POLYETHYLENE PIPELINE WITH NOMINAL DIAMETER DN250

P. Mosler[*], J. Melichar[**]

Abstract: *The article describes experimental measurements of head losses in polyethylene pipeline with diameter d280x25.4 SDR11. During experimental measurement were obtained values of frictional losses of polyethylene pipe PE100 and local pressure loss in butt welded joint. The experimental measurement results are loss coefficients in dependence on the Reynolds numbers. Measurement is continuation of long term research in determining head losses in plastic pipelines at the Faculty of Mechanical Engineering of the Czech Technical University in Prague. Obtained values of head losses in polyethylene pipelines shows that local losses represent important part of the total energy losses.*

Keywords: Polyethylene pipeline, Local head loss, Butt fusion joints, Friction loss, Internal bead

1. Introduction

Designers of plastic pipeline systems mostly do not have sufficient, comprehensive and verified data for reliable hydraulic calculation. The local head loss in plastic pipeline joints welded by butt fusion is nowadays typical example. Due to the recent problems during the operation of plastic piping system, designers often required accurate and verified data of friction losses and local head loss of butt welded joint. Hence, more accurate data are necessary for proper design of plastic piping system. One of frequently neglected minor loss is a loss of joint in butt welded pipeline system.

2. Local head loss in plastic pipelines joint welded by butt fusion

During the process of butt welding the inner and outer emanation (bead) of the pipe material is created (Figure 1c). The size of a butt weld joint bead is for certain material and wall thickness dependent on the welding process. The exact welding techniques are recommended for example by instructions of DVS (Deutscher Verband für Schweisstechnik). The inner bead in the tube represents the specific kind of inner resistance and results in additional minor losses of the fluid flow. The effect of local losses caused by butt welds on total energy balance for long pipelines is important. However, in design practice it is often underestimated or neglected (Mosler, 2014).

Allowed manufacturing tolerance of external diameter and wall thickness is prescribed by the ISO 4065 standard. The measured section was made of straight polyethylene tube *PE100 d280x25.4 DIN 0874/75 SDR11*. The average value of inner tube diameter of pipe is $d_i=227.93mm$ and inner diameter in joint $d_o=211.42mm$, average bead height $h=8.25mm$, average bead width $w=17.29mm$ and average thickness of the pipe $t=26.23mm$. Cross-sections of the pipe at the bead were taken in order to determine the real profile of bead around the entire circumference. Comparison of profiles around the circumference is shown in Figure 1b. It is obvious that internal bead is not symmetrical and the dimension of the bead varies around circumference. Comparison of the bead dimension around the circumference with the DVS standard is in figure 1a.

[*] Ing. Pavel Mosler: Faculty of Mechnical Engineering, Czech Technical University in Prague, Technická 4, 166 07, Prague; CZ, Pavel.Mosler@fs.cvut.cz

[**] Prof. Ing. Jan Melichar CSc: Faculty of Mechnical Engineering, Czech Technical University in Prague, Technická 4, 166 07, Prague; CZ, Jan.Melichar@fs.cvut.cz

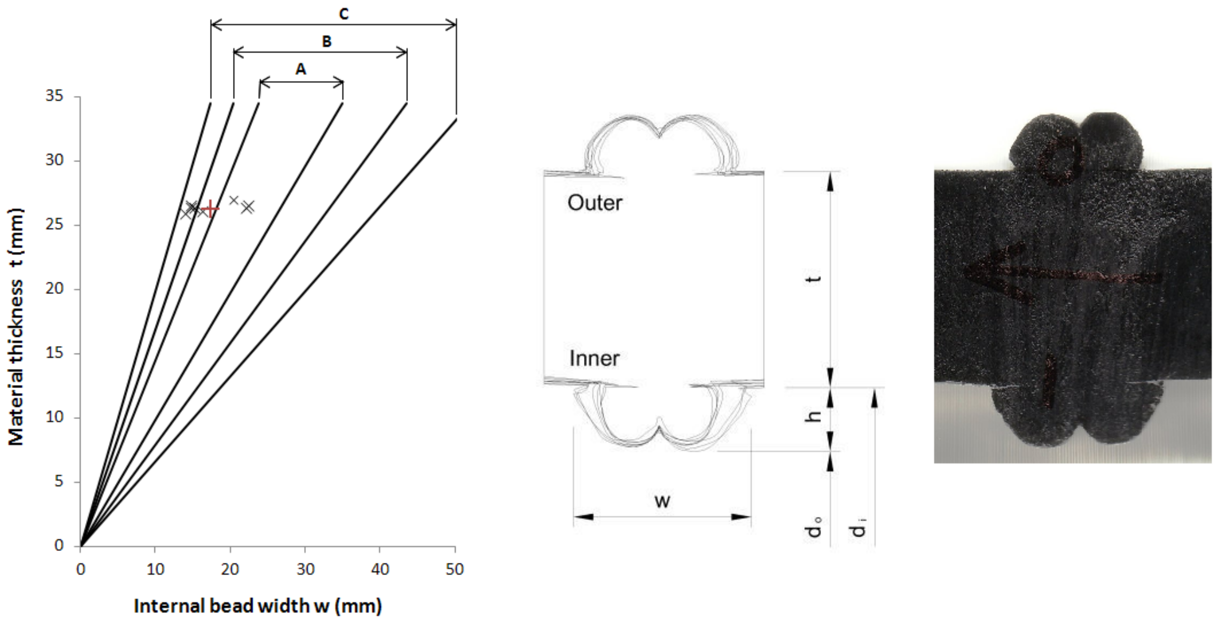

Fig. 1: a) Internal bead dimension in comparison with DVS prescription b) Cross sections of internal bead around circumference c) Cross section of butt welded joint of polyethylene pipeline dimension d280x25.4 SDR11 PE100

3. Design of experimental test loop

The test section of the circuit is composed of the proper metering pipe length sufficient straight pipeline length before and behind the jointing point where the influence of jointing point on flow pattern is anticipated. In front of this measuring section there is a straight pipeline with the corresponding length due to stabilization of the flow. Detailed drawing with distance between pressure measurement connection and jointing point is shown in Figure 2. Static pressure measuring connections in the experimental pipeline were made of four pipeline side inlets that were evenly placed. Figure 2 shows also the detailed arrangement of pressure measuring connections.

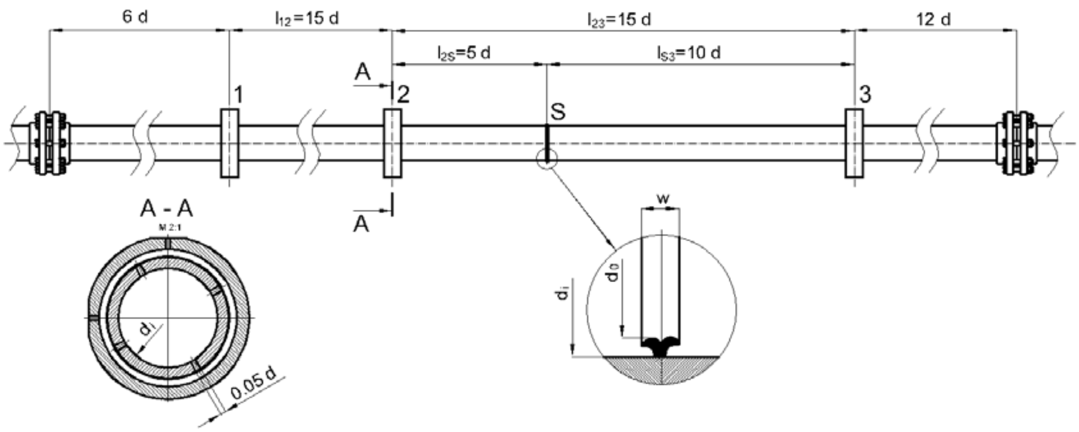

Fig. 2: Arrangement of test section with detail of pressure measuring connections

The static pressure differences Δp_{12} between the cross-section 1 and 2 and Δp_{23} between the cross section 2 and 3 were measured with the use of calibrated differential pressure sensors with range *0–16 kPa/4 – 20 mA*. The estimated accuracy of pressure difference measurements is up to *0.25 %* of a measuring range. The flow rate *Q* was measured using magnetic flow meter. The accuracy *0.5 %* of measured flow rate was guaranteed within the range of *10* to *100 %* of Q_{max}. The mercury thermometer was used to measure the water temperature in order to determine water viscosity. The analogue output signals from the magnetic flow meter and the differential manometers were compiled by A/D converter and transmitted and stored into PC using recording software (Mosler, Melichar 2014).

4. Calculation of local head loss from measured values

The head losses can be expressed in terms of fluid specific energy Y_z *(J.kg^{-1})*, which is consumed in a given pipeline section. The concrete values of Y_z are determined by computation from the measured values of pressure difference, Δp_{12} and Δp_{23}. The pressure drop between cross sections 1 and 2 due to frictional losses can be computed from the Darcy-Weisbach equation

$$Y_{zf} = \frac{\Delta p_{12}}{\rho} = \lambda \cdot \frac{l_{12}}{d_i} \cdot \frac{c^2}{2} \tag{1}$$

The friction factor λ in the case of turbulent flow in hydraulically smooth straight pipeline depends only on the Reynolds number.

The head loss generated at the joint of straight pipeline (local loss) is given by an increase of the loss at the straight pipeline section with given local loss against frictional loss at the same system without local loss. Pressure loss caused by the inner butt weld projection can be expressed as follows:

$$\Delta p_s = \Delta p_{23} - \Delta p_{12} \tag{2}$$

For the local loss computation in a given pipeline joint Y_{zl} it is possible to use the common formula where ξ is local loss coefficient of the joint (Melichar et. al. 2006).

$$Y_{zl} = \xi \cdot \frac{c^2}{2} = \frac{\Delta p_s}{\rho} \tag{3}$$

5. Results of experimental measurements

Results from the measurement of the friction factor of polyethylene pipeline *d280x25.4 SDR11* in dependence on Reynolds numbers is given in Figure 3. The results shows, that measured friction factor is higher than friction factor in hydraulically smooth pipes. Comparison with hydraulically smooth pipe friction factor given by Blasius's and Advani's formulas (Kolář, Vinopal 1963) is in Figure 3.

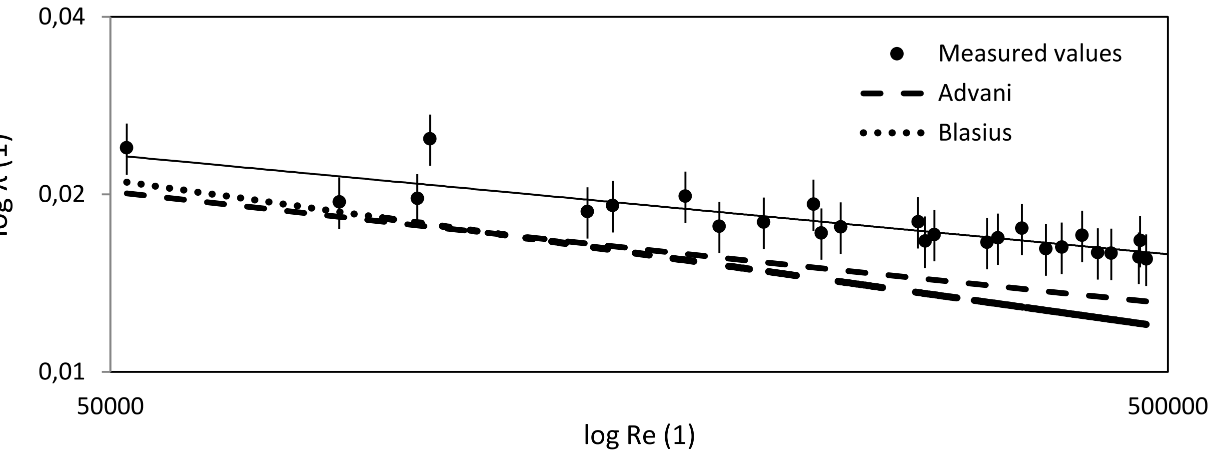

Fig. 3: Measured values of the friction factors in straight pipeline test section of length l_{12} in dependence on the Reynolds number compared to hydraulically smooth pipe

Experimental values of local loss coefficient ζ for examined pipeline joint in dependency on the Reynolds numbers are shown in Figure 4. The results in Figure 4 show values of the local loss coefficient ζ within a range of *0.01* to *0.03* for measured values of the Reynolds number within a range of $1.10^5 < Re < 5.10^5$ and/or flow velocity $0.2\ m\ s^{-1} < c < 2.4\ m\ s^{-1}$.

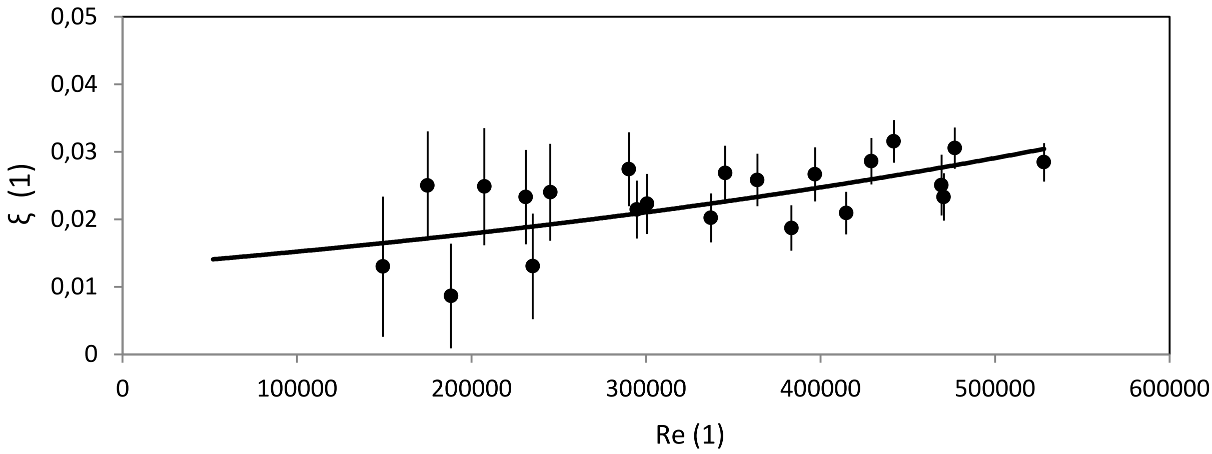

Fig. 4: Values of local loss coefficient for tube joint in dependence on the Reynolds numbers

6. Conclusions

The measured values show that the local losses in butt welded joints represent indispensable part of the total energy losses. This is significant in particular for long pipeline systems. For examples the pipeline with nominal diameter DN250 with butt-welded joints may result increase of head losses about 6% for the above-mentioned Reynolds numbers in comparison with the same pipeline without butt welds. The influence of local losses in butt welded joints is more significant in pipe with smaller diameter then in the larger one.

The paper shows result values of the local loss coefficient for the tube joints with butt welds that were experimentally determined for turbulent flow with Reynolds numbers within the range of $1.10^5 < Re < 5.10^5$. The local loss coefficient at pipeline joints had for the above-mentioned range of the Reynolds numbers the average value of $\zeta = 0.023$. This value was determined for tube *PE100 d280x25.4 SDR11* with average inner diameter of $d_i=227.93mm$ and for the joint and diameter proportion $d_0/d_i = 0.93$.

Acknowledgement

Experimental measurement was supported by the specific university grant provided by Czech Technical University No.: SGS13/063/OHK2/1T/12.

Appropriate equipment and instrumentation has been taken from Centre for research of multiphase flow and thermodynamic processes in renewable sources and energetic – NEW ENERGY reg. n. CZ.2/16/3.1.00/22130 supported by European Union.

References

Mosler, P., Melichar, J. (2014) Determination of Pressure Loss in Plastic Pipeline, in: 15th International Freight Pipeline Society Symposium, Prague, pp. 212-221

Melichar, J., Háková, J., Veselský, J., Michlík, L. (2006) Local head loss in plastic pipeline joint welded by butt fusion, Journal of Hydrology and Hydromechanics, vol. 54, no.3, pp. 299-308

Direction DVS 2202-1 (December 1989) Imperfection in thermoplastic welding joints; features, descriptions, evaluation, Deutscher verband fűr schweissen und verwanote verfahren e.v.

Standard ISO 4065 (1996) Thermoplastic pipes – Universal wall thickness table

Kolář, V., Vinopal, S. (1963) Hydraulika průmyslových armatur (Příručka praktických výpočtů), SNTL Praha.

22nd International Conference
ENGINEERING MECHANICS 2016
Svratka, Czech Republic, 9 – 12 May 2016

INFLUENCE OF WALL FLEXIBILITY OF LIQUID STORAGE TANKS ON HYDRODYNAMIC PRESSURES INDUCED DURING SEISMIC ACTIVITY

M. Musil*, M. Sivý**

Abstract: *The paper deals with the seismic analysis of the circular vertical ground-supported tanks containing liquid with the aim to determine the distribution of hydrodynamic pressures along the tank height during seismic excitation. Circular tanks are used for storage of liquids in various industrial sectors. Hence, it is a request for satisfactory performance during dynamic loadings. In general, these tanks are usually made of reinforced concrete or steel. For determination of distribution of hydrodynamic pressures there must be distinguished between rigid and flexible tanks due to different responses of tank-liquid systems. In cases of flexible tanks, the wall flexibility is taken into account. The paper is also dedicated to compare results of distribution of hydrodynamic pressure for both cases assuming models with identical geometric proportions. For computation and subsequent comparison Eurocode 8 standard and other procedures are used.*

Keywords: **circular liquid storage tank, hydrodynamic pressures, flexibility, seismic excitation, Eurocode 8**

1. Introduction

Liquid storage tanks are important components in various industrial sectors and are used as part of lifeline transmission and distribution systems. The main purpose of these systems is to store a variety of liquids (e.g. with toxic explosive nature) before subsequent treatment or utilization. Liquid storage tanks can be subjected to loadings of various nature which may threaten ordinary operation. In addition to static loading, which is usually represented by hydrostatic pressure, tanks may be subjected to the dynamic effects (e.g. seismic excitation) as well. There are many negative consequences which may be caused by dynamically loaded systems and can take one of the following ways: buckling of shells due to excessive axial compression taking the form of a bulge called elephant's foot; roof damage caused by sloshing of upper zone of contained liquid with inadequately designed freeboard between liquid surface and roof etc. There were proposed procedures for seismic resistance of tank-liquid systems. One of the basic seismic characteristics is the distribution of hydrodynamic pressures along the tank height. Time-dependent hydrodynamic pressures induce time-dependent stresses in tanks which can significantly affect their performance. Hence, estimate of distribution and magnitude of hydrodynamic pressures during loading are crucial in tank design in order to preserve their functionality before, during and after seismic event. These pressures and relative stresses depend on type of motion, liquid properties, proportions and material of tank.

2. Basic concepts and theory

Following the past earthquakes like El Centro, San Fernando and others, there was a huge effort to describe tank behavior in a more common way. The most widely used procedure for evaluating seismic effects in cylindrical liquid storage tanks is the one based on a spring-mass equivalent model (Housner, 1954). The proposed method shows that hydrodynamic pressures can be expressed as the sum of two contributions called impulsive and convective, separately. The impulsive pressures are those associated with inertial forces produced by accelerations of the walls of the container and are directly proportional to

* Doc. Ing. Miloš Musil, CSc.: Institute of Applied Mechanics and Mechatronics, Faculty of Mechanical Engineering, Slovak University of Technology, Námestie slobody 17; 812 31, Bratislava; SK, milos.musil@stuba.sk

** Ing. Martin Sivý: Institute of Applied Mechanics and Mechatronics, Faculty of Mechanical Engineering, Slovak University of Technology, Námestie slobody 17; 812 31, Bratislava; SK, martin.sivy@stuba.sk

these accelerations. The convective pressure is produced by oscillation of liquid and is a consequence of the impulsive pressure. However, Housner's method is limited to the rigid tanks. It is usually unconservative to consider all tanks to be rigid due to the wall deflection. Whereas walls of rigid tanks move in unison as the ground, motion of walls of flexible tanks is different. The wall deflection configuration of these tanks do not remain the same but vary from the base to the top of the tank (Veletsos, 1974). From procedures it follows, maximum acceleration in a given direction of a point on a rigid tank is the same as maximum acceleration of the ground, whereas in cases of flexible tanks it can be smaller than, equal to or greater than the maximum ground acceleration depending on tank flexibility. All these knowledge are reflected in seismic characteristics (base shear, overturning moment, stresses etc.). Tank flexibility affects the hydrodynamics effects and these may be increased significantly. Following investigation in the past, there were proposed procedures which underlie international standards in relation to design of structure for seismic resistance (e.g. Eurocode 8).

Following subchapters of paper are focused on the comparison of procedures for estimate of distribution of hydrodynamic pressures in rigid and flexible tanks in accordance with Eurocode 8 and other approaches. An investigated liquid storage tank is illustrated in Fig. 1. It is the cylindrical tank of radius *R* (8 m), height *H* (16 m) and thickness *t* (0,004 m). Tank is filled to the height H_L (16 m) with liquid (water). It is assumed that the base of the tank is continuously fixed to gravel-sand foundation, which is excited by a horizontal component of ground acceleration of 1 ms^{-2} with component importance factor III in accordance with Eurocode 8.

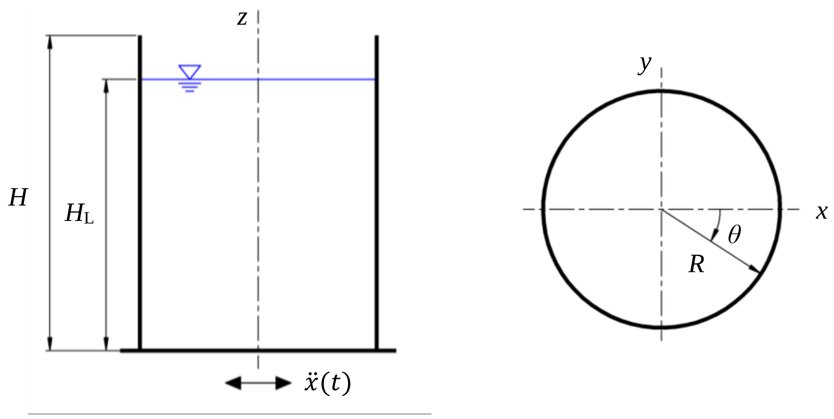

Fig. 1: Liquid storage tanks under horizontal seismic excitation

2.1. Hydrodynamic pressures in rigid tanks

During lateral base excitation, tank wall is subjected to the lateral hydrodynamic pressure. For rigid tanks in accordance with Eurocode 8, hydrodynamic pressures consists of two components analogous to Housner's theory. The spatial-temporal distribution of the rigid impulsive pressure is given by expression

$$p_\mathrm{i}(\xi,\varsigma,\theta,t) = C_\mathrm{i}(\xi,\varsigma)\rho_\mathrm{L} H_\mathrm{L} A_\mathrm{g}(t)\cos\theta \qquad (1)$$

where C_i gives the distribution along the height of p_i

$$C_\mathrm{i}(\xi,\varsigma) = 2\sum_{n=0}^{\infty}\frac{(-1)^n}{I_1'(v_n/\gamma)v_n^2}\cos(v_n\varsigma) I_1\left(\frac{v_n}{\gamma}\xi\right)$$

in which

$$v_n = \frac{2n+1}{2}\pi;\ \gamma = \frac{H_\mathrm{L}}{R};\ \ \xi = \frac{r}{R};\ \varsigma = \frac{z}{H_\mathrm{L}}$$

I_1 and I_1' represent a modified Bessel function of first kind and its derivative, $A_\mathrm{g}(t)$ denotes the ground acceleration time-history, ξ,ς are non-dimensional geometric parameters and γ denotes slenderness parameter (liquid height H_L to tank radius R). The part of liquid that does not move as a rigid body with the tank experiences sloshing effect. This motion can be expressed as a linear combination of the corresponding natural modes of liquid vibration. The spatial-temporal distribution of the convective pressure component is given by expression

$$p_\mathrm{c}(\xi,\varsigma,\theta,t) = \rho_\mathrm{L}\sum_{n=1}^{\infty}\psi_n\cosh(\lambda_n\gamma\varsigma) J_1(\lambda_n\xi)\cos\theta A_{\mathrm{c}n}(t) \qquad (2)$$

where

$$\psi_n = \frac{2R}{(\lambda_n^2-1)J_1(\lambda_n)\cosh(\lambda_n\gamma)}$$

J_1 is a Bessel function of the first order and λ_n are values for which the first derivative of J_1 is zero, $A_{cn}(t)$ is the acceleration time-history of SDOF oscillator with natural frequency ω_{cn}. To withstand roof damage caused by sloshing in the tank, a sufficient freeboard is required. The sloshing wave height may be given from the following expression

$$d(r,\theta,t) = R\sum_{n=1}^{\infty}\frac{2}{\lambda_n^2-1}\frac{J_1\left(\lambda_n\frac{r}{R}\right)}{J_1(\lambda_n)}\frac{S_\mathrm{e}(T_{cn})}{g}\cos\theta \qquad (3)$$

where $S_\mathrm{e}(T_{cn})$ is the elastic spectral acceleration at first convective frequency. In Fig. 2, distributions of maximum impulsive and convective pressure along the tank height of a described model are shown.

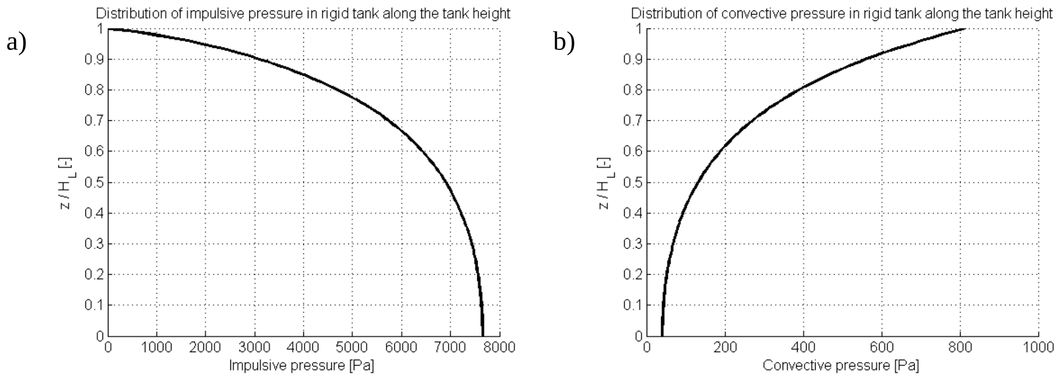

Fig. 2: Distribution of impulsive and convective pressures in the model of rigid tank

2.2. Hydrodynamic pressures in flexible tanks

According to the standard Eurocode 8, hydrodynamic pressure of flexible tanks is usually expressed as the sum of three contributions namely as rigid impulsive, flexible and convective. Flexible contribution satisfies the conditions of radial velocity of liquid along the height to be equal to the deformation velocity of the tank wall, zero velocity at the tank bottom and zero pressure at the free surface of liquid. Due to weak coupling between the second and the third component of hydrodynamic pressure, the flexible component may be determined independently. Weak coupling is a consequence of large differences between natural frequencies of sloshing liquid and tank-liquid system. The rigid impulsive and sloshing component in (1) and (2) remain unaffected. Assuming the modes of vibration $f(\varsigma)$, the flexible pressure distribution on the walls takes form

$$p_\mathrm{f}(\varsigma,\theta,t) = \rho_\mathrm{L}H_\mathrm{L}\psi\cos\theta\sum_{n=0}^{\infty}d_n\cos(\nu_n\varsigma)\,A_{\mathrm{f}n}(t) \qquad (4)$$

where

$$d_n = 2\frac{\int_0^1 f(\varsigma)\cos(\nu_n\varsigma)d\varsigma}{\nu_n}\frac{I_1(\nu_n/\gamma)}{I_1'(\nu_n/\gamma)}$$

$$\psi = \frac{\int_0^1 f(\varsigma)\left[\frac{\rho_S t(\varsigma)}{\rho_\mathrm{L}H_\mathrm{L}}+\sum_{n=0}^{\infty}b_n'\cos(\nu_n\varsigma)\right]d\varsigma}{\int_0^1 f(\varsigma)\left[\frac{\rho_S t(\varsigma)}{\rho_\mathrm{L}H_\mathrm{L}}f(\varsigma)+\sum_{n=0}^{\infty}d_n\cos(\nu_n\varsigma)\right]d\varsigma}$$

$$b_n' = 2\frac{(-1)^n}{\nu_n^2}\frac{I_1(\nu_n/\gamma)}{I_1'(\nu_n/\gamma)}$$

ρ_S is the mass density of the tank, $t(\varsigma)$ is the tank thickness and $A_{\mathrm{f}n}(t)$ is the pseudo-acceleration function corresponding to the natural frequency of the tank-liquid system. In most cases of flexible tanks, the pressure p_f provides predominant contribution to the total pressure, due to the fact, that while the rigid impulsive pressure (1) varies with ground acceleration, the flexible component varies with response acceleration $A_{\mathrm{f}n}(t)$, which may be significantly greater than maximum ground acceleration. Procedure for flexible tanks proposed by A. S. Veletsos (Veletsos, 1974) assumes the tank-liquid system vibrates in a fixed configuration along its height with no distortion of its cross-section. For deflection, it takes three different configurations between base and free surface liquid, like half-sine wave function $\psi_\mathrm{A} = \sin\left(\frac{\pi}{2}\frac{z}{H_\mathrm{L}}\right)$, linear function $\psi_B = \frac{z}{H_L}$ and reversed half-sine function $\psi_C = 1\text{-}\cos\left(\frac{\pi}{2}\frac{z}{H_L}\right)$, where z represents coordinate along the tank height. Fig. 3 a) represents mode of vibration of the tank-liquid system when liquid oscillates in unison with the tank and represents unfavorable response to the system which behaves like uniform cantilever flexural beam. Pressure distribution of flexible contribution of impulsive pressure along the tank height is shown in Fig. 3 b). For estimate of pressure distribution, maximum response acceleration of the tank-liquid system having the period of impulsive mode is assumed. It compares pressure distributions according to the Eurocode 8 and Veletsos's approach. Good conformity can be seen when comparing Eurocode 8 and deflection configuration ψ_A. Using another mentioned deflection configuration in Eurocode 8 computations, similar results as those shown in Fig. 3 b) will be attained.

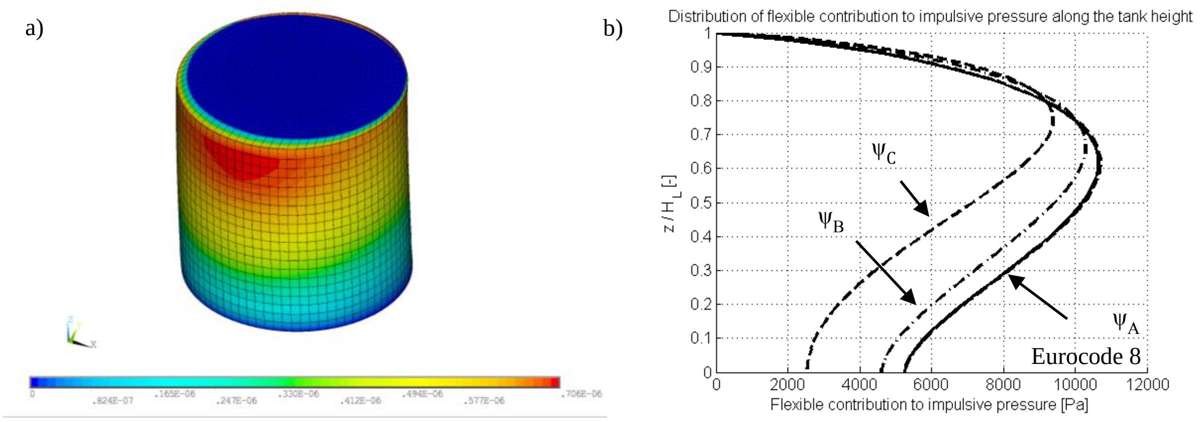

Fig. 3: Impulsive mode and distribution of flexible pressure contribution in the model of flexible tank

3. Conclusions

The aim of this paper was to estimate hydrodynamic pressures in the model of liquid storage tank and to compare acquired results when assuming rigid and flexible tank walls, respectively. It can be concluded that impulsive pressure in rigid tank increases from zero at liquid surface to a maximum at the base, whereas convective pressure reaches maximum at the liquid surface and decreases with depth. It was shown that flexibility of tank wall has impact on the impulsive liquid that experiences accelerations that are greater than peak ground acceleration. Therefore there is a different impulsive pressure distribution assuming additional flexible component which has tendency to shift a peak ordinate from the base to the top as γ increases. Convective pressure due to a weak coupling is not affected by wall flexibility. For design purposes, these effects can be evaluated by considering the tank to be rigid. To sum up, the base shear and overturning moment of flexible tanks calculated by assuming the tank as rigid can be non-conservative.

Acknowledgement

The paper was supported by grant from Grant Agency of VEGA no. 1/0742/15 entitled "Analysis for seismic resistance of liquid storage tanks with nonlinear and time-dependent parameters".

References

Eurocode 8 (1998) Design Provisions of Earthquake Resistance of Structures, Part 4: Silos, Tanks and Pipelines. European Committee for Standardization, Brussels.

Housner, G. W. (1954) Earthquake Pressures on Fluid Containers. Eight Technical Report under Office of Naval Research. California Institute of Technology, Pasadena, California.

Ibrahim, R. A. (2005) Liquid Sloshing Dynamics Theory and Applications. Cambridge University Press, Cambridge, UK, 948 p. ISBN 05-111-2492-9.

Malhotra, P. K., Wenk, T. & Wieland, M. (2000) Simple Procedure for Seismic Analysis of Liquid Storage Tanks, in Structural Engineering, IABSE, Vol. 10, No.3, pp. 197-201.

Musil, M. & Sivý, M. (2015) Dynamic Analysis of Liquid Storage Tank Using FE Method and Results Comparison with Analytical Models, in: ISET 2015, pp. 13-21.

Veletsos, A. S. (1984) Seismic Response and Design of Liquid Storage Tanks. Guidelines for the Seismic Design of Oil and Gas Pipeline Systems. Technical Council on Lifeline Earthquake Engineering (ASCE), New York, USA.

22nd International Conference
ENGINEERING MECHANICS 2016
Svratka, Czech Republic, 9 – 12 May 2016

THE COMPLEX EIGENVALUE ANALYSIS OF BRAKE SQUEAL USING FINITE ELEMENT METHOD

M. Musil*, A. Suchal , J. Úradníček***, P. Kraus******

Abstract: *This paper presents the study of brake squeal, its investigation and suppression, using FEM and complex eigenvalue analysis. This paper supplies with simple FEM model which is used for the main calculation. Complex eigenvalue analysis is applied in order to discover the instability represented by two unstable modes at different values of frequency. Further in this paper the analyses of the influence of two parameters, friction and stiffness, to the system are executed.*

Keywords: Brake squeal, Dynamic instability, Complex eigenvalue analysis, FEM, Mode coupling

1. Introduction

Brakes represent one of the most important safety and performance components of a vehicle. They are important in terms of reliability, braking power as well as in a fluent operation. The unwanted side effect of braking operation is its occasional squeal. Brake squeal is a noise problem caused by friction induced vibrations initiated by the disc rotation (Nouby, 2009). Usually brake squeal occurs in the frequency range between 1 and 20 kHz or even more.

Squeal is considered to be a difficult subject due to complexity of the brake mechanism, its mechanical interactions, significant dependence on many parameters and high sensitivity on operating conditions. Many investigators have been trying to solve this problem since the 1930s, using experimental, analytical and numerical methods in order to understand, prevent and predict squeal occurrence (Culla, 2009) but this problem has not been solved yet.

In studies of North (Ouyang, 2003) and other researchers we can find that the dynamics of brake systems puts in evidence a coincidence between the squeal frequencies and the natural frequencies of the system. Particularly, they associated the squeal phenomenon to the coalescence of two eigen frequencies of the system. Their studies suggested the complex modal analysis of brake systems as a tool for squeal investigation (Massi, 2005). To study the stability of the system by the complex eigenvalues analysis, the friction effects between the pad and the disc are accounted by introducing linear elements in an asymmetric stiffness matrix. Finite element method (FEM) has become the preferred tool in studying disc brake squeal, whereas it offers much faster and more cost efficient solutions than experimental methods and it can predict squeal noise performance at early stage of design development. It is feasible to apply transient analysis or complex eigenvalue analysis. Complex eigenvalue analysis is more convenient since transient is more time consuming.

* Ass. Prof. Ing. Milos Musil, PhD.: Institute of applied mechanics and mechatronics, Slovak University of Technology in Bratislava, Nam. slobody 17, 812 31 Bratislava 1, SK; milos.musil@stuba.sk

**Ing. Andrea Suchal, PhD.: Institute of applied mechanics and mechatronics,Slovak University of Technology in Bratislava, Nam. slobody 17, 812 31 Bratislava 1, SK; andrea.babalova@stuba.sk

***Ing. Juraj Úradníček, PhD.: Institute of manufacturing systems, environmental technology and quality management, Slovak University of Technology in Bratislava, Nam. slobody 17, 812 31 Bratislava 1, SK; juraj.uradnicek@stuba.sk

****Ing. Pavel Kraus: Institute of applied mechanics and mechatronics,Slovak University of Technology in Bratislava, Nam. slobody 17, 812 31 Bratislava 1, SK; pavel.kraus@stuba.sk

2. Basic model, theories and mechanisms of brake squeal

The first experimental investigation discovered that squeal could have been caused by the variation of friction coefficient μ at the contact interface. In 1938 Mills claimed that squeal was associated with the negative gradient characteristics of dynamic friction coefficient against the sliding velocity v. Later on, the stick-slip phenomenon had been described as unstable due to the static coefficient of friction μ_s (stick), higher than the dynamic μ_d (sliding) and this led to low sliding speed friction induced vibration instability. Both mechanisms led to unstable oscillation and had risen to self-excited vibration in the system (Duffour, 2002).

Later Fosberry and Holubecki (Frosberry, 1961) suggested that the disc brake tended to squeal when either a static coefficient of friction was higher than the dynamic coefficient or a dynamic coefficient decreaseed with increase of speed presented in the contact interface. But subsequent experiments proved that brake squeal could occur even though the friction coefficient was constant or even with a slight increase of relative velocity in the contact surface (Kinkaid, 2003). In 1962 Spurr came up with the sprag-slip model, which claimed that unstable friction induced oscillations occur even with a constant friction coefficient.

During squeal the friction material is deflected elastically along the disc surface by the frictional force (Ouyang, 2009). This deflection causes a second deflection with a component normal to the surface of the pad which reduces the friction and the stored elastic energy returns the system to the first configuration, and the cycle is repeated. Therefore, as a response to many tests and analysis, next studies were concerned to describe brake squeal as a friction induced self-excited mode coupling vibration with constant friction coefficient μ (Hoffmann, 2002).

Using complex eigenvalue analysis, it is possible to obtain the dependency of eigenvalues, which indicates the instability of such system as a function of various parameters, for instance force, relative velocity, particular stiffnesses as well as the friction coefficient.

3. Development of simple FE model

For investigation of squeal a simple FE model had been created (Fig. 1) using FEM. This model composes of a disc, brake pads and pads' back plates. It was created for nonlinear analysis and complex eigenvalue extraction in purpose of stability examination. The model was used for calculations when investigating the influence of two system parameters: the change of the friction coefficient and the stiffness of the disc. This model does not reflect dependency on disc angular velocity and normal force because we assume constant friction coefficient. All the mechanical, inertial, stiffness and geometrical properties including the contact properties, between the pad and the disc, were done in ANSYS environment. After creation of this model static and modal analysis were applied.

Particular geometry of the brake assembly parts were distinguished according to the real brake assemblies and material parameters gained from experiments (Suchal, 2013).

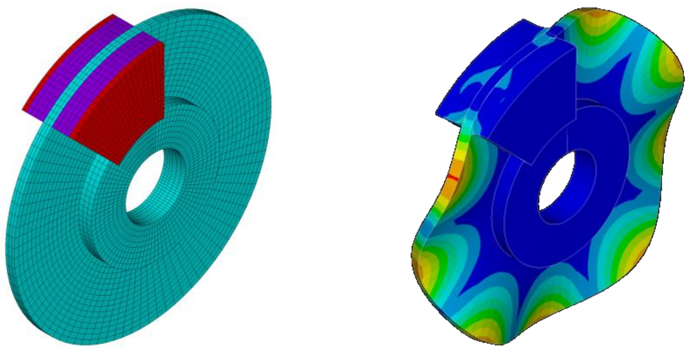

Fig. 1: Simple FE model and typical stable vibration mode

The first step was to create a FE model of a disc brake by defining all the stiffness and inertial properties of the system. The second step was the application of pre-stressed static analyses for definition of contact and contact elements. The third step was to apply dynamical analysis for the rotation of the disc what gave the asymmetric stiffness matrix. The final step was application of modal analysis for non-symmetric systems matrices, in order to calculate eigenvalues of the system.

4. Influence of different parameters on brake squeal

This section deals with the investigation of the effects of system parameters on squeal occurrence. It starts with changing the value of friction coefficient, followed by the analysis the influence of stiffness of the disc.

4.1. Investigation of instability due to variable value of friction coefficient

In the following the instability will be called mode-coupling type (among the other names in literature are non-conservative displacement dependent forces and binary flutter). This instability is characterized by the process of the creation of the unstable frequencies. The oscillation frequencies of two stable structural modes of an undamped system come, as a function of a control parameter (friction value), closer and closer until they merge together and a pair of an unstable and stable mode is created (Hoffmann, 2002).

The results include the frequencies at which the squeal phenomenon occurs. The evolution of two frequencies is investigated by changing the friction coefficient μ in range $\langle 0 - 1 \rangle$.

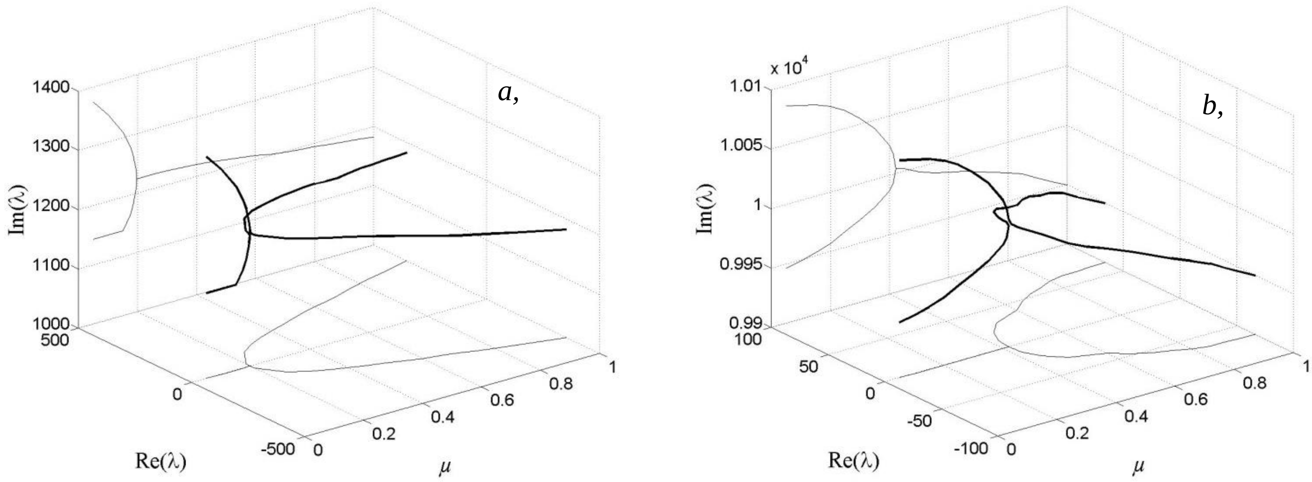

Fig. 2: Mode coupling gained from calculated data: a, first mode; b, second mode

For each value of the friction coefficient the complex eigenvalue analysis was executed. The results of the analysis are a list with complex eigenvalues and modes. Reviewing the list of complex eigenvalues the attention was paid to positive real part. Fig. 2 displays the evolution of real parts as a function of the friction coefficient. Firstly, the system features two separate modes in the frequency range; these two modes are stable since their real parts are zero. As the friction coefficient increases, the figure shows that the real parts remain zero and that the frequencies tend to get closer. The two modes reach the same frequency at a point known as the “bifurcation point” (Fig. 3). After that point, the system behavior is deeply altered (Fritz, 2002). Indeed, the frequencies remain equal but the real parts become non-zero and opposite.

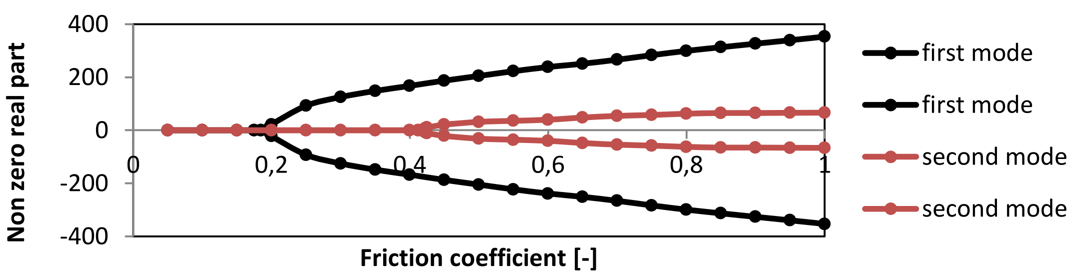

Fig. 3: The first two unstable Eigen modes of the disc brake assembly

4.2. Effect of changing stiffness of the disc and back plate on brake squeal

Investigation of the effect of the disc stiffness on brake squeal was studied by changing the Young modulus of elasticity in range $\langle 85 - 115\ \% \rangle$ according to reference value of $E_D = 1.975\text{e}11$ Pa. The analysis was performed on the first unstable mode because of the higher instability level (Fig. 3). As the Young modulus increased, the stiffness of the disc increased as well and the value of instability dropped significantly. The graphical results show the dependency between different values of the disc stiffness and the instability (Fig. 4). It is assumed that by increasing stiffness, it is possible to reduce squeal propensity and disc vibration magnitude.

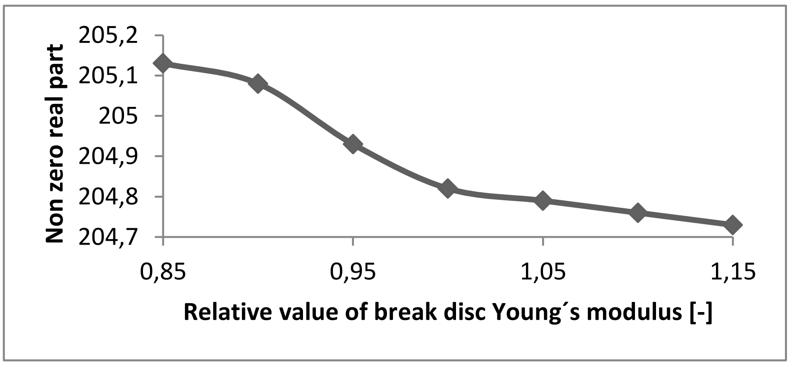

Fig. 4: Disc stiffness vs. instability dependency.

5. Conclusion

This work deals with the problem of brake squeal, its investigation and suppression. The instability causing brake squeal by gaining two unstable modes at different values of frequency is discovered by using the complex eigenvalue analysis on simple finite element model. It was found out that incensement of the friction coefficient results in higher squeal propensity.

The next investigation was the stiffness vs. instability dependence. Squeal can be reduced by increasing the Young's modulus of the brake disc.

The brake squeal problem is still under investigation. There has not been found any proper solution how to suppress this phenomenon completely. It is due to complexity of its mechanism and the influence of numerous parameters and side effects including thermal influence.

Acknowledgement

The paper was supported by grant from Grant Agency of VEGA no. 1/0742/15.

References

Culla A., Massi F. (2009) Uncertainty model for contact instability prediction. J. Acoust. Soc. Am. 126, 1111.

Duffour P. (2002) Noise generation in vehicle brakes, Dissertation, Cambridge University.

Fritz G., Sinou J.-J., Duffal J.-M., Jézéquel L. (2007) Investigation of the relationship between damping and mode coupling patterns in case of brake squeal, Journal of Sound and Vibration, Vol.307(3), pp.591-609.

Frosberry R.A.C., Holubecki Z. (1961) Disc brake squeal, its mechanism and suppression, Motor Industry Research Association, Lindley.

Hoffmann N., Fischer M., Allgaier R., Gaul L. (2002) A minimal model for studying properties of the mode-coupling type instability in friction induced oscillations, Mechanics Research Communications, Vol.29(4), pp.197-205.

Kinkaid N.M., O'Reilly O.M., Papadopoulos P. (2003) Automotive disc brake squeal. Journal of Sound and Vibration, Vol.267(1), pp.105-166.

Massi F., Baillet L. (2005) Numerical analysis of squeal instability, International Conference on Emerging Technologies of Noise and Vibration Analysis and Control, NOVEM2005, 1- 10.

Nouby M., Mathivanan D., Srinivasan K. (2009) A combined approach of complex eigenvalue analysis and design of experiments to study disc brake squeal. International Journal of Engineering, Science and Technology, 1, 1, pp. 254-271.

Ouyang H., Cao Q., Mottershead J. E., Treyde T. (2003) Vibration and squeal of a disc brake: Modelling and experimental results, Journal of Automobile Engineering, 1/1/2003, Vol.217(10), pp.867-875.

Ouyang H., Nack W., Yuan Y., Frank Ch. (2009) Numerical analysis of automotive disc brake squeal;a review, Int. J. Vehicle Noise and Vibration, Vol. 1, Nos. ¾,pp. 207-231.

Suchal A. (2013) Influence of thermal effects on dynamics of disc brakes and brake squeal, Dissertation, Slovak University of Technology, Bratislava.

22nd International Conference
ENGINEERING MECHANICS 2016
Svratka, Czech Republic, 9 – 12 May 2016

PRESS WEIGHTED AVERAGE SURROGATE: TRIAL TESTS IN 2D

E. Myšáková[*], M. Lepš[**]

Abstract: *Surrogate modeling (Meta-modeling) is an often used tool for analysis of behavior of complex systems which are usually described by computationally demanding models. Surrogate models provide an approximation of the original model's response in a fraction of time and therefore are suitable when multiple evaluations are needed. Many types of meta-models exist and each suits another type of problem. On the other hand it is not always possible to select the right meta-model in advance. Therefore parallel construction of several meta-models and their subsequent comparison and combining can be utilized with advantage. A typical method called PRESS weighted average surrogate which uses the prediction sum of squares obtained by cross-validation for computation of the weights for linear combination of individual surrogates is discussed in this contribution and illustrated on several 2-dimensional benchmark examples using a group of different meta-models.*

Keywords: **Meta-modeling, Ensemble of Surrogates, Cross-validation, Root Mean Square Error, Prediction Sum of Squares.**

1. Introduction

Surrogate modeling (Meta-modeling) constitutes a tool usable for analyses of complex systems which are described by computationally demanding models. Such models cannot be used when multiple evaluations are necessary, for example in Monte Carlo based reliability assessment of the system. In such case the meta-model represents a convenient substitution: it provides an approximation of the original model's response in a fraction of time.

A surrogate model is constructed based on training data which consist of i) training points spread over the design domain as uniformly as possible and ii) responses of the original model in training points. The positions of the points are selected via Design of Experiments (DoE) (Montgomery, 2012). Many types of surrogate models exist and each of them consists of surrogates differing in particular settings which results in a wide group of available meta-models. Therefore it is a logical step to use at least several of them at parallel.

This contribution is focused on an approach for combination of multiple meta-models. The methodology follows the procedure described in (Goel et al., 2007; Viana et al., 2009). The resulting surrogate is created as a linear combination of predictions of the individual meta-models and the weights of individual meta-models are computed based on their quality estimated by cross-validation. The methodology is tested on several illustrative 2-dimensional examples to get a good overview of the procedure. Ten different meta-models are used within the combination.

2. Methodology

The methodology described in this contribution deals with a set of meta-models constructed on the same training data which are selected via LHS design (Iman & Conover, 1980). The number of training points, i.e. the size of the DoE, is 11, 25 and 100. Each constructed meta-model is then tested using four randomly generated testing data sets (10, 100, 1000 and 10000 testing points). Such testing is possible

[*] Ing. Eva Myšáková: Faculty of Civil Engineering, Czech Technical University in Prague, Thákurova 7, 166 29, Prague, CZ, eva.mysakova@fsv.cvut.cz

[**] doc. Matěj Lepš, PhD.: Faculty of Civil Engineering, Czech Technical University in Prague, Thákurova 7, 166 29, Prague, CZ, leps@cml.fsv.cvut.cz

only because the original model is not computationally demanding; in practical use the large testing data sets cannot be used. The second way of testing the meta-models is cross-validation where the training data are used also for testing. In particular, the leave-one-out cross-validation is utilized. Cross-validation represents a type of testing usable with a real demanding original model because it requires no more original model's evaluations.

2.1. Root Mean Square Error

Having $y(\mathbf{x})$ the actual simulation at the point $\mathbf{x}$, $\hat{y}(\mathbf{x})$ the surrogate's prediction and $e(\mathbf{x}) = y(\mathbf{x}) - \hat{y}(\mathbf{x})$ the error associated with this prediction, the actual root mean square error over the domain with volume V is given by:

$$RMSE_{actual} = \sqrt{\frac{1}{V}\int_V e^2(\mathbf{x})d\mathbf{x}}\,. \tag{1}$$

When using Monte Carlo integration with p_{test} testing points the formula transforms into:

$$RMSE = \sqrt{\frac{1}{p_{test}}\sum_{i=1}^{p_{test}} e_i^2}\,, \tag{2}$$

where $e_i = y_i - \hat{y}_i$ is the error at the i-th testing point.

2.2. Predicted Residual Sum of Squares

When the testing set of points cannot be used a common way for evaluation of the surrogates' accuracy is a cross-validation where training points are used also for testing. Having p training points the leave-one-out cross-validation is performed by constructing p surrogates each of them with one of the training points excluded. Each surrogate is then used for prediction of the excluded point's response. The prediction sum of squares firstly proposed in (Allen, 1974) is then computed using the vector of cross-validation errors (PRESS vector) $\tilde{\mathbf{e}}$. An estimation of the $RMSE$ using PRESS vector is given by:

$$PRESS_{RMS} = \sqrt{\frac{1}{p}\tilde{\mathbf{e}}^T\tilde{\mathbf{e}}}\,. \tag{3}$$

2.3. PRESS Weighted Average Surrogate

When constructing n meta-models in parallel the possible and intuitive way of their utilization is their weighted averaging. Naturally, the weights are derived from the individual surrogate's prediction quality. The average surrogate's prediction $\hat{y}_{WAS}(\mathbf{x})$ is then given by a linear combination of individual meta-model's predictions $\hat{\mathbf{y}}(\mathbf{x})$ using weights $\mathbf{w}(\mathbf{x})$:

$$\hat{y}_{WAS}(\mathbf{x}) = \sum_{i=1}^{n} w_i(\mathbf{x})\hat{y}_i(\mathbf{x}), \quad \sum_{i=1}^{n} w_i(\mathbf{x}) = 1\,. \tag{4}$$

The heuristic computation of the weights proposed in (Goel et al., 2007) is based on the PRESS estimation of the root mean square error, $PRESS_{RMS}$. The resulting average surrogate is called PRESS Weighted Average Surrogate (PWS). The weights computation is given by:

$$w_i = \frac{w_i^*}{\sum_{j=1}^{n} w_j^*}, \quad w_i^* = (E_i + \alpha E_{avg})^{\beta}\,, \tag{5}$$

$$E_{avg} = \frac{1}{n}\sum_{i=1}^{n} E_i, \quad \beta < 0, \alpha < 1, \tag{6}$$

where E_i is the $PRESS_{RMS}$ of the i-th surrogate model and recommended values of parameters are $\alpha = 0.05$ and $\beta = -1$.

3. Used surrogates and examples

The methodology was tested using several types of surrogate models with various inner settings which resulted in ten different meta-models in total. Their short descriptions are listed in Table 1.

Tab. 1: Used surrogate models.

Meta-model No.	Description
1	Kriging (zero order polynomial regression function, cubic correlation function)
2	Kriging (first order polynomial regression function, spherical correlation function)
3	newrbe (Radial Basis Neural Network available in MATLAB)
4	RBFN (Radial Basis Function Network with zero order polynomial regression function)
5	RBFN (Radial Basis Function Network with first order polynomial regression function)
6	RSM (Response Surface Methodology with first order polynomial regression function)
7	RBFN (Radial Basis Function Network without regression part)
8	PCE (Polynomial Chaos Expansion using Hermite polynomials of 3^{rd} degree)
9	PCE (Polynomial Chaos Expansion using Legendre polynomials of 3^{rd} degree)
10	RSM (Response Surface Methodology with second order polynomial regression function)

Seven benchmarks from (Andre et al., 2001) were used for testing. All of them have 2 input parameters which result in 2-dimensional design domain as shown in Figure 1.

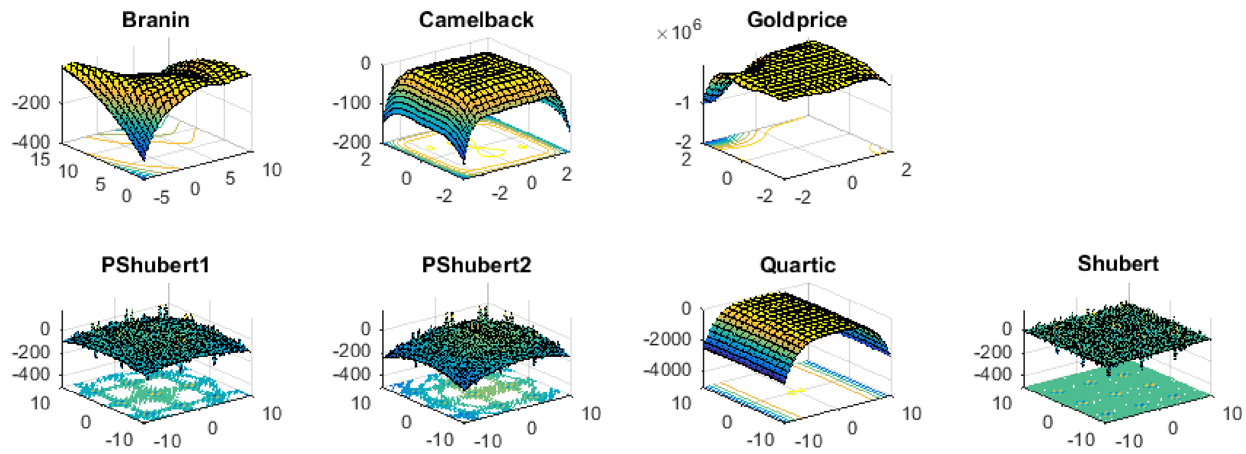

Fig. 1: Visualization of benchmark examples. Horizontal axes represent input parameters; vertical axis represents model's response.

4. Results and conclusions

The surrogate models were constructed based on 3 different optimized designs of experiments (with 11, 25 and 100 points). For each of them 100 random testing sets with 10^4, 10^3, 10^2 and 10 points were generated and used for computation of the *RMSE*. It was shown that the ranking of the meta-models remains almost the same no matter the number of training points or the testing points as depicted in Figure 2. Naturally, the spread of the values is significantly wider with decreasing number of testing points but the comparison of the surrogates' approximation quality is adequate even with the smallest testing set. Figure 3 shows the $PRESS_{RMS}$ obtained by the cross-validation of the training points which correspond to the weights of individual surrogates in the linear combination in the PWS. The results for the training set with 11 points were excluded because they would devalue the resulting graphs. The cross-validation led to very high errors in case of meta-models no. 8 and 9 (PCE). It is surprising because the *RMSE* for these meta-models come out well and ten training points used during the leave-one-out cross-validation is enough in case of the 3^{rd} degree of polynomials.

The stated simple testing on the PWS indicates possibility of usage of several surrogates at parallel and their follow-up combination. The results suggest that the weights for the linear combination could be computed using a small testing set rather than by the cross-validation based computation.

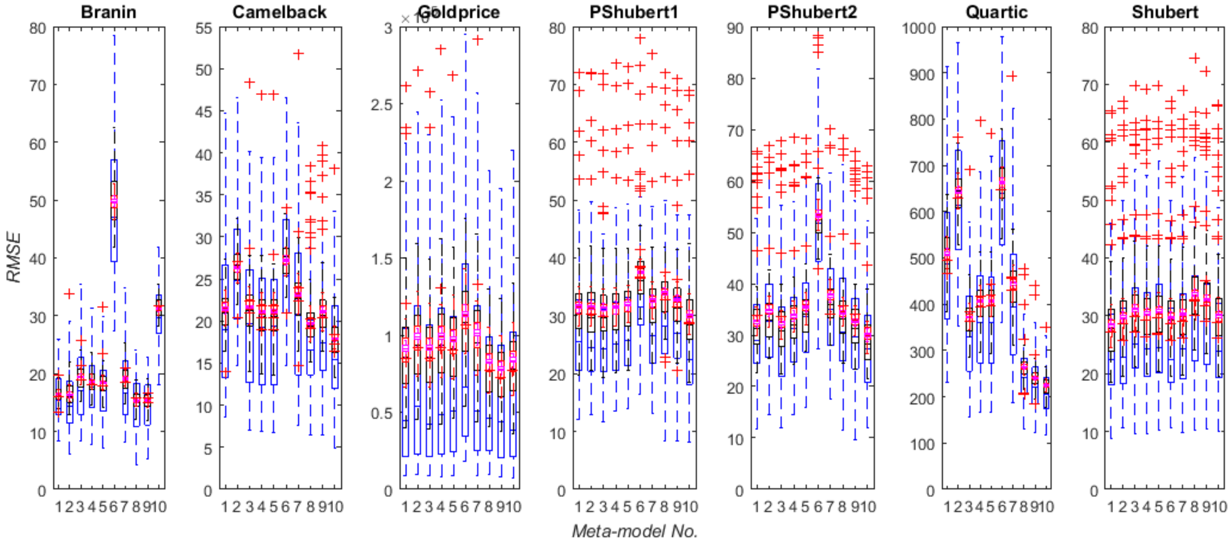

Fig. 2: Comparison of RMSE obtained by testing sets of different sizes (blue - 10^1, black - 10^2, red - 10^3, magenta - 10^4 points). Boxplots correspond to meta-models trained on the set with 11 points.

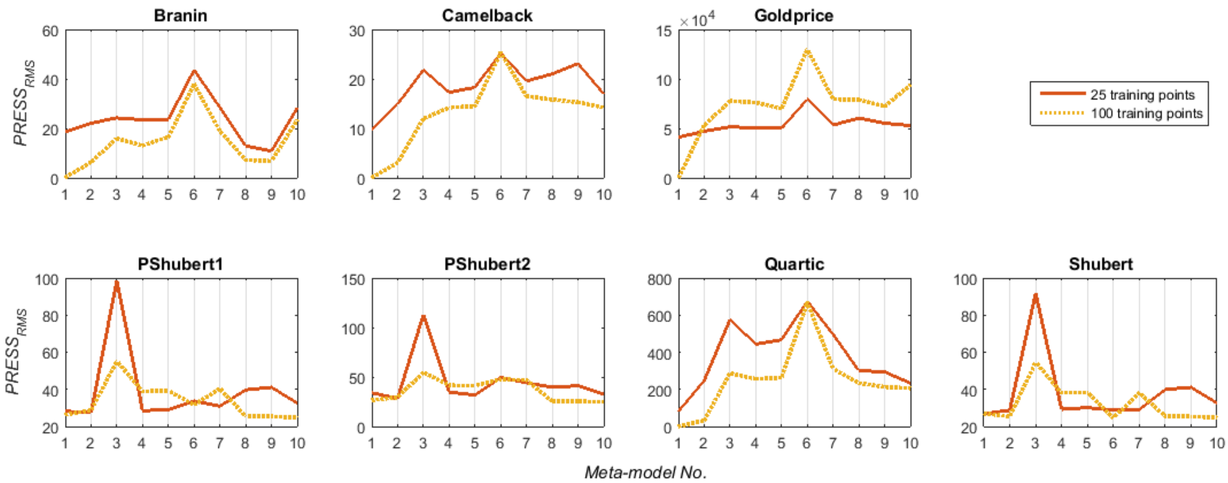

Fig. 3: Estimation of RMSE from PRESS vector obtained by leave-one-out cross-validation.

Acknowledgement

Financial support from the Ministry of Education, Youth and Sports of the Czech Republic, Project No. 8F15004, the Czech Science Foundation, Project No. 15-07299S, and the Grant Agency of the Czech Technical University in Prague, Project No. SGS16/037/OHK1/1T/11, is gratefully acknowledged.

References

Allen, D. M. (1974) The relationship between variable selection and data augmentation and a method for prediction. Technometrics, 16, pp.125-127.

Andre, J., Siarry, P. & Dognon, T. (2001) An improvement of the standard genetic algorithm fighting premature convergence in continuous optimization. Advances in Engineering Software, 32, 1, pp.49-60.

Goel, T., Haftka, R.Shyy, W. & Queipo, N. (2007) Ensemble of surrogates. Structural and Multidisciplinary Optimization, 33, 3, pp.199-216.

Iman, R. L. & Conover, W. J. (1980) Small sample sensitivity analysis techniques for computer models, with an application to risk assessment. Communications in Statistics: Theory and Methods, A9, pp.1749-1842.

Montgomery, D. (2012) Design and Analysis of Experiments, 8th Edition. John Wiley & Sons, Incorporated.

Viana, F., Haftka, R. & Steffen, V. J. (2009) Multiple surrogates: How cross-validation errors can help us to obtain the best predictor. Structural and Multidisciplinary Optimization, 39, 4, pp.439-457.

22nd International Conference
ENGINEERING MECHANICS 2016
Svratka, Czech Republic, 9 – 12 May 2016

NON-LINEAR NORMAL MODES IN DYNAMICS-
-CONTINUOUS SYSTEMS

J. Náprstek[*], C. Fischer[**]

Abstract: *The paper presents a continuation of an effort started last year, when the authors briefly informed about the Non-linear normal modes (NNM) concerning the version dealing with discrete systems. Although many features of the continuous formulation from the mathematical viewpoint are similar to the discrete case, a couple of specifics should be highlighted from the viewpoint of a real applicability of this tool to investigate particular dynamic systems. Three approaches are mentioned in the paper and the Galerkin-Petrov based procedure is outlined in more details. As a particular subject the cantilever prismatic beam is discussed. Non-linear normal modes for several amplitudes are shown to demonstrate the dependence of their shapes on the actual effective amplitude. Comparison with adequate linear counterpart is done.*

Keywords: Nonlinear dynamic systems, non-linear normal modes, discretization, multi-scale method

1. Introduction

The concept of the natural mode decomposition is very popular in linear area for many reasons, which are widely known. As it has been reported earlier this concept has been generalized to non-linear systems, for instance Nayfeh (1994), Shaw S.W. (1994) and many others. A large review can be found in pioneering papers by Vakakis and in the monograph by Vakakis et al. (1996). While most of the useful properties of linear modes cannot be reflected in the nonlinear area, invariant motions on a two-dimensional manifold can be found. Such motions have been named as nonlinear mode motions and the relevant method as Nonlinear Normal Mode (NNM) decomposition. This discipline is developing roughly some 30 years, although older papers dealing with this idea have appeared since early 60s, e.g., Rosenberg (1960, 1966), etc. Nevertheless, a lot of papers have been published during last years dealing with various special aspects of NNM, see for instance Kerschen (2009) - numerical implementations, Lenci (2007) - systems with internal resonance, etc.

In the previous paper the authors informed briefly about the version concerning discrete systems, see Náprstek (2015) with reference to the first paper appeared in Czech literature related with NNM, see Byrtus (2012). Regarding a continuous system, a couple of approaches are considered in the literature being based on methods commonly used in nonlinear dynamics:

(i) Time coordinate is anticipated in a form of a suitable periodic function $\varphi(t)$ (not necessarily harmonic) and the unknown displacement is sought in the form of $w(x,t) = v(x)\varphi(t)$. This expression is substituted into the governing system and then the method of the harmonic balance of an adequate level is used. This results in a boundary value problem for $v(x)$ which can serve to obtain a set of NNMs.

(ii) The Galerkin-Petrov procedure is applied to discretize the original problem. The displacement can be written in a form:

$$w(x,t) = \sum_{i=1}^{N} v_i(x)\varphi_i(t) \tag{1}$$

[*] Ing. Jiří Náprstek, DrSc.: Institute of Theoretical and Applied Mechanics, Prosecká 76; 190 00, Prague; CZ, naprstek@itam.cas.cz
[**] RNDr. Cyril Fischer, PhD.: Institute of Theoretical and Applied Mechanics, Prosecká 76; 190 00, Prague; CZ, fischerc@itam.cas.cz

where $v_i(x)$ are the linear undamped mode shapes. Then the expression (1) is substituted into the original nonlinear system and the Galerkin-Petrov procedure of orthogonalization in the space of admissible functions is subsequently performed. This results to a system of coupled ODEs for unknown time coordinates $\varphi_i(t)$. Thus, the NNMs are formulated as time variable linear combinations of linear modes. As the linear eigen modes are used as coordinate functions, all boundary conditions are implicitly fulfilled and optimal convergence is guaranteed.

(iii) NNMs and amplitude dependent eigen frequencies can be determined by applying the method of multiple scales directly to the governing partial differential equation and boundary conditions. Basically similar procedure as it is known in the perturbation method is performed.

As a particular case we treat a strait prismatic console with axial nonlinear effects due to the axial load and other effects depending on static and dynamic processes, see for instance Crespo da Silva & Glyn (1978). Following partial differential equation can be written:

$$\begin{aligned}
&\ddot{w}(x,t)+w''''(x,t)+Q[w(x,t)]=0,\\
&w(0,t)=0,\ \ w'(0,t)=0,\ \ w''(1,t)=0,\ \ w'''(1,t)=0,\\
&Q[w(x,t)]=[w'(x,t)\,(w'(x,t)\,w''(x,t))']'+\Big[w'(x,t)\int_1^x\int_0^\xi(\dot{w}(\zeta,t)'^2+w'(\zeta,t)\ddot{w}'(\zeta,t)\,d\zeta\,d\xi\Big]'
\end{aligned}\tag{2}$$

where $w(x,t)$ denotes the vertical displacement of the console and $Q[w(x,t)]$ represents the non-linear part of the equation comprising effects of the deformed system, the symbols $\bullet'$, $\dot{\bullet}$ indicate differentiation with respect to space or time, respectively. Concerning $Q[w(x,t)]$, a lot of more complex or simpler variants are available in literature. Their form is dependent on nonlinear effects which are important from the viewpoint of respective bifurcations and post-critical processes.

2. Discretized system

Let us demonstrate application of the 2nd solution process, see (ii) and Eq. (1). We consider the series:

$$w(x,t)=\sum_{i=1}^{\infty}v_i(x)\,\varphi_i(t)\tag{3}$$

where $\varphi_j(t)$ are the relevant time coordinates and $v_i(x)$ are linear mode shapes of Eq. (2):

$$\begin{aligned}
&v_i(x)=\cosh\lambda_i x+\cos\lambda_i x+\beta_i(\sin\lambda_i x+\sinh\lambda_i x)\\
&\beta_i=\frac{(\cosh\lambda_i+\cos\lambda_i)}{(\sin\lambda_i+\sinh\lambda_i)},\qquad 1+\cosh\lambda_i\cos\lambda_i=0
\end{aligned}\tag{4}$$

Substituting Eq. (3) into (2) and performing Galerkin's operations we obtain differential system for $\varphi_i(t)$:

$$\begin{aligned}
&\ddot{\varphi}_i+\omega_i^2\varphi_i+R_i(\varphi_i,\dot{\varphi}_i,\ddot{\varphi}_i)=0\\
&R_i=\int_0^\xi v_i(\xi)\cdot Q\Big[\sum_{i=1}^n v_j(\xi)\varphi_j(t),\sum_{i=1}^n v_j(\xi)\dot{\varphi}_j(t),\sum_{i=1}^n v_j(\xi)\ddot{\varphi}_j(t)\Big]d\xi
\end{aligned}\tag{5}$$

The term $Q\,[\cdot,\cdot,\cdot]$ in (5) symbolically comprises value and two time derivatives of $w(x,t)$. We approximate the nonlinear parts R_i in Eq. (5) employing decomposition:

$$\begin{aligned}
&R_i(\varphi_j,\dot{\varphi}_j)=(g_{1ij}-\omega_j^2 g_{2ij})\varphi_j^3+g_{2ij}\varphi_j\dot{\varphi}_j^2+\dots,\\
&\text{where:}\quad g_{1ij}=\int_0^1 v_i(\xi)\,Q_1(v_j(\xi))\,d\xi,\quad g_{2ij}=\int_0^1 v_i(\xi)\,Q_2(v_j(\xi))\,d\xi,\\
&Q_1(v_j(\xi))=(v_j'(v_j'v_j'')')',\qquad Q_2(v_j(\xi))=(v_j'\int_1^\xi\int_0^\zeta v_j'^2\,d\chi\,d\zeta)'
\end{aligned}\tag{6}$$

It can be shown, cf. Nayfeh (1994), that movement of the system in the *i*-th eigen mode can be written as:

$$
\begin{aligned}
&w_i(x,t) = v_i(x)\varphi_i(t) + \sum_{i\neq j} v_j(x)[\Gamma_{1ij}\varphi_j^3(t) + \Gamma_{2ij}\varphi_j(t)\dot{\varphi}_j^2(t) + \ldots] \\
&\Gamma_{1ij} = [(7\omega_j^2 - \omega_i^2)g_{1ij} - (5\omega_j^2 - \omega_i^2)\omega_j^2 g_{2ij}]/\Delta_{ij} \\
&\Gamma_{2ij} = [6g_{1ij} - (3\omega_j^2 + \omega_i^2)g_{2ij}]/\Delta_{ij}, \qquad \Delta_{ij} = (\omega_j^2 - \omega_i^2)(9\omega_j^2 - \omega_i^2)
\end{aligned}
\tag{7}
$$

We avoid until now cases $\omega_i \approx \omega_j$, $\omega_i \approx 3\omega_j$ leading to internal resonance. They produce homoclinic orbits and should be treated separately at the center manifold. Such cases occur in practice and cannot be omitted. However, a special study should be devoted to these effects, in particular regarding continuous systems. Nevertheless, the structure of Eq. (7) exhibits that every nonlinear eigen mode captures the contribution of all other linear modes. Hence the modal motion time history is given by expression:

$$
\begin{aligned}
&\varphi_i(t) = a_i \cos(\omega_{Ni}t + \beta_{i0}) + \frac{g_{1ii} - 2\omega_i^2 g_{2ii}}{32\omega_i^2} a_i^3 \cos(3\omega_{Ni}t + 3\beta_{i0}) + \mathrm{K} \ , \\
&\omega_{Ni} = \omega_i + \frac{1}{8\omega_i}(3g_{1ii} - 2\omega_i^2 g_{2ii})a_i^2 + \mathrm{K}
\end{aligned}
\tag{8}
$$

where ω_{Ni} is the nonlinear eigen frequency of the *i*-th mode. Depending on the initial conditions are a_i, β_{i0} constants, which represent first approximation to the amplitude and phase of the motion.

3. Numerical experiments

In order to illustrate the above considerations we outlined first three nonlinear modes for different amplitudes and compared them with adequate modes reflecting the linear approach. Certain amplitude estimates with respect to time have been evaluated using Eq. (7):

$$
w_i^*(x) = v_i(x)\varphi_i^* + \sum_{i\neq j} v_j(x)[\Gamma_{1ij}\varphi_j^{*3} + \mathrm{K}\,]
\tag{9}
$$

where it has been substituted: $w_i^*(x) = w_i(x,t^*)$, $\varphi_i^*(x) = \varphi_i(x,t^*)$ and $\dot{\varphi}_i^*(x) = 0$, t^*- time providing a maximum of $\varphi_i(t^*) = \varphi_{ic}$. The shape of modes (linear/nonlinear) is normalized in a usual way:

$$
\int_0^1 w_i^2(\xi,t^*)\,d\xi = 1
\tag{10}
$$

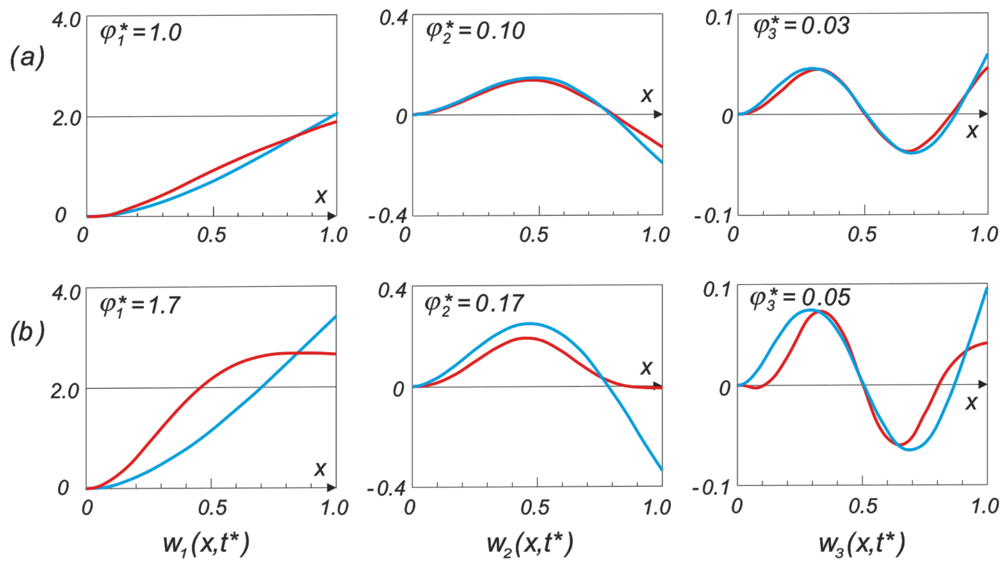

Fig. 1: Normal modes at a prismatic console: (a) linear approach - blue; (b) non-linear approach - red.

which enables to compare transparently the linear (blue) and nonlinear (red) modes for corresponding i and $\varphi_i^*(x)$ in Fig. 1. The upper triplet (a) corresponds to lower amplitude $\varphi_i^*(x)$ and the lower triplet (b) to higher amplitude $\varphi_i^*(x)$. In the latter case the differences between linear and nonlinear mode variants are higher. Differences between relevant modes increase starting zero with rising nonlinearity ratio. Because the whole solution process is approximate, there exists a critical limit φ_{ic} beyond which the convergence of the series (3) fails. Therefore it should be admitted that the above procedure works in a domain of weak nonlinearities. It is worthy to note that besides the variant (ii) - Galerkin-Petrov procedure, also the remaining variants (i) and (iii) have been processed and numerically validated. It can be concluded that especially the variants (ii) and (iii) provided very similar results of a semi-analytical investigation. Moreover, the numerical results coincided perfectly, when parameters put the system into a sub-critical domain.

4. Conclusions

Systems with continuously distributed parameters enable to construct the nonlinear normal modes. Their character and mathematical properties slightly differ from those defined for discrete systems with a couple of concentrated masses. To define the nonlinear normal modes, a discretization of the continuous system should be performed similarly like in the case of linear systems. One possibility being based at Galerkin-Petrov approach has been outlined and demonstrated at prismatic nonlinear console beam.

On the other hand, some shortcomings should also be taken into account. A system with an internal resonance between two or more modes becomes singular (remember a case of a multiple resonance of linear systems) and such modes cannot be uncoupled. Care should be taken as the system can change its character when additional energy is introduced. The internal resonance can occur due to non-linearity, despite of that under low level excitation no internal resonance exists. In such a case, a more complicated invariant manifold with more coordinates must be constructed or a center manifold formulation should be used usually together with homoclinic orbits appearance.

Finally, balancing strengths and weaknesses of NNM the advantages significantly dominate. This tool enables to concentrate analysis to the most important parts of the general response (NNM) and to consider only modes including the most of energy.

Acknowledgement

The kind support of the Czech Scientific Foundation No. GA CR 15-01035S and RVO 68378297 institutional support are gratefully acknowledged.

References

Byrtus, M. & Zeman, V. (2012) Alternative methods for vibration analysis of friction blade coupling. In: Proc. Dynamics of Machines 2012 (L. Pešek edt.), IT ASCR, Prague, 23-28.

Crespo da Silva, M.R.M. & Glyn, C.C. (1978) Nonlinear flexural-flexural-torsional dynamics of inextensional beams-I. Equations of Motion. Jour. Structural Mechanics, 6, 437-448.

Kerschen G., Peeters M., Golinval, J.C., Vakakis A.F. (2009) Non-linear normal modes, Part I: A useful framework for the structural dynamicist. Mechanical Systems and Signal Processing, 23, 170-194.

Lenci, S. & Rega, G. (2007) Dimension reduction of homoclinic orbits of buckled beams via the non-linear modes technique. Int. Jour. Non-linear Mechanics, 42, 515-528.

Náprstek, J. & Fischer, C. (2015) Non-linear normal modes in dynamics - discrete systems. Applied Mechanics and Materials, 821, 254-265.

Nayfeh, A.H. & Nayfeh, S.A. (1994) On nonlinear modes of continuous systems. Jour. Vibration and Acoustics, 116, 129-136.

Rosenberg R.M. (1960) Normal modes of non-linear dual-mode systems. Jour. Applied Mechanics, 27, 263-268.

Rosenberg R.M. (1966) On non-linear vibrations of systems with many degrees of freedom. Advances in Applied Mechanics, 9, 155-242.

Shaw S.W. (1994) Normal modes of vibration for non-linear continuous systems. Jour. Sound and Vibration, 169(3), 319-347.

Vakakis, A.F., Manevitch, L.I., Mikhlin, Y.V., Pilipchuk, V.N. & Zevin, A.A. (1996) Normal modes and localization in non-linear systems. Wiley, New York,.

22nd International Conference
ENGINEERING MECHANICS 2016
Svratka, Czech Republic, 9 – 12 May 2016

SOLUTION OF DYNAMICS AND ACOUSTICS BY VIRTUAL POWERTRAIN

P. Novotný[*], M. Zubík[**], A. Prokop[***], K. Řehák[****]

Abstract: *An advanced computational model suitable for the development of a modern powertrain in the field of noise and vibration is introduced. The advanced computational model of the powertrain is developed as a powerful tool for the solution of structural and also thermal and fatigue problems. The virtual powertrain is assembled, as well as numerically solved, in Multi Body System extended by user written subroutines. The virtual powertrain results are validated by measurements performed on compression ignition in-line six-cylinder engine.*

Keywords: Powertrain, dynamics, vibrations, acoustics, multibody.

1. Introduction

In today's fast paced automotive market, the computational methods are prerequisites to ensure low levels of sound, vibration and harshness (NVH) of modern powertrains. The complexity of computational models is always very important issue. The paper will present new and advanced approaches for evaluation of different powertrain noise sources and their influence on vibrations transmitted to the interior or exterior of the car.

2. Modelling approaches

This work evaluates noise sources in a powertrain and presents ways how the dominant noise source can be reduced by advanced computational models. The considered features of the computational models can be summarized as follows:

– Elastic deformations of main components enabling an evaluation of outer surface vibrations.
– Interactions between engine subsystems (cranktrain, valvetrain, gear timing drive etc.).
– Steady state or transient solution.
– Non-linear behaviour of interactions between components (slide bearings, gear tooth contacts, cam tappet contacts, etc.)

All the numerical approaches presented are integrated into a commercial program ADAMS extended by FORTRAN subroutines written by the authors.

2.1. Powertrain component modelling

Flexible bodies represented by FE (Finite Element) models have crucial importance for powertrain dynamics simulations. The proposed computational model uses reduced form of FE flexible bodies and the Craig-Bampton reduction method (Craig, 1981) is used for reduction of the FE models.

[*] doc. Ing. Pavel Novotný, Ph.D.: Institute of Automotive Engineering, Brno University of Technology, Technicka 2896/2; 616 69, Brno; CZ, novotny.pa@fme.vutbr.cz

[**] Ing. Martin Zubík: Institute of Automotive Engineering, Brno University of Technology, Technicka 2896/2; 616 69, Brno; CZ, zubik@fme.vutbr.cz

[***] Ing. Aleš Prokop: Institute of Automotive Engineering, Brno University of Technology, Technicka 2896/2; 616 69, Brno; CZ, prokop.a@fme.vutbr.cz

[****] Ing. Kamil Řehák: Institute of Automotive Engineering, Brno University of Technology, Technicka 2896/2; 616 69, Brno; CZ, rehak@fme.vutbr.cz

Crankshaft and engine block FE models present the fundamental components. The other flexible parts using reduced FE models are a camshaft, valve springs and rockers.

2.2. Torsional rubber damper model

A rubber damper model assembled in Multibody system (MBS) includes only general properties like torsional and axial stiffness but with very important dependencies on frequency and temperature. The frequency dependency in time domain is modeled via a series of four Maxwell's members (spring and damper). The overall static stiffness values originate from a detailed solution of the three dimensional FE model. Parameters of Maxwell's members are fitted by Matlab software functions to satisfy frequency dependency of the rubber. More details about torsional rubber damper modelling can be found in literature (Novotny, 2009).

2.3. Body interactions via slide bearing model

The loading capacity of a slide bearing included in the model is considered in a radial direction and including pin tiltings, which means that radial forces and moments are included in the solution. The slide bearing forces are based on a numerical solution of Reynolds differential Eq. (1), including elastic deformations of shells. The hydrodynamic forces are stored in hydrodynamic databases. Basic form of Reynolds equation is

$$\frac{\partial}{\partial x}\left(\frac{\rho h^3}{12\eta}\frac{\partial p}{\partial x}\right)+\frac{\partial}{\partial z}\left(\frac{\rho h^3}{12\eta}\frac{\partial p}{\partial z}\right)-\frac{U}{2}\frac{\partial(\rho h)}{\partial x}-\frac{\partial(\rho h)}{\partial t}=0 \qquad (1)$$

where p is pressure in oil film, h is oil film thickness, U is relative velocity of pin relative to shell, ρ is oil density, η is oil viscosity, x and z are coordinates and t is time.

The Reynolds equation is transformed into dimensionless coordinates, discretised by Finite Difference Method (FDM) and then numerically solved by Gauss-Seidel method employing Successive Over Relaxation (SOR) strategy. The pressure in oil film is integrated and the resulting forces are stored in reaction force databases. During the solution in time domain MBS solver reads the forces from databases for every solution time step.

2.4. Gear Timing Drive

A model of a gear meshing includes variable stiffness of meshing with backlash option. The variable stiffness of meshing gears enables to incorporate tooth meshing frequency, as well as its harmonic components. The computational model of meshing helical gear also includes all resultant forces between teeth (radial, axial and tangential forces). Detailed strategy and gear timing drive model influences can be found in a research works (Novotny, 2009).

2.5. Fuel Injection Pump

When taking into consideration the powertrain NVH, the injection pump can highly influence the dynamics of powertrain parts. In particular, the valvetrain and the gear timing drive can be influenced by high peak torques of the injection pump.

Essentially, the used type of injection pump includes injection pistons. The movement of the injection piston is controlled by a cam profile. Each cam interacts with a roller tappet. This interaction (cam – roller contact) produces time dependent torques on a pump shaft in each pump section.

Influences on the other powertrain components are the main aims of an injection pump MBS model. Therefore, the model includes a rigid body with inertia moment corresponding to a shaft and reduced inertia moments of other pump parts. Resultant torque in dependence on time and corrected for engine speeds is entered into the rigid body.

2.6. Virtual Powertrain

An advanced computational model of the powertrain, i.e. a virtual powertrain, is solved in time domain. This enables to incorporate different physical problems, including various nonlinearities. The virtual powertrain is assembled, as well as, numerically solved in MBS ADAMS. ADAMS is a general code and enables an integration of user-defined models directly using ADAMS commands or using user written FORTRAN or C++ subroutines. The virtual powertrain includes all significant components necessary for NVH analyses. The included modules are a cranktrain module, single valvetrain modules and a camshaft component, a gear timing drive module, a torsional damper module and a fuel injection pump module.

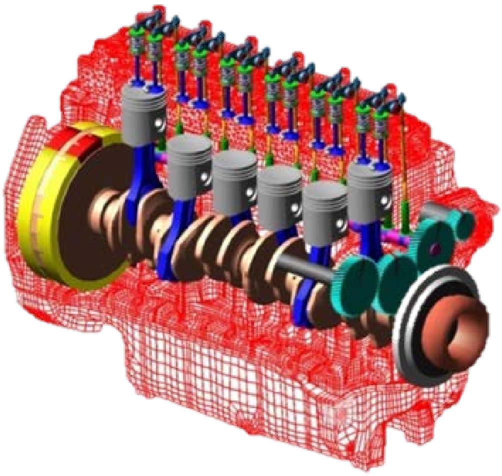

Fig. 1: Virtual powertrain assembled in multibody system

3. Validation of Virtual Powertrain Results

Proposed methods are applied to a turbocharged compression ignition (CI) six-cylinder engine. In general, powertrain surface vibrations and radiated noise are coupled.

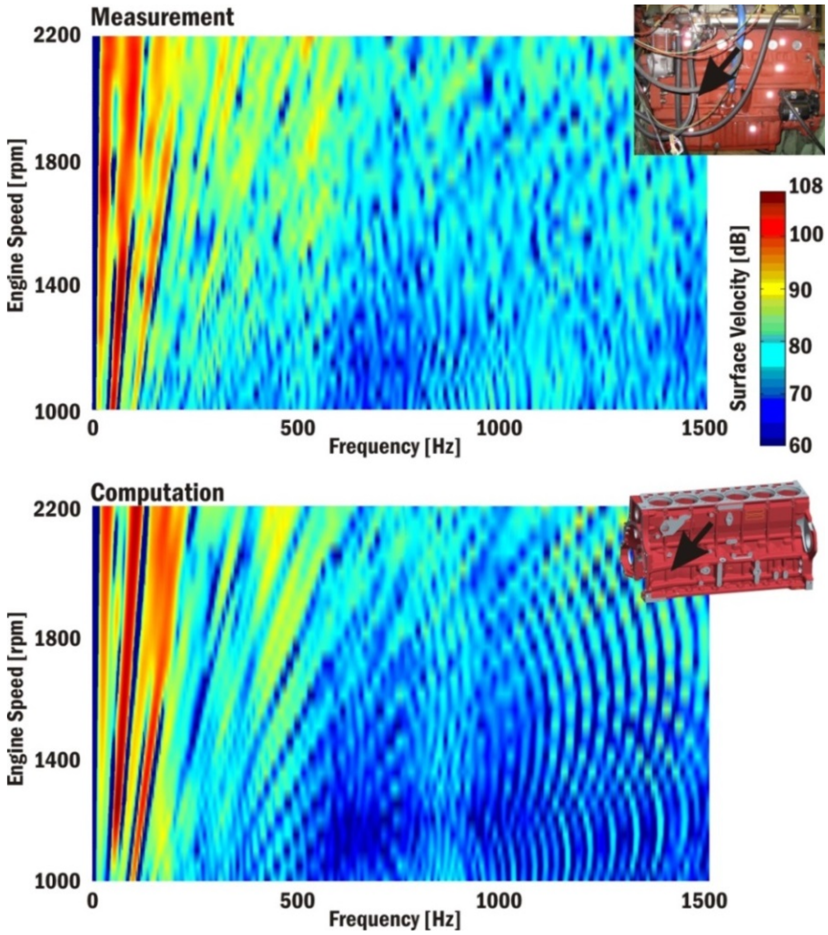

Fig. 2: Measured and calculated waterfall diagrams of crankcase surface velocities near the second cylinder and crankshaft axis

The noise produced by a powertrain can be estimated from crankcase surface velocities. Fig. 2 shows measured and calculated waterfall diagrams of crankcase surface velocities near the second cylinder and crankshaft axis. The value v_0 = 5.10^{-8} ms^{-1} is used as a reference velocity. Measured results have been determined by POLYTEC Vibrometer OFV-5000. The calculation results have been obtained by virtual powertrain and incorporating modules defined in a chapter 2.6.

4. Conclusions

The results of the work show that the most complex computational models on the level of virtual prototypes are necessary to fully simulate noise and vibrations of powertrains. These large models also enable to understand interactions among different powertrain subsystems. The fact that all the results are computed by one computational model and stored in one result file is also an advantage.

The greatest disadvantage lies in high model complexity. The complex computational models require a high number of parameters to be inputted, which are often hard to find. Other disadvantages are: long solution times to solve the models numerically and sometimes a large storage place required for computed results.

Influences of other powertrain subsystems, gear timing drive or injection pump influences, on noise and vibrations are significant. All significant noise sources, as combustion pressure forces, meshing gear forces or injection pump torques, have to be also included into the powertrain computational model.

Acknowledgement

The research leading to these results has received funding from the Ministry of Education, Youth and Sports under the National Sustainability Programme I (Project LO1202).

References

Craig R. R. (1981) Structural Dynamics. First edition, John Wiley & Sons, 1981, ISBN 0-471-04499-7.

Novotný P. (2009) Virtual Engine – A Tool for Powertrain Development. Inaugural Dissertation, Brno University of Technology, Czech Republic.

22nd International Conference
ENGINEERING MECHANICS 2016
Svratka, Czech Republic, 9 – 12 May 2016

SPEECH INTELLIGIBILITY IN THE POSITION OF CNC MACHINE OPERATOR

Ł. Nowakowski*, M. Mięsikowska, M. Blasiak*****

Abstract: *This article presents the results of the intelligibility of speech in the position of CNC milling machine operator. The study was conducted in two stages in a laboratory of numerically controlled machine tools in Kielce University of Technology. The first stage involved the measurement and analysis of changes in the sound pressure level in the work zone of the operator, which is emitted by the spindle of milling machine AVIA VMC 800. The measurement was carried out using the analyzer's NOR140 of NORSONIC during the operation of machine spindle without load with different speeds in the range of 1000 ÷ 10000 rpm / min. The second step was to study the possibility of verbal communication in a room where there are the machines, on the basis of the measurement recorded files in the first stage. Speech intelligibility was determined according to ISO 9921 based on the parameter SIL (Speech Interference Level).*

Keywords: Speech Intelligibility, Sound Pressure Level, Communication Man - Machine, CNC Milling Machines.

1. Introduction

Sounds accompanying man can be divided into useful, used, for example, to communicate and burdensome and harmful occurring e.g. in the position of the operator of numerically controlled machine tools. The latter often exceed the permissible sound level indication in the workplace, and become noise, adversely affecting human health. Noise also negatively affects the concentration of the operator in the workplace, which poses a serious threat. The most common source of noise in the workplace of the numerically controlled machine tool operator is work of drives of machine tools and machining process during which there are generated machine, the workpiece and the tool vibration (Miko & Nowakowski, 2012a).

For the measurement of vibrations in the cutting process, the non-contact face seals (Blasiak, 2015a, 2015b) piezoelectric transducers are used (Blasiak & Kotowski, 2009). Piezoelectric transducers are also used to measure the vibration of flying objects (Krzysztofik & Koruba, 2012) and to build gyroscopes (Koruba et al., 2010). The vibrations in the cutting process are an important factor in the process of machining, surface roughness (Miko & Nowakowski, 2012b) and the level of sound emission, which also reduces the concentration of the operator, causes fatigue, has a negative effect on hearing and the human nervous system and affects speech intelligibility.

In the study (www.ecophon.com.pl), the authors describe the method of calculating the speech intelligibility as an acoustic signal by the difference between the level of speech sound (signal) and the level of sound interference (noise).

According to the authors of the study (https://hipokrates, 2012) constant noise on the level of 70 dB to 80 dB prevents speech intelligibility from a distance of 0.5 m.

* Łukasz Nowakowski, PhD.: Chair of Mechanical Engineering and Metrology, Kielce University of Technology; Aleja Tysiąclecia Państwa Polskiego 7; 25-314 Kielce; PL, lukasn@tu.kielce.pl

** Marzena Mięsikowska, PhD.: Department of Applied Computer Science and Armament Engineering, Kielce University of Technology; Aleja Tysiąclecia Państwa Polskiego 7; 25-314 Kielce; PL, marzena@tu.kielce.pl

*** Małgorzata Błasiak, PhD.: Department of Mechanics, Kielce University of Technology; Aleja Tysiąclecia Państwa Polskiego 7; 25-314 Kielce; PL, mdrab@tu.kielce.pl

The aim of the study is to calculate speech intelligibility according to ISO 9921 in the position of the operator of CNC milling machines working without a load of different speeds.

2. Methods

The study of speech intelligibility were carried out at the Laboratory of Numerically Controlled Machine Tools in Kielce University of Technology in the workplace of operator of CNC milling machine VMC 800 Series, production FOP "AVIA SA. A characteristic feature of the machine is the solution of spindle drive, which has been based on engine HEIDENHAIN that using a belt drive with a toothed belt (POWERGRIP GT2) drives precisely balanced spindle of "cartrige" type. View of the machine, the design of the main drive and the basic parameters of CNC machine AVIA VMC 800 is presented in Table 1 (Extract from the machine metrics, 2008, Manual Machine, 2008).

Table 1. View and basic parameters of vertical machining center AVIA VMC 800 (Extract from the machine metrics, 2008, Manual Machine, 2008).

General view of the machine	The design of the drive spindle	
		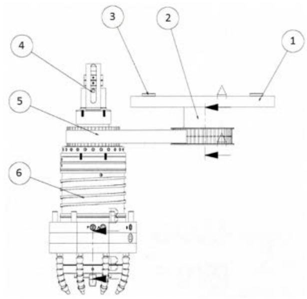
Spindle		**Description of construction**
Type	cartridge	1 – spindle plate, 2 –pulley of spindle drive motor, 3 – washer, 4 – bracket of tools presence sensor 5 – toothed belt 920-8MGT-30, 6 – spindle unit [6]
tip of the spindle	ISO 40 according to PN-92/M55085/01	
Spindle speed	50 - 10000 rev/min	
main motor power	10 / 17 kW	

Manufacturer of milling machines give in the manual of machine tools only the maximum noise level of 79 dB for a closed cabin and the maximum speed of the spindle. There is a lack of data for the full range of rotation speed, that is why laboratory tests were divided into two stages. The first stage involved the measurement and analysis of changes in the sound pressure level in the operator's work zone, which is emitted by a spindle of the milling machine CNC AVIA VMC800.

Fig. 1: Measurement position in the operator's work zone of CNC milling machine (Błasiak, M. et al., 2015).

Measurement of the sound level was made by the analyzer NOR140, of Norsonic company, which microphone was in the operator's work zone at a height of 170 cm corresponding to the position of the human ear. The measurement was performed for 10 different rotation speeds of the milling machine spindle without load in the range from 1000 to 10000 rev/min at 1000 rpm.

The second stage of the study was to examine and determine the possibility of verbal communication human-human / human-machine (Mięsikowska, 2015) in a room where there are the machines. The study was conducted on the basis of measurement files obtained in the first stage using the meter Nor140and acoustic parameter of speech intelligibility. Speech intelligibility was determined according to ISO 9921 based on the parameter SIL (Speech Interference Level).

3. Results

The results of the first phase of laboratory tests are shown in Figure 6, which shows the measured A sound level at the workstation of the operator of the CNC milling machine, which contains the sound emitted by the machine in the "standby" mode at a constant level equal to 67 dB (A), and in relation to the growing rotation speed of spindle. A level of A sound pressure for the milling machine spindle running without load in the speed range from 1000 to 5000 rev/min remains constant at the level of 71.4 ÷ 74 dB (A). For the speed 6000 rev/min, there is an increase of the sound level by 2.5 dB (A) to 76.5 dB (A) which progressively with increasing rotation of the spindle is increases to 80 dB (A) for a maximum spindle speed of 10000 r/min.

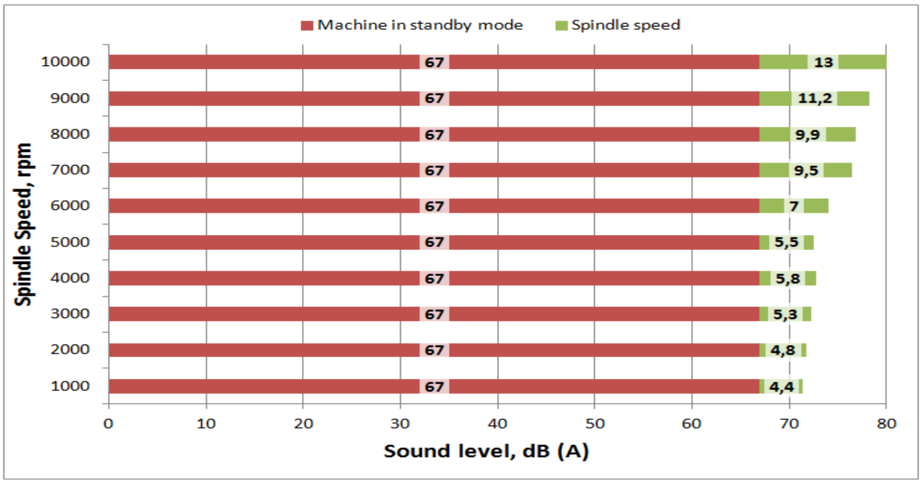

Fig. 6: level of A sound pressure measured at the workplace of the CNC milling machine operator

The second phase of the laboratory research, or the level of speech intelligibility determined according to ISO 9921 on the basis of the parameter SIL is presented in Table 2. Parameter SIL was determined as the difference between the L $_{S,A,L}$ parameter, - volume received by the listener (recorder) and a parameter L_{SIL} , which is an average sound level for the four octave band of frequency: 500Hz, 1000Hz, 2000Hz, 4000Hz. For the purpose of the study, there was estimated the value of the parameter $L_{S,A,L}$ equal to 72 dB, while the distance L = 1m. Thus, $L_{S,\ A,\ 1m}$ = 72 dB.

Table 1. Speech intelligibility at the workplace of the operator of numerically controlled machine tools

Spindle speed rev/min	Level of A sound pressure dB(A)	L_{SIL}, dB	SIL, dB	Speech intelligibility
1000	71,4	58,1	14,0	Fair
2000	71,8	59,5	12,5	Fair
3000	72,3	58,2	13,8	Fair
4000	72,8	60,9	11,2	Fair
5000	72,5	61,8	10,2	Fair
6000	74	60,8	11,2	Fair
7000	76,5	61,9	10,1	Fair
8000	76,9	63,0	9,0	Poor
9000	78,2	64,6	7,4	Poor
10000	80	67,5	4,6	Poor

Analyzing the results of the tests of Table 2, it has been found that the intelligibility of speech for the spindle speed in the range from 1000 rev/min to 7000 rev/min is Fair, and for the speed from 8,000 rev/min to 10,000 rev/min is Poor. Corresponding to the speech intelligibility, fair values of SIL parameter are in the range of 10.1 to 14.0 dB, values of L_{SIL} parameter in the range of 58.1 to 61.9 dB. Poor speech intelligibility corresponds to values of SIL parameter containing in the range of 4.6 to 9.0 dB, L_{SIL} values are in the range of 63.0 to 67.5 dB.

4. Conclusions

Conducted study showed a significant effect of spindle speed of milling machine on sound pressure level at the workstation of CNC operator, emitted by the CNC spindle working without load. A level of A sound for speed of spindle running without load in the range of 1000 to 7000 rev/min remains constant at the level of 71/76.5 dB (A). The maximum sound pressure level of 80 dB (A) was measured for the spindle speed equal to 10,000 rev/min. Analysis of the level of speech intelligibility determined according to ISO 9921 on the basis of the SIL parameter showed that the spindle speed in the range from 1000 rev/min to 7000 rev/min is at a Fair level, and for the rotational speed from 8,000 rev/min to 10,000 rev/min at a sound pressure level of 76.9/80dB (A) is poor. At a distance of 1 meter from the machine communication is maintained at a fair level to 7000 rev/min. A level of A sound pressure is maintained up to 7000 rev/min at a level of 71.4 dB (A) - 76.5 dB (A). At 8000 rev/min speech intelligibility decreases, so in terms of A sound level of 76.9 dB - 80 dB at a distance of 1m. Probably reduction of the distance to 0.5m, so coming closer to the source of the noise, it can cause a big drop in verbal communication, but this requires further study. Lack of speech intelligibility in the position of the operator is a serious threat to human health and can lead to accidents. Adverse acoustic conditions in the work zone of the operator, especially the possibility of verbal communication, can adversely affect the communication man/machine. It is advisable to carry out any work to reduce the sound pressure level in the work zone of the operator, in order to improve comfort and speech intelligibility. Sound pressure level at the workstation of the operator of CNC can be reduced by carefully balancing dynamic and static parts of these machines that rotate, for example, spindle. It may be also helpful to systematically check and tighten loose parts (screws) and lubrication. In addition, machine guards or the room in which there is the machine can be coated with sound-absorbing material and noise-reducing screens.

References

Blasiak, M. & Kotowski, R. (2009) Propagation of acoustic waves in piezoelectric crystals, Przeglad Elektrotechniczny ISSN 0033-2097, Vol 85, NR 12/2009, pp.40-43.

Błasiak, M., Mięsikowska, M. & Nowakowski, Ł. (2015) Analysis of sound levels of spindle of CNC Machine tool In the operator work area. Mechanik, Vol. 8-9, pp. 390-398.

Blasiak, S. (2015) An analytical approach to heat transfer and thermal distorions in non-contacting face seals. International Journal of Heat and Mass Transfer**,** Vol: 81, pp. 90-102.

Blasiak, S. (2015) The two dimensional thermohydrodynamic analysis of a lubrication in non-contacting face seals. Journal of Thermal Science and Technology, Vol: 10, pp. 1-8.

Extract from the machine metrics FOP AVIA S.A. (2008). Vertical Milling Machine VMC-800.

Koruba, Z., Dziopa, Z. & Krzysztofik, I. (2010) Dynamics and control of a gyroscope-stabilized platform in a self-propelled anti-aircraft system. Journal of Theoretical and Applied Mechanics, Vol. 48, No. 1, ISSN 1429-2955 pp.5-26.

Krzysztofik, I. & Koruba, Z. (2012) Model of Dynamics and Control of Tracking-Searching Head, Placed on a Moving Object. Journal of Automation and Information Sciences, Vol. 44, Issue 5, ISSN 1064-2315, pp.38-47.

Manual Machine AVIA S.A. (2008). Vertical Milling Machine VMC-800

Mięsikowska, M. (2015) Discriminant analysis of voice commands in a car cabin, Przegląd Elektrotechniczny ISSN 0033-2097,Vol 10, pp. 173-175.

Miko, E. & Nowakowski, Ł. (2012a) Analysis and Verification of Surface Roughness Constitution Model After Machining Process, XIIITH International scientific and engineering conference hermetic sealing, Vibration reliability and ecological safety of pump and compressor machinery-HERVICON-2011.Vol: 39, pp.395-404.

Miko, E. & Nowakowski, Ł. (2012b) Vibrations in the Machining System of the Vertical Machining Cente XIIITH International scientific and engineering conference hermetic sealing, Vibration reliability and ecological safety of pump and compressor machinery-HERVICON-2011 Vol: 39, pp. 405-413.

http://www.ecophon.com/pl/acoustic-solutions/acoustic-knowledge-bank/3-sposoby-oceny-akustyki/Zrozumialosc-mowy/Zrozumiao-mowy-/

https://hipokrates2012.wordpress.com/2013/10/23/ciszejjjjjjj-halas/

22nd International Conference
ENGINEERING MECHANICS 2016
Svratka, Czech Republic, 9 – 12 May 2016

THE ANALYSIS OF THE ZONE FOR INITIATING THE CUTTING PROCESS OF X37CrMoV51 STEEL

Ł. Nowakowski[*], E. Miko[**], M. Skrzyniarz[***]

Abstract: *This article has presented the results of the research based on the analysis concerning the zone for initiating the process of longitudinal turning and face milling of X37CrMoV51 steel. The research was conducted in two stages at the laboratories of the Kielce University of Technology. The first stage included performance of cutting attempts that were to gradually initiate the process of cutting thanks to a flowing change of depth of the cutting by tilting the working surface of samples at a slight angle. The second stage was about performing measurements of the cuboidal and conical working surface of samples on a non-sliding contact profilometer TOPO 01P. As a result, the measurements acquired 2D profiles of the sample presenting the zone for initiating the cutting process. Profiles of the surface were analyzed in order to identify and compare the characteristic contact areas of the tool on the cut item. The results of the conducted analysis of 2D profiles of the working surface have been presented graphically.*

Keywords: initiating the cutting process, the minimum thickness of the cut layer, turning, milling.

1. Introduction

When analyzing the stereometry of the cutting plate, we notice that it is not sharp enough, but it has a rounded edge with radius r_n and stereometry errors that result from the technology of its manufacture. During a precision treatment of the precise parts of machines and prototypes (Adamczak, Bochnia, & Kaczmarska, 2014; Adamczak, Kaczmarska, & Bochnia, 2015), i.e. contactless face seals (Błasiak, 2015, Błasiak, 2015), parts of gyroscopes (Krzysztofik & Koruba, 2012, Koruba et al., 2010) and cylindrical elements (Adamczak, Zmarzły, & Janecki, 2015), it is particularly significant to determine vibration in the process of cutting (M. Blasiak & Kotowski, 2009; Miko & Nowakowski, 2012a) and the real geometry of the cutter, which has an important influence on the minimum thickness of the cut layer (h_{min}) and the roughness of created surfaces (Miko & Nowakowski, 2012b) ensuring their high reliability of machine parts (S. Blasiak, Takosoglu, & Laski, 2014) and low manufacturing costs (Takosoglu, Dindorf, & Laski, 2009). The parameter h_{min} determines the beginning when the layer of the material is divided in form of shavings during cutting, so it determines the smallest layer of material that can be possibly removed in particular conditions.

When observing the zone of initiating the cutting process, one may distinguish three vivid stages of the effect of the cutter on the treated material, depending on the depth of cutting (a_p) (Cgae, Park, Freiheit, 2006; Grzesik, 2010):

I - when $a_p < h_{min}$: there are elastic deflections and malleable pressure of the treated material,

II - when $a_p = h_{min}$: there are elastic and malleable deflections with partial cutting of the treated material (chasing of the treated material),

III - when $a_p > h_{min}$: beginning of removing the material in form of shavings.

[*] Łukasz Nowakowski, PhD.: Chair of Mechanical Engineering and Metrology, Kielce University of Technology; Aleja Tysiąclecia Państwa Polskiego 7; 25-314 Kielce; PL, lukasn@tu.kielce.pl

[**] Edward Miko, Prof PŚk, dr hab..: Chair of Mechanical Engineering and Metrology, Kielce University of Technology; Aleja Tysiąclecia Państwa Polskiego 7; 25-314 Kielce; PL, lukasn@tu.kielce.pl

[***] Michał Skrzyniarz, M.Sc.: Chair of Mechanical Engineering and Metrology, Kielce University of Technology; Aleja Tysiąclecia Państwa Polskiego 7; 25-314 Kielce; PL, skrzyniarzmichal@gmail.com

There is a lot of theoretical research conducted in the world that is to determine the minimum thickness of the cut layer.

The aim of the scientific research is to experimentally determine the parameter of the minimum thickness of the cut layer for the process of longitudinal turning and face milling of X37CrMoV51 steel. The analysis concerned the zone of initiation of the process of rolling and milling in order to identify and compare the characteristic contact areas of the tool on the cut item.

2. Methods

The process of the practical determination of the parameter h_{min} meant gradual initiation of the cutting process through a flowing change of the depth of cutting. The flowing change of depth of cutting was achieved thanks to special preparing of the specimen geometry (Graba, 2011; Graba, 2012). The sample for rolling was of conical shape with an angle forming 0°19', while the milling sample was of a cuboid fixed on a wedge with an angle of 0°18'. The working surface of the samples was exposed to the process of precise grinding.

The cutting attempts were planned in such a way that they were to be as similar to each other as possible; the rolling and milling processes were performed with the feed of 0.12 mm/rev at the cutting speed of 300 m/min. Lathe works were conducted at DMG ALFA500 lathe centre. The attempts used a DCMT150408 cutting plate with a corner radius of 0.8 mm, while the milling works were conducted at an AVIA VMC800 vertical milling centre, where the cutter body (Adamczak, Janusiewicz, Makieła, Stępień, 2011) was facilitated with one 490-08T308M-PL plate with a corner radius of 0.8 mm in order to avoid axial run-out (Janusiewicz, Adamczak, Makieła, Stepień, 2011). The plan of cutting attempts has been presented in figure 1a.

a) b)

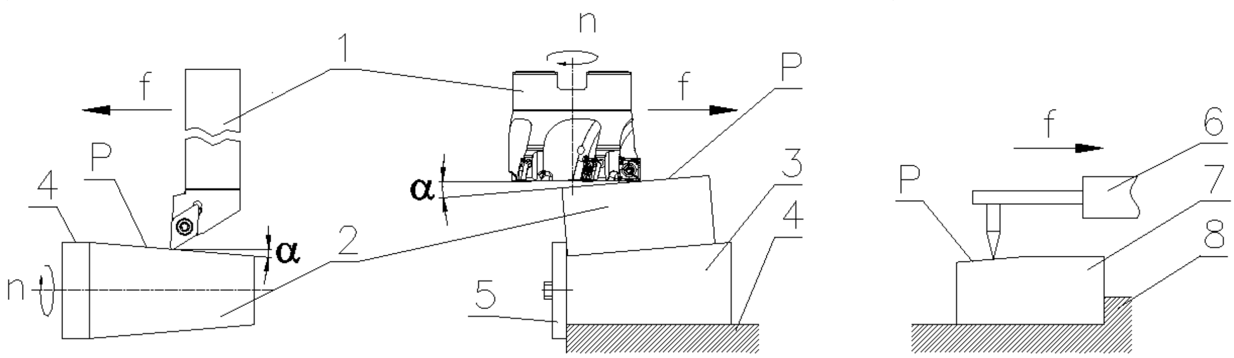

Fig. 1. View of: a) cutting attempts, b) measurement of samples in order to determine the minimum thickness of the cut layer. 1– tool, 2 – sample, 3 – wedge, 4 – handle, 5- stopper, 6 – head of the profilometer, 7 – measured sample, 8 – handle of the profilometer, f – feed, n – rotation, P – working surface of the sample, α – angle of the working surface

Another stage of the experiment was the performance of measurements of the cuboidal and conical working surface (Fig. 1b) on the contact profilometer TOPO 01P that was facilitated with a non-sliding measuring head. As a result, the measurements acquired 2D profiles of the working surface of the sample presenting the zone for initiating the cutting process. The profiles of the surface were analyzed with software TOPOGRAFIA and MATHEMATICA in order to identify the characteristic contact areas of the tool on the cut item.

3. Results

The results of the conducted analysis of 2D profiles of the working surface have been graphically presented in Figure 2. In order to compare the profiles, they were superimposed on each other in the software MATHEMATICA, so that the points of the first contact of the tool with the treated material were the same. Then, the identification of characteristic zones was conducted, their length was measured and the angles of working surfaces of samples were determined. Another step was to directly measure the h_{min} parameter, which is defined as the distance of the highest point of the profile from the middle line of the processed profile.

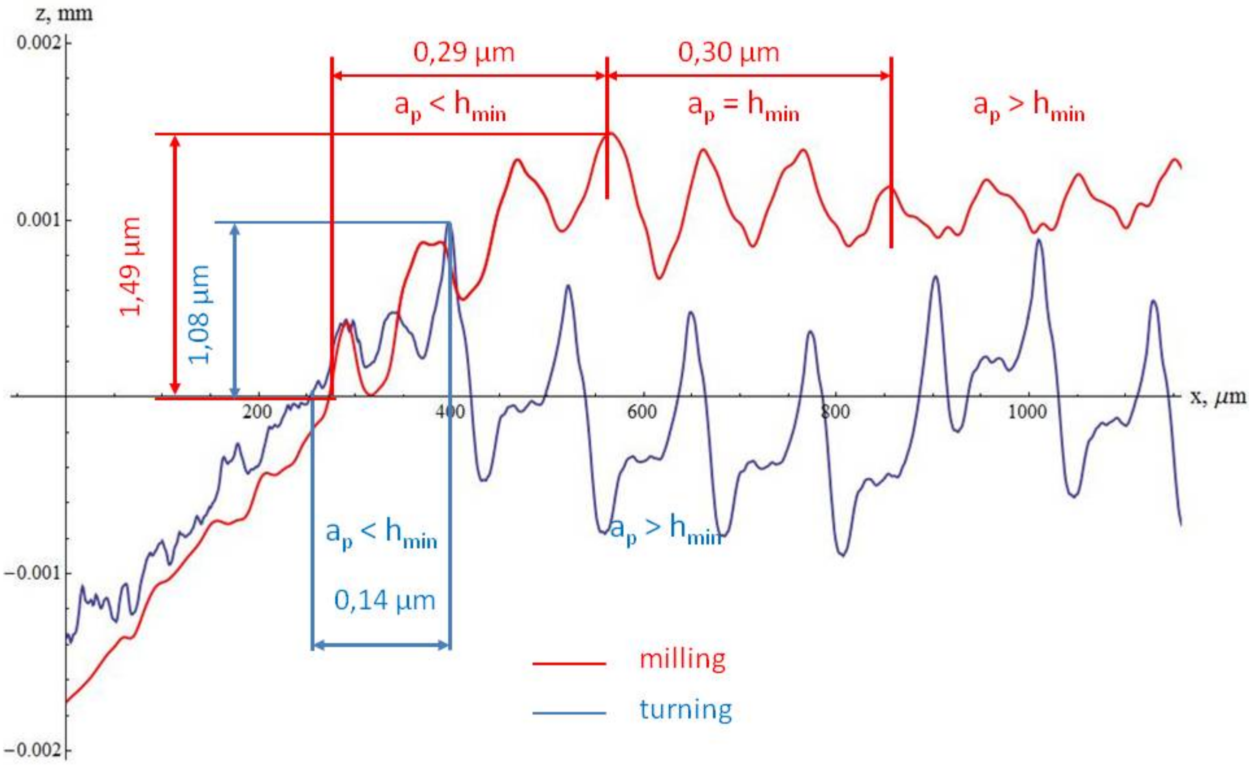

Fig. 2. View of the measured 2D profiles of the working surface of the rolled sample and milled sample

When analyzing Figure 2, it was noticed that there was a difference in the initiating zone of the process during rolling and milling. The profile acquired as a result of initiating the rolling process helped to identify only two characteristic zones I and III. Zone I of elastic deflections and malleable pressure of the treated material was 0.14 mm long, while the measured value of the parameter h_{min} was 1.08 µm. There was no zone II observed in case of rolling that would be responsible for elastic and malleable deflections of the treated material.

During the analysis of the milled profile, all characteristic areas of contact of the tool with the treated material were found. Zone I was 0.29 mm long, the second zone was 0.3 mm long. The parameter h_{min} during the head milling process was 1.49 µm.

During the comparison of the results of analyses, it was noticed that during milling the material or the machine worked within the area of elastic deflections, since the medium line of profile III of the zone is 11.4 µm higher than the medium line of zone III of the milled profile. The noticed different results arise from the elastic deflection of the spindle of the machine (which have been presented in one of the previous works of the Authors (Miko & Nowakowski, 2012b)) and this may significantly influence the dimension and form accuracy of milled objects.

4. Conclusions

The conducted research on initiating the process of longitudinal turning and face milling of X37CrMoV51 steel made it possible to measure, compare and analyze the characteristic contact zones of the tool on the treated item when initiating the cutting process. When analyzing the research results, a difference was noticed between the initiation process of rolling and milling. The profile acquired as a result of initiating the rolling process helped to identify only two characteristic zones I and III, there was no observation of zone II of elastic and malleable deflections with partial cutting of the treated material.

In the case of the milling process, all three characteristic areas of contact of the tool with the treated material were found.

During the comparison of the results of analyses, it was noticed that during milling the material or the machine worked within the area of elastic deflections, since the medium line of profile III of the zone is 11.4 µm higher than the medium line of the milled profile. The observed difference may have a considerable influence on the dimension and form accuracy of milled objects.

References

Adamczak, S., Bochnia, J., & Kaczmarska, B. (2014). Estimating the uncertainty of tensile strength measurement for a photocured material produced by additive manufacturing. *Metrology and Measurement Systems*, *21*(3), 553–560.

Adamczak S., Janusiewicz A., Makieła W., Stępień K.(2011): Statistical validation of the method for measuring radius variations of components on the machine tool. *Metrology and Measurement Systems, 23(1),* 35-40.

Adamczak, S., Kaczmarska, B., & Bochnia, J. (2015). An analysis of tensile test results to assess the innovation risk for an additive manufacturing technology. *Metrology and Measurement Systems*, *22*(1), 127–138.

Adamczak S., Zmarzły P., Janecki D.(2015): Theoretical and practical investigations of V-block waviness measurement of cylindrical parts. *Metrology and Measurements System, 22(2),* 181-192.

Blasiak, M., & Kotowski, R. (2009). Propagation of acoustic waves in piezoelectric crystals. *PRZEGLAD ELEKTROTECHNICZNY*, *85*(12), 40–43.

Błasiak, S. (2015) An analytical approach to heat transfer and thermal distorions in non-contacting face seals. International Journal of Heat and Mass Transfer**,** Tom: 81, pp. 90-102.

Błasiak, S. (2015) The two dimensional thermohydrodynamic analysis of a lubrication in non-contacting face seals. Journal of Thermal Science and Technology, Tom: 10, pp. 1-8.

Blasiak, S., Takosoglu, J. E., & Laski, P. A. (2014). Heat transfer and thermal deformations in non-contacting face seals. *Journal of Thermal Science and Technology*, *9*(2),

Cgae J., Park S.S., Freiheit T. (2006) Investigation of micro-cutting operations. *International Journal of Machine Tools & Manufacture 46,* 313-332,

Graba M., 2011, The influence of material properties and crack length on the Q-stress value near the crack tip for elastic-plastic materials for single edge notch plate in tension, Archives of Civil and Mechanical Engineering, vol. XI, No. 2, pp. 301-319, 2011

Graba M., 2012, The influence of material properties and crack length on the Q-stress value near the crack tip for elastic-plastic materials for centrally cracked plate in tension, J. Theor. Appl. Mech., 50, 1, pp. 23-46, 2012

Grzesik, W. (2010) Podstawy skrawania materiałów metalowych. Wydawnictwo Naukowo-Techniczne, Warszawa 2010

Janusiewicz A., Adamczak S., Makieła W., Stępień K.(2011): Determining the theoretical method error during an on-machine roughness measurement, *Measurement, 44(9),* 1761-1767.

Koruba, Z., Dziopa, Z. & Krzysztofik, I. (2010) Dynamics and control of a gyroscope-stabilized platform in a self-propelled anti-aircraft system. Journal of Theoretical and Applied Mechanics, Vol. 48, No. 1, ISSN 1429-2955 pp.5-26.

Krzysztofik, I. & Koruba, Z. (2012) Model of Dynamics and Control of Tracking-Searching Head, Placed on a Moving Object. Journal of Automation and Information Sciences, Vol. 44, Issue 5, ISSN 1064-2315, pp.38-47.

Miko, E., & Nowakowski, Ł. (2012a). Analysis and Verification of Surface Roughness Constitution Model After Machining Process. *Procedia Engineering*, *39*, 395–404.

Miko, E., & Nowakowski, Ł. (2012b). Vibrations in the Machining System of the Vertical Machining Center. *Procedia Engineering*, *39*, 405–413.

Takosoglu, J. E., Dindorf, R. F., & Laski, P. A. (2009). Rapid prototyping of fuzzy controller pneumatic servo-system. *INTERNATIONAL JOURNAL OF ADVANCED MANUFACTURING TECHNOLOGY*, *40*(3-4), 349–361.

22nd International Conference
ENGINEERING MECHANICS 2016
Svratka, Czech Republic, 9 – 12 May 2016

THE EVALUATION OF THE PROCESS OF SURFACE REGENERATION AFTER LASER CLADDING AND FACE MILLING

Ł. Nowakowski[*], M.Wijas[**]

Abstract: *This elaboration presents the results of experiments concerning milling of surfaces exposed to laser cladding. The aim of this elaboration has been to conduct the quality evaluation concerning the process of regenerating a flat surface of sheet metal made of steel C 45 through laser cladding and face milling. The assessment of the results of the regeneration process has been conducted on the basis of selected parameters of the geometric structure of the regenerated surface and the identification of surface defects.*

Keywords: regeneration of surface, laser cladding, face milling, geometric structure of surface.

1. Introduction

The connection of laser cladding with machining may be used to regenerate the surfaces of worn machine and device parts, i.e. the non-contact flat seals, pneumatic valves (Takosoglu et al., 2012, Takosoglu et al. 2014) and parts of gyroscopes (Koruba et al. 2011). Wear of precise parts may cause incorrect functioning of the device e.g. by generating vibration (Miko & Nowakowski, 2012, Błasiak & Kotowski 2009) . Laser cladding is one of the most modern, yet expensive, methods for coating of layers with special properties (Klimpel, 2000). It is about melting the additional material in form of powder or a wire, with energy from laser beam cladding, in a proper gas shield and, at the same time, melting the material of the surface. Mixing and melting together both materials causes formation of a surface layer of the clad surface that is called clad overlay (Klimpel, 2012). Consequently, a high-quality metallurgical connection is formed with the surface (Klimpel, 2000). After cooling, the metal layer should be machined in order to provide the regenerated surface with a particular dimension and form accuracy and required geometric structure of surface (SGP) (Miko & Nowakowski, 2012).

2. Methods

The procedure of quality assessment of the process of laser cladding was divided into several stages related to laser cladding, measurements and evaluation of SGP of the surface after laser cladding, as well as related to machining. The first stage included using a sample of steel C45 (non-alloy quality steel for tempering, easy to machine) for a simulated defect of the material in form of a 20x20 mm pocket with a corner radius of 5 mm and depth of 0.75 mm fig. 1.

Fig. 1. View of material defect

The second stage of research included filling the material defect of the sample through laser cladding by using LASERCELL 1005 manufactured by Trumph (fig. 2) facilitated with a powder conveyor produced by GTV (Sęk & Tofil 2014, Harnicarova et al. 2012). During the process of laser cladding, the powder used was metal powder PMNi of hardness of 57 HRC and granulation of 100–160 µm. In order to replenish the defect of 0.75 depth, 5 layers of clad overlay were applied. After the test, it appeared that such a number of layers is insufficient. Thus, two more layers were applied (fig. 3).

[*] Łukasz Nowakowski, PhD.: Chair of Mechanical Engineering and Metrology, Kielce University of Technology; Aleja Tysiąclecia Państwa Polskiego 7; 25-314 Kielce; PL, lukasn@tu.kielce.pl

[**] Marta Wijas, MSc: Chair of Mechanical Engineering and Metrology, Kielce University of Technology; Aleja Tysiąclecia Państwa Polskiego 7; 25-314 Kielce; PL, mwijas@tu.kielce.pl

Fig. 2. Head used for cladding and the process of cladding (Wijas & Nowakowski, 2015)

PARAMETERS OF CLADDING:
Feed: 1000, mm/min
Width of the laser beam for deposition: 3 mm
Laser power: 35 % Pmax
Frequency: 20000, Hz
Gas flow Ar: 12, l/min
Rotations of the feeder: 3, 1/min
Gas flow of the feeder He: 3, l/min

Fig. 3. Sample after the cladding

After the process of laser cladding as a part of the third stage of the research, measurements of the surface were made with the profiler Talysurf CCI – Lite Non–contact 3D Profiler manufactured by Taylor Hobson.

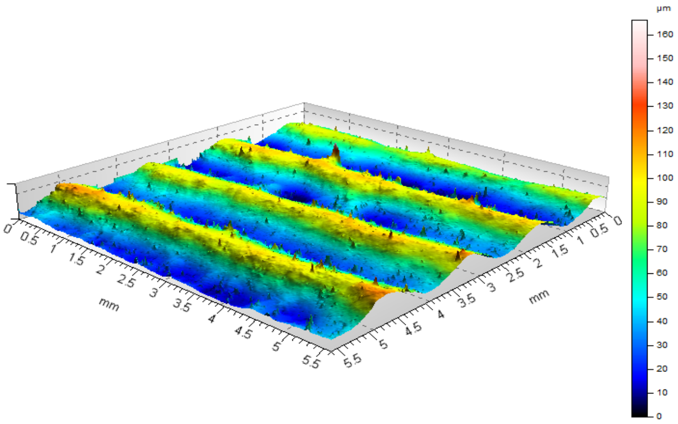

Measurement conditions:

- lens x10
- measurement resolution 1.65x1.65 µm
- measured area 5.5x5.5 mm - assembly

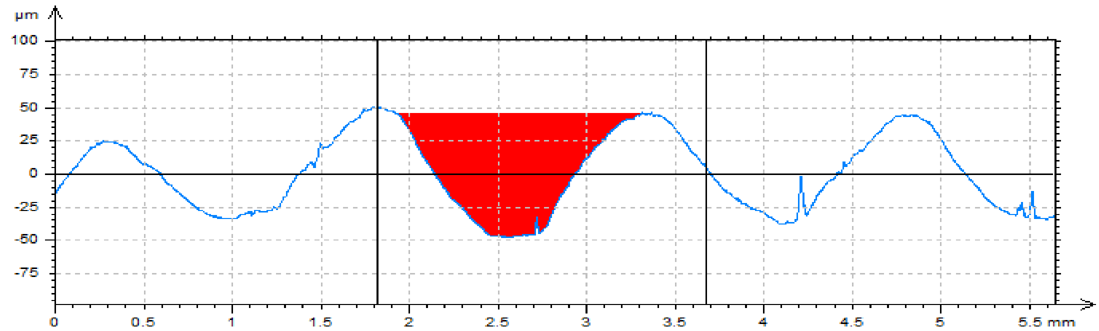

Fig. 4. View of the paded area measured with the profiler Talysurf CCI

When analyzing the results of measurements presented in fig. 4, it has been determined that due to the replenishment of a 0.75 deep simulated defect with laser cladding the acquired surface is characterized with a periodic profile. The measurement of gradient length was of average 1.5 mm, while the average distance from the top to the bottom of the profile - 83.94 µm. The measured space of the hole marked red in fig. 4. was 7398 µm^2. The isometric view of the surface also demonstrated chips of the material that were an unwanted effect of the laser cladding process.

The fourth stage was the process of face milling, with the usage of milling center HERMLE B 300 (table 1), of the clad surface that was conducted in order to achieve a flat surface. The research used the head R245-080Q27-12M produced by Sandvik Coromant that was facilitated with plates of type 245-12T3M-PL4230. The sample was milled with the feed of a cooling and lubricating liquid.

Table 1. View of the machine and the sample after milling with a milling head

General view HERMLE B300	Head R245-080Q27-12M	Parameters of machining	Sample after machining
	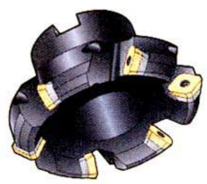 Plate R245-12T3M-PL4230 	v_c, 215 m/min n, 855 rotations/min f_z, 0.1 mm/cutter f_z, 513 mm/cutter a_p, 0.5 mm a_e, 50 mm	

The last fifth stage included measuring the selected parameters of the geometric structure of the clad surface after face milling. Conditions for the measurement remained unchanged.

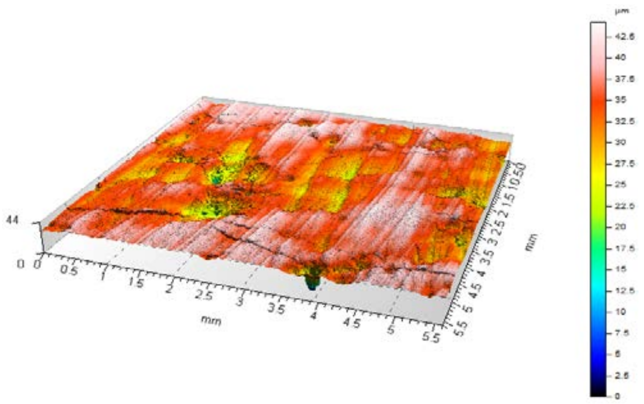

Table 2. 3D parameters of the surface ISO 25178

Sq	9.92	µm
Ssk	-1.02	-
Sku	6.42	-
Sp	9.35	µm
Sv	34.90	µm
Sz	44.26	µm
Sa	3.01	µm

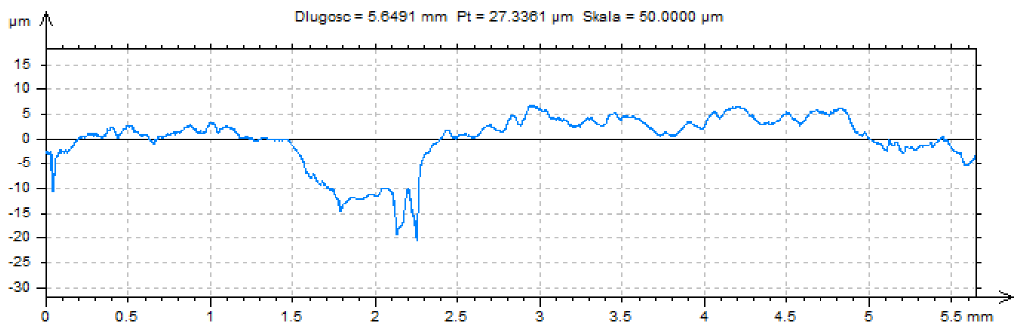

Fig. 5. View of the planned clad area measured with the profiler Talysurf CCI

By analyzing the results presented in table 2 and fig. 5, it has been noticed that after the machining of the clad surface, surface defects such as cracks, gas blisters and porosity were revealed (Graba 2011, 2012). The 2D profile presents the isometric cross-section of the clad surface after face milling in the place, where surface defects occurred in form of a gas blister. The measurement analysis showed that its length is 0.9 mm, while its depth is 21 µm. The surface of 5.5x5.5 mm had 4 gas blisters, three cracks with length of 1÷1.5 mm, and porosity. Table 2 presents the selected parameters of the geometric structure of the surface exposed to laser cladding that has surface defects.

3. Conclusions

Tests with the optical profiler allowed to conduct a quality assessment of the laser cladding process of C45 steel after machining. One of the significant factors that decrease the usage properties of clad surfaces are the hidden surface defects. Gas blisters, porosity and cracks in the clad surface are defects that are difficult to be revealed due to their size, but their presence greatly disqualifies the clad surface since its resistance properties become significantly lower and, consequently, the quality of the surface decreases (Adamczak et al., 2010).The surface defects observed after the measurements made with the profiler Talysurf CCI – Lite Non–contact 3D could result from the fact that the clad overlay was applied in two stages (5 layers, 2 layers). Additionally, so many layers of clad overlay resulted in material shrinkage. The research and scientific aim of the conducted work is to choose such parameters for the process of laser claddding that in the future it will be possible to avoid formation of surface defects.

References

Adamczak, S., Bochnia, J., Kaczmarska, B. (2014) Estimating the uncertainty of tensile strength measurement for a photocured material produced by additive manufacturing. Metrology and Measurement Systems [online]. 2014, roč. 21, č. 3, s. 553–560. ISSN 08608229. Dostupné z: doi:10.2478/mms-2014-0047

Błasiak, M., Kotowski, R. (2009). Propagation of acoustic waves in piezoelectric crystals. Przeglad elektrotechniczny, roč. 85, č. 12, s. 40–43. ISSN 0033-2097.

Graba, M. (2011), The influence of material properties and crack length on the Q-stress value near the crack tip for elastic-plastic materials for single edge notch plate in tension, Archives of Civil and Mechanical Engineering, vol. XI, No. 2, pp. 301-319.

Graba, M. (2012), The influence of material properties and crack length on the Q-stress value near the crack tip for elastic-plastic materials for centrally cracked plate in tension, J. Theor. Appl. Mech., 50, 1, pp. 23-46.

Harnicarova, M., Valicek, J., Zając, J., Hloch, S., Cep, R., Dzubakova, I., Tofil, S., Hlavacek, P., Klich, J., Cepova, L. (2012). Techno-economical comparison of cutting material by laser, plasma and oxygen. Tehnicki Vjesnik-Technical Gazette, 19/ 4, s. 813 – 817.

Klimpel, A. (2000), Napawanie i natryskiwanie cieplne. Technologie. Warszawa, WNT, s. 339- 365

Klimpel, A. (2012), Technologie laserowe. Gliwice, WPŚ, s. 1820-229

Koruba, Z., Krzysztofik, I., Dziopa, Z. (2011) An analysis of the gyroscope dynamics of an anti-aircraft missile launched from a mobile platform [online]. ISBN 0239-7528. Dostupné z: doi:10.2478/v10175-010-0069-4

Miko, E., Nowakowski Ł. (2012). Analysis and Verification of Surface Roughness Constitution Model After Machining Process. Procedia Engineering [online], roč. 39, s. 395–404. Dostupné z: http://www.sciencedirect.com/science/article/pii/S1877705812024290

Miko, E., Nowakowski Ł., (2012). Vibrations in the Machining System of the Vertical Machining Center. Procedia Engineering [online]. 2012, roč. 39, s. 405–413. ISSN 18777058. Dostupné z: doi:10.1016/j.proeng.2012.07.044

Sęk, P., Tofil, S. (2014) Laser Cold Ablation as a Cutting Edge Method of Forming Silicon Wafers used in Solar Cells. Advanced Materials Research. Terotechnology, s. 113-118

Takosoglu, J E., Łaski P A., Błasiak S. (2012). A fuzzy logic controller for the positioning control of an electro-pneumatic servo-drive. Proceedings of the institution of mechanical engineers part i-Journal of systems and control engineering [online], roč. 226, č. I10, s. 1335–1343. ISSN 0959-6518. Dostupné z: doi:10.1177/0959651812456498

Takosoglu, J E., Łaski P A., Błasiak S. (2014) Innovative modular pneumatic valve terminal with self – diagnosis, control and network communications. . In: FUIS, V, ed. Engineering Mechanics 2014. Dolejskova 5, PRAGUE 8, 182 00, Czech Republic: Acad sci Czech Republic, Inst thermomechanics, s. 644–647. Engineering Mechanics. ISBN 978-80-214-4871-1.

Wijas M., Nowakowski Ł., (2015). Suraface milling after laser cladding. Mechanik, Vol. 8-9, pp. 320-328

22nd International Conference
ENGINEERING MECHANICS 2016
Svratka, Czech Republic, 9 – 12 May 2016

ESTIMATION OF PRIMARY SUSPENSION PARAMETERS FROM LATERAL DYNAMIC RESPONSE OF A WHEELSET

A. Onat[*], P. Voltr[**], M. Lata[***]

Abstract: *Globally, maintenance tasks for railway vehicles have generally calendar based schedules. However, apparent changes may occur in vehicle structure and environment. Suspension malfunction and substantial change in adhesion conditions can be given as an example for such situations. Since these kinds of changes may affect especially safety, necessary actions must be taken as soon as possible without waiting schedule. This is possible with condition monitoring systems, which lead vehicles to be smarter, as they can inform decision makers for actions. Dynamic response of a vehicle, which includes information about changes in vehicle's structure and environment, can be used for condition monitoring. In this study, a condition monitoring scheme is proposed to identify primary lateral suspension parameter from dynamic response of a wheelset. Identification is based on the well-known model based filtering method, namely unscented Kalman filter.*

Keywords: Condition Monitoring, Wheelset Dynamics, Unscented Kalman Filtering, Wheel-Rail Contact, Parameter Estimation.

1. Introduction

Wheelset is the most important part of a railway vehicle which interacts with rails and has a highly nonlinear dynamic structure. In order to provide better and safer ride, wheelset is connected either to a bogie or a vehicle body with suspension elements in practice. These suspension elements provide the stability of vehicle during run. Especially, the primary suspension system has greater importance such that a problem in this system can cause lack of safety during ride.

Several studies consider the parameter estimation problem by using the dynamic models of railway vehicles. These studies can be divided into two groups. One group of studies focus on the adhesion estimation whereas the second group focus on estimating suspension parameters. (Ward et al., 2012) and (Hussain et al., 2013) are the examples of studies related with the estimation of adhesion. They are using the Kalman filtering scheme to estimate adhesion conditions by considering the lateral dynamical response of the vehicle. Kalman filtering method can only be used for systems which can be modelled and represented in linear state space form. Therefore, (Ward et al., 2012) choose to estimate firstly the creep forces and moments since they can be represented in linear state space form. Whereas (Hussain et al., 2013) choose to linearise the system around operating point and then estimate adhesion conditions by using a post processing method in conjuction with Kalman filtering method.

The second group of studies investigate the applicability of model based filtering methods for estimation of suspension or wheel/rail contact parameters. A literature review, which describes the advances in the related area up to 2007, can be found in (Bruni et al., 2007). (Li et al., 2004) and (Li et al., 2007) propose a filtering scheme that combine particle filter and Kalman filter for estimation and compare the results with the extended Kalman filter case. It is a well-known fact that particle filters are effective tools in identification of highly nonlinear, non-Gaussian systems. However, particle filters require excessive computational power. When the dynamic model of the system is described exactly and

[*] Altan Onat, M.Sc.: Jan Perner Transport Faculty, Transport Means and Diagnostics Department, University of Pardubice, Pardubice; CZ, altanonat@anadolu.edu.tr

[**] Petr Voltr, Ph.D. : Jan Perner Transport Faculty, Educational and Research Centre in Transport, University of Pardubice, Pardubice; CZ, Petr.Voltr@upce.cz

[***] Doc. Ing. Michael Lata, Ph.D. : Jan Perner Transport Faculty, Transport Means and Diagnostics Department, University of Pardubice, Pardubice; CZ, Michael.Lata@upce.cz

the initial conditions are selected carefully, (Zhongshun et al., 2014) show that extended Kalman filter can be applied for identification. However, the extended Kalman filter, which is the nonlinear version of the Kalman filter, suffers from the problems due to linearisation of the models.

In this study, possibility of estimation of primary lateral suspension parameters by using an unscented Kalman filter is presented. However, unlike the previous studies, this study inlcudes a detailed wheel/rail contact model which reduces the error due to modelling in estimation. Furthermore, unscented Kalman filter, which is considered here, is advantageous with respect to particle filter and extended Kalman filter. Details and advantages of unscented Kalman Filter can be found in (Julier & Uhlmann, 2004).

2. Methods

The overall methodology is given in Fig. 1. Necessary explanations can be found in the text.

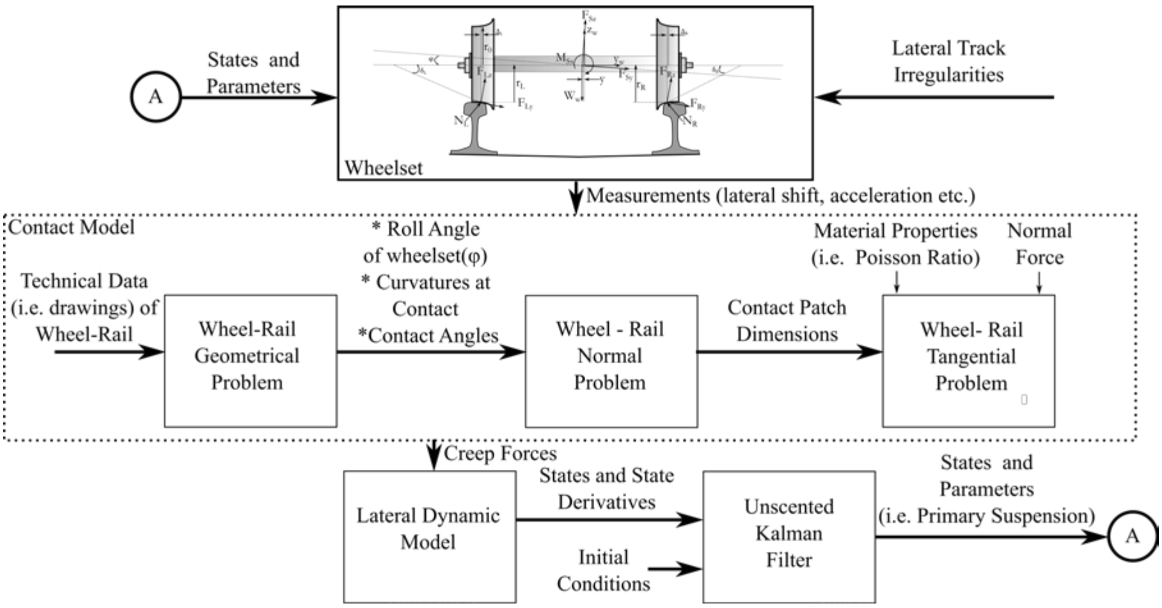

Fig. 1: General Scheme for Estimation.

2.1. Solution to geometrical, normal and tangential contact problem

The wheel/rail pair considered in this study is theoretical S1002/UIC60E1, where the details of these profiles can be found in related European standards. Firstly, by considering these profiles, geometrical problem, normal problem and tangential problem must be solved with respect to the lateral shift of the wheelset due to track irregularities. For the details of the methods to solve geometrical problem and normal problem considered in this study, readers are referred to read (Onat et al., 2015a). However, different from (Onat et al., 2015a), in this study, solution of normal problem is corrected by using the method given in (Piotrowski & Kik, 2008). (Piotrowski & Kik, 2008) converts the actual contact patch area into an equivalent ellipse whose length and width is equal to the length and width of penetration area. Due to the fact that contact area cannot be greater or equal to the penetration area, another penetration term is introduced, namely equivalent penetration, and this penetration is intentionally expanded by a factor. Therefore penetration area remains consistent. The corrected shape of the equivalent ellipse is given as

$$a_c = \sqrt{\frac{\delta_0}{A}}, b_c = \sqrt{\frac{\delta_0}{B}}, \quad (1)$$

where a_c and b_c are the corrected Hertzian contact patch dimensions in meters, δ_0 is the penetration in meters, A and B are the Hertzian curvatures in 1/meter. For all details of the method and explanations readers are refferred to read (Piotrowski & Kik, 2008).

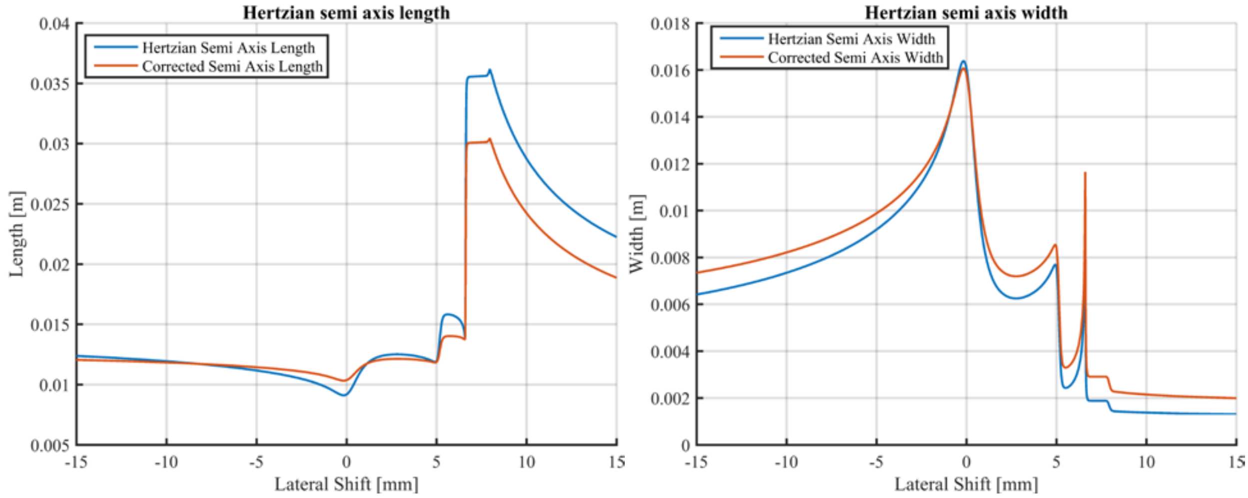

Fig. 2: Corrected width and length of contact patch.

For the solution of the tangential problem the well-known and experimentally validated creep force model of Polach, which is also mentioned in (Onat et al., 2015b), is used.

2.2. Wheelset dynamics and estimation

Details of the lateral dynamic model, which is considered here, can be found in (Onat et al., 2015b). On the other hand, instead of a rigid bogie assumption considered in (Onat et al., 2015b), bogie is modelled as a laterally suspended mass in this study. The lateral suspension force acting on the wheelset is given as

$$F_{sy} = -2k_y\left(y - y_m\right) - 2b_y\left(\dot{y} - \dot{y}_m\right), \tag{2}$$

where F_{sy} is the force due to lateral suspension in Newtons, k_y spring constant of a spring in lateral suspension in Newtons per meter, b_y is the damping coefficient of a damper in lateral suspension in Newton-seconds per meter, $y, \dot{y}$ and $y_m, \dot{y}_m$ are the lateral shift of the wheelset and bogie and their derivatives in meters and in meters per second, respectively. The estimation is based on the fact that change in lateral suspension parameters affects the dynamic response of the wheelset. Track measurements, which are taken from a 3 km track section between Choceň-Dobřikov (CZ), are used to excite the dynamic system. The longitudinal velocity of wheelset is taken 40 m/s. Parameters, which are considered here for wheelset, can be found in Table 1 of (Onat et al., 2015b). Different from that of (Onat et al., 2015b), in this study, the normal force per wheel is 50 kN and the lateral spring stiffness is equal to the $3\text{x}10^6$ N/m.

Continous dynamic system is discretized and by using a Runge-Kutta integration method, solution to the differential equations are obtained. System can be expressed as

$$\begin{aligned} x_k &= f\left(x_{k-1}, u_{k-1}, k-1\right) + q_{k-1} \\ y_k &= h\left(x_{k-1}, k-1\right) + r_k \end{aligned} \tag{3}$$

In Equation 3, x represents vector of states, which are lateral shift, yaw angle, lateral velocity and yaw rate of the wheelset. In the same equation, q and r vectors represent the process and measurement noises, respectively. In this case of application, the input to the system is lateral alignment irregularity, but measurements (all states) are assumed to be taken from wheelset, so that the system becomes output only. A non-augmented joint unscented Kalman filter (i.e. additive noise case) is considered for parameter estimation problem. In order to understand methodology used here, readers are referred to read the study in (Matzuka et al., 2012). (Matzuka et al., 2012) explain the application of unscented Kalman filter for parameter estimation in details and give examples for simple dynamic systems.

In order to test estimation scheme, firstly spring constant of lateral suspension is tried to be estimated statically, i.e. by having a distant initial guess of the parameter. Afterwards, it is assumed that a step change occurs in spring constant of primary suspension. In the first case, it is assumed that the initial guess for the spring constant of lateral suspension is $4\text{x}10^6$ N/m, whereas the real value is $6\text{x}10^6$ N/m. For the second case, it is assumed that real value of the total lateral spring value drops to the $4x10^6$ N/m from $6x10^6$ N/m after 20 seconds. Estimation results are fairly good and can be seen in Fig. 3.

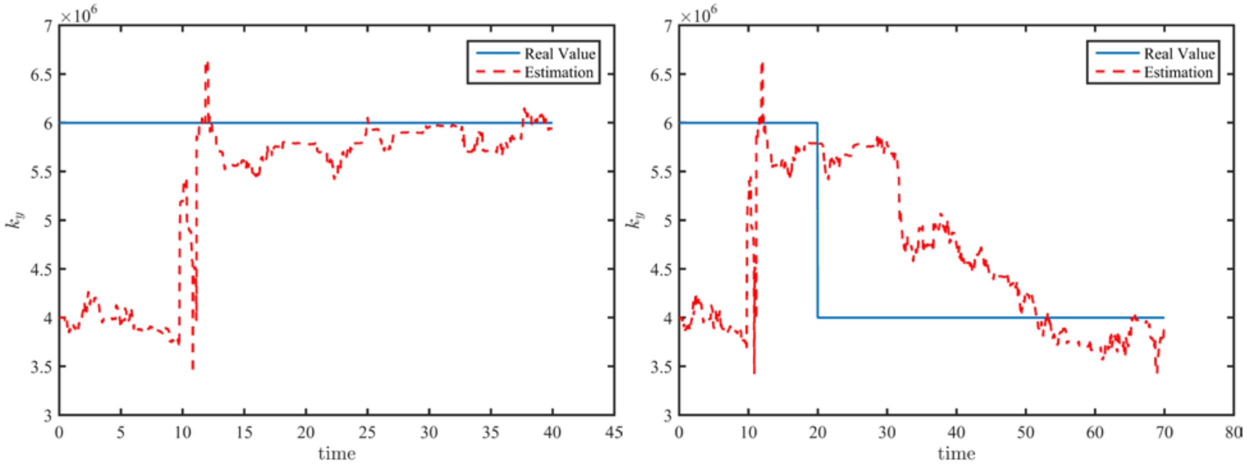

Fig. 3: Static estimation case (left), a step change in spring constant of lateral suspension (right).

3. Conclusions

In this work, a model based filtering scheme to identify primary lateral spring constant of a railway vehicle is investigated. Unlike the previous studies, a detailed model for the wheel/rail contact is considered in the estimation. Furthermore, the advantages of unscented Kalman filter with respect to the previously mentioned methods are used.

Additionally, use of real track irregularity measurements shows that the overall scheme may be appropriate for using the measurements from a real vehicle. By using this approach, if dramatic changes occur in suspension parameters before scheduled maintenance, necessary actions can be taken so that safety issues can be prevented.

References

Bruni, S., Goodall, R., Mei, T., & Tsunashima, H. (2007). Control and monitoring for railway vehicle dynamics. Vehicle System Dynamics, 45(7-8), 743-779.

Hussain, I., Mei, T., & Ritchings, R. (2013). Estimation of wheel–rail contact conditions and adhesion using the multiple model approach. Vehicle System Dynamics, 51(1), 32-53.

Julier, S., & Uhlmann, J. (2004). Unscented filtering and nonlinear estimation. Proceedings of the IEEE, 92(3), 401-422.

Li, P., Goodall, R., & Kadirkamanathan, V. (2004). Estimation of parameters in a linear state space model using a Rao-Blackwellised particle filter. Control Theory and Applications, IEE Proceedings, 151(6), 727-738.

Li, P., Goodall, R., Weston, P., Ling, C., Goodman, C., & Roberts, C. (2007). Estimation of railway vehicle suspension parameters for condition monitoring. Control Engineering Practice, 15(1), 43-55.

Matzuka, B., Aoi, M., Attarian, A., & Tran, H. (2012). Nonlinear filtering methodologies for parameter estimation. North Carolina State University.

Onat, A., Voltr, P., & Lata, M. (2015a). Nonlinear wheel/rail contact geometry characteristics & determination of Hertzian contact. Scientific papers of the University of Pardubice, 19(Series B), 145-152.

Onat, A., Voltr, P., & Lata, M. (2015b). Analysis of lateral dynamical response of a wheelset during traction. 22nd International Conference "Current Problems in Rail Vehicles - PRORAIL 2015", (pages 75-84). Zilina.

Piotrowski, J., & Kik, W. (2008). A simplified model of wheel/rail contact mechanics for non-Hertzian problems and its application in rail vehicle dynamic simulations. Vehicle System Dynamics, 46(1-2), 27-48.

Ward, C. P., Goodall, R. M., Dixon, R., & Charles, G. A. (2012). Adhesion estimation at the wheel–rail interface using advanced model-based filtering. Vehicle System Dynamics, 50(12), 1797-1816.

Zhongshun, Z., Bowen, X., Lei, M., & Shaoyang, G. (July 28-30, 2014). Parameter estimation of a railway vehicle running bogie using extended Kalman filter. Proceedings of the 33rd Chinese Control Conference, (stránky 3393-3398). Nanjing, China.

22nd International Conference
ENGINEERING MECHANICS 2016
Svratka, Czech Republic, 9 – 12 May 2016

INVESTIGATION OF STRESS LEVEL IN WHEEL-RAIL CONTACT

Y. Özdemir*, P. Voltr**

Abstract: *Initial calculation of the wheel and rail contact problem was solved with analytical theories. These include some assumptions during computations. A finite element analysis was performed to compare results of the analytical tools because of the assumptions. In addition, various finite element models have been developed by researchers to examine material response during wheel-rail contact. Damage of the rail surface and its effects on the contact forces are a common research area in numerical computations of wheel-rail contact. Maximum stress level of the model is a key factor of the permanent deformations. Neutral position of the wheelset is commonly selected in the studies. In this study, a wheel-rail contact tool is developed to investigate effects of cant angle and lateral position of wheel on maximum stress level that occurs in the rail part.*

Keywords: Wheel-rail contact, Contact stress, Lateral shift, Cant angle

1. Introduction

Wheel and rail contact is commonly researched for determining the pressure distributions on the contact patch. When the wheel comes into contact with rail, different contact geometry may occur. In the standards, lateral radius of the rail surface has a constant curvature in the central part. In the case of cylindrical wheel shape, the profile of the wheel brings about an elliptical contact shape. In contrast, if the profile of wheel is curvilinear, non-elliptical contact area could be observed at the contact interface. For this reason, contact pressure values are changed when the wheel is supposed to shift laterally.

Telliskivi and Olofsson developed a finite element method based tool for wheel and rail contact. The analysis includes two different cases which are rail gauge corner contact and rail head contact. Maximum contact pressure and values of the total contact area are compared with the results of the Hertz contact theory and Contact software. In the first case, there is significant difference between the Finite element method and validation methods (Telliskivi & Olofsson, 2001).

Yan and Fischer analyzed the wheel and rail contact conditions with FEM. UIC60 rail and UIC-ORE wheel profiles were implemented in the research. Four different values of lateral wheel displacement are considered. Contact pressure distributions of the positions are given for linear elastic, elastic-plastic material models and Hertz contact theory. The results show that if the curvature of the rail surface is constant within the contact area, numerical calculations including elastic material properties are compatible with those of Hertz contact theory (Yan & Fischer, 2000).

The main idea of this study is to determine maximum Von-Mises stress values for various lateral wheelset positions. Also, since rails are normally mounted on the sleepers with an inclination (cant angle) towards the track vertical axis, the effect of rail cant is observed. Results of the numeric simulations are expected to serve as a guide for researchers dealing with analysis of elastic-plastic wheel and rail contact.

* Yalçın Özdemir, M.Sc.: Educational and Research Centre in Transport, Jan Perner Transport Faculty, University of Pardubice, Studentska 95; 532 10, Pardubice; CZ, yalcinozdemir@anadolu.edu.tr

** Ing. Petr Voltr, Ph.D.: Educational and Research Centre in Transport, Jan Perner Transport Faculty, University of Pardubice, Studentska 95; 532 10, Pardubice; CZ, petr.voltr@upce.cz

2. Methods

Finite element simulations are performed via ABAQUS™ (Systèmes, 2013). Theoretical S1002 wheel profile (UIC, 2004) with 920 mm of diameter and UIC 60 rail (EN, 2011) profile with 200 mm of length are chosen for the numeric model. In addition, in order to assess effect of cant angle, two different wheel and rail contact assemblies are designed. One of them is characterized by a 1/40 canted rail whereas in the other one, the rail axis is vertical. The wheel is represented by a rim segment (without the disc or hub), but full rail geometry is utilized. Linear elastic material properties are considered in both of studies in which E = 210 GPa, ν = 0.3 (Deng et al., 2015).

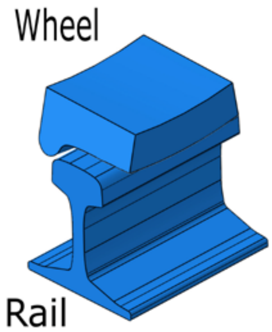

Fig. 1: Illustration of the wheel and rail contact model.

A vertical wheel load of 90 kN is applied at the center of the wheel. Transmission of the force from the reference point to the inner surface of the wheel body is set – constraint definition is used to connect the reference point with the surface of the wheel (Systèmes, 2013). All parts of the assembly are meshed with C3D8R type solid element whose edge size is 0.75 mm. Characteristic element size of the wheel and rail are 2 mm and 3.5 mm, respectively. Only measurement zones have finer FE discretization, so the assembly does not have uniform mesh structure. The FE models are presented in *Fig. 2*.

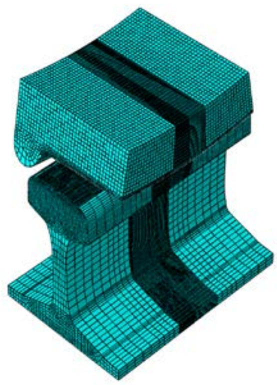

Fig. 2: 3-D meshed wheel and rail contact model.

Contact definition between the wheel and rail surface is defined as surface-to-surface (Systèmes, 2013). Contact definition includes only normal contact. Coefficient of friction is not defined as it does not play a role in the transmission of normal forces. During simulations, nine different lateral shift values (mm) are applied to the wheel part of the geometry. Maximum stress values are obtained in the rail part for each shifted position of wheel. Illustration of positions of the wheel are given in *Fig. 3*.

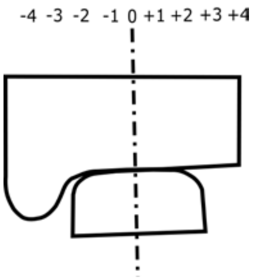

Fig. 3: Lateral wheelset positions [mm], positive values correspond to the wheel displacement away from the track centerline. .

3. Results

Figures 4 and 5 show maximum stress levels with respect to lateral positions of wheel. Two different inclination angles are examined in the study. The results present maximum equivalent stress in the rail part.

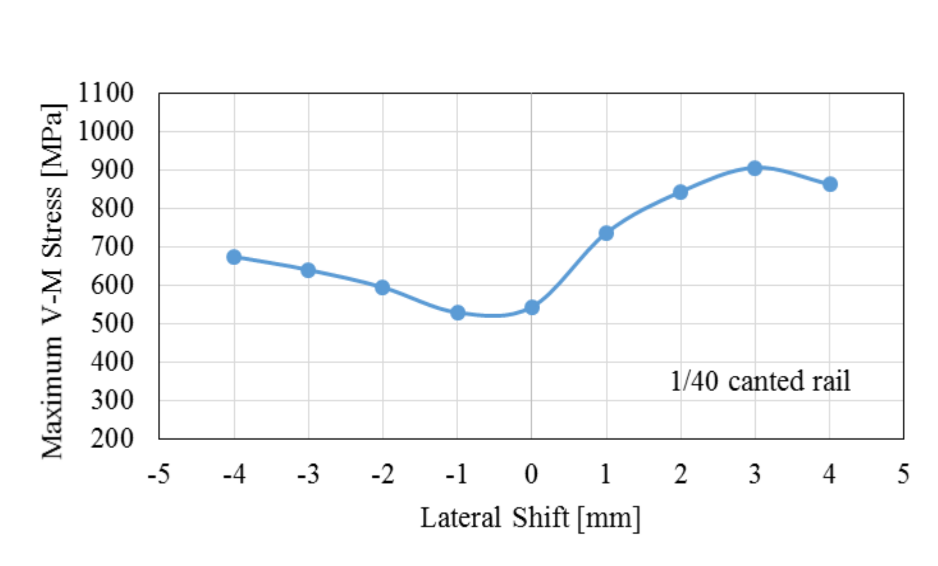

Fig. 4: Maximum Von-Mises stress levels according to lateral positions of the wheel for canted rail

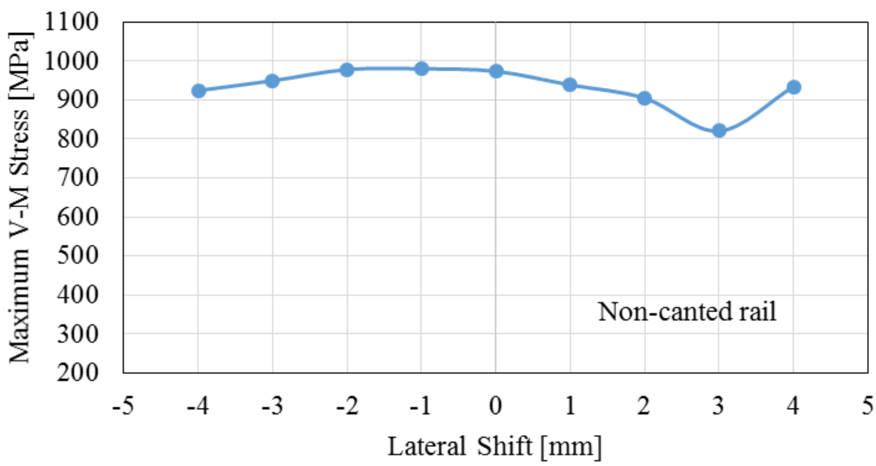

Fig. 5: Maximum Von-Mises stress levels according to lateral positions of the wheel for non-canted rail

For the canted rail, the maximum stress is observed in the +3 mm lateral shift position. In the positive side, stress levels are close to each other. However, when the wheel moves to negative direction, maximum stress in rail part decreases. Minimum values are seen between the zero and –1 mm positions, where the well-known non-Hertzian contact occurs, with the loading distributed in larger area of contact.

In *Fig. 5*, results of the non-canted rail are shown. The curve is different from that for the canted rail (*Fig. 4*) – particularly, the overall values are higher and there are not the peak levels which are seen in *Fig 5*. The results are close to each other between zero and –2 mm lateral positions of the wheel. Additionally, there is not big variation between 1 mm and –3 mm displacement values. Also, minimum stress emerges in the +3 mm position.

The effect of the inclination angle is clearly realized from *Fig. 4* and *Fig. 5*. Maximum stress has stable values for the non-canted rail, but canted rail does not have similar trend. The maximum stress peak values for canted and non-canted rail are close to each other.

4. Conclusions

Researchers focusing on material response of the wheel and rail contact can decide their working conditions according to *Fig. 4* and *Fig. 5*. Maximum equivalent stress level is an effective parameter for the plastic deformation, if the study in question considers elastic-plastic material behaviour. The results give an idea for deciding about lateral positions to analysis of plastic deformation, fatigue etc.

For the 1/40 rail inclination angle, working on the positive direction is better than the negative direction, because maximum stress levels are positioned in positive directions. As a result of that, more plastic deformation could be obtained in the positive direction. In addition, +3 mm lateral position of the wheel has maximum stress levels, so this should be considered.

For the non-canted rail, maximum peak does not appear clearly in *Fig. 5*. However, maximum level is located between zero and –2 mm shifted positions. The minimum stress level is shown in the +3 mm lateral position. Minimum plastic deformation is expected to be in this location. There is neither a significant increasing nor decreasing trend for the maximum stress distribution for the positive and negative directions.

References

510-2 UIC 2004 Code Trailing Stock: Wheels and Wheelset. Conditions Concern, UIC.

13674-1:2011 EN, PN. Railway applications-Track-Rail-Part 1, EN.

Systèmes, D., (2013). ABAQUS 6.13 user manuel. [Online] Available at: http://129.97.46.200:2080/v6.13/

Telliskivi, T. & Olofsson, U., (2001). Contact mechanics analysis of measured wheel-rail profiles using the finite element method. Proceedings of the Institution of Mechanical Engineers Part F, 215(2), pp. 65-72.

Yan, W. & Fischer, F., (2000). Applicabiility of the Hertz contact theory to rail-wheel contact problems. Archive of Applied Mechanic, 70, pp. 255-268.

Deng, X., Qian, Z., Dollevoet, R., (2015). Lagrangian explicit finite element modeling for spin-rolling contact. *Journal of Tribilogy* , 137 (4), pp. 041401(1-11).

22nd International Conference
ENGINEERING MECHANICS 2016
Svratka, Czech Republic, 9 – 12 May 2016

MODELING OF THE BLAST LOAD EFFECTS IN EXPLICIT DYNAMICS

M. Peč[*], P. Kubík[**], F. Šebek[***], T. Návrat[****], J. Petruška[*****]

Abstract: *The present paper deals with a detonation modeling. Comparison of the blast simulation and following propagation of pressure waves within an electric switchboard container is considered using Abaqus and LS-DYNA via the multi material arbitrary Lanrangian–Eulerian method. A simplified model is created in order to study the influence of domain and structure sizes and finite element mesh dependency using selected output variables.*

Keywords: Detonation, Pressure wave, arbitrary Lagrangian–Eulerian method, Explicit dynamics

1. Introduction

Short circuits result in a sudden overloading of structural parts of electric machines, cabling and switchboards, which resemble explosive detonation under some circumstances. Induced pressure waves act on the protection container of such devices. Wrong design of such parts may lead to the damage of the container and its surroundings. That is why the containers have to be properly protected against such failures as described the standards. Those sudden load states have to be considered in the development of new devices and the structure has to be designed to withstand in testing. However, such testing is expensive so it is suitable to use the numerical modelling in the design stage of new device. It is possible to computationally simulate the blast in detail and analyze the pressure waves propagation in time with evaluating its effect to critical sections of the structure. There are many issues in computational modeling of this, like calibration of the material model, finite element mesh setting, defining the boundary conditions and material models or substituting the short circuit by equivalent explosive. Besides calibration of the whole model, it is necessary to assess the behavior of particular computational models, which cannot be conducted on a complex structure but using simplified models. The aim of the present paper is to test the capabilities of particular computational models as the material models, boundary conditions and finite element mesh setting in commercial finite element codes LS-DYNA and Abaqus/Explicit. There are also studied options in creating the model and post processing.

2. Methods

Modeling of blast may be advantageously solved within Multi Material Arbitrary Lagrangian–Eulerian (MMALE) method, when there is a strong coupling between the structure and fluid. The advantage is in possibility of including more different materials in one finite element, such as air or gases generated by the explosion, using a certain volume fraction. In the model is also included a Lagrangian structure presenting the electric apparatus. Both structures, MMALE and Lagrangian, are then coupled using penalty-based algorithm which tracks the relative motion between the structures and applies the penalty forces that resist the penetration of MMALE material through the Lagrangian mesh (Sherkar et al., 2010).

[*] Ing. Michal Peč: Institute of Solid Mechanics, Mechatronics and Biomechanics, Faculty of Mechanical Engineering, Brno University of Technology; Technická 2896/2; 616 69, Brno; CZ, y133757@stud.fme.vutbr.cz

[**] Ing. Petr Kubík, Ph.D.: Institute of Solid Mechanics, Mechatronics and Biomechanics, Faculty of Mechanical Engineering, Brno University of Technology; Technická 2896/2; 616 69, Brno; CZ, kubik.p@fme.vutbr.cz

[***] Ing. František Šebek: Institute of Solid Mechanics, Mechatronics and Biomechanics, Faculty of Mechanical Engineering, Brno University of Technology; Technická 2896/2; 616 69, Brno; CZ, sebek@fme.vutbr.cz

[****] Doc. Ing. Tomáš Návrat, Ph.D.: Institute of Solid Mechanics, Mechatronics and Biomechanics, Faculty of Mechanical Engineering, Brno University of Technology; Technická 2896/2; 616 69, Brno; CZ, navrat@fme.vutbr.cz

[*****] Prof. Ing. Jindřich Petruška, CSc.: Institute of Solid Mechanics, Mechatronics and Biomechanics, Faculty of Mechanical Engineering, Brno University of Technology; Technická 2896/2; 616 69, Brno; CZ, petruska@fme.vutbr.cz

3. Computational model

The basic geometrical model consists of three parts. The first represents the structure itself which consists of sheet container of dimensions 500×500×500 mm with sheet thickness of 2 mm and square hole in the upper part for possible simulation of exhaust with propagation of pressure waves into surroundings. The explosive is modeled as a prismatic body with dimensions of 25×25×150 mm and the surrounding air as a cube with dimensions of 1500×1500×1500 mm. The assembly is depicted in Fig. 1. Everything is placed so that two planes of symmetry can be used. Points 1 and 2 correspond to centers of the structure surfaces and point 3 to center of the edge of exhaust. Point 4 is located 75 mm above exhaust in its axis in the Eulers's domain. Point 5 is placed 25 mm from all surfaces belonging to of the structure corners in the Euler's domain. Finally, point 6 is in the center of one of structure surfaces 25 mm in front of the structure and above the bottom surface in the Euler's domain.

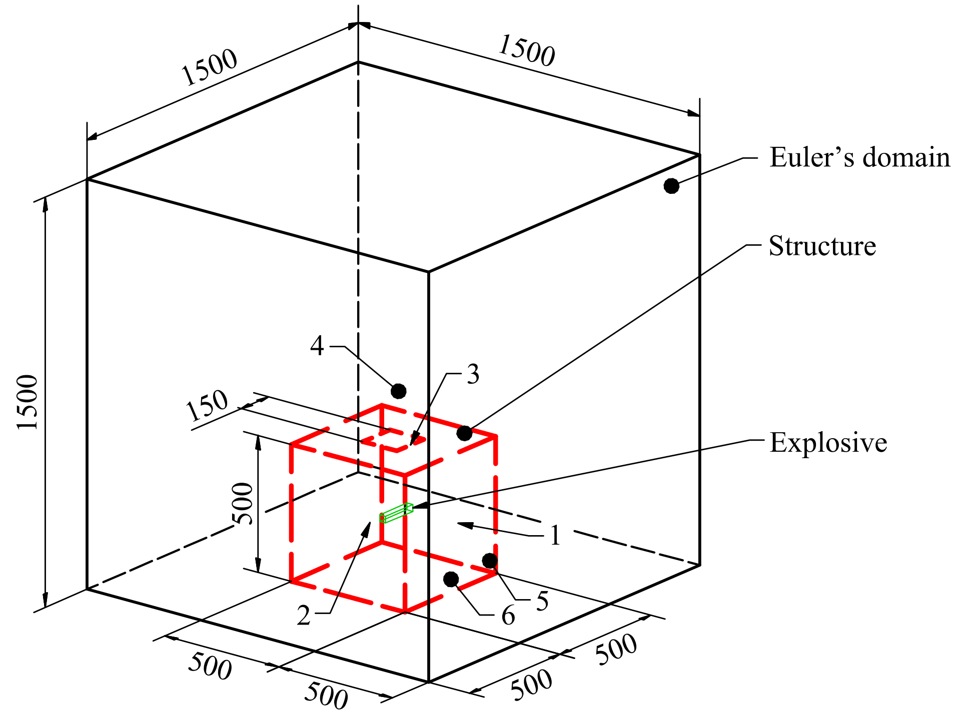

Fig. 1: The basic geometrical model (all dimensions are in mm).

Euler's domain represents both the explosive and air. The geometry was discretized by 8-node solid hexahedron elements in case of Euler's domain which is both inside and outside of the structure and by 4-node shell elements in case of structure. Mapped mesh with 25 mm characteristic element size for structure, surroundings and explosive. The presented model will be considered as the basic one and will differ for particular variants in testing of influence of various variables on the results.

The bottom is represented by surface which reflects the pressure waves. The pressure waves outflow was prescribed to other surfaces. The bottom surface of structure was fixed. The blast load was prescribed by detonation of the explosive in time zero (Puryear, 2012; Vasko, 2012). The blast hits dynamically the structure walls and there is mutual interaction between structure and surroundings. The time scaling factor of 0.6, recommended for extremely fast actions, was used within the time step of 10 ms.

Material properties were set according to real conditions. Isotropic homogeneous elastic-plastic model with linear hardening was used for structure. Elastic behavior was characterized by Young's modulus $E = 210\,000$ MPa, Poisson's ratio $\mu = 0.3$ and density $\rho = 7850$ kg·m^{-3}. Plastic behavior was described by yield stress σ_y = 300 MPa and plastic modulus H = 850 MPa. There is still room for sophisticated description of material behavior including the damage propagation (Kubík et al. 2014; Šebek et al. 2014) but it was not the aim of this paper. The explosive simulating the trinitrotoluene bomb was modeled as high explosive burn material model described by Equation Of State (EOS) for Jones Wilkens Lee as:

$$p = A\left(1-\frac{\omega\rho}{R_1\rho_0}\right)\mathrm{e}^{-R_1\frac{\rho_0}{\rho}} + B\left(1-\frac{\omega\rho}{R_2\rho_0}\right)\mathrm{e}^{-R_2\frac{\rho_0}{\rho}} + \omega\rho E_m \qquad (1)$$

Detailed description of particular variables is given in manuals (Abaqus, 2014; LS-DYNA, 2014). Following constants were used, ρ_0 = 931 kg·m^{-3}, A = 49460 MPa, B = 1891 MPa, ω = 0.33333, R_1 = 3.907, R_2 = 1.118 and E_m = 266809881847.476 MPa. Detonation wave speed was 200 m·s^{-1}. The air was modeled as an ideal gas using null material model with linear polynomial EOS in Abaqus and LS-DYNA, respectively, as:

$$p = \rho_a R(\theta - \theta_Z) \text{ and } p = E\frac{\rho_a}{\rho_0}(\gamma - 1) \tag{2}$$

In Eq. (2), following constants were used, ρ_a = 1.225 kg·m^{-3}, R = 287 J·kg^{-1}·°C^{-1}, θ_Z = 0.245°C and γ = 1.4. Additionally, specific heat at constant volume was 717.5 J·kg^{-1}·°C^{-1} and detonation energy per unit volume was 0.245 MPa.

4. Results

There are evolutions of total displacement magnitude and pressure in time in Fig. 2. Those are obtained from nodes, denoted by N in Fig. 2, in case of displacements and from elements, denoted by E in Fig. 2, in case of pressure. Their positions correspond to the points 1–6 in Fig. 1. Finally, ABQ and DYN represent abbreviations for Abaqus and LS-DYNA, respectively.

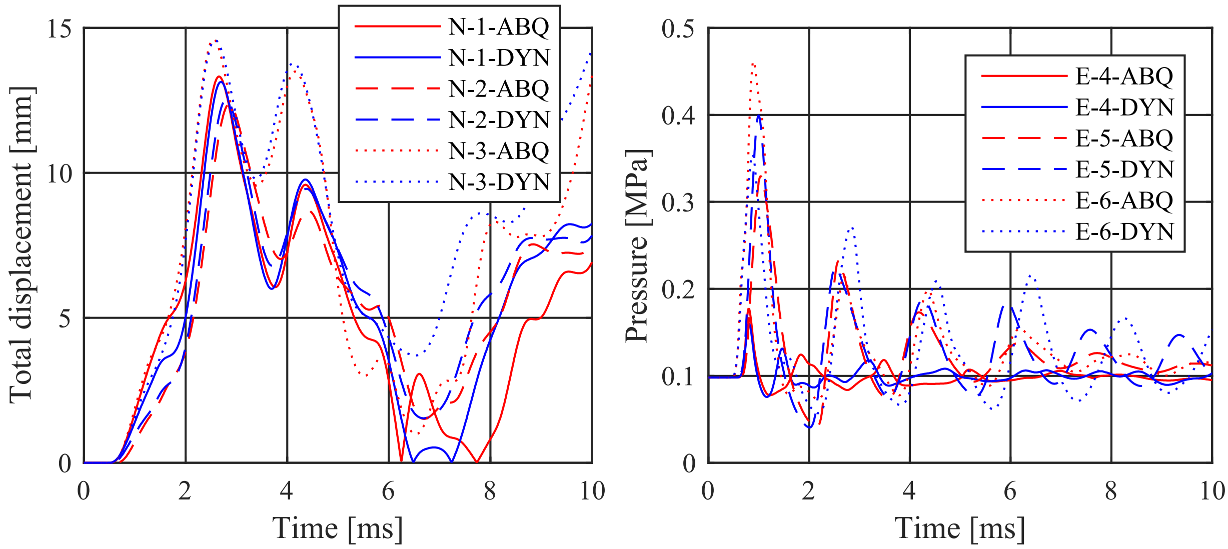

Fig. 2: Evolutions of the total displacement (left) and pressure (right) in time.

There is comparison of contours of pressure waves in time 3.09 ms in Fig. 3.

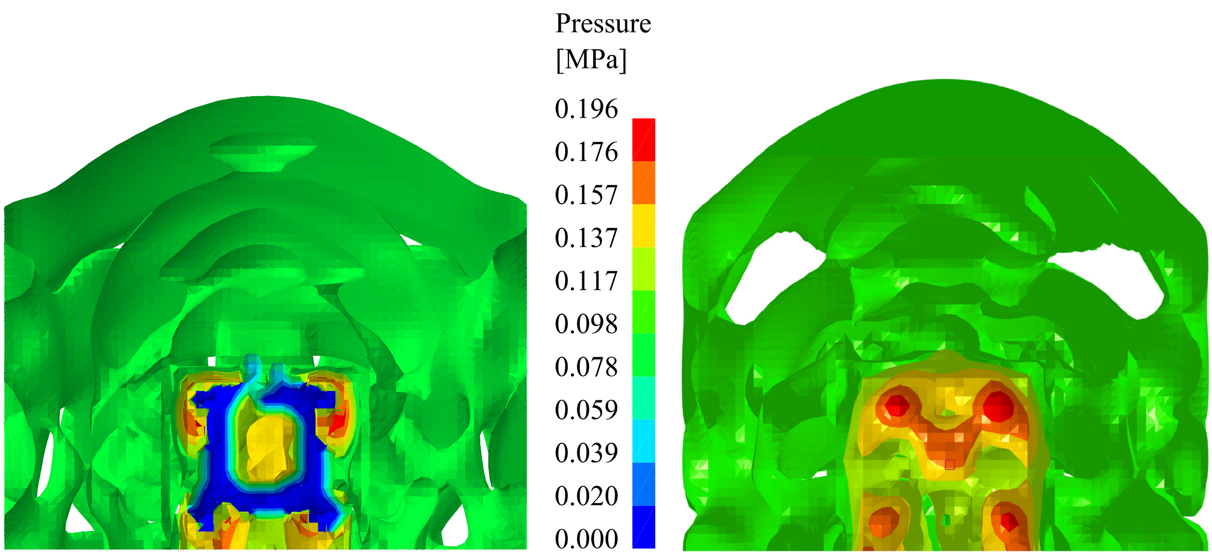

Fig. 3: Contours of pressure waves for Abaqus (left) and LS-DYNA (right).

The computation of basic configuration above took 1586 s within Abaqus. It was for 25 mm sized elements both for structure and domain. It was carried out using two cores of Intel® Core™ i7-980 processor with 3.33 GHz frequency and 24 GB of Random Access Memory (RAM). There were also conducted further analyses in Abaqus on the same computer in order to study the influence of element size both of structure and domain on the computational time. Results are summarized in Tab. 1. It was found that there is quadratic dependency of computational time on the element size of the structure. The dependency on the element size of the domain was not evaluated because the need of memory exceeded the capacity of used RAM in the case of 9717 s and using a hard drive slowed down the process. The influence of the domain dimensions on the computational time was studied as well. It was found that 7429 s was needed for Euler's domain with characteristic size of 3000 mm. The variant with 6000 mm did not even started because the lack of memory.

Tab. 1: Computational times for different variants of simulations.

Element size [mm]	Structure	5	10	20	25		
	Domain	25			15	20	50
Computational time [s]		8844	4363	1992	9717	3538	210

5. Conclusions

The comparison analysis of modeling options of the pressure waves propagation was conducted. The simulations of the blast caused by detonation of the explosion were carried out in two commercial codes, Abaqus and LS-DYNA, respectively. The contours of pressure waves were depicted for qualitative comparison from which it is clear that those are similar. This is confirmed by the quantitative comparison of pressure evolution in time. Nevertheless, it shows there is phase shift in the end of the simulations. Besides the pressure, there was also conducted a quantitative comparison of displacements and computational times. The values of total displacements differ in the second half of the simulations, therefore further investigation is needed. Man-power needed for creation of the models was similar in both finite element codes. Nevertheless, there are more possibilities within LS-DYNA for model and boundary conditions settings. Moreover, the possibilities of post processing in LS-DYNA are far more comprehensive and less time consuming.

Acknowledgement

This work is an output of project NETME CENTRE PLUS (LO1202) created with financial support from the Ministry of Education, Youth and Sports under the „National Sustainability Programme I".

References

Abaqus. (2014) Abaqus 6.14 Documentation. Dassaul Systèmes Simulia Corporation, Providence, Rhode Island.

Kubík, P., Šebek, F., Petruška, J., Hůlka, J., Růžička, J., Španiel, M., Džugan, J. & Prantl, A. (2014) Calibration of Selected Ductile Fracture Criteria Using Two Types of Specimens. Key Engineering Materials, 592–593, pp. 258–261.

LS-DYNA. (2014) LS-DYNA Keyword User's Manual R7.1, Livermore Software Technology Corporation, Livermore, California.

Puryear, J.M.H, Stevens, D.J., Marchand, K.A., Williamson, E.B. & Crane, C.K. (2012), ALE Modeling of Explosive Detonation on or near Reinforced-Concrete Columns, in: Proc. 12th Int. LS-DYNA Users Conf., Detroit, pp. 1–11.

Sherkar, P., Whittaker, A.S. & Aref, A.J. (2010) Modeling the Effects of Detonations of High Explosives to Inform Blast-Resistant Design. Technical Report MCEER-10-0009, University at Buffalo, State University of New York, Buffalo.

Šebek, F., Kubík, P. & Petruška, J. (2014) Localization Problem of Coupled Ductile Failure Models Compared to Uncoupled Ones, in: Proc. 20th Int. Conf. on Engineering Mechanics (V. Fuis ed), Brno University of Technology, Svratka, pp. 632–635.

Vasko, T.J. (2012) LS-DYNA Aerospace Working Group, Modeling Guidelines. LS-DYNA® Aerospace Working Group, New Britain.

22nd International Conference
ENGINEERING MECHANICS 2016
Svratka, Czech Republic, 9 – 12 May 2016

DIAGNOSTIC OF THE VVER REACTORS INTERNALS VIBRATIONS

L. Pečínka*, **M. Švrček****

Abstract: *Integrity of the VVER reactors internals is the important requirement of the NPPs long term operation. Two possible methods how to meet these requirements are: non destructive evaluation and diagnostic of the mechanical vibrations. The second one method is in the next analyzed. As the sensors are obviously used accelerometers, pressure pulsation sensors, ex-core ionization chambers and self powered neutron detectors. The significant changes of the frequency spectra are supposed to be symptom of the integrity changes..*

Keywords: **VVER type reactors, Accelerometers, Pressure pulsation sensors, Ex core ionization chambers, Frequency spectra.**

1. Introduction

Nuclear regulators in all countries require as the part of the PWRs long time operation permission the confirmation of the reactors internals integrity. The term reactor internals include core barrel, block of the protective tubes, and core basket or core shroud. As the part of the preoperation hot tests and initial start up tests the frequency spectra of the reactor internals are measured and evaluated in the form of the power spectral densities -(PSDs).This PSDs represent starting i.e. nonfailed state and all next measured PSDs during operation are with this ones compared. The significant deviations represent symptom of the possible failure.

2. Used sensors

As the sensors are obviously used accelerometers, ex core ionization chambers, pressure pulsation sensors, self powered neutron detectors (SPNDs) and during preoperation hot tests in some cases also strain gauges. In the next the principles of the rhodium SPNDs are described. The schema of the rhodium activation and chargé emission is as follows

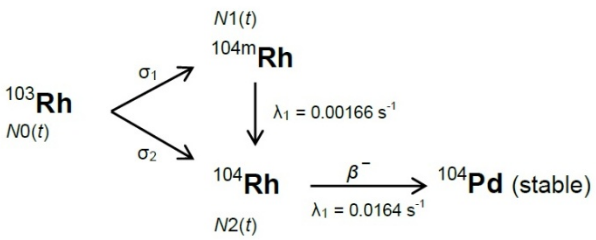

where
$\sigma_1 \sigma_2$: capture cross section
$\lambda_1 \lambda_2$: decay time

Emission is used which charges the rhodium electrode to a positive potential. The electrical system is a current generator with a high potential resistance $R_I = 10^8 \Omega$ much higher than the dynamic input resistance of the chargé circuit $R_c = 10^4 \Omega$ .The relationships between SPN detector current and neutron flux are as follows: the activation diagram is expressed by the following equations

* Ing. Ladislav Pečínka, CSc.: ÚJV Řež, a. s., Hlavní 130, 250 68 Husinec – Řež.; ladislav.pecinka@ujv.cz
** Ing. Miroslav Švrček, ÚJV Řež, a. s., Hlavní 130, 250 68 Husinec – Řež; miroslav.svrcek@ujv.cz.

$$\frac{dN1(t)}{dt} = N\sigma 1\varphi(t) - \lambda 1N1(t) \quad (1)$$

$$\frac{dN2(t)}{dt} = N\sigma 2\varphi(t) + \lambda 1N1(t) - \lambda 2N2(t) \quad (2)$$

where
N : number of Rh^{103} nuclei
N1(t): number of the Rh^{104m} nuclei
N2(t): number of the Rh^{104} nuclei
φ (t): neutron flux at time t
The measured current is expressed as

$$i(t) = K\lambda 2N2(t)$$

where K is a constant taking into account the emission yield, the transmission of the insulator, the number N0 of the rhodium nuclei and the units (current, charges).When resolving the differential system (1),(2), one deduced (with an appropriated mathematical method)

$$\varphi(t) = \frac{1}{KN\sigma 2\lambda 2}\frac{di}{dt} + \frac{i}{KN\sigma 2} - \frac{\lambda 1}{NG2}N1 \quad (3)$$

an non explicit equation since the term in N1 consist according to equation (1). It is evident that rhodium SPN detectors subjected to a variable neutron flux behaves like first order linear system. This introduces time constants between the output electric current and the input flux. The time laws of the current cannot then be identified with that of the flux and processing of the differential equations system is required to reconstitute the flux. Finally the PSDs of the measured current is evaluated.

3. NPP Dukovany

In NPP Dukovany are operated four units of the reactors VVER 440 Model 213 Č. For monitoring of the reactor internals vibrations are used sesmic sensors of absolut displacement and ex-core ionisation clambers. Cross section of the seismic sensor of absolut displacement is illustrated in Fig. 1:

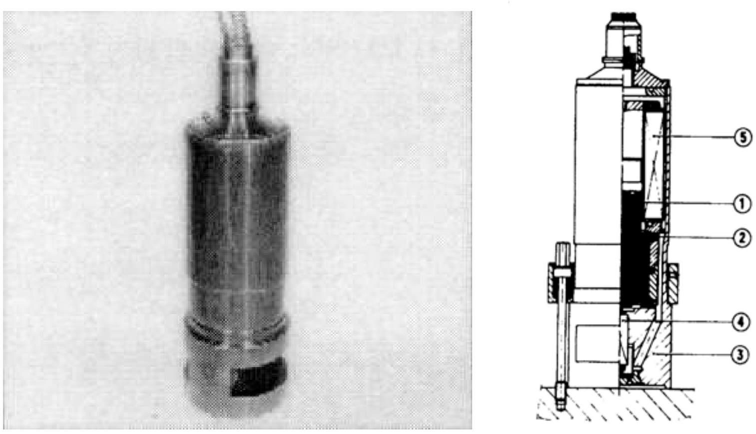

1… inertia mass

2... two springs

3... outer barrel

4... sensor of the relative displacemenet

5... magnetic coil

Fig. 1 : Crosssection of the displacement sensor

Details of the location of the displacement sencor on the reactor pressure vessel are illustrated in the Fig. 2.

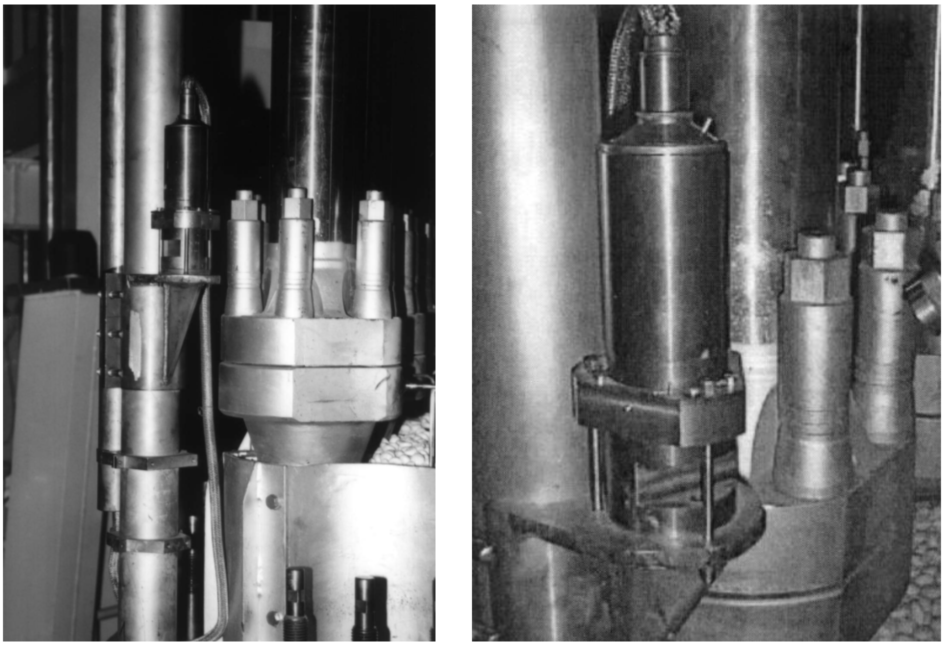

General view Detail

Fig. 2: Details of the location of displacement seinsors

Results of measurements are illustrated in the Table 1:

Tab. 1: operational vibrations of the VVER 440 Model 213 reactor

Frequency Hz	Description
6.3	First acoustic standing wave in primary circuit
8.6	RPV and reactor internals in vertical direction
11	nonidentified
12.8	Second acoustic standing wave in primary circuit
16	nonidentified
22.4	RPV and reactor internals in vertical opposite direction
24.8	Pressure pulsations generated by main circulation pump
27.9	vertical vibrations of the upper block
37.5	3/2 ultrasubharmonic to the frequency 24.8
45	nonidentified

RPV ... reactor pressure vessel

4. NPP Temelín

In NPP Temelín are operating two units of the VVER 440/320 reactor. For monitoring of the reactor internals vibrations is installed Reactor Vibration Monitoring System (RVMS) which consist four accelerometers installed on the RVP flange, pressure pulsation sensors (only on Unit 2), eight ex-core ionization chambers and SPNDs 64 fuel assemblies consist 7 detectors and one compensation detector, together 512 detectors. RVMS monitor SPNDs on the levels 1,3,5,7 local repressed 256 signals. They are organized in 16 selected groups with 16 signals. For monitoring vibrations is possible to choice each from these groups. Locations of the accelerometer, ex-core ionization chambers and SPNDs are illustrated in Figs 3 and 4.

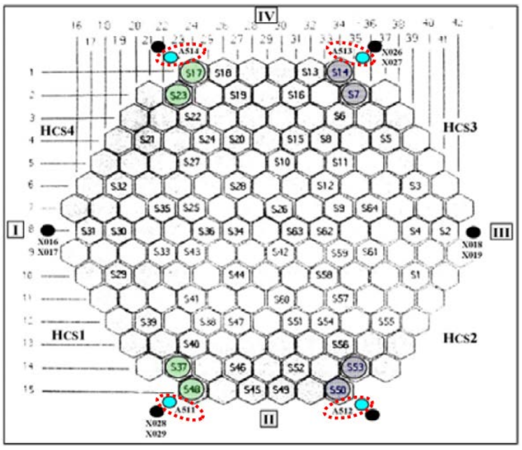

Fig. 3: Location of the accelerometers (Y)

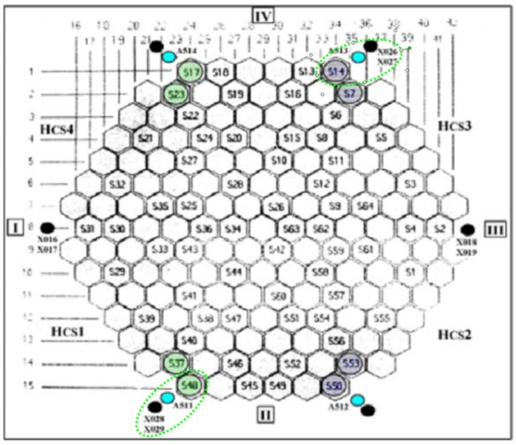

Fig. 4: Locations of SPNDs and ex-core IC (X)

IC … ionization chamber

Results of the SPNDs measurements are illustrated in Tab. 2:

Tab. 2: Results of the SPNDs measurements of the VVER 1000 MW reactor

Frequency Hz	Description
0.76	Standing wave in primary circuit including pressurizer
5.8	Second bending frequency of the fuel assembly
6.5	First acoustic standing wave in primary circuit
9.1	Standing wave in reactor pressure vessel
12.0	Third torsion frequency of the fuel assembly
12.5	Second acoustic standing wave in primary circuit
15.0	Fourth bending frequency of the fuel assembly
16.6	First frequency of the pressure pulsations generated by MCP
18.8	In-phase pendulum motion of the RPV and core barrel
22.5	Third acoustic standing wave in primary circuit
24.9	3/2 ultrasubharmonic to frequency 16.6 Hz
33.2	Second frequency of the pressure pulsations generated by MCP
49.8	Third frequency of the pressure pulsations generated by MCP

5. Conclusions

Monitoring of the reactor internals vibration is a important part of the nuclear safety of the operating PWR reactors. From the point of view of applied mechanics the following disciplines are used and in some cases

-Dynamic of mechanical systems with many degree of freedom as reactor etc [1]

-Acoustic phenomena in complicated piping systems [2].

Thanks to operation of two Czech NPPs in Dukovany and Temelín, many interesting works have been developed in WBU Plzeň. Dept. of Mechanics and ÚJV Řež, a. s.

References

Zeman Vl., Hlaváč Zd.: Prediction of the Nuclear Fuel Rod Abrassion in the Probability Sense. Enginearing Mechanics 2015, Svratka, Czech Republic

Pečínka L., Švrček M.: Acoustic Standing Waves in Primary Circuit of NPPs with WWER 1000 MW. Enginearing Mechanics 2015, Svratka, Czech Republic

22nd International Conference
ENGINEERING MECHANICS 2016
Svratka, Czech Republic, 9 – 12 May 2016

TEMPERATURE ANALYSIS IN THE VICINITY OF TRIAXIAL TRAILER DISC BRAKE

D. Perczyński*, K. Peszyński*, L. Knopik, S. Wawrzyniak***

Abstract: *The paper demonstrates the friction nodes statistical analysis of road tractor brakes as well as the temperatures analysis of selected wheel breaking systems. The measurement system consists of six temperature sensors mounted in the vicinity of the friction nodes and seventh to measure the ambient temperature. The output signals of the sensors are transmitted to a digital temperature meter based on ATmega 32 microcontroller. The measurement results were recorded on the SD memory card. The digital temperature sensors of the 1-wire interface manual DS18B20 of Dallas Semiconductor were used to measure the temperature. Moreover, the paper presents the research regarding the wheel temperature dependency of the outside temperature. The Principal Component Analysis was used for statistical testing of brakes temperatures. The method enables the statistical task dimension designation. The dependence analysis between the pairs of wheels was carried out using correlation methods and the spectral analysis of stochastic processes. The study of the coherence function proved that testing system is a linear system with constant parameters.*

Keywords: statistical analysis, road tractor brakes, principal factor analysis, brake temperature.

1. Introduction

The breaking system of a truck is an especially important system for road safety and operation of a vehicle. The intensive experiments and theoretical analysis of the system have been conducted in the Control Division of the Faculty of Mechanical Engineering at UTP University of Science and Technology in Bydgoszcz. It has been assumed that the temperature at the selected point of a wheel brake is a measure of correct operation of the system under operational conditions.

The electronic data acquisition system of temperature from selected friction nodes of the road track disk has been developed. The measuring system consists of six sensors located near friction nodes and 7th measuring the ambient temperature. The sensor output signals are transferred to the digital temperature meter based on ATmega 32 microcontroller. Braking and temperature of friction nodes are not correlated. It is due to the fact that temperature in wheels increases with some delay. Seeking to find the transfer function of the linear system with a binary signal at the input if the system (braking or not) has not given the answer what the transfer function for the system is. The reason of the above is a low correlation between braking and temperature. The analyzed process was observed at the $T_{\mathrm{ob}} = 2240\,\mathrm{s}$. Total period of braking was $T_{\mathrm{h}} = 39\,\mathrm{s}$.

2. Mathematical model

*Assist. Prof. Daniel Perczyński, PhD.: UTP University of Science and Technology, Faculty of Mechanical Engineering, Al. prof. S. Kaliskiego 7, 85-796 Bydgoszcz; PL, daniel.perczynski@utp.edu.pl

*Assoc. Prof. Kazimierz Peszynski, PhD.: UTP University of Science and Technology, Faculty of Mechanical Engineering, Al. prof. S. Kaliskiego 7, 85-796 Bydgoszcz; PL, kazimierz.peszynski@utp.edu.pl

**Assoc. Prof. Leszek Knopik, PhD.: UTP University of Science and Technology, Faculty of Management, Fordońska 430, 85-790 Bydgoszcz, PL, leszek.knopik@utp.edu.pl

*Assist. Prof. Sylwester Wawarzyniak, PhD.: UTP University of Science and Technology, Faculty of Mechanical Engineering, Al. prof. S. Kaliskiego 7, 85-796 Bydgoszcz; PL, sylwester.wawrzyniak@utp.edu.pl

The matrix of correlation coefficients is determined for a random variable $\left(T_1, T_2, T_3, T_4, T_{5,} T_{6,} T_z, H\right)$, where $T_i\left(i = 1,2,\ldots,6\right)$ is temperature of i^{th} fraction node, T_z – ambient temperature, H – binary signal ($H\left(t\right)=1$ – braking, $H\left(t\right)=0$ no braking). The values of obtained coefficients are presented in Table 1.

Tab. 1. Matrix of correlations between temperature and braking

	T_1	T_2	T_3	T_4	T_5	T_6	T_z	H
T_1	1.000							
T_2	0.997	1.000						
T_3	0.980	0.979	1.000					
T_4	0.996	0.997	0.980	1.000				
T_5	0.948	0.946	0.989	0.951	1.000			
T_6	0.997	0.998	0.977	0.999	0.945	1.000		
T_z	0.818	0.801	0.865	0.827	0.912	0.814	1.000	
H	-0.055	-0.048	-0.063	-0.039	-0.063	-0.040	-0.065	1.000

The analysis of the correlation matrix results shows that the correlation coefficients between wheel temperatures are very high, the correlation coefficients between wheel temperatures and the outside temperature are a little bit lower, but still high. The correlation coefficients between wheel temperatures and braking are not significant.

The statistical data $\left(T_1, T_2, T_3, T_4, T_{5,} T_{6,} T_z\right)$ are measurable and all of them are measured in degrees Celsius, while the characteristic H is binary dimensionless. A large number of statistical hypothesis based on the assumption of normality features can be tested for measurable characteristics. Significance of the correlation coefficients and the dimensionality of space is carried out by the principal component analysis. The correlation matrix for the characteristics $\left(T_1, T_2, T_3, T_4, T_{5,} T_{6,} T_z\right)$ contains high values of the correlation coefficients. Therefore, the question arises if seven-dimensional space of the characteristics $\left(T_1, T_2, T_3, T_4, T_{5,} T_{6,} T_z\right)$ is not redundant? The research attempts to answer the question by using the principal component analysis.

3. Principal component analysis

The principal component analysis consists in converting the input observations into the new unobservable variables. The new variables are uncorrelated. Each of the principal components is a linear combination of input variables. The principal components are arranged in the way that variances of further components get smaller and smaller. Usually the first few principal components give the most information about an examined phenomenon. The key assumptions of the method should be verified before starting the principal components analysis. The method is applicable when the correlation between variables are relatively high. The basic assumption is the normality of data. In the analyzed phenomenon the normality of tested data is ensured and, furthermore, there is a large number of analyzed test sample, $n = 2240$. There is given the matrix $\mathbf{X}$ with dimension of l_e lines for l_z columns, where: l_e – the number of experiments and l_z – the number of variables. For analyzed data there is $l_e = 2240$ and $l_z = 7$. $Y\left(i\right)$ means the average value in i^{th} column of the matrix $\mathbf{X}$. We create the matrix $\mathbf{X}_c$ based on the matrix $\mathbf{X}$ by subtracting the average value of $Y\left(i\right)$ in the column from each element of the matrix $\mathbf{X}$.

We make the matrix $\mathbf{S} = \left(\mathbf{X}_c{}^T\mathbf{X}_c\right)/\left(l_e - 1\right)$ known as a covariance matrix of a random vector $\left(T_1, T_2, T_3, T_4, T_{5,} T_{6,} T_z\right)$. The solution of the equation $\det\left(\mathbf{S} - \lambda\mathbf{I}\right) = 0$, where $\mathbf{I}$ is the identity matrix, are the eigenvalues of the matrix $\mathbf{S}$. The matrix $\mathbf{S}$ is a symmetrical matrix and positive definite. This is due to the fact that there are $l_z = 7$ actual and non-negative eigenvalues $\lambda_1 \geq \lambda_2 \geq \lambda_3 \geq, \ldots, \geq \lambda l_z$. The following values has been calculated for the data analyzed in the paper: $\lambda_1 = 6.6420$, $\lambda_2 = 0.3017$, $\lambda_3 = 0.0478$, $\lambda_4 = 0.0048$, $\lambda_5 = 0.0018$, $\lambda_6 = 0.0011$, $\lambda_7 = 0.0005$. Analysis of eigenvalues shows that the first eigenvalue is much higher than the other values.

4. Correlation analysis of temperature change process

The following part of the paper is dedicated to the relations between stochastic processes, especially processes regarding the changes of temperature values in the braking system of the trailer. Testing the processes and determining the characteristic of the process is possible, because the measurement data of the implemented process are available. The analysis contains $n = 2240$ temperature measurements, 6 process implementations every $\Delta t = 1\text{s}$. For testing the temperature signal accordance of the friction nodes on one of vehicle disk, we determine the coherence function specified by the formula (Bendat J.S., Piersol A.G. 1976):

$$\gamma_{xy}^2(\omega) = \frac{|S_{xy}(\omega)|^2}{S_{xx}(\omega)S_{yy}(\omega)} \tag{1}$$

where $S_{xx}(\omega)$ and $S_{yy}(\omega)$ are the spectral densities of temperature and braking, which are determined by formulas

$$S_{xx}(\omega) = \int_{-\infty}^{\infty} R_{xx}(\tau)e^{-j2\pi\omega}d\tau \tag{2}$$

$$S_{yy}(\omega) = \int_{-\infty}^{\infty} R_{yy}(\tau)e^{-j2\pi\omega}d\tau \tag{3}$$

where $R_{xx}(\tau)$ is the autocorrelation function determined as an average value:

$$R_{xx}(\tau) = E\{X(t)X(t+\tau)\}$$

The above formula can be written in limit form: $R_{xx}(\tau) = \lim_{T\to\infty} \frac{1}{T}\int_0^T x(t)x(t+\tau)dt$

The value $R_{xx}(0) = E\{X(t)^2\}$ is known as a mean square value of the process $X(t)$. Simultaneously, the mean square value of the process $X(t)$ is defined as:

$$R_{xx}(0) = \int_{-\infty}^{\infty} S_{xx}(\omega)d\omega$$

On the other hand, $S_{xy}(\omega)$ and $S_{yx}(\omega)$ are mutual spectral densities:

$$S_{xy}(\omega) = \int_{-\infty}^{\infty} R_{xy}(\tau)e^{-j2\pi\omega}d\tau \tag{4}$$

$$S_{yx}(\omega) = \int_{-\infty}^{\infty} R_{yx}(\tau)e^{-j2\pi\omega}d\tau \tag{5}$$

where $R_{xy}(\tau)$ is the cross-correlation function (mutual correlation) determined as an average value: $R_{xy}(\tau) = E\{X(t)Y(t+\tau)\}$, the coherence function satisfies the condition $0 \le \gamma_{xy}^2(\omega) \le 1$, for the linear system with constant parameters $\gamma_{xy}^2(\omega) = 1$ (Morrison D.F. 1990).

The calculated value of the coherence function is constant and approximately equal 1. In practice, it is very important to determine the autocorrelation function $R_{xx}(\tau)$ and the correlation function of measuring data. An unbiased estimator of the autocorrelation function $R_{xx}(\tau)$ is the statistics (Krzyśko M., 2000)

$$\hat{R}_{xx}(rh) = \frac{1}{N-r}\sum_{n=1}^{N-r} x_n x_{n+r} \,,$$

where: $x_1, x_2, x_3, \ldots, x_n$ are the measurements of implemented process $X(t)$ measured by the constant step $h = \Delta t$. An unbiased estimator of the cross-correlation function $R_{xy}(\tau)$ is the statistics

$$\hat{R}_{xy}(rh) = \frac{1}{N-r}\sum_{n=1}^{N-r} x_n y_{n+r}$$

where $y_1, y_2, y_3, \ldots, y_n$ are the measurements of implemented process $Y(t)$ measured by the constant step h. The formulas (2), (3), (4) are (5) implemented by the Fourier transform.

It is much easier to test the relations between the temperatures in the friction nodes than between temperature and braking. The Fig. 2 presents the value diagrams of the cross-correlation function for pairs of wheels from one disk (1, 2), (3, 4) and (5, 6). The diagrams have the same characteristic, however, clear differences between the disks can be noticed.

5. Conclusions

The temperatures values in the function of time presented in the paper are seen as a stochastic process, while the temperature changes for each friction node constitute implementation of this process.

The correlation matrix determined for the vector $(T_1, T_2, \ldots T_{6,})$ shows that all of the correlations are strongly significant. However, the correlation coefficient values are different for different pairs (T_i, T_j).

It has been proved that the use of the principal component analysis for the set of friction node temperatures is intentional, because the method shows redundancy of analyzed sample. It is the result of high correlation of the temperature processes in the vehicle wheels. The use of the correlation analysis for the processes of temperature changes in friction nodes of the braking system has explained the relation between temperatures and has given the basis for future research in this task. The previous research has been confirmed by the transfer function defined in the paper.

References

Bendat J.S., Piersol A.G. (1976): Metody analizy i pomiaru sygnałów losowych (Eng. Measurements and Analysis of Random Data). PWN, Warszawa.

Krzyśko M. (2000): Wielowymiarowa analiza statystyczna (Eng. Multivariate statistical methods), Wydawnictwo Naukowe UAM, Poznań.

Morrisom D.F. (1990): Wielowymiarowa analiza statystyczna (Eng. Multivariate statistical methods, New York: McGraw-Hill), PWE, Warszawa.

22nd International Conference
ENGINEERING MECHANICS 2016
Svratka, Czech Republic, 9 – 12 May 2016

MATHEMATICAL MODEL OF SELECTED OBJECT THERMAL PROPERTIES

K. Peszynski*, W. Szmyt*, S. Wawrzyniak*, D. Perczynski*

Abstract: *The paper presents the mathematical model of temperature changes of selected point in the home sauna obtained by the experimental identification. The basic simplifying assumptions, which lead to a linear model with constant coefficients in the form of the transfer function, are presented. The model parameters which are missing and impossible to measure have been determined by simulations conducted in ANSYS-FLUENT software. A qualitative assessment of compliance measurement results of the tested object and its model has been performed after a simulation in the Scilab-Xcos computing environment.*

Keywords: thermal properties, ANSYS-FLUENT, SCILAB-Xcox, on-off control, mathematical model.

1. Introduction

Thermal objects, for example: furnaces, heating chambers, heat exchangers, rooms, greenhouses are characterized by large time constants and significant delays. This is the reason why the on-off control is usually used for their control in case when there is no necessity of very precise control process, e.g. domestic equipment. However, there are processes for which this type of control in not precise enough, e.g. air conditioning of an operating room, technical devices in the pharmaceutical or bioengineering industry. Then, the on-off control with correction or the control by constant or discrete controllers (PLC – Programmable Logic Controller) is applied.

The task is more complicated when it is necessary to apply programme changes of set temperature, e.g. drying rooms. Then, the control process requires PLC. For the proper selection of a controller and its preliminary setting, there is the need for knowledge of the mathematical model of controlled object and the processes it undergoes. The mathematical model in the form of motion equations can be obtained as a result of thermal processes analysis occurring in a given technical object. In practice, however, the preparation of energy balance requires significant simplification, which affects the quality of the final model. Due to the fact that we very often have to deal with modernisation of existing buildings, it is useful to determine the model by using actual course analysis of selected thermal object.

2. Experimental studies

The home sauna presented in Fig. 1 has been investigated. Fig. 1a shows the heater with power of 2 kW. The characteristic dimensions and the measurement point arrangement are presented in Fig. 1b. The left bottom corner of the front wall of the sauna, where the heater is located nearby, was adopted as the beginning of coordinate system.

The measuring system (Szews M., et al., 2014) contains of five temperature sensors, which measure its value in different points of the sauna. Ambient temperature has been measured by a mercury

*Assoc. Prof. Kazimierz Peszynski, PhD.: UTP University of Science and Technology, Faculty of Mechanical Engineering, Al. prof. S. Kaliskiego 7, 85-796 Bydgoszcz; PL, kazimierz.peszynski@utp.edu.pl

*Wojciech Szmyt, BSc.: UTP University of Science and Technology, Faculty of Mechanical Engineering, Al. prof. S. Kaliskiego 7, 85-796 Bydgoszcz; PL

*Assist. Prof. Sylwester Wawarzyniak, PhD.: UTP University of Science and Technology, Faculty of Mechanical Engineering, Al. prof. S. Kaliskiego 7, 85-796 Bydgoszcz; PL, sylwester.wawrzyniak@utp.edu.pl

*Assist. Prof. Daniel Perczyński, PhD.: UTP University of Science and Technology, Faculty of Mechanical Engineering, Al. prof. S. Kaliskiego 7, 85-796 Bydgoszcz; PL, daniel.perczynski@utp.edu.pl

thermometer and it has been taken as a constant, because its changes during the measurements did not exceed the temperature of $0{,}5°C$. Locations of the measuring points $T_i(x,y,z)$ for $i=1,...,5$ are presented in Fig. 1b with respect to the marked coordinate system.

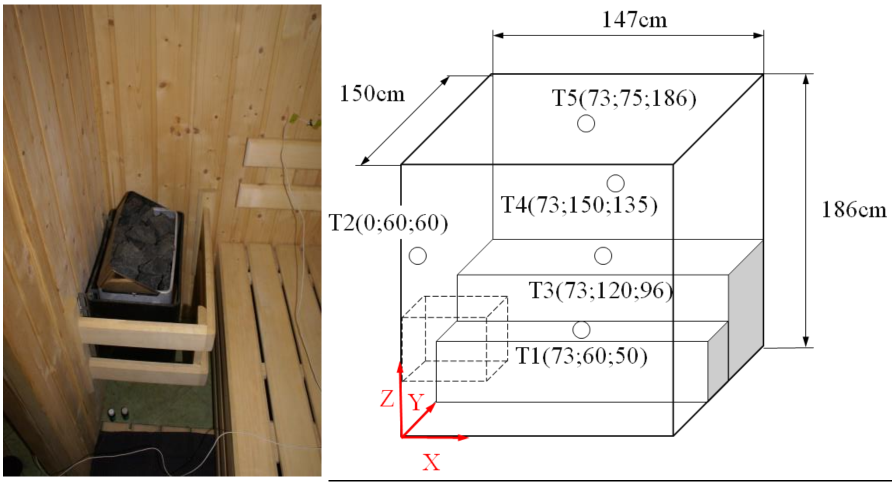

Fig. 1. Object of study: a) part of object with the heater, b) sensors placement

The research consisted of turning on the heating system of the sauna and recording the temperature of five selected measurement points. Time of the automatic sampling was 1 s. The heating system contains the control system, which provides automatic turning on and off of the heating process when the set temperature is reached, as well as its turning off after the set time.

3. Results

The results of experimental studies for selected measuring points are shown in Fig. 2. (Szmyt W. 2016). Each of presented curves consists of three intervals. The first interval (I.) consisting of heating the sauna to the operating temperature lasted 64 min. The second interval (II.), which lasted 196 min., occurred after reaching the operating temperature. Although, the temperature value was assumed to be constant during the control time, it was observed that the temperature was still increasing, however, much slower than during the heating time. The change of average temperature during the interval (II.) contradicts common on-off control system theory (Peszyński K., Siemieniako F. 2002), which does not consider transient states.

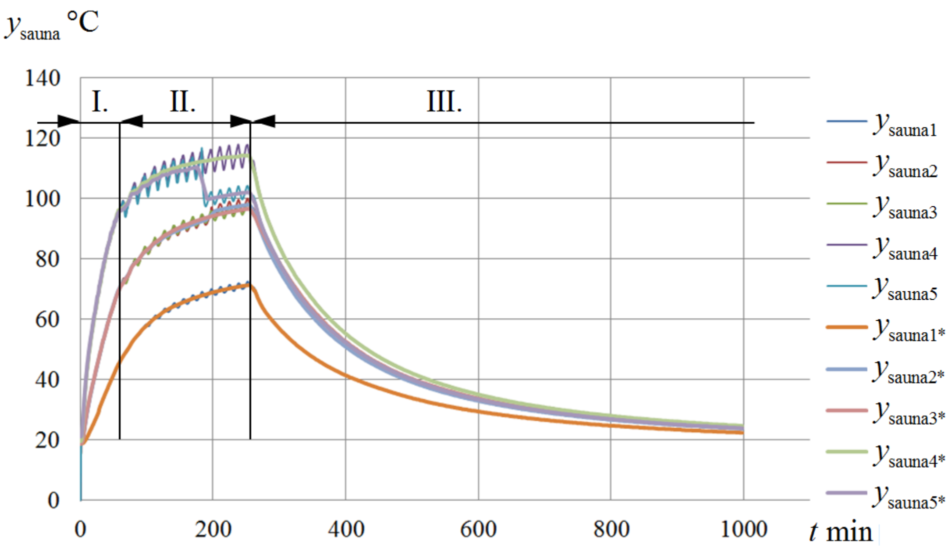

Fig. 2. Measurement results (measurement points as shown in Fig. 1b)

The phenomenon can be explained by the location of the temperature sensor, which controls on-off rely of the heater, near the heating element.

4. Analysis of measurement results

Seeking the mathematical model which describes the thermal properties it is assumed that the sauna is an object with one heat capacity (interior) determined by the transfer function

$$G_{\mathrm{sauna}}(s)=\frac{k}{Ts+1} \tag{1}$$

where k is the gain of the sauna and T is time constant.

Designation the parameters of k and T is difficult because of the measurement characteristic. The curves presented in Fig. 2 only during the initial phase (interval I.) and cooling time (interval III.) qualitatively correspond to the curves calculated from the formula (1). During the interval II., the on-off control is carried out and involves the periodic switching on and off the heating element. This type of control is difficult for mathematical description, especially during the transitional period when the average temperature changes. The simplification consisting of determining the average time for each switching on and off periods enables to determine the course of temperature presented in Fig. 2 through the curves designated as $y_{\mathrm{sauna}i*}$, where $i=1,2,\ldots,5$ is a number of the measuring point. Power of the heating element, as a result of part time heater operation, is assumed to be an input value. The above analysis enables the assumption of the following mathematical model of the sauna

$$\Delta y_{\mathrm{sauna}}=\begin{cases} y=0 & t<0 \\ y_{\mathrm{I}}=\Delta y_{\mathrm{sauna}}^{\infty}\left(1-e^{-\frac{t}{T}}\right) & 0\le t<t_{\mathrm{cP}} \\ y_{\mathrm{II}}=y_{\mathrm{I}}-c\cdot\Delta y_{\mathrm{sauna}}^{\infty}\left(1-e^{-\frac{t-t_{\mathrm{cP}}}{T}}\right) & t_{\mathrm{cP}}\le t<t_{0\mathrm{P}} \\ y_{\mathrm{III}}=y_{\mathrm{II}}-(1-c)\Delta y_{\mathrm{sauna}}^{\infty}\left(1-e^{-\frac{t-t_{0\mathrm{P}}}{T}}\right) & t\ge t_{0\mathrm{P}} \end{cases} \tag{2}$$

The period fulfilment coefficient c, shown in the formula (2), is calculated from the dependence

$$c=\frac{t_{\mathrm{on}}}{t_{\mathrm{cycle}}} \tag{3}$$

where the period of oscillation equals $t_{\mathrm{cycle}}=t_{\mathrm{on}}+t_{\mathrm{off}}$, time of heater operation t_{on}.

Because of enforcing periods and the responses of the controlled object are always the same, the output raising time y_{sauna} is assumed as the time of heater operation t_{on}, while the dropping time of the value (temperature) as the off time t_{off}.

Another problem was to determine the gain of the sauna $\Delta y_{\mathrm{sauna}}^{\infty}$, included in the formula (2), which corresponds to the coefficient k of the model written as the formula (1). $\Delta y_{\mathrm{sauna}}^{\infty}$ cannot be found in the diagrams because the heater was switched off before reaching the set state. The measurement without switching off the heater was impossible, because the sauna would have been destroyed by the temperature above 200°C. A solution to the problem has been found by using ANSYS-FLUENT software and numerical modelling. Only the steady state resulting from switching on the heater to the max has been modelled. The sauna is enclosed by four walls with different thicknesses, which are made of different materials, ceiling and floor, which are also made of different materials, the outside temperatures are also different, therefore it was assumed that heat flows through an averaged wall. The thermal parameters of the wall were chosen iteratively (Szmyt W. 2016), in the way to ensure the outflow of thermal energy complies with the average outflow during interval I. of heating the sauna. The temperature distribution in the sauna in steady state is presented in Fig. 3. It should be noted that the temperature in Fig. 3 is shown on Kelvin scale.

Time constant T of the model, the formulas (1) and (2), has been estimated from the courses of measured values (Fig. 2).

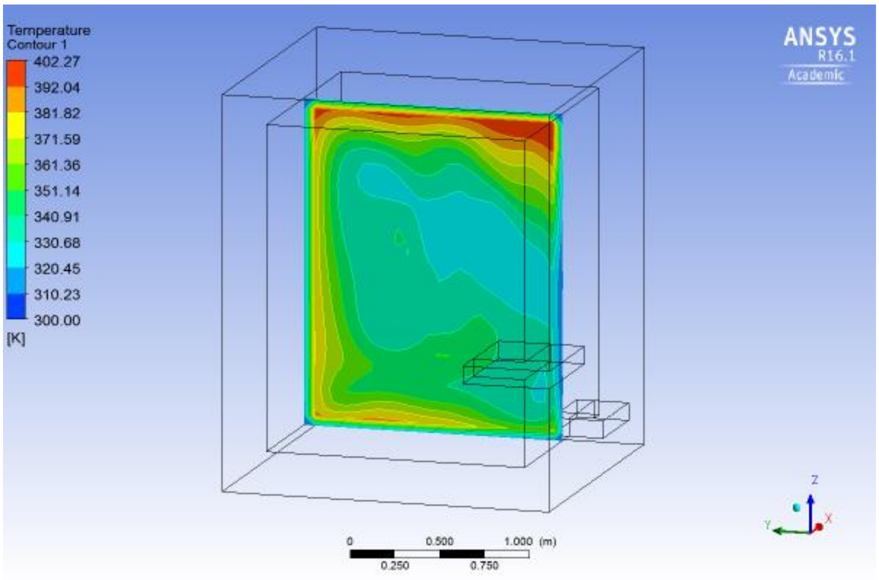

Fig. 3: Results of temperature simulation.

5. Conclusions

The mathematical model determined by the formula (2) enabled finding the courses of temperature changes in the sauna. SCILAB–Xcos computing environment has been used for determining the courses. The following parameters have been adopted the simulation: $\Delta y^{\infty}_{\text{sauna}} = 220°\text{C}$, $t_{c\text{P}} = 64\,\text{min}$, $t_{0\text{P}} = 260\,\text{min}$, $T = 160\,\text{min}$, $c = 0.476$.

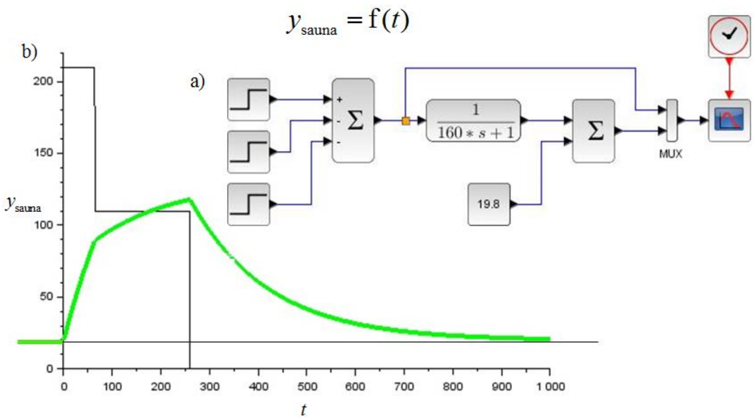

Fig. 4: Sauna temperature simulation: a) block diagram b), course of input power and output temperature

The courses presented in Fig. 2 and Fig. 4 are qualitatively compatible. Precise quantitative matching will be investigated in the next step of modelling. The modelling techniques (measurements, numerical simulations in ANSYS-FLUENT and SCILAB-Xcos computing environment) have been very useful for identification of thermal objects.

References

Peszyński K., Siemieniako F. (2002) Sterowanie procesów podstawy i przykłady (in English Processes control – basics, solved problems, ATR University Pres, Bydgoszcz

Szews M., Perczyński D., Wawrzyniak W., Peszyński K. (2014): Metoda diagnozowania stanu zdatności układu hamulcowego naczep i ciągników siodłowych. Studia i materiały polskiego stowarzyszenia zarządzania wiedzą 68. Bydgoszcz. ISSN 1732-324X

Szmyt W. (2016) Model matematyczny właściwości cieplnych sauny w domku jednorodzinnym. (in English: Mathematical Model of Thermal Properties in a Detached House Sauna). Bachelor Thesis. UTP University of Science and Technology.

22nd International Conference
ENGINEERING MECHANICS 2016
Svratka, Czech Republic, 9 – 12 May 2016

PARALLEL MANIPULATOR WITH PNEUMATIC MUSCLE DRIVE

D. S. Pietrala*

Abstract: *A parallel delta manipulator of six degrees of freedom with a pneumatic muscle drive was presented in this paper. A solid manipulator model was explained as well as a prototype of this device was presented. Drive units of the manipulator, which consist of two pneumatic counter-rotating muscles connected via belt spur drive and produced by the author of this paper, were characterized. The author presented a scheme of the control system and explained its elements. A kinematic model of the manipulator that is essential in the steering process, was shown. Some unique features of the device, such as high overload of pneumatic muscles, were outlined in this paper as well. They allow applying the manipulator when operating with items of unknown or irregular shapes. Possible collisions of the effecter with the items transferred will be effectively damped by the drives.*

Keywords: parallel manipulator, pneumatic muscle, kinematics of industrial robots.

1. Introduction

Industrial manipulators, both those of serial structure as well as with a closed kinematic chain, are one of the main elements of flexible production lines. Electric or hydraulic drives are applied in the majority of cases in those devices. (Laski, Pawel Andrzej et al., 2014) The author suggested application of parallel pneumatic muscles to the drive. Such drives are characterized by high flexibility and overload capacity as well as its natural abilities to move smoothly.

2. Solid model of the manipulator

A parallel delta manipulator of six degrees of freedom was presented in this article. Its construction was shown in Fig. 1. The device consists of a stationary base, six identical and independent arms and a moveable platform. Each arm is built of an active part that is connected with a drive unit, and of a passive part connected with the platform. The mobility of the operating platform of the manipulator is six. It might be calculated using the formula (1)

$$w = 6n - \sum_{i=1}^{5} ip_i \tag{1}$$

where: w – manipulator's mobility, n – number of moveable manipulator elements, i – pair class appearing in the kinematic chain, p_i – number of kinematic pairs of i-class. Each arm of the manipulator is driven by an independent drive unit, which consists of two pneumatic counter-rotating muscles, belt spur drive, bearing unit and an angle encoder. Linear movement of pneumatic muscles is changed into rotary movement of the active arm element with the use of the belt spur drive.

* M.Sc. Dawid Sebastian Pietrala: Department of the Automatic Control Engineering and Robotics, Kielce University of Technology, Aleja Tysiaclecia Panstwa Polskiego 7, 25-314, Kielce; PL, dpietrala@tu.kielce.pl

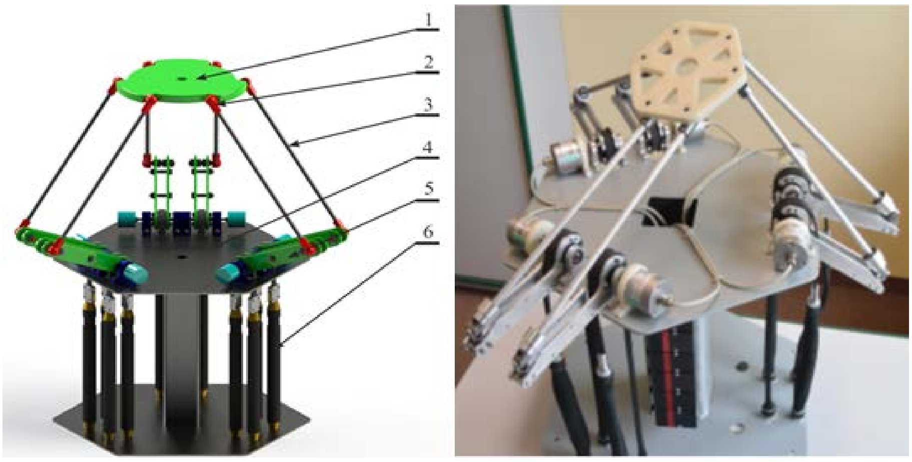

Fig. 1: Manipulator construction – general overview; 1 – operating platform, 2 – joint 3 – arm (passive element), 4 – base, 5 – arm (active element), 6 – drive unit

3. Kinematic model of the manipulator

The task of the manipulator is to move the operating platform against the stationary base. The platform movement constitutes the resultant of six controlled simultaneous movements of arms. As a result of such a movement, manual operation of the manipulator consisting in changing the angular position of each drive regardless of the others, is difficult or even impossible. That is why, in order to control the manipulator, determining and solving the inverse kinematics problem is essential. The problem consists in indicating drive articulated coordinates, knowing the setpoint position and orientation of the operating platform. The solution of the inverse kinematics problem was conducted in two stages. In the first one, knowing the setpoint position and orientation of the operating platform, the coordinates of points located in the upper joints of particular arms were determined. The correlations that allowed to determine those coordinates are presented with the following formula (2).

$$\begin{Bmatrix} C_{i,x} = P_x - R_2 \sin\zeta_i\left(\cos\alpha\sin\gamma + \cos\gamma\sin\alpha\sin\beta\right) + R_2\cos\beta\cos\zeta_i\cos\gamma \\ C_{i,y} = P_y + R_2 \sin\zeta_i\left(\cos\alpha\cos\gamma - \sin\alpha\sin\beta\sin\gamma\right) + R_2\cos\beta\cos\zeta_i\sin\gamma \\ C_{i,z} = P_z + R_2\cos\zeta_i\sin\beta + R_2\cos\beta\sin\alpha\sin\zeta_i \end{Bmatrix} \tag{2}$$

where: i – joint number (arm), $C_{i,x}, C_{i,y}, C_{i,z}$ – coordinates of i-joint, ζ_i – location angle of the joint on the platform, R_2 – radius of the circle, where the following joints are located $P_x, P_y, P_z, \alpha, \beta, \gamma$ – setpoint location and platform orientation.

Subsequently, taking advantage of the Denavit – Hartenberg parameters, dependencies, which allowed to calculate configuration coordinates, with a known position of the upper joint, were determined for each arm. Those dependencies are functions of three variables and for each arm they create a system of three equations with three unknown quantities that is presented with the following dependency (3)

$$\begin{Bmatrix} f_{i,x}\left(\theta_{i,1},\theta_{i,2},\theta_{i,3}\right) = -Wsp_{i,x} + R_1\cos\varepsilon_i + l_1\cos\left(\pm\left|\varepsilon_0\right|+\varepsilon_i\right)\cos\theta_{i,1} - l_2\sin\left(\pm\left|\varepsilon_0\right|+\varepsilon_i\right)\sin\theta_{i,3} + l_2\cos\left(\pm\left|\varepsilon_0\right|+\varepsilon_i\right)\cos\left(\theta_{i,1}+\theta_{i,2}\right)\cos\theta_{i,3} \\ f_{i,y}\left(\theta_{i,1},\theta_{i,2},\theta_{i,3}\right) = -Wsp_{i,y} + R_1\sin\varepsilon_i + l_1\sin\left(\pm\left|\varepsilon_0\right|+\varepsilon_i\right)\cos\theta_{i,1} + l_2\cos\left(\pm\left|\varepsilon_0\right|+\varepsilon_i\right)\sin\theta_{i,3} + l_2\cos\left(\theta_{i,1}+\theta_{i,2}\right)\sin\left(\pm\left|\varepsilon_0\right|+\varepsilon_i\right)\cos\theta_{i,3} \\ f_{i,z}\left(\theta_{i,1},\theta_{i,2},\theta_{i,3}\right) = -Wsp_{i,z} + h + l_1\sin\theta_{i,1} + l_2\sin\left(\theta_{i,1}+\theta_{i,2}\right)\cos\theta_{i,3} \end{Bmatrix} \tag{3}$$

where: i – joint number (arm), $\theta_{i,1}, \theta_{i,2}, \theta_{i,3}$ – articulated coordinates of a particular arm, $\varepsilon_0, \varepsilon_i$ – position angles of the arm on the base, R_1 – radius of the circle, where the following arms are located, l_1, l_1, h – geometrical dimensions of the arms and base. $\theta_{i,1}$ is, however, an articulated coordinate of the drive of the i-arm. The system was solved with the use of the Newton-Raphson method. (Blasiak, 2015) As a result, a set of three solutions was achieved. Each solution included three articulated coordinates. From a mathematical point of view, those solutions are correct. However, they need to be verified as far as their physical correctness is concerned and later, the proper solutions need to be chosen. (Blasiak & Pawinska,

2015) Fig. 2 presents the trajectories of manipulator drives for two set trajectories of the operating platform: helix and circle, with stable orientations.

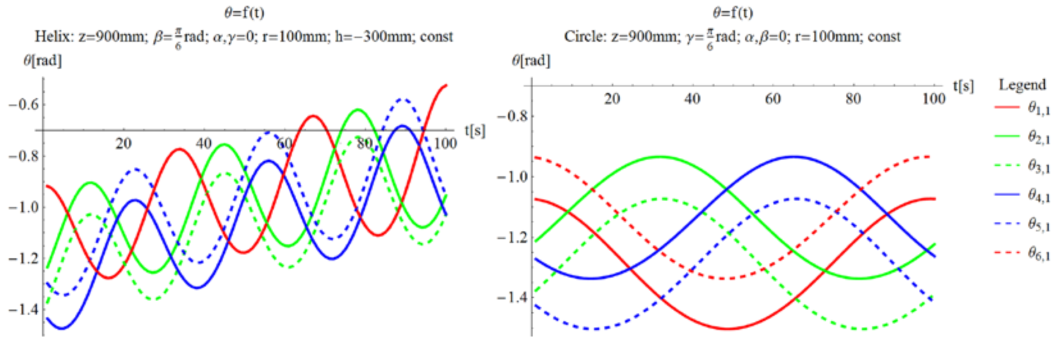

Fig. 2: Trajectories of particular drives for set displacements of the operating platform.

4. Operating space of the manipulator

Operating space of the manipulator determines a set of all points in the space that a robot is able to produce. This space, however, differs for various orientations of the operating platform. The operating platform presented in this paper was determined via discretization of points for zero orientation of the operating platform, i.e. for angles $\alpha, \beta, \gamma = 0$. (Laski, P A et al., 2014) A set of points surrounded by park position of the manipulator with dimensions bigger than the maximal width of the robot arms was randomly generated. Subsequently, out of that set of points, points for which it was possible to solve the inverse kinematics problem were chosen. What is more, the results of such calculations, which are articulated variables of the manipulator arms, need to fulfil the geometric conditions. (Janecki & Zwierzchowski, 2015) The operating space of the manipulator under consideration was presented in Fig. 3.

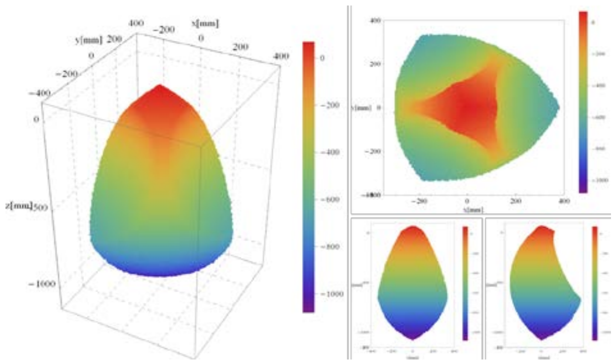

Fig. 3: The operating space of the manipulator determined for zero orientation of the effecter, in configuration of the robot with the platform pointed downwards.

5. Control system of the manipulator

The main element of the control system of the manipulator is a computer with real time system produced by *Speedgoat*. This device is equipped with AC & CA transducers (Takosoglu, J E et al., 2014). The system operation was divided into two stages. (Takosoglu, Jakub Emanuel et al., 2009) The first one is dedicated to solving the inverse kinematics problem and indicating new articulated coordinates. Solution of six systems of non-linear equations is required. The control system in the second stage generates proper signals that control the drive units (Andrs et al., 2012). Each control system consists of two counter-rotating pneumatic muscles. 3/2 proportional pressure valves, model tecno plus, manufactured by HOERBIGER were proposed to operate the pneumatic muscles. Those valves have piezoelectric control, which ensures quick response time. 16-bit absolute encoders of Posital Fraba, model OCD-S101G-1416-S060, served to measure the drive angular position. The scheme of the control system was presented in Fig. 4.

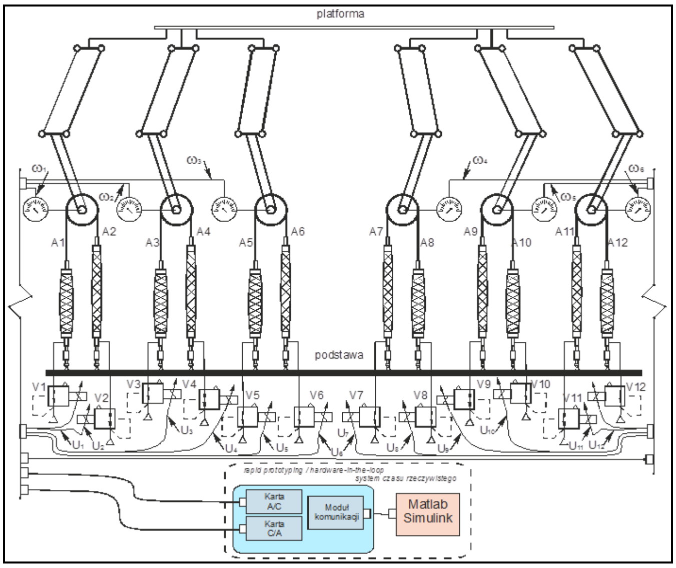

Fig. 4: Scheme of the control system of the manipulator

6. Conclusions

The manipulator of six degrees of freedom and with a closed kinematic chain was presented in this paper. The author presented the manipulator construction and the kinematic model, explained the operating space as well as showed the control system of the manipulator. The construction of the manipulator of six degrees of freedom allows free space orientation of the transported items. Artificial pneumatic muscles were applied as drives. The features of the applied drives provide the manipulator with high dynamics. They enable smooth start and stop as well as eliminate results of collisions of the manipulator with the surrounding areas. Due to the application of pneumatic drives, instead of electric, it is possible to use the manipulator in hazardous environment with danger of explosions or fire. A drawback of the applied drives is the difficulty of controlling them that results from their non-linear characteristic. From the research of a single muscle pair, it might be concluded that positive results of the drive positioning are obtained when using PID or Fuzzy Logic controllers.

References

Andrs, O., Brezina, T., & Kovar, J. (2012) Design of Fuzzy Logic Controller for DC Motor, In R. Jablonski & T. Bvrezina (Eds.), (pp. 9–18). Berlin, Heidelberg: Springer Berlin Heidelberg. doi:10.1007/978-3-642-23244-2_2

Blasiak, S. (2015) An analytical approach to heat transfer and thermal distortions in non-contacting face seals, International Journal of Heat and Mass Transfer, 81, pp. 90–102. doi:10.1016/j.ijheatmasstransfer.2014.10.011

Blasiak, S., & Pawinska, A. (2015) Direct and inverse heat transfer in non-contacting face seals, International Journal of Heat and Mass Transfer, 90, pp. 710–718. doi:10.1016/j.ijheatmasstransfer.2015.07.004

Janecki, D., & Zwierzchowski, J. (2015) A method for determining the median line of measured cylindrical and conical surfaces, MEASUREMENT SCIENCE {&} TECHNOLOGY, 26, 8. doi:10.1088/0957-0233/26/8/085001

Laski, P. A., Takosoglu, J. E., & Blasiak, S. (2014) A DELTA TYPE CLOSED KINEMATICS CHAIN WITH PNEUMATIC MUSCLE ACTUATOR MANIPULATOR, In Fuis, V (Ed.), *ENGINEERING MECHANICS 2014* (pp. 360–363). DOLEJSKOVA 5, PRAGUE 8, 182 00, CZECH REPUBLIC: ACAD SCI CZECH REPUBLIC, INST THERMOMECHANICS.

Laski, P. A., Takosoglu, J. E., & Blasiak, S. (2014) Design of a 3-DOF tripod electro-pneumatic parallel manipulator, Robotics and Autonomous Systems. Elsevier.

Takosoglu, J. E., Dindorf, R. F., & Laski, P. A. (2009) Rapid prototyping of fuzzy controller pneumatic servo-system, INTERNATIONAL JOURNAL OF ADVANCED MANUFACTURING TECHNOLOGY, 40, 3-4, pp. 349–361. doi:10.1007/s00170-007-1349-5

Takosoglu, J. E., Laski, P. A., & Blasiak, S. (2014) INNOVATIVE MODULAR PNEUMATIC VALVE TERMINAL WITH SELF-DIAGNOSIS, CONTROL AND NETWORK COMMUNICATIONS, In Fuis, V (Ed.), *ENGINEERING MECHANICS 2014* (pp. 644–647). DOLEJSKOVA 5, PRAGUE 8, 182 00, CZECH REPUBLIC: ACAD SCI CZECH REPUBLIC, INST THERMOMECHANICS.

22nd International Conference
ENGINEERING MECHANICS 2016
Svratka, Czech Republic, 9 – 12 May 2016

3D STABILITY OF PRESTRESSED STAYED COLUMNS

R. Pichal[*], J. Machacek[**]

Abstract: *A geometrically nonlinear analysis of the buckling and post-buckling behavior of the stayed columns is employed using FEM and ANSYS software. The buckling of these members depends on their geometrical and material properties, prestressing and boundary conditions. In the paper are discussed respective critical buckling loads and post-buckling paths with regards to 2D LBA (linear buckling analysis) and 3D GNIA (geometrically nonlinear analysis with imperfections). Former tests and recent detailed analyses of other authors are commented with respect to 3D analysis, level of imperfections and boundary conditions at the central crossarm.*

Keywords: Prestressed stayed columns; nonlinear buckling; finite element modelling; 3D analysis; sliding stays.

1. Introduction

The stayed columns in a practical layout are formed by a central steel tube of length L, a mid-span crossarm with 4 arms of length a in angle $\alpha = 90°$ and stays made of cables or rods, each with prestressing T. The basic setup shown in Fig. 1 was analyzed analytically by Smith et al. (1975) and Hafez et al. (1970), distinguishing 3 zones of behavior according to level of prestressing and resulting in principal formulas for buckling loads under arbitrary stay prestressing and „optimal" prestressing T_{opt} giving maximal buckling load $N_{cr,max}$. Influence of initial deflections was studied e.g. by Saito and Wadee (2009), showing predominant buckling modes with respect to ratio $2a/L$, stay area A_s, and shape of initial deflections (respective modes shown in Fig. 2). The stayed columns were also tested experimentally, e.g. by Araujo et al. (2008), Servitova & Machacek (2011), Osofero et al. (2012), the last one revealing post-buckling behavior of imperfect stayed columns depending on critical modes and level of prestressing.

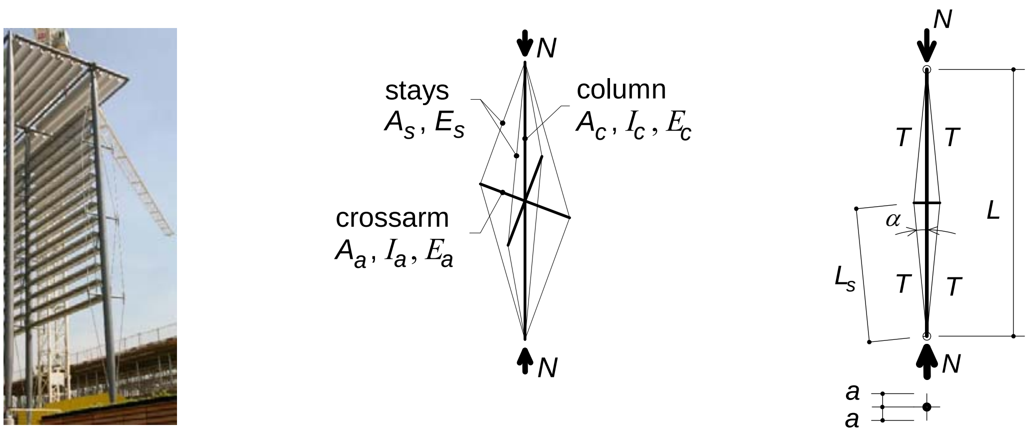

Fig. 1: Example (London site), space layout, geometry.

The buckling and post-buckling behaviour was studied using GNIA (geometrically nonlinear analysis with imperfections) by Saito and Wadee (2008, 2009). The results cleared up the stable or unstable paths of column behavior after buckling in symmetric, antisymmetric and interactive buckling modes (Fig. 2).

[*] Ing. Radek Pichal: Czech Technical University in Prague; Faculty of Civil Engineering; Thakurova 7; 16629 Prague; CZ, radek.pichal@fsv.cvut.cz

[**] Prof. Ing. Josef Machacek, DrSc: Czech Technical University in Prague; Faculty of Civil Engineering; Thakurova 7; 16629 Prague; CZ, machacek@fsv.cvut.cz

Recent parametrical study by Wadee et al. (2013) introduced three levels of global column initial deflections ($L/1000$, $L/400$, $L/200$), various ratios $2a/L$ (to cover all possible buckling modes) and initial stay prestress up to $3T_{opt}$. The maximum load-carrying capacity N_{max} was then established by GNIA and respecting relevant test results (Fig. 2), within all three prestressing zones.

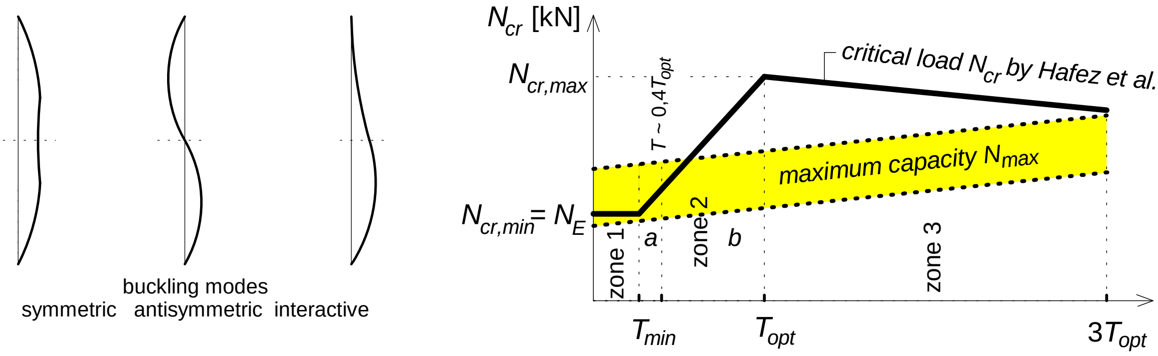

Fig. 2: Buckling modes, critical loads and load-carrying capacity.

All former analytical and numerical studies concerned elastic nonlinear 2D analysis, possibly extended for an influence of 4 space arms/stays of the space perpendicular crossarm but with buckling in the direction of the arms. The connections between the stays, columns and the crossarm were assumed to be fixed as ideal hinges.

The present paper deals with 3D behavior of the stayed columns using GNIA (geometrically nonlinear analysis with imperfections) with respect to dissimilarity of 2D and 3D behavior. Moreover, an arrangement with stays sliding on the crossarm which may be advantageous from assembly point of view is analyzed.

2. Nonlinear 3D analysis

Numerical GNIA ANSYS modeling used the following finite elements:

- column and crossarm tubes: BEAM188 (3D, 2x6 = 12DOF, large deflections, material nonlinearity),
- cable stays: LINK180 (3D, 2x3 = 6DOF, large deflections, material nonlinearity, introduced tension only),
- saddle at crossarm (in case of sliding stays): SHELL281 (3D, 8x6 = 48DOF, large deflections, material nonlinearity).

The prestressing was introduced by the stay's thermal change and external loading by axial column displacement. The respective prestressing loads and external column loading values were recalculated from the column reactions. Numerical procedure employed arc-length method to follow unloading path.

The column under investigation has following parameters (span L, cross-section area A, second moment of area I, Young's modulus E):

- tube column Ø 50x2 [mm]: $L = 5000$ mm, $A_c = 301.59$ mm^2, $I_c = 87009{,}6$ mm^4, $E_c = 200000$ MPa,
- crossarm tube Ø 25x1.5 [mm]: $a = 250$ mm, $A_a = 110.74$ mm^2, $I_a = 7675.7$ mm^4, $E_a = 200000$ MPa,
- cable Macalloy stay Ø 4 mm: $L_s = 2513$ mm, $A_s = 12.57$ mm^2, $E_s = 200000$ MPa.

2.1. Stayed columns with stays fixed to the crossarm

Analytical buckling analysis of this perfect stayed column in 2D according to formulas given by Hafez et al. (1970) provides the following results:

- Euler's critical buckling load of the column without stays $N_{cr} = 6.87$ kN,
- maximal critical load of the stayed column with symmetrical buckling $N_{cr,max,sym} = 39.78$ kN,
- maximal critical load of the stayed column with antisymmetrical buckling $N_{cr,max,anti} = 36.79$ kN,
- optimal prestressing $T_{opt} = 1.302$ kN.

Numerical FE analysis of such stayed column by LBA (linear buckling analysis) with medium prestressing (zone 2 in Fig. 2) is not possible as revealed by Saito and Wadee (2008), due to sudden slackening of the stays on the concave side at the instant of buckling. Therefore, introduction of initial deflections and GNIA is necessary. To determine 3D critical loads symmetric and antisymmetric initial deflection of very small values were introduced (see Fig. 2), with amplitudes in both cross-section directions w_0 = 0.01 (i.e. L/500 000), giving space amplitude of $w_0\sqrt{2}$. External load-axial deflection path for optimal prestressing under symmetric initial deflection (T_{opt} = 1.51 kN) is demonstrated in Fig. 3, showing bifurcation point with critical loading $N_{cr,max,sym}$ = 39.73 kN.

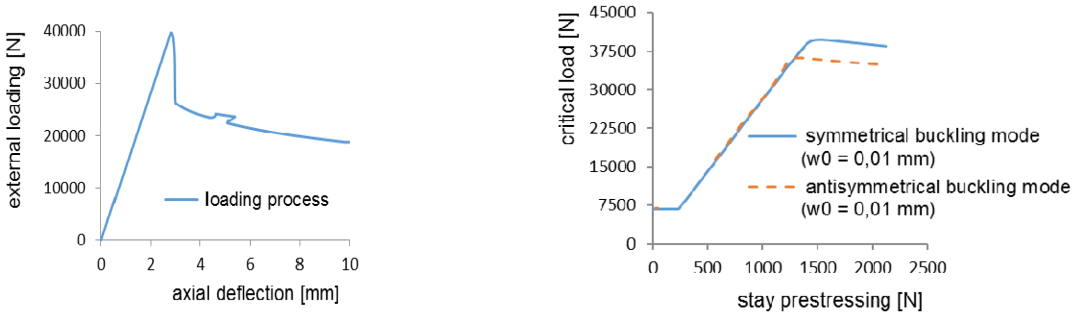

Fig. 3: Load-deflection path for the optimal prestressing (left), critical loads vs. pretensions (right).

The stayed column in its basic arrangement employs fixed hinged connections of the stays to the crossarm. The 3D GNIA was performed for 31 values of prestressing with both symmetrical and antisymmetrical initial deflections. Results are shown in Fig. 3, demonstrating zones 1, 2, 3 in accord with analytical solution. Sensitivity to amplitude of the initial deflection w_0 for the symmetrical buckling mode and comparison of the 3D GNIA maximal critical values with analytical 2D (Hafez et al., 1979) solution is presented in the Table 1. The 3D GNIA with the small initial deflections gives nearly identical critical loads $N_{cr,max}$ as the 2D analytical analysis. Negligible differences may arise due to imperfections, non-rigid crossarm and space buckling; the influence of the last one therefore seems to be rather unimportant.

Tab. 1: Maximal critical loads and optimal pretensions.

Initial deflection w_0 [mm]	Symmetrical mode		Antisymmetrical mode		Decisive $N_{cr,max}$ [kN]
	Optimal pretension T_{opt} [kN]	Maximal critical load $N_{cr,max,sym}$ [kN]	Optimal pretension T_{opt} [kN]	Maximal critical load $N_{cr,max,anti}$ [kN]	
0 (Hafez et al.)	1.41	39.79	1.30	36.79	36.79
0.01	1.51	39.73	1.35	36.18	36.18
0.05	1.58	39.25	-	-	-
0.10	1.61	38.62	-	-	-

Nevertheless, the space buckling is the fact confirmed by the tests and in the 3D GNIA demonstrated in Fig. 4, showing a stayed column with a predominant symmetrical initial deflection in the direction of the column cross section plane *x-z* (w_{0x} = 0.01 mm; w_{0z} = 5 mm). The column midspan deflection with increase of loading follows direction of the greater initial one and later traverse into space deflection (i.e. direction of the minimum rigidity), up to the buckling load value. The instant of change of the direction depends on value of prestressing: the greater prestressing, the higher value of the instant of change. Loss of prestressing in the stays is also shown in Fig. 4.

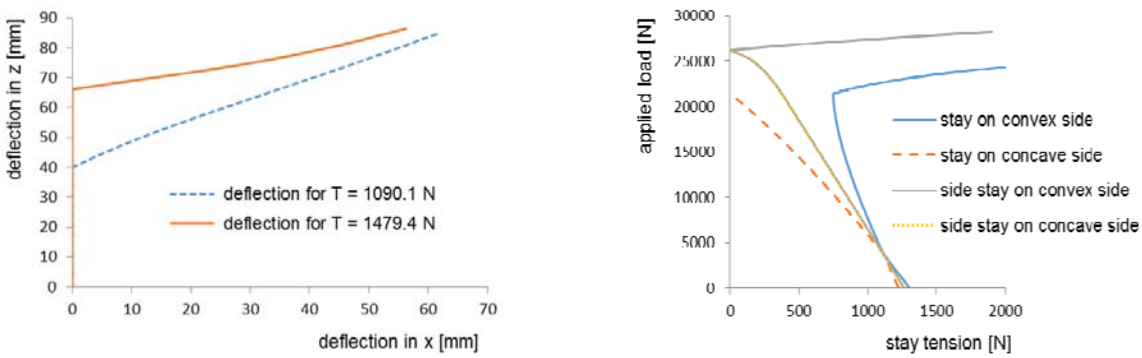

Fig. 4: The space buckling of initially symmetrically deflected column with w_{0x} = 0.01 mm; w_{0z} = 5 mm (left) and loss of prestressing in the stays (right).

2.2. Stayed columns with stays sliding at the crossarm

Modelling requires use of shell elements and introduction of friction (coefficient ν) at the saddle-stay interface. Comparison of results for symmetrical buckling mode with $\nu = 0.1$ is given in Fig. 5.

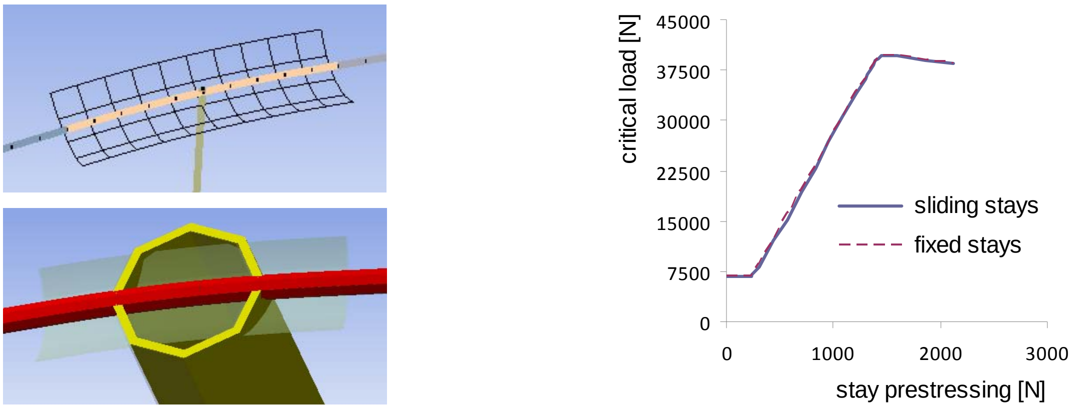

Fig. 5: Sliding saddle FE modeling (left), behavior and $N_{cr,max,sym}$ for fixed and sliding stays (right)

3. Conclusions

- Geometrically nonlinear analysis with imperfections (GNIA) in 3D proved buckling of the prestressed stayed columns in the space (in the direction between the arms of the central crossarm). Nevertheless, the critical loads received using 2D analysis and buckling in the direction of the arms gives nearly identical values.
- Amplitudes of initial deflections (w_0) using 3D GNIA affect substantially the buckling behavior and value of the respective critical load N_{cr}. In the investigated column the value of $w_0 \leq L/50000$ lowered the value $N_{cr,max}$ of less then 3 %. From the sensitivity study the values $w_0 \leq L/500000$ may be recommended for calculation of bifurcation load corresponding to LBA.
- Stays sliding on the crossarm with friction $\nu = 0.1$ and symmetrical buckling mode give nearly identical critical loads as for the fixed stays for various prestressing in all zones 1, 2, 3 including $N_{cr,max}$. Other modes of buckling and frictions are currently under detailed investigation.

Acknowledgement

Support of the Czech Grant Agency GACR No. 13-25781S is gratefully acknowledged.

References

Araujo, R.R., Andrade, S.A.L., Vellasco, P.C.G.S., Silva, J.G.S., & Lima, L.R.O. (2008). Experimental and numerical assessment of stayed steel columns. J. Construct. Steel Research, 64, pp. 1020-9.

Hafez, H.H., Temple, M.C. & Ellis, J.S. (1979) Pretensioning of single-crossarm stayed columns. J. Struct. Div. ASCE, 14362, ST2, pp. 359-75.

Píchal, R. & Macháček, J. (2015) Stability of stainless steel prestressed stayed columns, in: Proc. 21st Int. Conf. Engineering Mechanics 2015 (J.Náprstek & C.Fischer eds), Svratka, pp. 230-231.

Osofero, A.I., Wadee, M.A. & Gardner, L. (2012) Experimental study of critical and post-buckling behaviour of prestressed stayed steel columns. J. Construct. Steel Research, 79, pp. 226-41.

Saito, D. & Wadee, M.A. (2008) Post-buckling behaviour of prestressed steel stayed columns. Eng. Struct. 30, pp. 1224-39.

Saito, D. & Wadee, M.A. (2009) Numerical studies of interactive buckling in prestressed steel stayed columns. Eng. Struct., 31, pp. 432-443.

Servitova, K. & Machacek, J. (2011). Analysis of stainless steel stayed columns, in: Proc. 6th Int. Symp. Steel Structures, (E.T. Lee & S.J. Yoon eds), Seoul, pp. 874-81.

Smith, R.J., McCaffrey G.T. & Ellis J.S. (1975) Buckling of a single-crossarm stayed column. J. Struct. Div. ASCE, 11071, ST1, pp. 249-68.

Wadee, M.A., Gardner, L. & Osofero, A.I. (2013) Design of prestressed stayed columns. J. Construct. Steel Research, 80, pp. 287-98.

22nd International Conference
ENGINEERING MECHANICS 2016
Svratka, Czech Republic, 9 – 12 May 2016

STRENGTH CONTROL OF THE STANCHION OF POLE TRAILER

J. Pokorný*, O. Voltr, J. Vágner***, P. Jilek****, M. Tesař*****, I. Šefčík******

Abstract: *The Paper is focused on assessment of strength of the stanchion of the bunk. It describes measurements of the specimen consists of two bunks to answer distribution of forces along stanchion and its increase during inclination of the specimen about 30°. For better understanding of force distribution along stanchion more measurements with pure loading up logs in the specimen were performed too. Results of experiments were subsequently used as inputs for setting the load for analyses. For determination of strength of the stanchion construction was used FEM. Parts of stanchions were subjected to both static linear and nonlinear analysis.*

Keywords: Stanchion, Pole trailer, Tilting platform, FEM

1. Introduction

Manufacturers of lorries, trailers and semi-trailers are trying to offer products with the highest utility value. They try to offer products with the largest loading area or volume or with the lowest curb weight according to the restrictions given by rules of law. Manufacturers must search new solutions and design for their products and optimize them. Big range of calculations is necessary to make to develop new successful product.

Department of Transport Means and Educational and Research Centre in Transport (ERCT) of University of Pardubice were asked by company Hořické strojírny spol. s r.o. to make FEM analysis of their new prototype of a stanchion of bunk. But there was no knowledge about input load. It was possible to make theoretical model, but load (wooden logs) is usually a lot imperfect opposite to idealized model. And here was a question what is the load distribution on the stanchion in reality. This gap in knowledge about straining of the stanchion did not allow making any strength analyses and so it was necessary to undergo experiment with real wooden logs. This experiment should explain forces straining the stanchion which would be able to use as an input for strength analyses.

2. Experiment

It was important not only to find straining of the stanchion by simple loading up the bunk. The question was also what happens, when the centrifugal force on the logs is applied. This supposed to make a driving test in a circle or to replace the centrifugal force by another type of a force. The advantage of driving test is in its description of response on real conditions during driving the truck. But at the same time is also its disadvantage - it is important to measure kinematic and dynamic parameters of the vehicle, it is necessary to ensure safety when driving limits are attacked, costs are higher and so on.

* Ing. Jan Pokorný, Ph.D.: Research and education centre in transportation, University of Pardubice, Studentská 95; 532 10, Pardubice; CZ, jan.pokorny@upce.cz

** Ing. Ondřej Voltr: Department of transport means and diagnostics, University of Pardubice, Studentská 95; 532 10, Pardubice; CZ, ondrej.voltr@upce.cz

*** Ing. Jakub Vágner, Ph.D.: Research and education centre in transport, University of Pardubice, Studentská 95; 532 10, Pardubice; CZ, jakub.vagner@upce.cz

**** Ing. Petr Jilek, DiS.: Department of transport means and diagnostics, University of Pardubice, Studentská 95; 532 10, Pardubice; CZ, petr.jilek@upce.cz

***** Assoc. Prof. Miroslav Tesař, CSc.: Department of transport means and diagnostics, University of Pardubice, Studentská 95; 532 10, Pardubice; CZ, miroslav.tesar@upce.cz

****** Ing. Ivo Šefčík, Ph.D.: Department of transport means and diagnostics, University of Pardubice, Studentská 95; 532 10, Pardubice; CZ, ivo.sefcik@upce.cz

From this reason we decided to use possibilities and technologies of our laboratory in ERCT. In the laboratory of transport means – road vehicles is situated tilting platform for determination static threshold of a car rollover and also for determination of height coordinate of center of gravity of a car. It suggested itself to use this platform for simulation centrifugal force by using the part of gravity during tilting the platform.

For experiment was prepared specimen consisted of two whole bunks and auxiliary frame as a holder of bunks. Auxiliary frame was also used for fixation the specimen to the tilting platform. Measuring part was one of four stanchions. It was equipped by ten force sensors and five strain gauges along active length of the stanchion. These were protected by safety shields hung on stanchion and enabling force transmission from logs to the stanchion. The specimen was loaded with logs of total mass of 9 tons and length of 4 meters.

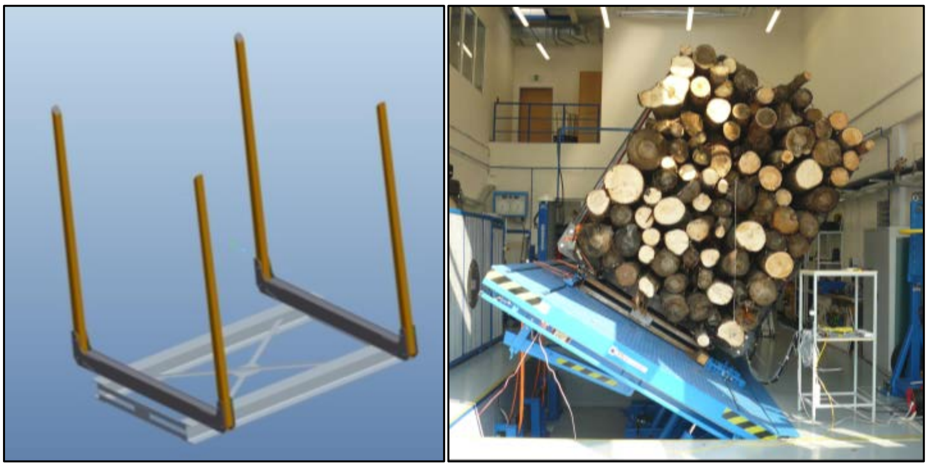

Fig. 1: CAD model of empty specimen and tilted specimen on the tilting platform (Pokorný et al., 2014)

Specimen with logs was fixed on the tilting platform in laboratory and during one month several times tilted up to 30°. Value of tilt angle of 30° was chosen according prescriptions relating to stability of tank trucks. For pole trailers is not similar prescription defined. This value of tilt angle is too big, that is not possible to reach it on real pole trailer during common driving without rollover. Such overstated value enabled to create safety space in straining of stanchions and took into account also some lateral dynamic effect.

This experiment simulated increase of straining of a stanchion during action of lateral or centrifugal force. In addition more measurements with repeated loading and unloading of logs were realized outside laboratory – both on specimen but also on a real trailer. These experiments should show usual distribution of forces along the stanchion and also extremes in this distribution.

Results of experiments showed, that general distribution is very difficult to determine. Distribution of forces straining the stanchion was stochastic and even summary of these forces was with wide dispersion (difference between two extremes of sums was over 6700 N). Increasing of straining of the stanchion owing to tilt the platform of 30° was around 44% that was little bit less compared to theoretical calculations (according calculations it should be around 50%) (Voltr O. & Pokorný J., 2015).

3. FEM analysis of bunk

Bunk consists of two main parts: stanchion and main beam called as a crossbeam. FEM analyses were focused primarily on a stanchion (material with R_e=900MPa) and connection parts between stanchion and crossbeam (materials with R_e=355 and 900 Mpa).

3.1. FEM analysis of stanchion

Computational model of stanchion was idealized opposite to real stanchion. Model of stanchion was proposed as a thin-wall shell. Cross-section of stanchion was taken into account as closed and linearly variable along whole length. At this model and phase of analyses were not taken into consideration parts forging lock between stanchion and crossbeam. For creation the mesh was used shell triangular element. Nearly whole model consists of element mesh of element size of 12 mm. Only in areas accordant with positions of strain gauges on real measuring stanchion was element mesh refined to element size of 5 mm. Boundary conditions were defined as fixation of lower end of stanchion. This increased safety of analyses. Input load was implemented in accordance with experiment.

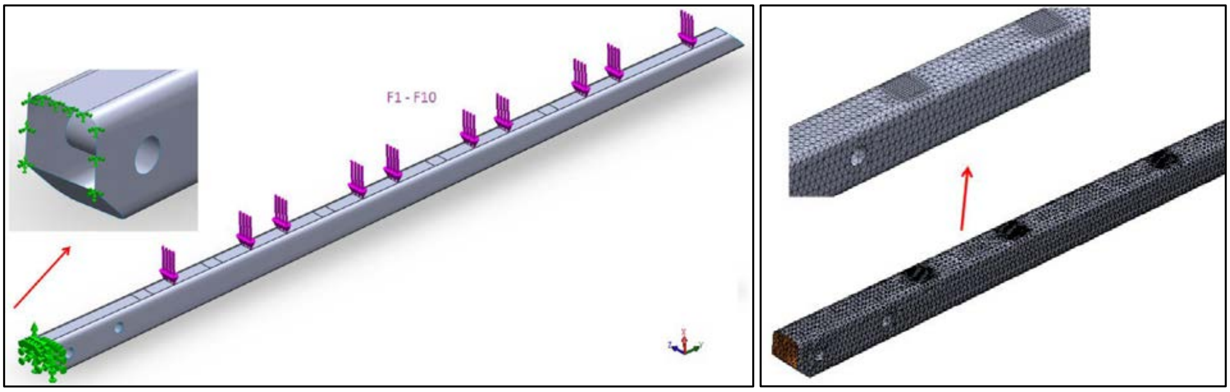

Fig. 2: Boundary conditions and distribution of load forces; mesh (Voltr O. & Pokorný J., 2015)

For validation of this model were used values of strain obtained from experimental strain gauge measurements. Three load cases from experimental data were chosen for this purpose. All of them generated maximal bending moment on the stanchion. Validation process was successful. Accuracy of results was obtained with relative error up to 15% (Voltr O. & Pokorný J., 2015).

Following analyses were focused on extreme loading of the bunk – up to its loading limit. In our measurements loading limit was used only from around 60%. According to experience and prescript of producer is impossible to fully use this limit. Because there was no experimental data for this case of loading, the straining of stanchion was necessary to predict. Used estimation was very rough, because we did not obtain general distribution of forces from experiments as was mentioned hereinbefore. For estimation was finally used rate between mass of load and resulted force acting on a stanchion. This was applied on the two load cases with the highest load on a stanchion.

These estimated loads on a stanchion were used for analyses. Results for estimated load of stanchion in normal position (without acting lateral or centrifugal force = tilt angle 0°) were safely to yield point. With applying additional load by tilting on angle of 30° got one predicted load case on the yield point of material in a wider area above fixation. Such stress is pseudo-elastic stress and for further analyses of stanchion behavior is important to make fully nonlinear analysis on more detailed and more accurate model.

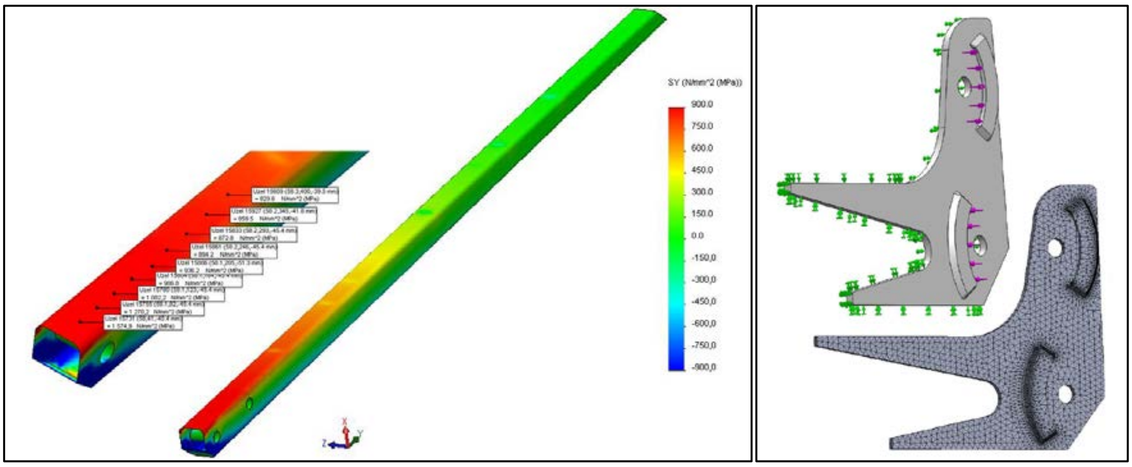

Fig. 3:Results for prediction of the most loaded state, stress on yield point (Voltr O. & Pokorný J., 2015); boundary conditions and distribution of load forces and mesh of ear of crossbeam (Pipek J., 2015)

3.2. FEM analysis of connection parts

Deeper analyses were made for part called as ear (ear of crossbeam – Fig. 3b) connecting stanchion and main beam. This part was chosen by reason of rugged shape, number of welds, and material with lower yield point than material of stanchion and crossbeam.

Models were not such simplified as a model of stanchion – only welds were made as a draft. Boundary conditions were chosen as fixed – according real possibilities of deformation of the ear. Input load corresponded to maximal bending moment calculated from real experimental data. Moment was applied on model as couple of forces acting on contact surfaces of locks. Mesh was created from elements of size 6 mm and in areas of welds was element size reduced to 1 mm.

In the first step was made linear analysis. This analysis showed some of potentially risk areas. In fact, as was supposed, it was areas of welded parts of lock, whereas the upper one was strained more. This part was subsequently analyzed by nonlinear analysis. Opposite part of this lock welded to the stanchion and welded connection between ear and crossbeam were analyzed this way too. This type of analysis enables to determine strength limit state, limit force, loss of stability and problems of fracture mechanics and works with material and geometric nonlinearity. In this case limit force was primary to determine. From each analyzed part was chosen node in the most shifted place and for this was subsequently plotted the graph of dependence between shift and load coefficient λ. Limit force is then calculated according formula:

$$F_{lim} = \frac{\alpha \cdot \lambda \cdot F}{k} \qquad [N], \tag{1}$$

where α is weld coefficient, F is load force and k is safety coefficient (k = 1,5).

In table 1 are shown results of these nonlinear analyses. In the second column are shown limited forces of parts and in the third column are forces for static load (calculated from experimental measurement).

Tab. 1: Results of nonlinear analyses of parts (Pipek J., 2015).

part	F_{lim} [N]	F_{st} [N]
weld - kidney	93600	26250
weld - crescent	73666.7	26250
weld ear - crossbeam	74100	26250
ear of crossbeam	74666.7	26250

4. Conclusions

This article was focused on problematic of strength of the stanchion of bunk. Producer of pole trailers demanded FEM analyses of stanchion and some another detailed parts of the bunk. But experiments had to be done before these analyses, because it was not known straining of the stanchion. Data obtained from experiments were used for validation of models and consequently in FEM analyses. In the case of stanchion it was the aim to make strength control on the heaviest load of stanchion responding the maximal loading limit of the bunk. Additional load in form of lateral force simulating centrifugal force was for this analysis used too. Linear analysis of the stanchion with such extreme and unreal straining showed, that lower part of stanchion is getting on yield limit of material. Further linear and nonlinear analyses of other detailed parts of bunk were made, where the result was the limit force. Analyses showed, that stanchion is well resistant to normal loaded up the bunk by logs and additional lateral forces. Also other parts as lock of stanchion or member connecting the stanchion and crossbeam spent strength requirements.

References

Pokorný, J., Vágner, J., Jilek, P., Kohout, M. & Šefčík, I. (2014) Experimentální měření silového zatížení klanic oplenového návěsu. Protokol o zkoušce VVCD-P-14/08, University of Pardubice, Pardubice

Voltr O. & Pokorný J. (2015) Experimentální měření silového zatížení klanic oplenového návěsu. Závěrečná zpráva, University of Pardubice, Pardubice

Pokorný, J., Vágner, J. & Jilek, P. (2015) Experimentální měření silového zatížení klanice oplenu v reálném provozu. Zpráva z měření VVCD-Z-15/08, University of Pardubice, Pardubice

Pipek, J. (2015) Optimalizace oplenu pro přepravu dřeva, diploma paper, University of Pardubice, Pardubice

FEM Computer program COSMOSWorks 2010. SolidWorks Corporation.

22nd International Conference
ENGINEERING MECHANICS 2016
Svratka, Czech Republic, 9 – 12 May 2016

INVESTIGATION OF DYNAMIC BEHAVIOUR OF AN INVERTED PENDULUM DRIVEN BY CABLES REPRESENTED BY POINT-MASS MODEL

P. Polach*, M. Hajžman**

Abstract: *The paper deals with point-mass modelling of cables, which are suitable for involving in dynamics of fibre mechanisms. The motivation is the development of a cable model, which could be efficient for the usage in a mechatronic model of a manipulator consisting of cables and an end-effector whose motion is driven by cables – particularly for the usage in the model of QuadroSphere. At previous research into the approach to the cable modelling, an inverted pendulum driven by two fibres (cables) attached to actuators was chosen as a suitable reference object. Its properties were investigated applying a calculation model. This paper is focused on using the point-mass model of cables, utilization of which generally proved to be very prospective for cable modelling. The effect of cable preload, the influence of the amplitude of the harmonic kinematic excitation of cables, the mass effect of cables and the influence of non-symmetric harmonic excitation on the pendulum motion were investigated. The influence of these crucial parameters of the system of an inverted pendulum driven by fibres (cables) on its dynamic behaviour is evaluated.*

Keywords: Cable, Inverted pendulum, Point-mass model, Multibody modelling, Vibration.

1. Introduction

Replacing rigid elements of manipulators or mechanisms (Chan, 2005) by flexible cables can be advantageous in the achievement of a lower moving inertia, which leads to a higher machine speed. Drawbacks can be associated with the fact that cables should be only in tension (Smrž & Valášek, 2009; Valášek & Karásek, 2009) in the course of a motion. The possible cable modelling approaches should be tested and their suitability verified in order to create efficient mathematical models of cable-based manipulators mainly intended for the control algorithm design.

At previous research into the approach to the cables modelling, an inverted pendulum driven by two fibres (cables) attached to actuators was chosen as a suitable reference object (see Fig. 1 left; e.g. Polach et al., 2012b), which is a simplified representation of a typical cable manipulator. Research into cable modelling and experimental verification of their usability has advanced (e.g. Polach & Hajžman, 2015; Dupal & Byrtus, 2015). Utilization of the point-mass model for cable modelling proved to be very prospective (Polach et al., 2015) in comparison with other approaches (see Chapter 2). Simulations with the inverted pendulum with the point-mass model of cables were applied in mapping the influence of some crucial parameters on dynamic behaviour of mechanical (or mechatronic) systems of this type. The effect of the cable preload (Polach & Hajžman, 2012b), the influence of the amplitude of the harmonic kinematic excitation of cables (Polach & Hajžman, 2012c), the effect of cable mass (Polach et al., 2012a) and the influence of non-symmetric harmonic excitation (Polach & Hajžman, 2012a) on the pendulum motion were investigated. In this paper, complete evaluation of the influence of crucial parameters on dynamic behaviour of the investigated system is given. This evaluation has not been presented yet.

* Dr. Ing. Pavel Polach: Section of Materials and Mechanical Engineering Research, Výzkumný a zkušební ústav Plzeň s.r.o., Tylova 1581/46; 301 00, Plzeň; CZ, e-mail: polach@vzuplzen.cz

** Ing. Michal Hajžman, Ph.D.: New Technologies for the Information Society, European Centre of Excellence, University of West Bohemia, Univerzitní 8; 306 14, Plzeň; CZ, e-mail: mhajzman@kme.zcu.cz

2. Possibilities of the cable modelling

The cable (fibre, wire etc.) modelling should be based on considering the cable flexibility and suitable approaches can be based on the flexible multibody dynamics (see Shabana, 1997; Gerstmayr et al., 2012). The simplest way how to incorporate cables in equations of motion of a mechanism is the force representation of a cable (e.g. Diao & Ma, 2009). It is assumed that the mass of cables is small to such an extent comparing to the other moving parts that the inertia of cables is negligible with respect to the other parts. The cable is represented by a force dependent on the cable deformation and its stiffness and damping properties. This way of the cable modelling is probably the most frequently used model in the cable-driven robot dynamics and control.

A more precise approach is based on the representation of the cable by a point-mass model (e.g. Kamman & Huston, 2001; Ottaviano et al., 2015). Point masses can be connected by forces or constraints. In order to represent bending behaviour of cables their discretization using the finite segment method (Shabana, 1997) or so called rigid finite elements (Wittbrodt et al., 2006) is possible. Other more complex approaches can utilize nonlinear three-dimensional finite elements (Freire & Negrão, 2006) or can employ absolute nodal coordinate formulation (ANCF) elements (Shabana, 1997; Gerstmayr et al., 2012; Liu et al., 2012).

In the case of the manipulator mechatronic model consisting of cables and an end-effector whose motion is driven by cables (particularly in the case of the QuadroSphere model) utilization of the point-mass model of a cable proved to be very prospective. The force model of a cable seems to be too simple, the sophisticated cable model created on the basis of the ANCF is dynamically correct but it is not usable for the calculations in a real time (Bulín et al., 2015). The cable models on the basis of the finite segment method or so called rigid finite elements can be supposed to be the same.

3. Inverted pendulum

The investigated inverted pendulum is driven by two fibres (cables) attached to actuators (see Fig. 1 left) and it is affected by a gravitational force.

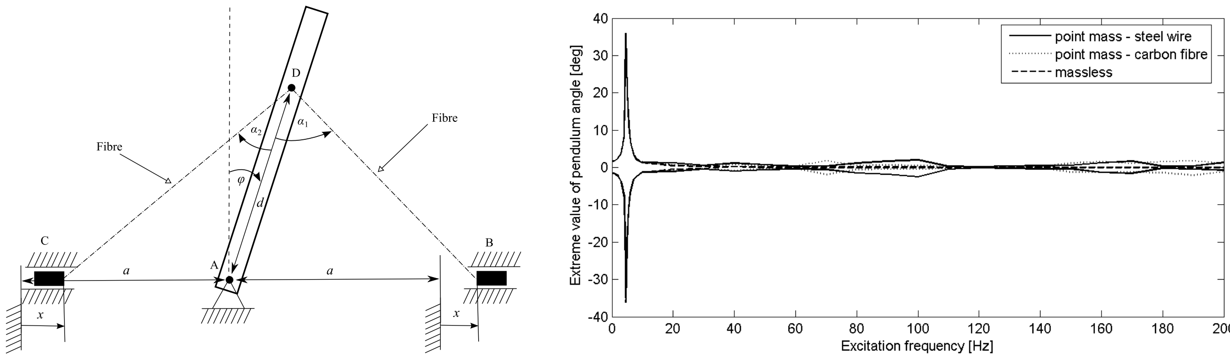

Fig. 1: Inverted pendulum actuated by the fibres (left) and time history of pendulum angle φ in dependence on the excitation frequencies (right).

When the pendulum is displaced from the equilibrium position, i.e. from the “upper” position, it is returned back to the equilibrium position by the tightened cable. As it has already been mentioned, this system was selected with respect to the fact that it is a simplification of possible cable-based manipulators.

The sophisticated point-mass cable model was validated on the basis of the results obtained using a massless cable model. In the cable model based on the point masses each cable is discretized using 10 point masses (e.g. Polach et al., 2012b). Each point mass is kinematically unconstrained (i.e. number of degrees of freedom is 3) in a two-dimensional model of the inverted pendulum system. The adjacent point masses are connected using spring-damper elements. Only axial (spring and damping) forces are considered in these spring-damper elements. The stiffness and the damping coefficients between the masses are determined in order to keep the global properties of the massless cable model. Validation of the point-mass model is given in Polach et al. (2012b). Correctness of the point-mass cable model was verified using another example in Polach et al. (2015). In order to investigate the pendulum motion the mentioned point-mass model of cables in the inverted pendulum models (Polach & Hajžman, 2012c) is used. For a better description of the solved problem a simple massless model is presented (the used model of the cable based on the point-mass model with lumped point masses corresponding to the mass of the cable is geometrically identical).

Kinematics of the system can be described by angle φ of the pendulum with respect to its vertical position (one degree of freedom), angular acceleration $\ddot{\varphi}$ and prescribed kinematic excitation $x(t) = x_0 \cdot \sin(2 \cdot \pi \cdot f \cdot t)$ (where x_0 is the chosen amplitude of motion, f is the excitation frequency and t is time). The equation of motion is of the form

$$\ddot{\varphi} = \frac{1}{I_{\mathrm{A}}} \cdot \left(F_{\mathrm{v1}} \cdot d \cdot \sin \alpha_1 - F_{\mathrm{v2}} \cdot d \cdot \sin \alpha_2 + m \cdot g \cdot \frac{l}{2} \cdot \sin \varphi \right), \qquad (1)$$

where I_{A} is the moment of inertia of the pendulum with respect to the axis in point A (see Fig. 1 left), α_1 and α_2 are the angles between the pendulum and the cables, m is the mass of the pendulum, F_{v1} and F_{v2} are the forces acting on the pendulum from the cables, g is the gravity acceleration, l is the length of the pendulum and d is the distance from the axis in point A to the position of attachment of cables to the pendulum (point D). Kinematic excitation acts in the points designated B and C (see Fig. 1 left).

The chosen model parameters are: l = 1 m, a = 1.2 m, d = 0.75 m, I_{A} = 3.288 kg·m^2, m = 9.864 kg, k_{v} = 8.264·10^4 N/m (stiffness), b_{v} = 5·10^{-4}·k_{v} N·s/m (damping coefficient). Excitation frequency f was considered in the range from 0.1 Hz to 200 Hz. Time histories and extreme values of pendulum angle φ and of the forces in the cables are the monitored quantities. Investigated parameters of the models of the inverted pendulum driven by two cables attached to actuators are given in Tab. 1.

Tab. 1: Investigated parameters of the cables.

Changed parameter	preload [N]	amplitude [m]	mass [g]	phase shift [deg]
The effect of the cables preload	0 to 8264	0.02	3.846	0
The influence of the amplitude of the harmonic kinematic excitation of cables	0	0.02 to 0.2	3.846	0
The effect of the cables mass	0	0.02	3.846 to 1269	0
The case of non-symmetric harmonic excitation	0	0.02	3.846	30

4. Conclusions

From comparing simulation results of inverted pendulum driven by two fibres (cables) attached to actuators it is evident that the greatest differences at utilizing the massless model and the point-mass model of cables are at investigating the influence of the cables mass (see Fig. 1 right). An unstable behaviour of the studied system was detected at investigating the cables preload influence on the pendulum vibration (Polach & Hajžman, 2012b) and at some combinations of the amplitude and the excitation frequency of the harmonic kinematic excitation of cables (Polach & Hajžman, 2012c). Changes in other investigated parameters of this system – i.e. the change in the cable mass (Polach et al., 2012) and non-symmetric harmonic excitation (Polach & Hajžman, 2012a) – do not cause the unstable behaviour of the pendulum.

Experimental verification of the cable dynamics within the manipulator systems is considered important in further research.

Acknowledgement

The paper has originated in the framework of the institutional support for the long-time conception development of the research institution provided by the Ministry of Industry and Trade of the Czech Republic to Research and Testing Institute Plzeň and solving project of the Czech Science Foundation No. 15-20134S entitled “Multi-level Light Mechanisms with Active Structures”.

References

Chan, E.H.M. (2005) Design and Implementation of a High-Speed Cable-Based Parallel Manipulator. PhD Thesis, University of Waterloo.

Bulín, R., Hajžman, M. & Polach, P. (2015) Analysis of vibrations of a cable-pulley system using the absolute nodal coordinate formulation, in: Proc. 13th Conference on Dynamical Systems – Theory and Applications, Dynamical Systems – Mechatronics and Life Sciences (J. Awrejcewicz, M. Kaźmierczak, J. Mrozowski & P. Olejnik eds), Faculty of Mechanical Engineering, Łódź University of Technology, Łódź, pp. 111-120.

Diao, X. & Ma, O. (2009) Vibration analysis of cable-driven parallel manipulators. Multibody System Dynamics, 21, 4, pp. 347-360.

Dupal, J. & Byrtus, M. (2015) Methodology of behaviour simulation of cable-driven manipulators with varying cable lengths, in: Proc. 31st Conference with International Participation Computational Mechanics 2015 (V. Adámek, M. Zajíček & A. Jonášová eds), University of West Bohemia in Plzeň, Špičák, CD-ROM (pp. 25-26).

Freire, A. & Negrão, J. (2006) Nonlinear Dynamics of Highly Flexible Partially Collapsed Structures, in: Proc. III European Conference on Computational Mechanics, Solids, Structures and Coupled Problems in Engineering (C.A. Mota Soares, J.A.C. Martins, H.C. Rodrigues, J.A.C. Ambrósio, C.A.B. Pina, C.M. Mota Soares, E.B.R. Pereira & J. Folgado eds), Laboratório Nacional de Engenharia Civil, Lisbon, CD-ROM.

Gerstmayr, J., Sugiyama, H. & Mikkola, A. (2012) Developments and Future Outlook of the Absolute Nodal Coordinate Formulation, in: Proc. 2nd Joint International Conference on Multibody System Dynamics (P. Eberhard & P. Ziegler eds), University of Stuttgart, Stuttgart, USB flash drive.

Kamman, J.W. & Huston, R.L. (2001) Multibody Dynamics Modeling of Variable Length Cable Systems. Multibody System Dynamics, 5, 3, pp. 211-221.

Liu, Ch., Tian, Q. & Hu, H. (2012) New spatial curved beam and cylindrical shell elements of gradient-deficient Absolute Nodal Coordinate Formulation. Nonlinear Dynamics, 70, 3, pp. 1903-1918.

Ottaviano, E., Gattulli, V., Potenza, F. & Rea, P. (2015) Modeling a Planar Point Mass Sagged Cable-Suspended Manipulator, in: Proc. 14th IFToMM World Congress (S.-H. Chang, M. Ceccarelli, Ch.-K. Sung, J.-Y. Chang & T. Liu eds), Chinese Society of Mechanism and Machine Theory, Taipei, Vol. 4, pp. 2696-2702.

Polach, P. & Hajžman, M. (2012a) Investigation of dynamic behaviour of inverted pendulum attached using fibres at non-symmetric harmonic excitation, in: Proc. EUROMECH Colloquium 524 Multibody system modelling, control and simulation for engineering design (J.B. Jonker, W. Schiehlen, J.P. Meijaard & R.G.K.M. Aarts eds), University of Twente, Enschede, pp. 42-43.

Polach, P. & Hajžman, M. (2012b) Effect of Fibre Preload on the Dynamics of an Inverted Pendulum Driven by Fibres, in: Proc. The 2nd Joint International Conference on Multibody System Dynamics (P. Eberhard & P. Ziegler eds), University of Stuttgart, Stuttgart, USB flash drive.

Polach, P. & Hajžman, M. (2012c) Influence of the excitation amplitude on the dynamic behaviour of an inverted pendulum driven by fibres. Procedia Engineering, MMaMS 2012, 48, pp. 568-577.

Polach, P. & Hajžman, M. (2015) Influence of the fibre spring-damper model in a simple laboratory mechanical system on the coincidence with the experimental results, in: Proc. ECCOMAS Thematic Conference on Multibody Dynamics 2015 (J. M. Font-Llagunes ed.), Universitat Politècnica de Catalunya, Barcelona School of Industrial Engineering, Barcelona, USB flash drive (pp. 356-365).

Polach, P., Hajžman, M., Šika, Z., Mrštík, J. & Svatoš, P. (2012a) Effect of fibre mass on the dynamic response of an inverted pendulum driven by fibres. Engineering Mechanics, 19, 5, pp. 341-350.

Polach, P., Hajžman, M. & Tuček, O. (2012b) Validation of the point-mass modelling approach for fibres in the inverted pendulum model, in: Proc. 18th International Conference Engineering Mechanics 2012 (J. Náprstek & C. Fischer eds), Institute of Theoretical and Applied Mechanics Academy of Sciences of the Czech Republic, Svratka, CD-ROM.

Polach, P., Byrtus, M., Dupal, J., Hajžman, M. & Šika, Z. (2015) Alternative modelling of cables of varying length, in: Proc. 31st Conference with International Participation Computational Mechanics 2015 (V. Adámek, M. Zajíček & A. Jonášová eds), University of West Bohemia in Plzeň, Špičák, CD-ROM (pp. 91-92).

Shabana, A.A. (1997) Flexible Multibody Dynamics: Review of Past and Recent Developments. Multibody System Dynamics, 1, 2, pp. 189-222.

Smrž, M. & Valášek, M. (2009) New Cable Manipulators, in: Proc. National Conference with International Participation Engineering Mechanics 2009 (J. Náprstek & C. Fischer eds), Institute of Theoretical and Applied Mechanics Academy of Sciences of the Czech Republic, Svratka, CD-ROM (pp. 1209-1216).

Valášek, M. & Karásek, M. (2009) HexaSphere with Cable Actuation. Recent Advances in Mechatronics: 2008-2009, Springer-Verlag, Berlin, pp. 239-244.

Wittbrodt, E., Adamiec-Wójcik, I. & Wojciech, S. (2006) Dynamics of Flexible Multibody Systems. Rigid Finite Element Method. Springer, Berlin.

22nd International Conference
ENGINEERING MECHANICS 2016
Svratka, Czech Republic, 9 – 12 May 2016

COMPARISON OF DIFFERENT SIMULATION TECHNIQUES FOR RELIABILITY-BASED DESIGN OPTIMIZATION

A. Pospíšilová[*], M. Lepš[**]

Abstract: *This contribution focuses on a double-looped reliability-based design optimization, in which the reliability of the system is evaluated in the inner loop and the designing process is performed in the outer loop. The double-looped formulation provides the most accurate results but it is computationally demanding especially if advanced simulation techniques are used for rare failure events. The selection of the method for the reliability assessment is therefore crucial to obtain the best results with the lowest possible computational efforts. A quasi-Monte Carlo simulation, an Asymptotic sampling and a Subset simulation are therefore utilized in the inner loop and the results are compared for two reliability-based design optimization benchmarks.*

Keywords: Multi-objective Optimization, Reliability-based Design Optimization, Subset Simulation, Monte Carlo Method, Asymptotic Sampling.

1. Introduction

A structural optimization is a process that seeks the best design under some predefined constraints. A deterministic model is usually unrealistic due to the uncertain inputs such as material properties, a structural topology, loadings etc. The optimal design with deterministic variables often terminates at a boundary between the failure domain and the safe domain and even a small perturbation in inputs can lead to a fatal failure. For that reason, the model uncertainties are introduced; the parameter uncertainties are associated with the input data whereas the structural uncertainties express that the model need not clearly describe the physics of the problem. The optimization under uncertainties looks into two main tasks; the first task (a *robust design optimization*) deals with the everyday fluctuations in inputs and provides a design with a minimum price that is less sensitive to small perturbations in inputs; the second task (a *reliability-based design optimization*) concentrates on worse-case scenarios and offers an economical design with large safety.

A reliability-based design optimization (RBDO) can be formulated by two linked loops. An optimizer provides a design in the outer loop, for which a probability of failure is evaluated in the inner loop. The double-looped procedure allows a very accurate safety appraisal of each design without any kind of approximation. However, this formulation suffers from large computational demands if a classical Monte Carlo method is used. Fortunately, advanced simulation techniques such as an Asymptotic sampling (Bucher, 2009) and a Subset simulation (Au & Beck, 2001) can be used for the reliability assessment and the accuracy can be almost maintained with the drastic computational effort reduction.

2. Multi-objective double-looped reliability-based design optimization

A classical formulation of the RBDO minimizes a cost function $f(\boldsymbol{d})$ such that the reliability constraints $\beta_i(\boldsymbol{x},\boldsymbol{d}) \geq \beta_i^{\min}$ as well as deterministic constraints $H_j(\boldsymbol{d}) \leq 0$ have to be satisfied. Design variables are arranged in vector $\boldsymbol{d}$ (e.g. deterministic variables or means of random variables), whereas uncertain parameters are arranged in vector $\boldsymbol{x}$. A generalized reliability index β_i for failure mode i is obtained by the inverse cumulative distribution function of the standard normal distribution $\beta = \Phi^{-1}(1 - p_f)$ where p_f is

[*] Ing. Adéla Pospíšilová: Faculty of Civil Engineering, Czech Technical University in Prague, Thákurova 7; 166 29, Prague; CZ, adela.pospisilova@fsv.cvut.cz

[**] Doc. Ing. Matěj Lepš, Ph.D.: Faculty of Civil Engineering, Czech Technical University in Prague, Thákurova 7; 166 29, Prague; CZ, leps@cml.fsv.cvut.cz

a probability of failure; $\beta_i^{\min}$ is the corresponding lower bound of the reliability index. In case that the setting of the lower limit $\beta_i^{\min}$ is unclear, the single-objective optimization can be reformulated into a multi-objective optimization; minimization of a cost function remains and maximization of the reliability indexes for all failure modes are added as the next objectives:

$$\min f(\boldsymbol{d}), \tag{1}$$

$$\max \beta_i(\boldsymbol{x}, \boldsymbol{d}), i = 1, \dots, n_I, \tag{2}$$

$$s.t. \quad H_j(\boldsymbol{d}) \leq 0, j = 1, \dots, n_J, \tag{3}$$

$$\boldsymbol{d}^{\min} \leq \boldsymbol{d} \leq \boldsymbol{d}^{\max}. \tag{4}$$

A probability of failure p_f is evaluated in an n-dimensional space of random variables $X_1, \dots, X_n$ as

$$p_f = \text{Prob}[F] = \text{Prob}[G(\boldsymbol{X}) \leq 0] = \int_{G(\boldsymbol{X}) \leq 0} f_X(\boldsymbol{x})\, \mathrm{d}\boldsymbol{x}, \tag{5}$$

where $f_X(\boldsymbol{x})$ is a joint probability density function, F denotes the failure, and $G(\boldsymbol{X})$ is a limit state function. A limit state $G(\boldsymbol{X}) = 0$ divides the space into the failure region $G(\boldsymbol{X}) \leq 0$ and the safe domain $G(\boldsymbol{X}) > 0$. A probability of failure is solvable analytically only for some specific problems and traditional numerical integration is not applicable for large n. Statistical sampling techniques based on a *Monte Carlo method* allow to estimate the expected value of p_f. Equation (5) is possible to reformulate as

$$p_f = \int_{-\infty}^{\infty} I_G(\boldsymbol{x}) f_X(\boldsymbol{x})\, \mathrm{d}\boldsymbol{x}, \tag{6}$$

where $I_G(\boldsymbol{x})$ is an indicator function that is equal to one for a failure domain and zero otherwise. For large number of samples, p_f in Equation (6) can be estimated by a ratio of the number of defective samples and the number of all samples. The number of total samples is recommended to set from $10/p_f$ with a coefficient of variation CV_{MC} around 30 %, over $100/p_f$ with CV_{MC} around 10 %, to $500/p_f$ with CV_{MC} around 5 %. In case that a sophisticated sampling strategy such as Halton or Sobol sequences or Latin hypercube sampling is used, the results are even more credible. The number of samples is however still enormous for small probabilities of failure.

A *Subset simulation* (Au & Beck, 2001) is based on a formulation of the failure event F as an intersection of the intermediate failure events F_i. The rare event problem is then reformulated as a series of more frequent events that are easier to solve. The probability of failure is as follows

$$p_f = \text{Prob}[F_1] \cdot \prod_{k=2}^{L} \text{Prob}[F_k \,|F_{k-1}]. \tag{7}$$

The failure probability of the first intermediate domain is evaluated by a classical Monte Carlo method with hundreds of samples N. These samples are sorted in an ascending order and a limit state function is shifted such as $\text{Prob}[F_1]$ is equal to a predefined value p_0. The first $(p_0 \cdot N)$ samples are used as seeds for the simulation of samples from conditional probabilities by a Markov chain Monte Carlo (MCMC) with modified Metropolis algorithm. In each level k, samples obtained by MCMC are sorted and first $(p_0 \cdot N)$ samples serve as seeds in k+1 step together with a proper shift of the limit state function. The last level L is reached if the probability of failure with the original limit state is greater than p_0.

An *Asymptotic sampling* (Bucher, 2009) is a novel methodology that predicts a reliability index from an asymptotic behavior of the probability of failure in an n-dimensional independent and identically distributed normal space. A principal idea is to sequentially scale random variables in a standard normal space over the standard deviation σ by a factor φ that is lesser than 1 to get more samples from a failure domain. In step k, scaled standard deviations σ_k equal to σ_{k-1}/φ are used to perform a Monte Carlo simulation with hundreds of samples. A corresponding reliability index β_k in step k and a factor φ raised to the power of k are saved as a support point for the following regression. After sufficient steps k, the approximation of the reliability index is obtained as a summation of the regression coefficients A and B after a regression via support points $\boldsymbol{\beta}$ and $\boldsymbol{\varphi}$

$$\boldsymbol{\beta} = A\boldsymbol{\varphi} + B\boldsymbol{\varphi}^{-1}. \tag{8}$$

A *First order reliability method* (FORM) (Hasofer & Lind, 1974) is not a simulation technique but an often used analytical approximation method in RBDO for its low computational demands. Nevertheless, it is inaccurate for highly nonlinear limit state functions. It is based on the linearization of the limit state function in a design point $\boldsymbol{u}^*$ in the standard normal space (SNS). The design point can be found by any optimization method as $\boldsymbol{u}^* = \min(\boldsymbol{u}^T\boldsymbol{u})^{-1}$ subject to $G(T_{SNS \rightarrow OS}(\boldsymbol{u})) = 0$. A transformation from the standard normal space to the original space and vice versa is possible via Rossenblat transformation $\boldsymbol{x} = T_{SNS \to \mathrm{OS}}(\boldsymbol{u})$. The approximation of the reliability index is then the shortest distance from the origin of SNS to the design point lying on the limit state surface.

3. Numerical benchmarks

Both benchmarks were optimized by Non-dominated sorting genetic algorithm II (Deb et al, 2002) with 200 individuals and 50 generations to obtain a rich approximation of the Pareto-set and the Pareto-front. The Pareto-front was bounded such that a reliability index is from an interval [0, 5.5] for both benchmarks. Both problems converged sufficiently in approximately the 10^{th} generation. An Asymptotic sampling as well as a Subset simulation was set to have CV_β equal to 5 % in the single objective optimum taken from literature with 1,000 independent runs.

The first example is taken from (Chen et al, 2013) and it is reformulated into a multi-objective optimization task in (Pospíšilová & Lepš 2015). The cost function is quadratic, the limit state function is highly nonlinear. The limit state $G(\boldsymbol{x}) = 0$ is also depicted in Fig. 1 with the solid line; the feasible domain is inside the shape. Both variables have the normal distribution and they are statistically independent. Means are design variables. Since a Monte Carlo method has high computational demands, an Asymptotic sampling was used to predict a probability of failure and the necessary number of samples was computed subsequently with $10/p_f$. The lower tail of the Pareto-front is almost identical for all used reliability assessment methods, FORM fails for reliability index slightly greater than 2.3 and it is problematical and unreliable for the rest of the Pareto-front. The Pareto-front with a Monte Carlo method oscillates between the front with an Asymptotic sampling and a Subset simulation approximately from reliability index equal to 4. At the upper tail, a Monte Carlo method is not reliable since these samples are in the failure domain according to the left figure in Fig. 1. The total number of samples during whole optimization process was measured in 10 independent runs: an Asymptotic sampling used ca. $2.3 \cdot 10^8$ samples, a Subset simulation used ca. $1.4 \cdot 10^8$ of samples, FORM in contrast used only $2.4 \cdot 10^5$ samples. A Monte Carlo method was used only once with enormous $5.4 \cdot 10^{11}$ samples leading to high CV.

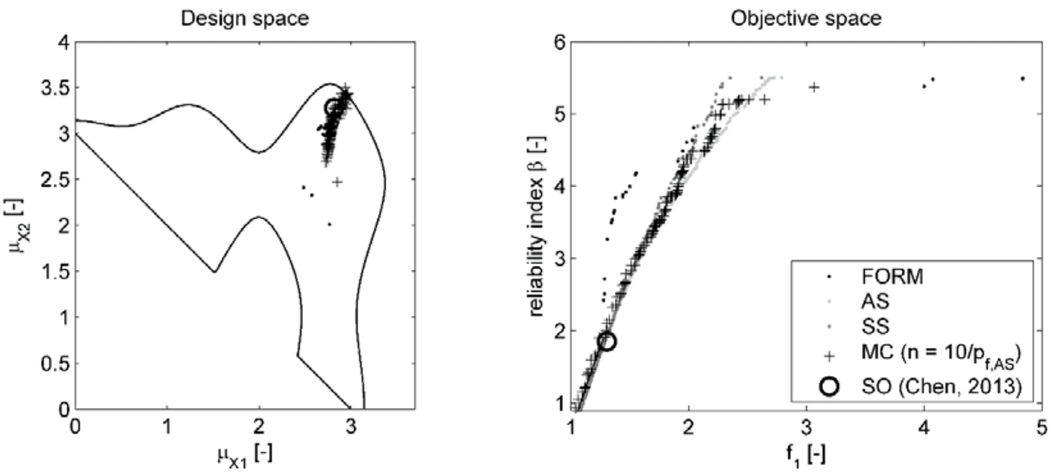

Fig. 1: Approximations of Pareto-set (left) and Pareto-front (right) for Example 1. Abbreviations: FORM – First order reliability method, AS – Asymptotic sampling, SS – Subset simulation, MC – Monte Carlo method, SO – single optimum from (Chen et al, 2013).

The second example is concentrated on a minimization of the material volume of a 23-bar planar truss bridge and maximization its safety. The limit state function is represented by a design rule that the mid-span deflection should not exceed 10 cm. The single objective formulation in (Dubourg, 2011) is reformulated into the multi-objective in (Pospíšilová & Lepš, 2013). Young's moduli E_1 and E_2 have Lognormal distribution; cross-sectional areas A_1 and A_2 have Lognormal distribution as well with means as design variables μ_{A1} and μ_{A2}; gravity loads P_1 - P_6 have a Gumbel distribution. All variables are statistically independent. A Subset simulation behaves the same as an Asymptotic sampling on interval [0, 3.1]. The rest of the Pareto-front with a Subset simulation probably needs more samples and/or levels and therefore an adaptive setting. FORM has a similar trend as an Asymptotic sampling but FORM slightly overestimates the reliability; this trend is obvious from the single optimum (Dubourg, 2011) lying on the Asymptotic sampling Pareto-front.

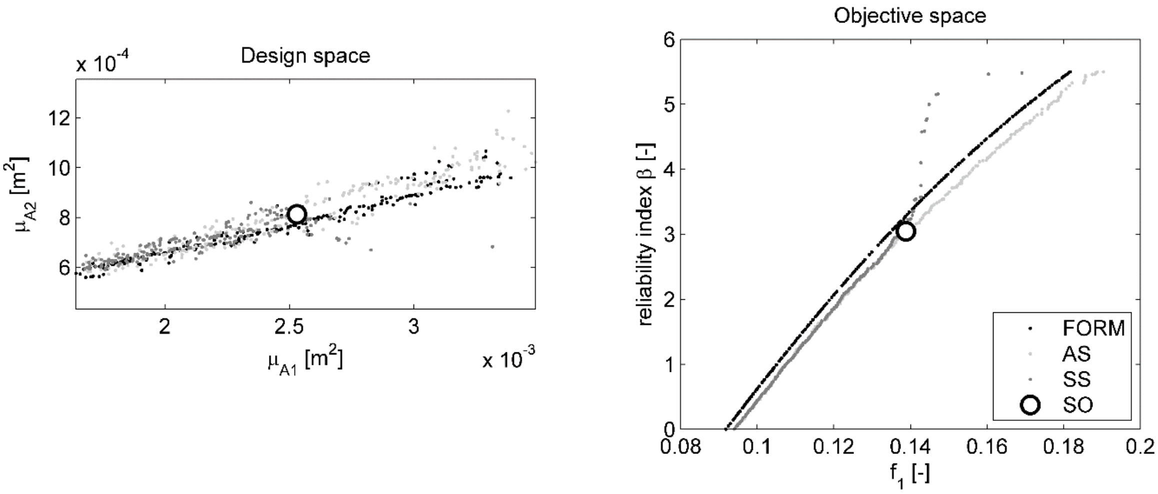

Fig. 2: Approximations of Pareto-set (left) and Pareto-front (right) for Example 2. Abbreviations: FORM – First order reliability method, AS – Asymptotic sampling, SS – Subset simulation, SO – single optimum from literature (Dubourg, 2011).

4. Conclusions

The multi-objective formulation of a reliability-based design optimization provides much more information than a single-objective case for a decision maker, who can subsequently decide which reliability level is worth it. On the other hand, computational efforts are much higher than for a single-objective formulation and therefore the most computationally demanding part, the reliability assessment, has to be chosen carefully. The double-looped formulation is affordable with advanced simulation techniques such as an Asymptotic sampling or a Subset simulation. Even with a basic implementation, the results are relatively credible with fewer number of samples than with a classical Monte Carlo method and more credible than with FORM.

Acknowledgement

This work was supported by Czech Science Foundation, grant No. 15-07299S and by the Grant Agency of the Czech Technical University in Prague, grant No. SGS16/037/OHK1/1T/11.

References

Au, S. K., & Beck, J. L. (2001). Estimation of small failure probabilities in high dimensions by subset simulation. Probabilistic Engineering Mechanics, 16, 4, pp. 263-277.

Bucher, C. (2009). Asymptotic sampling for high-dimensional reliability analysis. Probabilistic Engineering Mechanics, 24, 4, pp. 504-510.

Chen, Z., Qiu, H., Gao, L., & Li, P. (2013). An optimal shifting vector approach for efficient probabilistic design. Structural and Multidisciplinary Optimization, 47, 6, pp. 905-920.

Deb, K., Pratap, A., Agarwal, S., & Meyarivan, T. A. M. T. (2002). A fast and elitist multiobjective genetic algorithm: NSGA-II. Evolutionary Computation, IEEE Transactions on, 6, 2, pp. 182-197.

Dubourg, V. (2011). Adaptive surrogate models for reliability analysis and reliability-based design optimization PhD Thesis, Université Blaise Pascal-Clermont-Ferrand II.

Hasofer, A. M., & Lind, N. C. (1974). Exact and invariant second-moment code format. Journal of the Engineering Mechanics division, 100, 1, pp. 111-121.

Lee, T. H., & Jung, J. J. (2008). A sampling technique enhancing accuracy and efficiency of metamodel-based RBDO: Constraint boundary sampling. Computers & Structures, 86, 13, 1, pp. 463-1476.

Pospíšilová, A. & Lepš, M. (2013). Multi-Objective Optimization with Asymptotic Sampling for RBDO. In: Proceedings of the Third International Conference on Soft Computing Technology in Civil, Structural and Environmental Engineering.

Pospíšilová, A. & Lepš, M. (2015). Multi-Objective Reliability-Based Design Optimization utilizing an Adaptively Updated Surrogate Model**.** In: Proceedings of the Fourth International Conference on Soft Computing Technology in Civil, Structural and Environmental Engineering.

22nd International Conference
ENGINEERING MECHANICS 2016
Svratka, Czech Republic, 9 – 12 May 2016

INVESTIGATION OF SINGLE STAGE GEARBOX PARAMETERS INFLUENCING SURFACE NORMAL VELOCITY

A. Prokop[*], M. Zubík[**], K. Řehák[***], P. Novotný[****]

Abstract: *Presented paper examines the effect of the basic gearbox parameter on the surface normal velocity of the gearbox top cover. Firstly, in order to validate the inputs and results of the whole methodology a single stage gearbox was designed and manufactured. Secondly, a dynamic model is built for the single stage gearbox and each part of it is validated by an appropriate experiment. After the good correlation of the model and measurement, an additional simulation is performed to verify specified influences. The investigation focuses on finding the best conditions between thickness of gearbox housing top cover and dimensions of shafts, which are represented by the torsional stiffness. The method described is able to determine the impact of each modification, thus it can be useful at the design phase and also during measurement or investigation of an existent problem.*

Keywords: Single stage gearbox, Transmission, Noise, Vibration.

1. Introduction

Combustion engines, electric motors, compressors or transmissions are, nowadays, designed to have maximum possible efficiency, wide variety of running conditions, complexity and low production costs. The increasing number of such devices closely relates to the prevailing popular health issue topics. Moreover, the increasing global number of all the pollutants speeds up the development of electric car and accumulators. Since the combustion engines are absent in this regard, other noise components come into focus, mainly the transmissions. Currently, the gearboxes in the locomotive area are becoming a hot topic because trains are usually associated with densely inhabited district areas. In addition, transmissions in wind power plants, which are examined in papers by Feng et al. 2014 and Jin et al. 2016, as a renewable power source, are dealt with very often when the noise in surrounding areas is concerned, significantly influencing life quality there. Automobile industry with an extensive number of products is another part of this issue, where the transmission is one of the investigated topic (Kadmiri et al., 2012).

In cases where the transmission is expected to be the dominant noise source, usually it is the housing, which is responsible for more than 80% of the whole transmission emitted noise (Zubík et al., 2015). Housing NVH improvement is performed predominantly by a modal analysis, which can provide basic information about frequency and mode shape. This approach has some disadvantages, the frequency does not have to be, necessarily, excited by operation conditions or, on the other hand, the higher mode (over the operation mode) can be excited. Moreover, this approach does not provide any information about surface velocity, which is closely connected to the emitted noise. Modal analysis has an essential potential in a design phase when validating the differences between two possible options takes place (Yongxiang et al., 2014). The next level of gearbox investigation lies in using harmonic analysis, which can be performed

[*] Ing. Aleš Prokop: Institute of Automotive Engineering, Brno University of Technology, Technická 2896/2; 616 69, Brno, CZ, prokop.a@fme.vutbr.cz

[**] Ing. Martin Zubík: Institute of Automotive Engineering, Brno University of Technology, Technická 2896/2; 616 69, Brno, CZ, zubik@fme.vutbr.cz

[***] Ing. Kamil Řehák: Institute of Automotive Engineering, Brno University of Technology, Technická 2896/2; 616 69, Brno, CZ, rehak@fme.vutbr.cz

[****] doc. Ing. Pavel Novotný, Ph.D.: Institute of Automotive Engineering, Brno University of Technology, Technická 2896/2; 616 69, Brno, CZ, novotny.pa@fme.vutbr.cz

by experimental or numerical approach. Harmonic analysis can provide information about surface normal velocity, but the exciting forces have to be known, which is sometimes difficult to obtain.

For that purpose, the Multibody dynamics system can be used. Inputs causing excitation here can be formulated in an easier form – input torque and rotational speed, which are transferred into related forces acting on each model part. The numerical simulation of transmission is frequently examined and also extensive topic, but all models have to be at the end verified by an experiment. The most advantageous variant of the transmission seems to be the single stage gearbox, because of easy modification to different gearwheels, bearings, shafts and covers. This kind of transmission is widely used for examination of oil behavior, the influence of contact behavior, unbalance, backlash, torque value and transmission error (Razpotnik et al., 2015; Ma et al., 2012; Loutas et al., 2012; Lei, 2010; Andersson & Vedmar, 2003; Ma et al., 2012). This paper deals with the examination of dynamic simulations of the single stage transmission, where the normal surface velocity on the top cover is mainly observed.

2. Methods

In order to examine the concept of gearbox dynamics, single-stage gearbox unit was chosen. It is due to a relative simplicity of the shape but still comparable behavior with the standard transmissions. First step of such a study should always take into consideration how to provide reliable experimental validations. Comparison with real the measurements is necessary for the evaluation of computational dynamic characteristics when compiling the methodology for the first time. Once the procedure on this simplified gearbox unit is complete, it can be extended and applied to any transmission with experimental validation at the end. The information about the used gears, gearbox housing, testing state and measuring are summarized in paper by Zubík et al., (2015).

2.1. Multi body simulation model

The multibody simulation is a very powerful tools for description of dynamic behavior. The gearbox is predominantly represented by information about the gear mesh contact, shafts, bearings and housing. To attain the most corresponding behavior, the most important is that housing should be considered as flexible by using Craig Bampton reduction principle. This procedure replaces real deformations included in the basic equation of motion form by the simplified approximation established from the two variants of degrees of freedom multiplied by the special Craig-Bampton transform matrix, see equation 1 (Craig 1968):

$$\{\mathbf{u}_A\} = \begin{Bmatrix} \mathbf{u}_b \\ \mathbf{u}_L \end{Bmatrix} = \begin{bmatrix} \mathbf{I} & \mathbf{0} \\ \mathbf{\Phi}_R & \mathbf{\Phi}_L \end{bmatrix} \begin{Bmatrix} \mathbf{u}_b \\ \mathbf{q} \end{Bmatrix} = \mathbf{\Phi}_{CB} \begin{Bmatrix} \mathbf{u}_b \\ \mathbf{q} \end{Bmatrix}, \tag{1}$$

where $\boldsymbol{u}_{\mathrm{A}}$ is the original vector of deformation, $\boldsymbol{u}_{\mathrm{b}}$ are the boundary degrees of freedom (DOFs), $\boldsymbol{u}_{\mathrm{L}}$ stands for interior DOFs, $\mathbf{q}$ represents modal DOFs, $\mathbf{I}$ is the identity matrix element, $\boldsymbol{\phi}_R$ is rigid body matrix element and in the analogical way $\boldsymbol{\phi}_L$ are the fixed base mode shapes matrix element. Deformation approximation is inserted into the equation of motion. The aim of this process is to model the assembly parts independently, where the internal dynamic behavior is represented by the natural vibration modes.

The whole model consists of gears mounted on the rigid shafts, where shaft torsional stiffness is defined by spring-damper coupler. Transmission housing is represented by the flexible body with the experimentally specified damping ratio. Parts connection is done through bearings specified by radial and axial stiffness. The whole model is loaded by the constant torque moment on the output side and rotation speed is going up to 6000 rpm on the input side.

2.2. Results

The main aim of this comparison is to find the best variant of cover thickness and shafts stiffness in operational range up to 500 Nm torque. Appropriate model with gear contact stiffness based on FE simulation is used, including the real gear geometry. Boundary conditions are set to cover the whole torque range. At first the cover thickness is optimized based on the torque and afterwards the best shaft variant is checked for previously chosen best variant of cover thickness. The highest value of surface normal velocity at three points on the top cover during run up to 6000 rpm is observed for each case from the graph, shown in figure 1.

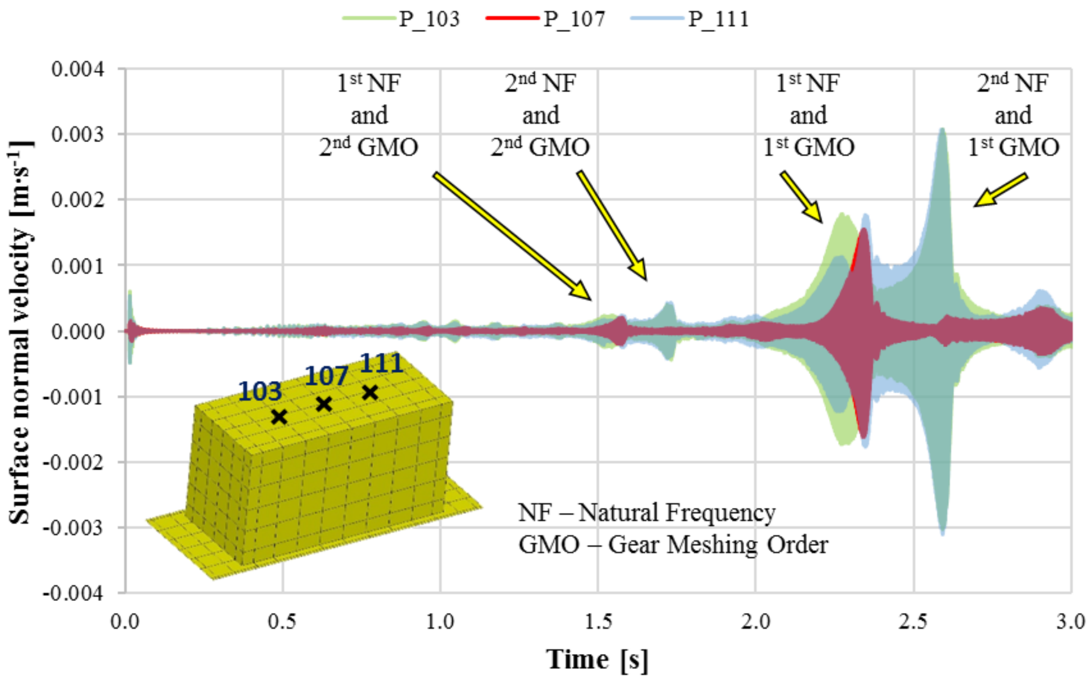

Fig. 1: Surface normal velocity amplitude identification on the top cover points.

The highest amplitudes are checked by applying partial FFT decomposition of the signal and comparison with the natural frequencies of the appropriate variant of housing. It has to be taken into account, that modal analysis in free boundary conditions used for the flexible body reduction does not include all of the natural frequencies and shapes. Some of them are a result of the bonded attachment of the gearbox housing, but still can be excited in the real operating conditions. To gain further knowledge, separate coupled modal analysis should be performed together with the uncoupled one.

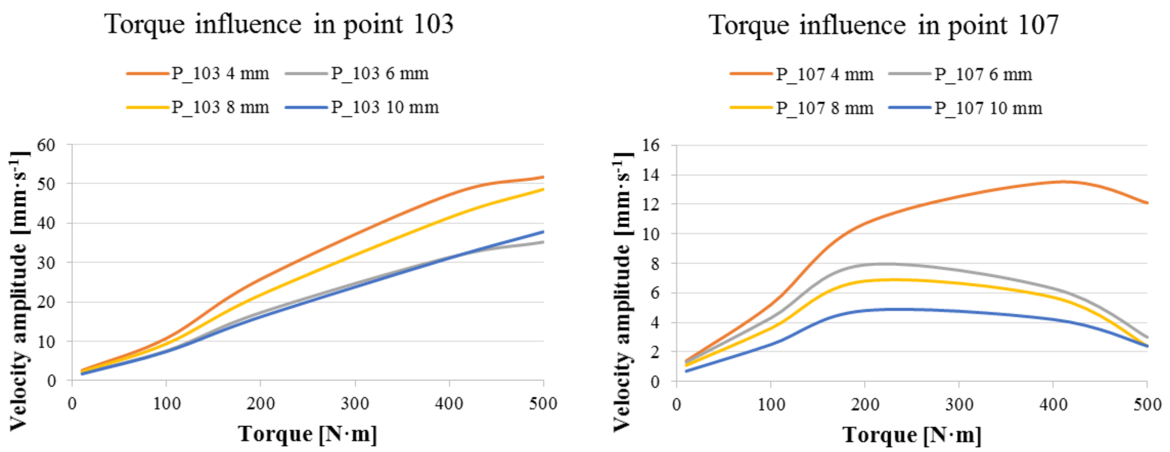

Fig. 2: Surface normal velocity amplitudes related to applied torque and gearbox housing cover thickness in two separate points 103 and 107.

Figure 2 shows the tendencies in the progress of surface normal velocity amplitudes when changing the housing cover thickness. From both result points, 103 and 107, can be assessed that the value 6 mm of thickness is the best option when considering material costs and the final level of velocities. Result data from point 111 are not presented because of very similar tendencies regarding the point 103. Engineering approach usually improves surface vibrations by adding stiffening ribs to the structure. Additional ribs on the cover would definitely change the results to have possibly even thinner cover with lower velocities, but this is not primarily the intention of the study. Presented solution is primarily chosen to maintain gearbox simple construction and not to achieve best cost effectivity.

The impact of shaft torsional stiffness is observed, where by 10 times increased and decreased value of stiffness is used, but without any significant change in the final surface velocities. In smooth operating conditions (with constant loading torque) is no need to consider torsional deformations of the shafts because they are hardly transferred further into the gearbox housing.

3. Conclusions

The method described in this paper can predict the gearbox dynamic behavior of a gear set before the manufacture. This phase predominantly focuses on the fast but still valid solution for finding the best components parameters. The thickness of cover or wall generally, is one of the most important factor for noise emission. The optimal value of cover thickness was found based on the increasing speed with constant loading by torque. The next step was based on the influence of shaft diameter, which was represented by the shaft torsional stiffness. There is no significant effect of torsional stiffness on normal surface velocity. Another case with varying input torque or speed could be more appropriate for this investigation. With some modifications, the methodology and experience gained from the experimental gearbox examinations can be easily used for common heavier single stage or two stage locomotive gearbox.

In the future step, a model of each component on a higher level of will be tested and it will undergo same testing of parameters afterwards.

Acknowledgement

The research leading to these results has received funding from the Ministry of Education, Youth and Sports under the National Sustainability Programme I (Project LO1202) and University Specific Research project Research of Progressive Methods for Drivetrain Dynamics, Reg. No. FSI-S-14-2334. This support is gratefully acknowledged.

References

Andersson, A. & Vedmar, L. (2003) A dynamic model to determine vibrations in involute helical gears. Journal of Sound and Vibration, vol. 260(issue 2), pp..195-212.

Craig, R., Bampton M. (1968) Coupling of substructures for dynamic analyses, AIAA Journal, Vol. 6, No. 7, p. 1313-1319

Feng, L., Yumo, Q., Linshan, G., Zhao, P., Shaokang, L. & Donglong, L. (2015) Influences of planetary gear parameters on the dynamic characteristics – a review. Journal of Vibroengineering, vol. 17(issue 2).

Jin, X., Li, L., Ju, W., Zhang, Z. & Yang, X. (2016) Multibody modeling of varying complexity for dynamic analysis of large-scale wind turbines. Renewable Energy, vol. 90, pp..336-351.

Kadmiri, Y., Rigaud, E., Perret-Liaudet, J. & Vary, L. (2012) Experimental and numerical analysis of automotive gearbox rattle noise. Journal of Sound and Vibration, vol. 331(issue 13), pp..3144-3157.

Lei, L. (2010) A Multibody System Model for Meshing Gears. Applied Mechanics and Materials, 44-47, pp. 1273-1278.

Loutas, T., Sotiriades, G., Kalaitzoglou, I. & Kostopoulos, V. (2009) Condition monitoring of a single-stage gearbox with artificially induced gear cracks utilizing on-line vibration and acoustic emission measurements. Applied Acoustics, vol. 70(issue 9), pp..1148-1159.

Ma, R., Chen, Y. & Cao, Q. (2012) Research on dynamics and fault mechanism of spur gear pair with spalling defect. Journal of Sound and Vibration, vol. 331(issue 9), pp..2097-2109.

Razpotnik, M., Bischof, T. & Boltežar, M. (2015) The influence of bearing stiffness on the vibration properties of statically overdetermined gearboxes. Journal of Sound and Vibration, vol. 351, pp..221-235.

Yongxiang, L., Lihong, J., Wenquan, S., Liwen, N. & Youjia, Z. (2014) An efficient optimal design methodology for abnormal noise control of automobile transmission in the neutral idle condition. Journal of Vibroengineering, vol. 16(issue 1).

Zubík, M., Prokop, A., Řehák, K. & Novotný, P. (2015) The effect of the gear parameters to the noise of transmission. In Vibroengineering Procedia. Katowice, Poland: JVE International, pp. 357-362.

22nd International Conference
ENGINEERING MECHANICS 2016
Svratka, Czech Republic, 9 – 12 May 2016

TENSILE BEHAVIOUR OF NATURAL FABRIC REINFORCED COMPOSITE

J. Purdek*, S. Samal, D. Reichmann

Abstract: *Tensile behaviour of natural fabric reinforced composite were investigated in this work. Natural fabric such as flax and jute were considered in bi-axial plain reinforcement in matrix of acrylic resin. The composite are prepared in hand layup techniques. Fabric weight fraction of 7 % was used in the matrix of composite. The samples were treated at RT and 60 °C for the final fabrication. Tensile test were carried out on the samples with dimension 200x30x5.5 mm with span of testing 120 mm using instrument Instron 5967 / 30 kN. The speeds of measurement were considered 5 mm/ min. The result of flax reinforced composite shows better tensile strength of 12 MPa. Scanning electron microscope image analysis was carried out to examine the micro structure effect of composite in terms of tensile strength.*

Keywords: Flax, Jute, Acrylic resin, Tensile Behaviour, Composite

1. Introduction

Every substitution of heavy metal materials by light-weighted composites of the equivalent mechanical properties is desired in the field of mechanical engineering. Furthermore, natural fabrics are renewable thus environmentally more convenient and friendly in nature. Flax and jute fabrics are investigated to reinforce acrylic resin matrix. Tensile strength is the focus of this work. Jute and flax plain weave fabrics were tested for tensile strength using Instron 5967 and then compared to tensile strength of the reinforced composite. The composite samples were prepared by hand layup technique.

Aim of the investigation is on tensile behaviour of fabrics such as flax and jute with the reinforced composite respectively. The microstructural observations were carried out to correlate the mechanical properties of the material.

2. Methods

Samples for tensile strength of fabrics prepared from jute (437g/m2) and flax (270g/m2) with dimension 200x30x0.5 mm. Plain weave fabrics were used for the composite of dimensions 200x200x5.5 mm. Hand layup technique was used to prepare jute and flax reinforced in acrylic resin matrix composite. Matrix is a combination of two materials such as Acrylic One LP01 Catalyst (Liquid composition: Water 54.4-56.7%, Acrylic Polymer 43.3-45.6%) and powder (Calcium Sulphate: Relative Density 2.75 g/cm3, Melting point 1610°C). The mixture of the solution is prepared using powder and catalyst in the ratio of 2:1 (300g of powder, 150g of liquid). Thicknesses of the composites were 5.8 (±0.2) mm for flax and 5.5 (±0.2) mm for jute where 3 layers of flax and 2 layer of jute were implied. Weight fraction for jute composite is 7.2% and 6.7% for flax is shown in equation (1). For some samples, heat treating was performed in the laboratory furnace for 24hours at 60°C, the rest dried at the room temperature (RT) 25°C. Final dimension of the samples used for testing is 200x25x5.5 mm. In average 7 samples were prepared from the plate by cutting using a hand saw instrument. Tensile tests were carried out on fabric samples and composite samples using Instron 5967 with a video-extensometer.

* Jiri Purdek, Sneha Samal, David Reichmann, Katedra mechaniky, pružnosti a pevnosti, Technická univerzita v Liberci, Studentská 2; 46117, Liberec; Czech Republic; samasneha@gmail.com

Table 1. Final dimensions of tested samples and weight fraction in case of composites.

Samples	Fabrics [mm]	Composite [mm]	Weight fraction %
Flax	200x30x0,5	200x25x5,8	6,7
Jute	200x30x0,7	200x25x5,5	7,2

The weight fraction of fabrics in the composite is calculated using equation (1) below

$$W_f = \frac{m_{fabric}}{m_{composite}} = \frac{m_{Flax}}{m_{powder} + m_{liquid} + m_{Flax}} \cong 6{,}7\% \tag{1}$$

The schematic diagram of the sample dimension and pictorial presentation of sample testing is shown in Fig.1.

(a)

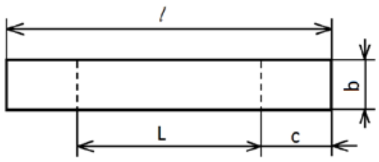

(b)

Fig. 1: (a) Schematic diagram of sample dimension (l – total length of the sample, L – measured length of the sample, b- width of the sample; (b), testing demonstration of composite sample using Instron 5967

The testing parameters are represented in Table 2 for measurement of tensile strength of the fabric and composite samples.

Table 2. Parameters for tensile test

	l [mm]	L	c	b	Speed [mm/min]
Fabric (Jute, Flax)	200	120	40	30	5
Composites	200	120	40	25	5

3. Results and discussion

Fig. 2 displays the force - displacement relation of the fabrics such as jute and flax. Flax fabric withstand the force of 87 N before the tearing happens in the fabric. However, the jute fabric tears up at force of 70 N. The tensile test of the fabric shows tearing happens in the zone of the clamping area. Fig. 3 represents the force - displacement of composite reinforced with flax and jute fabrics at room temperature. Flax fabric reinforced composite shows 3.5 times higher force compared to the composite reinforced by jute fabric. Jute reinforced composite show failure of the material at the force of 400N with extension of 0.3 mm. Fig. 4 shows force – displacement relation of flax and jute reinforced acrylic resin composite at 60°C. Results of heated samples show the changes in both of the composites. The flax reinforced acrylic resin composite withstands a lower pulling force of 525 N before any plastic deformation. In contrary, the plastic deformation of jute reinforced acrylic resin composite occurs after the force increases above 840 N. This may be caused due to interfacial adhesion between fabric and matrix surface. This observation has been supported by microstructural images of the composite.

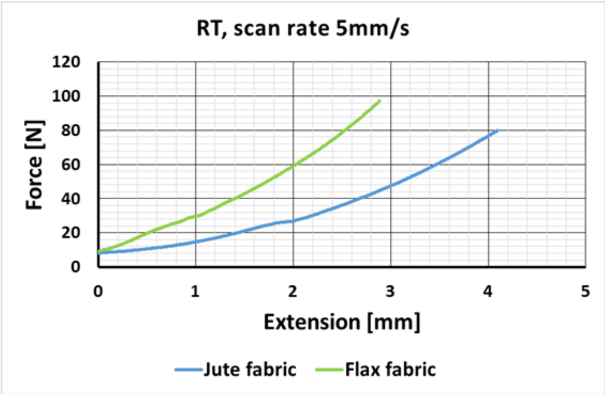

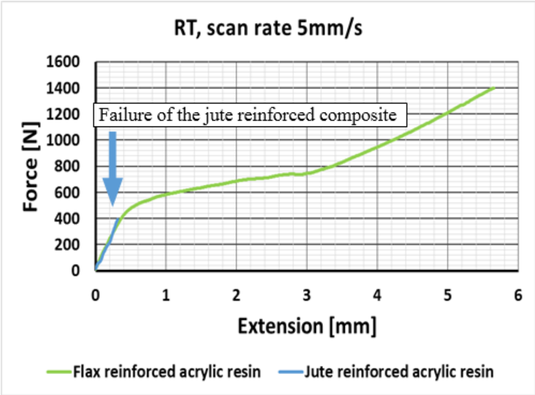

Fig. 2: Load vs displacement graph of fabrics

Fig. 3: Load vs displacement graph of composites

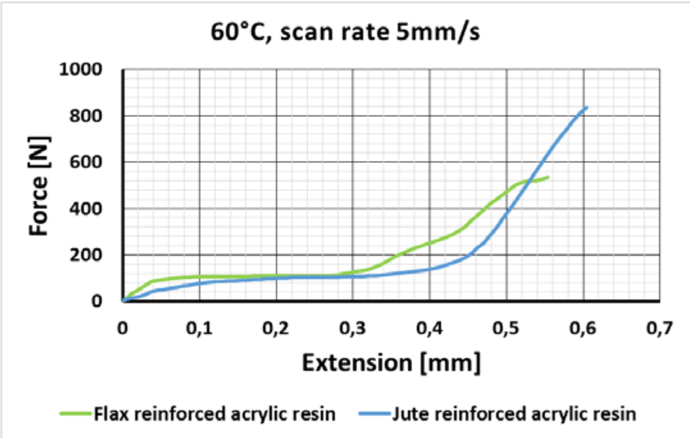

Fig. 4: Load vs displacement graph of composites at 60°C

The correlation between tensile and microstructural properties of the composite is investigated using scanning electron microscope. The adhesion between the fabric and the matrix is observed from this analysis. Fig. 5 shows the microstructure of the composite with flax fabrics (Fig. 5 a) and jute fabric (Fig. 5 b) is shown below. Adhesion between jute and matrix at RT is weak, however the samples treated at 60°C (Fig. 5 c) created stronger bonds with matrix. On the contrary the structural change due to the treatment to 60°C of the matrix reinforced with flax caused decreased overall tensile strength.

4. Conclusions

Flax fabric reinforced composite shows overall better tensile behaviour in comparison to jute reinforced acrylic resin composite. Despite the results with the heat treatment at 60°C at which point the jute reinforced acrylic resin composite reached the cracking point at the load of 840 N (tensile strength 6 MPa) , the flax reinforced acrylic resin composite reach the maximum value of 1390 N (tensile strength 10 MPa) at room temperature. This change of tensile behaviour may be caused by the microstructural changes. The bonds between the jute fibers and the matrix were weak at the room temperature. Heating helped matrix to bond with the jute fibers, however the structural change of the matrix reinforced with flax fabric weakened the overall tensile strength.

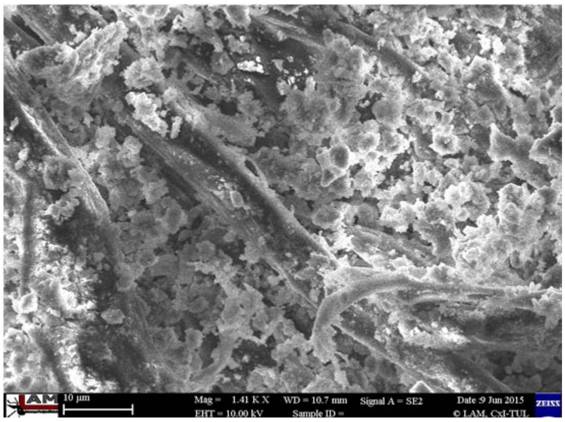

(a) Flax reinforced composite at RT

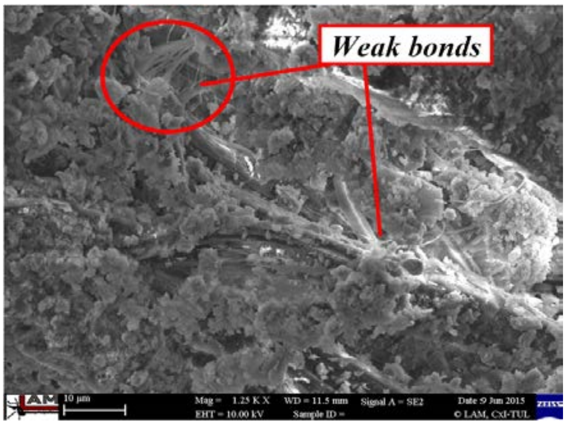

(b) Jute reinforced composite at RT

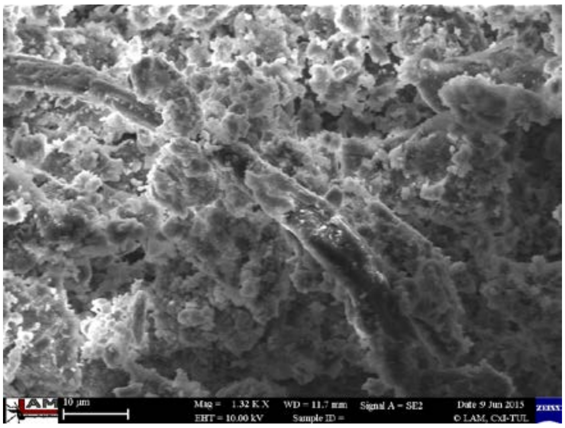

(c) Flax reinforced composite at 60°C

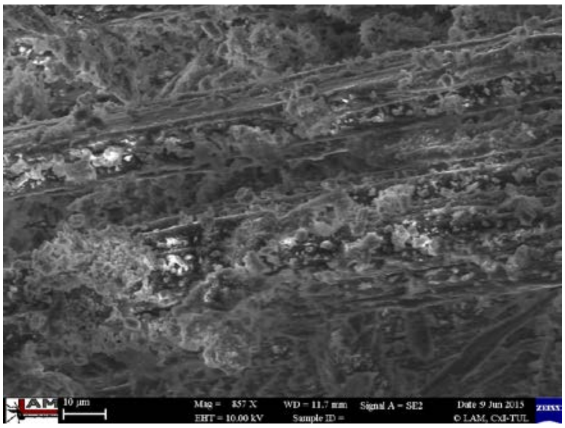

(d) Jute reinforced composite at 60°C

Fig. 5. Scanning electron microscope images for fabric reinforced composite at RT and 60 °C.

Acknowledgement

This work was supported by national financial resources of Ministry of Education Youth and Sports of Czech Republic for specific university research (SGS 21120).

References

Samal S., Nhan. P. T., Petrikova I. and Marvalova B. (2015) Improved mechanical proprties of various fabric-reinforced geocomposite at elevated temperature, JOM: The journal of the minerals, metals and materials society 67 ,7, pp. 1478-1485.

Samal S., Nhan P.T., Petrikova I., Marvalova B., Vallons K., Lomov S. V. (2015) Correlation of microstructure and mechincal properties of various fabric reinforced geo-polymer composites after exposure to elevated temperature, ceramics International 41, 9, pp. 12115-12129.

Zhu J., Zhu H., Njuguna J. and Abhyankar H. (2013), Recent Development of Flax Fibres and Their Reinforced Composites Based on Different Polymeric Matrices, Materials, 6, pp. 5171-5198, doi:10.3390/ma6115171.

Roe P. J., Ansell M. P. (1985) Jute-reinforced polyester composites, Journal of Materials Science, Volume 20, 11, pp 4015-4020.

22nd International Conference
ENGINEERING MECHANICS 2016
Svratka, Czech Republic, 9 – 12 May 2016

FIVE-BLADE BUNCH WITH DRY FRICTION INTER-CONNECTION FORCED BY RUNNING EXCITATION

L. Půst*, L. Pešek*, A. Radolfová*

Abstract: *The vibration of five-blade-bunch linked in the shroud by means dry-friction-elements is investigated. Quasi-stationary response curves are used for analysis of dynamic properties of isolated blade-bunches excited by running harmonic forces. This running wave excitation models the real excitation in the steam or gas turbine with different numbers of rotor and stator blades. Relation between the ratio of these blade-numbers and phase delay between neighboring blades is ascertained and the dynamic responses of isolated five-blade bunch are shown and analyzed in this paper. Gained theoretical results can be used for evaluation of data obtained from dynamic measurements on bladed disk.*

Keywords: Five-blade bunch, Coulomb dry friction damping, Delayed harmonic excitation, Response curves, Running wave.

1. Introduction

Reduction of resonance vibrations realized by dry friction between the blade-heads in the shroud is very often applied in technical practice [Sextro, 2007, Byrtus et al., 2013, Bruha & Zeman, 2014, Ding & Chen, 2008]. The dry friction contacts are strongly nonlinear and therefore the responses of such system are more complicated then responses of five-blade-bunch containing only linear viscous-elastic connections solved e.g. in [Pust et al., 2016].

Results of experimental or analytical investigation of vibration of blade-models with friction contact [Pesek & Pust., 2011] prove the efficiency of such devices for turbine blades vibrations improvement. In the Institute of Thermomechanics ASCR the detailed analysis and measurements of blade couple have been realized. Dynamics of the two blades model has been investigated with a lot of dry-friction-force characteristics, including also slip-stick models and possibility of instability and existence of dangerous self-excited vibrations. Because some laboratory experiments were carried out on the five-blade bunch [Pust & Pesek, 2013, Pust et al., 2013], the extension of two-blades-model investigation to the study of five-blades bunch is necessary.

According to real machines, the computational model of the turbine five-blades bunch is here excited by five delayed harmonic forces, with the same frequency and amplitude but with stepwise-enlarged delays Δt in time. As opposed to [Pust et al., 2016], the presented contribution is focused only on analysis of response curves of separate five-blades bunch (first and fifth blade unconnected).

In this contribution only the simplest model of many dry friction characteristics - Coulomb model – is applied. The properties of systems with the more sophisticated models will be shown at presentation.

* Ing. Ladislav Půst, DrSc., Ing. Ludek Pešek, CSc, Ing. Mgr. Alena Radolfová, Institute of Thermomechanics AS CR, v.v.i., Dolejškova 5, 18200 Praha 8, e-mail: pust@it.cas.cz, pesek@it.cas.cz, radolfov@it.cas.cz

2. Dry friction connection and elastic micro-deformations

Dry friction is very complicated process, which has to be mathematically described by a strongly nonlinear characteristic. The generally used Coulomb model is only the first approximation of description of real properties. There are two main sets of dry friction characteristics:

2D — "forc-velocity"

and 3D — "force-velocity-displacement" expressions.

The first 2D set of dry friction characteristics contains besides Coulomb model applicable in the ranges of great relative velocities also e.g. modified Coulomb model or arc-tangent model useful especially at vibrations with small amplitudes. However, including general dependence on friction velocity can further modify all these models. This 2D model enables an easy calculation for the majority of engineering problems, where the vibrating bodies are sufficiently stiff and only slip in contact surfaces exists.

In some friction couples especially at vibrations with small amplitudes and if friction surfaces are placed on some compliant parts of moving bodies, it is necessary to use more sophisticated 3D "stick-slip" computational model. There are also many kinds of this type; the simplest one consisting of an elastic linear spring connected with a dry friction element is applied.

3. Delayed harmonic excitation

The main part of excitation forces acting on blades in steam or gas turbines are aerodynamic forces generating by revolution of rotor bladed disk in the non-homogenous stationery gas flow through the stator blades cascade. The phase delay $\Delta\varphi$ of harmonic excitation depends on number l_r of blades of rotating disk and on number ls of stator blades according to the following relations:

$$\Delta\varphi = 2\pi * (1 - \frac{l_s}{l_r}) \tag{1}$$

In technical practice there are the numbers l_s, l_r in the ratio l_s / l_r usually selected in such a way, that their least common multiple is very high. In order such a system to be sufficiently resistant against resonance excited by the stator flow irregularity. However, in the case of isolated five-blade bunch, any arbitrary phase delay $\Delta\varphi$ (and corresponding arbitrary blades ratio l_s/l_r) can be selected.

4. Response curves of five-blade bunch with Coulomb 2D friction connection

Dry friction connections of blades are in the practice very often applied for introducing additional damping into mechanical systems.

An experimental bladed wheel with 60 models of blades has been investigated in the dynamic laboratory of the Institute of Thermomechanics ASCR.It contains two five-blade bunches situated on opposite sides of the wheel – see Fig. 1.

The boundary blades of these bunches are free on their external sides and each of the measured five-blade bunches is isolated from the other blades. The five-blade bunch can be modeled by a five masses system with blades replaced by 1 DOF systems, the eigenfrequencies of which correspond to the first bending eigenfrequency of real blade (mass *m*, stiffness *k*, damping coefficient *b*).

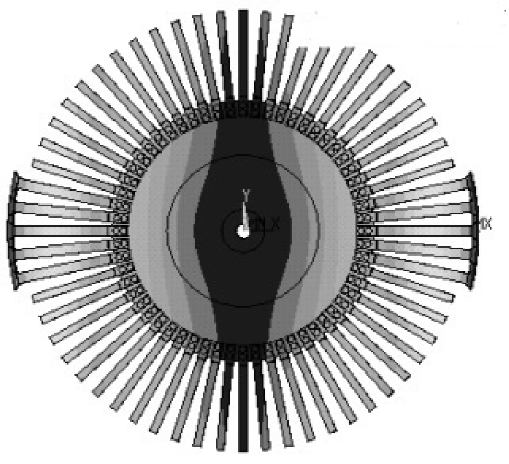

Fig. 1: Experimental bladed wheel with two five-blade bunches

Motion of the isolated blade bunch shown in Fig. 2 and excited by delayed harmonic forces $F_i(t) = F_{0i}\cos(\omega t - (i-1)\Delta\varphi)$, is described by a set of equations

$$
\begin{aligned}
&m\ddot{y}_1 + b\dot{y}_1 + ky_1 + g_1 = F_0\cos(\omega t),\\
&m\ddot{y}_2 + b\dot{y}_2 + ky_2 + g_2 - g_1 = F_0\cos(\omega t - \Delta\varphi),\\
&m\ddot{y}_3 + b\dot{y}_3 + ky_3 + g_3 - g_2 = F_0\cos(\omega t - 2\Delta\varphi),\\
&m\ddot{y}_4 + b\dot{y}_4 + ky_4 + g_4 - g_3 = F_0\cos(\omega t - 3\Delta\varphi),\\
&m\ddot{y}_5 + b\dot{y}_5 + ky_5 - g_4 = F_0\cos(\omega t - 4\Delta\varphi),
\end{aligned}
\tag{2}
$$

where functions g_i are given for Coulomb dry friction connections by

$$g_i = F_t sign(\dot{y}_i - \dot{y}_{i+1}), \qquad i = 1,...,4. \tag{3}$$

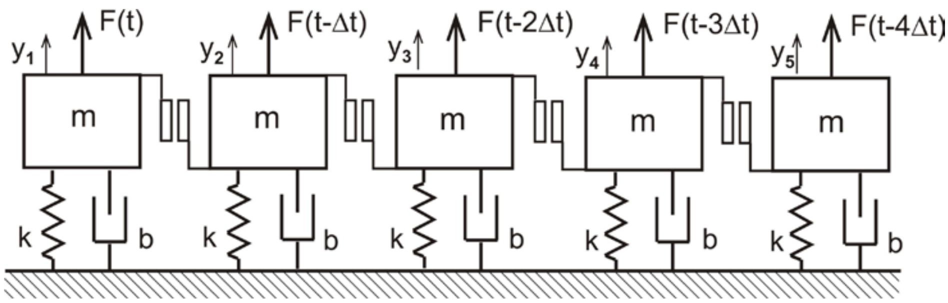

Fig. 2: Computational model of isolated five-blade bunch with dry friction connections

If $\Delta\varphi = 0$, all blades vibrate in the same phase and no deformations in dry friction connections occur. If the blades are excited with non-zero phase delay e.g. $\Delta\varphi = 2\pi/5$, all the joining elements are deformed and response curves of individual blades differ. This property is shown in Fig. 3, computed for parameters m = 0.182 kg, k = 105000 kgs^{-2}, b = 2 kgs^{-1}, F_0 = 1 N and several dry friction force F_f = 0.9 – 1.3 N. The height of resonance peaks decreases with increase of dry friction forces in the inter-connections.

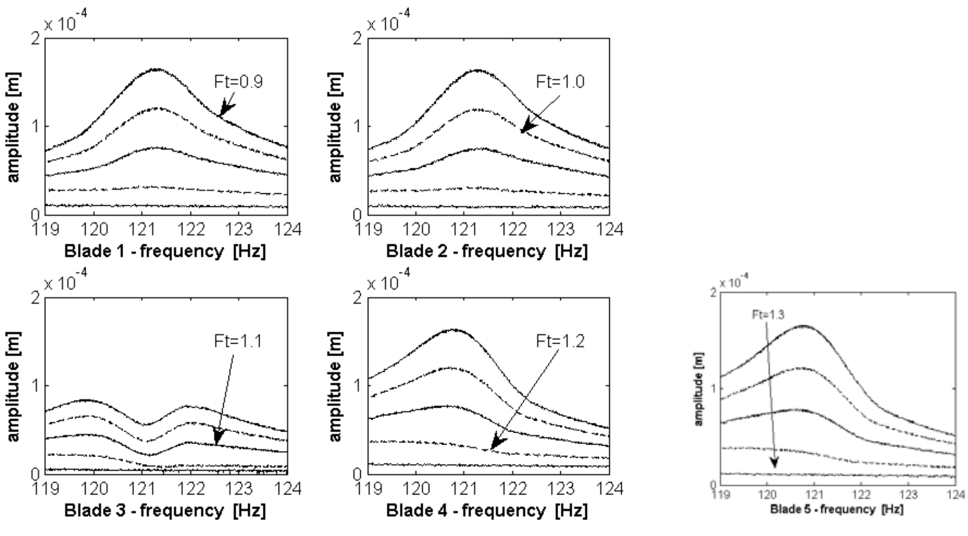

Fig. 3 : Response curves for phase shift Δφ =2π/5 and various Coulomb dry friction joining elements with F_f = 0.9 – 1.3 N.

No motion occurs for higher friction (approx. $F_t > 4/\pi * F_0$). Remarkable is the property of the central blade 3, which vibrates with minimum amplitudes and response curves have two maxims.

5. Conclusions

Dynamic properties of an isolated five-blade-bunch linked in the shroud by means of Coulomb dry friction connections and excited by running harmonic forces were investigated. The developed method of solution has been applied for computing of sets of response curves at different values of fry friction forces at running harmonic excitation with given phase angle shift produced by non-homogenous stationary gas flow through the stator blades cascade. Analysis of this set of curves reveals differences in dynamic responses of individual blades and creates base for evaluation of experimentally gained data from dynamic measurements on bladed disk.

This method of solution can be used also for investigation of dynamic properties of blade bunches with other types of inter-blades connections e.g. modified Coulomb, slip-stick contact, etc.

Acknowledgement

This work was supported by the research project of the Czech Science Foundation No. 16-04546S "Aero-elastic couplings and dynamic behaviour of rotational periodic bodies".

References

Bruha, J. & .Zeman, V. (2014) Vibration of bladed disk with friction elements, In Proc. Dynamics of Machines 2014, (L. Pesek),Prague, IT AS CR, pp.15-22

Byrtus, M., Hajzman, M. & Zeman, V., (2013) Linearization of friction effects in vibration of two rotating blades, *Applied and Computational Mechanics, Vol.*. 7, No. 1, pp. 5-22

Ding Q. & Chen Y., (2008) Analyzing Resonance Response of a System with Dry Friction Damper Using an Analytical Method.. Journal of Vibration and Control, 14(8), pp. 1111-1123

Pešek L. & Půst L. (2011) Mathematical model of a blade couple connected by damping element, in Proc. 8th International Conference on Structural Dynamics, EURODYN2011, Leuven, Katolieke Universiteit Leuven, (Roeck G. De, ed.), pp. 2006-2011.

Pust L., Pesek L. & Radolfova A. (2011) Various Type of Dry Friction Characteristics for Vibration Damping, Engineering Mechanics, 18, , No. ¾, pp. 203-224.

Pust L. & Pesek L.(2013) Model of Turbine Blades Bundles, in. ROM Proceedings Engineering Mechanics, (J. Fuis) VUT Brno, Svratka, CR, pp. 467-477

Pust L., Pesek L., Cibulka J. & Bula V.(2013) Mathematical Model of Blades Bundle with Damping Connections, Eastern-European Journal of Enterprise Technologies, 3/12(63), pp. 43-46

Pust L., Pesek L. & Radolfova A. (2016) Vibration of blade bunch forced by delayed excitation, in Proc. Colloquium Dynamesi 2016 (L.Pesek & I. Zolotarev), IT AVCR, Prague, pp. 12.

Sextro W.(2007) Dynamical Contact Problems with Friction, Springer-Verlag Berlin Heidelberg,

22nd International Conference
ENGINEERING MECHANICS 2016
Svratka, Czech Republic, 9 – 12 May 2016

PARALLEL COMPUTATIONS AND C++ STANDARD LIBRARIES

V. Rek*, I. Němec**

Abstract: *In this paper, the form of modifications of the existing code written in C programming language for the calculation of structures using the explicit form of the Finite Element Method is introduced. It uses the possibilities of multithread running, which is now supported at the level of native C++ programming language using standard libraries. Thanks to the high degree of abstraction that is provided by contemporary C++ programming language, a respective library created in this way can be generalized for other purposes of usage of parallelism in computational mechanics.*

Keywords: Finite Element Method, Explicit Form of the Finite Element Method, Central Difference Method, Parallel Computing, C++ Standard Libraries.

1. Introduction

Due to the significant expansion of multi-core processors in the past decade, many older applications designed to run sequentially have begun to become obsolete, mainly due to the performance of available hardware.

As in the past, and even now, development tools for the development of software applications are slightly lagging behind the choices of available hardware. Alternatives of how to benefit from multi-core processors were technologies such as Intel Threading Building Blocks or Intel Cilk++, or others which also require special installation. Another possibility was to use an application interface provided directly for the respective operating system such as Windows Win32 API (Hart, 2015) or POSIX (Kerrisk , 2010) for Unix-like operating systems, which are often quite cumbersome and limited to the possibilities of C programming language (Prata, 2004).

Since the year 2011, when the new standard of C++ programming language was introduced (version 11), developers have been given the possibility to use threads and all other necessary resources to support thread synchronization (mutex, semaphore, etc.) on the level of the native programming language using its standard libraries (Williams, 2010). Those abilities included programming languages like Java or C#. The main disadvantages are their performance and occasionally their limited portability.

Using the new version of the C++ programming language has been possible for some time in Microsoft Compiler since the Microsoft Visual Studio 2010 IDE (abbrev. for Integrated Development Environment) or in some freely available compilers.

The new standard libraries of C++ programming language already provide an effective interconnection of strong object-oriented programming language and multithread running, which until recently, had been largely limited. Computational software tools that are already written in C or C++ programming languages are now able to enrich the possibility to use parallelism while maintaining the portability of code. In a field of an explicit form of the Finite Element Method (Wu & Gu, 2012) the possibility of usage of parallelism is more than desirable, mainly because of time-consuming calculations, which is caused by the conditional stability of explicit methods used for the direct integration of equations of motion.

* Ing. Václav Rek: Institute of Structural Mechanics, Faculty of Civil Engineering, Brno University of Technology, Veveří 95; 602 00, Brno; CZ, rekv@seznam.cz

** Doc. Ing. Ivan Němec, CSc.: Institute of Structural Mechanics, Faculty of Civil Engineering, Brno University of Technology; Veveří 95; 602 00, Brno; CZ, nemec@fem.cz

2. Explicit Form of the Finite Element Method

This is an explicit algorithm that was originally designed for parallel computing on graphics cards using NVIDIA CUDA (Rek & Němec, 2016).

The algorithm is based on the explicit form of the Finite Element Method, which is based on an artificial transformation of the problem of statics to dynamic problem with damping. At the end we get semi-discrete second-order differential equations of motion, which we use for direct integration by the finite difference method (Har & Tamma, 2012).

$$M\{\ddot{q}\} + C\{\dot{q}\} + K\{q\} = \{F_E\}, \tag{1}$$

where $\{\ddot{q}\}$, $\{\dot{q}\}$ and $\{q\}$ are vectors containing nodal accelerations, velocities and displacements respectively. $K\{q\}$ represents internal forces $(\{F_I\})$ and $\{F_E\}$ the external forces. M is the lumped mass matrix and C is the damping diagonal matrix.

Using the Central Difference Method for direct integration of equations o motion we obtain the following explicit expression for the calculation of the new displacement. For the i_{th} degree of freedom, equation (1) leads to the explicit formula as follows:

$$q_{h,i}^{n+1,df} = \underline{\alpha}^{df}\left(F_{E,i}^{n,df} + F_{I,i}^{n,df}\right) + \underline{\beta}^{df} q_{h,i}^{n,df} - \underline{\gamma}^{df} q_{h,i}^{n-1,df}, \tag{2}$$

where

$$\underline{\alpha}^{df} = \frac{2\Delta t^2}{2m_i^{df} + c_i^{df}\Delta t}, \quad \underline{\beta}^{df} = \frac{4m_i^{df}}{2m_i^{df} + c_i^{df}\Delta t}, \quad \underline{\gamma}^{df} = \frac{2m_i^{df} - c_i^{df}\Delta t}{2m_i^{df} + c_i^{df}\Delta t}.$$

3. Parallel Algorithm

The algorithm is based on a parallel assembly of stiffness matrices for each of the finite elements and the subsequent calculation of the new displacements using explicit formula (2). Assembly of stiffness matrices and external force vector for continuous load is schematically shown in Fig. 1.

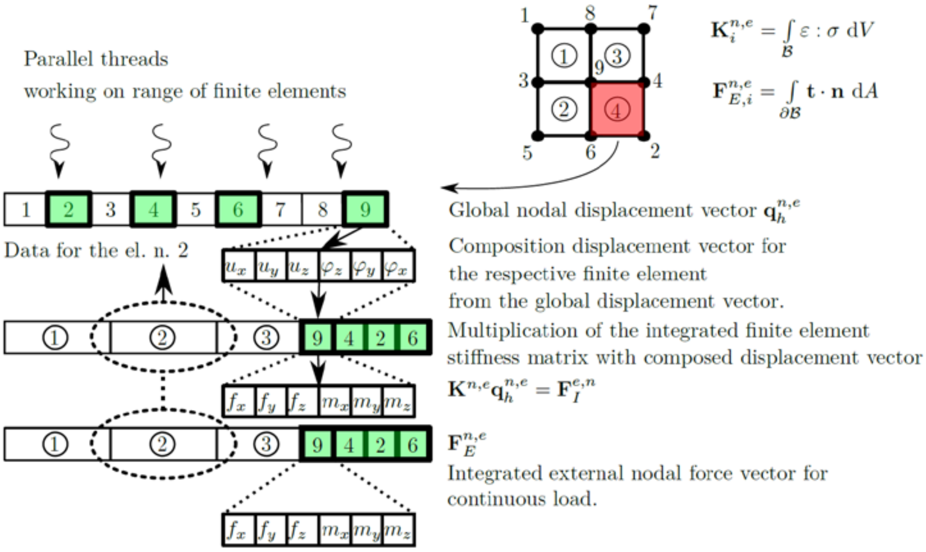

Fig. 1: Parallel composition of external and internal force vectors.

For each finite element node, the sum of the contributions from the neighboring finite elements for the respective node is performed. This procedure is simply shown in Fig. 2.

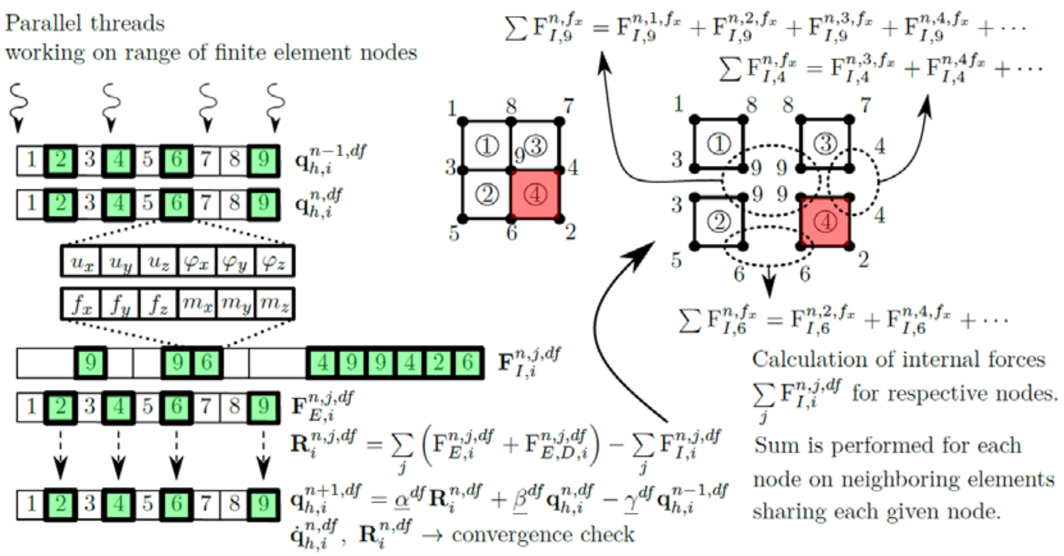

Fig. 2: Parallel composition of new deflections of finite element nodes.

4. C++ Implementation

For the purpose of compiling multithreaded run a general generic class "FEVRThreadFactory" was composed. It is based on the use of generic functions, which are then executed on the cores of a multi-core processor according to the settings which come from the object designed for scheduling of respective problem. The declaration and bindings of classes, which constitute the respective model of the solver, including the declaration of input data for each thread is in Fig. 3. A diagram of the synchronization object and global computing functions is in Fig. 4.

The underlying algorithm originally uses synchronization barrier only. This is frequently used synchronization procedure in GPGPU. Due to the nature of the algorithm used, a different type of synchronization is not needed. Using the C++ native threads and its standard libraries is well described in book C++ Concurrency in Action: Practical Multithreading (Williams, 2010).

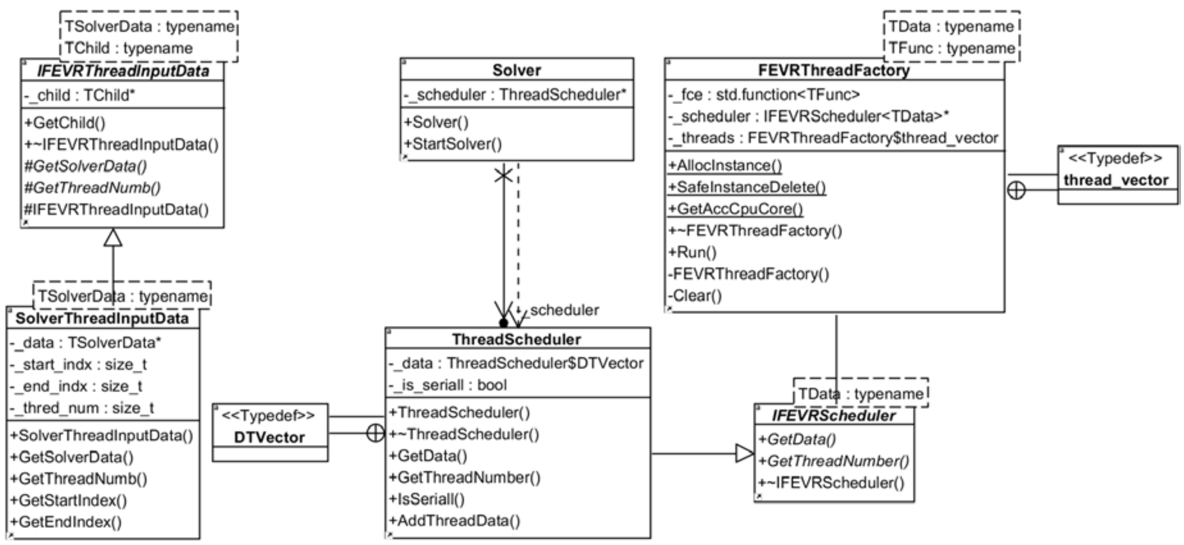

Fig. 3: UML class diagram of parallel solver.

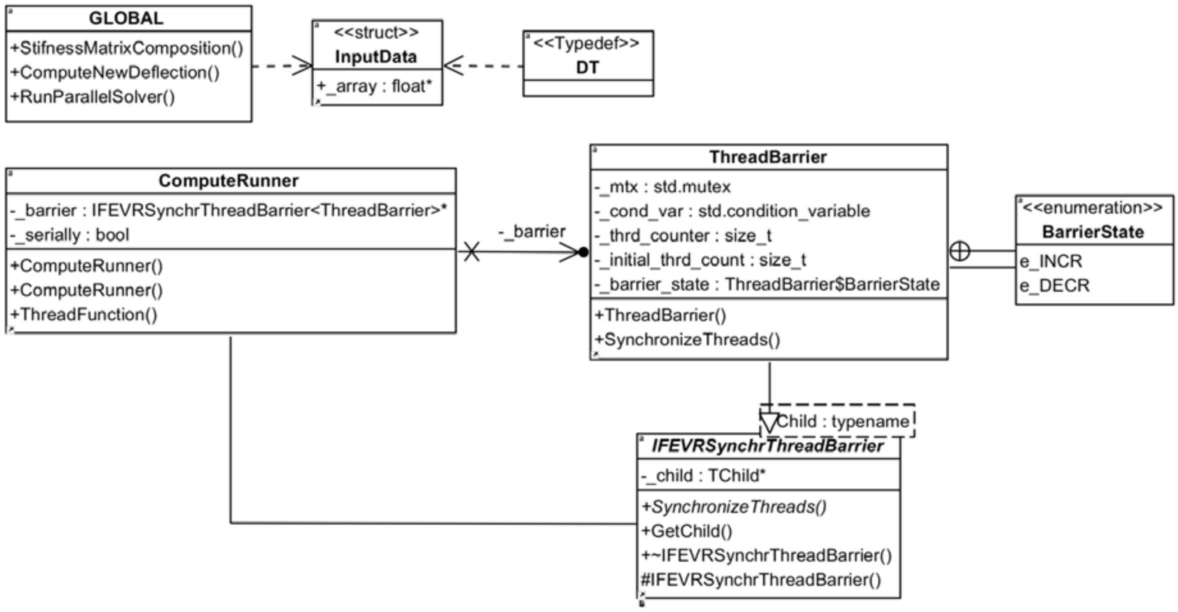

Fig. 4: UML class diagram of synchronization barrier object and encapsulating class for the computational global functions.

5. Performance Test

Test was performed on a model that consists 5 000 finite elements (30 906 DOF) with 100 time steps. The effectiveness of the used algorithm was tested on the three different processors as follows: Intel Core2 Duo SU9400 - 1.40 GHz (2 Cores / 2 Threads), Intel Core i5-3320M Ivy Bridge - 2.6 GHz (2 Cores / 4 Threads) and Intel Core i5-4690 3.5 GHz (4 Cores / 4 Threads). Achieved performance of execution (Sequential time [s] / Parallel time [s]): 1.119, 1.972, 3.826.

6. Conclusions

The introduced approach to the potential usage of the modern form of the C++ programming language and its new standard libraries allows us to make better use of the support of parallel computations on the level of native programming language. Functions from the NVIDIA CUDA library can be easily applied in a C++ code, and thus, the existing computational tool could be adapted to exploit the opportunities of multicore processors. Respective tests on different processors proved the effectiveness of the used approach.

References

Hart, J. M. (2015) Windows System Programming (Addison-Wesley Microsoft Technology), Fourth Edition, Addison-Wesley Professional.

Kerrisk, M. (2010) The Linux Programming Interface: A Linux and UNIX System Programming Handbook, No Starch Press.

Williams, A. (2010) C++ Concurrency in Action: Practical Multithreading, Manning Publications.

Wu, S. R. & Gu, L. (2012) Introduction to the Explicit Finite Element Method for Nonlinear Transient Dynamics, Wiley.

Rek, V. & Němec, I. (2016) Parallel Computing Procedure for Dynamic Relaxation Method on GPU Using NVIDIA’s CUDA, Applied Mechanics and Materials, 821, pp. 331-337, Trans Tech Publications.

Prata, S. (2004) C Primer Plus, Fifth Edition, Sams Publishing.

Har, J. & Tamma, K. K. (2012) Advances in Computational Dynamics of Particles, Materials and Structures, Wiley.

22nd International Conference
ENGINEERING MECHANICS 2016
Svratka, Czech Republic, 9 – 12 May 2016

PERPETUAL POINTS IN THE CAJAL-LIKE INTERSTICIAL CELL MODEL

J. Rosenberg[*], M. Byrtus[**]

Abstract: *Cajal-like interstitial cells (IC-LC) play important role in both physiological and pathological function of the bladder. The authors developed relative simple mathematical model consisting of five nonlinear ODEs. The model accuracy was verified using published experimental results. Deeper analysis of this model has shown existence of the multi-stable and hidden attractors which can have important influence on the behavior of the whole bladder. As the most effective way to obtain these attractors seems to be to use the method based on the calculation of the perpetual point. In the contribution is shortly introduced the definition of these points. Although this method is till now not fully proved it allows to calculate some multi-stable or hidden attractors. The goal is to show the application of this method on the more complex 5D system. This is presented on suitably chosen example.*

Keywords: Cajal-like interstitial cells, bladder, nonlinear dynamical system, hidden attractors, perpetual points.

1. Introduction

The simple model based on the current knowledge about these cells was introduced in Rosenberg & all (2016) where also the basic dynamical analysis was done. For this purpose was used the free software package MATCONT. The basic result is shown on Fig. 1. The area between the both curves starting from the Bautin bifurcation correspond to the oscillation.

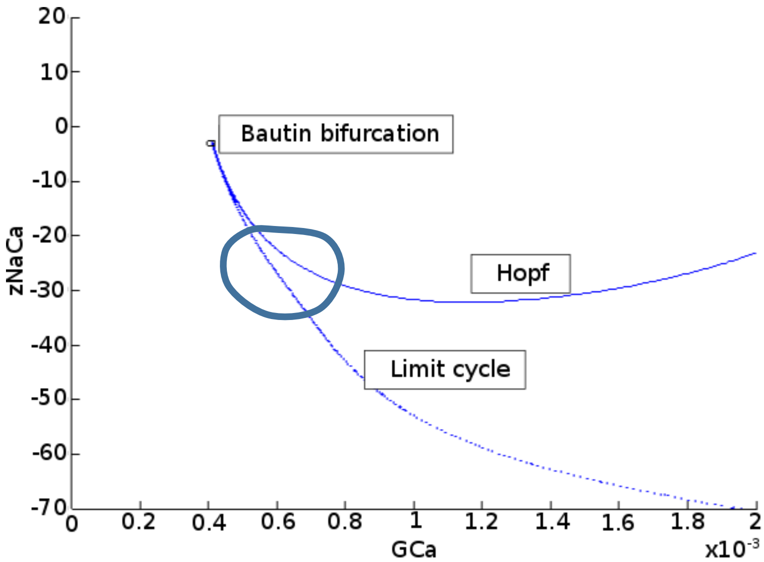

Fig. 1: Bifurcation diagram of the IC-LC model.

[*] Prof. Ing .Josef Rosenberg, DrSc.: Department of Mechanics, University of West Bohemia, Univerzitní 8; 306 14, Plzen; CZ, rosen@kme.zcu.cz

[**] Ing. Miroslav Byrtus, Ph.D.: Department of Mechanics, University of West Bohemia, Univerzitní 8; 306 14, Plzen; CZ, mbyrtus@kme.zcu.cz

While deeply studying the system in the area marked with circle in Fig.1, it can be seen very complicated behavior. There exist two stable attractors with the non-intersecting basins of attraction-one stable fix point and one self-excited attractor in the marked area. Multistability in dynamical system is a common feature. Uncovering all co-existing attractors and their basins of attraction are very important for understanding the systems. One of the major difficulties in understanding such systems is to locate the co-existing attractors.

The definition of the hidden attractors presented in Prasad (2015) is the following: An attractor is called a hidden attractor if its basin of attraction does not intersect with small neighborhoods of non-stable equilibria, otherwise it is called a self-excited attractor. It's important to mention that in the definition in Prasad (2015), the attractors are either oscillating or chaotic. In this contribution the usual definition of attractors including also the stable fixed points is used. Because of place shortage in here, the deeper explanation will be introduced during the conference presentation.

The examples and different methods for obtaining such attractor can be found e.g. in Kuznetsov (2015) or Kuznetsov & all (2014), where 1-3 dimensional systems are investigated. The following system is 5-dimensional and relatively very complex due to the interconnection of all the dimensions.

2. Description of the dynamical cell model

The schema of the simplified model of IC-LC is shown on the Fig. 2.

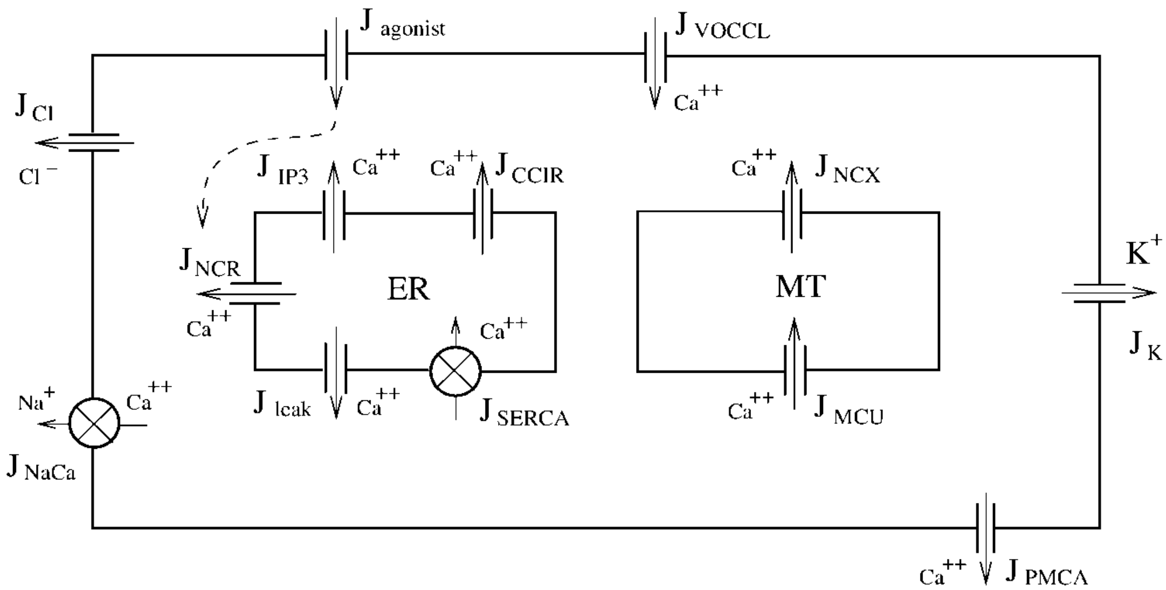

Fig. 2: The schema of the IC-LC. ***J*** *represent the fluxes of the ionts through the channels and pumps. For its meaning see Rosenberg & all (2016).*

The corresponding basic equations for Ca^{2+} concentration in cytoplasm (*c* ev. *cc*), in endoplasmic reticulum (cer), in mitochondria (cmt), for membrane potential (*v*) and for the membrane auxiliary variable *w* have the following form

$$\frac{dc}{dt} = \boldsymbol{G_{Ca}} \frac{v - z_{Ca1}}{1 + e^{-\frac{v - z_{Ca2}}{R_{Ca}}}} + G_{NaCa} \frac{c}{c + x_{NaCa}} (v - \boldsymbol{z_{NaCa}}) + g_c(c, cER, cMT, v, w) \ , \tag{1}$$

$$\frac{dc_{ER}}{dt} = g_{cER}(c, cER, cMT, v, w) \ , \tag{2}$$

$$\frac{dv}{dt} = \gamma \cdot \left[-2 \cdot \boldsymbol{G_{Ca}} \frac{v - z_{Ca1}}{1 + e^{-\frac{v - z_{Ca2}}{R_{Ca}}}} - G_{NaCa} \frac{c}{c + x_{NaCa}} (v - \boldsymbol{z_{NaCa}}) \right] + g_v(c, cER, cMT, v, w) \ , \tag{3}$$

$$\frac{dw}{dt} = g_w(c, cER, cMT, v, w), \tag{4}$$

$$\frac{dc_{MT}}{dt} = g_{cMT}(c, cER, cMT, v, w) \tag{5}$$

Functions $g_x(x = c, cER, cMT, v, w)$ are defined in Rosenberg & all (2016).

3. Dynamical analysis of the system

The equations (1) – (5) describe the nonlinear autonomous dynamical system

$$\dot{\boldsymbol{x}} = \boldsymbol{F}(\boldsymbol{x}; G_{Ca}, z_{NaCa}) \tag{6}$$

where the state space vector is $\boldsymbol{x} = [c, cer, v, w, cmt]^{\boldsymbol{T}}$.

The properties of this system can be studied using methods of the corresponding theory of dynamical systems. As the control parameters will be used as an example the conductance of the voltage operated calcium channel GCa and the reverse potential of the sodium/calcium exchanger zNaCa. The reason for this choice is the possibility to change their values using different drugs like nimodipin or the external calcium concentration. For this can be found the published experimental results allowing the verification. The meaning and values of the other parameters can be found in Rosenberg & all (2016).

According to Prasad (2015) the coexisting and hidden attractors can be approached starting from the perpetual points instead from nonstable fixed points. In the perpetual points the acceleration

$$\ddot{\boldsymbol{x}} = {}^{d\boldsymbol{F}}/_{d\boldsymbol{x}}\,\boldsymbol{F} = \boldsymbol{G}(\boldsymbol{x}) = \boldsymbol{0} \tag{7}$$

is equal zero but the velocities are non-zero, see Prasad (2015). Among the solutions of (7) there are both - the fixed points (**FP**) and perpetual point (**PP**). Let the eigenvalues of F are λ and of G are μ. In the **PP**, it is fulfilled

$$\mu = \lambda^2. \tag{8}$$

To demonstrate that, a point in the oscillating area was chosen. The coordinates of the fix and perpetual points were searched using special developed program starting from the different points in the domain $x_1 \in (-0.2; 0.2); x_2 = 0.2; x_3 \in (-70; 20); x_4 = 0.1; x_5 = 0.00001$.

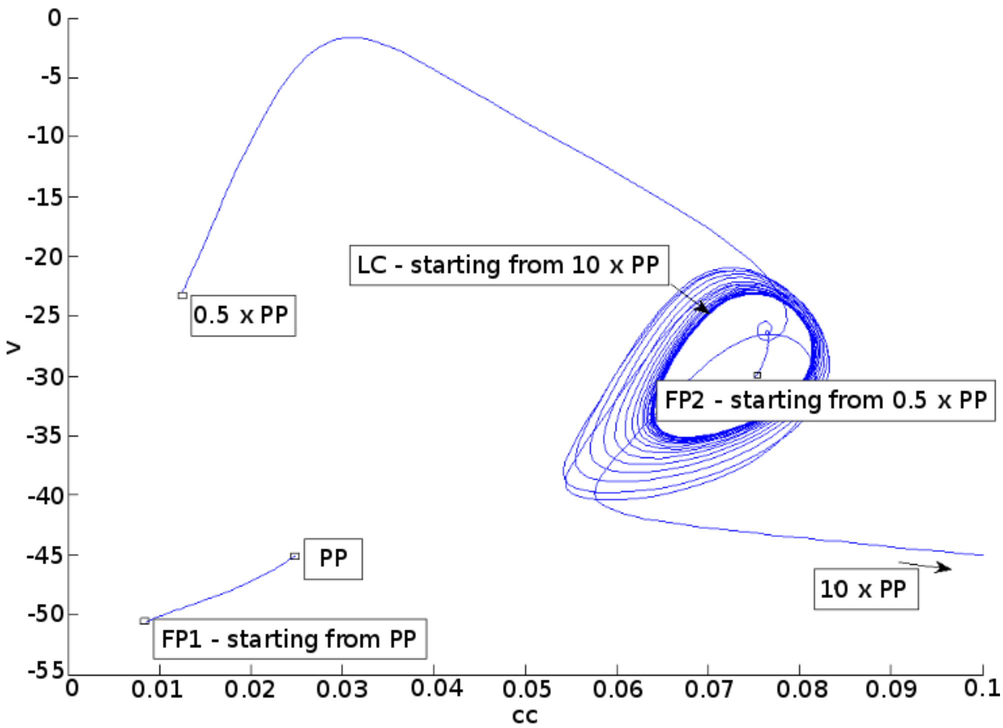

Fig. 3: Self-excited and coexisting attractors for GCa=0.0006 and zNaCa=-24.

Chosen the point (0;0.2;-45;0.1;0.00001) as an initial one, the perpetual point **PP** = $0.0249; 0.1669; -44.9989; 0.0011; 0.0005$ has been found. Starting the numerical solution from this point, one obtains the stable fixed point **FP**1- see Fig.3. Since we are in the oscillating area, this fixed point is one of the set of coexisting stable attractors.

Running along the line in the 5D configurational space (see Fig. 4 where the 3D subspace c – cer –v is shown only) what is performed by changing the length of the vector **PP**, one intersects the basins of attraction of the other attractors. As an example, the fix point **FP**2 corresponding with the starting point 0.5x**PP** – the non-stable attractor is shown.

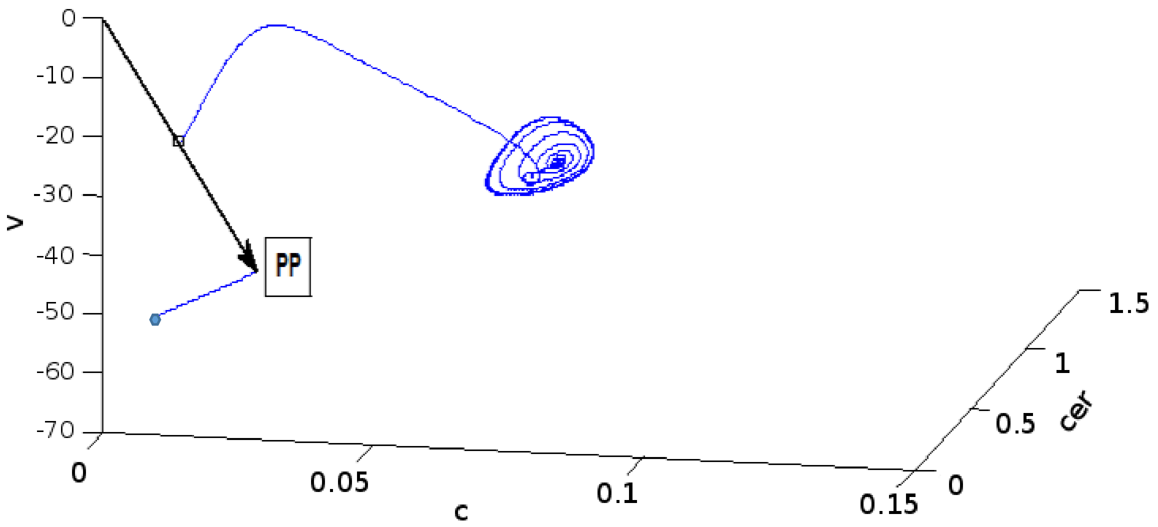

Fig. 4: Configurational 3D subspace with both coexisting attractors and the perpetual point.

Going further (10x**PP**), the self-excited attractor is obtained (its basin of attraction contains the neighborhoods of the non-stable equilibrium point FP2) and it corresponds with the Fig. 3.

4. Conclusions

The simple model (1)-(5) allows to simulate not only the basic properties of the ICCLC but also find the coexisting and hidden attractors. As an effective method for searching these attractors seems to be to use the perpetual points with their properties. In this contribution the application of the method to relatively complex 5D nonlinear model of the Cajal-like interstitial cell was shown.

The whole algorithm consisting from the finding of all perpetual points, corresponding attractors and their basins of attraction will be discussed in the in more detail during the conference presentation.

Acknowledgement

This work was developed within the CENTEM project, reg. no. CZ.1.05/2.1.00/03.0088, co-funded by the ERDF as part of the Ministry of Education, Youth and Sports OP RDI program and, in the follow-up sustainability stage, supported through CENTEM PLUS (LO1402) under the "National Sustainability Program" (author *) and by the project LO1506 of the Czech Ministry of Education, Youth and Sports (author **).

References

Kuznetsov, N.V. (2015) Hidden attractors in fundamental problems and engineering models. in: Proc. International Conference on Advanced Engineering - Theory and Applications, 2015 (Ho Chi Minh City, Vietnam), http://icaeta.org/

Kuznetsov, N.V. & Leonov, G.A. (2014) Hidden attractors in dynamical systems: systems with no equilibria, multistability and coexisting attractors. Preprints of the 19th World Congress The International Federation of Automatic Control Cape Town, South Africa. August 24-29, 2014.

Prasad, A. (2015) Existence of perpetual points in nonlinear dynamical systems and its applications. Int. J. Bifurcation Chaos, 25, 1530005

Rosenberg, J., Štengl, M. & Byrtus, M. (2016) Simple Model of the Cajal-Like Interstitial Cell and its Analysis. Applied Mechanics and Materials, Vol. 821, 677-684, Jan. 2016.

22nd International Conference
ENGINEERING MECHANICS 2016
Svratka, Czech Republic, 9 – 12 May 2016

TEMPERATURE DEPENDENCE OF MAGNETORHEOLOGICAL FLUID YIELD STRESS AND BINGHAM VISCOSITY

J. Roupec, I. Mazůrek, Z. Strecker, M. Kubík, O. Macháček [***]

Abstract: *This contribution describes results of measurement of magnetorheological fluid MRF-140CG by LORD Corporation. Results of this measurement are used as an inputs to the CFX model. MR fluid has been measured in special slit-flow rheometer at temperature range from 25 to 60 °C and at magnetic field of 0, 35, 70 and 105 kA/m. The flow curves were compiled with the respect of Bingham model of MR fluid Non-Newtonian behavior. Bingham model has two parameters – yield stress and Bingham (plastic) viscosity. Thanks to high precise measurement of pressure drop, the temperature dependence of yield stress is visible. All measured rheological properties were used as an input to the model described MR fluid behavior in dependence on temperature and magnetic field.*

Keywords: Magnetorheological fluid, slit-flow rheometer, high shear rates, yield stress

1. Introduction

Magnetorheological fluids (MRF) are a class of smart and intelligent materials. Their initial discovery is credited to Jacob Rabinow in 1948 (Rabinow, 1948). MR fluids mainly consist of three basic compounds: micron-sized iron particles, carrier oil and additives. Immediately upon the application of external magnetic field, the MR fluid can change its state from fluid to semi-solid or plastic state, in which the MR fluid shows viscoplastic behavior, characterized by the initial stress (yield stress), varying based on the extent of the applied magnetic field (Bossis, Lacis, Meunier, & Volkova, 2002; Carlson & Jolly, 2000; Klingenberg, 2001). MRF shows a Non-Newtonian behavior – the dependence of shear stress and shear rate is not linear. If the flow curve is measured and described at high shear rates, the Bingham model for MRF description can be used. Particularly, it is valid for On-state, when the considerable yield stress is occurred. The significant deviation of this model from the reality is only at low shear rates (Ngatu & Wereley, 2007), where the MRF exhibits viscoelastic behavior which can be described better by Herschel-Bulkley model than by Bingham model (Choi, Cho, Choi, & Wereley, 2005). When we need a CFX model describing a MRF flow (for example at process of designing of a new MR device), parameters describing MRF have to be inserted to the model. Parameters obtained from commercial rheometers are not suitable for their very low range of measured shear rates and inaccurate determination of a real shear rate and stress. Therefore, it is necessary to measure a MRF in a special rheometer.

This paper describes results from measurement at high shear rates and corresponding flow curves. The equation for calculation of yield stress and Bingham viscosity in dependence on temperature and magnetic field intensity was built.

2. Methods

The measured MRF was made by LORD Corporation, type MRF-140CG. Solids content by weight (Fe-particles) in MRF is 85 %. MRF was measured at temperature range from 25 to 60 °C and at magnetic fields of 0, 35, 70 and 105 kA/m. The corresponding shear rate (calculated from Bingham model) reaches up to 160 000 s^{-1}. The MRF was measured in a special slit-flow rheometer in version 2 (see Fig. 1). Unlike a previous version, the new rheometer has high precise measurement of temperature (before and behind the MR valve) and the shear stress is not calculated from measured force of piston but from the pressure drop in the MR valve, which is acquired by two accurate pressure sensors. The advantage of this

[***] all authors: Institute of Machine and Industrial Design, Brno University of Technology; Technická 2896/2; 616 69, Brno; CZ, roupec.j@fme.vutbr.cz

solution is an absence of all passive resistances, e.g.: influence of friction from piston and piston rod sealing, influence of friction from sealing and sliding tapes of floating pistons, absence of hydraulic loss caused by flow of hydraulic oil in the system, etc. The method of evaluation and determination of flow curves is described in the paper (Mazůrek, Roupec, Klapka, & Strecker, 2013; Roupec).

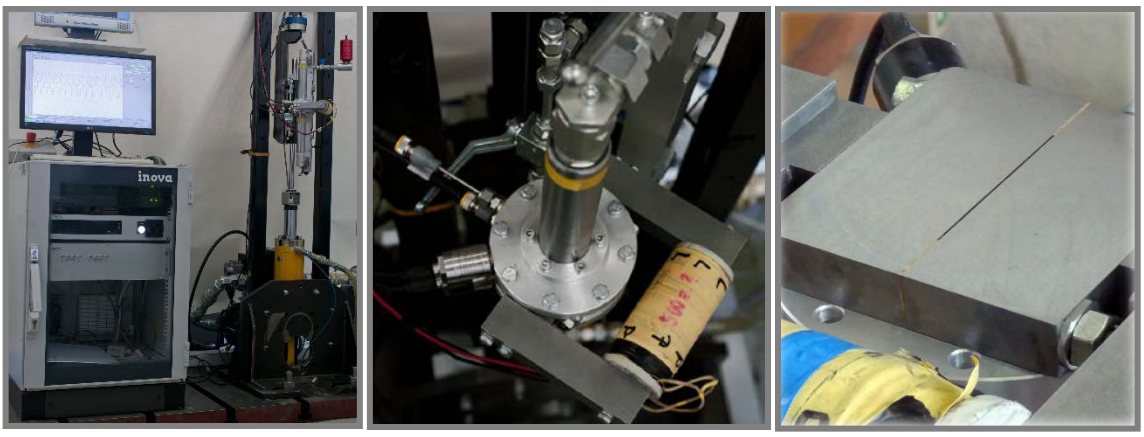

Fig. 1: Built-in rheometer in dynamometer with DAQ and RTC station (left); detail of MR valve with sensors (center); detail of MR valve – active zone (right)

3. Results and discussion

Figure 2(a) shows flow curves measurement of MRF-140CG at zero magnetic field. Without magnetic field, the MRF exhibits almost Newtonian fluid. A small deviation from linear course is visible at 25 and 30 °C. Figure 2(b) shows viscosity dependence on temperature. The dependence has exponential character with very good interlay of points.

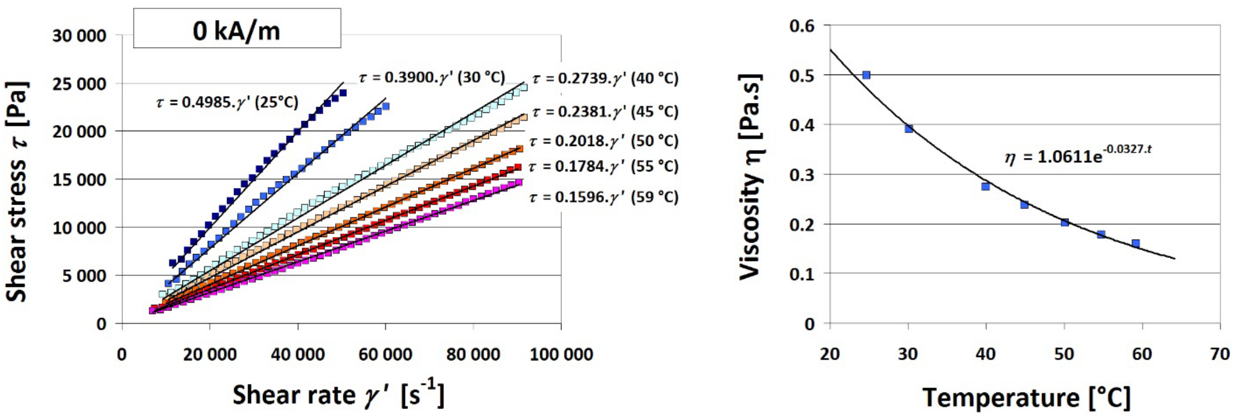

Fig. 2: MRF-140CG measured at zero magnetic field by slit-flow rheometer (a) flow curves; (b) viscosity dependence on temperature

Figure 3(a) shows flow curves measured at magnetic field of 146 kA/m. There are flow curves at different temperature and the difference among the temperature is obvious. Figure 3(b) shows a detail on flow curves and equation of linear regression. The last term in equations determine a yield stress and the first term determines a Bingham viscosity (plastic viscosity). There is evident dependence of yield stress and Bingham viscosity on temperature. The same measurements were carried out also for higher magnetic field intensities of 280 and 368 kA/m. Figure 4 shows a dependence of yield stress and viscosity on temperature for all measured magnetic fields. Unfortunately, the magnetic field is not increased about the identical step of intensity but it corresponds to exciting current to the electromagnet coil. However, we can calculate that the ratio of 368 and 280 kA/m is 1.31. But ratio of corresponding yield stress, for example at 50 °C, is only 1.22. So we can deduce that the Fe-particles approach to their saturation limit, in other words the saturation of Fe-particles is in the area of permeability decreasing. The course of viscosity is, excluding temperature, also magnetic field dependent. The higher magnetic field is, the lower viscosity dependence on temperature is and the lower absolute value of viscosity is. Maybe, some future study will describe this phenomenon by the model describing directly the interaction among single particles and carrier fluid.

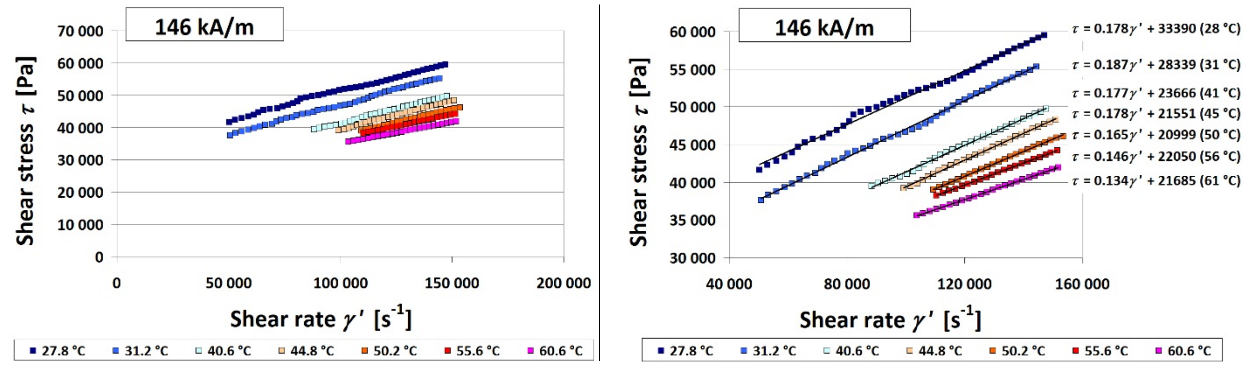

Fig. 3: MRF-140CG measured at magnetic field of 146 kA/m by slit-flow rheometer (a) flow curves; (b) detail with equations of regression

The equation valid for Bingham model is as follows:

$$\tau(\dot{\gamma}, H, t) = \tau_0(H, t) + \eta_{plastic}(H, t) \cdot \dot{\gamma} \tag{1}$$

The yield stress dependence on temperature is interlaid by power function characterized by this equation:

$$\tau_0(H, t) = A(H) \cdot t^{B(H)} \tag{2}$$

The viscosity dependence on temperature can be described by exponential function as follows:

$$\eta_{plastic}(H, t) = C(H) \cdot e^{D(H) \cdot t} \tag{3}$$

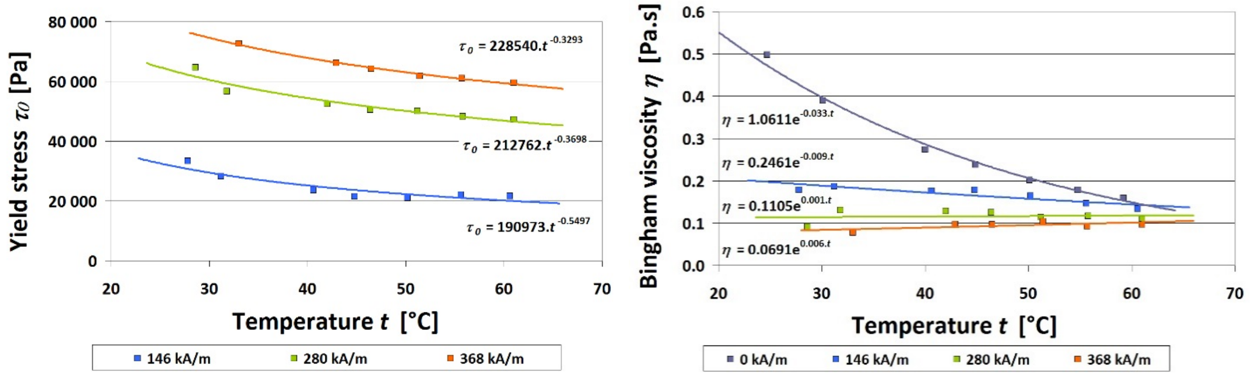

Fig. 4: Dependence of (a) yield stress and (b) viscosity on temperature at different magnetic fields

Figure 5(a) shows the dependence of parameter A and B' on magnetic field intensity.

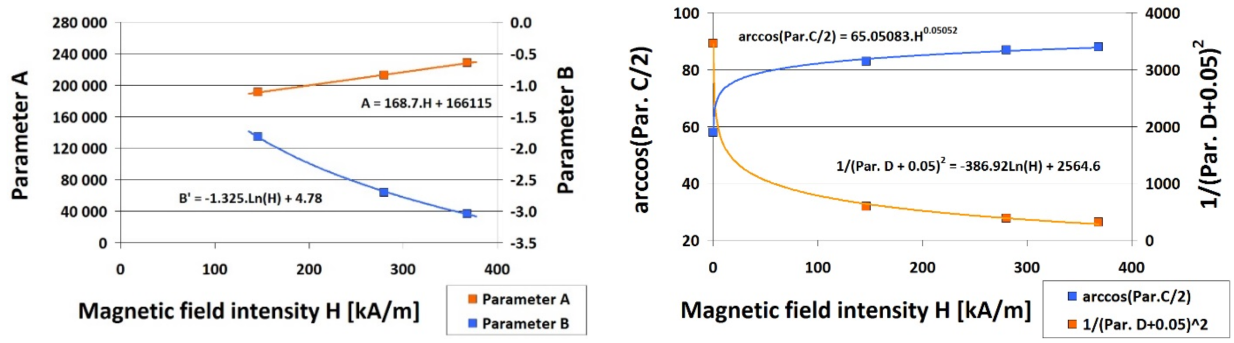

Fig. 5: (a) dependence of parameter A and B on magnetic field; (b) dependence of parameter C and D on magnetic field

Parameter B can be determined from the equation (4). This procedure were done for better fitting of points:

$$B(H) = \frac{1}{B'(H)} = \frac{1}{-1.325 \cdot \ln(H) + 4.78} \tag{4}$$

If these parameters are constituted to eq. (2), the yield stress is obtained. Parameters C and D were not able to fitted with simple function. Therefore more complicated procedure for the best fitting was used. Parameter C is characterized by this equation:

$$C = 2 \cdot \cos(65.051 \cdot H^{0.05052}) \tag{5}$$

Parameter D is characterized by this equation:

$$D = \frac{1}{\sqrt{-386.92 \cdot \ln(H) + 2564.6}} - 0.05 \tag{6}$$

The relationship for τ determination can be obtained by substituting equations (2) and (3) into (1) as follows:

$$\tau(\dot{\gamma}, H, t) = A(H) \cdot t^{B(H)} + C(H) \cdot e^{D(H) \cdot t} \cdot \dot{\gamma} \tag{7}$$

Complete model with substituting parameters A, B, C and D as follows:

$$\tau(\dot{\gamma}, H, t) = (169 \cdot H + 166115) \cdot t^{\frac{1}{-1.33 \cdot \ln(H) + 4.8}} + 2 \cdot \cos(65.1 \cdot H^{0.05}) \cdot e^{\left(\frac{1}{\sqrt{-387 \cdot \ln(H) + 2565}} - 0.05\right) \cdot t} \cdot \dot{\gamma}$$

Thanks to this equation the shear stress for corresponding magnetic field, temperature and shear rate can be calculated.

4. Conclusion

The MRF-140CG was measured in a special slit-flow rheometer. The results were evaluated for Bingham model describing accurately a flow at high shear rates. There were investigated several new phenomena: (a) yield stress dependence on temperature and (b) viscosity dependence on magnetic field intensity. The model of a MRF-140CG flow character was created and used as input to the analytical model and CFX model for simulation of flow in the MR valve with bypass.

Acknowledgement

There is very appreciated a kind sponsorship of many grants of numerous agencies, which granted as little as they could. The research leading to these results has received funding from the MEYS under the National Sustainability Programme I (Project LO1202), FSI-S-14-2329, FEKT/FSI-J-15-2777 and GAČR 13-31834P.

Abbreviations

CFX = high-performance Computational Fluid Dynamics (CFD); MEYS = Ministry of Education, Youth and Sports; MR = Magnetorheological; MRF = Magnetorheological Fluid

References

Bossis, G., Lacis, S., Meunier, a., & Volkova, O. (2002). Magnetorheological fluids. Journal of Magnetism and Magnetic Materials, 252, pp. 224–228.

Carlson, J. D., & Jolly, M. R. (2000). MR fluid, foam and elastomer devices. Mechatronics, 10, pp. 555–569.

Choi, Y. T., Cho, J. U., Choi, S. B., & Wereley, N. M. (2005). Constitutive models of electrorheological and magnetorheological fluids using viscometers. Smart Materials and Structures, 14, pp. 1025–1036.

Klingenberg, D. J. (2001). Magnetorheology : Applications and challenges. American Institute of Chemical Engineers, 47, pp. 246–249.

Mazůrek, I., Roupec, J., Klapka, M., & Strecker, Z. (2013). Load and rheometric unit for the test of magnetorheological fluid. Meccanica, 48, pp. 631–641.

Ngatu, G. T., & Wereley, N. M. (2007). Viscometric and sedimentation characterization of bidisperse magnetorheological fluids. IEEE Transactions on Magnetics, 43, pp. 2474–2476.

Rabinow, J. (1948). The Magnetic Fluid Clutch. Transactions of the American Institute of Electrical Engineers, 67,

Roupec, J., Mazůrek, I., Strecker, Z., & Klapka, M. (2013). The behavior of the MR fluid during durability test. Journal of Physics: Conference Series, 412, pp. 012024.

22nd International Conference
ENGINEERING MECHANICS 2016
Svratka, Czech Republic, 9 – 12 May 2016

FAILURE ANALYSIS OF STERNOTOMY

Z. Sant*, N. Farrugia**, K. Schembri***

Abstract: *Median sternotomy is a surgical procedure allowing direct access to the hearth via sternum dissection. The post-operative complications – infection and dehiscence – are associated with high morbidity and mortality rate. Out of the available techniques used to re-approximate the two sternum halves the wiring technique is preferred. This approach has specific problems demonstrated by the rupture of the wire or cutting through the bone. There is a limited knowledge about the biomechanical chest behaviour and the interaction at the interface between bone and sutures. These data are very difficult if not impossible to obtain via direct measurement 'in vivo' and even experimentally 'in vitro', due to complexity of the whole system and number of not well defined parameters that might play important role in the process. This paper will try to bring more information, by means of computational simulation, about the bone response to the presented suturing technique, the magnitude of stresses developed within the sutures, analysis of the relative displacement of the two halves, their behaviour, and the possibility of bone failure at the bone-wire interface.*

Keywords: Sternotomy, finite element, failure.

1. Introduction

Median sternotomy is a surgical procedure that provides direct access to the vital organs, which are protected by a chest wall. Thus the sternum is dissected along the midline and after the surgery the two halves of sterna bone are re-approached and secured in the position by a sternotomy technique. The postoperative complications, infection and dehiscence, although they have relatively low occurrence, are associated with a high mortality and morbidity rate once they occur (Schimmer et al., 2008). There are two commonly used closing methods – plating and wiring technique used by the majority of cardiac surgeons at the local Mater Dei hospital as it is easier to manage, and provides better opportunity to level the two halves, even though this approach represents very specific problems of postoperative complications such as the wire rupture or cutting through the bone. The failures, as reported by the surgeons, are mainly associated with convulsive cough that generates a high pressure within the chest reaching up to 40kPa. Due to the fact that the sternotomy attracted very little attention there is a limited number of papers discussing the sternotomy failure. Most of the papers are reporting mainly clinical observation (Pai, 2005), few present the results of an experimental testing using cadavers, foam models or animals (Casha et al., 2011; Dasika, 2003). In this paper we'll try to expand the available knowledge about the chest behaviour, the possibility of failure due to wire cutting bone, and identify the key factors affecting the mechanical response by using computational modelling.

2. Methods

Modelling of the failure scenario required three-dimensional sternum geometry that was obtained by manual segmentation of CT scan data. Following the segmentation an incision along the midline of the sternum has divided the bone into two halves. The suturing configuration shown in Fig.1 corresponds to the rehearsed thus preferred technique by the collaborating surgeon. The surgical suture is passed through the sternum at approximately 1cm from each side of the joined halves while the peristernal wires are

* Dr. Ing. Zdenka Sant: Mechanical Engineering Dept., University of Malta, Tal Qroqq; MSD2080, Msida; MT, zdenka.sant@um.edu.mt

** Nicholas Farrugia: Mechanical Engineering Dept., University of Malta, Tal Qroqq; MSD2080, Msida; MT, nicholas.farrugia.10@um.edu.mt

*** MUDr. Kevin Schembri.: Resident Cardiothoracic Specialist, Mater Dei Hospital, Triq Dun Karm; MSD2080; Msida; MT, kevinjschembri@gmail.com

sutures that wrap the wire around the whole sternum at the spaces between the ribs. The wire technique provides the possibility to make tighter closures while reducing the risk of the wires cutting through the cortical bone. Wire locking system is based on the twisting of the two ends of wire. This particular feature was omitted from our model as it does not contribute to the reported failure mechanism. Most wires were modelled via extruding the wire circular profile along the suture direction thus creating 3D wire volume. The sterna cortical bone covering the surface area of the sternum was assumed to have a uniform thickness of 1.38 mm as a result of CT scan analysis done during the manual segmentation. We were not able to compute an average density of cortical bone from CT scan as the image of 'phantom' was missing thus had to rely on evaluated guess based on the Hounsfield units (HU) and estimated the Young's modulus of cortical bone to be 5 GPa while the cancellous bone being of 50 MPa. Both tissue's were then modelled as an isotropic continuum. The suturing wire, normally used at Mater Dei Hospital, Malta is ETHICON® no.5 circular profile wire, made of stainless steel 316L with measured diameter of 0.79 ± 0.005 mm, had to be tested to obtain the corresponding mechanical properties. The material properties were obtained experimentally using Hounsfield Tensometer but the results turned out to be unreliable due to faulty gripping system, therefore the material model was created based on the data available in materials library that gives Young's modulus of 193.05 GPa for steel SS-316L, yield and ultimate strength of 290 MPa and 620 MPa respectively, with Poisson's ratio of 0.25 (SS-316L, www.hpmetals.com).

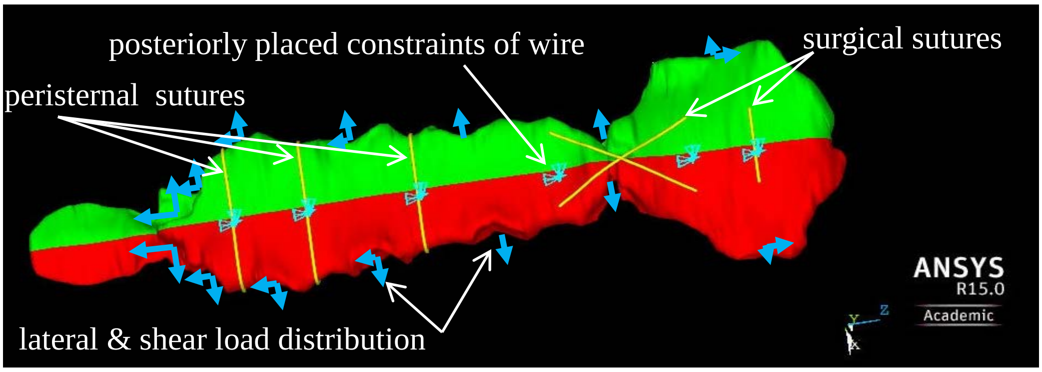

Fig.1: Model of the sterna with suturing configuration

The geometry model was segmented in Ansys 15 using SHELL181 elements with defined thickness of 1.38 mm thus mimicking the cortical bone on the 3D surface of the sterna while SOLID185 elements were assigned to 3D volume of the wire as well as to the sterna volume.

2.1. Model of the load and boundary conditions

The load of lateral force varying from 160 N to 1650 N and simulating the convulsive cough reaching a distending transmural pressure of 40 kPa was evaluated by different researcher using experimental or analytical approach (Casha, 1999; Trumble, 2002; Dasika, 2003; Pai, 2005). The load adopted for our computation is based on the reverse engineering where the chest wall is assumed to be an elliptical 'pressure vessel' while the varying thickness of the chest wall is taken into consideration (Casha et al., 2011). The force computation according to (1) takes into account the transmural pressure p, the wall thickness h at the equator, the minor semi-axis b as the geometric average of semi-transverse diameters, and the major semi-axis a as the height from apex to equator.

$$\sigma = \frac{p \cdot b}{h}\left[1 - \frac{b^3}{a^2(2b+h)}\right] \tag{1}$$

The computed force of 449 N is comparable to the experimental results and offers the load distribution on all seven coastal notches where the first seven ribs connect to the sternum via cartilages that provides the direct transfer of the load from the chest wall and intercostals muscles to the sternum. The lateral load applied to the sternum had to be accompanied by a shear force that corresponds to direction of each particular cartilage. The forces presented in the Tab.1 record the applied force components in lateral direction along x-axis, and shear force along the z-axis, while the force Fres is the total force applied via cartilage.

Tab. 1: Distribution of lateral and shear forces among first seven ribs

Rib Level	1	2	3	4	5	6	7
Fres [N]	46	55	69	78	74	87	124
Fx [N]	43	53	68	76	62	67	80
Fz [N]	17	15	5	-18	-40	-56	-94

To simulate the behavior of a sternum after the sternotomy required to set up number of contact pairs between the two re-approached parts of the sternum and the contact regions between bone and wires. The non-linear geometry behaviour of contact pairs is controlled mainly by normal stiffness factor FKN and FTOLN being of 0.9 and 0.01 respectively. The contact algorithm was set to Penalty method with contact detection on Gauss points while contact surface behaviour was set as a perfectly rough surface with no sliding for all contacts at the bone-wire interface. The contact at mid-plane of the sterna bone was set as unilateral with possibility of sliding. To simulate the 'fixed' position of the two halves, while each is attached to the corresponding half of the rib cage, a single node was selected at the posterior side of each suture and the constrains prohibited movement in all directions. Consequently, the FE model is defined by 593301 elements with total of 189435 degrees of freedom, and 8550 constraint equations. The analysis type was set for large displacements since the equation of stress conversion is valid for incompressible engineering materials with $\varepsilon < 0.005$ which doesn't tally for biological tissues that usually undergo large deflection but relatively small strains.

3. Results

As already mentioned earlier there are three mechanical factors influencing the healing process after the sternotomy. These are the condition between the two halves of the re-approached sternum, tension in the wire, and wire cutting the bone. Thus the first analysis of both sides of sternum demonstrate the maximum displacement that varies from 0.34 to 1.25 mm according to the varying pressure inside of the chest.

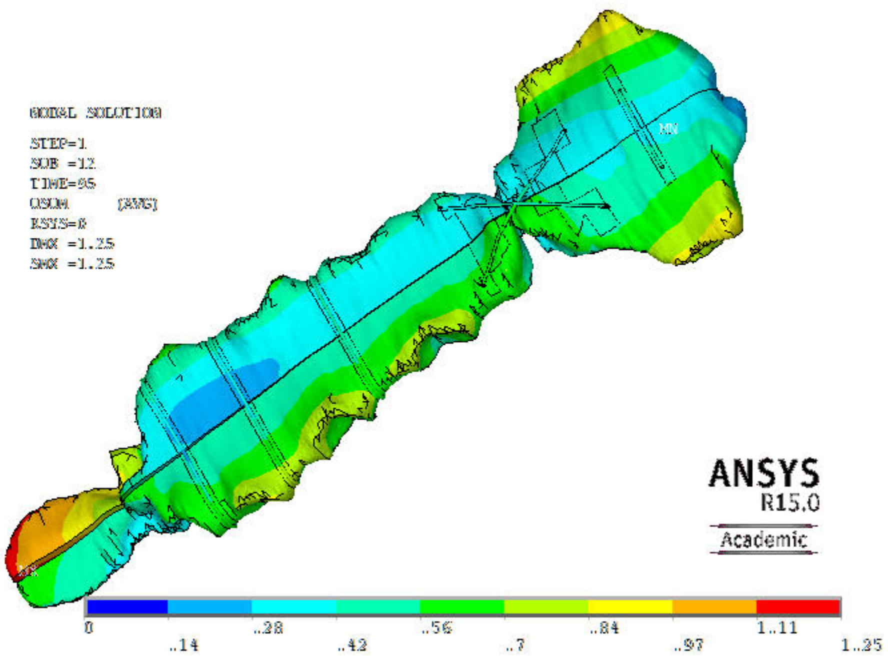

Fig. 2: Map of displacement after the sternotomy

The total maximum occurs at the attachments of the cartilages and at the caudal part of the xiphoid. The lateral gap between the two halves was computed as the difference between the displacements of left and right halve reaching its maximum of 1.87 mm at the caudal region of the xiphoid. The stress analysis within the sutures revealed very high stress reaching up to 7.98 GPa at the contact between the crossing wires while the last peristernal suture presents the highest stress of 715 MPa thus reaching beyond the level of ultimate stress though the other peristernal sutures have stresses within the yield limit. The bone – wire interface regions must be investigated for potential failure due to high contact stresses resulting in high strain. The region of the highest stress intensity corresponds with the highest strain of 0.6% developed at the contact between the suture and bone.

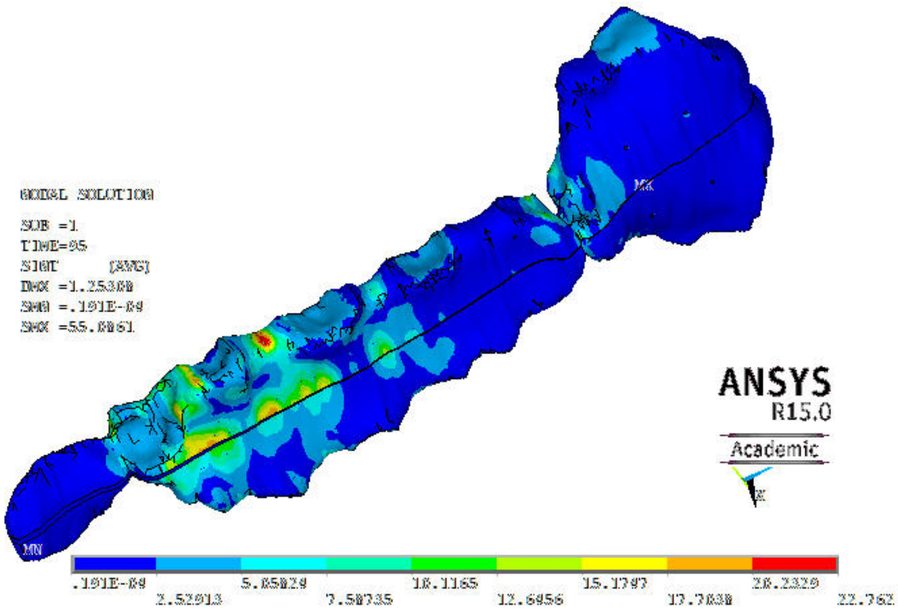

Fig. 3: Map of strain intensity

4. Conclusion

Results presented in this paper seems to be in agreement with clinical observation as the reported rupture of the wire or bone cutting occur mainly at the caudal region of peristernal sutures. Considering the reported elastic strain limit of cortical bone failure being within the limit of 2% we concluded that the wire cut through the bone would not occur but based on the results obtained from our simulation the rupture of the wire seems to be more likely the mode of failure. The maximum equivalent stress of 7.98 GPa occurs at the cross-link of the two wires at the manubrium joint where normally the real wire locking system secures the wire tension. Thus as the two wires don't cross each other in reality this stress was not considered to cause the failure. It cannot be said about the peristernal wire at the xiphoid location where the stress reached up to 715 MPA. At the same time we need to question the results at the inferior part of the sternum, which is loaded according to an elliptical analytical model of load that might not represent the real loading condition as the chest pressure represents only one component. Further research related to chest behaviour and loading condition is necessary to confirm the validity of our results.

References

Casha A. R., Manchéa A., Gauci M., Camilleri-Podesta M.-T., Schembri-Wismayer P., Sant Z., Gatt R., Grima J. N. (2011) Placement of trans-sternal wires according to an ellipsoid pressure vessel model of sternal forces. Interactive Cardiovascular and Thoracic Surgery, doi:10.1093/icvts/ivr108

Dasika U. K., Trumble D. R., Magovern J. A. (2003) Lower sternal reinforcement improves the stability of sternal closure. The Annals of Thoracic Surgery, vol. 75, pp. 1618-21

Kutz M. Biomedical Engineering and Design Handbook, vol. 1, 2nd ed., McGraw-Hill, 2009, pp 229

Pai S., (2005) In vivo characterization of respiratory forces on the sternal midline following median sternotomy. Faculty of Worcester Polytechnic Institute, Thesis

SS-316L, http://www.hpmetals.com/download/SS-316L.pdf

Schimmer et al., (2008) Prevention of Sternal Dehiscence and Infection in High-Risk Patients: A Prospective Randomized Multicenter Trial. Ann Thorac Surg, 86, 6, pp.1897-904

22nd International Conference
ENGINEERING MECHANICS 2016
Svratka, Czech Republic, 9 – 12 May 2016

APPLICATION AND DEVELOPMENT OF NUMERICAL MODELS IN BALLISTICS

V. Sháněl*, M. Španiel, K. Doubrava*****

Abstract: *This paper presents a case of shooting into a composite target using a rifle in terms of numerical modeling with a focus on the target and the gun barrel. The composite target is composed of several layers. In this case, it is steel armor or ceramics as the first layer and the second layer is made of aramid. These three materials are so different that for their modeling very different techniques are used. It is a Finite element method (FEM), Smoothed particle hydrodynamics (SPH), Discrete element method (DEM) and their combinations. All presented models are compared with experimental data of a real shooting or with data from a drop tester. During the firing of the projectile from the rifle there is a significant loading of the rifle barrel, which leads to vibrations of the barrel. This phenomenon is treated using numerical simulations as well as experimentally.*

Keywords: Impact, Ballistics, DEM, SPH, FEM

1. Introduction

Experimental methods play an essential role in developing new designs, but their applications are demanding in terms of time, cost and feasibility. Due to the development of knowledge in the field of phenomenological material models and methods themselves, especially numerical analysis methods of mechanical systems, the design process and structure analysis is commonly supported by their usage. As far as conventional constructions are concerned, numerical analysis is used routinely in cases when it is necessary to assess the stiffness, durability, frequency characteristics, etc. It is desirable to carry out experiments and numerical simulations together to validate them and determine material parameters. We expect a deepening understanding of experiments due to numerical simulations and also a continuous consequent promotion of rationally designed experiments, thus reducing their number.

Fig. 1: Shooting a rifle into a composite target – scheme.

Currently there is no unified theory that would cover the response of materials under impact loading for a wide range of impact velocity, projectile mass and geometry (Rosenberg & Dekel, 2012). Our focus will be on the damage of steel armor and ceramics which are used as one of the elements of sandwich armor called strike face – see Fig. 1. The main function of this layer is to absorb a part of the kinetic energy of a bullet, its destabilization and deformation. The second layer is called a back face and its function is to absorb the remaining kinetic energy of the projectile and catch fragments of the projectile. Hence, this layer must be resilient, yet strong enough to prevent the penetration by the projectile.

* Ing. Vít Sháněl: Faculty of Mechanical Engineering, CTU in Prague, Department of Mechanics, Biomechanics and Mechatronics, Technicka 4, 166 07 Prague 6; CZ, vit.shanel@fs.cvut.cz

** Doc. Ing. Miroslav Španiel, CSc.: Faculty of Mechanical Engineering, CTU in Prague, Department of Mechanics, Biomechanics and Mechatronics, Technicka 4, 166 07 Prague 6; CZ, miroslav.spaniel@fs.cvut.cz

*** Ing. Karel Doubrava, Ph.D.: Faculty of Mechanical Engineering, CTU in Prague, Department of Mechanics, Biomechanics and Mechatronics, Technicka 4, 166 07 Prague 6; CZ, karel.doubrava@fs.cvut.cz

In ballistic impact numerical simulations structural models need significant simplifications and their correctness is strongly dependent on modeling approach. The proper choice of a modeling method, approach, material model and damage criteria is crucial. That is why ballistic experiments using armor plates with different impact velocities, ballistic test of ceramics and their combination have been carried out. The dynamic test of aramid back face has been done on a drop tester.

The simulation of a sandwich composite penetration is a complex task involving an interaction of three main objects with each other: the bullet, the strike face, and the back face. For this reason, the numerical simulations of the bullet impact performance on a composite sandwich were divided into three steps. The real bullet impact into the steel, ceramics strike face and aramid back face penetration on a drop tester using different numerical methods.

2. Discrete element method

Steel armor targets can be described as a continuum and it is suitable to use FEM for their modeling, employing classical elements. These elements are able to describe material damage – material degrades its properties while the damage increases. If the element is damaged and its deformation begins to grow rapidly, it must be removed from the simulation to avoid premature termination. This causes a loss of the mass and the volume of the target. The loss is not fatal for steel armor, but it is unacceptable for ceramic targets because of the high number of damaged elements and the principle of the function related to the ceramic ballistic protection.

Ceramic targets work based on the following principle (Buchar & Voldřich, 2003): ceramics fragmentation occurs when a projectile impacts the ceramic target. The fragments go against the projectile, ridding it of its kinetic energy, and deforming and destabilizing the projectile. If all the damaged FEM elements were removed from the simulation, the ceramic target would be no obstacle for the projectile. The fragmentation of ceramics occurs immediately after the first contact with the projectile without the dissipation of a large amount of energy.

The main difficulties during the simulated shooting into ceramics are high strain rate, significant deformations, fragility and hardness of the targets. Not even the latest versions of commercial software products provide a tool to simulate this kind of situation. For this reason, a new modeling approach was developed. This method of modeling is suitable for the interaction of the projectile with the ceramic target simulation which removes all major issues with the classical approaches, such as deleting of damaged elements and the related loss of mass and volume. This new approach is based on DEM.

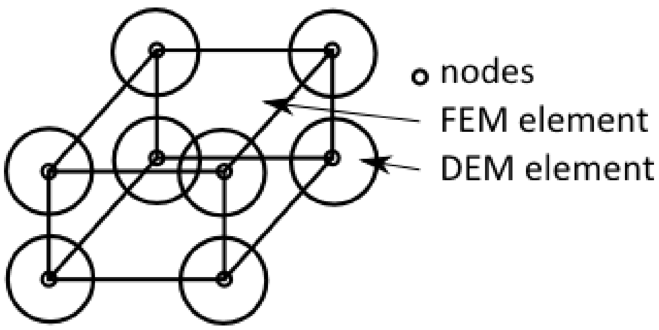

Fig. 2: The classic FEM element with the DEM elements with the common corner nodes.

DEM is a versatile tool for modeling the behavior of a particle material. ABAQUS software manual says that using DEM is appropriate for such modeling situations in which a large number of discrete particles come into contact, but this method is not suitable for describing continuum deformations (DASSAULT SYSTEMES, 2014). DEM does not require removal of elements during the simulation due to large distortions, thus maintaining the target mass and volume during the simulation. However, a disadvantage is that targets are not described as a continuum – consistency of the material is not captured and therefore no description of the damage is included either. Nevertheless, DEM can be used in combination with conventional finite elements to describe target deformations and damage. The ceramic target described using such a combination of FEM and DEM (Fig. 2) would maintain its mass, volume and capture the material damage. The respective qualitative behavior during the impact corresponds well with experiments.

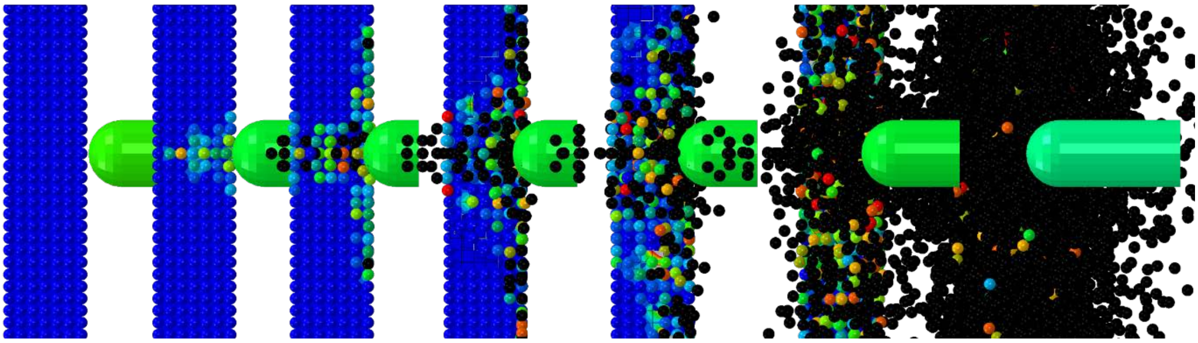

Fig. 3: Demonstration of projectile penetration into the ceramic target during the simulation.

A series of penetration simulation pictures is shown in Fig. 3. The view is perpendicular to the flying projectile, and ceramics can be seen in the cross section to show the spreading of the shock which is mainly propagated in the direction of the bullet flight as well as in directions perpendicular to each other and to the flight of the projectile.

3. Smoothed particle hydrodynamics

SPH is another method used in projectile penetration simulations. This was used to describe the lead core projectile during the penetration of the target armor and also proved to be suitable for modeling the aramid back face.

Due to the nature of the aramid material and the conditions prevailing during the clean shot of the back face with a real bullet – at a high speed and with the geometry of a real bullet – it is not possible to perform experiments using aramid panels with a bullet directly. A parting of the fabric and the simple passage of the bullet would occur; for that reason, the armor is always used on the strike face side which distorts and destabilizes the projectile. Moreover, many items of the available measuring equipment cannot be used during the experiments in combination with a real weapon so as not to risk their destruction. We therefore proceeded to perform experiments on the drop tester which allows considerably greater possibility of recording the entire experiment. For our testing purposes, we created a drop tester impactor of a real bullet.

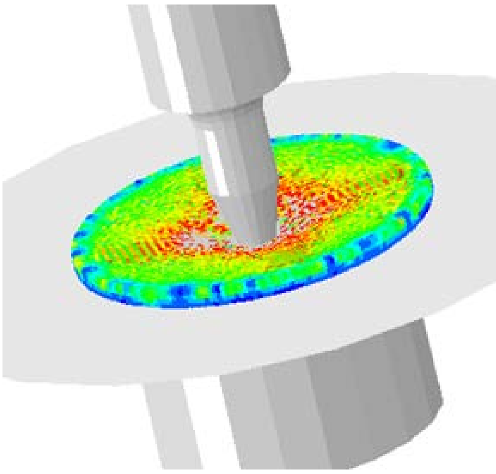

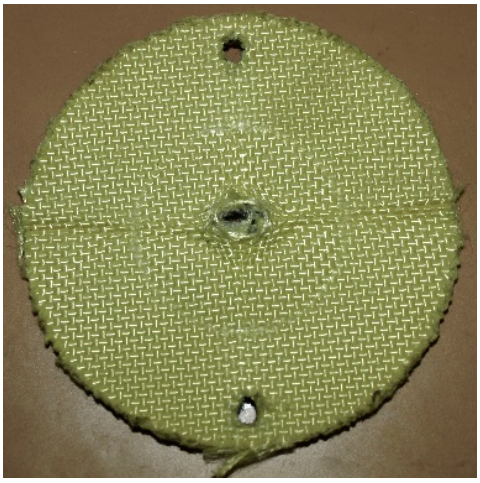

Fig. 4: Simulation of the drop test with aramid specimen using SPH formulation (left). Aramid specimen after impact on drop tester (right).

Subsequently a numerical model of the drop test experiments was created (Fig. 4) to enable identification of missing material parameters, and then allowed the usage of a model for the simulation of a complex sandwich. The impactor was modeled as a non-deformable body as well as a device for mounting the composite sample. We used a particle model based on a smoothed particle hydrodynamics method for the sample. This method is one of meshless methods which enables a simulation of problems involving a significant deformation.

The material damage was introduced into the model through SPH formulation wherein each particle has a predetermined area, interacting with other particles. If particles are moving away from each other their interaction strength decreases. Thanks to this description, a simulation of the aramid sample damage was achieved, although we did not use any standard description of the material damage. The model described above reached a good agreement during the drop test when comparing the absorbed energy during the impactor passing through the sample.

4. The barrel of the rifle

Shooting from a rifle into a composite target is interesting not only from the perspective of penetration the targets. A rifle barrel is under a heavy stress caused by the shot when the projectile is accelerated by the expanding gases that emerge as gunpowder is burned. During this process the pressure in the chamber reaches values exceeding the yield stress limit of conventional steels. The stress pulse is short but excites vibrations of the barrel. At that point, we focused on the bending vibrations which are captured by strain gauges during the shooting. We created a numerical model for the very same situation which extended the discreet results of the experiment to the entire rifle barrel.

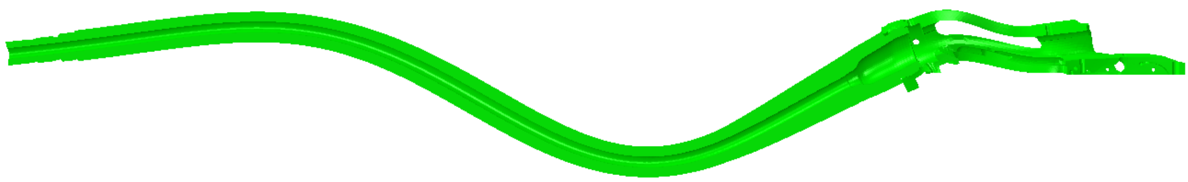

Fig. 5: Deformation of the rifle barrel during the shooting.

5. Conclusions

We focused on shooting from a rifle into a composite target from several perspectives. We paid attention especially to the perforation of a target composed of different materials as well as the barrel vibrations caused by the shot. In the course of the experiments, these processes were captured using different methods (high-speed camera, radar, optical gates, strain gauges, analysis of the deformed samples etc.). For the purpose of describing these processes, numerical models were devised. Due to high deformation rates and the impossibility to use standard approaches (deleting damaged elements), these simulations exhaust the possibilities of commercial software and even go beyond what such standard software tools can offer. We have developed special approaches (combination of DEM and FEM methods) that make it possible to numerically simulate such processes. The resultant numerical models enabled us to broaden the range of the data obtained from experiments (often at discrete points) on whole parts and thus allow for a more complex description of the monitored processes.

Acknowledgement

This work was supported by the Technological Agency of the Czech Republic in the project TH01010772 and by the Ministry of Industry and Trade of the Czech Republic in the project FR-TI4/317.

References

Buchar, J. & Voldřich J. (2003) Terminální balistika. Academia, Prague, ISBN 80-200-1222-2.

DASSAULT SYSTEMES (2014) Abaqus 6.14 Documentation.

Rosenberg Z. & Dekel E. (2012) Terminal ballistics, Springer, New York, ISBN 978-3-642-25305-8.

22nd International Conference
ENGINEERING MECHANICS 2016
Svratka, Czech Republic, 9 – 12 May 2016

FORCED VIBRATION ANALYSIS OF EULER-BERNOULLI BEAM WITH DISCONTINUITIES BY MEANS OF DISTRIBUTIONS WITHOUT DOING MODAL ANALYSIS

J. Sobotka*

Abstract: *The general equation of motion of forced vibration of Euler-Bernoulli beam has been used since it was derived by means of classical derivatives of shear force, bending moment, rotation of a cross section and deflection of the beam. However these derivatives are not defined at such points of center-line between ends of the beam in which there is a concentrated load or a concentrated support or a concentrated mass or a concentrated mass-moment of inertia or an internal hinge connecting beam segments, which are discontinuities that can be in practice. In this paper, distributional derivative for discontinuous shear force, discontinuous bending moment, and discontinuous rotation of a cross section of the beam has been applied to derive a generalized mathematical model for forced transverse vibration covering all the discontinuities mentioned. General closed-form solution to the generalized mathematical model for prismatic beam has been computed by means of symbolic programming approach via MAPLE. As a result of this new analytic approach, when computing forced steady-state response of the beam, we do not have to put together any continuity conditions at discontinuity points mentioned. The response of the beam is expressed directly without doing modal analysis.*

Keywords: Vibration, Beam, Discontinuities, Distribution, Dirac.

1. Introduction

Classical analytical method of calculating harmonic steady-state response of the beam is based on the following main steps (Rao, 2007). Firstly, we obtain a frequency equation for specific support conditions of the beam. Secondly, we solve the frequency equation for natural frequencies. Thirdly, we find orthogonal mode shapes corresponding to the natural frequencies of the beam. Finally, we express a forced response of the beam as a linear combination of the mode shapes by finding corresponding modal participation coefficients.

Applying distributional derivative for discontinuous shear force, discontinuous bending moment, and discontinuous rotation of cross section of a beam, we can derive a mathematical model for forced transverse vibration of a beam with discontinuities caused by concentrated supports or concentrated masses or concentrated mass moments of inertia or concentrated transverse forces or concentrated moments situated between ends of the beam, or hinges connecting beam segments. This mathematical model can be solved like only one differential task without dividing the beam into segments where all the continuity conditions among adjoining segments are fulfilled automatically. Using this approach, we have only four integration constants irrespective of the number of the discontinuities. Applying distributions, we do not have to compute natural frequencies, mode shapes or modal participation coefficients in analyzing forced harmonic response of beams.

2. The classical equation of motion for forced transverse vibration of Euler-Bernoulli beam

Equation of motion of a beam under distributed transverse force without discontinuities in shear force, in bending moment, in rotation of cross section or in transverse displacement of centerline of the beam is given by (Rao, 2007)

* Ing. Jiří Sobotka, Ph.D., ČEZ, a.s., 67550 Dukovany; CZ, e-mail: jiri.sobotka@cez.cz

$$\left(\frac{\partial^2}{\partial x^2}\left(E\,\mathrm{J}(x)\left(\frac{\partial^2}{\partial x^2}\mathrm{w}(x,t)\right)\right)\right)+\rho\,\mathrm{A}(x)\left(\frac{\partial^2}{\partial t^2}\mathrm{w}(x,t)\right)=\mathrm{f}(x,t)\quad, \tag{1}$$

where w(x, t) is transverse displacement of the beam centerline, A(x) is cross-sectional area, J(x) is area moment of inertia, E is modulus of elasticity (Young's modulus), ρ is density, f(x,t) is the distributed transverse force.

3. A mathematical model for forced transverse vibration of Euler-Bernoulli beam with discontinuities

In order to be able to express possible discontinuities in shear force, bending moment or in rotation of cross section along a centerline of a beam mathematically without cutting the beam into segments which would be without discontinuities in support, loading or without internal hinges, distributional derivative (Schwartz, 1966; Štěpánek, 2001; Kanwal, 2004) can be used, which consists of two main parts. Its first part is a classical derivative, while the second one is distributional as a sum of products of Dirac singular distribution moved to a point of a discontinuity and a magnitude of jump discontinuity of the quantity being differentiated.

When a beam supported at concentrated supports or carrying concentrated inertia masses or subjected to concentrated transverse forces between its ends is vibrating, jump discontinuities in shear force can occur at corresponding points of centerline of the beam. By expressing the first classical partial derivative of the shear force with respect to x from the equation of motion for an element cut out of the beam, and by adding distributional parts in the form of product, Eq. (2) can be derived, where $r_i(t)$ is a reaction force at i*th* concentrated support at the point $x=a_i$ ($0<a_i<L$), L is a length of the beam, m_i is a concentrated inertia mass at the point $x=b_i$ ($0<b_i<L$), $f_i(t)$ is a concentrated transverse load at the point $x=c_i$ ($0<c_i<L$), $\delta(x-a_i)$ denotes Dirac distribution moved to the point of the discontinuity, n_1 is a number of point supports without end supports, if any, n_2 is a number of concentrated inertia masses without end masses, if any, and n_3 is a number of concentrated transverse loads without end loads, if any.

If a beam carrying concentrated masses with moments of inertia of J_i at points $x=b_i$ or subjected to concentrated moment loads $s_i(t)$ at points $x=d_i$ ($0<d_i<L$) between its ends is vibrating, jump discontinuities in bending moment can occur at these points. By expressing the first classical partial derivative of the bending moment with respect to x from the moment equation for an infinitesimal element of the beam, and by adding products of a magnitude of the jumps and Dirac distribution situated at the point of the discontinuity, Eq. (3) can be deduced, the right hand side of which is the distributional derivative of the bending moment covering n_2 plus n_4 jump discontinuities.

When a beam containing hinges connecting segments of the beam at points $x=e_i$ ($0<e_i<L$) is vibrating, jump discontinuities in rotation of the cross section of a magnitude $\psi_i(t)$ may be found at these points. By expressing the first classical partial derivative of the rotation of the cross section with the respect to x from the deformation relation of the beam centerline curvature, and by adding corresponding distributional parts, Eq. (4) can be obtained, where n_5 is a number of internal hinges, if any.

$$\begin{aligned}\frac{\partial}{\partial x}\mathrm{Q}(x,t)=\rho\,\mathrm{A}(x)\left(\frac{\partial^2}{\partial t^2}\mathrm{w}(x,t)\right)+\left(\sum_{i=1}^{n_1} r_i(t)\,\delta(x-a_i)\right)+\left(\sum_{i=1}^{n_2} m_i\left(\frac{\partial^2}{\partial t^2}\mathrm{w}(x,t)\right)\Bigg|_{x=b_i}\delta(x-b_i)\right)\\-\left(\sum_{i=1}^{n_3} f_i(t)\,\delta(x-c_i)\right)\end{aligned}\quad, \tag{2}$$

$$\frac{\partial}{\partial x}\mathrm{M}(x,t)=\mathrm{Q}(x,t)-\left(\sum_{i=1}^{n_2} J_i\left(\frac{\partial^2}{\partial t^2}\phi(x,t)\right)\Bigg|_{x=b_i}\delta(x-b_i)\right)+\left(\sum_{i=1}^{n_4} s_i(t)\,\delta(x-d_i)\right)\quad, \tag{3}$$

$$\frac{\partial}{\partial x}\phi(x,t)=-\frac{\mathrm{M}(x,t)}{E\,\mathrm{J}(x)}+\left(\sum_{i=1}^{n_5}\psi_i(t)\,\delta(x-e_i)\right)\quad, \tag{4}$$

$$\frac{\partial}{\partial x}\mathrm{w}(x,t)=\phi(x,t)\quad. \tag{5}$$

4. Forced vibration solution

Supposing harmonic time variation of loading as

$$f_i(t) = F_i\, \mathbf{e}^{(\omega\, t\, I)} \quad , \qquad s_i(t) = S_i\, \mathbf{e}^{(\omega\, t\, I)}$$

and solution to equations (2) to (5) as

$$\mathrm{Q}(x, t) = Q_a(x)\, \mathbf{e}^{(\omega\, t\, I)} \quad , \quad \mathrm{M}(x, t) = M_a(x)\, \mathbf{e}^{(\omega\, t\, I)} \quad , \quad \phi(x, t) = \phi_a(x)\, \mathbf{e}^{(\omega\, t\, I)} \quad , \quad \mathrm{w}(x, t) = w_a(x)\, \mathbf{e}^{(\omega\, t\, I)}$$

$$r_i(t) = R_i\, \mathbf{e}^{(\omega\, t\, I)} \quad , \quad \psi_i(t) = \Psi_i\, \mathbf{e}^{(\omega\, t\, I)} \quad ,$$

where ω is circular frequency of vibration, $I^2 = -1$, and denoting amplitudes of vibration at points with concentrated inertia masses and moments of inertia as

$$\mathrm{W}_i = \lim_{x \to b_i} w_a(x) \quad , \quad \Phi_i = \lim_{x \to b_i} \phi_a(x) \quad , \tag{6}$$

a system of ordinary differential equations (7) to (10) can be derived for unknown general amplitudes of deflection, w_a , rotation of cross section, φ_a , bending moment, M_a , and shear force, Q_a , for a uniform beam as:

$$\frac{d}{dx} Q_a(x) = -\rho\, A\, w_a(x)\, \omega^2 + \left(\sum_{i=1}^{n_1} R_i\, \delta(x - a_i)\right) - \left(\sum_{i=1}^{n_2} m_i\, \mathrm{W}_i\, \omega^2\, \delta(x - b_i)\right) - \left(\sum_{i=1}^{n_3} F_i\, \delta(x - c_i)\right) \quad , \tag{7}$$

$$\frac{d}{dx} M_a(x) = Q_a(x) + \left(\sum_{i=1}^{n_2} J_i\, \Phi_i\, \omega^2\, \delta(x - b_i)\right) + \left(\sum_{i=1}^{n_4} S_i\, \delta(x - d_i)\right) \quad , \tag{8}$$

$$\frac{d}{dx} \phi_a(x) = -\frac{M_a(x)}{E\, J} + \left(\sum_{i=1}^{n_5} \Psi_i\, \delta(x - e_i)\right) \quad , \tag{9}$$

$$\frac{d}{dx} w_a(x) = \phi_a(x) \quad . \tag{10}$$

By using Laplace transform method, general solution to Eqs. (7) to (10) can be computed from which general amplitude of the deflection with integration constants in the form of initial parameters is as follows:

$$\begin{aligned}
w_a(x) = {} & \frac{(-\sinh(\beta\, x) + \sin(\beta\, x))\, \beta\, Q_a(0)}{2\, \omega^2\, m} + \frac{(\cos(\beta\, x) - \cosh(\beta\, x))\, \beta^2\, M_a(0)}{2\, \omega^2\, m} \\
& + \frac{(\sin(\beta\, x) + \sinh(\beta\, x))\, \phi_a(0)}{2\, \beta} + \left(\frac{\cos(\beta\, x)}{2} + \frac{\cosh(\beta\, x)}{2}\right) w_a(0) \\
& + \left(\sum_{i=1}^{n_4} \frac{\beta^2\, (\cos(\beta\, (x - d_i)) - \cosh(\beta\, (x - d_i)))\, S_i\, \mathrm{H}(x - d_i)}{2\, \omega^2\, m}\right) \\
& + \left(\sum_{i=1}^{n_5} \frac{\Psi_i\, \mathrm{H}(x - e_i)\, (\sin(\beta\, (x - e_i)) + \sinh(\beta\, (x - e_i)))}{2\, \beta}\right) + \left(\sum_{i=1}^{n_2} \right. \\
& (m_i\, \mathrm{W}_i\, (\sinh(\beta\, (x - b_i)) - \sin(\beta\, (x - b_i))) + (-\cosh(\beta\, (x - b_i)) + \cos(\beta\, (x - b_i)))\, \Phi_i\, J_i\, \beta)\, \beta \\
& \left. \mathrm{H}(x - b_i)/(2\, m) \right) + \left(\sum_{i=1}^{n_1} \frac{(-\sinh(\beta\, (x - a_i)) + \sin(\beta\, (x - a_i)))\, R_i\, \beta\, \mathrm{H}(x - a_i)}{2\, \omega^2\, m}\right) \\
& + \left(\sum_{i=1}^{n_3} \frac{F_i\, \mathrm{H}(x - c_i)\, (\sinh(\beta\, (x - c_i)) - \sin(\beta\, (x - c_i)))\, \beta}{2\, \omega^2\, m}\right)
\end{aligned} \quad , \tag{11}$$

where

$$m = \rho\, A \quad , \quad \omega = 2\, \pi\, f \quad , \quad \beta = \left(\frac{m\, \omega^2}{E\, J}\right)^{(1/4)} \quad . \tag{12}$$

As a simple example of using the proposed method, closed-form expression (13) for the amplitude of the deflection of forced steady-state response of a simply supported uniform beam (pinned-pinned) subjected to a concentrated harmonic force $F.\sin(\omega.t)$ at $x=c$ can be expressed as follows:

$$w_a(x) = \frac{(\sin(\beta\,(x-c)) - \sinh(\beta\,(x-c)))\,\beta\,F\,\mathrm{H}(c-x)}{2\,m\,\omega^2}$$
$$+\frac{\left(-\sin(\beta\,(x-c)) + \dfrac{\sinh(\beta\,x)\,\sinh(\beta\,(-L+c))}{\sinh(\beta\,L)} + \sinh(\beta\,(x-c)) - \dfrac{\sin(\beta\,x)\,\sin(\beta\,(-L+c))}{\sin(\beta\,L)}\right)\beta\,F}{2\,m\,\omega^2}\quad . \tag{13}$$

Correctness of expression (13) has been verified by evaluating classical infinite sequence (Rao, 2007; Weaver et al., 1990). A value of the expression (13) at $x=c$ has to be calculated by applying bidirectional limit because of the presence of Heaviside unit step function, i.e. $\mathrm{H}(c\text{-}x)$.

5. Conclusions

Contribution of this paper to harmonic forced response analysis of beams is that the mathematical model for forced transverse vibration, i.e. Eqs. (2) to (5), holds true also for discontinuous shear force, discontinuous bending moment and discontinuous rotation of cross section.

Discontinuities in shear force are supposed to be owing to idealized concentrated supports or inertia masses or concentrated transverse forces situated between ends of the beam. Likewise, discontinuities in bending moment are assumed to be due to idealized concentrated moments of inertia or concentrated moment loads situated between ends of the beam. On the contrary, discontinuities in rotation of the cross section are caused by real hinges connecting beam segments. Jump discontinuities in unknown dependently variable quantities have been expressed in corresponding distributional derivatives (2)-(4), where Dirac singular distribution, denoted as $\delta(x)$, is always moved to the point with the discontinuity mentioned, and multiplied by a magnitude of the discontinuity.

To be able to find forced response of Euler-Bernoulli beam analytically with discontinuities mentioned, Eqs. (7) to (10) have been derived for indeterminate amplitudes of the shear force, the bending moment, the rotation of the cross section and the deflection.

By using Laplace transform method, general solution to Eqs. (7) to (10) has been computed with integration constants in the form of initial parameters. A part of the general solution presented here, Eq. (11), contains H(x) as a symbol for Heaviside unit step function.

By computing limits (6), the unknown amplitudes of deflection and rotation can be expressed as functions of initial parameters. In order to determine the unknown initial parameters, four boundary conditions must be established. So as to determine the unknown reactions at concentrated supports between ends of the beam, and amplitudes of discontinuities in the rotation of the cross section at hinges connecting beam segments, corresponding deformation conditions at these points must be established. These deformation and boundary conditions create nonhomogeneous system of linear equations.

By making use of this approach, exact closed-form expressions can be found, e.g. (13), for harmonic steady-state response of uniform beams without summing infinite sequences and even without doing modal analysis.

References

Kanwal, R. P. (2004) *Generalized Functions*. Birkhäuser, Boston.

Kozien, M. S. (2013) Analytical Solutions of Excited Vibrations of a Beam with Application of Distribution. ACTA PHYSICA POLONICA A, Vol. 123, No. 6, pp. 1029- 1033.

Rao, S. S. (2007) *Vibration of Continuous Systems*. Wiley, New Jersey.

Schwartz, L. (1966) *Theorie des Distributions*, Hermann, Paris.

Štěpánek, J. (2001) *Distribuce a diferenciální rovnice*. Karolinum, Praha.

Weaver, W., Timoshenko, S.P. & Young, D.H. (1990) *Vibration Problems in Engineering*, 5th ed., John Wiley & Sons, Inc..

22nd International Conference
ENGINEERING MECHANICS 2016
Svratka, Czech Republic, 9 – 12 May 2016

STABILITY OF A DAMAGED SLENDER STRUCTURE LOADED BY A FORCE DIRECTED TOWARDS A POSITIVE POLE

K. Sokół[*], S. Uzny[**]

Abstract: *This paper presents the results of numerical simulations and theoretical studies on the natural vibration frequency and instability of a slender system, which is loaded by a force directed towards a positive pole. It is assumed that the column has a defect in the form of crack. The Hamilton's principle is used in the formulation of the boundary problem. The results focus on the shape of characteristic curves in the external load – natural vibration frequency plane as well as on the loading capacity.*

Keywords: column, crack, natural vibration, instability, positive pole.

1. Introduction

The column presented in this manuscript is classified as a slender supporting system due to its geometrical features (relation of total length to cross-sectional area). It is loaded by a force directed towards a positive pole (Tomski 2004). The pole in this case is a point located (below the loaded end) on the undeformed axis of the column. The line of action of the external load is defined by two points: the pole and the loaded end of the column. The implementation of the investigated type of external load has great influence on the natural vibration of the system (especially on the shape of the characteristic curves). By appropriately selecting the distance between the points, which define the line of action of the load, the divergence – pseudo-flutter instability can be obtained. A similar phenomena is present when Tomski's load is introduced (specific load). Both Tomski's load and the one investigated in this paper are fundamentally different from the one proposed by Beck in 1952. Beck's load (a follower load) is a non-conservative load while the ones presented here are conservative. The condition of conservation can be found in the paper (Tomski 2012). The load induced by the force directed towards the positive pole is a real life load which can be realized by means of the rigid rod used to transfer the load to the column from the rigid beam.

The presence of a crack is very undesirable defect in the supporting structure especially when its length is much greater than the cross-sectional area. A reduction in the cross-sectional area leads to a reduction in the loading capacity and a change in the dynamic properties of the structure. The supporting elements must be monitored in order to prevent the destruction of the supported construction. In the literature cracks are simulated by means of FEM packages like Abaqus or by using discrete elements such as rotational springs (Chondros 1998; Arif Gurel 2007; Sokół 2014, 2015). Moreover, the reduced cross-sectional area is also used. The type of simulation is selected according to the categorization of the crack (always open, always close or breathing). Depending on the type of model used, linear or non-linear phenomena can be studied.

In this paper the influence of the parameters of the introduced load, such as rigid rod length as well as crack size and crack location, on the natural vibrations and instability of a column with a defect are discussed.

2. Formulation of the boundary problem

[*] Krzysztof Sokół, PhD.: Institute of Mechanics and Machine Design Foundation, Częstochowa University of Technology Dąbrowskiego 73, 42-200 Częstochowa, Poland, sokol@imipkm.pcz.pl

[**] Sebastian Uzny, Prof.: Institute of Mechanics and Machine Design Foundation, Częstochowa University of Technology Dąbrowskiego 73, 42-200 Częstochowa, Poland, uzny@imipkm.pcz.pl

The column is shown in Figure 1. The slender structure is loaded by an external force P (force directed towards the positive pole) which is located on the upper end of the column. The defect in the form of crack is modelled by means of a rotational spring. The crack is considered to be an open one which divides the column into two elements (the natural boundary conditions at the common point facilitate the continuity of transversal and longitudinal displacements, bending moments and shear forces). A stiff rod of length l_c is installed on the loaded end in order to control the transversal displacements. The additional symbols in Figure 1 are as follows: E_i – Young's modulus, J_i – moment of inertia, A_i – cross-sectional area, ρ – material density, C – stiffness of rotational spring (crack size), P – external load, l_c – rod length, m – mass of loading head.

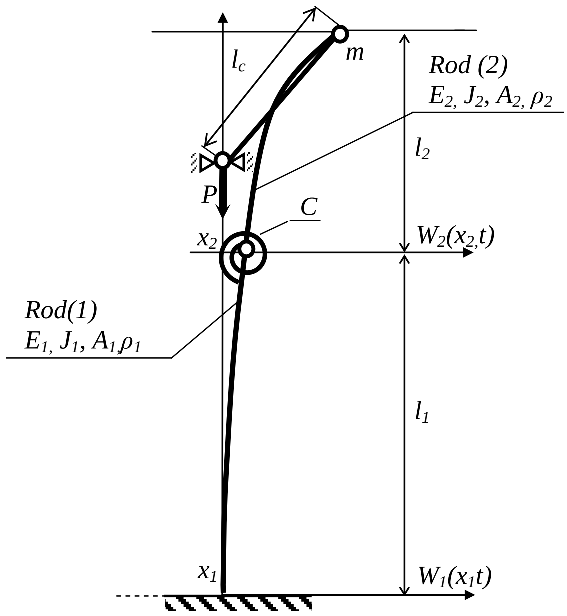

Figure 1. An investigated system

The Hamilton's principle $\delta\int_{t_1}^{t_2}(\mathrm{T}-V)dt=0$ is used in the formulation of the boundary problem, where kinetic T and potential V energies are expressed as follows:

$$T=\frac{1}{2}\sum_{i=1}^{2}\rho A_i\int_0^{l_i}\left(\frac{\partial W_i(x_i,t)}{\partial t}\right)^2 dx+\frac{1}{2}m\left(\frac{\partial W_2(x_2,t)}{\partial t}\bigg|^{x_2=l_2}\right)^2 \tag{1}$$

$$\begin{aligned}V=&\frac{1}{2}\sum_{i=1}^{2}EJ_i\int_0^{l_i}\left(\frac{\partial^2 W_i(x_i,t)}{\partial x_i^2}\right)^2 dx_i+\frac{1}{2}C\left(\frac{\partial W_1(x_1,t)}{\partial x_1}\bigg|^{x_1=l_1}-\frac{\partial W_2(x_2,t)}{\partial x_2}\bigg|_{x_2=0}\right)^2+\\&-P\frac{1}{2}\sum_{i=1}^{2}\int_0^{l_i}\left(\frac{\partial W_i(x_i,t)}{\partial x_i}\right)^2 dx_i+\frac{1}{2}P\frac{1}{l_c}\left(W_2(l_2,t)\right)^2\end{aligned} \tag{2}$$

Integration and variation lead, inter alia, to the differential equations of motion in the transversal direction (3):

$$EJ_iW_i^{''''}(x_i,t)+PW_i^{''}(x_i,t)+\rho A_i\ddot{W}_i(x_i,t)=0 \quad i=1,2 \tag{3}$$

as well as the natural boundary conditions which are obtained using the geometrical one 4(a-h):

$$W_1(0,t)=W_1^{'}(0,t)=0 \qquad W_1(l_1,t)=W_2(0,t) \qquad W_2^{''}(l_2,t)=0$$

$$EJ_1W_1^{'''}(l_1,t)+PW_1^{'}(l_1,t)-EJ_2W_2^{'''}(0,t)+PW_2^{'}(0,t)=0$$

$$-EJ_2W_2^{''}(0,t)+C\left[W_2^{'}(0,t)-W_1^{'}(l_1,t)\right]=0 \qquad EJ_1W_1^{''}(l_1,t)-C\left[W_2^{'}(0,t)-W_1^{'}(l_1,t)\right]=0$$

$$EJ_2 W_2'''(l_2,t) + P\left[W_2'(l_2,t) - \frac{1}{l_c} W_2(l_2,t)\right] - m\ddot{W}_2(l_2,t) = 0 \qquad \text{(4a-h)}$$

The problem is solved numerically by the introduction of (3) into the boundary conditions (4a-h) which leads to a set of homogenous equations, on the basis of which the obtained matrix determinant, equated to zero, creates the transcendental equation used to find, inter alia, the external load – natural vibration frequency relationship.

3. The results of numerical simulations

The results are discussed using the non-dimensional parameters:

$$p = \frac{Pl^2}{EJ_1}, c = \frac{Cl}{EJ_1}, d = \frac{l_1}{l}, \mu = \frac{EJ_2}{EJ_1}, m_b = m\rho A_1 l, l_{CB} = \frac{l_c}{l}, \omega = \sqrt{\Omega^2 \frac{\rho A_1 l^4}{EJ_1}} \qquad \text{6(a-f)}$$

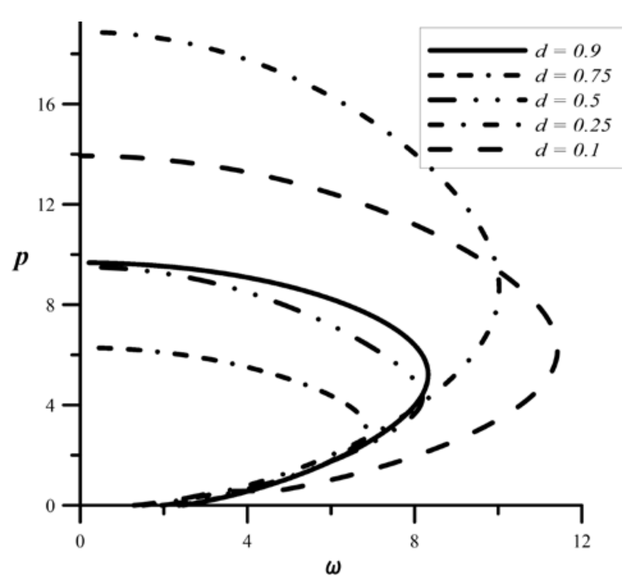

Figure 2. The characteristic curves at $c = 1$, $\mu = 1$, $m_b = 0.15$, $l_{CB} = 0.1$

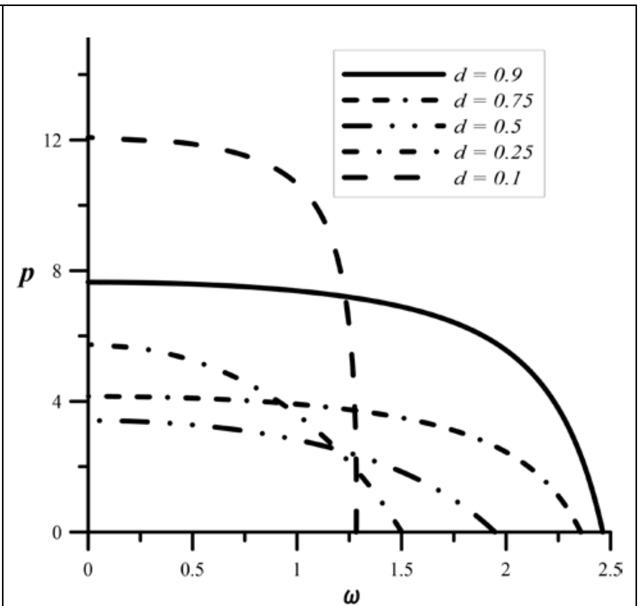

Figure 3. The characteristic curves at $c = 1$, $\mu = 1$, $m_b = 0.15$, $l_{CB} = 0.9$

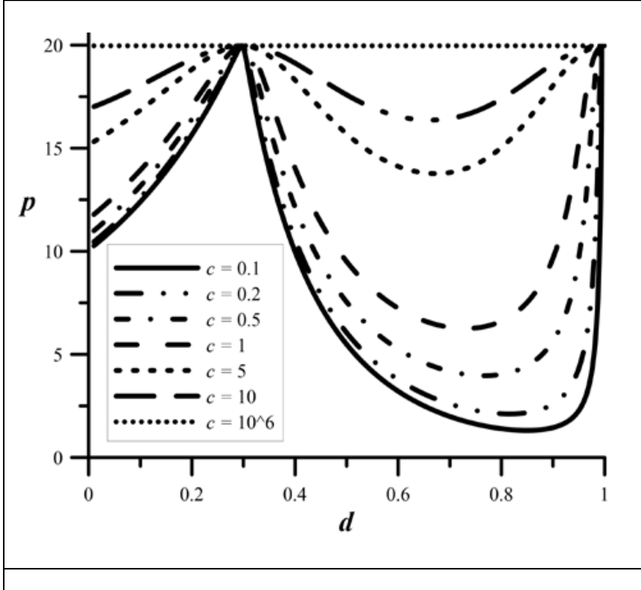

Figure 4. The influence of crack location on loading capacity at $\mu = 1$, $m_b = 0.15$, $l_{CB} = 0.1$

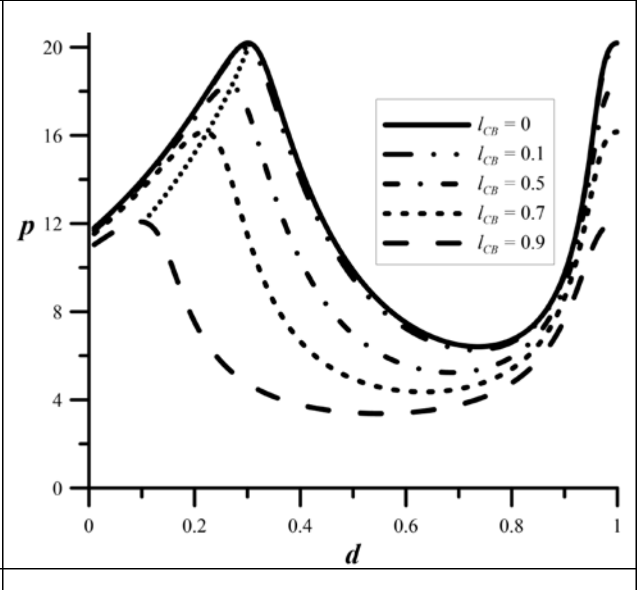

Figure 5. The influence of rod length on loading capacity at $\mu = 1$, $m_b = 0.15$, $c = 1$

As space is limited only small samples of the results are presented here. The studies start from calculations on the basis of which the external load – natural vibration frequency relationship was obtained. As shown in Figures 2 and 3, regardless of the rod length, the change in the crack location described by d parameter shows that the investigated column is very sensitive to this type of change (the shape modification of the characteristic curves). As shown, the change in the crack location does not affect the instability type but only the shape of the characteristic curves. Furthermore, the divergence – pseudo - flutter system (Figure 2) has low initial sensitivity of vibration frequency to the crack location in relation to the divergence system (Figure 3).

The initial shift of the crack location (Figure 4) from the fixed end in the direction of the loaded end results in an increase in the loading capacity up to a point at which the critical forces of both rods are identical (the location of this point largely depends on the rod length – see Figure 5). A further increase in parameter d causes a reduction in the maximum load and after reaching the lowest level an increase in the capacity can be observed. With a very short rod, the presented distribution of the loading capacity is very similar to the one that can be obtained for the fixed – pinned column. An increase in the rod length regardless of the crack size allows one to find the two points at which the column is insensitive to the crack size. An analysis of the vibration modes (not shown in this paper) leads to easy crack detection, especially in the divergence – pseudo - flutter system in which the change in the vibration modes is present along the characteristic curve.

4. Conclusions

The following conclusions can be drawn on the basis of the results of the numerical simulations:

– the location of the crack greatly affects the shape of the characteristic curves and the loading capacity,

– the character of those changes also depends on the rod length,

– two specific points can be found where the loading capacity does not depend on the crack size,

– the specific points are located as follows: the first on the loaded end, the second in relation to rod length shifts from d = 0.3 towards the fixed end,

– the crack does not change the type of instability (divergence or divergence – pseudo - flutter).

Future studies should be carried out on the higher components of natural vibration frequency in relation to parameters such as: rod length, crack size/location, bending rigidity factor. In addition different methods of crack simulation should be compared to the experimental studies in the one paper.

Acknowledgement

The study has been carried out within the statutory funds from the Czestochowa University of Technology (BS/PB-1-101-3020/11/P).

References

Arif Gurel, M. (2007) Buckling of slender prismatic circular columns weakened by multiple edge cracks. Acta Mechanica, 188, pp.1–19.

Chondros, T.G., Dimarogonas, T.G & Yao, J. (1998) A continuous cracked beam vibration theory. Journal of Sound and Vibration, 215 pp.17-34.

Sokół, K. (2014) Linear and nonlinear vibrations of a column with an internal crack. Journal of Engineering Mechanics 140, http://dx.doi.org/10.1061/(ASCE)EM.1943-7889.0000719.

Sokół, K. & Uzny, S. (2015) Instability and vibration of multi-member columns subjected to Euler's load. Archives of Applied Mechanics, DOI 10.1007/s00419-015-1068-6.

Tomski, L., Przybylski, J., Gołębiowska-Rozanow & M. Szmidla, J., (1997) Stability and vibration of a three-rod column of the divergence-pseudoflutter type. VIIth Symposium Stability of Structures, pp.283-286.

Tomski L., Szmidla. J.(2004), Vibration and stability of column subjected to generalized load by a force directed load. Journal of Theoretical and Applied Mechanics, 42, pp.163-193.

Tomski L., Uzny. S.(2008), Free vibrations and stability of a geometrically nonlinear column loaded by a follower force directed towards the positive pole. International Journal of Solid and Structures, 45(1),pp.87-112.

Tomski et. al. (2012), Free vibrations and stability of slender systems loaded by conservative and non-conseravtive loads. (Book in polish), PWN Warszawa.

22nd International Conference
ENGINEERING MECHANICS 2016
Svratka, Czech Republic, 9 – 12 May 2016

CRACK WIDTH CONTROL IN CONCRETE STRUCTURES WITH FRP REINFORCEMENT

R. Sonnenschein*, J. Bilcik**, K. Gajdosova***

Abstract: *Traditional material for concrete reinforcement is steel. In recent times, non-metallic fibers (steel, glass, aramid, carbon, polyethylene and polypropylene) as dispersed short fibers (together with different structures such as yarn, chopped yarn, strings, nets, fabrics, and polymer composite material reinforcement (bars and cages)) have been intensively investigated and some of them used for construction of structures. FRP rebar stress-strain curves have almost linearly elastic behaviour. The paper presents the mechanical properties and durability of different types of FRP rebars and calculations of the required reinforcement area in connection with the crack widths limitations for GFRP and steel reinforcement.*

Keywords: FRP composites, crack width, minimum reinforcement area

1. Introduction

Non-metallic fiber reinforced polymer (FRP) reinforcement is being used as an alternative to steel reinforcement in concrete structures, especially in aggressive environments, mainly due to its high corrosion resistance, and its high mechanical performance. (Pendhari, 2008)

FRP composites are durable materials which are different from the steel reinforcement for their resistance to the electrochemical corrosion. The advantages of FRP composites are high tensile strength, low density, electromagnetic neutrality and non-conductivity. With respect to steel, different mechanical behaviour of non-metallic reinforcement; however, involves some drawbacks- namely the lack of thermal compatibility between concrete and FRP reinforcement. Due to the difference between the transverse coefficients of thermal expansion of FRP bars and concrete, the temperature increase is inducing tensile stresses within the concrete member. These tensile stresses may cause splitting cracks within the concrete and eventually lead to degradation of the member's stiffness. As a consequence, important thermal strains occur just after the appearance of the first cracking of concrete which occurs in case the thermal stress within the concrete around FRP bars, in different locations, reaches the tensile strength of concrete (f_{ct}). These thermal cracks may cause degradation of the bond between FRP bars and the surrounding concrete, and eventually, failure of the concrete cover if the confining action of concrete is not sufficient (Zaidi, 2006).

Extensive analysis of cores removed from GFRP reinforced structures has confirmed that structures with small covers show no cracks despite being in service for 6-8 years. The studies also confirmed that no damage due to freeze-thaw cycles was experienced by the GFRP-reinforced structures. In light of the above discussion, the requirements for cover to FRP reinforcement shoul remain unchanged. (Mufti et al., 2007).

High tensile strength and lower modulus of elasticity cause that the decisive criteria for the design of the required area of FRP reinforcement is usually the serviceability limit state, not the ultimate limit state.

* Ing. Robert Sonnenschein, PhD.: Fakulty of Civil Engineering, Department of Concrete Structures and Bridges, Slovak University of Technology, Radlinskeho 11; 810 05, Bratislava; SK, robert.sonnenschein@stuba.sk

** prof. Ing. Juraj Bilcik, PhD.: Fakulty of Civil Engineering, Department of Concrete Structures and Bridges, Slovak University of Technology, Radlinskeho 11; 810 05, Bratislava; SK, juraj.bilcik@stuba.sk

*** Ing. Katarina Gajdosova, PhD.: Fakulty of Civil Engineering, Department of Concrete Structures and Bridges, Slovak University of Technology, Radlinskeho 11; 810 05, Bratislava; SK, katarina.gajdosova@stuba.sk

2. Composition, distribution and characteristics of FRP composites

There are several types of the composite reinforcements. Their common feature is that they consist of two components: the fibers and matrix. The fibers constitute 50 to 70% from the volume of the composite. (CNR-DT, 2006) They ensure its strength and stiffness, as well as electromagnetic neutrality, corrosion resistance and low weight. (ACI 440, 2006) The fibers can be made from carbon (CFRP), glass (GFRP), aramid (AFRP) or basalt (BFRP). The fibers are embedded in the polymer matrix that has a low modulus of elasticity. Matrix has more functions in the composite. It ensures the position and alignment of the fibers, protection from damage during manufacture and manipulation, durability of the composite as well as the protection from influence of external environment. It is also responsible for the distribution of the loads on the individual fibers. (fib No. 40, 2007) In the building industry the most commonly used are the thermosetting matrices based on epoxy, vinyl ester and polyester resins. Different types of the FRP composites have different characteristics resulting from the use of chosen type of fibers and matrixes.

Fig. 1 shows the relation strength-strain of the various kinds of the FRP composites in comparison with the steel reinforcement.

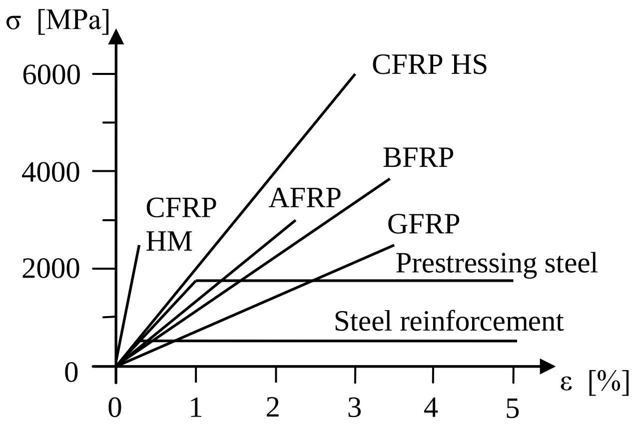

Fig. 1: Stress-strain diagram for the steel and FRP materials (Carolin, 2003)

FRP composites belong among anisotropic materials. Their properties depend on the type, volume and alignment of the fibers, the matrix type, form and quality of the construction. (ACI 440, 2006)

Due to economic reasons, the most commonly used composite reinforcement is from glass fibers. They can be made from the E-glass, S-glass or AR-glass (Alkali-Resistant Glass). The fibers from E-glass are the cheapest and therefore have the widest application. S-glass fibers, on the other hand, have a higher tensile strength and modulus of elasticity. (fib No. 40, 2007) Some environments may have a degrading influence on the glass fibers. Especially degrading is the effect of humidity and alkaline environment within the concrete. The effect of the concrete alkalinity can be reduced by applying a protective coating on the GFRP bars or by choosing the AR-glass fibers which have been created with addition of zirconium (e.g. Advantex and ArcoteX).

In comparison to other types of the reinforcement fibers, carbon fibers have a higher tensile strength and modulus of elasticity. They also appear to be less susceptible to aggressive environments and high temperatures. There are two types of carbon fibers: fibers with high tensile strength (HS) and fibers with high modulus of elasticity (HM). By increasing the modulus of the elasticity, the tensile strength and strain at failure are decreasing. The disadvantage of carbon fibers is their higher price. They tend to be 10 to 30 times more expensive than the fibers from E-glass. Aramid fibers have the best tensile strength to the density ratio. Among all above mentioned types of fibers, aramid fibers are of the lowest density. While resistant to many chemicals, they are sensitive to UV light and humidity, and further can degrade when exposed to certain acids and alkalis. (fib No. 40, 2007)

Basalt fibers are produced by melting of the withered volcanic lava. Their melting temperature is 1450°C, and therefore they are suitable for use in structures which are supposed to be resistant to fire. They have better physical and mechanical properties compared to glass fibers and significantly lower price than carbon fibers. (fib No. 40, 2007) However, their sensitivity to the effect of alkaline environment is considerably higher than that of the glass fibers. (Coricciati, 2007)

3. Serviceability limit state

Serviceability limit state deals with the usual operating conditions which occur within the structure throughout its serviceable life. It follows the criteria of appearance, durability and correct function of the structure. Compared to the steel reinforced concrete, the main difference in SLS criteria calculation for the elements reinforced with FRP lies in offsetting different properties for the FRP reinforcement. (ACI 440, 2006) Compared to steel, FRP reinforcement has a higher tensile strength; however, its modulus of elasticity is commonly smaller. Thus the higher tensile strength of FRP reinforcement cannot be in the design of reinforced elements fully utilized. (Design Manual No.3, 2007)

4. Cracks width control

Crack formation is expected, in case the maximum tensile stress within the cross-section exceeds the actual tensile strength of concrete. The crack width is controlled by the reinforcement area in the cross-section. In case of FRP reinforcement, the properties of the FRP bars such as the surface geometry, the reinforcement diameter and the concrete cover, influence the crack width. (McCallum, 2013) EN 1992-1-1 provides the limiting criteria for cracking together with equations for calculation of their width.

4.1 The calculation of the required reinforcement area in watertight structures – white tanks

In terms of the initiation and propagation of separation cracks, three design strategies are distinguished:

- construction without separation cracks - to be achieved by construction, technology processes, and execution measures,
- construction with separation cracks of limited width - achieved by the design and arrangement of reinforcement,
- construction with separation cracks, without crack control - the cracks are subsequently sealed.

The reinforcement design shall satisfy both the conditions of the serviceability limit state and the minimum reinforcement ratio requirement. The calculated areas of steel reinforcement and several kinds of FRP reinforcement required for the design of a white tank with separating cracks of reduced width will be later compared. The following parameters of the structure were chosen:

- constant parameters: concrete strength class C25/30, cement class S, exposure class XC2, structural class S4, investigation time of 5 days, the maximum permissible crack width $w_{k,max}$ = 0.15mm,
- changing parameters: different types of reinforcement (steel, FRP) and the slab thickness, which was considered between 0.1 m and 3.0 m.

Tensile strength and modulus of elasticity of the steel and FRP reinforcement are listed in tab. 1.

Tab. 1: Properties of the FRP reinforcements

Type of the FRP reinforcement	Tensile strength (MPa)	Modulus of elasticity (GPa)
BFRP	724	40,8
GFRP	1000	55
AFRP	1280	87
CFRP - HS	1400	100
CFRP - HM	1200	165
STEEL	500	200

In compliance with the higher tensile strength of FRP reinforcement, the replacement of the steel reinforcement for the FRP composite rebars has been implemented by the term of similar stresses. That being, a smaller diameter of FRP rebar having similar tensile strength compared to the replaced steel rebar has been chosen. Required reinforcement areas for the steel rebars of Ø16 and for selected types of the FRP rebars of Ø12 are shown in Fig. 2. Depending on the exposure class and the rebar diameter, the concrete cover for the steel reinforcement is 30 mm and for the FRP reinforcement it is 20 mm. From the figure it is clear that the required reinforcement area for a limited crack width increases along with decreasing of the modulus of elasticity.

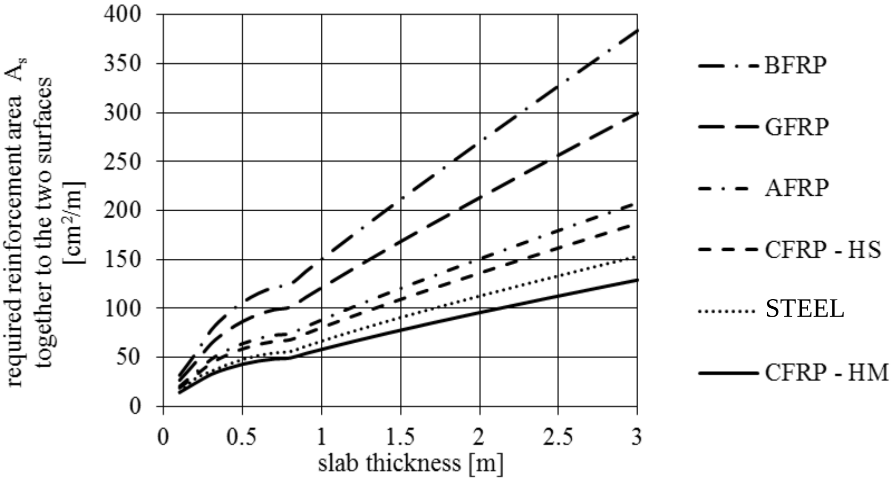

Fig. 2: Required reinforcement area for the limited crack width $w_{k,max}$ = 0,15 mm

5. Conclusion

The traditionally used steel reinforcement can be replaced by composite reinforcement, especially in cases of concrete structures exposed to environments with the increased environmental burden. Serviceability limit state is the deciding criteria for the design of FRP reinforced members. Control of both the limit crack width value and the maximum deflection of the member is necessary. The required reinforcement area for a limited crack width increases along with decreasing of the modulus of elasticity of the reinforcement.

Acknowledgements

The research proposed in this paper was created thanks to the support of research project VEGA No. 1/0583/15 “Analysis of the Reliability Risks in the Design and Execution of the Concrete Structures”.

References

Pendhari, S.S., Kant, T.; Desai, Y.M. (2008) Application of polymer composites in civil construction: A general review. Composite Structures, 84, pp. 114–124.

Zaidi, A., Masmoudi, R. (2006) Thermal effect on FRP-reinforced concrete slabs. In Proceedings of 1st International Structural Specialty Conference, CSCE, Alberta, Canada, pp. 23–26

CNR-DT 203/2006 (2006) Guide for the Design and Construction of Concrete Structures Reinforced with Fiber-Reinforced Polymer Bars. 39 p.

ACI 440.1R-06 (2006) Guide for the Design and Construction of Structural Concrete Reinforced with FRP Bars, 48 pp.

fib No. 40 (2007) FRP reinforcement in RC structures, 176 p.

Carolin, A. (2003) Carbon Fibre Reinforced Polymers for Strengthening of Structural Elements: Doctoral thesis. Lulea: Lulea University of Technology, 194 p.

Coriacciati, A., Corvaglia, P., Mosheyev, G. (2007) Durability of Fibers in Aggressive Alkaline Environment. In 17th International Conference on Composite Materials Conference. Edinburgh.

Design Manual No. 3 (2007) Reinforcing Concrete Structures with Fiber Reinforced Polymers. 151p.

McCallum, B. (2013) Experimental Evaluation Of The Bond Dependent Coefficient And Parameters Which Influence Crack Width, In GFRP Reinforced Concrete: Doctoral thesis. Halifax: Dalhousie University, 203 p.

STN EN 1992-1-1 (2007) Eurocode 2. Design of concrete structures - Part 1-1: General rules and rules for buildings, Bratislava.

Mufti, A. A et al. (2007) New Canadian Highway Bridge Design Code design provisions for fibre-reinforced structures. Canadian Journal of Civil Engineering, 34(3), p. 267-283, 10.1139/I06-137

22nd International Conference
ENGINEERING MECHANICS 2016
Svratka, Czech Republic, 9 – 12 May 2016

HYBRID RANS/LES MODELLING OF SECONDARY FLOW IN AXIAL TURBINE STAGE

P. Straka[*], J. Pelant[**]

Abstract: *The paper deals with application of hybrid RANS/LES model based on two-equation k–ω model in RANS mode and transport equation for the sub-grid scale turbulent energy in LES mode. Hybrid RANS/LES model is applied for computation of flow in an axial turbine stage with radial gaps under the stator and above the rotor blade. The model is implemented into the in-house numerical code which was originally designed for solution of RANS equation. Therefore the numerical inviscid fluxes are modified here in order to reduce a native numerical dissipation for use in LES approach.*

Keywords: hybrid RANS/LES, axial turbine stage, secondary flows.

1. Introduction

The contribution deals with simulation of flow in an axial stage of low power turbine (around hundreds kilowatts to units megawatts). To reduce of production costs this kind of turbines are often designed in a drum-type rotor configuration with prismatic blades, which are not equipped with a shroud. In that case there are radial gaps under the hub-end of the stator blade and above the tip-end of the rotor blade. Flow through these radial gaps leads to generation of large secondary flow structures which interact with following blade row. The interaction of blades with these secondary flow structures has major impact on the efficiency of the turbine stage. In paper (Straka et al., 2015) there was shown that drop in the efficiency due to interaction of the rotor blades with the secondary flows is up to ten percent.

Prediction of the blade/secondary flow interaction strongly depends on used turbulence model. In industrial applications, such as this, it is usual to solve system of RANS (Reynolds Averaged Navier–Stokes) equations, which is closed by two-equation turbulence model (such as k–ω). In paper (Straka & Němec, 2016) there was studied mechanism of the interaction between the rotor blades and the secondary vortices generated behind the radial gap under the stator blade using the k–ω model of Kok (2000). This model is based on linear relation for the Reynolds stress tensor. Although this model has provided interesting results, comparison with the experimental data revealed some differences in span-wise distribution of the efficiency behind the rotor blade. Therefore in paper (Straka, 2015) there was compared prediction of the secondary vortices development using the linear turbulence model of Kok (2000) and the nonlinear EARSM (Explicit Algebraic Reynolds Stress Model) model of Rumsey & Gatski (2001). It was found that the nonlinear EARSM model predicts deformation and unsteady behaviour of the secondary vortices, while the linear model doesn't have this capability. However, for better prediction of the interaction between the rotor blade and the secondary vortices generated behind the radial gap under the stator blade it is necessary to model not only deformation of large vortices but also their decay. Therefore, this contribution is focused on application of hybrid RANS/LES model for modeling of the rotor blade/secondary vortices interaction. In hybrid RANS/LES methods the flow field close to the wall is modeled via RANS approach, while the large detached eddies are simulated using LES (Large Eddy Simulation) approach which has capability to predict both deformation and decay of large secondary vortices. The hybrid RANS/LES model is implemented into the in-house RANS code described in (Straka, 2012; Straka, 2013) which was here modified with respect to requirements of the LES.

[*] Ing. Petr Straka, Ph.D.: Aerospace Research and Test Establishment, Beranových 130; 199 05, Prague; CZ, straka@vzlu.cz
[**] RNDr. Jaroslav Pelant, CSc.: Aerospace Research and Test Establishment, Beranových 130;19905, Prague;CZ, pelant@vzlu.cz

2. Turbulence model

The hybrid RANS/LES method according to (Davidson & Peng, 2003; Kok et al., 2004) is used in this work. This model switches between the system of RANS equations closed by two-equation turbulence model of Kok (2000) and LES when computational mesh is fine enough to simulate of large turbulent eddies. The sub-grid scale model of LES is based on transport equation for the sub-grid scale turbulent energy.

The transport equations for the kinetic energy k and the specific dissipation rate ω read:

$$\frac{D(\rho k)}{Dt} = P_k - \max\left(\beta^* \rho k \omega, \frac{\rho \sqrt{k^3}}{C_{DES} \Delta}\right) + \frac{\partial}{\partial x_j}\left[\left(\mu + \sigma_k \frac{\rho k}{\omega}\right)\frac{\partial k}{\partial x_j}\right], \tag{1}$$

$$\frac{D(\rho \omega)}{Dt} = \alpha \frac{\omega}{k} P_k - \beta \rho \omega^2 + \frac{\partial}{\partial x_j}\left[\left(\mu + \sigma_\omega \frac{\rho k}{\omega}\right)\frac{\partial \omega}{\partial x_j}\right] + C_D \, , \tag{2}$$

where ρ is the density, P_k is the production term, C_D is the cross diffusion term, α, β^*, β, σ_k and σ_ω are model constants. The local grid size Δ is defined by $\Delta = \max(\Delta_\xi, \Delta_\eta, \Delta_\zeta)$ where Δ_ξ, Δ_η and Δ_ζ are the distances between the cell faces in local ξ, η and ζ grid line directions. Constant $C_{DES} = 0.6086$ is chosen according to (Kubacki et al., 2013). Note that k is either the turbulent energy in RANS mode or the sub-grid scale energy in LES mode. The modeled stress tensor (Reynolds stress tensor in RANS mode, sub-grid scale stress tensor in LES mode) is given by $\tau_{ij}^t = 2\mu_t S_{ij} - 2/3 \rho k \delta_{ij}$, where S_{ij} is the strain rate tensor and $\mu_t = \min(\rho k/\omega, \rho \beta^* C_{DES} \sqrt{k} \Delta_{LES})$ is either the turbulent viscosity in RANS mode or the sub-grid scale viscosity in LES mode according to (Davidson & Peng, 2003; Kok et al., 2004), $\Delta_{LES} = (\Delta_\xi \Delta_\eta \Delta_\zeta)^{1/3}$.

From equations (1) it is evident that the solution is independent on equation (2) in LES mode although equation (2) is solved.

3. Numerical method

Flow through the axial turbine stage is modeled as unsteady, 3D, compressible, viscous, fully turbulent flow of the perfect gas. System of governing equations is discretized by the cell-centered finite-volume method on multi-block structured mesh of hexahedral elements. The inviscid numerical fluxes are calculated using the exact solution of the 1D Rieman problem in normal direction to the cell edges. The viscous numerical fluxes are calculated using the central scheme using the Green-Gauss theorem on a dual cells. Higher order of accuracy in space is obtained using linear reconstruction with the Van Leer's slope limiter. Temporal discretization is performed using the second-order backward Euler formula in implicit form, which is realized through a dual iterative process. The resulting numerical method is second order of accuracy in both time and space.

Although numerical methods based on exact or approximate solution of the Riemann problem have good features for RANS modelling, they are too dissipative for using in LES approach. Therefore a "centralization" of the numerical inviscid fluxes was used in this work for suppression of the native numerical dissipation. Let $F(W_{i+1/2}^L, W_{i+1/2}^R)$ is the inviscid numerical flux through cell face between i-th and (i+1)-th cells which is based on the Riemann problem solution. $W_{i+1/2}^L$ and $W_{i+1/2}^R$ denotes state vectors extrapolated to the cell face from the left and right in means of linear reconstruction with the slope limiter. The numerical dissipation is related to rate of difference between $W_{i+1/2}^L$ and $W_{i+1/2}^R$. Let $W_{i+1/2}^C$ is the state vector at the cell face computed as an average value of the state vectors in centers of i-th and ($i+1$)-th cells. The "centralization" of the inviscid numerical fluxes means replacing of $W_{i+1/2}^L$ and $W_{i+1/2}^R$ by $W_{i+1/2}^{CL}$ and $W_{i+1/2}^{CR}$, where $W_{i+1/2}^{CL} = \psi W_{i+1/2}^C + (1-\psi) W_{i+1/2}^L$ and $W_{i+1/2}^{CR} = \psi W_{i+1/2}^C + (1-\psi) W_{i+1/2}^R$. Parameter ψ is given as

$$\psi = \begin{cases} 0 & \text{for } L_t < L_{DES} \quad \text{(RANS mode)}, \\ [0.5 - 0.5\cos(2\pi(1 - L_{DES}/L_t))]^2 & \text{for } L_t \geq L_{DES} \quad \text{(LES mode)}, \end{cases} \tag{3}$$

where $L_t = \sqrt{k}/\beta^* \omega$ is the turbulent length scale and $L_{DES} = C_{DES} \Delta_{DES}$ is the sub-grid length scale.

4. Computational results

In left part of figure 1 there is shown scheme of the computational domain which contains one stator and one rotor blade. The chord of the stator and rotor blade is ≈30 mm. The hub diameter is 330 mm and diameter of the outer casing is 430 mm. The size of both radial gaps is 1.4 mm. The axial distance between the stator trailing edge and the rotor leading edge is 8 mm. The inlet boundary is placed 24 mm before the stator leading edge and the outlet boundary is placed 15 mm behind the rotor trailing edge. The sliding mesh interface between stator and rotor parts of the computational domain is placed in the middle of the axial gap between the stator and the rotor blades.

Presented results were calculated for the isentropic outlet Mach number $M_{is} = 0.7$, the outlet isentropic Reynolds number based on blade chord $Re_{is} \approx 3 \times 10^5$. The rotor blade and the hub-wall rotate at 7430 RPM.

In right part of figure 1 there is shown a distribution of the parameter ψ in meridian section. Red indicates areas where the inviscid numerical flux is fully centralized while in blue domains it remains in original form. In figure 2 there are shown instantaneous isosurfaces of $(|\Omega|^2 - |S|^2)$ which are colored with local turbulence intensity. It is evident that the "centralized" inviscid numerical fluxes allow to resolve more details in flow field. Figure 3 shows instantaneous distribution of the total-total efficiency behind the rotor blade and the time averaged span-wise distribution in section 11 mm behind the trailing edge. The total-total efficiency is defined as $\eta_{TT} = (T_{T0} - T_T) / (T_{T0} - T_{Tis})$ where T_{T0} is the inlet total temperature, T_T is local total temperature and T_{Tis} is the total isentropic temperature. The experimental data in figure 3 are from (Straka & Němec; 2016).

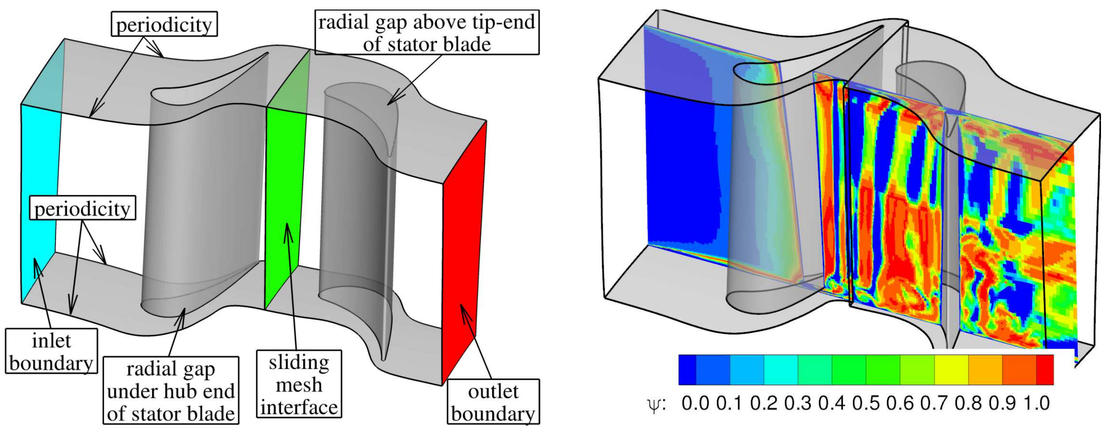

Fig. 1: Computational domain (left), distribution of parameter ψ in meridian section (right).

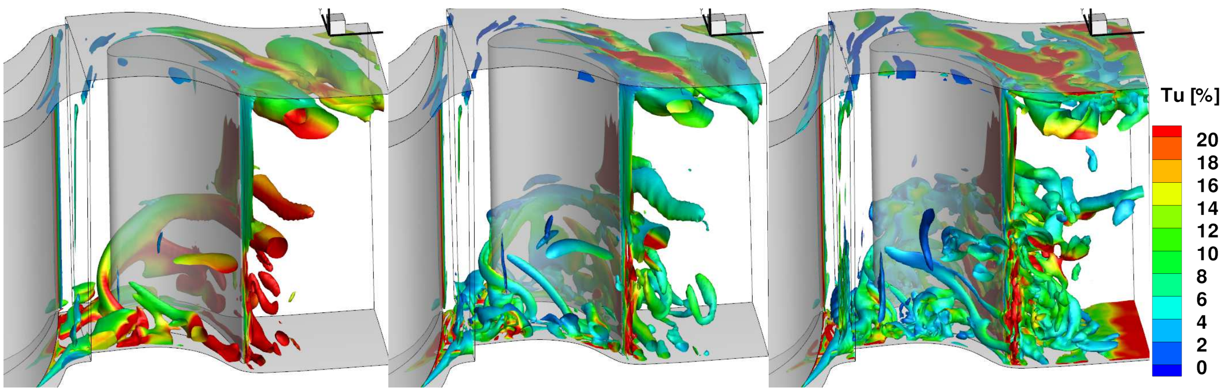

Fig. 2: Isosurfaces of $(|\Omega|^2 - |S|^2)$ colored by local turbulence intensity; RANS (left), RANS/LES with original inviscid numerical fluxes (middle), RANS/LES with centralized inviscid numerical fluxes (right).

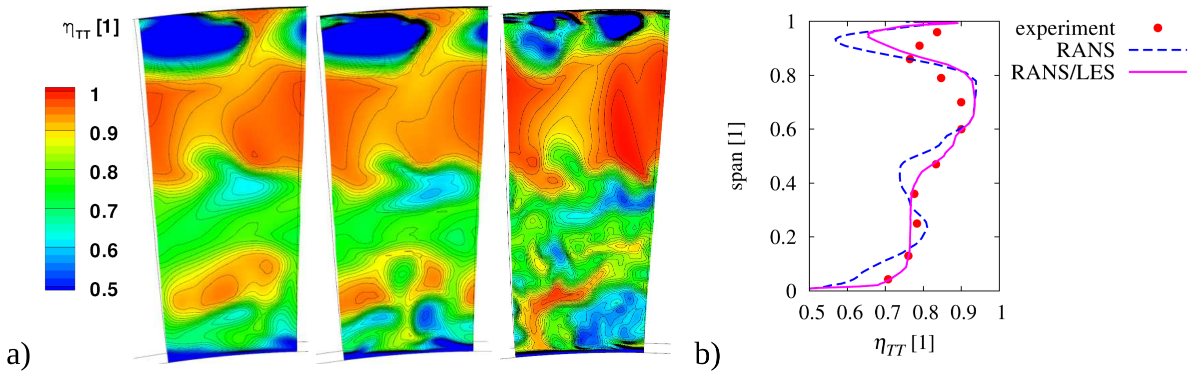

Fig. 3: Distribution of the total-total efficiency behind the rotor blade; a) instantaneous distribution in axial section: RANS (left), RANS/LES with original inviscid numerical fluxes (middle), RANS/LES with centralized inviscid numerical fluxes (right); b) time averaged span-wise distribution..

5. Conclusions

Hybrid RANS/LES model was implemented into the in-house numerical code which was here modified for using in LES approach. The model was applied for computation of flow in the axial turbine stage. Computational results shows that hybrid RANS/LES model predicts the interaction of the rotor blade with the secondary vortices much better then RANS model.

Acknowledgement

This work was supported by the Long-term Framework Advancement Plan provided by the Ministry of Industry and Trade of the Czech Republic.

References

Straka, P., Němec, M. & Jelínek, T. (2015) Investigation of flow in axial turbine stage without shroud-seal. EPJ Web of Conferences, 92, 02088.

Straka, P. & Němec, M. (2016) Influence of the radial gap under the stator blade on flow around the hub-end of the rotor blade. Applied Mechanics and Materials, 821, pp. 120-128.

Kok, J.C. (2000) Resolving the dependence of freestream values for the *k*–*ω* turbulence model. AIAA Journal, 38, 7.

Straka, P. (2015) Numerical simulation of high-swirl flow in axial turbine stage. Proc. Conf. Experimental Fluid Mechanics 2015 (Dančová, P. & Veselý, M. eds), Prague, pp. 752-759.

Rumsey, C.L. & Gatski, T.B. (2001) Recent turbulence model advances applied to multielement airfoil computations. Jour. of Aircraft, 38, 5, pp. 904-910.

Straka, P. (2012) Simulation of a 3D unsteady flow in an axial turbine stage. EPJ Web of Conferences, 25, 01090.

Straka, P. (2013) Calculation of 3D unsteady flow in axial stage of low power experimental turbine. Technical Report VZLU R-5904, Prague, (in Czech).

Davidson, L. & Peng, S.H. (2003) Hybrid LES-RANS modelling: a one-equation SGS model combined with a *k*-*ω* model for predicting recirculating flows. Int. Jour. Numer. Meth. Fluids, 43, pp. 1003–1018.

Kok, J.C., Dol, H.S., Oskam, B. & H. van der Ven (2004) Extra-large eddy simulation of massively separated flows. AIAA paper, 2004-264.

Kubacki, S., Rokicki, J., Dick, E., Degroote, J., Vierendeels, J. (2013) Hybrid RANS/LES of plane jets impinging on a flat plate at small nozzle-plate distances. Arch. Mech., 65, 2, pp. 143-166.

22nd International Conference
ENGINEERING MECHANICS 2016
Svratka, Czech Republic, 9 – 12 May 2016

TESTING OF CAR SUSPENSION WITH FAST MR DAMPER CONTROLLED BY MODIFIED GROUNDHOOK ALGORITHM

Z. Strecker*, P. Čípek, J. Roupec, M. Kubík, O. Macháček

Abstract: *The paper describes a comparison of traditional passive suspension to a suspension with MR damper controlled by on/off Modified groundhook algorithm. The MR damper used in an experimental trolley together with current controller has exceptionally short time response of force on control signal – up to 1.5 ms. The MR damper was mounted into experimental trolley, which is scaled quarter suspension car model. The experimental trolley was riding on a road simulator over a bump. The suspension quality was evaluated according to the standard deviation of sprung mass acceleration (the lower value means higher comfort) and according to the standard deviation of force (the lower value means better grip). The results show that suspension system controlled by Modified groundhook algorithm outperforms passive system, but the level of improvement is dependent on the setting of current respectively damping in on and off state.*

Keywords: Modified groundhook, fast MR damper, response time, tyre grip, comfort

1. Introduction

The possible wheel grip provided by suspension with passive dampers is limited. Many simulations proved that higher grip can be achieved when semiactive algorithms controlling the amount of dissipated energy are used (Poussot-vassal et al., 2012). These semiactive suspension systems can employ different types of controllable dampers. Valášek et al. (1998) used CDC damper for controlling the Truck suspension with Groundhook algorithm. Ahmadian et al. (2005) simulated semiactive suspension with magnetorheological damper.

Simulations, however, often use idealized models of dampers with zero time response. In real situations, the time response of MR damper can be in tens of milliseconds (Koo et al., 2006). Eslaminasab and Golnaraghi (2008) showed the significant influence of the damper time response on semiactive suspension performance on 1 DOF system. Strecker et al. (2015) implemented time response of a MR damper into the quarter model of car suspension. Results from simulations showed that suspension controlled by Groundhook algorithm cannot offer better wheel grip when MR damper with long time response is used. Experiment confirmed no improvement in tyre grip when automotive MR damper with response time 8 ms was used in experimental trolley. The improvement in grip, predicted by the simulations with MR damper with response time 2 ms, was not experimentally evaluated, because it was not possible to obtain MR damper with such low response time.

Reasons of long response time of MR devices were described in Maas and Güth (2011). They also designed a MR clutch with very short time response. Based on this knowledge, Strecker et al. (2015) designed a fast MR damper, with time response of damper force on control signal up to 1.5 ms. Such time response can be reached only in case when fast current controller with voltage overdrive is used.

The MR damper with fast time response was never experimentally evaluated in car suspension. This paper describes the performance of such damper in semiactive suspension in comparison with passive damper.

2. Methods

The experimental setup is in Fig. 1:

*All authors: Institute of Machine and Industrial Design, Brno Technical University, Technická 2896/2; 616 69, Brno; CZ, *strecker@fme.vutbr.cz

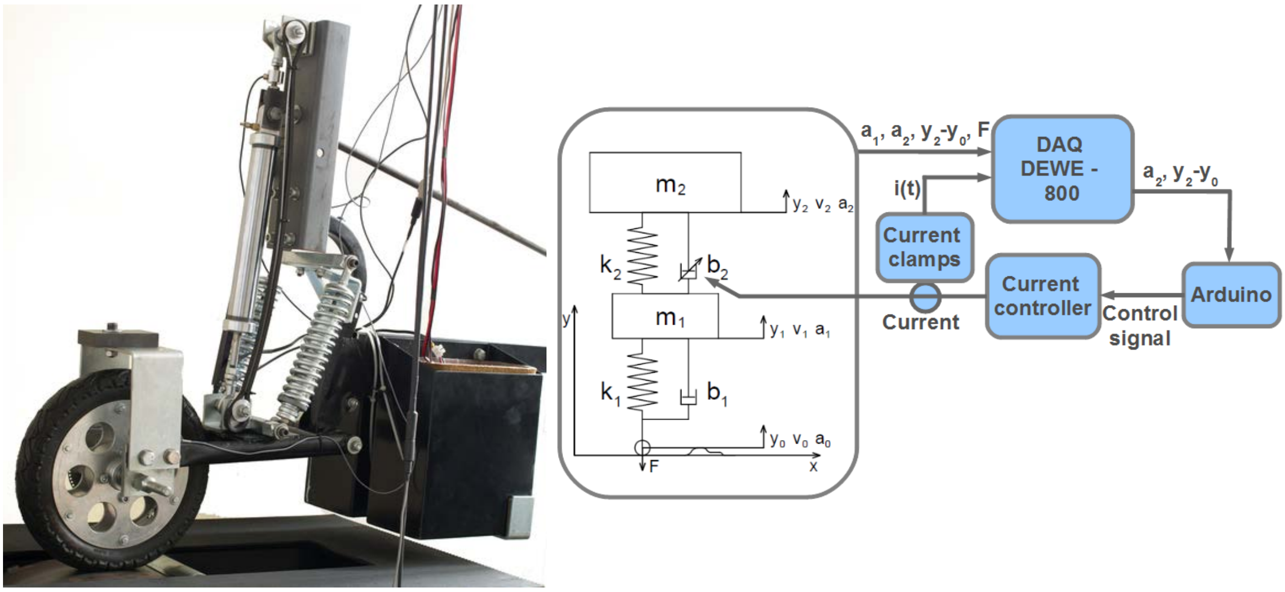

Fig. 1: The experimental trolley (left) and the block scheme of experimental setup

The experiment was conducted on a quarter car suspension model (Fig. 1) with unsprung mass m_1, sprung mass m_2, tyre stiffness k_1, main spring stiffness k_2, damping of the tyre b_1 and damper with variable damping b_2. The damping is dependent on piston velocity and electric current in the MR damper coil (Fig. 2). The other parameters are in Tab. 1. The experimental trolley was riding on the road simulator with the velocity 10 km/h over speed bump with the length 55 mm and height 21 mm.

Tab. 1: The parameters of experimental trolley

Dynamic tyre stiffness k_1 [N/mm]	50,2
Sprung mass m_2 [kg]	42.2
Unsprung mass m_1 [kg]	6.7
Overall stiffness k_2 [N/mm]	7,4

The measured force-velocity dependency for the currents between 0-2 A is in Fig. 2:

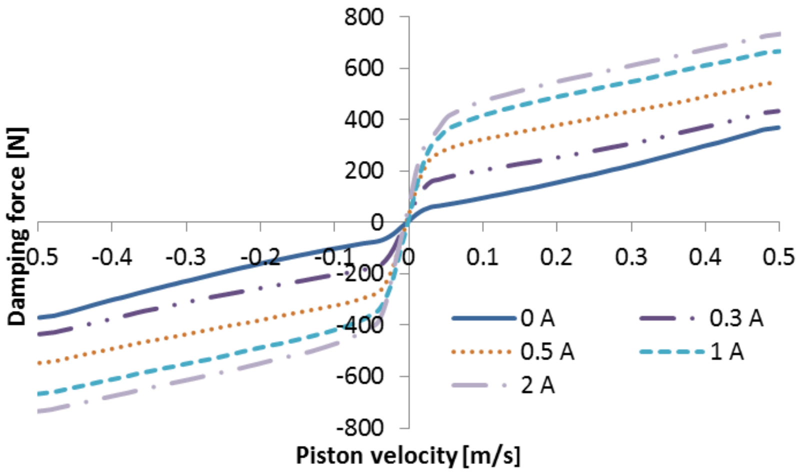

Fig. 2: F-v dependency of MR damper

The suspension quality was evaluated according to the standard deviation of sprung mass acceleration (1) which reflects comfort (the lower sprung mass acceleration standard deviation means better quality) and standard deviation of force on the road F (2) which reflects the tyre grip (the lower value means better grip), where F_{stat} is static force on the road:

$$\sigma(a_2) = \sqrt{\frac{1}{N}\sum_{i=1}^{N} a_{2(i)}^2} \tag{1}$$

$$\sigma(F) = \sqrt{\frac{1}{N}\sum_{i=1}^{N} (F_i - F_{stat})^2} \tag{2}$$

The suspension quality was evaluated for the whole range of the possible passive settings and for Modified groundhook algorithm. In this settings, the electric current to the coil was switched between two states – with low current I_L (low damping) and high current I_H (high damping). The rule for switching between these two states was according to the unsprung mass acceleration a_1, and relative velocity of sprung and unsprung mass v_2 - v_1 (3).

$$\begin{aligned} a_1(v_2 - v_1) \geq 0 \Rightarrow I = I_H \\ a_1(v_2 - v_1) < 0 \Rightarrow I = I_L \end{aligned} \tag{3}$$

The signals with acceleration of sprung mass, unsprung mass, relative displacement and force of the wheel to the road were sampled at 5 kHz and recorded by DEWE-800 measurement station. The signals with relative displacement and acceleration of unsprung mass were also used as input for control loop programmed in Arduino Due board (Fig. 2 right). The control loop was counting an output signal corresponding to the electric current I according to the equation (3). The relative velocity of sprung and unsprung mass was calculated from the rate relative displacement divided by control loop period. The signal with relative velocity was filtered by low-pass IIR filter with the cutoff frequency 360 Hz.

3. Results and discussion

The results are in Fig. 3. The passive setting for the current 0 A exhibits the best comfort, but the grip is the worst. With the rising current up to 0.5 A, the grip is improving, but the comfort is getting worse. The use of currents higher than 0.5 A does not bring any advantage, because both grip and comfort are getting worse.

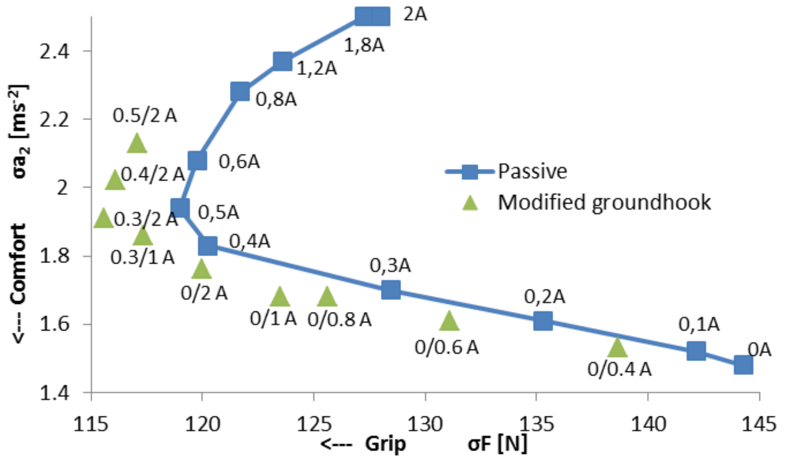

Fig. 3: Comparison of passive and modified groundhook controlled suspension

Suspension controlled by Modified groundhook algorithm exhibits better performance than passive suspension for all settings. When the current for low damping I_L was 0 A, the comfort of suspension was better than for passive settings with the same level of the grip. For achieving better grip than any passive setting, it was necessary to increase I_L. The best grip was reached for $I_L = 0.3\ A$ and $I_H = 2\ A$.

Fig. 4 shows the courses of unsprung mass acceleration and filtered relative velocity together with ideal desired current and the real current. It can be seen that the course of real current is delayed in comparison with desired current and especially for small amplitudes of relative velocity, the current is switched not exactly according to the algorithm. These differences are probably caused by delay from IIR low pass filter used for relative velocity and the noise in the signal.

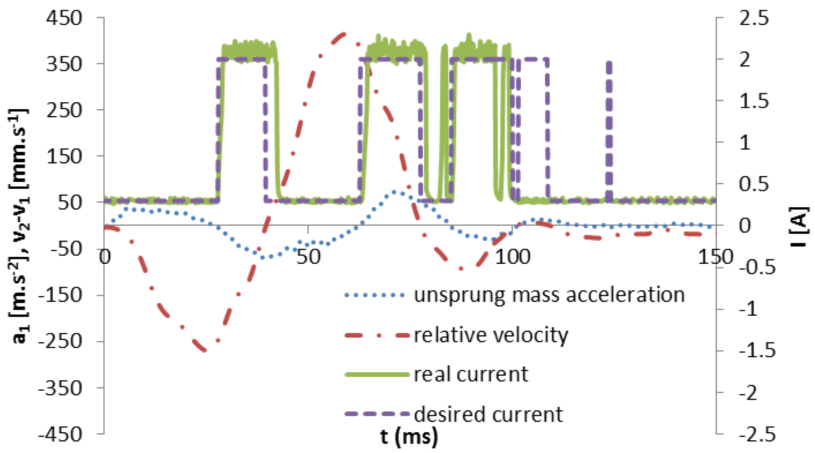

Fig. 4: The courses of current switching

4. Conclusions

The results from measurement showed that semiactive suspension with fast MR damper controlled by Modified groundhook algorithm is able to outperform any passive setting especially in tyre grip. The suspension performance is however sensitive on setting of the currents I_H and I_L. The measurement was conducted only for one type of bump with relatively high amplitudes of unsprung mass acceleration and relative velocity amplitudes. The switching of the current to the MR damper for small amplitudes was not exactly according to the algorithm. For smoother roads with smaller wheel disturbances, it will be necessary to use sensors with higher sensitivity and lower noise.

Acknowledgement

The research leading to these results has received funding from the MEYS under the National Sustainability Programme I (Project LO1202), FSI-S-14-2329, FEKT/FSI-J-15-2777 and GAČR 13-31834P.

References

Ahmadian, M., Goncalves, F.D. & Sandu, C. (2005) An experimental analysis of suitability of various semiactive control methods for magneto rheological vehicle suspensions, in: Smart Structures and Materials 2005: Damping and Isolation, pp. 208–216

Eslaminasab, N. & Golnaraghi, M.F. (2008) The effect of time delay of the semi-active dampers on the performance of on-off control schemes, in: Proceedings of the Asme International Mechanical Enginering Congress and Exposition 2007, Vol 9, Pts a-C, pp. 1911–1918.

Koo, J.-H., Goncalves, F.D. & Ahmadian, M. (2006) A comprehensive analysis of the response time of MR dampers. Smart Materials and Structures, 15,2, pp. 351–358.

Maas, J. & Güth, D. (2011) Experimental Investigation of the Transient Behavior of MR Fluids, in: ASME 2011 Conference on Smart Materials, Adaptive Structures and Intelligent Systems, Scottsdale, pp. 228-239.

Poussot-vassal, C., Spelta, C., Sename, O., Sergio, S. & Dugard, L. (2012) Survey and performance evaluation on some automotive semi-active suspension control methods : A comparative study on a single-corner model, Annual Rewievs in Control, 36, 1, pp. 148-160.

Strecker, Z., Roupec, J., Mazůrek, I., Machacek, O., Kubík, M. & Klapka, M. (2015) Design of magnetorheological damper with short time response, Journal of Intelligent Material Systems and Structures, 26, 14, pp. 1951–1958.

Strecker, Z., Mazůrek, I., Roupec, J. & Klapka, M. (2015) Influence of MR damper response time on semiactive suspension control efficiency, Meccanica, 50, 8, pp. 1949–1959.

Valášek, M., Kortüm, W., Šika, Z., Magdolen, L. & Vaculín, O. (1998) Development of semi-active road-friendly truck suspensions Control Engineering Practice, Elsevier 6, 6, pp. 735–744.

22nd International Conference
ENGINEERING MECHANICS 2016
Svratka, Czech Republic, 9 – 12 May 2016

A METHOD FOR DETERMINING A COMPLETE S-N CURVE USING MAXIMUM LIKELIHOOD

P. Strzelecki*, T. Tomaszewski, J. Sempruch*****

Abstract: *The study presents two methods to estimate the S-N curve. The first method is commonly known as the traditional approach and well documented in the normative sources. It consists in determining the curve using the least squares method in a limited fatigue life regime. A staircase method is used to determine the fatigue limit. The second approach assumes normal distribution of fatigue life and fatigue limit. A probability of failure is determined as a product of fatigue life probability distribution function and fatigue limit probability distribution function. The curve parameters are determined using the maximum likelihood estimation method. This is an alternative approach. The advantage of the latter approach is the ability to determine a complete S-N curve using less specimens than required in the traditional approach. The alternative method allows to use non-failed specimens for statistical calculations, which is not possible in the traditional approach. Comparison of those methods was presented using fatigue data for S355J2+C steel. The tests were carried out using the testing machine for rotating bending tests. The study also compares the accuracy of the alternative approach with the traditional approach, which is generally considered accurate.*

Keywords: Fatigue, Steel, High-cycles, S-N curve, Accelerated methods.

1. Introduction

Fatigue properties of materials within the high-cycle loading range are tested as scheduled based on standards, such as ISO-12107 (2003) or PN-EN-3987 (2010). For instance, offers a comparison between guidelines for such tests and analyses, as proposed by various standards. This scheduled testing based on standards is accurate but time-consuming and costly. Analytical methods, such as those proposed by Sempruch & Strzelecki (2011) or Strzelecki & Sempruch (2012a) can be used for initial computation. Unfortunately, following verification, these methods were proven as generating significant errors. This is why experiments are done where reliable machine components are required. The conventional approach to the determination of full S-N characteristics involves a number of tests (at least 14). Such tests are often done for comparing effects of process factors or geometry on fatigue strength, as described by Tomaszewski et al. (2014), for instance.

This paper proposes an alternative approach to determining full S-N characteristics, described in more detail in the following section. The paper aimed to demonstrate that the number of required tests can be reduced using another approach the processing of test results without compromising the acceptable estimation error.

2. Methods of determination S-N curve

ISO-12107 (2003) recommends at least 7 tests for the limited strength range and 15 tests with the up and down method for the unlimited strength range. This makes the total of 22 samples. Also, this document describes a full S-N characteristics determination procedure using 14 samples. Six samples are used for the fatigue limit range.

* Dr. Ing. Przemysław Strzelecki, Institute of Mechanical Engineering, University of Technology and Life Sciences, 85-789 Bydgoszcz, Poland; PL, e-mail:p.strzelecki@utp.edu.pl

** Dr. Ing. Tomasz Tomaszewski, Institute of Mechanical Engineering, University of Technology and Life Sciences, 85-789 Bydgoszcz, Poland; PL, e-mail:tomaszewski@utp.edu.pl

*** Prof. Ing. Janusz Sempruch, Institute of Mechanical Engineering, University of Technology and Life Sciences, 85-789 Bydgoszcz, Poland; PL, e-mail: semjan@utp.edu.pl

$$\hat{Z}_G = \frac{\sum_{i=2}^{n+1} S_i}{n} \tag{1}$$

where:
n – number of specimen used for unlimited fatigue life,
S_i – i^{th} stress level.

Stress for S_{n+1} is not tested; it is determined based on the last n^{th} level. It is the level that would be applied if tests were to be continued. Before this procedure can be followed, characteristics for the limited strength range has to be determined.

The least squares method is used for estimating parameters of the characteristics within the limited strength range. See Lee et al. (2005) for a detailed description of a procedure for this method of testing. Fig. 1 a) shows a graphic representation of this method. This method is hereinafter referred to as method "I" (conventional).

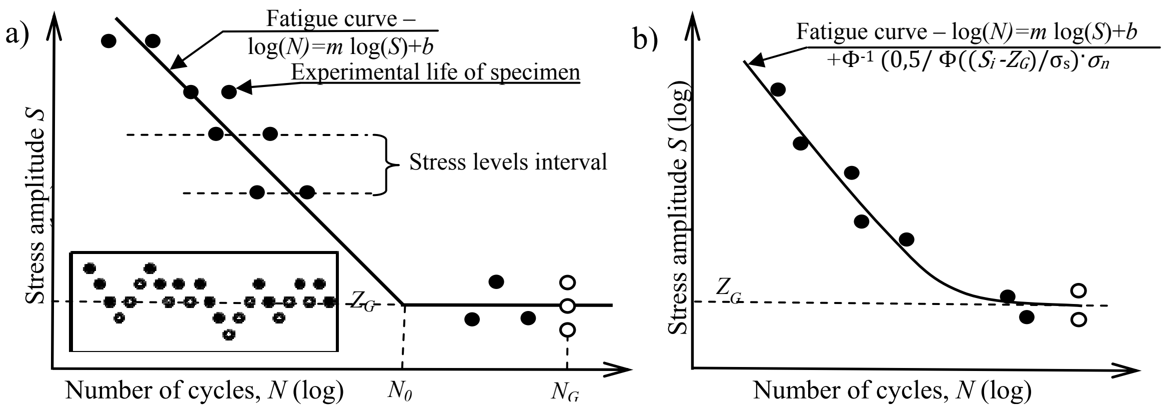

Fig. 1. Schematic representation determination of the fatigue curve of the using a) model I and b) model II

The method proposed by Pascual & Meeker (1999), shown schematically in Fig. 1 b), hereinafter referred to as method "II" (alternative), represents another approach. This method assumes that the distribution of strength in the limited strength range is normal. In addition, it assumes that also the distribution of fatigue limit is normal. See the following for equations describing these assumptions.

$$f(N) = \frac{1}{\sqrt{2\pi\sigma_n^2}} \exp\left(\frac{\left(\log(N) - \left(m\log(S) + b\right)\right)^2}{\sigma_n^2}\right) \tag{2}$$

$$f(S) = \frac{1}{\sqrt{2\pi\sigma_s^2}} \exp\left(\frac{\left(S - Z_G\right)^2}{\sigma_s^2}\right) \tag{3}$$

where:
σ_n – standard deviation for fatigue life in limited range,
N – fatigue life,
S – stress amplitude,
m – slope of regression line,
b – intercept of regression line,
σ_s – standard deviation for fatigue limited,
Z_G – fatigue limited.

The method of maximum likelihood method is used to estimate parameters of these distributions. The likelihood function used for this statistical method has the following form (Lorén & Lundström (2005)):

$$L(\theta)=\phi\left(\frac{\log N_i-(m\log S_i+b)}{\sigma_n}\right)^{\delta_i}\cdot\Phi\left(\frac{S_i-Z_G}{\sigma_s}\right)^{\delta_i}\cdot\left[1-\left(\Phi\left(\frac{\log N_i-(m\log S_i+b)}{\sigma_n}\right)\cdot\Phi\left(\frac{S_i-Z_G}{\sigma_s}\right)\right)\right]^{1-\delta_i},\tag{4}$$

where:

ϕ – density function of the normal distribution,

Φ – cumulative distribution function of the normal distribution,

$$\delta_i=\begin{cases}1 \text{ if specemen failure}\\ 0 \text{ if specimen runout}\end{cases}.\tag{5}$$

3. Experimental results

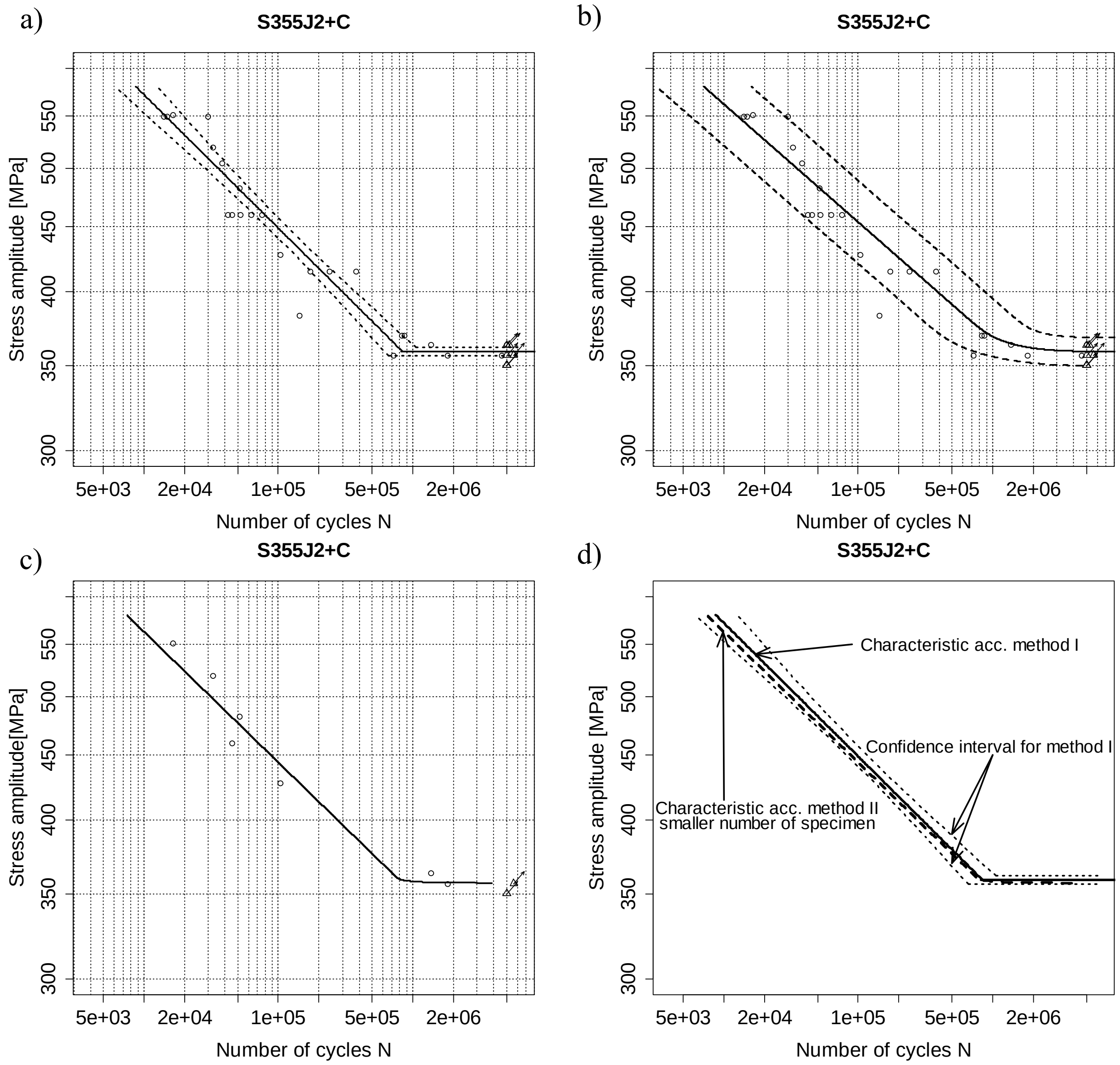

Fig. 2. Fatigue characteristics for S355J2+C steel acc. a) method I, b) method II with complete data, c) method II with smaller number of specimen, d) comparison of characteristic acc. Method I and II with smaller number of specimen

Tests were done for steel S355J2+C, using a rotary bending as the fatigue testing machine. See Strzelecki & Sempruch (2012b) for descriptions of the verification, work station and samples. Fig. 2 shows the resulting fatigue diagrams and Tab. 1 presents parameters estimated based on the proposed methods. In addition, the paper presents separately parameters estimated using the alternative method based on the data set contained in the graduation paper of Zawadzki (2015), constituting a part (9 tests) of the whole set (33 tests) used for analysis. Fig. 2 d) shows characteristics based on the conventional method (with the confidence interval) and the alternative method, for a smaller number of tests.

Tab. 1: Estimated parameters fo method I i II for steel S355J2+C.

Model	m	c	σ_v	Z_g	σ_z
I	-9.92	31.33	0.175	358.9	7.534
II – complete data	-11.14	34.62	0.244	359.0	7.245
II – first part data	-10.76	33.57	0.171	356.6	1.442

4. Conclusions

The conclusion from comparing the characteristics obtained by method "I" for 33 tests to the characteristics obtained by method "II" for 9 tests is that the diagram for the alternative method fits within the confidence interval obtained for the conventional method. This means that it is possible to obtain satisfactory fatigue characteristics based on 9 tests. This conclusion requires verification for other construction materials.

References

ISO-12107 (2003) Metallic materials - fatigue testing - statistical planning and analysis of data.

Lee, Y.L., Paw, J., Hathaway, Richard, B., Barkey, Mark, E. (2005) Fatigue Testing and Analysis - Theory and Practice. Elsevier Butterworth–Heinemann.

Lorén, S., Lundström, M. (2005) Modelling curved S-N curves. Fatigue Fract. Eng. Mater. Struct. 28, pp. 437–443. doi:10.1111/j.1460-2695.2005.00876.x

Pascual, F.G., Meeker, W.Q. (1999) Estimating Fatigue Curves with the Random Fatigue-Limit Model. Technometrics 41,4, pp. 277–290. doi:10.2307/1271342

PN-EN-3987 (2010) Aerospace series - Test methods for metallic materials - Constant amplitude force-controlled high cycle fatigue testing.

Sempruch, J., Strzelecki, P. (2011) Error of fatigue life determinated according to the FITNET method. 17th Int. Conf. Eng. Mech. pp. 531–534. doi:10.1017/CBO9781107415324.004

Strzelecki, P., Sempruch, J. (2012a) Verification of rapid method for determining the S-N curve in limited life region, in: Naprstek, J., Fischer, C. (Eds.), 18-Th International Conference Engineering Mechanics 2012. Institute of Theoretical and Applied Mechanics, Academy of Sciences of the Czech Republic, Prague, Svratka, Czech Republic, pp. 306–307.

Strzelecki, P., Sempruch, J. (2012b) Experimental Verification of the Analytical Method for Estimated S-N Curve in Limited Fatigue Life. Mater. Sci. Forum 726, pp. 11–16. doi:10.4028/www.scientific.net/MSF.726.11

Strzelecki, P., Sempruch, J., Nowicki, K. (2015) Comparing guidelines concerning construction of the S-N curve within limited fatigue life range. Polish Marit. Res. 22,3, pp. 67–74.

Tomaszewski, T., Sempruch, J., Piątkowski, T. (2014) Verification of selected models of the size effect based on high-cycle fatigue testing on mini specimens made of EN AW-6063 aluminum alloy. J. Theor. Appl. Mech. 52,4, pp. 883–894.

Zawadzki, K. (2015) Experimental verification of selected parameters determining the mechanical properties of steel. University of Science and Technology in Bydgoszcz.

22nd International Conference
ENGINEERING MECHANICS 2016
Svratka, Czech Republic, 9 – 12 May 2016

USING THE PROPER ORTHOGONAL DECOMPOSITION ANALYSIS FOR DETECTING PATHOLOGIC VOCAL FOLD VIBRATION

J. Štorkán*, T. Vampola, J. Horáček*****

Abstract: *A three-dimensional (3D) finite element (FE) fully parametric model of the human larynx based on computer tomography (CT) measurements was developed and specially adapted for numerical simulation of vocal folds vibrations with collisions. The complex model consists of the vocal folds, arytenoids, thyroid and cricoid cartilages. The vocal fold tissue is modeled as a four layered material where part of the cover was substituted by a liquid layer modelling the superficial layer of lamina propria. The proper orthogonal decomposition (POD) analysis of the excited modes of vibration was used for detecting changes in vibration properties of the vocal folds caused by pathologic changes of vocal fold structure (vocal nodule).*

Keywords: biomechanics of human voice, 3D FE model of human larynx, finite element method, proper orthogonal decomposition analysis

1. Introduction

Human voice plays an important role in society enabling interpersonal communication. Understanding the basic principles of voice production is important for better interpretation of clinical findings, detection of laryngeal cancers or other pathologies and for treatment of voice disorders.

Voice production is a complex physiological process, which involves several basic factors like airflow coming from the lungs, vocal folds (VF) vibration and acoustic resonances of the cavities of the vocal tract, see e.g. Fant (1960).

Design of more exact 3D computer models of the human VF folds enables modelling of some pathological situations. Changes in the structural and geometric properties are related to the changes of the vibratory properties of the vocal folds. In this contribution, the proper orthogonal decomposition method (POD) is used for predicting of the human vocal fold damage.

2. FE model of the human larynx

The geometry and relations between the arytenoids, thyroid and cricoid cartilages was derived from CT images. The geometry of the vocal folds was derived from the CT images registered during phonation of a female subject. The 3D complex dynamic FE model of the human larynx was developed by transferring the raw CT image data into volume models. After meshing of the volume models, the 3D FE model of the complete larynx was constructed within the framework of the program ANSYS (Vampola et al. 2015), see Fig. 1.

The frequency-modal properties and the results of the numerical simulation of the vocal fold oscillations with and without the VF nodule, excited by a prescribed periodic intraglottal aerodynamic pressure, are presented. For simplicity, no fluid structure interaction is considered here, and the primary focus is concentrated on the proper orthogonal decomposition (POD) analysis of the excited modes of vibration and on comparison of the vibration patterns in the vocal fold models.

* Ing. Jaroslav Štorkán: Department of Mechanics, Biomechanics and Mechatronics, Faculty of Mechanical Engineering, Czech Technical University in Prague. Technicka 4, Praha 6, Czech Republic, jaroslav.storkan@fs.cvut.cz

**prof. Dr. Ing. Tomáš Vampola: Department of Mechanics, Biomechanics and Mechatronics, Faculty of Mechanical Engineering, Czech Technical University in Prague. Technicka 4, Praha 6, Czech Republic, tomas.vampola@fs.cvut.cz

*** Ing. Jaromír Horáček, DrSc.: Institute of Thermodynamics, Academy of Sciences of the Czech Republic. Dolejšova 1402/5 Praha 8 Czech Republic, jaromirh@it.cas.cz

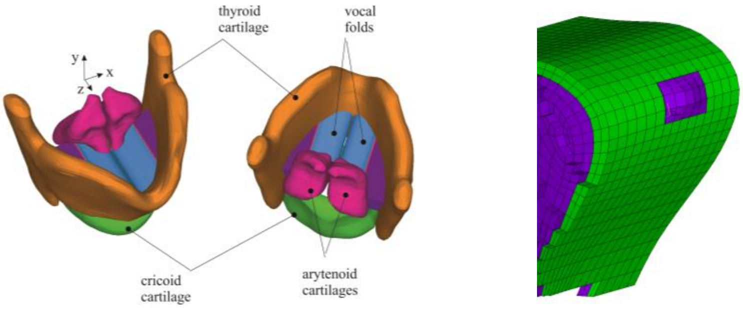

Fig. 1. The 3D FE model of the human larynx with the vocal folds fixed to the arytenoid and thyroid cartilages. False vocal folds were not considered in this study. The vocal fold nodule model (right).

The nonlinear elasticity theory for large-strain deformations with linear strain-stress relationship was implemented. The linear transversal isotropic material model was used for the vocal fold tissue. The tissues material constants for cover, ligament and muscle vocalis considered are summarized in Table 1. An incompressible liquid was included in the superficial layer of lamina propria and modelled by structural finite elements considering the bulk modulus of water (k_L =2.1*10^6 kPa). The VF nodule was modelled by an additional volume 2x1x0.5 mm^3 located in the lamina propria (see Fig. 1) with the material parameters of about 10% higher than the ligament parameters.

Table 1. Nominal values of material constants of individual tissue layers according to Luo et al. (2008)

	Cover	Ligament	Muscle
G_p [kPa]	0.53	0.87	1.05
G_l [kPa]	10	40	12
μ_p	0.3	0.3	0.3
$E_l(\varepsilon)$ [kPa]	26	104	31
ρ [kgm^{-3}]	1020	1020	1020

3. Frequency – modal characteristic of the models

The first fourth eigenfrequencies and the eigenmode shapes of vibration of the right vocal fold of the FE models for the model without the nodule are presented in Fig. 2. Because the vocal folds are not perfectly symmetric, the fundamental eigenfrequencies for the left and right vocal fold are slightly different, however the mode shapes are very similar. The influence of the VF nodule on the first four eigenfrequencies and the eigenmodes was found negligible.

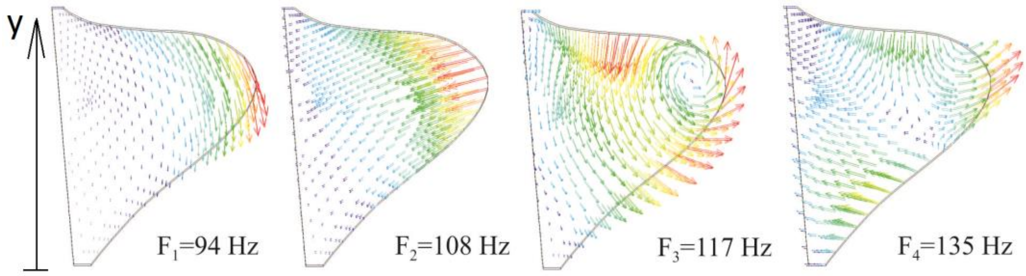

Fig. 2. First four eigenfrequencies and eigenmodes of vibration of the vocal fold model without the nodule.

4. Numerical simulation of vocal folds vibration

The self-sustained vibrations with collisions of the 3D vocal folds models were numerically simulated by using a prescribed intraglottal pressure given by a periodic function in the time domain. Transient analysis was used for simulation of the vocal folds vibration in time domain.

The intraglottal pressure loading of the vocal fold surface was generated by the 2D aeroelastic model of the VF self-oscillations developed by Horáček et al. (2009). The intraglottal pressure was calculated during the VF self-oscillations for the airflow rate Q=0.15 l/s, the prephonatory glottal half-gap g_0=0.2 mm and the subglottal pressure P_{sub}=270 Pa. The intraglottal periodic pressure $p(y,t)$, simulated by the 2D aeroelastic model, and used for excitation of the 3D FE models of the vocal folds is shown in Fig. 3.

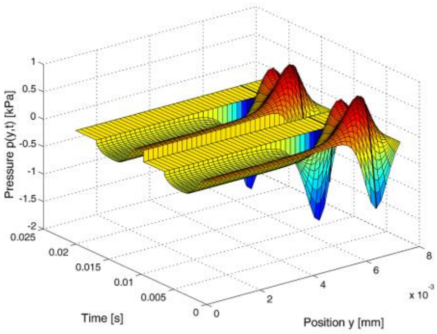

Fig. 3. Two periods of the intraglottal pressure pulses p(y,t) loading the vocal folds surface presented in the time-space domain.

5. Proper orthogonal decomposition analysis of the vocal fold vibration

The proper orthogonal decomposition (POD) is useful tool in analyzing vibration of the flexible structures, see e.g. Feeny & Kappagantu (1998). By means of the POD eigenvalues the amount of the energy in the POD modes can be evaluated. In this contribution we tested the hypothesis if the POD analysis can be used for prediction of the vocal fold damages.

For application of POD method it is necessary to assemble the displacement-history array in the N time snaps for displacements along x,y and z coordinates u_j, v_j, w_j (j=1,2,…,M):

$$\mathbf{D}=[\mathbf{d}(t_1),\mathbf{d}(t_2),\cdots,\mathbf{d}(t_i),\cdots,\mathbf{d}(t_\mathrm{N})] \tag{1}$$

An oscillatory component matrix **R** represents the time-varying displacements about the dynamic equilibrium of the system, can be separated from the **D** matrix where the MATLAB functions *mean*(**D**,2) and *ones*(1,N) were used.

$$\mathbf{R} \; = \mathbf{D} - mean(\mathbf{D},2) \; ones(1,\mathrm{N}) \tag{2}$$

The covariance matrix $\mathbf{C}=\mathbf{R}^T\mathbf{R}/\mathrm{N}$ is then formed. The eigenvectors and eigenvalues of the covariance matrix can be computed by means of singular value decomposition method ($\mathbf{C}=\mathbf{U}\,\mathbf{S}\,\mathbf{V}^T$). The normalized POD modes (also so called toposes) are then derived in the form

$$\boldsymbol{\varphi}_i = \mathbf{C}\,\tilde{\mathbf{u}}_i \,/\, \|\mathbf{C}\,\tilde{\mathbf{u}}_i\|, \quad i=1,2,\cdots,\mathrm{N}_{POD.} \tag{3}$$

The relative amount of energy involved in the POD modes can be expressed from the diagonal of the matrix **S**

$$energy\;[\%]=\left(s_{ii} \,/ \sum_{i=1}^{3M} s_{ii}\right)100 \tag{4}$$

Finally the modal assurance criterion (MAC) was used for evaluation a relation of the POD modes with the normal modes of vibration:

$$MAC_{ij}\;[\%]=\frac{(\mathbf{v}_i^T\boldsymbol{\varphi}_j)^2}{(\mathbf{v}_i^T\mathbf{v}_i)(\boldsymbol{\varphi}_j^T\boldsymbol{\varphi}_j)}100 \tag{5}$$

where $\mathbf{v}_i$, $i=1,2,\dots,N$ are the normal modes of vibration and $\boldsymbol{\varphi}_j$, j=1,2,…,$\mathrm{N}_{\mathrm{POD}}$ are the POD modes.

The POD analysis was applied on numerically simulated displacements for the FE models with and without the nodule. The results are summarized in Table 2 and in Fig. 4 for first three and two POD modes, respectively. Table 2 presents the MAC values (5) and the relative POD modes energies (4) computed for the first three POD modes (3) for the VF models without and with the VF nodule.

Table 2 shows that up to 97-98 % of the total energy is captured by the first two POD modes in both FE models. However, the main difference between the VF models is in the entrainment of the eigenmodes of vibration. The first POD mode for the VF model without the VF nodule entrains the 1st and 2th eigenmodes while the model with the nodule entrains a combination of the 1st and 3nd eigenmodes.

Table 2 Modal assurance criterion (MAC) coefficients $MAC_{ij}\ [\%]$ *computed for the full FE models of the vocal folds: a) with the nodule and b) without the nodule.*

a)	eigenmode				
POD mode	1	2	3	4	Energy [%]
1	31.04	2.87	41.34	9.91	73
2	37.30	24.85	18.97	1.28	25
3	1.04	0.15	8.97	5.81	0.4
b)	eigenmode				
POD mode	1	2	3	4	Energy [%]
1	36.35	40.78	12.25	0.28	53
2	26.61	0.52	28.92	17.70	45
3	0.41	2.35	9.63	0.001	0.99

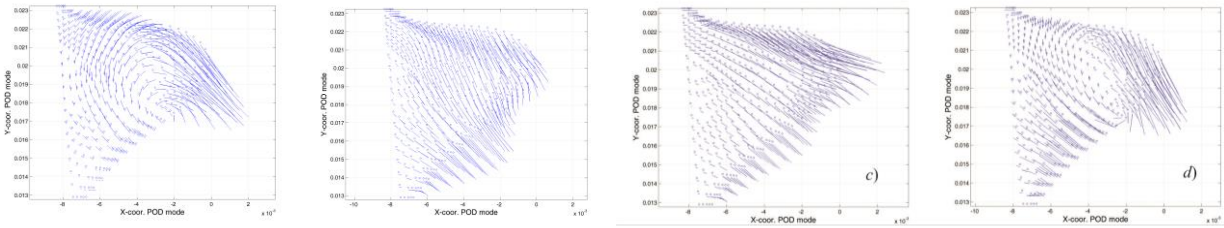

Fig. 4. First two POD modes of vibration computed for the full FE models of the vocal folds with the VF nodule (first and second) and without the nodule (third and fourth). For more clarity, only displacements of the nodes in the middle cross-section of the vocal folds are shown in the figure.

6. Conclusions

The geometry of the parametric 3D FE model of the vocal folds developed as a part of the complex 3D larynx model can be easily modified, enabling tuning and optimization procedures for finding proper geometric and material parameters related to the vocal fold vibration characteristics.

The POD analysis of the VF vibration patterns with and without the nodule proved a sufficient sensitivity of the developed computational VF model to a small variation of the model parameters and therefore the model can be used for prediction of the vocal fold damages.

Acknowledgement

The research is supported by the Grant Agency of the Czech Republic by project No 16-01246S “Computational and experimental modelling of self-induced vibrations of vocal folds and influence of their impairments on human voice “.

References

Fant, G. (1960) Acoustic Theory of Speech Production. Mouton, S'Gravenage, 2nd ed.

Feeny, B.F., Kappagantu, R. Proper orthogonal modes in vibrations. (1998) Journal of Sound and Vibration 211(4), 607-616.

Horáček J., Laukkanen AM., Šidlof P., Murphy P., Švec JG. Comparison of acceleration and impact stress as possible loading factors in phonation. A computer modeling study. (2009) Folia Phoniatrica et Logopaedica, 61(3), 137-145.

Luo, H., Mittal, R., Zheng, X., Bielamowicz, S.A., Walsh, R.J., Hahn, J.K. An immersed boundary method for flow-structure interaction in biological systems with application to phonation. (2008) J. Comput. Phys. 227(22), 9303–32.

Vampola T., Horáček J., Laukkanen A.M. Švec J.G. Human vocal tract resonances and the corresponding mode shapes investigated by three-dimensional finite-element modelling based on CT measurement. (2015) Logopedics Phoniatrics Vocology, 40, 14-23; DOI: 10.3109/14015439.2013.775333.

22nd International Conference
ENGINEERING MECHANICS 2016
Svratka, Czech Republic, 9 – 12 May 2016

EXPERIMENTAL ANALYSIS OF TORSION VIBRATION OF HARD RUBBERS UNDER LARGE DEFORMATIONS

P. Šulc*, L. Pešek, V. Bula, J. Cibulka, J. Košina

Abstract: *The paper deals with a stress analysis of hard rubber under large torsion deformations. This study was motivated by effort to enhance the theoretical background for experimental evaluation of material behaviour of hard rubbers on our test rig. First the Mooney Rivlin model (MRM) for shear case of loading was developed and then MRM constants were attained by fitting of the MRM to the experimental torsion-deformation curve. Then the tuned MRM cylindrical model was tested under torsion loading for evaluation of stress state. Besides the radial distribution of shear stress and strain the attention was paid to evaluation of axial stresses. It could help to assess the influence of the tension stresses on the tangential deformations of the test sample during large torsion.*

Keywords: hard rubber, torsion vibration, large deformation, hyperelasticity, parameter identification

1. Introduction

For rubber materials unlike conventional structural materials under dynamic loading, a nonlinear time-varying behavior occurs due to the size of straining, creep, temperature and aging (Pešek, 2008). Tests of rubbers with higher hardness Sh 50-80 (Nashif, 1985) were performed in the laboratories of IT AS CR in recent years. The dynamic tests of hard rubbers require usually a costly long-term operation of heavy hydraulic machines. Therefore we have started to look for realization of the tests in laboratory conditions with the lighter laboratory technique. Currently we have been developing a torsional dynamic test rig for torsional straining of hard rubber samples with a circular cross-section (Šulc, 2014). The reason for torsion straining was that hard rubber materials are softer in torsion than in pressure and therefore it is easier to achieve larger strains. Furthermore at this straining the shape changes are smaller in comparison with pressure loading when so-called barreling effect arises due to incompressibility of the material.

The torsional test rig should serve to dynamic material tests of hard synthetic rubbers for determination of the thermo-viscous-elastic material characteristics under small as well as finite strains, different amplitudes, frequencies and temperatures. This paper deals with the stress analysis of cylindrical samples at larger shear strains (up 10%), which leads to analysis of a nonlinear dependence of shear stress on shear strain and initiation of tensile component along the axis of the sample at larger torsion deformations.

Hence, the aim was to evaluate this stress component to assess its influence on the overall straining of the test sample. Therefore a numerical finite element model (FEM) of a rubber cylinder under the torsional stress considering hyperelasticity and finite strains was created in ANSYS. The five-parametric Mooney-Rivlin model (MRM) was considered. To calculate the constants of the MRM model, analytical relation between shear stress and shear strain were derived. The relation served for identification of the MRM constants on a base of tuning of the constant to achieve an optimal agreement between analytical and experimental stress-strain curves. Finally, the results and analysis of the numerical calculations of the three-parametric MRM model by the FEM are presented.

2. Hyperelastic model of rubber for shear straining

The strain energy of five-parametric MRM model can be expressed as

* Ing. Petr Šulc, PhD., Ing. Luděk Pešek, CSc., Ing. Vítězslav Bula, Jan Cibulka, Ing. Jan Košina : Institute of Thermomechanics of the CAS, v. v. i., Dolejškova 1402/5; 182 00, Prague; CZ, sulc@it.cas.cz

$$W = C_{10}(I_1 - 3) + C_{01}(I_2 - 3) + C_{20}(I_1 - 3)^2 + C_{11}(I_1 - 3)(I_2 - 3) + C_{02}(I_2 - 3)^2 \tag{1}$$

where W is a strain energy and I_1, I_2 are invariants of the Green strain tensor.

Torsion straining of the cylindrical surface is analogous to the straining in a simple shear. Deformation gradient F for the simple shear strain is determined by

$$\mathbf{F} = \begin{pmatrix} 1 & \gamma & 0 \\ 0 & 1 & 0 \\ 0 & 0 & 1 \end{pmatrix} = \mathbf{R} \cdot \mathbf{U} \tag{2}$$

where γ is the shear strain of a segment of the cylinder. Strain gradient **F** is decomposed by polar decomposition to a rotational tensor **R** and a strain tensor **U** (right "stretching" tensor). Then for Green's strain tensor $\mathbf{C} = \mathbf{F}^T\mathbf{F}$ and strain tensor **U** holds

$$\mathbf{C} = \mathbf{F}^T\mathbf{F} = (\mathbf{RU})^T\mathbf{RU} = \mathbf{U}^T\mathbf{R}^T\mathbf{RU} = \mathbf{U}^T\mathbf{U} = \mathbf{U}^2. \tag{3}$$

To determine the principal strains in the “main” directions under the simple shear consideration, first we calculate the Green's strain tensor **C**

$$\mathbf{C} = \mathbf{F}^T\mathbf{F} = \begin{pmatrix} 1 & \gamma & 0 \\ \gamma & 1+\gamma^2 & 0 \\ 0 & 0 & 1 \end{pmatrix}. \tag{4}$$

Then eigenvalues of the Green strain tensor are equal to principal strains of the strain tensor **U**

$$\lambda_1 = U_1 = \sqrt{C_1} = \frac{\sqrt{4+\gamma^2}+\gamma}{2},\ \lambda_2 = U_2 = \sqrt{C_2} = \frac{\sqrt{4+\gamma^2}-\gamma}{2},\ \lambda_3 = U_3 = \sqrt{C_3} = 1. \tag{5}$$

To get MRM constants, we determine the invariants of Green strain tensor by principal strains

$$I_1 = \lambda_1^2 + \lambda_2^2 + \lambda_3^2, \quad I_2 = \lambda_1^2\lambda_2^2 + \lambda_2^2\lambda_3^2 + \lambda_1^2\lambda_3^2, \quad I_3 = \lambda_1^2\lambda_2^2\lambda_3^2. \tag{6}$$

At simple shear deformation there is no volume change. It holds when the third invariant of the Green strain tensor equals to 1 and $\lambda_3 = 1$, too. So, we can express a relation between the remaining two principal strains $\lambda_1 = 1/\lambda_2$. Substituting the strain tensor eigenvalues (principal strains) of (5) into the invariants (6) we get these relations

$$I_1 = 3 + \frac{\gamma^2}{2}, \quad I_2 = 3 + \frac{\gamma^2}{2}, \quad I_3 = 1. \tag{7}$$

Constitutive relation for Cauchy stress expressed in principal strains is

$$\sigma_a = -p + \lambda_a \frac{\partial W}{\partial \lambda_a}, \qquad a = 1, 2, 3 \tag{8}$$

where p is the Lagrange multiplier also called hydrostatic pressure. The constant p is determined incompressible materials from the condition $\sigma_3 = 0$ (Holzapfel, 2000).

If we come from the expressions of the Cauchy principal stress (8) for the simple shear straining of cylindrical surface, after derivation of the strain energy over invariants I_1 and I_2 of the Green strain tensor and after substituting $\lambda = \lambda_1$, $\lambda_2 = \frac{1}{\lambda}$. We can express it in the form

$$\begin{aligned}\sigma_1 &= -p + 2\left(\lambda^2 - \frac{1}{\lambda^2}\right)\left(\frac{\partial W}{\partial I_1} + \frac{\partial W}{\partial I_2}\right)\\ \sigma_2 &= -p + 2\left(1 - \frac{1}{\lambda^2}\right)\left(\frac{\partial W}{\partial I_1} + \lambda^2 \frac{\partial W}{\partial I_2}\right)\end{aligned} \quad . \tag{9}$$

After substitutions and derivations of (9) the Cauchy principal stresses for five-parametric MRM model were arranged (Šulc, 2016) as

$$\begin{aligned}\sigma_1 &= -p + 2C_{10}\left(\lambda^2 - \frac{1}{\lambda^2}\right) + 4C_{20}(I_2 - 3) + 2C_{11}\left(\lambda^2 - \frac{1}{\lambda^2}\right)(I_1 - 3) + \\ &+ 2C_{01}\left(\lambda^2 - \frac{1}{\lambda^2}\right) + 4C_{02}\left(\lambda^2 - \frac{1}{\lambda^2}\right)(I_1 - 3)\\ \sigma_2 &= -p + 2C_{10}\left(1 - \frac{1}{\lambda^2}\right) + 4C_{20}(I_2 - 3) + 2C_{11}\left(1 - \frac{1}{\lambda^2}\right)(I_1 - 3)(1 + \lambda^2) + \\ &+ 2C_{01}\left(1 - \frac{1}{\lambda^2}\right)(I_1 - 3) + 4C_{02}\lambda^2\left(1 - \frac{1}{\lambda^2}\right)(I_1 - 3)\end{aligned} \quad . \tag{10}$$

The final relation for the maximal shear stress from principal stresses σ_1, σ_2 by use of (10) is

$$\tau_{\max} = \frac{1}{2}(\sigma_1 - \sigma_2). \tag{11}$$

The constants of the MRM are evaluated from the experimental shear stress-strain curve using the least square method (LSM) (Šulc, 2016).

3. Numerical results of torsion straining of rubber cylinder under larger strains

Experimental shear stress-strain curve of selected hard rubbers for the MRM constant tuning was obtained by our torsion test rig for a temperature -20°C. The test specimen was of cylindrical shape glued at both heads to steel consoles pins mounting in the collets. By usage of the consoles the test sample is not deformed in the vicinity of the heads due to clamping. The dimensions of the test sample of rubber were: ∅D = 0.05 m, length L = 0.036 m and weight 0.0763 kg. The material was isoprene butadiene rubber (IB) of hardness Sh60 and shear modulus of 11 MPa for a shear strain below 1%, temperature -20°C and frequency 20Hz of torsional loading. Experimental shear stress-strain curve (maximum value of strain is about 8%) is shown in Figure 1. Tuned constants of the three and five-parametric MRM models based on LSM method result in:

a) C_{10} = -0.0224e^9, C_{11} = -0.8023e^9, C_{01} = -0.0075e^9, C_{20} = -2.4963e^9, C_{02} = 1.3316e^9

b) $C_{10} = -1.5610e^7$, $C_{11} = -1.1975e^7$, $C_{01} = 0.5211e^7$.

The relations (1-10) result analogically for three-parametric MRM model where $C_{20} = C_{02} = 0$ (Šulc, 2016). For comparison, the shear stress-strain curves of three- and five-parametric models of MRM together with experimental counterpart are plotted on Figure 2.

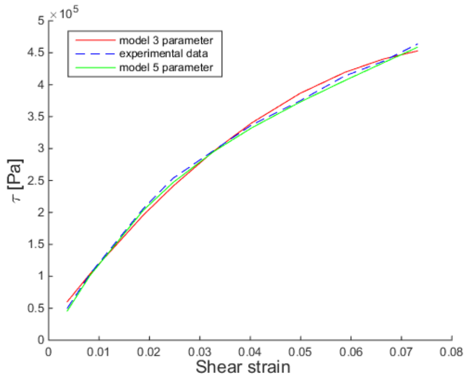

Fig. 1: Comparison of experimental shear stress-strain curve with counterparts of three- and five-parametric MRM models

It is obvious that the five-parametric MRM model fits better to the experimental data. For numerical simulations we come from the cylinder of diameter ∅D = 0.05 m and length l = 0.02. The cylinder was fixed in all nodes of the basis head and was loaded over a rigid plate connected to the upper head of the cylinder by the torque moment M_k=22.5Nm. Two material models, a) elastic model (G = 33MPa), b) three-parametric model MRM with the experimentally tuned constants, were used for the stress and deformation analysis. Linear model corresponds to the analytical solution to a size of shear stresses, tangential displacements and their space distribution. MRM model behaves almost linearly in this range of deformations and gives slightly smaller tangential deformation with respect to the linear model. This difference are caused by different methods of deformation solution (linear versus non-linear) including different representation of the stress-strain curve (Fig.1). The distribution of tension stress σ_{zz} over the surface of the specimen calculated for the non-linear MRM model (case b) is shown in Fig.2. It can be seen that the axial stresses are non-uniformly distributed in the volume of the specimen and their maximal stresses concentrate along the axial axis of the specimen and attenuate with the radial distance from the axis.

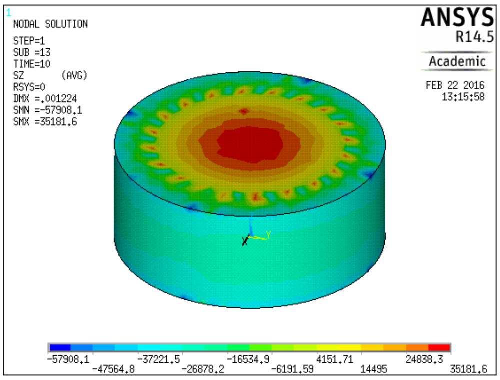

Fig. 2: The contour map of tension stress σ_{zz} distribution over the surface of the sample

By comparing maximal values of the shear and axial stresses for this study case, it is obvious that a size of axial stresses achieve very small values (about 25 times smaller) related to a size of shear stresses at shear deformations at cca 20%.

4. Conclusions

The aim of this paper was to evaluate the influence of the axial stresses arising at cylindrical samples of hard rubbers under large torsional deformations. Therefore the analytical relation for the simple shear stress-strain dependence of the five-parametric MRM model was derived. Both the constants of five-parametric model and analogically the three-parametric MRM model were calculated from the experimental stress-strain curve that we ascertained for the isopren-butadien rubber Sh60. The combined stress distributions of rubber cylinder under the torsional loading and larger strains were calculated by FE method using three-parametric MRM model. The results showed that a non-linearity is very weak for assumed shear strains (up to about 20%). As to the axial stresses it was found that they concentrate mainly around the cylinder specimen axis and reach relatively low maximal values with respect to the maximal values of shear stresses. It can be, therefore, assumed that the side effect of axial stresses does not significantly influences an accuracy of standard evaluation of rubber constants based on the linear theory of elasticity.

However, these theoretical findings are to be validated by the experiment. The torsion scale with a possibility to evaluate the axial tensile force has been developed in our lab and the first experimental results will be shown at the oral presentation at the conference.

Acknowledgement

This research work has been elaborated under financial support for conceptual development of research institutions RVO: 61388998 in the Institute of Thermomechanics, v.v.i., Prague.

References

Holzapfel A. G.(2000) Nonlinear Solid Mechanics, John Wiley&Sons.

Nashif, A. D., Johnes D. I. G., Henderson J. P. (1985): Vibration Damping, John Wiley&Sons.

Pešek, L., Půst, L., Balda, M., Vaněk, F., Svoboda, J., Procházka, P., Marvalová, B.(2008) Investigation of dynamics and reliability of rubber segments for resilent wheel, Procs. of ISMA 2008, KU Leuven, pp. 2887-2902.

Šulc P., Pešek L., Bula V., Cibulka J.,Košina J.(2015) Amplitude-temperature analysis of hard rubber by torsional vibration. Applied Mechanics and Materials - Archive of EM2015.

Šulc P., Pešek L., Bula V., Cibulka J., Košina J.(2016) Přídavná osová napjatost pryžového válce při torzním namáhání a velkých deformacích. Dymamesi 2016. Praha : Institute of Thermomechanics AS CR, v.v.i, s. 57-65.

22nd International Conference
ENGINEERING MECHANICS 2016
Svratka, Czech Republic, 9 – 12 May 2016

MECHANICAL RESPONSE OF COMPOSITES WITH RESPECT TO INCLUSION INTERACTION

S. Šulc*, T. Janda**, J. Novák***

Abstract: *This paper presents the major features of the µMECH micromechanical library, which gives the analytical solutions to micromechanical fields within media comprising ellipsoidal inclusions. The solutions are based on Eshelby´s stress-free eigenstrains and the equivalent inclusion method. Unlike the case of a single inclusion in an infinite matrix, for which the analytical solution is known, a fast and yet robust approach to the problem of multiple inclusions and their mutual interactions is still missing.*

Keywords: Micromechanics, Eshelby´s solution, Polynomial eigenstrains, Multiple inclusion problem.

1. Introduction

In composite materials the strain and stress concentration is of vital interest since it governs crack initializations. Numerical analyses allow us to predict material behaviour and identify regions where the concentration occurs. In the case of a composite consisting of a matrix phase and embedded heterogeneities of an ellipsoidal shape, an approach based on the solution of J. D. Eshelby (1957) to the single inclusion problem can be readily employed. We refer to an ellipsoidal heterogeneity using the term "inclusion". The present contribution describes principles of analytical methods for evaluating the mechanical fields in a particulate composite. The methods are implemented in the µMECH library.

2. Single-inclusion problem

The problem of a single ellipsoidal inclusion in an infinite matrix was successfully solved by J. D. Eshelby in 1951. Making use of Green´s function, Eshelby derived explicit formulae for the strain, stress, and displacement fluctuation fields. His fundamental contribution has been applied in many micromechanical models. In the following, we briefly review the fundamental notions related to the solution.

Assume that a material is subjected to a far field loading that would result in a constant strain $\boldsymbol{\varepsilon}^0$ if the material was homogeneous. However, due to the presence of the inclusion, strain fluctuations, denoted as $\boldsymbol{\varepsilon}^*$, occur in the material. In the sequel we use the term "perturbation" when referring to the fluctuations.

The strain perturbation together with the prescribed external load gives us the total strain as

$$\boldsymbol{\varepsilon}(\mathbf{x}) = \boldsymbol{\varepsilon}^0(\mathbf{x}) + \boldsymbol{\varepsilon}^*(\mathbf{x}). \tag{1}$$

The $\boldsymbol{\varepsilon}_0$ is mapped to the equivalent eigenstrain $\boldsymbol{\varepsilon}^\tau$ through

$$\boldsymbol{\varepsilon}^\tau = \mathbf{B}\colon \boldsymbol{\varepsilon}^0 , \tag{2}$$

where the tensor $\mathbf{B}$ depends on matrix and inclusion parameters. From $\boldsymbol{\varepsilon}^\tau$ we compute the strain, stress and displacement perturbations. In the following we need only the strain perturbation $\boldsymbol{\varepsilon}^*$ computed as

* Bc. Stanislav Šulc, CTU in Prague, Faculty of Civil Engineering, Thákurova 7, 166 29, Prague, CZ, sulcstanda@seznam.cz

** Ing. Tomáš Janda, Ph.D., CTU in Prague, Faculty of Civil Engineering, Thákurova 7, 166 29, Prague, CZ, tomas.janda@fsv.cvut.cz

*** Ing. Jan Novák, Ph.D., CTU in Prague, Faculty of Civil Engineering, Thákurova 7, 166 29, Prague, CZ, novakj@cml.fsv.cvut.cz

$$\boldsymbol{\varepsilon}^*(\mathbf{x}) = \mathbf{D}(\mathbf{x}) : \boldsymbol{\varepsilon}^\tau \; . \tag{3}$$

The tensor **D** depends on the coordinates of the point of interest and again on the matrix and inclusion parameters.

3. Multiple-inclusion problem

In the case of two or more inclusions in a matrix, we have to take their mutual interaction into account. Since there is no analytical solution, we propose a self-compatibility algorithm, which iteratively corrects $\boldsymbol{\varepsilon}^\tau$ of each inclusion, until an acceptable tolerance η between the Euclidean norms of the two consecutive eigenstrains $\boldsymbol{\varepsilon}_\mathrm{i}^\tau$ is achieved.

We approximate the effect of an inclusion *a* on an inclusion *b* as the strain perturbation caused by the inclusion *a* in the centre of inclusion *b*, which we denote $\boldsymbol{\varepsilon}^*_{\mathrm{a}\to\mathrm{b}}$. We take the perturbation as an additional external load on the inclusion *b*.

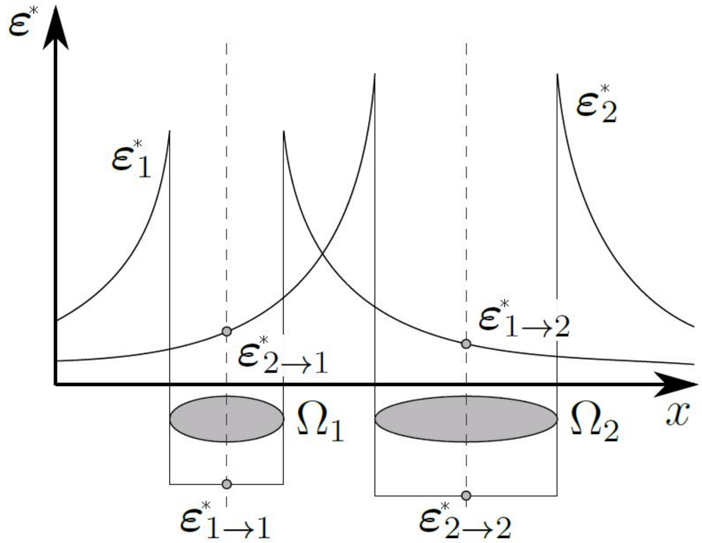

Fig. 1: Multiple-inclusion problem.

The structure of the self-compatibility algorithm for n inclusions can be summarized as follows:

1) **Do**

2) **For**(i ≤ n)

3) $\boldsymbol{\varepsilon}_\mathrm{i}^{\tau,\mathrm{prev}} = \boldsymbol{\varepsilon}_\mathrm{i}^\tau$

4) $\boldsymbol{\varepsilon}_\mathrm{i}^{0,\mathrm{tot}} = \boldsymbol{\varepsilon}^0 + \sum_{\mathrm{k}\in\{1\ldots\mathrm{n}\}\setminus\{\mathrm{i}\}} \boldsymbol{\varepsilon}^*_{\mathrm{k}\to\mathrm{i}}$

5) $\boldsymbol{\varepsilon}_\mathrm{i}^\tau = \mathbf{B}_\mathrm{i} : \boldsymbol{\varepsilon}_\mathrm{i}^{0,\mathrm{tot}}$

6) $\Delta\boldsymbol{\varepsilon}_\mathrm{i}^\tau = \boldsymbol{\varepsilon}_\mathrm{i}^\tau - \boldsymbol{\varepsilon}_\mathrm{i}^{\tau,\mathrm{prev}}$

7) **EndFor**

8) **While**$\left(\sum_{\mathbf{k}}^{\mathbf{n}} \left|\left|\Delta\boldsymbol{\varepsilon}_\mathrm{k}^\tau\right|\right| < \eta\right)$

At each iteration step, we update $\boldsymbol{\varepsilon}_\mathrm{i}^0$ of the *i*-th inclusion as a sum of the prescribed external load $\boldsymbol{\varepsilon}^0$ and the strain perturbations caused by the remaining inclusions evaluated in the centre of the *i*-th inclusion. With the modified $\boldsymbol{\varepsilon}_\mathrm{i}^0$ we update the equivalent eigenstrain $\boldsymbol{\varepsilon}_\mathrm{i}^\tau$. The comparison of results with and without using this algorithm are in Fig. 3.

5. Polynomial eigenstrains

Introducing the effect of the remaining inclusions only through strain perturbation at centre of the treated inclusion gives sufficiently good results if the inclusions are distant enough such that the gradient of the eigenstrain is negligible compared to the average value of the eigenstrain in this case. However, when the inclusions get closer, the gradient starts to play an important role, see Fig. 1. In the vicinity of the considered inclusion it is not even close to linear function. As a result, the average value for an inclusion deviates significantly from the value in its centre leading to the underestimated results.

This drawback can be diminished by replacing the constant eigenstrains with a polynomial function and using the known analytical solutions for polynomial eigenstrains. In particular, we have implemented the linear approximation, which seems to be sufficiently accurate even for short distance interaction.

As an example we have analyzed a 2D problem consisting of three circular inclusions. Geometry of the task is depicted in Fig. 2. All the inclusions have radius 1.0 m. Young´s modulus of the inclusion material is 10.0 with the Poisson´s ratio of value 0.3. The matrix Young´s modulus was assumed 1.0 and the Poisson´s ratio 0.2. The prescribed external load corresponded to the uniaxial strain with the only non-zero component $\varepsilon_x^0 = 1.0$.

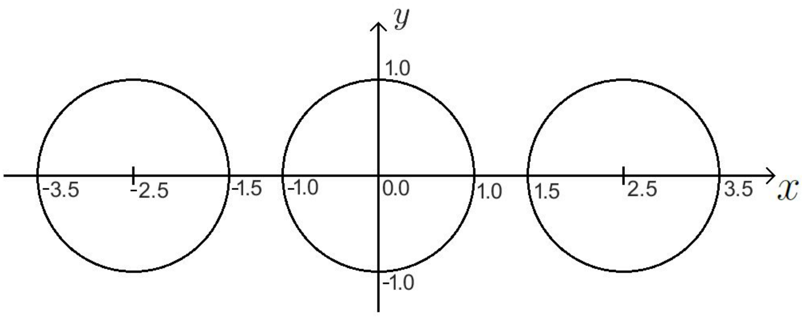

Fig.2: Scheme of the three-inclusion problem.

Fig. 3 shows a comparison of the proposed solutions and the reference solution obtained with Finite Element Method (FEM). Outside the group of inclusions the results provided by the polynomial solution closely resemble the FEM results. The importance of the self-compatibility algorithm and polynomial approximation of $\boldsymbol{\varepsilon}^{\tau}$ gets further pronounced in the regions among inclusion, where the interactions play a significant role.

4. Internal perturbation fields

In the multiple-inclusion problem the internal strain and stress perturbations are not constant and we cannot simply sum all the perturbations as we do in the case of points that are not in any inclusion. The first option to compute the internal fields is to use the polynomial solution also for the internal points. However, this leads to the loss of detailed distribution of eigenstrain which is limited by the polynomial approximation.

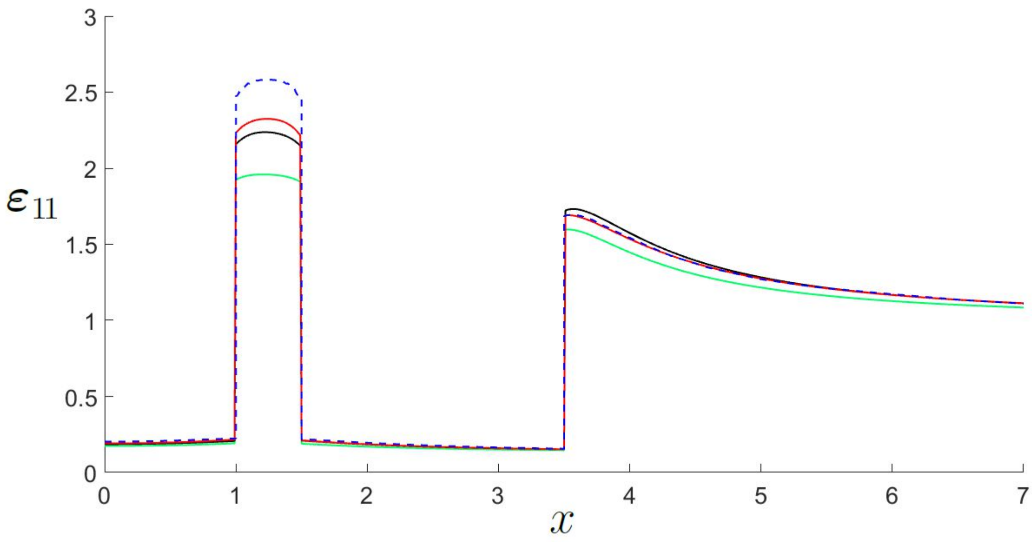

Fig.3: Results of the three-inclusion problem. Blue line: FEM.
Red line: Linear approximation of the $\boldsymbol{\varepsilon}^{\tau}$ with self-compatibility algorithm.
Black line: Constant $\boldsymbol{\varepsilon}^{\tau}$ with self-compatibility algorithm.
Green line: Constant $\boldsymbol{\varepsilon}^{\tau}$ without self-compatibility algorithm

We get the most accurate results employing the same principle as in the self-compatibility algorithm. We compute the strain perturbations of all other inclusions first. We sum them with the prescribed external load and take it as a new load for the inclusion with the point inside. Then, we map this load to $\boldsymbol{\varepsilon}^{\tau}$ and compute $\boldsymbol{\varepsilon}^{*}$ from Eq. 3.

We compute the stress and displacement perturbations in the usual way, the only difference is that we use this recalculated $\boldsymbol{\varepsilon}^{\tau}$ instead of the one evaluated in the self-compatibility algorithm.

6. Conclusions

The present results confirm the importance of accounting for the interaction among inclusions. We have presented two approximate solutions. In the first, the interaction was taken into account by employing the self-compatibility algorithm arising from the assumption of the constant equivalent eigenstrain within inclusions. In the second approach, we have extended this approach with the linear approximation. As expected, the latter approach gives better results when compared with the reference solution obtained with a Finite Element Method (FEM). Albeit the accuracy of the FEM solution was not reached the present methods yielded sufficiently accurate results with respect to their intended application. The µMECH library can solve much larger problems in a fraction of time when compared to FEM and thus provide fluctuation fields as a global enrichment functions for the generalized finite element methods. Our further effort aims improving the accuracy by quadratic polynomial approximation of the eigenstrains.

Acknowledgement

We gratefully acknowledge the financial support from the Grant Agency of the Czech Technical University in Prague, the grant SGS16/037/OHK1/1T/11.

We also gratefully acknowledge the financial support from the Czech Science Foundation, the grant GACR 13-22230S.

References

J. D. Eshelby, The determination of the elastic field of an ellipsoidal inclusion, and related problems, Proceedings of the Royal Society of London. Series A, Mathematical and Physical Sciences 241 (1226) (1957) 376-396.

22nd International Conference
ENGINEERING MECHANICS 2016
Svratka, Czech Republic, 9 – 12 May 2016

CONTROL SYSTEM OF DELTA MANIPULATOR WITH PNEUMATIC ARTIFICIAL MUSCLES

J. E. Takosoglu*

Abstract: *A project of control system and electro-pneumatic delta manipulator of three degrees of freedom with pneumatic muscle actuators was presented in this paper. Due to the features of the drives applied, the manipulator is characterised by quick action, smooth start and stop, high overload capacity as well as a great number of operating cycles in relation to traditional pneumatic cylinders. A standard PID controller was applied in the control system. The process of tuning PID controller with Ziegler-Nichols method that is based on the evaluation of the system, which is on the verge of stability, was presented herein. An analysis the quality of control for the suggested controller was conducted and the results of experimental research of positioning the effector of the delta manipulator are included as well.*

Keywords: pneumatic muscle actuator, electro-pneumatic manipulator, delta manipulator, PID controller, performance criteria.

1. Introduction

Manipulators and industrial robots with pneumatic drives are applied mainly in the processes of assembling, packing or palletizing (Miko & Nowakowski, 2012a, 2012b). The pneumatic actuators provide sufficiently large operating dynamics, however, they do not provide high positioning accuracy (Takosoglu et al., 2009). It results directly from the functional properties of pneumatic actuators and the working medium, namely compressed air. Friction force in the pneumatic actuators, which introduces huge nonlinearities (S. Blasiak et al., 2013; S. Blasiak et al., 2014a; S. Blasiak & Pawinska, 2015; S. Blasiak, 2015) and thus, prevents obtaining more precise and detailed motions with full trajectory control (Koruba et al. 2010; Krzysztofik & Koruba, 2012), constitutes an additional problem. Pneumatic manipulators are designed mainly as systems with serial kinematics. Rigidity of the structure is the decisive factor that influences the positioning accuracy of the manipulators. Serial kinematic structures of robots and manipulators, in which drive axes are mounted on each other, become deformed under the influence of load masses as well as the weight of the drives themselves. It might lead to a situation, when the deformities are cumulated at the end of the kinematic chain and thus, the positioning accuracy deteriorates. The analysis of the simulative and experimental research of multi-axis pneumatic manipulators with the Cartesian coordinate system revealed that the positioning accuracy of the effector is several times smaller than of a single drive axis. Kinematic structure, thanks to which construction and drives deformities might be decreased, is based on a closed kinematic chain – parallel structure (Laski et al., 2015).

2. Control system

The control system of delta manipulator with pneumatic muscle actuators (Laski, et al., 2014) was built on the basis of the diagram presented in Fig. 1a. Fig. 1b presents the general view of the manipulator. For building the control system the following elements were applied:

- artificial pneumatic muscles DMSP-10-300, diameter of 10 mm and length of 300 mm (Festo),

- piezoelectric proportional pressure valves tecno plus PRE-U2-00-11-21, pressure 0-10 bar, flow up to 1600l/min., voltage controlled 0-10 V (Parker Origa),

*BSc Jakub Emanuel Takosoglu, PhD.: Faculty of Mechatronics and Mechanical Engineering, Kielce University of Technology, Aleja Tysiaclecia Panstwa Polskiego 7, 25-314, Kielce; PL, qba@tu.kielce.pl

- angle encoders MAB36A, 12-bit, rotation angle of 360°, analog output 0-10V (Megatron),

- real time system for rapid control prototyping and hardware in the loop simulation *xPC Target* (MathWorks),

- laboratory computer system with 16-bit AC and CA cards *education real-time target machine* (Speedgoat).

Control of pneumatic muscles consists in changing the pressured air inside the muscle. That is why, piezoelectric proportional pressure valves were applied to control. The valves used in the control system are equipped with the system of electronic control of the outlet pressure (S. Blasiak et al., 2014b; Takosoglu et al., 2014) and thus, they automatically compensate the overload of working platform of the manipulator, e.g. in case of sudden hit or collision of the platform with an obstacle. The piezoelectric method applied in the valves provides very high dynamics (M. Blasiak & Kotowski, 2009) with a minimum energy consumption (max. power 0,8 W). Thanks to such solution, battery or accumulator power (Nadolski & Ludwinek, 2012) of valves is possible.

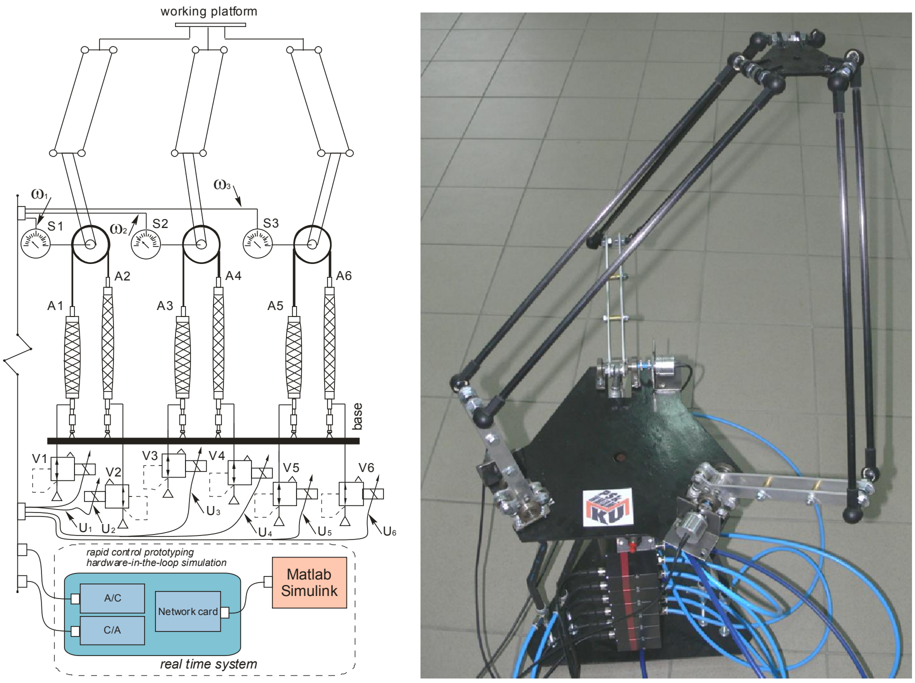

Fig. 1: Diagram of control system a): A – pneumatic muscles, S – angle sensors, V – proportional pressure valves, ω – feedback signal, U – control signal, General view of delta manipulator b)

A typical PID controller was used for controlling the proportional pressure valves. In the control system, three identical PID controllers were used due to the necessity to control three drive axes of the manipulator. The process of tuning PID controller was conducted with Ziegler-Nichols method that is based on the evaluation of the system, which is on the verge of stability (Farana et al., 2014). This method is applied in systems, where it is possible to find some gain, when Nyquist diagram intersects the tipping point or when the first root line intersects the axis of imaginary numbers. Such gain, defined as critical gain might be determined in an experimental way. In the control system, PID controller should be set only for proportional action (action I and D should be turned off), and the gain in action P should be gradually increased until oscillations of constant amplitude appear in the output. The point obtained in that way corresponds to the critical gain kp_{kr} and oscillations with the period T_{OSC}. In some practical applications, such operation might be very dangerous. The control system of the delta manipulator was brought to the verge of stability and the parameters of critical gain kp_{kr}=3.69 and the oscillation period T_{OSC}=0.2 sec. were determined. PID parameters were conducted by means of Ziegler-Nichols tuning rules.

The implementation of PID controller was conducted on the basis of real time system (Wisniewski & Plonecki, 2015) xPC Target of set Matlab/Simulink as well as the laboratory computer system education real-time target machine, taking advantage of the method of rapid control prototyping. The input signals from angle encoders were attached to AC cards, and the output signals from CA cards that were generated on the basis of the control algorithm PID were connected to proportional pressure valves controlling the pneumatic muscles. The control system works in real time with the sampling time of 0.001 sec.

3. Experimental research

The aim of the experimental research was to determine the accuracy and repeatability of positioning of the effector's manipulator in a closed loop with PID controller for particular mass loads. Studies with mass load of the operating platform of the manipulator of 0-3.6 kg, being changed every 0.2 kg, were conducted. Fig. 2a presents dynamic characteristics of first axis of the angular displacement of the manipulator arm for four chosen load masses of a working platform. The studies were conducted for the movement of the manipulator platform along the axis Z. That is why, the remaining two arms make the same movement (Trochimczuk, 2013). The trajectories of manipulator platform for the movement along the axis Z in Cartesian space (Gapinski et al., 2014; Krzysztofik, 2012) for 3 chosen load masses were presented in Fig. 2b.

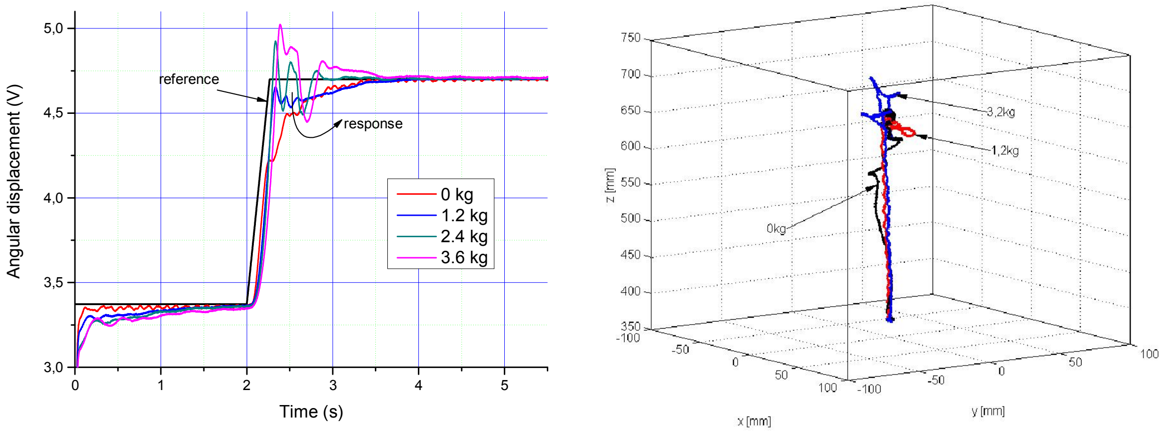

Fig 2: Dynamic characteristics a), Trajectories of manipulator platform b)

An analysis the quality of control in the function of mass load of the working platform was conducted. Fig. 3a presents the results of the experimental research of overshoot, whereas Fig. 3b contains the results of the integral quality indicator ISE (Integral of Squared Error) (Takosoglu et al., 2012).

4. Conclusions

Taking the achieved results into consideration, it was concluded that the manipulator operates well towards load mass of max. 3.6 kg. The positioning accuracy decreases as the load mass of the working platform of the manipulator increases. The integral indicator ISE shows that small load mass influencing the working platform of 0.2-1.4 kg is the most precise in terms of positioning (smaller indicator). In connection with this, the manipulator will operate very well with effector with the weight of 0.2-1.4 kg.

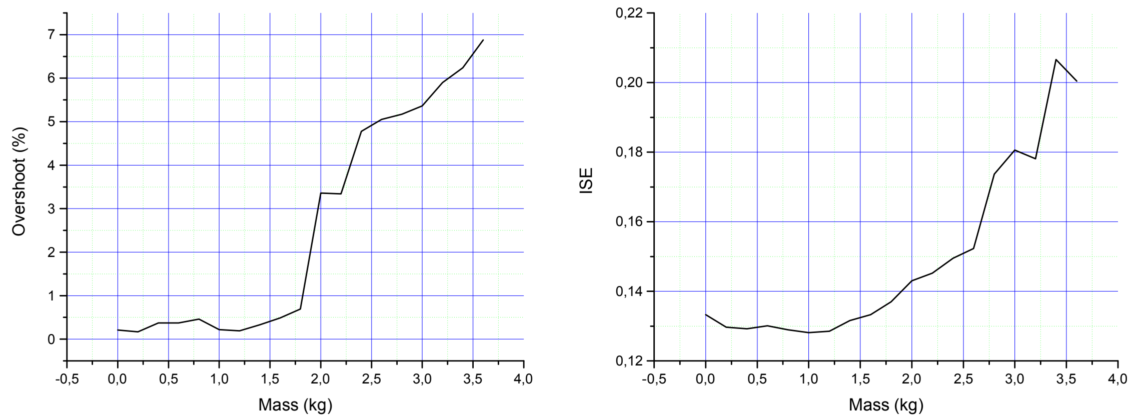

Fig. 3: The influence of load mass on: overshoot a), ISE b)

The designed control system allows changeover, follow-up, and teach/playback control. The manipulator is robust to external loads of the working platform, such as sudden hits against the platform or collisions of the platform with an obstacle. Such cases are automatically compensated due to: the type of drives applied therein (possibility to overload the pneumatic muscles without the necessity to use safety devices), the control valves that were used (proportional pressure valves with electronic control of the output pressure) and the control system applied.

References

Blasiak, M., & Kotowski, R. (2009). Propagation of acoustic waves in piezoelectric crystals. Przeglad Elektrotechniczny, 85(12), 40–43.

Blasiak, S. (2015). An analytical approach to heat transfer and thermal distortions in non-contacting face seals. International Journal of Heat and Mass Transfer, 81, 90–102.

Blasiak, S., Laski, P. A., & Takosoglu, J. E. (2013). Parametric analysis of heat transfer in non-contacting face seals. International Journal of Heat and Mass Transfer, 57(1), 22–31.

Blasiak, S., & Pawinska, A. (2015). Direct and inverse heat transfer in non-contacting face seals. International Journal of Heat and Mass Transfer, 90, 710–718. http://doi.org/10.1016/j.ijheatmasstransfer.2015.07.004

Blasiak, S., Takosoglu, J. E., & Laski, P. A. (2014a). Heat transfer and thermal deformations in non-contacting face seals. Journal of Thermal Science and Technology, 9(2). http://doi.org/10.1299/jtst.2014jtst0011

Blasiak, S., Takosoglu, J. E., & Laski, P. A. (2014b). Optimizing the flow rate in a pneumatic directional control valve, in: Proc. 20th International Conference on Engineering Mechanics 2014 (V. Fuis ed), Brno Univ Technol, pp. 96–99.

Farana, R., Walek, B., Janosek, M., & Zacek, J. (2014). Fuzzy-Logic control in fast technological processes. In Proceedings of the 2014 15th International Carpathian Control Conference (ICCC) (pp. 105–108). IEEE.

Gapinski, D., Koruba, Z., & Krzysztofik, I. (2014). The model of dynamics and control of modified optical scanning seeker in anti-aircraft rocket missile. Mechanical Systems and Signal Processing, 45(2), 433–447.

Koruba, Z., Dziopa, Z., & Krzysztofik, I. (2010). Dynamics and control of a gyroscope-stabilized platform in a self-propelled anti-aircraft system. Journal of Theoretical and Applied Mechanics, 48(1), 5–26.

Krzysztofik, I. (2012). The dynamics of the controlled observation and tracking head located on a moving vehicle. Solid State Phenomena, 180, 313–322. http://doi.org/10.4028/www.scientific.net/SSP.180.313

Krzysztofik, I., & Koruba, Z. (2012). Model of dynamics and control of tracking-searching head, placed on a moving object. Journal of Automation and Information Sciences, 44(5), 38–47.

Laski, P. A., Takosoglu, J. E., & Blasiak, S. (2014). A delta type closed kinematics chain with pneumatic muscle actuator manipulator, in: Proc. 20th International Conference on Engineering Mechanics 2014 (V. Fuis ed), Brno Univ Technol, pp. 360–363.

Laski, P. A., Takosoglu, J. E., & Blasiak, S. (2015). Design of a 3-DOF tripod electro-pneumatic parallel manipulator. Robotics and Autonomous Systems, 72, 59–70. http://doi.org/10.1016/j.robot.2015.04.009

Miko, E., & Nowakowski, L. (2012a). Analysis and verification of surface roughness constitution model after machining process. Procedia Engineering, 39, 395–404. http://doi.org/10.1016/j.proeng.2012.07.043

Miko, E., & Nowakowski, L. (2012b). Vibrations in the machining system of the vertical machining center. Procedia Engineering, 39, 405–413. http://doi.org/10.1016/j.proeng.2012.07.044

Nadolski, R., & Ludwinek, K. (2012). Utilization of BLDC motor in electrical vehicles. Przeglad Elektrotechniczny, (4), 180–186.

Takosoglu, J. E., Dindorf, R. F., & Laski, P. A. (2009). Rapid prototyping of fuzzy controller pneumatic servo-system. International Journal of Advanced Manufacturing Technology, 40(3-4), 349–361.

Takosoglu, J. E., Laski, P. A., & Blasiak, S. (2012). A fuzzy logic controller for the positioning control of an electro-pneumatic servo-drive. Proceedings of the Institution of Mechanical Engineers, Part I: Journal of Systems and Control Engineering, 226(10), 1335–1343. http://doi.org/10.1177/0959651812456498

Takosoglu, J. E., Laski, P. A., & Blasiak, S. (2014). Innovative modular pneumatic valve terminal with self-diagnosis, control and network communications, in: Proc. 20th International Conference on Engineering Mechanics 2014 (V. Fuis ed), Brno Univ Technol, pp. 644–647.

Trochimczuk, R. (2013). Conception of arm of medical robot dedicated to application of minimally invasive surgery. Solid State Phenomena, 198, 3–8. http://doi.org/10.4028/www.scientific.net/SSP.198.3

Wisniewski, H., & Plonecki, L. (2015). The dynamic properties of the IPMC polymer. In Proceedings of the 2015 16th International Carpathian Control Conference (ICCC) (pp. 594–598). IEEE.

22nd International Conference
ENGINEERING MECHANICS 2016
Svratka, Czech Republic, 9 – 12 May 2016

INVARIANTS OF SIMPLE NOZZLES

V.Tesař*

Abstract: *Paper presents a new concept: invariants of second order. The idea bypasses the necessity of geometric similarity (allowing only scaling up or down) in working with dimensionless criteria parameters. Practical aspects of the approach are demonstrated on family of simple nozzles, with different lengths of exit channels. While fluid flow in each nozzle is characterised by its primary invariant, the family as a whole is characterised by additional two secondary invariants.*

Keywords: Invariants, Secondary invariants, Nozzles, Single-parameter nozzle family

1. Introduction

Even though researchers themselves may be not aware of the fact, the ultimate goal of all research activities in physical sciences is to identify ***invariants*** of the investigated problem. In fluid mechanics, this usually means identifying the expressions (usually dimensionless combination of parameters) that remain constant (Fig.1) when magnitude of fluid flow rate passing through the investigated domain is varied. Generally believed to be sine-qua-non condition for the application of the similarity approach is *geometric similarity of* individual cases, varying only in their size. Author now extends the concept of invariants to quasi-similar geometries, demonstrated on family of shapes characterised by two secondary invariants, Fig. 2. It is demonstrated on the case of single-parameter family of simply shaped nozzles having different exit channel lengths There is an analogy with the quasi-similarity of turbulent jets discussed in Tesař and Kordík (2009). The two secondary invariants are a starting point: the number of the invariants increases with each added geometric degree of freedom.

2. Methods

Nozzles are not used alone. They are, instead, components of a hydraulic or aerodynamic system. For proper operation in a system, behaviour of any nozzle should be fully characterised by a numerical parameter - together with some size factor, usually exit diameter d. Until now is in this characterisation role used discharge coefficient (or Euler number Eu, with which it is uniquely related). This is not satisfactory: the coefficient varies with varying fluid flow rate. A really universal validity was demonstrated for the newly introduced coefficient c_T, derived in Tesař (2008). The idea of c_T is based on two hypotheses:

(1) Hydraulic loss in a nozzle is uniquely dependent on displacement thickness δ_* of the boundary layer that forms on internal walls exposed the to fluid flow. Euler number is evaluated from δ_* as $Eu = (1 - 2\delta_*/d)^{-4}$.

(2) The displacement thickness δ_* varies with nozzle exit Reynolds number as $\delta_* = c_T\, d/\sqrt{Re}$. This actually assumes laminar character, an acceptable assumption because the favourable pressure gradient in nozzles delays transition into turbulence.

The first hypothesis ceases to be valid at extremely low Reynolds numbers, due to mutual interference of the too thick boundary layer on opposite sides of the nozzle exit. Another limit of validity is at extremely large Reynolds numbers, where the flow in the exit channel ceases to be laminar.

* Prof. Ing. Václav Tesař CSc., Intitute of Thermomechanics CAS, Dolejškova 5, 182 00 Prague, CZ tesar@it.cas.cz

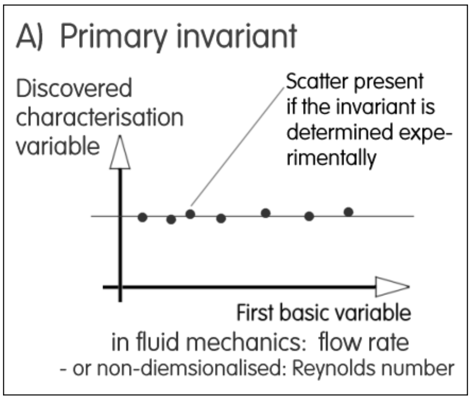

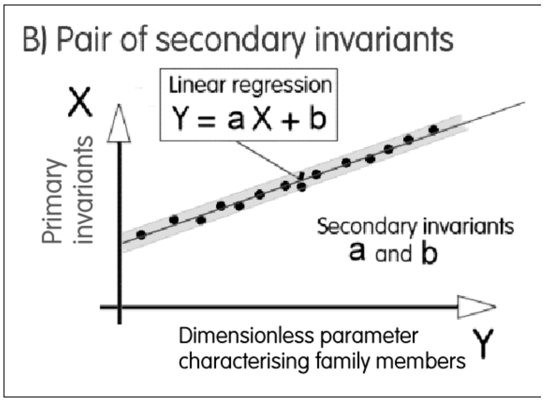

Fig. 1 (left): What all research activities should achieve as their final result is discovering – or deriving, using a mathematical model – the primary invariants of the solved problem.

Fig. 2 (right): Secondary invariants for single-parameter geometries exist in pairs. They are evaluated from dependence between variables which, with some good luck, may be transformed into a linear function with the secondary invariants **a** *and* **b**, *evaluated by the east-squares regression.*

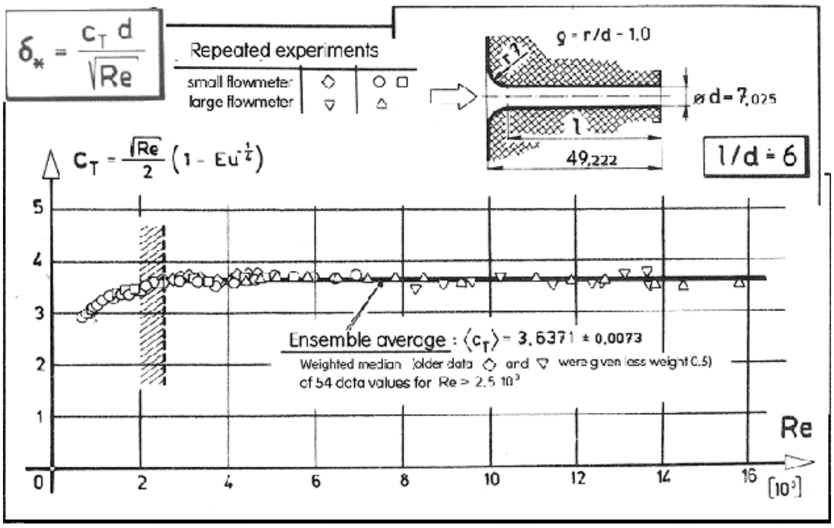

Fig. 3: Demonstrated invariance of the shape coefficient c_T *for a nozzle with quadrant-shaped inlet and constant-diameter exit channel. The deviation at small Reynolds numbers (roughly below* Re ~2500*) is due to mutual interaction of too thick boundary layers on the opposite sides of the nozzle exit, making one of the hypotheses invalid.*

3. The pair of secondary invariants

Derivation of the two hypotheses was based on the idea of nozzle exit blockage by the boundary layer. Validity is fully supported by constant c_T values obtained experimentally for a large number of various nozzles, with examples shown in Figs. 3 and 4. Shapes of the two nozzles there are different and classical hydrodynamics would therefore consider comparing these two cases impossible. Of course, the boundary layer in the shorter nozzle is thinner and with this agrees the lower value c_T in Fig. 4 — but going beyond this fact would similarity approach consider unreasonable**.** Author has, however, performed repeated measurements of pressure losses in altogether 7 quadrant-entrance nozzles (similar to shown in Fig, 3 but of various lengths). The data of primary invariants c_T are then presented in Fig. 5 as a function of the relative exit channel lengths. Transformation of the co-ordinates in the diagram have also made possible placing the data points on a common straight line, the Gauss' linear regression (Seal, 1967) thus enabling an easy evaluation of the two secondary invariants.

This procedure may seem to be simple and perhaps obvious. It should be, however, emphasised that what was achieved is actually breaking an old dogma of impossible comparison of flows in different domain shapes. Within reasonable limits of Reynolds number range, it is possible to predict with reasonable accuracy nozzle behaviour, thus marking the road to possible procedures as, e.g., optimisation of hydraulic circuits.

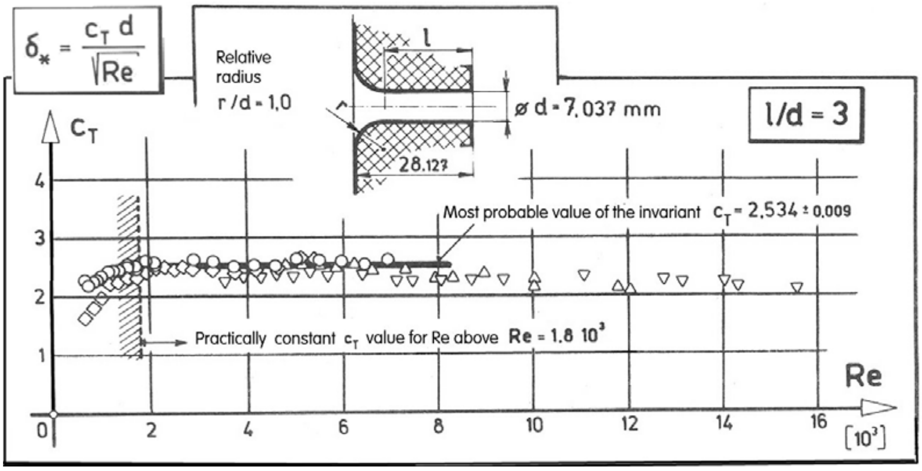

Fig. 4: Invariant c_T *of the short* l /d = 3 *nozzle. The scatter is larger than in Fig. 3 but the behaviour is fully characterised with accuracy needed in engineering calculations. Also here the boundary layer thickness becomes comparable with the nozzle exit diameter* d *at low Reynolds numbers, here below* Re ~ 1.8 10^3.

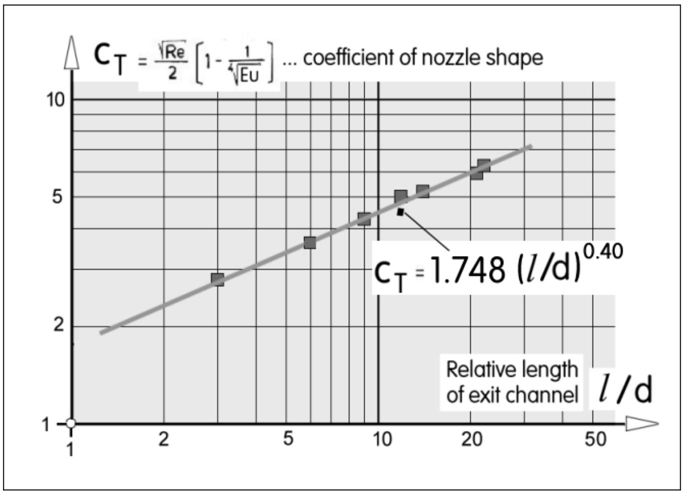

Fig. 5: Two secondary invariants a = 1.748 *and* b = 0.40 *found for the family of nozzles shaped as shown in Figs. 3 and 4, with various exit channel lengths l* /d.

4. Extension to very low Re

Recent development of low Reynolds number microfluidics, as discussed e.g. in Tesař (2007), has shifted interest in fluid mechanics towards the flows that were earlier considered negligible – as is the case of the very small Re values in Figs. 3 and 4, where the above described search for invariants fails because of the violation of the displacement thickness model. At low Reynolds numbers the boundary layer thickness grows extremely rapidly with decreasing Re so that he parts of the layer on the mutually opposed positions inside the exit channel begin to interact. The Reynolds number alone then ceases to be the determining parameter for the character of the flow – it is replaced in this role by Boussinesq number Bo = Re/(l/d). Below the approximate limiting value Bo ~ 50 the whole concept of boundary layer actually loses sense. If the flow rate is decreased further, then in the asymptotic limit the fully developed Hagen-Poiseuille flow takes place for which Eu = 64 / Bo. This is a useful starting point for the alternative approach to the search for invariants of the flow in the nozzle exit channels. The complicating factor

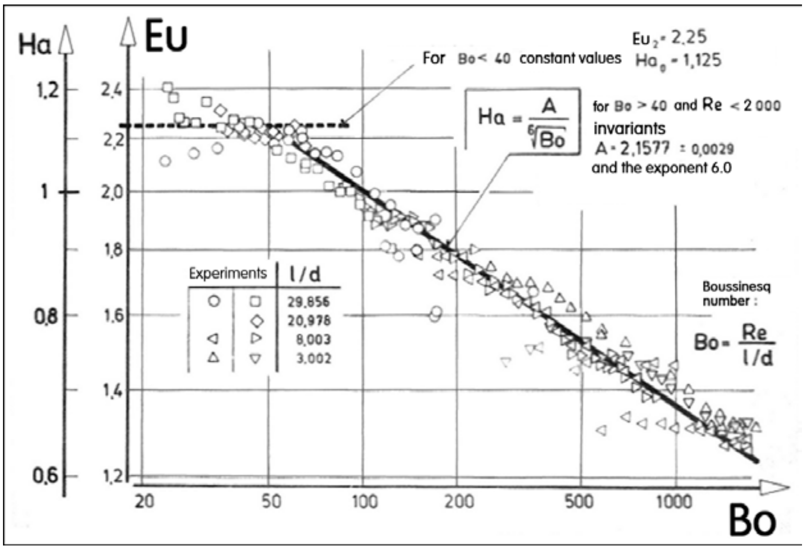

Fig. 5: The law of local quasi-similarity of discussed nozzles at very low Reynolds numbers, where the c_T invariance is lost. The two secondary invariants for this regime, the Boussinesq number Bo and Euler number Eu, were derived from a pipe flow model with initial development characterised by Hagenbach number Ha.

in real laminar pipe flows is the behaviour of the flow at the entrance part of the exit channel. Historically, this region of flow development caused trouble in capillary viscometry, where Hagenbach (1860) found good correspondence with experimental data if the classical law is supplemented by an additive correction term, so that: $\mathrm{Eu} = 64 / \mathrm{Bo} + 2\,\mathrm{Ha}$. Inadequacy of this approach was caused the wrong idea of Ha being constant. If it is, instead, taken to be a variable dependent on the Boussinesq number Bo, the Hagenbach's approach becomes very useful. Author's experimental data plotted in Fig. 5 show a very good correlation - with the fitted power law indicating another pair of the secondary invariants.

5. Conclusions

Author's experimental data demonstrate constant value of the characterisation invariant c_T of tested nozzles. Geometric quasi-similarity, with characterisation by secondary invariants, was then demonstrated for family of nozzles having different exit channel lengths and hence not similar. At very low Re, of interest in microfluidics, one of the underlying hypotheses is not valid and this required another approach to secondary invariance.

Acknowledgements

Author is grateful to GAČR — the Grant Agency of the Czech Republic — for financial support by the research grant Nr. 13-23046S. There was also institutional support RVO:61388998.

References

Tesař V. (2008) Characterisation of subsonic axisymmetric nozzles, Chemical Engineering Research and Design, 86, p. 1253.

Tesař V., Kordík J. (2009) Quasi-similarity model of synthetic jets, Sensors and Actuators A-Physical, 149, p. 255 Chapter "Impinging jets", in "Vortex rings and jets", (2015), Springer Singapore pp. 191-231

Tesař V. (2010) Characterisation of inexpensive, simply shaped nozzles, Chemical Engineering Research and Design, 88, p. 1433

Seal H. S. (1967) The historical development of the Gauss linear model, Biometrika 54, 1. Tesař V. (2007) Pressure-driven microfluidics, Artech House Publishers, Boston-London.

Hagenbach E. (1860) Über die Bestimmung der Zähigkeit einer Flüssigkeit duch den Ausfluss aus Röhren, Annalen der Physik und Chemie, 109, 25.

22nd International Conference
ENGINEERING MECHANICS 2016
Svratka, Czech Republic, 9 – 12 May 2016

GEOMETRIC SIZE EFFECT IN RELATION TO THE FATIGUE LIFE OF S355J2+C STEEL UNDER VARIABLE BENDING CONDITIONS

T. Tomaszewski*, P. Strzelecki, J. Sempruch*****

Abstract: *The fatigue tests are mainly carried out on the specimens with dimensions, which differ from actual tested items. Failure to allow for the item size in engineering practice can lead to significant errors in the assumed fatigue life of structural materials. The size effect is a complex phenomenon and no universal analytical or numerical models are currently available. The material strength decreases with the increase in size of the tested item subject to monotonic or fatigue loads. The reduction in strength is affected by the factors related to a random distribution of defects in the material, shape and type of load and the effects of technological processes during production. The study analyses the size effect in a geometrical approach. The test conditions (rotary bending) allow to estimate the stress gradient effect on the fatigue life. The tests were carried out on specimens to PN-H-04326 and specimens with reduced cross-sectional area (minispecimens).*

Keywords: Steel, High-cycle fatigue, Size effect, Minispecimen.

1. Introduction

Data about materials used for engineering computations should address the size effect or, otherwise, assumptions about various magnitudes can go astray. It is particularly true of heterogeneous materials (Carpinteri et al., 2009).

The size effect is a complex phenomenon depending on material structure, specimen size, load type and component manufacturing process (Kuguel, 1961), which means there are no universally applicable analytical or numerical models. How the size effect affects fatigue properties depends on material type and local structural features (such as grain size, microcracks, inclusions, discontinuities, dislocations and other flaws) (Bažant, 1984).

In general, fatigue is assumed to be reversely proportional to the structure size. This change is typically non-linear and valid up to a certain structure size limit (Sonsino et al., 2005).

This paper aims to determine the size effect for steel S355J2+C. Related monotonic and fatigue tests used specimens smaller than the standard ones. The size effect is described using some generic equations (coefficient of size of cross-section K (Tomaszewski et al., 2014a). The tests on the minispecimens described in the works of authors (Tomaszewski et al., 2012, 2014b).

2. Experimental tests

Experimental tests were done for steel S355J2+C. The specimens were cut out from a 10 mm diameter drawn bar. This material is generally used for the manufacture of machine components. See Fig. 1 and Tab. 1 for geometries of the fatigue test specimens. Each specimen for the static elongation test had a fixed-diameter bore for extensometer: 25 mm long for standard specimen or 12.5 mm long for minispecimen.

* Dr. Ing. Tomasz Tomaszewski, Institute of Mechanical Engineering, University of Technology and Life Sciences, 85-789 Bydgoszcz, Poland; PL, e-mail: tomaszewski@utp.edu.pl

** Dr. Ing. Przemysław Strzelecki, Institute of Mechanical Engineering, University of Technology and Life Sciences, 85-789 Bydgoszcz, Poland; PL, e-mail: p.strzelecki@utp.edu.pl

*** Prof. Ing. Janusz Sempruch, Institute of Mechanical Engineering, University of Technology and Life Sciences, 85-789 Bydgoszcz, Poland; PL, e-mail: semjan@utp.edu.pl

The effect of geometry was checked by determination of the aspect ratio α_k for the both specimen types, using the finite element method. The values of α_k were similar in the both cases, so the shape of the specimens should not produce any discrepancies in test results.

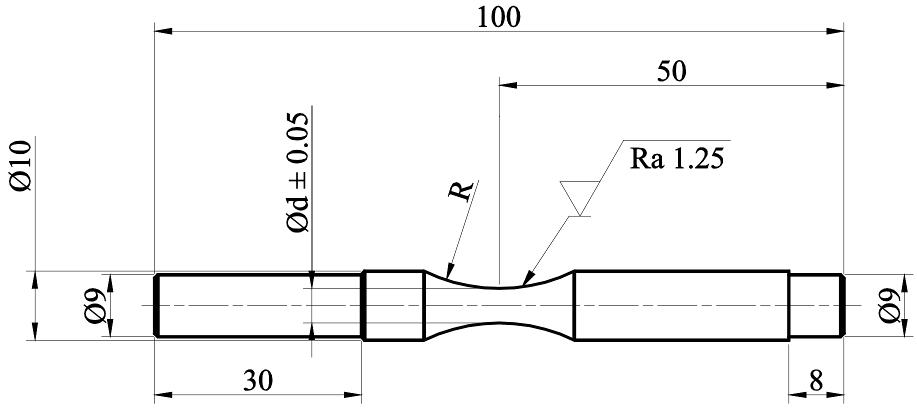

Fig. 1: Specimen geometry used in fatigue test (PN-74/H-04327).

Tab. 1: Specimen dimensions.

Type of geometry	d [mm]	R [mm]	S_o [mm^2]
Standard specimen	5	25	19.6
Minispecimen	2	12.5	3.1

The physical properties of steel S355J2+C were determined experimentally, by a static elongation test (acc. to PN-EN ISO 6892-1:2010). See Fig. 2 and Tab. 2 for the mean values.

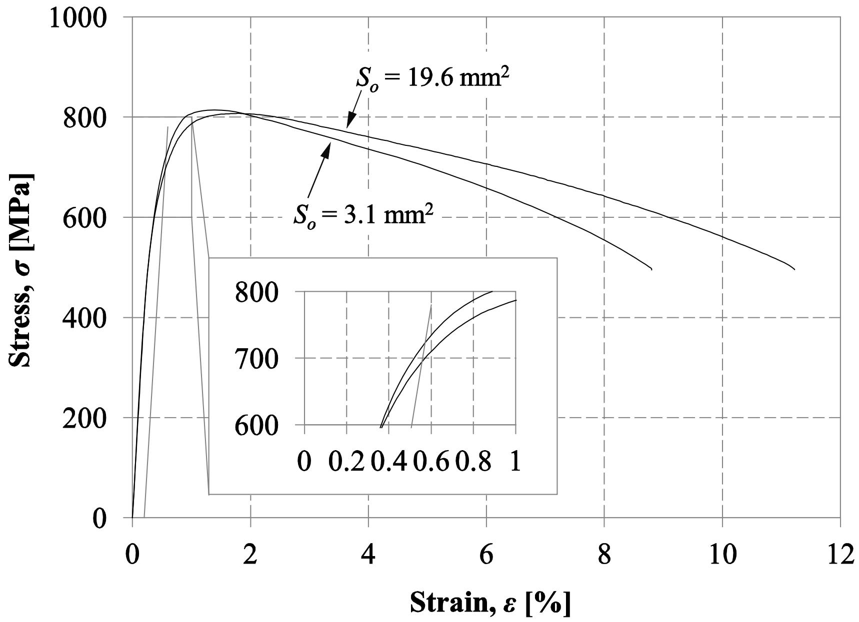

Fig. 2: Static tensile plot.

Tab. 2: Mechanical properties.

Minispecimen			
R_m, MPa	R_e, MPa	A, %	Z, %
820	713	10.8	65.5
Standard specimen			
809	684	12.2	63.8

3. Test result review

Ten experimental points provided input to the bilogarithmic linear regression and the Basquin's equation (Tab. 3). At least 7 such points are required for initial testing (Strzelecki et al., 2015). Fig. 3 shows a graphic representation of the resulting fatigue characteristics *σ-N* within the high-cycle loading range.

Tab. 3: σ-N characteristic parameters for various specimen sizes.

Type of geometry	Linear regression line $\log\sigma_a = a \log N + b$		Basquin relation $C = N(\sigma_a)^\beta$		Correlation coefficient, R^2
	a	b	C	β	
Standard specimen	-0.1008	3.1601	$2.26 \cdot 10^{31}$	9.92	0.901
Minispecimen	-0.1276	3.2761	$5.56 \cdot 10^{25}$	7.86	0.956

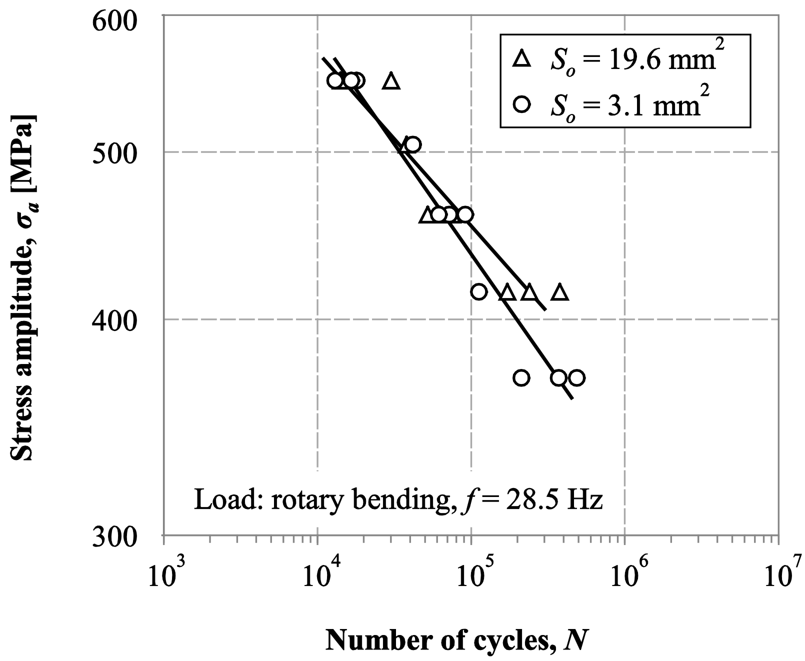

Fig. 3: σ-N characteristics compared for the specimens of different sizes.

The mutual relation of placement of the individual regression lines was evaluated statistically the line slope (a) parallelism test. The test was done for characteristics *σ-N*, for a standard specimen (S_o = 19.6 mm^2). The lines were parallel.

The coefficient of size of cross-section K (K_S = Minispecimen ultimate tensile strength / Standard specimen ultimate tensile strength, K_{HC} = Minispecimen fatigue strength / Standard specimen fatigue strength (Tomaszewski et al., 2014a)) was determined for examination of the size effect. See Tab. 4 for the results.

Tab. 4: Cross-section area ratios (K).

S_o [mm^2]	K_S	K_{HC}
3.1	1.014	0.974
19.6	1	1

4. Summary

The size effect did not apply to the tested material. Both fatigue and monotonic tests reported similar material properties. The values of coefficient K close to 1 confirm this claim. The tests were applied to a narrow range of specimen sizes. Typically, material property change depending on cross-section area is non-linear, so it would be reasonable to complement the tests by testing specimens with larger cross-section areas than those of the tested standard specimens.

References

Bažant, Z.P. (1984) Size effect in blunt fracture concrete, rock, metal. Journal of Engineering Mechanics ASCE, 110, pp. 518-535.

Carpinteri, A., Spagnoli, A. & Vantadori, S. (2009) Size effect in S-N curves: A fractal approach to finite-life fatigue strength. International Journal of Fatigue, 31, pp. 927-933.

Kuguel, R. (1961) A relation between the theoretical stress concentration factor and the fatigue notch factor deduced from the concept of highly stressed volume. Proc. ASTM 61, pp. 732-748.

PN-74/H-04327 The study of metal fatigue. The test of axial tension - compression at constant cycle of external loads (in Polish).

PN-EN ISO 6892-1:2010 Metals - Tensile testing - Part 1: Test method at room temperature (in Polish).

Sonsino, C.M. & Fischer, G. (2005) Local assessment concepts for the structural durability of complex loaded components. Materialwissenschaft und Werkstofftechnik, 36, pp. 632-641.

Strzelecki, P., Sempruch, J. & Nowicki, K. (2015) Comparing guidelines concerning construction of the S-N curve within limited fatigue life range. Polish Marit. Res, 22, 3, pp. 67-74.

Tomaszewski, T. & Sempruch, J. (2012) Determination of the fatigue properties of aluminum alloy using mini specimen. Materials Science Forum, 726, pp. 63-68.

Tomaszewski, T., Sempruch, J. & Piątkowski T. (2014a) Verification of selected models of size effect based on high-cycle fatigue testing on mini specimens made of EN AW-6063 aluminum alloy. Journal of Theoretical and Applied Mechanics, 52(4), pp. 883-894.

Tomaszewski, T. & Sempruch, J. (2014b) Verification of the fatigue test method applied with the use of mini specimen. Key Engineering Materials, 598, pp. 243-248.

22nd International Conference
ENGINEERING MECHANICS 2016
Svratka, Czech Republic, 9 – 12 May 2016

GLOBAL TOPOLOGY WEIGHT OPTIMIZATION OF 52-BAR BENCHMARK TRUSS WITH DISCRETE CROSS-SECTIONS

M. Tyburec*, M. Lepš**

Abstract: *Truss topology weight optimization problem with discrete cross-sections can be formulated as a mixed-integer linear program (MILP), which is solvable to global optimality. It is however very difficult to obtain proven globally optimal solution, as there usually exist a very large number of possible combinations. This contribution implements several types of additional cuts and solves the problem using a commercial branch-and-bound software Gurobi, hence making it possible to obtain a guaranteed globally optimal solution. Such solution can then be used as a lower bound for sizing optimization.*

Keywords: branch and bound method, mixed-integer linear programming, topology optimization, 52-bar truss, benchmark.

1. Introduction

Truss topology optimization with discrete variables is a NP-hard problem (Yates et al., 1982). In the case of 52-bar truss (see Fig. 1), which is being used in this contribution, simple enumeration of all possible solutions yields $5{,}69\times10^{21}$ combinations making it computationally non-manageable.

2. Problem formulation

According to (Rasmussen et al., 2008) the minimum-weight topology optimization problem is formulated as a mixed-integer linear program:

$$\min \rho \sum_{j=1}^{J} l_j \sum_{i=1}^{I} a_i x_{ij} \tag{1}$$

$$\text{s.t.}: Bs = f \tag{2}$$

$$x_{ij} a_i \sigma^{\min} \le s_{ij} \le x_{ij} a_i \sigma^{\max} \quad \forall (i,j) \tag{3}$$

$$(1 - x_{ij}) c_{ij}^{\min} \le \frac{E_j a_i}{l_j} b_j^T u - s_{ij} \le (1 - x_{ij}) c_{ij}^{\max} \quad \forall (i,j)\,. \tag{4}$$

$$u_{\min} \le u \le u_{\max} \tag{5}$$

$$\begin{gathered} \sum_{i=1}^{I} x_{ij} \le 1 \quad \forall j \\ x_{ij} \in \{0,1\} \quad \forall (i,j) \end{gathered} \tag{6}$$

The truss consists of J bars. Each bar j of the truss may have a cross-sectional area selected from the predefined list $\{a_1, a_2, \dots a_I\}$, where I represents the number of available areas. To describe which area is used by the bar j, an additional binary variable x_{ij} is introduced: if the ith area of the bar j is present, then x_{ij} is equal to one; zero otherwise. Each bar has at most one area present (6). If the bar does not have any area, it is removed, thus enabling to influence topology. The bars are divided into several groups with the same area, for implementation details the reader is referred to (Pospíšilová, Lepš, 2013).

* Bc. Marek Tyburec: Faculty of Civil Engineering, CTU in Prague, Thákurova 7/2077; 166 29 Prague; CZ, marek.tyburec@gmail.com

** Doc. Ing. Matěj Lepš, Ph.D.: Faculty of Civil Engineering, CTU in Prague; Thákurova 7/2077; 166 29, Prague; CZ, matej.leps@fsv.cvut.cz

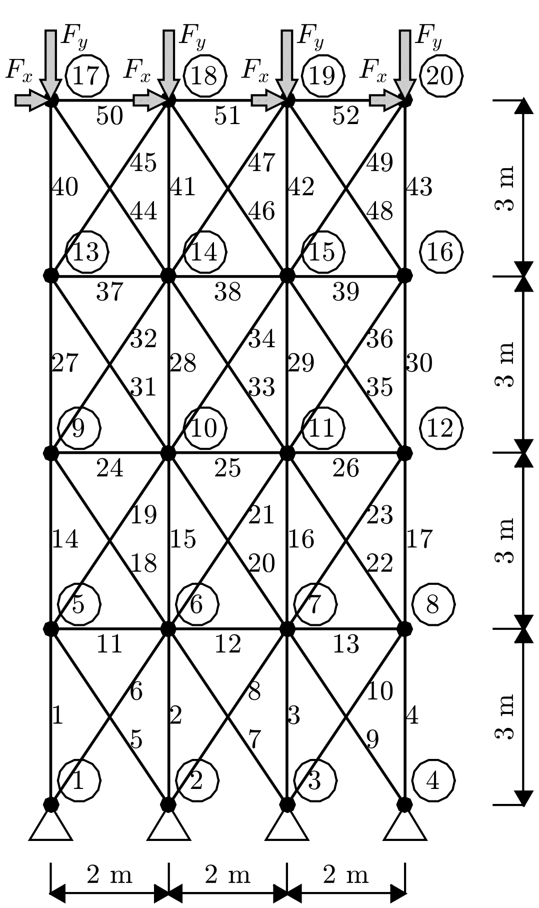

Group	Bars
A_1	1, 2, 3, 4
A_2	5, 6, 7, 8 ,9, 10
A_3	11, 12, 13
A_4	14, 15, 16, 17
A_5	18, 19, 20, 21, 22, 23
A_6	24, 25, 26
A_7	27, 28, 29, 30
A_8	31, 32, 33, 34, 35, 36
A_9	37, 38, 39
A_{10}	40, 41, 42, 43
A_{11}	44, 45, 46, 47, 48, 49
A_{12}	50, 51, 52

External forces
F_x = 100 kN; F_y = 200 kN

Possible bar cross-sections [mm^2]
71,613; 90,968; 126,451; 161,29; 198,064; 252,258; 285,161; 363,225; 388,386; 494,193; 506,451; 641,289; 645,16; 792,256; 816,773; 940; 1008,385; 1045,159; 1161,288; 1283,868; 1374,191; 1535,481; 1690,319; 1696,771; 1858,061; 1890,319; 1993,544; 2019,351; 2180,641; 2238,705; 2290,318; 2341,191; 2477,414; 2496,769; 2503,221; 2696.769; 2722,575; 2896,768; 2961,284; 3096,768; 3206,445; 3303,219; 3703,218; 4658,055; 5141,925; 5503,215; 5999,998; 6999,986; 7419,34; 8709,66; 8967,724; 9161,272; 9999,98; 10322,56; 10903,204; 12129,008; 12838,684; 14193,52; 14774,164; 15806,42; 17096,74; 18064,48; 19354,8; 21612,86

Material properties
E = 207 GPa
ρ = 7860 kg/m^3
$\sigma_{\max} = -\sigma_{\min}$ = 180 MPa

Fig. 1: Initial 52-bar truss.

The truss is also characterized by prescribed material properties – material density ρ, Young's modulus E and by minimal and maximal allowed stresses $\sigma^{\min}$ and $\sigma^{\max}$. Based on linear elasticity it is possible to limit internal normal forces of individual bars s_{ij}, see Equation (3).

It is usually needed to limit displacements u of the truss by a minimal $u^{\min}$ and a maximal displacements $u^{\max}$ (5), respectively. To preserve linearity of the formulation, the internal forces s are bounded by $c^{\min}$ and $c^{\max}$ (Rasmussen et al., 2008):

$$\begin{aligned} c_{ij}^{\min} &= \frac{E_j a_i}{l_j} \min_{u^{\min} \le u \le u^{\max}} \left\{ b_j^T u \right\} \quad \forall (i,j) \\ c_{ij}^{\max} &= \frac{E_j a_i}{l_j} \max_{u^{\min} \le u \le u^{\max}} \left\{ b_j^T u \right\} \quad \forall (i,j) \end{aligned}, \tag{7}$$

where b_j represents the jth row of the static matrix B. These bounds should be valid only when the area i is present (4). To preserve compatibility for trusses without specified displacement limits, the values of $c^{\min}$ and $c^{\max}$ are replaced by extreme normal forces from Equation (3). The force equilibrium in nodes is described by the static matrix B and Equation (2), where f represents the external nodal forces vector.

2.2 Branch-and-bound algorithm

Because the formulation of the problem (1)-(6) is linearly dependent on design variables x, s and u, respectively, the problem may be solved by branch-and-bound algorithm. The algorithm starts with a relaxed problem formulation, without considering binary (integer) variables, thus making it possible to solve an ordinary linear program (LP). If all the binary variables obtained by the solution of the relaxed problem have only binary values, global optimum is obtained. In the opposite case the initial relaxed problem is branched into multiple sub-problems (leave nodes) fixing specific binary variable on values 0 and 1. All the relaxed sub-problems are ordered by their objective value and solved from the smallest one, creating a lower bound of the problem.

Branch-and-bound algorithm uses heuristics for finding a feasible integer solution fulfilling all the prescribed constraints, hence solving the full problem (1)-(6) and creating the upper bound. Therefore, if any relaxed sub-problem takes higher objective value than the upper bound, it is discarded. The algorithm terminates only if the upper bound is equal to the lower bound and no spare leave nodes are left.

The benefits of branch-and-bound algorithm are obvious: limiting the number of combinations needed to solve the problem to global optimality and thus significantly speeding the computations up.

3. Tightening of the problem

To tighten the general formulation of the problem (1)-(6) even further, additional cuts are introduced. Their purpose is to limit the design space of the problem while preserving all feasible binary solutions and consequently keeping the same global optimum. The cuts have significant effect on both the number of branched nodes and the speed of the branch-and-bound algorithm itself.

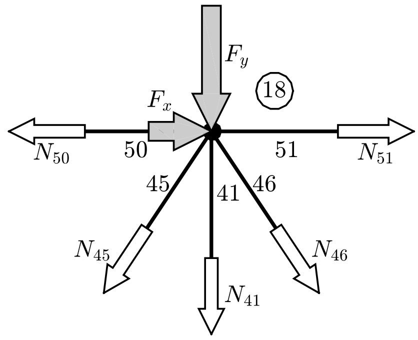

Fig. 2: Loaded node 18.

3.1 Loaded-nodes cuts

Each externally loaded node has to fulfill the force equilibrium (2). The vertical force F_y located at the node k has to be carried only by non-horizontal bars connected to the node k. It is evident that to carry the force F_y in Figure 2 at least one of the bars 41, 45 or 46 has to be present (Rasmussen et al., 2008) and the total area of these bars orthogonally displayed to vertical axis has to be greater than the minimal area needed to carry the external vertical force. The same procedure is also applied to the horizontal direction.

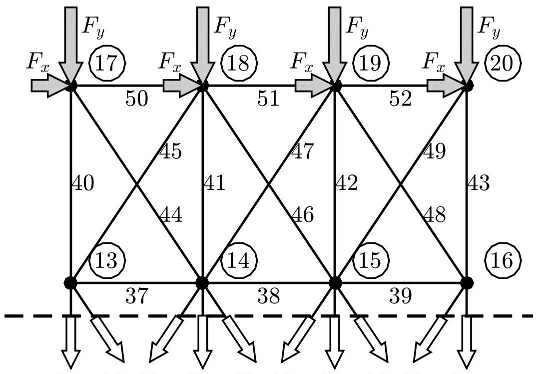

Fig. 3: Method of section – cut through bars 27-36.

3.2 Method-of-sections cuts

Similar idea is used for the method-of-sections cuts (Lepš et al., 2014). All the cuts are generated as follows: Firstly, the truss is divided into two sections. It is then checked if there exist a situation that all the supports in one direction (e.g. x) are on one section and there exist at least one external force, in the same direction as the supports, located on the other section. Consequently, there have to exist at least one bar in the direction of the external force connecting the two sections and the total area of the orthogonally displayed bars have to be greater than the minimum area needed to carry the external force. Considering Figure 3 and the fact that the area of bars 31-36 is equal (see Fig. 1), all the bars 31-36 have to be present and their minimal area needs to carry external forces F_x to the supports located on the other section.

3.3 Inner-nodes cuts

Inner-nodes cuts apply for all nodes without external forces or supports. They arise from an idea there cannot exist single horizontal (or vertical) bar in a node. If there would not be any horizontal force carried through the node then no bar was needed, otherwise there have to be at least two bars to carry the normal force (Rasmussen et al., 2008). However, inner-nodes cuts are useful only for topology optimization.

4. Results

Topology optimization of the 52-bar truss benchmark was launched on a computer with 16 cores, a limit of 128 GB RAM and GUROBI MILP solver (Gurobi Optimization, Inc., 2015). The globally optimal truss structure with a weight of 1902,606 kg has been obtained. The optimization progress is shown in the Fig. 4.

Note that the described implementation is not easily applicable for general use; still, it did significantly speed up the optimization. The global optimum of the benchmark truss is useful as a comparison for faster but not global heuristic algorithms or as a lower bound for sizing optimization.

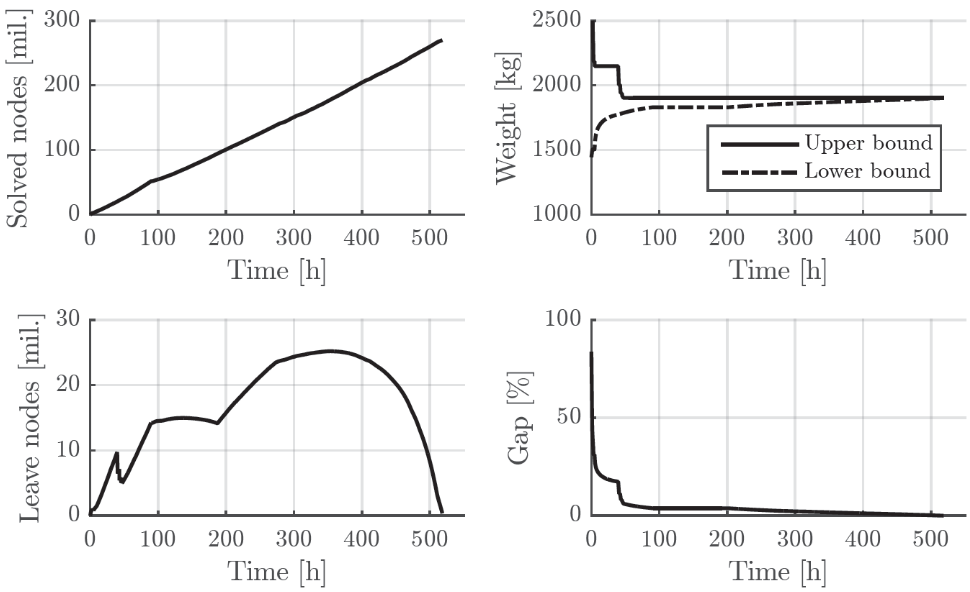

Fig. 4: 52-bar benchmark truss topology optimization.

Acknowledgement

The implementation has been built upon the MATLAB codes provided by Ing. Adéla Pospíšilová. The authors also acknowledge the financial support from the Grant Agency of the CTU in Prague, the grant SGS16/037/OHK1/1T/11.

References

Gurobi Optimization, Inc. (2015) Gurobi Optimizer Reference Manual, http://www.gurobi.com.

Lepš, M., Nosek, J. & Pohlídalová, E. (2014) 52-bar truss optimization benchmark: computational enhancements, in: Proceedings on the 5th Conference Nano & Macro mechanics, Czech Technical University, pp. 111-114.

Lepš, M. & Pospíšilová, A. (2013) Parallel Branch and Bound Method for Size Optimization Benchmarks. In: Proceedings of the Third International Conference on Parallel, Distributed, Grid and Cloud Computing for Engineering, Civil-Comp Press, Stirlingshire, UK, Paper 20.

Rasmussen, M. H. & Stolpe, M. (2008). Global optimization of discrete truss topology design problems using a parallel cut-and-branch method. Computers & Structures, 86(13), pp. 1527-1538.

Boffey, T. B., Templeman, A. B. & Yates, D. F. (1982). The complexity of procedures for determining minimum weight trusses with discrete member sizes. International Journal of Solids and Structures, 18(6), pp. 487-495.

22nd International Conference
ENGINEERING MECHANICS 2016
Svratka, Czech Republic, 9 – 12 May 2016

INFLUENCE OF AMPLITUDE ON FREE VIBRATION FREQUENCY OF A PARTIALLY TENSIONED COLUMN

S. Uzny[*], K. Sokół[**], M. Osadnik[***]

Abstract: *The non-linear vibrations of a slender system subjected to an external force applied between the elements of a structure are discussed in this paper. The boundary problem has been formulated on the basis of Hamilton's principle and the small parameter method. Taking into account the solution of the boundary problem, the parameter describing the relation between the amplitude and natural vibration frequency has been obtained. In the presented investigations, only the first vibration frequency is discussed. The numerical simulations of the vibration frequencies are done for variable location of the external load.*

Keywords: Non-linear column, natural vibration, amplitude, instability.

1. Introduction

The behaviour of certain structures can only be described using non-linear differential equations. This particularly holds for structures where vibrations have to be taken into account. Such an approach has been discussed by many authors in recent years. Various methods of solving non-linear boundary problems can be found in the literature. In the work by Szemplińska-Stupnicka (1983) a continuous non-linear system in the form of a beam was investigated. The author used the Ritz method in the solution to the problem. Examples of the relationship between the amplitude and the vibration frequency were presented. Nonlinear vibrations of a beam with an elastic axial restraint were discussed by Prathap (1978). The author investigated how the amplitude affects the vibration frequency for different slendernesses of the structure as well as the influence of different stiffening of the pinned support in the longitudinal direction. Awrejcewicz et.al. (2011) studied a flexible nonlinear Euler-Bernoulli-type beam for different boundary conditions. The continuous boundary problem was reduced to a finite-dimensional one and solved using the Runge-Kutta method. Sokół (2014) studied the influence of a crack present in one of rods of a multi-member structure on the amplitude – vibration frequency relationship. Tomski and Kukla (1989) performed theoretical and numerical studies of a column subjected to an eccentrically applied Euler's load on both ends of the system. Additionally, they used a translational spring in order to reduce the longitudinal displacement on one of the ends. In the solution to the boundary problem the small parameter method was used. As a result the parameters describing the relation between the linear and non-linear vibration frequency and longitudinal (linear/non-linear) force for different amplitudes and spring stiffness were obtained. Structures in the form of coaxial tubes or flat frames composed of elements with different rigidity are also geometrically non-linear and were presented in papers (Tomski et al. 2007, Uzny 2011). These types of structures are characterized by two forms of equilibrium: rectilinear and curvilinear.

[*] Sebastian Uzny, Prof.: Institute of Mechanics and Machine Design Foundation, Częstochowa University of Technology Dąbrowskiego 73, 42-200 Częstochowa, Poland, uzny@imipkm.pcz.pl

[**] Krzysztof Sokół, PhD.: Institute of Mechanics and Machine Design Foundation, Częstochowa University of Technology Dąbrowskiego 73, 42-200 Częstochowa, Poland, sokol@imipkm.pcz.pl

[***] Michał Osadnik, Eng.: Institute of Mechanics and Machine Design Foundation, Częstochowa University of Technology Dąbrowskiego 73, 42-200 Częstochowa, Poland, osadnik@imipkm.pcz.pl

The main scope of this paper is to estimate the differences between the linear and non-linear vibration frequency of a system subjected to axial load for a given magnitude of the parameter associated with the amplitude of natural vibrations. The proposed system can be modelled by a screw with a nut moving along its length. Additionally, in the real system, the nut is subjected to an external load.

2. Formulation of the boundary problem

The slender system discussed in this paper is presented in the Figure 1. It is constructed as a fixed – fixed rod loaded by means of force P, which is applied axially between the elements of the structure. The point of the force placement is described by parameter ζ ($\zeta = l_1/l$). The whole structure is characterized by constant bending stiffness ($(EJ)_1 = (EJ)_2 = (EJ)$), compression stiffness ($(EA)_1 = (EA)_2 = (EA)$) and mass ($(\rho A)_1 = (\rho A)_2 = (\rho A)$) (where: E_i – Young's modulus, ρ_I – density, A_i – cross sectional area, J_i – geometrical axial moment of inertia of the cross section of i-th element of the structure).

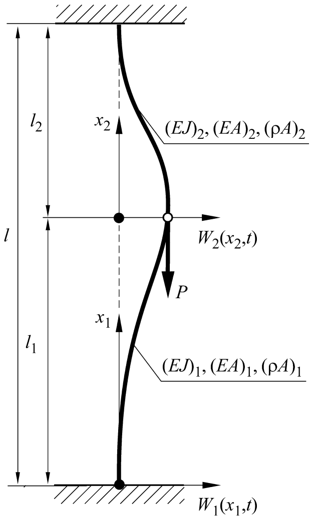

Figure 1. An investigated system

The differential equation of motion in transversal and longitudinal directions are as follows:

$$\frac{\partial^4 w_i(\xi_i,\tau)}{\partial \xi_i^4} + k_i^2(\tau)\frac{\partial^2 w_i(\xi_i,\tau)}{\partial \xi_i^2} + \Omega_i^2 \frac{\partial^2 w_i(\xi_i,\tau)}{\partial \tau^2} = 0 \tag{1}$$

$$u_i(\xi_i,\tau) - u_i(0,\tau) = -\frac{k_i^2(\tau)}{\theta_i}\xi_i - \frac{1}{2}\int_0^{\xi_i}\left(\frac{\partial w_i(\xi_i)}{\xi_i}\right)^2 d\xi_i \tag{2}$$

Equations (1) and (2) are written in the non-dimensional form by means of the relationships:

$$\xi_i = \frac{x_i}{l_i},\ w_i(\xi_i,\tau) = \frac{W_i(x_i,\tau)}{l_i},\ u_i(\xi_i,\tau) = \frac{U_i(x_i,\tau)}{l_i},\ k_i^2(\tau) = \frac{S_i(\tau) l_i^2}{(EJ)_i},$$

$$\Omega_i^2 = \frac{(\rho A)_i \omega^2 l_i^4}{(EJ)_i},\ \tau = \omega t,\ \Theta_i = \frac{A_i l_i^2}{J_i},\ i = 1, 2. \tag{3a-g}$$

Where: $S_i(\tau)$ – internal force in the i-th element of the structure, ω - vibration frequency, $W_i(x_i,\tau)$, $U_i(x_i,\tau)$ – transversal and longitudinal displacements, respectively.

The boundary conditions (in the non-dimensional form) are as follows:

$$u_1(0,\tau) = u_2(1.\tau) = w_1(0,\tau) = \left.\frac{\partial w_1(\xi_1,\tau)}{\partial \xi_1}\right|_{\xi_1=0} = w_2(1,\tau) = \left.\frac{\partial w_2(\xi_2,\tau)}{\partial \xi_2}\right|^{\xi_2=1} = 0\ ;\ u_1(1,\tau) = u_2(0.\tau)$$

$$u_1(0,\tau)=u_2(1.\tau)=w_1(0,\tau)=\left.\frac{\partial w_1(\xi_1,\tau)}{\partial \xi_1}\right|_{\xi_1=0}=w_2(1,\tau)=\left.\frac{\partial w_2(\xi_2,\tau)}{\partial \xi_2}\right|^{\xi_2=1}=0\,;\; w_1(1,\tau)=w_2(0,\tau)$$

$$\frac{(EJ)_1}{l_1^2}\left.\frac{\partial^3 w_1(\xi_1,\tau)}{\partial \xi_1^3}\right|^{\xi_1=1}-\frac{(EJ)_2}{l_2^2}\left.\frac{\partial^3 w_2(\xi_2,\tau)}{\partial \xi_2^3}\right|_{\xi_2=0}+P\left.\frac{\partial w_2(\xi_2,\tau)}{\partial \xi_2}\right|_{\xi_2=0}=0\,;\; S_1-S_2=P$$

$$\frac{(EJ)_1}{l_1}\left.\frac{\partial^2 w_1(\xi_1,\tau)}{\partial \xi_1^2}\right|^{\xi_1=1}-\frac{(EJ)_2}{l_2}\left.\frac{\partial^2 w_2(\xi_2,\tau)}{\partial \xi_2^2}\right|_{\xi_2=0}=0\,;\; \left.\frac{\partial w_1(\xi_1,\tau)}{\partial \xi_1}\right|^{\xi_1=1}=\left.\frac{\partial w_2(\xi_2,\tau)}{\partial \xi_2}\right|_{\xi_2=0} \tag{4a-r}$$

In the final formulation of the boundary problem the small parameter method is used due to the non-linearity in equation (2). All the non-linear elements are written in the power series of the small parameter. In this paper only the rectilinear form of static equilibrium is discussed, for which, the series are as follows:

$$w_i(\xi,\tau)=\sum_{j=1}^{N}\varepsilon^{2j-1}w_{i2j-1}(\xi,\tau)+O\left(\varepsilon^{2(N+1)}\right),\; u_i(\xi,\tau)=u_{i0}(\xi)+\sum_{j=1}^{N}\varepsilon^{2j}u_{i2j}(\xi,\tau)+O\left(\varepsilon^{2(N+1)}\right) \tag{5a}$$

$$k_i^2(\tau)=k_{i0}^2+\sum_{j=1}^{N}\varepsilon^{2j}k_{i2j}^2(\tau)+O\left(\varepsilon^{2(N+1)}\right),\; \Omega_i^2=\Omega_{i0}^2+\sum_{j=1}^{N}\varepsilon^{2j}\Omega_{i2j}^2+O\left(\varepsilon^{2(N+1)}\right) \tag{5b}$$

The above equations are solved sequentially for: the estimation of the distribution of the external force onto elements of the structure, linear vibration frequency ω_0, internal forces induced by vibrations, non-linear vibration frequency ω_2.

3. The results of numerical simulations

The discussion of the results is done with the use of the non-dimensional parameters:

$$\lambda=\frac{Pl^2}{EJ}\,,\; \zeta_\omega=\frac{\omega-\omega_0}{\omega_0}100\%\,,\text{ where: }\omega=\sqrt{\omega_0^2+\varepsilon^2\omega_2^2} \tag{6a-c}$$

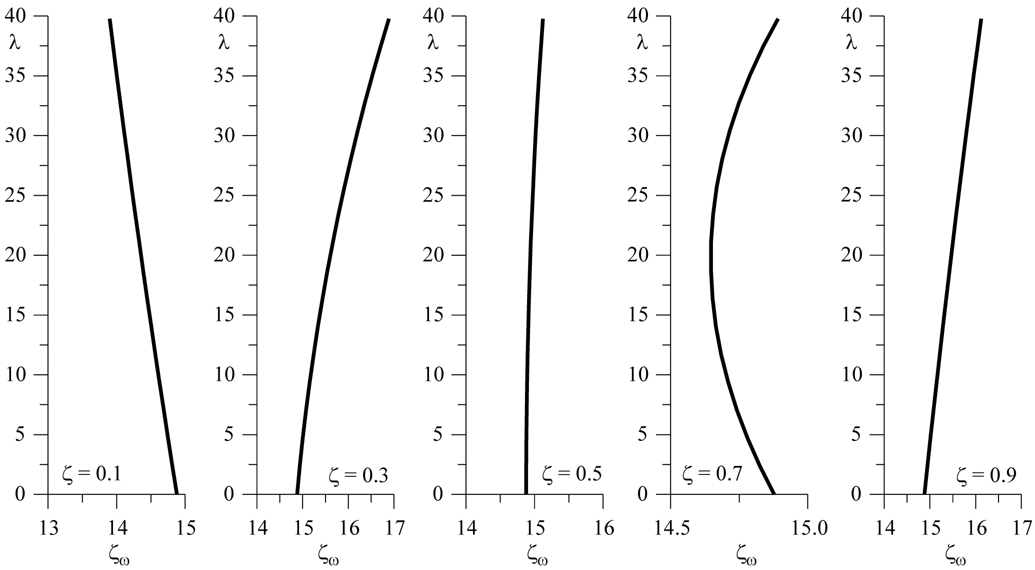

Figure 2. The change of ζ_ω parameter in relation to external load λ

The numerical investigations are done at external load level $\lambda \in \langle 0,25\rangle$ and at amplitude of vibration parameter $\varepsilon = 0.008$. The proposed magnitude of the small parameter $\varepsilon = 0.008$ refers to an amplitude of vibration approximately equal to double the magnitude of the minimum radius of inertia of the cross section of the column. In Figure 2, the change in parameter ζ_ω in relation to the location point of external load ζ (ζ = 0.1; 0.3; 0.5; 0.7; 0.9) is presented. In this study only an influence of an amplitude on the first vibration frequency is presented and discussed.

The degree of the influence of the amplitude on the vibration frequency of the system depends on the external load (parameter λ) and the point of its location (parameter ζ). In the investigated range of external load ($\lambda \in \langle 0,40 \rangle$), at amplitude corresponding to small parameter ε = 0.008 the smallest differences in the plotted curves $\lambda(\zeta_\omega)$ can be found when the external force is located in the middle of the structure (ζ = 0.5). For a smaller magnitude of ζ (ζ = 0.1) it can be seen that the differences between the frequency with non-linear part ω (where: $\omega^2 = \omega_0^2 + \varepsilon^2\omega_2^2$; ω_0 – linear component independent from amplitude of vibration, ω_2 – non-linear component dependent on amplitude of vibration) and basic ω_0 become smaller as the external load magnitude increases. In the case where ζ = 0.7, the considered difference between ω and ω_0 is smaller for the small magnitude of the external load than in the case when the external load is increasing.

4. Conclusions

The numerical studies presented in this paper concern the estimation of the influence of the amplitude of vibration on the natural vibration frequency of slender system which is partially tensioned in a rectilinear form of static equilibrium. It has been shown that the size of the influence of the amplitude on the first vibration frequency greatly depends on the location point of the external load as well as on its magnitude. On the basis of the results of numerical simulations it can be stated that the point which is the least sensitive to the placement of the external load is the one located in the middle to the total length of the column (see curves external load (λ) – frequency difference (ζ_ω) between ω and ω_0). In the investigated external load range and its location, parameter ζ_ω varies from ~14% up to ~17%. In the future it is planned to extend the studies presented in this paper to include the curvilinear form of static equilibrium and discreet elements which can affect the natural vibration frequency.

Acknowledgement

The study has been carried out within the statutory funds from the Czestochowa University of Technology (BS/PB-1-101-3020/11/P).

References

Sokół, K. (2014) Linear and nonlinear vibrations of a column with an internal crack. Journal of Engineering Mechanics 140, http://dx.doi.org/10.1061/(ASCE)EM.1943-7889.0000719.

Tomski L. & Kukla S. (1989) Free Vibrations of a Certain Geometrically Nonlinear System with Initial Imperfection, AIAA Journal, 28(7), 1240-1245.

Prathap G. (1978) Nonlinear Vibration of Beams with Variable Axial Restraint, AIAA Journal, 16(6), 622-624.

Szemplińska-Stupnicka W. (1983) Non-linear Normal Modes and the Generalized Ritz Method in the Problems of Vibrations of Non-linear Elastic Continuous System, International Journal of Non-Linear Mechanics, 18, 149-165.

Awrejcewicz J. & Saltykova O.A.&Chebotyrevskiy Yu.B.&Krysko V.A. (2011) Nonlinear vibrations of the Euler-Bernoulli beam subjected to transversal load and impact actions, Nonlinear Studies, 18(3), 329-364.

Uzny S. (2011) Local and global instability and vibrations of a slender system consisting of two coaxial elements, Thin-Walled Structures, 49, 618–626.

Tomski L. & Szmidla J. & Uzny S. (2007) The Local and Global Instability and Vibration of Systems Subjected to Non-Conservative Loading, Thin-Walled Structures, 45, 10-11, 945-949.

22nd International Conference
ENGINEERING MECHANICS 2016
Svratka, Czech Republic, 9 – 12 May 2016

FAILURES OF RAILWAY VEHICLES MEASURABLE ON TRACK

J. Vágner[*], J. Zelenka[**], A. Hába[***], M. Kohout[*****], P. Havlíček[*****]

Abstract: *This paper describes system for diagnostics of passing vehicles with help of measurements carried out at the track. There are the signals of vibration measured on rail foot and noise signals measured near to underside of vehicle. Further failures which could be measured by this method and estimation of their dominant frequencies are described too. The system has been tested on vehicles in metro and several methods of evaluation have been proposed. Signals are assessed in the time domain and in the frequency domain. Evaluation of results is carried out using neural networks.*

Keywords: Railway, Metro, Vibrodiagnostics, Noise, Neural network.

1. Introduction

This paper introduces possibilities of failures detection of running vehicles with help of measurement carried out at the track. The paper also describes system for diagnostics of passing vehicles, which is actually developed and tested in conditions of Prague metro. The detection of selected railway vehicle failures with help of vibration and noise measurement at the stationary part of infrastructure is the aim of this diagnostic system.

2. Description of diagnostic system

The diagnostic system has been created to placing directly in metro tunnel therefore it has been constructed as dustproof, moisture and water resistant. Low power consumption, appropriate efficiency and related low heat loss of all devices has been another requirements. For carried out measurements, we used available laboratory measuring technology, commercial utilization would have required full industrial conception of that system. The basic requirement, which results from the first measurement, performs 8 acceleration or noise sensors. We usually use 2 microphones and 6 acceleration sensors. Synchronization of trainset position with the recorded signals is at high importance to right assignment of the failures relate to each carriages, bogies or axles. However the right identification of the trainset has equally importance. For those purposes, the optical gates and automatic trainset identification by WiFi connection has been used. The issues of measured data transferring have been the next solution area. With respect to interference and cable length there is not any possibility to use a metallic connection in these conditions. Therefore the data transferring has been implemented through optical fibre cable.

3. Placement of sensors in the track

We carried out a lot of measuring campaigns in 2013-2015 which was utilized for optimization of sensors placement. For obtaining suitable data to assessment, one sensor has to be placed on each rail at least and one microphone has to be placed between rails at least. However these sensors have been doubled to

[*] Ing. Jakub Vágner, Ph.D.: Jan Perner Transport Faculty, University of Pardubice, Studentská 95; 532 10, Pardubice; CZ, jakub.vagner@upce.cz

[**] doc. Ing. Jaromír Zelenka, CSc.: Jan Perner Transport Faculty, University of Pardubice, Nádražní 547; 560 02, Česká Třebová; CZ, jaromir.zelenka@upce.cz

[***] Ing. Aleš Hába, Ph.D.: Jan Perner Transport Faculty, University of Pardubice, Nádražní 547; 560 02, Česká Třebová; CZ, ales.haba@upce.cz

[****] Ing. Martin Kohout, Ph.D.: Jan Perner Transport Faculty, University of Pardubice, Nádražní 547; 560 02, Česká Třebová; CZ, martin.kohout@upce.cz

[*****] Ing. Petr Havlíček: The Prague Public Transit Co., Prague, Czech Repulic, petr.havlicek@student.upce.cz

increasing of system reliability. Two optical gates have been used for detection of passing wheelset. The gates also enable identification of trainset speed. A typical sensor placing is shown in fig. 1. Four acceleration sensors ($z_1 \div z_4$) are situated on the rail foot in the two track crosssections appropriate to optical gates (G_A and G_B) localization. Acceleration sensor z_5 is situated on the rail foot above the fixing to a sleeper and acceleration sensor z_6 is situated on the concrete base (floor) of a tunnel. Microphones were previously situated on the tunnel lining, later they were placed only between rails.

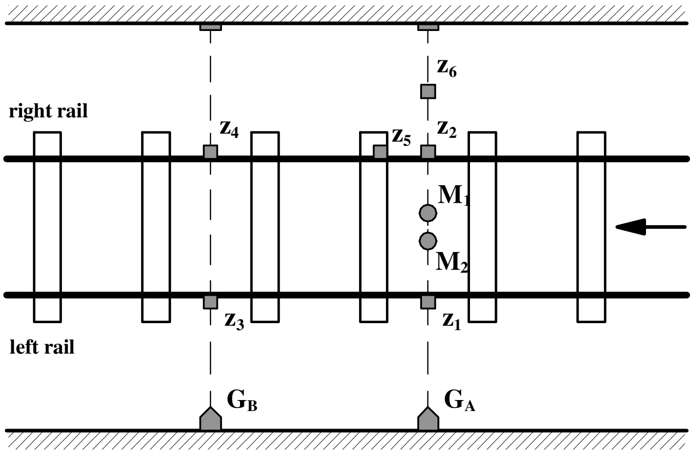

Fig. 1: Sensors placement in the track.

4. Measurable failures

At the fixed track part, it is possible to detect only the vehicles failure which shows sufficient and definite response in vibration and noise signals. With help of vibration signals we are able to detect especially failures in bogie or in mechanical part of drive. Noise signals can be used especially for detection the failures which generate such sufficient acoustic response that can be separated from the ambient noise. Searching of characteristic symptoms of appropriate failures and their quantification is the main aim of signal analyses. The evaluation of the signals has been carried out in time and frequency domain.

4.1. Wheelset failures

We can suppose several types of failure of wheelset which can create dynamical response to the track. These symptoms can be identified as a failure of wheel tread (material failure or flat caused by wheel slip) or unbalanced wheel or wheelset. If a failure occurs on the wheel tread only in one case, the dominant frequency is:

$$f_{\mathrm{W}} = \frac{1}{\pi \cdot D_{\mathrm{W}}} \cdot v, \qquad (1)$$

where D_{W} is wheelset diameter and v is vehicle speed. If the wheel tread (or whole wheelset) contains more than one failure then these failures are detected only by increased dynamical response to the track.

4.2. Axle bearing failures

Failures of axle bearings can have various character and these failures can be idetifyied in frequency domain. The response appears in signals of vibration as well as noise. In usual case we can identify these failure frequences (relate to failure type): failure frequency of inner bearing ring f_{BPBI} (2), failure frequency of bearing cage f_{FT} (3), failure frequency of outer bearing ring f_{BPFO} (4), failure frequency of bearing elements f_{BSF} (5).

$$f_{\mathrm{BPBI}} = \frac{n}{2} f_{\mathrm{W}} \left(1 + \frac{d_0}{d_s} \cos\alpha\right) \qquad (2)$$

$$f_{\mathrm{FT}} = \frac{1}{2} f_{\mathrm{W}} \left(1 - \frac{d_0}{d_s} \cos\alpha\right) \qquad (3)$$

$$f_{\mathrm{BPFO}} = \frac{n}{2} f_{\mathrm{W}} \left(1 - \frac{d_0}{d_s} \cos\alpha\right) \qquad (4)$$

$$f_{\mathrm{BSF}} = f_W \frac{d_s}{2d_0}\left(1 - \frac{d_0}{d_s}\cos\alpha\right)^2 \tag{5}$$

where d_s is pitch diameter of bearing elements, d_0 is diameter of bearing element, α is connection angle of bearing elements and n is number of bearing elements.

However the equations mentioned above can be used only in optimal conditions (optimal placing of sensor) and in these application usability has not been demonstrated yet. Result frequencies can be modulated by frequency of wheelset revolutions f_W (2) what can show also wheelset failure (misalignment or run-out).

4.3. Wheelset drive failures

A significant response in vibration and noise signals is caused by mechanical part of traction – gearbox. This so called tooth frequency is dominant in this case. It appears due to contact of the teeth of both wheels during its rotation (6).

$$f_\mathrm{T} = t_1 \cdot f_\mathrm{TM} = t_2 \cdot f_\mathrm{W} \tag{6}$$

where t_1 and t_2 are numbers of teeth of both gear wheels. In frequency spectrum we can also identify tooth harmonics $k \cdot f_\mathrm{T}$ what can show toothed wheel worn on their contact (evolvent) surface. Some frequencies, which develop by modulation of tooth frequency ($f_\mathrm{T} + f_\mathrm{W}$; $f_\mathrm{T} \pm f_\mathrm{TM}$) can identify misalignment of pitch circles of toothed wheels relate to rotation axle or failure of gearbox bearings (f_W is the rotational frequency of wheelset and f_TM rotational frequency of traction motor.

5. Results example

The fig. 2 and 3 present comparison of two spectrograms of passing of different trainsets (trainset No. 122 and 137).

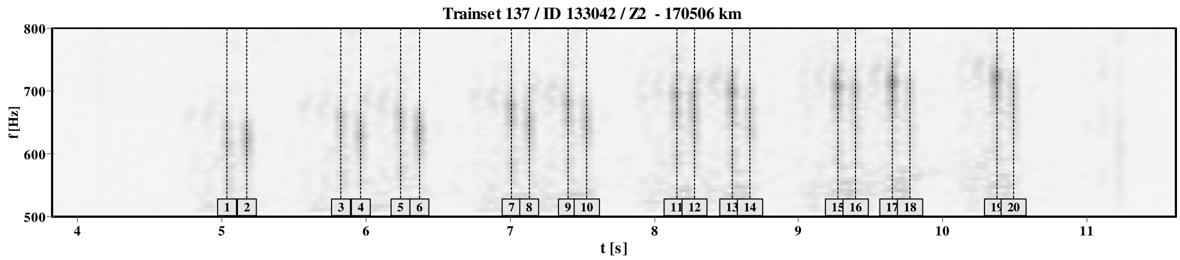

Fig. 2: Spectrogram of passing of trainset No. 137.

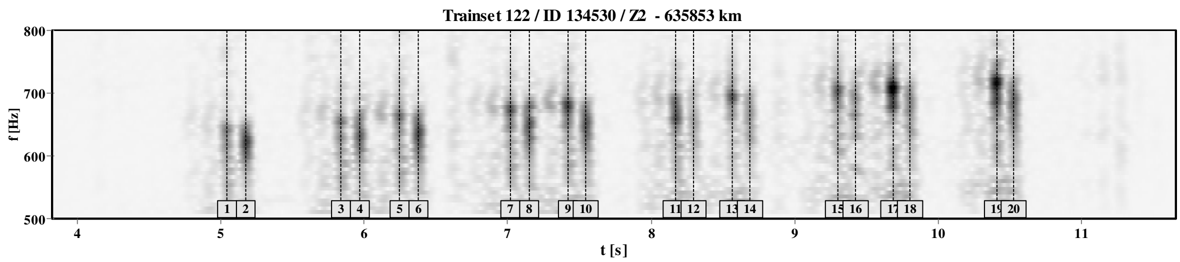

Fig. 3: Spectrogram of passing of trainset No. 122.

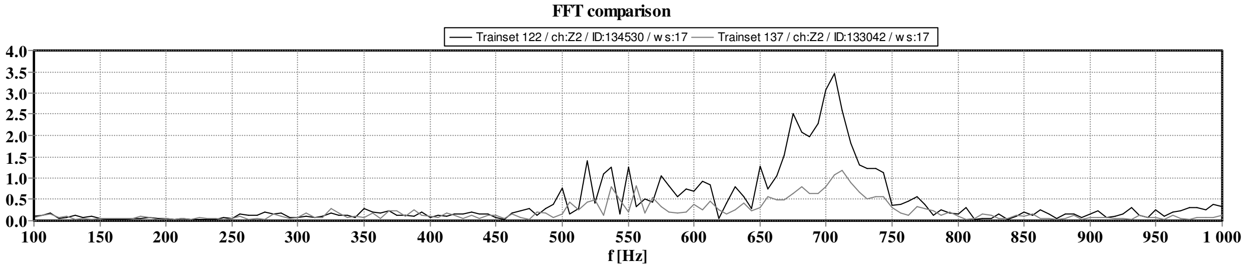

Fig. 4: Comparison of FFT spectrums for passing of 17th trainset axle.

The spectrograms of acceleration signal (sensor z_2) perform responses of gearboxes of all axles of the trainsets. There is lower response in the fig. 2 relate to fig. 3. The fig. 4 shows comparison of FFT spectrums only for 17th passing axle of each trainset. A difference between spectrums is clear especially in area of axle gearbox tooth frequency.

6. Conclusions

Results of evaluation of thousands passing show that the responses are possible to detect and frequency analysis with utilisation of neural network is the best way. Our diagnostic system is now able, using acceleration signals, to distinguish each trainset. For the correct behaviour, several trainset passing have to be measured with defined failure for learning and training of neural network to this failure symptom. To monitoring of failure development, it is necessary to carry out the measurement for a long time in defined time periods with an operation and maintenance data collection together. These activities will be solved in next stage of our project. The creation of the complete system for detection failures of passing vehicles according fig. 5 is our main aim.

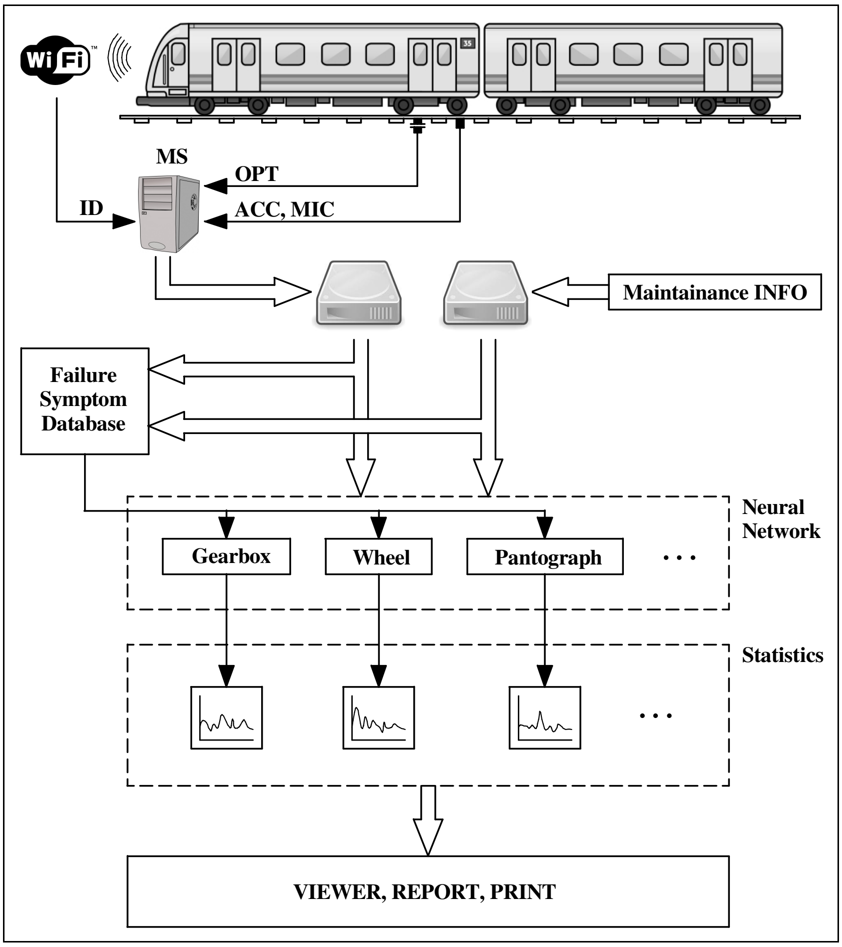

Fig. 5: Block diagram of diagnostic system for detection failures of passing vehicles.

Acknowledgement

This paper was supported by Technological Agency of Czech republic within the project No. TE 01020038.

References

VÁGNER, J., ZELENKA, J., HÁBA, A., KOHOUT, M., HAVLÍČEK, P. Stationary device for vibrodiagnostics of passing vehicle. In *Vibroengineering PROCEDIA Volume 6*. Kaunas : JVE International, 2015, p. 98-103. ISSN 2345-0533.

22nd International Conference
ENGINEERING MECHANICS 2016
Svratka, Czech Republic, 9 – 12 May 2016

USING GPU COMPUTING FOR THE SOLUTION OF A CDEM PROBLEM

V. Vančík*, B. Patzák**

Abstract: *In this paper we introduce an approach for the solution of a coupled discrete and finite element method (CDEM) designed for effective implementation on a graphics processing unit (GPU). A static problem is solved using dynamic relaxation while an optimum load-time history keeps the inertial forces small, thus eliminating the need for damping. Explicit time integration using central difference method is used. Each element is integrated independently and potential interelement contacts are enforced using penalty forces. This allows to avoid the need for forming global characteristic matrices and leads to a formulation well suited to GPU processing. To test the stability and accuracy of the proposed method, we start with a serial CPU implementation and examine a three-point bending test with the beam composed of dicrete deformable blocks (represented by traditional finite elements) connected by linear springs. The CPU code will serve as the starting point of the GPU implementation.*

Keywords: GPU computing, CDEM, dynamic relaxation, explicit integration.

1. Introduction

A GPU is a piece of hardware with a many-core architecture where all the cores have to perform the same instruction with their unique data within one instruction cycle (the SIMD approach to parallelism). The significantly higher computing performance as opposed to its CPU counterpart (see ("The CUDA C Programming Guide", 2015) for a detailed comparison of performances) has always made it attractive for scientific computations. However, since it was specifically designed for efficient processing of the graphics pipeline ("Graphics pipeline", 2016), the first attempts at using it for general-purpose computing had to deal with a lack of appropriate software development tools.

A big step towards easier development of general purpose GPU (GPGPU) code was made in 2006 with the introduction of the CUDA platform ("CUDA Toolkit Documentation", 2015) by the company nVidia. The platform introduces minor extensions for existing high-level programming languages (C/C++ and Fortran among others), which provide direct control over the GPU.

Nowadays, GPGPU computing is used to accelerate calculations in many scientific fields. The reference (Fu et al., 2014) reports an 87x speedup on the stiffness matrix assembly and an 51x speedup on the linear system solver in their GPU implementation of the FEM pipeline. The reference (Wang et al., 2013), which provided inspiration for our method, reports a speedup of up to 400 for single precision calculations. An important aspect of GPU programming is memory management. For the optimum performance, the data have to be kept in local memory, the non-local data access can be prohibitively expensive leading to high communication/computation ratio. Furthermore, an efficient algorithm obviously has to be well suited for the SIMD architecture.

2. Method of solution

The problem we focus on is a domain consisting of individual discrete finite elements with mutual contacts (See Figure 1). This approach allows for the modelling of discrete cracking, for example, but as we are still in the early testing phase, the contacts are realized as linear elastic springs. We believe that if

* Ing. Vladimír Vančík: Department of mechanics, Czech technical university in Prague, Faculty of civil engineering, Thákurova 7/2077; 166 29, Prague; CZ, vladimir.vancik@fsv.cvut.cz

** Prof. Dr. Ing. Bořek Patzák: Department of mechanics, Czech technical university in Prague, Faculty of civil engineering, Thákurova 7/2077; 166 29, Prague; CZ, borek.patzak@fsv.cvut.cz

we avoid the global stiffness matrix assembly, we can come up with an efficient GPU algorithm for the solution of the described problem. This is why we choose to use dynamic relaxation with explicit time integration to solve the linear static problem. Using the explicit integration allows us to calculate the internal forces for each element individually. The only information needed from the rest of the domain are the displacements

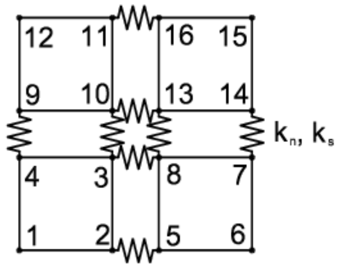

Figure 1: A sketch of the CDEM domain with numbered nodes. The values k_n and k_s denote the normal and shear (tangential) contact stiffness, respectively.

of the neighbor nodes (the nodes connected to the element's nodes by springs). In this study, we consider $2D$ plane stress elements. The element stiffness forces are obtained as

$$\boldsymbol{f_{es}} = -\boldsymbol{K_e}\boldsymbol{u_e}$$

and the damping forces as

$$\boldsymbol{f_{da}} = -\boldsymbol{C}\dot{\boldsymbol{u}}_{\boldsymbol{e}}$$

where $\boldsymbol{u_e}$ is the vector of nodal displacements of the element, $\dot{\boldsymbol{u}}_{\boldsymbol{e}}$ the vector of nodal velocities, $\boldsymbol{K_e}$ the element stiffness matrix and C the damping matrix. In this study, we model dumping using Rayleigh model, where the damping matrix is expressed as a mass matrix multiplied by a so called Rayleigh coefficient α_c. The contact stiffness forces, f_{cs}, are obtained node by node. In the simple case of full face contact, each node can have a maximum of two neighbors correspondingly to its two adjoining element edges. The contact stiffness is characterized by the local contact stiffness matrix

$$\boldsymbol{K_{c,l}} = \begin{pmatrix} k_n & 0 \\ 0 & k_s \end{pmatrix}$$

where the values k_n and k_s denote the normal and shear (tangential) contact stiffness, respectively. The transformation matrix is defined based on the normal vector $\boldsymbol{n}$ of the appropriate element edge as

$$\boldsymbol{T} = \begin{pmatrix} n_1 & n_2 \\ -n_2 & n_1 \end{pmatrix}$$

with n_1, n_2 being the components of the normal vector in the global coordinate system. The contact forces from each neighbor can now be calculated as

$$\boldsymbol{f_{cs,n}} = \boldsymbol{T^T}\boldsymbol{K_{e,l}}\boldsymbol{T}\boldsymbol{\Delta u}$$

where $\boldsymbol{\Delta u} = \boldsymbol{u_{neighbor}} - \boldsymbol{u_{node}}$ is the relative displacement of the node and its neighbor in the global coordinate system. The contributions from the individual neighbors can be assembled into the element-level vector of contact forces $\boldsymbol{f_{cs}}$. The next step is to calculate the inertial forces from the force balance equation as

$$\boldsymbol{f_{in}} = \boldsymbol{f_{es}} + \boldsymbol{f_{cs}} + \boldsymbol{f_{da}} + \boldsymbol{f_{ex}} + \boldsymbol{f_{re}}$$

where the vectors $\boldsymbol{f_{ex}}$ and $\boldsymbol{f_{re}}$ represent the external forces (load) and reactions, respectively. Finally, we get the nodal accelerations for the next time step as

$$\ddot{\boldsymbol{u}}_{\boldsymbol{e,i+1}} = \boldsymbol{M^{-1}}\boldsymbol{f_{in}}$$

where M is the lumped mass matrix.

We examine two possible approaches to obtaining the static solution with this method. First option is to apply the load all at once and examine a damped system until the transient dynamic part of the solution disappears. Alternatively, we can use the optimum load-time function proposed in the paper (Řeřicha, 1986), which should reach the static solution exactly at the end of loading, the error depending on the ratio of the natural frequency of the system and the total time of loading.

3. Test problem – three-point bending

As a testing example, we use a model of a beam with the length of $2\ m$, square cross section with the side of $0.2\ m$, Young's modulus $E = 25\ GPa$, Poisson's ratio $\nu = 0.2$ and density $\rho = 2500\ kg/m^3$. The beam is loaded in the center by a force of $400\ kN$.

The difference between a CDEM solution with springs and a standard FEM solution with the elements sharing nodes is influenced by the stiffness of the springs – higher stiffness means lower difference but also limits the length of stable time step. The natural period of the beam can be deduced from the time-deflection curve of the undamped solution seen in Figure 2. The figure further compares the curves of two solutions with a load function and a solution with impulse load and a damping factor $\alpha_c = 1000$. We see that the accuracy of the solution with load function increases for a longer loading time of double the natural period.

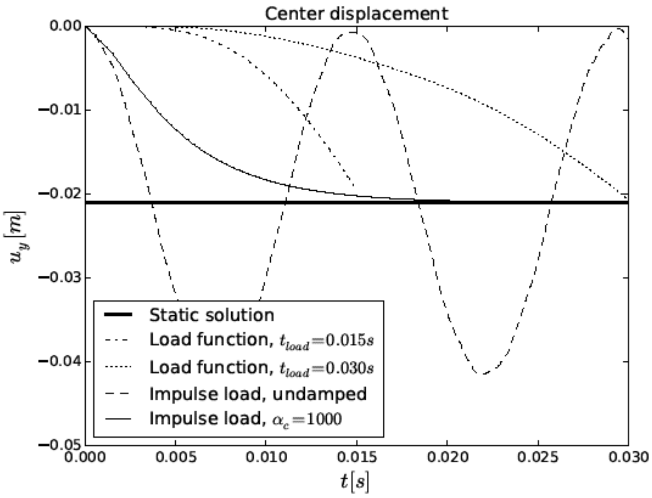

Figure 2: Deflection-time curves for various loading strategies for a beam with the spring stiffness factor of 10. Length of the time step is $1.5 * 10^{-8}$.

Following is the C++ code sample of the explicit integration as a loop across single degrees of freedom, ready for GPU parallelization.

```
for (int k = 1; k <= maxiter; k++) { // Loop of time steps
loadfunc = load_function(k*dt / t_load);
for (i = 0; i < nnodedofs*nnodes; i++) {
// Loop of dofs - increment displacement and velocity
  u[i] += dt*v[i] + 0.5*dt*dt*a[i];
  v[i] += dt*a[i];
}
for (i = 0; i < nnodedofs*nnodes; i++) {
// Loop of dofs - Calculate balance of forces and resulting acceleration
  int eid = i / stiffdim; // global number of element
  int nid = (i / nnodedofs) * nnodedofs; // number of dof 1 of this node
  int ned = i % stiffdim; // number of the dof within element
  int mdim = stiffdim*stiffdim; // no of elements of the stiffness matrix
  double kc11 = Kc[0], kc21 = Kc[1], kc12 = Kc[2], kc22 = Kc[3];

  // Element stiffness force:
  double F_k_e = 0;
  for (j = 0; j < stiffdim; j++) {
    F_k_e += -K[eid*mdim + j*stiffdim + ned] * u[eid*stiffdim + j];
  }
```

```
  // Contact stiffness force:
  double F_k_c = 0;
  for (j = 0; j < 2; j++) {
    int nbr = neighbors[nid + j];
    if (nbr != 0) {
      double t11 = n_vects[4 * (i / nnodedofs) + 2 * j];
      double t12 = n_vects[4 * (i / nnodedofs) + 2 * j + 1];
      double t21 = -t12, t22 = t11;
      double du_x = u[(nbr - 1)*nnodedofs] - u[nid];
      double du_y = u[(nbr - 1)*nnodedofs + 1] - u[nid + 1];

      if (i == nid) { // X-component
F_k_c += du_x * (t11*(t11*kc11 + t21*kc21) + t21*(t11*kc12 + t21*kc22)) +
       du_y * (t12*(t11*kc11 + t21*kc21) + t22*(t11*kc12 + t21*kc22));
// T_T * Kc * T * du_g

      } else { // Y-component
F_k_c += du_x * (t11*(t12*kc11 + t22*kc21) + t21*(t12*kc12 + t22*kc22)) +
       du_y * (t12*(t12*kc11 + t22*kc21) + t22*(t12*kc12 + t22*kc22));
// T_T * Kc * T * du_g
      }
    }
  }
  double F_c = -C[i] * v[i]; // Damping force
  // Reaction force - in supports, 1 means fixed dof and 0 means free dof
  double F_r = supports[i] * (-F_k_e - F_k_c - F_c - loadfunc*load[i]);
  z[i] = F_k_e + F_k_c + F_r + F_c;
  a[i] = Mi[i] * (z[i] + loadfunc*load[i]);
}
```

4. Conclusions

Two approaches to a dynamic solution of a linear static problem were compared. Although we could achieve an accurate solution, this was done with exclusive tuning of the calculation parameters (namely the time step length). Before we move on to the GPU implementation, we have yet to come up with a reliable method of estimating a stable time step length in order for the resulting code to be able to process arbitrary input.

Acknowledgements

Financial support received from the Grant Agency of the Czech Technical University in Prague under SGS project submitted with the number OHK1-093/16 is gratefully acknowledged.

References

CUDA Toolkit Documentation (2015). [Online]. Retrieved 2016-02-11 from http://docs.nvidia.com/cuda/

Fu, Z., James Lewis, T., Kirby, R. & Whitaker, R.. (2014). Architecting the finite element method pipeline for the GPU. *Journal of Computational and Applied Mathematics, vol. 257*, 195-211. http://doi.org/10.1016/j.cam.2013.09.001

Graphics pipeline (2016). [Online]. Retrieved 2016-02-11 from https://en.wikipedia.org/wiki/Graphics_pipeline

Řeřicha, P. (1986). Optimum load time history for non-linear analysis using dynamic relaxation. *International Journal for Numerical Methods in Engineering*, *23*(12), 2313-2324.

The CUDA C Programming Guide (2015). [Online]. Retrieved 2016-02-11 from http://docs.nvidia.com/cuda/cuda-c-programming-guide/

Wang, L., Li, S., Zhang, G., Ma, Z. & Zhang, L.. (2013). A GPU-Based Parallel Procedure for Nonlinear Analysis of Complex Structures Using a Coupled FEM/DEM Approach. *Mathematical Problems in Engineering, vol. 2013*, 1-15. http://doi.org/10.1155/2013/618980

22nd International Conference
ENGINEERING MECHANICS 2016
Svratka, Czech Republic, 9 – 12 May 2016

SYSTEM IDENTIFICATION OF A TRUSS BEAM

M. Venglár*, M. Sokol**, R. Ároch***

Abstract: *The article deals with structural health monitoring (SHM) using non-destructive vibration based method. Modal analysis of a truss beam was prepared in software ANSYS 13.0. The steel truss beam was supported as a cantilever for this experimental measurement. Accelerations of the structure were measured at 22 points (12 points in the horizontal direction, 6 points in the vertical direction and 4 points were situated at the mid-span of diagonal members). We also focused on model similarity. We compared natural frequencies, also mode shapes and their mutual compliance. The conformity was good enough in many cases and so the model similarity was high. The damage was investigated at the diagonals, which were fastened by bolts to the other members. Then, the bolts were loosened and the response of the structure to simulated damage was determined. Global mode-shapes were influenced minimally by structural damage of the joint and therefore the damage should be monitored directly at the specific elements. Such monitoring can be applied to monitor real truss bridges, but it requires more sensors and hence higher input cost.*

Keywords: Structural Health Monitoring, Modal Analysis, System Identification, Truss Beam, Model Similarity.

1. Introduction

Nowadays, system identification of bridge structures is achieving popularity among scientific teams. We can introduce several examples as reasons: increasing security demands of new structures and optimization of maintenance costs during the lifetime. In addition to the examples, it should be noted that bridge structures are usually obsolete. According to the paper (Ahlborn et al., 2010), the average age of bridges in USA is 43 years. The last circumstance from Pittsburgh confirms this fact. The 94-year-old Greenfield Bridge had to be demolished. Slovakia is in an analogous situation. Bridges in Slovakia are a few years older in average, according to the paper (Paulik, 2014). The mentioned fact has caused not so good technical conditions of bridges in Slovakia. In many cases, the main reason is insufficient maintenance during service time. This situation can result into a necessity of a later expensive complete reconstruction. The structural health monitoring (SHM) of structures can help to avoid the stated situation. Therefore, this paper deals with SHM of an experimental model of a truss beam.

2. Models

Firstly, we have prepared a numerical model of the truss beam and then we have started with experimental measurements in our laboratory.

2.1. Numerical model

As the first step, a FE model was created using software ANSYS. The elements BEAM4 were mainly used. We have analyzed the truss beam (Fig. 1). Cross-sectional dimensions and other characteristics of elements of the system were carefully measured. The numerical model has also considered the weight of the used accelerometers and the exciter. It was considered to achieve the best model similarity. Concentrated mass was modelled as an element MASS21. Modal analysis was done after the model was prepared.

* Ing. Michal Venglár: Slovak University of Technology, Faculty of CE, Department of Structural Mechanics; Radlinskeho 11, 810 05, Bratislava; SK, michal.venglar@stuba.sk

** prof. Ing. Milan Sokol, PhD.: Slovak University of Technology, Faculty of CE, Department of Structural Mechanics; Radlinskeho 11, 810 05, Bratislava; SK, milan.sokol@stuba.sk

*** doc. Ing. Rudolf Ároch, PhD.: Slovak University of Technology, Faculty of CE, Department of Steel and Timber Structures; Radlinskeho 11, 810 05, Bratislava; SK, rudolf.aroch@stuba.sk

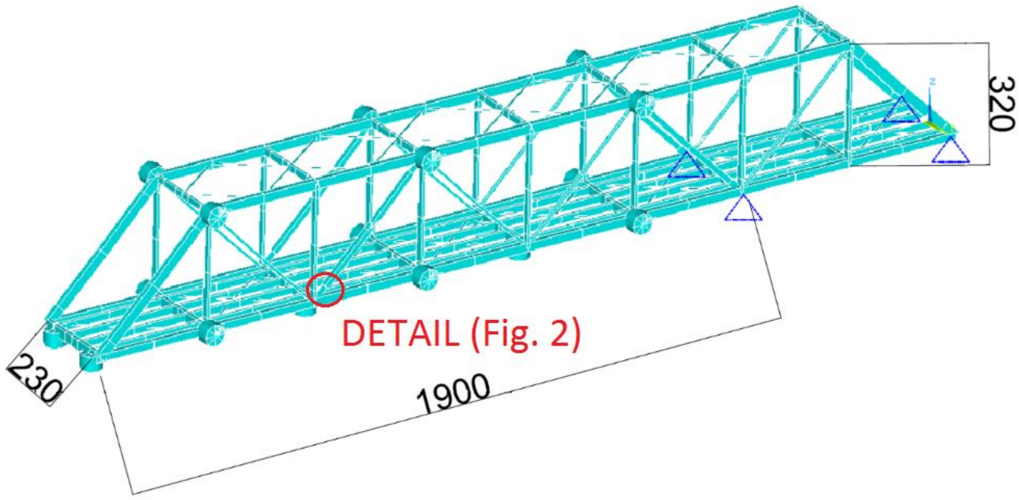

Fig. 1: Numerical Model.

2.2. Experimental model

The steel truss beam was supported as a cantilever for our measurements. The cantilever had the overhang 1900 mm long. The cross-section of the truss is closed (through truss) with a width of 230 mm and a height of about 320 mm. Diagonals of the truss beam form a 45° angle with the bottom and/or with the upper chords (Fig. 2 a). The experimental model has been weighed also.

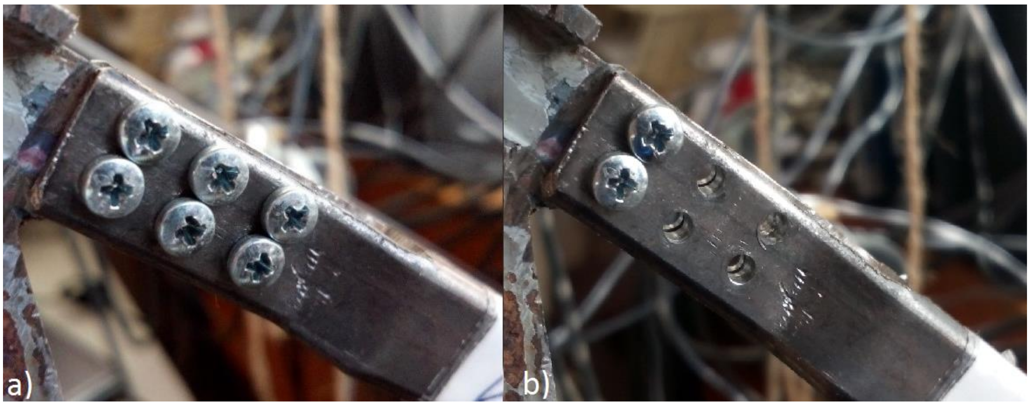

Fig. 2: Joint Detail a) intact structure, b) damaged structure.

2.3. Model similarity

The difference in weight of the FEM model and the experimental model was low (only 0.44%). The experimental model was measured after modal analysis on the FE model. Then we compared the first four global mode-shapes.

Tab. 1: Comparison of the measured and calculated natural frequencies for the cantilever truss beam.

No. of the mode-shape (direction)	Measured frequency (A)	Calculated frequency (B)	Error [%] $\frac{(A-B)}{\max(\mathrm{A,B})}$
1st – in Y direction	14.81 Hz	14.71 Hz	+0.675
2nd – in Z direction	25.33 Hz	25.08 Hz	+0.987
3rd – around X axis	35.42 Hz	34.93 Hz	+1.383
4th – in Y direction	77.63 Hz	77.16 Hz	+0.605

The MAC (Modal Assure Criterion) value was used to obtain a high model similarity, specifically Cross-MAC. The MAC value can also be used for the evaluation and identification of a damage of structures. The method is based on a direct comparison of mode-shapes. The MAC value can be either 0 (absolute incompatibility in mode-shapes) or 1 (for full compliance). In paper (Wang & Chan, 2009) the following formula is reported:

$$MAC(i,j) = \frac{({\phi^{A}}_{i}^{T} {\phi^{B}}_{j})^2}{({\phi^{A}}_{i}^{T} {\phi^{A}}_{j})({\phi^{B}}_{i}^{T} {\phi^{B}}_{j})} \qquad (1)$$

where ${\boldsymbol{\phi}^{A}}_{i}$ is the i-th mode-shape vector of the intact structure (or in the other case, the FEM model for the Cross-MAC value) and ${\boldsymbol{\phi}^{B}}_{j}$ is the j-th mode-shape vector of the damaged structure (or in the other case, the experimental model for Cross-MAC value). The software ModalVIEW R2 was used for comparison of the mode-shapes through Cross-MAC values.

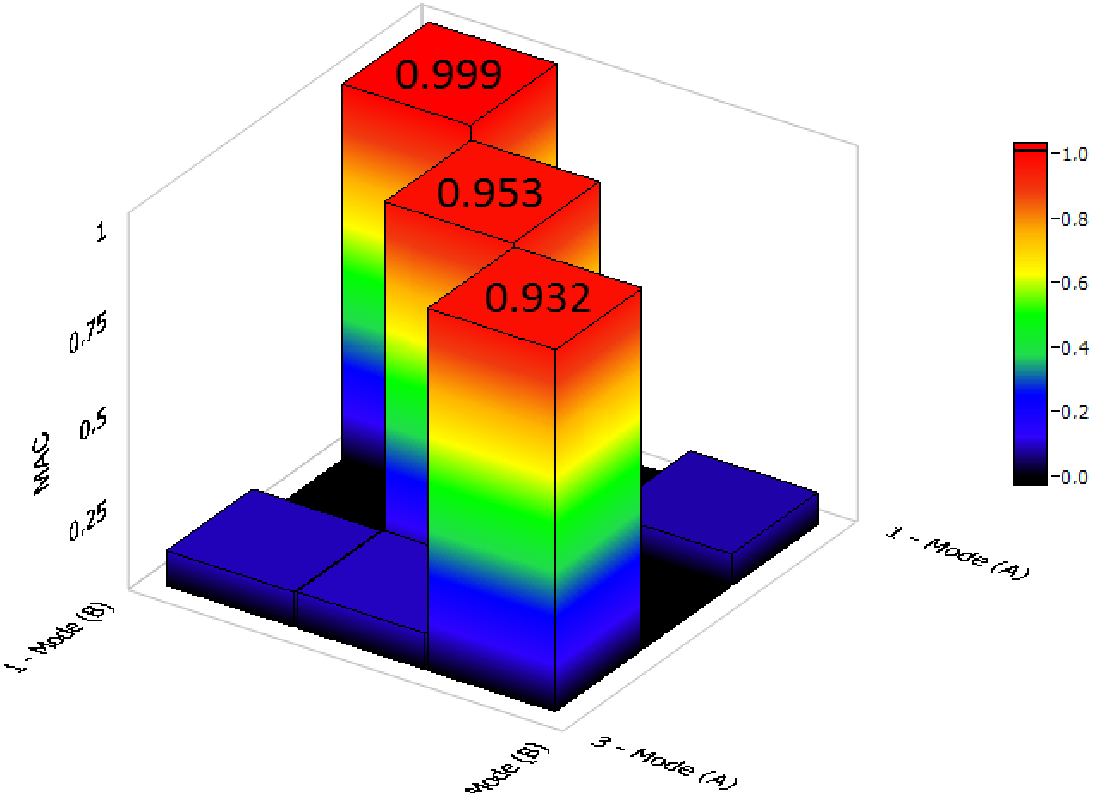

Fig. 3: Cross-MAC values (A means measured mode, B means calculated mode by FEM).

3. System identification

A number of publications are devoted to methods based on the natural frequency changes (Carden & Fanning, 2013; Kim et al., 2003; Wang, Lie & Zhang, 2016). The relationship among the changes in weight, stiffness and values of natural frequencies is fundamental for these methods. The advantage of this method is a lower demandingness of equipment for a measurement. It is theoretically sufficient to use only one sensor. So we have chosen the easiest method for initial system identification on the truss bridge model – via the mentioned method based on natural frequency changes.

Because of the high model similarity, the damage was modelled only in ANSYS software. The object of our interest for system identification was the simple supported truss bridge structure (Fig. 4). The first state was the intact structure (without damage). The second investigated state was a damaged structure. The damage was represented by loosened 4 bolts from the joint detail (Fig. 2 b). The comparison among these two states is showed in the following Tab. 2.

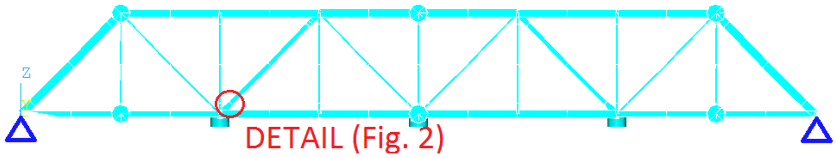

Fig. 4: Simple supported truss beam.

Tab. 2: Damage detection for the simple supported truss beam (Fig. 4).

Global mode-shapes (Global natural frequency)			Local mode-shapes (Natural frequency of diagonal member)		
Mode no. and state	Measured frequency	Calculated frequency	Mode no. and state	Measured frequency	Calculated frequency
1st – in Y direction (intact structure)	37.01 Hz	36.32 Hz	1st – in Y direction (intact structure)	145.62 Hz	144.97 Hz
1st – in Y direction (with damage)	36.97 Hz	36.32 Hz	1st – in Y direction (with damage)	141.68 Hz	141.00 Hz
2nd – around X axis (intact structure)	68.74 Hz	67.82 Hz	2nd – in Y direction (intact structure)	unmeasured	330.16 Hz
2nd – around X axis (with damage)	68.69 Hz	67.71 Hz	2nd – in Y direction (with damage)	unmeasured	325.21 Hz

4. Conclusions

The model similarity satisfied our expectations. Provided that complete characteristics of the cross-sections are available we can effectively use the model similarity for real structures in the next research.

The subsequent assessment of the damage (loosened 4 bolts) shows satisfying results. Real truss bridge structures can be, however, similarly identified by this method, but with enhancements in applied measuring equipment. There is a necessity to choose another method for identifying the damage of bridge structures over the Vah River channel which will be the aim of our next investigation.

Acknowledgement

This paper has been supported by the Slovak Research and Development Agency (SRDA) – grant from research program No. APVV-0236-12.

References

Ahlborn, T.M. et al. (2010) The State-of-the-practice of modern structural health monitoring for bridges: A comprehensive review, Michigan TECH, Michigan.

Carden, E.-P. & Fanning, P. (2004) Vibration based condition monitoring: A review. Structural Health Monitoring, 3, 4, pp. 355-377.

Kim, J.-T. et al. (2003) Damage identification in beam-type structures: frequency-based method vs mode-shape-based method. Engineering Structures, 25, 1, pp. 57-67.

Paulik, P. (2014) Bridges in Slovakia. Jaga, Bratislava.

Wang, L., Lie, S.T. & Zhang, Y. (2016) Damage detection using frequency shift path. Mechanical Systems and Signal Processing, 66–67, pp. 298-313.

Wang, L. & Chan, T.H.T. (2009) Review of vibration-based damage detection and condition assessment of bridge structures using structural health monitoring, in: The Second Infrastructure Theme Postgraduate Conference: Rethinking Sustainable Development: Planning, Engineering, Design and Managing Urban Infrastructure, Queensland University of Technology.

22nd International Conference
ENGINEERING MECHANICS 2016
Svratka, Czech Republic, 9 – 12 May 2016

THE EFFECT OF THE PITCH SUPPORT ELASTICITY ON THE NACA0015 PROFILE AEROELASTIC PROPERTIES

V. Vlček[*], I. Zolotarev[**], J. Kozánek[***]

Abstract: *The aeroelastic experiments realized in wind tunnel of the Institute of Thermomechanics with Mach numbers M ~ 0.20-0.22 and with the interval of Reynolds numbers Re = (2.4-2.6).10^5, are presented. These results correspond to the self-excited vibration of the profile NACA0015 with two degrees of freedom allowing the profile rotation in 1/3-chord axis and allowing the vertical displacement of the profile. The dependence of vibration frequency on the wind-flow velocity has been obtained. Comparing with the previous experiments the influence of the pitch support elasticity on the profile aeroelastic properties was determined.*

Keywords: aeroelasticity, self-excited vibration, flutter, subsonic flow.

1. Introduction

The aeroelastic and stability vibration problems of profiles are studied after a long time (Fung, 1993, Blevins, 1990, Dowell, 2015). Nevertheless the problems of self-excited vibration in our experimental configuration and investigated in this paper have not been published yet in detail. The scheme of the NACA0015 profile support is shown in Fig. 1. During the earlier experiments the pitch supports had the eigenfrequencies 14.5 Hz and 18.9 Hz for zero air flow velocity – (Vlček & Zolotarev et al., 2016 and Šidlof et al., 2016). In the current experiments the pitch eigenfrequency of the profile was 12.7 Hz. In these cases the shift eigenfrequency was 16.4 Hz. It means that in present measurements, the eigenfrequency of rotation was lower than shift eigenfrequency and also the lowest within the experiments realized in Institute of Thermomechanics – (Vlček & Štěpán et al., 2016; Zolotarev et al., 2012 and Kozanek et al., 2014).

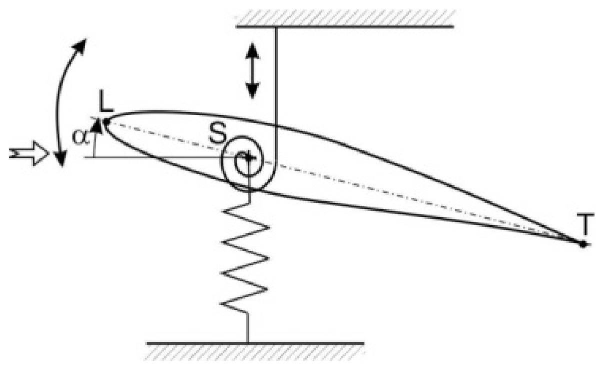

Fig. 1: The scheme of the profile support.

Self-excited aeroelastic vibration of this profile has been studied in lower subsonic speeds. Our aim was to determine the non-stable velocity region of the profile vibration. Attention has been paid to the kinematic behaviour of the profile represented by shift-pitch function.

[*] Ing. Václav Vlček, CSc.: Institute of Thermomechanics of the CAS, v. v. i., Dolejškova 5, 18200 Prague 8; CZ, vlcek@it.cas.cz
[**] Ing. Igor Zolotarev, CSc.: Institute of Thermomechanics of the CAS, v. v. i., Dolejškova 5, 18200 Prague 8; CZ, igor@it.cas.cz
[***] Ing. Jan Kozánek, CSc.: Institute of Thermomechanics of the CAS, v. v. i., Dolejškova 5, 18200 Prague 8; CZ, kozanek@it.cas.cz

2. Experimental results

In figure 2 the results of the experiment are presented in context with other measurements made (see Zolotarev et al., 2012 and Kozanek et al., 2014) in the Institute of Thermomechanics with the same profile, but with the different elasticity of the pitch support.

In the current experiments the pitch eigenfrequency of the profile was 12.7 Hz when air flow velocity M = 0. It was a rare case in the history of similar measurements in Institute of Thermomechanics, when the pitch eigenfrequency was lower than shift eigenfrequency. Other data in Fig. 2 had eigenfrequencies 14.5 Hz and 18.9 Hz for M = 0. In all these cases the shift eigenfrequency was 16.4 Hz. It is evident, that the increase in the pitch-support elasticity corresponding to the pitch-eigenfrequency 12.7 Hz would result in a substantial reduction of the velocity interval with occurrence of the self-excited vibration in the range M = 0.199-0.217.

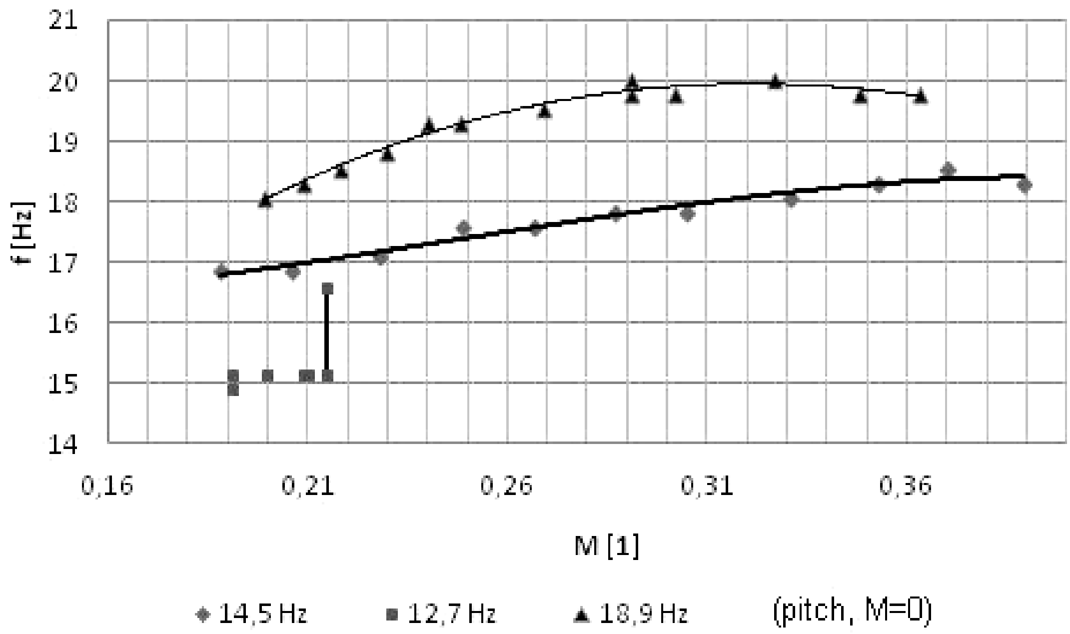

Fig. 2: Frequencies of the profile self-excited vibration.

2.1. Amplitude modulation of the pitch time vibration and the profile instability

The decreased stiffness of the pitch support has resulted in the amplitude modulation of the pitch time vibration (e.g. Fig. 3, Vlček & Zolotarev et al., 2016). This phenomenon for 12.7 Hz initial pitch eigenfrequency (M=0) appeared in the narrow velocity interval M =0.199-0.217, where the self-excited vibration occurred. This vibration is shown in Fig. 4 as the relationship between pitch and shift parametric time function. The shape of this curve has the form of a double-loop. The time evolution of circulation in both loops is in the counter-clockwise direction. The right loop is centered towards the origin of coordinates and the left one has an eccentric position.

At the bottom of the Fig. 3 there are depicted the results of the FFT analysis. The left side of the picture is dedicated to the pitch vibration and the pair of non-zero significant frequencies was determined. In this case, 15.1 Hz is related to the centered loop frequency, the 7.8 Hz corresponds to the eccentric loop frequency.

The amplitude of the pitch vibration and shift vibration are different time functions. The upper amplitude of vibration in the pitch alternates on two levels, while lower amplitude remains constant. On the other hand the shift vibration has only one significant frequency 15.1 Hz with the amplitude almost constant. This common value explains the connection of both loops in Fig. 4.

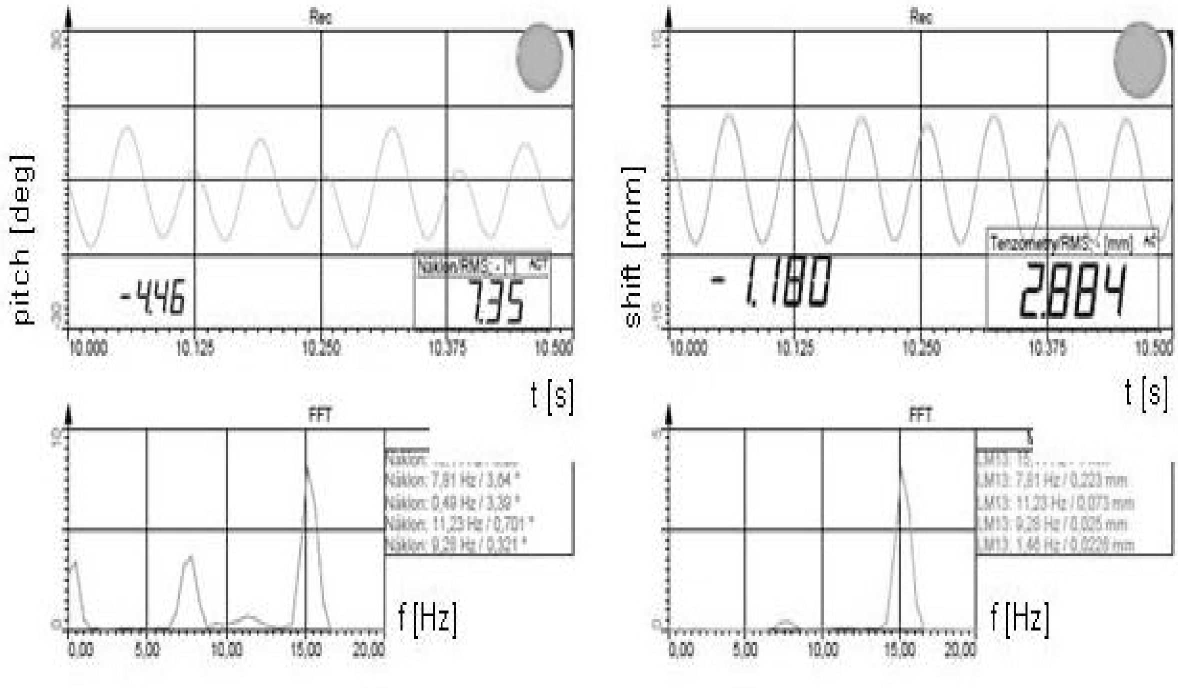

Fig. 3: Pitch vibration (left part) and shift vibration (right) of the profile in the case of the two-loop regime.

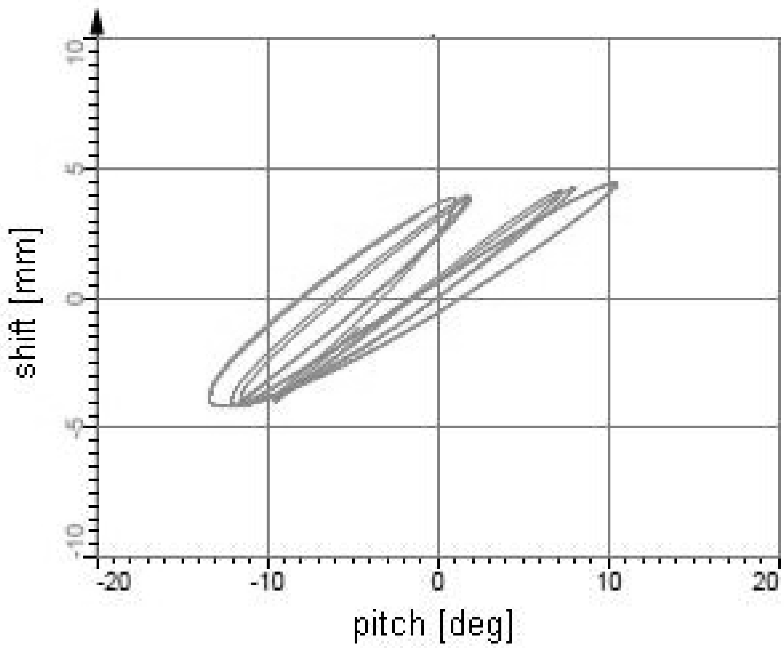

Fig. 4: The shift as a function of the pitch corresponding to Fig. 3.

The above double loop regime for small stiffness of the pitch support was specific. In almost all other experiments in Institute of Thermomechanics realized for higher stiffness the one loop vibration occurred – see e.g. Vlček & Zolotarev et al., 2016. However, in one of these cases already existed frequency of vibration, corresponding to the left eccentric loop in Fig. 4, but its amplitude was significantly lower than dominant one.

3. Conclusions

- The self-excited vibration of the 2D profile was studied (see also Vlček et al., 2015) and its dependency on the Mach number for one combination of the pitch and the shift elastic supports was obtained.
- The experiments indicate a possibility to suppress or increase self-excited oscillation of such profile. Using appropriate relationship between the elasticity of supports of both degrees of freedom it is possible to replace the stable „one-loop“ vibration by less stable „double-loop“ vibration or vice versa and by this way the occurrence of the self-excited vibration substantially suppress or increase.
- This changes of the vibration character are connected with the modulation either of the pitch or shift time course. The shift modulation was observed in previous experiments (Vlček et al., 2016) and pitch modulation is described here.

Acknowledgement

The authors have been sponsored by the Grant Agency of the Czech Republic under Grant № 13-10527S "Subsonic flutter analysis of elastically supported airfoils using interferometry and CFD". The measurements were performed in cooperation with P. Šidlof, M. Štěpán, M. Luxa, D. Šimurda and J. Horáček.

References

Fung, Y. C. (1993) An Introduction to the Theory of Aeroeleasticity, Dover Publications, Inc, Mineola, New York.

Blevins, R. D. (1990) Flow-Induced Vibration, Van Nostrand Reinhold, Amsterdam.

Dowell, E. (2015) A Modern Course in Aeroelasticity, Springer, Switzerland.

Vlček V., Zolotarev I., Kozánek J., Štěpán M. (2016) Some atypical flutter characteristics of the NACA0015 profile. Colloquium DYMAMESI 2016, Prague, March 1-2, 2016.

Vlček, V., Štěpán, M., Zolotarev. I., Kozánek. J. (2016) Innovation of the experimental facility for the study of flutter in the Institute of Thermomechanics AS CR and some results obtained from initial experiments. Applied Mechanics and Materials, Vol. 821 (2016), pp. 141-151.

Šidlof, P., Štěpán, M., Vlček, V. (2016) Experimental investigation of flow-induced vibration of a pitch-plunge NACA 0015 airfoil under deep dynamic stall. Preprint submited to Journal of Fluids and Structures.

Zolotarev, I., Vlček, V., Kozánek, J. (2012) Experimental results of a fluttering profile in the wind tunnel. Flow-induced Vibration, School of Engineering Trinity College, Dublin, (eds. Meskell, C., Bennett, G.), 2012, pp. 677-680.

Kozánek, J., Vlček, V., Zolotarev, I. (2014) Vibrating Profile in the Aerodynamic Tunnel — Identification of the Start of Flutter, Journal of Applied Nonlinear Dynamics 3(4), 2014, pp. 317–323.

Vlček, V., Štěpán, M., Zolotarev, I., Kozánek, J. (2015) Experimental Investigation of the Flutter Incidence Range for Subsonic Flow Mach Numbers, Proc. of the 21-st International Conference ENGINEERING MECHANICS 2015, Svratka, Czech Republic, 2015, pp. 350-351.

22nd International Conference
ENGINEERING MECHANICS 2016
Svratka, Czech Republic, 9 – 12 May 2016

DETERMINATION OF TEMPERATURES IN OSCILLATING BUBBLES: EXPERIMENTAL RESULTS

K. Vokurka *

Abstract: *The surface temperatures of the plasma core at the final stages of the first contraction phase of spark generated bubbles oscillating under ordinary laboratory conditions in a large expanse of water are determined experimentally. The measurement method is based on the analysis of optical radiation from the bubbles and on an assumption that the plasma core is radiating as a black-body. It is found that the maximum surface temperatures of the plasma core range from 4300 K to 8700 K and these temperatures decrease with a bubble size.*

Keywords: Bubble oscillations, Spark generated bubbles, Temperature in bubbles.

1. Introduction

Bubble oscillations remain an important topic in fluid dynamics. In experimental studies of free bubble oscillations spark generated bubbles represent very useful tools (Huang et al., 2014). The value of temperature in a bubble interior during the final stages of the first contraction has been attracting interest for years, see, e.g., Golubnichii et al. (1980), Baghdassarian et al. (2001), Brujan et al. (2005), Brujan & Williams (2005). In the present paper it is intended to deal with this interesting topic in a greater detail. The analysis is devoted to free bubble oscillation under ordinary laboratory conditions in a large expanse of liquid.

2. Experimental setup

Freely oscillating bubbles were generated by discharging a capacitor bank via a sparker submerged in a laboratory water tank. Both the spark discharge and subsequent bubble oscillations were accompanied by intensive optical and acoustic radiations. The optical radiation was monitored by a detector, which consisted of a fiber optic cable, photodiode (Hammamatsu photodiode type S2386-18L), amplifier, and A/D converter (National Instruments PCI 6115, 12 bit A/D converter with a sampling frequency of 10 MHz). The acoustic radiation was monitored with a Reson broadband hydrophone type TC 4034. The output of the hydrophone was connected via a divider 10:1 to the second channel of the A/D converter. In the experiments a larger number of almost spherical bubbles freely oscillating in a large expanse of liquid were successively generated. The size of these bubbles, as described by the first maximum radius R_{M1}, ranged from 18.5 mm to 56.5 mm, and the bubble oscillation intensity, as described by the non-dimensional peak pressure in the first acoustic pulse $p_{zp1} = (rp_{p1})/(p_\infty R_{M1})$, ranged from 24 to 153. Here p_{p1} is the peak pressure in the first acoustic pulse $p_1(t)$, p_∞ is the ambient (hydrostatic) pressure at the place of the sparker, and r is the hydrophone distance from the sparker centre. Both R_{M1} and p_{zp1} were determined in each experiment from the respective pressure record.

3. Results

An optical record (represented by a voltage $u(t)$ at the output of the optical detector) consists of a pulse $u_0(t)$ that is radiated during the electric discharge and the following explosive bubble growth, and of the pulse $u_1(t)$ that is radiated during the first bubble contraction and the following bubble expansion. The dynamic range of the optical detector was not sufficiently high to record both $u_0(t)$ and $u_1(t)$ in one experiment with a good fidelity. Therefore two sets of experiments were done. The first set of

* Prof. Ing. Karel Vokurka, DrSc.: Physics Department, Technical University of Liberec, Studentská 2; 461 17; Liberec; CZ, karel.vokurka@tul.cz

experiments was aimed at recording the pulse $u_0(t)$ undisturbed, and the second set of experiments was aimed at recording the pulse $u_1(t)$ with an acceptable noise. A link between the two sets of experiments was achieved by using statistical averages from the first set of records to compute the respective values for the second set of records.

An example of the optical pulse $u_1(t)$ from the second set of experiments is given in Fig. 1.

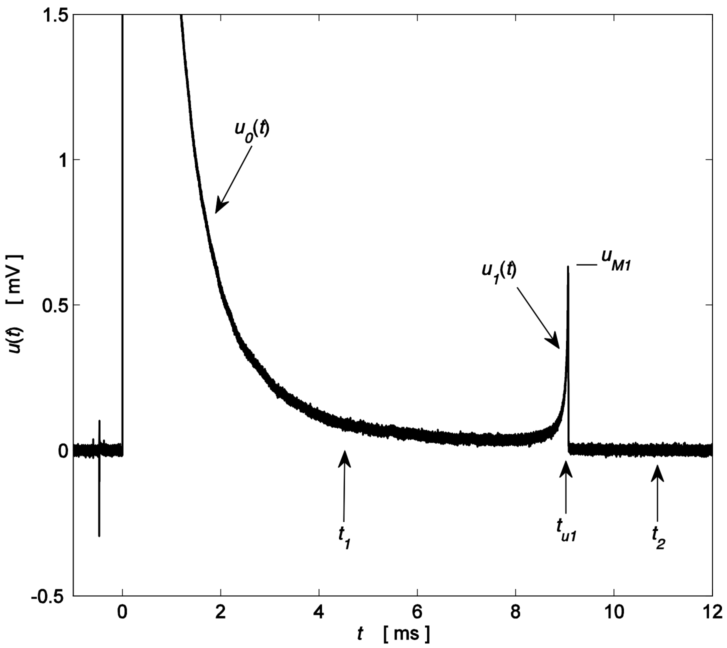

Fig.1: A voltage u(t) at the output of the optical detector. The spark generated bubble has a size R_{M1} = 55.2 mm, and oscillates with an intensity p_{zp1} = 153.2. The time, at which the bubble attains the first maximum radius R_{M1}, is denoted as t_1, and the time, the bubble attains the second maximum radius R_{M2}, as t_2. The pulse $u_0(t)$ is defined to be within the interval $(0,t_1)$, the pulse $u_1(t)$ within the interval (t_1,t_2).

In Fig. 1 the pulse $u_0(t)$ is clipped due to the limited dynamic range of the optical detector. The maximum value of the pulse $u_1(t)$ has been denoted as u_{M1} and the time of its occurrence as t_{u1}. As can be seen in Fig. 1, the optical radiation from the bubble decreases rapidly to zero after t_{u1}. Another interesting fact which can be seen in Fig. 1 is the occurrence of the optical radiation from the bubble during the whole first oscillation. The source of this persisting optical radiation is a plasma core. The bubble interior is filled with two substances. First, it is a transparent matter, which is, most probably, hot water vapour. And second, there is opaque plasma at the bubble centre. The existence of this hot plasma core during the whole first bubble oscillation, that is, even long after the electric discharge has terminated is an astonishing phenomenon observed already by Golubnichii et al. (1980).

Under an assumption that a hot plasma core in a bubble centre radiates as a black-body, an equation enabling the determination of the plasma surface temperature $\Theta(t)$ has been derived in Vokurka & Plocek (2013). The derivation is based on the Stefan-Boltzman Law, the equation of energy partition during the electric discharge, the time variation of the bubble radius $R(t)$, and the voltage $u(t)$ at the output of the optical detector. Particularly, for the voltage record $u_1(t)$ from the second set of experiments the corresponding temperature $\Theta(t)$ is given by the following equation

$$\Theta^4(t) = \frac{\langle \Theta_{M0} \rangle^4 \langle R_{M0} \rangle^2}{\langle u_{M0} \rangle} \frac{u_1(t)}{R_p^2(t)} \quad . \tag{1}$$

Here u_{M0} is the maximum voltage in the pulse $u_0(t)$ and this voltage corresponds to the bubble radius R_{M0}. The surface temperature of the plasma, when the bubble during its growth attains the radius R_{M0}, is Θ_{M0}. The angle brackets < > denote the average values on the first set of experiments. For a given bubble size

R_{M1} these average values can be computed using the regression lines and the polynomial derived in Vokurka & Plocek (2013): $<\Theta_{M0}> = -0.11R_{M1}+17.4$ [kK, mm], $<R_{M0}> = 0.1836R_{M1}$, and $<u_{M0}> = 1.25 \times 10^{-4}R_{M1}^2$ [V, mm].

In Eq. (1), R_p is a radius of a light emitting hot plasma core. An estimate of the radius R_p can be obtained from the knowledge of the bubble wall radius R and of the volume the plasma core occupies in the bubble interior. Denoting a reduction factor as q ($q < 1$), then $R_p = qR$. The variation of the bubble wall radius R with time can be computed using a theoretical bubble model. The exact value of the reduction factor q is not known at present. In this work an estimate of the reduction factor $q = 0.8$ will be used for the vicinity of the first minimum radius R_{m1}, irrespective of the bubble oscillation intensity p_{zp1}.

An example of the variation of the plasma core surface temperature Θ with time t during the first bubble contraction and the following expansion, as computed with eq. (1), is given in Fig. 2.

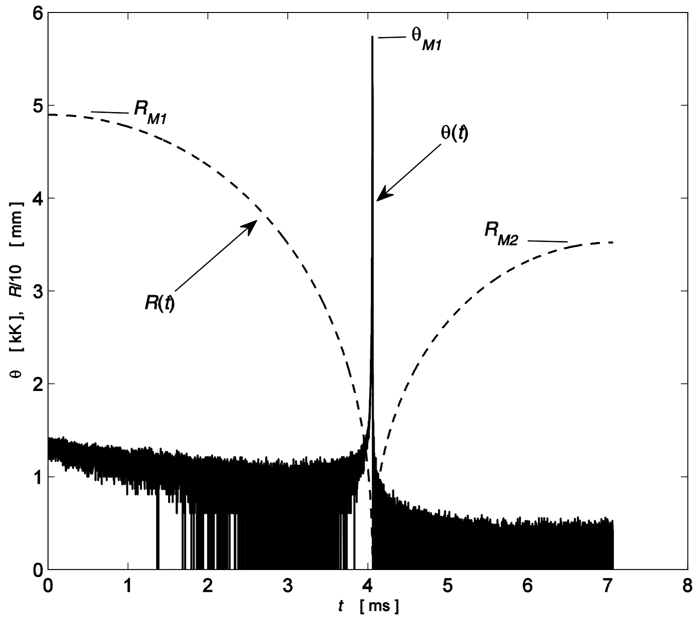

Fig. 2: A time variation of the plasma core surface temperature Θ and of the bubble wall radius R. The size of the experimental bubble is R_{M1} = 49.0 mm, the bubble oscillation intensity is p_{zp1} = 142.1.

A few comments concerning Eq. (1) and Fig. 2 should be presented now. Eq. (1) has been derived under an assumption that the plasma core is a black-body radiator. This assumption seems to be correct in those instants, when the pressure and temperature in the bubble interior are high. And this is fulfilled only in the vicinity of R_{m1}. Hence the computed temperature $\Theta(t)$ shown in Fig. 2 is correct only in the vicinity of the maximum value Θ_{M1}. In other instants the computed temperatures represent just a very rough estimate.

In Eq. (1), only the voltages $u_1(t)$ and u_{M0} are measured directly. The radii $R(t)$ and R_{M0} are computed using Herring's simplified model (Buogo & Vokurka, 2010). The parameters R_{M1} and p_{zp1} have been determined for each record $u_1(t)$ from the associated pressure record. Using these parameters the first bubble minimum radius $R_{m1} = f(R_{M1},p_{zp1})$ can be computed. An estimate of the corresponding plasma core radius is then $R_{pm1} = 0.8R_{m1}$. Thus, using the measured values of u_{M1}, R_{M1}, and p_{zp1} from the second set of experiments and the average values of $<\Theta_{M0}>$, $<R_{M0}>$, and $<u_{M0}>$ determined for a given bubble size R_{M1} from the regression lines and the polynomial given above, the temperature Θ_{M1} can be computed. The values of Θ_{M1} determined in this way for different bubble sizes R_{M1} are displayed in Fig. 3.

The temperatures Θ_{M1} given in Fig. 3 can be compared with experimental results of other researchers. For example, Golubnichii et al. (1980) found that the maximum in the spectrum of the optical radiation lies approximately at 500 nm. Then, using the Wien's Law, the temperature Θ_{M1} = 5800 K is obtained (in this case R_{M1} was 30 mm). Baghdassarian et al. (2001) determined that Θ_{M1} = 7800 K (now R_{M1} ranged from 0.6 mm to 0.8 mm). Finally Brujan et al. (2005) , and Brujan and Williams (2005) determined that Θ_{M1} = 8150 K (in this case R_{M1} ranged from 0.65 mm to 0.75 mm).

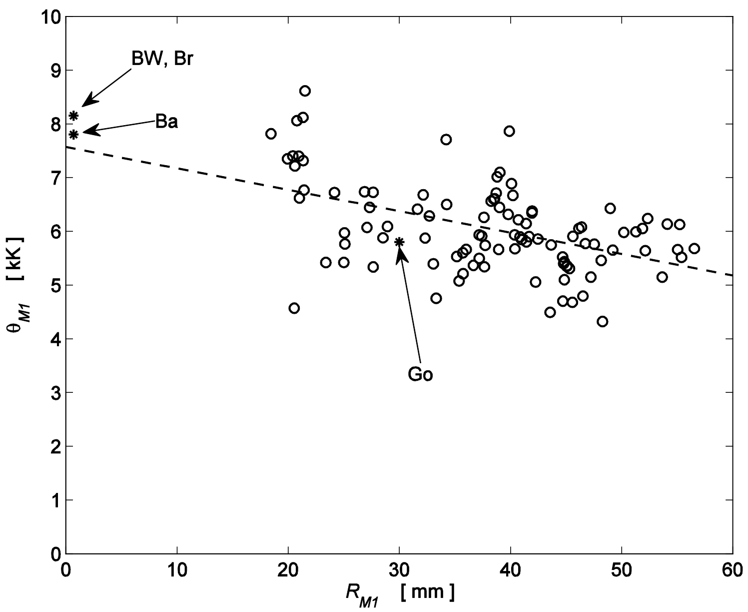

Fig. 3: Variation of experimentally determined maximum surface temperatures of the plasma core during the first bubble contraction Θ_{M1} with the bubble size R_{M1}: 'o' - the values of Θ_{M1} determined in this work, '' - the values of Θ_{M1} determined in works of other researchers.*

4. Conclusions

The surface temperatures of the plasma core inside the spark generated bubbles at the final stages of the first contraction phases have been determined experimentally. It has been found that these temperatures range from 4300 K to 8700 K. Even if the method used here gives only approximate results, these values are in a relatively good agreement with the temperatures published by other researchers.

Acknowledgement

This work has been supported by the Ministry of Education of the Czech Republic as the research project MSM 245 100 304. The author also wishes to thank Dr. Silvano Buogo from the Italian Acoustics Institute, CNR, Rome, Italy, for a very valuable help in preparing the experiments.

References

Baghdassarian, O., Chu, H.-C., Tabbert, B. & Williams, G.A. (2001) Spectrum of luminescence from laser-created bubbles in water. Phys. Rev. Lett., 86, pp. 4934-4937.

Brujan, E.A., Hecht, D.S., Lee, F. & Williams, G.A. (2005) Properties of luminescence from laser-created bubbles in pressurized water. Phys. Rev. E, 72, 066310.

Brujan, E.A. & Williams, G.A. (2005) Luminescence spectra of laser-induced cavitation bubbles near rigid boundaries. Phys. Rev. E, 72, 016304.

Buogo, S. & Vokurka, K. (2010) Intensity of oscillation of spark-generated bubbles. J. Sound Vib. 329, 4266-4278.

Golubnichii, P.I., Gromenko, V.M. & Filonenko, A.D. (1980) Nature of electrohydrodynamic sonoluminescence impulse (in Russion). Zh. Tekh. Fiz., 50, pp. 2377-2380.

Huang, Y., Zhang, L., Chen, J., Zhu, X., Zhen, L. & Yan, K. (2015) Experimental observation of the luminescence flash at the collapse phase of a bubble produced by pulsed discharge in water. Appl. Phys. Lett., 107, 184104.

Vokurka, K. & Plocek, J. (2013) Experimental study of the thermal behavior of spark generated bubbles in water. Exp. Therm. Fluid Sci., 51, pp. 84-93.

22nd International Conference
ENGINEERING MECHANICS 2016
Svratka, Czech Republic, 9 – 12 May 2016

STUDY OF PHYSICOCHEMICAL PROPERTIES OF ZIRCONIUM DIOXIDE ZRO2 3Y - TZP USED IN DENTISTRY

M.Wirwicki[*], A. Zalewska[**], T. Topolinski[***]

Abstract: *The article presents a chemical analysis and static mechanical strength tests on samples, with a geometry suggested by the authors. The market of dental materials is one of the most dynamically developing markets in the world. The materials used in the dental prosthetics must feature high biocompatibility, aesthetics and durability. In particular, the tests for materials used for dental crowns are widely developed. The test results related to the analysis of physical and chemical properties are used to improve the quality of services provided by the dental practices. The authors presented a newly developed method to prepare the mini-samples. 120 samples in 4 test groups were prepared: X-ray diffraction, derivatography, spectral analysis, 3-point bending static test. A chemical analysis showed that the tested material - zirconium dioxide is not susceptible to changes in temperature, and also showed numerous inclusions of other elements in the material.*

Keywords: physicochemical properties, zirconium dioxide, dentistry, 3 point bending tests

1. Introduction

The market of dental materials is one of the most dynamically developing markets in the world. The materials used in the dental prosthetics must feature high biocompatibility, aesthetics and durability. The development of dental materials requires improvement of the following features: chemical composition - biocompatibility, aging resistance of materials, which is reduced with the cyclic load (Munck et al., 2004). The main issue related to the development of dental materials is a lack of reliable analysis of physical and chemical properties of dental crowns and bridges. Zirconium dioxide (ZrO_2) and feldspar are the most commonly used dental prosthetic materials (Denry et al., 2008). Many laboratories around the world test the mechanical properties of dental materials. A review of the literature shows diversity of test methods related to the analysis of zirconium dioxide strength and stability. In particular, the tests for materials used for dental crowns are widely developed (Hisbergues et al., 2009). The test results related to the analysis of physical and chemical properties are used to improve the quality of services provided by the dental practices (Egilmez et al., 2014).

The article presents a method to prepare samples of zirconium dioxide, chemical analysis and static mechanical strength tests.

2. Materials and methods

The following material was used in the physicochemical analysis of zirconium dioxide: Cyrkon Lava by 3M ESPE. The material provided by the manufacturer is available as 60 mm x 25 mm x 16 mm blocks. The sample preparation technique includes three stages: the first involves cutting the material using Buehler ISOMET 5000 precision saw. The next involves polishing the surface with wet abrasive paper. The last stage involves laser cutting using Alfalas WS workstation. The processed samples were sent to the laboratory certified by the manufacturer for sintering (compacting). The process consists in firing the samples in a special furnace at 1410°C for 8 hours, during

[*] M.Sc. (Eng.) Mateusz Wirwicki, Faculty of Mechanical Engineering, UTP University of Sciences and Technology in Bydgoszcz, Al. Prof. S. Kaliskiego 7; 85- 796, Bydgoszcz; PL, Mateusz.Wirwicki@utp.edu.pl tp.edu.pl

[**] PhD Anna Zalewska, Department of Chemical Engineering and Technology, University of Science and Technology in Bydgoszcz, ul. Seminaryjna 2, Bydgoszcz, PL, Anna.Zalewska@utp.edu.pl

[***] Prof. Tomasz Topoliński: Faculty of Mechanical Engineering, UTP University of Sciences and Technology in Bydgoszcz, Al. Prof. S. Kaliskiego 7; 85- 796, Bydgoszcz; PL, Tomasz.Topolinski@utp.edu.pl

which the material shrinks by about 20% in volume. The tests were carried out on 120 samples (1.5 mm x 1.5 mm x 12 mm), divided into 4 groups depending on the physicochemical tests: X-ray diffraction, derivatography, spectral analysis and 3-point bending static test.

The phase composition of tested samples was determined based on the radiographic tests using x-ray diffractometer with URD 6 goniometer by Seifert with CuKα radiation and X-ray diffraction nickel filter. The analysis of data consisted in the comparison of X-ray patterns of tested samples with cards from the JCPDS database.

The thermal analysis was carried out in air atmosphere using Q 1500 D (MOM Budapest) 5°/min derivatograph, which measures change of the sample mass in time. A temperature curve (T), differential thermal analysis curve (DTA), thermogravimetric curve (TG) and thermogravimetric derivative curve (DTG) were plotted on a single graph. The temperature curve (T) allows to determine the transition temperatures.

The x-ray analysis was carried out to determine the chemical composition of the sample surface layer. The tests were carried out using Bruker S1 TITAN handheld X-ray fluorescent (XRF) analyser for a quick elemental analysis. The elements in the tested areas of the samples were quantified.

Static 3-point bending tests using Instron 8874 at ± 25 kN, ± 100 Nm were carried out to determine the mechanical strength of the samples.

3. Results

The X-ray diffractometry allowed to determine the crystallographic phases in the sample. Fig. 1 shows the X-ray pattern of the tested samples. The X-ray patterns were compared with the X-ray patterns for standard substances. A solid line in the graph is the X-ray pattern of the sample, whereas the points indicate peaks in the standard X-ray patterns.

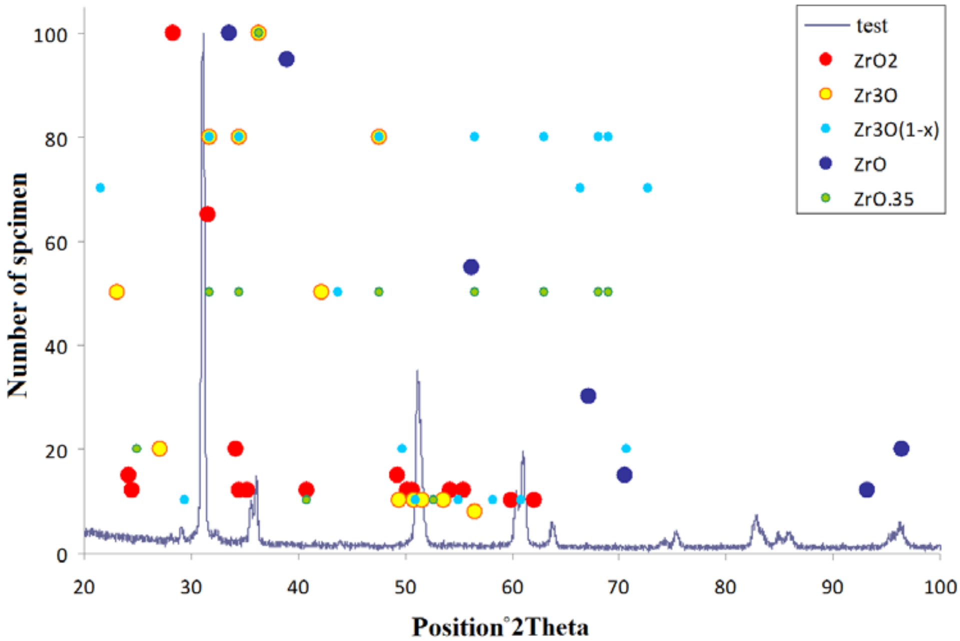

Fig. 1: Interpretation of the X-ray patterns for tested samples

The X-ray pattern allowed to determine the dominant phases in the analysed sample. An oxide phase, with the largest fraction is designated as phase I, whereas the fraction of phase II, which is also dominant is significantly lower. The result shows that the sample contains mostly ZrO and ZrO_2. It is possible, that other phases may be present, but were not identified due to the lack of suitable standards.

The thermogravimetric curves show the transitions temperatures, based on which a change in sample mass in mass percentage at initial, end and maximum temperature can be determined. The graph shows that the sample mass in the analysed temperature range does not change, which verifies the tested system resistance at this temperature range. Fig. 2 shows the thermogravimetric curves and record the temperature curve (T) curve Differential Thermal Analysis (DTA) , thermogravimetric curve (TG) , a derivative of a thermogravimetric (DTG).

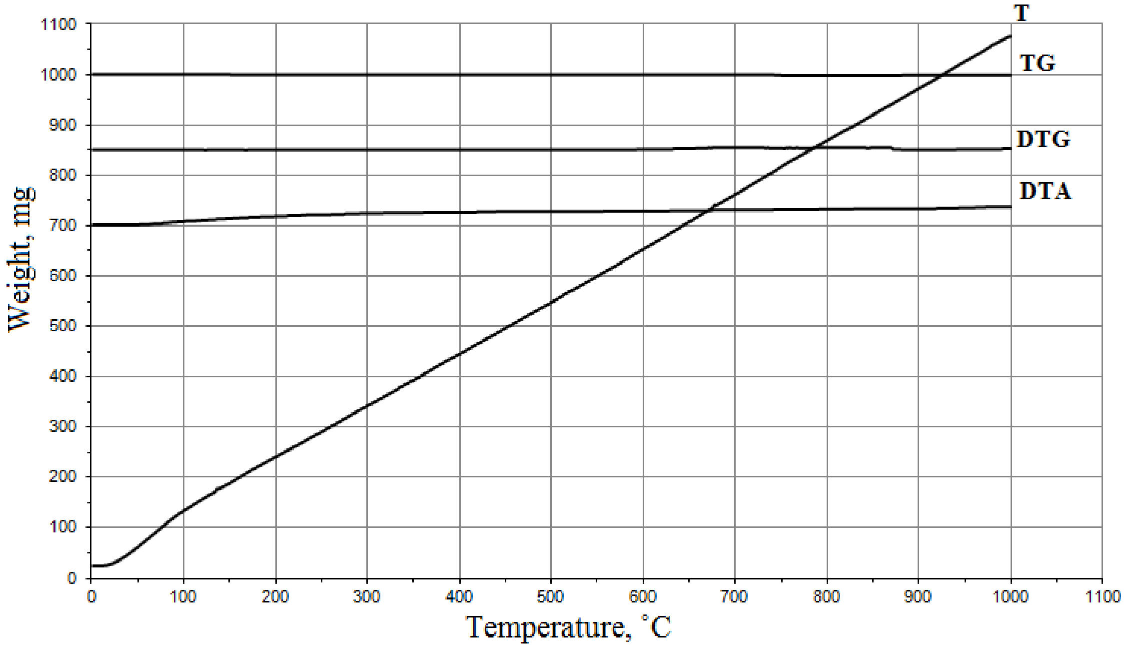

Fig. 2: Thermogravimetric curves of the sample, as change in the sample mass vs temperature.

The spectral analysis was carried out on a sample surface in point mode. Fig. 3 shows the example measurement point. The samples showed high and stable zirconium content at the surface. Due to the location of the measuring point, the statistical analysis showed no significant difference between the zirconium content at the sample surface. It indicates uniform distribution of this element in the tested system.

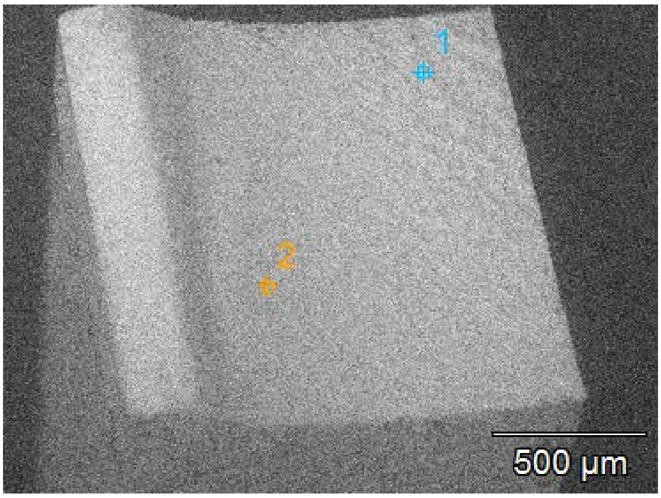

Fig. 3: Measuring points.

The results are represented as a spectrum. Each element emits a specific energy, and depending on its percentage content, its reflection on the graph differs in shape or height. Fig. 4 shows a spectrum for the analysis of a dental material with a non-diversified chemical composition. The main component of the tested sample is zirconium (Zr) with the highest energy, other peaks indicate Ca, C and O presence.

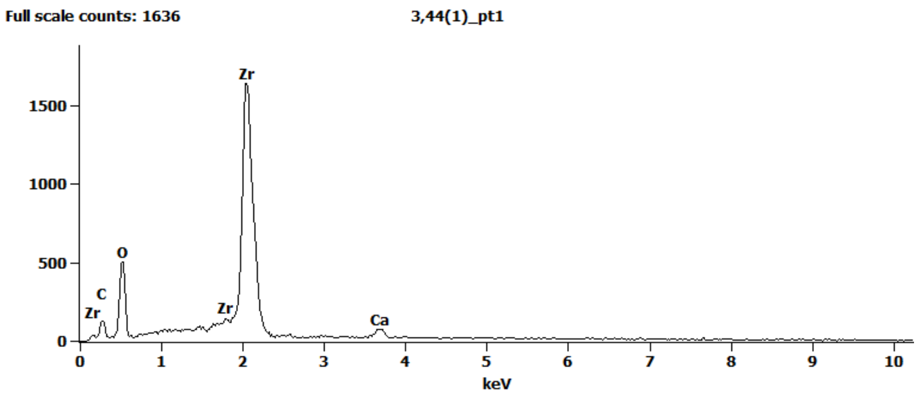

Fig. 4: Example XRF spectrum for Zr, C, O and Ca.

The results were exported to determine the percentage of major elements. The elemental composition and element ratio are similar for all samples. 50-60% zirconium content was determined in randomly selected points. The characteristics of zirconium content in relation to other elements in all measuring points is similar. The test results and statistical analysis show that the zirconium content is in fact the highest.

The last test was a static 3-point bending test to PN–EN 843–1. The standard specifies all test parameters, e.g. testing machine actuator speed, which is 0.5 mm/min. Table 1 shows the results of monotonic 3-point bending for a selected geometry from group 4: 1.5 mm x 1.5 mm x 12 mm. The tests were carried out on 30 samples.

Table 1. Monotonic 3-point bending test results for Cyrkon Lava and group 4 sample geometry: 1.5 mm x 1.5 mm x 12 mm

Material	**Average bending strength [MPa]**	**Standard deviation [MPa]**	**Relative standard deviation [%]**
Lava	978.17	78.32	8.11

4. Conclusions

The tests and analyses of physical and chemical properties of zirconium dioxide used in the dentistry for dental crowns and bridges were carried out. The analysis showed that the prepared zirconium dioxide based structure is characterized by good aesthetic, physical and chemical properties. The tests showed characteristic features of the material. The thermogravimetric analysis showed high thermal stability in a selected temperature range. The results were also verified by the analysis of the derivatographic curves. An interpretation of the X-ray patterns showed ZrO and ZrO_2 as the predominant oxides. The spectral analysis verified a significant fraction of zirconium in the tested samples. The physicochemical analysis (microscopic fractography, chemical analysis, roughness analysis and X-ray diffractometry) of the sample fracture shows changes in chemical composition of zirconium due to the loss of oxygen, increase in roughness and change in ZrO/ZrO_2 ratio. All the observed features of the sample fracture may indicate relation between the crack initiation and nature. A monotonic 3-point bending test and analysis of the results did not show any significant differences in mechanical strength. Comparison of the results with the results available in the scientific literature for similar materials did not show any significant differences in bending strength and standard deviation (Adams et al., 1997).

References

Adams, J.W., Ruh, R., & Mazdiyasni, K.S. (1997) Young's Modulus, Flexural Strength, and Fracture of Yttria-Stabilized Zirconia versus Temperature. J. Am. Ceram. Soc., 80, pp. 903–908.

De Munck, J., Van Landuyt, K., & Peumans, M. (2004) CRITICAL REVIEWS IN ORAL BIOLOGY & MEDICINE A Critical Review of the Durability of Adhesion to Tooth Tissue : Methods and Results. J. Dent. Res., 84, 118, pp. 118–132.

Denry, I. & Kelly, J.R. (2008) State of the art of zirconia for dental applications. Dent. Mater., 24, 3, pp. 299–307.

Egilmez, F., Ergun, G., Cekic-Nagas, I., Vallittu, P.K. & Lassila, L.V.J. (2014) Factors affecting the mechanical behavior of Y-TZP. J. Mech. Behav. Biomed. Mater., 37, 15, pp. 78–87.

Hisbergues, M., Vendeville, S. & Vendeville, P. (2009) Zirconia: Established facts and perspectives for a biomaterial in dental implantology. J. Biomed. Mater. Res. B. Appl. Biomater., 88, 2, pp. 519–29.

22nd International Conference
ENGINEERING MECHANICS 2016
Svratka, Czech Republic, 9 – 12 May 2016

INVESTIGATION OF BALLISTIC PERFORMANCE OF LAMINATED HYBRID COMPOSITES

C. Yanen*, M.Y. Solmaz**

Abstract: *In this study, the usability of layered hybrid composite as personal armor material has been investigated experimentally. In the scope of study, 4 hybrid composite materials with different thicknesses and number of layers, have been produced by using fabric with two different weaving type as plain and twill. Then, ballistic tests have been performed and the test results have been investigated. First, 2 test samples with [$Glass_{10}$/$Aramid_{10}$/$Carbon_{10}$] lineup and 30 layers have been produced, the ballistic tests have been performed and the results have been investigated. After observing the success of these two test samples, other two test samples have been produced by reducing the number of layers to 21 with [$Glass_{10}$/$Aramid_{10}$/$Carbon_{10}$] lineup. The ballistic tests have been conducted by using Beretta and 9 mm FMJ bullet according with the international standards (NIJ 0101-06). In the ballistic tests, the speed of bullets and the depth of penetration (DOP) accuring on the test samples have been measured and the damages have been assessed.*

Keywords: Hybrid composite, Ballistic performance, Armor material

1. Introduction

A composite material can be defined as obtaining a new material by combining two or more different materials. The purpose is to improve the weak properties of materials and to obtain a new material with better characteristics.

With the expansion of armament, mankind started to use protective armors and shields for defending. They made wars and used weapons and the technology of armors (Yavaş, 2009). Rapidly developing weapons technology has gained a new perspective with the invention of gunpowder and firearms. While the size and the weight of weapons decreased the effect and the range of them increased. Parallel to this, it has been aimed to increase the mobility with lighter body armor systems by investigating flexible materials with light in weight and also, to ensure protection against specific threats.

Temiz (2005), in his experimental study, produced a soft composite structure by using para-aramid and PBO fiber fabrics and a rigid composite structure by using para-aramid and E-glass fiber fabrics hardened with epoxy resin. He performed ballistic tests on these structures and investigated that rigid composite structure couldn’t provide reasonable protection against the bullets used in the test, while soft composite structure exhibit appropriate protection with a higher ballistic resistance.

In a study conducted by Özgültekin (2012), ballistic resistance of polypropylene honeycomb structure reinforced with aramid fiber, carbon fiber and epoxy resin and composite materials produced by using steel sieve wire laminated with epoxy resin were investigated. As a result of ballistic tests, it has been investigated that the combination in which Kevlar is in the rear of the layers, has failed due to the flexible property of Kevlar. Because the bullet has been able to punch the layers as Kevlar has not been reinforced with any other layer. The layered structure combined of three different materials has been investigated to exhibit better results and the test sample in which the Kevlar has been used as middleware material has exhibited a significant resistance to the bullet.

* Res. Assist. Cenk Yanen, MSc.: Fırat University, Engineering Faculty, 23100, Elazığ, TR, cyanen@firat.edu.tr
** Assoc. Prof. Murat Yavuz Solmaz, PhD.: Fırat University, Engineering Faculty, 23100, Elazığ, TR, mysolmaz@firat.edu.tr

In this study, to improve the personal protective armors used for defense has been aimed. With this study, experimental background for applications of personal protective armors with lighter and better protective properties has been presented and different ideas for making new armor combinations have been discussed.

2. Methods

In the experimental study, four hybrid composite layered structures were used, that have been produced in Firat University Mechanical Engineering Mechanical Laboratory by using hand lay-up method. In the production process of the test sample, carbon, glass fiber with two different weaving types as plain and twill and aramid fiber with plain weaving type as reinforcement material have been used. As matrix component Hexion MGS L326 Polyester Resin and Hexion H265 Hardener have been used.

After spreading the materials by using hand lay-up method, the mold has been inserted into a hydraulic press and pressed at 30 bar pressure. In the pressing process, the test sample has been cured by increasing the temperature gradually from 20C° to 110C° in 4 hours. The structure of layered hybrid composites used in the ballistic tests is shown in Figure 1. All of the ballistic tests have been carried out in the form of glass fiber, aramid fiber and carbon fiber from the front layer to the rear layer respectively.

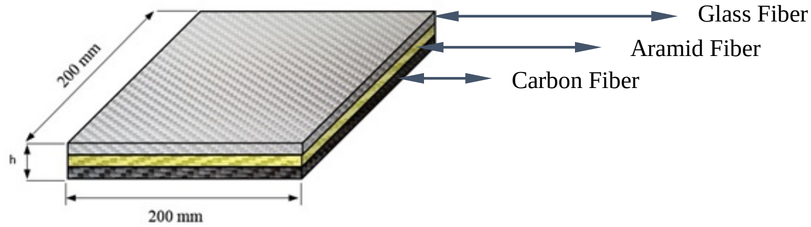

Fig. 1: The schematic of the structure of [Glass/Aramid/Carbon] layered hybrid polyester resin matrix.

Ballistic tests have been carried out by considering some standards. In the expermental study, National Institute of Justice (NIJ) has been taken as reference in the tests of the ballistic performance of composite samples. According to NIJ 0101.06 Level II-A standard, in the shots from 5 m by using 9 mm FMJ bullet, the bullet speed has to be 373 ± 9.1 m/s (NIJ 0101.06). According to NIJ 0101.06 standard, to consider the test sample successful, the bullet used in the test have to stay in the test sample and the depth of penetration have to be maximum 44 mm. For the depth of penetraion above 44 mm, the test sample is considered to be unsuccessful even if it is not punctured. The speed of the bullet has been determined by using Chrony F1 Master choronograph in the tests. The ballistic tests have been performed by the same person to make sure that carrying out the tests in the same condition. The experimental setup is shown in Figure 2.

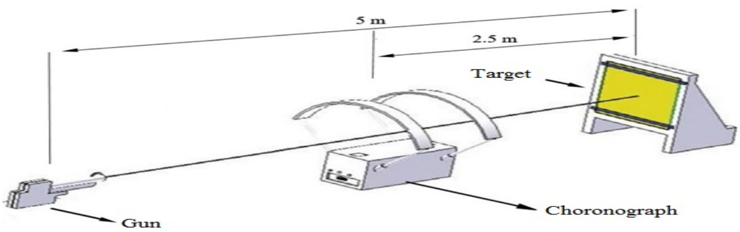

Fig. 2: The ballistic test system.

3. Findings

In this study, the ballistic tests of produced samples with the reference of NIJ 0101.06 standard have been performed. In the first stage of the study, two 30 layered hybrid composite structures with [Carbon(plain)$_{10}$/Aramid(plain)$_{10}$/Glass(plain)$_{10}$] and [Carbon(twill)$_{10}$/Aramid(plain)$_{10}$/Glass(twill)$_{10}$] lineup have been produced and the ballistic tests have been performed. The photos of the 30 layered test samples after the ballistic tests are shown in Figure 3 and Figure 4. After the ballistic tests, the test samples have been checked whether they are successful or not.

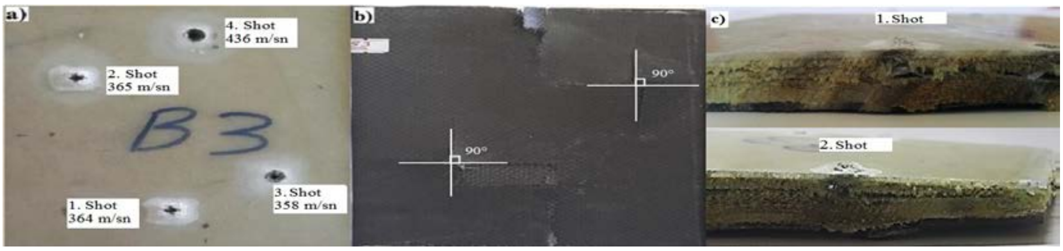

Fig. 3: B3 [Carbon(plain)$_{10}$/Aramid(plain)$_{10}$/Glass(plain)$_{10}$] test sample.

In the tests, the average bullet speed of the shots to B3 test sample with [Carbon(plain)10/Aramid(plain)10/Glass(plain)10] lineup has been determined 381m/s and the average depth of penetraion is 7.93mm. The depth of penetraion of the test sample indicates that the sample is in the ballistic limits without perforation. This test sample provides protection according to NIJ Level II-A standard. Fiber damage has been occurred in both horizontal and vertical directions becaouse the carbon fiber fabric has been in the rear of the test sample in plain type.

Fig. 4: B4 [Carbon(twill)$_{10}$/Aramid(plain)$_{10}$/Glass(twill)$_{10}$] test sample.

In none of the shots to B4 test sample, perforation has happened and this sample is successful. Carbon fiber fabric used as supporting plate at the rear of the test sample has not been damaged. B3 test sample has been determined 384 m/s and the average depth of penetration is 5.49 mm. This test sample provides protection according to NIJ Level II-A standard.

With protection property, another important factor in ballistic armor design is lightness property. Taking account of lightness property, after observing the success of firs two test samples, in the second stage other two test samples have been produced by reducing the number of layers to 21 and the ballistic tests have been conducted. The photos of the 21 layered test sample after ballistic test are shown in Figure 5 and figure 6.

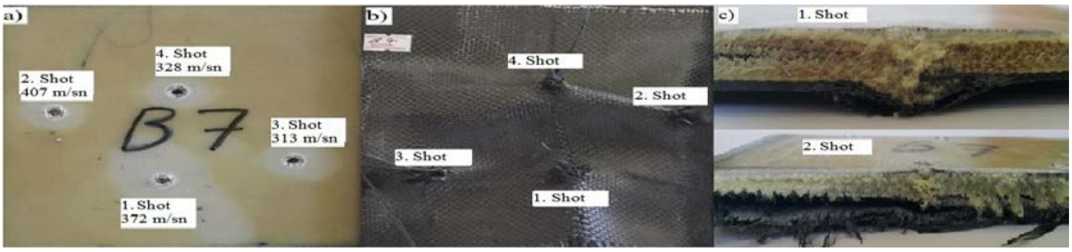

Fig. 5: B7 [Carbon(plain)$_{7}$/Aramid(plain)$_{7}$/Glass(plain)$_{7}$] test sample.

The bullet speeds of shots to B7 test sample have been between 313 m/s and 407 m/s. All of these shots have resulted with perforation and the samples have been unsuccessful.

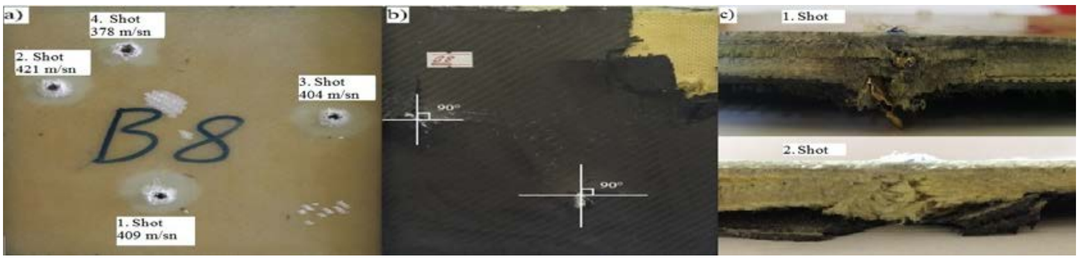

Fig. 6: B8 [Carbon(twill)$_{7}$/Aramid(plain)$_{7}$/Glass(twill)$_{7}$] test sample.

Perforation has been occurred in the Shot-1 and Shot-2 of 4 shots to B8 test sample with speed of 409 m/s and 421 m/s respectively. In the shots no puncture has occurred due to the carbon fiber fabric in the rear of the test sample is in twill type, fiber damage has been occurred in both horizontal and vertical directions. Carbon fiber plate has ruptured with Shot-2. In the Shot-1 damage has been occurred in fiber fabric due to twill weaving type and also, perforation has been observed. The average bullet speed has been 391 m/s and the average depth of penetration has been 8.75 mm of all shots accept Shot-1 and Shot-2 in which perforation has been occurred.

4. Conclusions

In this study, test samples have been produced to investigate the usability of layered hybrid composites as personal armor material. Ballistic tests of these samples have been performed with the reference of NIJ.0101-06 standard and the results of the tests have been investigated. The structural configuration of the test sample and the evaluations of the ballistic test results are given in Table 1.

Tab. 1: The ballistic test results

Test Sample	Material	Layer Number	Thickness (mm)	Mass (gr)	Evaluation Criteria
B3	***[Carbon(plain)$_{10}$/Aramid(plain)$_{10}$/Glass(plain)$_{10}$]***	***30***	***9***	***550***	***II-A***
B4	***[Carbon(twill)$_{10}$/Aramid(plain)$_{10}$/Glass(twill)$_{10}$]***	***30***	***9.5***	***598***	***II-A***
B7	***[Carbon(plain)$_7$/Aramid(plain)$_7$/Glass(plain)$_7$]***	***21***	***6***	***372***	***Puncture***
B8	***[Carbon(twill)$_7$/Aramid(plain)$_7$/Glass(twill)$_7$]***	***21***	***7***	***432***	***Puncture***

B4 with [Carbon (Twill)10/Aramid(Plain)10/Glass(Twill)10] lineup has been observed to be the most successful of 30 layered test samples in the ballistic tests.

After observing success of 30 layered hybrid composites in the ballistic tests, the layer number has been decreased to 21 from 30 and the ballistic tests have been performed for these samples.

None of the 21 layered test samples have been successful in the ballistic tests.

By considering the results of all test, twill weaving fabrics have been determined to have better ballistic resistance from plain weaving fabrics.

The damage types have been investigated after the ballistic tests and damage of fiber and separation of layers have been observed to be the most common damage types.

Behind the protection property, another important factor in the design of armor material is lightness property. The successful test samples of the ballistic tests in this study can be recommended to study to reach an optimum weight and thickness with better ballistic resistance by reducing the number of layers for new armors.

References

Yavaş, M.O., (2009) Hafif Silahlara Karşı Bireysel Savunma Amaçlı Kompozit Malzeme Tasarımı ve Balistik Dayanımı, Yüksek Lisans Tezi, Selçuk Üniversitesi, Fen Bilimleri Enstitüsü, Konya.

Temiz, S., (2005) Balistik Kumaş ve Test Yöntemleri Üzerine Bir Araştırma, Dokuz Eylül Üniversitesi, Fen Bilimler Enstitüsü, Mühendislik Fakültesi, Tekstil Mühendisliği Anabilim Dalı, Yüksek Lisans Tezi, İzmir.

Özgültekin, S.E., (2012) Balistik Zırhlarda Kullanılan Kompozit Malzeme Kombinasyonlarının İncelenmesi, *Yüksek Lisans Tezi*, Sakarya Üniversitesi, Fen Bilimleri Enstitüsü, Sakarya.

National Institue of Justice 0101.06 (2005) Ballistic Resistance of Body Armor

22nd International Conference
ENGINEERING MECHANICS 2016
Svratka, Czech Republic, 9 – 12 May 2016

ROBOT CONTROL IN TERMS OF HAMILTONIAN MECHANICS

V. Záda*, K. Belda**

Abstract: *The paper deals with a mathematical modeling of robot motion and control. Instead of frequently used Lagrangian formulation of robot dynamics, this paper presents robot dynamics by Hamiltonian formulation. This formulation leads to different physical descriptive quantities considered for control design. In the paper, as a comparative control approach, PD control with gravity compensation is considered. The control approach considering Hamiltonian formulation is demonstrated for simplicity on two-mass robot-arm system. However, the explained modeling approach is general and it can be applied, e.g., to usual industrial articulated robots-manipulators with multiple degrees of freedom.*

Keywords: Robot-manipulator, Hamiltonian formalism, Modeling, Robot control, PD control.

1. Introduction

Mechanical engineers usually prefer conventional Newton mechanics in their works. However, for robot control, there are preferred Lagrange's equations (Siciliano, 2008; Samson, 1991). In solutions of robot control, there exist some limits for positions, velocities or accelerations as well as some limits for control torques, respectively. The limits of velocities are usually constant for all configurations of robots without respecting the fact that inertia moments are discrepant for different configurations. The Lagrangian formalism is based on kinetic and potential energies and on a phase space formed by the positions and velocities. In the robot-manipulator dynamics, all momentums change very quickly, often in the rate 1/10 or more (Arimoto, 1996). Hence, it is interesting and useful to study control methods based not only on Lagrange formalism, but also on Hamiltonian one. It was investigated as the property of passivity of the robot (Landau, 1988).

Described approach can modify the natural energy of the robot so that it can satisfy the desired objectives (position or tracking control). Hamiltonian formalism with using a modified Hamiltonian (Takegaki, 1981) was used as new function there. Various choices are possible for the desired potential energy function (Wen, 1988). An alternative approach for potential function is in (Takegaki, 1981). In this contribution, we investigate and show differences in key features of Lagrangian and Hamiltonian formalism applied to robot control. Hence, we shall omit such changes as (Takegaki, 1981), but shall compare almost the same algorithms on the same problems of robot controls defined in both Lagrangian and Hamiltonian configuration spaces.

2. Lagrangian and Hamiltonian Formalism

The momentums and moments of momentums are very different in arbitrary configurations of robots. The classical methods of robot control use information on positions and velocities. It predetermines, that control methods based on feedback of positions and generalized momentums, will be different in results. In robotics, the generalized momentum is really momentum or moment of momentum, respectively. Hence, the Hamiltonian formalism may be better for aims of robot control than the Lagrangian one. In the following part we develop analogical differential equations of robot dynamics with using Hamilton's equations.

* Assoc. Prof. Václav Záda, CSc.: Institute of Mechatronics and Engineering Informatics, Faculty of Mechatronics, Technical University of Liberec, Studentská 1402/2; 461 17, Liberec 1; CZ, vaclav.zada@tul.cz

** Ing. Květoslav Belda, Ph.D.: Department of Adaptive Systems, The Institute of Information Theory and Automation of the Czech Academy of Science; Pod Vodárenskou věží 4, 182 08, Prague 8; CZ, belda@utia.cas.cz

2.1. Lagrange's equations of robot motion

Lagrange's equations of classical mechanics (Fasano, 2002) are frequently used for description of non-trivial mechanical systems. These equations are usually defined as follows

$$\frac{d}{dt}\left(\frac{\partial L}{\partial \dot{q}_j}\right)-\frac{\partial L}{\partial q_j}=F_j, \quad j=1,2,\cdots,n \tag{1}$$

where n represents degrees of freedom (DOF); $L = K - V$ is Lagrange's function expressing subtraction of kinetic K and potential V energies; F_j are generalized forces and q_j generalized coordinates. For technical applications, the generalized forces F_j represent only a sum of non-conservative forces and complementarily conservative forces are represented by the potential energy function V.

Then, Lagrange's equations of robot motion are written in the following form (Arimoto, 1996)

$$\mathbf{M}(\mathbf{q})\,\ddot{\mathbf{q}} + \mathbf{C}(\mathbf{q},\dot{\mathbf{q}})\,\dot{\mathbf{q}} + \mathbf{g}(\mathbf{q}) = \mathbf{u} \tag{2}$$

2.2. Hamilton's equations of robot motion

The Hamilton function is defined by (Fasano, 2002)

$$H=\sum_{i=1}^{n} p_i\,\dot{q}_i - L \tag{3}$$

where generalized momentums are defined by

$$p_j=\frac{\partial L}{\partial \dot{q}_j}, \quad j=1,2,\cdots,n. \tag{4}$$

The Hamilton's equations can be written as

$$\dot{q}_j=\frac{\partial H}{\partial p_j}, \quad p_j=F_j-\frac{\partial H}{\partial q_j} \tag{5}$$

These equations can be rewritten in the matrix form

$$\dot{\mathbf{q}}=\left(\frac{\partial H}{\partial \mathbf{p}}\right)^T, \quad \dot{\mathbf{p}}=\mathbf{F}-\left(\frac{\partial H}{\partial \mathbf{q}}\right)^T \tag{6}$$

Arbitrary robot may be considered as the time invariant system. Then, the Hamiltonian (3) is total energy: the sum of kinetic and potential energies. The Lagrangian L depends on positions and velocities, but the Hamiltonian depends on positions and generalized momentums, so we can write

$$H(\mathbf{q},\mathbf{p})=K(\mathbf{q},\mathbf{p})+V(\mathbf{q}) \tag{7}$$

The kinetic energy in coordinates $\mathbf{p}$ and $\mathbf{q}$ has the following form

$$K(\mathbf{q},\mathbf{p})=\frac{1}{2}\mathbf{p}^T\mathbf{M}^{-1}(\mathbf{q})\,\mathbf{p} \tag{8}$$

Let us define the gradient of potential energy

$$\frac{\partial V}{\partial \mathbf{q}}=\mathbf{g}^T(\mathbf{q}) \tag{9}$$

The derivation with respect vector $\mathbf{q}$ is different in Lagrange space and in Hamilton space

$$\frac{\partial K(\mathbf{q},\mathbf{p})}{\partial \mathbf{q}}=-\frac{\partial K(\mathbf{q},\dot{\mathbf{q}})}{\partial \mathbf{q}} \tag{10}$$

Hence, from the equation (6) we can obtain

$$\dot{\mathbf{p}} = \mathbf{F} - \mathbf{g}(\mathbf{q},t) - \left(\frac{\partial K(\mathbf{q},\mathbf{p})}{\partial \mathbf{q}}\right)^T . \tag{11}$$

Let a skew symmetric matrix **S** be defined as follows

$$S_{ij} = \frac{1}{2}\sum_{k=1}^{n} \dot{q}_k \left(\frac{\partial M_{ik}}{\partial q_j} - \frac{\partial M_{jk}}{\partial q_i}\right). \tag{12}$$

It can be derived that mentioned matrix **S** holds

$$\mathbf{S}\dot{\mathbf{q}} = \frac{1}{2}\dot{\mathbf{M}}\dot{\mathbf{q}} - \frac{1}{2}\left(\frac{\partial}{\partial \mathbf{q}}\left(\dot{\mathbf{q}}^T \mathbf{M}\dot{\mathbf{q}}\right)\right) \tag{13}$$

and hence (11) can be rewritten in the final form

$$\dot{\mathbf{p}} = \left(\frac{1}{2}\dot{\mathbf{M}} - \mathbf{S}\right)\mathbf{M}^{-1}\mathbf{p} - \mathbf{g}(\mathbf{q}) + \mathbf{u} \tag{14}$$

From the first equation of (5) follows the second vector equation

$$\dot{\mathbf{q}} = \mathbf{M}^{-1}\mathbf{p} . \tag{15}$$

The equations (14) and (15) represent the robot motion. Remember, these equations are described in Hamilton's phase space **p**, **q**.

3. Robot Control

For the sake of brevity, the simplest control algorithm often called *Position control* is studied. Other methods as tracking control or force control will be omitted. Recall, the Hamiltonian phase space is represented by coordinates (**q**, **p**). For simplicity, in this space, the control will be called simply *control in Hamilton space*. On the other hand, the control in Lagrangian phase space, which is represented by coordinates $(\mathbf{q}, \dot{\mathbf{q}})$, will be simply called *control in Lagrange space*.

The controlled system (robot) is described by eqs. (14) and (15). Let the controller be described as

$$\mathbf{u} = \mathbf{g} + \mathbf{A}\mathbf{e} - \mathbf{B}\,\mathbf{p} . \tag{16}$$

where **A** and **B** are positive definite diagonal matrices, **g** is gravity compensation for the robot and $\mathbf{e} = \mathbf{q_d} - \mathbf{q}$. This approach may be called *PD control with full gravity compensation*. The analogical versions for robot control described by Lagrange's equations are in (Siciliano, 2008; Arimoto, 1996) etc. The target position $\mathbf{q_d}$ in terms of joint coordinates is fixed. Consider a set point control problem, in which the posture of the robot arm is allowed to asymptotically approach towards the target position state $(\mathbf{q}, \mathbf{p}) = (\mathbf{q_d}, \mathbf{0})$. Substitution of the control law (16) into (14) yields

$$\dot{\mathbf{p}} = \left(\frac{1}{2}\dot{\mathbf{M}} - \mathbf{S}\right)\mathbf{M}^{-1}\mathbf{p} + \mathbf{A}\mathbf{e} - \mathbf{B}\,\mathbf{p} \tag{17}$$

Consider the following Lyapunov function

$$W_L = \frac{1}{2}\mathbf{p}^T\mathbf{M}^{-1}(\mathbf{q})\mathbf{p} + \frac{1}{2}\mathbf{e}^T\mathbf{A}\mathbf{e} \tag{18}$$

where its time derivation along the trajectory given by (17) is

$$\dot{W}_L = -\,\mathbf{p}^T\mathbf{M}^{-1}\mathbf{B}\,\mathbf{p} \tag{19}$$

If $\mathbf{B}$ is a diagonal positive definite matrix and the inverse of matrix $\mathbf{M}$ is positive definite, then the multiplication of these matrices in (19) is positive definite. Thus, the quadratic form in (19) is negative semi-definite and control process is stable according to Lyapunov theory of stability. We have now to prove that if $\mathbf{p} = \mathbf{0}$, the robot does not reach a position $\mathbf{q} \neq \mathbf{q_d}$. This can be done by the La Salle invariant set theorem (LaSalle, 1960). The set $\mathbf{S}$ of points in the neighborhood of the equilibrium, that satisfies $\dot{W}_L = 0$, is such that $\mathbf{p} = \mathbf{0}$ and $\dot{\mathbf{p}} = \mathbf{0}$. From (17) follows $\mathbf{e} = \mathbf{0}$. Hence, the equilibrium point $\mathbf{e} = \mathbf{0}$, $\mathbf{p} = \mathbf{0}$ is the only possible equilibrium for the controlled system and is the largest invariant set in $\mathbf{S}$. Hence, the equilibrium point is asymptotically stable. If we compare the similar method for control in Lagrangian space, we can obtain instead of (19) the following result

$$\dot{V}_L = -\dot{\mathbf{q}}^T \mathbf{B}\, \dot{\mathbf{q}} \tag{20}$$

and so from (19) and (20) we obtain the following criterion

$$\dot{W}_L \le \dot{V}_L \Leftrightarrow \dot{\mathbf{q}}^T \mathbf{B} \left(\mathbf{M} - \mathbf{E}\right) \dot{\mathbf{q}} \ge 0 \,. \tag{21}$$

Since $\mathbf{B}$ is positive definite, hence $\dot{W}_L \le \dot{V}_L$ holds if and only if the matrix $\mathbf{M} - \mathbf{E}$ is positive semidefinite ($\mathbf{E}$ is identity matrix). If this matrix is positive definite, the trajectory of W_L is under the trajectory of V_L in time.

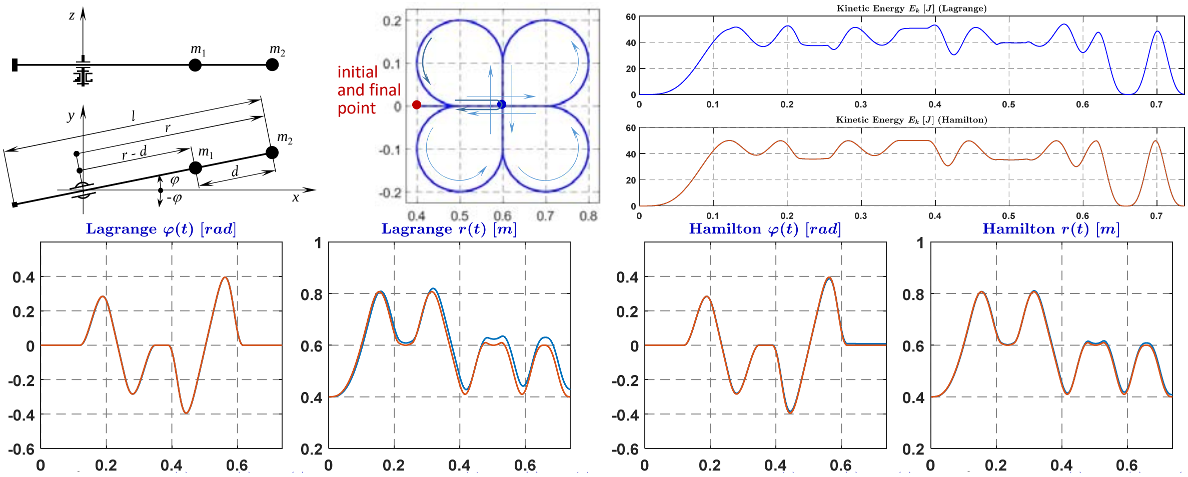

Fig. 1: Comparative examples of the PD control of the robot system shown at left top corner.

4. Conclusion

The developed theory and simulated examples show promising behavior of the control in Hamiltonian space against Lagrangian one, although generalized momentums cannot be directly measured but only computed from velocities and positions of the robot links. The difference of a quality of control increases for increased velocities of robot motion. The Fig. 1 is for max. tangential velocity 5 ms^{-1} of point m_2.

References

Siciliano, B. & Khatib, O. (Eds.) (2008). Handbook of Robotícs. Springer.

Samson, C. & M. Le Borgne, M. & Espiau, B. (1991) Robot Control, The task fun. approach. Clf. Press, Oxford.

Arimoto, S. (1996) Control Theory of Non-linear Mechanical Systems. Clarendorf Press, Oxford.

Landau, I. D. & Horowitz, R. (1988) Synthesis of adaptive controllers for robot manipulators using a passive feedback system approach. Proc. IEEE Int. Conf. on Robotics and Automation, Philadelphia, pp. 1028-1033.

Takegaki, M. & Arimoto, S. (1981) A new feedback method for dynamic control of manipulators. Trans. of ASME, J. of Dynamic Sytems, Measurement and control, Vol.102, pp. 119-125.

Wen, J. T. et al. (1988) New class of control laws for robotic manipulators. J. Control, Vol.47 (5), pp. 1361-1385.

Fasano, A. & Marmi, S. (2002) Analytical Mechanics. Oxford Press.

LaSalle, J. P. (1960) Some extension of Lyapunov's second method. IRE Trans. on Circuit Theory 7, pp. 520-527.

Záda, V. (2012) Robotics, Mathematical Aspects of Analysis and Control. Technical University of Liberec.

22nd International Conference
ENGINEERING MECHANICS 2016
Svratka, Czech Republic, 9 – 12 May 2016

SERVICE LIFE OF ROTORS UNDER MECHANICAL AND THERMAL STRESS

J. Zachwieja*, K. Peszynski**

Abstract: *Dynamic balancing of a rigid rotor should, at least in its final stage, be carried out at its operational speed, where its rotational frequency is often close to its resonance frequency. It is an adverse phenomenon, since even a minor constraint may induce high amplitude vibrations, limited by the attenuation. The service life of a rotor, mainly its bearings is thus significantly reduced. Balancing the rotor using the influence coefficient method at a frequency close to its resonance frequency is difficult due to the rapid changes in phase angle of a vector of the rotor response to constraints from the attached test weights. An optimal solution is to operate outside the rotor's resonance zone. A quick and efficient method is to change its rotational speed, however, it may have some side effects.*

Keywords: stress analysis, balancing, natural frequency, external anisotropy, resonance zone

1. Introduction

The power turbines are rotary turbomachines designed to operate at a natural frequency only slightly different from its rotational frequency. The deformable rotor, after passing its resonance zone is self-centred due to the gyroscopic moment. Its deflection is similar to the value of an eccentricity of unbalanced mass.

Operation of the power turbines and turbine generators at over 10.000 min^{-1} give rise to many problems. The most common issue, apart from the difficulties in maintaining stable conditions of the slide bearing operation is breaking off of the blade resulting in a major rotor unbalance. Despite an immediate turbine shutdown and activation of a brake system, the force exerted on the rotor is sufficient to cause its damage. It is also the case with the aircraft jet engine turbines. At the turbine rotor design stage, both numerical methods and high frequency variable load fatigue cycles are employed Non-linear finite element methods with various element types are used to determine the stress conditions in the rotor shaft and blade cross-sections.

The turbine tests show that together with the resonance vibrations excited by the variable load conditions (Poursaeidi, Salavatian 2009, Liu, Jiang, 2015) blade cracking is due to the progressive corrosion (Cuevas et all, 2013), pitting and rotor unbalance. Attempts are made within the fracture mechanics domain, to develop high-speed rotor blade crack propagation models (Barlow, Chandra, 2005).

2. Problem description

Gypsum is a raw material commonly used in the construction industry and is obtained in a calcination process of gypsum rock at 150^0-190^0C. The product is mostly hemihydrate. After milling, the product is used as a structural gypsum. The REA-gypsum mill is a machine used for milling gypsum rocks. Rock milling is possible due to the rotor design, which uses crushing hammers attached to the radial arms. Rotor speed is ~700 min^{-1}. Fig. 1 shows a medium mill with the rotor driven via a belt transmission. The batch material in form of gypsum rocks is crumbled by falling from several meters onto the rotating crushing hammers. The direction of material is indicated with an arrow.

* Assoc. Professor Janusz Zachwieja, PhD., Department of Applied Mechanics, University of Technology and Life Sciences in Bydgoszcz (Poland), Kaliskiego 7, Bydgoszcz; PL, janusz.zachwieja@utp.edu.pl,

** Assoc. Prof. Kazimierz Peszynski, PhD.: UTP University of Science and Technology, Faculty of Mechanical Engineering, Al. prof. S. Kaliskiego 7, 85-796 Bydgoszcz; PL, kazimierz.peszynski@utp.edu.pl

Fig. 1: REA-gypsum mill view.

The impact nature of the machine operation results in vibration speeds at amplitudes considered as transient-permissible or non-permissible. Mill rotor should be characterized by the lowest unbalance possible. Otherwise, the excitation will affect the dynamic state of the machine.

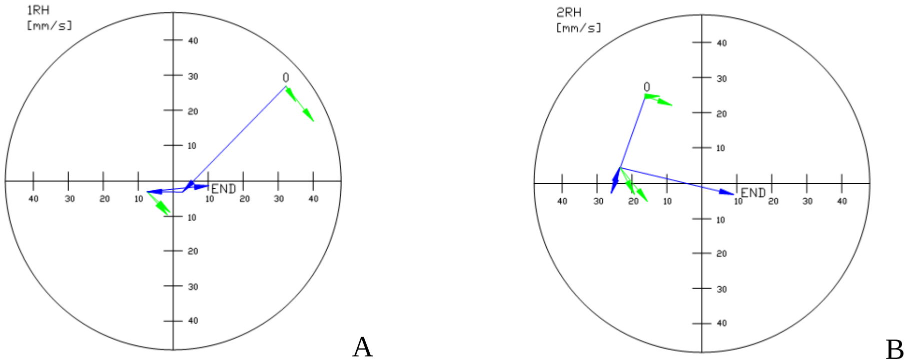

Fig. 2: Diagram of rotor balancing in horizontal plane. A) bearing on the pulley side, B) opposite bearing.

The tested mill is characterized by the disproportion of the vibration velocity amplitude in horizontal and vertical direction, indicating an external anisotropy or resonance in the horizontal plane. Whereas the vibration velocity amplitude for the bearings in vertical direction are permissible and reach values slightly over 1 $mm \cdot s^{-1}$, in horizontal direction they may reach several dozen $mm \cdot s^{-1}$. Fig. 2 shows the attempt to balance the mill rotor mounted on a steel platform.

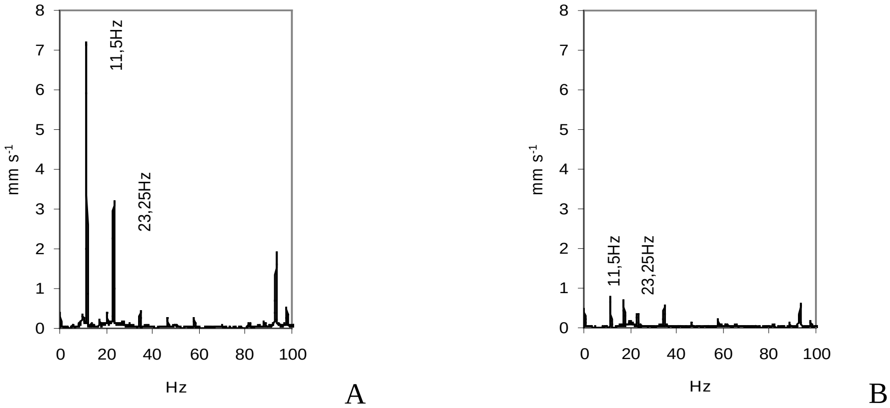

Fig. 3: Vibration velocity spectrum in: horizontal (A) and vertical (B) direction of the mill bearing on the belt transmission side at 696 min^{-1}.

After balancing, see Fig.3, the vibration velocity amplitude values for both rotor bearings in a horizontal direction were ten times lower than the values measured in a vertical direction. An impulse test was carried out to determine the cause and system response to the constraint in a short time period. The test results confirmed the resonance zone near 11 Hz for horizontal direction and 23.25 Hz for vertical direction.

3. Bringing the rotor out of resonance zone

The procedure of bringing the rotor out of resonance zone should be preceded by the analysis of the effects of increased rigidity of the machine mount, since the increase in mount rigidity increases the natural frequency of the mill. The rigidity can be increased by replacing the vibration damper with less flexible dampers. However, the mistuning value must be close to $\sqrt{2}$.

A simple method is to change the rotor speed, if adjustable. An attempt was made to gradually increase the speed frequency with a simultaneous measurement of the vibration velocity amplitude.

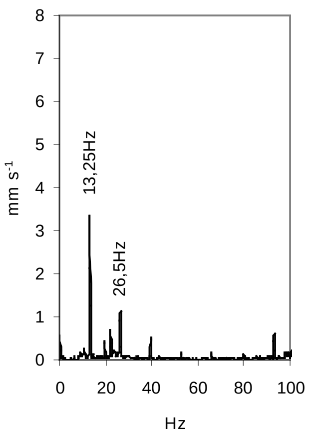

A

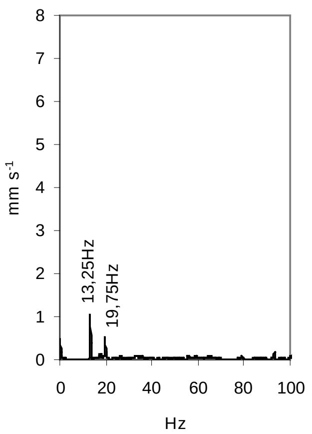

B

Fig. 4: Vibration velocity spectrum in: horizontal (A) and vertical (B) direction of the mill bearing on the belt transmission side at 795 min^{-1}.

Fig. 4 show the nature of mill bearing vibrations at rotor speed of 795 min^{-1}. The vibration velocity amplitude of the bearings in vertical (B) direction after changing the rotor speed has slightly increased due to the increase in constraint value, however the vibration velocity amplitudes in horizontal (A) direction have decreased 1.5÷2 times.

A continued increase in rotor speed was stopped at ~900 min^{-1} due to the breaking off of the mill hammer. It resulted in a rapid increase in rotor unbalance and significant increase in vibration amplitude. The consequence of increasing the rotor speed by just 15% was a major machine failure. The hammer blocked the rotor and caused deformation of the milling chamber and damage to the vibration dampers.

4. Analysis of rotor effort condition

A model of the REA-gypsum mill (Fig. 5) was developed to analyze the causes, with its dynamic properties selected to represent the actual object behavior. A resonant frequency of the model vibrations was 12.2 Hz and differed by 1 Hz from the actual value. Fig. 6 shows the form of mill vibrations (translational vibrations in X-axis) at this frequency.


A

Fig. 5: REA-gypsum mill model view

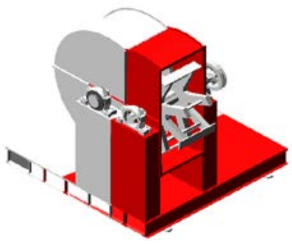
B

Fig. 6: Mill vibration form at 12.2 Hz

A state of stress in rotor cross-section at rotational frequency of 11 Hz, 13 Hz and 15 Hz was modelled (Fig. 7). In each case, the result shows that the correct joint between the hammers and the rotor arms provide sufficient strength, since the stress values did not exceed the yield point of the welded joint material. It is not the case if, as a result of cyclic impacts of the gypsum rocks and mill hammers, part of the kinetic energy is absorbed and results in the deformation of rotor components. A fracture of one of the welded joints, which may go unnoticed even after a long time operation at 11 Hz, at 15 Hz, will result in stresses at other welded joints, which may reach up to 700 MPa.

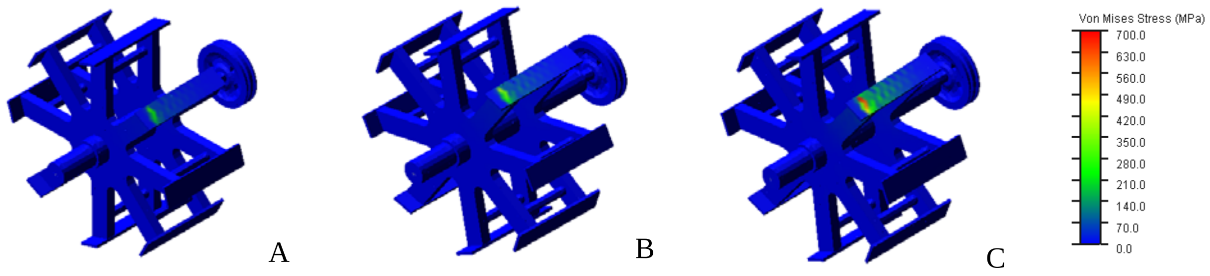

Fig. 7: Stress values in the welded joint at various rotational frequencies: A) 11 Hz, B) 13 Hz, C) 15 Hz.

The fatigue analysis of a question, if the impact between the calcined gypsum rock and the hammer of the rotating rotor may result in a fracture of the welded joint was carried out. It was shown that if the rotor operates at its rated speed, the joint between the hammer and the mount is correct, a several thousand impacts of the gypsum rock falling from 4 m and weighing 10 kg is required before the welded joint cracks. However, if the welded joint is not correct, the number of fatigue cycles before fracture may be significantly reduced.

5. Summary

The operation of rotary machines, except for the rare cases, should not occur in the resonant vibration conditions, which may cause premature wear of mill components. This problem generally applies to simple machines, including fans and crushers. The machine operator is often not aware that the resonance may cause high amplitude vibrations. The operator usually indicates rotor imbalance as a source of vibrations and recommends dynamic balancing, which does not yield the expected results.

The effectiveness of rotor balancing can be improved by using a method to optimize the vibration amplitudes in orthogonal directions. External anisotropy means that the resonance will rarely occur both in horizontal and vertical plane.

If allowed by the operating conditions, the operator can bring the machine out of resonance zone by adjusting its speed. It is usually possible to increase the rotor speed, however the operator must determine how much the load of the rotor disk components will increase and non-destructive methods must be employed to inspect the joints between the fan rotor blades or crusher hammers and the rotor disk frame. Insufficient strength of the welded joint, which may be sufficient for the loads exerted at lower speeds may be too low if the speed is increased.

6. References

Barlow K.W., Chandra R., (2005) Fatigue crack propagation simulation in an aircraft engine fan blade attachment, International Journal of Fatigue, 27, pp. 1661–1668.

Cuevas Arteaga C., Rodríguez J.A., Clemente C.M., Segura J.A., Urquiza G., Y.El. Hamzaoui Y.El.,(2013) Estimation of useful life in turbines blades with cracks in corrosive environment, Engineering Failure Analysis, 35, pp.576–589.

Diken H., Alnefaie K., (2011) Effect of unbalanced rotor whirl on blade vibrations, Journal of Sound and Vibration, 330, pp. 3498–3506.

Liu C., Jiang D., Chu F., (2015) Influence of alternating loads on nonlinear vibration characteristics of cracked blade in rotor system, Journal of Sound and Vibration, 353 pp. 205–219.

Poursaeidi E., Salavatian M., (2009) Fatigue crack growth simulation in a generator fan blade, Engineering Failure Analysis 16, 888–898.

22nd International Conference
ENGINEERING MECHANICS 2016
Svratka, Czech Republic, 9 – 12 May 2016

NEW APPROACH TO ASSESMENT OF RAILWAY VEHICLE DYNAMICAL RESPONSE IN THE COURSE OF PASSING OVER TURNOUT

J. Zelenka[*], A. Hába[**], M. Kohout[***]

Abstract: *In the course of a vehicle passing over a turnout, a significantly difference of dynamical response appears in vertical direction. Although a frog is the most loaded part of each turnout, a switch area is equally important part of a turnout from this point of view; so called suspended support of the switch area is tested at new turnout structures. The methodology for determination of the equivalent loading of a turnout frog in the course of a vehicle passing has been developed to evaluation of the frog loading. A vertical acceleration measured on the wheelset axle box of a vehicle passing over the frog is an input parameter for the calculation of the equivalent loading. Assessment of a vehicle dynamical response during passing over the suspended part in the switch area is also based on the vertical dynamical response measurement detected by acceleration sensors located on the wheelset axle box but this response is evaluated by statistical methods. Actually in cooperation with a turnout producer and one of the train operators, the turnouts of several types and in different operational condition are monitored since 2014 with application of the mentioned methodology. The reference vehicle for the monitoring of selected turnouts is an electric locomotive of axle load 22 t. The verification of optimized design of some turnouts in terms of loading of their parts is the main purpose of this research.*

Keywords: Turnout, Frog, Railway vehicle, Acceleration, Measurement.

1. Introduction

Perfect knowledge of operational conditions is the basic presumption of ensuring of operational reliability of a railway track structure if we need to increase a maximum operational speed. Passing of railway vehicle presents a high dynamic loading in wheel-rail contact in the course of passing over a turnout frog in straight direction. The turnout switch part (tongue area) is also important from this point of view. Suspended rail support in this area is actually tested at new turnouts.

Actually, there is no universal method, which would be able to evaluate the turnout loading level in the course of different vehicle types passing. Modelling of this phenomenon is very difficult because a turnout is an inhomogeneous element in common track, which is a place of dynamical impact in the course of contact of wheel with the frog. Therefore to explanation of these dynamical phenomena, we deal with experimental research in this field many years.

2. Determination of vehicle dynamical response in the course of passing over turnout

There is possible to use acceleration measuring principle for measurement of a vehicle dynamic response. Measured acceleration signal is friendly to assessment, therefore the acceleration measured on the wheelset axle boxes was chosen as an input quantity for evaluation of vehicle dynamical response. Wheelset axle box has unsuspended connection with wheelset and it is also friendly to installation of measuring chain (sensors, cable connections). It is necessary to find such place which has unsuspended

[*] doc. Ing. Jaromír Zelenka, CSc.: Jan Perner Transport Faculty, University of Pardubice, Nádražní 547; 560 02, Česká Třebová; CZ, jaromir.zelenka@upce.cz

[**] Ing. Aleš Hába, Ph.D.: Jan Perner Transport Faculty, University of Pardubice, Nádražní 547; 560 02, Česká Třebová; CZ, ales.haba@upce.cz

[***] Ing. Martin Kohout, Ph.D.: Jan Perner Transport Faculty, University of Pardubice, Nádražní 547; 560 02, Česká Třebová; CZ, martin.kohout@upce.cz

connection with the axle box (see fig. 1, left). For detection of maximum loading of turnouts components the a locomotive of axle load 22 t (see fig. 1, right) was chosen as measuring vehicle.

Fig. 1: Acceleration sensor placing on the wheelset axle box of measuring vehicle (illustration photo).

Signals of acceleration are recorded with the sampling rate of 20 kHz. For the next assessment, the signals are filtered by a band pass filter in the range 20 ÷ 500 Hz. Example of the filtered vertical acceleration signal measured on a wheelset axle box in the course of passing over a turnout frog is presented in fig. 2.

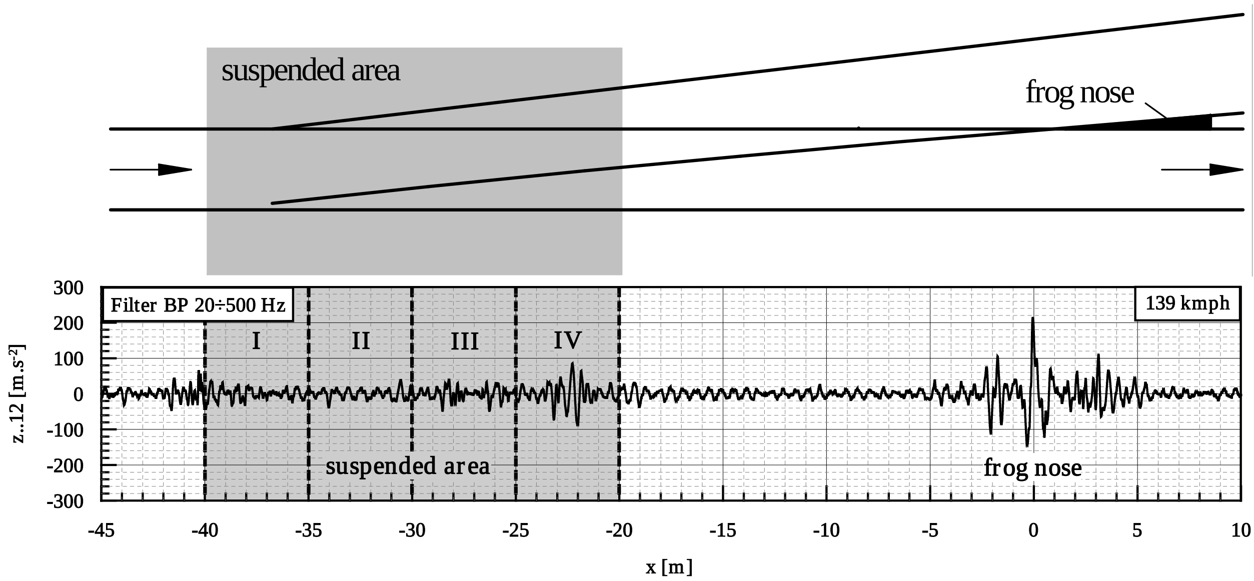

Fig. 2: Filtered vertical acceleration signal measured on the wheelset axle box in the course of passing over whole turnout

3. Assessment of vehicle dynamical response in the course of passing over turnout by calculation of equivalent loading

Base on long-time experience the new methodology of assessment of vehicle dynamical response in the course of passing over a turnout frog has been created. This methodology utilizes so called equivalent loading in wheel rail contact and it was certified in 2014.

The calculation of the equivalent dynamical force between wheel and rail in the course of passing of appropriate wheel over a frog area utilizes the vertical acceleration measured on a wheelset axle box of a vehicle (see fig. 2).

Due to the fact that natural frequencies of vertical motion of suspended vehicle parts are multiply lower than frequency of the vertical motion of a wheel in the course of passing over a turnout frog area, the calculation of the dynamic component of the equivalent force is carried out only with respect to inertia forces of unsuspended vehicle parts, i.e. relative mass of wheelset axle boxes included $m_{\mathrm{w\_r}}$ per a wheel (see fig. 3).

Dynamical component of the equivalent force ($\ddot{z}$ – measured acceleration):

$$F_{\mathrm{eq\_dyn}} = m_{\mathrm{w\_r}}.\ddot{z} \quad (1)$$

Equivalent loading of a frog area part ($m_{\mathrm{v\_r}}$ – relative mass of a vehicle per a wheel):

$$F_{\mathrm{eq}} = m_{\mathrm{v\_r}}.g + F_{\mathrm{eq\_dyn}} \quad (2)$$

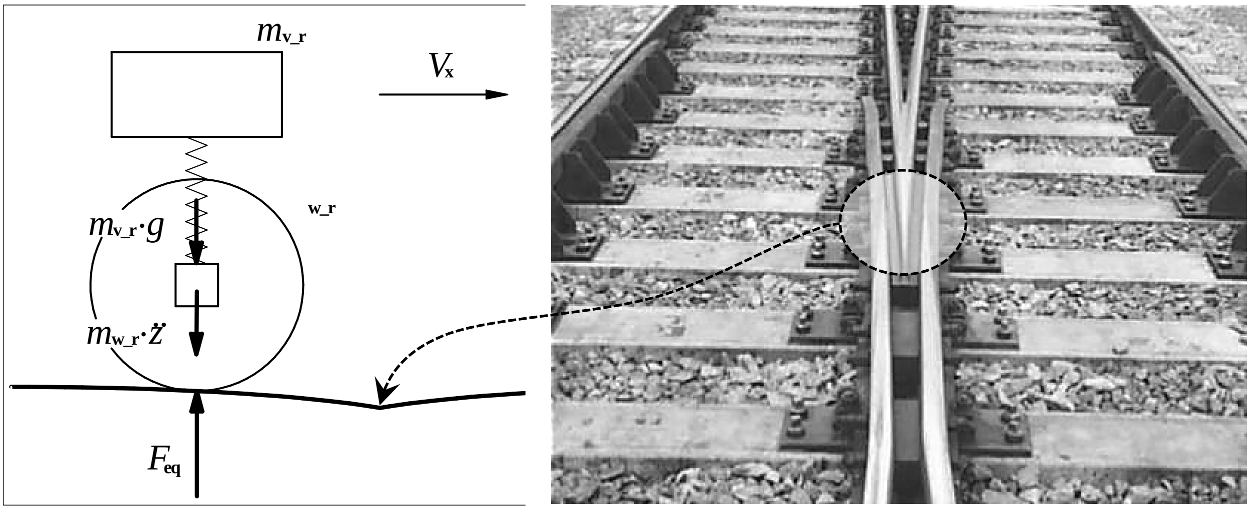

Fig. 3: Simplified dynamical model of a vehicle (left) in the course of passing over a turnout frog (right).

Example of results of carried out measurements in the course of passing over selected turnouts are presented in fig. 4. The values of turnout frog equivalent loading are displayed in form of columns and they are completed by vehicle actual speed. These columns present the equivalent loading caused by appropriate wheels in the range of vehicle passing over a turnout.

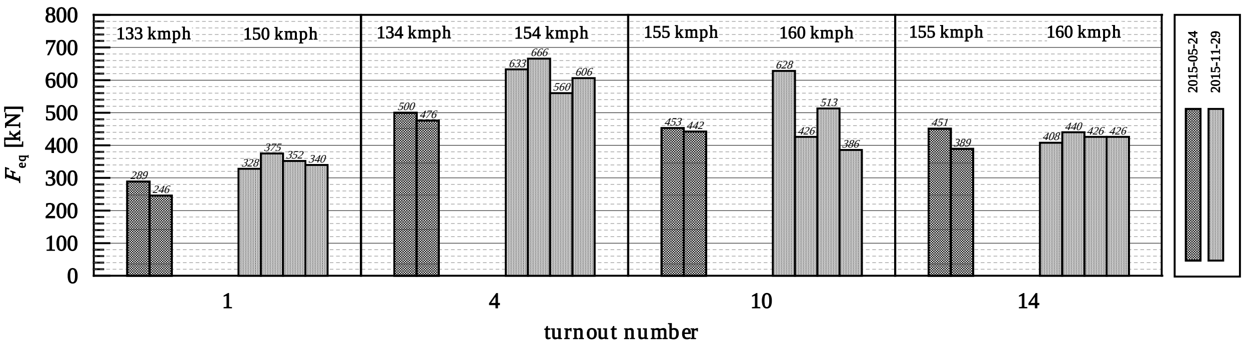

Fig. 4: Example results of the equivalent loading of the selected turnout frogs (measurement 2015-05 – sensors placed only at one bogie; measurement 2015-11 – sensors placed at both bogies).

4. Assessment of vehicle dynamical response in the course of passing over turnout suspended part

Determination of so called vertical acceleration estimated value ($OH\_z..$) (3) of a vehicle dynamical response in the course of passing over a turnout suspended part is a result of an assessment. The calculation of this quantity is based on statistical evaluation of measured acceleration on the wheelset axle box in four 5m sections in the suspended area of a turnout.

Estimated value ($SH\_z..$ – mean percentiles value; $SO\_z..$ – standard deviation):

$$OH\_z.. = SH\_z.. + 2{,}2 \cdot SO\_z.. \quad (3)$$

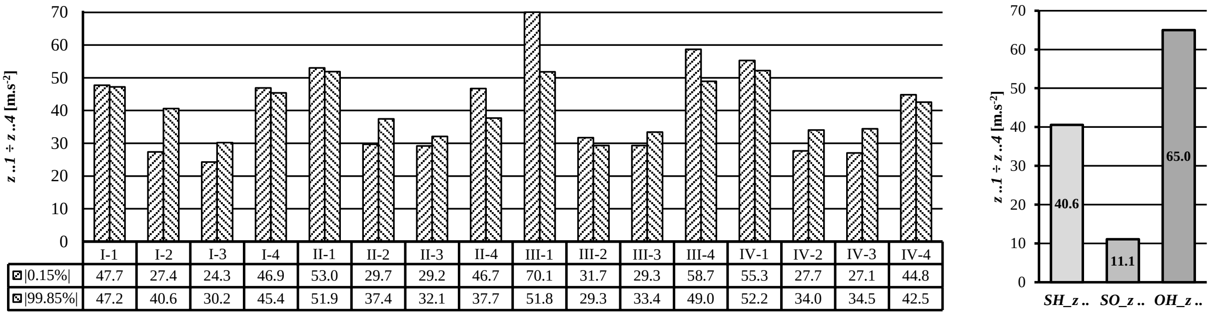

	I-1	I-2	I-3	I-4	II-1	II-2	II-3	II-4	III-1	III-2	III-3	III-4	IV-1	IV-2	IV-3	IV-4
|0.15%|	47.7	27.4	24.3	46.9	53.0	29.7	29.2	46.7	70.1	31.7	29.3	58.7	55.3	27.7	27.1	44.8
|99.85%|	47.2	40.6	30.2	45.4	51.9	37.4	32.1	37.7	51.8	29.3	33.4	49.0	52.2	34.0	34.5	42.5

Fig. 5 Presentation of statistical evaluation of vertical acceleration in turnout suspended area.

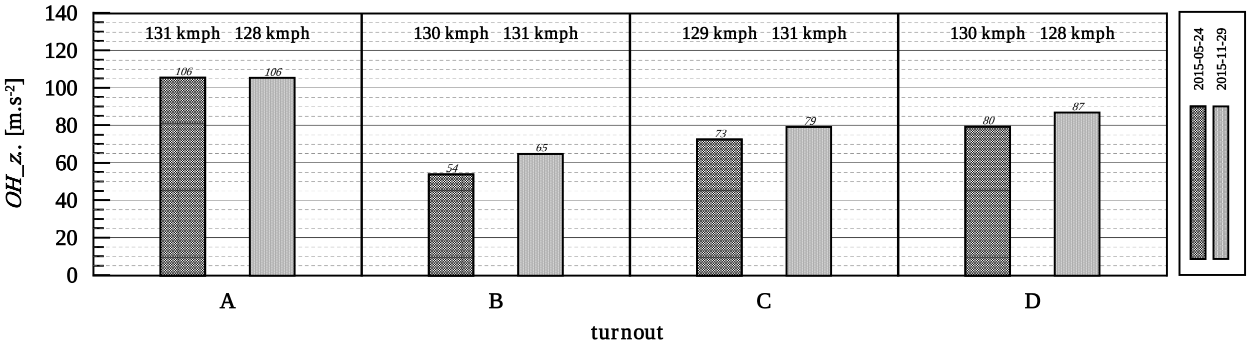

Fig. 6 Example of determination of acceleration estimated values and assessment for selected turnouts.

5. Conclusion

From the assessment of the equivalent loading of the turnout frogs we can recognize an increased value relate to passing speed for turnouts No. 1 and 4 (opposite to turnout e.g. No. 14). This equivalent loading growth partially appears at turnout No. 10, but only for the first and the third wheelset.

Realization of the certified methodology, which has been actually taken place within our research activities for company DT Výhybkárna a strojírna, a.s., is aimed to comparing of different turnouts structures with a point of view of vehicle dynamical response in the course of turnout passing during several years operation. Development of sensoric diagnostic system for optimization of turnout maintenance based on vehicle as well as track response is our future intension.

Acknowledgement

This paper was supported by Technological Agency of Czech republic within the project No. TE 01020038.

References

Grin, G. (2013) Verschleiß und Belastung von Weichenherzstücken. Diploma thesis, Technische Universität Dresden.

Gerber U., Zoll A., Fengler W. (2013) Fahrzuegbasierte Beurteilung des Herzstückverschleßes. Eisenbahningenieur 09/13, pp. 26 ÷ 30.

Müller R., Nelain B., Nielsen J., Said S., Rücker W., Bongini E. (2013) Description of the vibration generation mechanism of turnouts and the development of cost effective mitigation measures. Report RIVAS_UIC_ WP3-3_D3_6_V02.

Zelenka J., Hába A., Kohout M. (2014) Determination of equivalent loading of railway turnout frog area in the course of vehicle passing based on EN 14363 approaches. Certified methodology.

Hába A., Zelenka J., Kohout M. (2015) Determination of Equivalent Loading of Turnout Frog. In: Proc. Vibroengineering, Vol. 6, JVE International Ltd., Kaunas, pp. 217 ÷ 222.

Zelenka J., Hába A., Kohout M. (2015) Vyhodnocení ekvivalentního zatížení vybraných výhybek ve stanici Dlouhá Třebová. Technical report CKDV-WP5-2015-AH-01.

Zelenka J., Hába A., Kohout M. (2015) Vyhodnocení měření zrychlení na lokomotivě řady 380 při průjezdu vybranými výhybkami stanice Ústí nad Orlicí. Research report DP-03-15.

22nd International Conference
ENGINEERING MECHANICS 2016
Svratka, Czech Republic, 9 – 12 May 2016

FRICTION-VIBRATION INTERACTIONS OF THE NUCLEAR FUEL RODS

V. Zeman*, **Z. Hlaváč****

Abstract: *The paper deals with mathematical modelling of friction-vibration interactions of nuclear fuel rods in the hexagonal type nuclear fuel assembly. The fuel rods are transversally linked by three spacer grid cells to each other inside the fuel assembly skeleton in several vertical levels. The fuel assembly vibrations, caused by the fuel assembly support plates motion in the reactor core, generate variable contact forces between fuel rods cladding and spacer grid cells. Friction effects on stick-slip motion in contact surfaces are important to calculation of expected lifetime period of nuclear fuel assembly in terms of fuel rod cladding fretting wear.*

Keywords: Friction-vibration interactions, Nuclear fuel rod, Fretting wear

1. Introduction

Vibration of nuclear fuel assemblies (FA) was investigated in previous paper (Zeman & Hlaváč, 2012) and the monograph (Hlaváč & Zeman, 2013) as linear systems with proportional damping. Application of these mathematical models enables approximate calculation of the normal contact forces during slip motion without consideration possible stick phases and elastic deformations of spacer grid cells in tangential and vertical directions. Nevertheless, more exact computational friction-vibration analysis of fuel rod (FR) should have been based on more sophisticated computational stick-slip frictional model with force-slip velocity-displacement characteristic (Blau, 2014). The aim of this paper is presentation of the original approach to mathematical modelling of FR nonlinear vibration and fretting wear respecting the friction-vibration interactions in all contact surfaces between FR cladding and spacer grid cells.

2. Dynamic model of fuel rod

Fuel rods (Fig.1) in FA skeleton are fixed by means of the lower piece into mounting plate in reactor core barrel bottom (Hlaváč & Zeman, 2013). Each FR is surrounded by three spacer grid cells j = 1,2,3 (Fig.2) at several vertical levels g = 1,…,8 of the FA skeleton. FR mathematical model of beam type is derived by FEM for Euler-Bernoulli continua including mass forces on flexure (Raileigh theory) in space

$$\mathbf{q} = \left[\cdots, u_i, v_i, w_i, \varphi_i, \vartheta_i, \psi_i, \ldots\right]^T, i = L_u^{(s)}, 1, 2, \ldots, 16 \tag{1}$$

where u_i, v_i, w_i are axial and two lateral displacements of the central nodal point i. Angular displacements $\varphi_i, \vartheta_i, \psi_i$ represent torsional and two bending angles of FR cross-sections. Even nods $i = 2g$, g = 1,..,8 are at the level of spacer grid g and odd nodes are located in the middles. The mathematical model of spatially vibrating FR kinematically excited in the node $L_u^{(s)}$ is derived in the decomposed block form

$$\begin{bmatrix} \mathbf{M}_L & \mathbf{M}_{L,F} \\ \mathbf{M}_{F,L} & \mathbf{M}_F \end{bmatrix} \begin{bmatrix} \ddot{\mathbf{q}}_{L_u}^{(s)} \\ \ddot{\mathbf{q}}_F \end{bmatrix} + \begin{bmatrix} \mathbf{B}_L & \mathbf{B}_{L,F} \\ \mathbf{B}_{F,L} & \mathbf{B}_F \end{bmatrix} \begin{bmatrix} \dot{\mathbf{q}}_{L_u}^{(s)} \\ \dot{\mathbf{q}}_F \end{bmatrix} + \begin{bmatrix} \mathbf{K}_L & \mathbf{K}_{L,F} \\ \mathbf{K}_{F,L} & \mathbf{K}_F \end{bmatrix} \begin{bmatrix} \mathbf{q}_{L_u}^{(s)} \\ \mathbf{q}_F \end{bmatrix} = \begin{bmatrix} \mathbf{f}_L \\ \mathbf{f}_{C,FR} \end{bmatrix} \tag{2}$$

* Prof. Vladimír Zeman, DSc.: NTIS, -New Technologies for Information Society, University of West Bohemia, Univerzitní 8; 306 14, Plzeň; CZ, zemanv@kme.zcu.cz

** Assoc. Prof. Zdeněk Hlaváč, PhD.: NTIS-New Technologies for Information Society, University of West Bohemia, Univerzitní 8; 306 14, Plzeň; CZ, hlavac@kme.zcu.cz

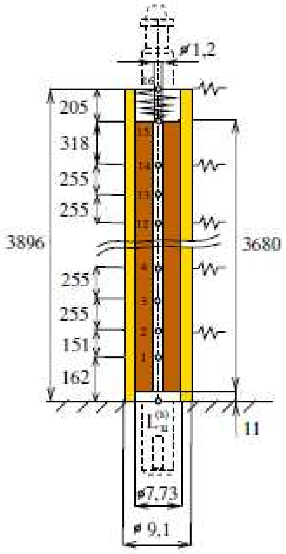

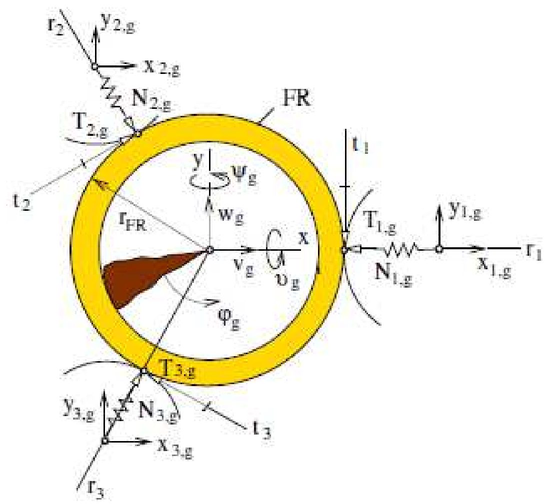

Fig. 1: Fuel rod model *Fig. 2: Contact forces between FR and spacer grid cells*

where displacements of the node $L_u^{(s)}$ (coupled with the mounting plate) are integrated in subvector $\mathbf{q}_{L_u}^{(s)}$ and displacements of the nodes $i = 1,\ldots16$ are integrated in subvector $\mathbf{q}_F \in R^{96}$. The force subvector $\mathbf{f}_L$ expresses forces acting in the kinematically excited node $L_u^{(s)}$. The subvector $\mathbf{f}_{C,FR} \in R^{96}$ expresses the coupling forces between surrounding spacer grid cells and FR at the level of all spacer grids $g = 1,\ldots,8$ (level of the even nodes). The second set of equations extracted from FR model in decomposed form (2) can be written as

$$\mathbf{M}_F\,\ddot{\mathbf{q}}_F + \mathbf{B}_F\,\dot{\mathbf{q}}_F + \mathbf{K}_F\,\mathbf{q}_F = -\mathbf{M}_{F,L}\,\ddot{\mathbf{q}}_{L_u}^{(s)}(t) - \mathbf{B}_{F,L}\,\dot{\mathbf{q}}_{L_u}^{(s)}(t) - \mathbf{K}_{F,L}\,\mathbf{q}_{L_u}^{(s)}(t) + \mathbf{f}_{C,FR}\;. \qquad (3)$$

The first three members on the right side express the kinematic excitation by the lower FA mouting plate motion calculated from the reactor global model (Zeman & Hlaváč, 2008).

3. Contact forces and prediction of the FR fretting wear

Contact forces between FR and spacer grid cells (see Fig. 2) can be expressed by normal $N_{j,g}$, tangential $T_{j,g}$ and axial $A_{j,g}$ components in all contact points $j = 1,2,3$ at the level of the spacer grids $g = 1,\ldots,8$. Friction-vibration interactions generally respect three states – ***stick, slip*** and ***separation*** – depending on the slip velocity components $c_{j,t,g}$ and $c_{j,z,g}$ and relative FR shifts $d_{j,r,g}$, $d_{j,t,g}$, $d_{j,z,g}$ in radial (r), tangential (t) and axial (z) directions compared with cell centres. Contact forces components in each contact points including all three states can be approximated by functions

$$N_{j,g} = \left(N_O + k_r d_{j,r,g}\right) H\left(N_O + k_r\, d_{j,r,g}\right), \qquad (4)$$

$$T_{j,g} = f\left(c_{j,g}\right) N_{j,g}\,\frac{c_{j,t,g}}{c_{j,g}} + k_t\left(c_{j,g}\right) d_{j,t,g}\,,\quad A_{j,g} = f\left(c_{j,g}\right) N_{j,g}\,\frac{c_{j,z,g}}{c_{j,g}} + k_z\left(c_{j,g}\right) d_{j,z,g} \qquad (5)$$

where $c_{j,\mathrm{g}}$ are resulting slip velocities. The Heaviside function H in (4) is zero for negative normal contact force $N_0+k_r d_{j,r,g}<0$ (separation state), where N_0 is static preloading of spacer grid cells about radial stiffness k_r. The approximative function for friction coefficient have to satisfy conditions $f(c_{j,g})<f_{\mathrm{st}}$ for $0<|c_{j,g}|<c_{\mathrm{krit}}$ and $f_{\mathrm{d}}<f(c_{j,g})<f_{\mathrm{st}}$ for $|c_{j,g}|>c_{\mathrm{krit}}$, where c_{krit} is critical sliding velocity separating the stick-state (phase of microslip) from slip-state (phase of macroslip) and f_{st} is static and f_{d} dynamic friction coefficient. The approximative functions for cell stiffnesses in tangential and axial directions satisfy conditions $k_t(c_{j,g})\approx k_t$, $k_z(c_{j,g})\approx k_z$ for $0<|c_{j,g}|<c_{\mathrm{krit}}$ and $k_t(c_{j,g})<<k_t$, $k_z(c_{j,g})<<k_z$ for $|c_{j,g}|>c_{\mathrm{krit}}$. The smooth functions

$$f\left(c_{j,g}\right) = \frac{2}{\pi}\,arctg\left(\varepsilon_f\, c_{j,g}\right)\left[f_d + \left(f_{st} - f_d\right)e^{-d\,c_{j,g}}\right] \qquad (6)$$

$$k_t\left(c_{j,g}\right)=k_t\,e^{-\left(\varepsilon_k c_{j,g}\right)^2},\;k_z\left(c_{j,g}\right)=k_z\,e^{-\left(\varepsilon_k c_{j,g}\right)^2} \tag{7}$$

satisfy approximately the required conditions for appropriately selected parameters f_{st}, f_d, ε_f, ε_k, d. The components of the contact forces are transformed into FR even nodes and produce the nonlinear vector $\mathbf{f}_{C,FR}\left(\mathbf{q},\dot{\mathbf{q}},t\right)$ in (3). The dynamic response is investigated by integration of motion equations (3) in time domain using standard Runge-Kutta integration scheme in Matlab. Because of a large number of nonlinearities (fully 3x8=24), the calculation is very time-consuming.

The fretting wear of the FR cladding is a particular type of FR wear that is expected in nuclear FA (Pečínka et al., 2014). The criterion of the fretting wear can be expressed using the work of friction forces during the representative time interval $< t_1, t_2 >$ calculated for normal component contact force $N_{j,g}(d_{j,r,g})$ and friction coefficient $f(c_{j,g})$.

The ***friction work*** in contact points can be written as

$$W_{j,g}=\int_{t_1}^{t_2} f\left(c_{j,g}\right)\left|N_{j,g}\left(d_{j,r,g}\right)\cdot c_{j,g}\right|dt,\; j=1,2,3,\; g=1,2,\ldots,8. \tag{8}$$

The ***fretting wear*** in grams of the FR cladding in particular contact points during the interval $< t_1, t_2 >$ can be expressed as

$$m_{j,g}=\mu W_{j,g}\;,\; j=1,2,3;\; g=1,2,\ldots,8, \tag{9}$$

where μ [g J^{-1}] is experimentally obtained fretting wear in grams (i.e. loss of FR cladding mass generated by the friction work W=1[J]) at the middle excitation frequency (Pečínka et al., 2014).

4. Application

The presented method has been applied to vibration analysis and fretting wear calculation of the Russian FA. The FA mounting plates motion and displacements of spacer grid cells centres were precalculated using FA global linearized model in the VVER-1000 type reactor for excitation by pressure pulsations generated by main circulation pumps (Zeman & Hlaváč, 2012). The basic mean excitation frequency corresponding to rotational speed of pumps is f=16.6 [Hz] , project values of cell stiffnesses are k_r=0.537 * 10^6 , k_t=k_z=10^6[N/m] and static contact force expressing preloading between FR and particular spacer grid cells is N_0=10 [N]. The friction-vibration characteristics of contact forces between FR and spacer grid cells in the form (5) are approximated by smooth function (6) and (7) for parameters $f_{st}=0.2,\, f_d=0.065, \varepsilon_f=10^4, \varepsilon_k=5000\,[s/m]$ and $d=100[s/m]$. The orbit of FR centre in nodal point i=10 (approximately in the FR middle) in time interval < 19.9, 20.1> [s] about the moment t_0=20 [s] of the maximal FA beating vibration is presented in the Fig. 3. Three orbit loops correspond to three harmonic components of the coolant pressure pulsations considered in the kinematic excitation in (3).

As an illustration, time behaviour of slip velocities $c_{1,g}$ in contact points of FR with the first cell at the level of spacer grids g = 1,4,8 is presented in the Fig. 4. As it is evident, maximal slip velocities increase with growing distance of spacer grid from lower FA mounting plate. The strong stick states are repeated in contact points with upper-most spacer grid g = 8.

5. Conclusion

The main objective of this contribution is to present the new basic method of friction-vibration interactions of the fuel rods in the nuclear fuel assembly. The method is based on mathematical modelling and computer simulation of nonlinear vibrations of the fuel rod in interactions with spacer grid cells inside the fuel assembly skeleton. The contact forces include three possible states depending on deformations of cells and slip velocities. The developed software in Matlab code is conceived in such a way that it enables to calculate fuel rod deformations, slip velocity and friction work in all fuel rod contact points with spacer grid cells. The fuel rod and spacer grid vibrations are kinematically excited by the fuel assembly support plates motion caused by pressure pulsations generated by main circulation pumps. The friction works can be used for fretting wear prediction of the Zr fuel rod cladding.

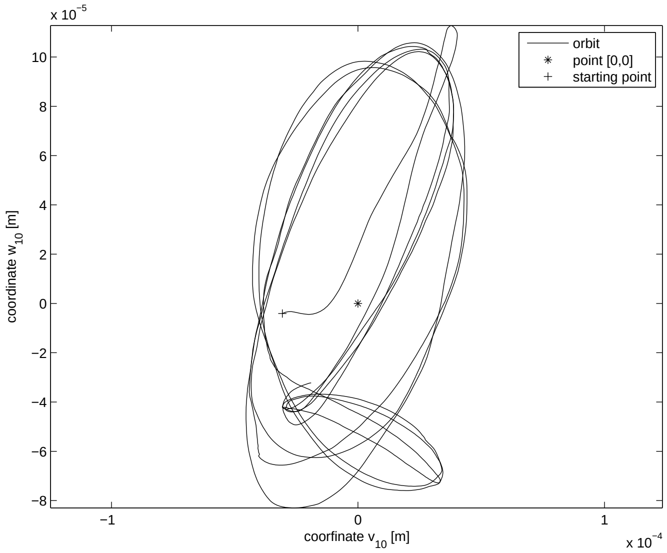

Fig. 3: Orbit of the fuel rod centre in the nodal point i=10 in time interval <19.9,20.1> [s]

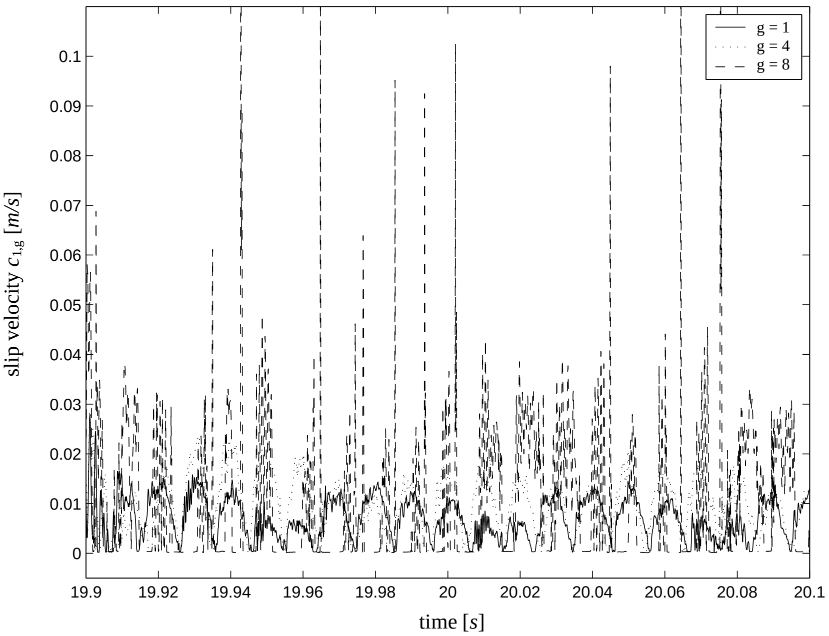

Fig. 4: Fuel rod slip velocities in contact points with the first cell at the level of spacer grid g=1,4,8

The presented method was applied for the fuel rods in Russian TVSA-T fuel assembly in the VVER 1000 type reactor in Czech NPP Temelín.

Acknowledgement

This study was supported by the project LO1506 of the Ministry of Education,Youth and Sports of the Czech Republic.

References

Blau, P. J. (2014) A multi-stage wear model for grid-to-rod fretting of nuclear fuel rods. Wear 313, 1/2, pp. 89-96.

Hlaváč, Z. & Zeman, V. (2013) Vibration of nuclear fuel assembly. LAP Lambert Academic Publishing, Saarbrucken.

Pečínka, L, Svoboda, J. & Zeman, V. (2014) Fretting wear of the Zr fuel rod cladding in Proc. 22nd Int. Conf. ICONE22.

Zeman, V, & Hlaváč, Z. (2008) Dynamic response of VVER 1000 type reactor excited by pressure pulsations. Eng. Mech. 15, 6, pp. 435-446.

Zeman, V, & Hlaváč, Z. (2012) Dynamic response of the nuclear fuel assembly excited by pressure pulsations. Applied and Computational Mechanics 6, 2, pp. 219-230.

22nd International Conference
ENGINEERING MECHANICS 2016
Svratka, Czech Republic, 9 – 12 May 2016

LAMINATED GLASS STRUCTURES IN BENDING: TIME/TEMPERATURE-DEPENDENT FINITE ELEMENT MODELS

A. Zemanová[*], J. Zeman[*], M. Šejnoha[*]

Abstract: *The lamination of glass sheets with ductile interlayers significantly changes the post-fracture response of glass structures and increases their safety. The aspects important for the modeling of laminated glass structures are: (i) heterogeneity in material parameters of glass and polymer foil (the ratio of shear moduli exceeds 1,000), (ii) time/temperature-dependent behavior of polymer foil, and (iii) effects of geometric non-linearity as a result of slenderness of laminated glass. One of the modeling approaches is finite element formulation based on refined theories. In the proposed model, kinematics relations are formulated for each layer individually and the compatibility on the interfaces of layers is ensured via Lagrange multipliers with the meaning of forces holding the neighboring layers perfectly bonded. The comparison of models with different assumptions is performed in this contribution: formulation based on large deflection or finite strains theories for kinematics, and constitutive assumption of constant bulk modulus or constant Poisson's ratio in relations for time/temperature-dependent behavior of polymeric interlayer. The developed models were verified against the detailed finite element model in ADINA and compared with a simplified model assuming elastic behavior of polymer foil with the secant shear modulus set according given temperature and loading time.*

Keywords: Laminated glass, Finite element method, Lagrange multipliers, Generalized Maxwell model, Williams-Landel-Ferry equation.

1. Introduction

Through continuous improvements in production technologies over the last decades, glass elements have attained a more structural role. The lamination of glass sheets with ductile interlayers significantly changes the post-fracture response of glass structures and increases their safety. The interfacial adhesion between glass and the interlayer is ensured by heating in combination with the application of high pressures, resulting in high gluing forces of chemical nature. Several types of interlayers have found their use in practice, for example polyvinyl butyral initially used for automotive glass or ionoplast polymer providing increased safety and security in structural applications. From car industry applications, laminated glass has expanded into the building constructions, such as roof and floor systems, staircases, or pedestrian bridges, and the application area keeps expanding in response to the pursuit of ever greater transparency in modern architecture.

2. Overview and methods for modelling

An extensive overview of the current state-of-the-art in structural glass design and engineering can be found e.g. in (Louter et al., 2014).

2.1. Behavior of laminated glass

What makes the modeling of laminated glass structures nontrivial? The common denominator is their heterogeneity. Namely, (i) polymer foils are much more compliant than the glass layers, rendering the assumptions of conventional beam or shell theories for laminates inapplicable, (ii) due to the polymer foil incorporation, their mechanical response is sensitive to load duration, temperature, strain, and strain rate e.g. (Delincé, 2014), and (iii) laminated structures display effects of geometric non-linearity as a result of

[*] Ing. Alena Zemanová, Ph.D., Doc. Ing. Jan Zeman, Ph.D., Prof. Ing. Michal Šejnoha, Ph.D., DSc.: Department of Mechanics, Faculty of Civil Engineering, Czech Technical University in Prague, Thákurova 7, 166 29 Prague 6; e-mail address: zemanova.alena@gmail.com

their slenderness. These phenomena have to be complemented with dynamic effects, arising from, e.g., impact of small projectiles in windstorms or fall of a human body – the so-called low-velocity impact that is the focus of our future research.

2.2. Overview of methods

Extensive research into the mechanical response of laminated glass structures has been undertaken to understand their unfractured behavior. Single-layer approaches, such as the concept of effective thickness, approximate the behavior of a unit by an equivalent homogeneous one. Their main advantage is their simplicity and satisfactory accuracy, but they are difficult to extend for the geometrically non-linear effects. The same arguments hold for the closed-form solutions for laminated glass plates. The most common approach is based on fully resolved 2D or 3D finite element models, which provide accurate response, but lead to expensive computations because of the large thickness-to-span ratio. The computational cost can be reduced by solid-shell elements, e.g. (Fröling and Persson, 2013), or refined beam and plate formulations, e.g. (Zemanová, 2014b). The latter approach builds on the variational formulation of refined plate theories, in which independent kinematics is considered for each layer and the inter-layer compatibility is enforced by the Lagrange multipliers when minimizing the total energy of the system. We adapted this concept to develop efficient and accurate finite element formulations for large-strain and large-deflection analyses of laminated beams and plates with temperature-dependent viscoelastic interlayer via time-incremental energy minimization. In this contribution, we focus on models for laminated glass beams.

3. Finite element formulations based on refined theories

3.1. Assumptions

The proposed geometrically nonlinear finite element models of laminated glass beams, derived from a refined plate theory by Mau (1973), assume planar cross sections of individual layers but not of the whole laminated glass unit. We treat each layer independently and enforce the compatibility by the Lagrange multipliers. This approach could capture possible delamination, however a perfect adhesion is supposed.

3.2. Kinematics

For kinematics equations, we used two approaches. The first of them, the Reissner finite-strain beam theory (FS), is more general, while the second one is based on von Kármán assumptions (VK) of large deflections and small in-plane displacements and rotations.

3.3. Constitutive relations

The main engineering property relevant to the composite behavior of the units is the shear-stress versus shear-strain characteristics of the soft interlayer. The shear modulus of the polymer interlayer is experimentally determined as a function of duration of loading and temperature, see (Pelayo et al., 2013). For that reason, the behavior of polymer foil is linearly viscoelastic, while glass is an elastic material in our models. Two different formulations assuming constant value of bulk modulus K (FS_K and VK_K) or Poisson's ratio υ (FS_υ and VK_υ) were proposed. The temperature dependence is taken into account by the time-temperature superposition principle; we employ the Williams-Landel-Ferry equation. These viscoelastic approaches are compared with a simplified model assuming elastic behavior of polymer foil with the value of the shear modulus set according given temperature and loading time.

3.4. Solution procedure

The geometrically nonlinear solver from (Zemanová et al., 2014a) was extended to the incremental viscoelasticity formulation. The sought displacement increment ${}^{k+1}\delta r$ and the vector of Lagrange multipliers ${}^{k+1}\lambda$ are determined from the linearized system

$$\begin{bmatrix} {}^{k}\hat{K} & {}^{k}C^{\mathrm{T}} \\ {}^{k}C & 0 \end{bmatrix} \begin{bmatrix} {}^{k+1}\delta r \\ {}^{k+1}\lambda \end{bmatrix} = -\begin{bmatrix} {}^{k}\hat{f}_{\mathrm{int}} - f_{\mathrm{ext}} \\ {}^{k}c \end{bmatrix}. \qquad (1)$$

The stiffness matrix for k-th iterative step ${}^{k}\hat{K}$ is composed of independent stiffness matrices of layers and therefore exhibits block structure. Matrix ${}^{k}C$ and vector ${}^{k}c$ implement the compatibility conditions for displacements on the interface of neighboring layers. For finite-strain formulation, these matrices have to be calculated for each iterative step, whereas for von Kárman assumptions, C is still the same matrix composed of constant values and ${}^{k}c$ is the zero vector. External nodal forces f_{ext} correspond to the loading of structure for given time step and ${}^{k}\hat{f}_{\text{int}}$ has the meaning of internal nodal forces for k-th iterative step. The notation ${}^{k}\hat{K}$ and ${}^{k}\hat{f}_{\text{int}}$ is used to emphasize that these quantities are determined for interlayer using the effective values of Young's modulus (or shear modulus) and include the additional terms due to relaxation effects.

4. Results, comparisons and verification

The most common laminated beams with three layers (glass/PVB/glass) are considered in this section. We compare the proposed models for two examples: the fixed-end beam and the simply-supported beam. In practical applications, the laminated glass elements are not perfectly fixed or simply-supported; therefore these two cases are limits of the real support conditions. The beams are loaded by uniformly distributed transverse pressure with a constant magnitude during the loading duration or with two-load history (with a jump in magnitude of loading).

It follows from the comparisons of results and from Fig. 1 that the viscoelastic approaches based on the assumption of constant value of bulk modulus K (FS_K, VK_K), or Poisson's ration υ (FS_υ, VK_υ) provide the same results for all examples. The errors in deflections and stresses are much smaller than 0.1%. The geometrically nonlinear approaches based on the assumptions of large deflections (VK_K, VK_υ) or finite strains (FS_K, FS_υ) give comparable results for tested examples. The errors are about 0.1%. For statically determinate example, the geometrically linear (LIN_K , LIN_υ) and nonlinear solvers provide the same results, whereas for statically indeterminate examples, the error of linear approach can be about 100% or up to 300%.

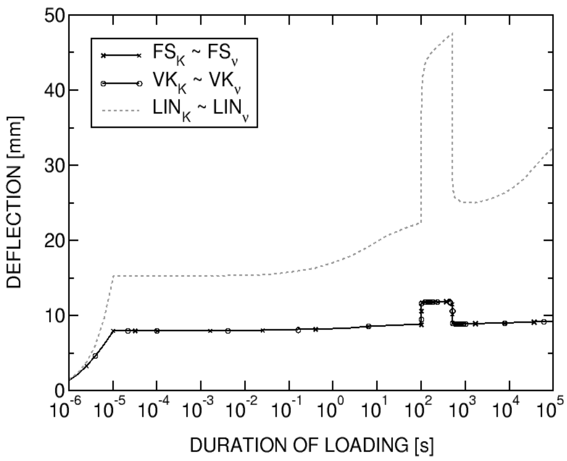

(a)

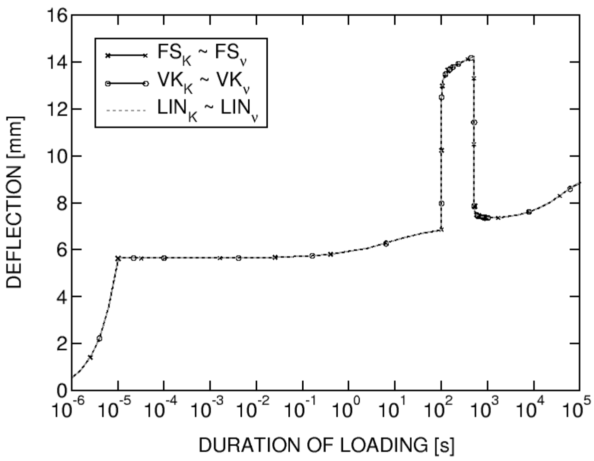

(b)

Fig. 1: Comparison of deflections at the mid-point of (a) a fixed-end beam and (b) a simply-supported beam for two-load history at the temperature 25°C: response of proposed finite element model under finite strains assumptions ($FS_K \sim FS_\upsilon$), large deflections assumptions ($VK_K \sim VK_\upsilon$), and geometrically linear case ($LIN_K \sim LIN_\upsilon$).

The response of proposed multi-layered model for both, deflection (Fig. 2 (a)) and stresses, is in a full agreement with the results of 2D analysis in ADINA. The error in values is under 0.5%. The results were compared for temperatures 0°C and 25°C; ADINA solver had problems with convergence for 50°C due to the low values of shear modulus of PVB.

The results obtained with and without accounting for the viscoelastic behavior of the interlayer are compared for a simply-supported beam in Fig. 2 (b). The elastic model gives good prediction for behavior of laminated glass beams, especially for small temperatures (error around 2% for maximum deflections).

For higher temperatures, the error can be significant (up to 27%) after the change of loading level. There are cases and zones where the elastic solution is not on the side of safety. The viscoelastic effects could be important for dynamic, impulsive, and reverse loading.

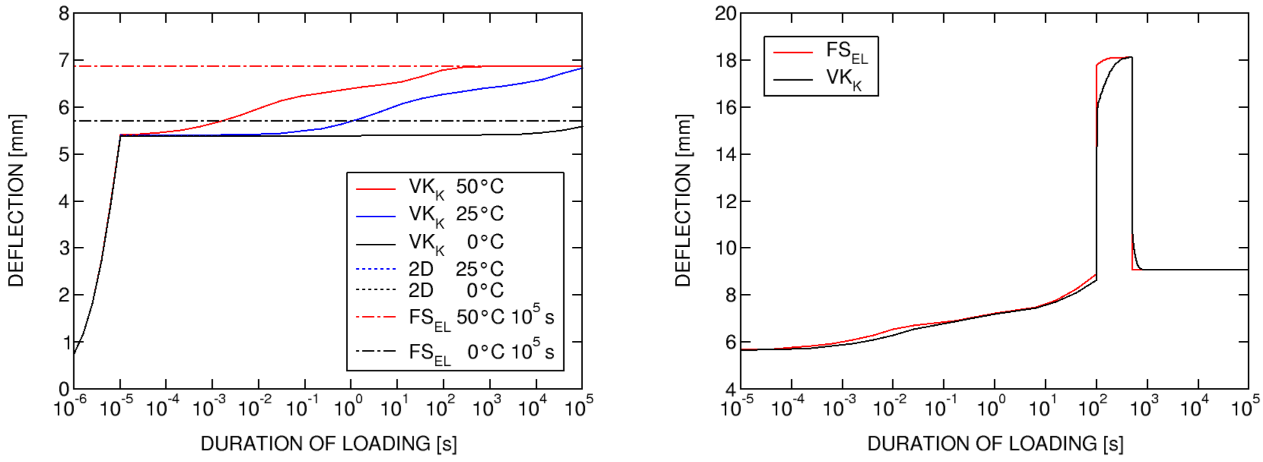

(a) *(b)*

Fig. 2: Deflections at the mid-point (a) of a fixed-end laminated glass beam under distributed loading at the temperature 0°C, 25°C, and 50°C, (b) of a simply-supported laminated glass beam with two-load history at the temperature 50° C. Response of geometrically nonlinear proposed model (VK$_K$) is compared with model in ADINA (2D), model for the elastic behavior of interlayer (FS$_{EL}$) with material parameters (a) for 0°C or 50°C and duration of loading 10^5 s or (b) for given loading duration.

5. Conclusions

(1) The viscoelastic approaches based on the assumption of constant value of bulk modulus or Poisson's ration provide the same results for all examples. (2) The geometrically nonlinear approaches based on the assumptions of large deflections or finite strains give comparable results for tested examples. (3) Effects of geometric nonlinearity can be significant for behavior of statically indeterminate laminated glass beams and plates; however the geometric non-linearity can be neglected for simply-supported beams. (4) Temperature affects the behavior of laminated glass significantly. (5) The simplified model assuming elastic behavior of polymer foil gives good prediction for behavior of laminated glass beams under static loading, especially for low temperatures. The viscoelastic effects could be important for dynamic, impulsive, and reverse loading under room or higher temperatures.

Acknowledgement

This contribution was supported by Czech Science Foundation (GA ČR), project No. 16-14770S.

References

Delincé, D. (2014) Experimental approaches for assessing time and temperature dependent performances of fractured laminated safety glass. Ph.D. thesis, Ghent University, https://biblio.ugent.be/publication/4346098.

Fröling, M., Persson, K. (2013) Computational methods for laminated glass. J. Eng. Mech. 139, 780–790.

Louter, C., Bos, F., Belis, J., and Lebet, J.-P. (2014) Challenging Glass 4 & COST Action TU0905 Final Conference. CRC Press.

Mau, S. T. (1973) A refined laminated plate theory. Journal of Applied Mechanics–Transactions of the ASME, 40(2):606–607.

Pelayo, F., López-Aenlle, M., Hermans, L., and Fraile, A. (2013) Modal scaling of a laminated glass plate. 5th International Operational Modal Analysis Conference, pp. 1–10.

Zemanová, A., Zeman, J., and Šejnoha, M. (2014a) Numerical model of elastic laminated glass beams under finite strain. Archives of Civil and Mechanical Engineering, 14(4):734–744.

Zemanová, A. (2014b) Numerical modeling of laminated glass structures. Ph.D. thesis, Czech Technical University in Prague, https://sites.google.com/site/zemanovaalena/research.

22nd International Conference
ENGINEERING MECHANICS 2016
Svratka, Czech Republic, 9 – 12 May 2016

COMPARATIVE THERMO-MECHANICAL ANALYSIS OF DIFFERENT TYPES OF DISC BRAKES

J. Ziółkowska*, P. Sokolski**

Abstract: *The paper is focused on analysis of mechanical and thermal processes occurring in disc brakes during braking. For a specific example of real braking parameters the authors conducted numerical simulations of performance of two differently shaped brakes. Finite elements method was used and coupled mechanical and thermal analyses were carried out. Basing on obtained results intensity of heat generation and distribution of temperature as well as stresses level in elements of the studied subassemblies were evaluated. Comparison of scientific findings was a keystone to point out some significant remarks concerning construction of disc brakes in the view of their safe and reliable operation.*

Keywords: Disc brakes, reliability, finite elements method, thermal processes, failures.

1. Introduction

Disc brakes are common mechanisms used in modern vehicles. It is because of their braking efficiency most of all and ease of servicing (Ghadimi et al., 2013). One can distinguish their self-cleaning capability, resistance to disadvantegous thermal processes and relatively low susceptibility to brake fade as other reasons why these subassemblies are so often applied (Scieszka, 1998; Ghadami et al., 2013).

Braking systems play key role in operation of all machines and vehicles. To ensure their reliable and safe work is an indispensible demand from the very beginning phase of machinery design process.

2. Problem identification

As it was described in (Belhocine & Bouchetara, 2013; Kennedy, 1984) during braking of disc brakes almost all of the friction energy (up to 95%) transforms into heat energy. Other components like triboemission, noise, mechanical vibrations or cumulated deformation energy are much less significant but also should be taken into account during complex analysis.

Generation of heat directly causes temperature changes what implicates occurrence of different thermo-physical processes. It is especially significant on the friction surfaces. In normal conditions temperature rises up to 800 ºC (Belhocine & Bouchetara, 2013) but of course it is advised to design and operate brakes to keep this value on lower level. In extreme cases such temperature rise can influence normal radiation and heat convection what can be described as thermo-elastic instability (Scieszka, 1998).

There were plenty of experimental research focused on physics of wear processes in disc brakes (among others Laguna-Camacho et al., 2015; Eriksson et al., 1999; Eriksson et al., 2012). Accurate results and detailed description of studied phenomena are usually achieved for a price of long-lasting and very expensive tests. In this situation it is reasonable to use numerical simulations to support experimental works. Some examples of coupled mechanical and thermal FEM analysis of disc brakes behaviour is presented among others in (Belhocine & Bouchetara, 2013; Ghadami et al., 2013; Ghadami et al., 2013).

The most common solution to change the intensity of thermal processes is to use so called ventilated disc brakes. In such a part there is an additional disc separated from the original one with a special gap. Both discs are connected through a set of cooling fins. That type of construction forces changes in aerodynamical flow in its surrounding which results in higher emission of heat from brakes into the

* Eng. Justyna Ziółkowska.: Faculty of Machine Design and Operation, Wroclaw University of Technology, ul. Wybrzeze Wyspianskiego 27, 50-370 Wroclaw, PL.

** Piotr Sokolski, PhD: Faculty of Machine Design and Operation, Wroclaw University of Technology, ul. Wybrzeze Wyspianskiego 27, 50-370 Wroclaw, PL, piotr.sokolski@pwr.edu.pl

ambient air. Although ventilated disc brakes have more compound structure than normal ones it is more favourable distribution of heat generated while braking and also lowering the level of temperature in the brakes' components what makes them widely used in automotive industry (Ghadami et al., 2013).

3. Method

In this paper temperature and stress distributions of the disc brake have been investigated. Finite elements method was used to perform numerical simulations (in Dynamic Explicit Coupled Temperature-Displacement Module of Abaqus 6.13 software). Computations were carried out for emergency braking of a passenger car (mass 1830 kg) from speed of 178 km/h until stop in time of 7 s. Because of narrow frames of this paper calculations of basic parameters of braking unit are not included in the text.

Computational parameters of disc and pads are shown in Tab. 1.

Tab. 1: Thermal and strength parameters of disc and pads assumed in the analyses

Parameter	**Disc**	**Pads**
Density [kg/m^3]	7800	1450
Young's modulus [GPa]	209	1,4
Poisson's ratio [-]	0,29	0,24
Thermal expansion [m/mK]	1,26e-5	1,1e-5
Thermal conductivity [W/mK]	48	1,1
Specific heat [J/kgK]	452	1200

Boundary conditions for tested elements were as follows:

- Disc - rotation allowed along the direction of car's movement.

- Pads - all degrees of freedom were fixed to simulate full clamp of pads.

Two types of discs were analyzed: a normal one (first case of analyses) and a ventilated one (second case of analyses). It was assumed in this paper that evaluation of disadvantageous processes during braking will be performed for disc only and expressed by stresses (von Mises stresses as pad is made of cast steel) and temperature level. Both of analyzed brakes where designs of the authors basing on literature guidelines. The original brakes made by the producer were not the case of this work.

The authors created solid numerical models. Then finite elements to generate mesh were selected. It is usually recommended to use cubic types of elements rather than pyramidal ones. The latter are so-called not adjusted elements and for this reason the results of analyses are error-prone (Biernacki, 2014; Biernacki, 2015; Rusinski et al., 2000). Having this in mind, to create the discrete model of pads and normal disc hexahedral finite elements were used. Because of more complicated geometry it was not possible to use only such elements while meshing the ventilated disc. In some regions of this part tetrahedral finite elements were applied but they were relatively small areas comparing to the rest of the model. To lower the negative influence of usage of tetrahedral finite elements their size was lowered what is typical in such cases (Rusinski et al., 2000).

The most important results are presented in Fig. 1-4. While scale for stresses figures (Fig.1, 3) is the same (up to 500 MPa), in temperature distribution figures (Fig. 2, 4), to make pictures more clear to analyze, in first case scale was up to 500 ºC and in second case it was 200 ºC.

It was observed that in the first case of analyses both used parameters were surpassing limits after only about 3 s of simulations, it is even before half point of braking. Almost from the very beginning of the tests von Mises stresses gradually arose around a hole which is the place were the disc is mounted to the wheel and on the perimeter of the disc where the friction surfaces were located (Fig.1). Temperature values surpassed the assumed level of 500 ºC on the contact surfaces where pads were sliding along (Fig. 2). Such an intensification of tribological processes is unacceptable.

Assessing the results of the second case of analyzes it turned out that addition of extra surfaces resulted in significant lowering of temperature level in disc (Fig.4). At the time of 3,2 s, it is when first type of brake was already overheated, temperature this time was below 100 ºC. In further parts of braking, including the final one, this parameter barely exceeded 200 ºC which is way below dangerous level. Von Mises stresses were lowered as well. In the midpoint of braking there were only small local areas where level of critical stresses was exceeded. In the end of braking process this area enlarged and also stresses were too high in some parts of surfaces paired with pads (Fig. 3). It means that the proposal of modification is improving thermal phenomena sufficiently. Modification also lowered stresses but not below safe level in the entire unit. There are some small parts of disc where yield strength is reached.

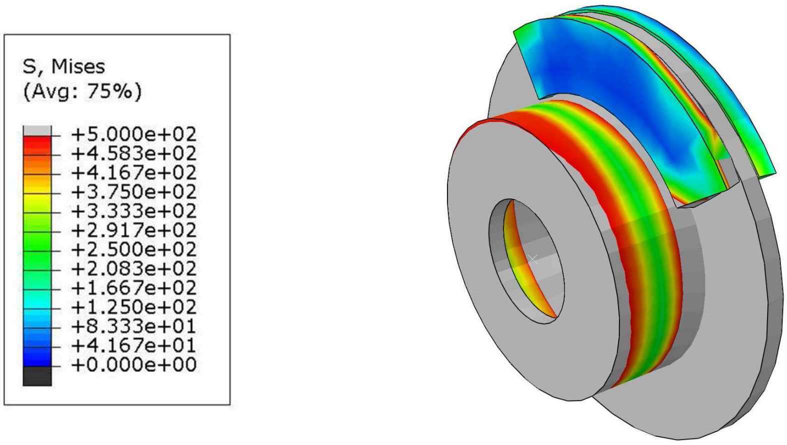

Fig. 1: Von Mises stress distribution [MPa] in disc brake unit after 3,2 s of braking in first case of analyses (detailed description in text)

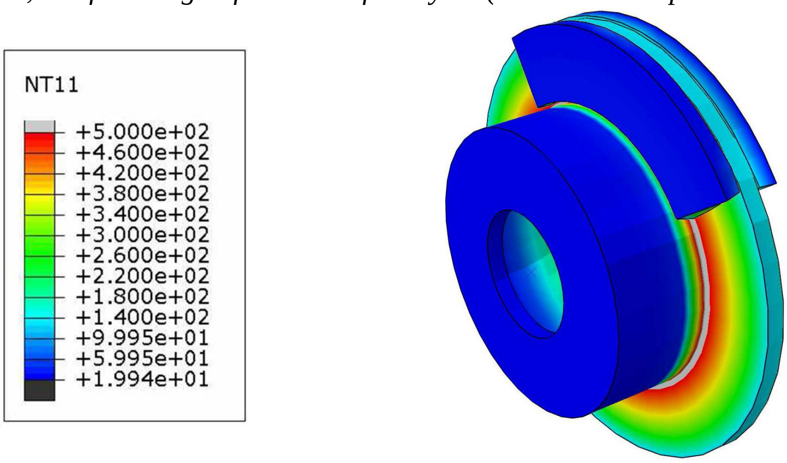

Fig. 2: Temperature distribution [ºC] in disc brake unit after 3,2 s of braking in first case of analyses (detailed description in text)

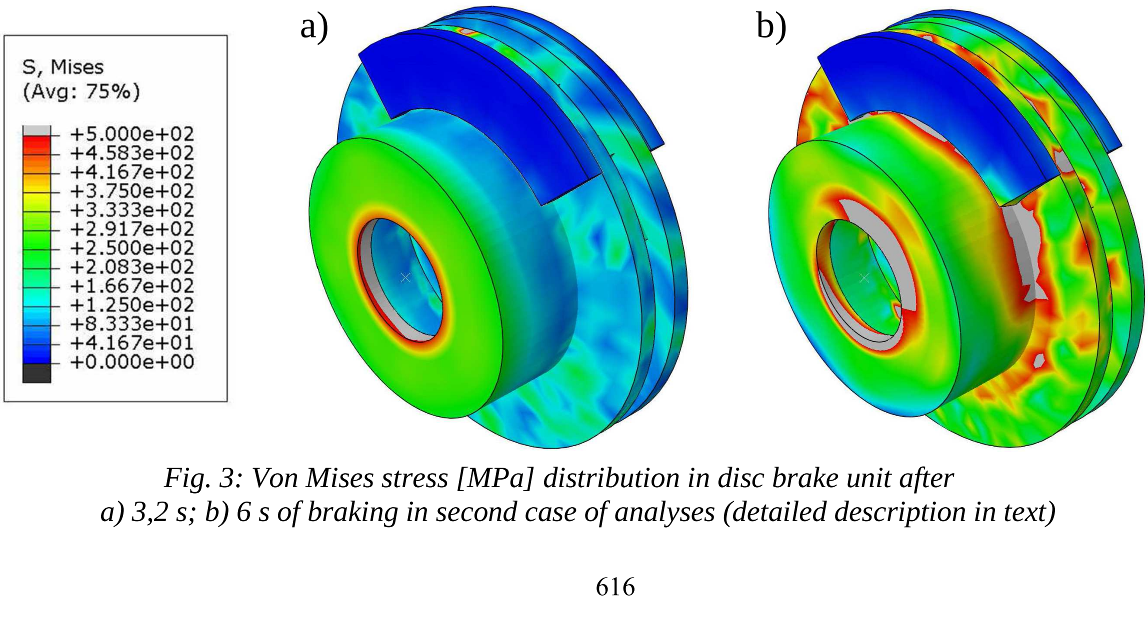

Fig. 3: Von Mises stress [MPa] distribution in disc brake unit after a) 3,2 s; b) 6 s of braking in second case of analyses (detailed description in text)

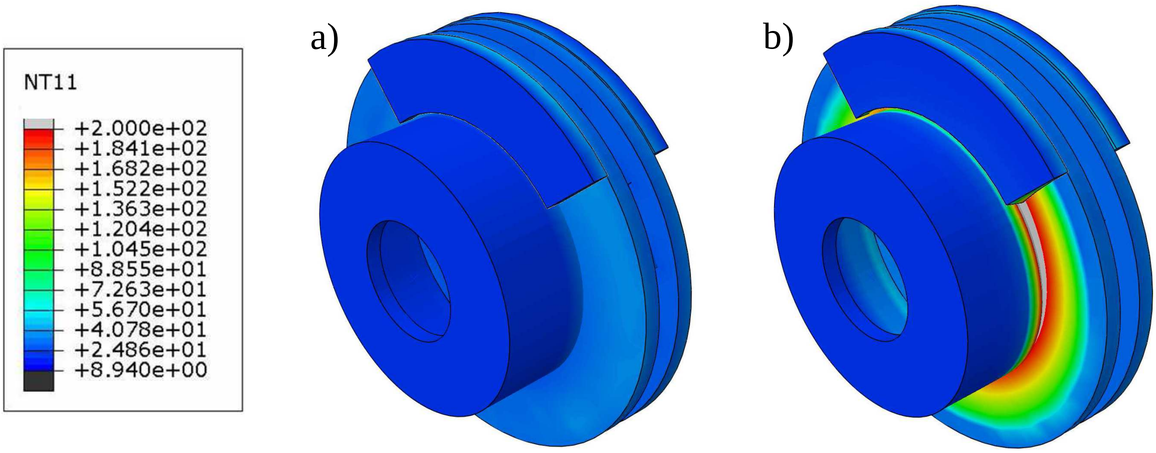

Fig. 4: Temperature distribution [ºC] in disc brake unit after a) 3,2 s; b) 6 s of braking in second case of analyses (detailed description in text)

4. Conclusions

It was observed that modification of the analyzed disc brake into the ventilated one resulted in substantial lowering of both temperature and von Mises stresses. Change of the design implied first of all changes in aerodynamic flow around the brake subassembly and heat development in its components. Thanks to that overheating within the analyzed brake was no more the problem. Additional surface turned out to strengthen the construction relevantly. Although stresses are locally over the permissible level it can be stated that the implemented modification almost fully reached expectations. Of course it also should be improved but it requires less important modifications than those which were done and they are not included in this paper because of its frames. Safety and reliability of analyzed brake units were increased.

References

Belhocine A. & Bouchetara M. (2013) Investigation of temperature and thermal stress in ventilated disc brake based on 3D thermomechanical coupling model. Ain Shams Engineering Journal, 4, pp. 475–483.

Biernacki K. (2014) Selection of the optimum tooth profile for plastic cycloidal gears. Proceedings of the Institution of Mechanical Engineers. Part C, Journal of Mechanical Engineering Science, Vol. 228, No. 18, pp. 3395-3404.

Biernacki K. (2015) Analysis of the influence of the material and design modifications on strength of the cycloidal gear system. International Journal of Precision Engineering and Manufacturing, Vol. 16, No. 3, pp. 537-546.

Eriksson M., Bergman F. & Jacobson S. (1999) Surface characterisation of brake pads after running under silent and squealing conditions. Wear, 232, pp.163–167.

Eriksson M., Bergman F. & Jacobson S. (2012) On the nature of tribological contact in automotive brakes. Wear, 252, pp.26–36.

Ghadimi B.,Kowsary F. & Khorami M. (2013) Thermal analysis of locomotive wheel-mounted brake disc. Applied Thermal Engineering, 51, pp. 948-952.

Ghadimi B., Sajedi R. & Kowsary F. (2013) 3D investigation of thermal stresses in a locomotive ventilated brake disc based on a conjugate thermo-fluid coupling boundary conditions. International Communications in Heat and Mass Transfer, 49, pp. 104–109.

Kennedy F. E. (1984) Thermal and thermomechanical effect in dry sliding. Wear, 100, pp. 453-476.

Laguna-Camacho J.R., Juárez-Morales G., Calderón-Ramón C., Velázquez-Martínez V., Hernández-Romero I., Méndez-Méndez J.V. & Vite-Torres M. (2015) A study of the wear mechanisms of disk and shoe brake pads. Engineering Failure Analysis, 56, pp. 348–359.

Rusinski E., Czmochowski J. & Smolnicki T. (2000) Advanced finite elements method in superstructures. Wroclaw University of Technology Publishing House, Wroclaw (in Polish).

Scieszka S. (1998) Friction brakes. Material, designing and tribological issues. Institute of Operation Technology Publishing House and Polygraphy Division, Radom. (in Polish)

22nd International Conference
ENGINEERING MECHANICS 2016
Svratka, Czech Republic, 9 – 12 May 2016

NUMERICAL ANALYSIS OF DRILLING RIG'S CARRYING STRUCTURE

J. Ziółkowska*, P. Sokolski**

Abstract: *Drilling rigs are constructions which play indispensable role in oil extraction process. The paper shows numerical calculations of crucial parts of drilling rigs which are derricks. These structures carry almost entire loading which occur during extraction of oil deposits. Level of von Mises stresses and total mass were the main criteria taken into account. A stability analysis was also done and buckling safety factors were estimated.*

Keywords: Drilling rig, derrick, buckling.

1. Introduction

Petroleum is one of the most needed energetic raw materials. Because of that its extraction is well-developed despite of many difficulties during realization of this process. The main problem is that oil deposits are usually situated several kilometres below ground level. To overcome this disadvantageous conditions special constructions called drilling rigs are used which enables to create drilling hole. Basic parts of a drilling device are mud pump, draw-works, drill lines and derrick. The latter is the main one in terms of mechanical stability as it serves as a carrying structure. It is under the influence of loading which acts through draw-works unit. The derrick has a truss structure with height up to several tens of meters. In the view of its working conditions, it has to be characterized by high mechanical strength and stability but on the other hand its mass must be as low as possible. These demands can be fulfilled by utilization of special profiles.

There are several loads that act on drilling rig's derricks. The most significant is influence of set of pipes. Among the others there are force of wind, travelling and fixed blocks or hooks.

One of other key problems in terms of durability of derricks is its dynamics. For this reason one have to include calculations of vibrations not only in the process of designing but also to examine their level during operation of the drilling rig. Example of such an attitude were described in details by plenty of researchers (among others Hu et al., 2013; Han et al., 2011). Usually the obtained results serve to conduct numerical simulations. In this way it is possible to calculate for instance first, second and so on order modes. This knowledge is the key to proper design of the construction.

2. Method

The goal of this work was to simulate and analyze loading and stresses in derrick under the influence of pipe set and then to optimize its geometry. The criterion was to keep level of stresses below permissible value while lowering construction's mass.

The simulations were carried out for the following parameters:

- Total length of the pipe set: 3000 m;
- Length of one pipe: 13 m;

* Eng. Justyna Ziółkowska.: Faculty of Machine Design and Operation, Wroclaw University of Technology, ul. Wybrzeze Wyspianskiego 27, 50-370 Wroclaw, PL.

** Piotr Sokolski, PhD: Faculty of Machine Design and Operation, Wroclaw University of Technology, ul. Wybrzeze Wyspianskiego 27, 50-370 Wroclaw, PL, piotr.sokolski@pwr.edu.pl

- Total mass of the pipe set: 230 000 kg;

- Yield stress of steel S235 used for construction: 235 MPa;

- Assumed safety factor: 2;

- Assumed buckling safety factor: 1.5;

- Permissible value of stresses: 117,5 MPa.

To perform simulations Siemens NX 9.0 software was used. Beam finite elements were utilized in numerical analyses.

An initial concept was to use I-beam profiles for main, oblique and transverse poles (Fig. 1a). In following simulations the dimension of this profile were modified. All of these dimensions are shown in Tab. 1. Another cross-section used in simulations was a closed one (Fig. 1b). Its dimensions are shown in Tab. 2.

There was a gap in the structure for placing the pipe set inside the derrick.

a) b)

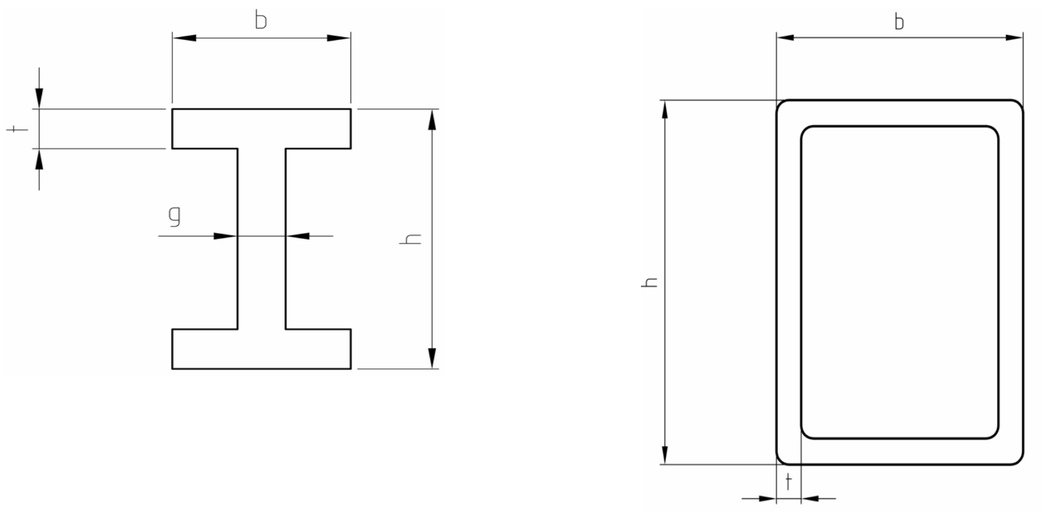

Fig. 1: Two types of profiles used in analyses: a) I-beam, b) closed

Tab. 1. Dimensions of I-beam profile (according to Fig. 1)

		h [mm]	b [mm]	g [mm]	t [mm]
First concept	**Main beams**	497,0	200,0	8,4	14,5
	Additional beams	196,4	100	4,5	6,7
Second concept	**Main beams**	357,6	170,0	6,6	11,5

Tab.2. Dimensions of closed profile (according to Fig. 1)

	Typ	t [mm]	b [mm]	h [mm]
Main beams	Square	10	200	200
Additional beams	Rectangular	10	180	260

Successive simulations were carried out. Their results are presented in Fig. 2-4 and also in Tab. 3. One can point out that for all of the cases von Mises stresses were below permissible level what means that strength criterion was fulfilled. For the first concept they were almost twice smaller than it is acceptable what meant the construction was too massive. Having in mind the other criterion (mass reduction), it turned out that the second concept was better than the first one. On this basis the authors decided to choose between the second and the third concepts.

As stability of derricks is of a great importance, buckling was analyzed as well. Safety factor was calculated for all 3 concepts using numerical simulations again (Tab. 4). This parameter has values below 1,2 for second concept what is not enough to ensure derrick's stability. For the other cases this requirement was met. Comparing the dimensions of the structure for first and third concept, it turned out that the best profile for the derrick's structure with the given initial parameters is the third one. Its buckling safety factor has value higher than 11 what means there is no danger of instability occurrence during the operation of the drilling rig.

a) b)

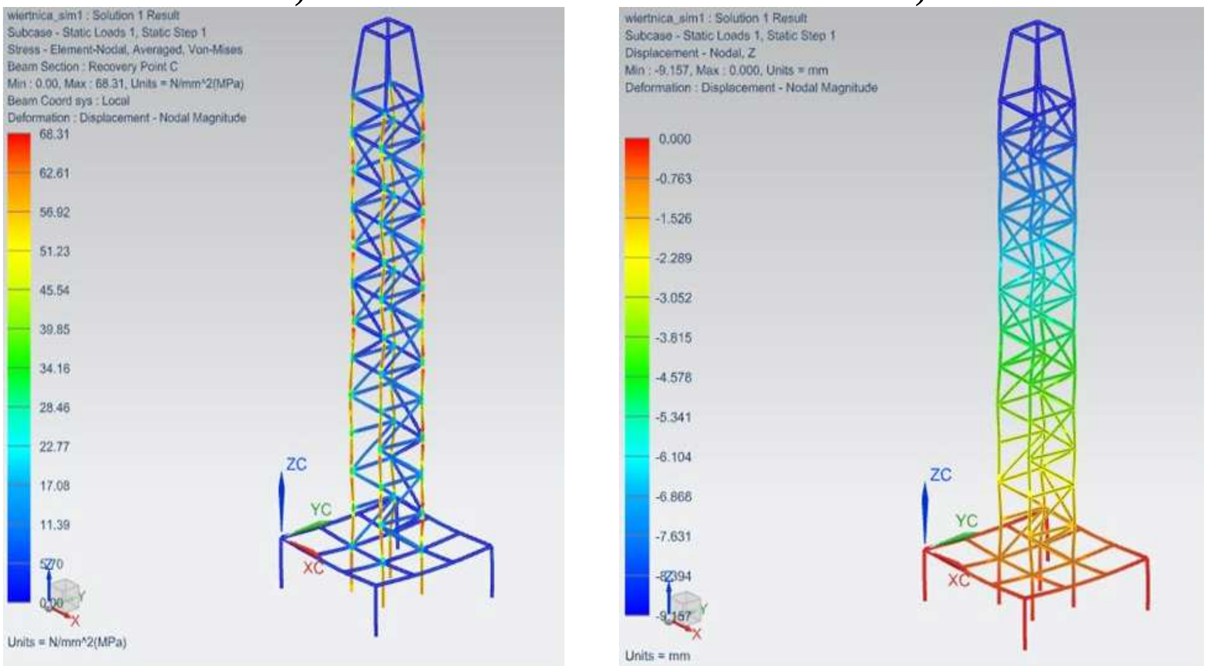

Fig. 2. First concept: a) von Mises stresses [MPa], b) displacement [mm]

a) b)

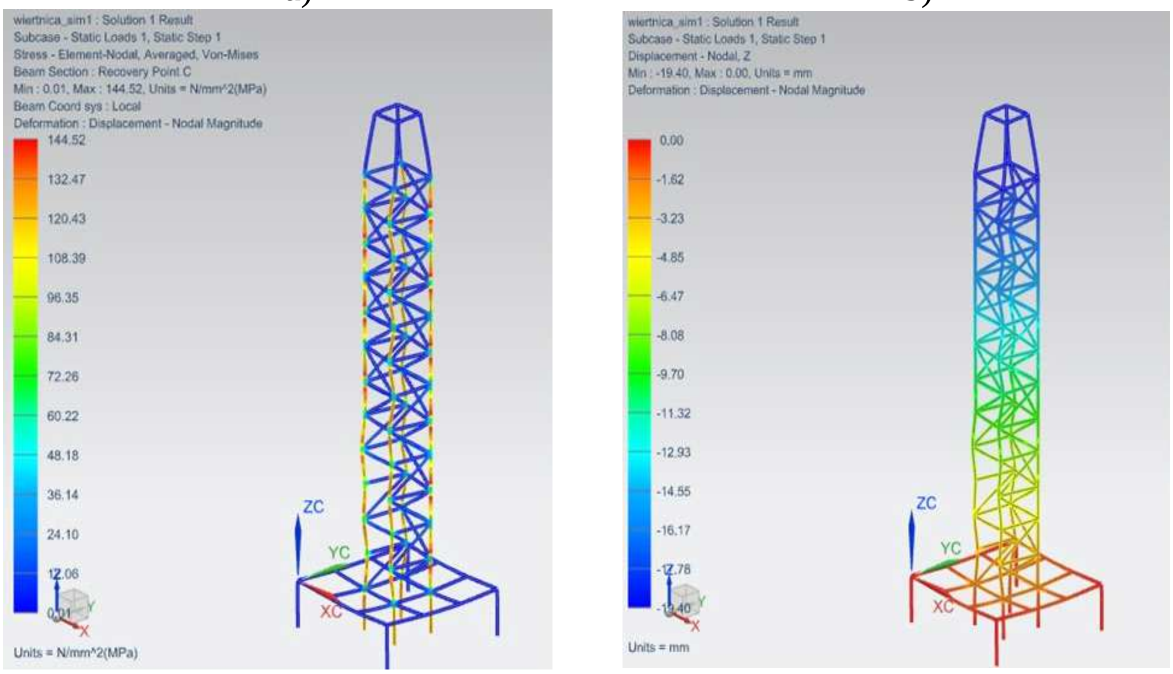

Fig. 3. Second concept: a) von Mises stresses[MPa], b) displacement [mm]

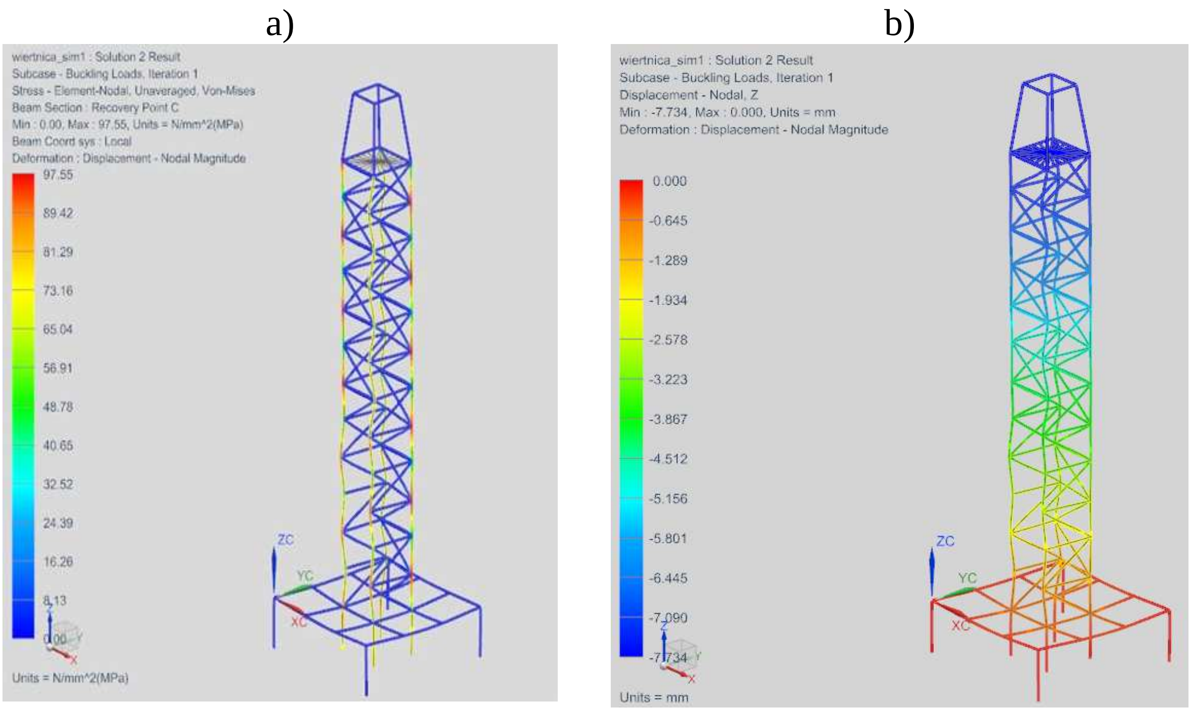

Fig. 4. Third concept: a) von Mises stresses [MPa], b) displacement [mm]

Tab. 3. Results of simulations for 3 concepts

	First concept	Second concept	Third concept
Maximum von Mises stresses [MPa]	68	109	98
Maximum displacement [mm]	9,2	14,6	11,5

Tab. 4. Values of buckling safety factor for 3 concepts analyzed

Concept	**Buckling safety factor**
1	1,57 ÷ 1,58
2	1,02 ÷ 1,18
3	11,5 ÷ 22,4

3. Conclusions

The carried out analyses helped to select the optimal profile for the derrick's structure in the view of the given criteria. The closed cross-section met all requirements: strength and buckling. Von Mises stresses were up to 100 MPa which is quite near to the permissible value of 117,5 MPa. I-beam profiles fulfilled the strength criterion as well but they were not enough safe in terms of buckling (the second concept) or they were too heavy (the first concept).

All in all, for the assumed values of input parameters, construction of derrick was designed. In addition dynamic analyses could be carried out but it was out of the scope of this paper.

References

Han D., Shi P., Zhou G., Li Z., Li Xu., Wang L. (2011) Safety Evaluation of Marine Derrick Steel Structures Based on Dynamic Measurement and Updated Finite Element Model. Procedia Engineering, 26, pp. 1891–1900.

Hu J., Tang Y., Li S. (2013) Vibration test and assessment for an ocean drilling rig derrick. Taking the ZJ50/3150DB drilling rig as an example. PETROL. EXPLOR. DEVELOP., 40(1), pp. 126–129.

22nd International Conference
ENGINEERING MECHANICS 2016
Svratka, Czech Republic, 9 – 12 May 2016

SYNTHESIZED MICROMECHANICAL FIELDS BASED ON THE SYNERGY OF WANG TILES AND FEM

L. Zrůbek*, A. Kučerová**, J. Novák***

Abstract: *In this contribution, we present the concept of replacing periodic unit cell (PUC) with a set of specifically designed cells and their utilization for modeling of materials with heterogeneous microstructures and for reconstruction of micromechanical fields. The approach is based on the Wang tiles method that compresses the stochastic microstructure into a small set of statistical volume elements – tiles. Tiles are placed side by side according to matching edge codes like in a game domino. Using the stochastic tiling algorithms the microstructure of arbitrarily large domain is recreated and opposite to the repeating pattern of PUC it preserves its randomness. To obtain the mechanical response of whole domain, the micromechanical quantities are evaluated only on tiles and then synthesized back. But because of the non-local character of mechanical quantities the resulting field contains jumps between adjacent tiles. To prevent this phenomenon, the surrounding layers of tiles of each addressed tile are included into the evaluation. In our latest work, we are focused on how the characteristic microstructural lengths influence the convenient size of individual tiles and how the number of included layers of tiles affects the resulting error between the synthesized and reference micromechanical field.*

Keywords: **Heterogeneous microstructures, Wang tiles, Synthesized Micromechanical Fields, Finite Element Method.**

1. Introduction

With the increasing pressure to the utmost material performance, we need a detailed understanding of characteristic mechanical processes taking place on a microstructural level. But when we look closely at materials used in engineering applications the majority of them is heterogeneous with a stochastic microstructure layout.

Several methods can be used for modeling of such microstructures. One of the most widely used methods is numerical homogenization. For materials with periodic patterns are the heterogeneities modeled as periodic unit cells (PUC). A small part of the original microstructure is representing the cell and just by duplication in cardinal directions we obtain original microstructure. For non-periodic microstructures is used the statistically equivalent periodic unit cell (SEPUC) which shares the statistical description with the original microstructure. However, in both cases, only a single cell is describing the whole microstructure which brings periodicity in all further operations. If we are searching only for the effective parameters the periodicity plays no role but when we want to study mechanical response of the microstructure itself (e.g. stresses, strains or displacements) we need to preserve the stochastic microstructure.

In contrast, a different method that does not operate with only one cell, but represents the media through a set of cells can be used. These cells are mutually compatible on the edges and using specific algorithm they can create an infinitely large reconstructed microstructure which preserve stochastic distribution. This method is called Wang tiles.

* Ing. Lukáš Zrůbek: Department of Mechanics, Faculty of Civil Engineering, CTU in Prague, Prague, Czech Republic, lukas.zrubek@fsv.cvut.cz

** Ing. Anna Kučerová, Ph.D.: Department of Mechanics, Faculty of Civil Engineering, CTU in Prague, Prague, Czech Republic, anicka@cml.fsv.cvut.cz

*** Ing. Jan Novák, Ph.D.: Experimental Centre, Faculty of Civil Engineering, CTU in Prague, Prague, Czech Republic, novakj@cml.fsv.cvut.cz

2. Wang tiles

The principle of the method of Wang tiles was introduced in the early sixties of the 20th century by Mr. Hao Wang (Wang. H., 1961; Wang H., 1965). It can be viewed as a game domino (Fig. 1a) where the goal is to place pieces side by side so they match in a number of dots on adjacent sides. The concept is nearly same for the Wang tiles, but in contrast to bilaterally coded rectangular domino pieces, the tiles are squares with four edge codes (Fig. 1b). Tiles are placed next to each other in cardinal directions according to matching codes on edges but cannot be rotated during the process. The created planar domain with no errors like incorrectly placed tiles or holes is called valid tiling.

Fig. 1: Principle of Wang tiles, a) domino game, b) Wang tiles.

2.1. Tile sets

As mentioned above, the Wang tiles compress the given structure into only a few small pieces, together called tile set, which holds the properties of the original structure. That means the tiles must be designed specifically.

One of the few approaches to design tiles is based on optimization of tile morphology according to statistical descriptors so the statistics of reconstructed microstructure corresponds to the original. But as shown in the paper from authors Novák J., Kučerová A., & Zeman J. (2012) with increasing pressure on optimization the tiles tends to become identical and the reconstructed microstructure show signs of periodicity. The second approach is called Automatic Tile Design (Cohen M. F. et al., 2003). Each tile is created as a cutout from a combination of four small samples of the original microstructure. This method is almost instantaneous if compared with first one which is much more time demanding because of the optimization. Another way of designing tiles is useful only for microstructures with individual particles that can be described by simple geometrical shapes. This method use the dynamics of each particle and by their movement and collisions the particles are distributed in tiles (Stránský J., 2014; Šedlbauer D. & Lepš M., 2013).

Whether we use any of these methods the created tiles must fulfill such conditions that we are able to create a stochastic valid tiling.

2.2. Stochastic tiling

When creating a tiling we start with a single tile. In the next step we place another tile (with one corresponding edge code) next to the first one in four possible directions. Let’s call these directions north (N), south (S), east (E) and west (W) (Fig. 2a). If we are not creating a long strip of tiles, we will at some point get in a situation where we need to place a tile in a position where two edge codes must correspond (Fig. 2b). To create the stochastic tiling and match the conditions of stochastic tiling algorithm (Cohen M. F. et al., 2003) we need at least two tiles that can be placed correctly in these corner positions. The smallest set that comply these requirements is set consisting of 8 tiles with two different vertical edge codes and two different horizontal edge codes. We call this set W8/2-2 and we use it in all following steps of our work.

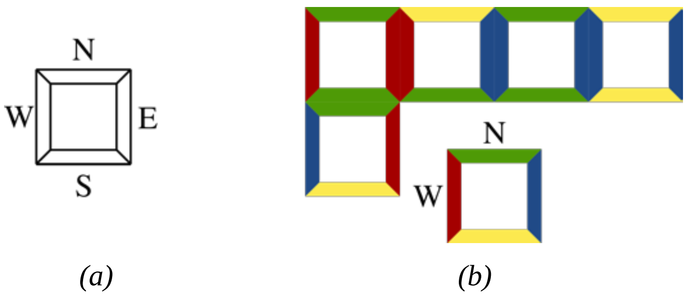

Fig. 2: Wang tiles edges and corner position,
a) cardinal directions and b) the NW corner position.

3. Synthesis of micromechanical fields

The Wang tiles method can be used in numerous ways. One of the first applications of the Wang tiles method was modeling of quasicrystals and generating naturally looking textures for computer graphic (Cohen M. F. et al., 2003). In material modeling, the method can be considered as a substitution of the PUC and SEPUC concepts or as a microstructure sensitive enrichment functions in Partition Unity (Melenk J. M. & Babuška I., 1996) and Hybrid finite element method (Freitas J.T. de., 1998).

In this paper, we focus on the analysis of microscale quantities as stresses, strains and displacements solved by finite element method (FEM). Simply said, the micromechanical response is evaluated on tiles instead of time-consuming evaluation of whole discretized domain and then, using the results from individual tiles, synthesized back. But because of the non-local character of mechanical quantities the grid of underlying tiles is clearly visible in the reconstructed mechanical field. The evaluated response of adjacent tiles does not coincide on edges and therefore, the micromechanical field is not continuous. That is because the mechanical response of each tile is affected by its surrounding tiles.

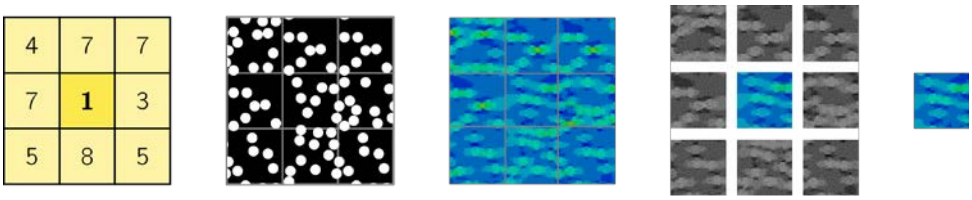

(a) (b) (c) (d) (e)

Fig. 3: Process of creating a tile from extended Wang tile set,
a) center tile with one layer of surrounding tiles, b) small synthesized domain,
c) solved small domain, d) cutting off included tiles and e) tile from extended Wang tile set.

One way to address this problem is to include the surrounding layers of tiles into the evaluation of the micromechanical response. For each tile from the tiling, we add the surrounding layers of tiles, in this case only one layer (Fig. 3a), synthesize small microstructural subdomain (Fig. 3b), solve the mechanical response for this subdomain (Fig. 3c) and cut off the included tiles from results (Fig. 3d). The outcome is the tile from so-called extended Wang tile set (Fig. 3e). After repeating this process for every tile from the tiling, the micromechanical field is synthesized using the tiles from the extended Wang tile set.

This technique gives us synthesized fields where the underlying grid is not so distinct and the jumps on edges of adjacent tiles are much smaller, as shown in paper Zrůbek, et al., (2012). However, this approach dramatically increases the number of small tasks that have to be evaluated. On top of that, as more than one layer of surrounding tiles can be included, the size m of the subdomain is increasing, which increase the evaluation time.

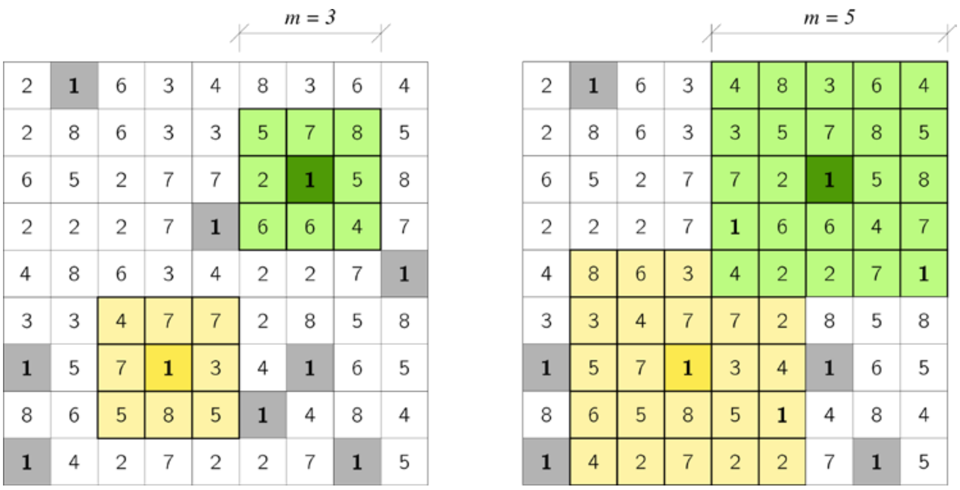

(a) (b)

Fig. 4: Included surrounding layers of tiles and size m *of the subdomain,*
a) single included layer (m=3), b) two included layers (m=5).

4. Future work and summary

At this stage, we are working on a sensitive analysis where we are focusing on two main topics. The first one is the evolution of error when including one, two or more layers of surrounding tiles. The error is obtained as difference between synthesized micromechanical field and reference solution. So far obtained results suggest that with increasing number of layers the error should have a decreasing tendency.

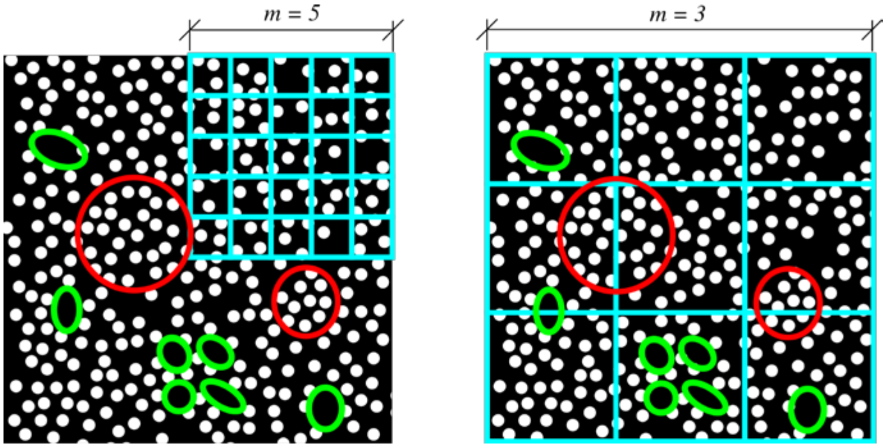

(a) *(b)*

Fig. 5: Characteristic microstructural lengths, tile size and subdomain size.

In the second topic, which is closely tied with the first one, we are trying to analyze how the characteristic microstructural lengths are affecting the optimal size of tiles. As shown in the Fig. 5, the microstructure contains some sort of clusters of empty matrix (green) and even clusters of particles (red). In the Fig. 5a the size of clusters is bigger than the size of tiles which means that the influence of these clusters may act over several tiles (cyan squares) and we need to extend subdomains with more layers of surrounding tiles. In Fig. 5b are tiles (cyan squares) bigger than clusters so a subdomain with only one layer extension of surrounding tiles is sufficient. But as larger the tiles are the more time-consuming is the evaluation of individual subdomains. Therefore, we are trying to find optimal size of tiles with an optimal number of subdomain layer extensions, to minimize the error and required computer time.

Acknowledgement

The authors gratefully acknowledge the financial support from the Grant Agency of the Czech Technical University in Prague, the grant No. SGS16/037/OHK1/1T/11 (L. Zrůbek, A. Kučerová and J. Novák).

References

Cohen M. F., Shade J., Hiller S. & Deussen O. (2003). Wang tiles for image and texture generation, volume 22(3). ACM.

Freitas J.T. de. (1998). Formulation of elastostatic hybrid-trefftz stress elements. Computer Methods in Applied Mechanics and Engineering, 153(1):127-151.

Melenk J. M. & Babuška I. (1996). The partition of unity finite element method: Basic theory and applications. Computer methods in applied mechanics and engineering, 139(1):289-314.

Novák J., Kučerová A., & Zeman J. (2012). Compressing random microstructures via stochastic wang tilings. Physical Review E, 86(4):040104.

Stránský J. (2014). Stochastic wang tiles generation using dem and yade software. Proceedings of the 5th Conference Nano and Macro Mechanics, pages 159-166.

Šedlbauer D. & Lepš M. (2013). Dynamic packing of stochastic wang tiling for heterogeneous material modelling. 20th International Conference on Computer Methods in Mechanics, pages 447-448.

Wang H. (1961) Proving theorems by pattern recognition-II. Bell system technical journal, 40(1):1-41.

Wang H. (1965) Games, logic and computers. Scientific American, 213(5), 98-106.

Zrůbek, L., Kruis J., Kučerová A. & Novák J. (2012) Complex microstructural enrichment functions based on extended wang tile sets. Proceedings of the 3rd Conference Nano and Macro Mechanics 2012, pages 263-270.

22nd International Conference
ENGINEERING MECHANICS 2016
Svratka, Czech Republic, 9 – 12 May 2016

INDSUSTRIAL ROBOT VISON SYSTEM FOR MOVING SPHERICAL ELEMENTS

J. Zwierzchowski*

Abstract: *In the application of industrial robots main and still increasing role play automation systems controlling their work. In order to enable the automation and a sense of intelligence we used vision systems. This paper describes industrial robot control software running on a PC. Information about the robot workspace is collected on by a video camera. The main robot task is to search items lying on the special table, and then move them to the place indicated by the operator. We developed appropriate objects searching algorithms for industrial robot. Those algorithms are based on object features (shape and color). We also describe communication between the robot, the computer and the camera. The proposed algorithms are implemented in C ++ (PC) and RAPID (robot) languages. The paper presents examples of using the application and tests system performance. It should also be noted that developed and described in the article system is based on very cheap to buy parts.*

Keywords: industrial robot, vision system, recognition, path generation

1. Introduction

The main task of the industrial robot used in this application is to move round parts, from an undefined position to a precise position determined by the system operator. This means that the place from which the element is taken must be indicated by software (Kovar, J et al., 2013), so the system will analyze the robot workspace and generate commands of its movements.

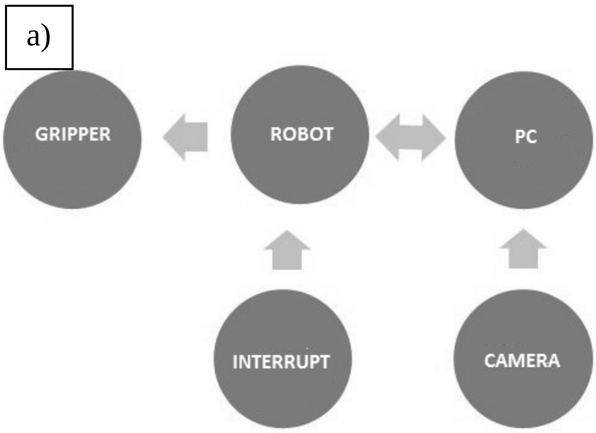

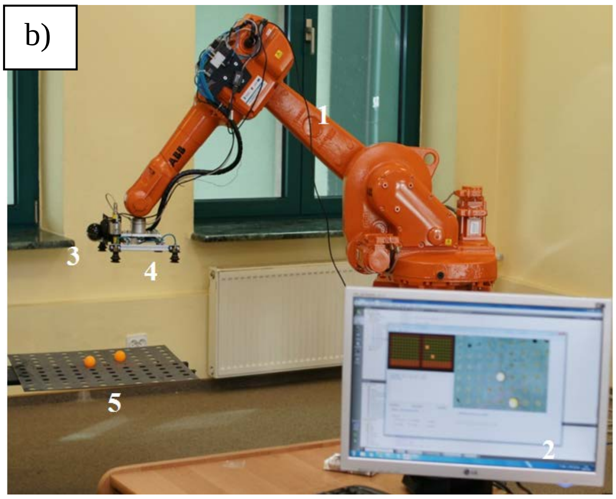

Fig. 1: a) System architecture for moving spherical elements; b) View of research station to move balls: (1) manipulator ABB IRB 1600, (2) managing application interface, (3) digital camera, (4) specially designed vacuum gripper, (5) work table with balls

The system architecture is shown in Figure 1a. Central point of this architecture is an industrial robot, which also is a communication server between robot and the PC application. In addition, the robot uses

* Dr inż. Jarosław Zwierzchowski, PhD.: Faculty of Mechatronics and Mechanical Engineering, Kielce University of Technology, Al. Tysiąclecia Państwa Polskiego 7; 25 – 314 Kielce; PL, j.zwierzchowski@tu.kielce.pl

digital input and output signals to control a vacuum gripper. There is also a digital camera, that works directly with the software installed on PC. Example of experimental station is shown in Figure1b.

Description of the system can be ordered and presented in several steps. The first step is to run the system. Then, after turning on, the robot sets its TCP (Tool Center Point) at the position, which is named *CameraHome*. This is one of the few points of the robot manipulator coordinates, which are permanently stored in the robot controller. This point is obtained in calibration process of the system. Locating at this point robot gripper ensures that captured image from the digital camera shows whole worktable, and Z coordinate of manipulator TCP is in the proper distance from one to table (Fig. 1b). This gives the possibility of calculating a correct diameters of spherical shapes, which ware found. At this point, the application communicates with the robot controller. The next step is to analyze the workspace. The application program searches appropriate elements using features as follows: color, shape and size of elements. These parameters are entered to the system by user. After identifying and recognizing the round objects, the control application takes action by sending the appropriate command to the industrial robot and then waits for the command performing movement. This order is appeared by system operator. The next step of the system is executing the robot program. After all activities related to transfer elements, the robot returns to the position *CameraHome* and again waits for orders coming from the operator.

2. Functional schema of the system and robot communication

In order to test system correctness of detecting and determining spherical objects position coordinates we designed and made a robot worktable. As can be seen in the drawing (Figure 2a) the worktable has holes, which are made in specific places (in the figure marked only selected holes). This approach greatly simplifies determining the position of an object in the shape of ball, inserted into the hole on the worktable. The figure (see Figure 2a) also shows the place of attached the Cartesian coordinate system $X_S Y_S Z_S$ onto worktable.

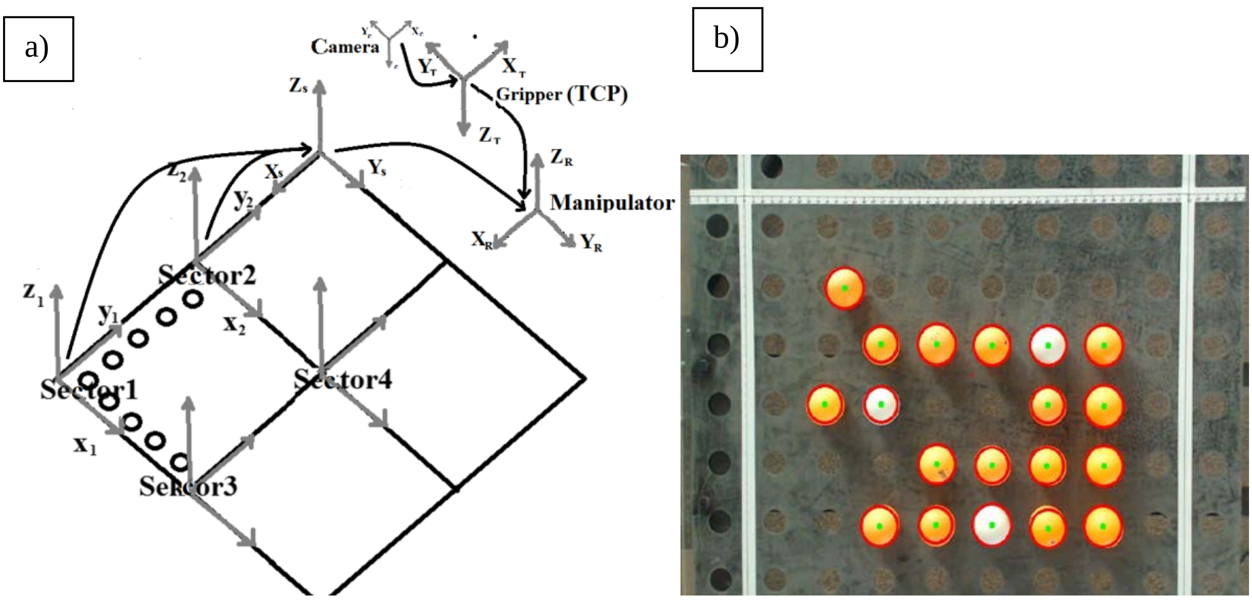

Fig. 2: a) Distribution of sectors onto the tablework. Gray marked the coordinate systems of each sector: worktable $X_S Y_S Z_S$, manipulator $X_R Y_R Z_R$, gripper $X_T Y_T Z_T$, camera $X_C Y_C Z_C$, b) The result of the Hough algorithm (a fragment of the worktable); (green) centers of detected objects, (red) detected round shapes

In described system, it is assumed that the gripper can "take away" spherical element only from the designated places. It means that there are cut grid holes in the table (see Fig. 2a). For simplicity, it is assumed that the table has N holes along both X_S and Y_S axes. Denote

$$p(pozX, pozY), \tag{1}$$

where:

$$pozX = 0,1,2 \ldots N-1, \; pozY = 0,1,2 \ldots N-1 \tag{2}$$

the essential points of the grid of holes. These points can be interpreted as the specific number from holes in the table. The actual position p_s in regard to coordinate system $X_sY_sZ_s$ (worktable) we can obtain form equation

$$p_s(x,y) = p[(pozX + 1) \cdot f, (pozY + 1) \cdot f], \tag{3}$$

where f is constant distance value between the centers of the holes in the worktable, expressed in mm.

The table is located in the working space of the manipulator in this manner, that it is impossible to set robot in a singular configuration. The robot is equipped with vacuum gripper. Initially, the gripper had only one sucker directly attached to the manipulator wrist. This approach meant that the manipulator had small movement range and a fragment of the table was located outside its working area. In order to eliminate this drawback, we designed and built a new gripper, increasing the manipulator movement range. Currently, the gripper is made from aluminum profiles arranged in the shape of a rectangle. At each of the rectangle corners there is mounted sucker. Robot controller controls each of the sucker separately.

The worktable is divided into four sectors and each sector has 25 holes (5 x 5 grid). The origin of each sector is called base position. Those base positions are permanently stored in the structure of the robot program. To each sector is assigned exact sucker.

Having the scene describe, now we should think which sucker would be move and where. Now new real points coordinates p_b^i are calculated related to coordinate system of sector base position i, where $i = 1,2,3,4$, and i is obtained from algorithm as follows:

$$i = \begin{cases} 1, & pozX \bmod b + pozY \bmod b = 0 \\ 2, & pozX \bmod b > pozY \bmod b \\ 3, & pozX \bmod b < pozY \bmod b \\ 4, & pozX \bmod b + pozY \bmod b = 2 \end{cases} . \tag{4}$$

The value i also indicate the number of sucker, which system should use during object movement. Real points coordinates related to sector i coordinate system can be calculated from equation

$$p_b^i(x,y) = p\left[(d_x + 1) \cdot f, \left(d_y + 1\right) \cdot f\right], \tag{5}$$

where

$$d_{x,y} = \frac{pozX, pozY}{b} \tag{6}$$

and f is constant distance between the centres of the holes in the worktable, d_x, d_y are hole coordinates (numbers) refer to i base coordinates system, $b = \frac{N}{2}$ and $b, d_{x,y} \in \mathrm{C}^+$.

3. Implemented vision system

For the purpose of the system was developed and implemented a simple algorithm to recognize objects, which projection on the worktable has a circular shape. The following figure (Fig. 3) shows subsiquent steps in the proposed image processing system. At the beginning propose system recognizes color. User system can indicate, which color is important to move and which color the system should avoid. After that, recognition algorithm changes original capture image into grayscale image. The next very important step is to perform edge detection procedure. For this task we use Canny transform (Canny, J., 1986). Then it is performed Hough (Pedersen, S. & Just, K., 2007) transform for circles. After this operation we have the list of circles center points and its radii obtained. Those points are transform form image coordinates system to manipulator coordinates system. Having all information about detected round objects position the system can generate moving instruction and send them to robot controller.

Figure 2 shows fragment of the worktable with detected table tennis balls. The manipulator transfers only orange balls. In figure 3 there are shown all used sequences in image processing task.

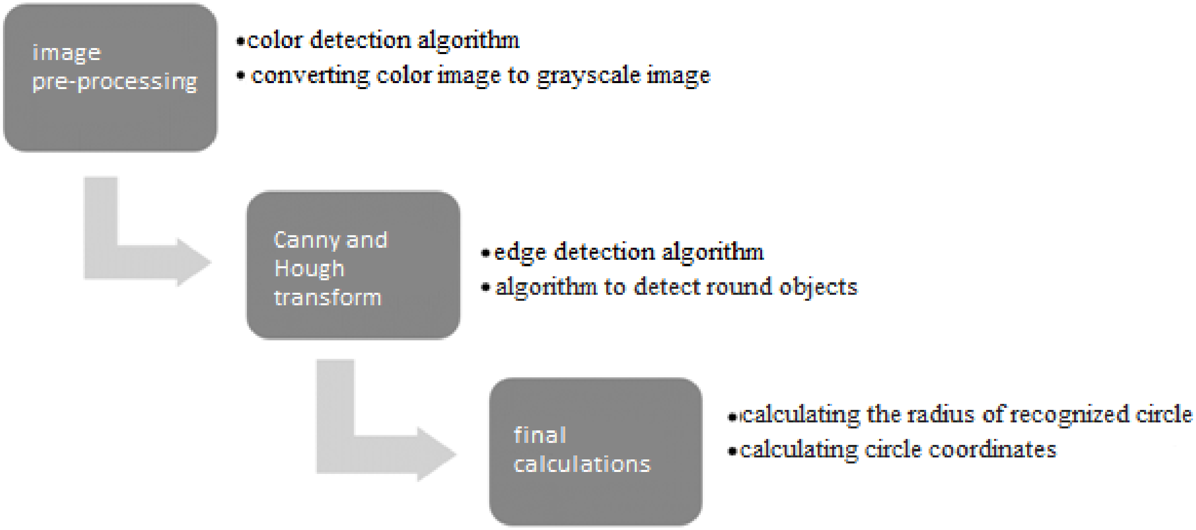

Fig. 3: Next steps in image processing used in designed system application.

4. Conclusions

We conducted tests using industrial robot ABB symbol IRB1600 with six degrees of freedom. The robot was equipped with a vacuum gripper and a digital camera Logitech symbol 920C. The camera sent the image to the computer at a resolution of 1920 x1080 pixels. In manipulator workspace was mounted worktable, which was a plate with cut-out holes spaced 60 mm (the centers of these holes), each hole was 18 mm in diameter. These 100 holes ware arranged in 10 by 10 grid. The tests had been prepared to use table tennis balls, each ball was 40 mm in diameter. We did 20 trials series. Every attempt was made at 12 the same set of balls located on the worktable. In each series there were orange balls (10 pieces), which robot had to move and white balls (2 pieces), which robot had to ignore.

The system software correctly rejected the white ball. Total recognition rate calculated as the average value of all the series, was 0.783. We can conclude that the system works properly, but in the future in order to raise this coefficient value we will install illuminator and add filtering algorithm (Janecki et al., 2015). We will test this system with delta robot (Łaski et al., 2015).

We managed to integrate an industrial robot with the application running on a PC, using the protocol TCP/IP. All programs were written in the RAPID ABB robot and C++ languages with OpenCV and Qt library. We would like also mention, that described system is primarily focused on testing communication reliability of all components and the correctness of the manipulator static paths generation.

Described system is an attempt to show program, which can be used for example in sorting or palletizing industry applications.

Creating system can be regarded as a testing platform for further research on machine vision in robotics. There can be also testing new algorithms like image analysis, communication, scheduling, artificial intelligence.

References

Canny, J. (1986) A computational approach to edge detection. Pattern Analysis and Machine Intelligence, IEEE Transactions on: pp. 679-698

Janecki, D. & Zwierzchowski, J. & Cedro, L. (2015) Separation of non-periodic and periodic 2D profile features using B-Spline functions. Metrology and Measurement Systems t: 22, issue: 2, pp: 289-302

Łaski, P. & Takosoglu, J. & Błasiak, S. (2015) Design of a 3-DOF tripod electro-pneumatic parallel manipulator. Robotics and Autonomous System issue: 72, pp: 59-70

Pedersen, S. & Just, K. (2007) Circular Hough transform. Aalborg University, Vision, Graphics, and Interactive Systems.

Kovar, J.; Andrs, O.; Dalecky, F. (2013) Using of Hough Transform for Automatic Robot Sorting System 19th International Conference on Soft Computing MENDEL 2013 pp: 375-378

22nd International Conference
ENGINEERING MECHANICS 2016
Svratka, Czech Republic, 9 – 12 May 2016

FLEXURAL BUCKLING AND BENDING INTERACTION OF STAINLESS STEEL MEMBERS

B. Židlický*, M. Jandera**, D. Syamsuddin***

Abstract: *There are several methods to cover the interaction of compression and bending for slender steel members. Usually an interaction formula is given and more recently also the general method can be used in terms of more advanced global analysis. In respect to stainless steel, the structural design standards have been developed largely based on the carbon steel standards. The current formula for interaction of axial force and bending moment given by EN 1993-1-4 was derived on limited results available and there is no limitation for the general method in the standard despite the non-linear stress-strain behaviour of stainless steels. Therefore the main aim of the paper is to show and compare numerical results for stainless steel beam-columns with existing Eurocode, the general method and some formulae proposed by other researchers taken from experimental and parametric studies. Their possible applicability will be shown as well as the way for further development. The conclusions may be used for other non-linear materials too, such as aluminium alloys, to some extent.*

Keywords: Stainless steel, Beam-column, General method, Non-linear stress-strain diagram.

1. Current methods of beam-column behavior description

The whole paper is limited to the interaction between major axis bending and axial compression of member subjected to major axis flexural buckling. So, the members are laterally and torsionally restrained along their length. Together with the Eurocode for stainless steels EN 1993-1-4 (2006), the current carbon steel code EN 1993-1-1 (2005) considering both methods (Boissonnade, Jaspart, Muzeau & Villett, 2004; Greiner & Lindner, 2006) for members subjected to both bending and compression is compared.

The main problem of stainless steel code interaction factor is the neglect of bending moment distribution along the member and material hardening. Also the boundary values of interaction factor may be limiting for members with dominant moment. So, the design approach given by EN 1993-1-4 (2006) is over conservative.

Therefore several research groups made experiments and numerical studies to develop more accurate interaction formula. All groups were focused on the accurate determination of the interaction factor:

- Salmi and Talja made experiments (Salmi & Talja, 1995; Talja, 1997) for hollow and open sections beam-columns for austenitic and duplex steel and a slight modification of ENV 1993-1-1 (1992) was suggested.
- An extensive experimental and numerical study was published by Gardner, Rossi, Young & Zhao (2015) for section interaction. It shows the effect of significant strain hardening of stainless steel for section resistance.
- The most general proposal was published by Lopes, Real & Silva (2009) that is also derived from ENV 1993-1-1 (2005).

* Ing. Břetislav Židlicky: Faculty of Civil Engineering, Czech Technical University in Prague, Thákurova 7; 166 29, Prague 6; CZ, bretislav.zidlicky@fsv.cvut.cz

** Ing. Michal Jandera, Ph.D.: Faculty of Civil Engineering, Czech Technical University in Prague, Thákurova 7; 166 29, Prague 6; CZ, michal.jandera@fsv.cvut.cz

*** Ing. Denny Syamsuddin: Faculty of Civil Engineering, Czech Technical University in Prague, Thákurova 7; 166 29, Prague 6; CZ

- Other numerical research by Greiner & Kettler (2008) was published for stocky sections only. Additionally the EN 1999-1-1 (2007) design rules for aluminium alloys are compared. It was believed that these rules developed for non-linear stress-strain diagram may show reasonable results as well.

2. Shell FE model parametric study

Firstly, a FE (finite element) model of open I sections and rectangular / square hollow sections (RHS / SHS) made in software Abaqus (used GMNIA, geometrically and materially non-linear analysis with initial imperfections) was validated. For validation were used the experiments from Salmi & Talja in Finland and the prediction of the FE model was reasonably accurate (Jandera & Syamsuddin, 2014), therefore it was accepted for subsequent parametric study.

The parametric study was made using three profiles representing different section slenderness and two section types. Three stainless steel grades (austenitic, ferritic and duplex) were considered and the material was defined by one stage Ramberg-Osgood stress-strain diagram.

The comparison between the design formulae for all selected methods and numerically established interaction factors is shown in Tab. 1.

- The EN 1993-1-4 (2006) provision showed good but most conservative results.
- The EN 1993-1-1 (2005) methods showed lower scatter but most of the results were on the unsafe side. A similar conclusion was found for ENV 1993-1-1 (1992) approach.
- Salmi & Talja (1995) expression indicated slightly better results that were on safe side. However, the results are still much conservative, the method may be perhaps the most suitable.
- The procedure used in EN 1999-1-1 (2009) for aluminium alloy structures and method published by Greiner & Kettler (2008) showed good value in average, but were very scattered for triangular and bi-triangular moment distribution.
- Lopes, Real & Silva (2009) proposal was found very unsafe, nevertheless the method with little modification (1) to (3) gives much better agreement (Fig. 1), but it may be still unsafe especially for non-uniform moment distribution. All the symbols used in the formulas are according to EN 1993-1-4.

$$k_y = 1.2 - \frac{1.2\,\mu_y N_{Ed}}{N_{b,Rd,y}} \tag{1}$$

$$\mu_y = \left(0.97\,\beta_{M,y} - 2.11\right)\bar{\lambda}_y + 0.44\,\beta_{M,y} + 0.09, \text{if } \bar{\lambda}_y \leq 0.3 \text{ then } \mu_y \leq 1.0 \text{ else } \mu_y \leq 0.9 \tag{2}$$

$$\beta_{M.y} = 1.8 - 0.7\psi \tag{3}$$

Tab. 1: Comparison between the design formulae and the numerical results

	EN 1993-1-4	EN 1993-1-1 Method 2	EN 1993-1-1 Method 1	ENV 1993-1-1	Salmi-Talja	Lopes-Real-Silva	Greiner-Kettler	Aluminium
	all cases considered							
$k_y/k_{y.FEM}$	1.235	0.969	0.925	0.997	1.129	0.828	1.053	0.966
Standard dev.	1.012	0.472	0.315	0.215	0.282	0.140	0.937	0.524
	uniform moment only							
$k_y/k_{y.FEM}$	1.015	0.885	0.878	1.001	1.162	0.834	0.872	0.845
Standard dev.	0.180	0.171	0.158	0.218	0.286	0.131	0.193	0.153

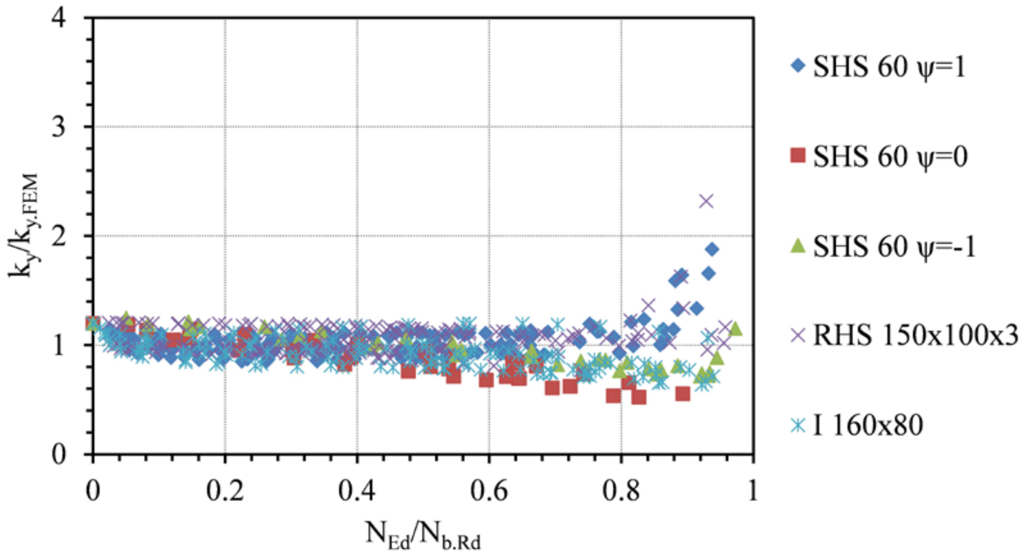

Fig. 1: Comparison for the modified method published originally by Lopes, Real & Silva

For further possible modifications of the EN 1993-1-4 (2006), more numerical results would be needed. Even more important would be to carry out more beam-column tests mostly for the case of small bending moments.

3. The general method of EN 1993-1-1

The general method is an alternative method of EN 1993-1-1 (2005) based on geometrically non-linear analysis of structure with imperfection (GNIA). The comparison was made for four members modelled in software Abaqus again. In formula the initial equivalent geometric imperfection amplitudes were calculated according to the buckling curve and for the section verification, the moment including the second order effect was used.

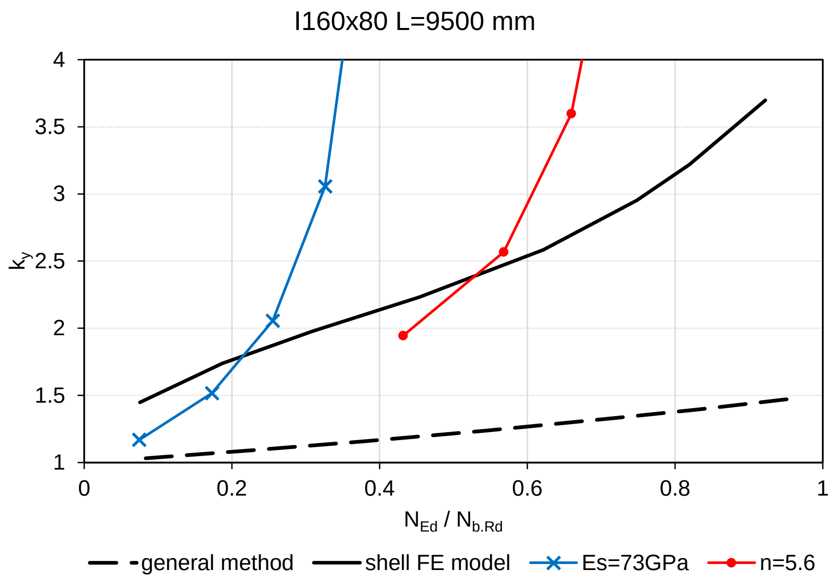

Fig. 2: Comparison of FE shell model of I 160x80 and the general method considering various Elasticity moduli

The comparison showed that the general method underestimates cases where the global buckling is almost negligible. Neglecting of the material non-linearity caused lower increase in the bending moment and is therefore generally unsafe. So, the stainless steel member is losing stiffness progressively with the load increase. For column, this is compensated by the equivalent geometric imperfection. However, it is not able to cover the effect of decreased stiffness caused e.g. by bending moment load. Therefore, the stiffness in the following beam models was considered as follows (the comparison is shown in Fig. 2):

- The secant elasticity modulus for stress level equal to the yield strength was tested.
- Non-linear stress-strain diagram was represented by the Ramberg-Osgood diagram but with hardening exponent $n = 5,6$.

Both modifications gave very conservative results. The secant modulus clearly underestimates the initial stage of the loading as well as the fibers and the sections which are loaded lower than the critical section. The beam model considering the non-linear diagram also underestimates the resistance. This is because the effect of the non-linearity on column buckling is once present in the buckling curve respectively in the equivalent geometric imperfections. The general method is recently not suitable for material described by the non-linear stress-strain diagram.

4. Conclusion

The main objective of this paper is to study relevant interaction factors for stainless steel beam-columns. The comparison showed that the current design code for stainless steel is over conservative, other published proposals are slightly more accurate but some of them are on the unsafe side and all of them still do not fit the real behavior of beam-columns accurately.

General method was compared too. It was shown that using of the initial Elasticity modulus underestimates the resistance of slender members. This may be compensated by reduction of the Elasticity modulus or by using the non-linear stress strain diagram (GMNIA) that is the most suitable method to be used if the equivalent geometric imperfections would be reduced.

References

EN 1993-1-4 (2006) Eurocode 3: Design of steel structures - Part 1-4: General rules -Supplementary rules for stainless steels, CEN, Brussel.

EN 1993-1-1 (2005) Eurocode 3: Design of steel structures - Part 1-1: General rules and rules for buildings, CEN, Brussels.

Boissonnade, N., Jaspart, J.P., Muzeau, J.P., Villett, M. (2004) New interaction formula for beam-columns in Eurocode 3: The French-Belgian approach. Journal of Constructional Steel Research. vol. 60, pp. 421–431.

Greiner, R., Lindner, J. (2006) Interaction formulae for members subjected to bending and axial compression in EUROCODE 3 - the Method 2 approach. Journal of Constructional Steel Research. vol. 62, pp. 757–770.

Salmi A., Talja, P. (1995) Design of stainless steel RHS beams, columns and beam-columns. Research Note 1619, VTT Building Technology, Finland.

Talja, A. (1997) Test report on welded I and CHS beams, columns and beam-columns. Report to ECSC. VTT Building Technology, Finland.

ENV 1993-1-1 (1992) Eurocode 3: Design of steel structures Part 1.1 General rules and rules for buildings, CEN, Brussels.

Gardner, L., Rossi, B., Young, B., Zhao, O. (2015) Behaviour of structural stainless steel cross-sections under combined loading – Part I: Experimental study. Engineering Structures. vol. 89, pp. 236-246.

Gardner, L., Rossi, B., Young, B., Zhao, O. (2015) Behaviour of structural stainless steel cross-sections under combined loading – Part II: Numerical modelling and design approach. Engineering Structures. vol. 89, pp. 247-259.

Lopes, N., Vila Real, P., da Silva, L.S. (2009) Stainless steel beam-columns interaction curves with and without lateral torsional buckling. 7th EUROMECH Solid Mechanics Conference, Lisbon, 17 p.

Greiner, R., Kettler, M. (2008) Interaction of bending and axial compression of stainless steel members. Journal of Constructional Steel Research, vol. 64, pp. 1217-1224.

EN 1999-1-1 (2007) Eurocode 9: Design of Aluminium structures, Part 1-1: General structural rules. CEN, Brussels.

Jandera, M., Syamsuddin, D. (2014) Interaction Formula for Stainless Steel Beam-Columns, Eurosteel 2014, Naples, pp. 145-146.

22nd International Conference
ENGINEERING MECHANICS 2016
Svratka, Czech Republic, 9 – 12 May 2016

COLD-FORMING EFFECT ON MECHANICAL PROPERTIES OF STAINLESS STEEL SECTION – MATERIAL TESTING

B. Židlický*, J. Mařík, M. Jandera*****

Abstract: *An experimental investigation of the cold-forming effect on mechanical properties of several grades of stainless steel is presented. The research is focused on basic grades of stainless steel, namely austenitic (1.4404), ferritic (1.4003), duplex (1.4462) and lean-duplex (1.4162) as correctly described cold-forming effect implies a possible strong increase of resistance. The test programme includes set of coupon tests of the material with various levels of induced plastic deformation. Measurement results serve to further modelling of stress-strain response and predicting of mechanical properties of cold-formed stainless steel. The general properties (0.2% proof tensile strength, ultimate tensile strength, ductility and nonlinearity) of cold-formed material were evaluated as well as values of the unformed material. In addition, other material properties were also described, such as the degree of stress-strain diagram non-linearity or anisotropy, modulus of elasticity of cold-formed or cold-worked stainless steel etc.*

Keywords: Cold-forming, Stainless steel, Stress-strain diagram, 0.2% proof strength, Mechanical properties.

1. Introduction

In structural design of stainless steel elements, in comparison with common carbon steel, the different material behaviour often demands more sophisticated design and offer possibilities how to prosper from specific material properties. The general investigated benefit for all stainless steel grades is the significant increase of 0.2% proof strength due to the cold-working within a fabrication process of structural elements. In the past, several proposals were developed (Van der Berg, Van der Merwe, 1992; Cruise, Gardner 2008; Rossi, Jaspart, 2010). Nevertheless, the design standards usually require tests for proving the increased strength properties and none of the proposal was established in the design rules with an exception of the British National Annex to EN 1993-1-4 using the method of Cruise and Gardner (2008). Generally, the proposed material models use various parameters and give different material strength. Some of them show good agreement in the range of strain expected in load-bearing structures. Other ones are in good agreement at higher strains. Results obtained from the recent investigations (Afshan et al. 2013; Rossi et al. 2013) demonstrate also different values for basic material characteristics, especially for modulus of elasticity, 0.2% proof strength, ultimate tensile strength or ductility. Especially, stainless steel in cold worked conditions can exhibit material properties with high scatter of the values among the steel grades and products. Current and extensive research of (Afshan et al. 2013) shows slightly different hardening exponent n depending on a grade of stainless steel, i.e. austenitic, ferritic, and duplex as opposed to recent European design standard. The same paper recommends also a lower modulus of elasticity for design purposes which may be assumed for the global analysis and in determining the resistances of members. Thus it is important to analyse more experimental data to establish generally valid relations for enhanced strength of cold-formed stainless steel.

* Ing. Břetislav Židlický.: Department of Steel and Timber Structures, Faculty of Civil Engineering, Czech Technical University in Prague; Thákurova 7, 166 29 Prague, CZ; bretislav.zidlicky@fsv.cvut.cz

** Ing. Jan Mařík.: Department of Steel and Timber Structures, Faculty of Civil Engineering, Czech Technical University in Prague; Thákurova 7, 166 29 Prague, CZ; jan.marik@fsv.cvut.cz

*** Ing. Michal Jandera, PhD.: Department of Steel and Timber Structures, Faculty of Civil Engineering, Czech Technical University in Prague; Thákurova 7, 166 29 Prague, CZ; michal.jandera@fsv.cvut.cz

This article presents test results of coupons made of a cold rolled sheet from the austenitic (1.4404), ferritic (1.4003), duplex (1.4462) and lean-duplex (1.4162) grade. Apart from a classic tensile test, coupon tests were also performed on cold-worked specimens respecting different behaviour parallel and transverse to the rolling directions, either parallel or transverse to the previous plastic strain induction. The results of the research might lead to more accurate material characteristics and material models of a cold-formed material appropriate for FEM modelling and structure design.

2. Experimental programme

The section describes set of experiments executed at the Czech Technical University in Prague. The testing programme is aimed on the establishment of stress-strain diagram of a cold-formed stainless steel section made of all kinds of stainless steel grades, i.e. ferritic (1.4003), austenitic (1.4404), duplex (1.4462) and a relatively new lean-duplex grade (1.4162). The project involved especially tensile coupon tests. All specimens were prepared of a cold-rolled steel sheet of 1.5 mm respectively 2.0 mm thickness. First of all, material tensile tests of all grades were performed, both for direction transverse and parallel to the rolling direction. Strain was measured by foil strain gauges attached to both sides of the specimens (see Fig. 1) for the best accuracy of the initial part of the stress-strain diagram and by an extensometer for higher strain ranges.

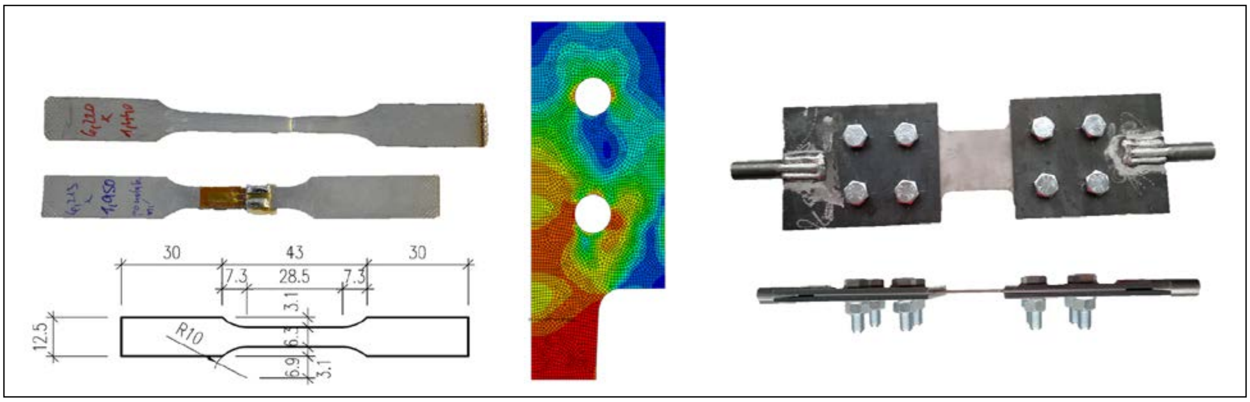

Fig. 1: Coupon before and after a tensile test including its initial geometry; stress distribution in the numerical model (quarter of the sample – symmetric conditions) and the test device with stainless steel plate attached.

The next step included tensile plastic deformation induction on the coupons or a special wide specimen from which the coupons were subsequently machined. A device able to induce uniform plastic deformation through the whole width of the wide specimen was used. That provides the desired (uniform) strain distribution in the area which the new coupon was created from (neck of the specimen) as it is shown in Fig. 2. The geometry of the specimen was based on a simple Abaqus 2D model presented as well. The device consists of 2 parts in which the sample was connected by 4 bolts M16 of 8.8 quality. There were two shear planes (represented by two plates and the sample) to minimalize the eccentricity in the connection. The device was able to clamp into a testing machine by a round bar which eliminated eventual moment influence. The middle part of the specimen served for extensometer set with gauge length of 50 mm at maximum. The device allowed load of the specimen over 100 kN.

Levels of the induced plastic strain varied significantly. Plastic strain equal to 1%, 3%, 5%, 10%, 15% and for other than ferritic grades also 20% or 50% (austenitic grade only) was used. From these “cold-worked” specimens where the plastic strain was induced, coupons were machined and tested. The cold-worked specimens are shown in Fig. 3, as well as the directions of the forming and the subsequent testing. The experimental set consisted of 5 or 6 specimens with various level of the induced plastic strain. The set was tested for each grade, in respect to the sheet rolling direction and in respect to the induced plastic strain direction. Coupon tests were executed in about four weeks after the plastic forming. In total, 92 coupons were prepared and tested in accordance with the recent European standard (EN ISO 6892-1:2009).

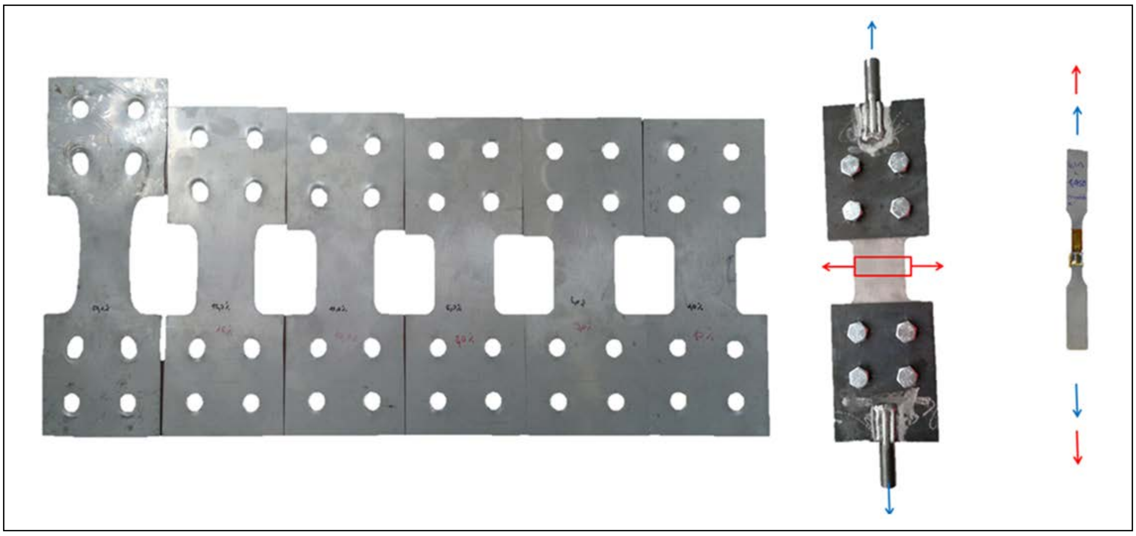

Fig. 2: Specimens after the plastic strain induced transversally (left) and along the tensile test direction (right).

All tests were performed using the MTS Qtest 100 kN electromechanical testing machine with all data recorded at 5 Hz using the SPIDER data acquisition system with CATMAN32 data acquisition software. The tests were strain controlled. The accepted strain rate for testing up to 1.5% strain was 0.007% s^{-1} and followed by 0.2% s^{-1} until fracture. The value of 1.5% strain ensured the lower stress rate for both 0.2% and 1.0% proof strength measurements. Both values are often used for stress-strain diagram description.

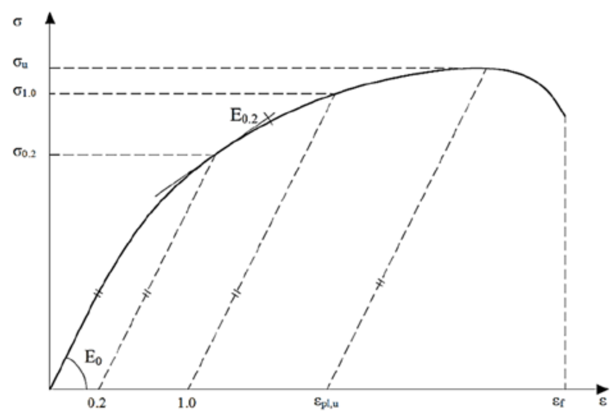

$$\varepsilon = \frac{\sigma}{E_0} + 0.002\left(\frac{\sigma}{\sigma_{0.2}}\right)^n \quad (1)$$

$$n = \frac{\ln(\varepsilon_{p2}/\varepsilon_{p1})}{\ln(\sigma_2/\sigma_1)} = \frac{\ln(20)}{\ln(\sigma_{0.2}/\sigma_{0.01})} \quad (2)$$

Fig. 3: Stress-strain behaviour description; Ramberg-Osgood model for a nonlinear metallic material.

3. Results and discussions

Figure 4 shows stress-strain diagrams for coupons of selected grades tested in the rolling direction. Stress-strain behaviour of the coupons tested transversally to the rolling direction was almost identical (as well as for other grades).

In contrast to the 0.2% proof strength increase, ultimate tensile strength increase is significant only when the engineering values are compared. For the true values of the ultimate strength, the “cold-formed” samples showed no important increase. Significant decrease of ductility and Ramberg-Osgood nonlinearity parameter *n* is typical for all grades.

Ductility decrease is significant for all investigated grades. The largest decrease is exhibited by ferritic grade in contrast to the austenitic grade with the smallest effect of cold-working affecting the ductility. Values for duplex and lean duplex grade lie within the area bounded by the ferritic grade from the bottom and the austenitic grade from the top. The fact reflects the ductility of the virgin material. Ferritic grades exhibit the lowest values, following by duplex and lean duplex grades. Austenitic grades are well-known for their ability to be cold-formed due to high ductility in general and they exhibit the highest ductility among all tested grades.

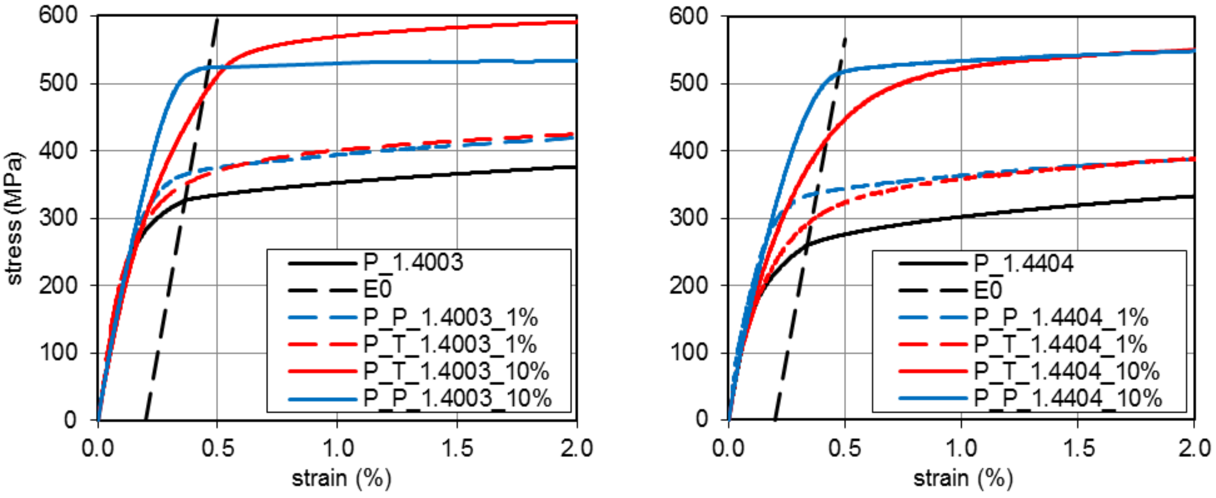

Fig. 4: Stress-strain diagram of selected 1.4003 and 1.4404 samples manufactured parallel to the rolling direction (P) with different direction and level of plastic strain induction (P – parallel, T –transverse).

4. Conclusions

The testing programme on 116 coupons was performed and its results presented. The main material characteristics and stress-strain curves were shown. Values of non-linearity parameters *n*, 0.2% proof strength, 1.0% proof strength, ultimate tensile strength, ductility and modulus of elasticity were evaluated and may be used for further research on cold-formed sections. The presented strength increase shows that the influence of cold forming is important not just for the austenitic grades, but also for the other stainless steel grades. However for the ferritic grade, the ductility could be limiting. After the plastic strain induction in a specimen corresponding to the level of strains induced during section cold-forming (in corners typically exceeding ten percent), the 0.2 proof strength increase typically reaches 30 to 90 %. Ultimate strength increase, when the true value is calculated, is almost none. The higher the plastic strain induced in the specimen the higher the values of Ramberg-Osgood nonlinearity parameter and the lower ductility. Material parameters also differ in respect to the forming direction and the anisotropy is evident.

Acknowledgement

This work was supported by the university grant SGS14/125/OHK1/2T/11 and it is gratefully acknowledged.

References

Afshan, S.; Rossi, B.; Gardner, L. (2013) Strength enhancements in cold-formed structural sections - Part I: Material testing, Journal of Constructional Steel Research 83: pp. 177-188.

Cruise, R. B.; Gardner, L. (2008) Strength enhancements induced during cold forming of stainless steel sections, Journal of Constructional Steel Research 64: pp. 1310–1316.

EN ISO 6892-1: (2009) Metallic materials - Tensile testing - Part 1: Method of test at room temperature. European Standard.

Rossi, B.; Afshan, S.; Gardner, L. (2013) Strength enhancements in cold-formed structural sections - Part II: Predictive models". Journal of Constructional Steel Research 83:pp. 189-196.

Rossi B.; Jaspart J. P. (2010) Enhanced proof strength after cold process of fabrication of non-linear metallic profiles—Comparison of two predictive models for hollow sections. Tubular Structures XIII: pp. 397–402.

Van den Berg, G. J.; Van der Merwe, P. (1992) Prediction of corner mechanical properties for stainless steels due to cold forming, in Proceedings of the eleventh international specialty conference on cold-formed steel structures: pp. 571–586.

Author Index

A

B

C

Č

D

E

F

G

H

CH

J

K

L

M

N

O

P

R

Ř

S

Š